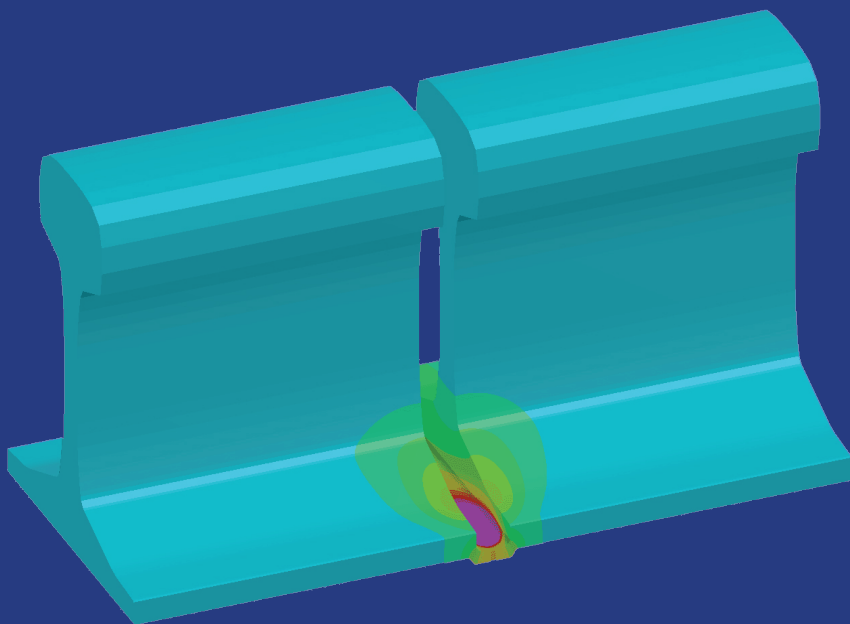


---

# MATHEMATICAL MODELLING OF WELD PHENOMENA 12

---

Edited by  
C. Sommitsch  
N. Enzinger  
P. Mayr



# **MATHEMATICAL MODELLING OF WELD PHENOMENA 12**



The delegates of the 12<sup>th</sup> International Seminar 'Numerical Analysis of Weldability' held from 23 - 26 September 2018 at Schloss Seggau near Graz, Austria

# MATHEMATICAL MODELLING OF WELD PHENOMENA 12

Selected peer reviewed papers from the  
**12<sup>th</sup> International Seminar**  
**Numerical Analysis of Weldability**  
September 23 – 26, 2018  
Graz - Schloss Seggau - Austria

Edited by

**Christof Sommitsch**

Institute of Materials Science, Joining and Forming  
Graz University of Technology

**Norbert Enzinger**

Institute of Materials Science, Joining and Forming  
Graz University of Technology

**Peter Mayr**

Institute of Joining and Assembly  
Technische Universität Chemnitz



©2019 Verlag der Technischen Universität Graz  
[www.tugraz-verlag.at](http://www.tugraz-verlag.at)

ISSN 2410-0544  
ISBN (print) 978-3-85125-615-4  
ISBN (e-book) 978-3-85125-616-1  
DOI 10.3217/978-3-85125-615-4



This work is licensed under a Creative Commons Attribution 4.0  
CC BY International License  
<https://creativecommons.org/licenses/by/4.0/>

Production Secretary & Typeset

**Bettina Schreiner-Föb1**

Institute of Materials Science, Joining and Forming  
Graz University of Technology

Layout creation assistance

**Lisa Minkowitz and Maurice Tödling**

Institute of Materials Science, Joining and Forming  
Graz University of Technology

Printed & bound

Koralpendruckerei, Deutschlandsberg, Austria  
[www.koralpendruckerei.at](http://www.koralpendruckerei.at)

## Table of Contents

<b>Introduction</b>	
<b>Introduction</b>	<b>1</b>
<b>I Arc Welding, Melt Pool and Solidification</b>	
<b>Complete 3D heat and fluid flow modeling of keyhole laser welding and methods to reduce calculation times</b>	<b>5</b>
<i>M. Courtois, M. Carin, P. Le Masson and S. Gaie</i>	
<b>Computational prediction of penetration shapes in MIG welding of practical aluminum alloy joints</b>	<b>17</b>
<i>H. Serizawa, S. Sato and F. Miyasaka</i>	
<b>Numerical investigation of the influence of welding parameters on the weld pool dynamics and the distribution of second phase particles</b>	<b>27</b>
<i>R. Kaboli, M. Massoudi Farid, R. Kramer, G. Ertugrul and P. Mayr</i>	
<b>A fine modification of the double ellipsoid heat source</b>	<b>39</b>
<i>O. Mokrov, M. Simon, A. Schiebahn and U. Reisgen</i>	
<b>Validation of heat source model for metal active gas welding</b>	<b>53</b>
<i>D. Kollár and B. Kövesdi</i>	
<b>A study of coupled influence of evaporation and fluid flow inside a weld pool on welded seam formation in GMAW</b>	<b>81</b>
<i>O. Mokrov, O. Lisnyi, M. Simon, A. Schiebahn and U. Reisgen</i>	
<b>II Microstructure Modelling in WM and HAZ</b>	
<b>Numerical simulation of ferrite/austenite phase fraction in multipass welds of duplex stainless steels</b>	<b>93</b>
<i>T. Ogura, T. Matsumura, L. Yu, D. C. Kim, H. Inoue, Y. Oikawa and K. Saida</i>	
<b>The influence of chemistry inhomogeneity on microstructure development and residual stress</b>	<b>125</b>
<i>J. Ni, J. Vande Voorde, J. Antonissen and M. A. Wahab</i>	
<b>Kinetic monte carlo simulation of pulse Cu30Ni bead on plate</b>	<b>139</b>
<i>A. Chiocca, F. Soulie, F. Deschaux-Beaume, J. Mitchell and C. Bordreuil</i>	

<b>Multi-pass ferritic steel weld modelling: phase transformation and residual stress</b>	<b>149</b>
<i>Y. L. Sun, C. J. Hamelin, T. F. Flint, Q. Xiong, A. N. Vasileiou, I. Pantelis, J. A. Francis and M. C. Smith</i>	
<b>Numerical modelling of welding of martensitic steel</b>	<b>167</b>
<i>B. Smoljan, D. Iljkić, S. Smokvina Hanza, L. Štic and M. Jokić</i>	
<b>Prediction of stress corrosion cracking in 304 stainless steel canisters in dry storage of spent fuel by modeling: analysis of weld residual stress and susceptible microstructure</b>	<b>179</b>
<i>S. Gordon, X. Wu, Z. Yu and S. Liu</i>	
<b>Computational analysis of the yield stress of ultra-high strength all-weld metals</b>	<b>199</b>
<i>D. Zügner, S. Holly, W. Ernst, R. Schnitzer and E. Kozeschnik</i>	
<b>Numerical simulation of Cu-rich precipitate evolution in Cu-bearing 316L austenitic stainless steel</b>	<b>219</b>
<i>Q. Xiong, J. D. Robson, T. F. Flint, Y. Sun, A. N. Vasileiou and M. C. Smith</i>	
<b>A coupled temperature-microstructure model for the heat-affected zone of low alloyed high strength steel during two-pass arc welding</b>	<b>233</b>
<i>J. Paananen, A. Pohjonen, J. Larkiola and S. Anttila</i>	
<b>III Residual Stresses and Distortion</b>	
<b>Distortion analysis of large scaled welded structures (not appen access)</b>	<b>254</b>
<b>N. Doynov, C. Stapelfeld, V. G. Michailov, H. Pasternak and B. Launert</b>	
<b>Finite element simulation of residual stresses and distortions in selective laser melting</b>	<b>281</b>
<i>M. Kaess, M. Werz and S. Weihe</i>	
<b>A shift technique for multi-pass welding simulation</b>	<b>293</b>
<i>P. Pereira Alvarez, T. Dinh Trong, S. Hendili, V. Robin and J. Delmas</i>	
<b>How reliable are prediction and measurement of weld residual stresses? Lessons from the NeT Network.</b>	<b>305</b>

*M. C. Smith, V. Akrivos and A. Vasileiou*

<b>Process chain simulation of laser cladding and cold metal forming</b>	<b>337</b>
<i>P. Khazan, A. Kzzo, R. Hama-Saleh, A. Weisheit, I. Ünsal and M. Bambach</i>	
<b>Influence of viscoplastic and hardening modelling on numerically predicted residual and thermal stresses in a single-pass grade S960QL steel weld (not open access)</b>	Fehler!
Textmarke nicht definiert.	
<i>N. Häberle, A. Pittner and M. Rethmeier</i>	
<b>Evaluation of two methods for welding distortion simulation</b>	<b>369</b>
<i>A. Baumgartner, F. Wirnsperger and N. Enzinger</i>	
<b>Simulation of welding residual stresses – From theory to practice</b>	<b>383</b>
<i>S. Gkatzogiannis, P. Knoedel and T. Ummenhofer</i>	
<b>Residual stress measurements and model validation of single and double pulse resistance spot welded advanced high strength steel</b>	<b>401</b>
<i>P. Eftekharimilani, H. Gao, R. M. Huizenga, E. M. van der Aa, M. Amirthalingham, I. M. Richardson and M. J. M. Hermans</i>	
<b>Numerical simulation of stress behavior during shot peening</b>	<b>417</b>
<i>K. Ikushima, Y. Yamada, M. Shibahara, S. Nishikawa and K. Akita</i>	
<b>Laser beam welding of steel-aluminum joints - Influence of weld metal elastic-plastic properties on the distortions</b>	<b>431</b>
<i>A. Evdokimov, R. Ossenbrink, N. Doynov and V. Michailov</i>	
<b>IV Cracking Phenomena and Hydrogen Effects</b>	
<b>Numerical simulation of hydrogen assisted stress corrosion cracking originating from pits (not open access)</b>	<b>442</b>
<i>M. C. Madigan, T. Mente and T. Boellinghaus</i>	
<b>Study of solidification cracking in advanced high strength automotive steels</b>	<b>465</b>
<i>G. Agarwal, H. Gao, M. Amirthalingham, I. M. Richardson and M. J. M. Hermans</i>	



<b>Simulation of weld solidification cracking in vareststraint tests of alloy 718</b>	<b>485</b>
<i>J. Draxler, J. Edberg, J. Andersson and L-E. Lindgren</i>	
<b>Use of modelling to characterize the risk of hot cracking in austenitic stainless steels during welding</b>	<b>505</b>
<i>G. Tran Van, D. Carron, P. Le Masson, J. Stodolna, A. Andrieu and J. Delmas and V. Robin</i>	
<b>V Solid State and Friction Stir Welding</b>	
<b>3D finite element modeling of the linear friction welding of a beta titanium alloy</b>	<b>533</b>
<i>W. Li, Q. Ye, X. Wang, X. Yang and T. Ma</i>	
<b>Analysis of acoustic softening, heat and material flow in ultrasonic vibration enhanced friction stir welding</b>	<b>549</b>
<i>C. S. Wu, L. Shi and J. Chen</i>	
<b>Thermo-mechanical model of the friction stir welding process and its application for the aluminium alloy AA5754</b>	<b>565</b>
<i>U. Reisgen, A. Schiebahn, A. Naumov, A. Maslennikov and V. Erofeev</i>	
<b>Development of a model to investigate the interaction between process and machine tool and the resulting dynamics of friction stir welding</b>	<b>585</b>
<i>F. Panzer, M. Werz and S. Weihe</i>	
<b>Advances in numerical modelling of linear friction welded high strength steel chains</b>	<b>615</b>
<i>P. S. Effertz, F. Fuchs and N. Enzinger</i>	
<b>Numerical Simulation of Rotary Friction Welding of Molybdenum (not open access)</b>	<b>637</b>
<i>M. Stuetz, F. Kogler, J. Wagner, K.-H. Leitz, N. Reheis and N. Enzinger</i>	
<b>A proposal for thermal computational model for API 5L-X80 steel friction stir welds based on thermocouples measurements</b>	<b>651</b>
<i>G. G. De Sousa, M. Montoya, N. Bouchonneau, T. F. C. Hermenegildo and T. F. A. Santos</i>	
<b>Influence of the probe geometrical features on the stress condition of the tool during friction stir welding</b>	<b>665</b>

*I. Golubev, M. Weigl and V. Michailov*

**Modelling approach to the microstructure evolution in commercially pure aluminium during the RFW process** 681

*E. Heppner and E. Woschke*

## **VI Special Joining Processes**

**A novel approach for calculating the thermal cycle of a laser beam welding process using a stationary CFD model (not open access)** 694

*A. Artinov, M. Bachmann, V. Karkhin and M. Rethmeier*

**Electrical contact resistance model for aluminum resistance spot welding** 711

*M. Piott, A. Werber, L. Schleuss, N. Doynov, R. Ossenbrink and V. G. Michailov*

**Weldability of a dissymmetric assembly with a very thin sheet during resistance spot welding** 729

*J. Queval, E. Geslain, P. Rogeon, T. Pierre, C. Pouvreau, L. Cretteur and S. Marie*

**Overheating induced by Al-Si coating during spot welding of a dissymmetrical three sheets assembly** 751

*E. Geslain, P. Rogeon, T. Pierre, C. Pouvreau and L. Cretteur*

**Advancing spot welding process assessment** 767

*J. Kaars, P. Mayr and K. Koppe*

**Multiphysics finite element simulation of resistance spot welding to evaluate liquid metal embrittlement in advanced high strength Steels** 783

*K. M. Prabitz, W. Ecker, M. Borchert, T. Antretter, H. Schubert, B. Hilpert, M. Gruber and R. Sierlinger*

**Magnetic pulse welding of tubular parts - Process modeling** 795

*R. Shotri and A. De*

**CFD simulation of particle movement during atmospheric plasma spraying** 805

*M. Stummer and N. Enzinger*

## VII Modelling Tools and Computer Programs

<b>Correlating large sets of experimental data with high resolution computational weld mechanics models</b>	<b>819</b>
<i>J. Goldak, M. Martinez, S. Tchernov, H. Nimrouzi, J. Zhou, D. K. Aidun and H. Eisazadeh</i>	
<b>Investigation of the influence of the welding speed and current on the parameters of the adaptive function</b>	<b>841</b>
<i>M. B. Nasiri, A. Putz and N. Enzinger</i>	
<b>Prediction of grain boundary evolution in an titanium alloy substrate using a novel phase field model coupled with a semi-analytical thermal solution</b>	<b>861</b>
<i>T. F. Flint, Q. Xiong, Y. L. Sun, A. N. Vasileiou, M. C. Smith and J. A. Francis</i>	
<b>Experimental validation of a simplified welding simulation approach for fatigue assessments</b>	<b>875</b>
<i>N. Friedrich and S. Ehlers</i>	
<b>Real-time welding simulation for education</b>	<b>893</b>
<i>O. Mokrov, M. Simon, A. Schmidt, U. Reisgen, A. Behmel, J. Martin, A. Becirovic and D. Rudolph</i>	
<b>Asymptotics and blending in the modeling of welding</b>	<b>907</b>
<i>Y. Wang, Y. Lu, M. Grams, A. Cesaro and P. Mendez</i>	
<b>Process simulation of TIG welding for the development of an automatic robot torch through heat pipe – Head cooling system</b>	<b>933</b>
<i>K. Alaluss and P. Mayr</i>	
<b>Evaporation-determined model for arc heat input in the cathode area by GMA welding</b>	<b>953</b>
<i>O. Mokrov, M. Simon, A. Schiebahn and U. Reisgen</i>	
<b>Potentials of the ALE-method for modeling plastics welding processes, in particular for the quasi-simultaneous laser transmission welding</b>	<b>965</b>

*A. Schmailzl, S. Hüntelmann, T. Loose, J. Käsbauer, F. Maiwald and S. Hierl*

## **VIII Additive Manufacturing**

**Improvement of numerical simulation model setup and calculation time in additive manufacturing-laser-metal-deposition components with an advanced modelling strategy** 979

*M. Biegler, P. Khazan, M. Gatzel and M. Rethmeier*

**Influence of the first weld bead on strain and stress states in wire + Arc additive manufacturing** 991

*C. Cambon, I. Bendaoud, S. Rouquette and F. Soulie*

**New approach for fast numerical prediction of residual stress and distortion of AM parts from steels with phase transformations** 1007

*M. Schänzel, A. Ilin and V. Ploshikhin*

**Multi-scale multiphysics simulation of metal L-PBF AM process and subsequent mechanical analysis** 1029

*M. Bayat, D. De Baere, S. Mohanty and J. H. Hattel*

**Development of a two-dimensional axial symmetry model for wire arc additive manufacturing** 1049

*S. Cadiou, M. Courtois, M. Carin, P. Le Masson, L. Guilmois and P. Paillard*



## INTRODUCTION

This volume contains the papers presented at the 12<sup>th</sup> International Seminar ‘Numerical Analysis of Weldability’, held from September 23 to 26, 2018 at Schloss Seggau near Graz, Austria. As always, this location provided an inspiring environment encouraging friendly and intensive discourse between scientists and engineers. The conference stood up to its reputation as one of the most important forums in the Science of Welding. The meeting was organized by the Institute of Materials Science, Joining and Forming (IMAT) of Graz University of Technology, and the working group ‘Mathematical Modelling of Weld Phenomena’ of Commission IX of the International Institute of Welding (IIW).

The unique tradition of publishing (all articles refereed, typeset and edited in uniformity; each article is required to be comprehensive in its content) could be maintained also for this edition to serve the welding community as reference literature. The continuity of the previous eleven volumes, Mathematical Modelling of Weld phenomena 1 – 11, has therefore been preserved thanks to the monumental efforts of the Seggau team of IMAT. Special thanks goes to Bettina Schreiner-Föböl, who was in charge of the entire work of coordinating the peer review and editing procedure in a highly ambitious manner as well as Lisa Minkowitz and Maurice Tödling for assisting her in the layout creation. Volume XII is again published by Verlag der Technischen Universität Graz and almost all papers have a DOI and are available open access.

The 2018 seminar was attended by 139 delegates coming from 22 countries participating in both, oral sessions and poster presentations in the following sessions:

- I Arc Welding, Melt Pool & Solidification
- II Microstructural Modelling in Weld Metal and Heat Affected Zone
- III Residual Stresses and Distortion
- IV Cracking Phenomena and Hydrogen Effects
- V Solid State and Friction Stir Welding
- VI Special Joining Processes
- VII Modelling Tools and Computer Programs
- VIII Additive Manufacturing

The most important observations of this seminar were the fact that modelling approaches in the meantime penetrate many fields of application in welding and recently in additive manufacturing. It helps to solve complex tasks and optimize the welding processes and materials used. By this, it helps to enhance the safety, reliability and economy of welded structures. This was impressively shown by many authors who in addition could verify the calculation results by experimental investigations.

The 2018 IIW Kenneth Easterling Best Paper Award was won by the paper "Multi-scale multiphysics simulation of metal L-PBF AM process and subsequent mechanical analysis", M. Bayat, D. De Baere, S. Mohanty and J.H. Hattel. This paper has been valued by an international committee as the best contribution made over the three years proceeding on

## Mathematical Modelling of Weld Phenomena 12

the advancement of knowledge or practice in respect of mathematical modelling of weld phenomena.

The next International Seminar 'Numerical Analysis of Weldability' will take place from September 26 – 29, 2021 at Schloss Seggau.

Christof Sommitsch, Norbert Enzinger and Peter Mayr  
Graz, June 2019

# **I Arc Welding, Melt Pool and Solidification**





# COMPLETE 3D HEAT AND FLUID FLOW MODELING OF KEYHOLE LASER WELDING AND METHODS TO REDUCE CALCULATION TIMES

M. COURTOIS\*, M. CARIN\*, P. LE MASSON\* and S. GAIE\*\*

*\*Univ. Bretagne Sud, UMR CNRS 6027, IRDL, F-56100 Lorient, France*

*\*\*ArcelorMittal Global R&D Montataire, F-60160 Montataire, France*

*DOI 10.3217/978-3-85125-615-4-01*

## ABSTRACT

The fluid flow calculation inside the melt pool in welding processes is a complex challenge. It can be useful for defects prediction in the weld seam or to study the influence of some process parameters. The cost in time of these calculations makes these models not widely used, although they are rich in information.

The aim of this paper is to present a complete model solving the heat and fluid flow equations in all the states (solid – liquid - gas) of the metal during keyhole laser welding. In order to track dynamically the keyhole shape, a level set function is employed and the momentum equations are solved to predict accurately the melt pool behaviour. The particularity of this model is a drastic optimization to reduce computation time (less than 1 day on a commercial workstation without reducing significantly the accuracy of the fluid flow computation. To achieve this goal, a simplified approach of the recoil pressure effect is employed and an original method with three different meshes adapted for each equation and physics problem is proposed and discussed. Finally, to validate the model simplification, a complete experimental validation is added with longitudinal and transverse micrograph cuts for different welding configurations, micro-thermocouples measurements in solid phase [20-1200°C], pyrometer measurements in liquid phase [1500-3000°C].

Keywords: Laser welding; heat and fluid flow; keyhole, numerical simulation

## INTRODUCTION

In automotive industry, laser welding is widely used for its high production rate and its capacity to produce clean and discreet welded beams. Moreover, the cost of the laser sources and the increased available power offer always more applications.

Laser welding of steel is currently employed in industry for 20 years. Nevertheless, the use of new materials or the necessity to weld new configurations raises sometimes difficulties to achieve a satisfying welded joint. In most cases, questions come when the weld seam presents some defects like porosity, lake of materials or partial penetration. In all these cases, the fluid flow in the melt pool during the welding process is the responsible:

gravity with large melt pools can create collapsing, the keyhole opening and behaviour can impact the melt pool stability.

With this observation, and the necessity to understand the liquid and keyhole behaviour in all the complexes configurations, many experimental works have been carried in the last 30 years. More recently (15 years), various numerical works have been proposed to provide a better understanding when experiments were unable to give sufficient information. Models that propose a self-estimation of the keyhole shape remains limited but numerous methods have been developed to describe the keyhole effect as summarized by Dal in 2016 [1]. The keyhole is the place where the laser energy is introduced and by its strong action, it is responsible for many movements in the molten pool. However, this free surface is difficult to calculate due to the very complicated vaporization effects. The first works that really propose a method to treat dynamically the keyhole are those of Ki in 2002 [2]. Although very accurate, the calculations were performed on a supercomputer not available to an industrial environment. The emergence of similar models with a complete prediction of the keyhole creation with numerical methods like level set or V.O.F. depending on the software begin from 2008 with works of Geiger [3], Pang [4], Cho [5]. Since this time, few (less than 10) teams have proposed this kind of complete models but the experimental validation is often too brief, and the calculation times keep often these models in the academic research field.

The model developed and presented here aims to conciliate keyhole prediction and reasonable calculation times. For that, a method is proposed with 3 meshes and a voluntary simplified method to treat the vaporization and recoil pressure effect. Equations and numerical procedure are presented and next, to discuss on the simplified parts (vaporization and energy deposition) a complete experimental validation is proposed. Finally, the model is used in different configurations and compared to micrograph cuts.

## MATHEMATICAL FORMULATION

In order to model all the required phenomena, a certain number of equations must be solved. Classically, in all phases, the heat transfer equation is solved (Eqn. (1)). Two specific source terms are introduced:  $S_{laser}$  Eqn. (2) (discussed in [6]) introduces the laser energy and  $Q_{vap}$  (Eqn. (3)) is a term to remove the energy of the latent heat of phase change during vaporization. This energy is depending of the mass flow rate of evaporation (Eqn. (4)) and the saturation pressure (Eqn. (5)). Regarding the latent heat of fusion-solidification, the equivalent heat capacity is used (Eqn. (6)).

$$\rho c_p^{eq} \left[ \frac{\partial T}{\partial t} + \vec{\nabla} \cdot (\vec{u} T) \right] = \vec{\nabla} \cdot (k \vec{\nabla} T) + S_{laser} + Q_{vap} \quad (1)$$

$$S_{laser} = 2.5 \cos(\theta) \alpha(\theta) \delta(\phi) \frac{P_{laser}}{\pi r_0^2} \exp \left[ \frac{-(x-x_0)^2 - (y-y_0)^2}{r_0^2} \right] \quad (2)$$

$$Q_{vap} = -L_v \dot{m} \delta(\Phi) \quad (3)$$

$$\dot{m} = \sqrt{\frac{m}{2\pi k_b}} \frac{p_{sat}(T)}{\sqrt{T}} (1 - \beta_r) \quad (4)$$

$$p_{sat}(T) = p_a \exp \left[ \frac{\Delta H_v}{k_b T_{vap}} \left( 1 - \frac{T_{vap}}{T} \right) \right] \quad (5)$$

$$c_p^{eq} = c_{p-s} + L_f \frac{\exp \left[ -\frac{(T-T_{melt})^2}{(T_l-T_s)^2} \right]}{\sqrt{\pi}(T_l-T_s)^2} \quad (6)$$

Where  $T$  is the temperature,  $k$  the thermal conductivity,  $\rho$  the density,  $c_p$  the heat capacity,  $\vec{u}$  the velocity vector,  $\theta$  the surface inclination,  $r_0$  the laser beam radius,  $\dot{m}$  the mass flow rate of the evaporation,  $\Phi$  the level set variable,  $k_b$  the Boltzmann constant,  $p_{sat}$  the saturation pressure of the vapor phase,  $m$  the atomic mass,  $\beta_r$  the retrodiffusion coefficient,  $p_a$  the ambient pressure,  $\Delta H_v$  the creation enthalpy of the vapor,  $T_{vap}$  the vaporization temperature,  $T_l$  the liquidus temperature,  $T_s$  the solidus temperature,  $T_{melt}$  the melting temperature average between  $T_s$  and  $T_l$ ,  $L_f$  the latent heat of fusion.

In liquid (melt pool) and gas (keyhole), the momentum conservation equation is solved (Eqn. (7)) for incompressible Newtonian fluids.  $p$  is the pressure,  $\vec{g}$  the gravity acceleration,  $\beta_l$  the expansion coefficient,  $\gamma$  the surface tension coefficient,  $\vec{n}$  the normal vector,  $\kappa$  the curvature,  $f_l$  the liquid fraction and  $C$  and  $b$  some numerical coefficients. Some terms have been introduced:  $\rho \vec{g}$  represents the gravity effect.  $\rho_l \beta_l (T - T_{melt}) \vec{g} \Phi$  considers the buoyancy effect but only in the molten steel with the term  $\Phi$ . This effect is neglected in gas.  $K\vec{u}$  is called the Darcy condition. This term will cancel the velocity if the temperature is below the fusion point. This well-known numerical technique allows a simple treatment of the solid with the fluid flow calculation and a moving fusion/solidification front. Finally, the last term is necessary with the level set method to take into account the surface tension effect.

Eqn. (10) is the mass conservation equation for an incompressible fluid and Eqn. (11) is the transport equation of the level set variable. The coupling with fluid mechanic is operate with the  $\vec{u}$  term. The term on the right of the equal sign is a numerical adjunction to facilitate the convergence. All these equations are solved in the commercial code Comsol Multiphysics. Some of them are already implemented in the software (Eqn. (1,7,10,11)), the other have to be added (Eqn. (2-6,8,9)).

$$\rho \left( \frac{\partial \vec{u}}{\partial t} + \vec{u} \cdot (\vec{\nabla} \cdot \vec{u}) \right) = \vec{\nabla} \cdot \left[ -pI + \mu \left( \vec{\nabla} \vec{u} + (\vec{\nabla} \cdot \vec{u})^T \right) \right] \quad (7)$$

$$+ \rho \vec{g} - \rho_l \beta_l (T - T_{melting}) \vec{g} \Phi + K \vec{u} + \gamma \vec{n} \kappa \delta(\Phi)$$

$$K = -C \left[ \frac{(1 - f_l)^2}{f_l^3 + b} \right] \quad (8)$$

$$f_l = \begin{cases} 0 & \text{for } T < T_s \\ \frac{T - T_l}{T_l - T_s} & \text{for } T_s < T < T_l \\ 1 & \text{for } T > T_l \end{cases} \quad (9)$$

$$\vec{\nabla} \cdot \vec{u} = 0 \quad (10)$$

$$\frac{\partial \Phi}{\partial t} + \vec{u} \cdot \vec{\nabla} \Phi = \gamma_{ls} \vec{\nabla} \cdot \left[ \varepsilon_{ls} \vec{\nabla} \Phi - \Phi (1 - \Phi) \frac{\vec{\nabla} \Phi}{|\vec{\nabla} \Phi|} \right] \quad (11)$$

## THERMOPHYSICAL PROPERTIES

The material used is a DP600 steel. This common material in automotive industry and is well known in the solid state [7]. When known, temperature dependent properties are used. When not known, at high temperature for example, some assumptions are made. The property is either for pure iron or the last known value. The main properties are listed in table 1.

**Table 1** Thermophysical properties used

Property [unit]	Symbol	Value or reference
Thermal conductivity of solid / liquid / gas [ $W \cdot m^{-1} \cdot K^{-1}$ ]	$k_{s/l/g}$	$f(T)$ [internal data] / $3.75 \cdot 10^{-3} T + 23.25 / 0.12$
Density of solid / liquid / gas [ $kg \cdot m^{-3}$ ]	$\rho_{s/l/g}$	$f(T)$ [internal data] / 7287 / 1
Specific heat of solid / liquid / gas [ $J \cdot kg^{-1} \cdot K^{-1}$ ]	$c_{p \ s/l/g}$	$f(T)$ [internal data] / 573 / 373
Dynamic viscosity of solid / liquid / gas [Pa.s]	$\mu_{s/l/g}$	$10^3 / 5 \cdot 10^{-3} / 1 \cdot 10^{-5}$
Latent heat of fusion [ $J \cdot kg^{-1}$ ]	$L_f$	$2.54 \cdot 10^5$
Latent heat of vaporization [ $J \cdot kg^{-1}$ ]	$L_v$	$6.1 \cdot 10^6$
Liquidus temperature [K]	$T_l$	1808
Solidus temperature [K]	$T_s$	1788
Melting temperature [K]	$T_{melting}$	$(T_l + T_s) / 2$
Vaporization temperature [K]	$T_{vap}$	3134
Surface tension coefficient [ $N \cdot m^{-1}$ ]	$\gamma$	1
Coefficients in Darcy's law (7)	$C / b$	$1 \cdot 10^6 / 1 \cdot 10^{-3}$
Coefficient of thermal expansion [ $K^{-1}$ ]	$b_l$	$1 \cdot 10^{-4}$

## SIMPLIFICATION STRATEGY

All the previous equations are widely used by many authors [2-6]. On the other hand, the way to treat the metal vaporization differs from one author to another because of the numerical complexity. The most rigorous method requires a very thin modelling of the Knudsen layer at the interface. This modelling is potentially very difficult to achieve (discussed in [7]) and can be very time-consuming). For this reason, a simplified modelling with a simple recoil pressure is proposed by applying only the resulting pressure (Eqn. (13)) in momentum conservation equation (Eqn. (12)). This surface force (in  $Pa$  or  $N/m^2$ ) is applied on the surface of the keyhole with the  $\delta(\Phi)$  term (in  $m^{-1}$ ), the spatial derivative of the  $\Phi$  function. This term is nonzero only on the free surface of the keyhole. This method, used by many other authors, does not generate vapor plume and takes only into account its effect on the liquid. Although less accurate, this method can be relatively fast and give interesting prediction of keyhole as discussed in the next section.

$$\rho \left( \frac{\partial \vec{u}}{\partial t} + \vec{u} \cdot (\vec{\nabla} \cdot \vec{u}) \right) = \vec{\nabla} \cdot \left[ -pI + \mu (\vec{\nabla} \vec{u} + (\vec{\nabla} \cdot \vec{u})^T) \right] \quad (12)$$

$$+ \rho \vec{g} - \rho_l \beta_l (T - T_{melting}) \vec{g} \Phi + K \vec{u} + \gamma \vec{n} \kappa \delta(\Phi) + F_{recoil}$$

$$F_{recoil} = p_a \exp \left[ \frac{\Delta H_v}{k_b T_{vap}} \left( 1 - \frac{T_{vap}}{T} \right) \right] \delta(\Phi) \quad (13)$$

## MESH USED

In this model, 3 main equations are solved: heat transfer Eqn. (1), fluid flow Eqn. (7) and level set transport equation Eqn. (11). Each equation does not have the same requirement in size of meshing. For example, the heat transfer problem needs a refined mesh in the laser deposition zone only. On the other hand, the fluid mechanic problem requires a finer mesh than heat transfer and with a refinement in the melt pool. Finally, the transport equation of level set needs a homogeneous mesh everywhere the interface (free surface) can potentially be.

The common way to solve this kind of model (with commercial codes) is by using a unique mesh often built for the more restrictive equation to solve. In this work, we suggest to use a specific and appropriate mesh for each main equation. Figure 1 presents the different meshes for each physics problem.

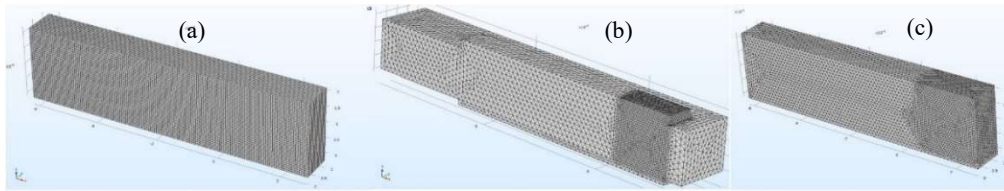


**Fig. 1** View of the 3 mesh used. (a) Level Set, (b) Heat transfer, (c) fluid flow.

## Mathematical Modelling of Weld Phenomena 12

During the solving process presented in figure 2 with an iterative method, the coupling variables must be transferred from a mesh to another. For that, Comsol Multiphysics offers interpolation tools to project a solution on another mesh. If the calculation points do not coincide, an interpolation between the two closest points is realized. Of course, when a solution is computed on a fine mesh and then projected on a coarser mesh to operate the coupling, the solution is degraded. Therefore, the next section will analyze if the model remains predictive by comparing numerical results to experimental data.

The addition of the 3 meshes represents 400 000 degrees of freedom (DOF) to be compared to the 2 000 000 DOF of a classical formulation (more details in [6]). Time steps are set to 100  $\mu$ s and the model is solved on 300 ms, which represents the physical time necessary to reach an established state. The solver used with the previously described meshes requires 7 GB of RAM. The model is solved on a common commercial workstation with a 2 cores, 4 threads i5-6500 at 3.20 Ghz and 16 GB RAM DDR4. The application of the simplified recoil pressure and the use of multi-meshes make it possible to increase the time step and so the calculation speed. In comparison of a model more complex and classic in the meshing method [6], the computation time is reduced from 3 weeks to 24 hours on the same computer.

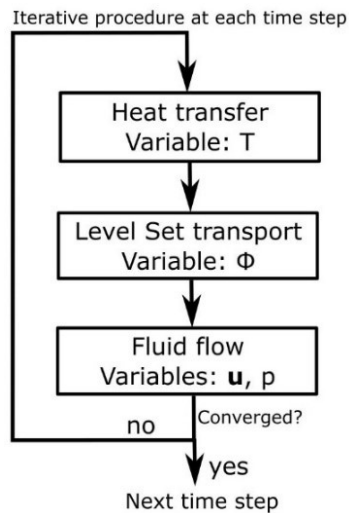


**Fig. 2** Iterative procedure principle allowing the use of three different meshes.

## RESULTS AND DISCUSS

All the previous equations and methods are solved to describe first a fusion line inside a 1.8 mm steel plate. A 4 kW laser with a 600  $\mu$ m diameter spot is used and the sheet moves with a speed of 6 m/min. As results, figure 3 presents the different stages of the creation of the keyhole and the melt pool growing. The vaporization temperature is reached in less than 2 ms and the keyhole begins to dig under the effect of the recoil pressure. When the keyhole is opened on the rear face, the melt pool finally stabilizes at 6 mm long in approximatively

200 ms. Figure 4 shows temperature and velocity fields. The temperature is around 3100 K inside the keyhole controlled by the evaporation latent heat. The velocity field is plotted only in the melt pool: indeed, although the fluid flow is calculated in it, the vapour plume velocity is not well described because of the choice of the recoil pressure simplification. To evaluate the interest of this model, a complete experimental validation must be carried out.

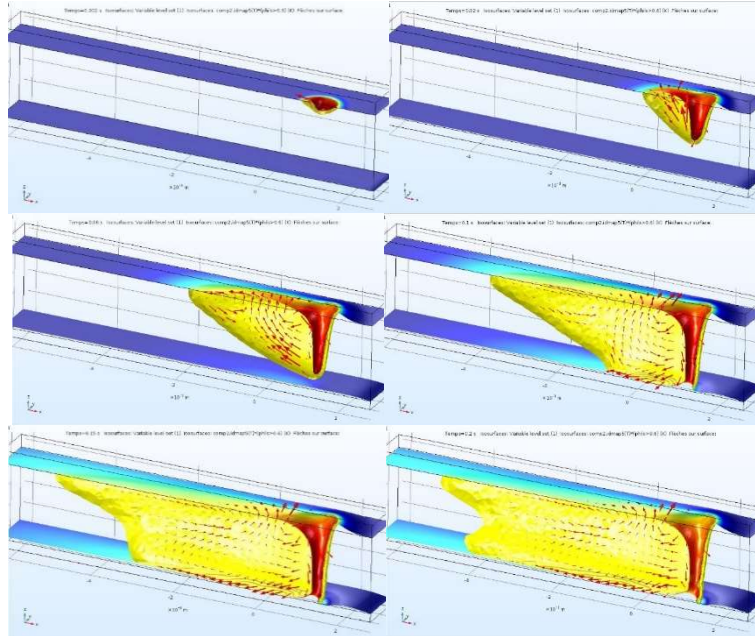


**Fig. 3** Keyhole and melt pool creation at 2, 20, 60,100, 150 and 200 ms.

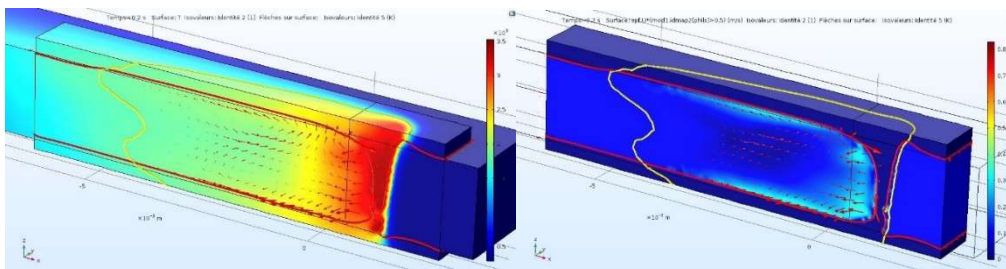


**Fig. 4** Temperature field (max : 3150K) and velocity field (max : 0,6 m/s).

### EXPERIMENTAL VALIDATION

To validate the model, a complete experimental set-up is proposed. First and classically, figure 5 compare the melted zone in a transversal cut after chemical etching. If the melted zone is well predicted for the case presented above (4 kW and 6 m/min), it is more interesting to note that a reduced velocity leads to a partial penetration on the experiment and in the model. The model predicts correctly the keyhole depth and can be used to predict



## Mathematical Modelling of Weld Phenomena 12

this kind of defects. To obtain an accurate keyhole shape, a thorough calculation of the energy deposition and the recoil pressure is essential.

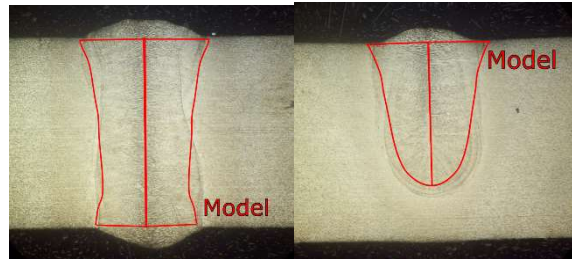


**Fig. 5** Comparison of melted zones. 4 kW – 6 m/min (left) 4 kW – 8 m/min (right)

Another indicator of the correct calculation of the energy deposition and the recoil pressure concerns the keyhole inclination angle. In figure 6, an experiment has been carried out with a sudden stop of the laser. With a small uncertainty thanks to the very thin liquid film beside the front wall of the keyhole, the longitudinal cut gives the inclination angle. Again, the model gives a consistent result.

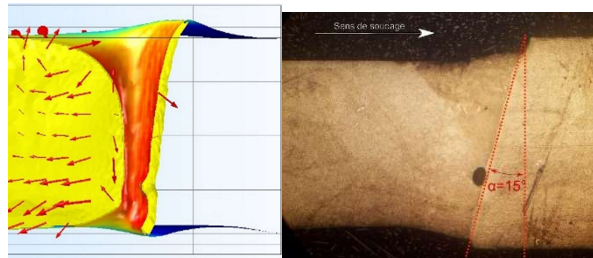


**Fig. 6** Calculated keyhole inclination (left) compared to experiment (right).

In addition, temperatures in liquid and solid are compared to experiments. At the surface of the melt pool, a pyrometry method developed at PIMM laboratory is used (detailed in [6]). Different areas close and away from the keyhole are compared. At all the chosen points, the difference is lower than 5% showing a good prediction of the melt pool temperature.

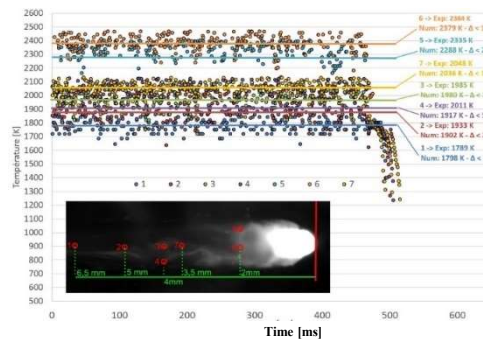


**Fig. 7** Comparison between calculated temperatures and measurements from pyrometry in different regions.

## Mathematical Modelling of Weld Phenomena 12

In the solid part, at lower temperatures, the figure 8 shows for 11 positions a comparison between micro-thermocouples and model calculation. Again, the prediction of the temperature level is correct but with more discrepancies. The bigger difference is observed during the cooling. Indeed, to reduce calculation times, a small heat transfer domain has been modelled and so the solution is very sensitive on the boundary conditions. The size of the domain is here responsible of the disparity. We can treat this problem either by increasing the domain size (best way but with an increase of time calculation) or by modifying the boundary conditions (more difficult and have to be done for each experiment). Nevertheless, near the melt pool, where the thermal gradient is high, the model gives a good prediction validating also the fluid flow computing.

For this configuration, the model gives interesting results with a possible prediction of the melt-pool shape and the global temperatures reached. The model will be now used for configurations close to industrial needs to see the versatility.

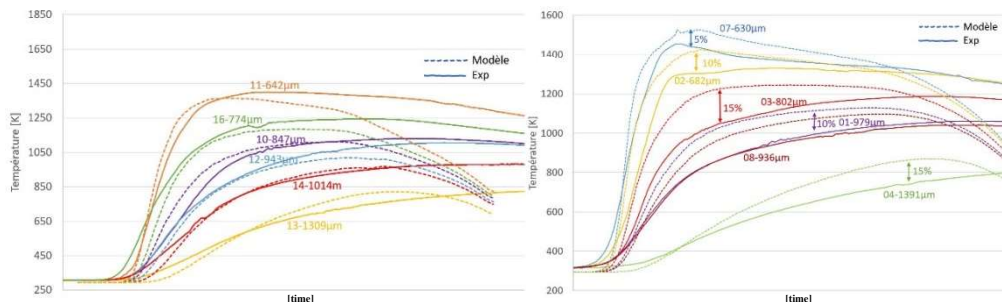


**Fig. 8** Comparison of temperatures calculated and measured by micro-thermocouples of  $25\mu\text{m}$ . (Left: below the sheet. Right: above the sheet. The indicated distance is the spatial shift from the welding axis)

### VERSATILITY ON OTHER CONFIGURATIONS

Without any other modifications than the operating parameters (here sheets geometries or laser speed), the model is now compared to more complicated geometries but closer to industrial issues. First, figure 9 shows a result for a 3 mm thick plate. For the same laser power than previously, the welding speed is decreased. Naturally, the keyhole is modified with almost a  $90^\circ$  inclination and the melt pool is shorter. The micrograph cut can be seen in figure. 10.

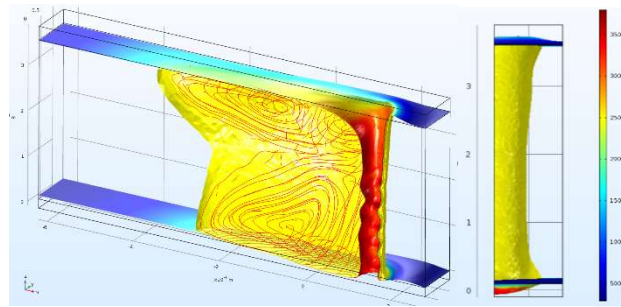


**Fig. 9** 3mm thickness – 4kW 3 m/min

Thanks to the level set method and the free surface method, it is easy to treat gap between sheets or a difference of thickness leading to the collapse of the thicker sheet on the other. Figure 10 shows various configurations and the micrograph cut in comparison. We can note again that many phenomena are correctly modelled like partial penetration (4 kW 7 m/min), melt pool wider at the surfaces or melt pool globally wider with an initial gap between sheets.

For the results presented in figure 10, the more expansive calculation requires 48h which is close to industrial requirements for analysing defects, or new welding assembly configurations.

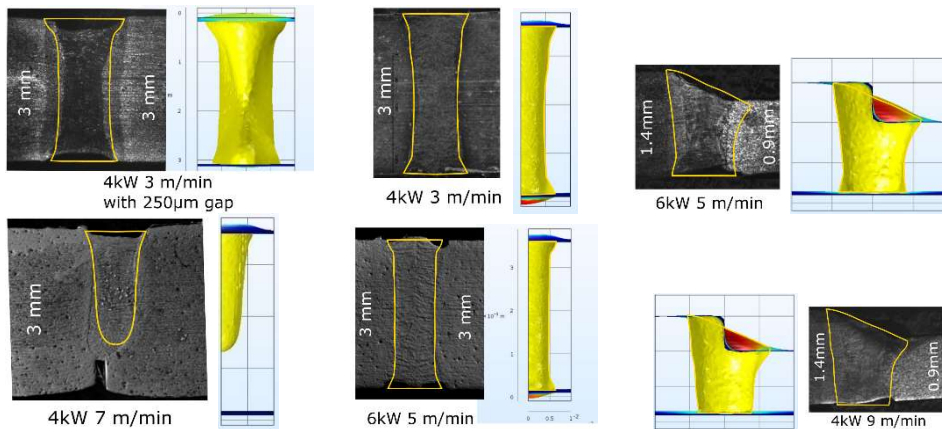


**Fig. 10** Comparison between model and experiment (PIMM Lab.) for 6 welding configurations.

### CONCLUSION

In this paper, a complete and predictive model is proposed to describe dynamically heat and fluid flow during laser welding. The keyhole is self-calculated. In order to propose a fast calculation running on classic computers, some approximations and improvement are proposed.

First, the vaporization – recoil pressure effect is simplified by a simple surface equivalent force. The very strong vapor plume is so neglected to facilitate the convergence. Then, a

new approach of meshing multiphysics models is proposed. The use of 3 meshes allows to refine only in the necessary locations and reduce drastically the number of DOF. This method can degrade the solution and so a complete experimental validation is performed. The prediction of the thermal levels and the sizes of the melted zones is satisfying. All the calculations are performed on classical computers (4 cores, 16 GB ram) in less than 48h allowing the use of these models in an industrial context.

### ACKNOWLEDGMENTS

The authors wish to thank the PIMM laboratory (Arts et Metiers – Paris France) for their support for the experimental validation of the model and ArcelorMittal for the funding of this study and the works associated.

### REFERENCES

- [1] M. DAL, R. FABBRO: ‘An overview of the state of art in laser welding simulation, *Optics & Laser Technology Vol 78*, Part A, 2-14, 2016.
- [2] H. KI, P. MOHANTY, J. MAZUMDER: ‘Modeling of laser keyhole welding: Part I. Mathematical modeling, numerical methodology, role of recoil pressure; multiple reflections and free surface evolution’, *Metall. Mater. Trans A* 33A 1817-1830, 2002.
- [3] M. GEIGER, K.H. LEITZ, H. KOCH, A. OTTO: ‘A 3D transient model of keyhole and melt pool dynamics in laser beam welding applied to the joining of zinc coated sheets’, *Prod. Eng. Res. Devel.* 3 127-136, 2009.
- [4] S. PANG, L. CHEN, J. ZHOU, Y. YIN, T. CHEN: ‘A three-dimensional sharp interface model for self-consistent keyhole and weld pool dynamics in deep penetration laser welding’, *J. Phys. D : Appl. Phys.* 44 025301, 2011.
- [5] W.I. CHO, S.J. NA, C. THOMY, F. VOLLERTSEN: ‘Numerical simulation of molten pool dynamics in high power disk laser welding’, *J. Mater. Process. Technol.* 212 262-275, 2012.
- [6] M. COURTOIS, M. CARIN, P. LE MASSON, S. GAIED, M. BALABANE: Guidelines in the experimental validation of a 3D heat and fluid flow model of keyhole laser welding’. *J. Phys : D Appl. Phy* 49 155503 (13pp), 2016.
- [7] M. COURTOIS, M. CARIN, P. LE MASSON, S. GAIED, M. BALABANE: ‘A new approach to compute multi-reflections of laser beam in a keyhole for heat transfer and fluid flow modeling in laser welding’. *J. Phys : D Appl. Phy* 46 505305 (14pp), 2013.



# COMPUTATIONAL PREDICTION OF PENETRATION SHAPES IN MIG WELDING OF PRACTICAL ALUMINUM ALLOY JOINTS

H. SERIZAWA\*, S. SATO\*\* and F. MIYASAKA\*\*

*\*Joining and Welding Research Institute, Osaka University*

*\*\*Graduate School of Engineering, Osaka University*

DOI 10.3217/978-3-85125-615-4-02

## ABSTRACT

As one of the methods for simulating the molten droplet from filler wire in metal insert gas (MIG) welding, a new line-type heat source has been developed and it is added in the three-dimensional, non-stationary thermal model which can demonstrate both molten pool and penetration shape in gas metal arc welding (GMAW) process. As the result of the examination about the applicability of this combined model for the practical aluminum joint, it is found that the penetration shape in the lap joint can be fairly demonstrated by assuming the adiabatic condition due to the oxide layer and/or the physical separation. In addition, it is revealed that the overhang length of numerical joggle joint model should be appropriately shortened in order to reproduce the penetration shape of practical joggle joint. Moreover, it can be concluded that the penetration shape of the practical aluminum joints can be reproduced by defining the dominant parameters in the combined model through the examinations of the basic welding.

## INTRODUCTION

Recently, the aluminum alloys have been widely employed in the transportation equipment, such as railway vehicle, car vehicle, motor bicycle and so on, in order to reduce the total weight of equipment and/or to decrease the carbon dioxide emission [1-3]. Although the friction stir welding (FSW) has been positively used for joining the aluminum alloy due to its various advantages such as less decrement of mechanical strength, small distortion after joining and so on [4,5], the thickness of plates is generally limited to be less than 10 mm and it is difficult to join the complicate shape structures by using FSW. Then, the metal insert gas (MIG) welding has been generally employed for joining the aluminum alloy parts in the motor bicycle [3], where the penetration shape becomes the finger type [6,7].

As for the methods to simulate gas metal arc welding (GMAW) process, many attempts have been made [8-10]. Dilthey and Roosen have studied a three-dimensional, quasi-stationary thermal model for GMAW [8]. In the model, the influence of process parameters such as the wire diameter and the composition of the shielding gas on the weld profile can be taken into account. Kim and Na have proposed a model of GMAW including the effect of weld pool convection [9]. Pardo and Weckman have developed a model for the prediction of weld pool and reinforcement dimensions in GMAW welds using a finite element method, which has been formulated for a moving coordinate framework [10]. In

spite of these efforts, some problems remain to be solved because of the complexity of arc welding processes. For example, the models mentioned above are for quasi-stationary conditions. In GMAW process, the electrode wire is melted and supplied to the molten pool intermittently and the welding process is fairly dynamic.

On the other hand, in order to examine the dynamic behaviour of weld pool precisely, Cao, Yang and Chen have developed a three-dimensional transient thermos-fluid model with free surface which can simulate the interaction of a metal droplet with the weld pool and shows a good agreement between the predicted finger penetration and actual welds [11]. Kumar and DebRoy have combined a heat transfer model with an optimization algorithm to determine several uncertain welding parameters from a limited volume of experimental data and the finger penetration characteristic of GMAW welds computed was in fair agreement with the experimental results for various welding conditions [12]. However, these models include many parameters which should be estimated through various computations or inverse analyses, and the typical features of GMAW process such as undercutting and humping cannot be reproduced.

As one of the methods for simulating GMAW process simply and practically, Yamamoto, Ohji, Miyasaka and Tsuji have developed a three-dimensional, non-stationary thermal model [13]. By using a finite difference model based on the heat flow equation and taking account of the balance of gravity, surface tension and arc pressure, both the molten pool and the penetration shape in the various types of GMAW are successively demonstrated [13-15]. In addition, by developing a new line-type heat source, which models the molten droplet from filler wire, and combining this line-type heat source with the three-dimensional, non-stationary thermal model, the penetration shapes in bead-on MIG welding and butt MIG welding with V-groove have been successfully reproduced [16]. In this research, in order to examine the applicability of this combined model for the practical aluminum joints, the penetration shapes in lap and joggled joints were studied.

## METHOD FOR ANALYSIS

### MODEL FOR GMAW PROCESS

In order to simplify the numerical model for GMAW process, the following two assumptions have been employed.

- The heat flow in the weld pool is assumed to be conductive. Namely, the influence of the metal flow in the weld pool is neglected.
- The weld pool is set to be in a static equilibrium under the influence of gravity, surface tension and arc pressure.

Based on the above two assumptions, the governing equations are as follows,

$$\rho \frac{\partial H}{\partial t} = \frac{\partial}{\partial x} \left( K \frac{\partial T}{\partial x} \right) + \frac{\partial}{\partial y} \left( K \frac{\partial T}{\partial y} \right) + \frac{\partial}{\partial z} \left( K \frac{\partial T}{\partial z} \right) \quad (1)$$

$$\sigma \left[ \frac{(1 + \xi_y^2) \xi_{xx} + (1 + \xi_x^2) \xi_{yy} - 2 \xi_x \xi_y \xi_{xy}}{(1 + \xi_x^2 + \xi_y^2)^{3/2}} \right] = \rho g \xi + P_a - \lambda \quad (2)$$

Where,  $\rho$ ,  $H$ ,  $K$ , and  $T$  in Eqn. (1) are density, enthalpy, thermal conductivity and temperature, respectively.  $\sigma$ ,  $\xi$ ,  $g$ ,  $P_a$  and  $\lambda$  in Eqn. (2) are surface tension, surface displacement, gravity acceleration, arc pressure and Lagrange multiplier, respectively. Equation (1) is used for estimating the temperature distribution in the base metal, while the theoretical configuration of the molten pool in the model is derived from Eqn. (2). Figure 1 shows the schematic illustration of the calculation flow during a unit time step in this model. The torch is fixed during the time step (Fig. 1(i)) and the thermal energy is transferred into the base metal from the arc (Fig. 1(ii)). In the final stage of this unit time step, the amount of the wire melted during this time step is transferred on the molten pool (Fig. 1(iii)) and the surface profile is calculated using Eqn. (2) (Fig. 1(iv)). Once the calculation for the unit time step is completed, the torch is moved and the calculation for the next time step is repeated in a similar manner.

As a numerical method for modelling GMAW process, three-dimensional finite difference method was employed. So, the grid points for both the target material and the air space surrounding the target material are configured in the numerical space as shown in Fig. 2, and the variables are set to each grid points.

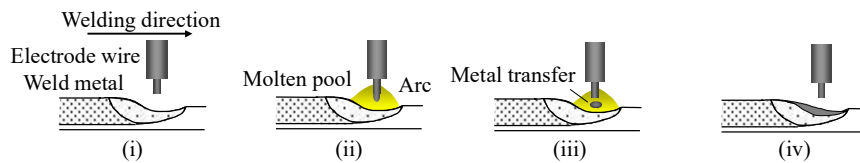


Fig. 1 Process of GMAW.

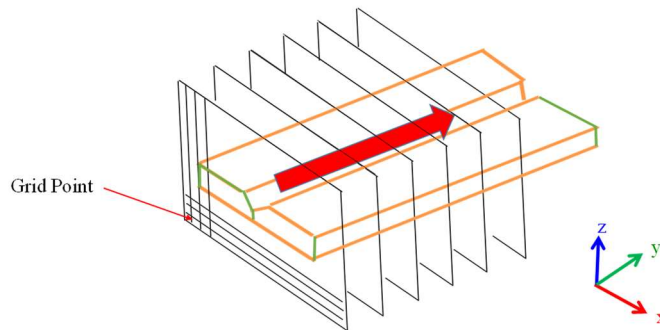


Fig. 2 Schematic illustration of numerical space in finite difference method.

#### LINE-TYPE HEAT SOURCE

In the above model, the heat source is assumed to be distributed in a circular zone on the molten pool. However, because the finger type penetration in MIG welding is caused by the molten droplet from the filler wire to the bottom of the molten pool and the molten droplet would have a high speed and a high temperature [6], the internal heat source in the



molten pool should be also taken into account. So, in this research, a new line-type heat source model has been developed and has been combined in the original model for GMAW process based on the following assumptions.

- The thermal energy is assumed to be divided into that from the arc and the molten droplet. Namely, the thermal energy from the arc is defined by the original heat source distributed on the molten pool, while that from the droplet is modeled by the line-type heat source.
- The line-type heat source is set to be uniformly distributed from the top surface to the bottom of the weld pool.

Then, the shape of line-type heat source changes as shown in Fig. 3. In the beginning of welding, the line-type heat source starts as a punctiform heat source at the center of the circular zone on the surface defined by the original heat source. With the growth of molten pool, the length of line-type heat source becomes longer. In this combined model, a ratio of the thermal energy from the original heat source to that from the line-type heat source is defined as a “ratio of heat source”.

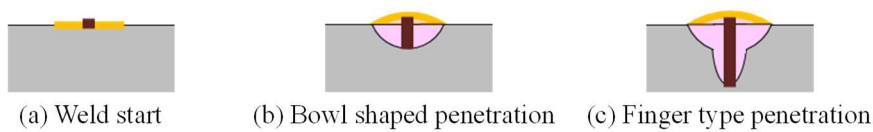


**Fig. 3** Change of heat source shape.

### OBJECTS FOR ANALYSIS

As the examples of practical aluminum joints, lap and joggled joints were examined in this research. The penetration shapes obtained in the experimental welding of lap and joggled joints are shown in Fig. 4, where forging and extruded aluminum alloys were employed as same as the practical joints, respectively. The thickness of aluminum alloys is 4 mm. The welding conditions of each joints are shown in Table 1. In addition, Fig. 5 is a schematic drawing of the joggle joint. Although two passes welding is employed for producing the practical joggle joint, both one pass and two passes welding were conducted in the experiment in order to examine the influence of welding pass on the penetration shape precisely, and both the penetrations are also shown in Fig. 4. In this research, in order to reproduce the penetrations shown in Fig. 4, the computational analyses using the combined model were conducted. In order to reduce the calculation time, the sizes of numerical models were set to be smaller than those of the experiments without affecting the penetration shape computed. Table 2 shows the model sizes and other parameters in the combined model.

## Mathematical Modelling of Weld Phenomena 12

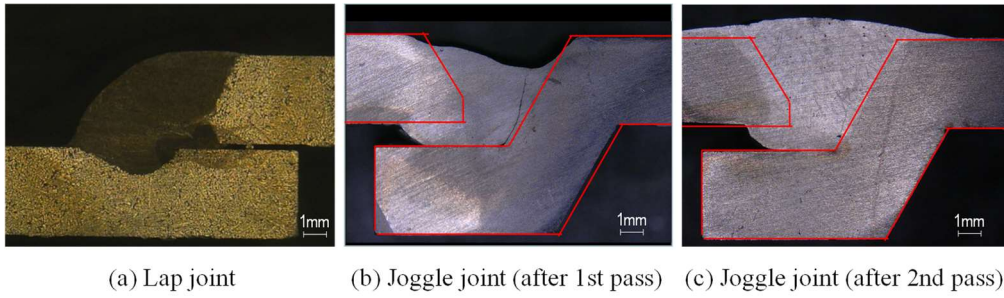


**Fig. 4** Penetration shapes obtained in practical aluminum joints.

**Table 1** Welding conditions for practical aluminum joints.

		Lap Joint	Joggle Joint
<b>Size of plate</b>	(mm)	200 x 200 x 4	150 x 100 x 4
<b>Welding speed</b>	(cm/min)	72	72
<b>Current</b>	(A)	150	140
<b>Voltage</b>	(V)	20	20
<b>Weaving</b>	<b>Full amplitude</b> (mm)	4	4
	<b>Frequency</b> (Hz)	2.8	2.8
<b>Overlap space</b>	(mm)	5	-
<b>Gap width</b>	(mm)	0	-
<b>Target position</b>		Overlaid corner	Bottom corner
<b>Torch angle</b>	(degree)	55	90
<b>Wire diameter</b>	(mm)	1.2	1.2

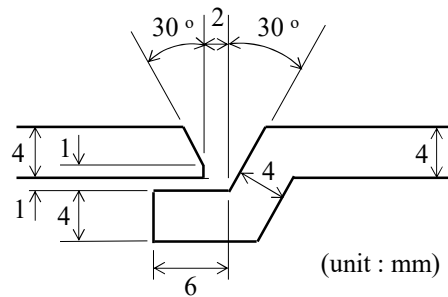


**Fig. 5** Schematic drawing of joggle joint.

**Table 2** Typical conditions for numerical analyses.

		Lap Joint	Joggle Joint
<b>Size of plate</b>	(mm)	100 x 50 x 4	150 x 75 x 4
<b>Thermal efficiency</b>	(%)		70
<b>Ratio of heat source</b>			7 : 3
<b>Radius of arc pressure</b>	(mm)	4	4 (1st pass)
			5 (2nd pass)

## RESULTS AND DISCUSSIONS

## LAP JOINT

According to the previous studies about the various GMAW processes using the three-dimensional, non-stationary thermal model and our research about bead-on MIG welding and butt MIG welding with V-groove using the combined model, it is revealed that the penetration shapes would be predicted regardless of the joint geometry by defining the dominant parameters in the model, which are dependent on the welding equipment [11]. In this research, the dominant parameters, which are thermal efficiency, ratio of heat source and radius of arc pressure, area assumed to be the values obtained from our previous research as shown in Table 2. The material properties were decided from our measurement for the aluminium alloy used in the experiment. The density, thermal conductivity, latent heat, specific heat and surface tension were set to be  $2.78 \text{ Mg/m}^3$ ,  $170 \text{ W/(m}\cdot\text{K)}$ ,  $333 \text{ kJ/kg}$ ,  $1000 \text{ J/(kg}\cdot\text{K)}$  and  $0.8 \text{ N/m}$ , respectively. Figure 6 shows the maximum temperature distribution and the penetration shape of lap joint computed, and it is found that the surface profile of weldment has a very good agreement with the experiment, while the depth of penetration to the bottom plate which seems to affect the lap joint strength is shallower than the experimental result. One possible reason for this shallow penetration is considered to be the difference of thermal conductivity of two plates before the welding. The two plates are set to be joined thermally in this numerical model, while upper and bottom plates are not integrated thermally due to the oxide layer on the surface of aluminum alloy and/or small physical separation of two plates in the experiment. In the practical welding, thermal energy from arc and molten droplet seems to concentrate on the weld pool because the thermal conductivity between two plates would be prevented by the oxide layer and/or the physical separation, and then the depth of penetration to the bottom plate might become to be deeper.

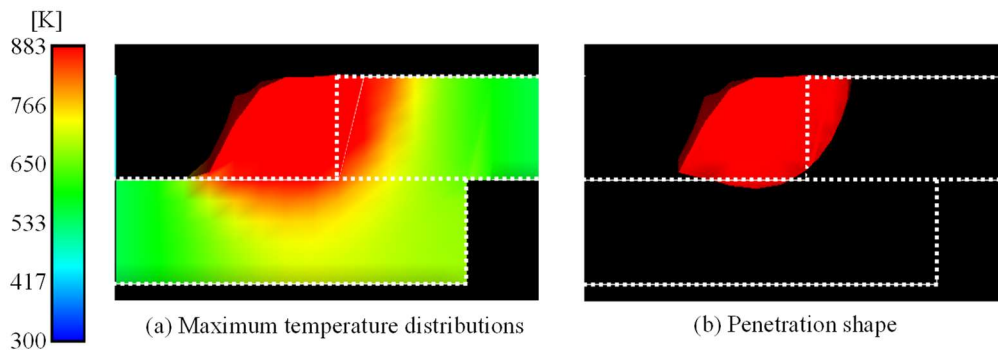


**Fig. 6** Maximum temperature distribution and penetration shape of lap joint computed.

In order to overcome this difference, the two plates are assumed to be separated and be insulated thermally before generating the weld pool between two plates and the two plates change to be integrated after producing the weld pool. In other words, the adiabatic condition due to the oxide layer and/or the physical separation is set at the overlap space

before welding. The penetration shape computed by using the modified model is shown in Fig. 7 and it is found that that its depth to the bottom plates seems to be slightly deeper than that of the original model shown in Fig. 6(b). Because there was a gap between the two plates obviously after welding as shown in Fig. 4(a), there would still be a difference of the thermal conductivity between the modified model and the experiment. In addition, the target position might be shift to the bottom plate although it is set to be the overlaid corner before welding. Although there still be a difference in the depth of penetration to the bottom plate between the numerical and experimental results, the modification of the model assuming the adiabatic condition before welding is considered to be effective for predicting the penetration shape of practical lap joint.

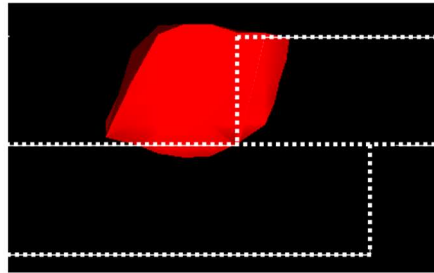


**Fig. 7** Penetration shape of lap joint with assuming adiabatic condition before welding.

### JOGGLE JOINT

According to the results of lap joint, the penetration shape is computed by assuming the adiabatic condition due to the oxide layer, and the results of maximum temperature distribution and penetration shape after first pass welding are shown in Fig. 8. From this figure, it is found that the depth of deposit metal calculated is shallower than that in the experiment. In addition, the filler metal fully flowed into the gap in the numerical result although only 2/3 of gap was filled in the experiment as shown in Fig. 4(b). In the practical process, the surface of filler metal in the gap would be slightly solidifying with flowing into the gap continuously. However, because the surface profile of filler metal flowed into the gap is only derived from Eqn. (2) and the flow process of filler metal is not modeled, the filler metal seems to achieve to the edge of gap in this computation.

In order to solve this problem, the amount of filler metal flowed is controlled by changing the overhang length of joggle joint. In this study, the overhang length which is 6 mm originally, is shortened to be 3 or 4 mm because about 2/3 of gap was filled in the experiment. Figure 9 shows the penetration shapes computed after first pass welding. In both cases, the filler metal fully flowed into the gap but it did not overflow. Then, the depth of deposit metal becomes deeper and the results show good agreements with the experiment. However, because the amount of filler metal flowed in the case of 3 mm overhang would be smaller than that in the experiment and the thermal energy would concentrate on the groove, the penetration would become to be larger than that in the case of 4 mm overhang. In order to examine the applicability of the combined model for the practical joggle joint, the penetration shape after second pass is also computed where the overhang length is assumed to be 3 or 4 mm as same as the cases for first pass. The results

are shown in Fig. 10 and it is revealed that the thermal energy applied in second pass would not almost affect the penetration produced in first pass and the filler metal deposited in the groove is mainly influenced by this second heat input. In addition, the numerical result of 4 mm overhang has a very good agreement with the experimental result after the second pass and it can be concluded that the penetration shape of the practical joggle joint can be reproduced by combined model with assuming the appropriate overhang length. Moreover, from our previous studies about the basic aluminum joints and these researches about the practical joints, it is found that the penetration shape of the practical aluminum joint can be reproduced by defining the dominant parameters in this combined model through the examinations of the basic welding such as bead-on welding, butt joint welding with the groove and so on.

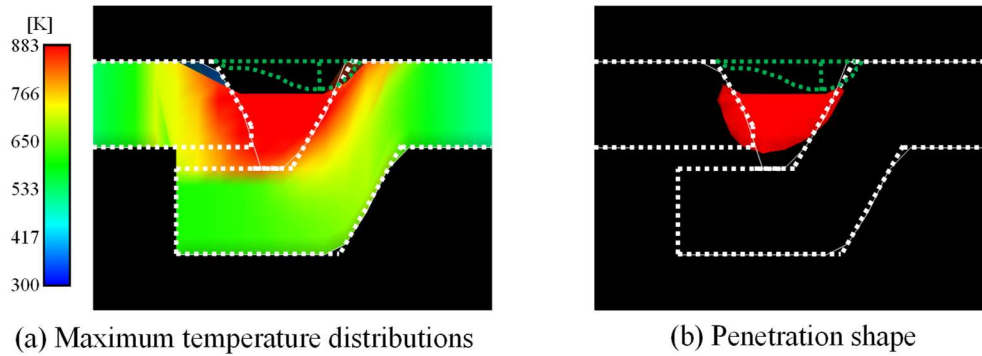


**Fig. 8** Maximum temperature distribution and penetration shape of joggle joint after 1st pass.

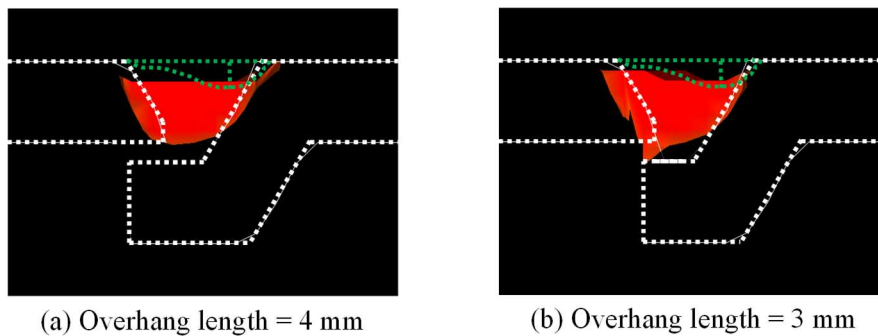


**Fig. 9** Effect of overhang length on penetrations of joggle joint after 1st pass.

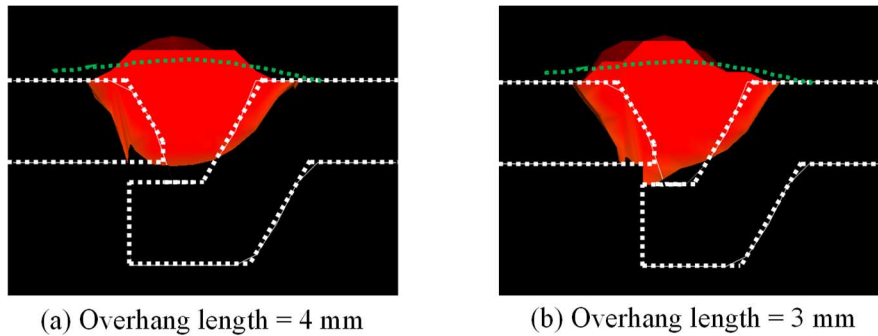


**Fig. 10** Effect of overhang length on penetrations of joggle joint after 2nd pass.

### CONCLUSIONS

In order to demonstrate the finger type penetration generated in MIG welding, a new line-type heat source has been combined with the three-dimensional, non-stationary thermal model and this combined model is applied for reproducing the practical aluminum lap and joggle joints. The conclusions can be summarized as follows,

- By assuming the adiabatic condition due to the oxide layer and/or the physical separation, the penetration shape in the lap joint can be fairly demonstrated, because the oxide layer on the aluminum alloy and/or the physical separation prevent the thermal conductivity.
- Because the combined model cannot simulate the flow process of filler metal and the filler metal achieves to the edge of gap regardless of overhang length in the joggle joint, the overhang length in the numerical model should be appropriately shortened in order to reproduce the penetration shape in the practical joggle joint.
- The penetration shape of the practical aluminum joints can be reproduced by defining the dominant parameters in the combined model through the examinations of the basic welding.

### ACKNOWLEDGEMENTS

The authors would like to express their sincere appreciation to T. Mizuno and M. Enyama (Suzuki Motor Corporation) for providing the experimental data of penetration shapes in the MIG welding of aluminum alloy.

### REFERENCES

- [1] U. DILTHEY AND L. STEIN: 'Technical Trends and Future Prospects of European Automotive Industry', *Proceedings of the 57th IIW International Conference on Technical Trends and Future Prospectives of Welding Technology for Transportation, Land, Sea, Air and Space*, pp. 19-30, 2004.

- [2] H. NISHIKAWA AND M. FUJIMOTO: ‘Control of Rotational Distortion in Friction Stir Welding’, *Proceedings of the 57th IIW International Conference on Technical Trends and Future Prospectives of Welding Technology for Transportation, Land, Sea, Air and Space*, pp. 79-85, 2004.
- [3] H. SERIZAWA, T. YAMAMOTO, H. MURAKAWA, T. MIZUNO, M. ENYAMA AND F. MATSUDA: ‘Prediction of Welding Distortion in a Part of Motorcycle Using Inherent Deformations Obtained from Inverse Analysis for Aluminum Alloy Welded Joints’, *Trends in Welding Research, Proceedings of the 8th International Conference*, pp. 774-780, 2009.
- [4] H. SERIZAWA, J. SHIMAZAKI AND H. MURAKAWA: ‘Numerical Study of Factors for Generating Inherent Strain in Friction Stir Welding’, *Trends in Welding Research 2012, Proceedings of the 9th International Conference*, pp. 922-929, 2013.
- [5] U. SUHUDDIN, L. CAMPANELLI, M. BISSOLATTI, H. WANG, R. VERASTEGUI, J.F. DOS SANTOS: ‘A Review on Microstructural and Mechanical Properties of Friction Spot Welds in Al-based Similar and Dissimilar Joints’, *Proceedings of the 1st International Joint Symposium on Joining and Welding*, pp. 15-21, 2013.
- [6] W.G. ESSERS AND R. WALTER: ‘Heat Transfer and Penetration Mechanisms with GMA and Plasma-GMA Welding’, *Welding Research Supplement*, February, pp. 37-s-42-s, 1981.
- [7] M. SHOEB, M. PARVEZ AND P. KUMARI: ‘Effect of MIG Welding Input Process Parameters on Weld Bead Geometry on HSLA Steel’, *International Journal of Engineering Science and Technology*, Vol. 5, No. 1, pp. 201-212, 2013.
- [8] U. DILTHEY AND S. ROOSEN: ‘Computer simulation of Thin sheet Gas-Metal-Arc-Welding’. *Proceedings of International Symposium on Theoretical Prediction in Joining and Welding*, Joining and Welding Research Institute, Osaka University, pp.133-154, 1996.
- [9] J.-W. Kim and S.-J. Na: ‘A Study on the Three-Dimensional Analysis of Heat and Fluid Flow in Gas Metal Arc Welding Using Boundary-Fitted Coordinates’, *Journal of Engineering for Industry*, Volume 116, Issue 1, pp.78-85, 1994.
- [10] E. PARDO AND D.C. WECKMAN: ‘Prediction of Weld Pool and Reinforcement Dimensions of GMA Welds Using a Finite-Element Model’, *Metallurgical Transactions B*, Vol. 20B, pp.937-947, 1989.
- [11] Z. CAO, Z. YANG AND X.L. CHEN: ‘Three-Dimensional Simulation of Transient GMA Weld Pool with Free Surface’, *Welding Journal*, June, pp.169-S-176-S, 2004.
- [12] A. KUMAR AND T. DEBROY: ‘Guaranteed Fillet Weld Geometry from Heat Transfer Model and Multivariable Optimization’, *International Journal of Heat and Mass Transfer*, Vol. 47, pp.5793-5806, 2004.
- [13] T. YAMAMOTO, T. OHJI, F. MIYASAKA AND Y. TSUJI: ‘Mathematical Modelling of Metal Active Gas Arc Welding’, *Science and Technology of Welding and Joining*, Vol. 7, No. 4, pp. 260-264, 2002.
- [14] T. YAMAMOTO, Y. YAMAZAKI, Y. TSUJI, F. MIYASAKA AND T. OHJI: ‘Simulation Software of MAG Arc Welding for Butt Joint’, *Quarterly Journal of the Japan Welding Society*, Vol. 23, No. 1, pp. 71-76, 2005 (in Japanese).
- [15] Y. YAMAZAKI, F. MIYASAKA AND T. OHJI: ‘A Simulation Model for High Speed MAG Welding for Thin Plate’, *Quarterly Journal of the Japan Welding Society*, Vol. 24, No. 4, pp. 368-372 2006 (in Japanese).
- [16] H. SERIZAWA, M. YOSHIYAMA AND F. MIYASAKA, ‘Development of Line-type Heat Source for Finger Type Penetration in MIG Welding’, *Mathematical Modelling of Weld Phenomena 11*, Verlag der Technischen Universität Graz, pp.51-61, 2017.

# NUMERICAL INVESTIGATION OF THE INFLUENCE OF WELDING PARAMETERS ON THE WELD POOL DYNAMICS AND THE DISTRIBUTION OF SECOND PHASE PARTICLES

R. KABOLI\*, M. MASSOUDI FARID\*\*, R. KRAMER\*,  
G. ERTUGRUL\* and P. MAYR\*

*\*Chemnitz University of Technology, Germany*

*\*\*Freiberg University of Technology, Germany*

DOI 10.3217/978-3-85125-615-4-03

## ABSTRACT

Plasma transferred arc welding (PTA) is widely used to deposit metallic materials on substrates in order to improve for example wear resistance, chemical resistance or thermal shock resistance. In terms of wear resistance, a homogeneous distribution of hard second phase particles in the deposited weld metal is favorable to achieve uniform properties. Therefore, it is important to know how the distribution of particles is affected by the welding parameters and the welding procedure in general. While experimental methods have only limited ability to provide a comprehensive insight into the weld pool dynamics, the numerical simulation of the PTA process does but is at the same time also a challenging task.

Within this work, the influence of PTA welding parameters on weld pool dynamics and distribution of second phase particles in the solidified weld metal is investigated applying thermodynamic and numerical simulation. As matrix material, a CoCr alloy (Stellite 6) is used and tungsten carbide particles are included as hard second phase. The finite volume simulation using the software package ANSYS Fluent considers several physical phenomena such as solidification/melting, magnetohydrodynamics (MHD), magnetic fields, etc. The solidification behaviour is studied using the thermodynamic software package ThermoCalc. The established numerical models solve the equations of the conservation of mass, momentum and energy by means of the Euler–Euler and Euler–Lagrange method.

Within this work, it was shown that thermodynamic and numerical simulations are valuable tools to describe weld pool dynamics as a function of different welding parameters for the PTA process. The distribution of second phase particles in a solidified metallic matrix was directly linked to the weld pool movement and can therefore be optimized. Simulation was verified by welding trials and subsequent metallographic characterisation.

Keywords: Plasma transferred arc welding, ANSYS Fluent, multiphase flow, Euler–Euler method, Euler–Lagrange method



## INTRODUCTION

Plasma transferred arc welding (PTA) is one of the most useful surface modification processes. A high power plasma column is used to melt feeding material and a thin layer of substrate to form a coating layer. The coating layer is characterized by low viscosity, which is perfectly bonded to the substrate. The power density of the PTA welding (50-100 kW/cm<sup>2</sup>) takes an intermediate position between arc welding (<15 kW/cm<sup>2</sup>) and laser/electron beam welding (>100 kW/cm<sup>2</sup>) [1]. The particular characteristics of PTA welding enables it to modify the surface, which lead to achieve excellent wear and corrosion resistance whereas the toughness of the bulk material is maintained. Therefore, PTA welding provides an excellent technology to optimize the properties of materials and to improve the functionality of them. The characterization, modeling, metallurgical and microstructure analyses have been the main research interests in PTA welding. Drastic progress has been made during the past years and has been reported [2,3].

A series of Co based alloys has been developed as surface modifying materials for steel components. Stellite 6 (Co-Cr) is widely used for surface modification due to its excellent properties. The strengthening mechanisms are solid solution and precipitation hardening [4]. The properties of the surface layer can be further improved by means of the additional embedded hard particles such as tungsten carbides (WC, W<sub>2</sub>C). The strength and wear resistance can be significantly improved by adding a small amount of hard materials to the surface layer. In this research, a combination of Stellite 6 (which will act as matrix) and tungsten carbide (WC) powder were used in this experiment. A schematic of the PTA process is shown in Fig. 1. Powders are supplied by a carrier gas to form a deposit layer on the base metal. A non-transferred plasma arc (pilot arc) is initially ignited between anode and cathode in the plasma torch to achieve ionisation of the gas. Then the transferred plasma arc (main arc) is started between the base metal and the tungsten electrode and it supplies the molten powders to the base metal. Thereby, a thin and dense coating layer with low dilution is generated on the base metal.

Because of the importance of film formation, several researchers have developed various models to predict film formation and relevant quantities [6,7]. Most of these models are valid for thin films. None of these models can be applied for the thick film modelling where 3D flow inside the film needs to be captured. A pure VOF approach can be used for modelling 3D flow inside the film. However, modelling these tiny droplets using pure VOF approach would need a very large number of mesh elements and is thus beyond the scope of practical computation limits. In this work, a lagrangian particle is tracked by a Discrete Phase Model. As this particle reaches the melting temperature, it is converted to an eulerian droplet using a User Defined Function (UDFs) in ANSYS Fluent. This droplet is further tracked in an Eulerian frame-work using a Euler-Euler model. This hybrid DPM-to-Euler-Euler approach enables taking the advantages of both the basic lagrangian and eulerian models into account. The DPM model, which is computationally less intensive, takes care of the particle movement in the bulk of the domain and the more accurate model Euler-Euler models takes care of the resulting droplet.

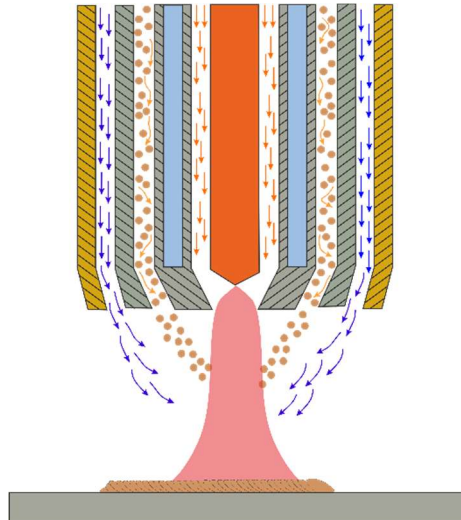


**Fig. 1** The schematic of the PTA process.

### NUMERICAL MODEL

The goal of this research project is the investigation of the physical phenomena such as heat and mass transfer, electromagnetic and hydrodynamic processes in PTA welding with multi-metal powders and the estimation of their influence on the weld bead formation by methods of numerical simulation. The number of different physics involved in PTA makes its simulation challenging especially when all four states of matter namely solid, liquid, gas and plasma must be considered and numerous physical phenomena interact together.

To solve such a complex model, the problem is divided into two sub-models. The first model covers the formation of plasma. The second model was developed to investigate the injection and the tracking of particles, melting and solidification as well as the formation of the weld bead (see Table 1).

**Table 1** sub-models and the modules

<b>Plasma model</b>	<b>Particle trace and melt model</b>
Electric currents	Particle injection
Magnetic field	Particle tracing
Joule heating	Particle melting
Laminar flow	Laminar flow
Heat transfer	Heat transfer
Magnetohydrodynamic (MHD)	Melting and solidification

## PLASMA MODEL

The Plasma model was developed in the simulation software COMSOL. The computation domain is shown in Fig. 1. The welding arc is formed between the tungsten electrode and the steel workpiece. The Direct Current Electrode Negative (DCEN) polarity is used, therefore the tungsten electrode is the cathode and the steel workpiece is the anode. The computation domain and the boundary conditions are shown schematically in Fig. 2.

The plasma model is based on the following assumptions:

- The computation domain is axially-symmetric
- The problem is solved in steady state since the arc enters into steady state just after arc formation
- The arc is stationary and under atmospheric pressure
- Gas flow is laminar and incompressible
- The arc plasma is in Local Thermodynamic Equilibrium (LTE)
- Metal vapors are not taken into account
- Gas properties change only with the temperature
- Debye sheath are not considered

## GOVERNING EQUATIONS

In the steady state and under axial-symmetric conditions, the governing equations, which describe arc plasma motion, are as follows:

Mass conservation:

$$\frac{\partial}{\partial z}(\rho \cdot u_z) + \frac{1}{r} \frac{\partial}{\partial r}(\rho \cdot r \cdot u_r) = 0 \quad (1)$$

Radial momentum conservation:

$$\begin{aligned} & \frac{1}{r} \frac{\partial}{\partial r}(\rho \cdot r \cdot u_r^2) + \frac{\partial}{\partial z}(\rho \cdot u_r \cdot z) = \\ & -\frac{\partial P}{\partial r} + \frac{1}{r} \frac{\partial}{\partial r} \left( 2r\mu \frac{\partial u_r}{\partial r} \right) + \frac{\partial}{\partial z} \left( \mu \left( \frac{\partial u_z}{\partial z} + \frac{\partial u_r}{\partial r} \right) \right) - 2\mu \frac{u_r}{r^2} - j_z B_\theta \end{aligned} \quad (2)$$

Axial momentum conservation:

$$\begin{aligned} & \frac{1}{r} \frac{\partial}{\partial r}(\rho \cdot u_r \cdot u_z) + \frac{\partial}{\partial z}(\rho \cdot u_z^2) = \\ & -\frac{\partial P}{\partial z} + \frac{\partial}{\partial z} \left( 2\mu \frac{\partial u_z}{\partial z} \right) + \frac{1}{r} \frac{\partial}{\partial r} \left( r\mu \left( \frac{\partial u_z}{\partial r} + \frac{\partial u_r}{\partial z} \right) \right) - j_i B_\theta \end{aligned} \quad (3)$$

Energy conservation equations:

$$\begin{aligned} & \frac{1}{r} \frac{\partial}{\partial r}(r \cdot \rho \cdot C_p \cdot u_r \cdot T) + \frac{\partial}{\partial z}(\rho \cdot C_p \cdot u_z \cdot T) = \\ & \frac{1}{r} \frac{\partial}{\partial r} \left( rk \frac{\partial T}{\partial r} \right) + \frac{\partial}{\partial z} \left( k \frac{\partial T}{\partial z} \right) + \frac{J_z^2 + J_r^2}{\sigma} + \frac{5k_B}{2e} \left( J_r \frac{\partial T}{\partial r} + J_z \frac{\partial T}{\partial z} \right) - U \end{aligned} \quad (4)$$

## Mathematical Modelling of Weld Phenomena 12

Where subscripts  $r$  and  $z$  denote radial and axial directions, respectively. The terms in the planes are special momentum and energy source terms concerning with plasma. In equations 1-4, the basic variables defined are temperature  $T$ , pressure  $P$ , radial velocity  $u_r$  and axial velocity  $u_z$ . The plasma property functions are density  $\rho$ , viscosity  $\mu$ , specific heat  $C_p$ , thermal conductivity  $k$  and electrical conductivity  $\sigma$  [5]. The current density components and the magnetic inductive intensity required in Eq. 2, 3. and 4 are obtained by Maxwell's equations described in the magnetic vector potential format:

$$E = -\nabla\varphi - \frac{\partial A}{\partial t} \quad (5)$$

$$B = \nabla \times A \quad (6)$$

Where  $E, \varphi, B, A$  are electrical field vector, electrical potential, magnetic inductive intensity vector, and magnetic vector potential. Under the steady state and axially symmetric conditions, the governing equations can be derived as:

Current continuity equations:

$$\frac{1}{r} \frac{\partial}{\partial r} \left( r \cdot \sigma \cdot \frac{\partial \varphi}{\partial r} \right) + \frac{\partial}{\partial z} \left( \sigma \cdot \frac{\partial \varphi}{\partial z} \right) = 0 \quad (7)$$

Ampere's law ( $\mu_0 = 4\pi \times 10^{-7}$ )

$$\frac{1}{r} \frac{\partial}{\partial r} \left( r \frac{\partial A_z}{\partial r} \right) + \frac{\partial}{\partial z} \left( \frac{\partial A_z}{\partial z} \right) = \mu_0 \cdot j_z \quad (8)$$

$$\frac{1}{r} \frac{\partial}{\partial r} \left( r \frac{\partial A_r}{\partial r} \right) + \frac{\partial}{\partial z} \left( \frac{\partial A_r}{\partial z} \right) = \mu_0 \cdot j_r \quad (9)$$

$$j_z = -\sigma \frac{\partial \varphi}{\partial z} \quad (10)$$

$$j_r = -\sigma \frac{\partial \varphi}{\partial r} \quad (11)$$

For converting  $A$  to  $B$  necessary in Eq. 5 and 6, a component of Eq. 6 is written as:

$$B_\theta = \frac{\partial A_r}{\partial z} - \frac{\partial A_z}{\partial r} \quad (12)$$

Thermodynamic properties and the transport coefficients of argon are taken from the COMSOL database. After it, the modules, which are mentioned in table 1, were coupled to solve the problem.

This numerical model is based on the Bauchire et al.'s model [5]. As mentioned in their work, the equations are highly non-linear. Attention must be paid for initiating and reaching convergence. An initial temperature of 10,000 K or greater must be set to ensure that the gases are fully ionized to reach convergence in the numerical solution. After solving the

## Mathematical Modelling of Weld Phenomena 12

plasma model, the calculated temperature and velocity fields were imported as input for the second model.

### PARTICLE TRACE AND MELT MODEL

The discrete phase model (DPM) with a lagrangian approach coupled with a Volume of Fraction (VOF) approach was applied to trace particles and melt in ANSYS Fluent. Particles were tracked in lagrangian frame as point sources. Two-way coupling was used to simulate the energy and momentum exchange with eulerian gas phase (Fig. 3). The DPM model is ideally suited for situations where particles enter and leave the computational domain. The discrete parcels of particles were uniformly distributed and injected through the powder inlet at each time step. Each parcel was tracked separately. The DPM model is suitable for dilute particulate flow when the particle mass fraction is lower than 10%.

After the injection of particles in the domain, some of the particles were heated up to melting temperature and were molten and some of them which have not reached the melting temperature were still considered as lagrangian particle. The molten particles were deleted from the Euler-Lagrange frame and imported to the Euler-Euler frame via a user defined function (UDF) in ANSYS Fluent. In order to simulate phase interfaces of particles, the Euler-Euler method was used.

As mentioned earlier, Euler-Euler method has been used in this work, which is the most complex of the multiphase models in ANSYS Fluent. It solves a set of  $n$  momentum and continuity equations for each phase. Coupling is achieved through the pressure and interphase change coefficients. The melting temperature, melting enthalpy and heat capacity of Stellite and tungsten carbide have been calculated via the thermodynamic software ThermoCalc and imported in ANSYS Fluent as input.

### EXPERIMENTAL SETUP

A welding robot equipped with a plasma torch was used to carry out experimental investigations. In order to validate the simulation results, thermocouples were welded on top of the metal sheet to capture the temperature during the welding process (Fig. 2).

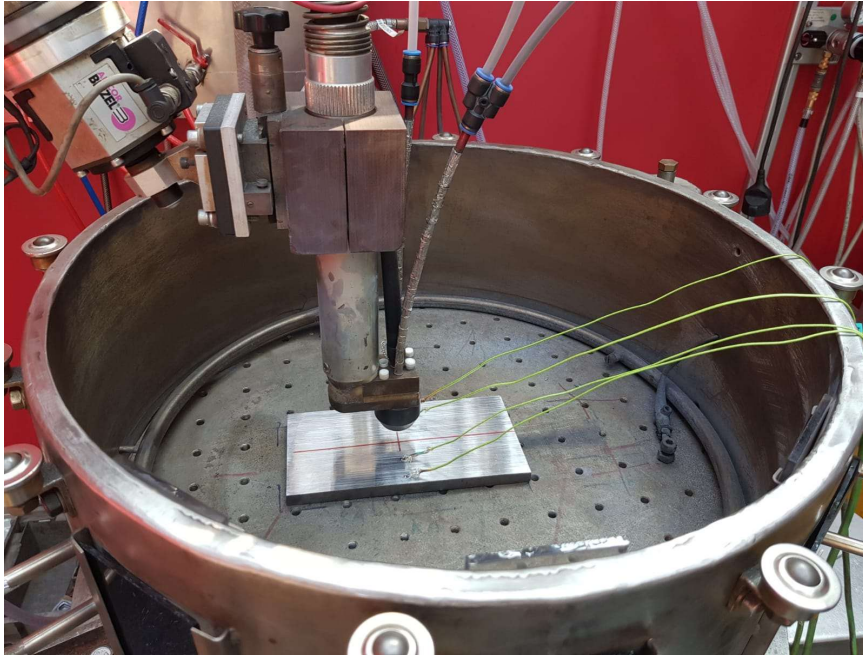


Fig. 2 The experimental setup.

## RESULTS AND DISCUSSION

In order to have a better understanding of the PTA process and to explain the experimental results, a CFD-Model was developed using the commercial software COMSOL and ANSYS Fluent.

The following welding conditions were assumed in the model: a current density of  $1e8$  [ $A/m^2$ ], a minimum value  $\sigma_{min}$  of 1 [ $s/m$ ] in the argon region and the plasma gas and shielding gas flow rate is fixed to 2 L/min and 8 L/min, respectively.

Figures 3 and 4 show the temperature and velocity fields under steady state conditions inside the arc plasma and the simulation domain. The maximum temperature of 12000 K and the maximum velocity of 7 m/s were observed.

## Mathematical Modelling of Weld Phenomena 12

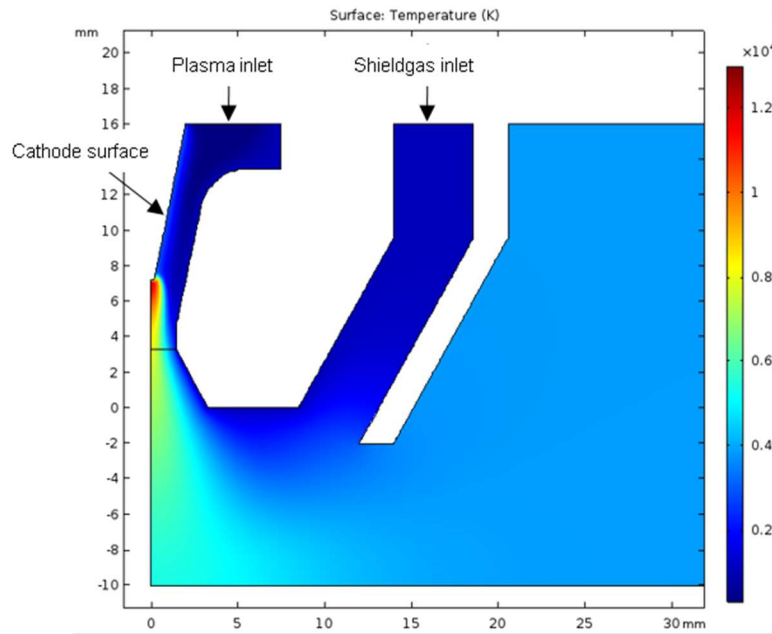


**Fig. 3** Calculated temperature fields in COMSOL.

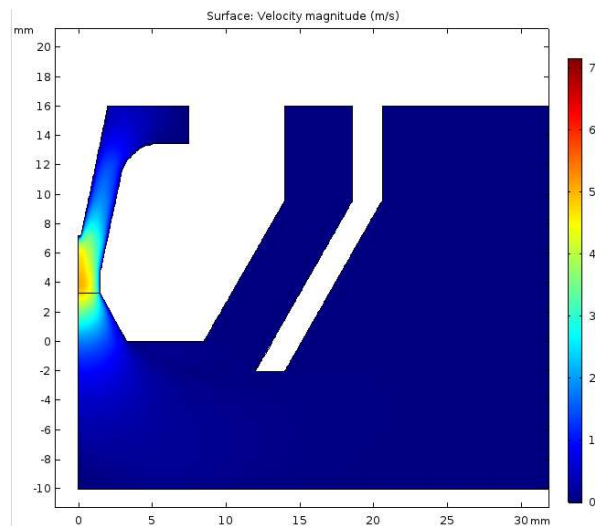


**Fig. 4** Contours of velocity magnitude fields in COMSOL.

These results were imported to ANSYS Fluent to simulate particle tracking and melting. A wide range of material/physical properties affected the particle melting. Among material properties and process conditions, melting rate of the particle, wetting angle, surface tension at the interface and viscosity were the main affecting parameters. Unfortunately, most of these parameters were unknown for Stellite 6 and WC. Therefore, some estimated values were used in the model. The particle temperature is shown in figures 5a and 5b at various times. It shows that the particles which reached the melting temperature were dissolved

from the Euler-Lagrange domain and added to the Euler-Euler domain. It also shows that some particles, which did not reach the melting temperature, left the domain which was observed by experimental investigations (Fig 6).

The weld bead after solidification and phase fraction of Stellite and tungsten carbide are shown in Figure 7. They are in agreement with numerical results (Fig 8).

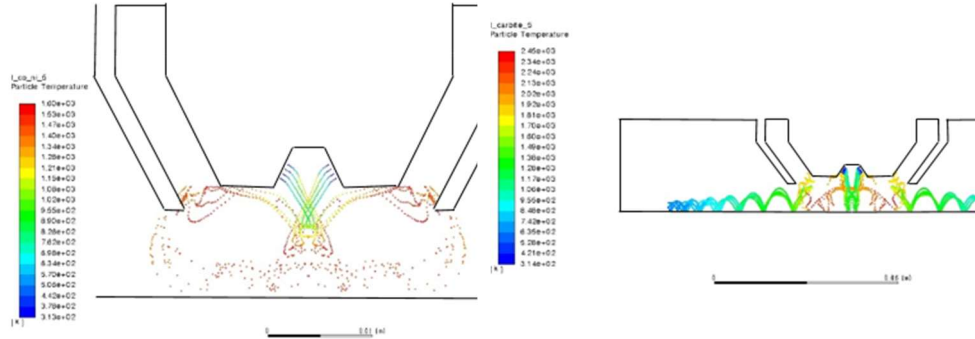


Fig. 5a and 5b particle temperature of Stellite (left) and WC (right).

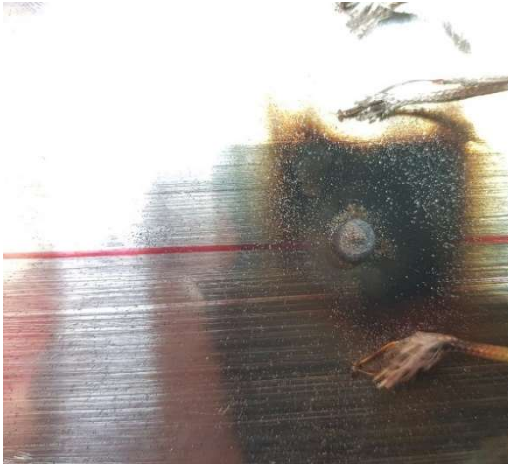


Fig. 6 unmolten particles on the surface of the test plate.

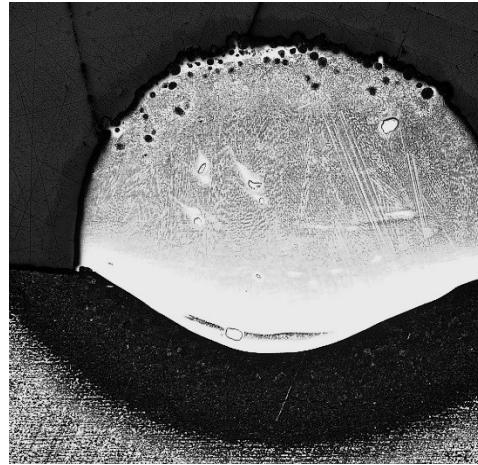


Fig. 7 weld bed after 10 seconds.

It was observed that the value of the surface tension between phases and wetting angle between phases and the bottom edge of domain had a very big influence on the shape of the welding bead. The values of these parameters need to be studied via experimental investigations.



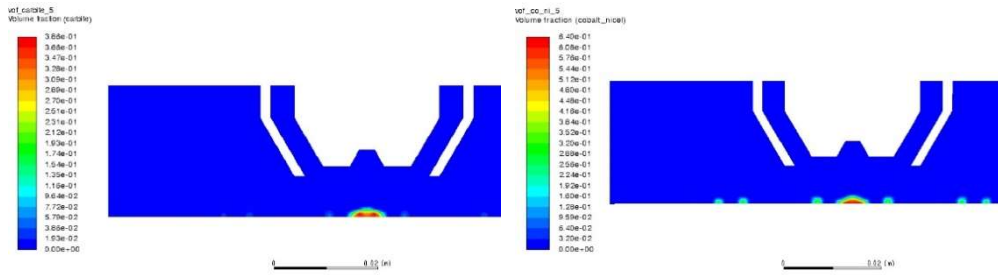


Fig. 8 phase fraction of WC (left) and Stellite 6 (right).

Figure 9 shows the velocity and temperature fields of argon. The velocity field under the plasma column is affected by the molten particles as expected. The model predicts the effect of melting enthalpy of the temperature fields correctly.

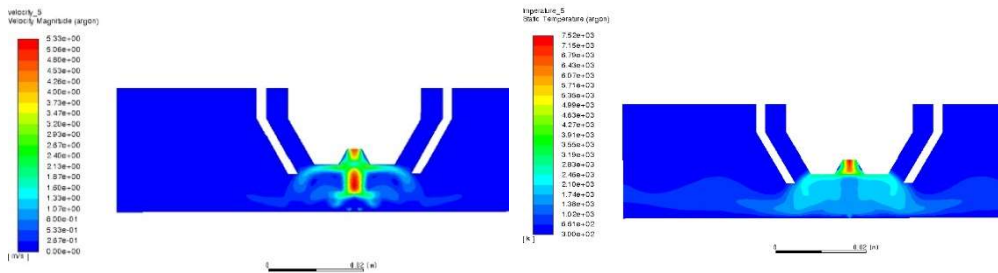


Fig. 9 velocity (left) and temperature fields (right) after 10 seconds.

### CONCLUSIONS

In this paper, a heat transfer and fluid flow model for PTA welding is presented. This model can explain the phenomena particle melting and weld pool shape formation. Gravity, electromagnetic forces, arc pressure and Marangoni effect were taken into account.

The DC plasma torch was modeled by developing a 2D axisymmetric model of laminar flow and heat transfer, coupled with the electromagnetic field. Lorentz force and joule heating effects were modeled, coupled with the physical model of the plasma torch. In order to ensure that the electric flow was ensured, an artificial minimum value of 8000 S/m for the electrical conductivity of argon was used. The numerical results of the gas temperature and axial velocity results were quite satisfactory, although more complete reproductions of the thermal and fluid phenomena might be obtained with three-dimensional modelling. In that case, computational requirements and computing times should be also taken into account.

A multi-phase flow model was established, and ANSYS Fluent was applied to simulate the multi-phase flow for gaining significant insight into understanding of particle melting and phase distribution bead formation mechanism. Melting rate of the particle, wetting angle, surface tension at the interface and viscosity were the main affecting parameters and must be set carefully. The calculation results were reasonable and reliable. It can be

concluded that the presented CFD method is a powerful approach to investigate mechanisms of the PTA process

### ACKNOWLEDGEMENTS

The authors gratefully acknowledge the funding by the German Research Foundation (Deutsche Forschungsgemeinschaft, DFG) within the project MA 5861/6-1 “Process-oriented modeling and simulation of unsteady modulated gas flows in plasma powder cladding to influence layer properties”.

### REFERENCES

- [1] S.H. KANG, T. SHINODA, Y. KATO and H.S. JEONG: ‘Thermal Fatigue Characteristics of PTA Hardfaced Steels’, *Surface Engineering*, Vol. 17, No. 6, pp. 498-504, 2001.
- [2] P.F. MENDEZ, N. BARNES, K. BELL, S.D. BORLE, S.S. GAJAPATHI, S.D. GUEST, H. IZADI, A.K. GOL, and G. WOOD: ‘Welding processes for wear resistant overlays’, *Journal of Manufacturing Processes*, Vol. 16, pp. 4-25, 2014.
- [3] S.H. NIKAM, N.K. JAIN, and S. JHAVAR, and G. WOOD: ‘Thermal modeling of geometry of single-track deposition in micro-plasma transferred arc deposition process’, *Journal of Materials Processing Technology*, Vol. 230, pp. 121-130, 2016.
- [4] J.L. ACEVEDO-DÁVILA A, R. MUÑOZ-ARROYO A, H.M. HDZ-GARCÍA A, A.I. MARTINEZ-ENRIQUEZ B, M. ALVAREZ-VERA A and F.A. HERNÁNDEZ-GARCÍA: ‘Cobalt-based PTA coatings, effects of addition of TiC nanoparticles’, *Vacuum*, Vol. 143, pp. 14-22, 2017.
- [5] J. BAUCHIRE, J. M. GONZALEZ and A. GLEIZES: ‘Modeling of a DC Plasma Torch in Laminar and Turbulent Flow’, *Plasma Chemistry and Plasma Processing*, Vol. 17, No. 4, pp. 409-432, 1997.
- [6] J. SENDA and H. Fujimoto: ‘Multidimensional modelling of impinging sprays on the wall in diesel’, *ASME*, 2009.
- [7] R. SCHMEHL, R. ROSSKAMP, and S. WITTING: ‘CFD analysis of spray propagation and evaporation including wall film formation and spray/film interactions’, *International journal of heat and fluid flow*, Vol. 20, No. 5, pp. 520-529, 1999.



# A FINE MODIFICATION OF THE DOUBLE ELLIPSOID HEAT SOURCE

O. MOKROV\*, M. SIMON\*, A. SCHIEBAHN\* and U. REISGEN\*

*\*RWTH Aachen University, ISF – Welding and Joining Institute, 52062, Aachen, Germany, mokrov@isf.rwth-aachen.de*

*DOI 10.3217/978-3-85125-615-4-04*

## ABSTRACT

The analysis of residual stresses or distortion of welded structures uses the prediction of the local temperature field. The calculation of the temperature field requires the definition of heat source. The double ellipsoid Goldak equivalent heat source (EHS) is the most used heat input model for arc welding. This model distributes the heat of the arc welding process in a volume, which is equal to a melted weld pool. The heat flow calculation with the EHS reaches a compliance of the experimental and the calculated temperature field, which is far from the weld seam. Close to the weld seam and especially at the fusion zone these results are hardly reachable with the Goldak model. Another disadvantage of Goldak's EHS is a very high non-physical energy density in the centre of the heat distribution. The reasons behind these disadvantages are analysed. It is shown how to modify the equation of the double ellipsoid heat source to secure the benefits of EHS and simultaneously eliminate the disadvantages of the model. A comparison between real experiments, calculations with Goldak's EHS and the modified EHS Modification-R<sup>10</sup> (EHS MR10) shows a significant improvement of the results using EHS MR10. The distribution of power density is described in the modified EHS by a function of the tenth power and therefore referred to as MR10.

## INTRODUCTION

Welding processes lead, because of the strong time-dependent and locally concentrated heat input in real components, almost always to a deformation of the structure. This deformation is generally unwanted and causes problems on the orientation and adaptation tolerance with neighboring structures. These problems are especially pronounced on comparatively heat-intensive welding procedures like electric arc welding. Detailed research projects have been already carried out in order to reduce the appearing welding warpages.

In this context, simulation offers a good opportunity to calculate and study the residual stresses and warpages as well as the structure transformations. The simulation of the residual stresses distortion, according to Radaj [1, 2], is defined as a structure simulation or welding simulation due to heat input, Fig. 1. The most important requirement for calculating the heat input via FEM-based simulation packages is an appropriate heat source description, which guarantees a good agreement of the numerical simulation results with the real temperature relationships in electric arc welding. Based on this, reasonable boundary conditions for the welding structure simulation can be defined.

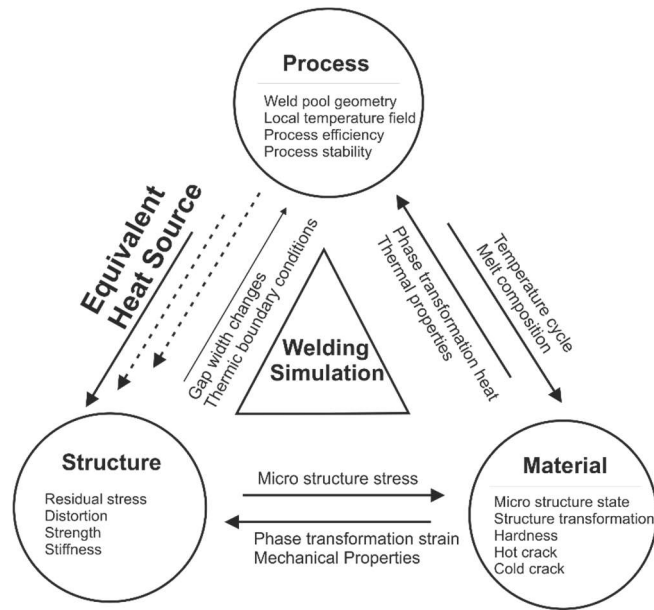


**Fig. 1** Welding simulation areas according to Radaj [1,2].

Usually different models for the heat sources are used: unidimensional point heat sources, two-dimensional superficial distributions and three-dimensional volumetric distributions as well as combinations of these. The application of these models for the simulation of residual stresses and warpage requires, in the corresponding FEM-programs, usually an elaborate calibration procedure.

Therefore a necessity arises for a heat source and its adaptation procedure, which facilitates a higher precision for the simulation of the heat input and a reduction of the calibration effort.

#### HEAT SOURCE APPLICATION IN WELDING SIMULATION

The first to accomplish a mathematical description of welding heat sources were Rosenthal [3, 4] and Rykalin [5]. The power density distribution of electric arc welding was described by means of an adaptation of the Gauss equation with the application of an intensity parameter to ensure that the whole power is inputted within the arc affected area. The phenomenological explanation for the application of the Gauss function in the construction of the heat source models is based on the original idea of the electric arc process as a combination of stochastic, physical processes.

The EHS by Goldak[6, 7, 8] is an extension of this concept to the case of volumetric heat input. The goal was to account for metal flow within the weld pool. Here the intensity parameter assures too that the whole power is inputted within both quarter-ellipsoids (fourths of the ellipsoid). A quick overview over different approaches for heat source modelling is shown in Table 1.

**Table 1** Overview over approaches for Equivalent Heat Sources.

Name	Method
Rosenthal [3, 4], Rykalin [5]	Function-analytical solutions by linearization of the heat conduction process in a homogeneous and isotropic continuum with the neglect of the convection in the weld pool
Rykalin [5]	Plane heat density distribution, based on the Gaussian distribution
Goldak et al. [6, 7, 8]	Distributed volumetric heat sources
Radaj [1]	Solidus surface as an equivalent heat source
Schwenk et al., Pittner et al. [9, 10]	Synthetical approach by decomposition of the process model into an empirical part, which is based on neuronal networks, and a phenomenological part, which describes the physical phenomena
Karkhin et al. [11]	Detailed description for the function-analytical creation of a volumetric heat source

The following examples show a few of many applications of the equivalent heat source (EHS) by Goldak in welding simulation. In a work of Schenk et al. [12], the impact of clamping technology on the appearing deformations were examined both experimentally and also through simulation. The necessary clamping technology for welding causes, in practice, substantial costs to some extent. For this, the choice of the clamping points and the resulting influences on the deformation have to be researched. In this work, the GMA welding of T-joint components of steel (S355) were examined for different clamping configurations. Measured welding temperatures and the resulting deformations were determined for two clamping configurations and compared with the simulations. For the modelling of the heat input, a two-dimensional simplification of the Goldak heat source was used. The work emphasizes, for a good agreement between simulation and experiment, the influence of the clamping configuration on marked-ness and shape of the appearing deformations.

Another work of the same group [13] presented a thermo-mechanical, metallurgic, microscopical model for steel, which well describes the material behavior in welding. The model is based on an existing model, which was extended for non-isothermal behavior in combination with phase transformation. The model and its numerical implementation in ABAQUS are described with vector notation for the stress and load tensors. In order to model the heat input, a Goldak heat source was implemented in ABAQUS in the user-subroutine DFLUX. Model parameters were presented for the steels DP600 and S355. Thermo-mechanical model parameters for DP600, namely hardening and stretching rate, were kept by adapting the temperature and stretching rate. A metallurgical model was implemented with help of the data gathered from the phase field models for the austenite-growth and the continuous cool-down transition diagrams for phase transformations from austenite. The model was applied to the welding simulations of DP600 for lap joint and S355 in T-joint geometries. The final warpage was compared with the experimental results and it was shown, that the presented model is capable of reproducing the experimental results very well.

This and many other examples show that for the illustration of the volumetric heat distribution in electric arc welding, here for the example of gas metal arc welding (GMAW), typically the double ellipsoid equivalent heat source model by Goldak is used. It is comparatively easy to determine and yields higher agreement (e.g. for the external boundaries of the heat affected zone when welding metallic materials) than other heat source models [6, 14].

The EHS by Goldak serves as de-facto standard for a model of heat input for the FEM-based welding structure simulation in the case of gas metal arc welding (GMAW). On SYSWELD or Simufact Welding is, for example, the EHS, one of the predefined heat sources. This applies also for comparatively complex calculation cases.

### DOUBLE ELLIPSOID EQUIVALENT HEAT SOURCE MODEL BY GOLDAK

The EHS by Goldak (Fig. 2) is described by six parameters (four geometrical and two energetic) and is based on the equation of Rosenthal and Rykalin for the superficial heat distribution in electric arc welding.

In the distribution by Rykalin and Rosenthal leads the intensity parameter of 3 to almost the whole supplied energy to be within the affected zone of the welding area. The EHS by Goldak underlies the same concept. Here the intensity parameter assures that the whole power is inputted within both quarter-ellipsoids (fourths of the ellipsoid), which corresponds to the normal conditions of electric arc welding.

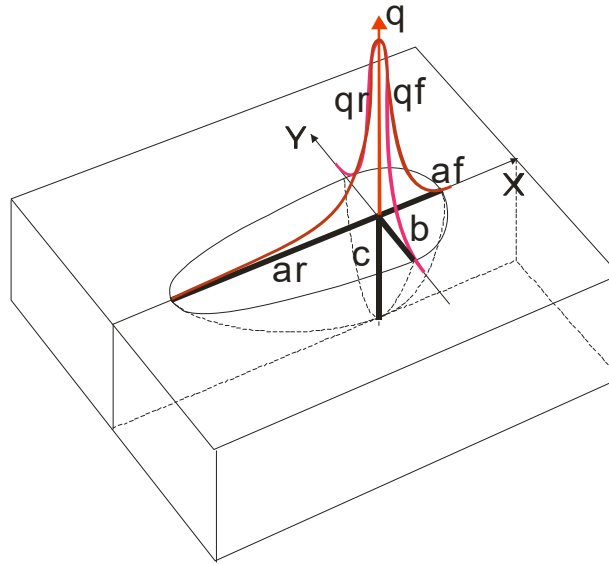


**Fig. 2** Schematic illustration of the distribution of the EHS by Goldak [6].

The four geometric parameters are normally defined before the calibration through experimentally defined or through simulation-aided prediction of the weld pool shape. They represent in detail the width and depth of the weld pool as well as the maximum distance between the broadest spot of the pool to the melt front and to the solidification front. The two energetic parameters represent the inputted energies in both quarter-ellipsoids. These were measured experimentally or estimated. Additionally, a measured, calculated or estimated efficiency factor is defined.

$$q_f(x, y, z, t) = \frac{6\sqrt{3}f_f Q}{a_f b c \pi \sqrt{\pi}} \exp\left(-3 \frac{(x+v(\tau-t))^2}{a_f^2}\right) \exp\left(-3 \frac{y^2}{b^2}\right) \exp\left(-3 \frac{z^2}{c^2}\right) \quad (1a)$$

## Mathematical Modelling of Weld Phenomena 12

$$q_r(x, y, z, t) = \frac{6\sqrt{3}f_r Q}{a_r b c \pi \sqrt{\pi}} \exp\left(-3 \frac{(x+v(\tau-t))^2}{a_r^2}\right) \exp\left(-3 \frac{y^2}{b^2}\right) \exp\left(-3 \frac{z^2}{c^2}\right) \quad (1b)$$

$$f_f + f_r = 2 \quad (1c)$$

$$2Q = \left(q_f(x, y, z, t) + q_r(x, y, z, t)\right) dx dy dz \quad (1d)$$

$$Q = \text{Heat}, [W]$$

Although the Goldak-EHS shows a better agreement for the heat affected zone (HAZ) compared to other heat source models, the precision is less satisfying in the area of the weld seam. In order to increase the precision, numerous experiments are carried out [1, 2, 7]. These serve for the calibration, the goal is thereby to achieve maximal agreement with the melt boundary and the weld pool shape, as well as the time-temperature cycles. As a rule, the achieved accordance comes with a calculated temperature that is too high, usually above the evaporation temperature, in the center of the EHS, as well as with a too low temperature on the edge of the EHS.

The problems are known to both engineers and scientists as well as developers of simulation programs. Different solutions were suggested, among others e.g. the variation of the intensity parameter (1 or 2, instead of 3) in the Goldak equation with the corresponding modification of the first normalization multiplier or an automatic calibration of the EHS in SYSWELD. These measures bring, however, only limited improvements and lead to an implausible form of the heat input. The problems, which appear during the calibration of the EHS by Goldak come as a consequence of the fact that the mathematical equation is based on the Gaussian distribution, which has in combination with the intensity parameter a strong maximum in the center of the distribution and the integration of the equation yields 1 as a result. This particularity is very helpful for analytical solutions and allows for an easy normalization for any powers.

The equation yields values, which decrease exponentially depending on the distance to the center. The approach of the distribution brings often a high accordance for the solid phase for the temperature calculation. The maximum value in the center of the distribution corresponds also to the idea of the maximal heat input in the center of the heat source for electric arc welding, which is not necessarily always the case. The model idea for the heat input in this form does not sufficiently consider the hydrodynamics in the weld pool, which could significantly decrease the heat input and the temperature gradient in the weld pool. The maximal temperature in the center follows from the balance between the heat input and the heat dissipation, so for example an even volumetrically distribution in the simulation causes also a maximal temperature in the center of the distribution. Also, hydrodynamics in the weld pool and their impact are, not stochastic processes and therefore don't follow a Gaussian distribution, but on the contrary tend to smooth out the power density gradients. It is therefore plausible to develop a volumetric distribution equation with decreased gradients in the center of the heat source distribution, but at the same time higher power density at the edge of the weld pool.

The development of a modified EHS followed in this application based on the approach by Goldak allows for an increased precision in the representation of the real heat source with a significantly lower calibration effort.



MODIFICATION IDEA

Through a mathematical modification of the distribution equation, the compensation of the temperature gradient through hydrodynamics in the weld pool is considered. From the FEM-simulation with the modified EHS, a decrease of the maximum calculated temperature in the center of the EHS and at the same time an increase of the temperature at the edge of the EHS are expected. This leads to a better representation of the physical reality and simulation precision of temperature-time-cycles and weld seam geometry without increasing the number of parameters for the description of the heat source.

The main idea for the modification of the EHS by Goldak is the replacement of the underlying normal distribution equation, Fig. 3 (a), so that the heat density is decreased in the center of the heat source (flat-topped curve) and increased at the edge (provisory model of the weld pool surface), Fig. 3 (b).

The class of exponential symmetrical distributions can be described with a common equation (Eqn. 2) according to [15]:

$$f(x) = \frac{\lambda}{2\sqrt{2}\theta_1\Gamma(1/\lambda)} \exp\left(-\left(\frac{|x-\theta_0|}{\sqrt{2}\theta_1}\right)^\lambda\right) \quad (2)$$

In this, the expected value for the energy distribution in electric arc welding corresponds to the value at the center of the distribution and the standard deviation is the Gamma function, for example.

The form parameter  $\lambda$  is important here. A form parameter of  $\lambda = 1$  represents, for example, the Laplace distribution and a parameter of  $\lambda = 2$  represents the Gaussian distribution, Fig. 3.

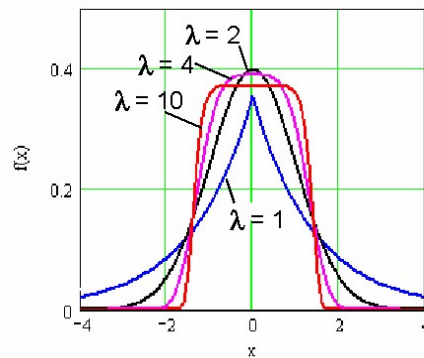


**Fig. 3** The class of exponential symmetrical distribution, as well as the distribution function for different parameters  $\lambda$  [15].

The function from this class

$$f(x) = \frac{1}{\sqrt{2\pi}\theta_1} \exp\left(-\frac{1}{2} \frac{(x-\theta_0)^2}{\theta_1^2}\right) \quad (3)$$

usually underlies the models of heat density distribution in electric arc welding, among others in the two-dimensional Rykalin-Rosenthal distribution or the three-dimensional Goldak-EHS.

Regarding the modelling of the heat input in welding, the heat distribution can be regulated with the help of the parameter  $\lambda$  without changing its integral value. For electric arc welding, parameters of  $\lambda > 2$  lead to a more realistic representation of the heat source. These functions have often been called Super-Gauss distributions, see Fig. 4 where the integral value is the same for each half.

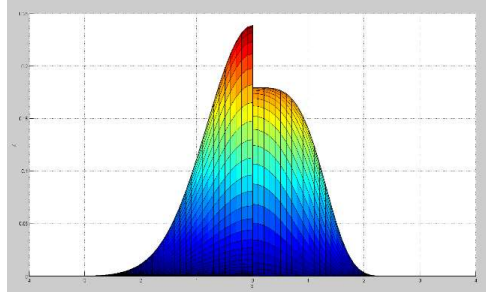


**Fig. 4** Comparison of the Gauss distribution ( $\lambda=2$ , left half) and Super-Gauss distribution ( $\lambda=4$ , right half).

The superficial two-dimensional heat density distribution, which can be described with a parameter  $\lambda = 4$  in equation (2) yields, in comparison with the normal distribution, a better accordance in the simulation of the temperature field and of the weld pool in the program SimWeld [16, 17].

The same methodology is applied for the modification of the equivalent heat source by Goldak.

#### FIRST MODIFICATION: ENERGY DENSITY DISTRIBUTION

The goal of the first modification is to reach a more equally distributed heat source in the area which can be described by the distribution radii. The equations (1a) and (1b) can be formally described as:

$$\begin{aligned}
 f_{Gol}(x, y, z, t) &= KG \exp\left(-\left((x_0 + v(\tau - t))^2 k_x + y^2 k_y + z^2 k_z\right)\right) \\
 c &= 3; k_x = \frac{c}{r_x^2}; k_y = \frac{c}{r_y^2}; k_z = \frac{c}{r_z^2}; \\
 b &= (r_x \cdot r_y \cdot r_z)\pi^{1.5}; KG = \frac{2c^{1.5}}{b};
 \end{aligned} \tag{4}$$

Analogously, the modified equation can be written as follows

$$\begin{aligned}
 f_{MR10}(x, y, z, t) &= KM \exp\left(-\left((x_0 + v(\tau - t))^2 k_x + y^2 k_y + z^2 k_z\right)\right) \\
 c &= 2; k_x = \frac{c}{r_x^2}; k_y = \frac{c}{r_y^2}; k_z = \frac{c}{r_z^2}; \\
 b &= (r_x \cdot r_y \cdot r_z)\pi^{1.5}; KM = \frac{2c^{1.5}}{b \cdot 0.691368};
 \end{aligned} \tag{5}$$

The comparison between the three-dimensional power density distribution with the equation of EHS by Goldak and the modification MR10 is shown in Fig. 5. The color represents the intensity of the power density. For equal distribution parameters and fully distributed power of EHS, the EHS MR10 (right) shows an almost even density inside the distribution area and a sudden decrease at its borders. That kind of distribution significantly corresponds to the conception that the intensive mass fluxes redistribute and average out the heat fluxes in the weld pool. The attempt to reach a deeper melting depth in simulation by increasing the depth distribution parameter is shown in Fig. 6.

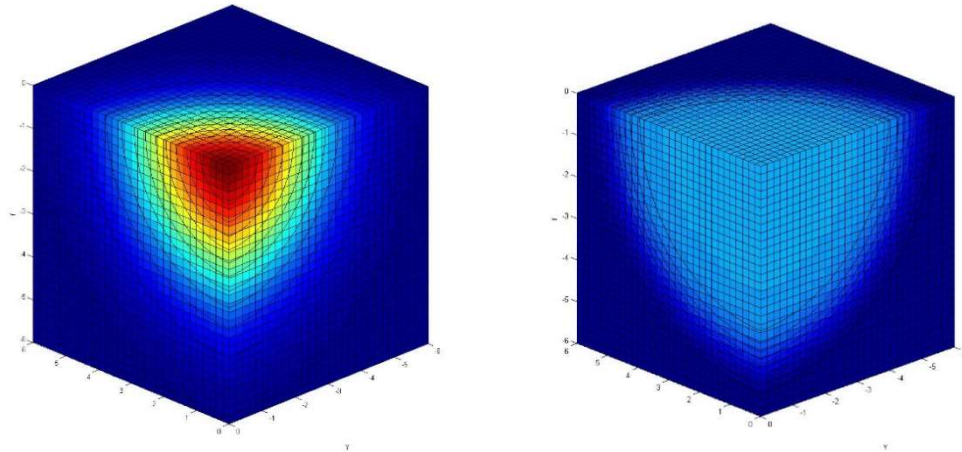


**Fig. 5** Comparison between the power density distribution of the EHS by Goldak (left) and modified EHS MR10 (right) .

While the distribution density of the EHS by Goldak increases only slightly at the desired depth, the distribution of the EHS MR10 practically precisely follows the required depth of the weld seam melting zone which is equivalent to the depth parameter of the distribution.

The given examples show the benefits of EHS MR10 by enabling the possibility of a required density of power in the desired area. The dependency between the distribution parameters of EHS MR10 and the weld seam geometry are rather direct, however only if the density power is sufficient for the melting.

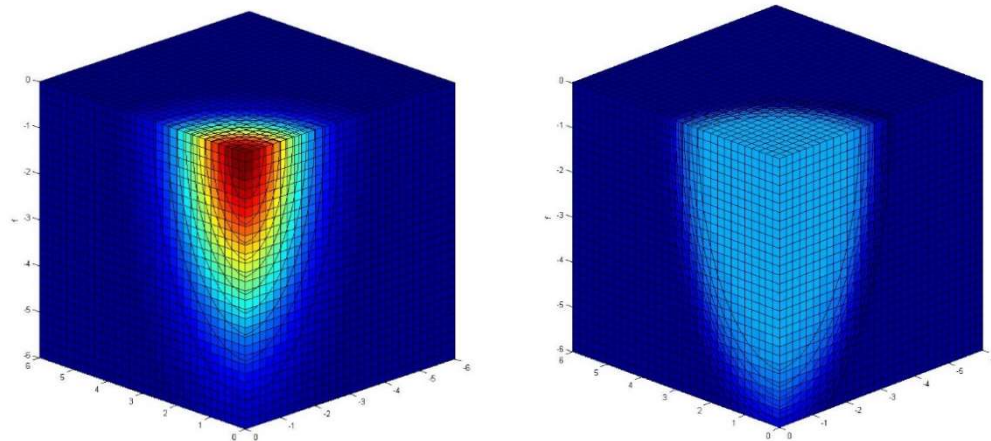


**Fig. 6** Representation of the distribution efficiency in the depth direction of the EHS by Goldak (left) and modified EHS MR10 (right).

### SECOND MODIFICATION: HEAT SOURCE AREA

Another fundamental problem in using the EHS by Goldak for the calculation of the heat input in FEM-simulation arises when considering the weld reinforcement, created by the additional wire metal. This consideration is necessary if the exact balance of mass and energy is to be achieved. In this case the weld reinforcement is already included in the FEM-simulation mesh. By taking the additional metal given in the mesh into account a conflict with the normalization condition (Eqn. 1d) arises. According the Eqn. (1d) both parts (the front side and the rear side) of the EHS by Goldak should be distributed onto the welding plate. In fact, the normalized conditions (Eqn. 1d) allow that only the lower parts of the distributed energy will be part of the calculation. Therefore, the upper parts of the given ellipsoids remain out of consideration.

If the weld reinforcement is included in the FEM-mesh, two cases are possible: 1. The EHS center has a trajectory (welding line) inside the mesh above the previous surface in the state before the welding (without weld reinforcement) and 2. The EHS center has a trajectory (welding line) above the surface with the consideration of weld reinforcement (top position). In the first case, it has to be guaranteed that the zone of weld reinforcement will be blocked from receiving heat. In the second case, a part of the distributed power to the left and right side of the weld reinforcement border will be lost. Additionally, it makes it difficult to reach the required depth of the melted welding zone.

The study of the cross section of the welding pools with GMAW and SAW welding, especially under the conditions of increased welding speeds and heat input intensities, makes it possible to establish the following assumption: the metal, melted under the welding arc and mixed with the wire metal leaves the melting area as a result of hydrodynamics in the welding pool and forms the weld reinforcement. In fact, these hydrodynamics change the heat input distribution into the weld pool by convection. If the hydrodynamic flow in the welding pool is not taken into consideration during the FEM-simulation, then the process can be compensated by adding heat to the weld reinforcement.

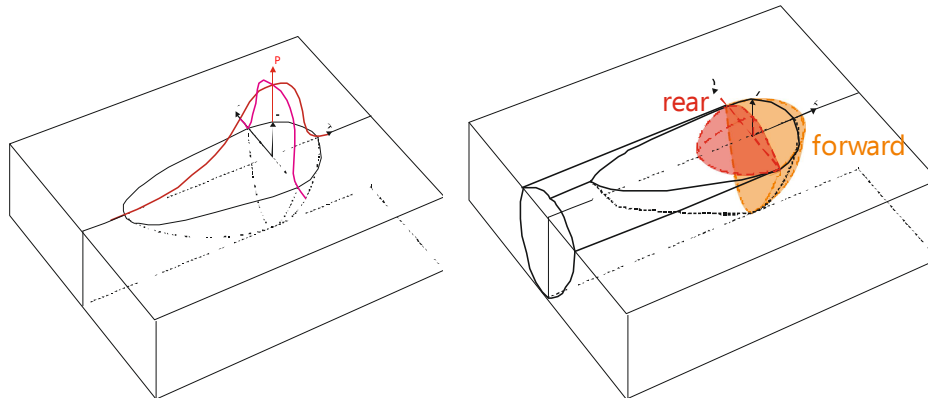


**Fig. 7** Schematic representation of the second modification.

In case of a double ellipsoid EHS it is proposed to distribute the heat at the rear ellipsoid only in the metal of the weld reinforcement and block the heat entry of the lower rear part of EHS in the welded plates. The Fig. 7 shows the application of the second modification. This second modification can be used also for the „standard“ EHS by Goldak, but in relation with the suggested first modification it makes it possible to reach better results with less time needed for the calibration.

#### APPLICATION EXAMPLES

The modifications were implemented and simulated for verification by using the tool ANSYS. The comparisons between experimentally determined and simulated geometries in the weld pool for the cases of Goldak’s EHS with the 2nd modification and EHS MR10 are shown exemplary in Fig. 8.

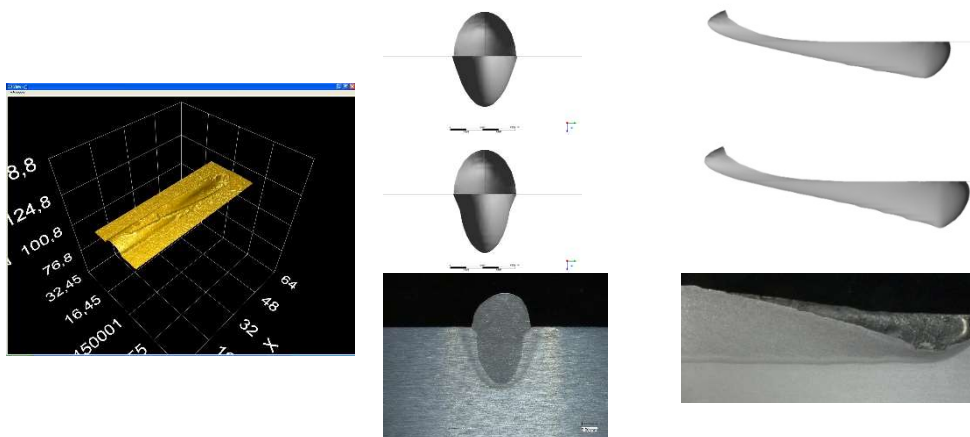


**Fig. 8** The comparison between experimentally determined (left: 3D, bottom: 2D) and simulated geometries of the welding pool for the cases of Goldak’s EHS with the 2nd modification (top) and EHS MR10 (middle).

A very specific experimental weld seam was chosen for the demonstration of the modification's advantages. Such a cross section is commonly a result of the combination of a high wire feed rate and corresponding current as well as a short arc length and corresponding voltage. The cross section as well as the long section show good correspondence in the simulation for the case of EHS MR10 and also EHS according to Goldak with the 2nd modification. Usually for the calibration a cross section from the real experiment is necessary or a result from a process simulation for example from SimWeld [16, 17]. Also, for the calibration of the energy input, the thermo-cycles are necessary. For this reason the length of the melt pool conveys the whole information about the agreement, much more than the comparison with the thermo-cycles. Furthermore, the thermos-cycles far away from the fusion line are nearly not sensitive to the distribution of the input power density. Both simulations produce good results for the length of the weld pool. In the case of EHS MR10 it was even possible to reproduce the mushroom shaped seam.

This method was also validated for the cases of different welding velocities and the corresponding energy per unit length.

Fig. 9 shows further a good agreement of the comparison between experimentally determined and simulated cross sections for the cases of Goldak's EHS with the 2nd modification and the agreement further increases for the comparison with the EHS MR10 cases.

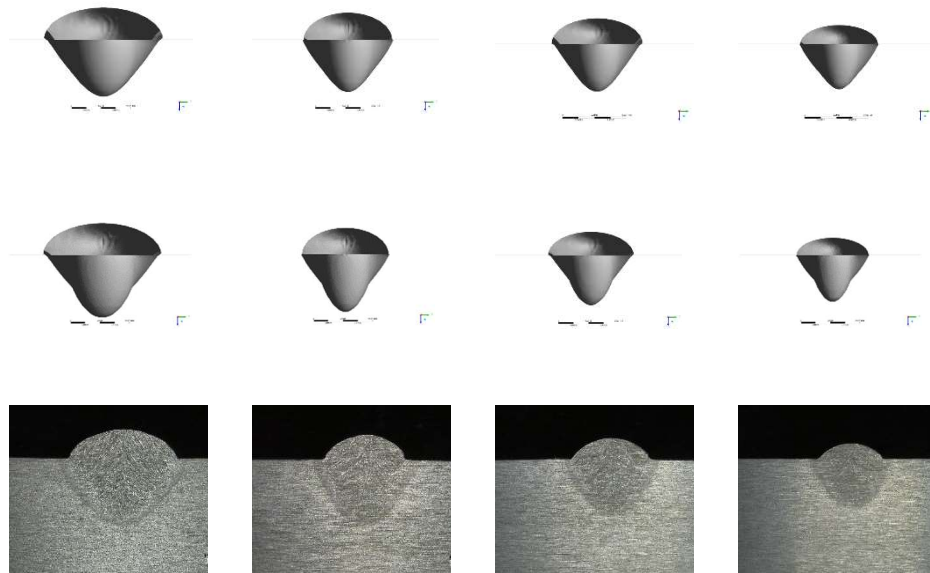


**Fig. 9** The comparison between experimentally determined (bottom) and simulated cross sections of the weld seam for the cases of EHS according to Goldak with the 2nd modification (top) and EHS MR10 (middle) for different welding velocities.

The EHS MR10 is implemented as FORTRAN- subroutine for the usage by the FEM-Software SYSWELD. A similar C-subroutine is implemented for the usage by the FEM-Software DynaWeld [18].

### CONCLUSION

The suggested and described modifications of the EHS according to Goldak were qualified for the calculation of the GMA welding's temperature field. Since the modifications depict the real processes of the GMA welding closer to reality, the simulation also shows better results with a significantly lower calibration effort.

However, it should not be expected that all kinds of geometries of the weld seam can be depicted by using this modification. The EHS MR10 is primarily an „equivalent“ heat source, which purpose is to enable the most real heat distribution outside of the weld pool. The calculated temperature in the weld pool area can be understood as an estimation only and any predictions of the temperature distribution in the case of the EHS approach are unsubstantial.

### REFERENCES

- [1] D. RADAJ: *Schweißprozesssimulation - Grundlagen und Anwendungen*, Düsseldorf: DVS-Verlag 1999.
- [2] D. RADAJ: *Eigenspannungen und Verzug beim Schweißen, Rechen- und Messverfahren*, Düsseldorf: DVS-Verlag, 2002.
- [3] D. ROSENTHAL: 'Mathematical theory of heat distribution welding, cutting', *Welding Research Supplement*, Vol. 20, No. 5, pp.220-234, 1941.
- [4] D. ROSENTHAL: 'The theory of moving sources of heat and its application to metal treatments', *Transactions of the ASME*, Vol. 68, Nr. 8, pp.849-866, 1946.
- [5] N.N. RYKALIN: *Berechnung der Wärmevorgänge beim Schweißen*, Berlin: VEB Verlag Technik, 1957.
- [6] J. GOLDAK et al.: 'A New Finite Element Model for Welding Heat Sources', *Metallurgical Transactions B*, Vol. 15, No. 2, pp.299-305, 1984.
- [7] J. GOLDAK et al.: 'Heat and fluid flow in welds', *Advanced Joining Technologies*, London: Chapman and Hall, pp.69-82, 1990.
- [8] J. GOLDAK et al.: 'Computer modelling of heat flow in welds', *Metallurgical Transactions B*, Vol. 17, pp.587-600, 1986.
- [9] C. SCHWENK, M. RETHMEIER, D. WEISS: 'Rapid generation of temperature fields for simulation of welding distortions', *Mathematical Modelling of Weld Phenomena 8*, Verlag der Technischen Universität Graz, pp.835-846, 2007.
- [10] A. PITTNER, D. WEIß, C. SCHWENK, M. RETHMEIER: 'Methodology to improve applicability of welding simulation', *Science and Technology of Welding and Joining*, Vol. 13, No. 6, pp. 496-508, 2008.
- [11] V. A. KARKHIN, P. N. HOMICH, V. G. MICHAILOV: 'Models for volume heat sources and modelling functional-analytical technique for calculating the temperature fields in butt welding', *Mathematical Modelling of Weld Phenomena 8*, Verlag der Technischen Universität Graz, pp.819-834, 2007.
- [12] T. SCHENK, I. M. RICHARDSON, M. KRASKA AND S. OHNIMUS: 'Influence of clamping on distortion of welded S355 T-joints', *Science and Technology of Welding and Joining*, Vol. 14, No. 4, 369-375, 2009.

- [13] T. SCHENK, I. M. RICHARDSON, M. KRASKA AND S. OHNIMUS: ‘Non-isothermal thermomechanical metallurgical model and its application to welding simulations’, *Science and Technology of Welding and Joining*, Vol .14, No. 2, 152-160, 2009.
- [14] J. GOLDAK AND M. AKHLAGHI: *Computational Welding Mechanics*, New York: Springer, 2005
- [15] B. U. LEMESCHKO, C.C. PODMADIN: *Sibirische Zeitschrift industrieller Mathematik*. T.5.-No. 3, pp.115-130, 2002.
- [16] U. DILTHEY et al.: ‘Software Package SimWeld for Simulation of Gas-Metal-Arc-Welding Processes of Steels and Aluminium Alloys’, *Mathematical Modelling of Weld Phenomena 7*, Verlag der Technischen Universität Graz, pp. 1057-1079, 2005.
- [17] U. REISGEN, O. MOKROV, E. ROSSITER et al.: ‘Welding process simulation for the calculation of an equivalent heat source’, *Mathematical Modelling of Weld Phenomena 9*, Verlag der Technischen Universität Graz, pp.801-818, 2010.
- [18] T. LOOSE, O. MOKROV: ‘SimWeld® and DynaWeld Software tools to setup simulation models for the analysis of welded structures with LS-DYNA’, *European LS-DYNA Conference, Würzburg 15.-17.6.2015*, Stuttgart: Dynamore GmbH, pp. 145-146. 2015.





# VALIDATION OF HEAT SOURCE MODEL FOR METAL ACTIVE GAS WELDING

D. KOLLÁR\* and B. KÖVESDI\*

*\*Budapest University of Technology and Economics (Department of Structural Engineering, H-1111, Budapest, Hungary, 0000-0002-0048-3327, kollar.denes@epito.bme.hu)*

DOI 10.3217/978-3-85125-615-4-05

## ABSTRACT

The most sufficient welding parameters and settings of manufacturing technologies are currently mainly determined by experiments for standardised production in the practice. It is a time-consuming method, while there is a large amount of waste during the 'trial and error' process of distinct welding technologies. Virtual fabrication and virtual testing of weldments using finite element method provide a sustainable solution for advanced applications. Calibration and validation of heat source models using finite element analysis is a crucial task, because theoretically the calibration has to be done for all the individual cases related to different welding processes and welding variables. Nevertheless, it can reduce the need of on-site experiments and waste during fabrication. A comprehensive literature review has been carried out focusing on the introduction of different heat source models. The aim of the current research is to develop a common calibration process for a wide range of heat source model parameters to ensure general applicability for a typical joint of a weldment. A systematic research program is carried out on small scale specimens using different welding input parameters. The experimental research program contains temperature measurements during welding, macrographs and deformation measurements after welding. In addition, a numerical study using uncoupled transient thermo-mechanical analysis, including sensitivity analyses and parametric studies focusing on fusion zone size, residual stresses and distortions, is performed. Based on the large number of experimental data, thermal efficiency and heat source model parameters are calibrated and verified. As a generalization, a validated heat source model is developed for a metal active gas welding power source. The developed validation process can have significant role in case of robotic welding, where welding trajectory, heat input, travel speed and quality can be controlled precisely.

Keywords: welding simulation, heat source model, calibration, validation, metal active gas welding

## PROBLEM STATEMENT

There is a remarkable industrial demand on speeding up and improving manufacturing processes. Lindgren [1] revealed that welding technologies are generally developed by performing experiments and tests on prototypes, while computational methods are still rarely used in the development process. It is a substantial expectation that simulations will complement experiments using the 'trial and error' process for obtaining Welding Procedure Specifications (WPS) as a final result. Namely, both residual stresses and deformations are evaluated in the design phase to optimize welded structures. However, nowadays deformations are usually in focus whereas residual stresses are of interest in subsequent phases.

In most of the cases it is time efficient and economical to use Computer-aided Engineering (CAE) opportunities rather than determining optimal parameters experimentally. Developing a sustainable virtual manufacturing process is an innovative way to reduce waste in workshops and specify optimal conditions depending on the requirements. Goldak and Akhlaghi [2] denoted that in the automotive industry the number of prototypes has been reduced from a dozen to one or two applying CAE sources as powerful, robust and efficient tools. The general aim of Computational Welding Mechanics (CWM) is to set up reasonably precise methods and models that are capable of controlling and designing welding technologies whilst ensuring suitable performance [3]. Obviously, it is an overall aim to perform numerical simulations faster and easier than to carry out welding experiments, especially when dealing with large welded structures [4]. The welding simulation procedure can be implemented in full-scale modelling frameworks describing the entire manufacturing process including steel rolling, cold forming, thermal cutting, machining, etc. [5]. An additional tremendous advantage of CWM is comparing different variants in the design phase, while performing subsequent analyses on virtual specimens, such as buckling [6-8] or fatigue analysis, is also a potential.

The determination of residual stresses and deformations are highly recommended for manufacturers as well as for designers. In case of steel structures there are often assembly difficulties and resistance problems due to large weld sizes, high heat inputs or poor clamping conditions during fabrication. These effects can result in large deformations and residual stresses, which can reduce the resistance of steel structural elements. Most of the standards, such as EN 1993-1-5:2005 [9], give only approximations for the initial (equivalent) geometrical imperfections. Therefore, it is an important task to take these effects into account as accurately as possible. Several years ago it was almost impossible to simulate the welding of large and complex structures because of hardware requirements and long computational time. Nowadays, due to the improvement of computational background it is feasible to examine large-scale welded joints and structures in an adequately accurate way, but it has to be declared that computations still have boundaries.

The aim of the current research is to develop a common calibration process for a wide range of welding variables and heat source model parameters to ensure general applicability for a typical T-joint of a weldment. A systematic research program is carried out on small scale specimens using different welding input parameters. The experimental research program contains temperature measurements during welding, macrographs and deformation measurements after welding. In addition, a numerical study using transient thermo-mechanical analysis, including sensitivity analyses and parametric studies focusing on fusion zone size, residual stresses and distortions, is performed. Based on the large number of experimental data, thermal efficiency and heat source model parameters are calibrated and verified. As a generalization, a welding process model is developed for a metal active gas welding power source. The developed validation process can have significant role in case of robotic welding, where welding trajectory, heat input, travel speed and quality can be controlled precisely.

### LITERATURE REVIEW

Experiments and measurements are intended to assist in getting acquainted with heat sources. There is a fundamental need for better understanding the influence of certain parameters and more precise approaches to predict the realistic behaviour. Mathematical models are used to enhance the knowledge of heat sources taking distinct effects into account. For instance, mathematical models can include 'the energy equation, surface tension of the weld pool surface, hydrostatic forces, Lorentz and Marangoni forces in the weld pool, pressure and shear forces from the arc or plasma, and droplet transfer to the weld pool' according to Goldak and Akhlaghi [2]. Generally, the aim is to model the welding heat source as accurate as it is necessary depending on one's purpose. Naturally, the level of negligence is related to the analysis aspects. Therefore, Goldak and Akhlaghi classified heat source models into five categories of First to Fifth Generation Weld Heat Source Models. The fifth class is the newest and most complex. The older ones are considered as sub-classes of each newer generation as latter generations include the attributes of former models. Table 1 sums up the pros, cons, applicability and the need for calibration of each weld heat source model generation. The following subsections introduce the history and the most important features of each heat source modelling level. The introduction focuses on the Second Generation Weld Heat Source Models as these are relevant for the presented finite element calculations; however, the subsequent generation models are presented briefly as well. Heat source models can be generalized for welding processes in a parameter range. According to Lindgren [3], welding process models are coupling the physics of the problem, the power density distribution in the weld pool and welding process parameters. Sudnik et al. [10-11] set up such a model earlier for laser beam welding taking energy transport, vapour pressure and capillary pressure into account. Welding process models have much importance as experiments can be combined or fully replaced by calibrated heat source models in the region of interest [12].

First generation heat sources comprehend point, line and plane heat source models. Point heat source models are designated to model arc welding. Line heat source models can be used for full penetration welds, e.g., electron beam welding or laser beam welding. Generally, plane heat source models are effective to simulate welding with sheet electrodes. The temperature can be predicted in any point in the specimen utilizing these heat source models. The development of instantaneous point heat source models for two- and three-dimensional heat flow, solving the heat flow differential equation for quasi-stationary state, is credited to Rosenthal [13] and Rykalin [14]. Rosenthal made a few assumptions such as (i) the energy input from the heat source is uniform and moves with a constant velocity along a trajectory, (ii) all the energy is deposited into the weld at a single point, (iii) thermal properties are temperature-independent, (iv) heat flow is governed by conduction, meanwhile radiation and convection are ignored, in addition (v) latent heats due to phase transformations and fusion/solidification is neglected. Analytical approaches are effective for instance in determining the approximate size of the heat-affected zone or fusion zone, thermal gradients, phase proportions and hardness. Heat source models of Rosenthal and Rykalin have been widely used for modelling infinite or semi-infinite bodies. The temperature field far from the weld could be determined with acceptable accuracy, but the accuracy of these approaches may decrease severely in the fusion zone and the heat-affected zone. On the other hand, for welded structures with complex welding trajectories quasi-

stationary state may not even exist according to Goldak et al. [15], thus, the utilization of First Generation Weld Heat Source Models is restricted.

**Table 1** Pros, cons, applicability and the need for calibration of weld heat source model generations (WHSMG).

WHSMG	Pros	Cons	Applicability/Calibration
First	analytical solution low computational cost	distribution of energy ☒ constant material properties phase transformations ☒ radiation and convection ☒ simple weldment geometry straight weld path discontinuities in geometry ☒ constant travel speed quasi-steady state heat transfer	approximates temperature for finite, infinite or semi-infinite bodies without discontinuities and nonlinearities; supports welding control systems and optimizing welding variables; <b>calibration is not really possible</b>
Second	distribution of energy nonlinear material properties phase transformations radiation and convection complex weld path complex weldment geometry discontinuities in geometry varying travel speed unsteady state heat transfer Stefan problem Cauchy momentum equation	fluid flow complex weld pool shapes ☒/☒	FDM* or FEM*: nonlinearities; realistic temperature fields outside of the weld pool; complex weld pool shapes: prescribed temperature model/combination of surface and/or volumetric heat sources; <b>calibration is needed</b>
Third	complex weld pool shapes higher computational cost	additional input data may be needed for pressure distribution of the arc, mass flow rate into the weld pool and surface tension on the fluid surface	welding positions; weld pool shape becomes output data; <b>calibration is not needed</b>
Fourth	fluid dynamics complex weld pool shapes	mathematical difficulties high computational cost	FVM*: droplet flow can be included; <b>calibration is not needed</b>
Fifth	model of the arc is included magneto-hydrodynamics complex weld pool shapes	mathematical difficulties high computational cost	most general heat source model generation; application is actually limited to researches; <b>calibration is not needed</b>

\*FDM: Finite Difference Method; FEM: Finite Element Method, FVM: Finite Volume Method

Second Generation Weld Heat Source Models define distribution functions instead of solving Dirichlet problems of first generation models. It is mainly applied in finite element analysis and is suitable to handle complex geometries, weld pool shapes and welding trajectories, while temperature-dependent material properties, radiation and convection, phase transformations and latent heats due to phase transformations, fusion and evaporation can be taken into account. Effective specific heat or enthalpy makes it possible to take latent heat into consideration. These models have to fulfil solely the heat equation, thus, power density, prescribed flux and prescribed temperature functions are in this class according to Refs. [2] and [16]. The first innovative conception was a distributed flux model developed by Pavelic et al. [17] and Rykalin [18] to model weld pools without nail-head shape or deep penetration. The description of distributed flux models, e.g., normal Gaussian distributed

surface heat source, bivariate Gaussian distributed surface heat source, etc. is given in Ref. [2] in a detailed manner. Prescribed temperature model was used by e.g., Refs. [19-20]. Goldak, Chakravarti and Bibby [21] presented power density functions to model even complex weld pool shapes for arc welding or laser beam welding. General power density functions of spherical, hemispherical, single ellipsoidal and double ellipsoidal heat sources are gathered in Refs. [2] and [16] as well. Recently, hybrid heat source models [22-25] are also published, as combination of heat source models is feasible for non-conform cases.

In addition to the first two generations, Third Generation Weld Heat Source Models predict the liquid weld pool shape solving the Stefan problem at the boundary of liquid and solid phases. It is treated as a free boundary problem, also known as moving boundary problem, as the interface of two phases moves with time and is an unknown hypersurface. The heat equation is solved assuming an initial temperature distribution, a Dirichlet condition for melting temperature at the interface, the Stefan condition describing the interface velocity and an initial weld pool shape. Enthalpy is not continuous at the interface, hence, distinct heat equations belong to each phase. Goldak and Akhlaghi [2] denoted that this model type was initiated by Ohji, Ohkubo and Nishiguchi [26] introducing discrepancies between horizontal and vertical welding positions. Their model includes the Cauchy momentum equation and mass continuity in addition to the free boundary problem. Using a Third Generation Weld Heat Source Model makes it possible to have the weld pool shape as output information contrary to the first and second generations. Navier-Stokes momentum equation, including buoyancy forces and Lorentz forces in the liquid phase, Marangoni forces, shear forces and pressure due to the arc acting on the weld pool surface, can be added to previous models to describe macroscopic fluid dynamics, thus, developing the fourth class of weld heat source models. Fifth Generation Weld Heat Source Models include even the model of the arc. Fourth generation models are improved by the equations of magneto-hydrodynamics to generalize the mathematical problem. These equations are a coupling of Navier-Stokes equation of fluid dynamics and Maxwell's equations of electromagnetism. Magneto-hydrodynamics deals with the movement of electrically conductive fluids due to external electromagnetic field. The added feature turns the fourth generation model into a highly complex mathematical problem, which results in numerical methods facing serious difficulties and calculation time.

### EXPERIMENTAL RESEARCH PROGRAM

#### SPECIMENS AND EXPERIMENTAL SET-UP

Small scale welded T-joints (Figure 1) of a stator segment of a wind turbine are investigated in the current study. The major aim of the experimental research program is to evaluate the effect of different filler metals, welding variables and types of welding joints on productivity and the structural behaviour. High-cycle fatigue is crucial in case of wind turbines, therefore, four types of joints are analysed (Figure 2) having considerably different resistance against cyclic loading: (i) double-beveled butt weld, (ii) double-sided fillet welds, (iii) single-beveled butt weld and (iv) a novel T-joint using a groove and double-sided fillet welds. Number of weld passes and heat input per unit length are the

## Mathematical Modelling of Weld Phenomena 12

investigated variables resulting in a database of input parameters including the cross sectional area of the fusion zones. It is the basis of the heat source model verification. Thirty-six welded specimens are manufactured altogether. The following notations are used for the joints (e.g., JTX-Y-0Z): JT – T-joint; X – 1/2/3/4 – double-beveled butt weld/double-sided fillet welds/single-beveled butt weld/novel T-joint using a groove, with a groove angle of  $90^\circ$ , and double-sided fillet welds; Y – 1/2 – solid wire/flux cored electrode; Z – number of specimen. All the specimens are made from S355J2+N steel grade with a length of 100 mm. Base plates are manufactured from steel plates with dimensions of  $300 \times 100 \times 40$  mm, while stiffeners have dimensions of  $140 \times 100 \times 15$  mm. Plasma cutting is used for carving the plates. A Fronius TransPuls Synergic 5000 welding power source, M21 - ArC - 18 (Corgon 18) shielding gas and PA flat or PB horizontal-vertical welding positions are used for metal active gas (MAG) welding. Solid wire (Esab OK Aristorod 12.50) and flux cored (Böhler Ti52 T-FD) electrodes with diameters of 1.2 mm are used during manufacturing. Preheat and interpass temperatures are both  $150^\circ\text{C}$ . Ambient temperature is between  $20\text{-}22^\circ\text{C}$  during the experiments. Heat input per unit length varies between 6.01 and 26.94 kJ/cm depending on filler metal, joint type and number of passes.



**Fig. 1** Tack welded T-joints before welding.

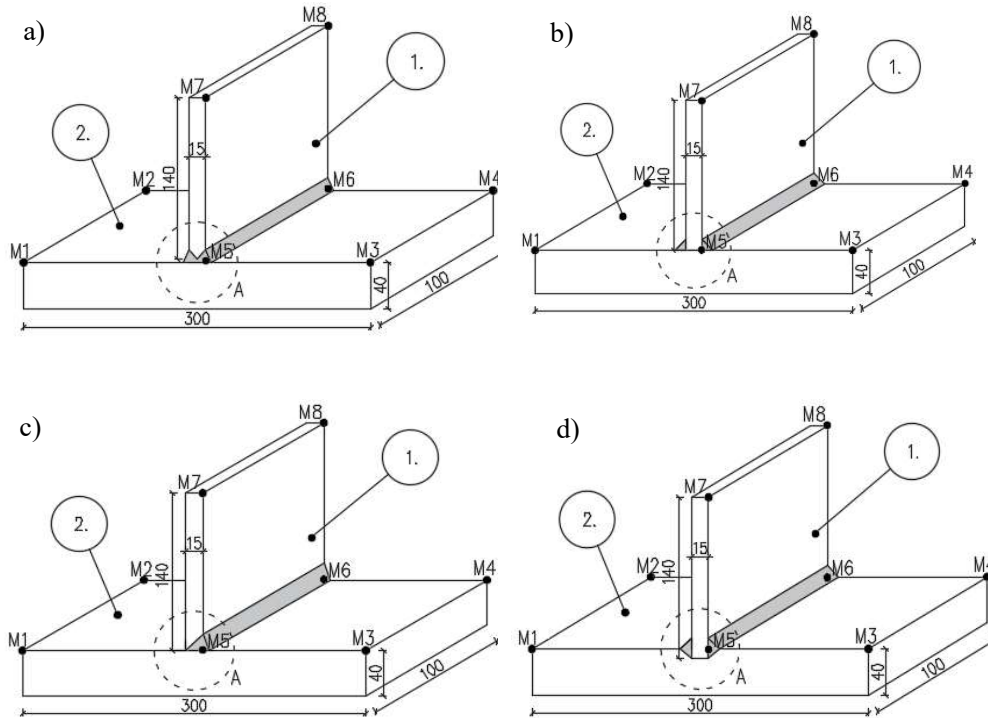


**Fig. 2** Types of investigated joints: (a) double-beveled butt weld, (b) double-sided fillet welds, (c) single-beveled butt weld and (d) a novel T-joint using a groove and double-sided fillet welds.

The initial and deformed configurations of the joints are measured with a coordinate-measuring machine in specific points, denoted with M1-M8 in Figure 2, thus, welding-induced deformations can be calculated after using common coordinate transformations. Temperature is measured by a thermocouple and an infrared thermal camera during welding. The camera uses a fix value for emissivity, therefore, a code is developed to calibrate the measurements of the camera using data recorded by the thermocouple. The measurement range of Type K (Chromel/Alumel) thermocouples is  $-200\text{ }^{\circ}\text{C} - 1200\text{ }^{\circ}\text{C}$ , while the sensitivity is around  $41\text{ }\mu\text{V}/^{\circ}\text{C}$ . Thermoelectric voltages are converted to temperatures via a Thermo-MXBoard thermocouple adapter and a QuantumX MX840A data acquisition system, that operates as a universal amplifier. The temperature variation in time is plotted in, therefore, real-time monitoring of fixed points is possible during experiments. A ThermoPro™ TP8S infrared thermal camera with high-temperature filter is part of the measurement system as well. It uses a focal plane array uncooled microbolometer with  $384 \times 288$  pixels. Its spectral range is  $8 - 14\text{ }\mu\text{m}$ , while its sensitivity is  $0.08\text{ }^{\circ}\text{C}$  at  $30\text{ }^{\circ}\text{C}$ . The measurement range is  $-200\text{ }^{\circ}\text{C} - 2000\text{ }^{\circ}\text{C}$ , whilst the operating temperature is between  $-20\text{ }^{\circ}\text{C}$  and  $60\text{ }^{\circ}\text{C}$ . Basically, it is only capable of recording static thermal images that can be analysed in its program. It is not sufficient for time-dependent analysis, therefore, an approach is developed. A video capture card digitizes the composite video signal via Image Acquisition Toolbox in MATLAB R2016b [27]. A code is



developed to record videos, hereafter the .AVI videos are split into frames. Frames can be analysed regarding the red, green and blue (RGB) colour code, because the temperature palette unequivocally determines actual temperature values for each pixel. Spot and time-temperature curve analysis are implemented in the code for further data processing. The calculated virtual temperatures are calibrated according to thermocouple measurements, thus, a temperature scaling is necessary. The principle of scaling is having the same computed areas under each curve, thereunto trapezoidal rule integration is used. Surface and material properties can be handled easily, while the temperature-dependent emissivity is also taken into consideration. The cross sectional area of the fusion zone is measured after fabrication using macrographs. Vickers hardness tests and microstructural analyses are also carried out.

EXPERIMENTAL RESULTS

Welding variables, such as voltage, current, travel speed, are registered during welding, therefore, total heat input per unit length can be calculated. The deformations due to welding differ in a great extent in case of the presented types of joints, as the number of weld passes, total heat input and single/double sided welding have a large influence on residual strains. The most important component of deformations is the transverse deformation of the top due to angular distortion; the base plates are much stiffer, thus, vertical deformations are quasi-zero. Maximum  $U_{x,max}$  transverse deformations of the top and the  $A_{FZ}$  cross sectional area of the fusion zone for every single case is shown in Figure 3; measurements are sorted in groups regarding the types of the joints. A linear regression analysis is carried out using the least squares method to determine the relationship between  $A_{FZ}$  and the  $UI/v$  total heat input per unit length, marked with continuous solid line, for double-sided fillet welds with single weld passes. Measurements and derived heat input data are showed in Figure 3 as well. Error bars are denoting the  $s = 7.05 \text{ mm}^2$  standard deviation of discrepancies between measured data and corresponding values of the regression line due to uncertainties in welding variables as arc length and travel speed are not constant during welding.

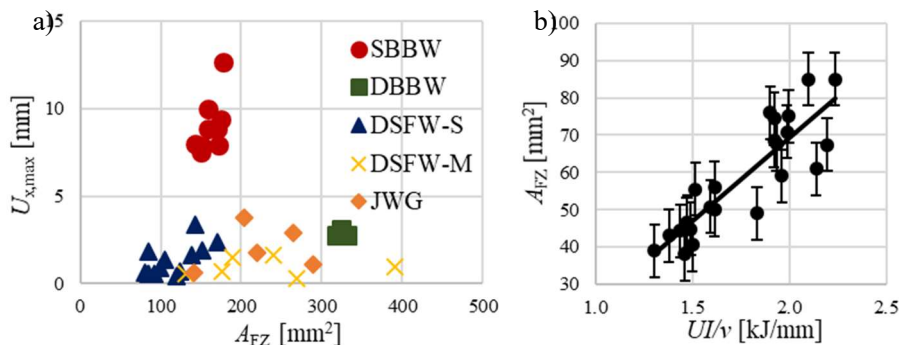
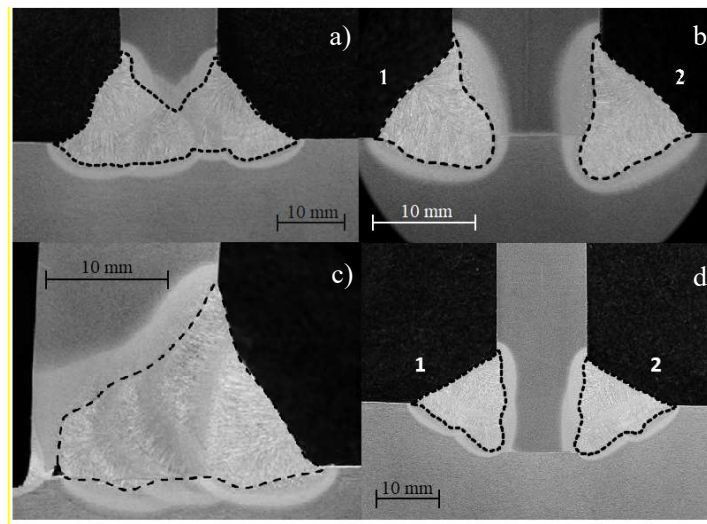


Fig. 3 Fusion zone size vs. a) maximum transverse deformations of the top and b) net heat input.

Maximum transverse deformations of the top are evaluated regarding the joint type and the cross sectional area of fusion zone. Specimen JT3-1-03 with single-beveled butt weld (SBBW) has not been taken into account in the assessment process as tack welds have fractured during transportation. The plates are repositioned and new tack welds are laid, therefore, the measurements of the deformed configuration cannot be used for deformation calculations, it would be erroneous. In addition, JT1-2-01, JT1-2-02 and JT1-2-03 T-joints are manufactured with single-bevel butt welds instead of double-beveled butt welds (DBBW), hence, they are treated as JT3 specimens. An obvious trend cannot be determined in case of multi-pass welding of double-sided fillet welds (DSFW-M) and double-beveled butt welds due to insufficient data. Larger transverse deformations and heat input are characteristic for larger fusion zones in case of joints with groove (JWG) and double-sided fillet welds with single weld passes (DSFW-S) regarding the whole joint.

The cross sectional areas of fusion zones are measured after manufacturing using macrographs. Typical macrographs and fusion lines, denoted by dashed lines, are introduced in Figure 4 for a double-beveled butt weld, double-sided fillet welds, a single-beveled butt weld and a novel T-joint using a groove and double-sided fillet welds.



**Fig. 4** Typical macrographs of joints: (a) double-beveled butt weld, (b) double-sided fillet welds, (c) single-beveled butt weld and (d) a novel T-joint using a groove and double-sided fillet welds.

Thermal cycles are determined for six specimens using a thermocouple located 15 mm far from the stiffener in transverse direction and positioned in the centre longitudinally. Virtual temperatures of the infrared camera are calibrated according to thermocouple measurements via temperature scaling for different temperature ranges. Figure 5 shows temperature measurements for JT4-2-02, while error bars are denoting the  $s = 20.6$  °C standard deviation of temperature differences derived from the two approaches. Hereafter, temperature scaling factors can be used for other specimens, hence, solely infrared thermal camera is applied for further weldments.

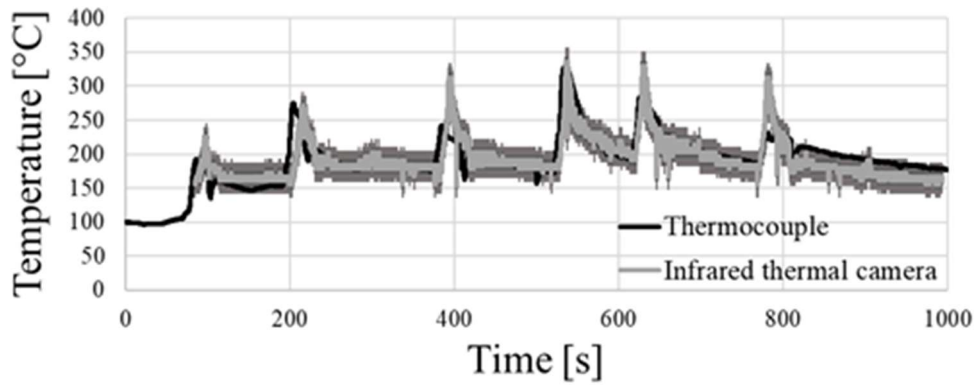


Fig. 5 Temperature measurements of a thermocouple and the calibrated infrared thermal camera.

Vickers hardness tests and microstructural analyses are also carried out for eight specimens (two for each type of welding joint). A ferritic and pearlitic microstructure is specific for the base material; its hardness varies between 153 and 173 HV. The highest hardness values are measured at the boundary of the heat-affected zone and the fusion zone; the maximum values are between 253 and 363 HV. A significant decrease of 30-110 HV can be observed in the fusion zone. The fusion zone contains ferrite, pearlite and bainite, while a ferritic and pearlitic microstructure is typical for the heat-affected zone with bainitic patterns in some cases. Cooling rate is lower in the weld pool and on its surface than in the heat-affected zone. The so-called  $\Delta t_{8/5}$  cooling time, that is necessary for cooling from 800 °C to 500 °C, has to be shorter for the base plate as higher hardness values are measured, in the corresponding heat-affected zone, than in the stiffener. There is no significant difference in hardness between face and root side, except in case of single-beveled butt welds naturally. The type of filler metal does not have any notable influence on hardness in these cases. Hardness profiles of double-sided fillet welds and joints with grooves do not differ in a great extent. Hardness profiles for face and root sides and the points used for measurements are presented in Figure 6.

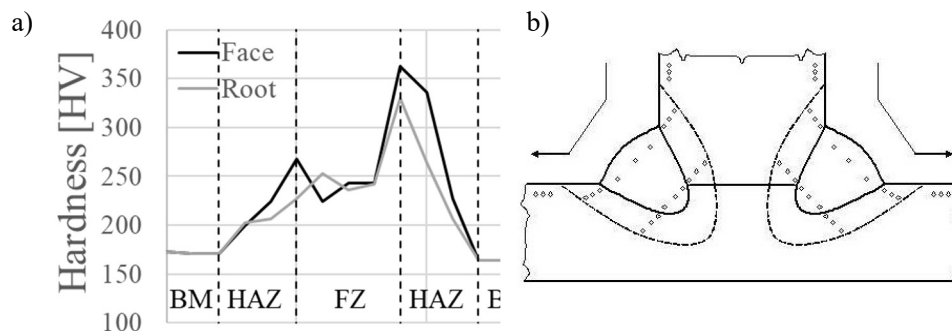
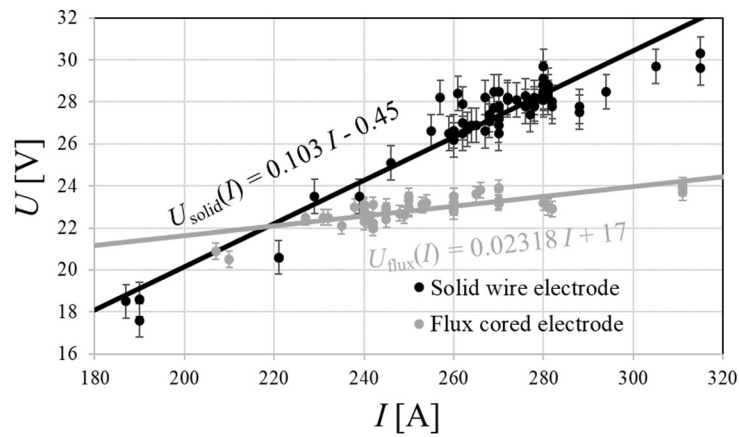


Fig. 6 a) A typical hardness profile and b) points for measurements.

The weldments are manufactured by using a Fronius TransPuls Synergic 5000 welding power source for MAG welding using constant-voltage (slightly drooping) characteristics.

Direct current and reverse polarity (DC+) are applied for the current applications. Welding current ( $I$ ) and voltage ( $U$ ) are registered during welding, thus, the operating points for each weld pass, assuming that arc length is constant, can be determined for configuration with solid wire and flux cored electrodes as arc characteristics for different filler metals, wire diameters and shielding gases are distinct. The solid wire electrode is an Esab OK Aristorod 12.50 (EN ISO 14341-A G 42 4 M G3Si1) and the flux cored electrode is a Böhler Ti52 T-FD (EN ISO 17632-A T 46 4 P M 1 H5). Diameter of electrodes is 1.2 mm, while shielding gas is EN ISO 14175 - M21 - ArC - 18. Eighty-two weld passes are laid using solid wire electrodes and eighty-one weld passes are carried out applying flux cored electrodes, hence, the number of data points is equal to the number of weld passes in Figure 7. A linear regression analysis is carried out using the least squares method to determine the welding current-voltage relationship for globular and spray arc metal transfer modes, marked with continuous solid lines, for both electrodes. Error bars are denoting the  $s = 0.81$  V and  $s = 0.38$  V standard deviations, for solid wire and flux cored electrodes, of discrepancies between measured data and corresponding values of the regression line representing the uncertainties in arc characteristic ranges, i.e., increase and decrease of contact tip-to-workpiece distance and arc length.



**Fig. 7** Operating points and working conditions for solid wire and flux cored electrodes.

The current-voltage equations of the solid lines for the solid wire and flux cored electrodes are

$$U_{solid}(I) = 0.103I - 0.45 \quad (1)$$

$$U_{flux}(I) = 0.02318I + 17 \quad (2)$$

representing the operating points after the linear regression analysis. These equations can be applied in the preliminary design phase when calculating heat input. In addition, they are implemented in the numerical model developed for the welding simulation of T-joints.

NUMERICAL APPROACH

A complex finite element framework has been developed in ANSYS 17.2 [28] to simulate welding processes for civil engineering and mechanical engineering applications. Uncoupled transient thermo-mechanical analysis is performed, which is a comprehensive technique for welding simulations that is used for determining and evaluating temperature fields, residual stresses and deformations. The most important features of the method implemented in the code are presented hereunder.

Uncoupled thermomechanical analysis means that calculated temperature fields are applied as nodal loads in the subsequent mechanical analysis. The typical couplings in a thermo-metallurgical-mechanical analysis (Figure 8) according to Refs. [1,3,29] are listed below; weak couplings and phase transformation-related phenomena are not taken into account in this paper:

- 1a Thermal expansion depends on microstructure of material.
- 1b Volume changes due to phase transformations.
- 1c Elastic and plastic material behaviour depend on microstructure.
- 1d Transformation-induced plasticity.
- 2a Microstructure evolution depends on deformation (weak coupling).
- 2b Phase transformations depend on stress state (weak coupling).
- 3a Thermal material properties depend on microstructure.
- 3b Latent heats due to phase transformations/solidification/melting.
- 4 Microstructure evolution depends on temperature.
- 5a Deformation evolution depends on temperature.
- 5b Mechanical material properties depend on temperature.
- 6a Deformation changes thermal boundary conditions (weak coupling).
- 6b Heat due to thermal, elastic and plastic strain rate (weak coupling).

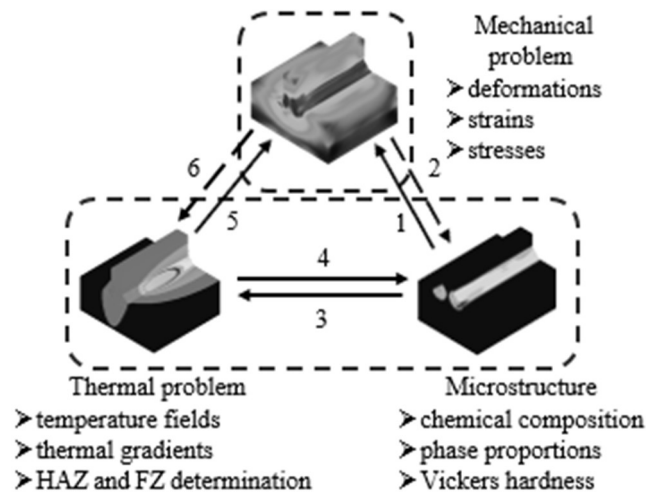


Fig. 8 Couplings in a thermo-metallurgical-mechanical analysis.

In the current study, solid elements are used in the finite element model. SOLID70, a thermal solid element, has a three-dimensional thermal conduction capability. The element has eight nodes with a single thermal degree of freedom at each node. It allows for prism,

tetrahedral and pyramid degenerations when used in irregular regions. In the mechanical analysis SOLID185 is used as an equivalent structural solid element, which has eight nodes with three translational degrees of freedom (in nodal x, y, and z directions) at each node.

Thermal boundary conditions are defined for heat flow calculations. The initial temperature (room temperature or preheating temperature) of nodes is specified before the first load step of the thermo-metallurgical analysis. Nodal temperatures of not yet deposited weld passes are prescribed in the first step of the calculation to avoid ill-conditioned matrices. A combined temperature-dependent heat transfer coefficient of  $h_{cr}(T)$  is defined in the Function Editor of ANSYS to model the effect of convection and radiation to ambient in the developed code as described in Eqn. (3). In the equation below

$$h_{cr}(T) = h_c(T) + \sigma \varepsilon(T)(T + T_{amb})^2 (T^2 + T_{amb}^2) \quad (3)$$

where  $h_c(T)$  is convective heat transfer coefficient or film coefficient,  $T$  is absolute surface temperature,  $T_{amb}$  is absolute ambient temperature,  $\sigma$  is the Stefan-Boltzmann constant and  $\varepsilon(T)$  is emissivity. The film coefficient is assumed to be  $25 \text{ W m}^{-2} \text{ K}^{-1}$ , while emissivity is taken as a temperature-independent value with a magnitude of 0.8 in the current research. On the other hand, moving volumetric heat sources induce heat generation which is defined as element body force load during the transient thermo-metallurgical analysis. The double ellipsoidal heat source model is implemented in the current study. Eqns. (4) and (5) determine the power density distribution in the front and rear quadrants, respectively

$$q_f(x, y, z) = q_{\max} \cdot e^{-3\frac{x^2}{c_f^2} - 3\frac{y^2}{a^2} - 3\frac{z^2}{b^2}} \quad (4)$$

$$q_r(x, y, z) = q_{\max} \cdot e^{-3\frac{x^2}{c_r^2} - 3\frac{y^2}{a^2} - 3\frac{z^2}{b^2}} \quad (5)$$

where characteristic parameters  $c_f$ ,  $c_r$ ,  $b$  and  $a$  represent the physical dimensions of the heat source model in each direction shown in Figure 9, while  $q_{\max}$ , maximum power density, is used for numerical scaling of power density, thus, the law of conservation of energy is fulfilled and heat generation error due to mesh formulation can be zeroed out in the transient analysis at every time step. The size of front and rear ellipsoids could be calibrated and fitted separately, while it could be applied even to simulate deep penetration welding. Several analogous functions exist to describe the power density distribution of a double ellipsoidal heat source, e.g., Bradac [30] used different constants in the exponent for each direction instead of a value of 3. Due to lack of sufficient data, Goldak, Chakravarti and Bibby [21] assumed that it is reasonable to take the distance in front of the source equal to one half of the weld width ( $c_f = a$ ) and the distance behind the source equal to twice the weld width ( $c_r = 4a$ ) as a first approximation. The idea of using a double ellipsoidal heat source model instead of a single ellipsoidal one is explained by Goldak [31] as an attempt to generate typical weld pool shapes capturing the ‘digging action of the arc’ in front and ‘slower cooling of the weld by conduction of heat into the base metal’ at the rear. In general,

it is recommended by Goldak et al. [32] that the heat source may not move more than half of the weld pool length to function appropriately in three-dimensional welding simulations using the transient method.

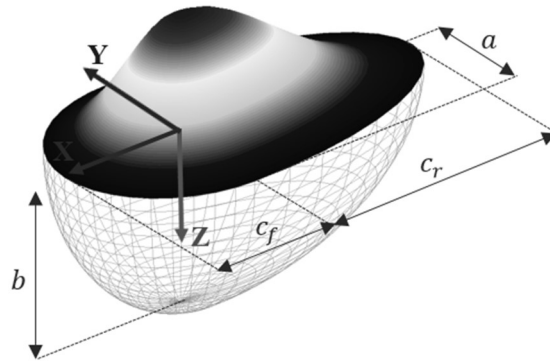


**Fig. 9** Notation and power density distribution of the double ellipsoidal heat source model.

In the mechanical analysis temperature fields are applied as nodal loads as explained before. Clamping conditions (i.e., rotational and translational degree of freedom constraints) have an important impact on the evolution of deformations and stresses. Even the release time of clamps has an appreciable influence on residual stresses and deformations. First of all, rigid body motion has to be avoided. Therefore, defining the minimum number of constraints is necessary to analyse a statically determinate structure. In addition, clamps can fundamentally act like rigid (or elastic) supports. In case of statically indeterminate structures, the additional constraints have to be deleted in an intermediate (hot release) or in the last sub-step (cold release) of the simulation to assess residual stresses and deformations.

Depending on the welding process, welded joints can be created with or without filler material addition. Therefore, initial gaps and deposited material have to be modelled in the welding simulation. The ‘birth and death’ procedure [28] is added in the thermal analysis. Element activation and deactivation can be executed using the EALIVE and EKILL commands, respectively. EKILL uses a stiffness matrix multiplier of  $10^{-6}$  (it can be changed via ESTIF command) by default for deactivated elements. In the mechanical analysis the quiet element technique [33] is implemented instead of ‘birth and death’ procedure presented previously, since all elements are active from the beginning of the calculation. Regarding the works of Refs. [34-35], extremely reducing Young’s modulus can cause numerical problems, therefore, a reduction of two orders of magnitude is sufficient. Therefore, the Young’s modulus of 1000 MPa is used for un-deposited material, while linear thermal expansion coefficient is temperature-independent and taken as zero to ensure thermal strain free bead elements before welding. Material model changes for weld bead elements only above 1200 °C as it is considered to be the reference temperature.

In the current investigation, material properties are based on EN 1993-1-2:2005 [36]. The code is basically recommended for structural fire design, but there are several examples (e.g., Refs. [6-8]) demonstrating its applicability for welding simulation purposes as well. The material properties are defined between 20 °C and 1200 °C in the standard. Temperatures can be much higher during welding, therefore, material properties are set as

constant values above 1200°C. Eurocode uses reduction factors for considering temperature dependent Young's modulus, yield strength and stress-strain curves. This material model has a notable advantage: only yield strength (355 MPa in the current paper) and Young's modulus are needed to be known on room temperature to describe the mechanical behaviour of the material. The required parameters are given in the Annex A of EN 1993-1-2 to describe stress-strain curves. It also gives a recommendation for modelling hardening below 400 °C. A multilinear isotropic hardening model is used in the simulations assuming a von Mises yield criterion. Large deflection effects are taken into account in the mechanical analysis.

## RESULTS

### SENSITIVITY ANALYSIS

The sensitivity analysis focuses on the effect of thermal efficiency and characteristic parameters of the heat source model. The dimensions of T-joints with double-sided fillet weld are identical to the experimental ones, while throat thickness is 5 mm. A gap of 0.5 mm filled with 'un-deposited material' is modelled between the base plate and the stiffener. The model consists of 27010 finite elements (Figure 10). The minimum number of constraints are defined to analyse a statically determinate structure.

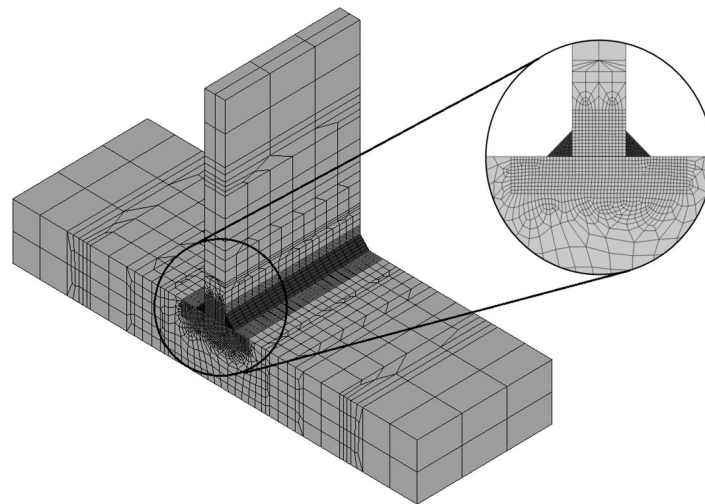


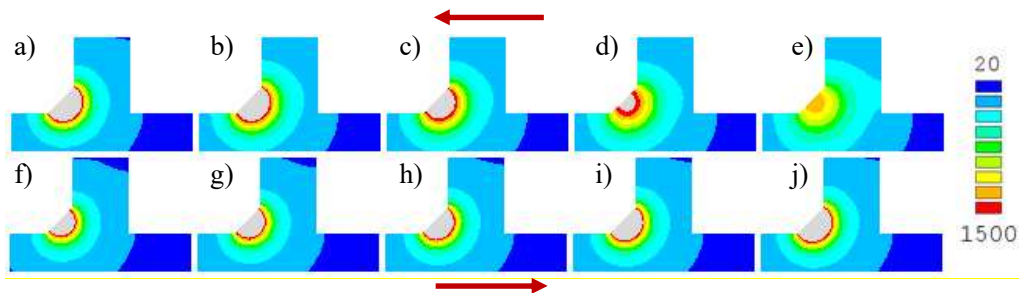
**Fig. 10** Finite element model of a T-joint with double-sided fillet weld.

Interpass temperature is not controlled, the 2nd weld pass is laid right after the 1st weld pass with the same welding direction. Welding variables are  $I = 270$  A,  $U$  is calculated using Eqn. (1) and  $v = 4$  mm s<sup>-1</sup>. Ambient temperature is taken as 20 °C, while preheat temperature is 150 °C. The reference values for the characteristic parameters of Goldak's double ellipsoidal heat source model are  $a = b = c_f = 2.5$ mm and  $c_r = 4c_f$ . These parameters are scaled in the sensitivity analysis to investigate the effect of power density



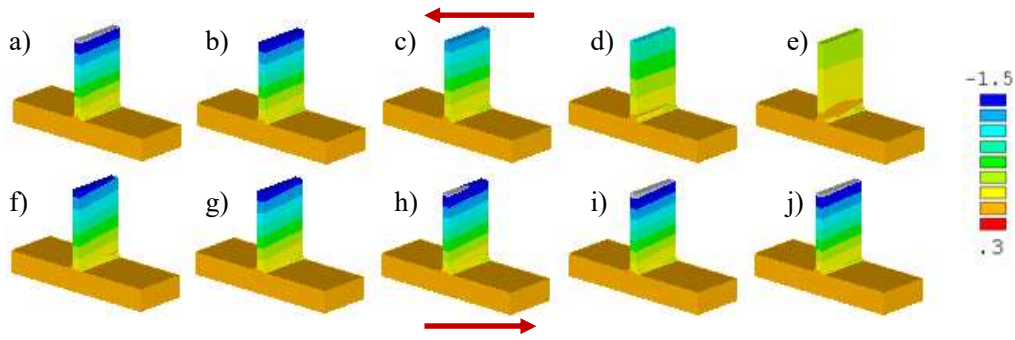
distribution. Scaling factors of 1.00, 1.50, 2.00, 2.50 and 3.00 are applied; thermal efficiency is 1.00. Five additional analyses are performed in order to analyse the influence of thermal efficiency, which is increased in 0.10 steps from 0.60 to 1.00.

Figure 11 shows weld pool size and isothermal lines in the vicinity of the weld in the midsection during welding of the 1st weld bead. Arrows show increasing tendency of fusion zone size. Scaling the reference heat source parameters results in lower power density. Thus, weld pool size decreases as scaling factor increases. Temperature does not even reach the liquidus temperature, assumed to be 1500 °C, in the weld bead elements when the scaling factor is equal to 3.00. The cross sectional area of the weld pool is 47.5 mm<sup>2</sup>, 45.5 mm<sup>2</sup>, 36 mm<sup>2</sup>, 12.5 mm<sup>2</sup> and 0 mm<sup>2</sup> for scaling factors of 1.00, 1.50, 2.00, 2.50 and 3.00, respectively. Variation of thermal efficiency has a similar effect as it has an influence on power density distribution; weld pool size increases as thermal efficiency increases. The cross sectional area of the weld pool is 25 mm<sup>2</sup>, 32 mm<sup>2</sup>, 37 mm<sup>2</sup>, 42.5 mm<sup>2</sup> and 47.5 mm<sup>2</sup> for thermal efficiency of 0.60, 0.70, 0.80, 0.90 and 1.00, respectively.



**Fig. 11** Size of the fusion zone using heat source parameter scaling by a) 1.00, b) 1.50, c) 2.00, d) 2.50 and e) 3.00 and thermal efficiency of f) 0.60, g) 0.70, h) 0.80, i) 0.90 and j) 1.00.

Figure 12 sums up the transverse deformations of the joint after cooling. Configurations a)-e) have maximum transverse deformations of 1.56 mm, 1.46 mm, 1.26 mm, 0.93 mm and 0.45 mm, respectively. Transverse deformation of the stiffener decreases as scaling factor increases. Arrows show increasing tendency of deformations. For instance, scaling factor of 2.00 results in a 20% decrease in deformations in comparison to the reference configuration. Obviously, configurations d) and e) are erroneous as temperature just reaches the reference temperatures in the finite elements representing the weld bead (Figure 11), while the elevated temperature is lower than liquidus temperature in the corresponding finite elements. Configurations f)-i) have maximum transverse deformations of 1.41 mm, 1.46 mm, 1.54 mm, 1.58 mm and 1.56 mm, respectively. Transverse deformation of the stiffener slightly increases as thermal efficiency increases, however, the variation is within 10% due to 67% increase in thermal efficiency.



**Fig. 12** Transverse deformations using heat source parameter scaling by a) 1.00, b) 1.50, c) 2.00, d) 2.50 and e) 3.00 and thermal efficiency of f) 0.60, g) 0.70, h) 0.80, i) 0.90 and j) 1.00.

Figure 13 shows the von Mises residual stresses in the vicinity of the weld beads in midsection after cooling. The plastic zones are shown in the figure, where the residual stress is higher than the yield strength, which is 355 MPa in this case. The same conclusions can be drawn as for Figure 11. Arrows show increasing tendency of plastic zone size. Plastic zone size decreases as the weld pool size decreases. The signs of lack of fusion is presented for configuration e) for instance, where several finite elements in the weld bead remains elastic, while the quasi-zero penetration is simulated in the joint. The gap, initially filled with un-deposited material, is the widest in this case as practically the material is not melted.

Results show that thermal efficiency and the scaling factor may have a similar effect on residual stresses and transverse deformations. However, it is important to emphasize that sufficient power density is requisite to reach the reference temperature of un-deposited material, otherwise, the material model for weld bead elements remain elastic with a low Young's modulus. It results in quasi-zero stresses in weld beads due to lack of fusion affecting overall residual stresses in conjunction with obtaining equilibrium of resultant internal forces and bending moments in any section of the specimen. On the other hand, 100% increase in scaling factor for the first three cases results in a variation of 32% in the weld pool size, while the variation is within 90% due to 67% increase in thermal efficiency.

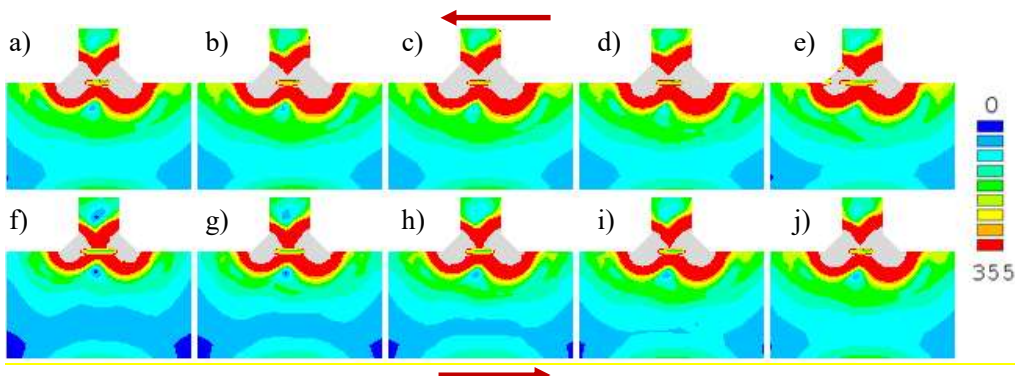


**Fig. 13** von Mises residual stresses using heat source parameter scaling by a) 1.00, b) 1.50, c) 2.00, d) 2.50 and e) 3.00 and thermal efficiency of f) 0.60, g) 0.70, h) 0.80, i) 0.90 and j) 1.00.

## DETERMINATION OF THERMAL EFFICIENCY

Generally, thermal efficiency of a welding process can be evaluated using several approaches. In this study, the thermal efficiency is determined by the comparison of experimental and numerical data. Thermocouples and infrared thermal imaging are utilized to carry out temperature measurements during welding, as presented in section 3.2, thus, thermal cycles determined by finite element models can be compared with experimental data. In addition, macrographs are used to evaluate the thermal efficiency as well. Nevertheless, the EN 1011-1:2009 standard [37] recommends to use 0.80 as thermal efficiency, while Radaj [29] introduced a range between 0.65-0.90 for metal active gas welding. The sensitivity analysis in the previous section shows that thermal efficiency has a larger effect on fusion zone size than scaling the characteristic parameters of the heat source, while the latter has a negligible effect on total (elastic and thermal) strains and temperatures further from the weld bead as presented by Kollár and Kövesdi [8].

T-joints with double-sided fillet weld (JT2-1-06 and JT2-2-02 welded with flux cored and solid wire electrodes, respectively) are chosen for the determination of thermal efficiency. The actual dimensions of the joints, which are measured, are modelled with the corresponding throat thicknesses. Throat thicknesses are measured on the macrographs for the weld beads which are single pass welded; models are built up with average throat thicknesses. The 2<sup>nd</sup> weld pass is laid after the 1<sup>st</sup> weld pass with opposite welding direction. Welding variables are summed up in Table 1 in section 5.3. Ambient temperature is taken as 20 °C, while preheat and interpass temperatures are both 150 °C. The characteristic parameters of Goldak's double ellipsoidal heat source model are  $a = b = 10\text{mm}$  and  $c_r = c_f = 2.5\text{ mm}$  for both specimens. Nodes in the stiffener in the midsection, 10 mm above the base plate, are chosen for the comparison of experimental and numerical data (Figure 14).

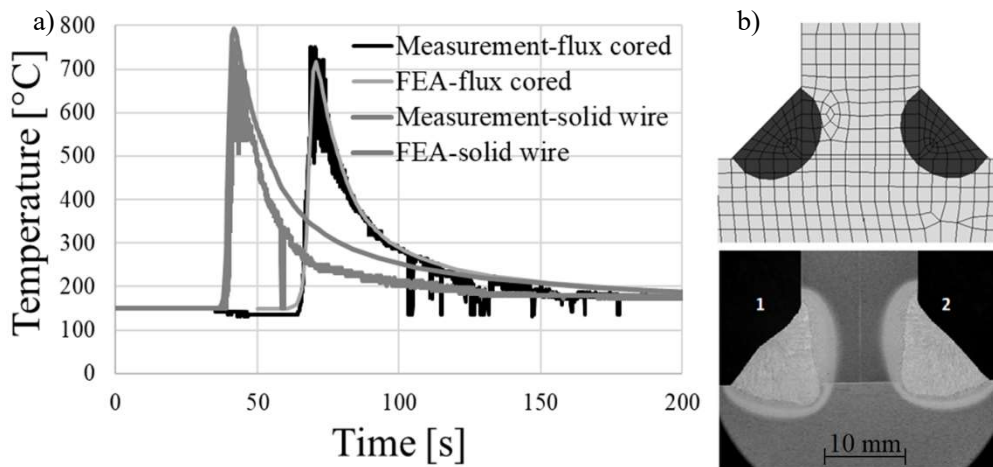


**Fig. 14** Determination of thermal efficiency by a) temperature measurements for flux cored and solid wire electrodes and b) a macrograph of specimen JT2-1-06.

Figure 14 shows the time-temperature curves based on infrared thermal imaging ('Measurement') and the finite element analysis (FEA). The peak temperature is

approximately 700-800 °C for both cases and the cooling phenomenon is also simulated successively. The temperature is about 200 °C at 200 s in case of the investigated configurations for both approaches. The figure sums up the macrograph of the JT2-1-06 specimen as well and a cross section of the finite element model showing the fusion zone (and the heat-affected zone in case of the macrograph). The basis of calibration is related to the fusion zone size. The aim is to approximate the measured fusion zone size within an arbitrary  $\pm 10\%$  range specified for treating uncertainties in welding variables (the same way as it is treated in the relationship between welding current and voltage in section 3.2). The cross sectional areas of the fusion zones for JT2-1-06, by measurements, are 76 mm<sup>2</sup> and 75 mm<sup>2</sup> for the 1st and 2nd weld beads, respectively. In addition, fusion sizes are 43 mm<sup>2</sup> and 39 mm<sup>2</sup> for JT2-2-02. The corresponding simulated weld pool sizes are 77 mm<sup>2</sup>, 72 mm<sup>2</sup>, 42 mm<sup>2</sup> and 37 mm<sup>2</sup>, respectively, which are within the reasonable range. According to the results of the sensitivity analysis the influence of thermal efficiency is already known in case of the actual T-joint, therefore, thermal efficiency was changed in 0.10 steps. Thermal efficiency of 0.90 is accepted related to the comparison of numerical and experimental data and it is applied in the simulations hereafter for both electrodes; in addition, it is in conjunction with the values published in Ref. [29] mentioned before.

### CALIBRATION AND VERIFICATION OF THE DOUBLE ELLIPSOIDAL HEAT SOURCE MODEL

In this section, the characteristic parameters of the implemented double ellipsoidal heat source model are calibrated for a typical range of welding variables in case of double-sided fillet welds with single weld passes. The developed welding process model for welding simulation of double-sided fillet welds with single weld passes is verified. A total of twelve specimens are modelled.

Double-sided fillet welded T-joints with single pass welds are investigated. The actual dimensions of the joints, which are measured, are modelled with the corresponding throat thicknesses. The parametric model of section 5.2 is used in the simulations. The 2<sup>nd</sup> weld pass is laid after the 1<sup>st</sup> weld pass with opposite welding direction. Ambient temperature is taken as 20 °C, while preheat and interpass temperatures are 150 °C. Table 2 sums up specimen notations, # number of weld pass, type of filler metal,  $I$  welding current,  $U$  voltage,  $v$  travel speed,  $a$  characteristic parameter,  $q = \eta UI/v$  net heat input per unit length,  $A_{FZ}$  and  $A_{FZ,FEA}$  fusion zone sizes based on measurements and numerical analyses and error in simulated fusion zone size, respectively. Voltage is calculated using Eqns. (1) and (2) depending on the type of filler metal. After performing dozens of iterations a function of heat input per unit length is developed to evaluate  $a$  and  $b$  characteristic parameters. The  $a$  and  $b$  characteristic parameters for JT2-2-02 are outliers (**bold letters**) in data, therefore, the specimen is ignored when  $a(q)$  polynomial function is approximated. The  $A_{FZ,FEA}$  fusion zone sizes in the table are determined by characteristic parameters using Eqn. (6),

$$a(q) = 11.094q^3 - 62.383q^2 + 117.52q - 60.812 \text{ [mm]}; c_r = c_f = 2.5 \text{ mm} \quad (6)$$

for flux cored electrodes. The model for this configuration assumes that  $a=b$  and  $c_r = c_f = 2.5$  mm regarding previous simulations of the joints. The characteristic

## Mathematical Modelling of Weld Phenomena 12

parameters of Goldak's double ellipsoidal heat source model are independent of the  $q$  net heat input per unit length for the configurations welded with solid wire electrode ( $a = b = 10\text{mm}$  and  $c_r = c_f = 2.5\text{mm}$ ). Obviously, the small  $c_r$  and  $c_f$  parameters result in a requirement of dense mesh along welding trajectory.

**Table 2** Input and output data for the calibrated cases.

Specimen	#	Filler metal	$I$ [A]	$U$ [V]	$v$ [mm/s]	$q$ [kJ/mm]	$a$ [mm]	$A_{FZ}$ [mm <sup>2</sup> ]	$A_{FZ,FEA}$ [mm <sup>2</sup> ]	Error [%]
JT2-1-01	1	solid wire	305	30.97	+4.77	1.78	10	76	77	1.3
	2	solid wire	280	28.39	-4.17	1.72	10	75	72	-4.0
JT2-1-02	1	solid wire	280	28.39	+4.00	1.79	10	71	73	2.8
	2	solid wire	261	26.43	-3.85	1.61	10	68	65	-4.4
JT2-1-03	1	solid wire	239	24.17	+3.70	1.40	10	55	51	-7.3
	2	solid wire	229	23.14	-3.33	1.43	10	50	49	-2.0
JT2-1-04	1	solid wire	315	32.00	+4.17	2.18	10	85	87	2.4
	2	solid wire	315	32.00	-4.55	1.99	10	85	83	-2.4
JT2-1-05	1	solid wire	221	22.31	+2.13	2.08	10	61	67	9.8
	2	solid wire	221	22.31	-2.32	1.91	10	59	64	8.5
JT2-1-06	1	solid wire	270	27.36	+4.00	1.66	10	69	67	-2.9
	2	solid wire	270	27.36	-4.00	1.66	10	74	68	-8.1
JT2-2-01	1	flux cored					13.5	67		
	2	flux cored	282	23.54	+2.92	2.05		56	68	1.5
JT2-2-02	1	flux cored	282	23.54	-4.00	1.49	12.5		51	-8.9
	2	flux cored	<b>210</b>	<b>21.87</b>	<b>+2.94</b>	<b>1.41</b>	<b>10.0</b>	<b>43</b>	<b>40</b>	<b>-7.0</b>
JT2-2-03	1	flux cored	<b>210</b>	<b>21.87</b>	<b>-3.33</b>	<b>1.24</b>	<b>10.0</b>	<b>39</b>	<b>35</b>	<b>-10.3</b>
	2	flux cored						45		
JT2-2-04	1	flux cored	311	24.21	+5.00	1.36	11.5		48	6.7
	2	flux cored	311	24.21	-5.00	1.36	11.5		47	4.3
JT2-1-05	1	flux cored	265	23.14	+4.17	1.32	11.2		41	2.4
	2	flux cored	265	23.14	-4.35	1.27	10.5		44	-2.3
JT2-1-06	1	flux cored	232	22.38	+3.57	1.31	11.0		38	2.6
	2	flux cored	232	22.38	-3.70	1.26	10.5		43	-4.7
JT2-1-06	1	flux cored	311	24.21	+4.55	1.49	12.5		51	0.0
	2	flux cored	270	23.26	-4.17	1.36	11.5		49	-6.1

Figure 15 shows a nomogram for the developed approach. Selecting welding current, this may be wire feed rate for MIG/MAG welding power sources, determines voltage for solid wire or flux cored electrodes. Typical travel speeds and corresponding net heat inputs per unit length are shown as well for the two types of filler metals. Finally, characteristic parameters are evaluated using the curves of the figure or Eqn. (6). The  $U(I)$ ,  $a(q)$  and  $b(q)$  equations are implemented in the finite element code for further parametric studies and the sustainable virtual manufacturing of stator segments of a wind turbine as a final application in the future.

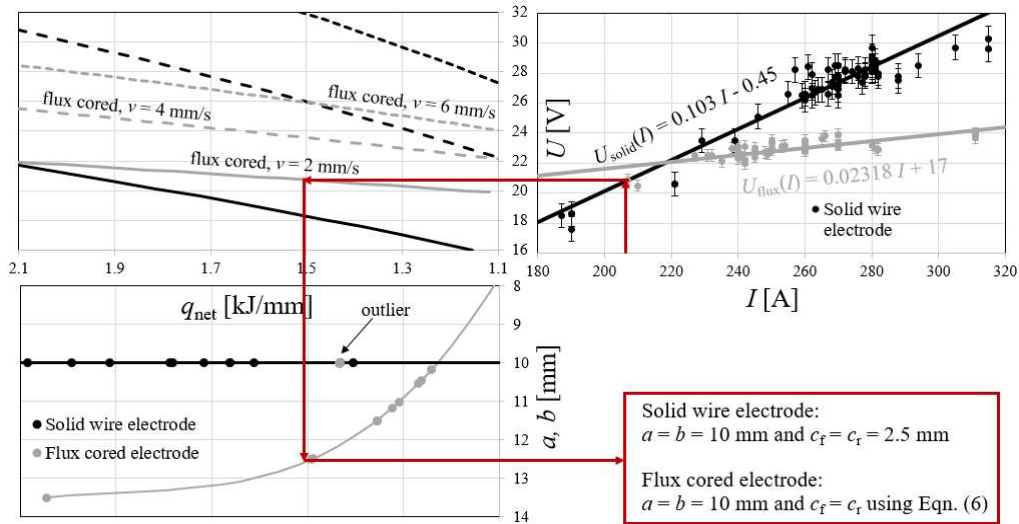


Fig. 15 Workflow of determining characteristic parameters for virtual manufacturing.

#### VALIDATION OF THE WELDING PROCESS MODEL

Calibration and verification of the heat source model makes it possible to investigate the effect of additional parameters and variants in qualitative and quantitative parametric studies and virtual prototyping. It is a time-consuming method, while there is a large amount of waste during the 'trial and error' approach in the product development phase. Developing a sustainable virtual manufacturing process is an innovative way to reduce waste in workshops and specify optimal conditions depending on the requirements for advanced applications.

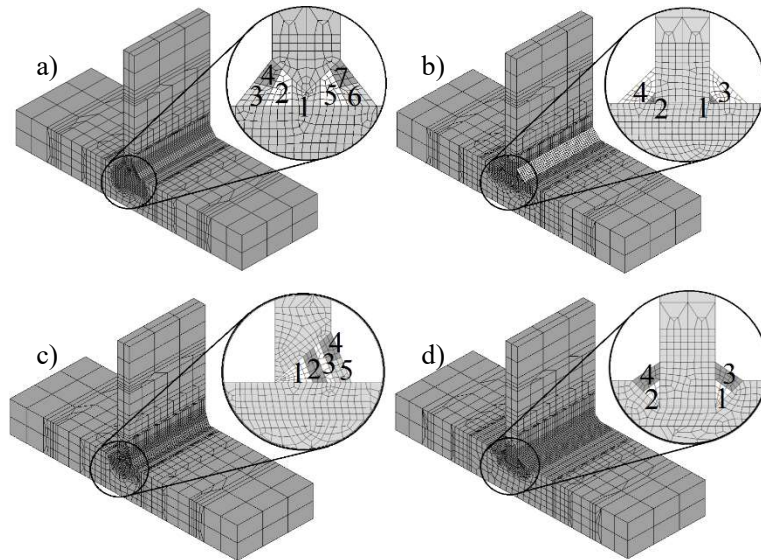
The verified parameters for double-sided fillet welds with single weld passes are validated using an extended set of parameters in case of the four types of T-joint; one from each configuration is presented in this paper. Figure 16 shows the finite element models of the weldments contributing in the validation process, while welding sequence is also denoted. T-joints with double-beveled butt weld (JT1-1-03), with double-sided fillet welds using multiple passes (JT2-1-07), with single-beveled butt weld (JT3-2-01) and a novel configuration with groove (JT4-2-01) are studied. Models consist of 26052, 23112, 18632 and 23640 finite elements, respectively.

Table 3 sums up specimen notations, # number of weld pass, type of filler metal,  $I$  welding current,  $U$  voltage,  $v$  travel speed, denoting (+) positive and (-) negative welding directions,  $a$  characteristic parameter,  $q = \eta UI/v$  net heat input per unit length,  $A_{FZ}$  and  $A_{FZ,FEA}$  fusion zone sizes based on measurements and numerical analyses and error in simulated fusion zone size, respectively. Voltage is calculated using Eqns. (1) and (2) depending on the type of filler metal. Fusion zone sizes in the table are related to the whole joints as multi-pass welding is used for the weldments. Welding sequence is summed up in Figure 17 for the investigated cases.

## Mathematical Modelling of Weld Phenomena 12

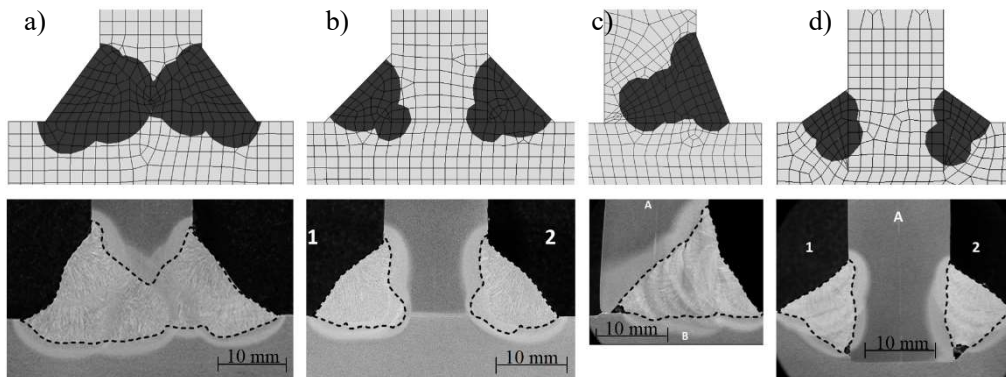
**Table 3** Input and output data for the validated cases.

Specimen	#	Filler metal	$I$ [A]	$U$ [V]	$v$ [mm/s]	$q$ [kJ/mm]	$a$ [mm]	$A_{FZ}$ [mm <sup>2</sup> ]	$A_{FZ,FEA}$ [mm <sup>2</sup> ]	Error [%]
JT1-1-03	1	solid wire	190	19.12	+3.57	0.92	10	331 (298)	302	-8.8 (1.3)
	2	solid wire	280	28.39	+4.55	1.57	10			
	3	solid wire	280	28.39	+5.26	1.36	10			
	4	solid wire	270	27.36	+5.26	1.26	10			
	5	solid wire	280	28.39	-3.33	2.15	10			
	6	solid wire	280	28.39	-4.17	1.72	10			
	7	solid wire	270	27.36	-5.56	1.20	10			
JT2-1-07	1	solid wire	278	28.18	+8.33	0.85	10	95 + 94	86 + 100	-1.3
	2	solid wire	262	26.54	+7.69	0.81	10			
	3	solid wire	276	27.98	-3.85	1.81	10			
	4	solid wire	278	28.18	-3.45	2.04	10			
JT3-2-01	1	flux cored	260	23.03	+3.85	1.40	11.9	158	163	3.2
	2	flux cored	238	22.52	+3.13	1.54	12.7			
	3	flux cored	245	22.68	+5.00	1.00	5.4			
	4	flux cored	242	22.61	+4.17	1.18	9.2			
	5	flux cored	242	22.61	+4.17	1.18	9.2			
JT4-2-01	1	flux cored	270	23.26	+5.88	0.96	4.4	69 + 72	67 +73	-0.7
	2	flux cored	270	23.26	+4.17	1.36	11.5			
	3	flux cored	270	23.26	+4.35	1.30	10.9			
	4	flux cored	270	23.26	+5.00	1.13	8.3			



**Fig. 16** Finite element models of a) JT1-1-03, b) JT2-1-07, c) JT3-2-01 and d) JT4-2-01.

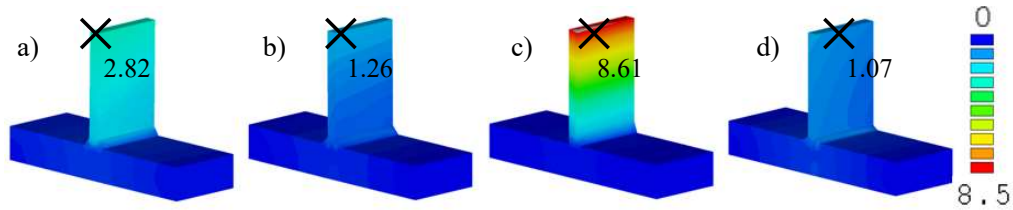
Figure 17 shows the simulated fusion zones and the macrographs highlighting fusion lines with dashed lines; liquidus temperature is assumed to be 1500 °C. Measurements and numerical results are in a good agreement for the specimens, the absolute maximum error in the cross sectional area of the fusion zone is 8.8%, which is a quite convincing result. Namely, the calibrated and verified double ellipsoidal heat source model is validated for multi-pass welding using an extended set of parameters. The largest discrepancy comes forward in case of JT1-1-01, which is T-joint with a double-beveled butt weld. However, the complex geometry of weld face is not taken into account in the simulations. Neglecting the difference between the perfect and imperfect weld geometry reduces the difference to 1.3% as the measured fusion zone size becomes 298 mm<sup>2</sup>. On the other hand, geometry of weld face does not have a large influence on results for the other T-joints.



**Fig. 17** Simulated and measured fusion zones for a) JT1-1-03, b) JT2-1-07, c) JT3-2-01 and d) JT4-2-01.

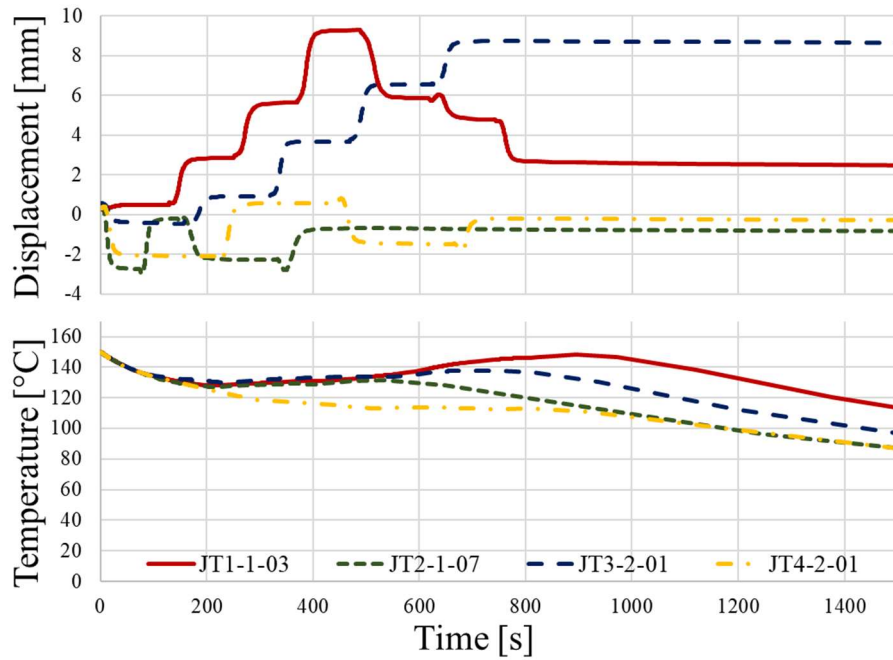


Figure 18 sums up the total deformations of the joints after cooling. Specimens a)-d) have maximum transverse deformations of 2.82 mm, 1.26 mm, 8.61 mm and 1.07 mm, respectively. Results show that the novel T-joint, using a groove and double-sided fillet weld, has performed well in a distortion controlled design. Obviously, the T-joint with single-beveled butt weld is the worst configuration in this sense. On the other hand, it is important to highlight that throat thickness varies for the four specimens.



**Fig. 18** Simulated and measured fusion zones for a) JT1-1-03, b) JT2-1-07, c) JT3-2-01 and d) JT4-2-01.

The top nodes, representing the maximum transverse deformations and denoted with an ‘x’ mark in Figure 18, are selected and typical thermal and displacement data as a function of time are also given in Figure 19 to show the importance of different joint configurations. The time limit in the figure is maximized in 1500 s for clarity, however, cooling to room temperature is modelled. Temperature is 150 °C in the first load step due to the preheat temperature. Welding time varies in a function of travel speed and number of weld passes for the validated cases. Transverse nodal displacement decreases after the 4<sup>th</sup> weld pass for JT1-1-03 and it is alternating for JT2-1-07 and JT4-2-01 because of the welding sequence shown in Figure 16. Obviously, transverse nodal displacement increases permanently during welding for the JT3-2-01 specimen which is a T-joint with a single-beveled butt weld. Eventually, phenomena shown in the figure is an unambiguous explanation for the beneficial effect of alternating welding sequence in a distortion controlled design.



**Fig. 19** Temperature and transverse displacement data as a function of time for the validated models.

A three-dimensional heat transfer model is used to predict the weld pool size in fillet and butt weld configurations during metal active gas welding. Eventually, the developed model is applicable to simulate the fusion zone size with fair precision in S355 structural steel weldments using M21 - ArC - 18 (Corgon 18) shielding gas, PA flat or PB horizontal-vertical welding positions and two different electrode types.

## CONCLUSIONS

Welding simulation has become an ultimate tool for virtual manufacturing, testing and prototyping in the recent years, nevertheless, the calibration of heat source models used in finite element analysis is a common problem as the variation of welding variables have a large influence on the weld pool shape and size. The aim of the current research program is to develop a welding process model for a typical T-joint of a weldment. An experimental and numerical study is performed focusing on the size of fusion zone, deformations and residual stresses during metal active gas welding investigating several types of T-joints and two different filler metals. The relationship between welding current and voltage for solid wire and flux cored electrodes, with diameters of 1.2 mm using a mixture of pure argon and carbon dioxide as shielding gas, is determined. A sensitivity analysis is performed focusing on the effect of thermal efficiency and characteristic parameters of the double ellipsoidal heat source model using uncoupled thermo-mechanical analysis. Results show that thermal efficiency and the scaling factor may have a similar effect on residual stresses and transverse deformations. However, it is important to emphasize that sufficient power

density is requisite to reach the reference temperature of un-deposited material, otherwise, the material model for weld bead elements remain elastic with a low Young's modulus. It results in quasi-zero stresses in weld beads due to lack of fusion affecting overall residual stresses in conjunction with obtaining equilibrium of resultant internal forces and bending moments in any section of the specimen. The thermal efficiency of the welding process is determined by the comparison of experimental and numerical data. The characteristic parameters of the implemented double ellipsoidal heat source model are calibrated for a typical range of welding variables in case of double-sided fillet welds with single weld passes. The developed welding process model for welding simulation of double-sided fillet welds with single weld passes is verified. The verified parameters for double-sided fillet welds with single weld passes are validated using an extended set of parameters in case of a multi-pass welded double-beveled butt weld, double-sided fillet weld, single-beveled butt weld and a novel T-joint using a groove and double-sided fillet weld. A three-dimensional heat transfer model is used to predict the weld pool size in fillet and butt weld configurations during metal active gas welding with fair precision in S355 structural steel weldments using a mixture of pure argon and carbon dioxide as shielding gas, PA flat or PB horizontal-vertical welding positions and two different electrode types. The approach is implemented in the finite element code for further parametric studies and the sustainable virtual manufacturing of stator segments of a wind turbine as a final application in the future.

### ACKNOWLEDGEMENTS

The presented research program received funding from Hungarian R&D project under grant agreement No. GINOP-2.1.1-15-2016-008854. The second author of the paper was supported by the ÚNKP-18-4 New National Excellence Program of the Ministry of Human Capacities and by the János Bolyai Research Scholarship of the Hungarian Academy of Sciences; the financial supports are gratefully acknowledged.

### REFERENCES

- [1] L.E. LINDGREN: 'Finite Element Modeling and Simulation of Welding Part I: Increased Complexity', *Journal of Thermal Stresses*, Vol. 24, No. 2, pp. 141-192, 2001.
- [2] J.A. GOLDAK and M. AKHLAGHI: *Computational Welding Mechanics*, Boston MA, 2005.
- [3] L.E. LINDGREN: *Computational welding mechanics: Thermomechanical and microstructural simulations*, Cambridge, 2007.
- [4] T. KIK, M. SLOVACEK and M. VANEK: 'Use of Welding Process Numerical Analyses as Technical Support in Industry. Part 3: Industrial Examples – Transport Industry', *Biuletyn Instytutu Spawalnictwa*, Vol. 6, pp. 38-45., 2015.
- [5] F.W. BRUST and P. SCOTT: 'Weld Distortion Control Methods and Applications of Weld Modeling', *Transactions*, SMiRT, Toronto, paper #B05/1, 2007.
- [6] D. KOLLÁR and B. KÖVESDI: 'EXPERIMENTAL AND NUMERICAL SIMULATION OF WELDED COLUMNS', *41st International Conference Zavarivanje – Welding 2016*, Opatija, pp. 123-132, 2016.
- [7] D. KOLLÁR, B. KÖVESDI and J. NÉZŐ: 'NUMERICAL SIMULATION OF WELDING PROCESS – APPLICATION IN BUCKLING ANALYSIS', *Periodica Polytechnica Civil Engineering*, Vol. 61, No. 1, pp. 98-109, 2017.

- [8] D. KOLLÁR and B. KÖVESDI: ‘Effect of imperfections and residual stresses on the shear buckling strength of corrugated web girders’, *Proceedings of the Eighth International Conference on Thin Walled Structures*, Lisbon, paper 42, 20 p., 2018.
- [9] European Committee for Standardisation. *EN 1993-1-5:2005. Eurocode 3: Design of steel structures – Part 1-5: Plated structural elements*.
- [10] W. SUDNIK, D. RADAJ, S. BREITSCHWERDT and W. EROFEEV: ‘NUMERICAL SIMULATION OF WELD POOL GEOMETRY IN LASER BEAM WELDING’, *Journal of Physics D: Applied Physics*, Vol. 33, No. 6, pp. 662-671, 2000.
- [11] W. SUDNIK, D. RADAJ and W. EROFEEV: ‘COMPUTERIZED SIMULATION OF LASER BEAM WELD FORMATION COMPRISING JOINT GAPS’, *Journal of Physics D: Applied Physics*, Vol. 31, No. 24, pp. 3475-3480, 1998.
- [12] A. LUNDBACK and H. RUNNEMALM: ‘VALIDATION OF THREE DIMENSIONAL FINITE ELEMENT MODEL IN ELECTRON BEAM WELDING OF INCONEL 718’, *Science and Technology of Welding and Joining*, Vol. 10, No. 6, pp. 717-724, 2005.
- [13] D. ROSENTHAL: ‘THE THEORY OF MOVING SOURCES OF HEAT AND ITS APPLICATION TO METAL TREATMENTS’, *Transactions of the ASME*, Vol. 48, pp. 848–866, 1946.
- [14] R.R. RYKALIN: *Calculations of thermal processes in welding* (in Russian), Moscow, 1951.
- [15] J.A. GOLDAK, A. ODDY, M. GUM, W. MA, A. MASHAIE and E. HUGHES: ‘COUPLING HEAT TRANSFER, MICROSTRUCTURE EVOLUTION AND THERMAL STRESS ANALYSIS IN WELD MECHANICS’, *Mechanical Effects of Welding*, pp. 1-30, 1992.
- [16] N.T. NGUYEN: *Thermal Analysis of Welds*, Southampton, 2004.
- [17] V. PAVELIC, R. TANBAKUCHI, O.A. UYEHARA and P.S. MYERS: ‘EXPERIMENTAL AND COMPUTED TEMPERATURE HISTORIES IN GAS TUNGSTEN-ARC WELDING OF THIN PLATES’, *Welding Journal*, Vol. 48, No. 7, pp. 295s-305s, 1969.
- [18] R.R. RYKALIN: ‘ENERGY SOURCES FOR WELDING’, *Welding in the World*, Vol. 12, No. 9/10, pp. 227-248, 1974.
- [19] J. NÉZŐ: *Virtual Fabrication of Full Size Welded Steel Plate Girder Specimens*, PhD, Heriot-Watt University School of Engineering and Physical Sciences, 2011.
- [20] M. GU, J.A. GOLDAK and E. HUGHES: ‘STEADY STATE THERMAL ANALYSIS OF WELDS WITH FILLER METAL ADDITION’, *Canada Metallurgica*, Vol. 32, No. 1, pp. 49-55, 1993.
- [21] J.A. GOLDAK, A. CHAKRAVARTI and M. BIBBY: ‘A NEW FINITE ELEMENT MODEL FOR WELDING HEAT SOURCES’, *Metallurgical Transactions B*, Vol. 15, No. 2, pp. 299-305, 1984.
- [22] J.R. CHUKKAN, M. VASUDEVAN, S. MUTHUKUMARAN, R.R. KUMAR and N. CHANDRASEKHAR: ‘SIMULATION OF LASER BUTT WELDING OF AISI 316L STAINLESS STEEL SHEET USING VARIOUS HEAT SOURCES AND EXPERIMENTAL VALIDATION’, *Journal of Materials Processing Technology*, Vol. 219, pp. 48-59, 2015.
- [23] M. DAL and R. FABBRO: ‘AN OVERVIEW OF THE STATE OF ART IN LASER WELDING SIMULATION’, *Optics & Laser Technology*, Vol. 78, pp. 2-14, 2016.
- [24] N.T. NGUYEN, Y.W. MAI and A. OHTA: ‘ANALYTICAL SOLUTION FOR A NEW HYBRID DOUBLE-ELLIPSOIDAL HEAT SOURCE IN SEMI-INFINITE BODY’, *Proceedings of International Conference on Advances in Composite Materials and Structures VII*, Bologna, pp. 207-217, 2000.
- [25] P. THASANARAPHAN: *A Study on the Welding Characteristics of Tailor Welded Blank Metal Sheets Using GTAW and Laser Welding*, PhD, Lehigh University, 2012.
- [26] T. OHJI, A. OHKUBO and K. NISHIGUCHI: ‘MATHEMATICAL MODELING OF MOLTEN POOL IN ARC WELDING’, *Mechanical Effects of Welding*, Berlin, pp. 207-214, 1992.
- [27] MATLAB VERSION R2016B, The MathWorks Inc., Natick, Massachusetts, USA, 2016.
- [28] ANSYS VERSION 17.2, ANSYS Inc., Canonsburg, Pennsylvania, USA, 2016.
- [29] D. RADAJ: *Heat Effects of Welding: Temperature Field, Residual Stress, Distortion*, Berlin, 1992.

## Mathematical Modelling of Weld Phenomena 12

- [30] J. BRADAC: 'USING WELDING SIMULATIONS TO PREDICT DEFORMATIONS AND DISTORTIONS OF COMPLEX CAR BODY PARTS WITH MORE WELDS', *Machines, technologies, materials*, Vol. 4, pp. 29-32, 2012.
- [31] J.A. GOLDAK: 'WEB BASED SIMULATION OF WELDING AND WELDED STRUCTURES', <http://www.ewp.rpi.edu/hartford/~ernesto/F2014/MPT/MaterialsforStudents/Patella/Goldak2013-web-based-simulation.pdf>, 24 p., 2013.
- [32] J.A. GOLDAK, B. PATEL, M. BIBBY and J. MOORE: 'COMPUTATIONAL WELD MECHANICS', *AGARD Conference Proceedings*, Vol. 398, pp. 1-32, 1986.
- [33] L.E. LINDGREN, H. RUNNEMALM, and M.O. NASSTROM: 'SIMULATION OF MULTIPASS WELDING OF A THICK PLATE', *International Journal for Numerical Methods in Engineering*, Vol. 44, pp. 1301-1316, 1999.
- [34] M. RHODIN: *Calculation of welding deformations in a pipe flange*, MSc, Chalmers University of Technology, 2012.
- [35] A. ROBERTSON and J. SVEDMAN: *Welding Simulation of a Gear Wheel Using FEM*, MSc, Chalmers University of Technology, 2013.
- [36] European Committee for Standardisation. *EN 1993-1-2:2005. Eurocode 3: Eurocode 3: Design of steel structures – Part 1-2: General rules –Structural fire design*.
- [37] *EN 1011-1:2009. Welding – Recommendations for welding of metallic materials – Part 1: General guidance for arc welding*.

# A STUDY OF COUPLED INFLUENCE OF EVAPORATION AND FLUID FLOW INSIDE A WELD POOL ON WELDED SEAM FORMATION IN GMAW

O. MOKROV\*, O. LISNYI\*, M. SIMON\*,  
A. SCHIEBAHN\* and U. REISGEN\*

*\*RWTH Aachen University, ISF – Welding and Joining Institute, 52062, Aachen, Germany, lisnyi@isf.rwth-aachen.de*

*DOI 10.3217/978-3-85125-615-4-06*

## ABSTRACT

Simulation of the gas metal arc welding (GMAW) process in the welding pool and welded plates requires to define such distributed parameters of the welding arc as heat, mass and electric current fluxes as well as arc pressure and drag forces on the free surface of the welding pool. Comprehensive approaches to define these parameters require to use three dimensional magneto-hydrodynamic arc plasma models. The high complexity of these models does not allow to use them widely for calculation. Nevertheless the most amount of available works use a simplified definition of arc source parameters as a predefined shape (e.g. circular or double ellipsoid law due to the Gauss distribution), that does not change during the calculation. In this work, a new approach is proposed to define the distributions of arc parameters not in the usual predefined shape, but in distributions, that are modified according to the calculated temperature of the free surface of the welding pool on which the arc heating, evaporation of the welding metal and hydrodynamics of the welding pool have their own coupled impact. The discussed approach was used in developing a mathematical model of GMAW process that can provide a numerical analysis of thermal, electromagnetic and hydrodynamic processes in the weld pool and welded plates. The model was used to study the proposed approach of arc parameters redistribution on the welded seam formation.

Keywords: arc welding, numerical simulation, cathode area, heat flux distribution, welded seam formation.

## INTRODUCTION

The gas metal arc welding (GMAW) process is widely used in industries for manufacturing of metal constructions. The quality of a welded joint depends on a set of welding process variables that define conditions of the welding arc burning, the transfer mode of electrode droplets, the shape of the melted zone, the geometry of the welded seam, the chemical composition and heterogeneity, thermal cycles, that define the microstructure and the mechanical properties of the welded metal. A rational choice of welding process variables requires investigations of physical processes taking place in the weld pool and welded

plates. Limitations of experimental research methods caused the need to use mathematical modelling.

One of the main goals of the arc welding process modelling is the prediction of the temperature field, the weld seam geometry and the shape of the weld pool in dependence of the welding process variables. A solution of this task requires to develop appropriate physics-based models for the GMAW process. Calculation of physical processes in the welding pool and welding plates requires to define some parameters of the welding arc such as pressure, drag forces, heat, mass and electric current fluxes on the free surface of the welding pool.

The most comprehensive approach to define these parameters requires to use three dimensional MHD arc plasma models which consider evaporating anode (A) and cathode (C) areas. The high complexity of these models does not allow to use them widely for calculation. Nevertheless, most of the available works use a simplified definition of arc source parameters with usually circular shaped distribution [1, 2].

In this work, a new approach is proposed to define the distributions of heat flux, current density and arc pressure within the cathode area on the free surface of the welding pool. It was proposed to define them not in the usual circular shape, but in a distribution, that is modified according to the calculated temperature of the free surface of the welding pool on which the hydrodynamics of a welding pool and evaporation of welding metal have their own impact.

The intention of the present work is to use the discussed approach to develop a mathematical model of GMAW process that can provide a numerical analysis of thermal, electromagnetic and hydrodynamic processes in the weld pool and welding plates and estimate their influence on the weld seam formation.

### DESCRIPTION OF A MATHEMATICAL MODEL

The model of the GMAW process considers physical phenomena of heat transfer, electromagnetics, hydrodynamics and deformation of weld pool free surface.

In order to simplify the mathematical model formulation, the following assumptions were made: fluctuations of the welding arc burning due to the electrode melting and droplet detachment are neglected; the hydrodynamics flow is Newtonian, incompressible and laminar, the Boussinesq buoyancy approximation is applied; the droplets' frequency, initial velocity, temperature and diameter in dependence on welding parameters are calculated by given empirical equations. To speed up the calculation of weld pool hydrodynamics, ideas that were proposed in [3-4] were used. It is supposed, that the incoming droplet in the weld pool is considered as a non-mixed particle that keeps its mass and size. The trajectory of the droplet in the weld pool is determined numerically by integrating the equation of motion. The interaction between the droplet and liquid metal of the weld pool is determined by the droplet's trajectory due to viscosity and heat conductivity of liquid metal. When the velocity of the droplet becomes the same as the melt flow velocity it is considered that the droplet is accepted by the weld pool volume.

The calculation area includes the welding plates, the welding pool and the solidified metal of welded seam. The Cartesian stationary coordinate system ( $x, y, z$ ) is used in the

## Mathematical Modelling of Weld Phenomena 12

calculation. The welding arc moves along x axis and gravity force is directed downward in z direction (Figure 1).

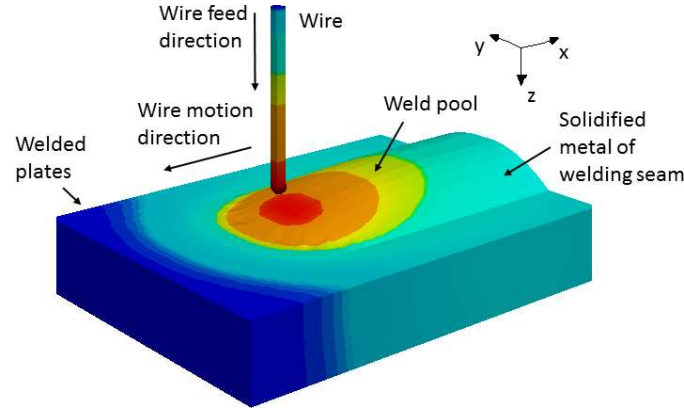


**Fig. 1** Schematic representation of GMAW process.

Based on the above assumptions, the governing equations used to describe the GMAW process are given as follows: they include heat transfer (1), momentum transfer (2) and mass conservation (3), electrical current continuity (4), Maxwell's equations (5) and the deformation of weld pool free surface (6-7).

$$\frac{\partial h}{\partial t} + \nabla(\vec{u}h) = \nabla(\lambda\nabla T) + \frac{j^2}{\sigma} + S_{dh}; \quad (1)$$

$$\rho \left( \frac{\partial \vec{u}}{\partial t} + \nabla(\vec{u} \cdot \vec{u}) \right) = -\nabla P + \nabla(\mu\nabla\vec{u}) + \rho\vec{g}\beta_A T + \vec{j} \times \vec{B} + \vec{S}_{du}; \quad (2)$$

$$\nabla(\rho\vec{u}) = 0; \quad (3)$$

$$\nabla(\sigma\nabla\phi) = 0; \quad (4)$$

$$\vec{B} = \nabla \times \vec{A}, \nabla^2 \vec{A} = \mu_0 \vec{j}; \quad (5)$$

$$\nu \nabla(K^{-1}\nabla\xi) - \rho(\vec{g} \cdot \vec{n})(\xi - \xi_{max}) = P_{arc} + P_d; \quad (6)$$

$$\int_{y_m}^{y_p} (\xi(x_m, y) - \xi_0) dy = \pi r_f^2 \frac{u_f}{u_w}; \quad (7)$$

where  $t$  is the time;  $h = \int_{T_0}^T c\rho dT + \chi\rho\eta$  is the enthalpy;  $c$  is the heat capacity;  $\rho$  is the mass density;  $T$  is the temperature;  $T_0$  is the initial temperature;  $\chi$  is the latent heat;  $\eta$  is the fraction of liquid metal ( $\eta = 0, T \leq T_S$ ;  $\eta = 1, T \geq T_L$ ;  $\eta = (T - T_S)/(T_L - T_S), T_S < T < T_L$ );  $T_L, T_S$  are the liquidus and solidus temperatures;  $u$  is the fluid flow velocity of liquid metal inside the weld pool;  $\lambda$  is the thermal conductivity;  $j$  is the electrical current density;  $\sigma$  is the electrical conductivity;  $P$  is the pressure;  $\mu$  is the viscosity;  $g$  is the acceleration due to gravity;  $\beta_A$  is the thermal volumetric expansion coefficient of liquid metal;  $B$  is the magnetic induction;  $\phi$  is the electrical potential (it is linked to the current



via Ohm's law  $j = -\sigma \nabla \phi$ ;  $A$  is the vector potential;  $\mu_0$  is the permeability of vacuum;  $\xi$  is the free surface position in  $z$  direction;  $\upsilon$  is the surface tension;  $K = \sqrt{1 + (\nabla \xi)^2}$  is the curvature of the free surface;  $P_{arc} = \frac{3\mu_0 I^2}{4\pi} \frac{1}{\pi r_p^2} \exp(-3(x_t^2 + y^2)/r_p^2) \beta(T, T_B)$  is the arc pressure;  $r_p$  is the arc pressure radius;  $x_t = x_0 - u_w t$ ,  $x_0$  is the current and beginning position of the welding arc;  $u_w$  is the welding velocity;  $\beta$  is the arc redistribution function;  $T_B$  is the boiling temperature;  $P_d = \frac{3}{4} \pi r_d^3 \frac{3\rho u_d f_d}{\pi r_d^2} \exp(-3(x_t^2 + y^2)/r_d^2)$  is the droplet impact pressure;  $u_d$ ,  $f_d$ ,  $r_d$  are the droplet velocity, frequency and radius.

The source terms considering the droplets' interaction with the weld pool are given as  $S_{du} = \frac{1}{\delta V} \sum_{k=1}^N f_d A_k$ ,  $S_{dh} = \frac{1}{\delta V} \sum_{k=1}^N q_d A_k$ ; where  $S_{du}$ ,  $S_{dh}$  are the local values of mechanical momentum and heat sources due to the interaction between the droplets and the liquid metal of the weld pool;  $N$  is the instantaneous number of droplets that are present in a local volume  $\delta V$ ;  $A_k$  is the surface area of a droplet;  $f_d = (u_d - u)\mu/r_w$  is the mechanical interaction between the droplet and the liquid metal of the weld pool;  $u_d$  is the droplet velocity;  $r_w$  is the length of predefined boundary layer. The change of droplet kinematic momentum is tracking by expression  $du_d/dt = f_d/\rho$ . The heat flux between the droplet and the weld pool is given as  $q_d = (T_d - T)\lambda/r_w$ ,  $T_d$  is the droplet temperature,  $T$  is the local temperature of liquid metal. The change of the droplet's heat content is given by  $\partial h_d/\partial t = q_d A_k/\delta V$ .

The deformation of the weld pool free surface is calculated using an equilibrium surface equation (6), considering the influence of surface tension, surface curvature, gravity, arc pressure and droplet impact pressure.  $\xi_{\max}$  is determined by the integral equation of mass conservation (7) due to the assumption that the volume of metal fed from the wire is equal to the volume of weld reinforcement;  $y_p$ ,  $y_m$  are the boundaries of molten metal in  $y$  direction,  $x_m$  is the boundaries of molten metal in  $x$  directions at the edge of solidification;  $\xi_0$  is the initial coordinates of top surface before melting;  $r_f$  is the radius of electrode wire;  $u_f$  is the velocity of electrode wire feeding.

Boundary conditions for heat flux on the left ( $y=2Lg$ ), right ( $y=-2Lg$ ), front ( $x=0$ ), back ( $x=8Lg$ ) and bottom ( $z=Lg$ ) surfaces were defined by eq. (8), where  $Lg$  is a space parameter. The heat flux on the top surface ( $z = \xi$ ) was defined by eq. (9).

$$\lambda \frac{\partial T}{\partial n} = q_{NR} - q_{radi}; \quad (8)$$

$$\lambda \frac{\partial T}{\partial n} = q_{arc} - q_{NR} - q_{radi} - q_{evap}; \quad (9)$$

$$q_{NR} = \alpha(T - T_{out}); \quad (10)$$

$$q_{radi} = e \sigma_S (T^4 - T_{out}^4); \quad (11)$$

$$q_{arc} = \frac{\eta I U - W_d}{\pi r_h^2} \exp(-3(x_t^2 + y^2)/r_h^2) \beta(T, T_B); \quad (12)$$

## Mathematical Modelling of Weld Phenomena 12

where  $n$  is the outward unit normal vector of the surface,  $\alpha$  is the Newton-Richmann heat exchange coefficient,  $\sigma_s$  is the Stefan-Boltzmann constant,  $e$  is the surface emittance,  $T_{out}$  is the ambient temperature,  $q_{evap}$  is the evaporation heat flux, which is calculated by the evaporation model from [5],  $q_{arc}$  is the arc heating flux,  $\eta$  is the arc efficiency,  $I$  is the welding current,  $U$  is the drop of arc voltage,  $W_d = c\rho\pi r_f^2 u_f(T_d - T_{our})$  is the heat power consumed for heating of electrode wire and droplets,  $r_h$  - is the arc heating radius. The melt flow velocity along solidus temperature is set as  $u = 0$ . On the top surface the normal component of vector velocity is set as  $u_n = 0$  and the tangential component of vector velocity  $\tau$  is defined by surface thermo-capillary force  $\frac{\partial u_\tau}{\partial n} = \beta_M \frac{\partial T}{\partial \tau}$ ; where  $\beta_M = d\sigma/dT$  is the temperature coefficient of surface tension. The electric potential at the bottom surface is set as  $\varphi = 0$ . At the top surface we adopt the following electric potential  $\sigma \nabla \varphi = I/(\pi r_j^2) \exp(-3(x_t^2 + y^2)/r_j^2) \beta(T, T_B)$  where  $r_j$  is the arc electrical radius. At other boundaries  $\nabla \varphi = 0$ . The gradient of the magnetic potential at all sides is set as  $\nabla A = 0$ . At the beginning of calculation  $t=0, T=T_0, u=0, P=0, \varphi=0, \xi = \xi_0 = 0, x_0 = 6L_g$ . The calculation leads until  $x_0 > 2L_g$ .

### CALCULATION METHODS

The mathematical model of the GMAW process was approximated by the finite volume method. A non-uniform rectangular spaced grid is used to describe the geometrical model approximation. A finer spacing grid (0.2 mm) was applied in melted area. The SIMPLER algorithm [6] is employed to calculate the fluid velocity fields. A restriction on the overheating of the weld pool free surface was considered due to the evaporation of the base metal. It was taken into account that the increase of evaporated mass flow leads to a decrease of the density of the electric current and heat generation in local areas of the cathodic layer. The used assumptions are aligned with the existing hypotheses of a preferential binding of the welding arc to the free surface of the welding pool. The initial distribution of arc parameters were defined by normal Gauss' law. During the calculation, a special iteration procedure was applied to obtain values of  $\beta$  function (it can be changed from 1 when  $T < T_B$  up to 0 when  $T \gg T_B$ ). It limits the overheating of the welding pool surface above the boiling temperature. The values of  $r_p, r_H, r_j$  were recalculated according to changing  $\beta$  to keep the integral value of arc pressure, heating and electrical current as given constants).

The geometry of the weld pool was defined as  $D, B, G, L$  - the depth, width, height of reinforcement and length. The initial internal model parameters  $r_h, r_j, r_d, r_p$  were defined by experimental data due to providing less than 5% of numerical error for the weld pool geometry calculation, other parameters are given in Tables 1-2.

**Table 1** Parameters of mathematical model

Property	Symbol, unit	Value
space parameter	$L_g, cm$	1.0
electrode radius	$r_e, cm$	$8.0 \cdot 10^{-2}$
arc voltage	$U_0, V$	32
welding velocity	$u_w, mm/min$	600
length of boundary layer	$r_w, cm$	$1.0 \cdot 10^{-2}$
velocity of electrode wire melting ( $I = 250-375 A$ )	$u_f, cm/s$	$-6.3 + 0.053 \cdot I$
arc efficiency	$\eta$	0.8
Stefan-Boltzmann constant	$\sigma_s, W cm^{-2} K^{-4}$	$5.67 \cdot 10^{-4}$
coefficient of radiation emission	$\chi e$	0.4
coefficient of Newton-Richman heat exchange	$\alpha, W cm^{-2} C$	$1.0 \cdot 10^{-3}$
magnetic permeability	$\mu_0, g s^{-2}$	$1.26 \cdot 10^{-3}$
gravitational acceleration	$g, cm c^{-2}$	980.0
initial and ambient temperature	$T_0, T_{out}, C$	20.0
liquidus temperature	$T_L, C$	1514.0
solidus temperature	$T_S, C$	1443.0
boiling temperature	$T_B, C$	2860.0

**Table 2** Parameters of mathematical model

Property	Symbol, unit	Value
latent heat of melting and solidification	$\chi, J g^{-1}$	270.0
density of material	$\rho, g cm^{-3}$	7.6
coefficient of surface tension	$\nu, g s^{-2}$	$1.8 \cdot 10^3$
heat capacity	$c, J g^{-1} C^{-1}$	0.5
thermal conductivity	$\lambda, W cm^{-1} C^{-1}$	0.45
electrical conductivity ( $T > 1000C$ )	$\sigma, om^{-1} cm^{-1}$	$1.0 \cdot 10^4$
cinematic viscosity	$\mu, cm^2 s^{-1}$	$1.1 \cdot 10^{-2}$
coefficient of thermal volumetric expansion	$\beta_A, C^{-1}$	$1.4 \cdot 10^{-4}$
coefficient of thermal surface expansion	$\beta_M, C^{-1}$	$2.1 \cdot 10^{-3}$

## EXPERIMENTAL PROCEDURE

The experiments were made for 100x100x10 mm plates of S235JR steel, 1.6 mm diameter welding wire of SG2 steel, electrode stick out 25 mm, direct current electrode positive (DCEP) power source supply. The experimental data of geometry of the weld bed was obtained. A digitized measurement of full 3-dimensional shape of weld bed was defined by a non-contact 3d laser profiling system, Figure 2. The welding parameters and sizes of the weld pool are given in Table 3.

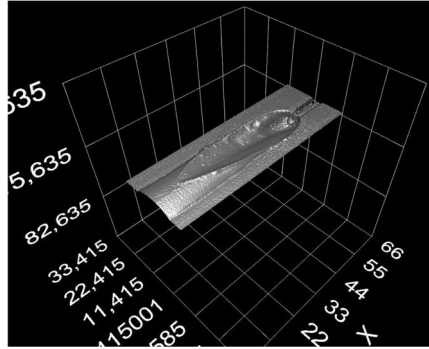


Fig. 2 3D scan of the weld bed .

Table 3 Experimental data of weld pool geometry

I, A	D, mm	B, mm	G, mm	L, mm
250	3.3	9.1	1.3	21.0
375	7.9	11.0	3.7	43.0

### RESULTS AND DISCUSSION

Figure 3-4 shows the calculated results obtained due to the use of heat flux  $q_{arc}$  that is distributed by Gauss' law (GL).

Figure 3 shows the calculated results at 250 A. As the maximal temperature of the weld pool free surface 2840 C is lower than the boiling temperature of the welding material. The heat lost due to the evaporation is not significant and the effect of heat flux redistribution in the cathode area for this case does not appear. The velocity of electrode melting is 7 cm/s. The free surface of the liquid welding pool metal has no significant deformation as the arc pressure and droplet impact flow have no significant influence.

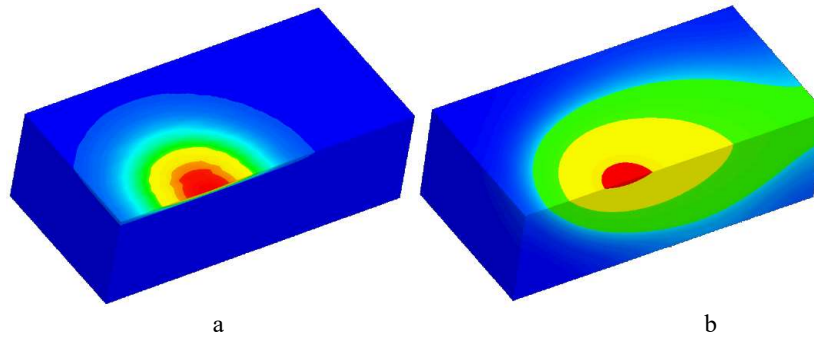
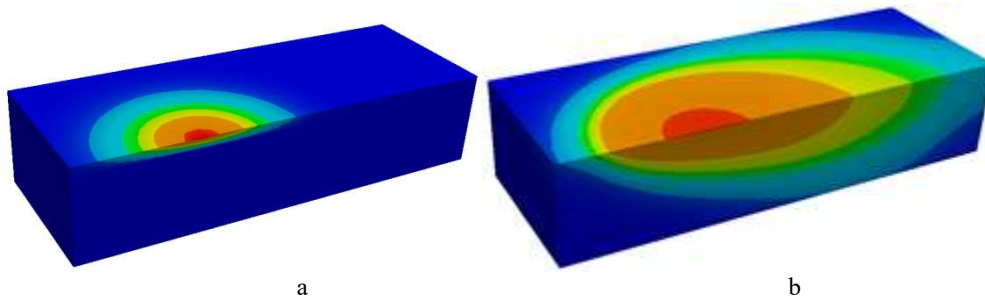


Fig. 3 Heat flux (a) and temperature field (b) ( $I=250$  A,  $v_{max} = 40$  mm/s,  $q_{max} = 1.43 \cdot 10^5$  W/cm<sup>2</sup>,  $T_{max} = 2840$  C).

In this case the shape of the free surface is mostly defined by the surface tension force and the intensity of metal mass income due to the electrode melting rate. It indicates the surface mode of heat and mass transfer in the area of burning arc during GMAW process.

The convective flow of liquid metal inside the weld pool is formed mainly under the influence of thermo-gravitational and thermo-capillary forces. In this case the maximum velocity of liquid metal flow is 40 mm/s. The impact of the electromagnetic Lorentz force and forced convection due to the droplets income do not lead to a significant axial flow in the downward direction of the weld pool. In the central part of the weld pool, ascending liquid streams are formed. They transport the most overheated metal from the arc area along the free surface to the periphery of the weld pool. Near solidification borders, the convective streams of liquid metal change in the opposite direction and move along the bottom surface of the welding pool. Near solidification borders, the convective streams of liquid metal change in the opposite direction and move along the bottom surface of the welding pool.

Figure 4 shows the calculated results at the higher welding current 375 A. The velocity of electrode melting rate reaches 19 cm/s, the depression of weld pool free surface is 3.5 mm.



**Fig. 4** Heat flux (a) and temperature field (b)  $q_{arc}$  settled by Gauss' law ( $I=375 A$ ,  $v_{max} = 250 mm/s$ ,  $q_{max} = 2.15 \cdot 10^5 W/cm^2$ ;  $T_{max} = 3150 C$ ).

The comparison between 250 A and 375 A shows a significant increase of the penetration depth, while the width of the melted zone becomes smaller (Table 3). This result is caused by the complex influence of two main factors that lead to the concentrated arc source impact on welding plates. The first factor is the significant deformation of the weld pool free surface due to the more intensive arc dynamic pressure and the droplet impact flow. It increases the temperature gradient and heat flux from the free surface of the weld pool to the melting front due to the decreasing of the thickness of liquid metal under the arc source. The second factor is the change of the liquid metal hydrodynamic flow pattern. In this case the convective flow inside the welding pool is formed mainly due to the electromagnetic Lorentz force and the forced convection due to the droplets mass income. Under the influence of these force factors the maximal velocity of convective flow reaches 200 mm/s. Inside the welding pool near the electrode tip a downward convective flow is formed. It transfers the most overheated metal from the arc area to the melting front. At the solid interface, the convective flow turns and goes along the bottom surface to the peripheral zones of the weld pool.

Figure 5 shows the calculated results obtained due to the use of heat flux  $q_{arc}$  that is redistributed due to the evaporated mass flow (EMF) at welding current 375 A. The maximal overheating above the boiling temperature in case GL is 290 C, in case EMF it is less than 35 C.

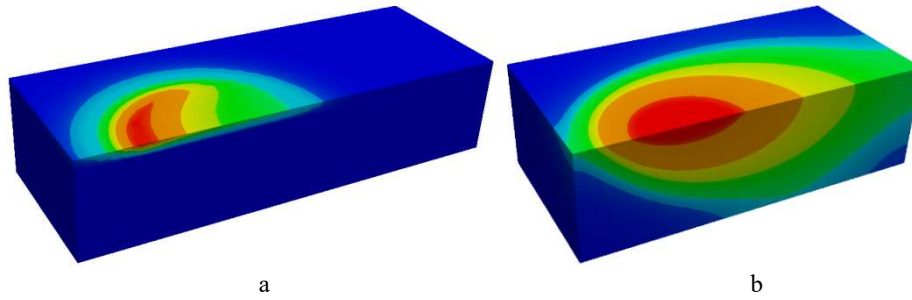


**Fig. 5** Heat flux (a) and temperature field (b)  $q_{arc}$  redistributed due to the evaporated mass flow, ( $I=375\text{ A}$ ,  $v_{max} = 200\text{ mm/s}$ ,  $q_{max} = 1.5 \cdot 10^5\text{ W/cm}^2$ ;  $T_{max} = 2895\text{ C}$ ).

The higher overheating produces higher heat losses and as a subsequent result in the EMF case the depth of penetration increased by 15%, the lengths of the weld pool is increased by 20% and the width of the weld pool is increased by 5%. Also, it has to be mentioned that in the EMF case the heat distribution has no axial symmetry and is stretched along the melting front of the weld pool. The highest density of the heat flux of the arc in the cathode area is shifted from the central region of the weld pool (under the electrode) towards the melting front of the weld pool. Due to this cause, the direction of heat and mass flow in the weld pool changes, which promotes an increase of the melting ability of the welding arc.

## CONCLUSIONS

The developed mathematical model of GMAW process allows to investigate the formation of the temperature field in the welding plates, fluid flow inside the weld pool, geometry of the welding bed and welded seam in dependence on GMAW process variables.

The results of the calculations show that in case of redistributed heat flux  $q_{arc}$  with an increase of thermal power of the arc the highest density of the heat flux of the arc in the cathode area is shifted from the central region of the weld pool (under the electrode) towards the melting front of the weld pool. Due to this cause, the direction of heat and mass flow in the weld pool changes, which promotes an increase of the melting ability of the welding arc. With increasing depression of the free surface of the weld pool this effect amplifies.

The obtained calculations show that for a plate with a thickness of 10 mm, arc voltage 32 V, welding velocity 600 mm/min and at a current of 375 A, the effect of arc parameters redistribution leads to an increase in depth of penetration by 15%, in length of the weld pool by 20% and in width of the weld pool by less than 5%. The increase of melted metal volume in comparison with original Gauss' law distribution is caused by decreased heat losses due to evaporation. The calculation show that considering of arc bending can have influence on weld bed calculation.

The simulations show that with an increase of welding current the enthalpy transferred from the droplet to the weld pool has a stronger influence on the weld pool depth and the momentum transferred by the droplets has a stronger influence on the melt flow in the weld pool.

## Mathematical Modelling of Weld Phenomena 12

The developed model can be used as a base for the following investigation of the influences of the welding arc in GMAW process.

### ACKNOWLEDGEMENTS

This work was carried out with the financial support of the Collaborative Research Centre SFB1120 (DFG (Deutsche Forschungsgemeinschaft) Sonderforschungsbereich) "Precision Melt Engineering" at RWTH Aachen University. For the sponsorship and the support we wish to express our sincere gratitude.

### REFERENCES

- [1] ZHEN NING CAO, PINGSHA DONG: *Modeling of GMA Weld Pools With Consideration of Droplet Impact*. J. Eng. Mater. Technol 120(4), 313-320 (Oct 01, 1998) (8 pages) doi:10.1115/1.2807020
- [2] Z. YANG, T. DEBROY: *Modeling macro-and microstructures of Gas-Metal-Arc Welded HSLA-100 steel*. Metallurgical and Materials Transactions B, June 1999, Vol. 30, Issue 3, pp 483–493
- [3] A.B. MURPHY: *A self-consistent three-dimensional model of the arc, electrode and weld pool in gas-metal arc welding*. J. Phys. D: Appl. Phys. 44, (2011), 194009 (11pp). doi:10.1088/0022-3727/44/19/194009
- [4] A.B. MURPHY: *Influence of droplets in gas-metal arc welding: new modelling approach, and application to welding of aluminium*. Science and Technology of Welding and Joining, 2013 Vol. 18, No. 1, p.32-37.
- [5] H.G. FAN, R. KOVACEVIC: *A unified model of transport phenomena in gas metal arc welding including electrode, arc plasma and molten pool*. J. Phys. D: Appl. Phys. 37 (2004) 2531–2544 PII: S0022-3727(04)77964-4
- [6] M. CHOI, R. GREIF: *A study of the heat transfer during arc welding with applications to pure metals or alloys and low or high boiling temperature materials*. Numerical Heat Transfer, Vol. 11, 1987, pp. 477-489
- [7] S.V. PANTANKAR: *Numerical Heat Transfer and Fluid Flow*. McGraw-Hill, 1980, New York

## **II Microstructure Modelling in WM and HAZ**





# NUMERICAL SIMULATION OF FERRITE/AUSTENITE PHASE FRACTION IN MULTIPASS WELDS OF DUPLEX STAINLESS STEELS

T. OGURA\*, T. MATSUMURA\*, L. YU\*, D. C. KIM\*,  
H. INOUE\*\*, Y. OIKAWA\*\*\* and K. SAIDA\*

*\*Dept. of Materials & Manufacturing Science, Osaka University*

*\*\*Joining & Welding Research Institute, Osaka University*

*\*\*\*Nippon Steel & Sumikin Stainless Steel Corporation*

DOI 10.3217/978-3-85125-615-4-07

## ABSTRACT

Kinetic approach to the  $\alpha/\gamma$  phase transformation phenomena ( $\alpha/\gamma$  phase fraction) in the heat affected zone (HAZ) and weld metal (WM) of multipass welds was made using duplex stainless steels (lean, standard and super duplex stainless steels). The kinetic equations including rate constants of the dissolution behaviour as well as precipitation behaviour of  $\gamma$  phase were determined by isothermal heat treatment test. Based on the kinetic equations determined, the distribution of the  $\gamma$  phase fraction in multipass welds of duplex stainless steels was calculated applying the incremental method combined with the heat conduction analysis during welding. The depleted zone of  $\gamma$  phase was formed adjacent to the fusion line in the base metal HAZs and the reheated WMs. However, the  $\gamma$  phase fraction in the depleted zone was increased (recovered) by the subsequent weld passes. Accordingly, the  $\alpha/\gamma$  phase balance has been complexly varied in multipass welds, and the profile of the  $\gamma$  phase fraction was arranged in laminae in the WM roughly along the fusion lines. Furthermore, the  $\gamma$  phase fraction in multipass weld of standard DSS was slightly lower than those of lean and super DSSs. The over-precipitated zone, where the  $\gamma$  phase fraction slightly exceeded the base metal level, was not observed in the low temperature HAZ of standard DSS weld, whereas it was observed in other welds. Microstructural observation revealed that the calculated results of the  $\gamma$  phase fraction in multipass welds were consistent with experimental ones. It follows that the  $\alpha/\gamma$  phase transformation in duplex stainless steel welds could be successfully predicted by the present approach.

## INTRODUCTION

Duplex stainless steels (DSSs) have been widely applied in various industrial fields such as chemical, energy, food, pharmacy and marine plants. DSSs indicate the dual phase microstructure consisting of the balanced austenitic ( $\gamma$ ) and ferritic ( $\alpha$ ) phases, and possess the superior properties such as high strength and toughness, high corrosion resistance and good weldability. However, during fusion welding (especially multipass welding), DSSs undergo the complex microstructural change and phase transformation affecting the  $\alpha/\gamma$

phase balance due to a series of thermal cycles [1-4]. The microstructure of the weld metal (WM) is quite different from that of the base metal, *i.e.*, solidified as the single-phase  $\alpha$  (F mode) and precipitated the Widmanstätten  $\gamma$  [5]. On the other hand, in the heat affected zone (HAZ), the  $\gamma$  phase fraction is reduced (the  $\alpha/\gamma$  phase balance deviates from the adequate ratio), and Cr-carbides and nitrides and/or intermetallic compounds such as  $\sigma$  and  $\chi$  phases would be easily precipitated in the  $\gamma$  phase-depleted HAZ [6-9]. As a result, the mechanical and corrosion properties of welds would be seriously deteriorated. It follows that prediction and control of the  $\alpha/\gamma$  phase transformation in DSS welds are required. There are a number of studies concerning the  $\alpha/\gamma$  phase transformation phenomena in DSS welds [5,10-14], while only a few studies have been conducted for investigating the kinetics of the  $\alpha/\gamma$  phase transformation. According to the previous reports, the kinetics of formation (precipitation) of  $\gamma$  phase in the HAZ of DSS welds was followed by the Austin-Rickett type equation [15,16], and the  $\gamma$  phase fraction in the DSS WM was successfully predicted in the cooling thermal cycle with various cooling rates [17]. However, these investigations dealt with only the precipitation phenomena of  $\gamma$  phase in the HAZ under the limited thermal cycles. In particular, the  $\alpha/\gamma$  phase transformation in multipass welds (*i.e.*, multiple thermal cycle) has not been clarified yet. In addition, the dissolution and re-precipitation behaviours of  $\gamma$  phase during thermal cycle were not investigated at all. In the HAZ of DSS welds,  $\gamma$  phase has been dissolved once at the higher temperature in weld thermal cycle, and then precipitated again (re-precipitated) during cooling. In order to predict the  $\alpha/\gamma$  phase transformation in welds, especially multipass welds, it is necessary to clarify the kinetics of dissolution and precipitation of  $\gamma$  phase separately. Furthermore, the precipitation kinetics of  $\gamma$  phase in the WM would differ from that in the HAZ (base metal), because  $\gamma$  phase comes to precipitate in the solidified (solidification-segregated)  $\alpha$  structure originated from the F mode solidification.

In the previous studies [18,19], the authors have investigated the kinetics of  $\alpha/\gamma$  phase transformation (dissolution and precipitation behaviours of  $\gamma$  phase) in the HAZ of DSS welds (lean, standard and super DSSs), and the  $\gamma$  phase fraction in the HAZ of single pass melt-run welds was numerically calculated and compared between the types of steel and/or welding techniques. As a result, the dissolution as well as precipitation behaviour of  $\gamma$  phase was followed by the Austin-Rickett type equation, and the rate constants of them involving the temperature dependency were determined for various DSSs. From the fact that the calculated results of the  $\gamma$  phase fraction in the HAZ of gas tungsten arc (GTA) and laser beam (LB) melt-run welds were approximately consistent with experimental ones, the authors have concluded that the  $\alpha/\gamma$  phase transformation in the HAZ of DSS welds could be successfully predicted by the numerical computation. However, the  $\alpha/\gamma$  phase transformation behaviour in the DSS WM has never been predicted in the previous study.

In the multipass welding, the WM as well as HAZ is reheated numerous times by the subsequent weld passes, as a result, the dissolution and/or precipitation of  $\gamma$  phase will alternate in welds. Furthermore, the dissolution and precipitation kinetics of  $\gamma$  phase would differ between in the multipass WM and HAZ (base metal) as pointed out above. Because of such very complicate phase transformation behaviours during multiple thermal cycle, the  $\alpha/\gamma$  phase transformation in multipass DSS welds is hard to predict quantitatively.

In the present study, the kinetic approach was made to the  $\alpha/\gamma$  phase transformation phenomena in the multipass welds of DSSs. Both of the dissolution and precipitation

behaviours of  $\gamma$  phase were kinetically investigated for the reheated WM as well as the base metal HAZ, and the  $\gamma$  phase fraction in multipass welds of DSSs was numerically calculated by coupling with the heat conduction analysis during multipass welding. Finally, the predicted results of  $\alpha/\gamma$  phase transformation in multipass welds were verified by the experimental examination.

## MATERIALS AND EXPERIMENTAL PROCEDURES

### MATERIALS

Three types of DSSs, lean, standard and super DSSs, were used for the base metal. Table 1 shows the chemical compositions of the base metals used in this study. A standard and super DSSs are comparable to type 329J3L and 327L1 steels, respectively. All DSSs were heat-treated at 1323 K $\times$ 5 min after hot rolling. The autogenous filler metals (diameter, 1.2 mm) were used for gas tungsten arc welding (GTAW). The chemical compositions of filler metals are shown in Table 2. The filler metal compositions for lean DSS welding were identical to the base metal compositions (because manufactured from the base metal plate). The  $\gamma$  phase fraction of as-received base metals of DSSs was approx. 50-60%. The dimensions of DSS plates were 50 mm  $\times$  70 mm  $\times$  4 mm<sup>t</sup> (for single pass melt-run welding) and 80 mm  $\times$  100 mm  $\times$  12 mm<sup>t</sup> (for multipass welding).

### EXPERIMENTAL PROCEDURES

In order to manufacture the WM of DSS, single pass melt-run GTAW was carried out using

**Table 1** Chemical compositions of duplex stainless steels used (mass%)

Steel	C	Si	Mn	P	S	Ni	Cr	Mo	Cu	N	Fe
Lean DSS	0.014	0.35	1.49	0.024	0.0004	3.06	20.85	0.30	0.09	0.177	Bal.
Standard DSS	0.008	0.56	1.82	0.025	0.0002	5.75	22.55	3.08	0.16	0.161	Bal.
Super DSS	0.009	0.31	0.51	0.024	0.0009	6.56	25.11	3.72	0.21	0.259	Bal.

a DSS plate under the welding conditions of arc current, 90 A; arc voltage, 14 A; welding

**Table 2** Chemical compositions of filler metals used (mass%)

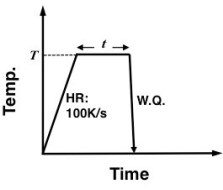
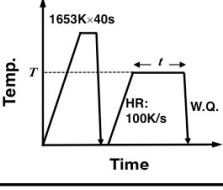
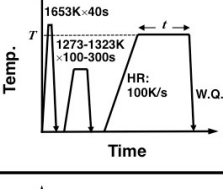
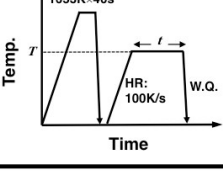
Steel	C	Si	Mn	P	S	Ni	Cr	Mo	Cu	N	Fe
Lean DSS	0.014	0.35	1.49	0.024	0.0004	3.06	20.85	0.30	0.09	0.177	Bal.
Standard DSS	0.012	0.56	1.81	0.024	0.0005	5.72	22.46	3.07	0.17	0.169	Bal.
Super DSS	0.013	0.31	0.48	0.025	0.0005	6.83	24.98	4.03	0.20	0.265	Bal.

speed, 6 cm/min; shielding gas, Ar+2%N<sub>2</sub> (flow rate, 15 L/min). The full weld metal specimen for isothermal heat treatment was machined from the melt-run welded plate. The dimensions of specimen were 3 mm  $\times$  8 mm  $\times$  1.5 mm<sup>t</sup>. On the other hand, the base metal specimen for isothermal heat treatment was directly machined from the as-received plate. The dimensions of specimen were 3 mm  $\times$  3 mm  $\times$  4 mm<sup>t</sup>.

## Mathematical Modelling of Weld Phenomena 12

The isothermal heat treatment of DDS specimen was conducted in the Ar atmosphere using a high frequency induction heating apparatus. The heat-treatment conditions including thermal cycle patterns are summarised in Table 3. Different kinds of isothermal heat treatment were conducted for the kinetic investigation of the dissolution and precipitation phenomena. As for the base metal specimen, the solution treatment at 1373-1633 K for 0-2000 s was performed to investigate the dissolution behaviour of  $\gamma$  phase, and the precipitation treatment at 1073-1423 K for 0-3000 s subsequent to the  $\alpha$  single-phasing treatment (solution treatment) at 1653 K for 40 s was performed to investigate the precipitation behaviour of  $\gamma$  phase in the single-phase  $\alpha$  structure. As for the weld metal specimen, the solution treatment at 1473-1623 K for 0-2000 s was performed subsequent to the  $\alpha$  single-phasing treatment at 1653 K for 40 s and the pre-precipitation treatment at 1273-1323 K for 100-300 s (aimed to the initial amount of  $\gamma$  phase being uniformed at

**Table 3** Conditions of isothermal heat treatment

Heat treatment		Thermal cycle	Conditions	
Base metal (Base metal HAZ)	Solution treatment		Heating temp., $T$	1373-1633K
			Holding time, $t$	0-3000s
Base metal (Base metal HAZ)	Precipitation treatment		Heating temp., $T$	1073-1423K
			Holding time, $t$	0-3000s
Weld metal (Reheated WM)	Solution treatment		Heating temp., $T$	1473-1623K
			Holding time, $t$	0-30s
Weld metal (Reheated WM)	Precipitation treatment		Heating temp., $T$	1123-1423K
			Holding time, $t$	0-1000s

approx. 50%), and the precipitation treatment at 1123-1423 K for 0-1000 s was performed subsequent to the  $\alpha$  single-phasing treatment (solution treatment) at 1653 K for 40 s.

## Mathematical Modelling of Weld Phenomena 12

The multipass GTAW was carried out for investigation of the microstructure and  $\alpha/\gamma$  phase fraction in welds. The GTAW conditions were as follows: arc current, 160 A; arc voltage, 12 V; welding speed, 12 cm/min (root pass) / arc current, 220 A; arc voltage, 12 V; welding speed, 15 cm/min (other passes); shielding gas, Ar+2%N<sub>2</sub> (flow rate, 15 L/min); interpass temp., 373 K; U-groove (angle, 50°; root face, 1 mm).

The microstructure of specimens was observed by an optical microscope (OM) and scanning electron microscope (SEM) after electrolytic etching with a 20%H<sub>2</sub>SO<sub>4</sub> + methanol solution at 25 V for 40 s. The amount of  $\gamma$  phase (the  $\gamma$  phase fraction) in specimens was measured as the area fraction of  $\gamma$  phase in metallographic structure using the electron back scatter diffraction analysis (EBSD) with OIM crystallography software.

### DISSOLUTION BEHAVIOUR OF AUSTENITIC PHASE

#### DISSOLUTION KINETICS IN BASE METAL HEAT AFFECTED ZONE

The change in microstructure of DSSs during the solution treatment was investigated. Fig.1 shows an example of microstructural change (phase mapping by EBSD analysis) in super DSS with the solution treatment condition. The red regions indicate a  $\gamma$  phase, green ones a  $\alpha$  phase and yellow ones a  $\sigma$  phase in the microstructure. A typical microstructure of DSS could be observed in all specimens, namely, a  $\gamma$  phase was aligned along the rolling direction. The amount of  $\gamma$  phase decreased with an increase in the heating temperature. Very few  $\sigma$  phase was formed in the present conditions. It has been confirmed that similar dissolution behaviour was observed in lean and standard DSSs. The area fraction of  $\gamma$  phase in the phase map was measured for all steels with varying the heat treatment condition.

In the previous report [18,19], the authors have been reported that the precipitation of  $\gamma$  in steels is followed by the Austin-Rickett type equation as given by eq.(1) or (2) [15,16];

$$\frac{y}{1-y} = (kt)^n \quad (1)$$

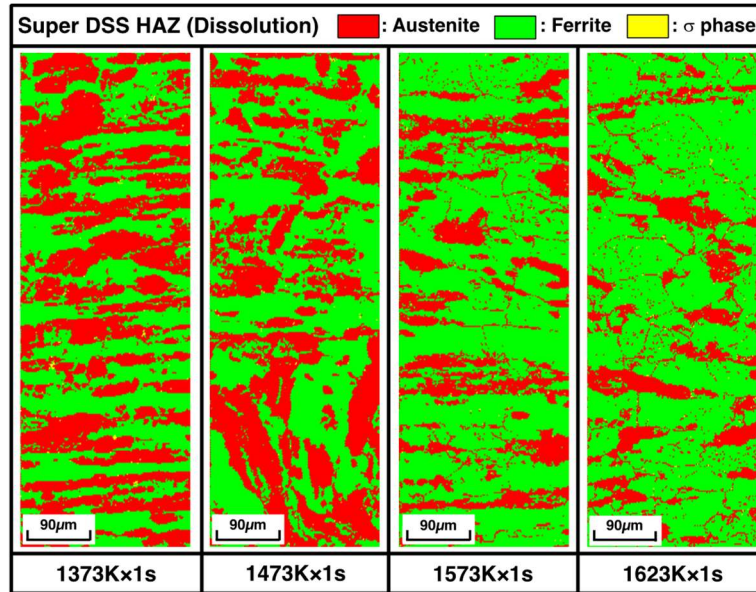


Fig. 1 Change in microstructure of super DSS with solution treatment

$$\log \frac{y}{1-y} = n \log t + n \log k \quad (2)$$

where  $y$  is the fraction transformed,  $k$  is the kinetic constant,  $t$  is the time and  $n$  is the time exponent. Then, applicability of the Austin-Rickett type equation to dissolution phenomena of  $\gamma$  phase was evaluated. Fig.2 shows the Austin-Rickett plot of dissolution behaviour of  $\gamma$  phase in lean, standard and super DSSs (base metal HAZs). There were good linear relationships in the Austin-Rickett plot, and gradients of lines were almost identical independent of the heating temperature. The time exponents,  $n$  of lean, standard and super DSSs were determined as 0.49, 0.64 and 0.71, respectively. Consequently, it can be concluded that dissolution kinetics of  $\gamma$  phase in all base metal HAZs of DSSs is followed by the Austin-Rickett type equation.

It has been well-known that the kinetic constant,  $k(T)$  can be generally expressed by the Arrhenius type equation as given by eq.(3);

$$k(T) = k_0 \exp\left(-\frac{Q}{RT}\right) \quad (3)$$

where  $k_0$  is the frequency factor,  $Q$  is the activation energy,  $T$  is the absolute temperature and  $R$  is the gas constant. The Arrhenius plots of dissolution rate of  $\gamma$  phase in DSSs are shown in Fig.3. There were good linear relationships between  $\ln k$  and  $1/T$  for all steels. Therefore, the temperature dependency of dissolution rate of  $\gamma$  phase in DSSs could be obtained in the present study as follows;

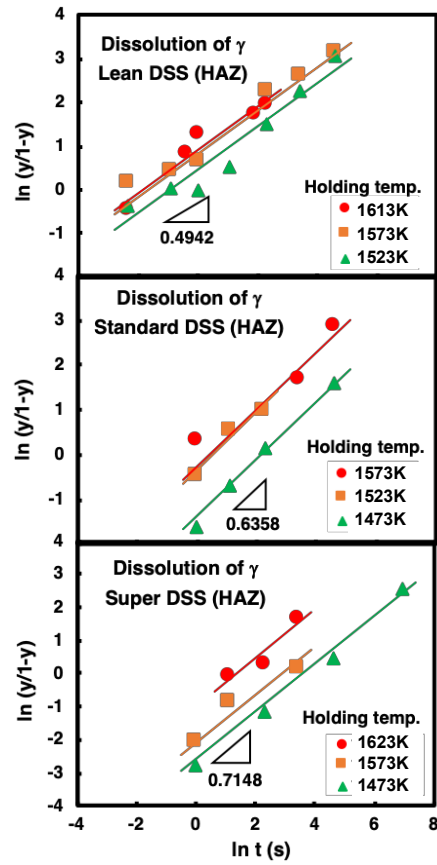
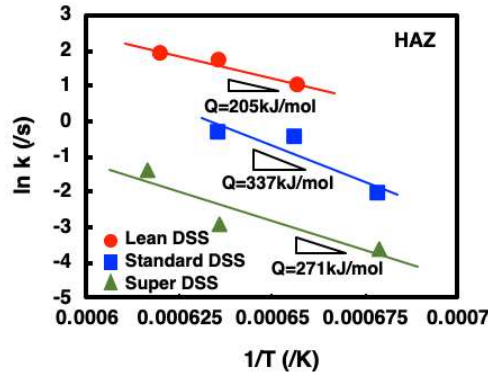


Fig. 2 Austin-Rickett plots of dissolution behaviour of  $\gamma$  phase in base metal HAZs

Lean DSS HAZ:

$$k(T) = \exp\left(\frac{-2.47 \times 10^4}{T} + 17.2\right) \quad (4)$$





**Fig. 3** Arrhenius plots of dissolution rates of  $\gamma$  phase in base metal HAZs  
Standard DSS HAZ:

$$k(T) = \exp\left(\frac{-4.05 \times 10^4}{T} + 25.6\right) \quad (5)$$

Super DSS HAZ:

$$k(T) = \exp\left(\frac{-3.26 \times 10^4}{T} + 18.4\right) \quad (6)$$

#### DISSOLUTION KINETICS IN REHEATED WELD METAL

As described in INTRODUCTION, the WMs of DSSs are generally solidified as the F mode, and a  $\gamma$  phase comes to precipitate in the solidified  $\alpha$  structure during cooling. Then, precipitation kinetics of  $\gamma$  phase was also investigated in the WM (reheated WM). Fig.4 shows the Austin-Rickett plot of dissolution behaviour of  $\gamma$  phase in the WMs of lean, standard and super DSSs. There were good linear relationships in the Austin-Rickett plot for all WMs. The time exponents,  $n$  of the WMs of lean, standard and super DSSs were determined as 0.20, 0.36 and 0.35, respectively. It follows that precipitation kinetics of  $\gamma$  phase in the reheated WM is also followed by the Austin-Rickett type equation.

The Arrhenius plots of dissolution rate of  $\gamma$  phase in the DSS WMs are shown in Fig.5. The temperature dependency of dissolution rate of  $\gamma$  phase in the reheated WMs of DSSs could be obtained in the present study as follows;

Lean DSS WM:

$$k(T) = \exp\left(\frac{-4.81 \times 10^4}{T} + 27.8\right) \quad (7)$$

Standard DSS WM:

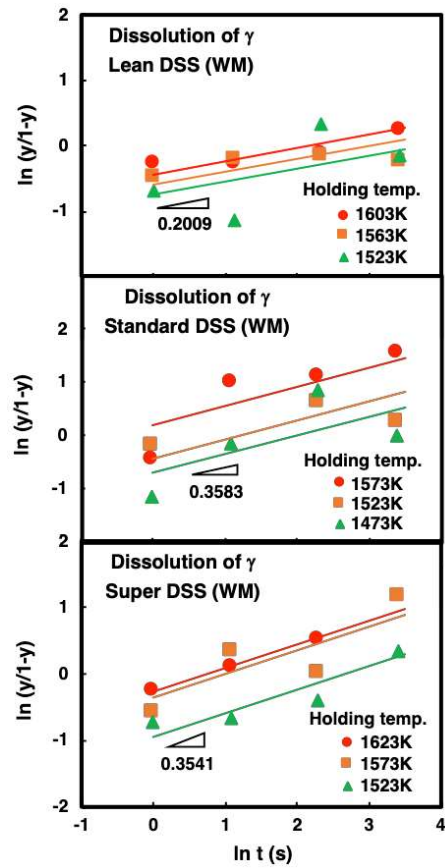


Fig. 4 Austin-Rickett plots of dissolution behaviour of  $\gamma$  phase in WMs

$$k(T) = \exp\left(\frac{-5.82 \times 10^4}{T} + 37.4\right) \quad (8)$$

Super DSS WM:

$$k(T) = \exp\left(\frac{-4.75 \times 10^4}{T} + 28.8\right) \quad (9)$$

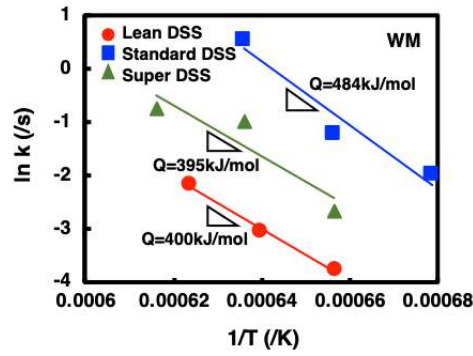


Fig. 5 Arrhenius plots of dissolution rates of  $\gamma$  phase in WMs

COMPARISON OF DISSOLUTION RATE BETWEEN HEAT AFFECTED ZONE AND WELD METAL

The dissolution rates of  $\gamma$  phase in the base metal HAZ and reheated WM were compared. Fig.6 shows the temperature dependency of dissolution rate in the HAZ and WM of DSSs. The dissolution of  $\gamma$  phase was enhanced at the higher temperature range in any case. The dissolution rates in the WM of standard and super DSSs were comparable to those in the HAZ, while the dissolution rate in the WM of lean DSS was much reduced to that in the HAZ. The reason why the dissolution rate of lean DSS differed between in the HAZ and WM has not been clarified in the present study, and therefore, the further detailed investigation would be required. In addition, the dissolution rate in the HAZ decreased in the order of lean>standard>super DSSs, *i.e.*, the dissolution of  $\gamma$  phase in the lean DSS HAZ proceeded rapidly compared with the standard and super DSS HAZs.

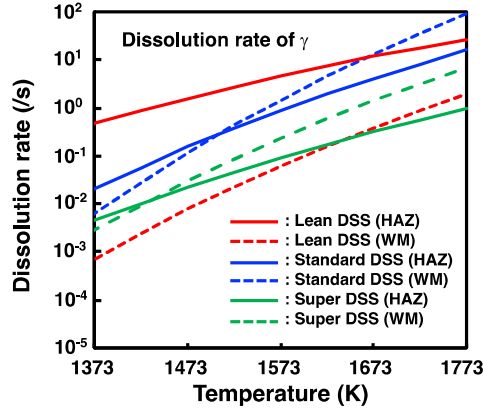


Fig. 6 Comparison of dissolution rates in HAZ and WM

PRECIPITATION BEHAVIOUR OF AUSTENITIC PHASE

PRECIPITATION KINETICS IN BASE METAL HEAT AFFECTED ZONE

The change in microstructure of DSSs during the precipitation treatment was investigated. Fig.7 shows an example of microstructural change (phase mapping by EBSD analysis) in super DSS with the precipitation treatment condition. A  $\gamma$  phase was precipitated not only at the grain boundaries (GBs) (Widmanstätten-like) but also in the grains of  $\alpha$ , and the amount of  $\gamma$  phase increased with an increase in the heating temperature. Similar precipitation behaviour has been observed in lean and standard DSSs.

The several researchers have been reported that precipitation kinetics of  $\gamma$  phase in DSS welds was followed by the Austin-Rickett type equation [15-19], and therefore, applicability of the Austin-Rickett type equation to the present precipitation phenomena was verified. Fig.8 shows the Austin-Rickett plots of precipitation behaviour of  $\gamma$  phase in lean, standard and super DSSs. There were good linear relationships in the Austin-Rickett plot, and gradients of the lines were almost identical for all steels. The time exponents  $n$  of lean, standard and super DSSs were determined as 0.82, 1.16 and 0.53, respectively. It follows that precipitation kinetics of  $\gamma$  phase in the base metal HAZ is also followed by the Austin-Rickett type equation.

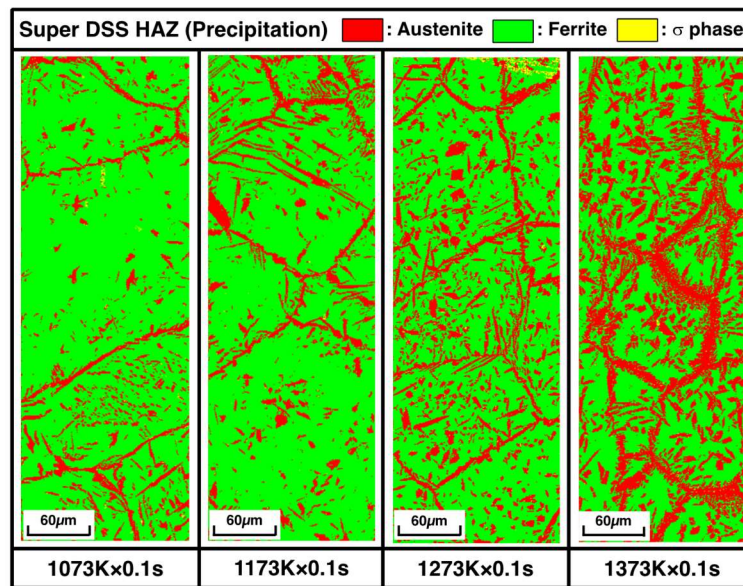


Fig. 7 Change in microstructure of super DSS with precipitation treatment

According to Fig.8, the precipitation of  $\gamma$  phase in standard and super DSSs was fastest at the heating temperature around 1273 K, while that in lean DSS around 1173 K. The fact that the precipitation of  $\gamma$  phase in DSSs becomes fastest at the certain intermediate temperature (*i.e.*, possesses a “nose”) means that the temperature dependency of precipitation rate would not followed by the simple Arrhenius type equation as indicated by eq.(3). Therefore, the temperature dependency of precipitation rate of  $\gamma$  phase in DSSs, which indicates a C-curved diagram with a nose, was theoretically discussed. Assuming that precipitation of  $\gamma$  phase is controlled by the non-uniform nucleation in an  $\alpha$  grain and at the  $\alpha$ -GB, and grows inward an  $\alpha$  grain, the non-uniform nucleation rate  $I$  can be expressed by eq.(10) [20];

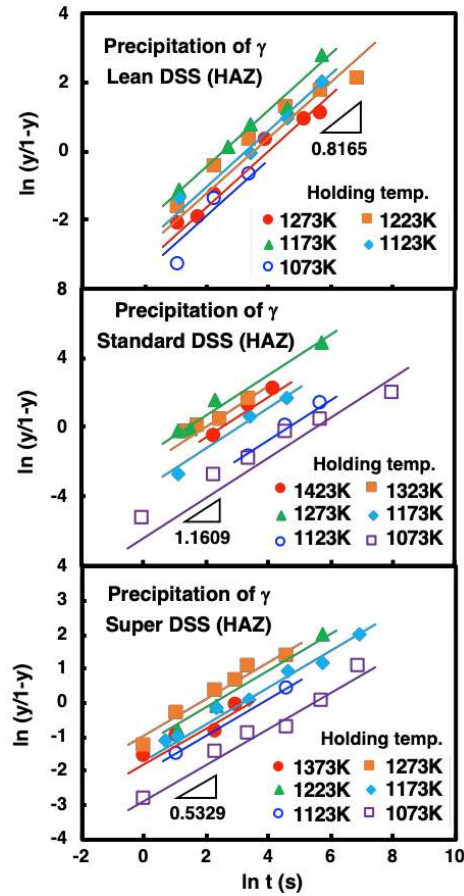


Fig. 8 Austin-Rickett plots of precipitation behaviour of  $\gamma$  phase in base metal HAZs

$$I = \nu m \left( \frac{d}{L} \right)^{3-j} \exp \left( - \frac{\Delta G^* + \Delta G_a}{RT} \right) \quad (10)$$

where  $\nu$  is the frequency factor,  $m$  is the number of atoms per unit volume,  $d$  is the effective GB thickness,  $L$  is the grain diameter,  $j$  is the dimensionality of site,  $\Delta G^*$  is the minimum free energy required to form a nucleus, and  $\Delta G_a$  is the free energy of activation for a nucleus to continue to grow. Terms in eq.(10) which have temperature dependency are  $m$ ,  $L$  and  $\Delta G^*$ . However, the variation of  $m$  is negligible compared with the temperature dependency of exponential term, and  $L$  is regarded as constant because the starting specimen is a solution treated specimen at 1653 K for 60 s. Consequently, temperature dependent term in eq.(10) is only  $\Delta G^*$ , and can be expressed by eq.(11) from the Spherical-Cap model [21];

$$\Delta G^* = \frac{16\pi\sigma_{\alpha/\gamma}^3}{3\Delta G_{V_{\alpha \rightarrow \gamma}}^2} f(\theta) \quad (11)$$

where  $G_{V_{\alpha \rightarrow \gamma}}$  is the volume free energy change from  $\alpha$  to  $\gamma$  phase,  $\theta$  is the wetting angle of  $\gamma$  phase at the  $\alpha$ -GB, and is expressed by the following relationships;

$$G_{V_{\alpha \rightarrow \gamma}} = \frac{\Delta H_{\alpha/\gamma} (T_E - T)}{V_m T_E} \quad (12)$$

$$\cos \theta = \frac{\sigma_{\alpha/\alpha} - \sigma_{\alpha/\gamma}}{\sigma_{\alpha/\gamma}} \quad (13)$$

$$f(\theta) = \frac{2 - 3\cos\theta + \cos^3\theta}{4} \quad (14)$$

where  $T_E$  is the starting temperature of precipitation of  $\gamma$  phase ( $\gamma$  solvus),  $\Delta H_{\alpha/\gamma}$  is the change in enthalpy from  $\alpha$  to  $\gamma$  phase at  $T_E$ ,  $V_m$  is the molar volume,  $\sigma_{\alpha/\alpha}$  and  $\sigma_{\alpha/\gamma}$  are the interfacial energies between  $\alpha$  and  $\alpha$  phases,  $\alpha$  and  $\gamma$  phases, respectively. Assuming that  $\sigma_{\alpha/\alpha}$  and  $\sigma_{\alpha/\gamma}$  are independent on temperature,  $\Delta G^*$  in eq.(10) is inversely proportional to the square of degree of undercooling from the starting temperature of precipitation of  $\gamma$  phase,  $(T_E - T)^2$ , and expressed by;

$$\Delta G^* = \frac{B^*}{(T_E - T)^2} \quad (15)$$

where  $B^*$  is an arbitrary coefficient. Consequently, the non-uniform nucleation rate  $I$  in eq.(10) can be expressed by;

$$I = A^* \exp \left( - \frac{\Delta G_a}{RT} \right) \cdot \exp \left\{ \frac{-B^*}{RT(T_E - T)^2} \right\} \quad (16)$$

Assuming that the progress in transformation from  $\alpha$  to  $\gamma$  phase is controlled by the non-uniform nucleation, the temperature dependency of rate constant  $K(T)$  can be also given by;

$$K(T) = A^* \exp \left( - \frac{\Delta G_a}{RT} \right) \cdot \exp \left\{ \frac{-B^*}{RT(T_E - T)^2} \right\} \quad (17)$$

where  $A^*$  is an arbitrary coefficient. Fig.9 schematically shows the temperature dependency of the rate constant  $K(T)$  expressed by eq.(17). The rate constant approaches asymptotically to two types of Arrhenius equation in the temperature ranges below/above a nose.

On the other hand, from the fact that a  $\gamma$  phase in DSS welds grows as the Widmanstätten structure from  $\alpha$ -GBs into grains, the precipitation amount of  $\gamma$  phase depends on both nucleation and growth. Namely, the fraction transformed  $y$  depends on the nucleation rate, diffusion speed and time, and dissolving a diffusion equation assuming the local equilibrium at the  $\alpha/\gamma$  interface, the rate constant  $K(T)$  can be approximately expressed by eq.(18) [22];

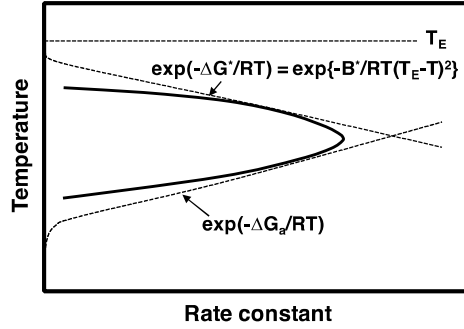


**Fig. 9** Temperature dependency of rate constant

$$K(T) = -\frac{16\sqrt{2}}{15} \pi D^{2/3} \left( \frac{C_\alpha - C_E}{C_\gamma - C_E} \right) \cdot I \quad (18)$$

where  $D$  is the diffusion constant (of N or Ni),  $C_\alpha$  and  $C_\gamma$  are the solute concentrations (N or Ni) in  $\alpha$  and  $\gamma$  phases, respectively,  $C_E$  is the equilibrium concentration of solute element (N or Ni) in  $\alpha$  phase at the  $\alpha/\gamma$  interface. The diffusion constant can be given by;

$$D = D_0 \exp\left(-\frac{\Delta G_a}{RT}\right) \quad (19)$$

Approximately assuming that  $C_\alpha$ ,  $C_\gamma$  and  $C_E$  are independent of the temperature and the amount of  $\gamma$  phase (*i.e.*, negligible small compared to the temperature dependency of exponential term), eq.(18) can be transformed to;

$$K(T) = A^{**} \exp\left(-\frac{\Delta G_a}{RT}\right)^{2/3} \cdot \exp\left(-\frac{\Delta G_a}{RT}\right) \cdot \exp\left\{\frac{-B^*}{RT(T_E - T)^2}\right\} \quad (20)$$

where  $A^{**}$  is an arbitrary coefficient. Eq.(20) can be transformed to;

$$K(T) = A^{**} \exp\left(-\frac{5\Delta G_a}{3RT}\right) \cdot \exp\left\{\frac{-B^*}{RT(T_E - T)^2}\right\} \quad (21)$$

Eq.(21) can be simplified by eq.(22) using three undetermined coefficients  $A$ ,  $B$  and  $C$ ;

$$K(T) = A \exp\left(\frac{B}{RT}\right) \cdot \exp\left\{\frac{C}{RT(T_E - T)^2}\right\} \quad (22)$$

Based on the experimental results (Fig.8), three coefficients ( $A$ ,  $B$  and  $C$ ) were determined by a regression analysis ( $T_E$  can be calculated by the phase computation software, *Thermo-Calc*, Database: TCFE6). Fig.10 shows the temperature dependency of the precipitation rate constants of  $\gamma$  phase in DSSs (regression analysis results of rate constants), and summarises the three coefficients and  $T_E$  determined. The precipitation rate of  $\gamma$  phase in DSSs decreased in the order of standard>super>lean DSSs. The temperature dependency of precipitation rate of  $\gamma$  phase in base metal HAZs of DSSs, which indicates a C-curved diagram with a nose, could be obtained in the present study.

PRECIPITATION KINETICS IN REHEATED WELD METALS

The change in microstructure of the WMs of DSSs during the precipitation treatment was investigated. Fig.11 shows the microstructural change (phase mapping by EBSD analysis) in the WMs of lean, standard and super DSSs with the precipitation treatment condition. A

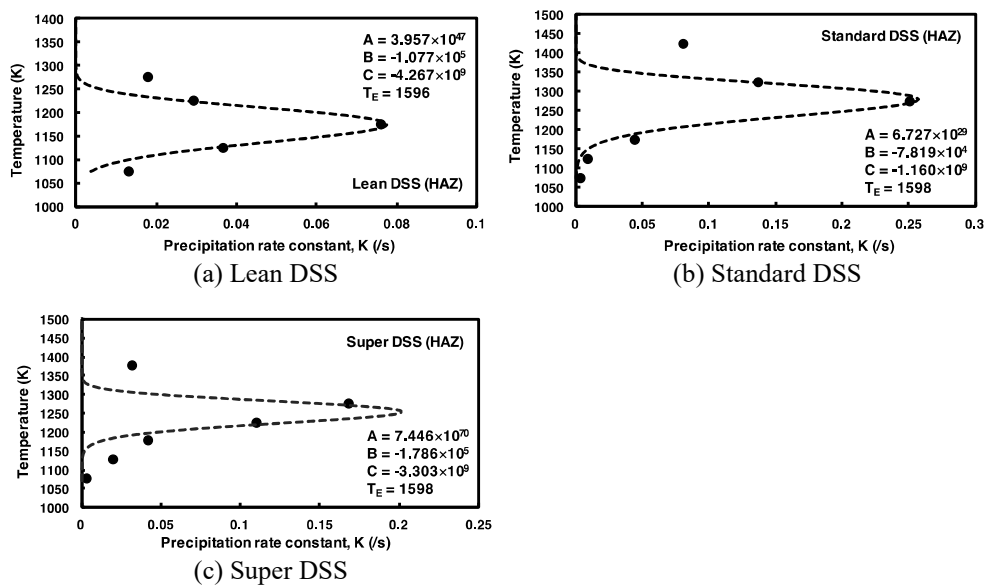
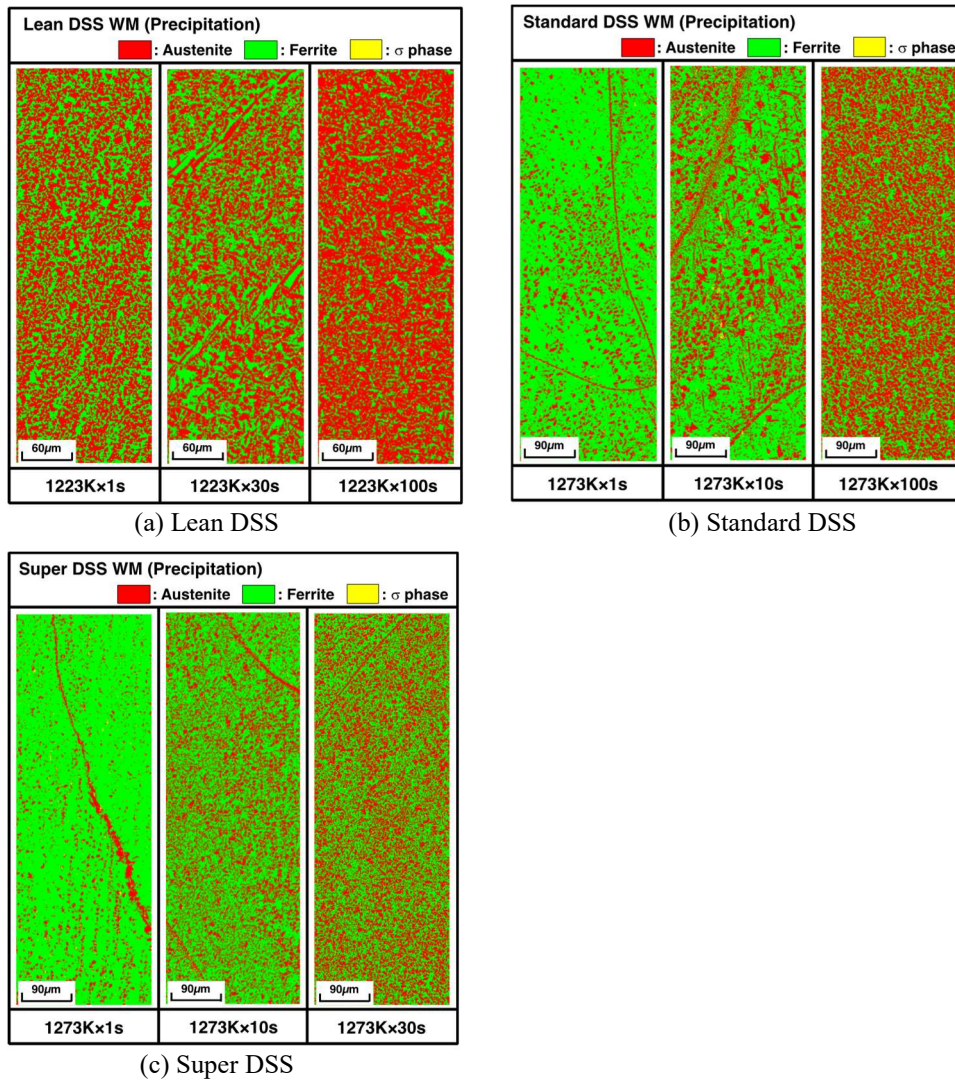


Fig. 10 Regression analysis of precipitation rate constants of  $\gamma$  phase in base metal HAZs

$\gamma$  phase was precipitated in  $\alpha$  grains as well as at GBs, and the amount of  $\gamma$  phase increased with an increase in the holding time for all WMs. In addition, very few  $\sigma$  phase was formed in the present conditions.





**Fig. 11** Changes in microstructure of DSS WMs with precipitation treatment

The Austin-Rickett plots of precipitation behaviour of  $\gamma$  phase in the WMs of lean, standard and super DSSs are shown in Fig.12. There were good linear relationships in the Austin-Rickett plot again, and gradients of the lines were almost identical for all steels. The time exponents  $n$  of the lean, standard and super DSS WMs were determined as 0.73, 0.39

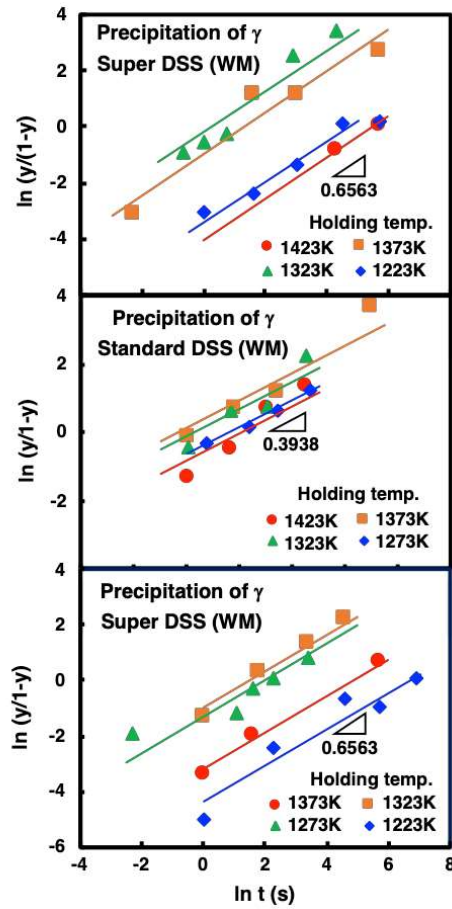


Fig. 12 Austin-Rickett plots of precipitation behaviour of  $\gamma$  phase in WMs

and 0.66, respectively. The precipitation rates of  $\gamma$  phase in the DSS WMs also possess the temperature dependency with a nose. The nose temperature of precipitation in the standard DSS WM was around 1373 K, while that in super and lean DSSs around 1323 K. It follows that precipitation kinetics of  $\gamma$  phase in the reheated WM is also followed by the Austin-Rickett type equation.

Based on the experimental results (Fig.12), three coefficients ( $A$ ,  $B$  and  $C$ ) in eq.(22) were determined by a regression analysis again ( $T_E$  was calculated by *Thermo-Calc*). Fig.13 shows the temperature dependency of the precipitation rate constants of  $\gamma$  phase in the DSS WMs, and summarises the three coefficients and  $T_E$  determined. The precipitation rate of  $\gamma$  phase in DSSs decreased in the order of standard>lean>super DSSs. The temperature dependency of precipitation rate of  $\gamma$  phase in the reheated WMs of DSSs could be also obtained in the present study.

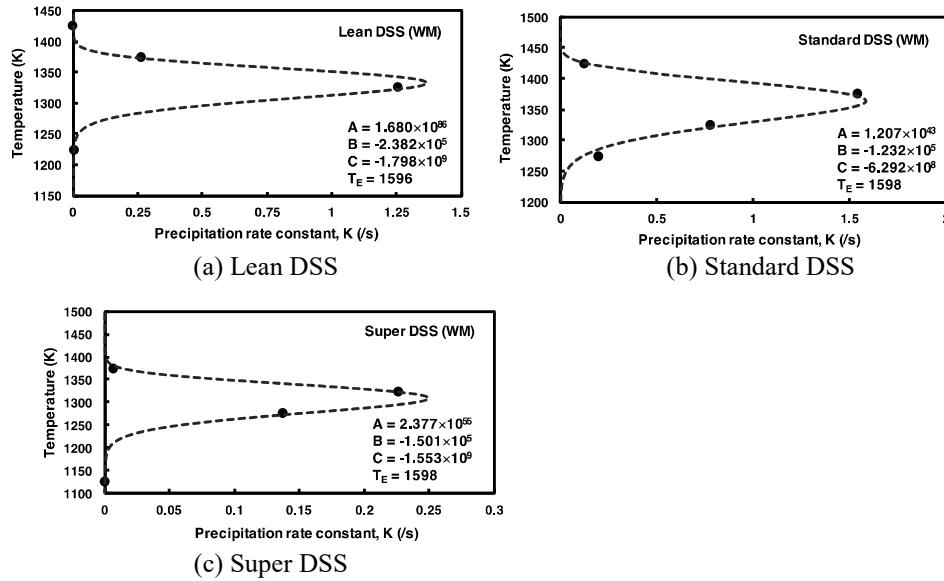


Fig. 13 Regression analysis of precipitation rate constants of  $\gamma$  phase in WMs

COMPARISON OF PRECIPITATION RATE BETWEEN HEAT AFFECTED ZONE AND WELD METAL

The precipitation rates of  $\gamma$  phase in the base metal HAZ and reheated WM were compared. Fig.14 shows the temperature dependency of precipitation rate in the HAZ and WM of DSSs. The precipitation rate of  $\gamma$  phase in standard DSS was largest of the three DSSs. The nose temperature and rate constant of the  $\gamma$  phase precipitation in WMs increased compared with those of HAZs in all DSSs. The reason why they differed between the HAZ and WM, especially in lean and standard DSSs, has not been clarified, and therefore, the further detailed investigation would be required.

PREDICTION OF PHASE TRANSFORMATION IN MULTIPASS WELDS

COMPUTATION METHOD OF PHASE TRANSFORMATION IN MULTIPASS WELDS

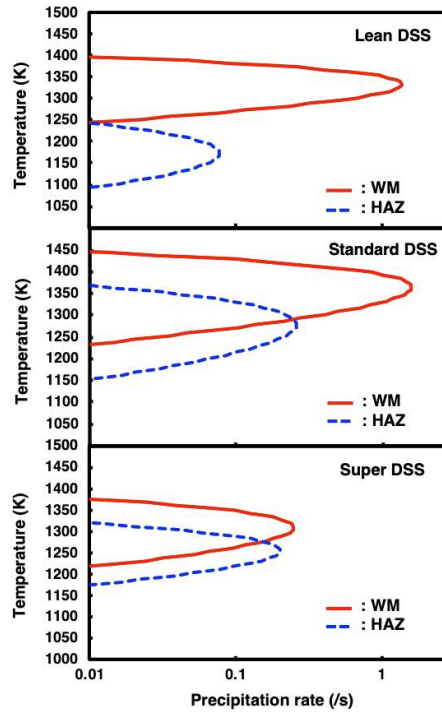


**Fig. 14** Comparison of precipitation rates in HAZ and WM

In order to expand the isothermal kinetics of dissolution and precipitation determined above to the non-isothermal process such as welding, the increment method [18,19] was applied. A concept of the incremental method is that; dividing the thermal cycle into minute isothermal intervals during the  $\alpha/\gamma$  phase transformation process, the transformation quantity (increment in the amount of  $\gamma$  phase) is calculated in a minute isothermal step, and sum up them through thermal cycle. A flowchart of computation of the phase transformation (the amount of  $\gamma$  phase) in multipass welds is shown in Fig.15. The thermal cycles in the HAZ and WM during multipass welding were computed using the welding mechanical analysis software, *JWRAN*. Compared the  $\gamma$  phase fraction at the time to the equilibrium  $\gamma$  phase fraction at the temperature in each isothermal step, it was determined that either dissolution or precipitation occurred. Based on the kinetic equations (dissolution and precipitation kinetics) determined, the increment or decrement in the  $\gamma$  phase fraction was calculated and summed up through welding process. From these procedures, the alternate behaviours of dissolution and precipitation of  $\gamma$  phase during multiple thermal cycle would be numerically simulated. In the present study, the distribution of the  $\gamma$  phase fraction in multipass welds was visualised by repeating these calculation over the whole

area of welds (the base metal HAZ and reheated WM). In the previous reports [18,19], the predicted results of the  $\alpha/\gamma$  phase transformation based on the present computation method have been verified in the melt-run welds (GTAW and LBW) of DSSs.

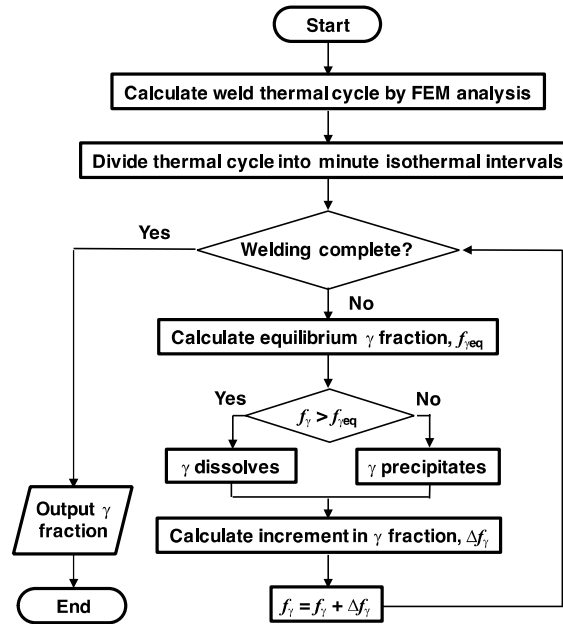


**Fig. 15** Flowchart of computation of phase transformation in multipass welds

Thermal properties of lean, standard and super DSSs [23] used for calculation are shown in Fig.16 (assuming to be identical regardless of the steel grade). The  $\alpha$  single-phasing and solidus temperatures of lean, standard and super DSSs, which were calculated by *Thermo-Calc* (Database; TCFE6), are summarised in Table 4. Temperature dependency of the equilibrium  $\gamma$  phase fraction of lean, standard and super DSSs (which was determined based on the measured results combined with the calculated values by *Thermo-Calc* (Database; TCFE6)) is shown in Fig.17. The multipass welding conditions used for computation are described above in EXPERIMENTAL PROCEDURES. In addition, Fig.18 shows the cross-sectional views and mesh division (weld pass sequence) of multipass welds (GTAW) of lean, standard and super DSSs used for numerical analyses of the thermal cycle and  $\alpha/\gamma$  phase transformation (distribution of the  $\gamma$  phase fraction). The total number of weld passes in multipass welding was 15 for all DSSs. The minimum mesh size divided was approx.  $0.5 \text{ mm} \times 0.5 \text{ mm}$ .

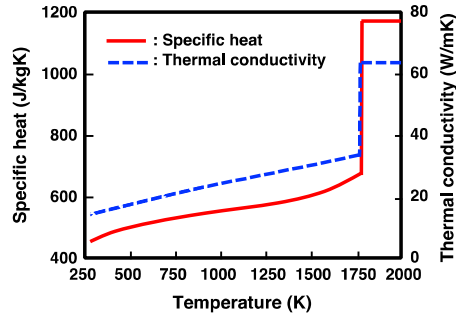


Fig. 16 Physical properties of DSSs used for calculation

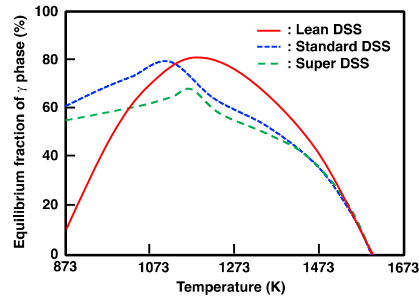


Fig. 17 Temperature dependency of equilibrium  $\gamma$  phase fraction of DSSs

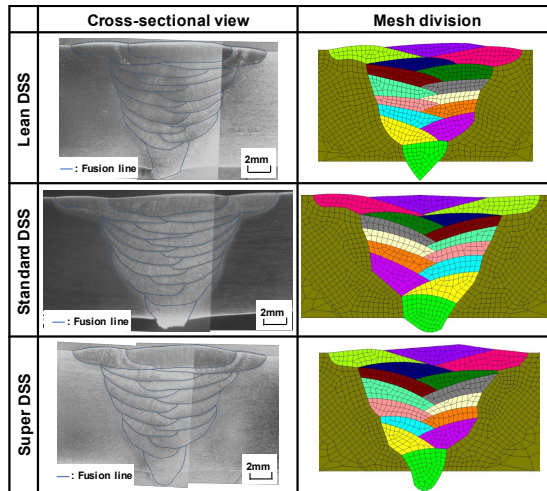
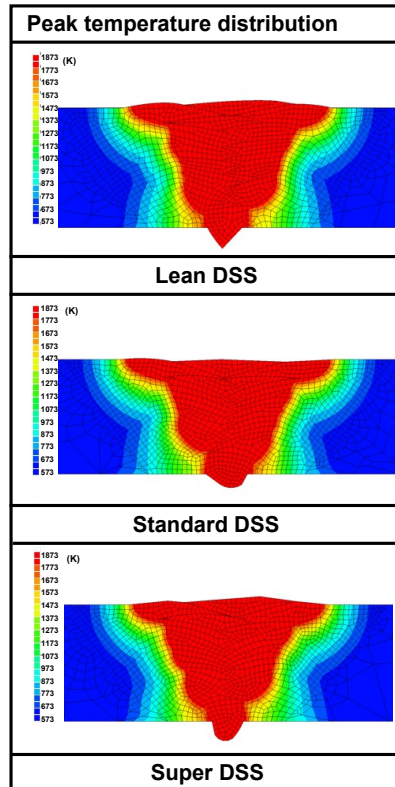


Fig. 18 Cross-sectional views and mesh division of multipass welds of DSSs

**Table 4**  $\alpha$  single-phasing and solidus temperatures of DSSs

Steel	$\alpha$ single-phasing temp.	Solidus temp.
Lean DSS	1596K	1683K
Standard DSS	1598K	1647K
Super DSS	1598K	1604K

COMPUTED RESULTS OF AUSTENITIC PHASE FRACTION IN WELDS



**Fig. 19** Peak temperature distribution in multipass welds of DSSs

The thermal cycles during multipass GTA welding (the number of weld passes is 15) of DSSs were calculated. Fig.19 shows the peak temperature distribution in the base metal HAZs of lean, standard and super DSSs during multipass welding computed by the heat conduction analysis using *JWRIAN*. The peak temperature distribution and thermal cycle in multipass welds could be successfully computed for all DSSs. Based on the multiple thermal cycles calculated in the base metal HAZs and reheated WMs, the  $\alpha/\gamma$  phase transformation in multipass GTA welds of DSSs was computed. Fig.20 shows the distribution of the  $\gamma$  phase fraction (indicated by colour contours) calculated in the multipass weld of lean DSS. This figure exhibits the entire history of the distribution of the  $\gamma$  phase

fraction at the completion of each weld pass during multipass welding. The dashed lines in the figure indicate the fusion lines of weld passes. The  $\gamma$  phase fraction in the just solidified WM was considerably small in any weld passes, and the depleted zone of  $\gamma$  phase was formed adjacent to the fusion line ("under-bead" region) in the base metal HAZs and reheated WMs. However, the  $\gamma$  phase fraction in the depleted zone was increased by the subsequent weld passes (the  $\gamma$  phase was re-precipitated by the thermal cycles in subsequent welding). Accordingly, the  $\alpha/\gamma$  phase balance has been complexly varied in multipass welds, and the profile of the  $\gamma$  phase fraction was arranged in laminae in the WM roughly along the fusion lines. The minimum  $\gamma$  phase fraction in multipass welds was approx. 20% located in the base metal HAZ of the final weld layer, and the  $\gamma$  phase fraction in WMs was reduced to approx. 25%. On the other hand, the  $\gamma$  phase fraction in a part of base metal HAZ (low temperature HAZ) was exceeded to that in the base metal, because of the additional precipitation of  $\gamma$  phase during multipass welding. The distribution of the  $\gamma$  phase fraction calculated in the multipass welds of standard and super DSSs is also shown in Fig.21 and Fig.22, respectively. Quite similar tendencies to lean DSS weld were observed in the distribution of the  $\gamma$  phase fraction, that is, the  $\gamma$  phase fraction was reduced in the solidified WM and under-bead region of WM as well as the base metal HAZ, while the  $\gamma$  phase fraction in the depleted zone was recovered by the subsequent weld passes. As a result, the  $\alpha/\gamma$  phase balance has been complexly varied in multipass welds. Furthermore, the  $\gamma$  phase fraction in multipass weld (especially WM) of standard DSS was slightly lower than those of lean and super DSSs, namely, the  $\gamma$  phase fraction in standard DSS weld was reduced to approx. 10-15%, while those in lean and super DSS welds were reduced to approx. 25-30%. On the other hand, the over-precipitated zone, where the  $\gamma$  phase fraction slightly exceeded the base metal level, was not observed in the low temperature HAZ of standard DSS weld, whereas it was observed in other welds.



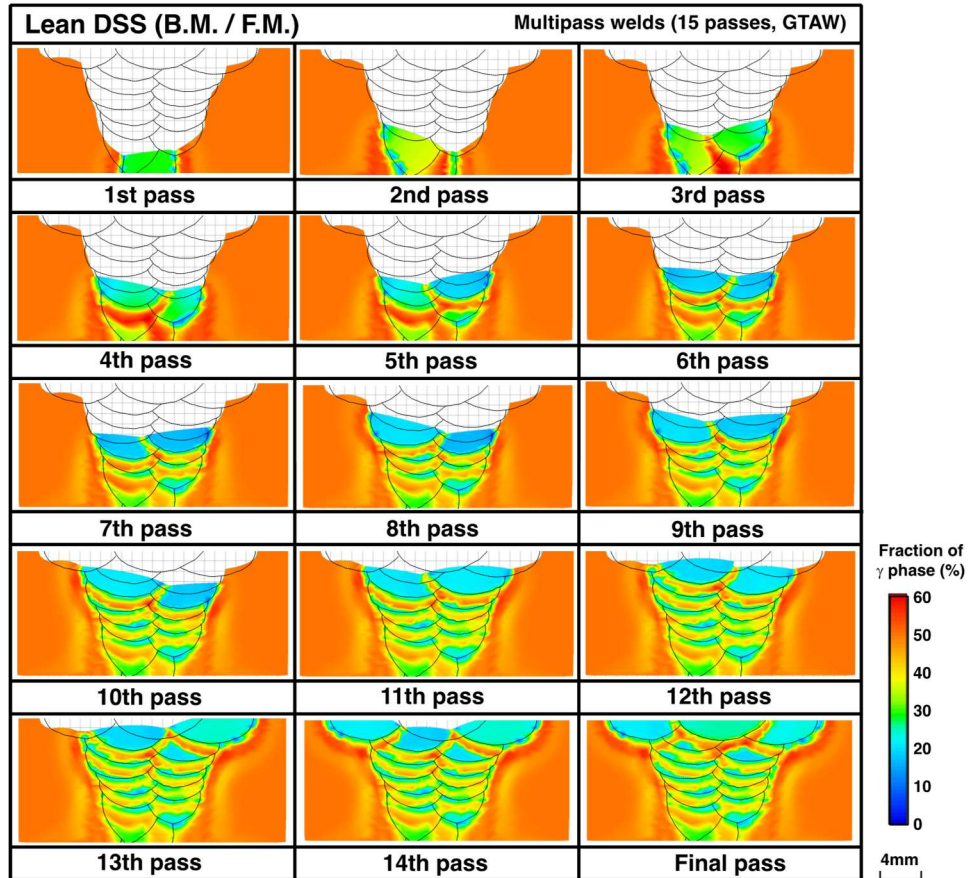


Fig. 20 Distribution of  $\gamma$  phase fraction calculated in multipass weld of lean DSS

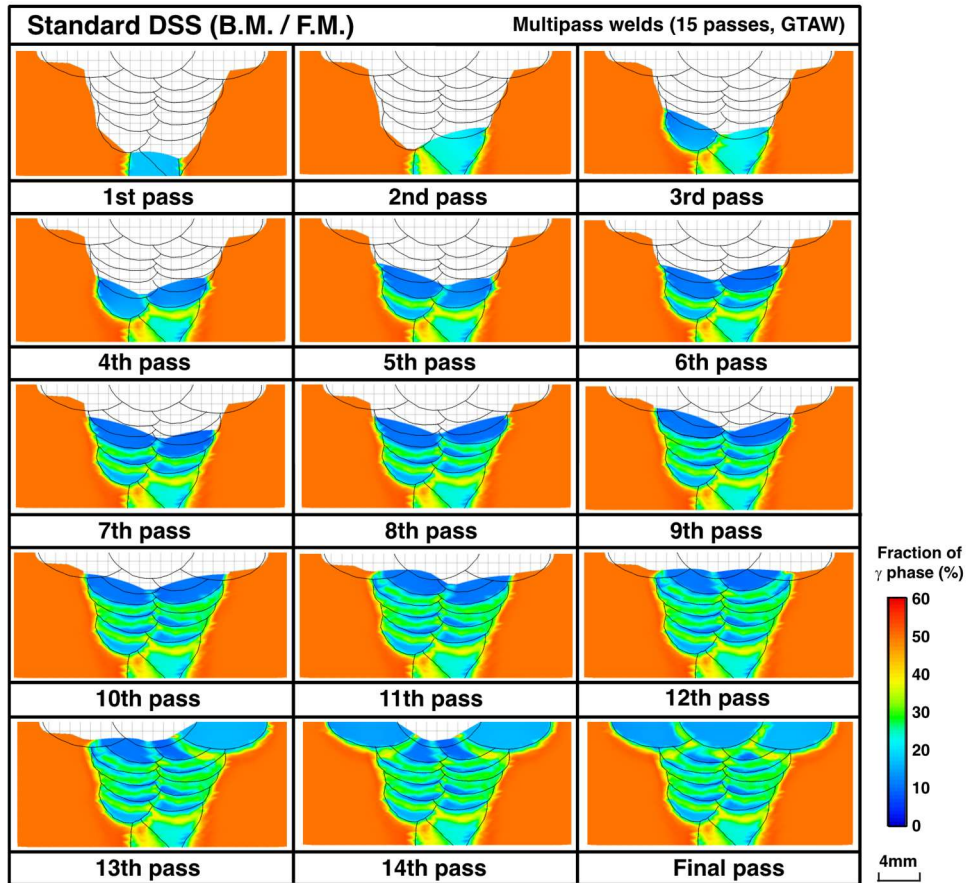


Fig. 21 Distribution of  $\gamma$  phase fraction calculated in multipass weld of standard DSS

COMPARISON OF AUSTENITIC PHASE FRACTION IN MULTIPASS WELDS BETWEEN CALCULATED AND MEASURED

In order to validate the predicted results of the  $\alpha/\gamma$  phase transformation, the  $\gamma$  phase fraction in the multipass welds was compared between calculated and measured. Fig.23 shows the example of microstructure (phase mapping by EBSD analysis) of multipass welds. This figure shows the microstructure of lean, standard and super DSSs observed at the final weld layer in multipass welding as schematically shown in Fig.24. A dashed line in Fig.23 indicates the fusion line. The  $\gamma$  phase fraction was relatively reduced in the higher temperature HAZ (base metal HAZ) as well as WM of all steels. In particular, the  $\gamma$  phase

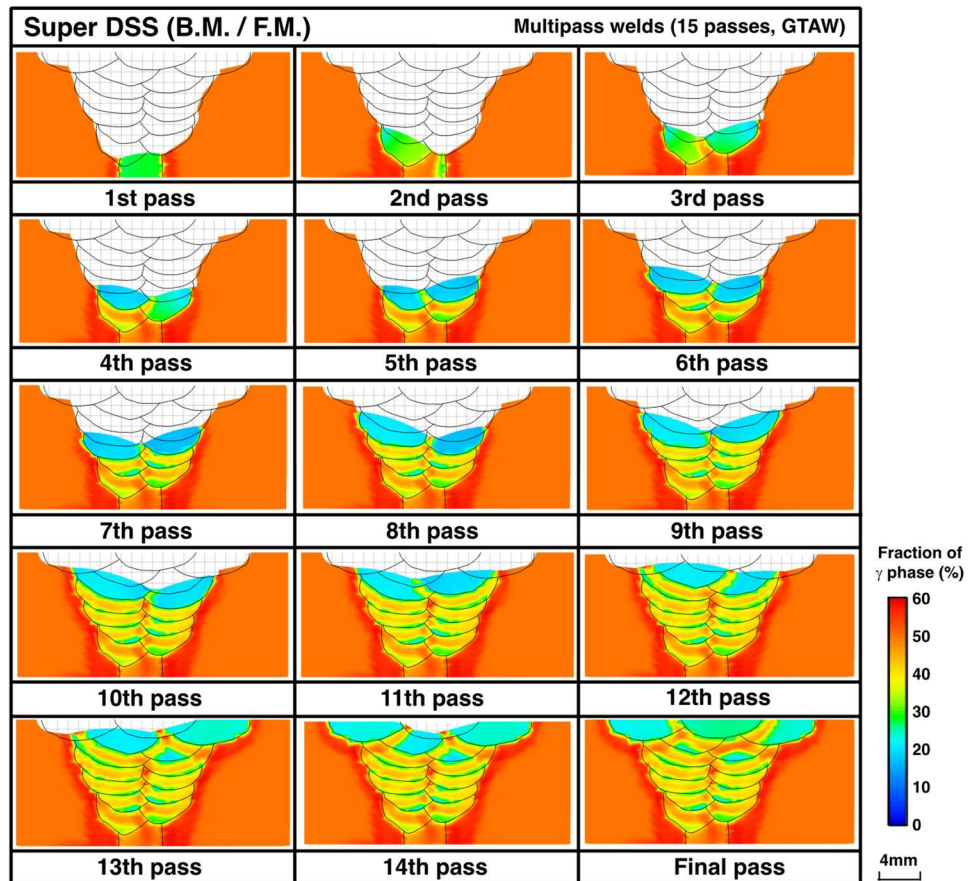
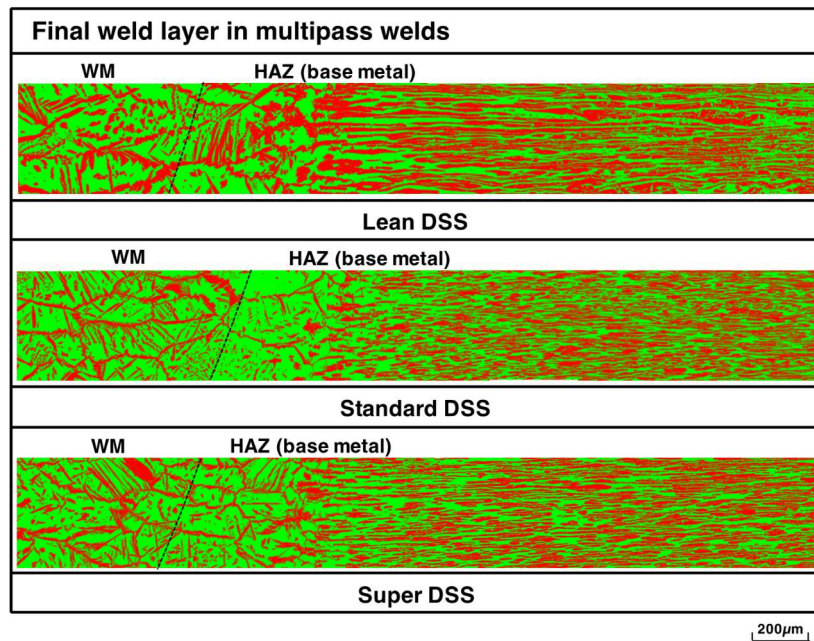
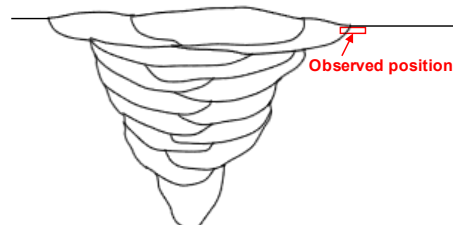


Fig. 22 Distribution of  $\gamma$  phase fraction calculated in multipass weld of super DSS



**Fig. 23** Microstructures of final layer (WM and HAZ) in multipass welds

fraction in the HAZ of standard DSS was much reduced compared to other steels. The  $\gamma$  phase fraction at the various positions was measured in multipass welds. Figs.25-27 show the comparison of the  $\gamma$  phase fraction between calculated and measured in the multipass welds (GTAW) of lean, standard and super DSSs, respectively. In these figures, a figure (a) indicates the analysis spots (positions) of the  $\gamma$  phase fraction, and a figure (b) indicates the correlation between the calculated  $\gamma$  phase fraction and measured one. The analysis spots were dotted across the welds in the reheated/un-reheated WMs and base metal HAZ. Although there were small scatters between the calculated and measured values, the calculated results were fairly consistent with measured ones (correlation coefficients; 0.81-



**Fig. 24** Observed position of microstructure in multipass weld

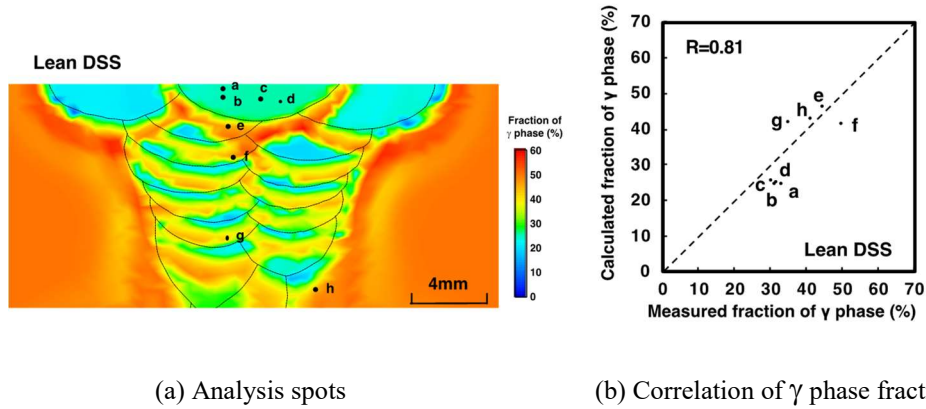


**Fig. 25** Comparison of  $\gamma$  phase fraction between calculated and measured in lean DSS multipass weld

0.90) in all welds (in the WM, reheated WM as well as the base metal HAZ). It follows that the  $\alpha/\gamma$  phase transformation in the DSS multipass welds could be successfully predicted by the present kinetic approach and computer simulation. In particular, the  $\gamma$  phase-depleted zone in the multipass welds, where the mechanical and corrosion properties would be potentially deteriorated, could be estimated with a high degree of accuracy.

### CONCLUSIONS

In the present study, the kinetic approach was made to the  $\alpha/\gamma$  phase transformation phenomena in the multipass welds of DSSs. Both of the dissolution and precipitation

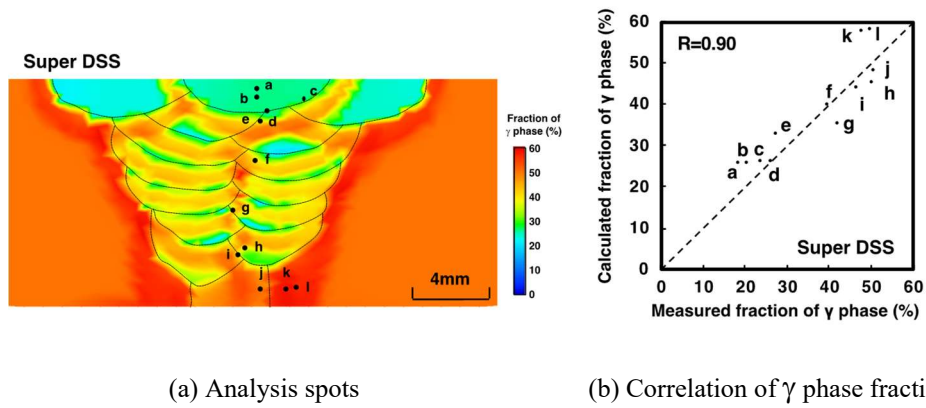


**Fig. 26** Comparison of  $\gamma$  phase fraction between calculated and measured in super DSS multipass weld

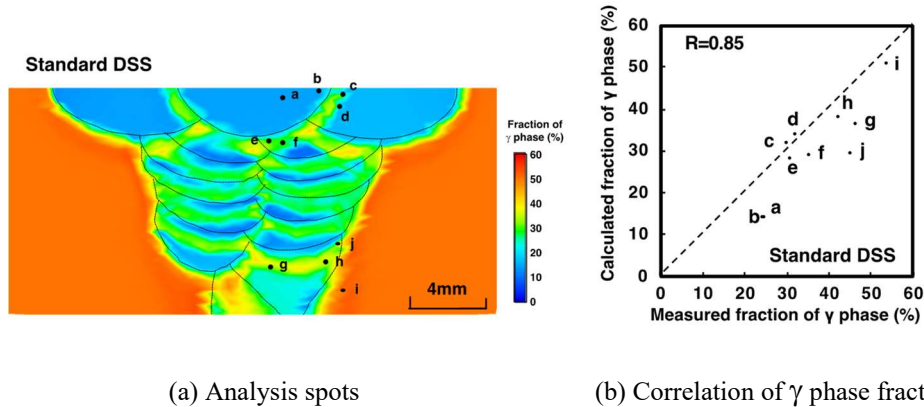


**Fig. 27** Comparison of  $\gamma$  phase fraction between calculated and measured in standard DSS multipass weld

behaviours of  $\gamma$  phase were kinetically investigated for the reheated WM as well as the base metal HAZ, and the  $\gamma$  phase fraction in multipass welds of DSSs was numerically calculated by coupling with the heat conduction analysis during multipass welding. Finally, the predicted results of  $\alpha/\gamma$  phase transformation in multipass welds were verified by the experimental examination. The results obtained are summarised as follows;

(1) The dissolution and precipitation kinetics of  $\gamma$  phase in the base metal HAZ and WM were followed by the Austin-Rickett type equation.

(2) The temperature dependency of the dissolution and precipitation rates of  $\gamma$  phase was determined. The dissolution rate in the HAZ of lean DSS was slightly larger than those in the HAZs of standard and super DSSs. The precipitation rate of  $\gamma$  phase in standard DSS was largest of the three DSSs. The nose temperature and rate constant of the  $\gamma$  phase precipitation in WMs increased compared with those of HAZs in all DSSs.

(3) Based on the kinetic equations determined, the distribution of the  $\gamma$  phase fraction in multipass welds of DSSs was calculated combined with the heat conduction analysis in welding process. The incremental method was applied to expand the dissolution and precipitation kinetics to the non-isothermal process. The  $\gamma$  phase fraction in the just solidified WM was considerably small in any weld passes, and the depleted zone of  $\gamma$  phase was formed in the “under-bead” region in the base metal HAZs and reheated WMs. However, the  $\gamma$  phase fraction in the depleted zone was increased (recovered) by the subsequent weld passes.

(4) The  $\gamma$  phase fraction in multipass weld of standard DSS was slightly lower than those of lean and super DSSs. The over-precipitated zone, where the  $\gamma$  phase fraction slightly exceeded the base metal level, was not observed in the low temperature HAZ of standard DSS weld, whereas it was observed in other welds.

(5) Microstructural observation revealed that the calculated results of  $\gamma$  phase fraction in multipass welds were consistent with experimental ones. It followed that the  $\alpha/\gamma$  phase transformation in DSS welds could be successfully predicted by the present approach.

## ACKNOWLEDGEMENTS

The authors would like to thank Messrs. Y. Tanabe and J. Tokunaga (Osaka Univ.) for their cooperation in this research.

## REFERENCES

- [1] M.MIURA, M.KOSO, T.KUDO AND H.TSUGE: 'Effect of Nickel and Nitrogen on Microstructure and Corrosion Resistance of Duplex Stainless Steel Weldment', *Quarter. J. JWS*, Vol.7 No.1 (1989), p.94-100 (in Japanese).
- [2] O.KAMIYA, K.KUMAGAI, T.ENJO AND Y.KIKUCHI: 'Effect of Microstructure on Fracture Toughness of SUS329J1 Duplex Stainless Steel Welds', *Quarter J. JWS*, Vol.8 No.1 (1990), p.105-111 (in Japanese).
- [3] N.A.MCPHERSON, Y.LI AND T.N.BAKER: 'Microstructure and Properties of As Welded Duplex Stainless Steel', *Sci. & Technol. Welding & Joining*, Vol.5 No.4 (2000), p.235-244.
- [4] R.BADJI, M.BOUABDALLAH, B.BACROIX, C.KAHLOUN, B.BELKESSA AND H.MAZA: 'Phase Transformation and Mechanical Behavior in Annealed 2205 Duplex Stainless Steel Welds', *Mater. Characterization*, 59 (2008), p.447-453.
- [5] J.W.ABTIBOL MENEZES, H.ABREU, S.KUNDU, H.K.D.J.BHADESHIA AND P.M.KELLY: 'Crystallography of Widmanstätten Austenite in Duplex Stainless Steel Weld Metal', *Sci. & Technol. Welding & Joining*, Vol.14 No.1 (2009), p.4-10.
- [6] R.J.RAMIREZ, S.D.BRANDI AND J.C.LIPPOLD: 'Secondary Austenite and Chromium Nitride Precipitation in Simulated Heat Affected Zones of Duplex Stainless Steels', *Sci. & Technol. Welding & Joining*, Vol.9 No.4 (2004), p.301-313.
- [7] J.-O.NILSSON, T.HUHTALA, P.JONSSON, L.KARLSSON AND A.WILSON: 'Structural Stability of Super Duplex Stainless Weld Metals and Its Dependence on Tungsten and Copper', *Metall. Mater. Trans.*, Vol.27A No.10 (1996), 2196-2208.
- [8] R.BADJI, M.BOUABDALLAH, B.BACROIX, C.KAHLOUN, K.BETTAHAR AND N.KHERROUBA: 'Effect of Solution Treatment Temperature on the Precipitation Kinetic of  $\sigma$ -Phase in 2205 Duplex Stainless Steel Welds', *Mater. Sci. Eng.*, A 496 (2008), p.447-454.
- [9] K.NISHIMOTO, K.SAIDA AND O.KATSUYAMA: 'Prediction of Sigma Phase Precipitation in Super Duplex Stainless Steel Weldments', *Welding in the World*, Vol.50 No.3/4 (2006), p.13-28.
- [10] S.H.WANG, P.K.CHIU, J.R.YANG AND J.FANG: 'Gamma ( $\gamma$ ) Phase Transformation in Pulsed GTAW Weld Metal of Duplex Stainless Steel', *Mater. Sci. Eng.*, A 420 (2006), p.26-33.
- [11] H.LIU AND X.JIN: 'Secondary Austenite Morphologies in Fusion Zone of Welded Joint after Postweld Heat Treatment with a Continuous Wave Laser', *J. Mater. Sci. Technol.*, Vol.28 No.3 (2012), p.249-254.
- [12] T.A.PALMER, J.W.ELMER AND J.WONG: 'In Situ Observation of Ferrite-Austenite Transformations in Duplex Stainless Steel Weldments using Synchrotron Radiation', *Sci. & Technol. Welding & Joining*, Vol.7 No.3 (2002), p.159-171.
- [13] C.M.GARZÓN AND A.J.RAMIREZ: 'Growth Kinetics of Secondary Austenite in the Welding Microstructure of a UNS S32304 Duplex Stainless Steel', *Acta Mater.*, Vol.54 (2006), p.3321-3331.
- [14] D.J.KOTECKI: 'Ferrite Control in Duplex Stainless Steel Weld Metal', *W.J.*, Vol.65 No.10 (1986), p.273s-278s.
- [15] Y.NAKAO, K.NISHIMOTO AND S.INOUE: 'Kinetics of the Formation of Austenite at Constant Temperature, -Study on the Phase Transformation in Welded Joints of Duplex Stainless Steels (Report 1)-', *J. JWS*, Vol.50 No.5 (1981), p.514-520 (in Japanese).

- [16] Y.NAKAO, K.NISHIMOTO AND S.INOUE: 'Quantitative Analysis of Austenite Formation in HAZ, -Study on the Phase Transformation in Welded Joints of Duplex Stainless Steels (Report 2)-', *J. JWS*, Vol.50 No.11 (1981), p.1107-1111 (in Japanese).
- [17] K.YASUDA, R.N.GUNN AND T.G.GOOCH: 'Prediction of Austenite Phase Fraction in Duplex Stainless Steel Weld Metals', *Quarter. J. JWS*, Vol.20 No.1 (2002), p.68-77 (in Japanese).
- [18] K.SAIDA, K.NISHIMOTO, H.INOUE AND Y.OIKAWA: 'Prediction of Phase Transformation in Duplex Stainless Steel Welds', *Mathematical Modelling of Weld Phenomena 11*, ed. by C.Sommitsch, N.Enzinger and P.Mayr, (2016), p.109-122.
- [19] T.OGURA, Y.TANABE, H.INOUE, Y.OIKAWA AND K.SAIDA: 'Kinetics of Phase Transformation in Weld Heat Affected Zone of Duplex Stainless Steels', 9th European Stainless Steel Conference - Science & Market (ESSC2017) & 5th European Duplex Stainless Steel Conference & Exhibition (DUPLEX 2017), 21-23rd May (2017), Bergamo (Italy).
- [20] J.W.CAHN: 'The Kinetics of Grain Boundary Nucleated Reactions', *Acta Metall.*, Vol.4, (1956), p.449-459.
- [21] W.C.JOHNSON, C.L.WHITE, P.E.MARTH, P.K.RUF, S.M.TUOMINEN, K.D.WADE, K.C.RUSSELL AND H.I.AARONSON: 'Influence of Crystallography on Aspects of Solid-Solid Nucleation Theory', *Metall. Trans. A*, Vol.6A No.4 (1975), p.911-919.
- [22] K.HIRANO: 'GOUKIN NO GIKOU KATEI TO SONO KAISHAKU', KINZOKUGAKKAI SEMINAR, (1968), p.1-28 (in Japanese).
- [23] J.J.DEL COZ DIAZ, P.MENENDEZ RODRIGUEZ, P.J.GARCIA NIETO AND D.CASRO-FRESNO: 'Comparative Analysis of TIG Welding Distortions between Austenitic and Duplex Stainless Steels by FEM', *Applied Thermal Eng.*, Vol.30, (2010), p.2448-2459.





# THE INFLUENCE OF CHEMISTRY INHOMOGENEITY ON MICROSTRUCTURE DEVELOPMENT AND RESIDUAL STRESS

J. NI\*, J. VANDE VOORDE\*\*, J. ANTONISSEN\*\* and  
M. A. WAHAB\*

*\*Laboratory Soete, Faculty of Engineering and Architecture, Ghent University, 9052, Zwijnaarde, Belgium*

*\*\*Research Centre for the Application of Steel (OCAS), 9060, Zelzate, Belgium*

DOI 10.3217/978-3-85125-615-4-08

## ABSTRACT

The chemistry distribution is of importance in the welding process. By varying the chemical composition, the evolution of microstructure and the residual stress change correspondingly. To examine the effect of chemistry, a three-dimensional metallo-thermo-mechanical model is created. The model is established according to a bead-on-plate welding experiment. Samples of S700 steel are manufactured by gas metal arc welding (GMAW). In total, three welds with three heat inputs were conducted so that different chemistries are obtained. The final weld geometry and the uniform chemistry in the fusion zone (FZ) are predicted by the software SimWeld. The parameters in the double ellipsoidal heat source are also calibrated by SimWeld. An inhomogeneous chemistry field is created using the data predicted by SimWeld and the chemical composition of base material (BM), and is further imported to the coupled model by writing user subroutine in ABAQUS. The metallurgical algorithm is implemented in the same way for calculating the phase volume fraction using both the homogeneously and the inhomogeneously distributed chemistry fields. After the temperature and microstructure are determined, the mechanical analysis is conducted using linearly interpolated material properties. Finally, the results of microstructure distribution and the residual stress predicted for homogeneous and inhomogeneous field are compared to clarify the influence of chemical composition.

Keywords: Chemistry Inhomogeneity, Residual stress, Phase transformation

## INTRODUCTION

The filler wire and the base material are mixed during the welding process, leading to an area whose chemical composition is neither that of the filler nor that of the base. This variation in the chemical composition will definitely cause a change in microstructure evolution. However, due to the complexity of the welding process, the chemical composition in FZ is hard to predict. Buki [1] developed an algorithm to calculate the composition, and applied it as a universal procedure to design new electrodes. However, this method is not widely adopted. An alternative way to predict the chemistry in FZ is provided by the commercial software SimWeld. This approach is adopted in this research work.

When conducting the metallurgical simulation, several authors [2-4] simply treated the chemistry in FZ the same as in BM, which is obviously not reasonable. An improvement was done by using two chemical compositions, the one of filler for FZ, and the other of BM for the rest of the welded structures [5]. Both compositions are homogeneously distributed in corresponding regions. However, this assumption may not hold since the chemical compositions of BM and filler mix in the FZ, leading to an area with chemistry of neither BM nor filler. To consider this effect, SimWeld is used to estimate the chemical composition in FZ for constructing the complete chemistry field. This field is then imported to the metallurgical algorithm of Bhadeshia et al. [6-9] by assigning the chemical composition to each node of finite element (FE) model.

In this work, the arc welding was conducted with three levels of input power. Therefore, the wire filler and the base material contribute in different ratios to the FZ. As a result, different chemistry fields are achieved. The chemical composition in FZ as well as the final geometry of the weldments are predicted by SimWeld. Those data are imported into ABAQUS to create coupled models. Finally, the phase volume fractions and the residual stress distributions predicted using only the BM and the non-uniform chemistry fields are compared to demonstrate the influence of chemistry inhomogeneity.

### TRANSFORMATION KINETICS

The kinetic functions of the austenite decomposition are briefly introduced in this section. As the temperature decreases, austenite transforms to allotriomorphic ferrite, Widmannstätten ferrite, pearlite, bainite and martensite, which are written in symbols of  $\gamma$ ,  $\alpha$ ,  $\alpha_w$ ,  $\alpha_p$ ,  $\alpha_b$  and  $\alpha'$ , respectively.

$\gamma$  continues to decompose until the space of the austenite grain is fully filled. The space is evaluated by the grain boundary area  $O_B$  of austenite as [10]:

$$O_B = \frac{2}{\bar{L}} \tag{1}$$

where  $\bar{L}$  is the mean linear intercept for an equiaxial grain.

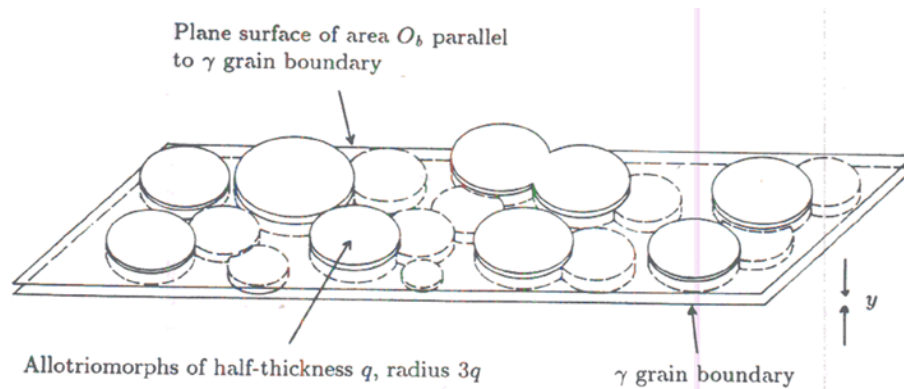


Fig. 1 Representative plot of  $\alpha$  grain growth [11]

$\alpha$  is assumed to grow layer by layer as shown in Figure 1, in which the growth of it is modelled as expansion and thickening of discs. Those discs are assumed to be able to grow on both sides of  $\gamma$  grain boundaries with the half-thickness  $q_\alpha$  as [6]:

$$q_\alpha = v_\alpha (t - \tau)^{1/2} \quad (2)$$

where  $v_\alpha$  is the parabolic thickening rate, and  $\tau$  is the incubation time. The change rate of the area that intersects with the plane at a distance of  $y$  away from grain boundary at time  $t = m\Delta t$  is given as [6]:

$$A_{\alpha,k,y} = \begin{cases} \pi\eta_\alpha^2 v_\alpha^2 & q_{\alpha,m\Delta t} > y \\ \pi\eta_\alpha^2 q_{\alpha,m\Delta t}^2 / \Delta t & q_{\alpha,m\Delta t} = y \\ 0 & q_{\alpha,m\Delta t} < y \end{cases} \quad (3)$$

where  $k$  denotes nucleation time  $\tau = k\Delta t$ .  $\Delta\tau$  and  $\Delta t$  are set to be numerically identical.  $\eta_\alpha$  is the ratio between disc radius and half-thickness. The growth of  $\alpha_p$  and  $\alpha_w$  is treated similarly as  $\alpha$  but with different nucleation rates [6]. Besides, the growth of  $\alpha_w$  is modelled as the lengthening of tetragonals instead of discs.

The growth kinetic function of  $\alpha_b$  is expressed as [9]:

$$\frac{d\xi}{dt} = \frac{uK_1}{X_{\alpha_b,\max}} (1 - \xi) \left[ 1 + \lambda_1 (1 - \lambda_2 x_\gamma) X_{\alpha_b,\max} \xi \right] \times \exp \left[ -\frac{K_2}{RT} \left( 1 + \frac{\Delta F_{\max}}{C_e} \right) + \frac{K_2 (\Delta F_{\max} - \Delta F_N)}{C_e RT} \right] \quad (4)$$

where  $\xi$  is the ratio between volume fraction  $X_{\alpha_b}$  of current  $\alpha_b$  and its maximum value  $X_{\alpha_b,\max}$ , namely  $\xi = X_{\alpha_b} / X_{\alpha_b,\max}$ .  $u$  is the volume of a bainitic subunit.  $x_\gamma$  is the carbon concentration in steel.  $C_e$ ,  $K_1$ ,  $K_2$ ,  $\lambda_1$  and  $\lambda_2$  are fitted constants.  $R$  is the gas constant.  $\Delta F_{\max}$  is the maximum molar energy difference between  $\gamma$  and  $\alpha_b$ .  $\Delta F_N$  is the energy required for the nucleation of  $\alpha_b$ . For  $\alpha'$ , its final volume fraction is estimated as [8]:

$$-\frac{\ln(1 - X_{\alpha'})}{X_{\alpha'}} = 1 + C_f (M_s - T) \quad (5)$$

where  $X_{\alpha'}$  is the volume fraction of  $\alpha'$  at temperature  $T$  and  $C_f$  is also a fitted constant.

## EXPERIMENTAL SETUP

The bead-on-plate specimens of low-alloyed sheet metal S700 were produced using the GMAW, with a thickness of 8.0 mm and a length of 800 mm. The chemical compositions

## Mathematical Modelling of Weld Phenomena 12

of plate and filler are listed in Table 1. The welding speed is controlled at 300 mm/min and the other welding conditions are detailed in Table 2, in which ‘HI’ means heat input.

**Table 1** Chemical composition of S700 plate and filler

	Chemical elements (wt.%)			
	C	Si	Mn	Ni + Mo + Cr
Plate	0.06	0.05	1.90	0.70
Filler	0.10	0.90	1.50	

**Table 2** The currents and voltages used at three heat input level

Sample	Current (A)	Voltage (V)
Low HI	180	20
Medium HI	210	22
High HI	240	25

As mentioned, BM and filler are mixed in the FZ and the chemical composition is predicted by SimWeld. The uniform values are listed in Table 3.

**Table 3** The chemical composition in FZ predicted by SimWeld

	Chemical elements (wt.%)			
	C	Si	Mn	Ni + Mo + Cr
Low HI	0.077	0.47	1.66	0.27
Medium HI	0.077	0.48	1.66	0.26
High HI	0.078	0.49	1.65	0.26

### MODEL ESTABLISHMENT

The coupled thermo-metallo-mechanical model incorporates three aspects. In the thermal analysis, the temperature is regenerated in ABAQUS by implementing the double ellipsoidal heat source as:

$$q(x, y, z, t) = \frac{6\sqrt{3}f_f Q_{inp}}{a_f b c \pi \sqrt{\pi}} \exp\left(-\frac{3[x + v(\tau - t)]^2}{a_f^2} - \frac{3y^2}{b^2} - \frac{3z^2}{c^2}\right) \quad (6)$$

with the parameters which were calibrated by SimWeld and are summarized in Table 4.

**Table 4** The calibrated parameters of double ellipsoidal model by SimWeld

	$a_f$ (mm)	$a_r$ (mm)	$b$ (mm)	$c$ (mm)	$f_f$	$Q_{inp}$ (W)
Low HI	3.5	14.3	3.7	5.1	1.3	3400
Medium HI	4.0	18.0	4.3	6.0	1.2	4400
High HI	7.0	19.5	4.8	3.2	1.5	5400

$f_f$  is the power fraction of the front ellipsoid.  $a_f$ ,  $b$  and  $c$  are the ellipsoid semi-axes. The distribution function in the rear quadrant has the same form but with different values for the semi-axis length  $a_r$  and the power fraction  $f_r$ .  $f_f$  and  $f_r$  satisfy  $f_f + f_r = 2.0$  [12]. The description and the function of power distribution is shown in Figure 2. The function is implemented in ABAQUS writing user subroutine DFLUX.

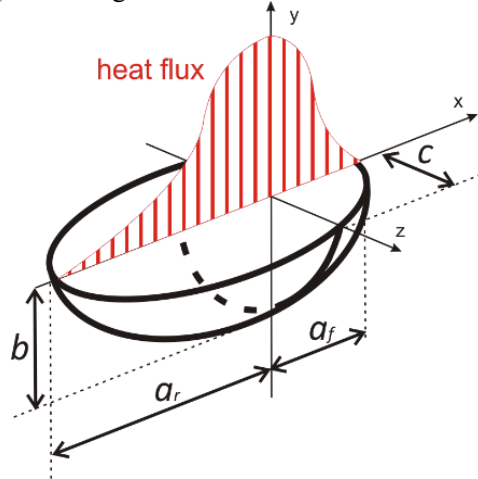


**Fig. 2** The power distribution function of double ellipsoidal heat source

As mentioned, the geometry after welding is also predicted by SimWeld. The results are output as '.igs' files and the 2D figures are presented in Figure 3. Those files are imported to ABAQUS to create 3D models.

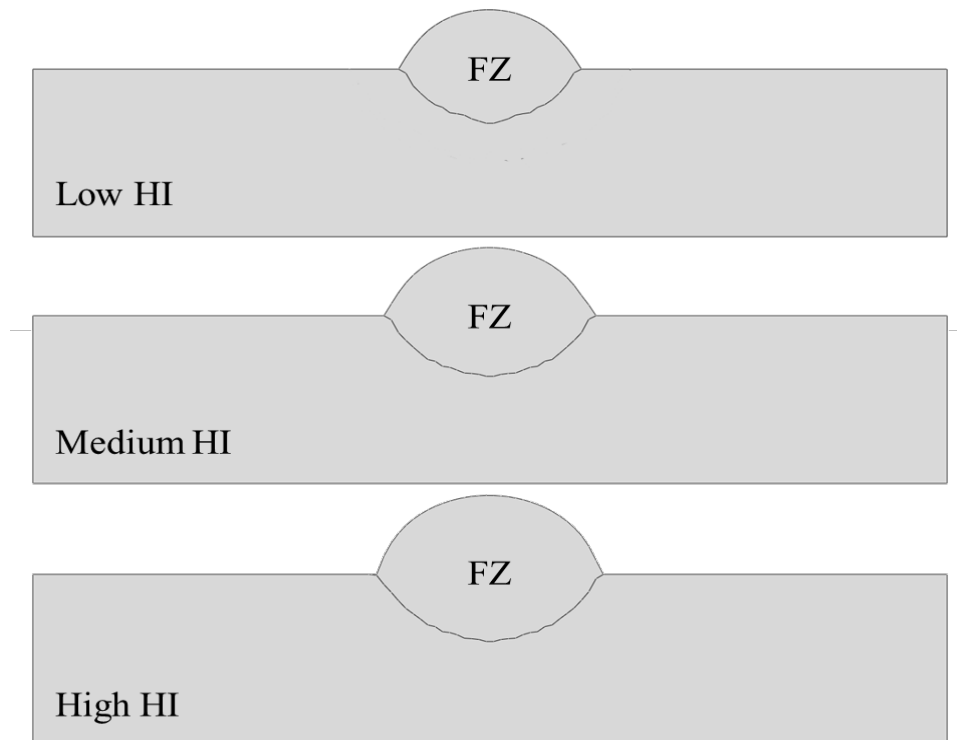


**Fig. 3** The geometry of the weld at three heat input levels

The uniform field simply uses the chemical composition of BM for every node. The non-uniform chemistry field is created by the following steps:

- Create the FE model in ABAQUS, and group the nodes belonging to FZ and BM in separate sets. The model is exported as '.inp' file.
- A python script is written to select the nodes belonging to each set and rearrange them in nodal sequence as illustrated in Figure 4 b).
- In the last step, the chemical compositions of FZ (denoted as 'CFUSION' in Figure 4 c)) and BM (denoted as 'CBASE' in Figure 4 c)) are assigned to corresponding nodes.

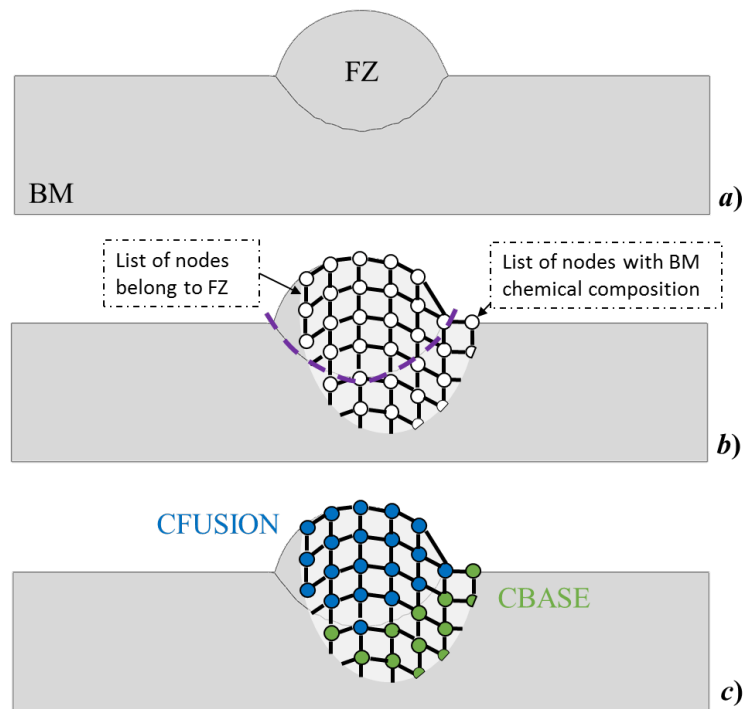


**Fig. 4** The steps to construct a chemistry field for simulation

The chemistry distribution created in this 2D geometry is output as a '.dat' file in nodal sequence. The inhomogeneity in the third direction is ignored. The homogeneous chemistry distribution in the FZ is stored in a '.dat' file as well.

The metallurgical algorithm in section 2 is implemented in ABAQUS using another subroutine ABAMAIN. In the algorithm, the start and finish transformation temperatures are estimated based on thermodynamic theories rather than empirical functions. For transforming kinetics, the model assumes the reconstructive transformation to occur at grain boundaries but also includes the possibility of inclusion nucleation. The nucleation rates were treated as temperature-dependent and the growth rates were determined by solving carbon diffusion equations [6]. The initiation of bainite growth was assumed to be displacive with a strain energy of 400 J/mol [13]. The advantages of this framework are that:

- it omits the troubles of parameter validation;
- it requires only the chemical composition, the temperature history and the austenite grain size at each node as its input.

The BM mainly consists of bainite. The SEM micrograph shows that bainite accounts for 99% and that ferrite contributes to 1% [14]. Therefore, the initial values of bainite and ferrite in the metallurgical analysis are assigned to be 0.01 and 0.99 in the FE model. The



values of the other phases are set to 0.00. Again, the five products, allotriomorphic ferrite ( $\alpha$ ), Widmannstätten ferrite ( $\alpha_w$ ), pearlite ( $\alpha_p$ ), bainite ( $\alpha_b$ ) and martensite ( $\alpha'$ ) are arranged in sequence as in Table 5.

**Table 5** The sequence of field variables and corresponding phase stored in ABAQUS

FV1	FV2	FV3	FV4	FV5	FV6
$\alpha$	$\alpha_w$	$\alpha_p$	$\alpha_b$	$\alpha'$	$\gamma$

The mechanical analysis is conducted using the built-in elasto-plastic algorithm in ABAQUS. The material is treated as an assembly of phases or constituents. Therefore, the overall properties are obtained by linearly interpolating the properties of individual phases with their respective volume fractions.

The mechanical properties are listed in Table 6. The values of  $\alpha_w$  are not listed in Table 6 because it is treated the same as  $\alpha$  and  $\alpha_p$ . The tangent modulus of all phases is assumed to be 2000 MPa [15].

**Table 6** The properties of individual phase [16]

Property	Phase	Temperature (°C)			
		0	300	600	800
Elastic modulus, GPa	$\gamma$	200	175	150	124
	$\alpha$ and $\alpha_p$	210	193	165	120
	$\alpha_b$	210	193	165	120
	$\alpha'$	200	185	168	--
Poisson's ratio	$\gamma$	0.29	0.31	0.33	0.35
	$\alpha$ and $\alpha_p$	0.28	0.30	0.31	0.33
	$\alpha_b$	0.28	0.30	0.31	0.33
	$\alpha'$	0.28	0.30	0.31	--
Expansion coefficient, K <sup>-1</sup>	$\gamma$	2.1×10 <sup>-5</sup>			
	$\alpha$ and $\alpha_p$	1.4×10 <sup>-5</sup>			
	$\alpha_b$	1.4×10 <sup>-5</sup>			
	$\alpha'$	1.3×10 <sup>-5</sup>			
Yield strength, MPa	$\gamma$	190	110	30	20
	$\alpha$ and $\alpha_p$	360	230	140	30
	$\alpha_b$	440	330	140	30
	$\alpha'$	1600	1480	1260	--

The implementation algorithm is plotted in Figure 5. One thermal analysis is run before the coupled analysis to produce the temperature field. Therefore, the proposed model is sequentially coupled, ignoring the effects of latent heat and plastic work. This is reasonable since the amount of energy produced by those mechanisms is far lower than the input heat power [17, 18]. The experiments were conducted at a room temperature of 20°C, with an estimated convection coefficient of 30W/m<sup>2</sup>°C.

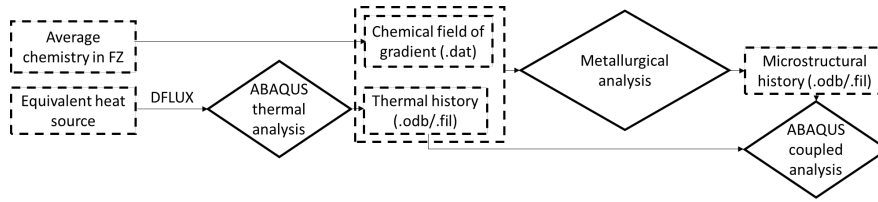


**Fig. 5** Flow chart of the fully coupled model

## RESULTS AND DISCUSSION

The microstructure evolution of two selected nodes, ‘A’ and ‘B’, predicted in high heat input are plotted in Figure 6. Here, only the distribution of  $\alpha$  and  $\alpha_w$  are presented because they are the main transformation products. The evolution line of the homogeneously distributed chemistry field is drawn in black, comparing to the results of the inhomogeneous chemistry distribution in red. The nodes are chosen at the middle cross-section of the weld. ‘A’ is located at the top of the section. ‘B’ lies at the FZ/HAZ boundary. The difference of  $\alpha$  and  $\alpha_w$  volume fractions at node ‘A’ can be obviously noticed. It is due to the fact that point ‘A’ in inhomogeneous model possesses a chemical composition different from BM as presented in Table 3. Moreover, higher volume fraction of  $\alpha$  at ‘A’ is found in the case of inhomogeneous chemistry, while the value of  $\alpha_w$  is lower. This phenomenon indicates that the chemistry of the filler wire favors the formation of  $\alpha$  and inhibits the production of  $\alpha_w$ . For location ‘B’, the microstructure evolutions predicted by both chemistry fields are identical according to the algorithm in section 4. As a result, their volume fractions overlap with each other.

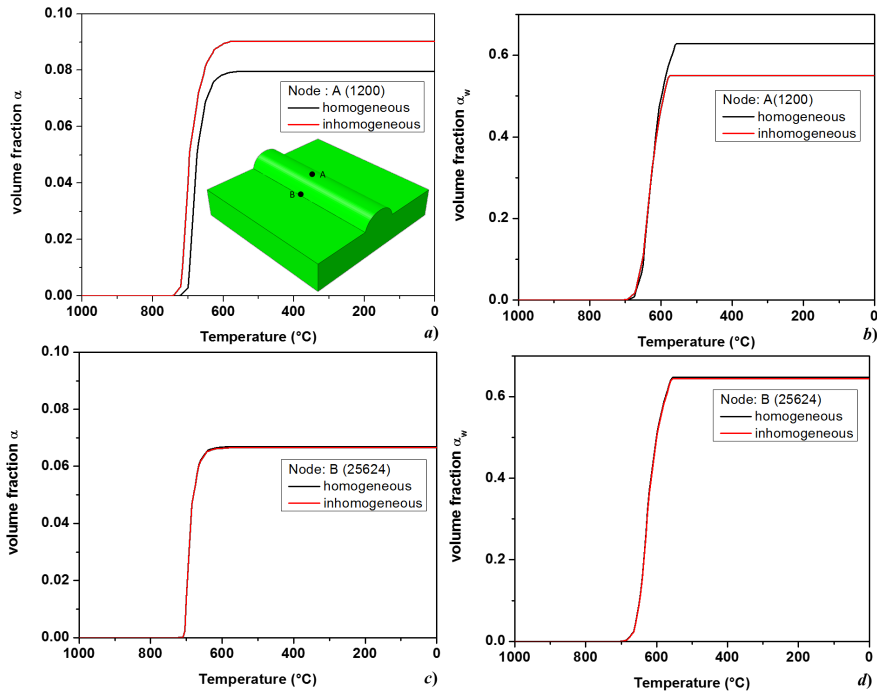


**Fig. 6** The evolution of  $\alpha$  and  $\alpha_w$  at specific positions ‘A’ and ‘B’

Previously, the microstructure evolution was plotted only for the high level heat input. To demonstrate the effect of chemistry inhomogeneity at different heat input levels, the final distributions of  $\alpha'$  in all cases are presented in Figure 7. With the decrease of input power, the cooling rate increases in the FZ and the volume fraction of  $\alpha'$  increases accordingly. However, due to the reduction of heat input, the transformation occurs within a smaller area. The maximum value of  $\alpha'$  predicted by the inhomogeneous field is always greater than the one by the homogeneous field. This is caused by the fact that in the inhomogeneous field, the carbon concentration is higher than the one in the uniform field. The distributions of  $\alpha'$  volume fraction are different either, especially in FZ, which is again caused by the chemistry inhomogeneity. However, this distribution difference becomes not so significant in the low heat input level, which may be due to the fact that the cooling rate turns out to be the main fact influencing on the phase transformation.

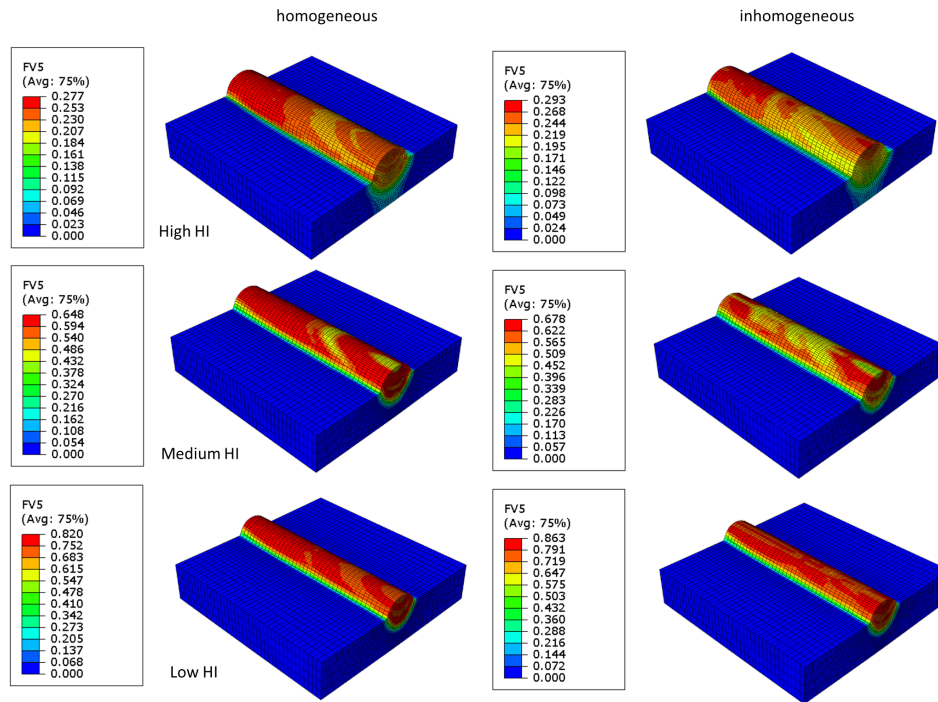


**Fig. 7** The contour plots of  $\alpha'$  predicted using homogeneous and inhomogeneous fields

Finally, the stress distributions at the middle cross-section are plotted in Figure 8. 'S11' is the stress component vertical to the section, and 'S33' is the parallel value. The maximum stress values predicted using the inhomogeneous field, no matter in tensile or compressive, stay lower than the values of the homogeneous one. Furthermore, compared to the distribution of 'S11' of the homogeneous field, the area subjected to tensile stress predicted by the inhomogeneous field expands. Similar situation is found for the 'S33' distribution.

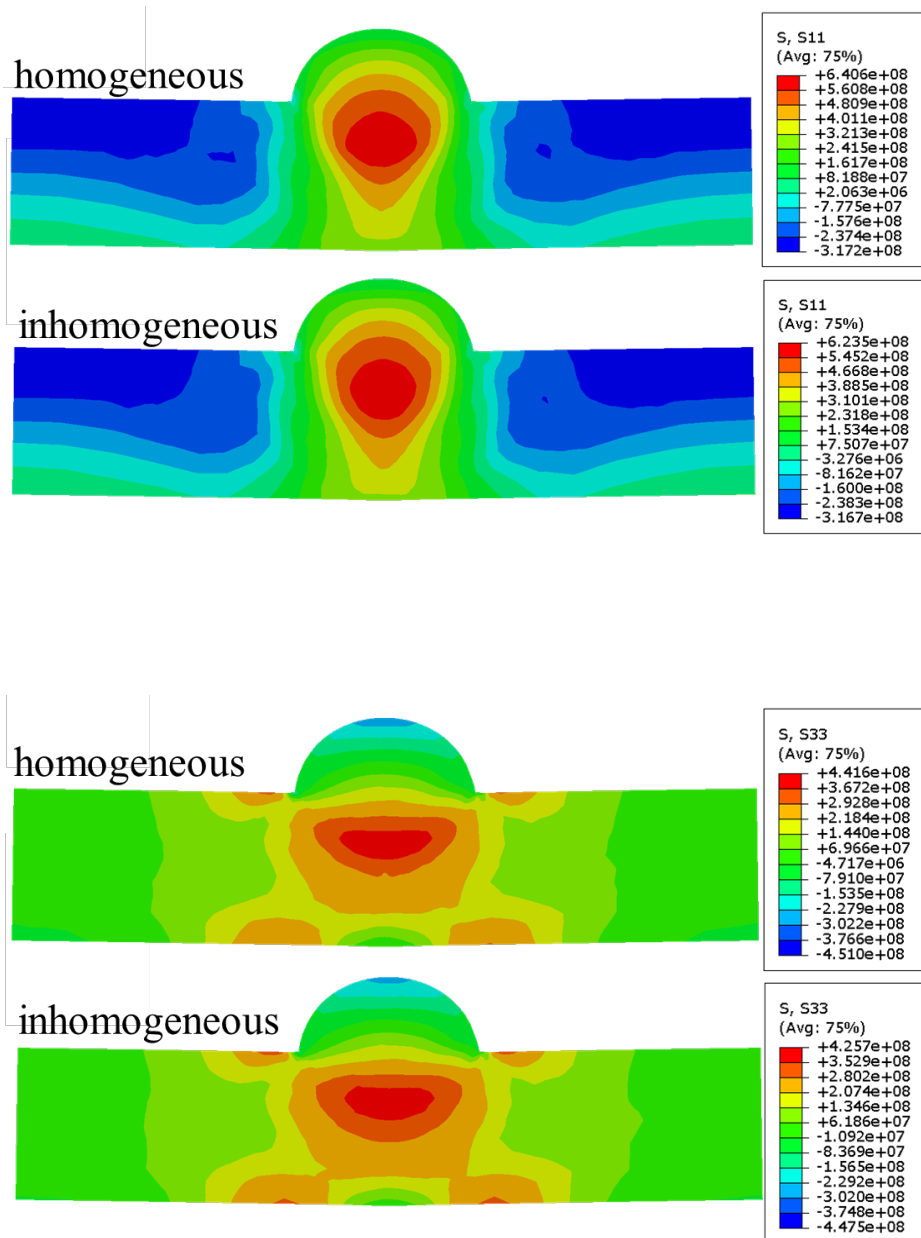


Fig. 8 The stress distribution at the middle cross-section

### CONCLUSION

A metallurgical algorithm by Bhadeshia et al. [6-9] is implemented in ABAQUS to establish a coupled thermo-metallo-mechanical model. To analyze the effects of chemical composition on the phase transformation and the residual stress, the chemical composition predicted by SimWeld is adopted to construct a reasonable inhomogeneous chemistry field. This field is further imported to the coupled FE analysis. By comparing the simulation results using homogeneous and inhomogeneous fields, the following conclusions can be drawn:

- At high heat input level, more  $\alpha$  and less  $\alpha_w$  are produced in FZ due to the chemistry inhomogeneity, while at the FZ/HAZ boundary, no difference of the volume fractions of  $\alpha$  and  $\alpha_w$  is found.
- Higher heat input reduces  $\alpha'$  volume fraction.
- The non-uniform chemistry increases the maximum value as well as the distribution of  $\alpha'$  volume fraction in the simulation results.
- The inhomogeneous chemistry distribution reduces the maximum magnitudes of the residual stress components and extends the areas subjected to tensile stress.

### ACKNOWLEDGEMENTS

The authors acknowledge the MaDurOS project and the support from SIM and VLAIO.

### REFERENCES

- [1] H. K. D. H. BHADESHIA: 'A Rationalization of Shear Transformations in Steels', *Acta Metallurgica*, Vol. 29, No. 6, pp. 1117-1130, 1981.
- [2] A. A. BHATTI, Z. BARSOUM, H. MURAKAWA, and I. BARSOUM: 'Influence of Thermo-Mechanical Material Properties of Different Steel Grades on Welding Residual Stresses and Angular Distortion', *Materials & Design*, Vol. 65, pp. 878-889, 2015.
- [3] L. BORJESSON, AND L. E. LINDGREN: 'Simulation of Multipass Welding with Simultaneous Computation of Material Properties', *Journal of Engineering Materials and Technology-Transactions of the ASME*, Vol. 123, No. 1, pp. 106-111, 2001.
- [4] A. A. BUKI: 'Calculating the Chemical Composition of Deposited Metal When Welding with Coated Electrodes', *Welding International*, Vol. 6, No. 10, pp. 818-820, 1992.
- [5] HUI DAI: 'Modelling Residual Stress and Phase Transformations in Steel Welds', *INTECH Open Access Publisher*, 2012.
- [6] D. DENG: 'FEM Prediction of Welding Residual Stress and Distortion in Carbon Steel Considering Phase Transformation Effects', *Materials & Design*, Vol. 30, No. 2, pp.359 -366, 2009.
- [7] P. FERRO, H. PORZNER, A. TIZIANI, AND F. BONOLLO: 'The Influence of Phase Transformations on Residual Stresses Induced by the Welding Process - 3d and 2d Numerical Models', *Modelling and Simulation in Materials Science and Engineering*, Vol. 14, No. 2, pp.117 -136, 2006.
- [8] JOHN A GOLDAK, AND MEHDI AKHLAGHI: *Computational Welding Mechanics*, Springer Science & Business Media, 2006.

- [9] W. GUO, J. A. FRANCIS, L. LI, A. N. VASILEIOU, D. CROWTHER, AND A. THOMPSON: 'Residual Stress Distributions in Laser and Gas-Metal-Arc Welded High-Strength Steel Plates', *Materials Science and Technology*, Vol. 32, No. 14, pp. 1449-1461, 2016.
- [10] C. J. HAMELIN, O. MURANSKY, M. C. SMITH, T. M. HOLDEN, V. LUZIN, P. J. BENDEICH, AND L. EDWARDS: 'Validation of a Numerical Model Used to Predict Phase Distribution and Residual Stress in Ferritic Steel Weldments', *Acta Materialia*, Vol. 75, pp.1-19, 2014.
- [11] S. J. JONES, AND H. K. D. H. BHADSHIA: 'Kinetics of the Simultaneous Decomposition of Austenite into Several Transformation Products', *Acta Materialia*, Vol. 45, No. 7, pp.2911-2920, 1997.
- [12] S. A. KHAN, AND H. K. D. H. BHADSHIA: 'Kinetics of Martensitic-Transformation in Partially Bainitic 300m Steel', *Materials Science and Engineering A Structural Materials Properties Microstructure and Processing*, Vol. 129, No. 2, pp. 257-272, 1990.
- [13] J. S. KIRKALDY, AND R. C. SHARMA: 'A New Phenomenology for Steel It and Cct Curves', *Scripta Metallurgica*, Vol. 16, No. 10, pp. 1193-1198, 1982.
- [14] R. C. REED, AND H. K. D. H. BHADSHIA: 'Kinetics of Reconstructive Austenite to Ferrite Transformation in Low-Alloy Steels', *Materials Science and Technology*, Vol. 8, No. 5, pp. 421-435, 1992.
- [15] G. I. REES, AND H. K. D. H. BHADSHIA: 'Bainite Transformation Kinetics .1. Modified-Model', *Materials Science and Technology*, Vol. 8, No. 11, pp. 985-993, 1992.
- [16] F.N. RHINES, R.T. DEHOFF: *Quantitative Microscopy*, University of Florida, 1968.
- [17] M. TAKAHASHI, AND H. K. D. H. BHADSHIA: 'A Model for the Microstructure of Some Advanced Bainitic Steels', *Materials Transactions*, Vol. 32, No. 8, pp. 689-696, 1991.
- [18] G.E. TOTTEN: *Handbook of Residual Stress and Deformation of Steel*, ASM International, 2002.

# KINETIC MONTE CARLO SIMULATION OF PULSE CU30NI BEAD ON PLATE

A. CHIOCCA\*, F. SOULIE\*, F. DESCHAUX-BEAUME\*,  
J. MITCHELL\*\* and C. BORDREUIL\*

*\*Université de Montpellier, Montpellier France*

*\*\*Sandia labs Albuquerque, United States*

DOI 10.3217/978-3-85125-615-4-09

## ABSTRACT

The purpose of this paper is to show a modelling scheme to predict rapidly three dimensional grain structure. The modelling is based on a plane thermal finite element for the process coupled with a monte carlo simulation for grain structure. To demonstrate the interest of this type of modelling the simulations are done for a squared pulse mode and results are compared with experimental results (EBSD) done during the work of A.Chiocca. The originality of the paper is that predictions of grain structure are investigated with current and arc voltage evolving with time. Results show the interest of using monte carlo simulation.

Keywords: Monte carlo simulation, grain structure, Binary alloy

## INTRODUCTION

The grain structure has an important impact on complex phenomena as hot cracking during welding [1]. The grain structure depends on thermal transfer induced by the process variables. Different modelling of grain structure evolution during solidification can be found in the literature. The two main modellings commonly encountered to predict grain structure are the cellular automaton (CA) [2] and kinetic monte carlo simulation [3]. The first one describes the physics of solidification but it is costly from the numerical point of view. The second one is fast and can then be implemented for an engineering point of view. Sandia Labs proposes an open source software ssparks [4] that can model efficiently grain structure during welding based on a potts model. In ssparks software, different applications are available and can treat three dimensional grain structures. Pulse welding is implemented in kinetic MC simulation (kMC). KMC has also the advantage to take into account grain growth in the heat affected zone that is quite difficult with CA. This last phenomenon can play an important role on epitaxial growth.

The purpose of this paper is to compare experimental results obtained during the PhD of A.Chiocca [5] and results carried out with ssparks program for complex process solidification conditions. Experiments are simple beads on CuNi plate with pulse current. Process thermal simulation is carried out and temperatures and weld pool size are compared with experimental results. Then, melting isotherm based on the process simulation are integrated in the kMC simulation.



Based on EBSD maps, the experimental results seem to indicate an equiaxed grain structure in the whole bead. It is also demonstrated that grain size and shape depend on location inside the bead. Based on different kMC simulations, explanations about the different grain size would be attributed to the process or to the metallurgy. Results demonstrate that kMC opens nice perspectives from engineering point of view.

### EXPERIMENTAL RESULTS

A. Chiocca [5] conducted solidification experiments on Cu30Ni plate with 1.6mm of thickness, 150mm of length and 70mm of width. TIG was used to create the melt pool in the middle of the plate. To investigate the link between the current intensity and solidification front behaviour, it was chosen to use squared pulsed current. The welding power source was set to have a peak current of 133A during 300ms and a low current of 29A during 500ms. The welding speed is 3.5mm/s. Different experimental observations were done during the process. The plate is moved in order to ease image acquisition. Images were synchronized with data acquisition (current evolution). A high speed camera with a microscopic lens was located to observe the solidification front during the pulse. In figure 1, images obtained by the device with microscopic lens are shown.

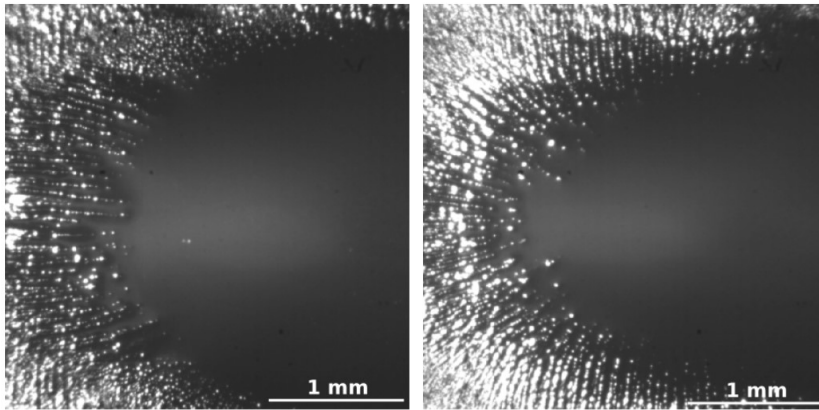


**Fig. 1** Solidification front in the opposite side relative to the torch at the end of a low (right) and high current period (left).

Two cameras were located to observe the weld pool in the rear at the top and the bottom face of the plate. Basic image processing (canny) enables us to find the position at the rear of the weld pool in the frame of the camera. In order to have this position in a fixed frame in the plane of the plate, a calibration procedure was used. Based on the contour and with data acquisition synchronisation, it is possible to compare the evolution of the position at the rear as function of the current. Figure 2 shows the evolution of the position of the point at the rear of the weld pool and the evolution of the current. The curve of the position is noisy and it looks like a sine function. To investigate the position of the point, an interpolation was performed to identify the sine function with a least square method. The fit is good. The position varies only from 0.5mm but this is for the point in the rear. In reality, there is a large evolution of the size of the weld pool. Cameras observations indicated that even at

the end of the low current period there is still residual liquid at the center of the pool. In figure 2, the velocity of the front is derived from the fitted cosine function for the position and the experimental current shows a squared waveform. The front velocity is then approximated by a cosine function and shows a shift from the current that is due to the thermal transfer and in particular to thermal solidification time scale induced by the latent heat.

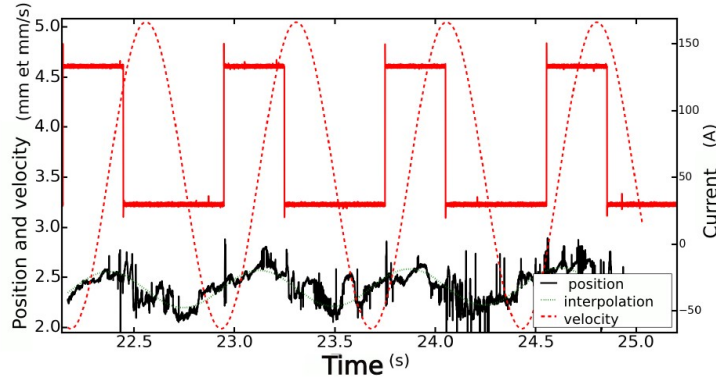


**Fig. 2** Position of the point at the rear of the weld pool synchronised with current.

Figure 3 shows an EBSD map of a bead obtained with the present conditions. In figure 3, the assumed borders of the weld pool are drawn. The border is not easy to locate due to the large change in thermal transfer and due to possible grain growth in the heat affected zone. Compared to constant current weld bead with almost constant width, the width of the pool changes with the torch travelling. This will induce complex front velocity along the border of the weld pool that can modify considerably grain growth. The size of grain in the base material can be estimated with the EBSD measurement. For this plate, it is around 10 micrometers. In figure 3, the middle of the weld bead is shown. It seems that the weld pool is not symmetrical probably due to important fluid flow. The size of the grains can be estimated from the file given by the EBSD measurement. It seems that the grains are larger in the middle of the pool. The size of the grains is controlled by two phenomena. The first one corresponds to the growth of grains and the second one is due to nucleation. In liquid, nucleation can be due to inoculant (particles) or to dendritic arm broken due to active flow.

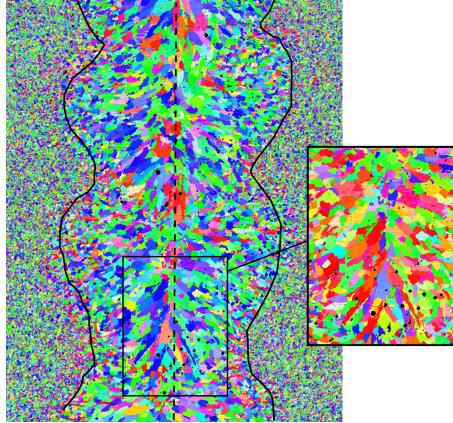


**Fig. 3** EBSD map for the pulse test conditions at the top side of the plate. In black, assumed contour of the weld bead. Some porosities are visible (black disks) in the middle of the weld pool. The width of the weld pool is approximately 10mm. The image in the right has another color because it is another orientation.

To compare the grain structure inside the weld bead, regions of interest must be defined. Because the width of the weld pool changes with time, the grain structure is highly inhomogeneous with large grain size distribution. It is then complicated to investigate the relation between solidification conditions and grain size distribution. Nevertheless, to study this relationship, a region of interest will be located at the common width of the weld pool. The region of interest corresponds to a rectangle that will be translated along the welding direction. Inside this rectangle, the number of grains are counted. A filter was applied to delete all small grains from the analysis and it is then possible to plot the number of grain inside the window in function of the position in the bead. The number of grains inside this window tells us about the average grain size in function of the traveling distance. If the number of grains in the window are low, it means that the grains are large. This can be due to less nucleation site combined with important grain growth velocity. It has also to be noticed that the EBSD maps were carried out on the plane close to the torch and that three dimensional effect due to thermal transfer can be important.

Figure 4 shows the result. A 2.8 mm characteristic length corresponding to the distance between two current peaks can be measured. The location of small grains (low number of grains) corresponds to the location of the peak current. The difference between the low and high value for the number of grains is round 50%.

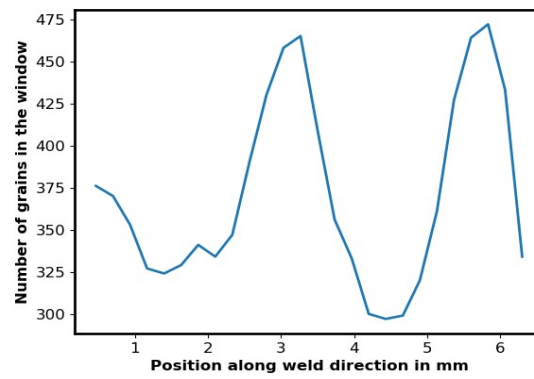


**Fig. 4** Number of grains in function of the position along the weld direction computed with EBSD measurement.

### PROCESS SIMULATION

In this part, the process simulation is explained. The purpose is to model the evolution of the solidification front in order to obtain the solidification front as function of time in order to feed the kinetic monte carlo simulation. The thermal transfers without taken into account fluid velocity are carried out. The different thermal properties of the Cu30Ni are given in table 1. With these properties, it is possible to estimate the characteristic solidification time due to the latent heat that is around 3s for the pool. It means that compared to the 1.2Hz of the pulsed current, latent heat has to be taken into account. In this purpose, an enthalpy formulation is modelled. This formulation integrates the phase change to compute the thermal fields.

**Table 1** Thermal properties of Cu30Ni.

Property	Value and unit
Solidification interval	1472-1520K
Density	8940kg/m <sup>3</sup>
Conductivity	60W/m.K
Capacity	600J/kg.K
Latent heat	2,75e5J/kg

Due to symmetry, only the half of the plate is modelled and to accelerate computation, we considered in plane conduction. Welding simulation follows classical theory. A surface gaussian flux (q) is used to model the heat input of the Gas tungsten arc in function of time t :

$$q = \frac{3 \eta U(t) I(t)}{\pi r_0^2} \exp\left(-3 \frac{(X - X_0)^2 + (Y - Y_0 - v_w t)^2}{r_0^2}\right) \quad (1)$$

where  $\eta$  is the efficiency of the process,  $U(t)$ ,  $I(t)$  are the arc voltage in function of time,  $r_0$  is radius to model where the maximum of heat input entered the plate,  $X_0$  and  $Y_0$  are the coordinate of the start position of the torch and  $v_w$  is the welding speed assumed to be constant all along the process. The efficiency of the process is also assumed constant all along the process despite its possible fluctuations due to high convection during the peak current. Time increment is kept constant at 0.025s. More details about the modelling can be found in [5]. Based on melting isotherm, the evolution of the solidification front can be investigated as function of the time for several periods. Figure 5 shows the half width and length of the pool. The mean half width is around 2mm and the mean half length is 2.8mm. The two characteristics have an amplitude of 0.6mm. With the simulation, it is possible to know the position and the size of the melting isotherm with respect to time. The contour looks like an ellipsoid. The half width of the weld pool seems to be a sinusoid function while the half length of the weld pool seems to be more complex. For a first assumption, it is assumed to be fitted by a cosine function similar to the half width. Due to the difference of duration between the hot and cold period (0,3 vs 0,5 ms), it could be imagined a complex function to fit the evolution of the contour. In particular, it would be better to use a non symmetrical function. To investigate the possibility to use kMC simulation for complex solidification conditions, a cosine function is chosen for the radii of the ellipse that model geometrically the size of the melting isotherm.  $a(t)$  and  $b(t)$  are the two radii functions of time. The evolution of one radius is also shown in figure 5. If a mathematical function wants to fit the evolution of one radius of the ellipsoid, it can be chosen as:

$$a(t) = \left( \cos\left(\frac{2\pi}{\tau} t\right) \right) (a_{max} - a_{min}) + a_{min} \quad (2)$$

In figure 5, the result of the fit is excellent to approximate the evolution of the contour. By combining this evolution with the displacement of the center of the melting isotherm, it is possible to know the position of the solidification front. The center of the contours is assumed to move at a constant speed of 3.5mm/s.

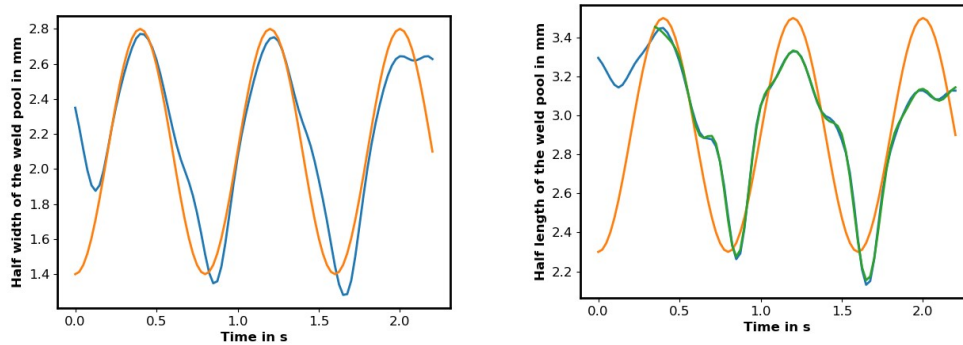


**Fig. 5** Evolution of the fusion isotherm in function of the current for several periods. The size of the weld pool is very similar to the experimental one.

KINETIC MONTE CARLO SIMULATION FOR GRAIN STRUCTURE PREDICTION

The kinetic monte carlo simulation tool used in this work is spparks [4]. The base concept of the software is to minimize the grain boundary energy. The algorithm changes randomly spins in the neighbouring of a grain boundary site and looks if the change is energetically favorable or not with a probability function. Different applications are embedded in the code. In particular, the weld module is presented in [3]. In spparks, pulse arc power is directly integrated in three dimensions. The weld pool is represented as an implicit function. The shape of the weld pool with the dissymetry between the top and the bottom is taken into account. The implicit function describing the one implemented in [3] looks like:

$$\rho(u, v) = V_0(v)P_0(u) + V_1(v)P_1(u) + V_2(v)P_2(u) \quad (3)$$

where  $u, v$  are two curvilinear abscissa and  $V$  and  $P$  are Bernstein polynomials and control points respectively. The two important features to model weld solidification with kinetic monte carlo simulation is the melting and the grain growth. The melting is modelled by assigning a random spin for point inside the weld pool. Grain growth is modelled by defining the grain boundary mobility function as:

$$M(T) = 1 - \frac{d(x)}{haz(t)} \quad (4)$$

where  $haz$  is a distance function depending on energy and  $d(x)$  is the distance function from the weld pool. To take into account the evolution of energy during pulse current,  $haz$  function is defined in function of simulation time in a similar manner as the evolution for the radii (eq 2). During high current, the heat affected zone is larger. For the geometrical point of view, the workpiece is defined as a three dimensional structured grid also called a lattice. A cell of the grid is also called a site. The lattice has to model the width of the pool along  $x$ , the travelling in  $y$  direction and the thickness along  $z$ . Only a part embedding the weld pool is modelled in the geometry. The initial microstructure is computed by letting the grain growth occurs during a number of monte carlo steps (MCS). To have grains with a larger size, simulation are run with  $2MCS$ .

In the function describing the evolution of the weld pool, the time is also expressed as MCS and dimensions are expressed as function of a number of sites. A relationship exists between this time and real time, see [6] for more details. For given process conditions, it is assumed to be constant. For spatial synchronisation, a site represents a distance of 40 micrometers. This leads to a lattice of 400000 sites that is low cost to run and compare simulations. With these definitions, the weld pool dimensions  $a$  and  $b$  are to be defined in function of a number of sites and to model the evolution in figure 4 with time as MCS. The different parameters entering the monte carlo simulation are shown in table 2. The simulation time is expressed as monte carlo steps (MCS) as well as the welding velocity (scan rate).

**Table 2** Parameters for kMC simulation

Parameter	Value and unit
Mean a radius	50 sites
Mean b radius	70 sites
Pulse period	32
Max Haz Distance	1
Scan rate	1.5.sites/MCS
Alpha coefficient for weld pool shape	0.5
Beta coefficient	0.1

With these parameters, a first simulation is done. The results are shown in figure 6. The left hand side of figure 6 shows the initial grain structure obtained by letting the algorithm compute with a given initial number of seeds. The weld pool can be seen on the bottom of the domain. On right hand side, on the top of the figure, the weld pool was not gone out of the lattice. Despite the symmetry of the implicit function describing the solidification front, the result of grain structure is not symmetric due to the algorithm and due to the initial microstructure

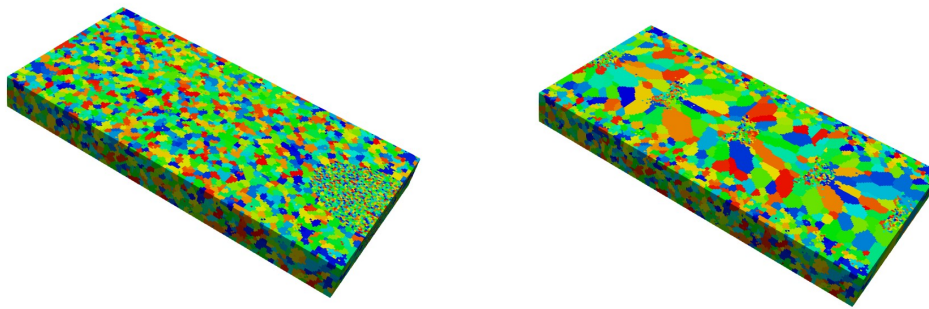


**Fig. 6** Initial and final grain structure prediction after a pulse welding.

As for the experiment, large grains are visible and small grains are more located in the middle of the lattice. Figure 6 correspond to a top view of the plate. Due to the shape of the weld pool, the results are different on the bottom side. In fact, grain shapes on the bottom side look like more elongated denoting a large effect of the grain growth. The first result is to compare the overall distribution of the number of grains in a window as it was done for the experiment (see figure 4).

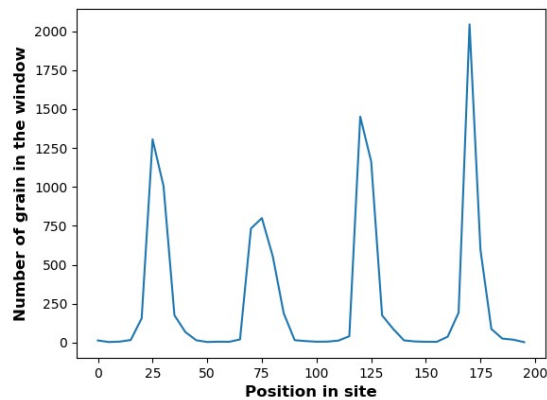


**Fig. 7** Grain number in function of the direction of welding.

Figure 7 shows the distribution of grain number inside a cuboid with a side of 5 sites in length of welding, a side with the thickness of the plate and a side with the width of the weld pool. The period is equal to 70 sites that correspond to 2.4mm for the given velocity. Investigations indicates that small grains are generated at the end of the low current period. It is observed that large grains are then created during the rest of the low current period. One large grain is shown in figure 8.

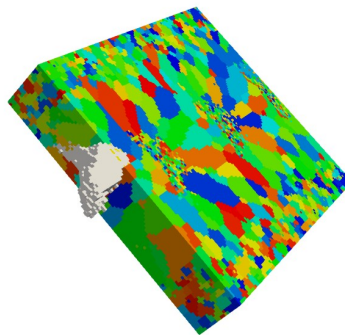


**Fig. 8** A large grain inside the microstructure

In figure 8, the grain is extracted from the lattice by looking at the change of spins. The grain shown in figure 8 is large. It starts to grow from the bottom side of the plate and then grows to the top. It seems that most of the grains are columnar when investigating their three dimensionnal shapes and not equiaxed as can be indicated by observation of the top side.



### CONCLUSION

The paper shows some comparison between experiments, process modelling and grain structure prediction. The base experiment is complex to model and lead to complex solidification conditions due to the squared current waveform. To predict the final grain structure in the bead, the most important is the weld pool border. Process simulation results with pulse mode show the complex evolution of the ellipsoid representing the weld pool border. The choice of implementing a sine function for radius is due to simplicity but more complex function can be implemented in order to have more precise evolution. The different model used in grain structure prediction (process and kMC simulation) are staggered and then uncoupled. This gives really fast computational time that to can be used for engineering purpose. Up to now, kMC does not take into account crystallographic orientation in the simulation. This orientation can be important to model some phenomena as hot cracking. Work in progress try to integrate crystallographic orientation in kMC simulation.

### REFERENCES

- [1] C.BORDREUIL, A.NIEL. 'Modelling of hot cracking in welding with a cellular automaton combined with an intergranular fluid flow model', *COMP.MAT.SCI*, vol. **82** p.442 – 450,2014.
- [2] S.CHEN, G. GUILLEMOT G., C-A GANDIN., '*Three-dimensional cellular automaton-finite element modeling of solidification grain structures for arc-welding processes*', *Acta Materialia*, 115, 448-467, 2016
- [3] T.M.RODGERS, J.A.MICHELL, V.TIKARE 'A Monte Carlo model for 3D grain evolution during welding', *Modelling and Simulation in Materials Science and Engineering*, Volume 25, Number 6 , 2017
- [4] S.PLIMPTON, A.THOMPSON AND A.SLEPOY, SPPARKS, 2016. <http://spparks.sandia.gov>.
- [5] A.CHIOCCA : PhD Thesis, Université de Montpellier, 2016
- [6] Z.YANG S.SISTA, J.W.ELMER, T.DEBROY, 'Three dimensional monte carlo simulation of grain growth during GTA welding of titanium', *Acta Materialia*, Vol 48, p4813-4825, 2000
- [7] K.ICHIKAWA, A.NOGAMI,T.KOSEKI Y.FUKUDA, "Modelling of solidification and grain growth in steel welds", p189-207, *Mathematical modelling in welding 5*, Graz 2001.

# MULTI-PASS FERRITIC STEEL WELD MODELLING: PHASE TRANSFORMATION AND RESIDUAL STRESS

Y.L. SUN\*, C.J. HAMELIN\*\*, T.F. FLINT\*, Q. XIONG\*,  
A.N. VASILEIOU\*, I. PANTELIS\*, J.A. FRANCIS\* and  
M.C. SMITH\*

*\*School of Mechanical, Aerospace and Civil Engineering, The University of Manchester, M13 9PL, Manchester, UK,  
yongle.sun@manchester.ac.uk (Y.L. Sun)*

*\*\*Australian Nuclear Science and Technology Organisation, NSW 2234, Lucas Heights, Australia; current affiliation: EDF  
Energy, Gloucester, GL4 3RS, UK*

DOI 10.3217/978-3-85125-615-4-10

## ABSTRACT

The solid state phase transformation (SSPT) occurring during welding thermal cycles gives rise to distinctive microstructures across the fusion zone and heat affected zone (HAZ), as well as significant effects on the residual stress generated in the weldment. We have developed a numerical model to simulate multi-pass welding in low alloy ferritic steel with consideration of SSPT. In this study, we applied a semi-empirical modelling approach to three-pass gas tungsten arc welding in a grooved plate made of SA508 steel (widely used in nuclear power plants). The microstructure, hardness and residual stress were predicted using a 2D finite element model and the predictions were compared with experimental results. We examined the sensitivity of the predicted hardness and stress to austenitisation kinetics and weld-metal plasticity. Two sets of empirical parameters were considered in the kinetic model of austenitisation to represent different levels of the heating-rate dependence of the critical temperatures (i.e.  $A_{c1}$  and  $A_{c3}$ ) for austenite formation. A rule-of-mixtures method based on dilution and hardness was proposed to estimate the plastic properties of weld metal for each pass, using the predicted phase fractions and the yield stress dataset for each transformation product of base material. The modelling results show that the extent of the inter-critical HAZ, hardness and residual stress are affected by the austenitisation kinetics. The use of weld-metal plastic properties estimated by the rule-of-mixtures method can improve the residual stress prediction for the weld metal.

Keywords: Arc welding, phase transformation, microstructure, hardness, residual stress, modelling

## INTRODUCTION

Weld-induced heterogeneous mechanical properties and residual stresses are two key factors affecting the performance and life of welded structures [1, 2]. Weld modelling has been playing an important role in the engineering design and structural integrity assessment of high-value and safety-critical weldments, such as those used in nuclear reactor pressure vessels [3, 4]. However, it is still challenging to accurately model multi-pass welding in

ferritic steel, which involves complicated metallurgical variation such as dilution, grain growth and solid state phase transformation (SSPT).

The impact of SSPT on weld residual stress has been confirmed in both experiments [5, 6] and modelling [7-9]. The effects of dilution, grain growth and inter-pass temperature on the microstructure and residual stresses in ferritic steel weldments have also been investigated experimentally and numerically [10-16]. Despite some key physics captured by the weld models, which are useful to establish qualitative understanding, the uncertainty in material parameters required by the models has been a serious issue when evaluating the prediction accuracy in a quantitative sense. In particular, the temperature- and microstructure-dependent properties of weld metal are notoriously difficult to measure, and consequently, estimation or approximation is usually needed to define the elastic-plastic model for weld metal. Ideally, the material properties for each phase (e.g. martensite, bainite or ferrite) of the weld metal should be individually determined by experimental tests. However, it is not feasible to produce samples for such tests. On one hand, the chemical compositions of the weld metals produced by different passes are normally different due to the chemical mismatch between the base and filler materials, as well as the dilution effect [10, 16, 17]. This implies that the weld-metal properties may differ from pass to pass, and a large matrix of tests is needed. On the other hand, tests must be performed on each phase of the unstressed weld metal to determine its evolutionary hardening behaviour for model definition purpose, rather than on the final hardened weld metal (potentially a mixture of different phases) present after the welding is complete. It is thus a daunting task to obtain material parameters for weld metal. Another issue causing uncertainty is the empirical parameters used in metallurgical models, such as the kinetic model of austenitisation that was proposed by Leblond and Devaux [18]. Dilatometry tests are a common method to experimentally determine the empirical parameters for phase transformation. However, in these tests, the temperature is strictly controlled to be uniform in the sample, while a steep temperature-gradient exists across the fusion zone (FZ) and heat affected zone (HAZ) of a weldment. Recent studies have demonstrated the effect of temperature gradient on metallurgical behaviour [19, 20]. Therefore, the metallurgical calibration tests may also need to take into account temperature gradient, which substantially increases the difficulty of experiment.

In this study, three-pass gas tungsten arc welding (GTAW) in a grooved SA508 steel plate is simulated using a thermal-metallurgical-mechanical finite element (FE) model. The sensitivity of the predictions for microstructure and residual stress to austenitisation kinetics and weld-metal plasticity is examined. We consider four analysis cases, i.e. two sets of empirical parameters are used in the kinetic model of austenitisation, and the plastic properties of each ferritic phase (e.g. martensite, bainite and ferrite) in the diluted weld metal for each pass are either assumed to be same as those for base material or estimated using a rule-of-mixtures method based on dilution and hardness.

MATERIALS AND METHODS

WELDING EXPERIMENT

A 200 × 150 × 20 mm plate made of a nuclear reactor pressure vessel steel, SA508 Gr.3 Cl.1, was used for the three-pass GTAW. The plate was grooved along the mid-width to a depth of 6 mm and at an angle of 45°, as shown in Fig. 1a and Fig. 1b. The welding parameters are given in Table 1. A SD3 filler wire with a diameter of 1.2 mm was used in weld bead deposition. Fig. 1c shows a transverse weld macrograph of the three-pass welded plate (half the weld is shown). To facilitate examination of the evolutionary metallurgical and mechanical response to welding, a single-pass plate was also produced using identical process parameters to the first pass of the three-pass weld. The chemical compositions of the base and filler materials are listed in Table 2, showing that the base material ( $C_{eq}=0.34$ ) has a much higher hardenability than the filler material ( $C_{eq}=0.17$ ).

**Table 1** Gas tungsten arc welding parameters [21]

Pass	Voltage [V]	Current [A]	Torch speed [mm/min]	Wire feed rate [mm/min]	Nominal heat input [kJ/mm]
1	11.0	227	75	1000	2.0
2	11.5	217	75	1000	2.0
3	11.5	217	75	1000	2.0

**Table 2** Chemical compositions (wt.%) of SA508 Gr.3 Cl.1 steel and SD3 filler metal [22]

	C	Si	Mn	Ni	Cr	Mo	V	Fe	$C_{eq}$
SA508 (base material)	0.2	0.25	1.4	0.8	0.2	0.5	0.003	Bal.	0.34
SD3 (filler material)	0.08	0.3	1.4	0.03	0.04	0.01	-	Bal.	0.17

Note: The Ito-Bessyo equation, i.e.  $C_{eq} = C + Si/30 + (Mn + Cu + Cr)/20 + Ni/60 + Mo/15 + V/10 + 5B$  [23], is used to calculate the carbon equivalent  $C_{eq}$ .

WELD MODELLING

*Thermal Model*

The general purpose FE software Abaqus was employed to simulate the multi-pass welding, along with a series of user-defined subroutines to capture the thermal, metallurgical and mechanical response. The geometry and mesh of the FE weld model is shown in Fig. 1d. A 2D simplification [24] was adopted and one half of the welded plate was considered to take advantage of the symmetry of the geometry and process. The geometric profiles of the weld beads for the first and third passes were determined from the macrographs of the single-

pass and three-pass welded plates, respectively. The geometric profile of the weld bead for the second pass was inferred to ensure that the volume of the bead for each pass is same, since identical torch speed and wire feed rate were employed for all three passes (Table 1). The bead deposition was simulated via an “element birth and death” approach (i.e. “model change” in Abaqus [25]).

The thermal model was based on a 2D heat source which is equivalent to a 3D ellipsoidal heat source. A specialised weld modelling tool, FEAT-WMT [26], was used to derive the 2D heat source such that the 2D model predicts a transient temperature field identical to that on the cross-section of the plate under steady welding conditions, as modelled in 3D using FEAT-WMT. The thermal model comprises 1088 quadratic, quadrilateral elements (Abaqus element designation: DC2D8). Convection and radiation on plate surfaces were considered to an environment at 20 °C. The material parameters were obtained from Ref. [7].

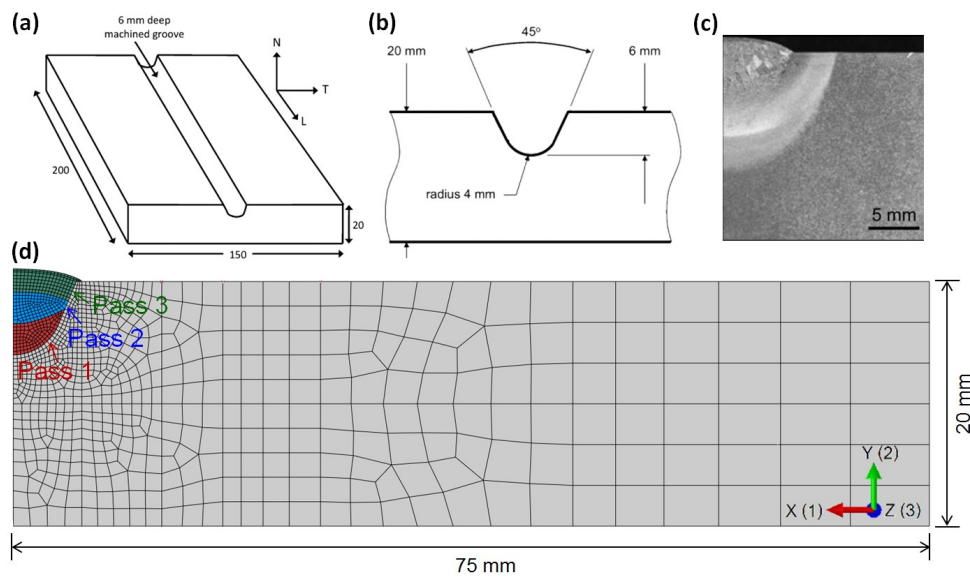


**Fig. 1** Three-pass SA508 steel weldment and finite element model (X, Y and Z directions correspond to transverse, normal and longitudinal directions, respectively): (a) dimensions of grooved plate [22]; (b) transverse sectional profile [22]; (c) macrograph on transverse section (half part) [21]; (d) geometry and mesh of 2D weld model (half part).

### *Metallurgical Model*

A semi-empirical approach was employed to model the reaction kinetics of austenite decomposition. The theoretical framework was initially established by Kirkaldy and Venugopalan [27] and later refined by Li et al. [28], based on which Hamelin et al. [7] have developed a weld model to predict the microstructure and residual stress in an autogenous edge-welded beam benchmark. The isothermal transformation for a ferritic phase is described by:

$$\tau(X, T) = \frac{F(C, Mn, Si, Ni, Cr, Mo, G)}{\Delta T^m \exp(-Q/RT)} S(X) \quad (1)$$

where  $\tau$  is the transformation time required to form a fraction  $X$  of a ferritic phase (e.g. ferrite, pearlite or bainite);  $F$  is a function of the weight percentages of C, Mn, Si, Ni, Cr and Mo, as well as the ASTM number  $G$  of the prior austenite grain size (PAGS), see Table 3;  $S(X)$  is a sigmoidal function;  $\Delta T$  is undercooling and  $m$  is an empirical exponent;  $Q$  is the activation energy;  $T$  is absolute temperature; and  $R$  is the universal gas constant. The values of material parameters are shown in Table 3. For anisothermal transformation occurring during welding, a series of isothermal events are discretised and an additivity rule [7] is used to capture the kinetics. Empirical equations in terms of chemical composition are used to estimate the transformation start temperatures for ferrite, pearlite and bainite, see Ref. [7] for more details.

**Table 3** Paramers [28] in the ferritic phase transformation model, i.e. Eq. (1)

Phase	$m$	$Q$ [cal/mol °C]	$F(C, Mn, Si, Ni, Cr, Mo, G)$
Ferrite	3	27500	$\exp(1.00+6.31C+1.78Mn+0.31Si+1.12Ni+2.70Cr+4.06Mo) / 2^{0.41G}$
Pearlite	3	27500	$\exp(-4.25+4.12C+4.36Mn+0.44Si+1.71Ni+3.33Cr+5.19\sqrt{Mo}) / 2^{0.32G}$
Bainite	2	27500	$\exp(-10.23+10.18C+0.85Mn+0.55Ni+0.90Cr+0.36Mo) / 2^{0.29G}$

The martensite transformation is modelled using the Koistinen-Marburger equation [29], i.e.

$$X_M = X_{RA} [1 - \exp(-A(M_s - T))] \quad (2)$$

where  $X_M$  is the fraction of martensite,  $X_{RA}$  is the fraction of remaining austenite for martensitic transformation and  $A$  is a material parameter. The martensite start temperature for full austenite is estimated using an empirical linear equation of chemical composition [30]. Furthermore, the martensite start temperature is assumed to decrease linearly with the fractions of pre-formed ferritic phases, if any exist, before martensitic transformation [31].

Austenitisation kinetics are modelled using the Leblond-Devaux [18] approach, and the rate of austenite formation is expressed as

$$\dot{x} = \frac{x_{eq} - x}{\tau_{LD}} \quad (3)$$

where  $x_{eq}$  is the equilibrium austenite fraction and  $\tau_{LD}$  is an empirical positive time constant. The parameter  $x_{eq}$  is assumed to increase from zero to one when temperature varies from 760 °C to 830 °C, which are the  $A_{c1}$  and  $A_{c3}$  temperatures, respectively, determined from dilatometry test data at low heating rates [31, 32]. Table 4 shows two cases of Leblond-Devaux model defined here, for which  $x_{eq}$  is taken to be same in both cases but the empirical parameter  $\tau_{LD}$  is varied to represent different heating-rate sensitivity of the predicted austenitisation kinetics. It should be mentioned that the characteristic temperature of 1020°C for Case B is the estimated grain-coarsening temperature of SA508 steel [10].

## Mathematical Modelling of Weld Phenomena 12

For the FZ produced by each pass, 100% austenite formation is assumed when temperature drops below the melting temperature ( $T_m=1450\text{ }^\circ\text{C}$  [7]).

**Table 4** Two sets of parameters to define the Leblond-Devauz model for austenitisation kinetics

Temperature [ $^\circ\text{C}$ ]	Case A		Temperature [ $^\circ\text{C}$ ]	Case B	
	$x_{eq}$	$\tau_{LD}$ (s)		$x_{eq}$	$\tau_{LD}$ (s)
<760	0	1	<760	0	2
760	0	1	760	0	2
830	1	0.2	830	1	1.8
>830	1	0.05	1020	1	1.5
			>1020	1	0.05

Note: Linear interpolation is used between tabulated parameters at different temperatures.

Fig. 2 shows the predicted continuous heating transformation diagram for two cases of the austenitisation kinetics model defined using Eq. (3). The difference in the predicted austenitisation temperature ranges between Case A and Case B is negligible when the heating rate is lower than  $1\text{ }^\circ\text{C/s}$ , but it becomes significant when the heating rate is higher than  $10\text{ }^\circ\text{C/s}$ . The Case B model is more sensitive to heating rate than the Case A model, and thus it is expected that more extensive partial austenitisation will occur in the welding simulation using the Case B model.

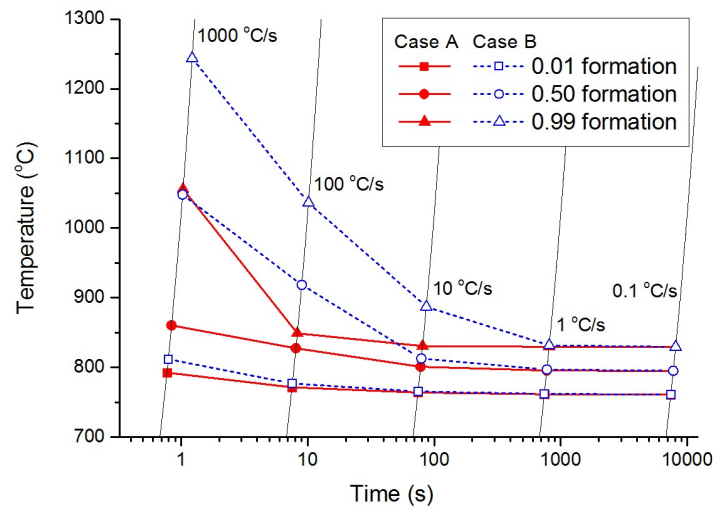


**Fig. 2** Continuous heating transformation diagram for austenitisation kinetics predicted by Eq. (3) considering two cases of model definition (Table 4).

Austenite grain growth is modelled using the following equation [32]:

$$\frac{dL}{dt} = A \exp\left(-\frac{Q_g}{RT}\right) \left(\frac{1}{L} - \frac{1}{L_{lim}}\right) \quad (4)$$

## Mathematical Modelling of Weld Phenomena 12

where  $L$  is grain size,  $t$  is time,  $Q_g$  is activation energy,  $T$  is absolute temperature,  $R$  is the universal gas constant and  $L_{lim}$  is the limit of grain size due to pinning effect of precipitates [32]. The  $1/L_{lim}$  term in Eq. (4) vanishes when the precipitates dissolve above the grain coarsening temperature of 1020 °C. For SA508 steel,  $Q_g = 190$  kJ/mol,  $L_{lim} = 3 + 0.58(T - A_{c3})$  in  $\mu\text{m}$ , and  $A$  is taken to be 4.2  $\mu\text{m}^2/\text{s}$  and 16.8  $\mu\text{m}^2/\text{s}$  for peak temperature below and above 1020 °C, respectively [16]. However, Eq. (4) is not applicable if peak temperature exceeds melting point during heating. In such a case, for simplicity, the PAGS is taken to be 0.4 mm, as an estimate in accordance with previous microscopic observations [22].

Empirical equations [33] are adopted to predict the Vickers micro-hardness of each ferritic phase, i.e.

$$Hv_M = 127 + 949C + 27Si + 11Mn + 8Ni + 16Cr + 21 \log(Vr) \quad (5)$$

$$Hv_B = -323 + 185C + 330Si + 153Mn + 65Ni + 144Cr + 191Mo + (89 + 53C - 55Si - 22Mn - 10Ni - 20Cr - 33Mo) \log(Vr) \quad (6)$$

$$Hv_{F/P} = 42 + 223C + 53Si + 30Mn + 12.6Ni + 7Cr + 19Mo + (10 - 19Si + 4Ni + 8Cr + 130V) \log(Vr) \quad (7)$$

for martensite, bainite and ferrite/pearlite, respectively; where the element symbol denotes the weight percentage of the chemical element and  $Vr$  (in °C/h) is the cooling rate at 700 °C.

The hardness of the mixture of different micro-constituents is calculated using a rule-of-mixtures as follows

$$Hv = Hv_M X_M + Hv_B X_B + Hv_{F/P} (X_F + X_P) + Hv_A X_A + Hv_{b0} X_{b0} \quad (8)$$

where  $X_M$ ,  $X_B$ ,  $X_F$ ,  $X_P$ ,  $X_A$  and  $X_{b0}$  are the fractions of martensite, bainite, ferrite, pearlite, austenite and base material, respectively. According to previous work [7, 10], we have  $Hv_{b0} = 200$  and  $Hv_A = 160$ . The hardness of martensite, bainite and ferrite/pearlite is predicted by Eqs. (5), (6) and (7), respectively.

As the SSPT kinetics model and hardness prediction are primarily dependent on chemical composition, see Eqs. (1) and (5)-(7), it is necessary to take account of the chemical heterogeneity within the weldment. For weld metal, the content of each chemical element is calculated using a dilution-based rule-of-mixtures, i.e.

$$p_n = p_b D_n + p_f (1 - D_n) \quad (9)$$

where  $p_n$  is the content of the element for pass  $n$ ;  $p_b$  and  $p_f$  are the contents of the element in the base and filler materials (Table 2), respectively; and  $D_n$  is the dilution for pass  $n$ . The dilution has been determined to be 0.44, 0.17 and 0.09 for the first, second and third passes, respectively [10].



### *Mechanical Model*

The thermo-metallurgical deformation upon thermal cycling acts as the major driving force to generate stresses in the weldment. The total strain can be decomposed as follows

$$\varepsilon = \varepsilon_e + \varepsilon_p + \varepsilon_{th} + \varepsilon_{tr} + \varepsilon_{tp} \quad (10)$$

where  $\varepsilon_e$ ,  $\varepsilon_p$ ,  $\varepsilon_{th}$ ,  $\varepsilon_{tr}$  and  $\varepsilon_{tp}$  are the elastic strain, plastic strain, thermal strain, metallurgical strain and transformation-induced plastic strain, respectively. On the right-hand side of Eq. (10), the third and fourth strain components are determined by the changes in temperature and phase, respectively. By contrast, the first two strain components are generated in conjunction with thermal-metallurgical deformation to satisfy the compatibility condition (i.e. internal constraint) implied in the continuum assumption, as well as the external constraint imposed, if any exists. The fifth strain component only arises in the presence of both SSPT and deviatoric stress.

In this study, the thermal strain and metallurgical strain were defined according to previous dilatometry test data on SA508 steel [7]. The dilation curve was decoupled between ferritic and austenitic phases, and a rule-of-mixtures was employed to estimate the individual contribution from the ferritic and austenitic phases. The transformation-induced plastic strain is calculated using the following constitutive equation [34]

$$\dot{\varepsilon}_{ij}^{tp} = \frac{3}{2} K s_{ij} f'(z) \dot{z} \quad (11)$$

where  $\dot{z}$  is the rate of phase transformation,  $f'(z)$  is a normalised function,  $s_{ij}$  is the deviatoric stress, and  $K$  is a material constant. For SA508 steel, we assume that  $f(z) = z(2-z)$  and  $K = 10^{-4} \text{ MPa}^{-1}$  [34].

The FE mesh of the mechanical model is same as that of the thermal model, except that quadratic, quadrilateral, generalised plane strain and hybrid elements (Abaqus designation: CPEG8H) were used in the mechanical model. The bottom corner node on the symmetry plane was fully fixed, while only displacement constraint in the X direction (i.e.  $U1 = 0$ ) was imposed on the whole symmetry plane.

The elasto-plastic properties are dependent on both temperature and microstructure, and the material parameters reported in Ref. [7] were adopted for base material and its transformation products. No plastic property dataset is available for the filler material, so a scaling method is developed to make an approximation. Since yield strength is generally proportional to hardness [35], the yield stress for each ferritic phase of the filler material can be estimated using the filler-to-base ratio of calculated hardness and the plastic property dataset for each ferritic phase of the base material. Table 5 shows the calculated hardness using Eqs. (5)-(7) and the corresponding hardness ratio (i.e. scaling ratio).

**Table 5** Vickers hardness for each ferritic phase of base/filler material

	Martensite	Bainite	Ferrite/pearlite
Base material	453.3	319.4	214.9
Filler material	332.0	236.6	142.2
Filler-to-base ratio	0.73	0.74	0.66

Note: Hardness is calculated using Eqs. (5)-(7) wherein cooling rate is taken to be 27 °C/s according to the thermal modelling result [10].

For weld metal corresponding to each pass, a dilution-based rule-of-mixtures method was employed to estimate the contribution from both base and filler materials to the plastic behaviour of the weld metal, as illustrated in Fig. 3. Table 6 shows the different modelling scenarios considered in the mechanical analysis, with regard to different definitions of austenitisation kinetics and plastic property.

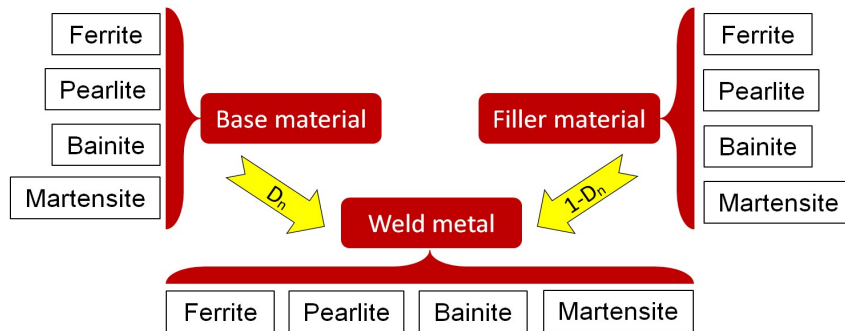


**Fig. 3** Illustration of the dilution-based rule-of-mixtures estimation of plastic properties of weld-metal.

**Table 6** Modelling Scenarios for mechanical analysis

Model No.	Austenitisation case	Yield stress scaling
1	A	No
2	B	No
3	A	Yes
4	B	Yes

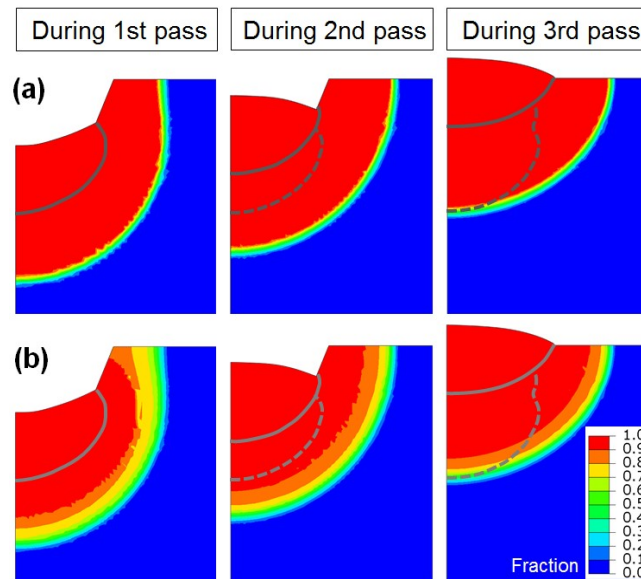
## RESULTS AND DISCUSSION

### MICROSTRUCTURE AND HARDNESS

Our previous study [10] has shown a good accuracy of the temperature prediction by the weld model, as verified by thermocouple data and FZ/HAZ observations. Here, particular attention is paid to the heating during which austenitisation occurs. Heating rates were calculated at 700 °C for material points experiencing peak temperatures higher than 700 °C, and the averaged heating rates are 169±56 °C/s, 146±53 °C/s and 122±42 °C/s for the

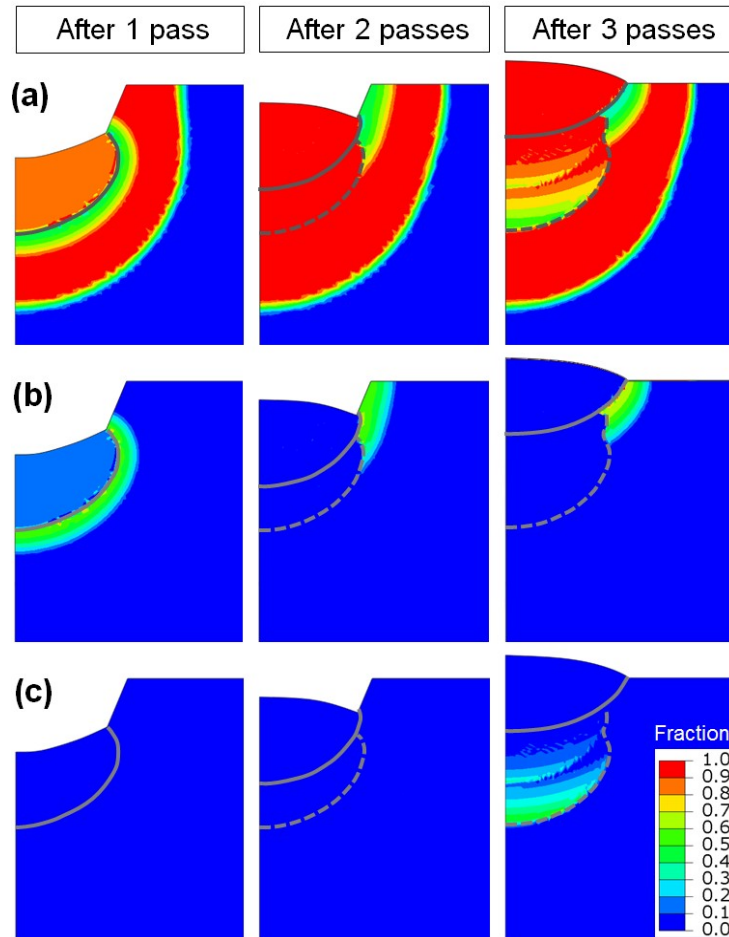
first, second and third passes, respectively, based on the thermal solution of the weld model. According to Fig. 2, the difference in the predicted austenitisation kinetics between Case A and Case B (Table 4) is significant for the heating rates larger than 100 °C/s, which is similar to those involved in the simulated welding. Therefore, unsurprisingly, a much wider inter-critical HAZ (ICHAZ, i.e. partially austenitised zone) is predicted in Case B, as shown in Fig. 4. This is because the empirical time constant, i.e.  $\tau_{LD}$ , adopted in Case B is larger than that in Case A, and the  $\tau_{LD}$  dictates the retardation effect during austenitisation.

Fig. 5 and Fig. 6 show the predicted fractions of different ferritic phases (i.e. bainite, martensite and ferrite) for austenitisation Case A and Case B, respectively. For base material HAZ, a mixture of bainite and martensite is formed in the coarse-grained HAZ (CGHAZ, adjacent to FZ boundary), while bainite is dominant in the fine-grained HAZ (FGHAZ, relatively far from FZ boundary). For as-deposited weld metal, the fraction of martensite is considerable after first pass, but it became minor when more passes were deposited; in the reheated weld metal (i.e. HAZ formed in previous FZ), bainite is the major constituent predicted and some ferrite is also present. It is noted that, different microstructures are predicted in the weld metal and the base material, particularly for the CGHAZ, although similar temperature histories are involved. The difference is due to the chemical heterogeneity as controlled by the dilution for each pass, see Eq. (9), given the chemical mismatch between the base and filler materials (Table 2). These predicted microstructures are overall consistent with microscopic observations in experiment, except that acicular ferrite was present in the actual weld metal but it has not been explicitly considered (i.e. acicular ferrite is treated being equivalent to bainite) in the weld model; more discussion about this issue can be found in our previous work [10].



**Fig. 4** Predicted distributions of maximum fractions of austenite formed during each pass: (a) austenitisation Case A; (b) austenitisation Case B. Note that the solid and dashed grey lines indicate the current and accumulated fusion boundaries, respectively.

Here, we focus on the effect of austenitisation kinetics on the final microstructure. The effect is pronounced for bainite (Figs. 5a and 6a) and discernible for ferrite (Figs. 5c and 6c), but negligible for martensite (Figs. 5b and 6b). This is because the difference in austenitisation kinetics mainly affects the ICHAZ which is adjacent to the FGHAZ where bainite is dominant, ferrite is present (only in reheated weld metal) but martensite is absent. In other words, in the ICHAZ, the base material or the preceding transformation products persist, and hence the fraction of newly transformed phase (mainly bainite) is limited. In the austenitisation Case B, a more extensive ICHAZ develops (Fig. 4), and consequently, markedly less bainite and slightly less ferrite are formed, in comparison with the austenitisation Case A, as shown in Figs. 5 and 6.



**Fig. 5** Predicted distributions of ferritic phase fractions (austenitisation Case A) after different number of passes: (a) bainite; (b) martensite; (c) ferrite. Note that the solid and dashed grey lines indicate the current and accumulated fusion boundaries, respectively.

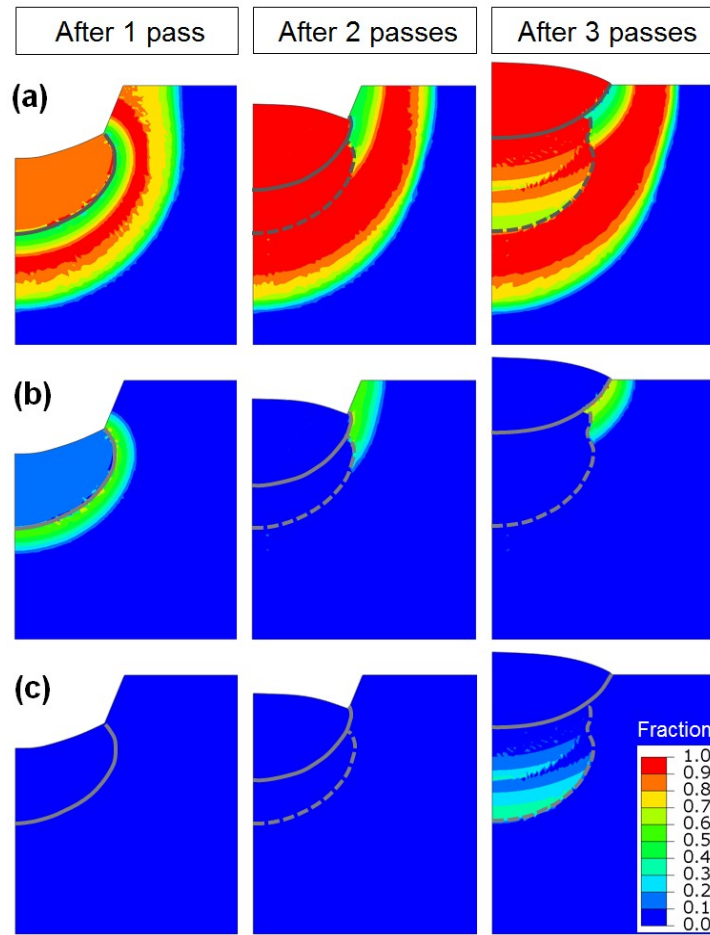


**Fig. 6** Predicted distributions of ferritic phase fractions (austenitisation Case B) after different number of passes: (a) bainite; (b) martensite; (c) ferrite. Note that the solid and dashed grey lines indicate the current and accumulated fusion boundaries, respectively.

Fig. 7 shows the comparison between the predicted and measured hardness distributions. It is evident that a better agreement is achieved in the austenitisation Case B. The narrower ICHAZ (consequently, wider FGHAZ) formed in the austenitisation Case A leads to a significant overestimate of hardness close to the base material, in contrast to the lower hardness found in the wider ICHAZ formed in the austenitisation Case B. Similar results were also obtained by Hamelin et al. [36]. For both Case A and Case B, the hardness in the reheated weld metal is underestimated (Fig. 7c), due to a considerable fraction of ferrite predicted therein (Figs. 5c and 6c). This may indicate an overestimate of ferrite in the reheated weld metal. It is also noted that Case B assumption somewhat reduces the underestimation of hardness in the reheated weld metal (Fig. 7c), implying that more significant retardation of austenitisation may also occur in the weld metal. As re-austenitisation and grain growth in columnar-grained weld metal is complicated, a more sophisticated model may be needed to capture the exact metallurgical behaviour, opening a direction for future work.

## Mathematical Modelling of Weld Phenomena 12

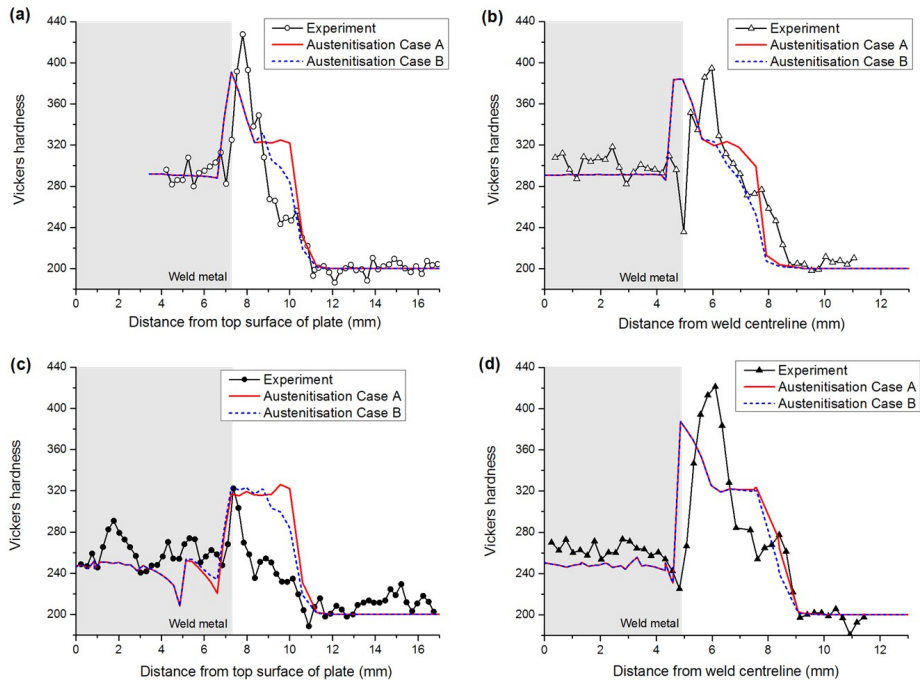


**Fig. 7** Predicted and measured hardness distributions: (a) through-thickness distribution after one pass; (b) transverse distribution after one pass; (c) through-thickness distribution after three passes; (d) transverse distribution after three passes. The hardness measurement results are taken from the Ref. [22]. Note that the transvers distributions are examined at depths of 4.5 mm and 2.0 mm to the top surface after one pass and three passes, respectively.

### RESIDUAL STRESS

Fig. 8 compares the predicted and measured residual stress distributions through thickness, as well as the predictions between different modelling scenarios. Good agreement is achieved for transverse stress after one pass, while for other cases the predictions are less accurate and only have a qualitative agreement. It is believed that the inaccuracy is mainly caused by the longitudinal over-constraint under generalised plane strain assumption and the uncertainty in weld-metal material properties adopted in the mechanical model, which have more significant effects when more weld beads are deposited. In addition, experimental observations show a significant presence of acicular ferrite in the weld metal [22], which has not been explicitly considered in the current metallurgical model, hence limiting the accuracy of the predicted SSPT kinetics.

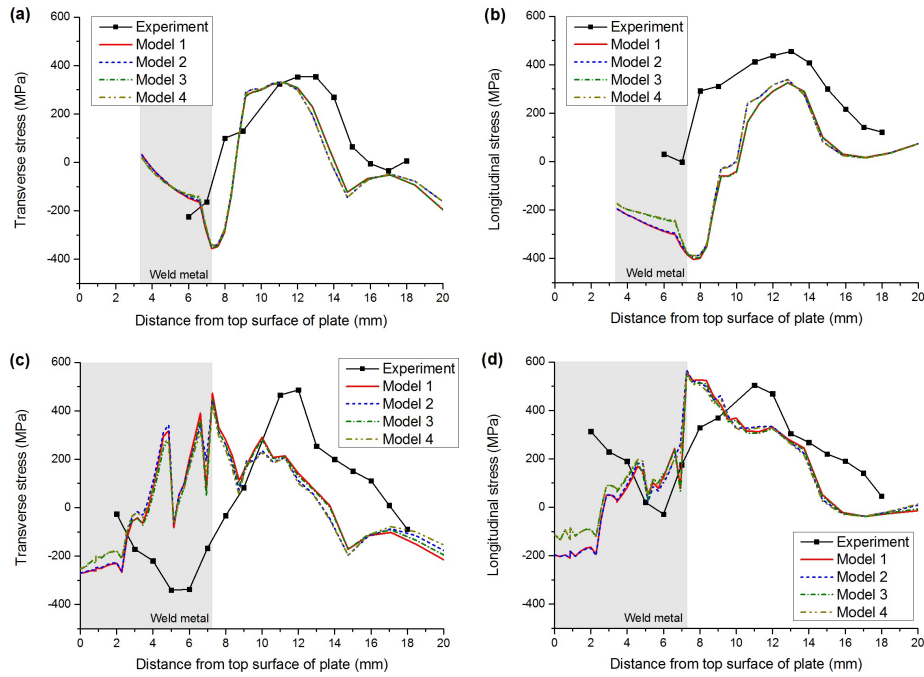


**Fig. 8** Predicted and measured through-thickness distributions of residual stresses: (a) transverse stress after one pass; (b) longitudinal stress after one pass; (c) transverse stress after three passes; (d) longitudinal stress after three passes. The neutron diffraction stress measurement results are taken from Ref. [22]. The different modelling scenarios are described in Table 6.

The difference between the four modelling scenarios (Table 6) is more pronounced for longitudinal stresses than for transverse stresses. The different austenitisation kinetics (i.e. Case A and Case B) primarily affect the stress level in the ICHAZ and the adjacent base material. The prediction of stresses in the weld metal has been slightly improved in modelling scenarios 3 and 4 wherein the rule-of-mixtures method based on pass-by-pass dilution is used to estimate the distinctive yield stress in the weld metal.

Fig. 9 and Fig. 10 show the contours of longitudinal and transverse stresses, respectively, after three passes. The results further confirm that the different cases of austenitisation kinetics model (Table 4) have discernible but overall insignificant effect on the residual stresses. By contrast, the effect of weld-metal yield stress is more considerable, particularly in the FZ produced by the third pass. The plastic properties of the weld metal are expected to be more complicated than that approximated using simple rule-of-mixtures, and thus more significant difference in residual stress prediction may be expected if more accurate plastic constitutive parameters are used.

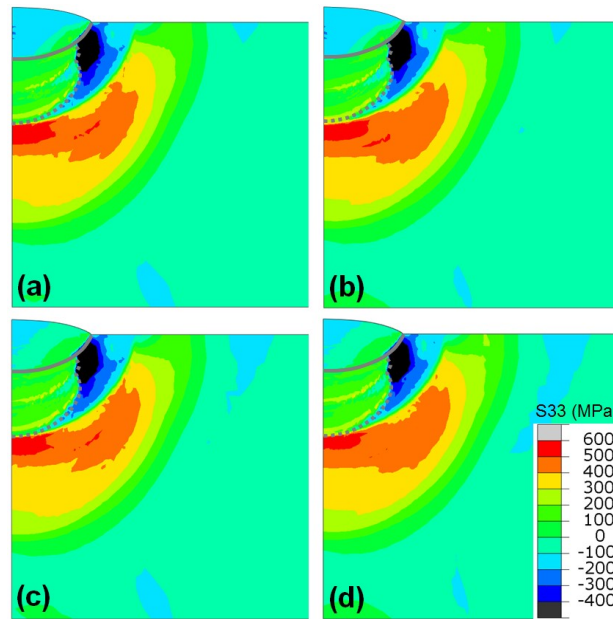


**Fig. 9** Predicted distributions of longitudinal stress after three passes: (a) Model 1; (b) Model 2; (c) Model 3; (d) Model 4.

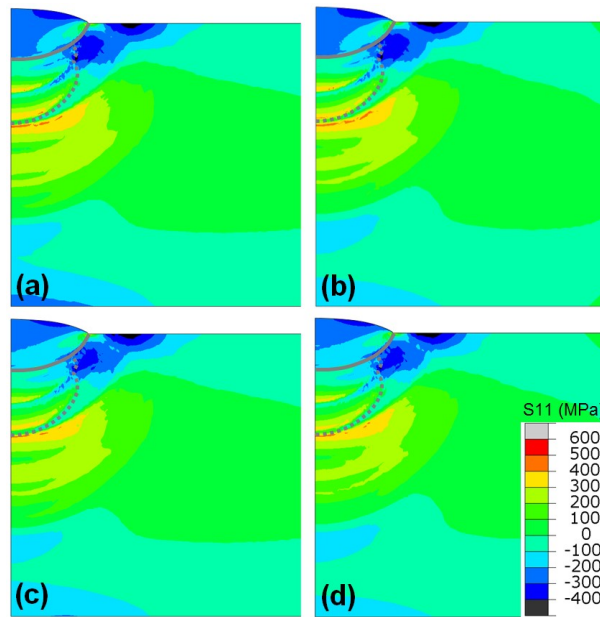


**Fig. 10** Predicted distributions of transverse stress after three passes: (a) Model 1; (b) Model 2; (c) Model 3; (d) Model 4.



### CONCLUSIONS

Three-pass gas tungsten arc welding in a grooved plate made of a low alloy ferritic steel (SA508 Gr.3 Cl.1) has been modelled with consideration of solid state phase transformation. The analysis focused on the sensitivity of the predicted microstructure, hardness and residual stress to the empirical parameter in the austenitisation kinetics model and the assumed yield stress of the weld metal. Four modelling scenarios have been examined (Tables 4 and 6). The numerical predictions were also compared with experimental measurements.

The modelling results show that a stronger heating-rate dependence of  $A_{c1}$  and  $A_{c3}$  temperatures leads to a wider ICHAZ; and consequently, in the ICHAZ, the austenitisation kinetics markedly affects the microstructure and hardness, while only slightly affects the residual stress. The approximation of weld-metal plastic properties using dilution-based rule-of-mixtures method can improve the residuals stress prediction for the weld metal, but the accuracy is still limited due to other issues (e.g. 2D simplification and acicular ferrite transformation). Future work will be devoted to more accurate material properties and SSPT kinetics for weld metal in a 3D model.

### ACKNOWLEDGEMENTS

The authors gratefully acknowledge the funding support from EPSRC grant EP/J021172/1, for the development and characterisation of welds under the NNUMAN programme. The assistance given by the IT Services and the use of the Computational Shared Facility at the University of Manchester are also acknowledged.

### REFERENCES

- [1] S. KOU. *Welding metallurgy*, John Wiley & Sons, New Jersey, 2003.
- [2] J.A. Goldak, M. Akhlaghi. *Computational welding mechanics*, Springer Science & Business Media, 2006.
- [3] J.A. FRANCIS, H.K.D.H. BHADOSHIA, P.J. WITHERS. Welding residual stresses in ferritic power plant steels, *Materials Science and Technology* 23 (2007) 1009-1020.
- [4] Y. RONG, J. XU, Y. HUANG, G. ZHANG. Review on finite element analysis of welding deformation and residual stress, *Science and Technology of Welding and Joining* 23 (2018) 1-11.
- [5] J.A. FRANCIS, H.J. STONE, S. KUNDU, H.K.D.H. BHADOSHIA, R.B. ROGGE, P.J. WITHERS, L. KARLSSON. The Effects of Filler Metal Transformation Temperature on Residual Stresses in a High Strength Steel Weld, *Journal of Pressure Vessel Technology* 131 (2009) 041401-041408.
- [6] S.W. OOI, J.E. GARNHAM, T.I. RAMJAUN. Review: Low transformation temperature weld filler for tensile residual stress reduction, *Materials & Design* 56 (2014) 773-781.
- [7] C.J. HAMELIN, O. MURÁNSKY, M.C. SMITH, T.M. HOLDEN, V. LUZIN, P.J. BENDEICH, L. EDWARDS. Validation of a numerical model used to predict phase distribution and residual stress in ferritic steel weldments, *Acta Materialia* 75 (2014) 1-19.
- [8] A.N. VASILEIOU, M.C. SMITH, J. BALAKRISHNAN, J.A. FRANCIS, C.J. HAMELIN. The impact of transformation plasticity on the electron beam welding of thick-section ferritic steel components, *Nuclear Engineering and Design* 323 (2017) 309-316.

- [9] D. DENG, H. MURAKAWA. Prediction of welding residual stress in multi-pass butt-welded modified 9Cr–1Mo steel pipe considering phase transformation effects, *Computational Materials Science* 37 (2006) 209-219.
- [10] Y. SUN, C.J. HAMELIN, M.C. SMITH, A.N. VASILEIOU, T.F. FLINT, J.A. FRANCIS. Modelling of dilution effects on microstructure and residual stress in a multi-pass weldment. ASME 2018 Pressure Vessels and Piping Conference. Prague, Czech Republic: American Society of Mechanical Engineers, 2018.
- [11] T. RAMJAUN, H. STONE, L. KARLSSON, J. KELLEHER, S. OOI, K. DALAEI, J. REBELO KORNMEIER, H. BHADESHIA. Effects of dilution and baseplate strength on stress distributions in multipass welds deposited using low transformation temperature filler alloys, *Science and Technology of Welding and Joining* 19 (2014) 461-467.
- [12] T. RAMJAUN, H. STONE, L. KARLSSON, J. KELLEHER, R. MOAT, J.R. KORNMEIER, K. DALAEI, H. BHADESHIA. Effect of interpass temperature on residual stresses in multipass welds produced using low transformation temperature filler alloy, *Science and Technology of Welding and Joining* 19 (2014) 44-51.
- [13] H. DAI, R. MOAT, P. WITHERS. Modelling the interpass temperature effect on residual stress in low transformation temperature stainless steel welds. ASME 2011 Pressure Vessels and Piping Conference: American Society of Mechanical Engineers, 2011. p.1451-1458.
- [14] Y. SUN, C.J. HAMELIN, M.C. SMITH, L. EDWARDS. Predicting an optimal inter-pass temperature to mitigate residual stress and distortion in ferritic steel weldments. ASME Pressure Vessels and Piping Conference. Vancouver, Canada, 2016.
- [15] C.J. HAMELIN, O. MURÁNSKY, L. EDWARDS. The Influence of Austenite Grain Size during Welding Simulations of Ferritic Steels, *Advanced Materials Research* 996 (2014).
- [16] Y.L. SUN, G. OBASI, C.J. HAMELIN, A.N. VASILEIOU, T.F. FLINT, J. BALAKRISHNAN, M.C. SMITH, J.A. FRANCIS. Effects of dilution on alloy content and microstructure in multi-pass steel welds, *Journal of Materials Processing Technology* 265 (2019) 71-86.
- [17] J.N. DUPONT, A.R. MARDER. Dilution in single pass arc welds, *Metallurgical and Materials Transactions B* 27 (1996) 481-489.
- [18] J.B. LEBLOND, J. DEVAUX. A new kinetic model for anisothermal metallurgical transformations in steels including effect of austenite grain size, *Acta Metallurgica* 32 (1984) 137-146.
- [19] T.F. FLINT, C. PANWISAWAS, Y. SOVANI, M.C. SMITH, H.C. BASOALTO. Prediction of grain structure evolution during rapid solidification of high energy density beam induced re-melting, *Materials & Design* 147 (2018) 200-210.
- [20] S. CHAKRABORTY, P. KUMAR, A. CHOUDHURY. Phase-field modeling of grain-boundary grooving and migration under electric current and thermal gradient, *Acta Materialia* 153 (2018) 377-390.
- [21] B.M. PELLEREAU, C.M. GILL, M. DAWSON, P.R. HURRELL, J. FRANCIS, A. MARK. Finite element modelling and measurements of residual stress and phase composition in ferritic welds. ASME 2010 Pressure Vessels and Piping Division/K-PVP Conference: American Society of Mechanical Engineers, 2010. p.1385-1392.
- [22] A. MARK, J. FRANCIS, H. DAI, M. TURSKEI, P. HURRELL, S. BATE, J. KORNMEIER, P. WITHERS. On the evolution of local material properties and residual stress in a three-pass SA508 steel weld, *Acta Materialia* 60 (2012) 3268-3278.
- [23] Ş. TALAŞ. The assessment of carbon equivalent formulas in predicting the properties of steel weld metals, *Materials & Design* 31 (2010) 2649-2653.
- [24] S. SARKANI, V. TRITCHKOV, G. MICHAELOV. An efficient approach for computing residual stresses in welded joints, *Finite Elements in Analysis and Design* 35 (2000) 247-268.
- [25] Dassault Systèmes, ABAQUS Analysis User's Manual, (v6.13 Documentation).
- [26] R. SMITH. FEAT-WMT: Weld-modelling tool user guide, FEATWMT: weld-modelling tool user guide: FeatPlus Limited (2010).
- [27] J. KIRKALDY, D. VENUGOPALAN. Prediction of microstructure and hardenability in low-alloy steels, *Phase Transformations in ferrous alloys* (1983) 125-148.
- [28] M.V. LI, D.V. NIEBUHR, L.L. MEEKISHO, D.G. ATTERIDGE. A computational model for the prediction of steel hardenability, *Metallurgical and Materials transactions B* 29 (1998) 661-672.

- [29] D.P. KOISTINEN, R.E. MARBURGER. A general equation prescribing the extent of the austenite-martensite transformation in pure iron-carbon alloys and plain carbon steels, *Acta Metallurgica* 7 (1959) 59-60.
- [30] C. KUNG, J. RAYMENT. An examination of the validity of existing empirical formulae for the calculation of Ms temperature, *Metallurgical Transactions A* 13 (1982) 328-331.
- [31] N. O'MEARA, H. ABDOLVAND, J.A. FRANCIS, S.D. SMITH, P.J. WITHERS. Quantifying the metallurgical response of a nuclear steel to welding thermal cycles, *Materials Science and Technology* (2016) 1-16.
- [32] H. POUS-ROMERO, I. LONARDELLI, D. COGSWELL, H.K.D.H. BHADESHIA. Austenite grain growth in a nuclear pressure vessel steel, *Materials Science and Engineering: A* 567 (2013) 72-79.
- [33] P. MAYNIER, J. DOLLET, P. BASTIEN. Creusot-Loire system for the prediction of the mechanical properties of low alloy steel products. in: Doane DV, Kirkaldy JS, (Eds.). *Hardenability concepts with applications to steels*. The Metallurgical Society of AIME, Warrendale, Pennsylvania, 1978. pp. 518-545.
- [34] J.-B. LEBLOND, G. MOTTET, J. DEVAUX, J.-C. DEVAUX. Mathematical models of anisothermal phase transformations in steels, and predicted plastic behaviour, *Materials science and technology* 1 (1985) 815-822.
- [35] E.J. PAVLINA, C.J. VAN TYNE. Correlation of Yield Strength and Tensile Strength with Hardness for Steels, *Journal of Materials Engineering and Performance* 17 (2008) 888-893.
- [36] C.J. HAMELIN, O. MURÁNSKY, P. BENDEICH, K. SHORT, L. EDWARDS. Predicting solid-state phase transformations during welding of ferritic steels. *Materials Science Forum*, vol. 706: Trans Tech Publ, 2012. p.1403-1408.

# NUMERICAL MODELLING OF WELDING OF MARTENSITIC STEEL

B. SMOLJAN\*, D. ILJKIĆ\*\*, S. SMOKVINA HANZA\*\*, L. ŠTIC\*\*  
and M. JOKIĆ\*

*\*Polytechnic of Pula, College of applied sciences, Riva 6, 52100 Pula, Croatia, bsmoljan@politehnika-pula.hr,  
mjokic@politehnika-pula.hr*

*\*\*University of Rijeka - Faculty of Engineering, Department of Materials Science and Engineering, Vukovarska 58, 51000  
Rijeka, Croatia, darioi@riteh.hr, suncana@riteh.hr, lstic@riteh.hr*

DOI 10.3217/978-3-85125-615-4-11

## ABSTRACT

The mathematical model and computer simulation for prediction of mechanical properties and microstructure composition of steel welded joint was developed. Because of wide range of applicability and ease of use of finite volume method (FVM), this numerical method was suitable to create integrated computer program for simulation of transient temperature field, microstructure transformation and mechanical properties during welding of steel.

The computer simulation of mechanical properties and microstructure of welded joint is consisted of numerical calculation of transient temperature field in process of cooling, and of numerical calculation of hardness. The computer simulation of hardness of welded joint is based on both, CCT diagrams and the thermo-kinetic expressions using linear alignment with the actual chemical composition. Microstructure and hardness of welded joint has been predicted based on calculated characteristic time of cooling from 800 °C to 500 °C, ( $t_{8/5}$ ). Results of steel welding were estimated by taking into account the process of reheating of workpiece during the welding. The established procedure was applied in computer simulation of martensitic steel welded joint.

Keywords: Mathematical modelling, computer simulation, welded joint, hardness distribution, microstructure composition

## INTRODUCTION

Computer simulation of the welding can be done by considering the issues such as achievement of tolerable defects, desired mechanical properties distribution and required microstructure distribution. Many very useful software exist for the calculation of grain structure, porosity, hot tearing, and solid-state transformation. But, there are still questions on which answers should be given to satisfy all industry needs in mathematical modelling and simulation of welding [1, 2].

During the welding, many different physical processes, such as, melting, solidification, solid state phase transformation, evolution of microstructure, diffusion, heat conduction, and mechanical stressing and distortion are at once taking place inside metal [3-7]. Simulations of microstructural transformations can be based on the both, CCT diagrams and thermo-kinetic expressions. The first approach is more consistent, but the second approach gives good results using the real chemical composition of the steel.

The input of the simulation is composed of the following categories: geometry, physical characteristics of the steel and, kinematic boundary conditions and thermal boundary conditions. It is necessary to establish the appropriate algorithm which describes heating and cooling processes and to involve appropriate input data in the model. Inverse heat transfer problems should be solved to determine thermal properties for welding material and filler material based on experimentally evaluated results [8].

Proposed numerical model of welding in this work is based on finite volume method (FVM). The finite volume method (FVM) has been established as a very efficient way of solving fluid flow and heat transfer problems. The key feature of the FVM approach is that the FVM is based on flux integration over the control volume surfaces. The method is implemented in a manner that ensures local flux conservation, regardless of the grid structure [9]. FVM is used as a simple and effective tool for the solution of a large range of problems in the analysis of welding processes [10-12].

### COMPUTER MODELLING OF THERMAL PROCESSES

Numerical simulation of welding gives consideration to both, the melting and solidification processes.

Mathematical formulation of process of welding, i.e., melting, solidification and cooling is based on the following system of differential equations [4, 5, 13]:

- the Navier-Stokes equations

$$\begin{aligned} \mu \left( \frac{\partial^2 v_r}{\partial r^2} + \frac{1}{r} \frac{\partial v_r}{\partial r} + \frac{\partial^2 v_r}{\partial z^2} - \frac{v_r}{r^2} \right) - \frac{\partial p}{\partial r} + \rho g_r \beta (T - T_\infty) &= \rho \frac{dv_r}{dt} \\ \mu \left( \frac{\partial^2 v_z}{\partial r^2} + \frac{1}{r} \frac{\partial v_z}{\partial r} + \frac{\partial^2 v_z}{\partial z^2} \right) - \frac{\partial p}{\partial z} + \rho g_z \beta (T - T_\infty) &= \rho \frac{dv_z}{dt} \end{aligned} \quad (1)$$

- the continuity equation

$$\frac{\partial v_r}{\partial r} + \frac{v_r}{r} + \frac{\partial v_z}{\partial z} = 0 \quad (2)$$

- the Fourier's heat conduction equation including the convection term

$$\frac{\lambda}{r} \frac{\partial T}{\partial r} + \frac{\partial}{\partial r} \left( \lambda \frac{\partial T}{\partial r} \right) + \frac{\partial}{\partial z} \left( \lambda \frac{\partial T}{\partial z} \right) = \rho c_{ef} \left( \frac{\partial T}{\partial t} + v_r \frac{\partial T}{\partial r} + v_z \frac{\partial T}{\partial z} \right) \quad (3)$$

Characteristic boundary condition for the top face is:

$$-\lambda \frac{\delta T}{\delta n} \Big|_s = \alpha_{ef} (T_s - T_a) + q_{source} \quad (4)$$

and for the other faces

$$-\lambda \frac{\delta T}{\delta n} \Big|_s = \alpha(T_s - T_a) \quad (5)$$

where  $T_s/K$  is surface temperature,  $T_a/K$  is air temperature,  $q_s/Wm^{-3}$  is volumetric density of heat source,  $\alpha/Wm^{-2}K^{-1}$  is heat transfer coefficient of air,  $\alpha_{ef}/Wm^{-2}K^{-1}$  is effective heat transfer coefficient by which convection and radiation are taken into account and  $q_{source}/Wm^{-2}$  is arc source heat flux.

where  $T/K$  is the temperature,  $t/s$  is the time,  $\rho = \rho(T)/kgm^{-3}$  is the density,  $\lambda/Wm^{-1}K^{-1}$  is the thermal conductivity coefficient,  $T_s/K$  is surface temperature,  $T_a/K$  is air temperature,  $\alpha/Wm^{-2}K^{-1}$  is heat transfer coefficient,  $v_r, v_z/ms^{-1}$  are the  $r$ - and  $z$ -component of velocity, respectively,  $\mu(T)/Nsm^{-2}$  is dynamical viscosity coefficient,  $c_{ef} = c + L/(T_\beta - T_a)/Jkg^{-1}K^{-1}$  is the effective specific heat of a mushy zone,  $L/Jkg^{-1}$  is the latent heat of solidification,  $c/Jkg^{-1}K^{-1}$  is the specific heat,  $p/Nm^{-2}$  is the pressure,  $g_r, g_z/ms^{-2}$  are the  $r$ - and  $z$ -component of gravitational acceleration, respectively,  $\beta/K^{-1}$  is the volume coefficient of thermal expansion,  $r, z/m$  are the coordinates of the vector of the considered node's position,  $T_\infty/K$  is the reference temperature  $T_\infty = T_{in}$ ,  $r/m$  is the radius.

In this model it was presumed that convection term has no relevant role and that liquid metal flow could be neglected after melting.

Quantity of growth of solidified part of welded joint was predicted by calculation of solidification rate in control volume (Fig. 1).

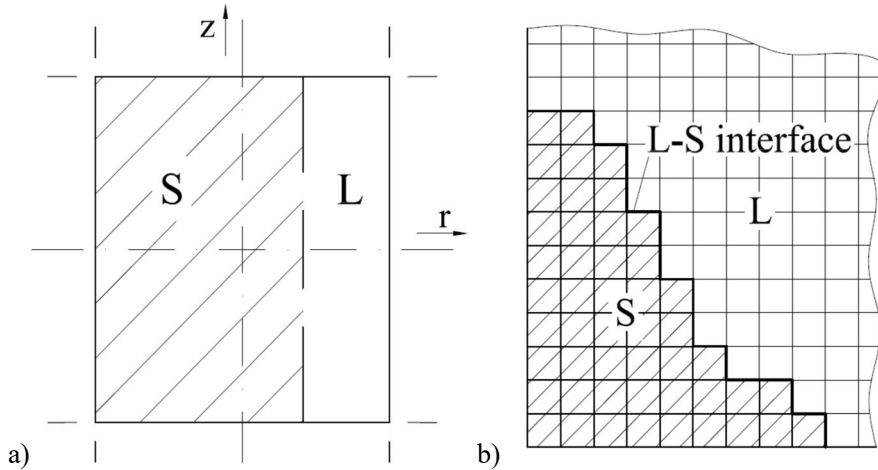


Fig. 1 Liquid-solid interface, a) control volume, b) welding joint [14].

## Mathematical Modelling of Weld Phenomena 12

Increment of melted or solidified part,  $f_i$  in control volume can be calculated by:

$$f_i = \frac{m_i}{m_{\text{vol}}} = \frac{c_m(T_1 - T_2)}{L} \quad (6)$$

where  $m_i/\text{kg}$  is mass quantity increase of solidified part in control volume,  $m_{\text{vol}}/\text{kg}$  is mass quantity of control volume,  $c_m/\text{Jkg}^{-1}\text{K}^{-1}$  is heat capacity of liquid and solid mixture,  $T_1/\text{K}$  is the temperature at the beginning and  $T_2/\text{K}$  is the temperature at the end of time step  $\Delta t$ . In proposed model it was presumed that convection term has no relevant role and that liquid metal flow could be neglected after pouring [15]. Equations 1 to 3 were found out using the finite volume method. Physical properties included in equations 1 to 6 should be defined [9]. Accuracy of the heat transfer prediction directly influences to the accuracy of both, calculations of phase transformation kinetics and calculations of mechanical properties of steel. Involved variables in model should be additionally adjusted.

Quantity of growth of solidified part of casting was predicted by calculation of solidification rate in control volume. When  $\Sigma f_i = 1$ , the mass of solidified part of casting will grow up for mass of control volume.

The temperature field change in an isotropic rigid body with coefficient of heat conductivity,  $\lambda/\text{Wm}^{-1}\text{K}^{-1}$ , density,  $\rho/\text{kgm}^{-3}$  and specific heat capacity,  $c/\text{Jkg}^{-1}\text{K}^{-1}$  can be described by Fourier's law of heat conduction:

It is assumed that the arc has a Gaussian distribution on the top face of the workpiece:

$$Q = q_0 \int_0^{\infty} e^{-\frac{d}{r_0^2} r^2} 2\pi r dr \quad (7)$$

where  $Q/W$  is the total heat input into the workpiece,  $r_0/\text{m}$  is the radius of the heat input distribution,  $d$  is the exponential factor and  $q_0/\text{Wm}^{-2}$  is the volumetric energy generation rate [10].

Solution of equation 1 can be found out using the finite volume method [9, 11, 12]. If the total volume is divided in  $N$  number of control volumes, discretization system has  $N$  linear algebraic equations, with  $N$  unknown temperatures of control volumes. Time of cooling from  $T_a$  to specific temperature in particular point is determined as sum of time steps, and in this way, the diagram of cooling curve in every grid-point of a specimen is possible to find out [10].

Accuracy of the heat transfer prediction directly influences to the accuracy of both, calculations of solidification kinetics, phase transformation kinetics and calculations of mechanical properties of steel. If the variables  $\rho$  and  $c$  were accepted, variable  $\lambda$  and specially variable  $\alpha$  must be estimated, i.e., calibrated according to variables  $\rho$  and  $c$  [10]. Total heat conductivity coefficients of steel at some temperature  $T$  should be calculated in accordance to composition and distribution of microstructure. Heat transfer coefficients of air are given in Table 1 [10].

**Table 1** Calibrated values of heat transfer coefficient of air

Temperature, T/°C	20	100	200	400	600	800	1000
Heat transfer coefficient, $\alpha/Wm^{-2}K^{-1}$	12	15	21	33	50	84	113

### MATHEMATICAL MODELING OF MICROSTRUCTURE COMPOSITION AND HARDNESS

Microstructure composition after the welding depends on chemical composition of steel and nature of cooling process. Kinetics of transformations was calculated by Avrami's isothermal equation. Transformed part of microstructure,  $x$  can be calculated by:

$$x = 1 - \exp(-k \cdot t^n) \quad (8)$$

where  $k$  and  $n$  are kinetic parameters.

For purpose of numerical analysis by computer, it is convenient when kinetics of austenite decomposition is defined in an incremental form of Avrami's isothermal equation. By differentiating the Avrami's equation it follows that:

$$\frac{dx}{dt} = \exp(-kt^n) nkt^{n-1} \quad (9)$$

and by extracting the time component from equation 9 it follows that:

$$\frac{dx}{dt} = nk^n \left( \ln \frac{1}{1-x} \right)^{\frac{1}{n}} (1-x) \quad (10)$$

Equation 10 can be written in an incremental form and the volume fraction  $\Delta x$  of austenite transformed in the time interval  $\Delta t_i$  at temperature  $T_i$  can be calculated as follows:

$$\Delta x_{(m)} = nk^n \left( \ln \frac{1}{1-x_{(m-1)}} \right)^{\frac{1}{n}} (1-x_{(m-1)}) \Delta t_{(m)} \quad (11)$$

In accordance to the Scheil's additivity rule, characteristic microstructure transformation is completed when transformed part of microstructure,  $\Sigma \Delta x$  is equal to one [16, 17]:

$$\sum_{m=1}^M nk^n \left( \ln \frac{1}{1-x_{(m-1)}} \right)^{\frac{1}{n}} (1-x_{(m-1)}) \Delta t_{(m)} = 1 \quad (12)$$



## Mathematical Modelling of Weld Phenomena 12

The non-isothermal transformation kinetics can be described as the sum of a series of the small isothermal transformations. The temperature range of cooling is divided into a series of small finite steps. Maintaining the time interval,  $\Delta t_i$  to sufficiently short times permits the assumption that the conditions are isothermal over each time step. It was assumed that each time step produces such a transformation as occurs in the isothermal condition of transformation at the same temperature and microstructure composition. Kinetic parameters  $k$  and  $n$  from equation 11 can be determined inversely by using data of time of isothermal transformation,  $t_T$ :

$$k = \frac{\ln(1-x)}{t_T^n} \quad (13)$$

Characteristic time of isothermal transformation could be calculated by kinetic equations based on chemical composition of steel or could be found out by using IT diagram of steel with standard chemical composition [17]. The IT diagram should be additionally adjusted based on actual chemical composition or based on Jominy test results for applied steel [18].

The martensitic transformation relation is based on the following expression [19]:

$$x_M = (1 - x_F - x_P - x_B) (1 - \exp(-0.01 (M_S - T))) \quad (14)$$

Increment of martensite is equal to:

$$\Delta x_M = x_M(T_{m+1}) - x_M(T_m) \quad (15)$$

Between critical temperatures of austenite decomposition and hardenability properties, regression relations are established [20]:

$$A_3 = 862 - 0.04(\text{HRC}_{\max} - 20)^2 - \frac{6E_d}{\text{HRC}_{\max} - 20} \quad (16a)$$

$$B_s = 586 - 0.02(\text{HRC}_{\max} - 20)^2 - \frac{30.6E_d}{\text{HRC}_{\max} - 20} \quad (16b)$$

$$M_s = 502 - 0.09(\text{HRC}_{\max} - 20)^2 - \frac{9E_d}{\text{HRC}_{\max} - 20} \quad (16c)$$

$$M_f = 502 - 0.2(\text{HRC}_{\max} - 20)^2 - \frac{9E_d}{\text{HRC}_{\max} - 20} \quad (16d)$$

It was accepted that equilibrium temperature of eutectoid transformation  $A_1$  is equal to 721 °C.

Simulation of as welded hardness at different welding joint points is estimated by the conversion of the calculated equivalent cooling time,  $t_{8/5e}$  to the hardness. This conversion is provided using the relationship between the equivalent cooling time  $t_{8/5e}$  and distance from the quenched end of the Jominy test specimen,  $E_d$ , i.e. by the using the diagram of cooling time  $t_{8/5}$  versus distance from the quenched end of the Jominy test specimen [21].

$$E_d = f(t_{8/5e}) \quad (17)$$

Hardness  $HRC_q$  was predicted by using the Jominy curve diagram:

$$HRC_q = f(E_d) \quad (18)$$

In the developed computer simulation of welding, the hardness at different points of steel plate is estimated by the conversion of the calculated cooling time  $t_{8/5}$  to the hardness and microstructure composition by using CCT diagram and thermo-kinetic equation [10, 22].

Since steel plate is repeatedly heated during the welding processes, influence of reheating of workpiece during welding on microstructure transformation should be taken into account. The reference value of hardness of welded steel plate can be estimated based on hardness at the start of welding,  $HRC_{start}$ , by [10, 23, 24]:

$$HRC = \frac{HRC_{start} - HRC_{min}}{K} + HRC_{min} \quad (19)$$

where  $HRC_{min}$  is the material constant with known physical meaning,  $K$  is the coefficient or ratio between reference hardness at the start of welding,  $(HRC_{start} - HRC_{min})$  and reference welded hardness,  $(HRC - HRC_{min})$ . Factor  $K$  is equal to:

$$K = \exp \left[ AB \left( \frac{T_{tr}}{a} \right)^{n_1} \right] \quad (20)$$

where  $T_{tr}/K$  is the reference value of reheating temperature, while  $A$ ,  $B$ ,  $a$  and  $n_1$  are the material constants, that are established by regression analysis of hardness of quenched and tempered steel. The algorithm for prediction of hardness of welded steel given by equations 19 and 20 was established by regression analysis [25]. Since the duration of processes of annealing or tempering at some temperature  $T_p$  is equal to  $\Delta t$ , temperature  $T_{tr}$  can be expressed by the following equation:

$$T_{tr} = \frac{T_p (C + a \ln \Delta t)}{C} \quad (21)$$

where  $a$  is a constant. Constant  $C$  depends on chemical composition and has the same meaning as constant  $C$  in Hollomon-Jaffe expression.

## APPLICATION

The developed method for prediction of hardness and microstructure distribution was applied in computer simulation of welded joints of steels with different hardenabilities. Welded joints were made of normalized steels, EN 52CrMoV4 and EN X15Cr13. Joint design is shown in Fig. 2. Welding rate was 30 cm/min and heat input was 4.8 kJ/cm. It was accepted that chemical composition of filler metal was the same as was of the base metal. Steel joints are tempered after welding at 380 °C for one hour. Computer simulation of hardness and microstructure distribution of the welded joints were done using the computer software BS Thermal, module BS-Welding.

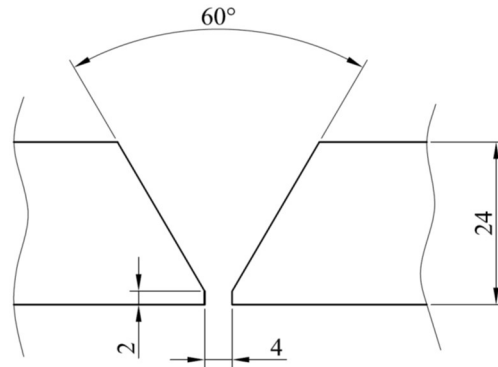


**Fig. 2** Joint design.

# Mathematical Modelling of Weld Phenomena 12

## WELDING JOINT MADE OF STEEL EN 52CrMoV4

The distribution of hardness and microstructure of the welding joint made of steel EN 52CrMoV4 are shown in Fig. 3.

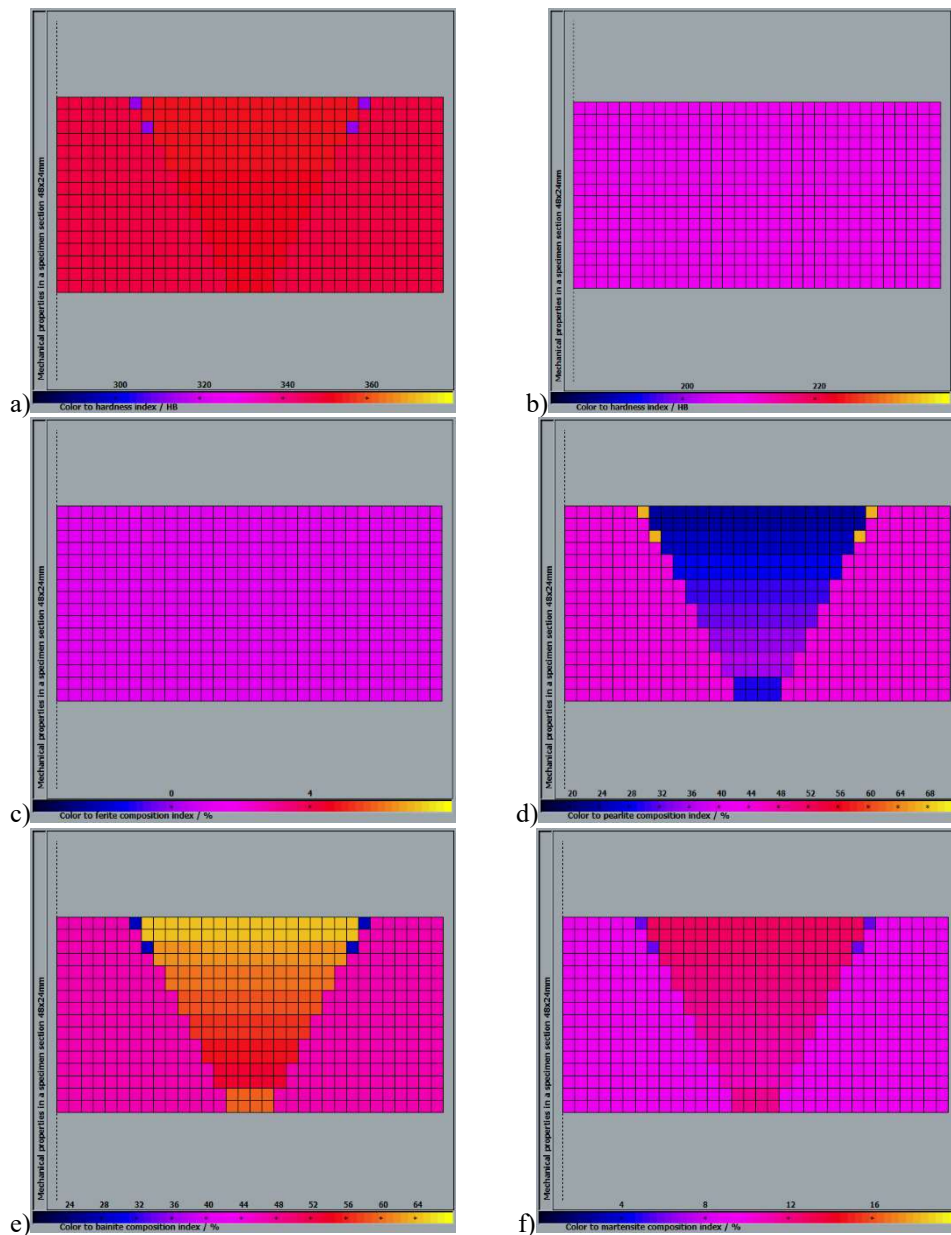


**Fig. 3** Distribution of hardness and microstructure of welded joint of steel EN 52CrMoV4, a) hardness as-welding, b) hardness after tempering, c) ferrite, d) pearlite, e) bainite, f) martensite.

# Mathematical Modelling of Weld Phenomena 12

## WELDING JOINT MADE OF STEEL EN X15Cr13

The distribution of hardness and microstructure of the welding joint made of steel EN X15Cr13 are shown in Fig. 4.

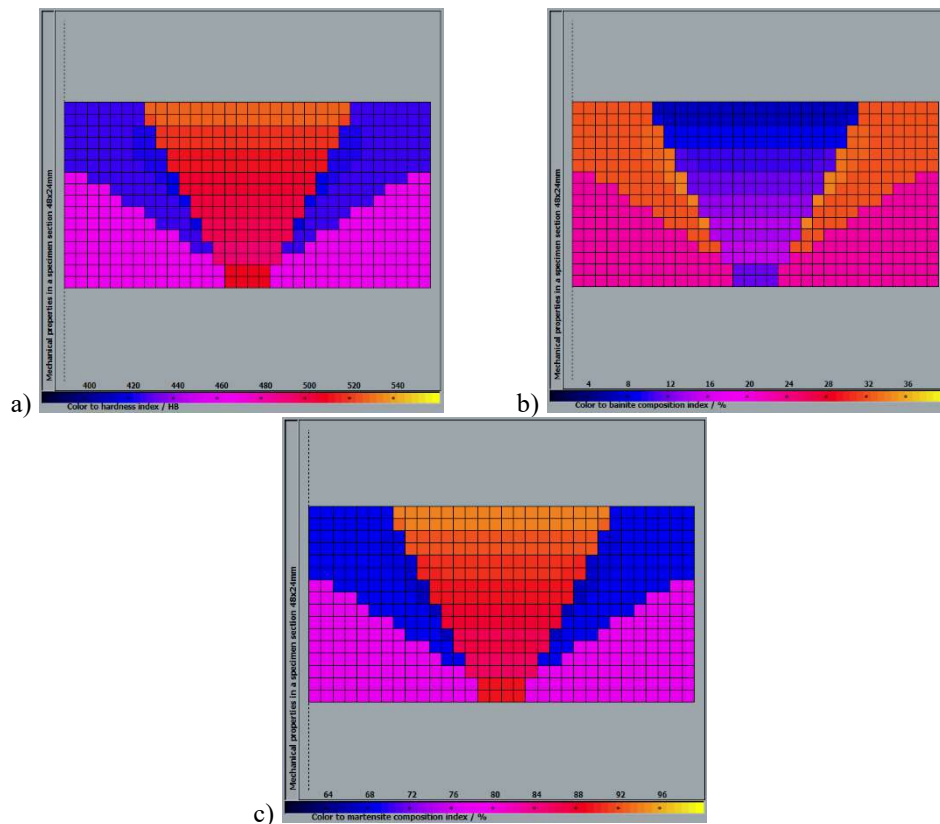


**Fig. 4.** Distribution of hardness and microstructure of welded joint of steel EN X15Cr13, a) hardness as-welding, b) ferrite+cementite, c) martensite [26]

## CONCLUSIONS

The mathematical model of steel welding has been developed to predict the hardness and microstructure distribution in welded joint. The model is based on the finite volume method. The numerical simulation of welding is consisted of numerical simulation of transient temperature field of cooling process, numerical simulation of mechanical properties and microstructure transformation in solid state.

Input material data involved in mathematical model of welding, i.e., density and specific heat capacity of steel, heat transfer coefficient and heat conductivity coefficient were

accepted from literature. Moreover, heat transfer and heat conductivity coefficients are additionally calibrated.

Hardness and microstructure composition in specimen points were calculated by the conversion of calculated time of cooling from 800 to 500 °C,  $t_{8/5}$  to hardness and microstructure composition using the CCT diagram and thermo-kinetic expressions. Hardness of steel weldings was estimated by taking into account the process of reheating of workpiece during the welding. Also, influence of tempering on welding joints properties was studied.

A developed mathematical model has been applied in computer simulation of welding of steel plates. It can be concluded, that hardness and microstructure composition in welded steel can be successfully calculated by proposed method.

### ACKNOWLEDGEMENTS

This work has been supported in part by Croatian Science Foundation under the project 5371.

This work has been supported in part by University of Rijeka, Support No 13.09.1.1.02.

### REFERENCES

- [1] M. SCHNEIDER, C. BECKERMANN: 'Formation of Macrosegregation by Multicomponent Thermosolutal Convection during the Solidification of Steel', *Metallurgical and Materials Transactions A*, Vol. 1, 26, 9, pp. 2373-2388, 1995.
- [2] A. SOMMERFELD, B. BÖTTGER, B. TONN: 'Graphite nucleation in cast iron melts based on solidification experiments and microstructure simulation', *J. Mater. Sci. Technol.*, 24(2008), pp. 321-324.
- [3] M. ROSSO: 'Modelling of Casting'H, in Handbook of Thermal Process Modelling Steels, eds. C.H. Gur, J. Pan, CRC Press, 2008.
- [4] J. FALKUS, K. MIŁKOWSKA-PISZCZEK, M. RYWOTYCKI, E. WIELGOSZ: 'The influence of the selected parameters of the mathematical model of steel continuous casting on the distribution of the solidifying strand temperature', *Journal of Achievements in Materials and Manufacturing Engineering*, 55/2 (2012) 668-672.
- [5] N. M. VANAPARTHY, M. N. SRINIVASAN: 'Modelling of solidification structure of continuous cast steel', *Modell. Simul. Mater. Sci. Eng.*, 6(1998), pp. 237-249.
- [6] T. C. TSZENG, S. KOBAYASHI: 'Stress analysis in solidification process: Application to continuous casting', *Int. J. Mach. Tools Manuf.*, 29(1989), pp. 121-140.
- [7] I. TELEJKO, H. ADRIAN, K. SKALNY, M. PAKIET, R. STAŠKO: 'The investigation of hardenability of low alloy structural cast steel', *Journal of Achievements in Materials and Manufacturing Engineering*, 37/2 (2009) 480-485.
- [8] C. H. GUR, J. PAN: 'Handbook of Thermal Process Modelling Steels', CRC Press, 2008.
- [9] B. SMOLJAN, D. ILJKIĆ, H. NOVAK: 'Estimation of coefficient of heat conductivity and heat transfer coefficient in the numerical model of the steel quenching', *Proceedings of the 2nd Mediterranean Conference on Heat Treatment and Surface Engineering*, 11-14 June 2013, Dubrovnik - Cavtat, Croatia.
- [10] B. SMOLJAN, D. ILJKIĆ, L. ŠTIC, N. TOMAŠIĆ, S. SMOKVINA HANZA: 'Mathematical modelling of mechanical properties and microstructure of welded joint', *Proceedings of the 41st*

## Mathematical Modelling of Weld Phenomena 12

- International Conference WELDING 2016, Modern Joining Processes, Development of Filler Materials and Simulations*, 8-11 June 2016, Opatija, Croatia.
- [11] I. DEMIRDŽIĆ: 'Application on finite volume method to calculation of temperature fields generated during welding', *Zavarivanje*, 27/6, 1984, pp 481 – 489, (in Croatian)
- [12] S. PATANKAR: 'Numerical Heat Transfer and Fluid Flow', McGraw Hill Book Company, New York, 1980.
- [13] L. SOWA: 'Mathematical Model of Solidification of the Axisymmetric Casting While Taking Into Account its Shrinkage', *Journal of Applied Mathematics and Computational Mechanics*, 13(2014) 4, pp. 123-130.
- [14] B. SMOLJAN, D. ILJKIĆ, M. MARETIĆ: 'Computer simulation of hardness and microstructure of casted steel 100Cr6', *Archives of Materials Science and Engineering*, 78/1 (2016) 23-28.
- [15] M. FLEMINGS: 'Solidification Processing', McGraw-Hill Book Company, 1984..
- [16] 'Heat Treating', *ASM Handbook Vol. 4*, ASM International, Materials Park, OH, 1991.
- [17] S. SMOKVINA HANZA: 'Mathematical Modeling and Computer Simulation of Microstructure Transformations and Mechanical Properties During Steel Quenching', *thesis*, Department of Materials Science and Engineering, University of Rijeka - Faculty of Engineering, 2011, (in Croatian)
- [18] SMOLJAN, B.: 'Numerical Simulation of Steel Quenching', *Journal of Materials Engineering and Performance*, Vol. 11, No. 1, 2002, pp. 75–80.
- [19] KOISTINEN, D. P., AND MARBURGER, R. E.: 'A General Equation Prescribing the Extent of the Austenite-Martensite Transformation in Pure Iron-Carbon Alloys and Plain Carbon Steels', *Acta Metall.*, Vol. 7, 1959, pp. 59–60.
- [20] SMOLJAN, B., ILJKIĆ, D., AND TOMAŠIĆ, N.: 'Prediction of Mechanical Properties and Microstructure Composition of Quenched and Tempered Steel', *presented at the 28th ASM Heat Treating Society Conference*, Heat Treating 2015, Detroit, MI, October 20–22, 2015, ASM International, Materials Park, OH, pp. 266–273.
- [21] SMOLJAN, B., AND ILJKIĆ, D.: 'Computer Modeling of Mechanical Properties and Microstructure of Quenched Steel Specimen', *presented at the Fifth International Conference on Thermal Process Modeling and Computer Simulation*, Orlando, FL, June 16–18, 2014, ASM International, Materials Park, OH, pp. 103–111.
- [22] B. SMOLJAN, D. ILJKIĆ, L. ŠTIC: 'Mathematical modelling and computer simulation of non-monotonic quenching', *Proceedings of the 23rd IFHTSE Congress*, 18-21 April 2016, Savannah, Georgia, USA.
- [23] B. SMOLJAN, D. ILJKIĆ AND S. SMOKVINA HANZA: 'Computer simulation of working stress of heat treated steel specimen', *Journal of Achievements in Materials and Manufacturing Engineering*, 34/2, 2009, pp 152 – 156.
- [24] T. RETI, I. FELDE, M. GUERRERO, AND S. SARMIENTO: 'Using Generalized Time-Temperature Parameters for Predicting the Hardness Change Occurring during Tempering', *International Conference on New Challenges in Heat Treatment and Surface Engineering (Conference in honour of Prof. Božidar Liščić)*, B. Smoljan, B. Matijević, Eds., June 9-12, pp 333-342, Dubrovnik-Cavtat, Croatia, 2009.
- [25] D. ILJKIĆ: 'A contribution to the development of the mechanical properties prediction of quenched and tempered steel and cast steel', *Doctoral Thesis*, Department of Materials Science and Engineering, Faculty of Engineering, University of Rijeka, 2010. (in Croatian).
- [26] B. SMOLJAN, D. ILJKIĆ, L. ŠTIC, S. SMOKVINA HANZA, L. GRŽINIĆ, G. VRATOVIĆ, 'Numerical modelling of welded joints properties', *Proceedings of the MATRIB 2018*, 27-29 June 2018, Vela Luka, Croatia.

PREDICTION OF STRESS CORROSION  
CRACKING IN 304 STAINLESS STEEL  
CANISTERS IN DRY STORAGE OF SPENT  
FUEL BY MODELING: ANALYSIS OF WELD  
RESIDUAL STRESS AND SUSCEPTIBLE  
MICROSTRUCTURE

S. GORDON\*, X. WU\*, Z. YU\* and S. LIU\*

*\*George S. Ansell Department of Metallurgical and Materials Engineering  
Center for Welding, Joining and Coatings Research  
Colorado School of Mines, Golden, CO 80401, U.S.A.*

*DOI 10.3217/978-3-85125-615-4-12*

ABSTRACT

Atmospheric chloride-induced stress corrosion cracking (CISCC) in the weldments of spent fuel canisters is one of the primary safety concerns during the dry storage of used nuclear fuel at Independent Spent Fuel Storage Installations (ISFSI) in coastal areas. For SCC to occur, three criteria must be met: an aggressive chemical environment, susceptible microstructure, and sufficient tensile stress. Instead of the environment, this paper will focus only on the material microstructure and stress state. Firstly, finite element analysis (FEA) based numerical simulation models were developed for the welding of the mockup canister. Multi-pass arc welding process was considered. The thermal history and residual stress distribution induced by the longitudinal, circumferential, and the intersection between longitudinal and circumferential welds were developed based on a thermal-mechanical coupling model using ABAQUS software. The simulation results were compared with the deep-hole drilling (DHD) and contour measurement data. Based on the model-predicted stress results, a four-point bend (4PB) setup was then designed to duplicate the weld residual stress onto the 4PB specimen, on which the maximum tensile stress is close to the predicted maximum stress level of 250 MPa in the weld heat-affected zone (HAZ). A stress gradient also existed along the thickness of the 4PB specimen which allowed for the consideration of stress variation. The designing of the 4PB test was done by FEA method using ABAQUS software, and verified by digital image correlation (DIC) measurements. Besides, to identify the most susceptible microstructure of the canister to corrosion under the weld residual stress in the controlled environment, the modified implant test (CEMIT) was designed. A FEA model considering the welding process and the following uniaxial tensile load was then developed using the SYSWELD software. The residual stress and thermal history were obtained during and after the CEMIT welding process, and after the uniaxial tensile loading process. These tests yielded instructive information for the prediction of the initiation site of the crack. The initiation of the crack observed in the experiments was explained based on the simulation data. While each of the three simulations provided an independent story, the three together produced a complete and complementary picture. Stress corrosion cracking is a series of complex interactions which simultaneously occur. The thermal mechanical model of the canister provides information for predicting



## Mathematical Modelling of Weld Phenomena 12

the location at which stress corrosion cracking will most likely occur. The model for the 4PB test predicts the stress gradient which occurs in a bent bar. The SYSWELD CEMIT model predicts the welding cycle, the thermal history, residual stress and loading behavior of the specimen. By design, each independent CEMIT provides the location of the most crack susceptible location under a specified environment.

Keywords: Stress corrosion cracking, Spent fuel canister, Weld residual stress, Susceptible microstructure, Modelling

### INTRODUCTION

CISCC in the weldments of spent nuclear fuel (SNF) canisters is one of the primary safety concerns during the dry storage of used nuclear fuel at Independent Spent Fuel Storage Installations (ISFSI) in coastal areas [1]. For SCC to occur, three criteria must be met: an aggressive chemical environment, susceptible microstructure, and sufficient tensile stress. Field sampling analysis of surface deposits on in-service spent nuclear fuel storage canisters at three near-marine ISFSI sites in the United States have demonstrated the presence of chloride-rich salts on the canister surfaces [2-4]. As part of the surface of the canisters cools sufficiently for the salts to deliquesce, chloride-rich aqueous brine layer could form locally on the surface, leading to potential failures by CISCC in regions with high tensile stress. On the other hand, for austenitic stainless steel SNF interim canisters, the multi-pass welding procedures introduce high tensile residual stresses and sensitization in the HAZ. Therefore, the potential for CISCC in the weldments of the stainless steel interim storage canisters has been identified as a high priority data gap.

To gain fundamental understanding of the pitting and cracking behavior in the canisters and to accurately predict their long-term performance, the first step is to obtain the accurate residual stress distribution within the canisters, especially in the weldments. In the last decade, there have been several studies on the residual stresses in the canister welds. For example, Kosaki et al. [5] reported that the experimentally measured weld residual stresses were close to the yield stress through thickness on a cylindrical canister of 1.3 m in diameter and with walls approximately 75 mm thick. The Nuclear Regulatory Commission (NRC) simulated the residual stresses for typical canister welds by employing a two-dimensional, sequentially-coupled thermal-structural FE model [6], and predicted that tensile stresses of sufficient magnitude to initiate SCC are likely to be present in the HAZ of both longitudinal and circumferential welds through the wall thickness of the canisters, allowing for crack propagation through the wall thickness over time. There is very limited literature on 3D simulation of the residual stress induced by multi-pass longitudinal and circumferential welds in the dry storage fuel canisters. As for the microstructure of the canister material, possible factors that may influence the CISCC include the sensitization, ferrite, martensite, inclusions, grain size, phase orientation, texture, and so on. It is, thus, necessary to determine the most susceptible microstructure for the weld region of the canister under the influence of weld heat input and mechanical stresses. In this study, a 3D FE model using ABAQUS software was built to simulate the residual stress contours in the 304 stainless steel canisters with the presence of both longitudinal and circumferential multi-pass welds. Experimental measurements by deep hole drilling (DHD) and contour methods provide valuable comparisons with the simulation results. Then, a modified four-point bend setup was built to duplicate the weld residual stresses into a small sample, by which subsequent corrosion tests will be carried out. At

last, a modified implant test was designed, together with FEA, to characterize the most susceptible microstructure for the initiation of SCC.

## SIMULATION DETAILS AND EXPERIMENTAL METHODOLOGIES

### WELD RESIDUAL STRESS SIMULATION

The ABAQUS software was used to build the residual stress models for longitudinal and circumferential double-V groove multi-pass welds. Fig. 1(a) demonstrates the meshed structure with 52100 brick elements established based on the actual geometry of the mockup and the welding conditions as schematically illustrated in Fig. 1(b). The mockup consists of three cylindrical shells that were 4 feet (~1220 mm) long each and 5/8 inch (~15.9 mm) thick as shown in Fig. 1(b). The shells were rolled from a plate into a cylinder and then welded at the longitudinal seam. The three cylinders were joined together by two circumferential welds. Details of the welding parameters including pass sequence, voltage, current, travel speed and heat input for each weld pass can be found in reference [7]. Take longitudinal welds for example, the three inner passes were made first, followed by the four passes in outer diameters. Since the three longitudinal welds were arranged 180 degrees apart (see Fig. 1(b)) and the two circumferential welds were separated by the middle section, the interference between the same welding types can be negligible. Hence, in this FE model, only the longitudinal and circumferential intersecting joint in half of the mockup section was simulated, as shown in Fig. 1(a), and the welding length was sufficient to reach steady state. Note that the heat source travelled through the whole length of the welds to ensure the elements experience the same thermal history as did the actual welds.

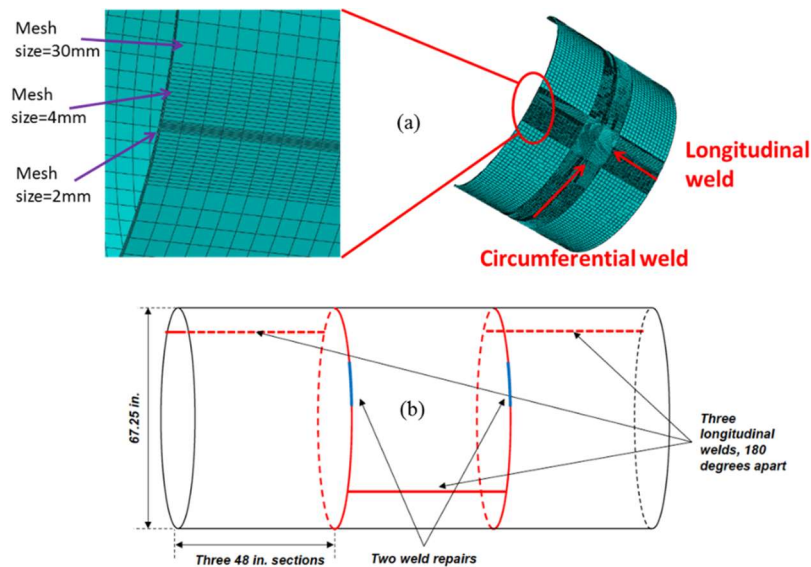


**Fig. 1** (a) The FEA model for the mockup with fine meshes near welds, and (b) schematic drawing of the mockup.

The multi-pass weld beads have sharp transition angles, as shown in Fig. 2, which demands extremely fine meshes. More importantly, the intersecting longitudinal and circumferential welds needs compatible meshing. Due to such complications, the weld bead was divided into small rectangle-shaped areas matching the experimental bead morphology as closely as possible. The experimental bead morphology of each pass is outlined by the dotted curves in Fig. 2 and the corresponding simulation passes are highlighted in various colors. Such simplification avoided elements with sharp angles and assisted the FE model to converge more easily.

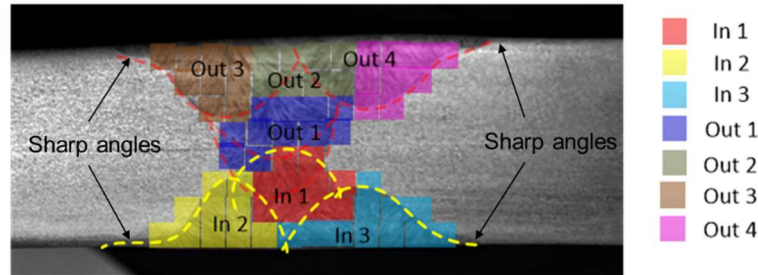


**Fig. 2** Experimental bead morphology and the corresponding computational weld bead. In the figure, “in” means inner diameters of the mockup, and “out” refers to the outer diameters of the mockup.

The mockup base material is 304 stainless steel (SS). The material properties used in the simulation were taken from Deng’s work [8]. Temperature-dependent hardening modulus used in this model was obtained from Liu’s work [9]. The material solidus and liquidus temperatures were set at 1400 and 1450 °C, respectively. The latent heat of fusion was set to be 260 kJ/kg. The material properties were assumed to be the same for both base and weld metals due to lack of information in 308 weld metal physical properties.

Double-ellipsoidal heat source model developed by Goldak [10] as illustrated in Fig. 3 was used to simulate the heat input of submerged-arc welding process. The front and rear parts of the heat flux are described by Eqs. (1) and (2), respectively:

$$q_r(x, y, z) = \frac{6\sqrt{3}f_r\eta Q}{a_rbc\pi\sqrt{\pi}} \exp\left(-\frac{3x^2}{a_r^2} - \frac{3y^2}{b^2} - \frac{3z^2}{c^2}\right) \quad (1)$$

$$q_f(x, y, z) = \frac{6\sqrt{3}f_f\eta Q}{a_fbc\pi\sqrt{\pi}} \exp\left(-\frac{3x^2}{a_f^2} - \frac{3y^2}{b^2} - \frac{3z^2}{c^2}\right) \quad (2)$$

where the front and rear quadrant fractions,  $f_f$  and  $f_r$ , were set to be 0.6 and 1.4, respectively. The heat input was defined as  $Q = V \cdot I \cdot \eta$ , where  $V = 30$  V,  $I = 400$  A and  $\eta = 0.8$ . The constants  $a_f$ ,  $a_r$ ,  $b$ , and  $c$  were set to be 13, 26, 13, and 13, respectively, to closely match the experimental fusion boundary in Fig. 2.

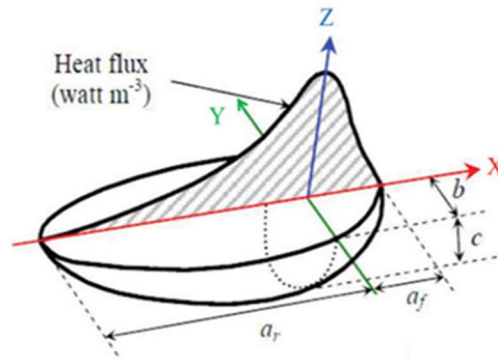


**Fig. 3** Heat source model for the weld simulation.

The weld residual stresses were also characterized by DHD and contour measurement method developed by Sandia National Laboratory [7], which can be used to validate the simulation data. Detail comparison between simulation and experimental data are discussed in Section 3.

#### REPLICATION OF RESIDUAL STRESSES BY FOUR-POINT BENDING TEST

The stresses experienced by the mockup materials were duplicated to laboratory scale specimens through four-point bend (4PB) test. In this modified 4PB test setup, pitting initiation/growth was characterized within the thickness of the specimen, which covered stress levels from compression to tension. The maximum tensile residual stress, as indicated in another report by the same authors [11], was predicted to be around 250 MPa in the HAZ, so the design of this 4PB setup was to obtain maximum stress on the tensile side close to 250 MPa. FE method was adopted to design the geometry of this setup to allow for a sufficient sampling area within a small stress increment. Fig. 4 illustrates the finalized geometry design. The frame and actuator material is 316 stainless steel, and they were coated with Kolor-Proxy high build polyamide-epoxy primer that provides abrasion, impact and chemical resistance.

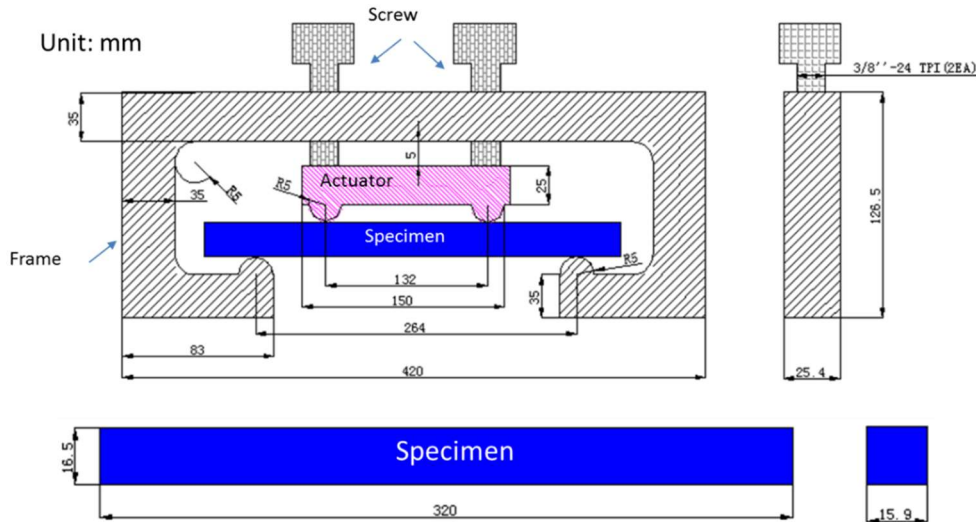


Fig. 4 Optimized geometry of the modified 4PB setup by FEA.

The stress loading of the specimen was accomplished by turning the two screws downward to certain displacement predicted by FEA. DIC method was used to in-situ monitor the strain development in the designed 4PB setup during incremental loading for the purpose of validation. Fig. 5(a) shows the DIC measurement setup. Fig. 5(b) demonstrates the surface preparation for DIC measurement, where a white background and black speckle pattern was generated by carefully spraying the white coating primer and low chloride metal marker black paint.

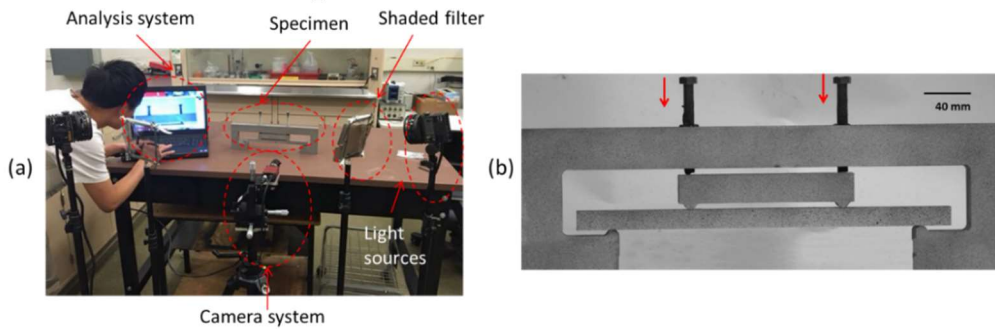


Fig. 5 (a) Photograph of the DIC setup for 4PB testing, and (b) the speckle pattern on the side surface of 4PB setup prepared for DIC analysis.

#### MODIFIED IMPLANT TEST

The following discussion will show how the Controlled Environment Modified Implant Test (CEMIT) can correlate the weld thermal exposure with the developed microstructure in the heat affected zone (HAZ) of the welds as well as the sensitization experienced. Together with the stresses developed during welding and subsequent canister handling, the sensitized microstructure consisted of austenite with precipitated  $\text{Cr}_2\text{C}_6$  particles and small

amounts of deformation-induced martensite contributes to stress corrosion in the corrosive environment.

As a result of the high temperature, the base material near the fusion line may recover and/or recrystallize, and if near enough to the weld zone, may melt. Softening generally occurs in this region. Further away from the weld there is a region where the kinetics for carbide ( $\text{Cr}_{23}\text{C}_6$ ) precipitation is favorable. The material within this region is heat treated to between 450 to 850oC and is commonly known as the sensitized region and under proper conditions can be more prone to corrosion. The upper and lower limits of the temperature range can change according to the chemical composition, in particular, carbon content, of the stainless steel. Alloys with lower carbon content will see lower temperatures and longer delay times for carbide precipitation. To account for residual stress development, a thermal mechanical model was developed to simulate the conditions in the canister during and after welding. Due to the size of the canister, the complex residual stress states, and ever changing natural environment, determining the exact location and time when SCC will happen is difficult.

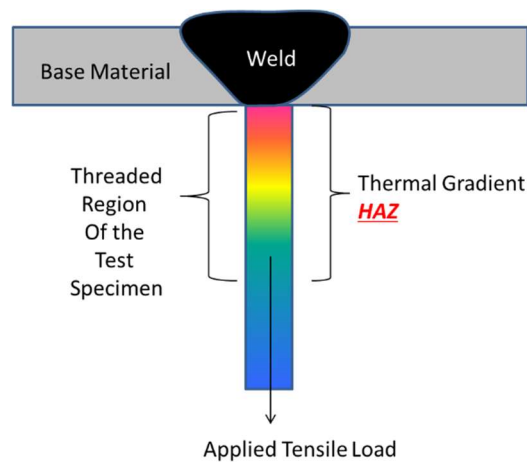


**Fig. 6** A threaded cylindrical specimen with a weld bead on top. A tensile load is applied at the conclusion of the welding. The arrow indicates the direction of loading.

The Implant testing was substantially modified from its original intention [12-13] with the addition of an environmental chamber to introduce the corrosive elements (salt load, relative humidity, and temperature). To simulate the environment of the canister, salts would be deposited in the threaded region of the welded cylinder and the specimen would be placed into the chamber with preset temperature and humidity. The specimen would then be loaded to a pre-determined stress level. Under load, the notch concentrates the stress to the root of the threads. Fig. 6 shows a generalized schematic drawing depicting the basic concept of the implant test. When the specimen is provided with the proper conditions for corrosion, pitting and cracking can be observed in the notched region.

A thermal mechanical model using SYSWELD was developed to simulate the welding process for the Implant test. The thermal histories determined from both models: the canister and the Implant test can be compared. Similar thermal cycles found in the models should produce similar microstructures in both weldments (on the canister and in the Implant test). By using the thermal cycle determined from the Implant test model at the

location in the threads where pitting corrosion and cracking occurred, a corresponding location for crack-susceptible microstructure can be determined on the model developed for the canister. Grain size as well as degree of sensitization can be used to support the microstructural behavior prediction.

By using the temperature-time profiles determined by the models, bulk material with the crack-susceptible microstructures can then be produced for testing by using the Gleeble or other heat treatment techniques. Testing of this material can lead to the determination of pitting initiation times, crack growth rates, and resistance to cracking once cracks are initiated.

For atmospheric SCC testing, the basic Implant testing equipment would be modified. However, the basic fundamentals of the test would remain the same, i.e. a welded threaded specimen is pulled in tension. The major differences are, (1) after welding, the threaded region of the specimen is coated in a corrosive media (salt loading), and (2) instead of ambient conditions, the tensile loading of the specimen is conducted under a controlled environment. By loading the end of this vertical cylindrical specimen of Type 304 stainless steel in the corrosive media, the spiral notch will locate the position of the microstructure most susceptible to cracking.

*Implant specimen*

The Implant specimen is a Type 304 stainless steel cylinder machined with a spiral notch as shown in Fig. 7(a). Fig. 7(b) is a schematic drawing showing the orientation of the weld cup and implant specimen with respect to rolling direction of the base plate. The specimen would be machined from 0.625 inch thick plate transverse to the direction of rolling. The specimen is approximately 3.5 inches long with a 1/4-28 thread on one end and 1/2-13 thread on the other. The end with the 1/4-28 thread was the welded end and the other end connected to the load cell. Table 1 shows the chemical composition of the implant specimen.

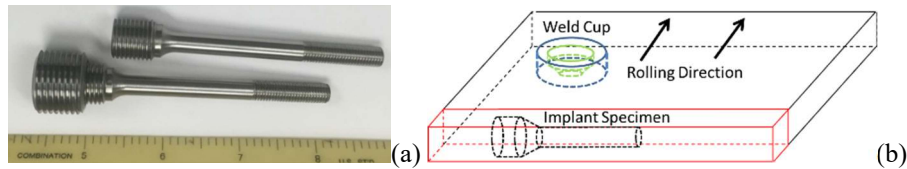


**Fig. 7** (a) Photograph showing Implant specimens and adapter collar screwed onto the bottom of the specimens. (b) Schematic drawing showing the implant specimen and weld cup extraction location with respect to base plate orientation.

**Table 1** Chemical composition (in weight percent) of Type 304L stainless steel used in this study

Material	C%	Co%	Cr%	Cu%	Mn%	Mo%	N%	Ni%	P%	S%	Si%
304/304L	0.0216	0.1980	18.3105	0.3915	1.8280	0.2855	0.0889	8.1125	0.0325	0.0010	0.2510

*Thermal mechanical model*

A commercial finite elements software, SYSWELD, was used to model the weld thermal experience and stresses developed during the welding process. This software is also able to predict the resulting weld microstructure as a function of the location on the modelled component. Combining the thermal conditions data with the microstructural evolution history in the specimen, bulk specimens can be created with the targeted microstructural for corrosion susceptibility, pitting-to-cracking transition, fracture mechanics testing, and advanced nondestructive evaluation. These specimens can also be further processed to characterize in-situ corrosion and crack propagation mechanism.

Using as input the welding heat input, physical dimension and geometry of the material, physical material properties, and applying the necessary thermal boundary conditions, SYSWELD was used to model the temperature profiles, microstructure, mechanical properties and the residual stresses developed in the cylindrical specimen.

*Model description*

Fig. 8 shows the meshed model used in the FEA. The Implant test specimen is constituted of three parts: Base metal, weld metal and the screw. All the three parts are made of type 304 stainless steel; the material properties are chosen from reference [8]. The cross-section view and top view as shown in Fig. 8(a) and Fig. 8(c) depict that the base metal (described earlier also as weld cup) is modeled as a cylinder with a hole created in the middle. This hole is simulated by a cylinder on the top and an inverted cone at the bottom. The screw is connected with the base metal at the bottom of the cone. Welding is conducted on the top of the screw and the weld metal is represented by the brown-colored region. As shown in Fig. 8(d), the top 10 threads in the screw are meshed with very small size elements to clearly describe the most sensitive region under the thermal and mechanical load. Different parts are connected together by the co-node method. The thread is meshed with 4-node tetrahedral elements due to the complicated geometry structure, while the rest is meshed with hexahedral solid elements. The total number of elements is 754,374. The FEA studies for the modified Implant test are conducted using the SYSWELD software.

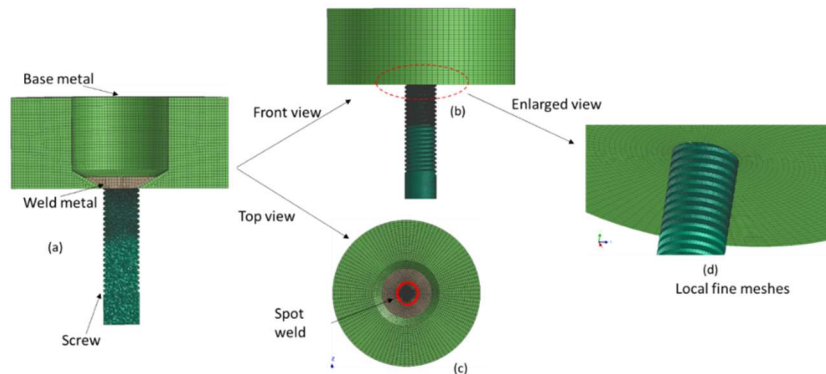


**Fig. 8** Meshed model for the modified Implant test simulation. (a) Cross-section view. (b) Front view. (c) Top view. (d) Enlarged view.



**Table 2** SYSWELD simulation parameters

Parameter	Welding Current (A)	Welding voltage (V)	Welding velocity (m/s)	Welding time (s)	Cooling time (s)	Tensile load (MPa)
Value	250	32	0.225	4.534	600	170

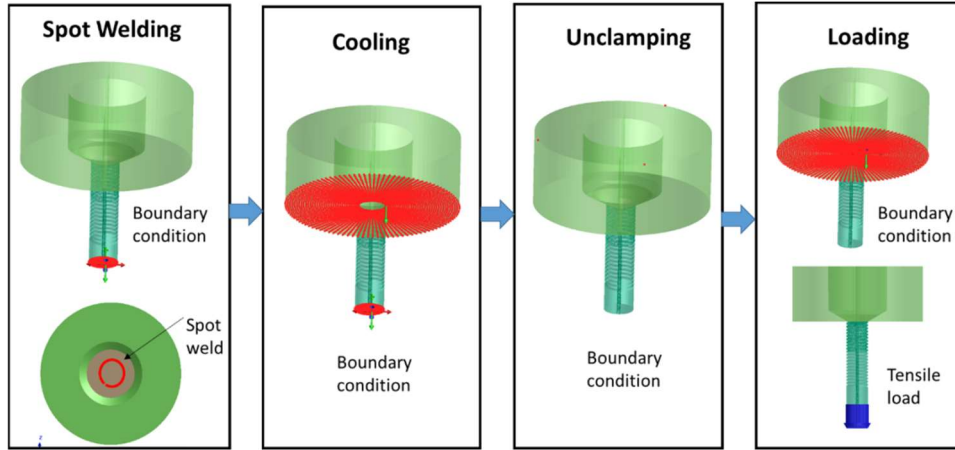


**Fig. 9** Schematic drawing showing the progression of welding, cooling, and loading boundary conditions.

The X, Y, and Z directions for the implant specimen shall be defined as the following. The Y direction is the direction in which the specimen is a uniaxial loaded condition, the X and Z directions are transverse to the loading direction. Fig. 9 describes the simulation procedures used in SYSWELD. Firstly, spot arc welding is conducted on the top of the screw; the spot welding is realized following a small circular trajectory. During the welding process, the bottom surface of the screw is fixed. After welding, the three pieces are air cooled for sufficient time. At this stage, the ambient temperature is kept as 20 °C with the bottom surface of the screw fixed. Meanwhile, movement of the base metal in the -Y direction is restricted. Then, after cooling, the whole piece is unclamped with three nodes, during which no thermal or mechanical load is applied. Lastly, a uniaxial tensile load is applied to the bottom surface of the screw. The tensile load value is adjusted to achieve a stress level on the screw to be a fraction of the yield strength of the material (250 MPa). During the loading process, movement of the base metal along the -Y direction is also restricted. By taking the four simulation procedures, a process similar to that observed in the experiment is reproduced on the computer. Table 2 gives the simulation parameters used in SYSWELD. The choice of these parameters is also closely related to the real conditions in experiment.

During the welding process three clamping conditions can arise. The first, both pin and plate (weld cup) are free to expand and contract without restraint during welding or cooling. Second, pin and plate are fixed during welding or cooling. Third, the pin and plate can both move during welding but are fixed during cooling. The third case fits best the intended testing condition. While the specimen is held by the fixture, the pin is free to expand through the hole in the plate upon heating, and the plate is held by gravity to the fixture. Once the

melt pool incorporates both the pin and the plate, and solidification begins, the specimen is deemed as fixed together. As the specimen begins to cool the weld metal has sufficient strength to support the stress in the specimen.

RESULTS AND DISCUSSIONS

WELD RESIDUAL STRESS

*Residual stress contours*

Fig. 10 summarizes the overall stress contours in the mockup after seven longitudinal weld passes and eight circumferential weld passes. The thermal contraction during solidification and cooling of arc welding induced high tensile residual stress in the weld metals. In the longitudinal welds, as shown in Fig. 10(a), the axial stress is as high as 423.7 MPa in the weld center, which is much higher than the hoop stress. In comparison, a maximum residual stress of 366.1 MPa lies in in hoop direction in the circumferential welds. Both stresses in the two welds are way higher than yield strength (~ 250 MPa), so plastic deformation has initiated. The influence of two intersecting multi-pass weldments on the residual stress distribution is clearly demonstrated in Fig. 10. It should be noted that the highest tensile stress always coincided with the welding direction.

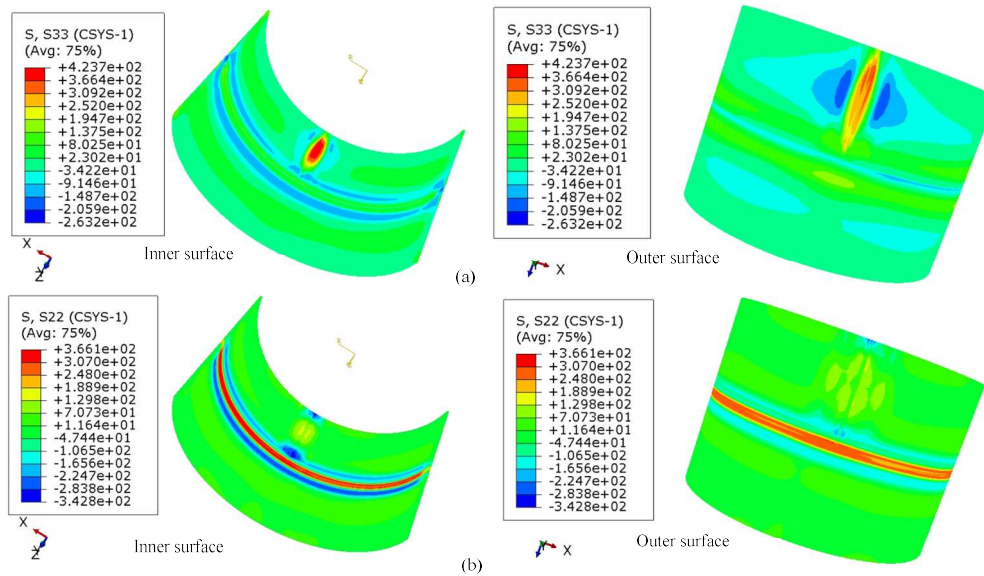
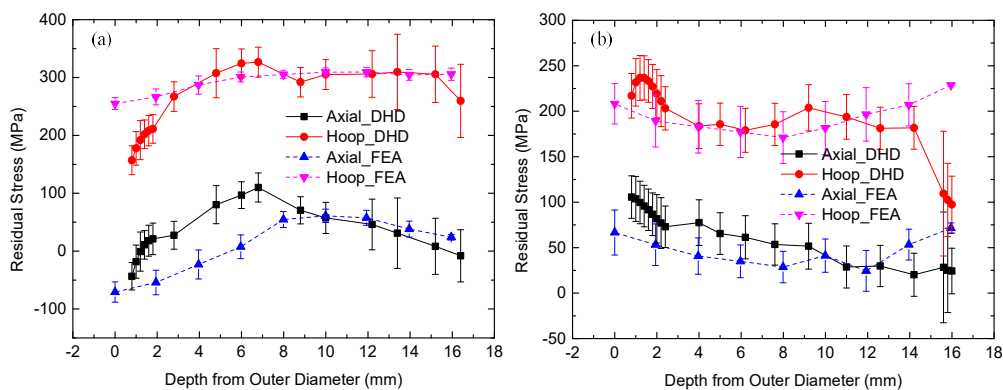


Fig. 10 Overall residual stress contours for (a) axial stress and (b) hoop stress from FEA.

*Comparison of FEA with measurement results*

Fig. 11 summarizes the residual stress profiles as a function of depth in circumferential weld centerline and HAZ (approximately 4mm away from weld toe on the outer surface) obtained from FEA and DHD measurements, which demonstrates a good agreement. Note that the experimental residual stress data close to the surfaces ( $\leq 2$ mm) were obtained from conventional hole drilling method. Through-wall high hoop tensile stress was observed in the circumferential welds. The maximum hoop stresses in circumferential welds are about 230 to 340 MPa in the weld centerline and approximately 200 MPa in HAZ, respectively. The pre-existing residual stress in the base metal (up to 50MPa indicated by the DHD measurements) induced by the rolling process during manufacturing which was not considered in the FE model, may lead to the difference in residual stress values near surfaces between experimental and simulation results. In comparison, for the longitudinal welds (which is not shown here), high through-thickness axial stresses were observed in the weld metal (320 to 420 MPa) and HAZ (170 to 200 MPa).



**Fig. 11** Residual stress profiles as a function of depth in (a) weld centerline and (b) HAZ of circumferential weld from FE simulation (dashed lines) and DHD measurements (solid lines). The data of FE simulation is averaged from ten points in the steady-state location.

The cross-section stress contour is extracted from FEA results, and compared with the results from contour method for both circumferential and longitudinal weld. Fig. 12 demonstrates the comparison of longitudinal weld. Good agreement is achieved between the FEA and contour measurement results. The residual stresses are strongly tensile through thickness near the longitudinal weld centerline. The simulation result predicts a slightly wider tensile residual stress regime than the contour method, especially on the inner and outer surfaces, which is in agreement with the experimentally observed fusion boundary morphology as illustrated in Fig. 2. Note that tensile stress is observed at the two ends of the welded plate only in the contour method, as shown in in Fig. 12(a), which could be introduced potentially by cutting process.

## Mathematical Modelling of Weld Phenomena 12

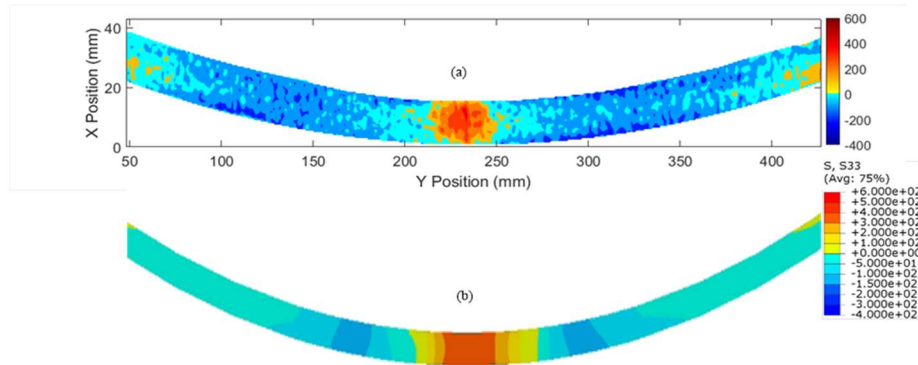
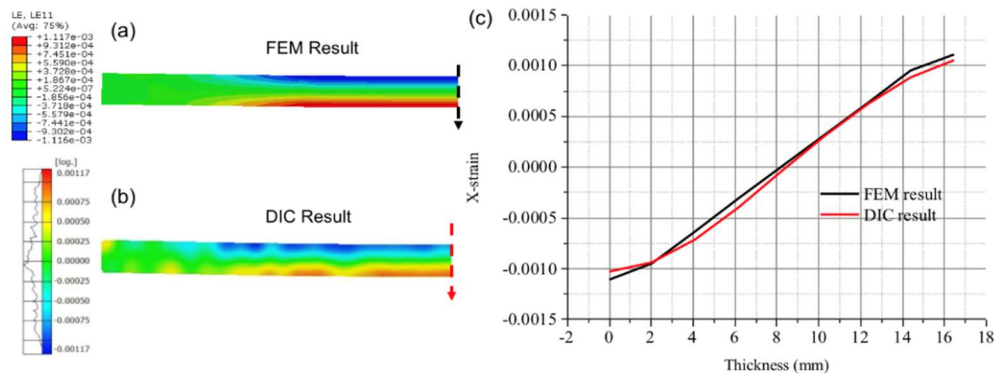


**Fig. 12** Cross-section axial stress contour distribution for longitudinal weld from (a) contour method and (b) FEA.

### STRESS AND STRAIN DISTRIBUTION OF FOUR-POINT BEND SAMPLE

#### *Verification of FEA results by DIC*

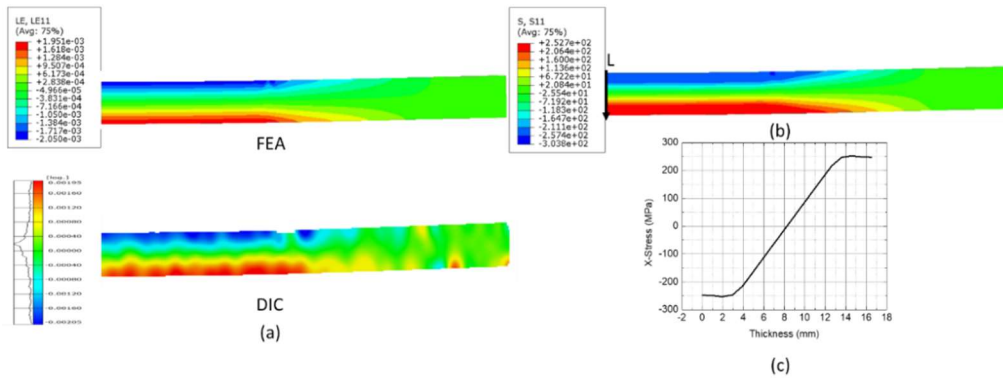
The DIC method was able to provide the strain evolution along x axis ( $\parallel$ LD, longitudinal weld direction) as a function of displacement load along y axis ( $\parallel$ ND, normal direction) in a modified 4PB specimen. The displacement load was carefully applied by turning the two screws in Fig. 5(b) downward slowly and evenly. Good agreement was achieved between the strain profiles obtained from DIC measurement and FEA, as plotted in Fig. 13. As demonstrated by the stress profile, for every 2 mm increase along the thickness direction (y axis), the variation of the stress load would be with a range  $\pm 25$  MPa, meanwhile, the constant stress region could extend to around 120 mm along x axis, which could result in a sampling area as 2 mm  $\times$  120 mm.



**Fig. 13** Comparison of strain contours obtained from (a) FEA and (b) DIC measurement on the modified 4BP specimen, and (c) the strain variations as a function of depth from top surface in the center of the specimen subtracted from the strain maps in (a) and (b).

*Stress and strain distributions for the 4pb samples*

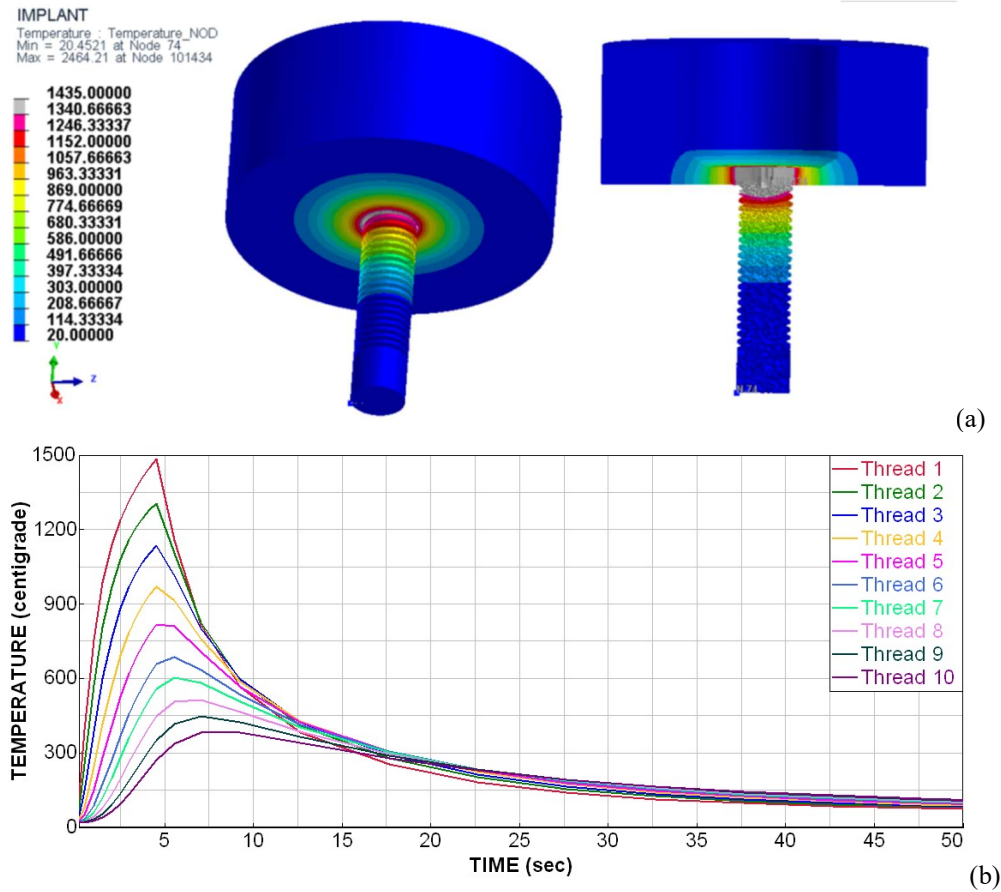
Fig. 14 gives the strain and stress distributions of the 4PB samples. The DIC method was applied to track the strain evolution during the loading process so as to validate the FEA design. As shown in Fig. 14(a), good agreement was achieved between the strain contour obtained from FEA and DIC measurement. The stress contour was given in Fig. 14(b), which indicates a stress variation from compression to tension along the thickness of the sample. The maximum stress locates at the bottom surface of the sample, which is close to 250 MPa. The stress profile along the thickness in center (Fig. 14(c)) also demonstrates the stress gradient.



**Fig. 14** Strain and stress distribution of the loaded 4PB samples. (a) Comparison of the strain field predicted by FEA and DIC. (b) The stress field predicted by FEA. (c) Stress profile along path L. Only half of the specimen was shown due to symmetry.

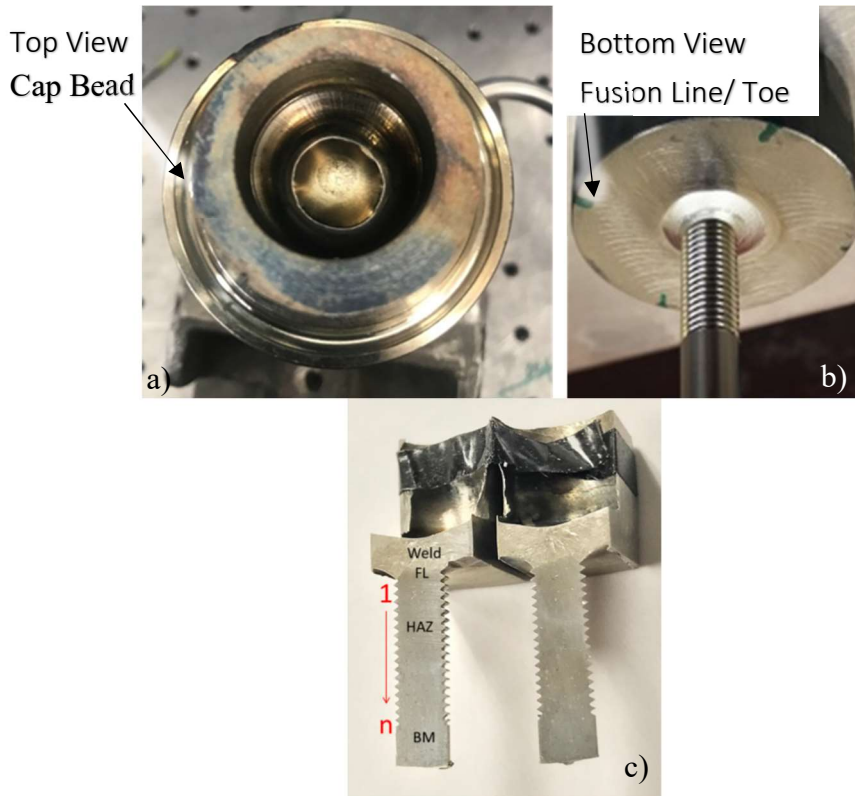
THERMAL HISTORY AND SUSCEPTIBLE MICROSTRUCTURES

Fig. 15 is a temperature contour map generated by SYSWELD showing the specimen in 3D and a cross-section of the specimen at the end of the welding time. Fig. 15(b) is a graph showing the temperature profile at the surface of each thread as a function of time. Fig. 16(a) is a photograph showing the root and cap bead of a completed CEMIT specimen before testing. Fig. 16(b) shows a cross section of a tested specimen. The numbering of the threads begins at the toe of the weld and increases as the distance increases, away from the weld. The fusion line is annotated as (FL), weld metal as (WM), heat affected zone as (HAZ), and base material as (BM), respectively. Where the base metal and the weld metal meet on the surface, this location will be referred to as the toe of the weld. Since the weld is actually a melt-through, this location will be referred to as the root of the weld. The fusion line begins internally in the weld cup and exits towards the threads. Note the smooth wetting angle between the threaded portion of the specimen and the weld cup. Fig. 17 is a series of contour maps showing the development in strain and thermal experience. Note that tensile stresses develop between the fusion line and Thread 8. Compression is observed after Thread 8. By matching the actual



**Fig. 15** (a) Temperature contour maps generated by SYSWELD. Graph showing temperature profile at the surface of each thread as a function of time. (b) Simulated time-temperature profiles for each thread generated by SYSWELD.

fracture location observed in the modified Implant test specimens with the SYSWELD calculated temperature contours, the region where the microstructure was most sensitive to cracking could be identified. Fig. 17(a) show the stress contour maps of the specimen upon release from the fixture after cooling, with clear indication that the specimen is loaded during testing. Note the regions in Threads 5 to 8 that does not stress to the same levels as the upper portions of the threads. High surface and subsurface tension in the specimen close to the fusion line may promote crack opening in this region if the microstructure is predisposed to cracking. Thus, it is important to match the microstructure with the developed stresses to confirm the effect of sensitization. Fig. 17(b) shows the stress contour within the specimen after unloading and then the stress reapplied to 170 MPa. Note that while loading the stress applied is below the yield stress, the stress levels within the first 7 threads reach a level at or above the yield strength due to the residual stresses. This is important since the actual welds within the canister also have residual stress.



**Fig. 16** (a) Photographs showing a completed weld with acceptable appearance viewed from both the top into the weld cup and from the bottom with threaded test region and weld root in view. (b) Photograph showing the cross-section of a completed weld. The weld threads have been numbered beginning at the fusion line and increasing in number as the base material is approached. The weld, fusion line (FL), heat affected zone (HAZ) and base metal (BM) are labelled. Where the base metal and the weld metal meet on the surface, this will be referred to as the toe of the weld. The HAZ is between the fusion line and the base material. This is the region where sensitization occurs. The BM is the material which is unaffected by any processing.

Several implant specimens were produced and tested. Minor corrosion and cracking were observed throughout all of the specimens, and in particular at the base of the threads, the fusion line, and in regions where residual stress and cold work were produced during the machining process. Observation showed that corrosion and SCC occurred in the HAZ, between Threads 5 and 10, which correspond well with the region that experienced between 450 to 850 °C as predicted by the software. Fig. 18 shows two SEM images of the CEMIT specimen. Fig. 18(a) is an image taken at 23x showing indications of corrosion in Threads 6 to 8. Fig. 18(b) is an SEM photograph taken from the cross-section of the same implant specimen in Thread 7. A crack can be observed splitting the grain boundary between the austenite (light color) and the delta Ferrite (darker color). Since the initial processing conditions for wrought 304L includes a water quench, it is reasonable that small amounts of delta ferrite remain in the base material. Using a Feritscope and SEM, it was confirmed that ferrite was present. Small precipitates and carbides were observed decorating the grain

boundary. As shown in Fig. 15(b), Thread 7 reached a peak temperature just below 600 °C. This condition was consistent with that needed for the nucleation and growth of the  $M_{23}C_6$ , thus leading to sensitization and potentially, SCC. The formation of the  $M_{23}C_6$  was verified by performing a selective digestion method and then analysed using XRD. Further verification was performed by creating carbon extraction replicas and observing the precipitates using TEM. The carbides were observed in the etch pits and decorating the grain boundaries. It was found that the carbide morphology was consistent with literature and EDS results were reasonable. While a kinetic model would help to show that favourable conditions existed for the formation of the carbides, this was not the focus of this study. Future work should and will include this type of model.

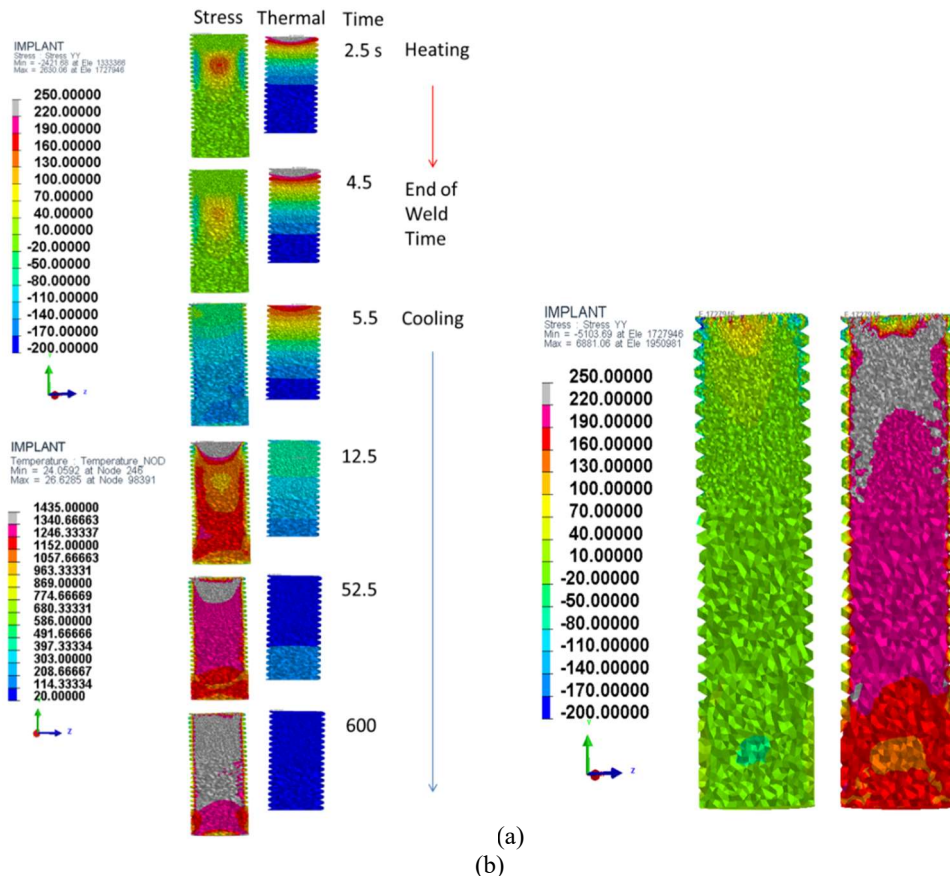


**Fig. 17** (a) Contour maps showing the development in strain and thermal experience (temperature history) along the screw. (b) Stress contour map showing the specimen after welding (L) and upon release from the fixture (R) showing the stress developed upon reloading to 170 MPa.



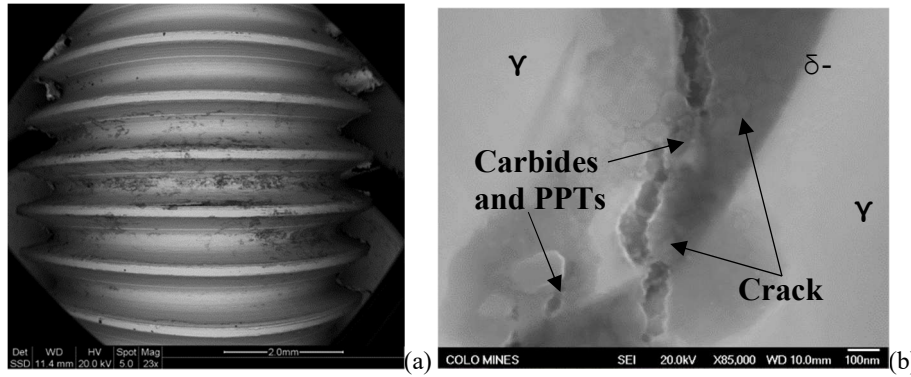


**Fig. 18** (a) SEM image taken at 23X magnification showing corrosion on Threads 5 to 9 from top to bottom. (b) SEM micrograph taken at 85000x showing a crack propagating through the boundary between ferrite and austenite. Note the small carbides decorating the grain boundary.

### CONCLUSIONS

From the numerical studies performed on the canister welding, 4PB test and CEMIT, it was concluded that:

- (1) Based on the thermal and stress results of the CEMIT predicted by the FEA model, the crack initiation site observed in the microscope can be clearly explained. These numerical studies could offer important information about the susceptible microstructure and tensile stresses for the canister, which is meaningful for the future investigation of the initiation and growth rate of CISCC.
- (2) The canister simulation was validated by measured stress data obtained using deep-hole drilling and contour methods. High through-thickness hoop stresses were found within the weld metal (230 to 340 MPa) and HAZ (approximately 200 MPa) in circumferential welds. In comparison, high through-thickness axial stresses were observed in the weld metal (320 to 420 MPa) and HAZ (170 to 200 MPa) in longitudinal welds.
- (3) A 4PB test setup was reasonably designed by FEA and DIC to duplicate the stress conditions in the mockup canister. For every 2mm increase along the thickness direction, the variation of the stress load would be with a range  $\pm 25$  MPa, which could result in a sampling area as 2 mm $\times$ 120 mm.
- (4) Corrosion and cracking was observed in the CEMIT process concentrated within threads 5 to 9. This region falls within the temperature range suitable for the precipitation of the  $M_{23}C_6$  carbides. The combination of this sensitized microstructure, a sufficient load, and the corrosive environment lead to fracture in the CEMIT specimen.

### ACKNOWLEDGEMENTS

This work was supported by the DOE, Nuclear Engineering University Program (NEUP) under grand number DE-NE0008442 of Integrated Research Program (IRP), no. IRP-15-9318. The authors would like to gratefully acknowledge ESI Group for making the SYSWELD software available to the researchers of the Center for Welding, Joining and Coatings Research of the Colorado School of Mines. Their technical support and discussion are also kindly appreciated.

### REFERENCES

- [1] R. M. KAIN: 'Marine Atmospheric Stress Corrosion Cracking of Austenitic Stainless Steels', *Materials Performance*, Vol. 29, No. 12, pp. 60-62, 1990.
- [2] D. G. ENOS, C. R. BRYAN and K. M. NORMAN: 'Data Report on Corrosion Testing of Stainless Steel SNF Storage Canisters', *FCRD-UFD-2013-000324*, U.S. Department of Energy, Office of Used Nuclear Fuel Disposition, 2013.
- [3] C. R. BRYAN and D. G. ENOS: 'Analysis of Dust Samples Collected from Spent Nuclear Fuel Interim Storage Containers at Hope Creek, Delaware, and Diablo Canyon, California', *SAND2014-16383*, Albuquerque, NM, Sandia National Laboratories, 2014.
- [4] C. R. BRYAN and D. G. ENOS: 'Analysis of Dust Samples Collected from an Unused Spent Nuclear Fuel Interim Storage Container at Hope Creek, Delaware', *SAND2015-1746*, Albuquerque, NM, Sandia National Laboratories, 2015.
- [5] A. KOSAKI: 'Evaluation method of corrosion lifetime of conventional stainless steel canister under oceanic air environment', *Nuclear Engineering and Design*, Vol. 238, No. 5, pp. 1233-1240, 2008.
- [6] NUCLEAR REGULATORY COMMISSION (NRC): 'Finite Element Analysis of Weld Residual Stresses in Austenitic Stainless Steel Dry Cask Storage System Canisters', *NRC Technical Letter Report (ADAMS ML13330A512)*, Washington, D.C., 2013.
- [7] D. G. ENOS and C. R. BRYAN: 'Characterization of Canister Mockup Weld Residual Stresses', *FCRD-UFD-2016-000064*, *SAND2016-12375 R*, Albuquerque, NM, Sandia National Laboratories, 2016.
- [8] D. DEAN and M. HIDEKAZU: 'Numerical simulation of temperature field and residual stress in multi-pass welds in stainless steel pipe and comparison with experimental measurements', *Computational Materials Science*, Vol. 37, No. 3, pp. 269-277, 2006.
- [9] C. LIU, J. X. ZHANG and C. B. XUE: 'Numerical investigation on residual stress distribution and evolution during multi-pass narrow gap welding of thick-walled stainless steel pipes', *Fusion Engineering and Design*, Vol. 86, No. 4-5, pp. 288-295, 2011.
- [10] J. GOLDAK, A. CHAKRAVARTI and M. BIBBY: 'A new finite element model for welding heat sources', *Metall Trans B*, Vol. 15, No. 2, pp. 299-305, 1984.
- [11] X. WU, Z. YU: 'Final Report: Weld Residual Stress Analysis in the Canister Mockup', *DE-NE0008442 of Integrated Research Program No. IRP-15-9318*, Golden, CO, Colorado School of Mines, 2018.
- [12] H. GRANJON: 'The Implants Methods for Studying the Weldability of High Strength Steels', *Metal Construction and British Welding Journal*, Vol. 1, No. 11, pp. 509-515, 1969.
- [13] J. M. SAWHILL, JR., A. W. DIX, W. F. SAVAGE: 'Modified Implant Test for Studying Delayed Cracking', *Welding Journal*, Vol. 53, No. 12, pp. 554-s-559-s, 1974.



# COMPUTATIONAL ANALYSIS OF THE YIELD STRESS OF ULTRA-HIGH STRENGTH ALL- WELD METALS

D. ZÜGNER\*<sup>+</sup>, S. HOLLY\*\*, W. ERNST\*\*\*, R. SCHNITZER\*\*\*\*  
and E. KOZESCHNIK\*

*\* Institute of Materials Science and Technology, TU Wien, 1060, Vienna, Austria*

*\*\* voestalpine Böhler Welding Austria GmbH, 8605, Kapfenberg, Austria; now at: voestalpine Wire Technology GmbH,  
8600, Bruck an der Mur, Austria*

*\*\*\* voestalpine Stahl GmbH, 4020, Linz, Austria*

*\*\*\*\* Department of Physical Metallurgy and Materials Testing, Montanuniversität Leoben, 8700, Leoben, Austria  
+ corresponding author, dominik.zuegner@tuwien.ac.at*

DOI 10.3217/978-3-85125-615-4-13

## ABSTRACT

Lightweight constructions providing a high yield stress play a crucial role in transportation systems and steel constructions optimized for low energy consumption. For the fabrication of such components, the development of matching welding consumables is an essential task. In this investigation, the aim is to understand the influence of different alloying elements on the strength of all-weld metal samples of ultra-high strength filler metals with a yield strength of 1100 MPa. In the end, this should provide insight into the operating mechanisms providing the desired strength and make it possible to predict the expected yield stress with reasonable accuracy.

Apart from precipitation and solid solution strengthening, special attention is paid to the contributions of dislocation hardening and grain boundary strengthening, since these are expected to be the major contributors to the overall strength in a predominantly martensitic structure. In order to apply those classical strengthening mechanisms to the specific microstructure of martensite, additional considerations have to be made concerning the effective grain size and initial dislocation density used for calculation. Finally, the developed model is tested and the results are compared with over 90 actually produced and measured alloys.

Keywords: yield strength, welding, simulation

## INTRODUCTION

In today's world there is an ever growing need for high strength materials in order to fulfil the demand for lightweight, energy-saving constructions. With this arises a need for high-strength filler materials to join those metals. Up until now, those filler metals are available with a yield strength of up to 960 MPa and the aim of the project was to develop a new material that can provide a yield strength of at least 1100 MPa. Since the process of producing flux cored wire samples, fabricating all-weld-metal samples and mechanically testing them can be rather cumbersome, consuming both time and funds, thermokinetic simulations are employed to assess the achievable yield strength.

The simulation itself is carried out using the software package MatCalc and is split into two major parts. The first part is the simulation of the solidification process using the Scheil-Gulliver method, which not only yields the fraction but also the chemical composition of all phases that form during this early stage. These results are then transferred to the second part of the simulation, which is a complete thermokinetic simulation considering precipitation kinetics, grain size and dislocation density evolution under the given heat treatment which has been recorded during the welding process. These microstructural parameters are then used to calculate the overall yield strength of the material by employing the four classical strengthening mechanisms of grain size strengthening, dislocation strengthening, solid solution strengthening and precipitation strengthening. Considerations have been made to account for the effective grain size and dislocation density in the case of a martensitic microstructure. These simulations are then compared with over 90 different alloys that actually have been produced, welded and tested.

### STATE OF THE ART

The plastic deformation of metals is dependent on the movement of dislocations throughout the material and there are various mechanisms at work that interact with these movements in one way or another. Besides the intrinsic strength of the perfect lattice, there are usually four individual strengthening mechanisms: solid solution strengthening ( $\tau_{SS}$ ), grain refinement ( $\tau_{gb}$ ), dispersion (or precipitation) strengthening ( $\tau_p$ ) and work (or dislocation) hardening ( $\tau_{disl}$ ). In the following sections, consideration is given to each of these strengthening mechanisms and their ability to increase the applied stress required for the onset of plastic deformation.

### SOLID SOLUTION STRENGTHENING

According to Bhadeshia and Honeycombe [1], misfitting solute atoms can interfere with the motion of dislocations by the strain fields they create around them and this mechanism is called solid solution strengthening. Substitutional alloying elements (e.g. silicon, manganese) cause local expansions or contractions in the lattice. These are isotropic strains and thus they only interact with the hydrostatic components of the strain fields of dislocations.

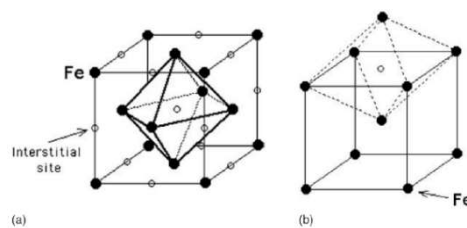


**Fig. 1** (a) The regular octahedron interstice in austenite. (b) Octahedral interstice in ferrite - notice that two of the axes are longer than the third (vertical axis). This leads to a tetragonal distortion when the site is occupied by carbon [1].

Whereas interstitial atoms located at the irregular octahedron interstices in the ferritic structure cause a tetragonal distortion (Figure 1) that has a strong interaction with the shear stress, which is the dominant component of a dislocation strain field. In this lies the main reason, why interstitial solid solution strengthening is so much more potent in ferrite. The corresponding interstitial site in the austenite structure is the regular octahedron. An interstitial atom in austenite therefore acts like a substitutional element, providing only hydrostatic strain in the nearby area. This is why carbon is much less effective in strengthening austenite.

Like described by Hornbogen and Warlimont [2], because of the different sizes and other atomic parameters of the solute atoms, local strain fields are introduced to the lattice which can effectively increase the resistance to plastic deformation. The effect of atomic size differences, commonly expressed by an atomic misfit parameter  $\delta$  is defined as

$$\delta = \frac{1}{a} \frac{da}{dc}, \quad (1)$$

where  $a$  is the lattice constant and  $c$  is the concentration of the solute atom in the matrix. Analogously, the shear modulus effect can be expressed as

$$\eta = \frac{1}{G} \frac{dG}{dc}, \quad (2)$$

where  $G$  is the shear modulus. To determine the strength increase by solid solution strengthening, the general formulation

$$\Delta\tau_{ss} \sim \left( \sqrt{\delta^2 + \eta^2} \right)^m \cdot c^n \quad (3)$$

may be used. In equation (3),  $m$  is an interaction exponent between 1 and 2 ([2], [3]) and  $n$  a concentration exponent, generally between 1/2 and 1 [2–9] depending on the solute concentration and temperature [6]. In literature [10–15], it is also found that the first term in equation (3) containing the atomic misfit parameter  $\delta$  as well as the modulus mismatch parameter  $\eta$  and the exponent  $m$  is replaced by a constant strengthening coefficient  $k$  which only depends on the solute element itself and the lattice (bcc/fcc) it is dissolved in. Therefore equation (3) reduces to

$$\Delta\tau_{ss} = k \cdot c^n. \quad (4)$$

#### PRECIPITATION STRENGTHENING

As adequately described by Bhadeshia [1], in general there is more than one phase present in steel and the matrix is further strengthened by controlling the dispersion of these other phases in the microstructure – an effect called precipitation or dispersion strengthening. The most common other phases are carbides which are a result of the low solubility of carbon in  $\alpha$ -iron. In plain carbon steel this carbide usually is  $\text{Fe}_3\text{C}$  (cementite) and it can occur in a wide range of structures, from a coarse lamellar form (pearlite), to fine rod or spheroidal precipitates (tempered steels). However in alloyed steel, the same variety of structures is observed, with the exception that usually the iron carbide is replaced by other

carbides which are thermodynamically more stable. Other dispersed phases that can be encountered include nitrides and intermetallic compounds. For the case of fine particles, ideally small spheres that are randomly dispersed in the matrix, there are well-defined relationships between the yield stress and the parameters of the dispersion.

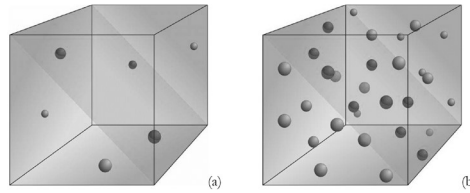


**Fig. 2** Schematic illustrations of an intersected dislocation glide plane by second phase particles [16].

The effect of these densely distributed particles on the mechanical properties of the material (i.e. yield strength) is due to those precipitates acting as obstacles intersecting the glide plane of a dislocation, as can be schematically seen in Figure 2 (a) and (b). It becomes apparent that the amount of strengthening that can be achieved by dispersed second phase particles is directly related to the amount of precipitates intersecting the glide plane of a dislocation, which can be represented by the inter-particle distance. The model used for precipitations strengthening in *MatCalc* is very well described in the work of Ahmadi [17], a very simplified version of which will be outlined here.

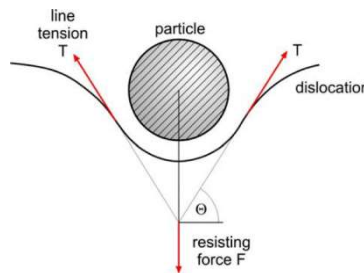


**Fig. 3** General illustration of the particle-dislocation interaction. Balance of forces acting during particle resistance to dislocation movement [16].

In order to determine the absolute contribution of precipitation strengthening to the overall yield strength, the nature of the interaction between the moving dislocation and the dispersed particles must be considered. When a single dislocation encounters a second phase particle while moving through the glide plane of a stressed metal (see Figure 3), the precipitate-dislocation interaction can be described in the most general form as

$$F = 2T \sin \theta , \quad (5)$$

where  $T$  is the line tension of the dislocation section and  $F$  is the resistance force of the dispersed particle [18]. With increasing resistance force  $F$ , the dislocation gets bowed more or in other words  $\theta$  increases. In dependence of the strength of the second phase particles characterized by the resistance force  $F$ , two major cases of particle-dislocation interaction can be determined - hard and weak particles [16].

The dislocation line tension (per unit length of dislocation) has been calculated by Cottrell [19] and Foreman [20] as

$$E(\theta) = \frac{Gb^2}{4\pi} \left( \frac{1 - \nu(\cos \theta)^2}{1 - \nu} \right) \ln \left( \frac{r_o}{r_i} \right), \quad (6)$$

where  $G$  is the shear modulus,  $\theta$  is the angle between the dislocation line and its Burgers vector,  $b$  is the magnitude of the Burgers vector,  $\nu$  is Poisson's ratio and  $r_o$ ,  $r_i$  is the outer and inner cut-off distance respectively [17]. Ahmadi finally formulates the line tension as

$$T(\theta) = \frac{Gb^2}{4\pi} \left( \frac{1 + \nu - 3\nu(\sin \theta)^2}{1 - \nu} \right) \ln \left( \frac{r_o}{r_i} \right). \quad (7)$$

For the case of shear-able particles, the shear stress can then be formulated as

$$\tau = \frac{2T(\theta)}{bL_s} \left( \frac{F_m}{2T(\theta)} \right)^{\frac{2}{3}}, \quad (8)$$

with  $L_s$  being the surface to surface distance between two precipitates along the dislocation, and  $F_m$  is the maximum resistance force of the precipitate in different mechanisms. And for the case of non-shear-able precipitates, the shear stress can be written as

$$\tau_{\text{Orowan}} = \frac{JGb}{2\pi\sqrt{1-\nu}L_s} \ln \left( \frac{2r_s}{r_i} \right), \quad (9)$$

where  $J$  is a correction constant for random arrangement of particles instead of ordered, periodic arrangement (=0.8 or 1) and  $r_s$  is the equivalent radius of the precipitate in different models. For a more detailed and complete description of the model please refer to [17], [21], [22].

The mechanisms that contribute to strengthening include coherency strengthening, which arises from the coherency strains developed in the matrix around a coherent particle, chemical hardening, which relates to the development of antiphase boundaries when a dislocation cuts through a precipitate, and dispersion hardening, which arises from looping of the dislocation between hard non-deformable particles as described by Orowan [23].

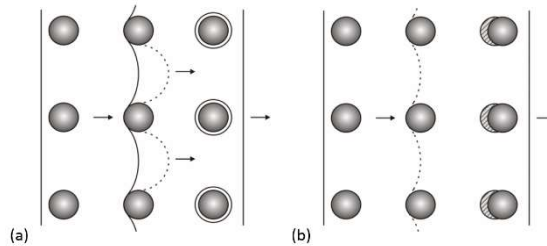


**Fig 4** Particle-dislocation interaction for hard (a) and weak (b) particles [16].

Holzer [16] summarizes the two cases described by Ahmadi [17] as follows. If the strength (i.e. the resistance force  $F$ ) of the dispersed particle exceeds twice the line tension



of the dislocation ( $F \geq 2T, \theta = 90^\circ$ ), the particle will not be cut through or sheared by the dislocation. Therefore the obstacle is denoted as a strong particle. In this case, the dislocation may bypass the precipitate either by the Orowan mechanism or cross slip. The second phase particle will remain unchanged, namely non-deformed (Figure 4 (a)), thus the properties of the precipitate will not affect the amount of precipitation strengthening exerted by it. In contrary if the precipitates are weak ( $F < 2T, \theta < 90^\circ$ ) and therefore sheared by the dislocation, the particle will deform as can be seen schematically in Figure 4 (b). In this case the properties of the second phase particles will strongly affect the amount of precipitation strengthening and numerous effects may be involved in raising the stress required for yielding related to phenomena like chemical strengthening, coherency strengthening or modulus mismatch hardening.

#### GRAIN BOUNDARY STRENGTHENING

For a basic description of the effect of grain size refinement of ferrite, which represents one of the most important strengthening routes in the heat treatment of steel, we will resort to the work of Bhadeshia [1] once more. The first scientific analysis of the relationship between grain size and strength, performed by Hall and Petch, led to the famous Hall-Petch relationship between the grain diameter  $d$  and the yield stress  $\sigma_y$ ,

$$\sigma_y = \sigma_0 + k_y d^{-\frac{1}{2}}, \quad (10)$$

where  $\sigma_0$  and  $k_y$  are constants. This type of relationship has been confirmed to be appropriate for a wide range of steels as well as for many non-ferrous metals and alloys. The term  $\sigma_0$  is called friction stress and it represents the stress required to move free dislocations along the slip planes in the bcc crystals, and can also be seen as the yield stress of a single crystal ( $d^{-\frac{1}{2}} = 0$ ). This friction stress is particularly sensitive to temperature and chemical composition. The constant  $k_y$  represents the slope of the  $\sigma_y$ - $d^{-\frac{1}{2}}$  plot which has been found to be insensitive to temperature, chemical composition and strain rate. In agreement with the Cottrell-Bilby theory of the yield point involving the unpinning of dislocations from interstitial carbon atmospheres,  $k_y$  has been referred to as the unpinning parameter. Nevertheless, the fact that  $k_y$  is not sensitive to temperature suggests that unpinning rarely occurs, and emphasizes the theory that new dislocations are generated at the yield point. That statement is consistent with the theories that explain the yield point in terms of the movement of new dislocations, the velocities of which are stress dependent.

For the strength contribution by grain refinement in the case of all weld metals, which in our case consist of a primarily martensitic microstructure, attention has to be paid to what effective grain size is used for the Hall-Petch relationship. There is a strong relationship between the prior austenite grain size and the hierarchical microstructure of lath-martensite (Figure 5) as reported by Galindo-Nava et al. [24]. The interesting conclusion concerning this relationship will be outlined in the following.

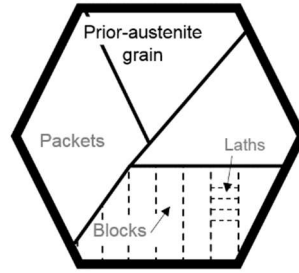


**Fig. 5** Hierarchical microstructure of martensite. The prior austenite grains contain packets, which consist of blocks of laths [24].

Martensite packets are formed by laths sharing a common habit plane, with four possible variants of the  $\{1\ 1\ 1\}_\gamma$  planes in the Kurdjumov-Sachs (K-S) relation, the number of packets per austenite grain is equal to  $N_p = 4$ . Additionally the strain controlling the martensitic transformation is composed by a dilatation, remaining constant for each K-S relation, and a shear strain differing from each variant [25]. This means that all six lath orientation variants in a given packet should be present in order to minimize the elastic energy and decrease the overall strain. This indicates that the possible number of blocks per packet should be  $N_b = 6$  [24]. Combining these results the packet and block size in dependence of the austenite grain diameter ( $D_g$ ) should be equal to

$$d_{\text{packet}} = \sqrt{\frac{3\sqrt{3}}{8N_p}} D_g = \sqrt{\frac{3\sqrt{3}}{32}} D_g = 0.40D_g , \quad (11)$$

$$d_{\text{block}} = \frac{1}{N_b} d_{\text{packet}} = \frac{1}{6} d_{\text{packet}} = 0.067D_g .$$

We used an effective block size of  $0.067D_g$  in accordance with equation (10) upon the transformation to martensite for our calculations.

#### DISLOCATION STRENGTHENING

Strengthening by dislocation represents another very important route when trying to increase the strength of steel, bearing a tremendous potential. In fact, plain carbon steel can be raised to strength levels above  $1500\text{ Nm}^{-2}$ , without the addition of special alloying elements, simply by the phenomenon of work hardening [1]. Despite the fact that the weld joint is not subjected to any external mechanical deformations, the transformation to the martensitic structure introduces internal stress and deformation and therefore work hardening or dislocation strengthening can and should not be neglected.

The strength increase by dislocation hardening can be determined according to the formulation of Taylor ([13], [26], [27])

$$\tau_{\text{disl.}} = \alpha \cdot G \cdot b \cdot \sqrt{\rho} , \quad (12)$$

## Mathematical Modelling of Weld Phenomena 12

where the strength contribution  $\tau_{disl}$  is a function of the shear modulus  $G$ , the Burgers vector  $b$ , the free dislocation density  $\rho$  and  $\alpha$  which is a constant. The initial dislocation density  $\rho_0$  is taken from a formulation by Takahashi and Bhadeshia [28]

$$\log \rho_0 = 9.28480 + \frac{6880,73}{M_S} - \frac{1780360}{M_S^2}, \quad (13)$$

where  $M_S$  is the martensite start temperature in °C, which can also be calculated empirically using any of the available regressions, i.e. the one by Arjomandi et al. [29].

After the transformation, the dislocation density is assumed to evolve under the given heat treatment according to the approach proposed by Sherstnev et al. [30], adapted by Buker and Kozeschnik [31], that describes the rate of the total dislocation density evolution  $\dot{\rho}$  as

$$\dot{\rho} = \frac{M\sqrt{\rho}}{Ab} \dot{\phi} - 2B \frac{d_{ann}}{b} \rho M \dot{\phi} - 2CD_{Dis} \frac{Gb^3}{k_B T} (\rho^2 - \rho_{RS}^2), \quad (14)$$

with the Taylor factor  $M$ , the Burgers vector  $b$ , the critical dislocation annihilation distance  $d_{ann}$ , the substitutional self-diffusion coefficient at dislocations  $D_{Dis}$ , the strain rate  $\dot{\phi}$ , the amount of geometrically necessary dislocations  $\rho_{RS}$  and material parameters  $A$ ,  $B$  and  $C$ .

### SCHEIL GULLIVER ANALYSIS

Primary precipitates are particles that form during the solidification process of the weld metal. They are usually of rather large size and do not participate in any further reactions, therefore it is assumed that they do not significantly contribute to dispersion strengthening. However their formation does alter the chemical composition of the remaining material thus they should be taken into account.

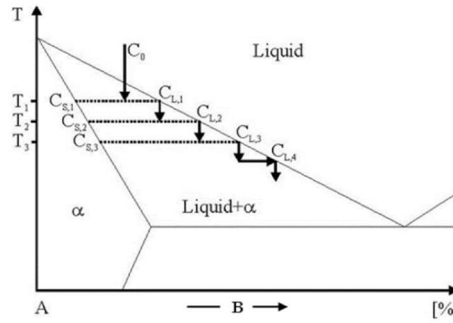


**Fig. 6** Scheme of Scheil solidification of a hypothetical Fe-C alloy. During solidification the actual liquid phase, beginning with  $C_0$ , is undercooled and solidifies according to the lever rule enriching the liquid phase with solute atoms [32].

By employing the Scheil-Gulliver analysis, it is possible to calculate the fraction and composition of all phases during solidification step by step from the liquidus temperature

to the temperature where solidification of the residual liquid phase occurs [33]. The residual liquid fraction at final solidification depends on the cooling rate. Higher cooling rates in general lead to higher fractions, whereas low rates of cooling enable the liquid film to become very thin and the residual liquid enriches more than in the case of higher fraction residual liquid at solidification. Figure 6 schematically shows how the Scheil-Gulliver analysis is performed. Liquid metal with the initial composition  $C_0$  is undercooled which leads to a local equilibrium and the formation of a solid fraction with the composition  $C_{S,1}$  and a liquid fraction with the composition  $C_{L,1}$  (with the ratio between liquid and solid following the lever rule). Due to their low mobility in the solid phase, the diffusion of substitutional elements is halted from this point on, but it is assumed that the interstitial elements (i.e. carbon, nitrogen and boron) are still mobile in both phases which causes back-diffusion of those atoms, striving for an equilibrium between the liquid and solid phase. Then this process is repeated with the concentration  $C_{L,1}$  and so on and so forth.

## EXPERIMENTAL

### MATERIALS AND WELDING

All materials used for the experiments and simulations were experimental alloys that were fabricated during the development of the new filler material at the *voestalpine Böhler Welding* GmbH. To give the reader an idea as to what materials we are dealing with here, Table 1 contains approximate ranges for the content of each chemical element.

**Table 1** Approximate chemical composition of all alloys.

<b>Element</b>	<b>Content range in wt%</b>
<b>C</b>	0.05 - 0.15
<b>N</b>	0.00 - 0.03
<b>Si</b>	0.20 - 0.80
<b>Mn</b>	0.80 - 2.10
<b>P</b>	0.00 - 0.01
<b>Cr</b>	0.11 - 0.98
<b>Mo</b>	0.00 - 0.78
<b>Ni</b>	0.99 - 3.20
<b>Nb</b>	0.00 - 0.07
<b>V</b>	0.10 - 0.34
<b>W</b>	0.00 - 0.02
<b>Cu</b>	0.00 - 0.81
<b>Co</b>	0.00 - 0.35
<b>Ti</b>	0.00 - 0.11
<b>As</b>	0.00 - 0.01
<b>Sn</b>	0.00 - 0.01
<b>Zr</b>	0.00 - 0.01
<b>Sb</b>	0.00 - 0.01
<b>B</b>	0.00 - 0.01
<b>Al</b>	0.00 - 0.01

As described in other publications within this project ([34] and [35]), numerous metal-cored wires with different chemical compositions were produced and samples were welded. All-weld metal samples were prepared in accordance with EN 15792-1 in position PA using Ar + 18 % CO<sub>2</sub> as shielding gas. They were fabricated with eight weld passes, each consisting of three beads. The welding parameters are shown in Table 2. S235 was used as base material and three layers were applied as buffer.

**Table 2** Welding parameters used.

Current [A]	Voltage [V]	Welding speed [mm/min]	Heat input per unit length [kJ/mm]	Interpass-temperature [°C]
250	26.5	550	0.71	150

MECHANICAL TESTING

The welded samples for mechanical testing were subjected to a soaking heat treatment at 150°C for 16 h according EN ISO 15792-1. Tensile and charpy V impact toughness testing were performed on all-weld samples. The tensile tests were carried out on single specimens and were done at ambient temperature in accordance to EN ISO 6892-1. The impact tests were conducted on three samples in order to get a set of statistics. Impact tests of samples were performed at ambient temperature and -20°C defined by EN ISO 9016. See also [34].

SIMULATION

THERMOKINETIC CALCULATIONS USING MATCALC

All simulations were conducted using the thermokinetic software package *MatCalc* ([36], [37]), version 6.00.0218, utilizing CALPHAD-type [38] Gibbs energies (database: 'mc\_fe.tdb') to calculate chemical potentials, driving forces for precipitation and interfacial energies. A script is used for all calculations, performing a Scheil-Gulliver analysis for the solidification process followed by a precipitation kinetics simulation under the given heat treatment which can be seen in Figure 7. The peaks of reheating after the initial cooling are due to the passing of additional weld beads. This temperature evolution has been recorded with a thermocouple placed within the first welding seam.

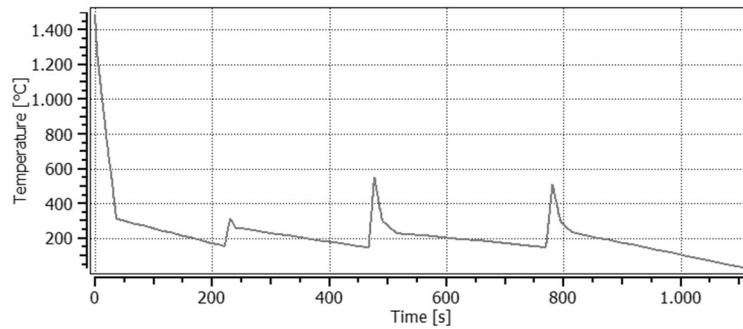


**Fig. 7** Evolution of temperature used for simulations in *MatCalc*.

The individual strength contributions, namely solid solution strengthening ( $\tau_{ss}$ ), grain refinement ( $\tau_{gb}$ ), dispersion (or precipitation) strengthening ( $\tau_p$ ), work (or dislocation)

hardening ( $\tau_d$ ) and intrinsic lattice strength ( $\tau_i$ ) are summed up in *MatCalc* in the following way

$$\tau = (\tau_A^\alpha + \tau_B^\alpha)^{\frac{1}{\alpha}}, \quad (15)$$

where  $\tau_A$  equals  $\tau_d$  and  $\tau_B = \tau_i + \tau_{ss} + \tau_p + \tau_{gb}$ . The factor  $\alpha$  is set to a value of 1.8.

The parameters used for the simulation, including values for solute drag and others are summarized in Table 3. Additional settings include activated back-diffusion for carbon, nitrogen and boron during Scheil calculation, phases include AlN, cementite and composition sets for TiN, TiC, NbN, NbC and VCN, for evolution of grain size the multi-class model was used. The amount of primary precipitates is directly imported from the Scheil calculation.

## Mathematical Modelling of Weld Phenomena 12

**Table 3** Parameters used for the MatCalc simulation.

Parameter	Value	Unit	Description
$T_{S,s}$	<b>1600</b>	°C	Starting temperature for Scheil analysis
$T_{S,f}$	<b>1000</b>	°C	Finish temperature for Scheil analysis
$T_{S,st}$	<b>1.0</b>	°C	Step value for Scheil analysis
$f_{res.liq.}$	<b>0.03</b>	–	Residual liquid fraction at which to stop Scheil
$r_{prim.}$	<b>600E-9</b>	<i>m</i>	Radius of primary precipitates from Scheil
$D_{\gamma}$	<b>10E-6</b>	<i>m</i>	Starting grain diameter for austenite
$V_{mis.,Cem.}$	<b>0.01</b>	–	Volumetric misfit of cementite
$V_{mis.,NbC}$	<b>0.1</b>	–	Volumetric misfit of NbC
$V_{mis.,NbN}$	<b>0.1</b>	–	Volumetric misfit of NbN
$V_{mis.,TiC}$	<b>0.05</b>	–	Volumetric misfit of TiC
$V_{mis.,TiN}$	<b>0.05</b>	–	Volumetric misfit of TiN
$V_{mis.,AlN}$	<b>0.27</b>	–	Volumetric misfit of AlN
$V_{mis.,VCN}$	<b>0.03</b>	–	Volumetric misfit of V[C,N]
$T_{crit.,TiN}$	<b>4000</b>	°K	$T_{crit.}$ for diffuse interface effect of TiN
$T_{crit.,TiC}$	<b>3500</b>	°K	$T_{crit.}$ for diffuse interface effect of TiC
$T_{crit.,NbN}$	<b>3360</b>	°K	$T_{crit.}$ for diffuse interface effect of NbN
$T_{crit.,NbC}$	<b>3500</b>	°K	$T_{crit.}$ for diffuse interface effect of NbC
$T_{crit.,VCN}$	<b>2425</b>	°K	$T_{crit.}$ for diffuse interface effect of V[C,N]
$\dot{\epsilon}_{\gamma}$	<b>1E-3</b>	$s^{-1}$	Assumed strain rate of weld joint during cooling
$A_{SLK,fcc}$	<b>33</b>	–	A-parameter for evolution of $\rho$ in fcc
$B_{SLK,fcc}$	<b>-0.646 ln <math>\dot{\epsilon}_{\gamma}</math> + 7.5</b>	–	B-parameter for evolution of $\rho$ in fcc
$C_{SLK,fcc}$	<b>5E-5</b>	–	C-parameter for evolution of $\rho$ in fcc
$A_{SLK,bcc}$	<b>30</b>	–	A-parameter for evolution of $\rho$ in bcc
$B_{SLK,bcc}$	<b>2</b>	–	B-parameter for evolution of $\rho$ in bcc
$C_{SLK,bcc}$	<b>1e-3</b>	–	C-parameter for evolution of $\rho$ in bcc
$S_{SLK}$	<b>33</b>	–	Similitude-parameter for evolution of $\rho$
$k_d$	<b>2.0</b>	–	$k_d$ parameter for evolution of $\rho$
$k_r$	<b>1.5</b>	–	$k_d$ parameter for evolution of $\rho$
$CLS_V$	<b>1500</b>	<i>J/mol</i>	Interaction energy for solute drag of V
$CLS_{Ti}$	<b>12000</b>	<i>J/mol</i>	Interaction energy for solute drag of Ti
$CLS_{Nb}$	<b>18000</b>	<i>J/mol</i>	Interaction energy for solute drag of Nb
$CLS_{Mo}$	<b>9000</b>	<i>J/mol</i>	Interaction energy for solute drag of Mo
$CLS_{Mn}$	<b>6000</b>	<i>J/mol</i>	Interaction energy for solute drag of Mn
$CLS_{Si}$	<b>2500</b>	<i>J/mol</i>	Interaction energy for solute drag of Si
$CLS_{Ni}$	<b>3000</b>	<i>J/mol</i>	Interaction energy for solute drag of Ni
$CLS_{Cr}$	<b>3000</b>	<i>J/mol</i>	Interaction energy for solute drag of Cr



## RESULTS

### COMPARISON OF CALCULATED AND MEASURED VALUES

A comparison of measured and simulated values for the yield strength can be found in Figure 8.

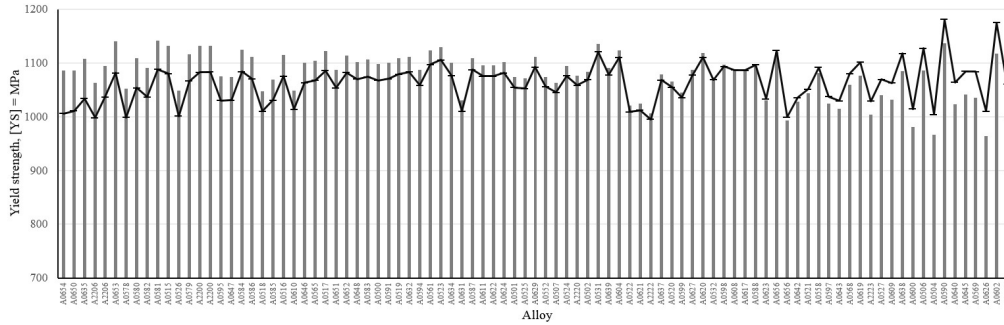


**Fig. 8** Comparison of measured (bars) and calculated (line) values for the yield strength.

There was an overall good agreement between measured and calculated values, with an approximate mean deviation of 3% for the values shown in Figure 8. Although the ductility of the samples was measured, it was not simulated due to the much more complex nature of fracture.

### EXEMPLARY SIMULATION RESULTS

This section shows some detailed simulation results for a selected alloy to give an impression as to how some parameters evolve during the initial cooling and reheating of the weld joint. Exemplary results for the simulation of the solidification process with the formation of primary precipitates by the means of a Scheil-Gulliver analysis are found in Figure 9.

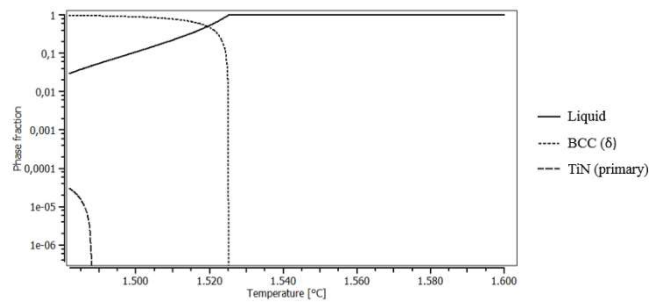


**Fig. 9** Results of the Scheil-Gulliver analysis.

The only primary precipitate that forms in the investigated alloys is titanium nitride. This result is then transferred to the precipitation simulation, the results of which follow. The

simulated phase fraction of all phases with a greater fraction than  $1E-8$  and the evolution of temperature, in other words the heat treatment, can be seen in Figure 10. In this context, (dis) means nucleation at dislocations in the bulk and (gb) means nucleation at grain boundaries.

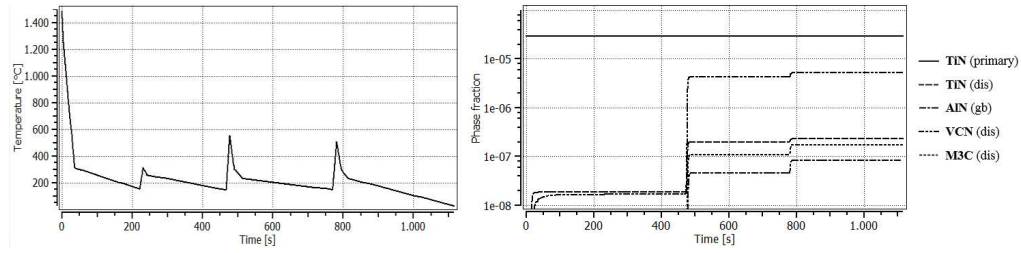


**Fig. 10** Heat treatment (left) and simulated evolution of phase fractions (right).

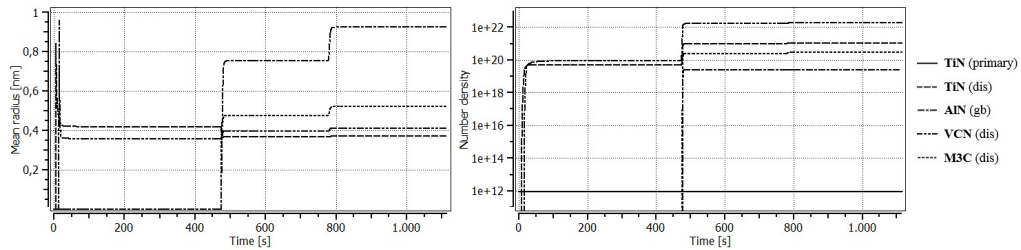


**Fig. 11** Simulated mean radii of precipitates (left) and number densities (right).

For the development of the mean grain diameter within the first minute please refer to Figure 12. Please note that upon transformation to martensite (at approximately 34 seconds) the diameter switches according to equation (11).

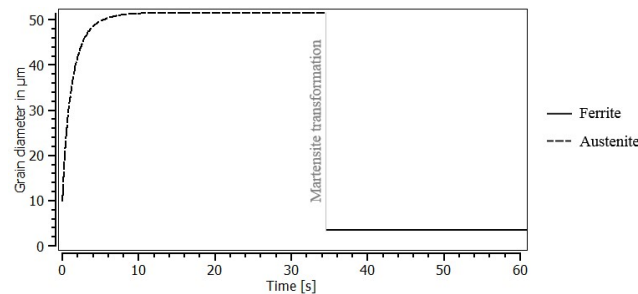


**Fig. 12** Evolution of mean grain diameter in austenite (multi-class) and transformation to martensite.

Finally, the simulated evolution of the total dislocations density and the total calculated yield strength with all contributions (excluding intrinsic lattice strength – which is constant anyways) can be seen in Figure 13.

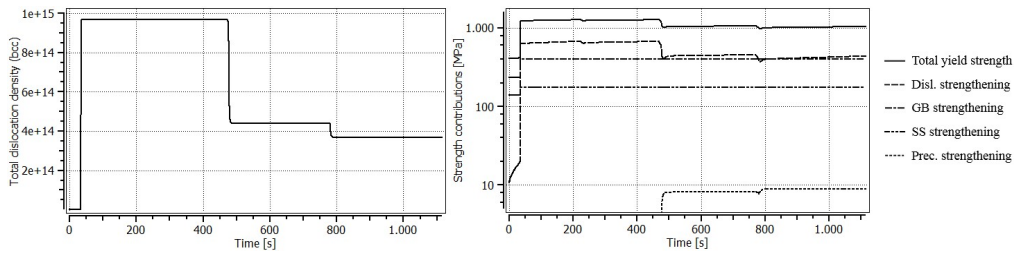


**Fig. 13** Simulated total dislocation density (left) and simulated total yield with individual contributions (right).

## DISCUSSION

The overall agreement of simulated values for the yield stress with the measured ones was good. However there were still some extreme outliers, some of which were not included in the evaluation and most of these can be attributed to fluctuations besides chemical composition, like deviations in the welding parameters for example. Therefore it would be advisable to employ robotic welding for fabrication of the samples in the future.

Simulations of the solidification process via the Scheil-Gulliver method have revealed that the only primary precipitates in these alloys were titanium nitride which can be explained by the low solubility product compared to other nitrides and carbides and a high affinity of titanium to nitrogen. It is assumed that those precipitates do not participate in any further reactions due to their large size and therefore their number density and phase fraction remains constant.

As for the precipitation kinetics simulations, when looking at Figure 10 it becomes apparent that especially the peaks of reheating after the initial cooling of the weld, which are due to the passing of additional weld beads in proximity to the first one, have a high impact on the outcome of the calculation. This fact can be seen in Figure 10 on right side where especially the first peak that exceeds temperatures over 500°C increases the phase fraction of certain precipitates by two to three orders of magnitude. Nevertheless we are dealing with a relatively low alloying content in these welds and a fast initial cooling rate which results in a very small precipitate size but higher number densities as depicted in Figure 11. The approach to assess the yield stress contribution of martensite by its grain size and high dislocation density (Figure 12 and Figure 13 left) is yielding good overall results. It is noteworthy that that plateau value of the austenite grain size is not really depending on the chosen initial grain size, within reasonable boundaries of course. Obviously these two mechanisms are the dominating ones in this model, followed by solid solution strengthening and lastly precipitation strengthening (Figure 13 right). For investigations to come, additional attention should be paid to the development of the grain size and the model should be calibrated and adjusted with extensive measurements of the prior austenite grain size and the martensite block size. It might also be advisable to exclude geometrically necessary dislocations from the strength contribution by dislocation strengthening, since those are already considered by grain size strengthening.

### SUMMARY AND CONCLUSION

Thermokinetic simulations using MatCalc provide a very useful tool for the development of new filler materials since they not only provide a reasonable assessment of the overall strength that can be achieved with a specific chemical composition but also provide some insight into what is happening during the welding process. It was revealed that e.g. especially the second peak of reheating has a high impact on precipitation behavior.

More work on the model is needed, backed up by experimental investigations, however the framework provided is already yielding very good results and has the potential to significantly reduce the requirement for actual manufacturing of samples in future development processes.

### REFERENCES

- [1] BHADESHIA, H.K.D.H. ; HONEYCOMBE, SIR ROBERT: The Strengthening of Iron and its Alloys. In: *Steels* : Elsevier, 2006 — ISBN 9780750680844, S. 17–38
- [2] HORNBOGEN, ERHARD ; WARLIMONT, HANS: *Metallkunde*. Berlin, Heidelberg : Springer Berlin Heidelberg, 2001. — ISBN 978-3-662-08696-4
- [3] GYPEN, L.A. ; DERUYTTERE, A.: The combination of atomic size and elastic modulus misfit interactions in solid solution hardening. In: *Scripta Metallurgica* Bd. 15 (1981), Nr. 8, S. 815–820.
- [4] GOMIERO, P. ; BRECHET, Y. ; LOUCHET, F. ; TOURABI, A. ; WACK, B.: Microstructure and mechanical properties of a 2091 AlLi alloy—II. Mechanical properties: Yield stress and work hardening. In: *Acta Metallurgica et Materialia* Bd. 40 (1992), Nr. 4, S. 857–861.
- [5] BUTT, M.Z. ; FELTHAM, P.: Solid-solution hardening. In: *Acta Metallurgica* Bd. 26 (1978), Nr. 1, S. 167–173.
- [6] BUTT, M. Z. ; FELTHAM, P.: Solid-solution hardening. In: *Journal of Materials Science* Bd. 28 (1993), Nr. 10, S. 2557–2576.
- [7] SIEURIN, HENRIK ; ZANDER, JOHAN ; SANDSTRÖM, ROLF: Modelling solid solution hardening in stainless steels. In: *Materials Science and Engineering: A* Bd. 415 (2006), Nr. 1–2, S. 66–71
- [8] TRAUB, H. ; NEUHÄUSER, H. ; SCHWINK, CH.: Investigations of the yield region of concentrated CuGe and CuZn single crystals—I. Critical resolved shear stress, slip line formation and the true strain rate. In: *Acta Metallurgica* Bd. 25 (1977), Nr. 4, S. 437–446.
- [9] ZANDER, JOHAN ; SANDSTRÖM, ROLF ; VITOS, LEVENTE: Modelling mechanical properties for non-hardenable aluminium alloys. In: *Computational Materials Science* Bd. 41 (2007), Nr. 1, S. 86–95.
- [10] GYPEN, L. A. ; DERUYTTERE, A.: Multi-component solid solution hardening. In: *Journal of Materials Science* Bd. 12 (1977), Nr. 5, S. 1028–1033.
- [11] GYPEN, L. A. ; DERUYTTERE, A.: Multi-component solid solution hardening. In: *Journal of Materials Science* Bd. 12 (1977), Nr. 5, S. 1034–1038.
- [12] HUTCHINSON, C ; GOUNE, M ; REDJAIMIA, A: Selecting non-isothermal heat treatment schedules for precipitation hardening systems: An example of coupled process–property optimization. In: *Acta Materialia* Bd. 55 (2007), Nr. 1, S. 213–223.

- [13] LI, Q: Modeling the microstructure–mechanical property relationship for a 12Cr–2W–V–Mo–Ni power plant steel. In: *Materials Science and Engineering A* Bd. 361 (2003), Nr. 1–2, S. 385–391.
- [14] GLADMAN, T.: *The physical metallurgy of microalloyed steels*, 1997 — ISBN 0910716812
- [15] YOUNG, C. H. ; BHADSHIA, H. K. D. H.: Strength of mixtures of bainite and martensite. In: *Materials Science and Technology* Bd. 10 (1994), Nr. 3
- [16] HOLZER, I: *Modelling and Simulation of Strengthening in Complex Martensitic 9-12% Cr Steel and a Binary Fe-Cu Alloy*, Dissertation, TU Wien, 2010
- [17] AHMADI, M.R. ; POVODEN-KARADENIZ, E. ; ÖKSÜZ, K.I. ; FALAHATI, A. ; KOZESCHNIK, E.: A model for precipitation strengthening in multi-particle systems. In: *Computational Materials Science* Bd. 91 (2014), S. 173–186
- [18] GLADMAN, T.: Precipitation hardening in metals. In: *Materials Science and Technology* Bd. 15 (1999), Nr. 1, S. 30–36
- [19] COTTRELL, A.H.: Theory of dislocations. In: *Progress in Metal Physics* Bd. 4 (1953), S. 205–264
- [20] FOREMAN, A.J.E: Dislocation energies in anisotropic crystals. In: *Acta Metallurgica* Bd. 3 (1955), Nr. 4, S. 322–330
- [21] AHMADI, M.R. ; POVODEN-KARADENIZ, E. ; SONDEREGGER, B. ; ÖKSÜZ, K.I. ; FALAHATI, A. ; KOZESCHNIK, E.: A model for coherency strengthening of large precipitates. In: *Scripta Materialia* Bd. 84–85 (2014), S. 47–50
- [22] AHMADI, M.R. ; SONDEREGGER, B. ; POVODEN-KARADENIZ, E. ; FALAHATI, A. ; KOZESCHNIK, E.: Precipitate strengthening of non-spherical precipitates extended in  $\langle 100 \rangle$  or  $\{100\}$  direction in fcc crystals. In: *Materials Science and Engineering: A* Bd. 590 (2014), S. 262–266
- [23] Internal Stresses in Metals and Alloys. In: *Nature* Bd. 161 (1948), Nr. 4080, S. 70–71
- [24] GALINDO-NAVA, E.I. ; RIVERA-DÍAZ-DEL-CASTILLO, P.E.J.: A model for the microstructure behaviour and strength evolution in lath martensite. In: *Acta Materialia* Bd. 98, Acta Materialia Inc. (2015), S. 81–93
- [25] KINNEY, C.C. ; PYTLEWSKI, K.R. ; KHACHATURYAN, A.G. ; MORRIS, J.W.: The microstructure of lath martensite in quenched 9Ni steel. In: *Acta Materialia* Bd. 69 (2014), S. 372–385
- [26] Focus on Recent Breakthroughs in Materials Science and Technology. In: *Science and Technology of Advanced Materials* Bd. 9 (2008), Nr. 1, S. 010301
- [27] MARUYAMA, KOUICHI ; SAWADA, KOTA ; KOIKE, JUN-ICHI: Advances in Physical Metallurgy and Processing of Steels. Strengthening Mechanisms of Creep Resistant Tempered Martensitic Steel. In: *ISIJ International* Bd. 41 (2001), Nr. 6, S. 641–653
- [28] TAKAHASHI, M. ; BHADSHIA, H. K. D. H.: Model for transition from upper to lower bainite. In: *Materials Science and Technology* Bd. 6 (1990), Nr. 7, S. 592–603
- [29] ARJOMANDI, M. ; KHORSAND, H. ; SADATI, S.H. ; ABDOOS, H.: Prediction of martensite formation start temperature in steels using artificial neural networks. In: *Defect and Diffusion Forum* Bd. 273–276 (2008), S. 329–334
- [30] SHERSTNEV, P ; LANG, P ; KOZESCHNIK, E: No Title. In: *Eur. Congr. Comput. Methods Appl.*, 2012
- [31] BUKEN, HEINRICH ; KOZESCHNIK, ERNST: A Model for Static Recrystallization with Simultaneous Precipitation and Solute Drag. In: *Metallurgical and Materials Transactions A: Physical Metallurgy and Materials Science* Bd. 48, Springer US

- (2017), Nr. 6, S. 2812–2818
- [32] WARCZOK, PIOTR: *Simulation of solidification of 0.7C 3Mn steel*. URL <http://matcalc.tuwien.ac.at/wiki/doku.php?id=tutorials:t11>. - abgerufen am 2015-04-04
- [33] KOZESCHNIK, E. ; RINDLER, W. ; BUCHMAYR, B.: Scheil–Gulliver simulation with partial redistribution of fast diffusers and simultaneous solid–solid phase transformations. In: *International Journal of Materials Research* Bd. 98 (2007), Nr. 9, S. 826–831
- [34] HOLLY, S. ; HASLBERGER, P. ; ZÜGNER, D. ; SCHNITZER, R. ; KOZESCHNIK, E.: Development of high-strength welding consumables using calculations and microstructural characterisation. In: *Welding in the World* Bd. 62 (2018), Nr. 3, S. 451–458
- [35] SCHNITZER, RONALD ; ZÜGNER, DOMINIK ; HASLBERGER, PHILLIP ; ERNST, WOLFGANG ; KOZESCHNIK, ERNST: Influence of alloying elements on the mechanical properties of high-strength weld metal. In: *Science and Technology of Welding and Joining* Bd. 22 (2017), Nr. 6, S. 536–543
- [36] SVOBODA, J ; FISCHER, F D ; FRATZL, P ; KOZESCHNIK, E: Modelling of kinetics in multi-component multi-phase systems with spherical precipitates I: Theory. In: *Materials Science and Engineering A* Bd. 385 (2004), S. 166–174
- [37] KOZESCHNIK, E ; SVOBODA, J ; FRATZL, P ; FISCHER, F D: Modelling of kinetics in multi-component multi-phase systems with spherical precipitates II: Numerical solution and application. In: *Materials Science and Engineering A* Bd. 385 (2004), S. 157–165
- [38] LUKAS, HANS ; FRIES, SUZANA G. ; SUNDMAN, BO: *Computational Thermodynamics*. Cambridge : Cambridge University Press, 2007 — ISBN 9780511804137



# NUMERICAL SIMULATION OF CU-RICH PRECIPITATE EVOLUTION IN CU-BEARING 316L AUSTENITIC STAINLESS STEEL

Q. XIONG\*, J. D. ROBSON\*, T. F. FLINT\*, Y. SUN,  
A. N. VASILEIOU\* and M. C. SMITH\*

*\*School of Mechanical, Aerospace and Civil Engineering, The University of Manchester*

DOI 10.3217/978-3-85125-615-4-14

## ABSTRACT

A numerical model based on the coupling of the thermodynamic software ThermoCalc and the Kampmann and Wagner Numerical (KWN) framework has been developed in this work to predict the evolution of Cu-rich precipitates in 316 stainless steels. The effect of precipitation hardening on mechanical properties at 700°C is investigated as well. The predicted average particle size, volume fraction and number density of precipitates agree well with the experimental observations. In addition, the precipitation strengthening effects of Cu-rich precipitates were quantitatively evaluated and agree with experimental data as well. The slow increase in average radius of Cu-rich precipitates was consistent with the modest change in yield strength with extended aging. These cumulative results and analyses could provide a solid foundation for much wider applications of Cu-bearing stainless steels. The developed model can be used to predict the precipitation behaviour in other similar austenitic stainless steels.

Keywords: Cu-rich precipitates, 316 stainless steel, modelling

## INTRODUCTION

The outstanding mechanical formability, good high temperature strength and oxidation resistance of AISI 316 austenitic stainless steels make them widely used materials in nuclear power plants [1]. However, the degradation of these materials can result from thermal aging and other external factors (irradiation, stress, temperature, coolant media, etc.), which could affect the reliability of components [2, 3]. After heat treatment, Cu-rich precipitates in the steel matrix will be produced if sufficient amount of copper is present in the steel. It is well known that the stability, size, type and number density of Cu-rich precipitates are mainly attributed to superior antibacterial property to the stainless steel and high temperature strength improvement [6-9]. The stability of these phases in multicomponent materials such as AISI 316SS under thermal aging is affected by many variables such as alloy composition, temperature, time, and processing history. However, there is currently a lack of in-depth understanding of Cu precipitation behaviour in austenitic steels [10].

Several investigations have reported Cu-rich precipitation during isothermal heat treatment and its effects on mechanical properties in austenitic stainless steel [2, 9-11], but



clearly there are practical limits to the duration of such experiments. To be able to extrapolate these results to longer timeframes, a numerical method is required to predict precipitate evolution. The simulation of Cu-rich precipitation requires a suitable modelling framework for capturing the complexity of the multicomponent system and involving the simultaneous occurrence of nucleation, growth and coarsening. Many efforts have been devoted to the modelling of the microstructure during the precipitation process for different types of materials [12, 13]. Accurate modelling of the precipitation process requires a synchronous consideration of all these contributions to simulate the temporal evolution of microstructure. Moreover, the phase equilibrium information as well as the composition and mobility data of the matrix phase need to be constantly updated as nucleation, growth and coarsening proceed. Therefore, a smooth integration of thermodynamic calculation, kinetic simulation and property modelling of the material is necessary. However, an integrated framework coupling reliable thermodynamic calculation, kinetic simulation and property prediction of 316SS is rarely available.

In this work, the ThermoCalc and Kampmann and Wagner approach (KWN model) are combined to predict the phase stability, phase compositions and precipitation. First, the phase properties under different compositions and temperatures are calculated from ThermoCalc. These may then be used as inputs for the precipitation kinetics and accelerate the understanding of the stability of precipitate phases in 316SS steels under extended thermal aging [14]. The simulation results demonstrate the potential applications of the current methodology to the understanding of phase stability in similar structural materials. The KWN model is used to predict the precipitation behaviour, and can deal with nucleation-growth-coarsening phenomena within the same formulation. A few models based on this framework have been applied to a number of systems [12, 15, 16]. An important limitation in those approaches is that the overall kinetics is computed by imposing a constant concentration at the precipitate/matrix interface, and by employing a driving force obtained from binary dilute solution approximation. Because of the decrease of solute supersaturation in the matrix during precipitation, the local equilibrium concentration at the precipitate/matrix interface may change significantly. Moreover, the chemical free energy change during nucleation based on the dilute solution approximation in high-alloy systems is also not precise, especially for ternary or higher order systems. The model presented here intends to overcome this problem via computing multicomponent thermodynamic equilibrium in the time domain, to obtain the instantaneous local equilibrium condition at the matrix/precipitate interface during precipitation. Homogeneous precipitation is considered in this work. The results of this model show good agreement with experimental observations for late precipitation stages. The precipitation behaviour of Cu-rich particles in 316SS is thus well understood. The effects of the precipitation on the mechanical properties are studied as well.

## MATERIAL DETAILS AND EXPERIMENTAL DATA

## SAMPLES

The chemical composition of the Cu-bearing 316 L austenitic stainless steel (SS) investigated in this work is shown in Table 1.

**Table 1.** Composition (wt%) of 316LCu alloy with Fe as balance

Alloy	C	P	S	Cr	Ni	Mo	Cu
316LCu	0.016	0.005	0.001	18.18	14.5	3.02	4.36

## EXPERIMENTAL DATA

Tong Xi etc. solution-treated the 316L-Cu specimens at 1100 °C for 30 min, followed by water quenching. The specimens were then aged isothermally at 700 °C for 20 min, 3 h, 6 h, 10 h, and 15 h, respectively. TEM (transmission electron microscopy) was used to analyse the morphology, size and the orientation relationship of Cu-rich precipitates in the 316L-Cu SS. APT (atom probe tomography) was used to characterize the evolution and calculate the size of Cu-rich precipitates [17]. The experimental results show that, with increasing aging time, the spherical morphology of Cu-rich precipitate remains unchanged. Moreover, the lattice constant of the austenitic matrix after solid solution treatment is very close to that of the FCC Cu-rich precipitates, and the lattice constant misfit  $\Delta a/a$  is small [24, 25]. The composition of Cu-rich precipitates obtained by proxigram analysis was 94.1671.26 at.% Cu and 1.7870.22 at.% Fe after 20 min aging, 98.0471.94 at.% Cu and 1.9671.92 at.% Fe after 6 h aging, and 99.1770.82 at.% Cu and 0.8370.81 at.% Fe after 15 h aging.

The average radius increased slightly from 1.38 nm to 2.39 nm as the aging time increased. The relatively slow growth and coarsening behaviour of Cu-rich precipitates was largely attributed to the slower diffusion kinetics of Cu than Fe, low interfacial energy and high strain energy of Cu-rich precipitates in the austenite matrix [17]. The measured average radius, number density, and volume fraction  $\Phi$  of the Cu-rich precipitates as a function of aging time will be compared with calculated results in the next section.

## THERMODYNAMIC RESULTS

To produce a reliable kinetic model, it is first necessary to have a sufficient understanding of the phase equilibrium of the system being modelled. Quantities such as equilibrium solubility and driving forces must be predicted and used as inputs to the kinetic model. The ThermoCalc® software [20] employing the TCFE8 thermodynamic database was used to calculate phase stabilities and compositions. This produces the solute concentration in the matrix ( $\alpha$ ) and in the precipitate ( $\beta$ ) under equilibrium. In addition, the chemical potentials of all the components are obtained and employed to determine the chemical driving force for the nucleation of the precipitates.

The calculated equilibrium phases and their mole fractions in 316LCu are demonstrated in Fig.1. Here, the open symbols denote the precipitate phases while the solid symbols denote the matrix phase in 316LCu. The main precipitates are sigma,  $M_{23}C_6$ , HCP, Laves and Cu-rich precipitate.

The predicted composition of precipitate phases is shown in Fig.2 and is compared with experimental results. The predicted equilibrium Cu-rich precipitates contain 94.02 at% Cu, and 0.516 at% Fe. While the Cu-rich precipitates obtained by proxigram analysis contain  $94.167 \pm 1.26$  at.% Cu and  $1.787 \pm 0.22$  at.% Fe,  $98.047 \pm 1.94$  at.% Cu and  $1.967 \pm 1.92$  at.% Fe and  $99.177 \pm 0.82$  at.% Cu and  $0.837 \pm 0.81$  at.% Fe after 20 min, 6 h and 15 h aging, respectively. The agreement between the calculated and experimental results are reasonable.

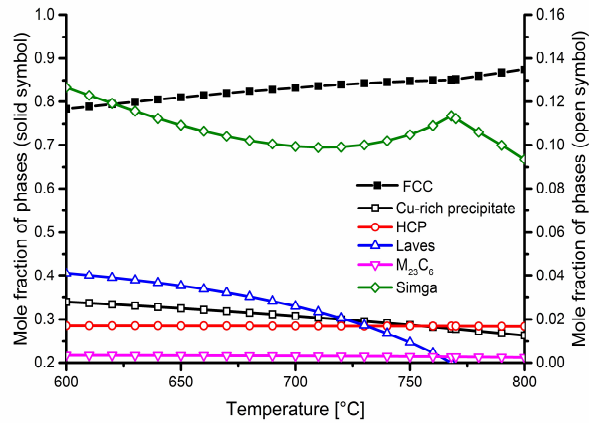


Fig.1 Calculated equilibrium phase mole fraction vs temperature for 316LCu

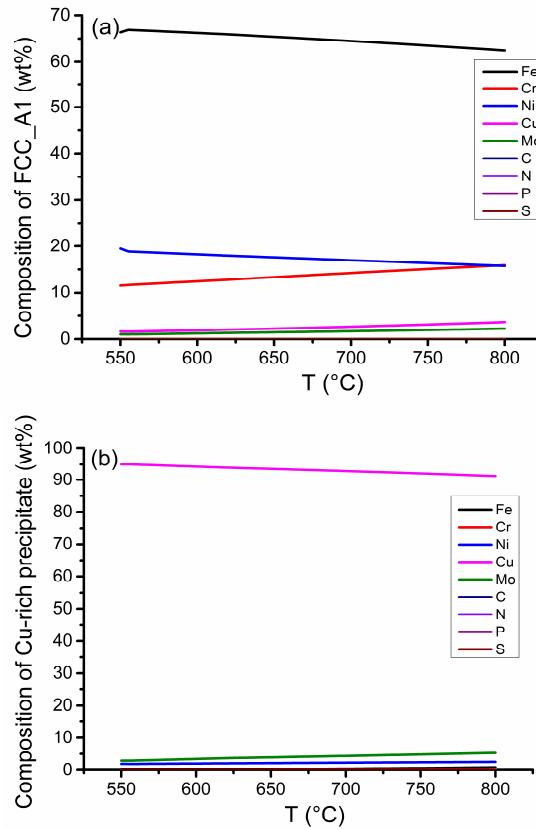


Fig.2 Calculated phase compositions in 316LCu for (a) FCC\_A1 (b) Cu-rich precipitate

### PRECIPITATION KINETICS SIMULATION

The preferred nucleation sites of precipitate phases were specified based on experimental evidence. In 316LCu, high number densities of spheroidal Cu-rich precipitates were homogeneously distributed in the austenitic matrix and the interface between Cu-rich precipitates and austenitic matrix remained coherent during the aging process [2, 17].

In this work, the KWN model is applied to predict precipitation of multiple phases [16]. The process of nucleation, growth, and coarsening of particles can be predicted simultaneously in this model. The number of new Cu-rich precipitates is calculated according to classical nucleation theory. The growth of particles is assumed to be governed by the diffusion rate of Cu to or from the particle/matrix interface. The particle size distribution and the volume fraction of the precipitate particles are updated at each time step. They are used to recalculate the matrix compositions during discrete time steps which are determined by a mean-field approach. After each time-step, the Cu concentration remaining in the matrix is recalculated and used in the next time-step. Coarsening arises naturally in the model. Using this method, the transition from nucleation and growth to a

coarsening-dominated regime is naturally predicted as the precipitate volume fraction increases.

### NUCLEATION

Classical nucleation theory gives the homogeneous nucleation rate as [15]:

$$I = N_v Z \beta^* \exp\left[-\frac{4\pi\gamma_n r^{*2}}{3kT}\right] \exp\left(-\frac{\tau}{t}\right) \quad (1)$$

where  $N_v$  is the number of nucleation sites per unit volume (equal to the number of atoms per volume for homogeneous nucleation);

$Z$  is the Zeldovich nonequilibrium factor,  $Z = \frac{V_a \Delta G_v^2}{8\pi \sqrt{\gamma_n^3 kT}}$ ;

$\beta^*$  is the rate of atomic attachment to a growing embryo,  $\beta^* = 16\pi\gamma_n^2 cD / \Delta G_v^2 a^4$ ;

$k$  is the Boltzmann constant;

$T$  is the thermodynamic temperature;

$\gamma_n$  is the interfacial energy of the matrix/nucleus interface; The interfacial energy of Cu-rich precipitated is cited from [11, 20].

$r^*$  is the radius of the critical nucleus,  $r^* = -2\gamma_n / \Delta G_v$ ;

$\tau$  is the incubation time for nucleation,  $\tau = 8kT\gamma_n a^4 / V_a^2 \Delta G_v D c$ ;

$\Delta G_v$  is the chemical volume free energy change driving nucleation,

$$\Delta G_v = -\frac{RT}{V_m} \left[ c_e^\beta \frac{\ln(c_i)}{\ln(c_e^\alpha)} + (1 - c_e^\beta) \frac{\ln(1 - c_i)}{\ln(1 - c_e^\alpha)} \right];$$

$V_m$  is the molar volume of the precipitating phase;

$c_i$  is the instantaneous concentration of Cu in the matrix. This is the far field matrix concentration, strictly speaking an infinite distance from the precipitate/matrix interface;

$c_e^\alpha$  is the concentration of solute in the matrix ( $\alpha$ ) in equilibrium with the precipitate ( $\beta$ );

$c_e^\beta$  is the equilibrium concentration of solute in the precipitate phase;

$V_a$  is the volume per atom in the matrix;

$c$  is the concentration (atomic fraction) of Cu solute in the matrix;

$a$  is the lattice constant of the product phase which is equal to 0.36 nm in this work [10];

$D$  is the diffusivity of Cu precipitate in matrix.

### GROWTH

The Cu-rich particles appear approximately spherical in shape. The modelling of precipitate growth with local equilibrium at the interface is based on the theory for spherical precipitates. The development of the radius of the spherical precipitate is assumed to follow the parabolic equation. The growth rate is limited by the rate at which Cu can diffuse to the particles and is given by

$$\frac{dr}{dt} = \frac{D}{r} \frac{c_i - c_r^\alpha}{c^\beta - c_r^\alpha} \quad (2)$$

where  $D$  is the chemical diffusion coefficient of Cu [m<sup>2</sup>/s],  $r$  is the particle radius [m],  $c_r^\alpha$  is the concentration of solutes in the matrix at the interface (which depends on the particle radius due to the effect of capillarity),  $c^\beta$  is the concentration of solute in precipitates and  $c_i$  is the instantaneous concentration of Cu in the matrix.  $c_r^\alpha$  is calculated using the Gibbs–Thomson equation:

$$c_r^\alpha = c_\infty^\alpha \exp\left(\frac{2\gamma_n V_m}{RT} \frac{1}{r}\right) \quad (3)$$

where  $\gamma_n$  is the interfacial energy of the growing (or shrinking) particle [J/m<sup>2</sup>].

The mean solute concentration of the components in the matrix,  $c_i$ , is updated after each time step:

$$c_i = c_0 - (c^\beta - c^\alpha) \int_0^\infty \frac{4}{3} \pi r^3 \phi dr \quad (4)$$

where  $\phi$  is the size distribution function. The newly obtained multicomponent matrix composition is employed as an input for the thermodynamic computations in the next time step.

The chemical diffusion coefficient of Cu in  $\gamma$ -iron is measured in [18]

$$D = 0.19 \exp\left(\frac{-65100}{RT}\right) \times 10^{-4} \quad (5)$$

#### PRECIPITATE COARSENING

Coarsening occurs when large precipitates grow at the expense of small ones, without a change the overall volume fraction. As the fraction of solute in the matrix decreases during precipitation, the driving force for nucleation and growth of the precipitate particles decreases and the critical particle radius increases. The growth rates of all the particles size classes were calculated at the edges (i.e. upper and lower bounds) of each class. For particles with radii smaller than the critical radius,  $r^*$ , the size of the particles will have a negative growth rate according to Eq.(2). Particles radii larger than  $r^*$  will retain a positive growth rate and increase in size. When the size of a group of shrinking particles reaches zero they are removed from the size distribution. The particles are then reallocated to the size classes.

Secondly, the precipitates size distribution at each iteration is updated by a third order Runge–Kutta scheme [19] with an adaptive time step. The time step was adjusted to ensure that the error in the change in radius was less than 0.1 nm between steps and the error in the prediction of number density was less than 0.01 particle/ $\mu\text{m}^3$ . In the early stages of precipitation, the time step is very small to ensure these criteria are met when nucleation and growth rates are most rapid. In the later stages of precipitation and during coarsening, the time step expands, where changes occur more slowly, allowing more efficient calculation.

**Table 2** Parameters used in this work

Parameter	value	Reference
$N_v$		Calculated in this work
$a$	0.36e-9 m	[20]
$\gamma_n$	0.017 J/m <sup>2</sup>	[11, 20]
$V_m$	7.457e-6 m <sup>3</sup> /mol	Calculated by Thermo-Calc
$V_a$	1.17×10 <sup>-29</sup> m <sup>3</sup>	[21]
$k$	1.38×10 <sup>-23</sup> m <sup>2</sup> *kg/(s <sup>2</sup> *K)	[22]
$R$	8.314 J/(mol*K)	[22]
$T$	700 °C	In this work
$M$	3	Taylor factor
$G$	75.3GPa	Shear modulus
$b$	0.254nm	Burgers vector
$\Delta a/a$	0.38%	Misfit parameter

### STRENGTH MODEL

The increment of macroscopic yield strength  $\sigma_p$  can be calculated as [10]

$$\sigma_p = 4.1MG\varepsilon^{3/2}v_f^{1/2}\left(\frac{R}{b}\right)^{1/2} + \frac{2M}{bLT^{1/2}}(\gamma_n b)^{2/3} \quad (6)$$

where M is the Taylor factor, G is the shear modulus of the austenitic matrix and b is the Burgers vector in the matrix, T is the line tension of the dislocation, approximately equal to  $Gb^2/2$  [49],  $\varepsilon = 2/3 (\Delta a/a)$  is the coherency strain,  $L = 0.866/(RN)^{1/2}$  is the mean particle spacing in the slip plane,  $v_f$ , N and R are the volume fraction, number density and average radius of Cu-rich precipitates, respectively. These input parameters are shown in Table 2.

### RESULTS AND DISCUSSION

The integrated model can now be used to predict precipitation for a range of alloy compositions and investigate the effect of changing the bulk alloy composition on the precipitation kinetics. The input parameters are shown in Table 2. Fig. 3 shows plots of the predicted evolution of volume fraction, number density and particle radius along with the experimental data at 700°C. The average measured radius of Cu-rich precipitates is 1.387±0.46 nm after aging for 20min, while it increased to 2.077±0.71nm and 2.397±0.81 nm after aging for 6h and 15h, respectively. Meanwhile, the number density of the Cu-rich precipitate decreases continuously from 1.29×10<sup>24</sup> m<sup>-3</sup> after 20 min aging to 4.27×10<sup>23</sup> m<sup>-3</sup> after 6h aging and further to 2.65×10<sup>23</sup> m<sup>-3</sup> after 15h aging [10]. The predicted radius of Cu-rich precipitates is 1.4 nm after aging for 20min, while it increased to 2.0 nm and 2.4 nm after aging for 6h and 15h, respectively. The predicted number density of the Cu-rich precipitate decreases continuously from 1.3×10<sup>24</sup> m<sup>-3</sup> after 20 min aging to 4.3×10<sup>23</sup> m<sup>-3</sup> after 6h aging and further to 2.7×10<sup>23</sup> m<sup>-3</sup> after 15h aging.

The predicted volume fraction, number density and average size of Cu-rich particles are in good agreement with published experimental results. The volume fraction of Cu-rich particles increases rapidly initially and then remains relatively constant at different aging time, indicating that the Cu-rich precipitates are in a regime where growth and coarsening are dominant. At first, the number density of Cu-rich particles increases rapidly in a very short time. Then the number density begins to decrease as described by the experiment. The decrease of number density is very fast and followed by a relatively stable state. Meanwhile, the average precipitate size increased with increasing the aging time. After increasing rapidly in size at the early stage of aging, the growth rate of Cu-rich particles slowed down and kept at a relatively stable state. The slight increase in mean radius and decrease in number density were consistent with the tiny change in mechanical properties under different aging time [10].

The predicted total precipitation strengthening is shown in Fig.4, which is 15.81MPa, 20.37MPa and 21.23MPa for 20min, 6h and 15h aging, respectively. The calculated results are a bit higher than the experimental results but within reasonable agreements. The reason resulting in the slowly increment of yield strength with extended aging time is the weak precipitation strengthening effect of Cu-rich precipitate and the slow growth of the Cu-rich precipitate.



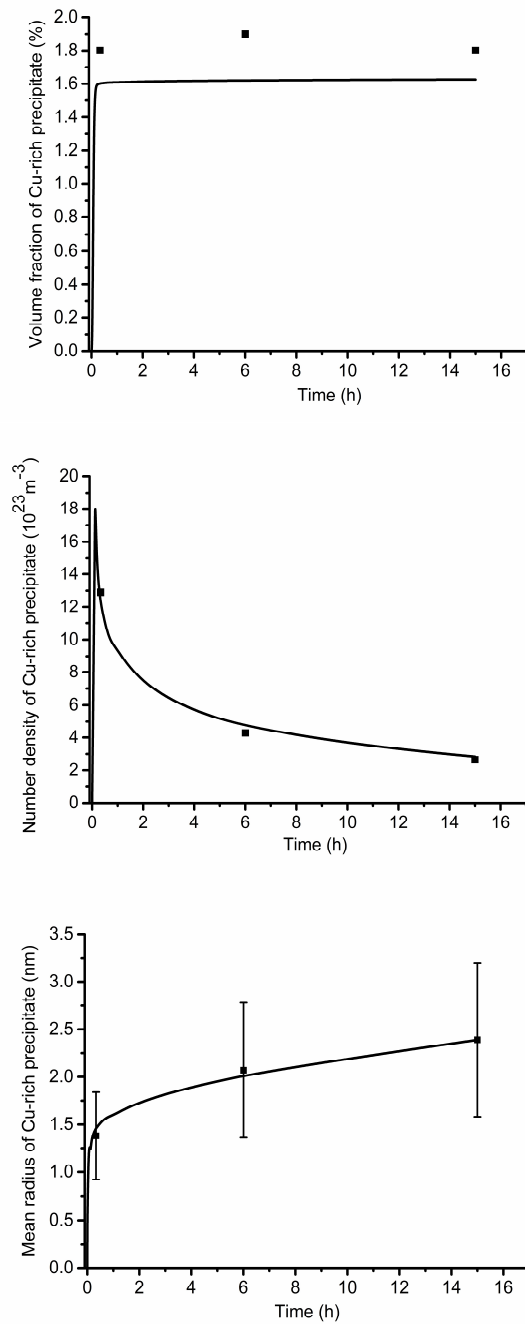


**Fig. 3.** Predicted and measured evolution of: (a) volume fraction of Cu-rich precipitate (b) Cu-rich precipitate number density; and (c) mean radius with time at 700°C. Measured data from [17]

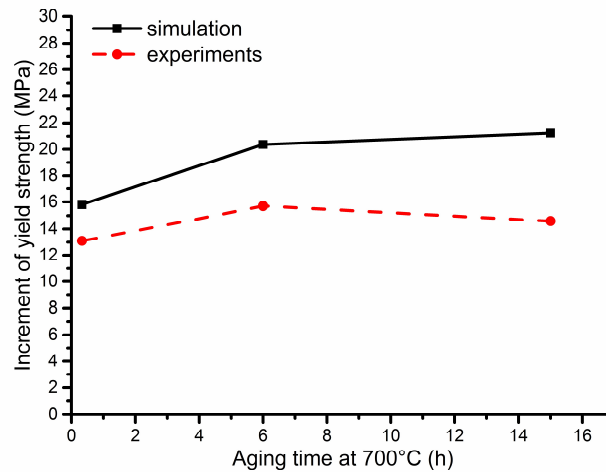


Fig. 4. Strengthening contributions of Cu-rich precipitates in 316L-CuSS.

### CONCLUSIONS

A model describing the precipitation kinetics is developed. The model is based on a KWN framework with continuous nucleation in the matrix and a growth rate computation incorporating capillarity effects. The model is coupled with ThermoCalc<sup>®</sup> thermodynamic databases for obtaining the instantaneous equilibrium condition at interface. Models have been developed to predict the full precipitation process for the Cu-rich precipitate phase, from the initial nucleation stage to the final coarsening dominated stage. The size distributions and particle size evolution predicted by the model in this study agree well with the experimental data reported in the literature. The model is able to predict the overlapped nucleation-growth-coarsening kinetics in a natural way and trace the particle size distribution throughout the process. The model is of a general nature, and it can be applied to other precipitate phases present in similar stainless steels. The precipitation hardening effects of Cu-rich precipitates are simply and quantitatively analysed. The strengthening effects are found to be relatively small and consistent with the experimental results.

### ACKNOWLEDGEMENTS

The authors gratefully acknowledge the contributions of all the participants in this work. The support of the UK Engineering and Physical Sciences Research Council for M C Smith is also acknowledged, via the Fellowship in Manufacturing “A whole-life approach to the development of high integrity welding technologies for Generation IV fast reactors”, EP/L015013/1. The authors acknowledge the use of the EPSRC-funded JEOL JXA-8530F FEG-EPMA, award EP/M028097/1.

REFERENCES

- [1] MAZIASZ, P. and J. BUSBY: *Properties of austenitic steels for nuclear reactor applications*, in *Comprehensive Nuclear Materials*. 2012, Elsevier Oxford. p. 267-283.
- [2] SAHLAOU, H., ET AL., *Effects of ageing conditions on the precipitates evolution, chromium depletion and intergranular corrosion susceptibility of AISI 316L: experimental and modeling results*. *Materials Science and Engineering: A*, 2004. 372(1–2): p. 98-108.
- [3] MAZIASZ, P.J.: *Overview of microstructural evolution in neutron-irradiated austenitic stainless steels*. *Journal of Nuclear Materials*, 1993. 205: p. 118-145.
- [4] REN, L., ET AL.: *Preliminary study of anti-infective function of a copper-bearing stainless steel*. *Materials Science and Engineering: C*, 2012. 32(5): p. 1204-1209.
- [5] XI, T., ET AL., *Study of the processing map and hot deformation behavior of a Cu-bearing 317LN austenitic stainless steel*. *Materials & Design*, 2015. 87: p. 303-312.
- [6] ARGON, A.: *Strengthening mechanisms in crystal plasticity*. 2008: Oxford University Press on Demand.
- [7] MULHOLLAND, M.D. and D.N. SEIDMAN: *Nanoscale co-precipitation and mechanical properties of a high-strength low-carbon steel*. *Acta Materialia*, 2011. 59(5): p. 1881-1897.
- [8] JIAO, Z.B., ET AL.: *Precipitation mechanism and mechanical properties of an ultra-high strength steel hardened by nanoscale NiAl and Cu particles*. *Acta Materialia*, 2015. 97: p. 58-67.
- [9] PADILHA, A.F., ET AL.: *Precipitation in AISI 316L(N) during creep tests at 550 and 600 °C up to 10 years*. *Journal of Nuclear Materials*, 2007. 362(1): p. 132-138.
- [10] XI, T., ET AL.: *Copper precipitation behavior and mechanical properties of Cu-bearing 316L austenitic stainless steel: A comprehensive cross-correlation study*. *Materials Science and Engineering: A*, 2016. 675: p. 243-252.
- [11] HONG, Y.J.O.J.H.: *Nitrogen effect on precipitation and sensitization in cold-worked Type 316L(N) stainless steels*. *Journal of Nuclear Materials*, 2000. 278: p. 242-250.
- [12] ROBSON, J.D.: *Modelling the overlap of nucleation, growth and coarsening during precipitation*. *Acta Materialia*, 2004. 52(15): p. 4669-4676.
- [13] KOZESCHNIK, E., ET AL.: *Modelling of kinetics in multi-component multi-phase systems with spherical precipitates: II: Numerical solution and application*. *Materials Science and Engineering: A*, 2004. 385(1–2): p. 157-165.
- [14] ANDERSSON, J.O., ET AL.: *Thermo-Calc & DICTRA, computational tools for materials science*. *Calphad: Computer Coupling of Phase Diagrams and Thermochemistry*, 2002. 26(2): p. 273-312.
- [15] ROBSON, J.D., M.J. JONES, and P.B. PRANGNELL: *Extension of the N-model to predict competing homogeneous and heterogeneous precipitation in Al-Sc alloys*. *Acta Materialia*, 2003. 51(5): p. 1453-1468.
- [16] ROBSON, J.D.: *A new model for prediction of dispersoid precipitation in aluminium alloys containing zirconium and scandium*. *Acta Materialia*, 2004. 52(6): p. 1409-1421.
- [17] LAI, J.K.L.: *A review of precipitation behaviour in AISI type 316 stainless steel*. *Materials Science and Engineering*, 1983. 61(2): p. 101-109.
- [18] SALJE, G. and M. FELLER KNIEPMEIER: *The diffusion and solubility of copper in iron*. *Journal of Applied Physics*, 1977. 48(5): p. 1833-1839.
- [19] ROBSON, J.D. and P.B. PRANGNELL: *Modelling Al3Zr dispersoid precipitation in multicomponent aluminium alloys*. *Materials Science and Engineering: A*, 2003. 352(1–2): p. 240-250.
- [20] LEWIS, M.H. and B. HATTERSLEY: *Precipitation of M23C6 in austenitic steels*. *Acta Metallurgica*, 1965. 13(11): p. 1159-1168.

## Mathematical Modelling of Weld Phenomena 12

- [21] LEE, E., P. MAZIASZ, and A. ROWCLIFFE, *Structure and composition of phases occurring in austenitic stainless steels in thermal and irradiation environments*. 1980, Oak Ridge National Lab., TN (USA).
- [22] CHRISTIAN, J.W.: *The Theory of Transformations in Metals and Alloys*, in *The Theory of Transformations in Metals and Alloys*. 2002, Pergamon: Oxford. p. ix.



# A COUPLED TEMPERATURE- MICROSTRUCTURE MODEL FOR THE HEAT- AFFECTED ZONE OF LOW ALLOYED HIGH STRENGTH STEEL DURING TWO-PASS ARC WELDING

J. PAANANEN \*, A. POHJONEN\*, J. LARKIOLA\* and  
S. ANTTILA\*\*

*\*University of Oulu, Materials and Production Technology, Pentti Kaiteran katu 1, 90014 Oulu, Finland,  
firstname.lastname@oulu.fi*

*\*\*SSAB Europe, P.O. Box 93, 92101 Raahе, Finland, firstname.lastname@ssab.com*

DOI 10.3217/978-3-85125-615-4-15

## ABSTRACT

A coupled temperature-microstructure model was developed in order to simulate the evolution of the microstructure in the heat-affected zone during two-pass gas-metal arc welding. The model is developed to serve the steel industry's need to evaluate the weldability of new steel grades. Heat transfer and heat input models were used for modelling the arc welding and the temperature changes in the heat-affected zone. A microstructure model was fully coupled with the temperature model, including latent heat of transformation as well as the dependence of thermophysical properties on temperature and phase fractions. The microstructure model simulates phase transformations and grain growth including a simplified model for the effect of fine particles. The modeled temperature paths are in good agreement with the measured ones. The final phase fractions and grain size distribution obtained from the model correspond to the actual microstructure and the model predicts the shapes of the heat-affected zone and fusion zone with relatively good accuracy.

Keywords: Microstructure, Phase Transformations, Grain Growth

## INTRODUCTION

There is a need in the steel industry to shorten the steel development cycle to meet the increasing customer demands. Therefore, weldability models that can predict the microstructure evolution without real welding experiments would help to achieve this goal. Modelling can also give valuable information of the microstructure evolution that is difficult or impossible to obtain experimentally. Although feasible welding models have been developed in the past, the increase in computational power has made it possible to create more detailed models and still maintain relatively low calculation times.

Goldak et al. [1] developed a model that predicts the heat flow in welds. They used a non-linear heat equation to take into account the effect of temperature on thermal conductivity and specific heat capacity. The authors presented two and three-dimensional approaches and were able to get a good agreement between the experimental and modelled results.

Watt et al. [2] developed quite comprehensive algorithm for the evolution of microstructure. Their model predicts the final microstructure, the phase fractions and the grain size, based on chemical composition of the steel. Henwood et al. [3] verified the algorithm in their paper. However, there were some aspects that were simplified. For instance, the authors assumed that austenitization occurs near equilibrium conditions and that the grain growth occurs only after the particles have dissolved. In addition, they assumed that after reaching the martensite start temperature the remaining austenite will transform into martensite.

The model presented in this paper includes a heat transfer model for the conduction in the steel, convection and radiation at the surfaces and the heat input from the arc. The heat transfer model is fully coupled with a microstructure model that includes phase transformations, grain growth and a rough model for precipitates. The paper aims to bring some new aspects on weldability modeling and overcome some of the drawbacks of the earlier methods. For example, the grains may grow in the presence of pinning particles. The phase transformation model is based on experiments and it for instance, allows simultaneous decomposition of austenite to ferrite, bainite and martensite and the grain growth in the presence of pinning particles. In addition, the thermophysical properties are functions of temperature and present phase fractions.

### DESCRIPTION OF THE MODEL

Due to high temperature gradients together with high heating and cooling rates that exist in actual welds, very fine grid and short time step are required. Therefore, it was a necessity to reduce the calculation time by using a two-dimensional model. The dimension where the temperature gradient was assumed to be zero was the direction of the movement of the torch as in Fig 1. Obviously, this was a very rough assumption. However, the results to be presented show that the used two-dimensional approach gave reasonable accuracy. Goldak et al. [1] also showed that two dimensional approach is sufficient for points far from the heat source for high speed productive welds in steel. The presented model is intended for the heat-affected zone and only little attention is paid on fusion zone phenomena. Thus, it is assumed that the points in the heat-affected zone are sufficiently far from the heat source but the accuracy of the temperature model in the fusion zone may not be sufficient. The model also assumes that inter-critical zones behave as the fully austenitized zones. This may not hold true in all cases and therefore, this model may not be suitable for the microstructure of inter-critical heat-affected zone.

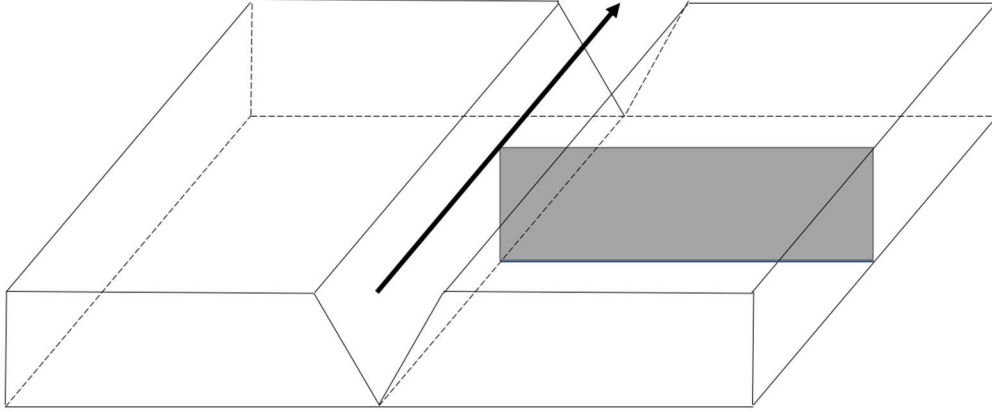


**Fig. 1** Gray area represents the modelled area and the arrow indicates the welding direction.

### TEMPERATURE MODEL

The heat equation (Eqn. (1)) was solved by using forward-time – centered-space (FTCS) finite difference scheme.

$$\rho c \frac{\partial T}{\partial t} - \nabla \cdot (k \nabla T) = Q \quad (1)$$

### BOUNDARY CONDITIONS

The schematics of the boundary conditions used in the simulation are presented in Fig. 2. The boundary condition in all surfaces experiencing air cooling is a combination of convection (Eqn. (2)) and radiation (Eqns. (3) and (4)). Only exemption is that the radiative heat loss in the horizontal direction ( $h_{rad,x}$ ) was assumed to be zero at the groove because the radiation from the opposite hot surface of the groove diminishes the heat loss in this direction. The total heat flux is then calculated by Eqn. (5) [4].

$$h_{conv} = h(T - T_{ext}) \quad (2)$$

$$h_{rad,x} = \cos(\alpha) \sigma \epsilon (T^3 + T^2 T_{ext} + T T_{ext}^2 + T_{ext}^3) (T - T_{ext}) \quad (3)$$

$$h_{rad,y} = \sin(\alpha) \sigma \epsilon (T^3 + T^2 T_{ext} + T T_{ext}^2 + T_{ext}^3) (T - T_{ext}) \quad (4)$$

$$h_{tot} = h_{rad,x} + h_{rad,y} + h_{conv} \quad (5)$$

Symbols in Eqns. (2)-(5) are as follows:  $\sigma$  is the Stefan-Boltzmann's constant,  $\epsilon$  is the emissivity,  $h$  is the convective heat transfer coefficient,  $T$  is the absolute temperature at the boundary, the  $T_{ext}$  is the ambient temperature in Kelvin and  $\alpha$  is the angle between the surface and the y-axis (vertical direction). In this model  $\epsilon$  and  $h$  were taken as 0.75 and 10



$Wm^{-2}K^{-4}$  respectively, following the approach given in Ref. [4]. It was assumed that the filler material is in place at the beginning of each pass. Goldak et al. [1] proposed this as the simplest approach and stated that this would cause error ahead of the weld pool. However, it was assumed that the effect is not as significant in present model, bearing in mind that the model was intended for the heat-affected zone.



**Fig. 2** Boundary conditions used in the simulation (during the first pass of two pass weld). The dashed line represents convection and radiation and the solid line seen on the left of the figure represents a symmetry boundary condition.

#### HEAT INPUT MODEL

Widely used double-ellipsoidal heat source model formulated by Goldak et al. [5] was used as a heat input model. The volumetric heat input to each node was calculated by using Eqn. (6) or (7). The term  $y_0$  was added to the heat source model because the global and local y-coordinate may not be the same.

$$Q = \frac{f_f UI \mu 3\sqrt{3}}{ABC_f \pi \sqrt{\pi}} \exp\left(-\frac{3x^2}{A^2} - \frac{3(y - y_0)^2}{B^2} - \frac{3(St - C_f)^2}{C_f^2}\right), St < C_f \quad (6)$$

$$Q = \frac{f_r UI \mu 3\sqrt{3}}{ABC_r \pi \sqrt{\pi}} \exp\left(-\frac{3x^2}{A^2} - \frac{3(y - y_0)^2}{B^2} - \frac{3(St - C_f)^2}{C_r^2}\right), St \geq C_f \quad (7)$$

where  $Q$  is the volumetric heat input,  $x$  and  $y$  are the coordinates of the node,  $y_0$  is the coordinate of the top of the heat source,  $S$  is the travel speed and  $t$  is time from the beginning of the welding,  $f_f$  and  $f_r$  are the parameters used to divide equal amount of energy to front and rear quadrant (Eqn. (8)),  $U$  is the arc voltage,  $I$  is the welding current,  $A$ ,  $B$ ,  $C_f$  and  $C_r$  are the heat source parameters. Parameters  $A$  and  $B$  are obtained by calculating the area that the consumable will fill and then simply measuring these dimensions as seen in Fig. 3.  $C_f$  is equal to the  $A$  and  $C_r$  is two times the  $A$ .

$$f_f = \frac{2C_f}{C_f + C_r}, f_r = \frac{2C_r}{C_f + C_r} \quad (8)$$

The parameters  $A$  and  $B$  were calculated as follows: First the area of the cross-section of the molten consumable was calculated by Eqn. (9). Then based on the joint preparation and

## Mathematical Modelling of Weld Phenomena 12

the area of the bead, the geometric shape of the bead's cross-section was obtained. Finally, based on the shape of the cross-section the parameters were calculated as shown in Fig. 3.

$$A_{bead} = \frac{D_{wire}\pi^2}{4} * \frac{F}{S} \quad (9)$$

where  $D_{wire}$  is the diameter of the wire,  $F$  is the wire feed rate and  $S$  is the travel speed.

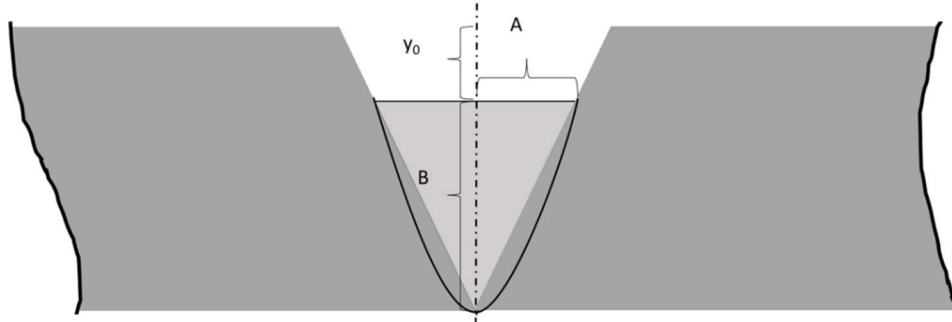


**Fig. 3** A schematic showing how the parameters A, B and  $y_0$  are calculated based on the area of the bead.

### THERMOPHYSICAL PROPERTIES

In low alloyed steels, density, thermal conductivity and specific heat capacity are highly dependent on the temperature and present phase. Therefore, it is necessary to calculate the properties at each node based on the temperature and phase fractions of that node. In addition, transformation enthalpy of austenite-to-ferrite is temperature dependent. All these properties and their dependence on phase and/or temperature are shown in the Fig. 4.

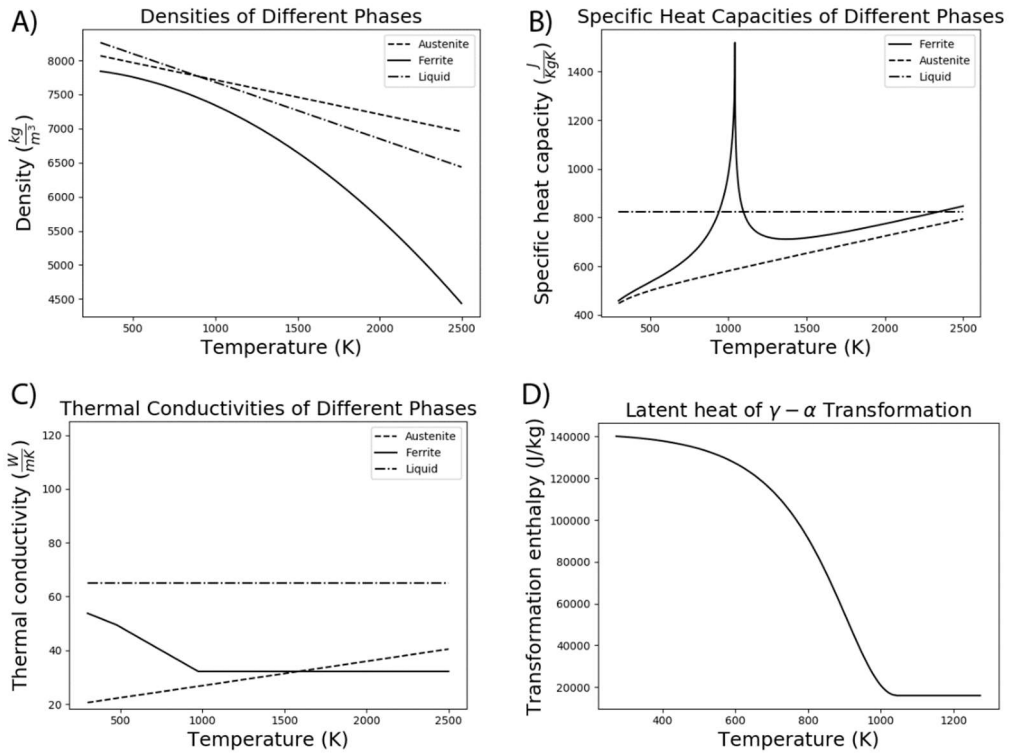


**Fig. 4** A) Densities of different phases B) Specific heat capacities of different phases C) Thermal conductivities of different phases D) Latent heat of  $\gamma - \alpha$  transformation as a function of temperature

The density of phase mixture was calculated by using Eqn. (10).

$$\rho = 1 / \sum \frac{X_i}{\rho_i} \quad (10)$$

where  $X_i$  is the volume fraction of the phase  $i$  and  $\rho_i$  is the density of phase  $i$ . Densities of the individual phases are calculated as in Ref. [6].

The specific heat capacity of a phase mixture was calculated by using Eqn. (11)

$$c = \sum c_i X_i \quad (11)$$

where  $c_i$  is the specific heat capacity of phase  $i$ . Specific heat capacities of ferrite and austenite are calculated as in Ref. [7] and the specific heat capacity of the liquid phase is taken as constant,  $825 \text{ Jkg}^{-1}\text{K}^{-1}$ , as presented in Ref. [8].

Finally, the thermal conductivity of phase mixture was calculated by using Eqn. (12)

$$k = \sum k_i X_i \quad (12)$$

where  $k_i$  is the thermal conductivity of the phase  $i$ . Calculation of the thermal conductivity of austenite and ferrite phase is described in Ref. [6]. Miettinen [6] proposed that thermal conductivity of liquid steel is  $35 \text{ Wm}^{-1}\text{K}^{-1}$  and Watt et al. [2] used  $120 \text{ Wm}^{-1}\text{K}^{-1}$  to simulate the heat transfer by stirring. For this model, a value between these two was chosen i.e.  $65 \text{ Wm}^{-1}\text{K}^{-1}$ . The main reason was that the usage of even higher thermal conductivity would add instability to the temperature model if FTCS scheme is used. On the other hand, the low value,  $35 \text{ Wm}^{-1}\text{K}^{-1}$ , gave unrealistically high temperatures in the fusion zone.

The latent heat of fusion was taken as constant and it was obtained from Thermo-Calc ® software (TCFE9 database). For steel that was used in the experiments the latent heat of fusion was 275 kJ/kg. The latent heat of fusion includes the transformation heats of the transitory delta-ferrite. The latent heat of austenite-to-ferrite or ferrite-to-austenite transformation can be seen in Fig. 4D [7]. The same value was used also for the austenite-to-bainite and austenite-to-martensite transformations.

### MICROSTRUCTURE MODEL

Microstructure model calculates the phase transformations and the grain growth. It also includes a very coarse model for precipitates. Possible phases in phase transformation model are ferrite, bainite, martensite, austenite and liquid. Formation of pearlite was neglected because it was not found in the continuous cooling experiments and thus, it was impossible to find parameters for the formation. As in Ref. [2], the delta-ferrite was omitted from the model. Instead, it is handled as a part of the liquid phase. The reason is that this adds stability to the model because the phase transformations at high temperatures occur presumably in very short time and this combined with the latent heats of transformation is likely to cause instability. In addition, the modelling of the delta-ferrite would require knowledge of the kinetics of austenite to delta-ferrite transformation at high heating rates.

### MELTING AND SOLIDIFICATION

Melting and solidification are important phenomena in welding. However, the present model was aimed for HAZ microstructure simulations so the melting and solidification are modelled quite simply. In metals, the melting occurs at the equilibrium melting temperature even at high heating rates [9]. To increase the stability of the model the melting rate is calculated as follows: The melting occurs between solidus ( $T_S$ ) and liquidus ( $T_L$ ) temperatures and the rate is  $(T_L - T_S)10^{-3}\text{K}^{-1}\text{s}^{-1}$ . The  $1000 \text{ Ks}^{-1}$  is the approximated heating rate in the fusion zone.

During welding, the nucleation barrier for solidification is very low. Therefore, there is very little undercooling [9]. To avoid the instability caused by latent heat of fusion, the solidification begins only after temperature is 10 degrees below the  $T_S$ . It was assumed that

this is within the range of ‘very little undercooling’. In reality, the solidifying phase depends on cooling rate [10]. In this model, the solidifying phase is always austenite because, as described previously, the delta-ferrite is combined with the liquid phase.

### AUSTENITIZATION

Austenitization kinetics during heating depend on initial microstructure, composition and heating rate. In the experiments it was found that during welding the heating rates are relatively high ( $\sim 80$  K/s) in the regions where temperature rises over the  $A_1$  temperature.

The austenitization kinetics were investigated by using the Gleeble thermomechanical simulator (Gleeble® 3800). The test specimens were heated to 1250 °C at heating rates from 10 to 1000 °C/s and the diameter of the specimen was measured by dilatometry and later the change in the diameter was converted to transformed fraction by lever rule. It was found that for the examined low alloyed steel, the austenitization is time-independent on these heating rates. Therefore, the austenitization is modelled rather simply using the Johnson-Mehl-Avrami-Kolmogorov (JMAK) equation that is fitted to the experimental data. While this works very well for the initial microstructure, it remains somewhat questionable how well this represents the austenitization from the microstructure formed after the first pass. The prior austenite grain size in the heat-affected zone of the first pass differs from initial pancaked structure and this may have effect on the transformation rate. The austenitization is modelled by using Eqn. (13)

$$X_A(T) = 1 - \exp(-k\Delta T^n) \quad (13)$$

where  $X_A$  is the volume fraction of austenite at temperature  $T$ ,  $k$  and  $n$  are parameters fitted to the experimental data,  $\Delta T$  is the temperature difference between the  $T$  and the equilibrium temperature, i.e.  $A_1$  in the intercritical zone and  $A_3$  above that temperature. Note that different values for parameters  $k$  and  $n$  are used between  $A_1$  and  $A_3$  temperatures and above  $A_3$  temperature.

It is assumed that during austenitization from a mixed microstructure, the initial phases transform into austenite in relation to their volume fractions, for instance, initially 70% bainite – 30 % martensite will be 35% bainite and 15% martensite after 50% of total volume is austenitized.

### DECOMPOSITION OF AUSTENITE

During cooling, three different austenite decomposition mechanism are possible and may occur simultaneously. These are the formation of ferrite, bainite and martensite. As noted earlier, the formation of pearlite is neglected because it was not found in experiments, though it could be modelled using the same principles.

Diffusional transformations (austenite to ferrite or bainite) are separated into two parts. The first part is incubation that occurs until the volume fraction of the phase is more than

1%. The second part is nucleation and growth that may occur until austenite is completely decomposed.

The incubation phase is calculated by using Eqns. (14), (15) and (16) following similar approach as in Ref. [11]: The ideal TTT-diagram is obtained from the continuous cooling experiments using the following equation

$$\frac{1}{\tau(\Delta T)} = \frac{d\theta'}{d(\Delta T_{CCT})} \quad (14)$$

where  $\theta'$  is the constant cooling rate,  $\Delta T_{CCT}$  is the magnitude of the undercooling at the beginning of the transformation during continuous cooling. According to the Scheil's additivity rule, one percent is transformed when

$$\sum \frac{\Delta t}{\tau(T)} \geq 1 \quad (15)$$

where  $\Delta t$  is the time step and

$$\tau(T) = A_i(T_i - T)^{m_i} \exp\left(\frac{Q_i}{RT}\right) \quad (16)$$

where  $T$  is the temperature at the beginning of time step,  $A_i$ ,  $T_i$ ,  $m_i$  and  $Q_i$  are parameters fitted for incubation of each phase, separately. After incubation is finished, the phase transformation rate is calculated using Eqn. (17) as presented in Ref. [12].

$$\frac{\Delta X}{\Delta t} = (X_{max} - X) \ln\left(\frac{X_{max}}{X_{max} - X}\right)^{\frac{n-1}{n}} nk(T)^{1/n} \quad (17)$$

where  $\Delta X$  is the fraction transformed during one time step ( $\Delta t$ ),  $X_{max}$  is the maximum volume fraction of the phase,  $X$  is the current volume fraction of the phase, the  $n$  is a parameter fitted to experimental data and the  $k$  is the rate constant calculated by Eqn. (18) as in Ref. [13].

$$k(T) = \exp(a(T - T_0)^2 - c) \quad (18)$$

where  $a$ ,  $c$  and  $T_0$  are parameters fitted to experimental data. For the formation of the bainite, the term presented in Eqn. (19) is added to Eqn. (17). This takes into account the fact that transformation rate is decreased as the austenite is enriched with carbon [14].

$$\frac{C_0}{C_\gamma} \quad (19)$$

where  $C_0$  is the bulk carbon content and

$$C_\gamma = \frac{C_0 - X_f * 0.02}{1.0 - X_f} \quad (20)$$

where  $X_f$  is the volume fraction of ferrite that possibly formed before the austenite-to-bainite transformation begun. In addition, the term presented Eqn. (21) is added to Eqn. (17) to take into account the effect of grain size on the formation of ferrite and bainite [2]

$$\frac{G_{current} - G_{parameters}}{2} \quad (21)$$

where  $G$  is the ASTM grain size number. Subscripts *current* and *parameters* denotes to the grain size at the moment phase transformation is occurring and the grain size that was in specimens when parameters were obtained, respectively.

For the martensitic transformation, the derivative of Koistinen-Marburger equation (Eqn. (22)) is used as presented in Ref. [4].

$$\frac{\Delta X_m}{\Delta t} = -\mu X_{m,max} [1 - \exp(-\mu(T_{Ms} - T))] \frac{\partial T}{\partial t} + X_m(T = T_{Ms}) \quad (22)$$

where  $\Delta X_m$  is the transformed volume fraction during one time step ( $\Delta t$ ),  $\mu$  is a coefficient that is fitted to experimental data,  $T_{Ms}$  is the martensite start temperature,  $X_{m,max}$  is the maximum amount of martensite that may form and the term  $X_m(T = T_{Ms})$  takes into account the possibility that there may be already some martensite in the inter-critical zone as the transformation begins.

More detailed description of the austenite decomposition model can be seen in Ref. [15] and result for different steels can be seen in Refs. [15] and [16].

#### GRAIN GROWTH

As noted above, the prior austenite grain size has an effect on phase transformation kinetics. Therefore, it is important to model the grain growth in austenite. The grain size is also important factor determining the impact toughness of the heat-affected zone and model would also be suitable for indicating if the grain size would be too high. Grain growth during one time step is calculated by using the Eqn. (23)

$$\frac{\Delta D}{\Delta t} = nK \left( \frac{1}{D} - \sum \frac{f}{K_z r} \right)^{\frac{1}{n}-1} \quad (23)$$

where  $D$  is the average grain diameter,  $K_Z$  is the Zener coefficient,  $f$  is the volume fraction of precipitate and  $r$  is the mean particle radius. Zener coefficient is 2.1 for TiN [17] and 4/3 for NbC [9]. Parameters  $n$  and  $K$  are calculated as in Ref. [17].

Particle pinning is important grain growth controller. Therefore, it is necessary to have reasonable estimation of particle structure during the thermal cycle. In this model, pinning from NbC and TiN particles is taken into account. Volume fraction of the precipitate is estimated during thermal cycle by solving the following integral (Eqn. (24)) numerically [18]

$$f = f_0 \left( 1 - \frac{2}{r_0^2} \int_{t_1}^{t_2} \alpha D_m dt \right)^{\frac{3}{2}} \quad (24)$$

where  $r_0$  is the initial particle diameter,  $D_m$  is the diffusivity of the less mobile element and  $\alpha$  is the ratio between the fraction of the less mobile element in the matrix and in the precipitate. It was assumed that the dissolved particles will not precipitate between two passes but remain in solution. The initial volume fractions of the precipitates were approximated by using Thermo-Calc ® (TFCE9 Database). For the dissolution temperature ( $T_D$ ) Eqn. (25) was used.

$$T_D = \frac{D}{C - \log[M\%][C\%]} \quad (25)$$

where  $M$  and  $C$  are the concentrations of metal and non-metal, respectively. The  $C$  and  $D$  are constants that depend on the precipitate and were taken directly from Ref. [18].

The coarsening of particles is calculated by using Eqn. (26)

$$r^3 = r_0^3 + c_1 \int_{t_1}^{t_2} \frac{1}{T} \exp\left(-\frac{Q}{RT}\right) dt \quad (26)$$

where  $Q$  is the activation energy for diffusion of the less mobile element,  $R$  is the universal gas constant and  $c_1$  is parameter fitted for experimental data [18].

The previous equation for growth is valid only below the equilibrium dissolution temperature. In the present model, it is assumed that precipitates grow below the  $T_D$  temperature and the coarsening will not occur simultaneously with the dissolution. Although the precipitation model was not directly verified experimentally, it increased the overall accuracy of the grain growth model significantly. The initial precipitation structure was estimated as follows: the volume fraction of the precipitate was calculated using solubility product. Parameters for solubility product as well as initial particle diameters (5 nm for TiN and 60 nm for NbC) were after Grong [18].



EXPERIMENTAL PROCEDURE

To validate the present model, experimental data was obtained from practical welding trials. Test coupons of 100×120×8 mm were welded to each other by using a Motoman Yasnac RX robot equipped with a Kemppi ProMig 500 gas metal arc welding machine. The chemical composition of the steel is presented in Table 1. The joint preparation was a 50 degree V-groove without a root gap (see Fig. 5A). Four thermocouples were attached on the top surface. The shielding gas was Mison® 25 (Ar + 25%CO<sub>2</sub> + 0.03% NO) with gas flow of 20 l/min. The welding consumable was 1.2 mm Esab OK AristoRod™ 89 solid core wire. Other welding parameters are presented in Table 2.

The welded samples were then cut to 40x8 mm cross-sections, mounted, polished and etched in picric acid for 6 minutes to reveal the prior austenite grain size or in 2% Nital etchant for 10 seconds to reveal the microstructure. The prior austenite grain size (PAGS) was measured using the mean linear intercept method. 400 μm lines were drawn parallel to fusion line and the amount of grain boundary interceptions was calculated. (see Fig. 9D)

Final microstructure characterization was done by using a laser confocal microscope (VK-X200, Keyence Ltd.) to validate the result of the phase transformation model. The phase fractions were calculated by using simple image analysis. A grid of dots was drawn on microstructure images and the amount of dots on each phase were calculated. In case it was not clear what the phase under the dot is it was not taken into consideration. Finally, the phase fractions were estimated by calculating the fraction of the amount of dots per phase and the total amount of calculated dots.

Three welding experiments were carried out and three cross-section specimens were made from each test coupon. However, there was some deviation in the welding current (±10 A) and this had an effect on temperatures. Therefore, the measurements were checked against each other to confirm that there was no significant error in them and then the model was compared with randomly chosen test coupon.

**Table 1** Data of the steel used in the experiments

Yield strength (MPa)	C (wt-%)	Mn (wt-%)	Si (wt-%)	Nb+Ti+Mo+Vn (wt-%)	Cr+Ni (wt-%)
960	0.1	1.4	0.3	0.05	1.00

**Table 2** Welding parameters

Bead no.	Voltage (V)	Current (A)	Travel speed (cm/min)	Feed rate (m/min)
1	21.9	196	40	5.8
2	22.0	188	50	5.8

## Mathematical Modelling of Weld Phenomena 12

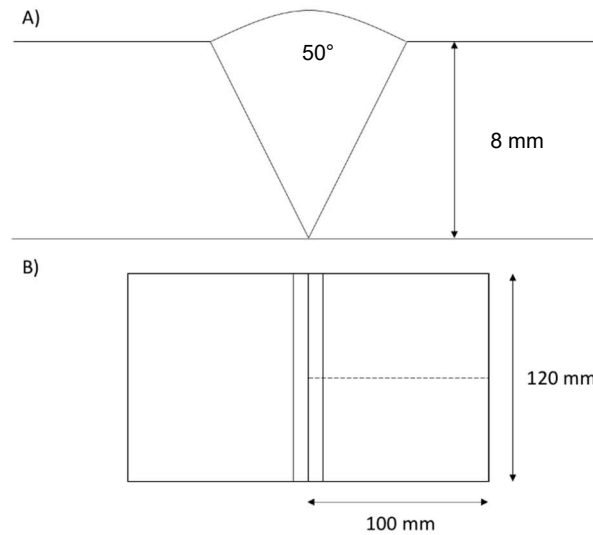


**Fig. 5** A) Joint preparation B) Dimensions of the plate. Dashed line represents the line where the thermocouples were attached.

### RESULTS AND DISCUSSION

The welding experiment was modelled using the described parameters. The grid spacing in simulations was 0.1 mm and the time step was 0.1 ms. A value of 0.80 was used for the heat input efficiency. This value was chosen because it gave the best correlation between the modelled and measured peak temperatures near the fusion line (5 mm line in Fig. 7). The simulation time was approximately 5 hours. Fig. 6 and Fig. 7 show that there is relatively good agreement between the experimental and modelled results. Evidently, the heat source model is merely an approximation of the complex phenomena in the weld pool and it causes some differences between shapes of the real and modelled fusion zones.

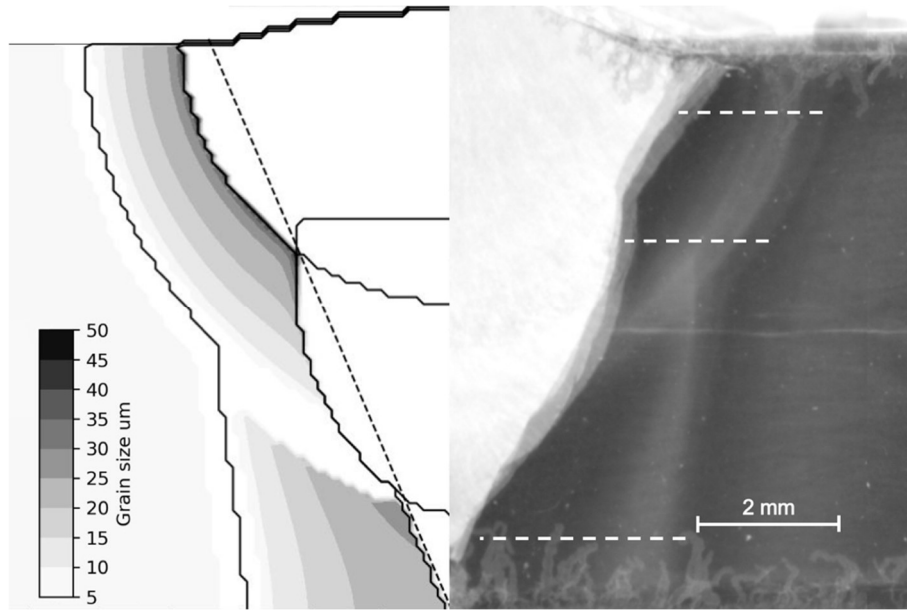


**Fig. 6** A figure showing a comparison between a cross-section from the model (left) and a blend of four cross-sections from the practical welding experiments (right). Blending was done due to the fact that the real fusion zones are not perfectly symmetric. Contours in the model image shows the modelled PAGS.

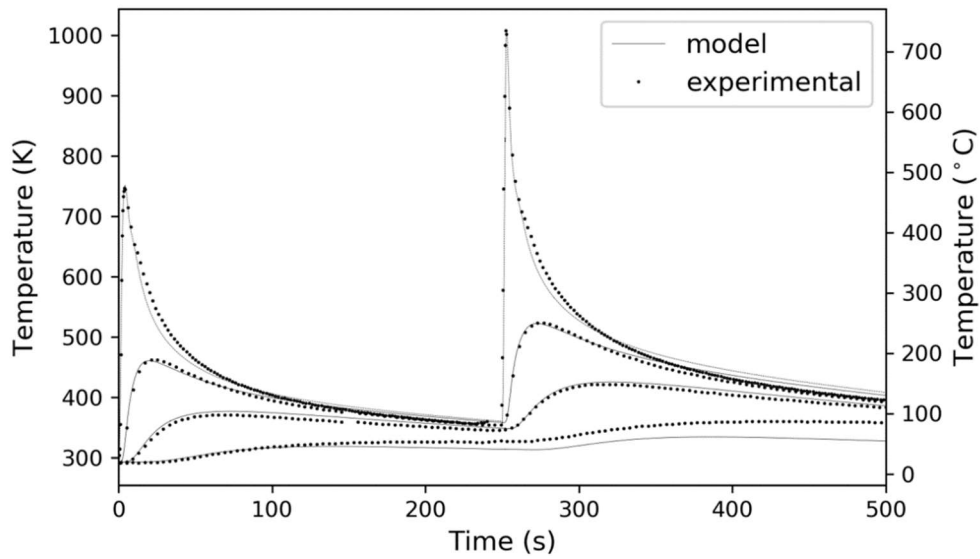


**Fig. 7** Temperature curves on the top surface during two-pass welding. Distances of the thermocouples are 5, 20, 40 and 80 mm from the symmetry line on top surface (in decreasing temperature order).

**Table 3** Volume fractions from model at the positions presented in Fig. 8

<b>Figure</b>	<b>Bainite model (vol-%)</b>	<b>Bainite exp (vol-%)</b>	<b>Martensite model (vol-%)</b>	<b>Martensite exp (vol-%)</b>
A	95	92	4	8
B	75	80	23	20
C	95	94	4	6
D	80	86	17	14
E	80	93	20	7
F	75	80	24	20

Table 3 shows the comparison between modelled and experimental phase structure. The images are shown in Fig. 8A-F. There is generally a good agreement between these values as the accuracy of the image analysis is approximately  $\pm 15\%$ . The most significant error is in Fig. 8E, which may be due to the fact that the area is tempered during the second pass and that makes the distinguishing of bainite and tempered martensite difficult. In some points, the sum of the phase fractions from the model are not equal to 100%. There are two reasons behind this. The volume fraction of ferrite is always at least slightly over zero due to incubation and this may lose one percentage point due to rounding. The model may also propose that there would be some retained austenite. However, the amount of retained austenite may also be numerical error of the phase transformation model.

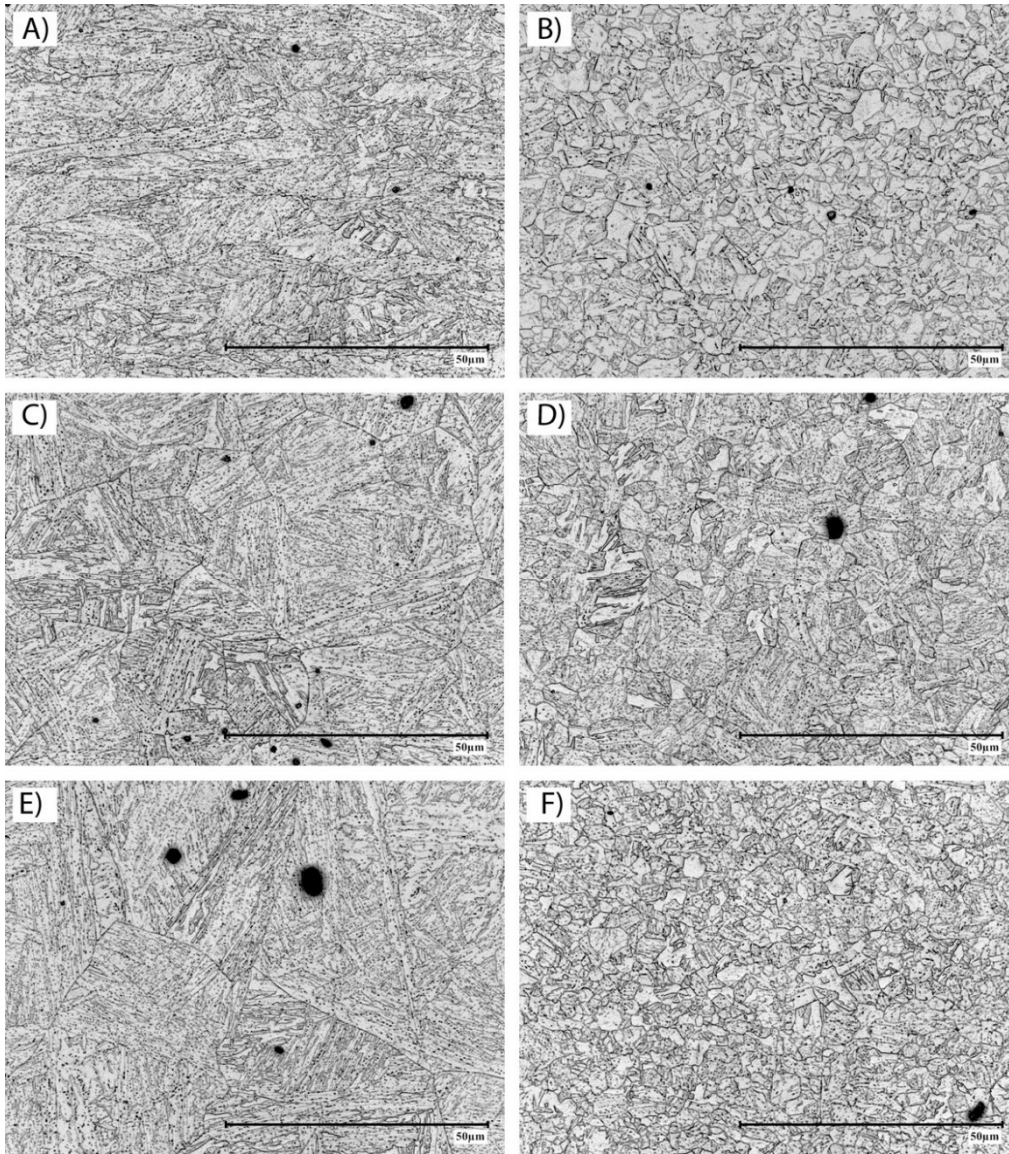


**Fig. 8** Microstructure at different areas of the heat-affected zone. Lines referred later are shown in Fig. 6. A) Top line near fusion line. B) Top line near inter-critical zone C) Middle line near fusion line. D) Middle line near inter-critical zone. E) Bottom line near fusion line. F) Bottom line near inter-critical zone.

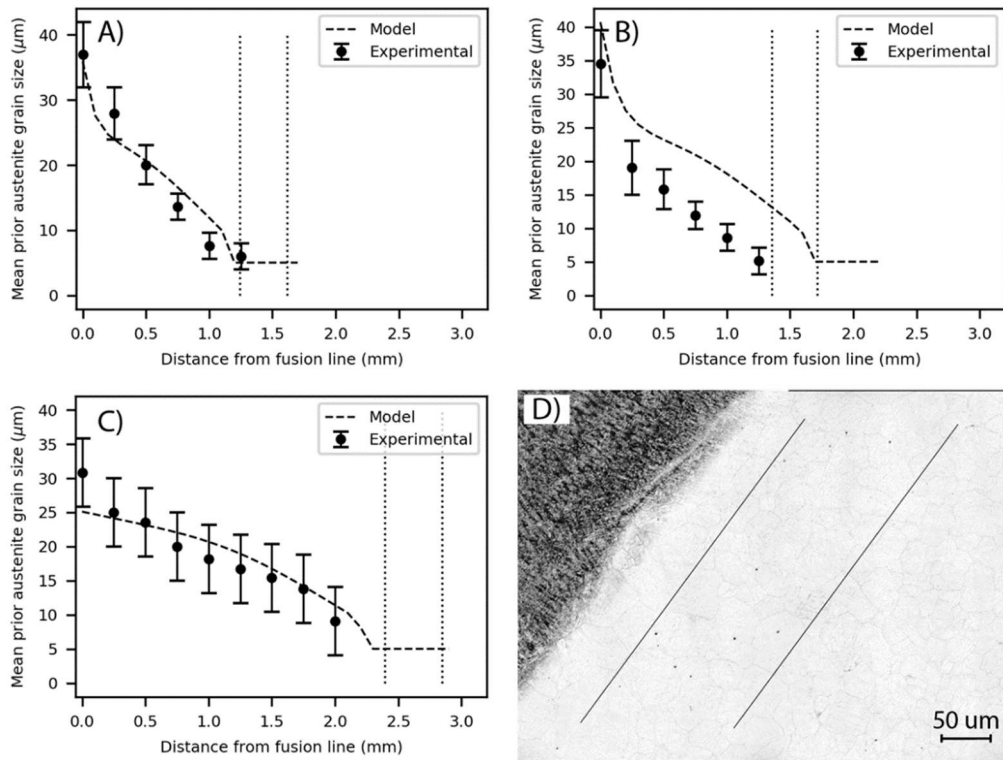


**Fig. 9** Mean prior austenite grain size A) near the top surface. B) near the centerline C) near the bottom surface. The grain size of unaffected base material is not shown in the figure and the flat areas in the modelled grain size curves show the inter-critical zone. Dashed vertical line show the real position of the ICHAZ. Lines where the grain sizes were measured from are shown in Fig. 6 D) Image showing how lines were drawn to measure the mean grain size.

The grain growth model seems to work relatively well (Fig. 9A-C). The model predicts a little wider heat-affected zone near the center than is found in actual cross-sections. This indicates that the temperatures have been too high in the model. It is supposed that this is a result from the double-ellipsoidal shape that is not ideal for these types of welds, where the shape of the fusion zone is not perfectly ellipsoidal. In addition, the performance in the initially coarse-grained zone that is partially austenitized during the second pass is very poor and would require more profound model. It is also worth noting that there may be much bigger grains than the average grain size in the coarse-grained zone (abnormal grain growth). Therefore, the grain growth model may not be optimal for situations where the grain size distribution would be needed.

## SUMMARY

The model can be used to evaluate the weldability of a steel prior to extensive practical testing because the necessary parameters can be obtained from small specimens. Moreover, model can also aid when finding the proper heat input ranges to produce desired microstructure and properties. It was shown that chosen approach gives reasonable

accuracy in fully austenitizing zones. However, the chosen methods are not necessarily suitable for inter-critical zones and the development of better models for that area would be the topic of future research.

### ACKNOWLEDGEMENTS

The authors are grateful to Mr. Juha Uusitalo for the Gleeble experiments and to Mr. Tun Tun Nyo for the valuable help in sample preparation. Also, the authors are grateful for the support of the SSAB Europe Oy.

### REFERENCES

- [1] J. GOLDAK, M. BIBBY, J. MOORE, R. HOUSE, and B. PATEL: "Computer modeling of heat flow in welds," *Metallurgical Transactions B*, vol. 17, no. 3. pp. 587–600, 1986.
- [2] D. F. WATT, L. COON, M. BIBBY, J. GOLDAK, and C. HENWOOD: "An algorithm for modelling microstructural development in weld heat-affected zones (part a) reaction kinetics," *Acta Metall.*, vol. 36, no. 11, pp. 3029–3035, 1988.
- [3] C. HENWOOD, M. BIBBY, J. GOLDAK, and D. WATT: "Coupled transient heat transfer-microstructure weld computations (part B)," *Acta Metall.*, vol. 36, no. 11, pp. 3037–3046, 1988.
- [4] D. C. MARTIN: "Selected heat conduction problems in thermomechanical treatment of steel," Doctoral Thesis, University of Oulu, 2011.
- [5] J. GOLDAK, A. CHAKRAVARTI, and M. BIBBY: "A New Finite Element Model for Welding Heat Sources," *Metallurgical Transactions B*, vol. 15, no. 2. pp. 299–305, 1984.
- [6] J. MIETTINEN: "Calculation of solidification-related thermophysical properties for steels," *Metall. Mater. Trans. B*, vol. 28B, pp. 281–297, 1997.
- [7] K. M. BROWNE: "Modeling the thermophysical properties of iron and steels," in *Proceedings of materials '98*, 1998, pp. 443–438.
- [8] M. BEUTL, G. POTTLAGHER, and H. JAGER: "Thermophysical properties of liquid iron," *Int. J. Thermophys.*, vol. 15, no. 6, pp. 1323–1331, 1994.
- [9] D. PORTER, K. EASTERLING, and M. SHERIF: *Phase Transformations in Metals and Alloys*, pp. 140, 192, 230-231 3rd ed. CRC Press, 2009.
- [10] H. K. D. H. BHADESHIA and L. E. SVENSSON: "Modelling the Evolution of Microstructure in Steel Weld Metal," *Math. Model. Weld Phenomena*, eds Cerjak, H., Easterling E.K., *Inst. Mater. London*, pp. 109–182, 1993.
- [11] T. T. PHAM, E. B. HAWBOLT, and J. K. BRIMACOMBE: "Predicting the onset of transformation under noncontinuous cooling conditions: Part II. Application to the Austenite Pearlite Transformation," *Metall. Mater. Trans. A*, vol. 26, no. 8, pp. 1993–2000, 1995.
- [12] J. LEBLOND, G. MOTTET, and J. DEVAUX: "Mathematical Models of Anisothermal Phase Transformations in Steels, and Predicted Plastic Behaviour," *Mater. Sci. Technol.*, vol. 1, no. 10, pp. 815–822, 1985.
- [13] M. UMEMOTO, K. HORIUCHI, and I. TAMURA: "Pearlite Transformation during Continuous Cooling and Its Relation to Isothermal Transformation," *Trans. Iron Steel Inst. Japan*, vol. 23, no. 8, pp. 690–695, 1983.

- [14] B. DONNAY, J. C. HERMAN, V. LEROY, U. LOTTER, R. GROSSTERLINDEN, and H. PIRCHER: “Microstructure evolution of C-Mn steels in the hot-deformation process: the stripcam model,” *2nd International Conference on Modelling of Metal Rolling Processes*. pp. 23–35, 1996.
- [15] A. POHJONEN, M. SOMANI, and D. PORTER: “Modelling of austenite transformation along arbitrary cooling paths,” *Comput. Mater. Sci.*, vol. 150, no. March, pp. 244–251, 2018.
- [16] A. POHJONEN, J. PAANANEN, J. MOURUJARVI, T. MANNINEN, J. LARKIOLA, and D. PORTER: “Computer Simulations of Austenite Decomposition of Microalloyed 700 MPa Steel During Cooling,” in *Proceedings of 21st international ESAFORM Conference on Material Forming (ESAFORM 2018)*, 2018.
- [17] J. MOON, J. LEE, and C. LEE: “Prediction for the austenite grain size in the presence of growing particles in the weld HAZ of Ti-microalloyed steel,” *Mater. Sci. Eng. A*, vol. 459, no. 1–2, pp. 40–46, 2007.
- [18] O. GRONG: *Metallurgical modelling of welding, second edition.*, pp.301-334 London: Institute of Materials, 1997.





# **III Residual Stresses and Distortion**

*intentionally blank page*

*intentionally blank page*

*intentionally blank page*

*intentionally blank page*

*intentionally blank page*

*intentionally blank page*



*intentionally blank page*

*intentionally blank page*

*intentionally blank page*

*intentionally blank page*

*intentionally blank page*

*intentionally blank page*

*intentionally blank page*

*intentionally blank page*



*intentionally blank page*

*intentionally blank page*

*intentionally blank page*

*intentionally blank page*

*intentionally blank page*

*intentionally blank page*

*intentionally blank page*

*intentionally blank page*



*intentionally blank page*

*intentionally blank page*

*intentionally blank page*

*intentionally blank page*

*intentionally blank page*

# FINITE ELEMENT SIMULATION OF RESIDUAL STRESSES AND DISTORTIONS IN SELECTIVE LASER MELTING

M. KAESS\*, M. WERZ\*\* and S. WEIHE\*\*

*\*Institute for Materials Testing, Materials Science and Strength of Materials (IMWF), University of Stuttgart, Germany*

*\*\*Materials Testing Institute (MPA), University of Stuttgart, Germany*

DOI 10.3217/978-3-85125-615-4-16

## ABSTRACT

With additive manufacturing, the production of individual lightweight structures and complex parts with integrated functions can be realized. In selective laser melting (SLM), a highly concentrated and fast moving laser spot is used to melt the powder layers which leads to high temperature gradients during the manufacturing process. This causes thermal residual stresses and distortions which can affect the intended use of additive manufactured parts. If cracks and distortions develop during the manufacturing process, a collision of the powder coater with the manufactured part can lead to a process abortion. A simulation predicting residual stresses and distortions can be used to consider these problems before manufacturing and therefore avoid scrap parts. Parameter configurations could be developed systematically to reach specific component properties. A common approach for simulating these effects in welding is the thermomechanical finite element simulation. Using this approach with a high spatial and temporal resolution, which is necessary to accurately represent the heat source, only small additive manufactured parts can be simulated with a reasonable computational effort. In order to allow numerical simulations of parts with larger dimensions, it is necessary to use appropriate simplifications and simulation strategies. One possible simplification presented in literature is to expose a whole layer to a heat source simultaneously instead of considering the whole scan path. To evaluate the effect of this simplification, the SLM-manufacturing of cuboids is simulated with different temporal resolution. Moreover, the effects of a base plate cutting and of different scanning strategies on residual stresses and distortions are examined numerically.

Keywords: selective laser melting, simulation, temperature fields, residual stresses, distortions

## INTRODUCTION

Due to its unique advantages, compared to conventional manufacturing methods, additive manufacturing has become rather popular. Additive manufacturing methods allow the production of individually produced complex components which also allows the construction of lightweight structures and components with integrated features. Compared to traditional manufacturing processes, such as forging or drilling, part or process specific tools are not needed in additive manufacturing. This provides geometry and designing choices which, in return, allows for complex, innovative and bionically optimized structures. Since only the CAD data is needed to manufacture these components, smaller quantities can be produced rather quickly.

During selective laser melting, a powdered base material is applied in layers and melted locally by means of a laser source. During the following cool down, the new material solidifies and forms solid connections with the already existing layers. This process can be compared to multilayer welding and shape welding. Only the area where the part is created is melted in each layer. The other surrounding areas stay in powder form. This powder is removed once the process is completed.

Due to the highly focused and rapidly moving heat source, there are thermal expansions and contractions during SLM [1]. If these thermal expansions or contractions are in any way obstructed during the heating or cooling of the components, local plastifications can occur due to an exceeded yield strength and thermal residual stresses could be the result [1], [2], [3]. The extent of the thermal expansions depends on locally varying heat gradients. During the SLM process, the thermal expansion, caused by the heating of the upper layers of the components, is blocked by the solidified layers underneath or the base plate respectively. Due to the higher temperatures, the material in the upper areas has a lower yield strength which tends to lead to increased yielding [4]. Residual stresses can result in cracks or can have negative effects on the tolerable loads during operation [1], [5]. Furthermore, distortions of the components can be caused by residual stresses [1], which, in return, can lead to unwanted deviations of the shape and even to the collision of the component with the mechanism that applies the powder during production. A process simulation to predict residual stresses and deviations could help to factor in these influences before the start of production. With a good simulation, parameter configurations could be developed, tested and used to achieve specific component characteristics. The different length scales of process and part, however, still pose a challenge for FE-simulations of SLM manufacturing. Currently, the dimension of additively manufactured parts can reach several centimeters or even decimeters and, on the other hand, the laser spot diameter and layer thickness are in the order of about 100 micrometers. In order to display the exact movement of the laser, a high-resolution simulation of the processing time and the working area is inevitable. Such a simulation, however, requires an immense computing effort, especially when done for larger parts. Adequate simplifications and calculation strategies need to be developed to reduce these computing efforts of numerical simulations for real life components.

### STATE OF THE ART

Numerous approaches for numerical simulations of temperature fields [6], [7], [8], [9] and residual stresses as well as deformations [10], [11], [12], [13], [14] during selective beam welding processes are described by many authors. Especially thermomechanically coupled finite element calculations are often used to determine residual stresses and deformations.

Goldak [15], [16] developed a heat source with Gaussian distribution for the fusion welding process to describe the heat input in great detail. Several different forms of heat sources for the numerical simulation of the laser beam during the SLM process for additive manufacturing have been described in literature. Examples for such forms are circular surface heat sources [8], [9], [17] and circular volumetric heat sources [18], [19] which use Gaussian intensity distribution. Furthermore, some authors describe the usage of heat sources with evenly distributed intensities [7], [20].

However, a high temporal and spatial resolution, which is necessary to precisely represent the laser spot diameter, laser movement as well as the layer thickness of a real life component, can cause very high computational costs. This is why residual stresses and temperature fields are often only calculated for smaller components. Some authors discuss methods that would allow to compute residual stresses and deformations for bigger parts as well: Keller et al. [11], for instance, use a multiscale approach with three stages to cope with the different length scales in selective laser melting to calculate residual stresses and distortions. In order to do so, the parameters of a Goldak heat source are calibrated in a microscopic model. What follows is a thermomechanical calculation using a simplified equivalent heat source in a meso-model to calculate a strain field for each layer considering the laser path. These inherent strains are finally used as input for a mechanical multi-layer calculation (macro-model), which requires less computing resources and is therefore more suitable for simulations of whole components [11].

Li et al. [13] also use a multi-scale approach with three stages. The microscale model is used to calculate the temperature field of the melt pool considering a heat source with Gaussian distribution on one single scan line. In the larger mesoscale model, the heating of a layer is simulated by using a simplified heat source which is applied for an exposure time determined in the microscale model. With the macroscale model, the layer-by-layer build process is simulated in a thermomechanically coupled analysis using the thermal input calculated in the mesoscale layer model. First, the transient temperature field of the whole build process is calculated in a thermal simulation and in a following mechanical simulation this thermal load is used to calculate stresses and strains for the whole model [13]. Neugebauer et al. [12] describe another way of simplification: To allow the usage of larger elements, multiple layers of the SLM process are combined in a macroscopic model. Furthermore, a highly detailed resolution of laser path is omitted in this approach. Instead, the layers are fully or partially heated simultaneously by one heat source. In the second case, the influence of the laser's path can, at least partially, be taken into account. The total amount of heat energy applied in this model is identical to the energy that would be applied by a high-resolution heat source. Due to the fact that in the real process the laser needs more time to run the scanning path, extra time is added in the simulation without a heat source being active. In this way, cooling processes, which occur during the heating in a real manufacturing process, can be taken into account [12].

Some authors use a method of local mesh refinement to allow for a detailed resolution of the heat source while at the same time granting a reasonable computing effort for large components [9], [10], [14], [21]. With this approach, the different length scales of SLM can be dealt with in one model. If a dynamic mesh refinement method is used, only the area immediately around the heat source is refined, the outer areas are less detailed. Due to boundary conditions or interpolations, information between the lesser and the more refined areas still need to be exchanged [21]. This is why in most commercial FE-codes the method of local mesh refinement is not realizable for AM processes [10]. This restricts the usage of dynamic mesh refinement methods to the case when no specific software is available.

Process simulations allow to manufacture components that are optimized for residual stresses. Moreover, a deeper understanding of the development of residual stresses is necessary to realize process simulations with acceptable computing efforts for large components. Only a thorough understanding can lead to the development of adequate



simplifications and computing methods, which, in return, would allow calculations for larger parts.

In our earlier works [22], [23], [24], it was investigated how deformations, residual stresses and temperature fields during the SLM process could be predicted by means of numerical simulations. Since the thermomechanically coupled finite-element-method for simulating the processes during welding has proven to be adequate, the same method was used to simulate the manufacturing of cuboids using SLM. In order to conduct numerical simulations with an agreeable amount of computing, simplifications had to be made. Therefore, the influence of the spacial and temporal discretization on the computing time and the preciseness of the simulation were investigated. A possible way to simplify the simulation is to combine the sections of the laser movement into larger intervals. Previous studies [22], [23], [24] show that this method is a possible way to simplify the process while losing only a small amount of detail. If the scanning strategy is simplified too much, however, not all aspects of the transient influences can be captured. The studies regarding the influence of element size, temperature gradients, residual stresses and deformations show consistent results as long as the size of the used elements does not exceed the diameter of the laser source or the thickness of the layers.

### MODEL DESCRIPTION

Numerical studies have been performed to develop an understanding of influences of the base plate cutting and the scanning strategy on residual stresses and distortions in SLM. Moreover, the effects of a simplification method have been examined.

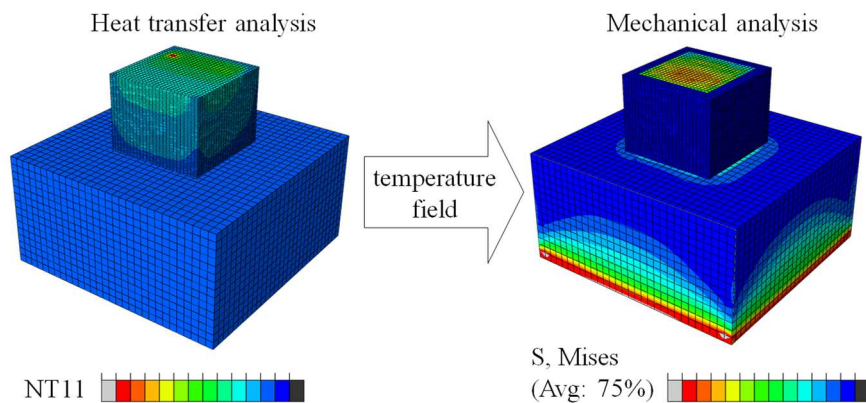


**Fig. 1** Sequentially coupled thermomechanical simulation method shown schematically

In the presented studies, a sequentially coupled thermomechanical simulation approach is used in the finite element program Abaqus. Fig. 1 shows schematically the two models used for the implicit heat transfer analysis first, and the following implicit mechanical analysis second. In the heat transfer analysis, thermal boundary conditions and a heat source model to simulate the laser beam are applied. The result file from the heat transfer analysis is read into the sequentially coupled mechanical analysis to consider temperature dependent material properties and to calculate thermal expansions and constrictions from temperature

gradients. The mechanical analysis is being used to calculate stresses, strains and displacements considering mechanical boundary conditions.

In the studies, the model of a cube with 3 mm edge length, shown in Fig. 2, has been created. A tie contact is used in the model to simulate the connection to the base plate on which the cube is directly built. The element size in the cube is  $0.15 \times 0.15 \times 0.05 \text{ mm}^3$  and in the built plate it is  $0.3 \times 0.3 \times 0.3 \text{ mm}^3$ . The element height of 0.05 mm represents the simulated powder layer thickness. Heat dependent material properties of the aluminum alloy AlSi10Mg in solid state are assigned to the base plate and the cube. Additionally, a material definition of AlSi10Mg with reduced thermal conductivity and reduced mechanical strength properties is used for the surrounding powder ring, which is modeled to account for the influence of the powder bed. The used material properties are shown in Table 1. The temperature dependent material properties are interpolated linearly in the given range and kept constant for lower and higher values.

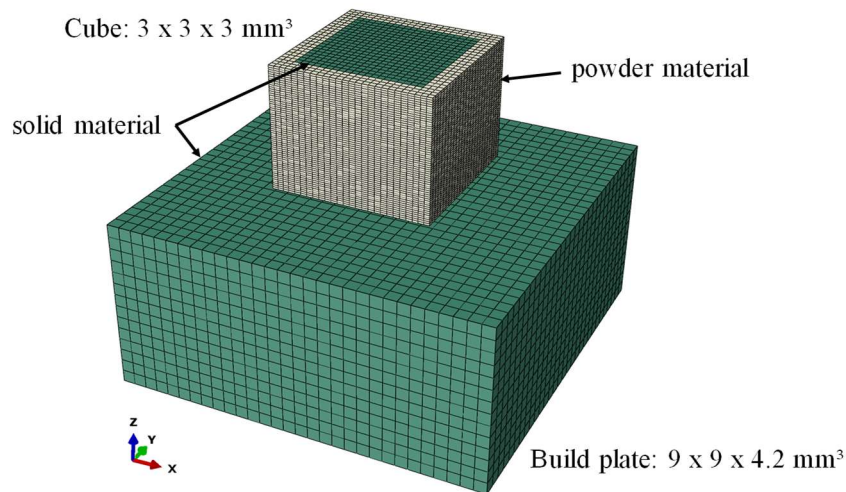


**Fig. 2** Finite element model of a cube with build plate and different material assignments

The layer-by-layer build process is simulated by successively activating the elements of the cube. In the model, the final geometry of the cube is defined, but elements of a layer remain inactive until the coating of this layer is simulated. Inactive elements are not considered in the calculation. The new plug-in feature “AM Modeler” of Abaqus 2017 is used to control this element activation.

**Table 1** Temperature-dependent material properties for powder and solid (derived from [25], [26])

<b>temperature</b>	20 °C	600 °C	
<b>heat conduction solid material</b>	110 W/(m*K)	150 W/(m*K)	
<b>heat conduction powder material</b>	1,1 W/(m*K)	1,5 W/(m*K)	
<b>heat capacity</b>	900 J/(kg*K)	1200 J/(kg*K)	
<b>heat expansion</b>	$21 \cdot 10^{-6}$ 1/K	$26 \cdot 10^{-6}$ 1/K	
<b>temperature</b>	20 °C	500 °C	580 °C
<b>yield strength powder material</b>	1 MPa	1 MPa	1 MPa
<b>Young's modulus powder material</b>	10 GPa	10 GPa	10 GPa
<b>yield strength solid material</b>	250 MPa	20 MPa	1 MPa
<b>Young's modulus solid material</b>	72 GPa	10 GPa	10 GPa

With this Abaqus feature, it is also possible to define a heat source and the related scanning strategy for simulating the thermal impact of the laser beam. In this way, a hemispherical volumetric heat source with Gaussian intensity distribution was implemented in the model. A scanning speed of 1000 mm/s, a diameter of 0.2 mm and a power of 300 W were used for the heat source model.

At the top surface of the cube, convection and radiation to the build chamber are modelled in the heat transfer analysis. Furthermore, heat transfer to the surrounding powder bed is modelled at the lateral surfaces of the cube and heat transfer to the continuing built plate is modelled at the bottom. In the mechanical analysis, an encastre boundary condition is used for the bottom surface of the build plate to simulate a fixation in the SLM-machine.

For all simulations, a preheating of powder, build plate and build chamber to 50 °C is applied. After the build process of 60 layers with alternating element activation and layer heating, a cooling period follows in which the whole model is cooled down to room temperature (20 °C). Finally, the cutting process is simulated according to [27] by successively deleting the top element layer of the base plate, as shown in Fig. 3.

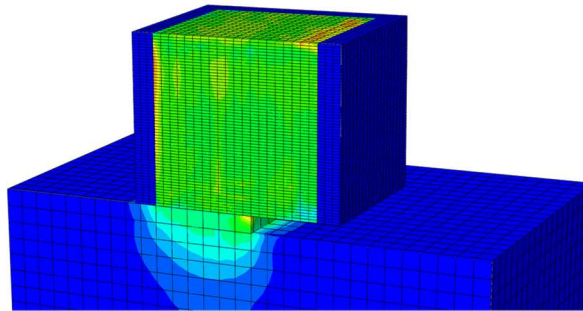


**Fig. 3** Cutting from the build plate by deleting elements

## Mathematical Modelling of Weld Phenomena 12

With the model described above, studies of different scanning strategies were performed. These five examined scanning strategies are shown in Fig. 4. The scanning pattern remains unchanged for all layers in (a), (c) and (d) and alternates for (b) and (e). For scanning strategies a) to c), the scanning path starts in the upper left corner and ends in the lower right corner. The order of the islands is numbered for scanning strategy e).

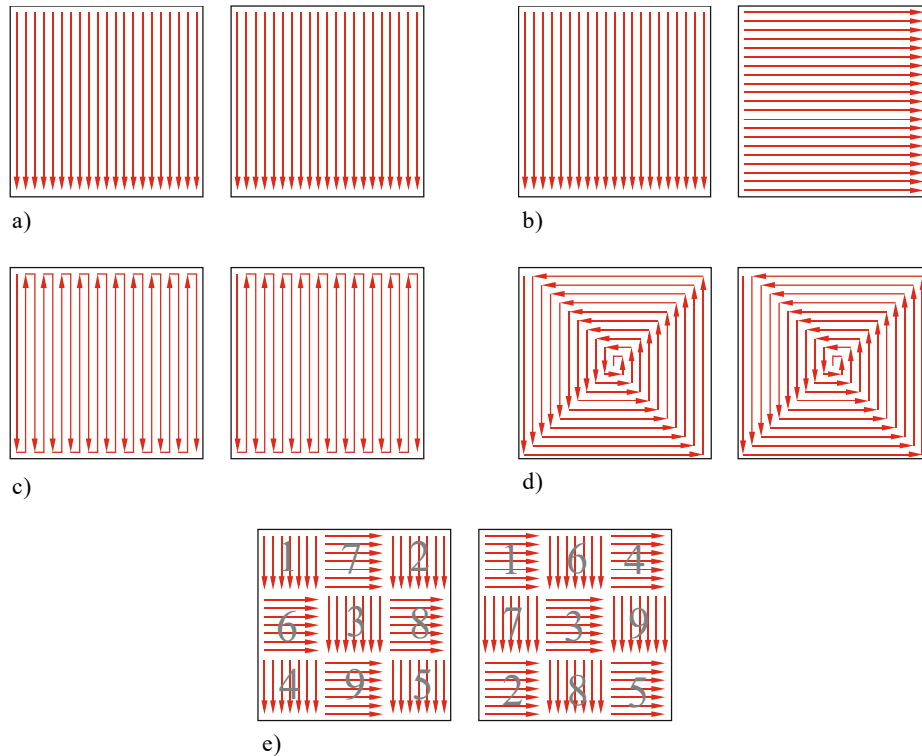


**Fig. 4** scanning strategies - left and right figure represent alternating layers:  
 (a) linear scanning; (b) across scanning; (c) meander scanning; (d) screw scanning; (e) island scanning

## RESULTS

Stresses and deformations are being analyzed along different paths, which are schematically shown in the cubic model in Fig. 5. Before build plate cutting, the cube is connected to the substrate on the x, y plane. Stresses are always taken along path 1 which is located in z-direction at the center of the cube. Distortions are calculated as a difference of displacements on two paths located on opposite surfaces. Path 2a and 2b are used to calculate the shrinkage or expansion in z-direction and along path 3a and 3b, the deformation in x-direction is analyzed.

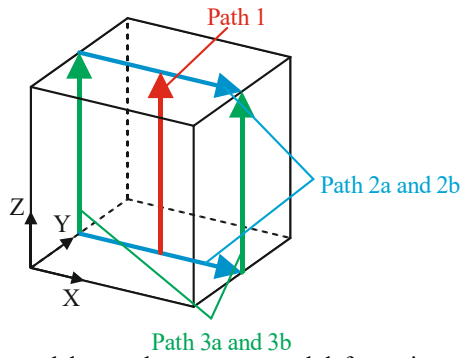


**Fig. 5** Paths in the cubic model to analyze stresses and deformations

Fig. 6 and Fig. 7 show how stresses and distortions change in the model due to a base plate cutting. These simulations have been conducted with a linear scanning strategy and a time increment of 0.001 s. Mercelis et al. [4] determined that parts which are removed from the base plate basically show tensile stresses in the upper region, compressive stresses in the center and tensile stresses in the lower areas. The occurrence of high tensile stresses in the top layers and compressive stresses in the center of parts is confirmed by [1]. The stresses in x-direction illustrated in Fig. 6 show a good qualitative accordance to the distribution described in [1] and [4].

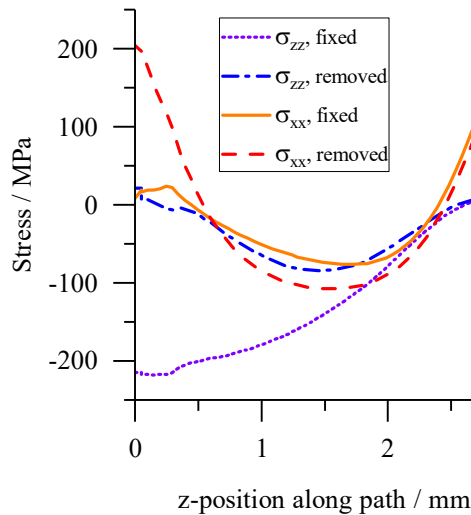


**Fig. 6** Influence of base plate cutting on stresses along path 1 – linear scanning strategy

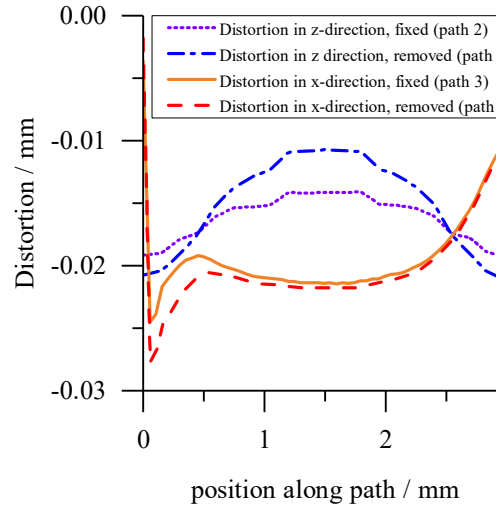


**Fig. 7** Influence of base plate cutting on distortions along paths 2 and 3 – linear scanning strategy

Fig. 6 shows high compressive stresses in z-direction along path 1 in the bottom area of the cube before cutting from the base plate. A relaxation of these stresses occurs when the base plate is removed. On the other hand, high tensile stresses emerge in x-direction after base plate cutting. In Fig. 7, the geometrical deviation from the ideal shape is shown. This means that an expansion in z-direction and a shrinkage in x-direction occurs due to the base plate cutting. In summary, it could be shown that significant changes of stresses occur at

the bottom of the cube whereas the upper area remains almost unchanged when the base plate is removed. These variations of the stress field cause shrinkage and expansion of the cube.

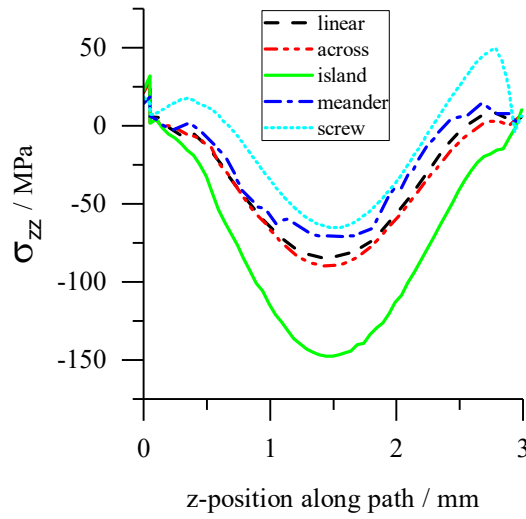


Fig. 8  $\sigma_{zz}$  along path 1 for different scanning strategies – used time increment: 0.001 s

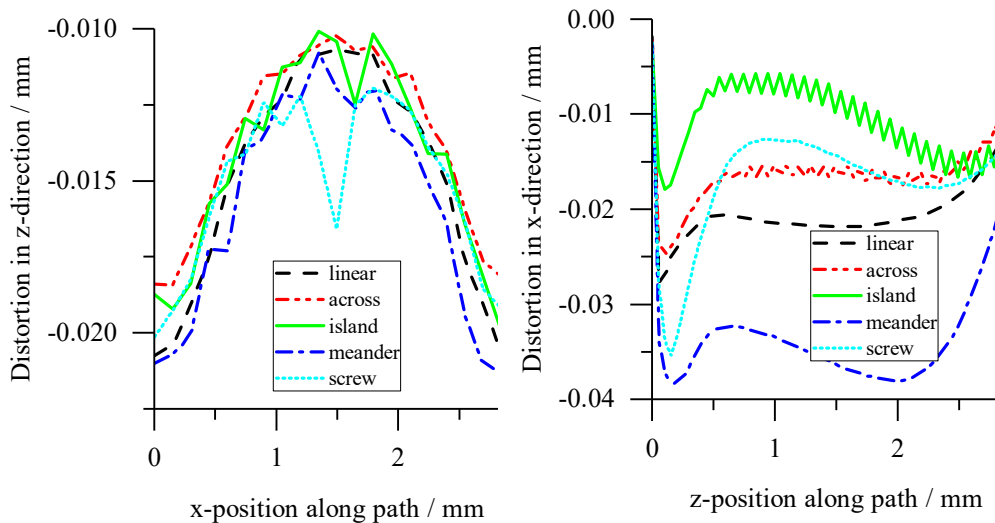


Fig. 9 distortion in z-direction along paths 2 – used time increment: 0.001 s

Fig. 10 distortion in x-direction along paths 3 – used time increment: 0.001 s

The influence of different scanning strategies on residual stresses after base plate cutting is shown in Fig. 8. All calculated stress curves have a similar shape but show different minimum and maximum values. The highest compressive stresses in z-direction occur in the center of the cube for an island scanning strategy.

Fig. 9 and Fig. 10 show the geometrical deviations for different scanning strategies after base plate cutting. Only small differences are calculated for the deformation in z-direction,

but significant variations occur for the deformation in x-direction. The largest shrinkage in x-direction has been calculated for a meander scanning strategy and the smallest deviation is shown for an island scanning pattern. This means that the simulation method can be used to capture effects of different scanning strategies. A validation of the numerical results has to be done in a future study to allow a quantitative comparison.

In the following, an examination of different temporal discretizations is presented. Fig. 11 shows the stress in z-direction along path 1 for a linear scanning strategy. Only with a small time increment, the scanning strategy can be considered in detail. For larger time increments, the heat flux is averaged over larger segments of the scanning path which are passed by the fast moving laser beam. Using a time increment of 0.1 s means that one whole layer is heated at the same time. In Fig. 11 it can be seen that wide variations of the calculated residual stresses occur. Convergence of the results can be seen for a time increment equal or smaller than 0.0005 s. Averaging the heat fluxes over a long period of time means that the spot heating with high intensity cannot be considered in the calculation and the maximum temperatures that are reached decrease. This has already been shown in [22], [23] and [24].

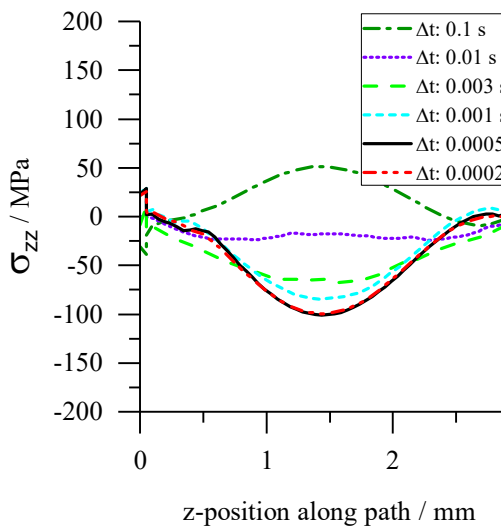


**Fig. 11**  $\sigma_{zz}$  along path 1 for different temporal discretizations – linear scanning strategy

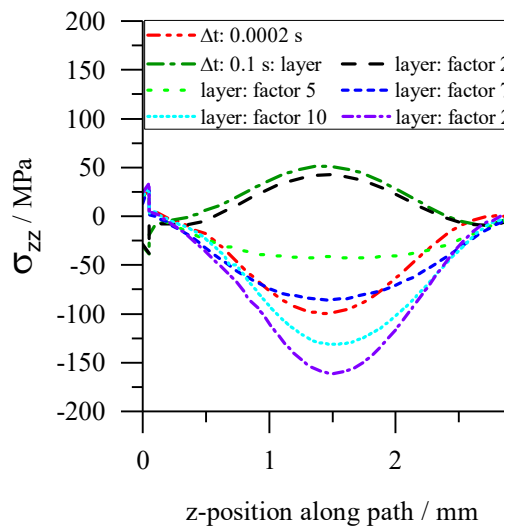


**Fig. 12**  $\sigma_{zz}$  along path 1 for different temporal discretizations and layer-by-layer heating – linear scanning strategy

A layer-by-layer heating with higher intensity for a respectively shorter period of time was tested to compensate this effect of averaged heat fluxes and decreasing temperatures. For this purpose, the intensity of the layer heat source was increased by a factor between 2 and 20 and the exposure time was reduced by the same factor. As a result, the energy input per unit length and the total energy input per layer were kept constant. In

Fig. 12, it is shown that this technique allows to adjust the calculated residual stresses to the shape calculated with a high temporal resolution (0.0002 s). However, if the factor is too high, the calculated residual stresses exceed the curve with high resolution (0.0002 s).

In Fig. 12 the curve with a factor of 7 shows the best results for the stresses in z-direction. For other magnitudes, like  $\sigma_{xx}$  or deformations, the factor also shows an effect and can be used to match the curves. However, the ideal factor varies for the different magnitudes. For example, a factor of 15 or even 30 is best to fit the stress or deformation in x-direction in this model. This means that a layer-by-layer heating could be an appropriate method of simplification to reduce computational effort if the intensity of the heat source is calibrated well. In future studies, different calibration methods, based on the maximum temperatures reached in the process or the energy input per unit length, will be examined. However, the effect of different scanning strategies, as shown in Fig. 8 and Fig. 10, cannot be considered by a layer heat source. This effect could perhaps be dealt with if a calibration of the layer heat source is conducted with a detailed model of one or a few layers.

### CONCLUSION

It could be shown that a base plate cutting and different scanning strategies can be considered in a thermomechanical finite element simulation of a selective laser melting process. A high temporal resolution is necessary to model the effect of different scanning strategies. On the other hand, it was shown that a layer-by-layer heating could be an appropriate method to reduce computational costs. Simplifications are important to make the thermomechanical finite element method feasible for simulating the SLM-production of large components. In future studies, it is planned to additively manufacture cubes and other geometries and experimentally examine these parts on residual stresses and distortions. These experimental studies are necessary to validate and develop the models and the proposed simplification strategies.

### REFERENCES

- [1] Y. LIU, Y. YANG, and D. WANG, 'A study on the residual stress during selective laser melting (SLM) of metallic powder', *Int J Adv Manuf Technol*, vol. 87, no. 1-4, pp. 647–656, 2016.
- [2] E. ROOS, K. MAILE, and M. SEIDENFUß, *Werkstoffkunde für Ingenieure*, 6th ed. Berlin: Springer-Vieweg, 2017.
- [3] D. BUCHBINDER, G. SCHILLING, W. MEINERS, N. PIRCH, and K. WISSENBAACH, 'Untersuchung zur Reduzierung des Verzugs durch Vorwärmung bei der Herstellung von Aluminiumbauteilen mittels SLM', *RTejournal*, 2011.
- [4] P. MERCELIS and J. KRUTH, 'Residual stresses in selective laser sintering and selective laser melting', *Rapid Prototyping Journal*, vol. 12, no. 5, pp. 254–265, 2006.
- [5] C. CASAVOLA, S. L. CAMPANELLI, and C. PAPPALLETTERE, 'Preliminary investigation on distribution of residual stress generated by the selective laser melting process', *The Journal of Strain Analysis for Engineering Design*, vol. 44, no. 1, pp. 93–104, 2008.
- [6] S. KOLOSSOV, E. BOILLAT, R. GLARDON, P. FISCHER, and M. LOCHER, '3D FE simulation for temperature evolution in the selective laser sintering process', *International Journal of Machine Tools and Manufacture*, vol. 44, no. 2-3, pp. 117–123, 2004.
- [7] N. CONTUZZI, S. L. CAMPANELLI, and A. D. LUDOVICO, '3D Finite Element Analysis in the selective laser melting process', *Int. j. simul. model.*, vol. 10, no. 3, pp. 113–121, 2011.



- [8] I. A. ROBERTS, C. J. WANG, R. ESTERLEIN, M. STANFORD, and D. J. MYNORS, ‘A three-dimensional finite element analysis of the temperature field during laser melting of metal powders in additive layer manufacturing’, *International Journal of Machine Tools and Manufacture*, vol. 49, no. 12-13, pp. 916–923, 2009.
- [9] D. PITASSI *et al.*, ‘Finite Element Thermal Analysis of Metal Parts Additively Manufactured via Selective Laser Melting’ in *Finite Element Method - Simulation, Numerical Analysis and Solution Techniques*, R. Păcurar, Ed.: InTech, 2018.
- [10] A. BAUEREIß, E. PARTELI, D. RIEDLBAUER, and M. STINGL, ‘Numerische Simulation pulver- und strahlbasierter additiver Fertigungsprozesse’, in *Dietmar Drummer*, pp. 117–130, 2012.
- [11] N. KELLER and V. PLOSHIKHIN, ‘New method for fast predictions of residual stress and distortion of AM parts’. Austin, Texas, 2014.
- [12] F. NEUGEBAUER, N. KELLER, V. PLOSHIKHIN, F. FEUERHAHN, and H. KÖHLER, ‘Multi Scale FEM Simulation for Distortion Calculation in Additive Manufacturing of Hardening Stainless Steel’. Bremen, 2014.
- [13] C. LI, J. F. LIU, X. Y. FANG, and Y. B. GUO, ‘Efficient predictive model of part distortion and residual stress in selective laser melting’, *Additive Manufacturing*, vol. 17, pp. 157–168, 2017.
- [14] E. R. DENLINGER, M. GOUGE, J. IRWIN, and P. MICHALERIS, ‘Thermomechanical model development and in situ experimental validation of the Laser Powder-Bed Fusion process’, *Additive Manufacturing*, vol. 16, pp. 73–80, 2017.
- [15] J. GOLDAK, A. CHAKRAVARTI, and M. BIBBY, ‘A new finite element model for welding heat sources’, *Metallurgical Transactions*, no. 15B, pp. 299–305, 1984.
- [16] J. GOLDAK and M. AKHLAGHI, *Computational welding mechanics*.
- [17] K. ZENG, D. PAL, N. PATIL, and B. STUCKER, ‘A new Dynamic Mesh Method Applied to the Simulation of Selective Laser Melting’. Austin, Texas, 2013.
- [18] T. TÖPPEL, B. MÜLLER, K. P. HOEREN, and G. WITT, ‘Eigenspannungen und Verzug bei der additiven Fertigung’, *Schweißen und Schneiden* 68, no. 4, pp. 176–186, 2016.
- [19] A. HUSSEIN, L. HAO, C. YAN, and R. EVERSON, ‘Finite element simulation of the temperature and stress fields in single layers built without-support in selective laser melting’, *Materials & Design (1980-2015)*, vol. 52, pp. 638–647, 2013.
- [20] A. FOROOZMEHR, M. BADROSSAMAY, E. FOROOZMEHR, and S. GOLABI, ‘Finite Element Simulation of Selective Laser Melting process considering Optical Penetration Depth of laser in powder bed’, *Materials & Design*, vol. 89, pp. 255–263, 2016.
- [21] N. PATIL, D. PAL, and B. STUCKER, ‘A New Finite Element Solver using Numerical Eigen Modes for Fast Simulation of Additive Manufacturing Processes’.
- [22] M. KÄß, ‘Entwicklung einer Simulationsmethode zur Vorhersage der Eigenspannungen beim selektiven Laserschmelzen (SLM)’, Master’s Thesis, Institute für Materials Testing, Materials Science and Strength of Materials (IMWF), University of Stuttgart, 2017.
- [23] M. KÄß, M. WERZ, and S. WEIHE, ‘Vergleich verschiedener Ansätze zur Simulation der Temperaturfelder und Eigenspannungen beim selektiven Laserschmelzen’, *2. Tagung des DVM Arbeitskreises - Additiv gefertigte Bauteile und Strukturen*, pp. 99–112, 2017.
- [24] M. KÄß, M. WERZ, and S. WEIHE, ‘Parametrische Untersuchung der Diskretisierung für die numerische Simulation von Temperaturfeldern, Eigenspannungen und Verzügen beim selektiven Laserschmelzen’, *DGM Fachtagung Werkstoffe und Additive Fertigung*, 2018.
- [25] EOS GmbH, ‘Materialdatenblatt EOS Aluminium AlSi10Mg’, Krailing/München, 2014.
- [26] Renishaw plc, ‘AlSi10Mg-0403 Pulver für die generative Fertigung’, Pliezhausen, 2015.
- [27] T. BARETH, ‘Entwicklung eines Modells zur Simulation von Eigenspannungen und Verzügen beim selektiven Laserschmelzen’, Student Research Project, Institute für Materials Testing, Materials Science and Strength of Materials (IMWF), University of Stuttgart, 2018.

# A SHIFT TECHNIQUE FOR MULTI-PASS WELDING SIMULATION

P. PEREIRA ALVAREZ<sup>\*\*\*</sup>, T. DINH TRONG<sup>\*\*\*</sup>, S. HENDILI<sup>\*</sup>,  
V. ROBIN<sup>\*</sup> and J. DELMAS<sup>\*</sup>

<sup>\*</sup>EDF R&D, Chatou, France

<sup>\*\*</sup>MINES ParisTech, Centre des matériaux, CNRS UMR 7633, Evry, France [pablo.pereira\\_alvarez@mines-paristech.fr](mailto:pablo.pereira_alvarez@mines-paristech.fr)

DOI 10.3217/978-3-85125-615-4-17

## ABSTRACT

The simulation of complex industrial welding processes using the Finite Elements method is not usually feasible within a reasonable time limit due to the strong non linearities of the physical models and the dimensions of the problem. To study many of these industrial cases, we would like to apply simplified methods to compute the simulations in acceptable time. We propose a simplified method called Physical Fields Shift which allows us to accelerate the computations and obtain an approximation of the strain and residual stress state at the scale of the component after the repair process. This method has been applied to an overlay welding repair with successful results.

Keywords: multi-pass welding, shift technique, overlay welding repair

## INTRODUCTION

The numerical simulation of welding processes is an extremely complex problem because of the strong non linearities of the physical models and their large spatio-temporal dimensions. In some industrial cases of welding repair, a large number of passes is involved. This large number of passes implies an even greater time expense and thus their study through simulations is almost impossible to achieve in an industrial context. An example of this type of problem is the simulation of a welding repair process called overlay. In this kind of process, more than a hundred passes over two different layers of weld beads are required. Bearing in mind that the simulation of a single pass takes around 10 hours, we immediately realize that the simulation of the whole process using the classical Finite Elements method is not feasible in a reasonable time.

A simplified method called the Physical Fields Shift is proposed. Firstly the Physical Fields Shift method will be explained. Then, we will present a welding procedure that is being studied through numerical simulation: an overlay repair operation. In that section, the parameters of the reference procedure and the consequences of it are discussed. The goal of the following section is to explain the physical models employed in the simulation of an overlay repair, focusing on the mechanical behavior. Finally the performance of both methods (the proposed Physical Fields Shift method and the classical Finite Elements method) will be compared to empirical data obtained from an industrial overlay procedure.

## PHYSICAL FIELDS SHIFT

In the context of one of EDF's research projects on welding, numerical simulation is used as a way to study the thermo-mechanical consequences of many different welding repair processes. These multi-pass simulations usually involve a large number of welding beads arranged in several layers of them. The computation time increases at least quadratically with the number of beads and thus the whole simulation of the welding procedure is not feasible in a reasonable time. To overcome this problem, we propose a simplified method called Physical Fields Shift which allows us to accelerate the computations and obtain an approximation of the strain and residual stress state at the scale of the component after the repair process.

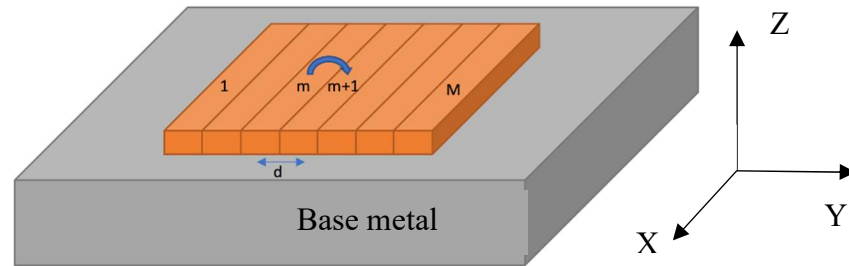


Fig. 1 Schema showing a multi-pass welding toy case (one layer).

The Physical Fields Shift method is based on the similarities observed between two consecutive passes. After a certain number of simulated passes, we observe a propagation of the solution in the sense of the deposit of welding beads. In fact, after each pass, the main difference between two consecutive passes is a spatial translation. Indeed, on the new bead almost the same fields reappear and on the previous beads, the stress and strain accumulate. This evolution will be capitalized to obtain an approximation of the next passes. However, a reasonable number of beads must be computed before applying the method because this observation is not valid on the first beads. Fig. 2 and Fig. 3 show these phenomena in a welding test case consisting of a base metal and 20 welding beads similar to the one in Fig. 1. The curves are plotted over a line that goes from one end of the base to the other, crossing the welding area at the center. A zoom is made on the welding area. The first bead is placed at 60 mm from the end of the plate and is 4 mm large. The last one is placed at 136 mm. In the figures, the tenth bead starts at a 100 mm and the thirteenth starts at 112 mm.

Let  $M \in \mathbb{N}$  be the total number of passes. In order to use the method, we need to compute the first  $m$  passes by the Finite Elements method, with  $m < M$ . The objective of the first step is to obtain an approximation of the final state of the  $(m+1)^{th}$  pass using the solutions of the  $m$  and  $m-1$  passes. We assume that the difference between the displacement and stress fields of the  $m+1$  and  $m$  passes is going to be similar to that of the  $m$  and  $m-1$  passes. Let  $\mathbf{s}_m$  and  $\mathbf{s}_{m-1}$  be the fields representing the final state after the simulation of the  $m+1$  and  $m$  passes respectively. The first step of the method is to compute a field  $\Delta\mathbf{s}_m$  containing the difference between the  $m$  and  $m-1$  passes. This field is called the increment field and it

represents the evolution of displacement and stress from the  $m-1$  pass to the  $m$  and it is computed as follows:

$$\Delta \mathbf{s}_m = \mathbf{s}_m - \mathbf{s}_{m-1}$$

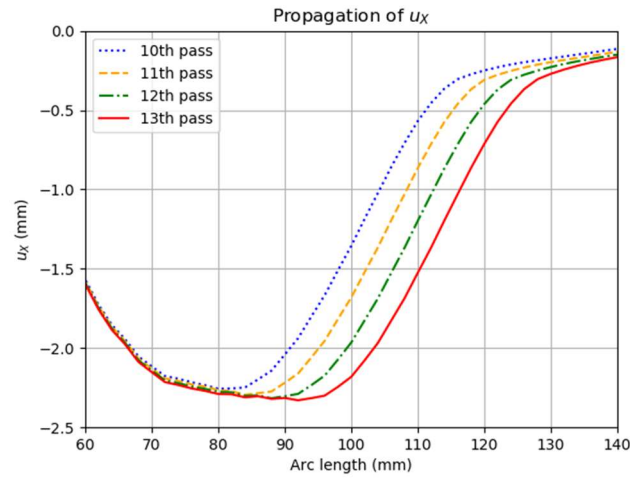


**Fig. 2** Final state of displacement of four consecutive passes (X component).

When the increment field is calculated, we need to shift it of a distance  $d$  in the direction of the deposit of welding beads. This distance  $d$  represents the distance between two beads as shown in Fig. 1. The shifted increment field  $\Delta \hat{\mathbf{s}}_m$  approximates the evolution that will happen between the  $m$  and  $m+1$  passes. Finally, the shifted increment field is used to obtain an approximation  $\tilde{\mathbf{s}}_{m+1}$  of  $\mathbf{s}_{m+1}$ :

$$\tilde{\mathbf{s}}_{m+1} = \mathbf{s}_m + \Delta \hat{\mathbf{s}}_m$$

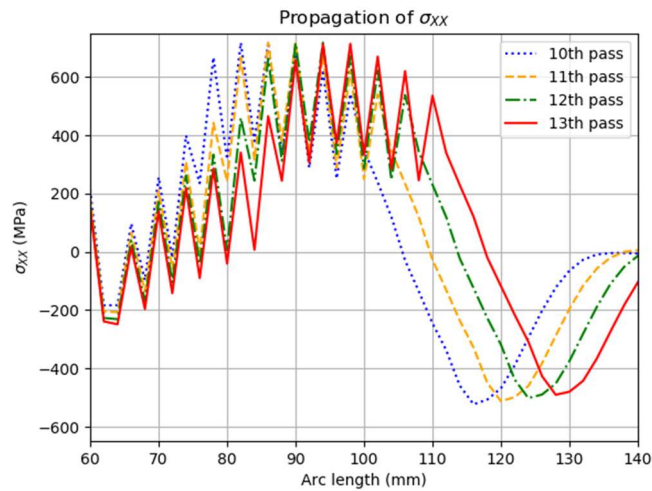


**Fig. 3** Final state of longitudinal stresses of four consecutive passes.

## Mathematical Modelling of Weld Phenomena 12

The method is applied successively until all of the beads are done. The predictions are accurate in the welding area (see Fig. 4), but not so much outside of it after applying the method many consecutive times. The final step, once all the passes are done, consists in using the predictions as input on the welding area for an elastoplastic re-equilibrium to obtain an approximation of the final state of the physical fields on the whole structure.

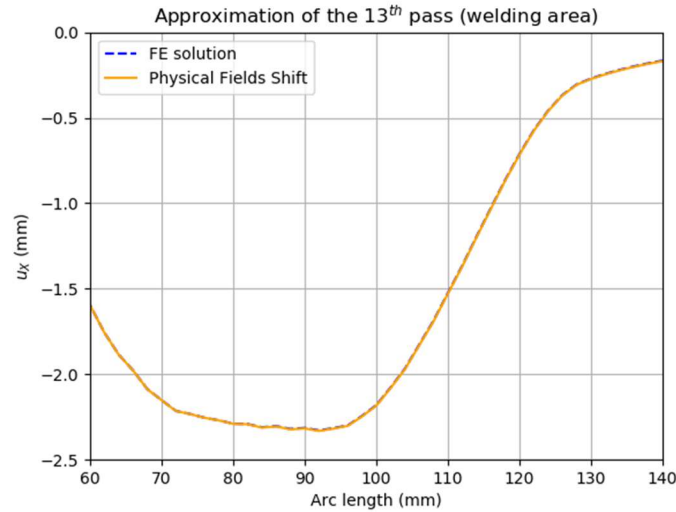


**Fig. 4** Approximation of the displacement of the 13<sup>th</sup> pass (X component).

### OVERLAY WELDING REPAIR

Pipes in nuclear power plants sometimes have a thickness defect which could be caused during its fabrication or by erosion. When this kind of defect is detected, it needs to be repaired using a method called overlay to ensure their mechanical resistance. This technique consists in covering the defected area with one or more layers of welding beads in order to achieve a physical and mechanical continuity. We differentiate between partial overlay, when only a section of the circumference is welded and complete overlay, when the whole circumference is welded. Only the partial overlay is being considered as an example of an industrial case in this document.

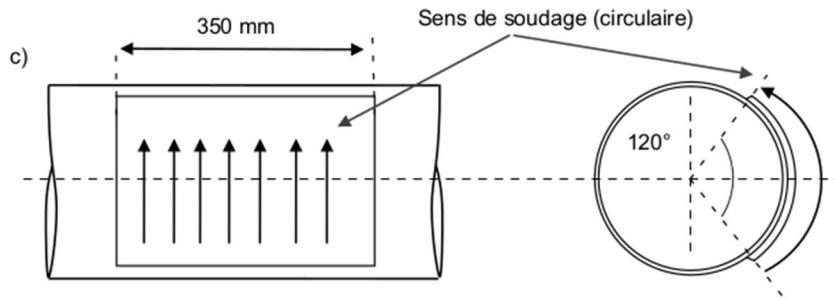


Fig. 5 Schema of the welding area.

The pipe on which the procedure is performed is made from P265GH Schedule 80S steel. It is 1900 mm long, its external diameter is 323.8 mm and its thickness is 12.7 mm. After the operation, we will have a deposition with a thickness of 5.6 mm. A first layer of 3.4 mm and a second one of 2.2 mm. The welding beads are deposited on an area of 350 mm and 120° of the circumference, as shown in the schema in Fig. 5. The welding parameters of the operation are shown in Table 1.

At the end of the procedure, three different types of deformation on the pipe will be observed. Due to the suffered stress during the welding the pipe will bend, changing the angle between the extremities of the pipe. Furthermore, the pipe is deformed at the welding area and its internal diameter is reduced.

Table 1 Welding parameters of the reference experiment.

Parameters	First layer	Second layer
Intensity ( $A$ )	193	182
Tension ( $V$ )	17,8	17,8
Speed ( $cm \cdot min^{-1}$ )	13	12
Maximum inter-pass temperature ( $^{\circ}C$ )	250	250
Energy ( $KJ \cdot min^{-1}$ )	15,9	16,1
Number of passes	114	91

## NUMERICAL MODEL

To simulate a welding procedure, a thermo-mechanical problem is solved using the Finite Elements method with code\_aster, EDF's Finite Elements software[1]. The pipe is modeled by a 1900 mm cylinder with an external diameter of 323.8 mm and a thickness of 12.7 mm. The welding beads are modeled as a volume 5.6 mm thick covering an area of 120 ° and 350 mm placed in the middle of the pipe. This volume is divided in two layers of 3.4 mm

and 2.2 mm respectively. Each layer will be partitioned in a 100 sub-layers in the transverse sense of welding. These sub-layers will represent the welding beads. The pipe and the welding beads are meshed using quadrangular linear elements. The mesh is more refined in the welding area and has a total of 345842 elements. A screenshot of the mesh can be found in the first appendix.

The thermo-mechanical problem is solved in two steps. We first solve the thermal problem and then use the solution as input data for the mechanical problem. The heat problem consists of the classical heat equation in which the heat source is represented as an equivalent heat source using a Goldak function [2]. The other boundary conditions are the heat exchange with the surrounding air (supposed to be at 20°C) and radiation. Table 2 shows the parameters used to solve the heat problem.

The mechanical behavior is supposed to be thermo-elasto-plastic. The thermo-elastic behavior is determined by Young’s modulus, Poisson’s coefficient and the coefficient of thermal expansion whilst the plastic behavior is described by the von Mises yield criterion and isotropic non-linear hardening. The hardening function  $R(p, T)$ , dependent on the plastic strain ( $p$ ) and temperature ( $T$ ), is computed from stress-strain curves  $\sigma(\varepsilon, T)$  obtained from experimental measures. In the third appendix an example of the stress-strain curves for various temperature values are given. The mechanical evolution is produced by the temperature gradients calculated during the resolution of the heat problem. Three points are fixed on one side of the pipe, enough to avoid rigid body movements.

The values of the physical parameters used in the numerical models are shown in the second appendix.

**Table 2** Parameters of the heat problem.

Parameters	Values
Heat source’s length	10 mm
Efficiency of the heat source	0.55
Heat source speed	13/6 mm · s <sup>-1</sup>
Convective transfer coefficient	20 W · m <sup>-2</sup> · K <sup>-1</sup>
Emissivity	0.8
Boltzmann constant	5.67 10 <sup>-8</sup> W · m <sup>-2</sup> · K <sup>-4</sup>

## RESULTS

The goal of this section is to compare the performance of the Physical Fields Shift method to the classical Finite Elements method. To do so, we will compare the computation time of each method and the error between the obtained solution and a reference solution, in this case the experimental data. The computation of the Finite Elements method takes a really long time, so only the first layer of beads is simulated. This method has already been tested with success on an overlay welding procedure in [3].

To apply the Physical Fields Shift method, the twenty first passes are simulated using the Finite Elements method. The choice of twenty beads is to done to be sure that the quasi-steady state is achieved. The final instant of the solutions of the 19<sup>th</sup> and 20<sup>th</sup> passes are used to approximate the final instant of the 21<sup>st</sup> pass. Then, the final instant of the 22<sup>nd</sup> is

computed from the final state of the 20<sup>th</sup> pass and the approximation of the 21<sup>st</sup> pass. The final state of the rest of the passes are calculated in the same way using the approximations. After the final pass is finished, a quick elastoplastic re-equilibrium is computed introducing the predicted stress and strain fields as imposed values on the welding area to calculate the final strain on the whole pipe.

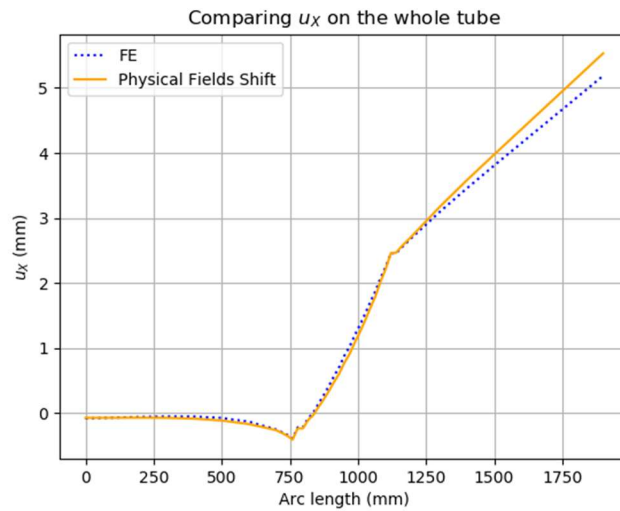


**Fig. 6** Comparison of the final state of displacement computed using the Finite Elements method and the Physical Fields Shift method applied 80 times (X component).

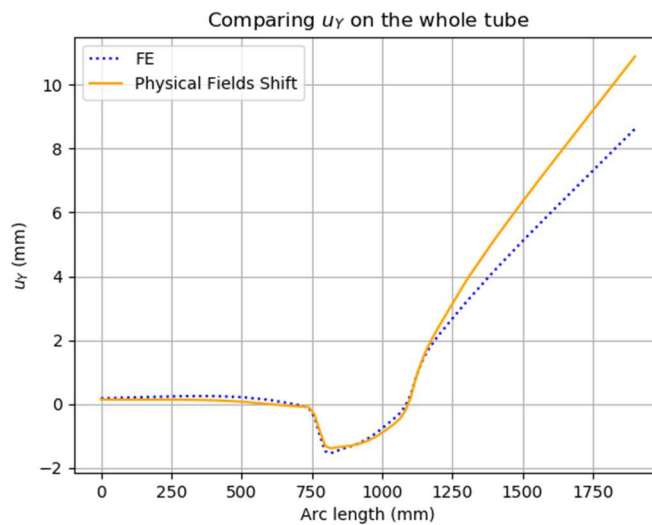


**Fig. 7** Comparison of the final state of displacement computed using the Finite Element method and the Physical Fields Shift method applied 80 times (Y component).



The computation time of the Finite Elements simulation is, on average, 2 hours per pass for the heat problem and 7 hours per pass for the mechanical problem. The CPU execution time of the Physical Fields Shift method is 13 seconds per pass on average. The Table 3 allows to compare the time needed to study the welding of the first layer using the Finite Elements method and the Physical Fields Shift method on the last 80 passes.

**Table 3** Computation times.

Method	Heat problem	Mechanical problem	Complete problem
Finite Elements	200h	700h	~ 37 days
Physical Fields Shift	40h	140h + 18min	~ 7 days

As it can be observed, around 30 days of computations are saved if only the first 20 passes are computed and then the Physical Fields Shift method is applied. That is effectively 5 times quicker than using the Finite Elements method to compute the total number of welding beads. This gain time may be the difference between a study that can be carried out and one that is impossible to do in an industrial context. These computation times could be further improved reducing the number of passes that are simulated before the first use of the Physical Fields Shift method.

One of the important measures taken during overlay welding is the bending angle of the pipe after the welding. To measure this value, only the displacement fields are necessary. The displacement values at the end of the simulation are shown on Fig. 6 (X component) and Fig. 7 (Y component). In both cases, the Physical Fields Shift method overestimates the values obtained using the Finite Elements method. Those values are plotted over a line going from one end of the tube to the other one. The first bead is placed at 775 mm from the end of the tube. We will now compare the bending angles that we calculated using the Finite Elements method and the Physical Fields Shift method. The Y component of the displacement on one extremity of the pipe is used to compute the arctangent of  $Y/(L/2)$  where L is the length of the pipe. Both of those results, as well as the data obtained during the procedure, are shown in Table 4.

**Table 4** Bending angles (in degrees).

Method	Experimental data	Finite Elements	Physical Fields Shift
<b>Bending angle</b>	0.537	0.56	0.697

In this case, both methods overestimate the bending angle of the experimental data. We need to bear in mind that the computation of the angle is very sensitive to small variations to the displacement values. The most important results of the Physical Fields Shift method is the reduction of the computation time.

### CONCLUSION AND FUTURE WORK

In the context of the EDF's research projects on welding we are confronted with industrial multi-pass problems that are impossible to solve in reasonable time limits, for instance overlay welding procedures. The complexity of the classical Finite Elements method, the size of the problems and the huge computation times make most of these studies not feasible.

We have presented a simplified method that allows us to obtain reasonable approximations of the final state of an overlay welding procedure in acceptable time limits. The results prove that computation times are improved and solutions are valid.

In addition to this method, these approximations could be used to build reduced order models to apply the hyper-reduction method [4] to obtain more precise results in still reasonable times. Reduced order models for the first passes could also be built and used for parametric studies. Both of these ideas have already been tested in [3] on simple multipass welding examples, but not yet on industrial cases.

### REFERENCES

- [1] EDF: 'Finite elements code\_aster, Analysis of Structures and Thermomechanics for Studies and Research', [www.code-aster.org](http://www.code-aster.org), 1989–2018.
- [2] J. GOLDAK, A. CHAKRAVARTI, and M. BIBBY: 'A new finite element model for welding heat sources', *Metallurgical and Materials Transactions*, B 15, 2 (1984), 299–305.
- [3] T. DINH TRONG: *Modèles hyper-réduits pour la simulation simplifiée du soudage en substitut de calcul hors d'atteinte*, thesis, Centre des Matériaux, Mines ParisTech, 2018.
- [4] D. RYCKELYNCK: 'A priori hyperreduction method: an adaptive approach', *Journal of computational physics*, 202(1) :346–366, 2005.

### APPENDIX 1: MESH USED FOR THE SIMULATIONS

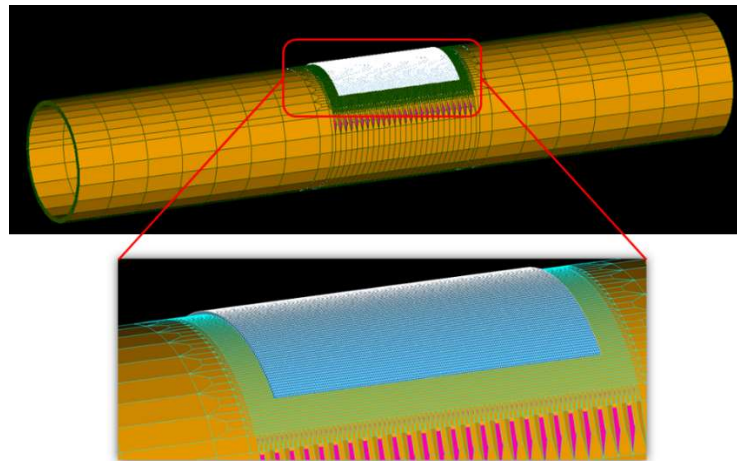


**Fig. 8** Mesh used in overlay simulations with zoom on the welding area.

APPENDIX 2: PHYSICAL PARAMETERS FOR THE NUMERICAL MODEL

The following tables include the physical parameters of P265GH Schedule 80S steel:

**Table 5** Thermo-physical parameters (temperature dependent).

Temperature (°C)	Thermal conductivity ( $W \cdot mm^{-1} \cdot K^{-1}$ )	Heat capacity ( $J \cdot mm^{-3} \cdot K^{-1}$ )
20	4.93E-02	3.71E-03
100	4.83E-02	3.80E-03
200	4.67E-02	3.88E-03
300	4.35E-02	4.02E-03
400	3.98E-02	4.19E-03
500	3.59E-02	4.38E-03
600	3.23E-02	4.58E-03
700	2.88E-02	4.79E-03
800	2.37E-02	5.28E-03
900	2.54E-02	5.22E-03
1000	2.67E-02	5.17E-03
1100	2.80E-02	5.12E-03
1200	2.94E-02	5.06E-03
2200	2.94E-01	5.06E-03

**Table 6** Thermo-elastic parameters (temperature dependent).

Temperature (°C)	Young's modulus (MPa)	Coefficient of thermal expansion (°C <sup>-1</sup> )	Poisson's coefficient
20	2.12E+05	1.11E-05	0.3
100	2.02E+05	1.15E-05	0.3
200	1.94E+05	1.22E-05	0.3
300	1.88E+05	1.28E-05	0.3
400	1.81E+05	1.33E-05	0.3
500	1.71E+05	1.38E-05	0.3
600	1.59E+05	1.43E-05	0.3
700	1.42E+05	1.49E-05	0.3
800	1.22E+05	1.25E-05	0.3
900	1.00E+05	1.34E-05	0.3
1000	7.92E+04	1.42E-05	0.3
1100	6.24E+04	1.50E-05	0.3
1200	4.91E+04	1.57E-05	0.3

APPENDIX 3: STRESS-STRAIN CURVES FOR THE HARDENING FUNCTION

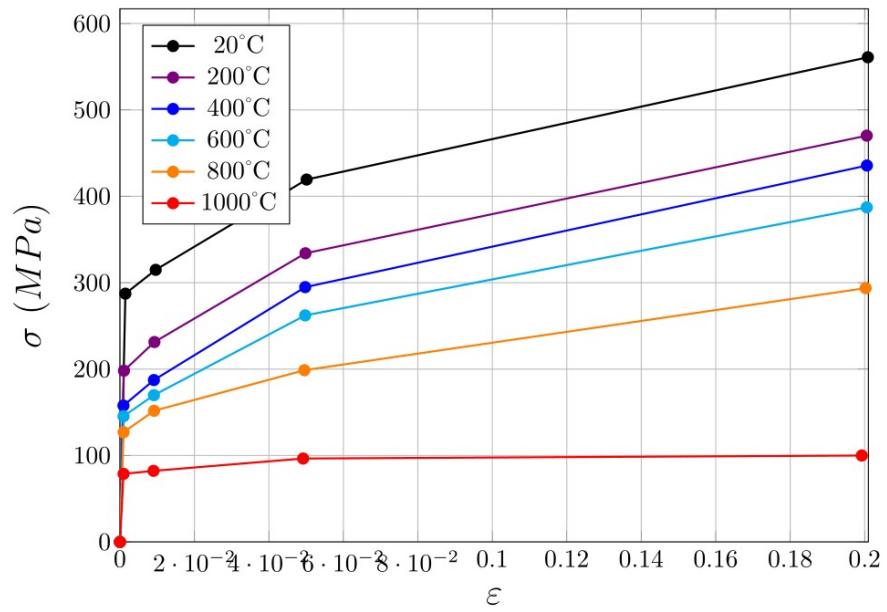


Fig. 9 Stress-strain curves used to compute the hardening function.



# HOW RELIABLE ARE PREDICTION AND MEASUREMENT OF WELD RESIDUAL STRESSES? LESSONS FROM THE NET NETWORK.

M C SMITH\*, V AKRIVOS\* and A VASILEIOU\*

*\* The University of Manchester, Oxford Road, Manchester, M13 9PL, United Kingdom, mike.c.smith@manchester.ac.uk*

DOI 10.3217/978-3-85125-615-4-18

## ABSTRACT

The Task Groups of the NeT European Network undertake closely controlled round robin studies examining the prediction and measurement of residual stresses in thoroughly characterised welded benchmarks. Task Groups 4 and 6 are examining three-pass slot welds in plates made from AISI316L(N) and Alloy 600 respectively. A very large body of independent RS measurements and simulations have been performed, giving a unique insight into the real-world reliability of both RS measurements and finite element simulation of welding. This paper reviews NeT Task Groups 4 and 6, and considers their implications for modelling of welding processes.

## INTRODUCTION

Finite element methods are used increasingly to predict weld residual stresses for use in weld structural performance assessments [1-3], since they offer the prospect of more accurate, less conservative residual stress profiles than the upper bound profiles currently provided in structural integrity assessment procedures such as R6 [4] and API 579 [5]. However, the potential uncertainties in finite element predictions remain a serious concern. The R6 structural integrity assessment procedure used in the UK includes guidelines for finite element prediction of weld residual stresses [6, 7] and imposes strict validation requirements on those predictions. The level of validation required depends on the structural integrity significance of weld residual stresses in the weldment being considered, but wholly unvalidated finite element predictions may not be used in structural integrity assessments.

Continuum-mechanics-based finite element prediction of the welding process is sometimes considered as a relatively straightforward “engineering” technique, with the attention of researchers focussed on modelling of sub-continuum features such as microstructure development in the weld pool and the adjacent strain/heat affected zone. However, the forcing functions for the development of such meso-scale features are the transient thermal and stress-strain fields developed during welding. Accurate continuum

level modelling of the welding process is thus a pre-requisite for useful modelling at lower length-scales.

The mission of the European Network on Neutron Techniques Standardization for Structural Integrity (NeT) is to develop experimental and numerical techniques and standards for the reliable characterisation of residual stresses in structural welds. NeT was first established in 2002. It involves over 30 organisations from Europe and beyond. NeT operates on a “contribution in kind” basis from industrial, academic, and research facility partners. Each problem examined by the network is tackled by creating a dedicated Task Group (TG), which undertakes measurement and modelling studies and the interpretation of the results. Since its formation, NeT has examined a number of benchmark weldments, of steadily increasing complexity.

NeT TG1 [8-23] examined a single weld bead laid onto the surface of an AISI 316L austenitic steel plate. AISI 316L is normally considered a “simple” material to model: no solid-state phase transformation takes place at temperatures relevant to the development of residual stresses and distortion, so there is normally assumed to be no need to model microstructure development as part of the process of predicting the weld residual stress state. This weld geometry produced a strongly three-dimensional residual stress distribution, with similar characteristics to a weld repair, and proved to be very challenging to simulate accurately.

NeT TG4 [24-33] was designed as a natural follow-on to TG1, using similar material (AISI 316L(N)), but with the single weld bead of TG1 replaced by three superimposed weld beads laid into a slot. It introduced a multi-pass weld and a significant volume of weld metal, while retaining the portability of TG1. Participants in TG4 were set the following challenges:

- To make accurate measurements of residual stress in weld metal, where grain size and microstructural texture make diffraction-based measurements difficult. The volume of weld metal in TG1 was so limited that the residual stress field could be largely characterised without attempting to make measurements in the weld itself.
- To extend the line-based residual stress measurements made in TG1 to full 3D spatial mapping of the residual stress field.
- To improve statistical descriptions of measured stresses, and thereby reduce uncertainty and provide reliable validation targets for residual stress predictions.
- To make accurate predictions of the development of material properties and the final residual stress field in weld metal, which starts life molten, and in the adjacent heat/strain affected zone which, like weld metal, undergoes multiple high temperature thermo-mechanical cycles.

NeT TG4 largely succeeded in these objectives, and the project is probably the most detailed and extensive study on weld residual stress simulation and measurement yet carried out.

NeT TG5 [34, 35] examined the prediction and measurement of residual stresses in a material that undergoes both bainitic and martensitic solid state phase transformations during welding, the low alloy steel SA508 Gr 3 Cl 1. The TG5 benchmark is a simple beam specimen with a single autogenous weld bead laid along one edge. Two different welding speeds are used, to promote either bainitic or martensitic structures in the fusion zone and HAZ.

NeT TG6, started most recently, in 2012, examines the behaviour of Tungsten inert gas (TIG) welds made using nickel-based Alloy 82 filler on an Alloy 600 substrate, using a three pass slot weld geometry similar to the TG4 specimen. Residual stresses in welds made using Alloy 82 or Alloy 182 filler are of considerable interest because these alloys are susceptible to primary water stress corrosion cracking when used in pressurized water reactor primary circuit dissimilar metal welds. Considerable effort has been expended in the measurement and prediction of residual stresses in PWR DMW's [36-39], with mixed results. These may be attributed partly to the complexity of the weldments being examined, and partly to the difficulties associated with neutron diffraction measurements in nickel alloy weld metals. NeT TG6 thus addresses an important need: it allows a challenging material to be examined within the well-established NeT framework of detailed characterization of both the welding process and the materials used, multiple, diverse residual stress measurements, and extensive finite element simulation.

NeT TG6 has now reached a stage where sufficient results are available to allow assessment of the performance of measurement and simulation techniques. This paper thus reviews the outputs of the NeT TG4 and TG6 projects together, and considers their implications for the accuracy and reliability of finite element predictions of weld residual stresses in "simple" metal alloys, where explicit consideration of microstructure is not necessary in order to predict continuum stresses and distortions. It first briefly describes the design, manufacture and metallographic/microscopic characterisation of the benchmark specimens themselves, concentrating upon the information required to make and validate FE simulations, and then summarises the extensive mechanical testing campaigns that were undertaken to provide the materials data necessary for accurate simulation. The accuracy and reliability of the thermal simulations are then reviewed – accurate thermal simulation is a pre-requisite for any further modelling. The residual stress measurement campaigns are then reviewed, again to assess their accuracy and reliability, before examining the performance of the mechanical simulations.

### THE NET TG4 AND TG6 BENCHMARK SPECIMENS

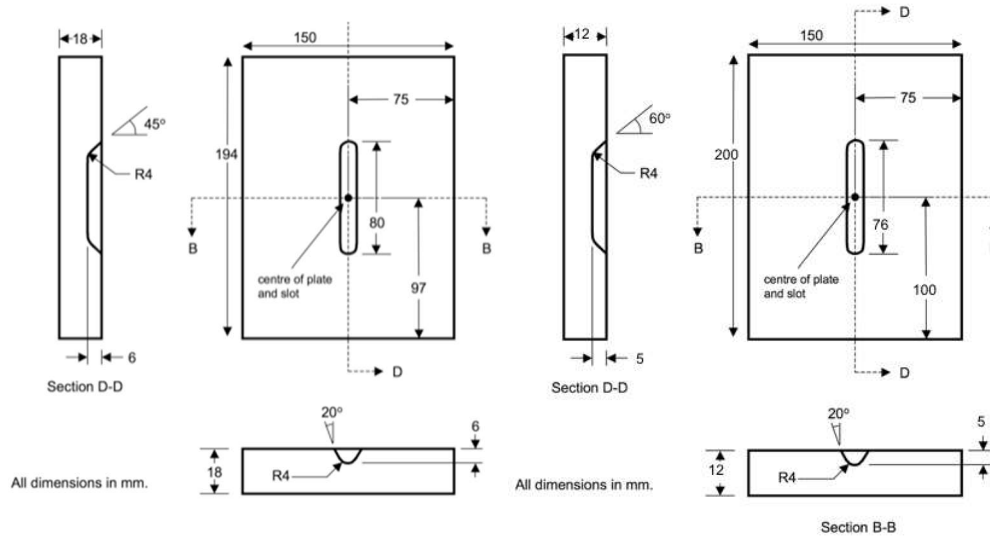
#### SPECIMEN DESIGN AND MANUFACTURE

TG4 specimens were fabricated from AISI 316L(N) plate, while TG6 specimens used Alloy 600 plate. Basic dimensions are shown in Figure 1. The specimen designs were intended to allow sufficient constraint to develop an intense three-dimensional residual stress field around a short multi-pass weld, while remaining easily portable, with a plate thickness that allowed full-field measurements of residual stress using diffraction-based methods, without excessive count times. The TG6 specimen is thinner than TG4, at 12mm rather than 18mm. The reduction in thickness was made to aid diffraction-based residual stress measurements, in what is known to be a challenging material. A completed TG4 specimen is shown in Figure 2, while Figure 3 shows a TG6 specimen prior to welding.

All TG4 specimens were fabricated from a single plate of AISI 316L(N) material, originally procured for the ITER fusion reactor project and donated to the NeT network. TG6 specimens were fabricated from two different heats of Alloy 600 plate.



*Plate A* material was used to fabricate production specimens, and for critical materials characterization testing. *Plate B* material was used for the manufacture of trial specimens and initial materials characterization testing. A total of fifteen TG4 specimens were fabricated over the course of the project. Nine TG6 specimens have been fabricated from Plate A material so far.



TG4 specimen

TG6 specimen

**Fig. 1** Dimensions of NeT TG4 and NeT TG6 benchmark specimens prior to welding. Note that line BD is a through-wall line at the centre of the plates, at the intersection of Sections B-B and D-D

Both benchmarks contain three superimposed weld passes deposited in a central slot using a tungsten inert gas (TIG) process, using AISI 316L filler in TG4 and Alloy 82 filler in TG6. A three-pass weld was selected for TG4, based upon knowledge of the cyclic hardening behaviour of AISI 316 steel. This is rapid, so three passes are sufficient to achieve significant hardening without placing an undue time burden on subsequent modelling. Alloy 600 is expected to cyclically harden slower than AISI 316, but the desire to maintain maximum commonality with TG6 led to a three-pass slot weld in TG6.

Weld parameters were developed for both benchmarks via a series of trials performed on additional multi-slot plates, using pedigree material for TG4, and on Plate B material for TG6, with the aim of developing processes that gave slight overfill in three passes without excessive heat input. Production welding for TG4 was performed using a programmable TIG welding machine. Full automation was not achieved, as the welding engineer retained control over the exact torch path and traverse length. The production weld parameters for TG6 were fully programmed into a welding robot to ensure repeatability. Table 1 summarises the steady-state weld process parameters for both benchmarks. Detailed process parameter records were kept, and these are reported elsewhere [32, 40]. It is evident that the heat inputs achieved in TG6 were higher than for TG4, especially in passes two and three.



**Fig. 2** Completed TG4 specimen prior to neutron diffraction measurements



**Fig. 3** TG6 specimen prior to welding, showing machined slot and top surface thermocouples

**Table 1** Steady-state welding parameters at mid-length for TG4 and TG6 benchmarks

Benchmark	Pass	Mean current (A)	Mean voltage (V)	Traverse speed (mm/s)	HI (kJ/mm)
TG4	1	220	10	1.27	1.73
TG4	2	195	10	1.27	1.54
TG4	3	185	10	1.27	1.46
TG6	1	220	10.8	1.17	2.03
TG6	2	220	13.4	1.17	2.52
TG6	3	220	12.3	1.17	2.31

TRANSIENT TEMPERATURES DURING WELDING

Surface-mounted thermocouple arrays were used to monitor transient temperatures during welding. The array design philosophy for both benchmarks was the same: a redundant, symmetric array at mid-length where the welding temperature transient response is expected to be quasi-steady-state, positioned in the far field where the thermocouples respond as if the weld torch/pool is a point heat source; and additional thermocouple arrays at the slot ends to record the three-dimensional temperature transients there. The thermocouple locations are shown in Figure 4. K-type thermocouples were used. Three TG4 plates were instrumented, with the thermocouples spot-welded to the plate surface. All the TG6 plates were instrumented, with an attachment technique that aimed to learn lessons from TG4 and improve thermocouple accuracy and reliability (see Figure 2)<sup>1</sup>.

Figure 5 shows the transient temperatures recorded at the lower surface thermocouples during pass 1 for seven TG6 specimens. The responses show good repeatability. The measured temperature rises at the mid-length thermocouple arrays are tabulated for TG4 in Table 2, and for TG6 in Table 3. Responses from symmetric thermocouples are grouped. We note:

- The temperature rises measured for TG6 are much greater than for TG4, a reflection of the higher heat inputs and the thinner plate. This is particularly evident on the back face, where the central thermocouple T9 records a peak temperature above 900°C during pass 1. This is much greater than for TG4 (about 450°C).
- The uncertainties in measured temperature rises are lower for TG6, due to both the improved attachment technique and the larger number of instrumented specimens.
- It appears to be necessary to instrument a number of nominally identical specimens with redundant, symmetric thermocouple arrays in order to make reliable measurements of the transient temperature fields.

Separate, single TG4 and TG6 specimens were instrumented with two buried thermocouple arrays each. The buried arrays were designed to allow optimization of local

<sup>1</sup> The thermocouple wires were encased in protective sheaths, the junctions were spot welded into shallow dimples machined into the plate surface, and the top surface arrays were protected with insulating paste to prevent errors due to arc shine.

weld heat source parameters such as size, shape, and flux distribution. Details are given elsewhere [32, 40].

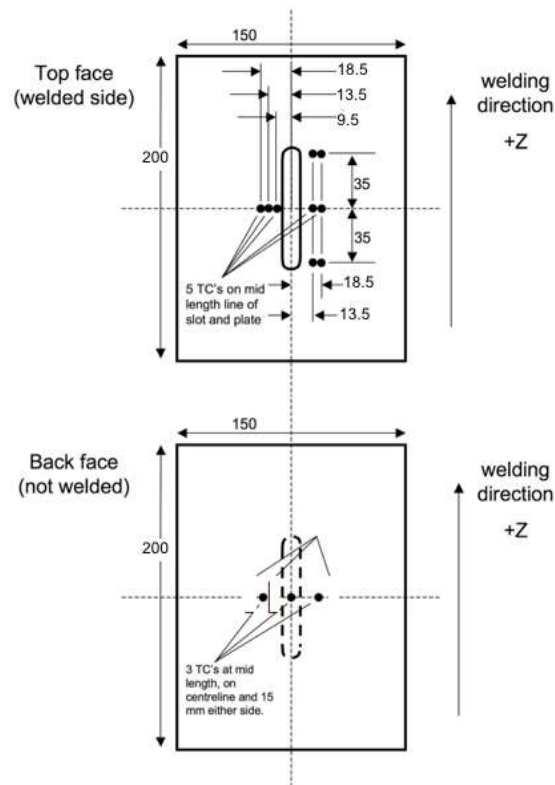


**Fig. 4** Locations of surface-mounted thermocouples on NeT TG6 specimen (array design for TG4 was identical except top surface thermocouples were positioned at 9mm, 13mm, and 18mm from the weld centreline).

**Table 2** Measured temperature rises at mid-length thermocouples for NeT TG4, from arrays on three welded plates

Thermocouple group	Nominal lateral position  x	Mean measured temperature rise (°C) (+/-1 sd)		
		Pass 1	Pass 2	Pass 3
T10 (top)	9 mm	583.2 +/-35.3	604.0 +/-78.5	632.1 +/-155.7
T2, T11 (top)	13 mm	384.7 +/-31.6	358.9 +/-36.6	340.3 +/-42.8
T5, T12 (top)	18 mm	236.2 +/-17.4	206.2 +/-14.6	188.9 +/-16.8
T7, T8 (bottom)	15 mm	275.7 +/-10.7	225.7 +/-7.5	198.8 +/-8.1
T9 (bottom)	0	451.3 +/-3.4	346 +/-6.5	299.4 +/-4.0

## Mathematical Modelling of Weld Phenomena 12

**Table 3** Measured temperature rises at mid-length thermocouples for NeT TG6, from arrays on seven welded plates (pass 1), and 4 plates (passes 2 and 3).

Thermocouple group	Nominal lateral position  x	Mean measured temperature rise (°C) (+/-1 sd)		
		Pass 1	Pass 2	Pass 3
T10 (top)	9.5 mm	841.2 +/-34.2	932.2 +/-22.4	1004.1 +/-25.8
T2, T11 (top)	13.5 mm	540.7 +/-34.0	557.4 +/-12.4	607.2 +/-51.4
T5, T12 (top)	18.5 mm	395.7 +/-14.6	394.1 +/-12.8	386.0 +/-11.2
T7, T8 (bottom)	15 mm	480.9 +/-18.6	468.3 +/-21.6	443.9 +/-22.0
T9 (bottom)	0	910.2 +/-18.5	789.5 +/-10.5	717.5 +/-11.2

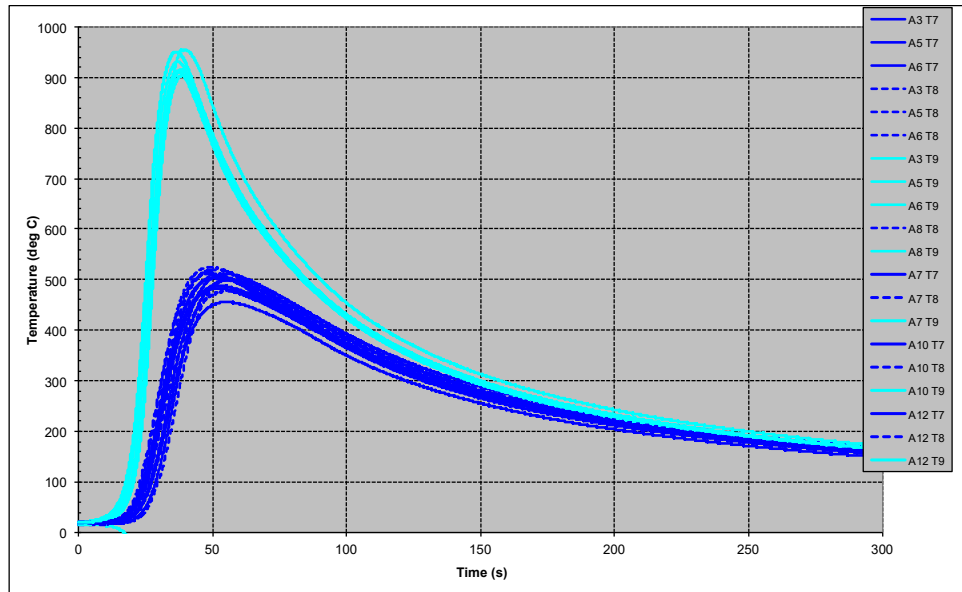


**Fig. 5** measured transient temperatures for pass 1 at back face (lower surface) thermocouples for seven TG6 specimens

### DISTORTION MEASUREMENTS

Distortion during welding was measured for both benchmarks. For TG4, a coordinate measuring machine was used to profile selected specimens before and after welding. The final deformed shapes of all TG6 specimens were measured using a hand-held laser scanner, while one specimen was measured prior to welding, at inter-pass conditions between each pass, and after completion of welding.

### METALLOGRAPHIC CHARACTERISATION

The fusion boundary profile and melted area are key parameters for finite element weld models. Both TG4 and TG6 made use of multi-slot specimens containing welds with one,

two, and three passes which could be sectioned for metallography. The transverse cross-sections for TG4 are shown in Figure 6. AISI 316L(N) is considered a well-understood material for weld modelling. Neither excessive grain growth, nor re-crystallisation are expected in the heat/strain affected zone, and solid-state phase transformation is absent. Cyclic hardening leads to a steady increase in yield strength in the HAZ as the fusion boundary is approached and the plastic path length increases, and the weld metal used is closely matched to parent material [41]. Thus detailed microscopy was not performed as part of the NeT TG4 round robin.

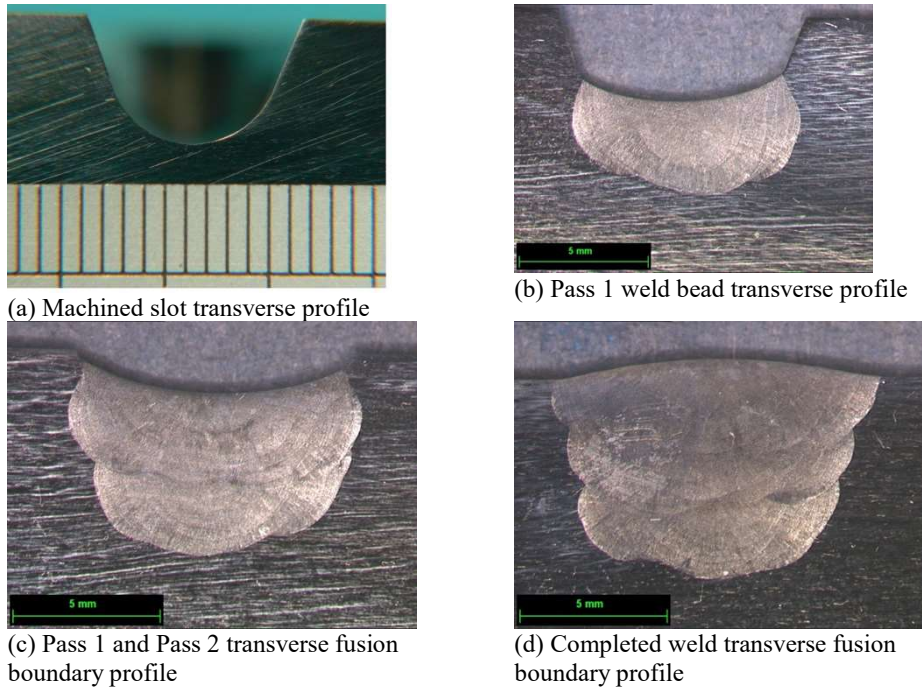


**Fig. 6** Transverse fusion boundary profiles for passes 1, 2 and 3 in NeT TG4 AISI 316L(N) welded benchmark

Alloy 600 is a less well understood material for weld modelling, so more detailed microscopy was performed for TG6, comprising conventional polishing and etching to reveal the microstructure, hardness mapping, and electron back-scatter diffraction (EBSD) studies. Transverse macrographs are presented in Figure 7.

The Alloy 600 parent material has a bi-modal grain size distribution with large grains (100-500  $\mu\text{m}$ ) in a matrix of much smaller grains (tens of  $\mu\text{m}$ ). The bi-modal distribution is clearly visible in the parent plate on the low magnification images in Figure 7a-c, and in a higher magnification image in Figure 7d. In contrast, the grain size in the Alloy 82 weld metal is significantly larger, with columnar grains close to the weld fusion boundaries and more equi-axed grains near the centre of the final weld bead. Individual columnar grains appear to span more than one weld bead. There is also a region of grain coarsening in the HAZ adjacent to the weld fusion boundary.

Crystallographic texture measurements were made on a sample extracted from a three pass TG6 weld. These revealed relatively weak texture in the parent material, and the bottom of the weld, but strong texture in the final weld bead.

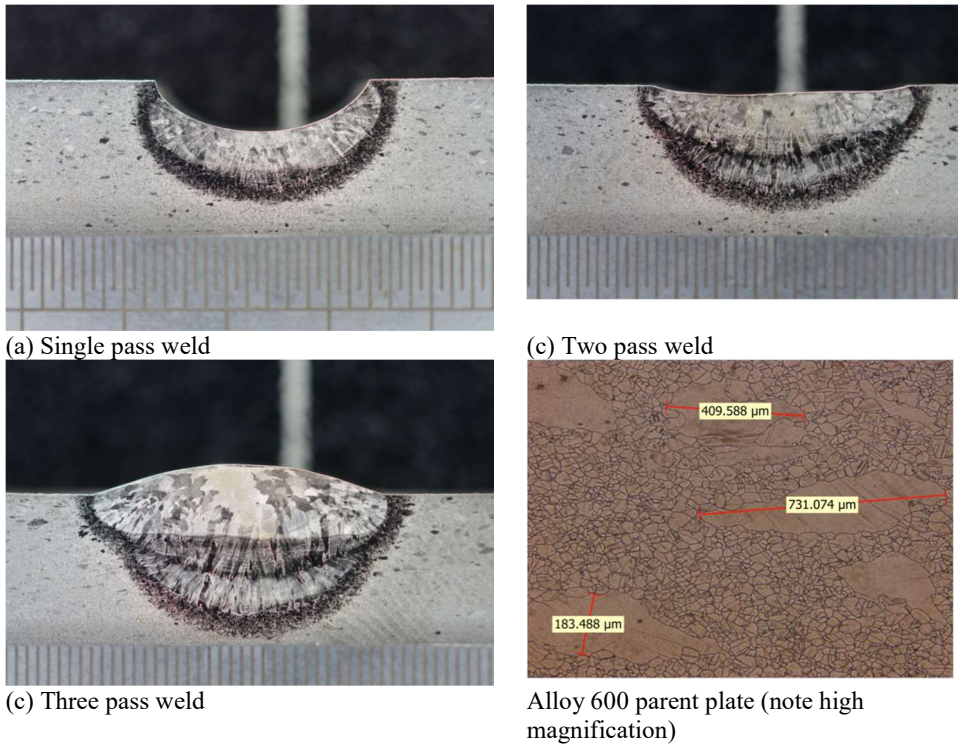
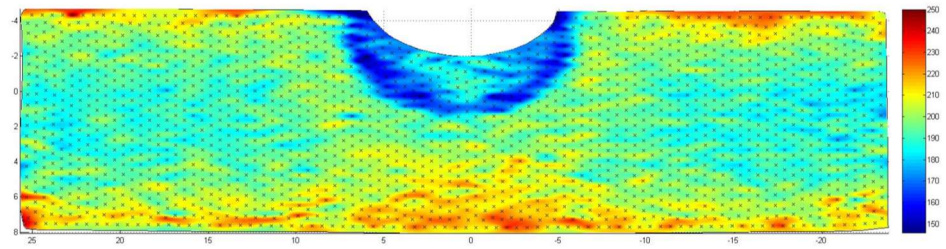
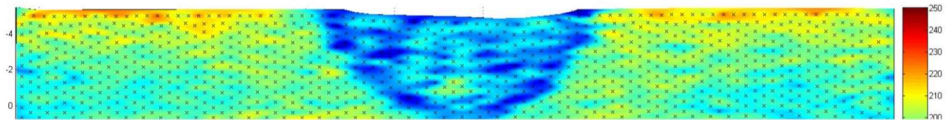


**Fig 7:** Transverse fusion boundary profiles for passes 1, 2 and 3 and Alloy 600 parent plate grain morphology in NeT TG6 Alloy 600/82 welded benchmark

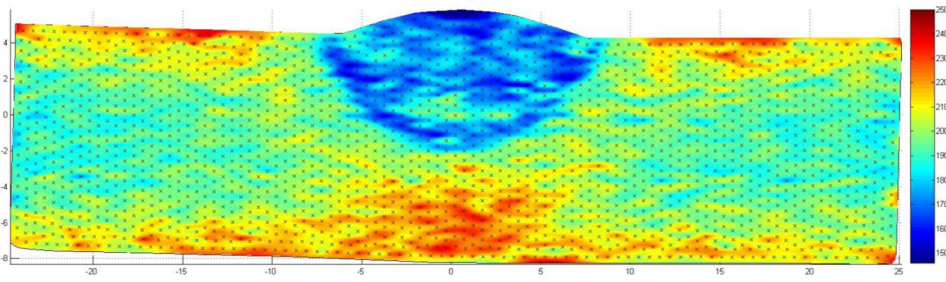
Vickers hardness maps for one-pass, two-pass and three-pass TG6 welds are presented in Figure 8. They reveal that the Alloy 82 weld metal and the coarse-grained region of the HAZ are significantly softer than the parent plate. There is also evidence of progressive cyclic hardening in parent material beneath the weld, and to a lesser extent in weld metal, plus a thin zone of hardened material near the surface of the plate. The latter is probably a result of the plate forming operations, as the upper and lower surfaces of the plate were left un-machined prior to welding.



(a) Single pass weld



(b) two-pass weld



(c) three-pass weld

**Fig 8:** Vickers hardness variation on transverse planes in 1, 2 and 3-pass NeT TG6 Alloy 600/82 welded benchmarks, showing cyclic hardening in parent ligament, and softening in CGHAZ and under-matched weld metal.



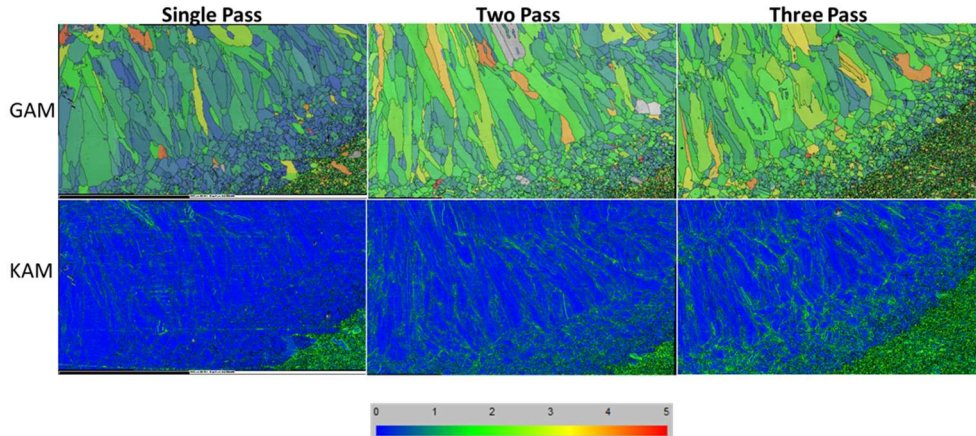


**Fig 9:** Qualitative mapping of the accumulated plastic strain in the pass 1 weld and HAZ of one, two, and three pass NeT TG6 benchmark welds using (top) grain average misorientation and (bottom) kernel average misorientation EBSD metrics. The low levels of misorientation in the coarse grained HAZ and weld metal are clearly visible, especially in the single pass weld.

Figure 9 presents EBSD maps of crystallographic misorientation made using two common metrics. Both show very clearly the low misorientation in the coarse-grained region of the HAZ and the columnar fusion zone of a single pass weld, compared with adjacent parent material, and the subsequent increase in misorientation as successive passes are deposited on top of each other. The EBSD data thus show very similar trends to the conventional hardness maps.

They Alloy 600/82 combination thus appears to show significant differences to AISI 316 in the weld and HAZ regions.

## MATERIALS CHARACTERISATION

Materials characterisation performed for both TG4 and TG6 was focussed upon providing data over a full range of temperature sufficient to allow temperature-dependent mixed isotropic-kinematic hardening models to be derived for both constituents of each benchmark. If started from scratch this would be an onerous task, so maximum possible use was made of existing material property databases held by NeT participants, especially EDF Energy in the UK. New characterisation tests concentrated on gaps in existing data.

### NET TG4

The AISI 316L(N) plate used for NeT TG4 has very similar physical and mechanical properties to the plate previously used for NeT TG1. The materials testing performed to support TG4 thus concentrated on the monotonic tensile and isothermal cyclic behaviour for both the parent AISI 316L(N) plate and the AISI 316L TIG weld metal. All other materials data were obtained from the database assembled for NeT TG1. A detailed materials compendium was compiled, comprising approximately 180Mb of test data.

Thermal and physical properties were assumed to be identical to those of the AISI 316L plate and TIG weld metal used for NeT TG1. Those in turn were derived from internal material properties databases held by NeT members, especially EDF Energy [32].

Only room temperature monotonic tensile tests were performed on the TG4 AISI 316L(N) material. These revealed behaviour very similar to the NeT TG1 material, so TG1 data obtained at temperatures up to 750°C were also supplied to participants in NeT TG4. These detailed test data were supplemented by simplified proof stress vs. temperature data derived for TG1 that extended up to the melting point of 1400°C [32].

EDF Energy have performed monotonic tensile testing on ER316L TIG weld metal made using welding wire of the same specification used for TG4, although not the same batch. Several different processing histories were used to produce weld metal suitable for testing, namely:

- Material extracted from a multi-pass weld pad, and tested in the as-welded condition
- Material extracted from a multi-pass weld pad, and tested after solution heat treatment
- Material extracted from two-pass welds laid into grooves (the minimum number of passes that produced sufficient weld cross-sectional area to manufacture test specimens), and tested in the as-welded condition
- Material extracted from the same two-pass welds, and tested after solution heat treatment

The processing history has a marked effect upon the tensile properties of weld metal, discussed in detail elsewhere [29]. It was judged that solution-treated 2-pass material offers the best facsimile of unhardened, just-deposited weld metal, and these data were therefore provided to TG4 participants, both as simplified proof stress vs. temperature data, and as full stress-strain responses.

AISI 316L cyclically hardens strongly, and its mechanical behaviour during welding is best described using mixed isotropic-kinematic material hardening models [42, 43]. Isothermal cyclic test data are required to fit the parameters in mixed hardening models. Cyclic testing was performed on both the parent plate material and on solution-treated two-pass TIG weld metal. The test parameters (strain rate and strain range), were chosen to be relevant to the expected response during welding, using the recommendations in the weld modelling guidelines incorporated into the R6 structural integrity assessment procedure [4, 7]. Testing extended up to 700°C, above which AISI 316L ceases to cyclically harden.

### NET TG6

The NeT TG6 specimen is fabricated from two materials, Alloy 600 plate and Alloy 82 weld metal. This material combination results in an under-matched weld. The presence of both an under-matched weld and possible softening in the HAZ make the mechanical behavior of NeT TG6 significantly different to the NeT TG4 AISI 316L(N) benchmark. In particular, treating weld and parent material as identical is not a good assumption. It was judged that the evolutionary hardening behavior of the alloy 82 weld metal would best be evaluated by testing solution-treated weld metal, a similar conclusion to that reached for NeT TG4.

Both Alloy 600 and Alloy 82 cyclically harden in a broadly similar manner to austenitic stainless steels, although at slower initial rates, albeit with a greater change between cycle 1 and saturation.

A further complication for NeT TG6 is the heat-to-heat variation in yield strength between Plate A and Plate B material. Most of the material available for characterization at the beginning of the project was from plate B. This required adjustment before use in simulation of the welded specimens made from Plate A material.

A large body of testing was performed, comprising:

- Thermo-physical property measurements for the Alloy 600 plate material
- Monotonic and isothermal cyclic testing of Plate B material in conventional testing machines over a range of temperatures up to 700°C
- Monotonic and isothermal cyclic testing of Plate A material in conventional testing machines over a range of temperatures
- Thermo-mechanical testing of Plate A material in a Gleeble thermo-mechanical simulator
- Manufacture of a multi-pass weld pad from Alloy 82 weld metal
- Monotonic and isothermal cyclic testing of solution-treated Alloy 82 material in conventional testing machines over a range of temperatures up to 700°C
- Thermo-mechanical testing of alloy 82 material in a Gleeble thermo-mechanical simulator

This testing supplemented data already available from other sources, in particular testing performed on material from an Alloy 182 weld pad by EDF Energy. Alloy 182 is the manual metal arc filler metal equivalent to alloy 82 wire, and data from these tests were used in Phase 1 simulations for the TG6 benchmark. In total, the TG6 characterisation programme was intended to provide the necessary mechanical properties data to allow the fitting of both conventional and visco-plastic Lemaitre-Chaboche mixed hardening models.

### ORGANISATION OF MEASUREMENT AND SIMULATION ROUND ROBINS

The measurement and simulation round robins for both TG4 and TG6 were carried out independently and in parallel. Each was controlled by its own protocol. The protocol documentation was extensive and detailed:

- The measurement protocols specified where to measure, how to measure and what to report.
- The simulation protocols comprised the protocol itself (which specifies the conduct, reporting and accuracy targets for the analyses), and supporting manufacturing case histories and material properties compendia.

The TG4 measurement round robin commenced in 2009, and the reported measurements include high energy synchrotron X-ray diffraction measurements made on two specimens at the European Synchrotron Radiation Facility in Grenoble, neutron diffraction measurements performed at eight different facilities (including several re-measurements), deep hole drilling and incremental deep hole drilling measurements on two specimens, transverse and longitudinal contour method measurements on a number of specimens, and ultrasonic measurements. This is believed to be the largest measurements database ever developed on a welded benchmark specimen. The diffraction measurements database is

large enough to generate reliable mean profiles, to identify clear outliers, and to establish that there is no statistically significant difference in the residual stress field in the two specimens used for most of the non-destructive measurements.

The TG6 measurement round robin commenced in 2015. To date, neutron diffraction measurements have been performed at five different facilities. All measurements to date have been performed on the same specimen. One contour method measurement has been carried out with others planned, and incremental deep hole drilling measurements have been performed on a single specimen.

The TG4 simulation round robin also commenced in 2009. This was performed in two phases. In Phase 1, participants were first required to validate their thermal simulations of welding by matching the measured thermocouple responses and weld fusion boundary profiles, in order to demonstrate that the thermal load was essentially correct before proceeding to any mechanical analyses. The mechanical analyses were then performed using only materials data for the AISI 316L(N) parent material, in effect assuming that weld and parent material behaved identically. A large body of weld-metal-specific materials data were assembled for Phase 2 simulations, which concentrated upon varying both the high temperature behaviour of both constituent materials, and on the most appropriate materials data and constitutive behaviour to assume for weld metal.

The TG6 simulation round robin commenced in 2015. This is also being performed in two phases. Phase 1 consists of thermal analyses, to be validated against the extensive database of transient measured temperatures, and mechanical analyses using the available materials data at an early stage in the project. In a departure from previous NeT practice, participants were supplied with both raw mechanical test data and recommended fitted parameters for Lemaitre-Chaboche mixed hardening models. These were based upon test data available at the time, namely cyclic isothermal testing on Plate B parent material, and on Alloy 182 weld metal. Additional materials data specific to the Plate A parent material and Alloy 82 weld metal has now been obtained, and will be supplied for the Phase 2 round robin, which has not yet commenced.

## RESULTS

### ACCURACY OF TEMPERATURE PREDICTION

An accurate thermal solution is a pre-requisite for any subsequent simulations, irrespective of the length scale involved. The thermal solution calibration procedure recommended for both TG4 and TG6 was the same: to employ moving volumetric heat sources (typically ellipsoidal gaussian or Goldak sources); to calibrate the global heat source parameters using the temperature rises recorded at far-field thermocouples, and to calibrate local heat source parameters using the fusion boundary profile data. In both round robins, the only unknown global parameter is the welding efficiency: the welding power, torch speed, path, and start-stop transients are all known. The number of local parameters needed to define the source shape depends upon the heat source adopted: examples include the three radii of a simple ellipsoidal gaussian source, the position of its centroid with respect to the deposited weld bead, its angular inclination, and weave characteristics, if any.

## Mathematical Modelling of Weld Phenomena 12

Target solution accuracies were imposed based upon experience gained in the NeT TG1 benchmark, and were similar for both TG4 and TG6:

- The predicted cross-sectional area of fused weld/parent metal at mid-length of each of the three beads should be within  $\pm 20\%$  of the mean measured fused area of the trial beads.
- The analysis should reproduce the observed mid-length transverse fusion boundary profiles.
- The predicted increases in temperature,  $\Delta\theta = (\theta_{peak} - \theta_0)$ , at mid-length thermocouple positions T5, T7, T8, T9, and T12 should agree with the mean measured increases,  $\Delta\theta_{mean}$ , to within 10%. Results from T5 and T12, and from T7 and T8, were combined, since these thermocouples are symmetrically arranged on opposite sides of the bead.
- Analysts should strive to achieve similar levels of agreement for the mid-length near-field thermocouples T2, T10 and T11, and for the thermocouple arrays at the start and stop ends

The performance of the finite element thermal predictions for TG4 is reviewed in detail in [31]. With some identified exceptions, all eight participants met the accuracy criteria, so that variations in the thermal solution could be discounted when accounting for variations in subsequent mechanical analyses. Figure 10 plots predicted and measured temperature histories for a pair of lower surface thermocouples. This emphasises the general quality of the thermal predictions.

A further accuracy measure is the overall RMS error for the mid-length thermocouple arrays, defined as:

$$Error_{RMS} = \sqrt{\frac{1}{n} \sum_{i=1}^n \left\{ \frac{(\theta_{Ti,peak} - \theta_{Ti,0}) - \Delta\theta_{Ti,mean}}{\Delta\theta_{Ti,mean}} \right\}^2}$$

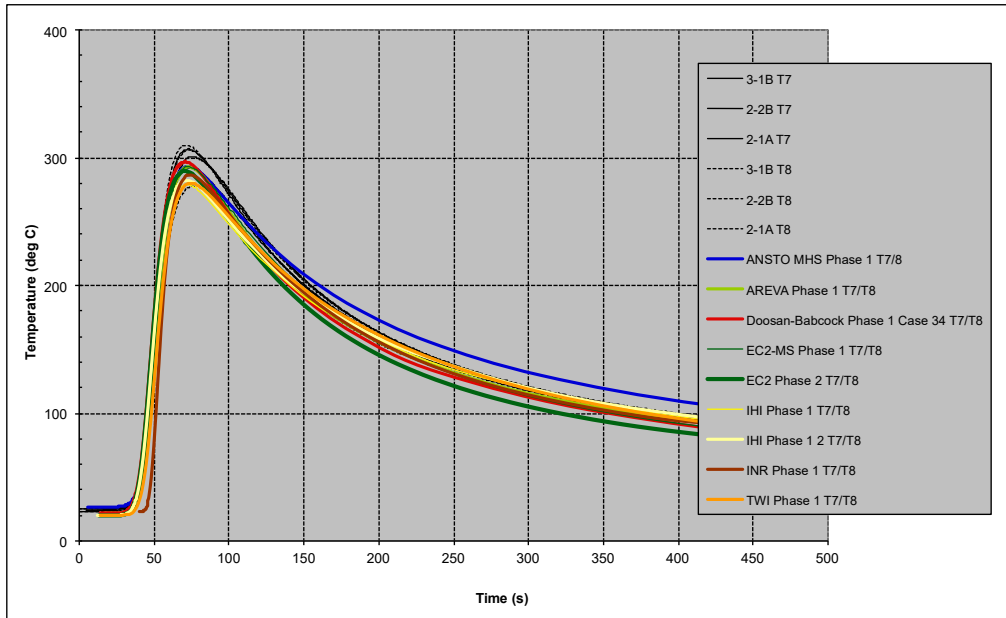
where  $\theta$  is temperature,  $\Delta\theta$  is temperature rise, the suffices  $Ti$  identify individual thermocouple locations, the suffix *mean* indicates mean measured data, and the suffices  $0$  and *peak* refer to FE predictions of initial and peak temperature respectively.

Table 4 presents sample RMS errors achieved for the NeT TG1, TG4 and TG6 round robins. We note:

- The TG1 thermal simulation was performed in two phases. As can be seen, the spread in predicted temperatures for the phase 1 simulations was large, with an RMS error of over 17%. It proved necessary to undertake a second thermal simulation campaign, in order to achieve acceptable agreement between simulations and between simulations and measurements, with an overall RMS error of 4.3% [14].
- Thermal solution performance in the TG4 round robin was much better, with an overall error over all simulations of 5.5%, which reduced to 3.7% when two participants submitted improved solutions and one solution with identified errors was removed [31]. The best simulation achieved an RMS error of 1.3%.
- A single TG6 simulation is reported, from the same team of researchers that achieved 1.3% error in TG4. The RMS error is somewhat higher, at 4.3%, but is

still at a level where the thermal solution is unlikely to contain serious errors, at least at weld mid-length.

It is important to remember that these low levels of solution error can only be achieved if the measured thermocouple data are accurate. In both TG4 and TG6, large amounts of data from different instrumented specimens and from equivalent thermocouples within individual specimens were combined to derive reliable target temperatures. If only limited thermocouple data are available, it is unlikely that they will be reliable enough to achieve these levels of assurance.



**Fig. 10:** Predicted and measured temperatures during pass 1 at thermocouples T7 and T8, lower surface mid-length, for NeT TG4 AISI316L(N) welded benchmark

**Table 4** RMS errors in predicted temperature rises at mid-length thermocouple arrays for NeT TG1, TG4, and TG6 benchmarks, in all cases for the final weld pass

Benchmark	Analysis details	RMS error
TG1 single bead on plate, AISI 316L	Phase 1 round robin	17.2%
TG1 single bead on plate, AISI 316L	Phase 2 round robin	4.3%
TG4 3-pass slot weld, AISI 316L(N)	All simulations	5.5%
TG4 3-pass slot weld, AISI 316L(N)	"Phase 2"	3.7%
TG4 3-pass slot weld, AISI 316L(N)	Best simulation	1.3%
TG6 3-pass slot weld, Alloy 600/82	Best TG4 participant	4.3%

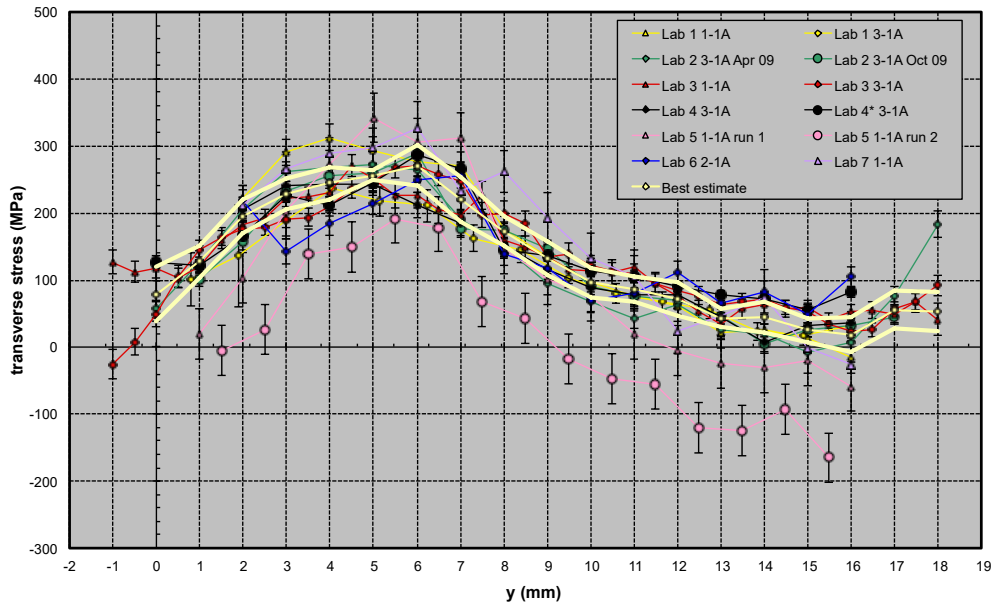
#### *NeT TG4*

A large body of measured data was assembled for NeT TG4, see [30, 32]. Here we consider only results for a through-wall line at the centre of the specimen, identified as line BD (see Figure 1). This passes through all three weld beads, through the high temperature heat/strain affected zone, and through the remaining ligament, in a region where welding had achieved steady-state conditions, and where longitudinal variation in the residual stress field is small. Measured stresses in the longitudinal and transverse directions obtained using diffraction techniques are plotted in Figure 11, which shows:

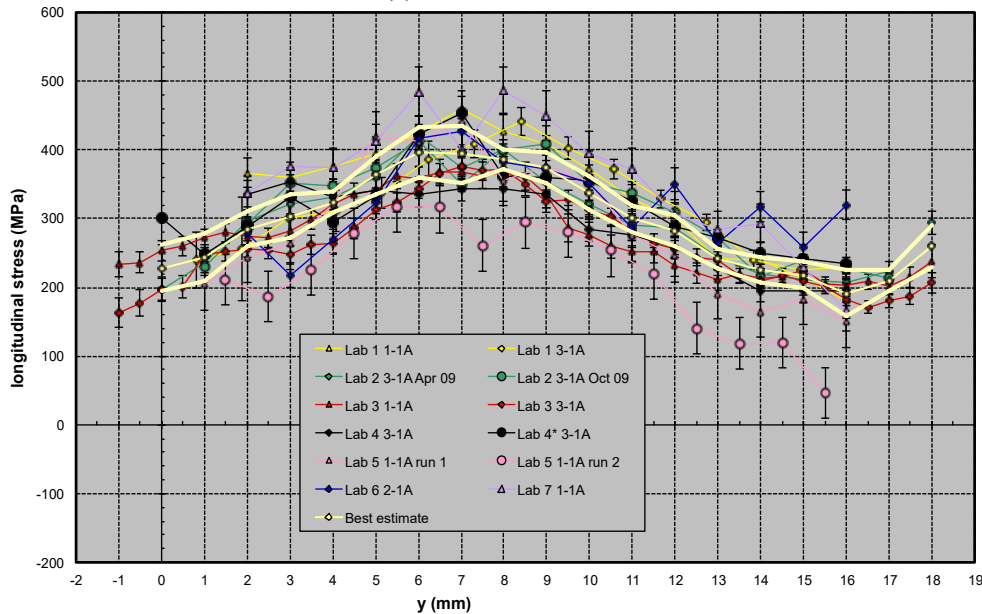
- Individual measured data, with the uncertainties declared by the participating laboratory (usually, but not always, the fitting error for the raw diffraction peaks). The laboratories are anonymised, but the measured specimen is identified.
- The best-estimate measured profile, calculated using techniques originally developed in [23].
- An uncertainty of +/- one standard deviation on the best estimate.

The calculated uncertainties in the final best estimates are of order +/- 20 to 40 MPa. They are largest near free surfaces and in “pass 1” weld metal (weld metal with three thermo-mechanical load cycles). The final best-estimate profiles have very small normal stresses (not shown), which is as expected and an encouraging outcome. While this low level of final uncertainty is very encouraging, it is based upon analysis of a large dataset, and it is evident from Figure 11 that the uncertainty in individual measurements is higher.

Structural Integrity Assessment procedures such as R6 [4] recommend that residual stresses are measured using both diffraction and strain-relief methods, since they tend to have different characteristic errors. Good agreement between such independent techniques is deemed to be strong evidence of reliable measurements and helps negate the significant uncertainties associated with single measurement datasets.



(a) transverse stress



(b) longitudinal stress

**Fig. 11:** Residual stresses measured using diffraction methods on through-wall line BD in TG4 specimens. Best estimate and +/- 1 SD shown in yellow.

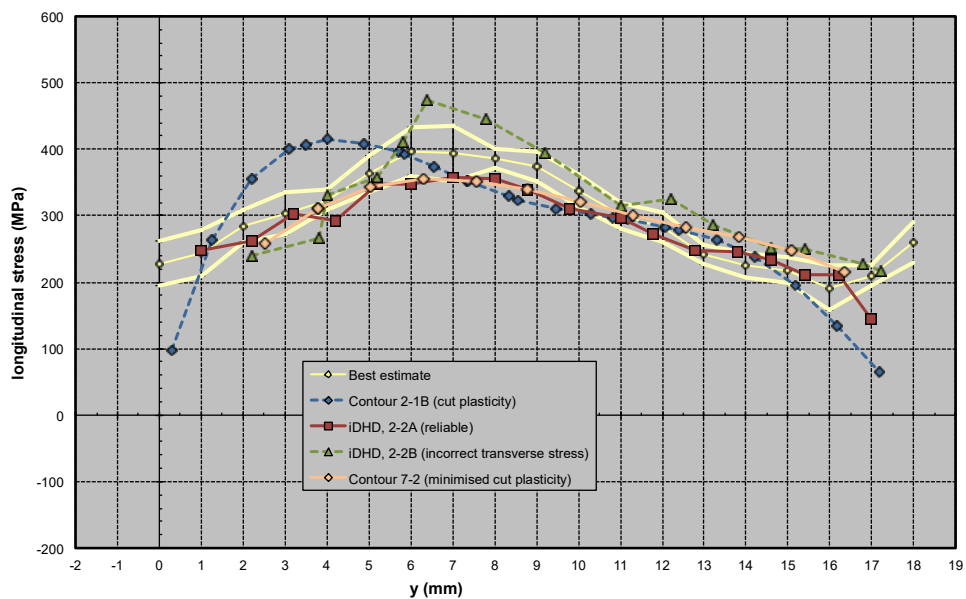
Both the contour method and the incremental deep hole drilling method were applied to NeT TG4. In both cases two specimens were measured. The measured longitudinal stresses on line BD are compared with the best estimate from diffraction-based measurements in



Figure 12. For both strain relief methods, one measurement agrees closely with the diffraction consensus, and one does not.

In the case of the contour measurements, the first measurement took no special precautions against the development of plasticity during the EDM cut. The contour method assumes that all deformation during the measurement process is elastic, so plastic deformation causes systematic errors in the measurement results. This measurement deviates from the diffraction-based best estimate (especially at other locations in the plate). The second measurement was optimized to minimize cut plasticity, and achieved good agreement with the diffraction consensus [44].

The incremental deep hole drilling technique is capable of returning accurate measured stresses when the residual stresses are high enough for plastic redistribution to occur during the measurement, so would be expected to have “worked” on line BD in TG4. Here, the first measurement returned visibly incorrect transverse stresses. No satisfactory explanation for this could be found, so the measurement was repeated on another specimen. As can be seen from figure 12, the second iDHD measurement agrees closely with the diffraction consensus.



**Fig 12:** Comparison of measured longitudinal stresses on through-wall line BD in TG4 using strain relief methods with diffraction-based best estimates. Best estimate (with symbols and lines) and +/- 1sd (lines) shown in yellow.

*NeT TG6*

The measurement activities for NeT TG6 are not as complete as for TG4. The TG6 benchmark has proved to be a challenge for both diffraction-based and strain-based measurement methods. Neither the contour method nor deep hole drilling have yet yielded satisfactory results. The very large grain size and texture in Alloy 82 weld metal have

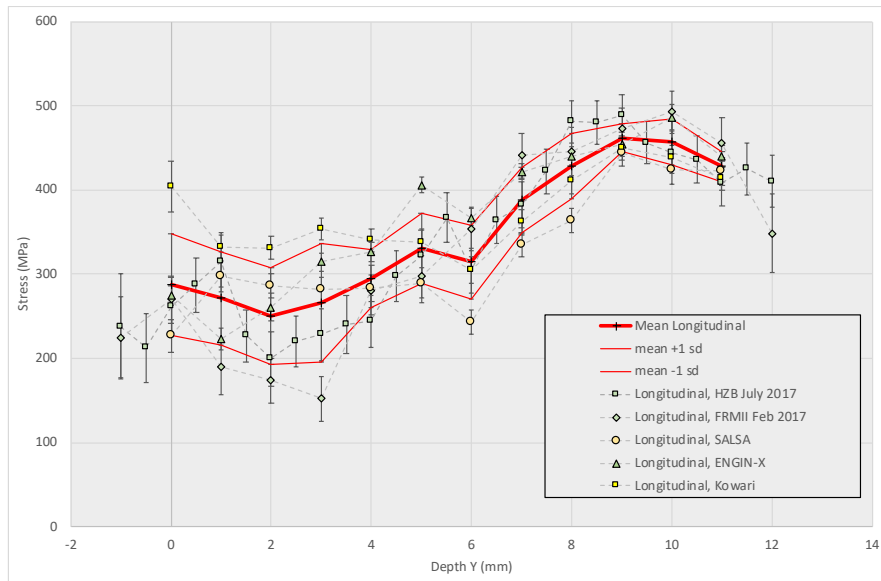
caused problems for neutron diffraction measurements, as has the large change in stress-free lattice parameter observed between Alloy 600 and Alloy 82.

Here we consider only the neutron diffraction measurements made at five facilities. Figure 13 plots measured stresses on line BD. These should be compared with stresses on the equivalent line in TG4 plotted in Figure 11. We note

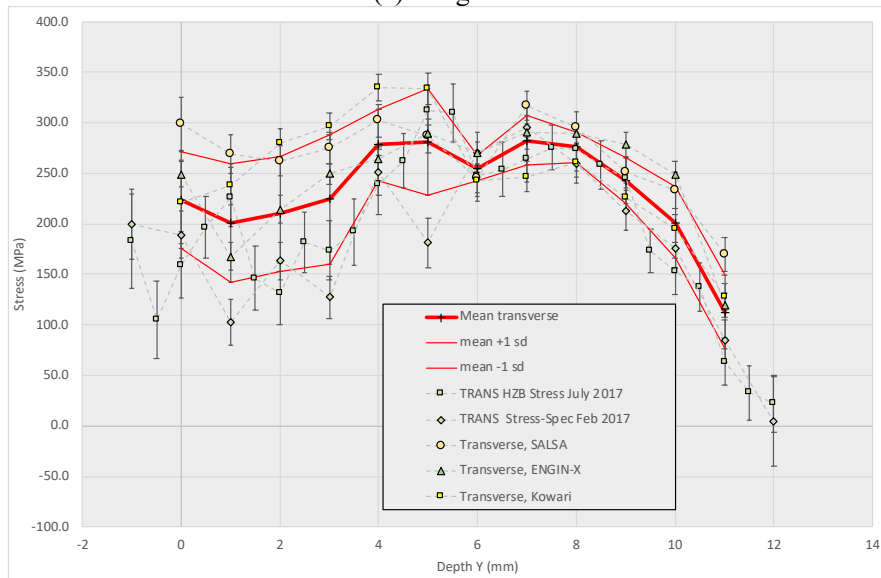
- The through-wall distribution of stress in TG6 differs from that in TG4. Longitudinal stresses peak near the bottom surface in the parent ligament, with significantly lower stresses in weld metal and in the coarse-grained HAZ. In TG4, peak stresses develop in Pass 1 weld metal and the associated strain/heat affected zone. Transverse stresses peak near the middle of the plate, and fall near top and bottom surfaces, again in contrast to TG4.
- The uncertainties in measured stresses tend to be higher in TG6, especially in weld metal. This is probably due mostly to the difficulties in measuring in the TG6 material, especially in the weld, but the smaller data set may also be a factor, as may the much simpler technique used to generate a mean stress profile.

Clearly the combination of under-matched weld, softened HAZ, lower cyclic hardening rates, higher welding heat input, and thinner plate has led to a very different stress field in TG6 compared with the superficially similar TG4 benchmark.

## Mathematical Modelling of Weld Phenomena 12



(a) Longitudinal stress



(b) Transverse stress

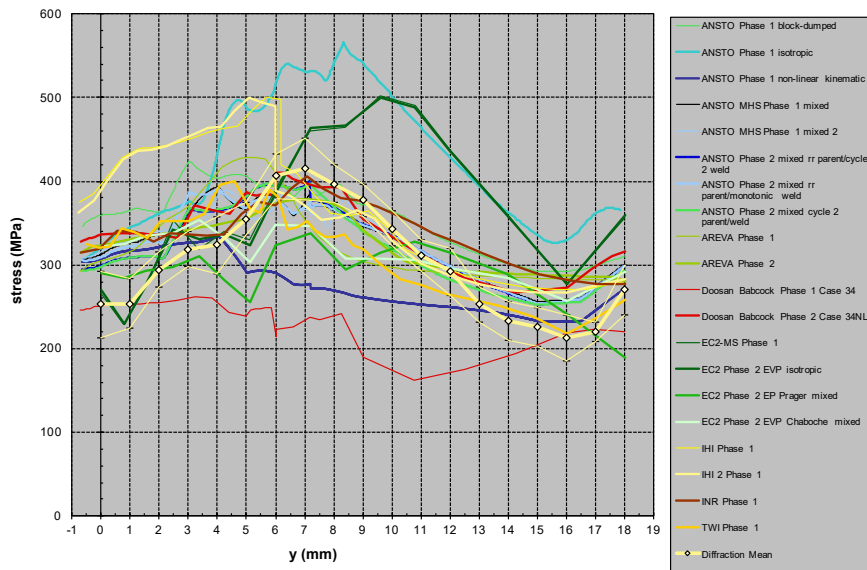
**Fig. 13:** Residual stresses measured using diffraction methods on through-wall line BD in TG6 specimen. Mean and +/- 1 SD shown in red

### PREDICTIONS OF RESIDUAL STRESS

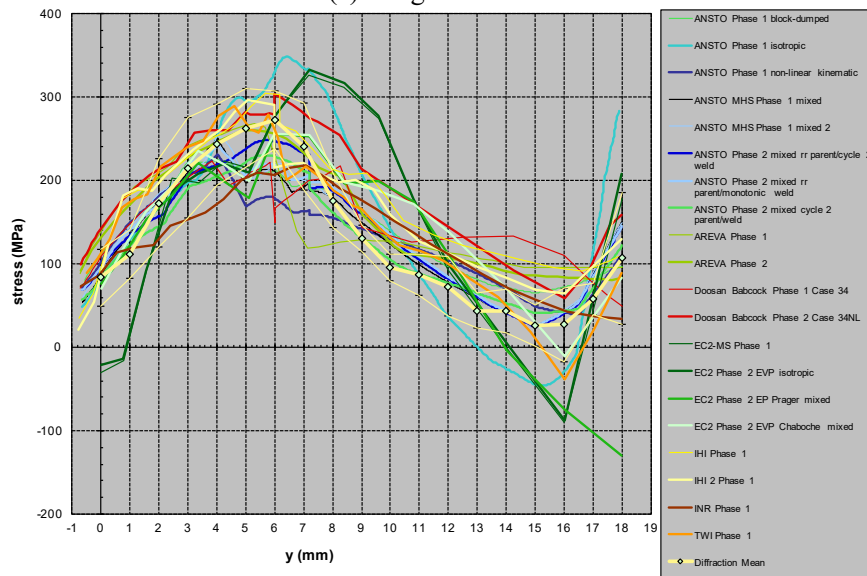
*TG4*

A total of eight organisations submitted 21 simulations as part of the main simulation round robin [30], with a further six simulations performed to examine details of weld metal hardening behaviour [29]. The stresses predicted on line BD by the main round-robin are compared with the measurement best estimate in Figure 14. At first sight the large spread in predictions is somewhat dispiriting, although not unexpected. The general picture is of “consensus plus outliers”. The structural boundary conditions of the problem are well defined, and with a few known exceptions the thermal analyses are correct. Once analyses with known errors are identified and removed, then the most important source of error is the assumptions made about material hardening behaviour and about the mechanical properties of weld metal. Neither pure isotropic nor pure kinematic hardening are appropriate behaviours for AISI 316L(N): once these analyses are eliminated, the general accuracy improves greatly. The assumptions made about weld metal are also important: if weld metal properties are derived from tests on multi-pass weld metal or weld metal with any significant strain hardening, then stresses in the weld are over-predicted (in fact, the simple assumption that AISI 316L weld metal behaves like solution-treated parent material turns out to be remarkably good). A full description of the main simulation round robin and its performance is given in [30]

# Mathematical Modelling of Weld Phenomena 12



(a) Longitudinal stress



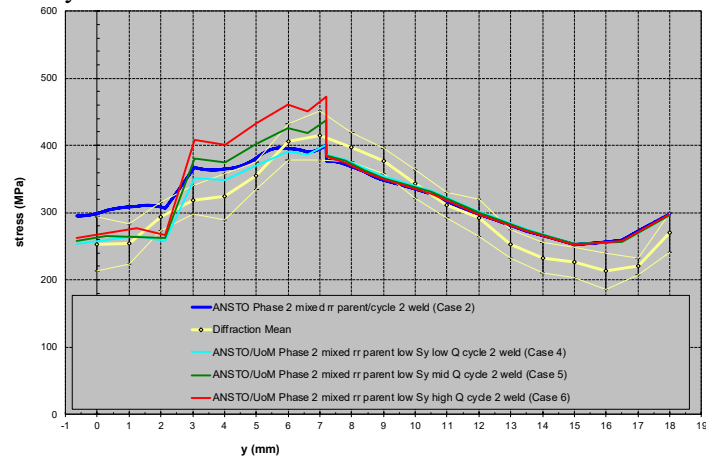
(b) Transverse stress

**Fig. 14:** Comparison of predicted and measured stresses in TG4 specimen on line BD, all main round robin analyses

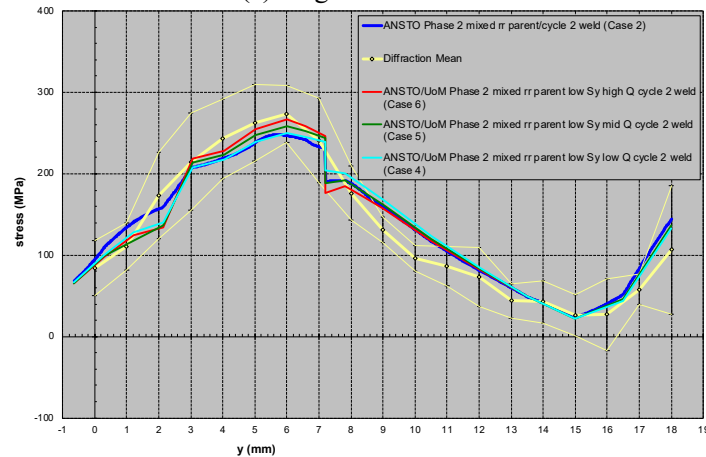
The sensitivity studies reported in [29] made use of weld specific cyclic test data to fit Lemitre-Chaboche mixed hardening models for the weld metal in NeT TG4. These not only used test data from solution-treated 2-pass TIG welds (which effectively contain only a single weld bead because of remelting during the second pass), but also considered carefully both the initial “just solidified” yield strength, the cyclic hardening rate, and the final state of multi-pass weld metal, remembering that the thermo-mechanical cyclic

response of a steel will not necessarily be the same as its isothermal response. Figure 15 plots predictions from three of these fitted models, and compares them with the measured stresses on line BD (full details are in [29]). A high predictive accuracy is achieved, despite the analyses still using simple static plasticity with no viscous effects at high temperature other than a simple two-stage annealing functionality. This stops further isotropic hardening above a lower threshold temperature, and removes the hardening history completely at an upper limit temperature.

The sensitivity study results are probably at the limit of what can be achieved using conventional Lemaitre-Chaboche hardening models. They still retain unrealistic stress jumps associated both with changes in material model and with the simple annealing models used to eliminate hardening at high temperatures. Further improvements in predictive accuracy can probably only be achieved by explicit consideration of viscous effects at high temperatures, and a better understanding of thermo-mechanical hardening behaviour, especially in weld metal.



(a) longitudinal stress



(b) Transverse stress

**Fig. 15:** Showing the impact of optimised mixed-hardening models for weld metal on predicted stresses on line BD in a TG4 specimen

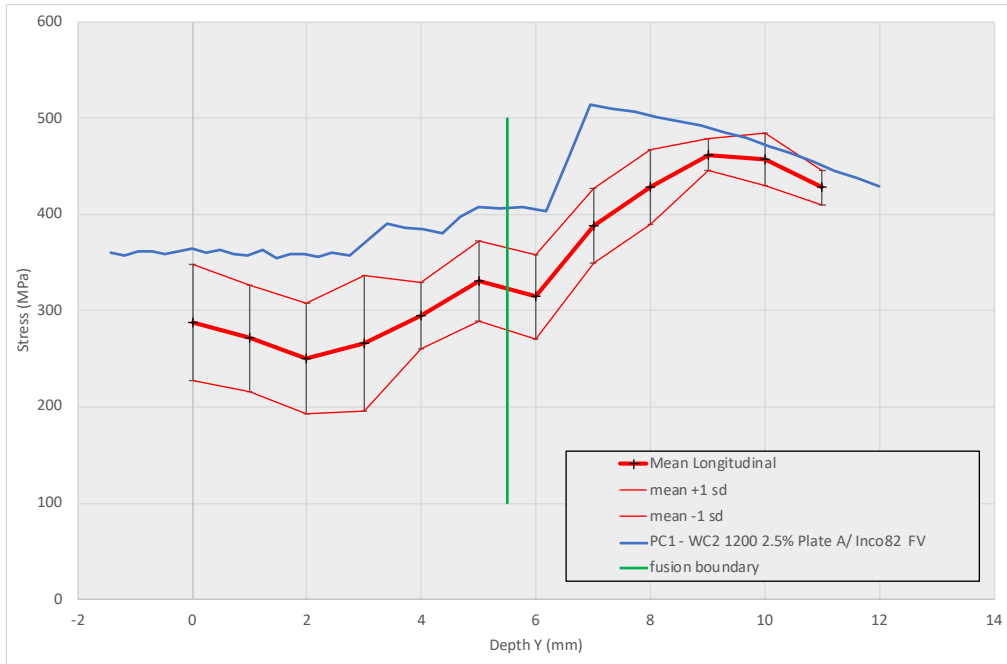
### *TG6*

The simulation work on NeT TG6 is still ongoing, but the results available so far indicate that the knowledge gained in TG4 cannot be simply be applied to the TG6 geometry and materials and achieve the same predictive accuracy.

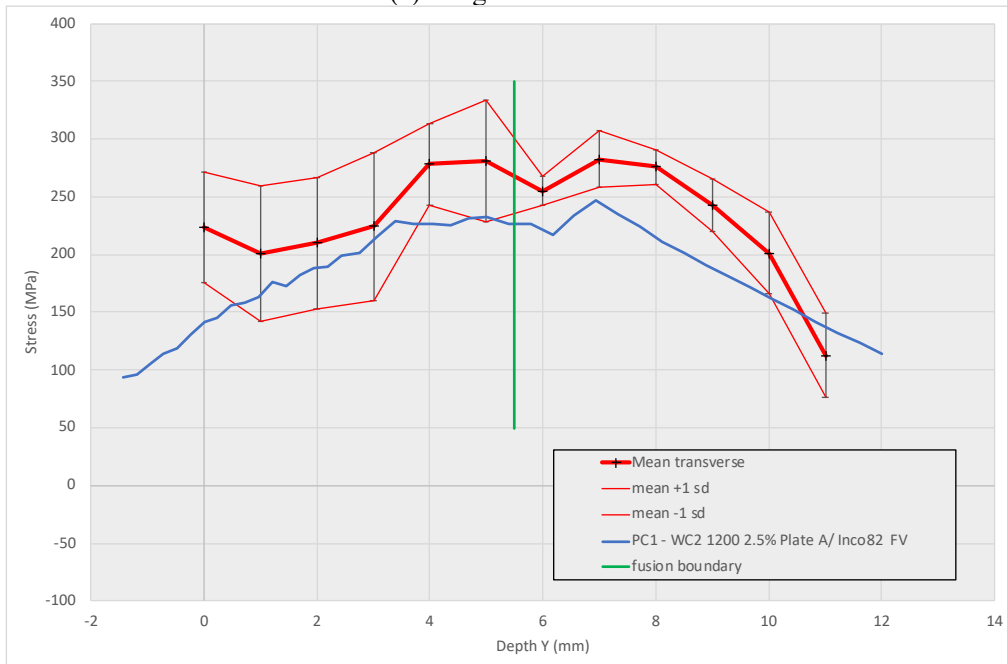
Figure 16 compares a single, representative prediction with the measured stresses on line BD. This has the following features:

- The simulations were performed by the research team responsible for the most accurate TG4 models (see [29]), using the same FE software and the same welding heat source fitting strategy.
- The thermal solution achieved acceptable accuracy
- Parent material mechanical behaviour was described using a Lemaitre-Chaboche model fitted to representative Plate A test data using the approach developed for AISI 316.
- Weld metal mechanical behaviour was also described using a Lemaitre-Chaboche model fitted to solution-treated Alloy 82 test data, although the material was extracted from a weld pad rather than two-pass welds. No initial yield strength or hardening limit adjustments were made.
- Softening in the CGHAZ was modelled using field variables to allocate weld properties to material that exceeded a critical temperature, determined by comparing the results of microscopy and hardness mapping with the predicted maximum temperatures achieved.
- Simple “annealing” behaviour was assumed, in which the hardening history was eliminated above 1200°C.

It is evident that longitudinal stresses are generally over-predicted, especially in weld metal, the CGHAZ, and in the ligament adjacent to the HAZ, which has also reached high temperatures. In contrast, transverse stresses are consistently under-predicted. The reasons for this are not yet clear.



(a) Longitudinal stresses



(b) Transverse stresses

**Fig. 16:** Comparison of predicted and measured stresses in TG6 specimen on line BD, for a single sample analysis.



### DISCUSSION AND CONCLUSIONS

The end results of simulations of the welding process are quantities that are of use to engineers and scientists. The weld residual stress field is an obvious output, since this can adversely affect the service life of welds. Much of the industrial interest in weld modelling has been driven by the need to understand and manage in-service degradation of welds in nuclear powerplants, where residual stress is a key variable. Clearly there are others, such as in-process distortion or the development of important microstructural features. Whatever the desired output, the complexity of welding means that making accurate predictions is a multi-stage process, requiring validation at each stage to ensure simulations do not diverge from reality.

The NeT benchmarks reflect this need, and they offer unique test beds for the development and validation of weld simulation techniques. The plate and weld materials are thoroughly characterized, the welding conditions are well defined, and the transient thermal response is reliably characterized via redundant thermocouple arrays on multiple specimens. The weld residual stresses and accompanying structural distortions are also reliably characterized: indeed the residual stress measurements for both TG4 and TG6 are unusual in both their number and their extent.

Results from both TG4 and TG6 show that it is possible to make accurate predictions of the transient thermal fields developed during arc welding in both austenitic steels and nickel alloys. However, the scatter routinely exhibited by thermocouple measurements during welding mean that multiple specimens need to be instrumented with redundant arrays of thermocouples in order to accurately calibrate the welding heat source models. Thermocouple measurements also need to be supplemented by conventional weld metallography to establish the size and shape of the weld fusion zones.

If these data are available, then the combination of thermocouple data to calibrate “global” heat source parameters (here only the efficiency) and metallography to calibrate local heat source parameters (size and shape parameters) leads to thermal solutions with sufficient accuracy to be used for either continuum predictions of residual stresses and distortions, or indeed meso-scale predictions of microstructural features in the heat-affected zone.

Measured residual stresses are historically the most important validation measure for finite element weld models. Here the work of NeT has emphasized the need both for great care and for diversity in making such measurements. The residual stress state in NeT TG4 is known with high accuracy only because multiple diffraction-based measurements were made at multiple instruments. If only a single set of measurements had been made, then it would be a matter of “luck” whether they reflected the consensus or were an outlier<sup>2</sup>.

Strain relief measurements show a similar pattern. In TG4 both the contour method and incremental deep hole drilling produced mixed results, and the availability of a reliable diffraction-based best estimate was an important part of the process of identifying errors in the first measurements made.

---

<sup>2</sup> Of course “luck” is not correct. It is perhaps more correct that a properly qualified team of experienced researchers should have followed best practice in making measurements at an instrument with a good track record, without being rushed by the pressure of competitive time allocation.

The validation requirements of the UK R6 procedure are shown to have a sound engineering basis: if measurements made using diffraction techniques agree well with strain relief measurements, then it is likely that an accurate estimate of the residual stresses has been made.

The first stages of the measurements round robin on NeT TG6 has served to emphasise that residual stress measurements can be made more difficult by the characteristics of the welded structure and the materials used. Neutron diffraction, as yet, has higher uncertainties than in TG4, at least partly due to the microstructural characteristics of the Alloy 600/82 welded plates. Strain relief measurements have yet to produce reliable results, probably because the characteristics of the welded plates lead to more opportunity for unwanted local plastic deformation during the measurements. Nevertheless, the NeT collaborative approach means that sufficient independent measurement data are available to identify systematic errors and outliers.

The simulation round robins performed on NeT TG4 have shown that highly accurate predictions of weld residual stress may be achieved in AISI 316L(N). However, to achieve this it is necessary to use mixed isotropic-kinematic hardening models for both weld and parent material. Simple isotropic and kinematic models lead to significant deviation from the measurements consensus. Mixed hardening models carry a significant burden of materials testing: it is necessary to perform isothermal cyclic testing over a range of temperatures up to 700°C, and monotonic tensile testing to higher temperatures, to obtain sufficient data to fit the models (those used for TG6 require 7 parameters at each temperature).

The handling of weld metal requires care. It is not acceptable to test multi-pass weld metal (its end state) in order to develop the parameters for an evolutionary hardening model. Any models fitted to multi-pass weld test data will grossly over-predict stresses in the weld metal. In TG4, weld metal testing was performed on two-pass welds (effectively a single bead due to re-melting), that had been solution-treated to remove any hardening).

Initial results for NeT TG6 indicate that approaches developed for AISI 316 may not transfer to the Alloy 600/82 combination without modification. TG6 exhibits significant under-matching, softening and re-crystallisation in the HAZ, and much higher temperatures in the ligament beneath the weld than developed in TG4. It is evident that high temperature effects, such as recovery and re-crystallisation, are more important than in TG4 where they could be ignored or handled very simply. Research to understand this and improve the accuracy of prediction continues.

### ACKNOWLEDGEMENTS

The NeT Network receives no external project funding. All participants in its round robin activities are either self-funded or co-funded by other participants. The authors therefore wish to acknowledge the contributions made by all the participants in NeT TG4 and NeT TG6.

Mike Smith is supported by the UK Engineering and Physical Sciences Research Council (EPSRC) Fellowship in Manufacturing “A whole-life approach to the development of high integrity welding technologies for Generation IV fast reactors”, EP/L015013/1.

Successful management of NeT collaborations requires a unique blend of skills. Until 2014, these were provided by Ann Smith. She guided the TG4 project from its inception, and was instrumental in setting up the TG6 project and guiding its participants through the early stages of the project stages. Sadly, Ann died in July 2014, shortly after being diagnosed with metastatic pancreatic cancer. She is greatly missed by all her co-workers in NeT

### REFERENCES

- [1] L-E LINDGREN: Finite element modeling and simulation of welding part 2: improved material modelling, *J Therm Stress* 24, 195-231 (2001).
- [2] L-E LINDGREN: Finite element modeling and simulation of welding Part 1: increased complexity, *J Thermal Stresses* 24, 141-192 (2001).
- [3] L-E LINDGREN: Computational welding mechanics. Thermomechanical and microstructural simulations, Cambridge, Woodhead Publishing Ltd (2007).
- [4] R6, Assessment of the integrity of structures containing defects, EDF Energy (2015).
- [5] Fitness for Service, API 579-1/ASME FFS-1, Second Edition (2007).
- [6] P HURRELL, C WATSON, P J BOUCHARD, M C SMITH, R J DENNIS, N A LEGGATT, S K BATE and A WARREN: Development of weld modelling guidelines in the UK, ASME PVP 2009, Prague, PVP2009-77540 (2009).
- [7] S BATE and M SMITH: Determination of residual stresses in welded components by finite element analysis, *Materials Science and Technology* 32(14), 1505-1516 (2016).
- [8] C E TRUMAN and M C SMITH: The NeT residual stress measurement and analysis round robin on a single weld bead-on-plate specimen, *Int Jnl Press Vess and Piping* 86(1), 1-2 (2009).
- [9] M C SMITH and A C SMITH: NeT bead on plate round robin: Comparison of transient thermal predictions and measurements, *Int Jnl Press Vess and Piping* 86(1), 96-109 (2009).
- [10] M C SMITH and A C SMITH: NeT bead on plate round robin: Comparison of residual stress predictions and measurements, *Int Jnl Press Vess and Piping* 86(1), 79-95 (2009).
- [11] X FICQUET, D J SMITH, C E TRUMAN, E J KINGSTON and R J DENNIS: Measurement and prediction of residual stress in a bead-on-plate weld benchmark specimen, *Int Jnl Press Vess and Piping* 86(1), 20-30 (2009).
- [12] M C SMITH, B NADRI, A C SMITH, D G CARR, P J BENDEICH and L EDWARDS: Optimisation of mixed hardening material constitutive models for weld residual stress simulation using the NeT Task Group 1 single bead on plate benchmark problem, ASME PVP 2009, Prague, PVP2009-77158 (2009).
- [13] P J BENDEICH, M C SMITH, D G CARR and L EDWARDS: Sensitivity of predicted weld residual stresses in the NeT Task Group 1 single bead on plate benchmark problem to finite element mesh design and heat source characteristics, ASME PVP 2009, Prague, PVP2009-77584 (2009).
- [14] M C SMITH, A C SMITH, R WIMPORY and C OHMS: A review of the NeT Task Group 1 residual stress measurement and analysis round robin on a single weld bead-on-plate specimen, *Int Jnl Press Vess and Piping* 120–121(0), 93-140 (2014).
- [15] P J BOUCHARD: The NeT bead on plate benchmark for weld residual stress simulation, *Int Jnl Press Vess and Piping* 86(1), 31-42 (2009).
- [16] P GILLES, W EL-AHMAR and J-F JULLIEN: Robustness analyses of numerical simulation of fusion welding NeT-TG1 application: "single weld-bead-on-plate", *Int Jnl Press Vess and Piping* 86(1), 3-12 (2009).

- [17] M HOFFMAN and R C WIMPORY: NeT TG1: Residual stress analysis on a single bead weld on a steel plate using neutron diffraction at the new engineering instrument "STRESS-SPEC", *Int Jnl Press Vess and Piping* 86(1), 122-125 (2009).
- [18] R M MOLAK, K PARADOWSKI, T BRYNK, L CIUPINSKI, Z PAKIELA and K J KURZYDŁOWSKI: Measurement of mechanical properties in a 316L stainless steel welded joint, *Int Jnl Press Vess and Piping* 86(1), 43-47 (2009).
- [19] C OHMS, R C WIMPORY, D E KATSAREAS and A G YOUTSOS, NET TG1: Residual stress assessment by neutron diffraction and finite element modelling on a single weld on a steel plate, *Int Jnl Press Vess and Piping* 86(1), 63-72 (2009).
- [20] S PRATHAR, M TURSKI, L E EDWARDS and P J BOUCHARD: Neutron diffraction residual stress measurements in a 316L stainless steel bead-on-plate weld specimen, *Int Jnl Press Vess and Piping* 86(1), 13-19 (2009).
- [21] X SHAN, C M DAVIES, T WANGSDAN, N P O'DOWD and K M NIKBIN: Thermo-mechanical modelling of a single-bead-on-plate weld using the finite element method, *Int Jnl Press Vess and Piping* 86(1), 110-121 (2009).
- [22] M TURSKI and L E EDWARDS: Residual stress measurements of a 316L stainless steel bead-on-plate specimen utilising the contour method, *Int Jnl Press Vess and Piping* 86(1), 126-131 (2009).
- [23] R C WIMPORY, C OHMS, M HOFFMAN, R SCHNEIDER and A G YOUTSOS: Statistical analysis of residual stress determination using neutron diffraction, *Int Jnl Press Vess and Piping* 86(1), 48-62 (2009).
- [24] K ABBURI VENKATA, C E TRUMAN, R C WIMPORY and T PIRLING: Numerical simulation of a three-pass TIG welding using finite element method with validation from measurements, *Int Jnl Press Vess and Piping* 164, 68-79 (2018).
- [25] L DEPRADEUX and R COQUARD: Influence of viscoplasticity, hardening, and annealing effects during the welding of a three-pass slot weld (NET-TG4 round robin), *Int Jnl Press Vess and Piping* 164, 39-54 (2018).
- [26] O MURÁNSKY, C J HAMELIN, F HOSSEINZADEH and M B PRIME, Evaluation of a self-equilibrium cutting strategy for the contour method of residual stress measurement, *Int Jnl Press Vess and Piping* 164, 22-31 (2018).
- [27] O Muránsky, F Hosseinzadeh, C J Hamelin, Y Traore and P J BENDEICH, Investigating optimal cutting configurations for the contour method of weld residual stress measurement, *Int Jnl Press Vess and Piping* 164, 55-67 (2018).
- [28] O MURÁNSKY, M TRAN, C J HAMELIN, S L SHRESTHA and D BHATTACHARYYA, Assessment of welding-induced plasticity via electron backscatter diffraction, *Int Jnl Press Vess and Piping* 164, 32-38 (2018).
- [29] M C SMITH, O MURÁNSKY, C AUSTIN, P BENDEICH and Q XIONG, Optimised modelling of AISI 316L(N) material behaviour in the NeT TG4 international weld simulation and measurement benchmark, *Int Jnl Press Vess and Piping* 164, 93-108 (2018).
- [30] M C SMITH and A C SMITH, Advances in weld residual stress prediction: A review of the NeT TG4 simulation round robins part 2, mechanical analyses, *Int Jnl Press Vess and Piping* 164, 130-165 (2018).
- [31] M C SMITH and A C SMITH, Advances in weld residual stress prediction: A review of the NeT TG4 simulation round robin part 1, thermal analyses, *Int Jnl Press Vess and Piping* 164, 109-129 (2018).
- [32] M C SMITH, A C SMITH, C OHMS and R C WIMPORY, The NeT Task Group 4 residual stress measurement and analysis round robin on a three-pass slot-welded plate specimen, *Int Jnl Press Vess and Piping* 164, 3-21 (2018).
- [33] R C WIMPORY, R V MARTINS, M HOFMANN, J R KORNMEIER, S MOTURU and C OHMS, A complete reassessment of standard residual stress uncertainty analyses using neutron

- diffraction emphasizing the influence of grain size, *Int Jnl Press Vess and Piping* 164, 80-92 (2018).
- [34] M C SMITH, S K BATE and P J BOUCHARD, Simple benchmark problems for finite element weld residual stress simulation, *ASME Pressure Vessels and Piping Conference*, Paris, PVP2013-98033 (2013).
- [35] C J HAMELIN, O MURÁNSKY, M C SMITH, T M HOLDEN, V LUZIN, P J BENDEICH and L EDWARDS, Validation of a numerical model used to predict phase distribution and residual stress in ferritic steel weldments, *Acta Materialia* 75(0), 1-19 (2014).
- [36] H J RATHBUN, D RUDLAND, L FREDETTE, A CSONTOS and P SCOTT, NRC welding residual stress validation program – International round robin details and findings, 2011 *ASME Pressure Vessels and Piping Division Conference*, Baltimore, 17th-20th July 2011, PVP 2011-57642 (2011).
- [37] L FREDETTE, M KERR, H J RATHBUN and J E BROUSSARD, NRC/EPRI Welding Residual Stress Validation Program - Phase III Details and Findings, *ASME Pressure Vessels and Piping Conference*, Baltimore, PVP2011-57645 (2011).
- [38] O MURANSKY, M C SMITH, P J BENDEICH and L EDWARDS, Validated numerical analysis of residual stresses in Safety Relief Valve (SRV) nozzle mock-ups, *Computational Materials Science* 50(7), 2203-2215 (2011).
- [39] P J BENDEICH, O MURANSKY, C J HAMELIN, M C SMITH and L EDWARDS, Validated numerical analysis of residual stresses in safety relief valve (SRV) nozzle mock-ups: influence of axial restraint on distortion and residual stress predictions, *Computational Materials Science* 62, 285-288 (2012).
- [40] M C SMITH and O MURANSKY, The NeT task group 6 weld residual stress measurement and simulation round robin in alloy 600/82, *ASME Pressure Vessels and Piping Conference*, Vancouver, PVP2016-63941 (2016).
- [41] M TURSKI, M C SMITH, P J BOUCHARD, L EDWARDS and P J WITHERS, Spatially resolved materials property data from a uniaxial cross-weld tensile test, *Journal of Pressure Vessel Technology* 131(6), (2009).
- [42] M C SMITH, P J BOUCHARD, M TURSKI, L EDWARDS and R J DENNIS, Accurate prediction of residual stress in stainless steel welds, *Computational Materials Science* 54, 312-328 (2012).
- [43] O MURANSKY, M C SMITH, P J BENDEICH, T M HOLDEN, V LUZIN, R V MARTINS and L EDWARDS, Comprehensive numerical analysis of a three-pass bead-in-slot weld and its critical validation using neutron and synchrotron diffraction residual stress measurements, *International Journal of Solids and Structures* 49(9), 1045-1062 (2012).
- [44] F HOSSEINZADEH, Y TRAORE, P J BOUCHARD and O MURÁNSKY, Mitigating Cutting-Induced Plasticity in the Contour Method, Part 1: Experimental, *International Journal of Solids and Structures*.

# PROCESS CHAIN SIMULATION OF LASER CLADDING AND COLD METAL FORMING

P. KHAZAN\*, A. KZZO\*\*, R. HAMA-SALEH\*\*\*,  
A. WEISHEIT\*\*\*\*, I. ÜNSAL\*\*\*\*\* and M. BAMBACH\*\*\*\*\*

\*Simufact Engineering GmbH, 21079 Hamburg, Germany, pavel.khazan@simufact.de

\*\*Simufact Engineering GmbH, 21079 Hamburg, Germany, abdullah.kzzo@simufact.de

\*\*\*Fraunhofer-Institut fuer Lasertechnik, Steinbachstrasse 15, 52074 Aachen, Germany, rebar.hama-saleh@ilt.fraunhofer.de

\*\*\*\*Fraunhofer-Institut fuer Lasertechnik, Steinbachstrasse 15, 52074 Aachen, Germany,  
andreas.weisheit@ilt.fraunhofer.de

\*\*\*\*\*Chair of Mechanical Design and Manufacturing, BTU Cottbus-Senftenberg,  
Konrad-Wachsmann-Allee 17, 03046 Cottbus, Germany, uensal@b-tu.de

\*\*\*\*\*Chair of Mechanical Design and Manufacturing, BTU Cottbus-Senftenberg,  
Konrad-Wachsmann-Allee 17, 03046 Cottbus, Germany, bambach@b-tu.de

DOI 10.3217/978-3-85125-615-4-19

## ABSTRACT

Lightweight construction is still an important driver for innovations in production technologies. Recent developments in Laser Metal Deposition (LMD) and forming technology allow the production of lightweight sheet metal components with locally adapted properties, reducing the weight of parts. For example, using laser cladding, it is possible to reinforce critical areas of a sheet metal component, while other areas can still remain untouched and thus consume less material, reducing the overall weight of the component. Conventional production of such reinforced structures would require expensive and time-consuming machining steps. However, especially if it comes to sheet metal components that are to be mechanically formed, the induction of heat during laser cladding might lead to undesired properties of the final product due to distortion, residual stresses as well as changed material properties. Such effects can be investigated by means of structural welding simulation, but, if it comes to process chains, i.e. reinforced metal sheets that undergo forming processes, a process chain simulation covering forming and cladding steps is desirable. This approach would also answer the question of preferred process sequences. This article presents an approach for such a process chain simulation for a demonstrator made of aluminium EN AW 6016 undergoing one laser cladding and one cold forming process. The simulation considers the influence of the process sequence (forming-cladding vs. cladding-forming) and helps to select the proper process sequence as well as predicts properties of the final product.

Keywords: Laser cladding, cold forming, process chain simulation, sheet metals

## INTRODUCTION

Nowadays, lightweight design is one of the most important drivers for further developments in manufacturing technology. On the one hand, it allows the reduction of material usage, leading directly to overall reduction of material costs. On the other hand, lighter structures with structural properties that are comparable with conventionally built components lead to weight reduction of the final product, reduce the processing and material costs and finally the efficiency of the product itself. A combination of cold forming and cladding processes can be useful to achieve such goals.

In this article we take a brief look at a common forming process, initially consisting of a single cold metal forming step. Usually, in mass production of complex features, sheet metal of constant thickness is used. This leads to increased material usage and weight as well as higher needed forces and decreased tools life cycle during forming. Alternatively, tailored blanks, especially patchwork blanks, can be used, which allow for a variable sheet thickness. Tailored welded and rolled blanks only allow for relatively simple thickness variation. With patchwork blanks more complicated designs are feasible, but the patches cannot be joined to the basic sheet metal yielding a full metallurgical bond. However, technologies like laser cladding [1] allow for flexible local adjustments of material thickness and thus structural properties. While challenges that arise from increased process complexity are to be addressed, the method clearly enables a reduced overall weight of a component. On the one hand, laser cladding, basically a surface welding process, might induce undesired residual stresses as well as change local material properties in an undesired way. On the other hand, one has to investigate which process chain direction is the most desirable one: a sheet of metal can be cladded and then formed or vice versa.

From the manufacturing point of view such investigations, especially concerning the question of the preferred process sequence, would need at least two sets of forming tools to be applied to undeformed wrought material as well to deformed but cladded material. At this point, numerical simulation of cladding and forming process is helpful to identify the optimal process sequence, also allowing the estimation of hidden target variables that are difficult or expensive to measure, like residual stresses, strains, and material state.

Processing of aluminium alloys by means of laser cladding has been described in the past [2] and is in general a common process nowadays. Calculation of such kind of properties is a relatively new field and – due to long process times – often needs some kind of model simplification and reduction [3]. However, in general such calculations are possible [4] and can, if detailed enough, also cover not only deformation effects but also evolution of residual stresses [5].

Incremental simulation of sheet metal forming processes is well-described [6] and is widely used in research and industrial applications. However, the coupling between a forming and a welding or cladding simulation might be challenging (due to possible different element formulations, strain decomposition approaches, different meshes and so on), but possible [7].

In the current investigation, a sheet made of aluminium grade EN AW 6016 undergoes local forming as well as local cladding. Finite element welding and forming simulation with data transfer in between the processes is applied in order to identify the desired process chain to achieve best possible component properties at the end.

### GEOMETRIES, MATERIALS AND EXPERIMENTAL SETUP

Laser cladding and forming of an aluminium sheet made of EN AW 6016 provided by Hydro Aluminium Rolled Products GmbH is investigated. Dimensions of the sheet are 80 mm x 80 mm x 1 mm. A drilled hole with a radius of 2.5 mm is positioned at the centre of the sheet, see fig. 1, left.

The mechanical properties of EN AW 6016 T4 are shown in Table 1.

**Table 1** Mechanical properties of EN AW 6016 T4

$R_{p0.2}$	$R_m$	$A_{g0}$
90-130 MPa	>190 MPa	> 24%

LASER CLADDING PROCESS

In the vicinity of the hole, a ring-shaped cladding with a radius of 10 mm is welded onto the sheet using powder material made of the same alloy as the base material (fig. 1, right). During cladding, the component is clamped on a copper plate with internal meandering cooling channels. Water is used as cooling liquid with an entrance temperature of 16°C. A flow of 6 l/min is maintained. The component is fixed on the cooling plate using a steel clamping device with an opening at the centre (fig. 2). This opening can have different shapes, depending on the area that has to be cladded. It is important to clamp an area as big as possible to ensure that the warpage of the sheet metal during the cladding process is minimized. The cooling plate and the clamping device are bolted together.

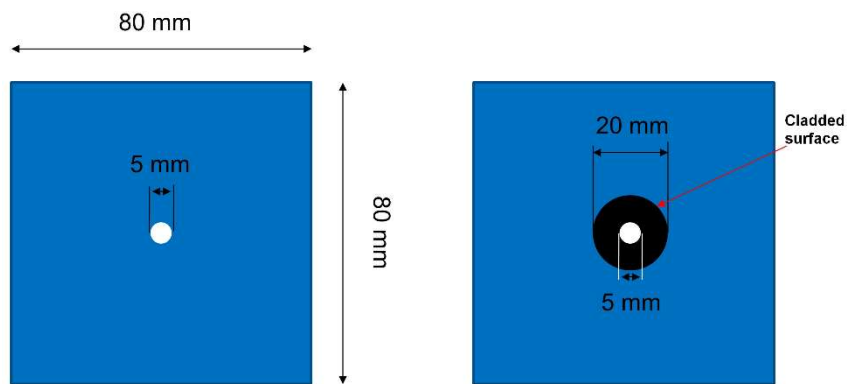


**Fig. 1** Left: Geometry of the aluminium sheet, right: cladded area.

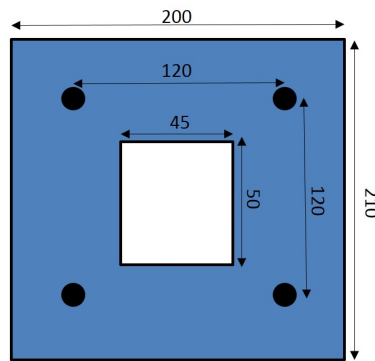


**Fig. 2** Geometry of the clamping tool.

Laser cladding is performed using a 2 kW Laserline LDF-2000 – 30 diode laser with the wavelength of 1030 nm. In a parameter study suitable process parameters were identified. To clad a thin sheet the local heat input must be minimized to avoid massive melting and



warpage. Thus a laser spot diameter on the surface of 0.85 mm was selected for the process and the velocity is set to 4000 mm/min. The laser power required to clad a dense and bonded layer is 1200 W. A Laserline optic and an ILT powder feed nozzle are used. The powder is fed in an inert gas stream (Ar) with a GTV Twin powder feeder system into the interaction zone. To prevent oxidation of the melt pool the process zone is additionally protected by a local shielding gas stream (Ar) through the beam path opening. The complete experimental setup is shown in fig. 3. The cladding path itself is represented by an Archimedean spiral starting the edge of the hole and moving outwards. The distance between cladding tracks is approx. 0.3 mm while approx. 23 revolutions are required to achieve the outer diameter of 20 mm of the cladded area. With these settings, a cladding height of 0.25 mm in one layer was achieved. All this data was taken as input for the cladding model.

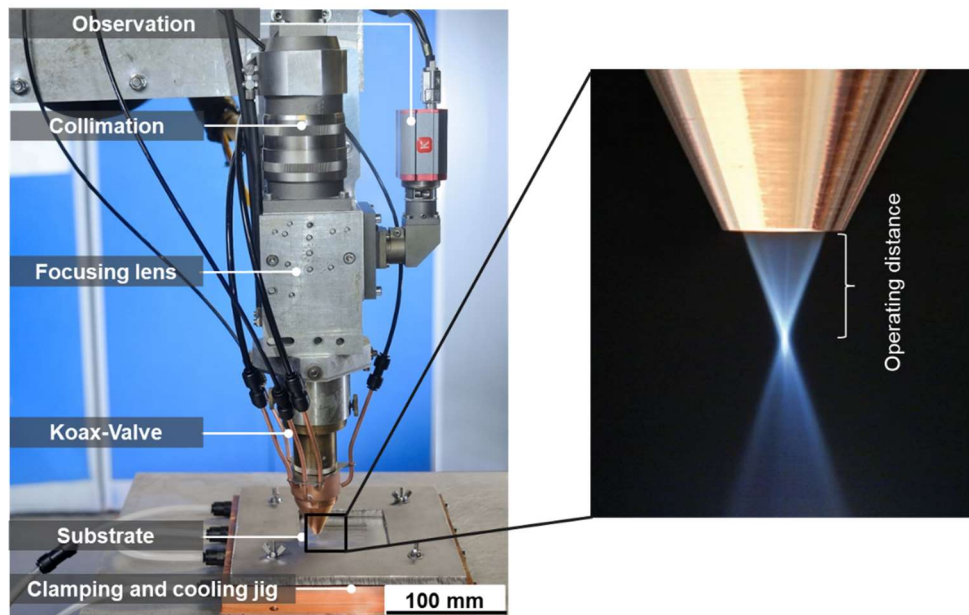


**Fig. 3:** Experimental setup for the laser cladding process with substrate, clamping and cooling-jig.

### FORMING PROCESS

The hole flanging experiments are executed on a Zwick Z250 universal testing machine. The machine can generate a testing force of max. 250 kN, which can be applied using a constant velocity for the forming tool. Additionally, the force used in the forming process can be measured continuously.

A special tool was designed for the forming process. The aim is to clamp and fix the cladded specimen during the action of the forming die. This is achieved by bolting. Furthermore, different inserts can be used to operate with different hole diameters. Tool and die are depicted in fig. 4.

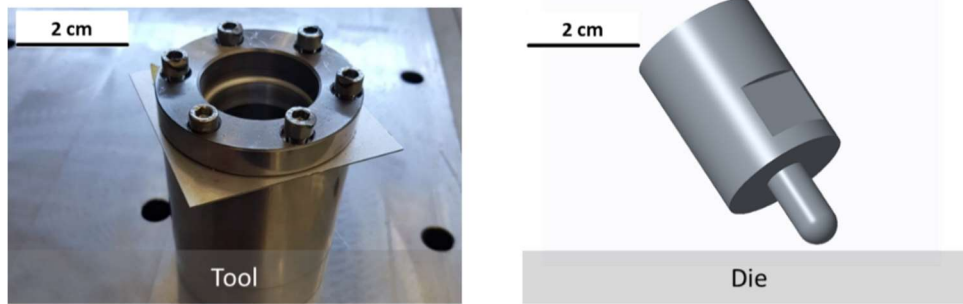


Fig. 4: Tool for collar forming (left) and CAD-Model of used die for forming process (right).

*Forming of cladded sheet*

In this case, the hole flanging process is applied on a reinforced sheet metal. The die can be applied on the cladded and non-cladded side, leading to a different end geometry. It can be stated, that the flanging with the die on the cladded sides can lead to cracking of the cladded layer. The process chain is shown in fig. 5.

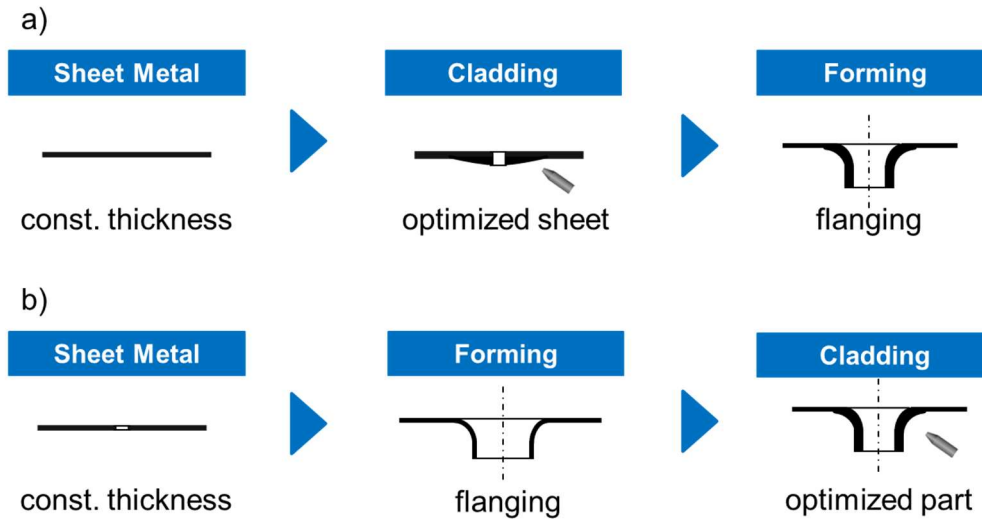


Fig. 5: Process chain for the sequence cladding-forming (a) and forming-cladding (b).

FINITE ELEMENT MODELING

The welding as well as the forming processes were modelled using FE based software packages Simufact Welding and Simufact Forming, both in the most recent versions. The material model of aluminium EN AW 6016 was created using material simulation software JMatPro v. 9.1 by Sente Software. The material model respects dependences of thermal

and mechanical properties on temperature. Additionally, stress-strain relations are described with respect to strain rate.

The fundamentals of FE-modelling of both – thermal and thermo-elasto-plastic – problems are well-described. Concerning heat transfer problems we refer to [8], while the fundamentals of plasticity can be found in [9] and the solution procedure by terms of finite element method is given in [10-11].

Both process chain directions – cladding and forming as well as forming and cladding – were calculated.

### PROCESS CHAIN CLADDING - FORMING

#### *Cladding model*

The cladding operation takes about 13.825 seconds with a total length of clad path of 921.6 mm. This is a relatively long clad line with relatively high cladding velocity, thus, the time discretization of the cladding process itself needs to be rather fine. In order to keep the calculation time sufficiently low, the main goal during model creation is the reduction of model complexity, thus, especially in the reduction of element number in the model.

The aluminium sheet was created from CAD data and meshed using Simufact Welding sheetmesher. The typical element edge length in the X-Y-plane of the sheet is between 0.13 and 0.33 mm in the cladding area and in the heat affected zone, while the general element edge length outside the relatively narrow heat affected zone is around 1.5 mm. Solid shell elements with seven layers are used for this component, reducing the number of needed element layers in the model to one. Through the usage of solid shell element approach the overall element number in this mesh can be reduced to 11,660, with approx. 23,700 nodes.

The cladding area (fillet mesh) is modelled as a disc with the height of 0.25 mm and radius of 10.85 mm using two layers of hexahedral elements with full integration and a typical element edge length of 0.125 mm, leading to 46,500 elements and 70,779 nodes within the cladding geometry. MSC Apex as well as Simufact Welding meshers were used for mesh generation.

In order to reduce the overall number of solid elements, the cooling plate is modelled as a rigid body using thermal properties of pure copper material. The temperature of the rigid body is set to 16 °C. The heat transfer between the cooling plate and the component is sufficiently high, governed by material properties of copper and aluminium assigned to the cooling device and the clad component respectively. Such modelling approach creates an infinite heat sink.

The clamping device is also modelled as rigid body with usual 20 °C temperature. Both rigid bodies allow separation and sliding of the contacting surfaces, but no penetration. The general geometrical model is shown in fig. 6.

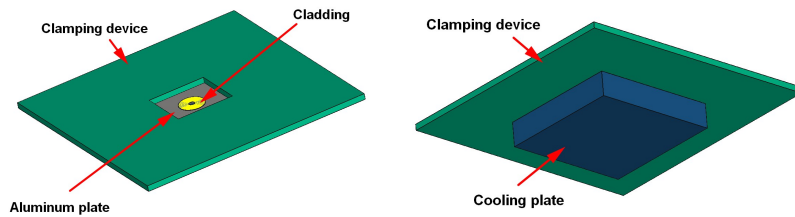


**Fig. 6:** Model geometry including base plate, cladded surface as well as cooling and clamping tools.

The cladding trajectory is directly imported from machine data; however, the number of sampling points has been reduced from over 9,000 to about 3,000. The equivalent heat source with an efficiency of 25% is positioned directly on the cladding, normal to the surface of the component, using a cylindrical shape with penetration depth of 0.4 mm and a radius of 0.42 mm. A constant clad flux distribution over the radius is assumed.

A fully adaptive time stepping scheme is used during the calculation. Initial and maximal allowed time steps are set to 2 ms and 5 ms, respectively, to allow for a good resolution of the process in terms of heat source movement. Convergence tests for the thermal solution are set to fulfil 20 K max. error in the temperature calculation as well as 1% max. tolerance in the force balance.

After the cladding process itself, the clamping tool as well as the cooling plate are both removed. This happens at 15 s and 20 s respectively. To avoid rigid body motion, at 20 s process time, nodal boundary conditions at three corners of the aluminium plate are activated, allowing free deformation but preventing any rigid body motion and rotation, thus being a classical three-point mounting support. The cooling duration is set to 1000 s; however, the calculation aborts after clamping tool and cooling plate removal as soon as the maximal temperature in all nodes of the model falls below 22 °C.

During the complete process, gravity, acting in the negative Z direction, is taken into account. Since solid shell elements in Simufact Welding and Forming solvers only support additive strain decomposition, this approach was also applied to solid elements present in the model.

### *Forming model*

Due to interoperability between Simufact Welding and Simufact Forming, the results of the cladding simulation can be easily transferred into a forming model. The mesh density of the welding model is also sufficient for the sheet metal forming simulation. The model geometry is rotated 180° around the centre point (so that the cladded surface showed in the negative Z direction) and is repositioned using contact and gravity positioners on the lower die. The movable upper die is attached to a press moving with velocity  $v = 44$  mm/min in the  $-Z$  direction until the stroke of 15 mm is achieved, thus leading to a deformation of the metal sheet including cladding. Both dies are modelled as rigid bodies without any deformations. Temperature effects are neglected. Fig. 7 shows the overall geometry of the model as well as die geometries in the contact area.

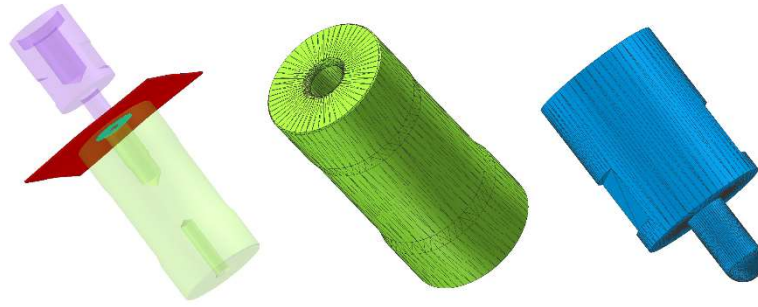


**Fig. 7** Forming model geometry (left), stationary die (centre), movable die/press (right).

After the desired stroke of 15 mm is achieved, the deep-drawing process stops, and the dies are removed. To avoid rigid body motion, stabilizer springs were added to the model.

### PROCESS CHAIN FORMING - CLADDING

#### *Forming model*

The model has the same configuration as the model used in the reversed process chain. In contrast to the cladding model in the cladding – forming chain, the cladding material is removed from the model and the dies were repositioned accordingly.

#### *Cladding model*

The-setup of the deformed sheet cladding model is significantly different from to the basic cladding model used in the previous process chain. Several challenges have to be solved in order to get useful model and results:

- The deformed sheet has to be repositioned on the cooling plate. This could be achieved using several positioning tools in Simufact Welding.
- The cladding geometry has to be created and positioned on the deformed shape. To achieve this, an expected shape of the contact area between base material and cladding material has been exported from the forming results: This contact surface has been meshed using 2D-shell elements, extruded normal to the surface and remeshed using the Simufact Welding mesher. Using gravity and contact positioner, the resulting geometry has been roughly pre-positioned on the deformed surface of the aluminium sheet. An intermediate solver run is then used to establish clean contact between component and cladding.
- Before welding, the assembly is clamped with the clamping tool, the four screws can apply a significant force and straighten the sheet. During the intermediate solver run this was achieved applying a certain force in the  $-Z$  direction of the clamp.

## Mathematical Modelling of Weld Phenomena 12

- After the intermediate solver run, the position of the clamp, the shape and positions of clamped sheet as well as the shape and position of the cladding material can be extracted and used for the cladding model.
- At this point no real process existed for this direction of process chain, thus, the description of welding paths was not available. The helix-shaped path was thus replaced by a number of circular paths beginning on the top of the deformed sheet and reaching the end of expected cladding geometry. The paths were calculated to get the same overlap as in the case of an Archimedean spiral.

The overall cladding period increased significantly (13.8 s vs. 17.0 s) compared to cladding of the undeformed sheet because of increased area after deep drawing process. The same holds for the weld path lengths (921 mm vs. 1134 mm). Thus, the overall heat input into the model increased by approx. 23%.

### SIMULATION RESULTS

#### *Chain Cladding - Forming*

After welding, cooling and unclamping the expected bending of the plate towards the laser beam occurs. Due to the fact that the corners of the plate are referenced at zero in Z direction, the distortion is visible as negative Z displacement of the plate, while the corners stay at the initial position (fig. 8).

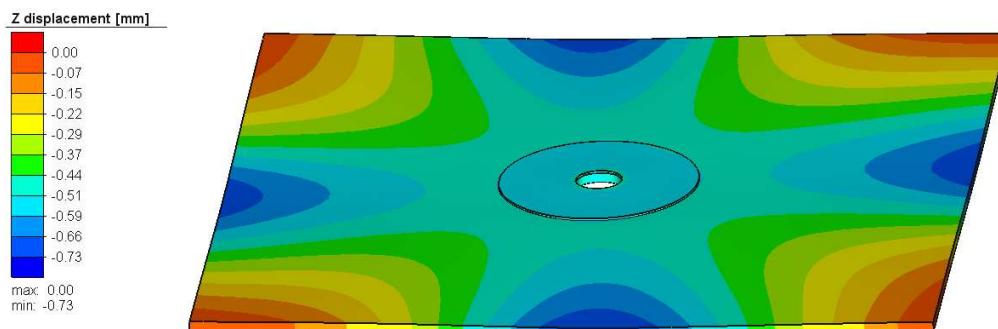


**Fig. 8:** Z-Distortion of the plate after unclamping, upper side.

On the lower side of the plate a sag is visible underneath the cladded surface, which can also be observed in the experiment (fig. 9). However, the absolute height is underestimated.

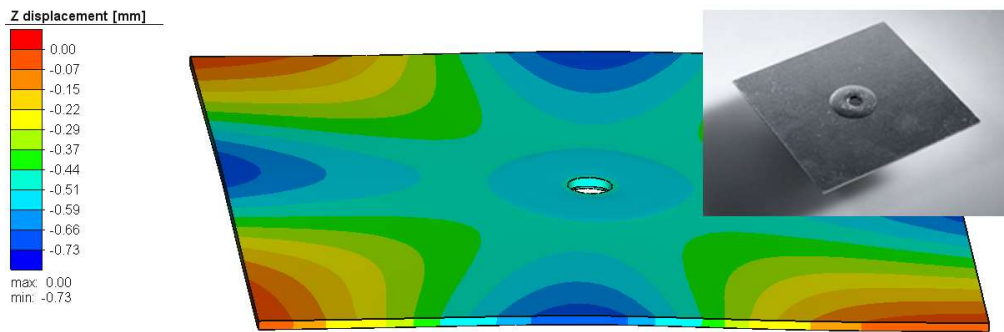


**Fig. 9:** Z-Distortion of the plate on the lower side (simulation and experiment).

The simulation also provides insight into residual stresses and the achieved yield stress during and after welding (fig. 10).

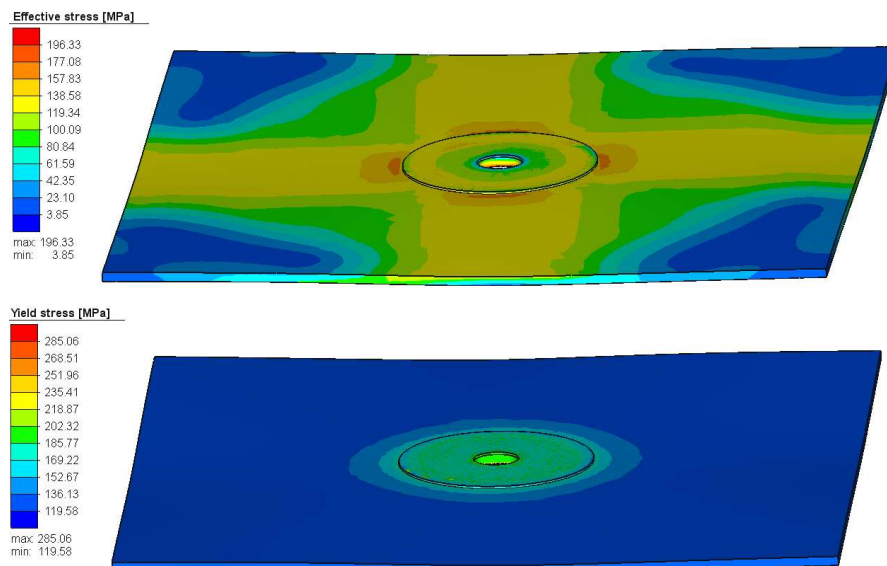


**Fig. 10:** Von Mises residual (top) and yield stresses after welding.

After forming and removing of dies, the deformation reaches 4.24 mm in the stroke direction at the centre of the plate. However, the plate itself is bent largely, showing 3.5 mm sag at the boundary of the plate (fig. 11).

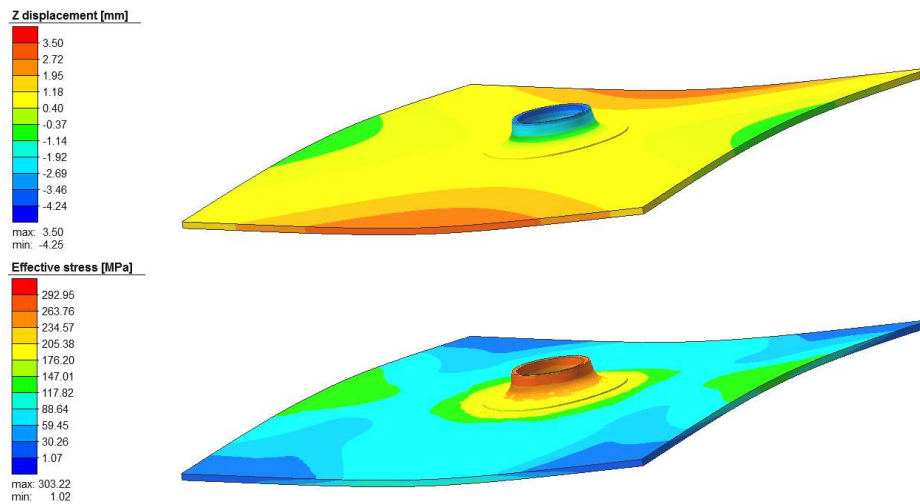


**Fig. 11:** Z-displacement (top) and von Mises residual stress (bottom) after forming.

In fig 11 high residual stress accumulation in the centre of the plate is also shown. In the cladding itself relatively high radial tensile stresses up to 400 MPa can be found in the base material directly in the contact area between base material and cladding.

The calculation time of this process chain using parallelization capabilities of Simufact FE-solver on a 16 core dual Intel® Xeon E5-2667 at 3.2 GHz machine was 27 hours for the cladding process and at about 2 hours for the forming process.

### *Chain Forming – Cladding*

The plate deformation after forming is nearly axially symmetric with respect to the Z-axis showing 4.4 mm Z-distortion in the stroke direction but less overall deformation of the plate reaching only about 1 mm at the edges of the plate (fig. 12). No significant additional distortion can be observed during welding. The von Mises stress after forming shows (at least in the area around the tools) similar peak values as before.



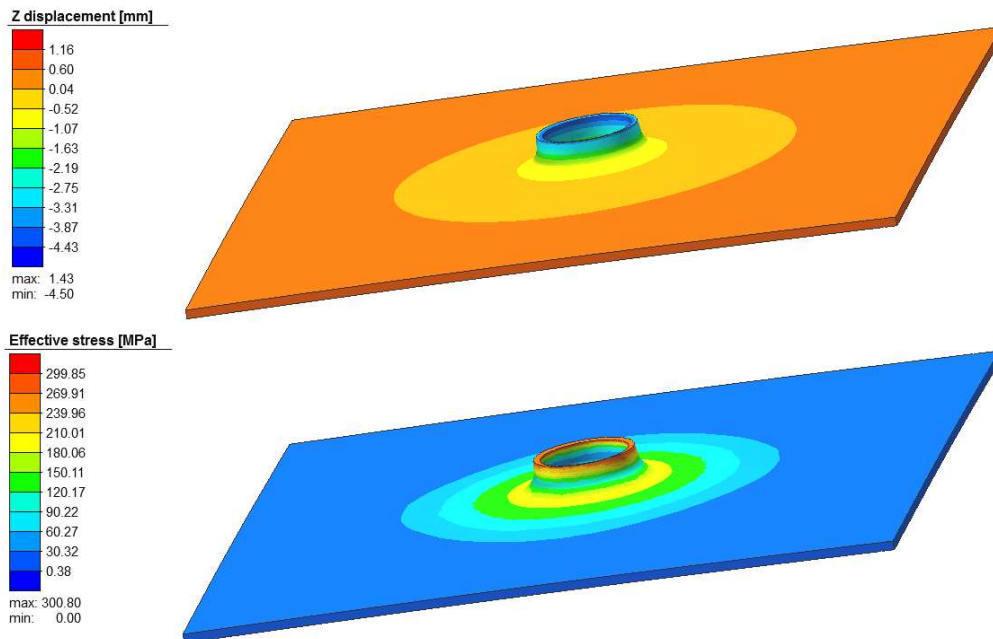


**Fig. 12:** Z-distortion (top) and von Mises residual stress (bottom) after forming.

After cladding, a reduction of residual stresses around the hole in the centre of the component (fig. 13) can be observed compared to uncladded, formed sheet.

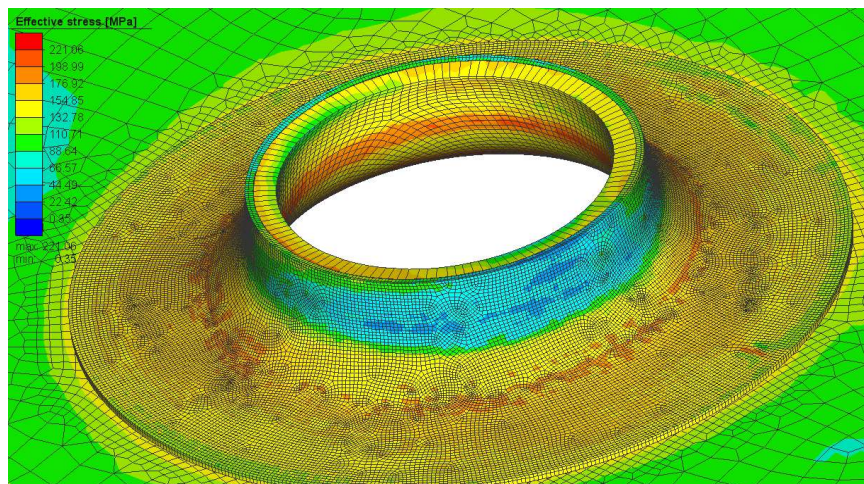


**Fig. 13:** Von Mises stress after forming, cladding, cooling and unclamping.

This can be explained due to the process chain direction, which leads to heating and partial melting of deformed material. Accumulated residual stresses and work hardening due to plastic deformations during forming are reduced. These reduced stresses also reduce the distortion, especially in the uncladded regions of the plate.

The calculation time of this process chain is approx. 0.6 h for the forming and 48 h for the cladding process.

### *Comparison of the two process chains*

Fig. 14 shows the deviation from the initial undeformed shape. Here, it is visible that the chain direction starting with forming leads to lower deformation of the initial geometry. The equivalent residual stress at the end of both process chains is widely different as shown in the figure 15.

Both effects are related, reduced residual stresses also reduce the deformation. Reduced residual stresses promise overall better characteristics of the component. Especially if the effective plastic deformation of the cladding is considered, the values achieved during the chain cladding  $\rightarrow$  forming are approx. three times higher compared to the reversed direction (fig. 16).

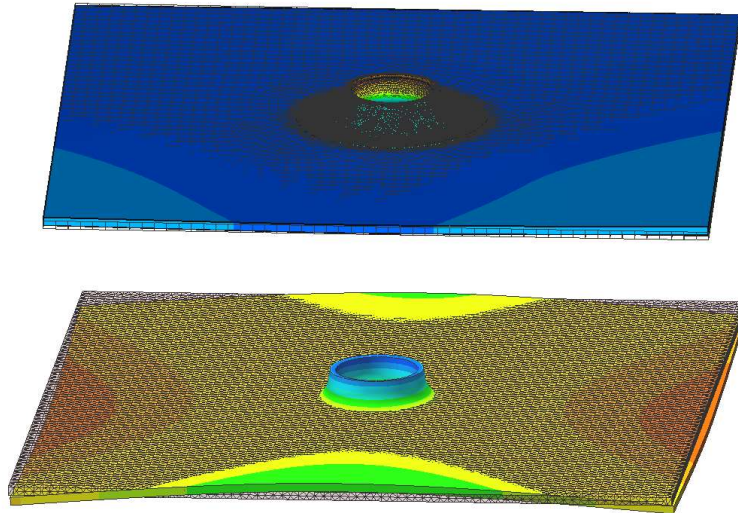


**Fig. 14:** Deviation from the undeformed state, top: forming  $\rightarrow$  cladding, bottom: cladding  $\rightarrow$  forming process chains. Solid: Simulation results. Wireframe: Initial shape.

## Mathematical Modelling of Weld Phenomena 12

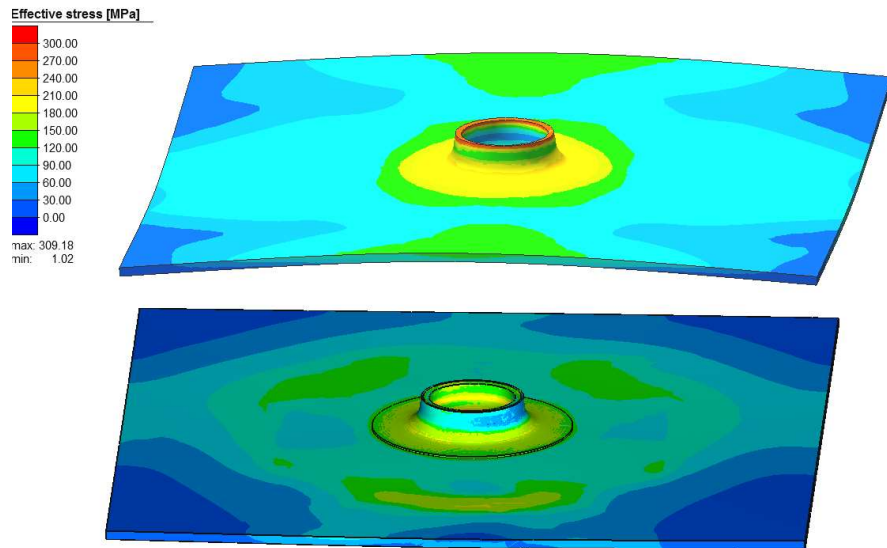


**Fig. 15:** Residual stress after cladding→forming (top) and forming→cladding (bottom) process chain.

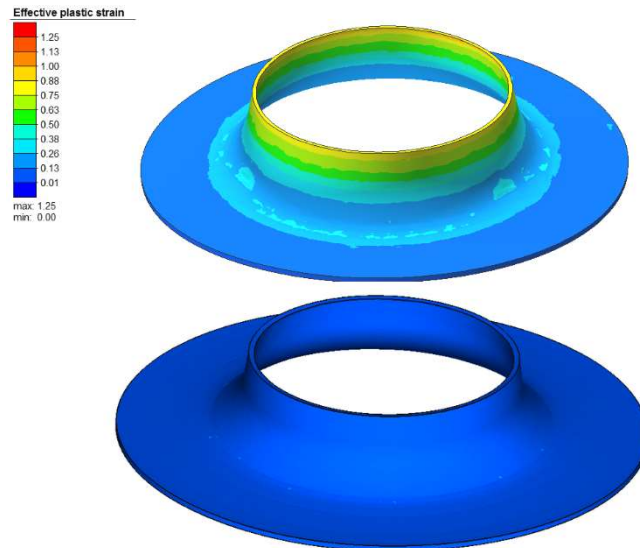


**Fig. 16:** Effective plastic strain at the end of the process, Cladding→Forming (top), forming→cladding (bottom).

### CONCLUSION AND OUTLOOK

This work shows that it is possible to couple sheet metal forming and cladding process simulations if certain assumptions are met and if sufficient care is taken concerning correct plasticity formulation in both processes.

Besides already briefly discussed strain decomposition and element types, a proper material model that suits the needs of forming and welding simulation is needed. Such a material model can be obtained using material simulation software and adjusting the material properties according to measured data or material data sheets provided by manufacturer.

Due to partially missing experimental results it is difficult to make quantitative statements, however, qualitative conclusions can be made. Especially it is possible to select the best suited chain direction. The current investigation shows that cladding after forming seems to yield better results, i.e., less deviation of the underformed shape and lower residual stresses. For such a relatively simple model geometry this can be explained with two major effects. Firstly, deformations and residual stresses after forming are distributed nearly axial symmetric with respect to the Z-axis of the model. This leads to more balanced deformations and residual stresses after cladding. On the other hand, cladding process helps to relax forming residual stresses in the cladding area and also partially reduces the plastic strain and thus work hardening effects there. The reversed process chain suffers from asymmetrical residual stresses and deformations after cladding. Those imperfections are growing also during forming afterwards.

Future work will focus on validation of the models with experiments. Furthermore, a trimming stage between cladding and forming will be included. Investigations on the influence of tool geometry and hole diameter are planned, thus, the components are undergoing a cutting process after cladding and cooling, before the forming process starts. This might require remeshing and result mapping, while in the current work the same mesh could be used for all process steps.

The authors would like to thank BMWi (Federal Ministry for Economic Affairs and Energy) and AiF for funding of the IGF project 19292BG AiF/EFB “Lokale materialeffiziente Verstärkung belastungsangepasster Bauteile durch Laserauftragschweißen und Tape-Beschichten”.

The contribution of Simufact engineering GmbH (Kzzo and Khazan) is funded through the BMBF-project 03ZZ0210J “Zwanzig20 – Additiv-Generative Fertigung – Verbundvorhaben: ImProVe; TP10: Entwicklung Simulationstool“ by the German Federal Ministry of Education and Research.

Furthermore the authors would like to thank Hydro Aluminium Rolled Products GmbH who provided the material for specimens used in this investigation.

### REFERENCES

- [1] D. S. GNANAMUTHU: *Cladding, US Patent 3,952,180, 1976*
- [2] J. MAZUMDER, D. DUTTA, N. KIKUCHI, A. GOSH: 'Closed loop direct metal deposition: art to part', *Optics and Lasers in Engineering*, Vol. 34, pp. 397-414, 2000
- [3] P. KHAZAN and R. RAJPUT: 'Experimental and numerical investigations of reconditioning of ship engine components by laser cladding', *Proc. of the 4<sup>th</sup> International Workshop on Thermal Forming and Welding Distortions*, Eds.: F. Vollertsen, H. Tetzl, BIAS Verlag, Bremen, pp. 1-12, 2014.
- [4] G. BRANNER: 'Modellierung transienter Effekte in der Struktursimulation von Schichtbauverfahren', *Dissertation*, TU München, 2010
- [5] F. BRÜCKNER, D. LEPSKI, E. BEYER: 'Modelling the Influence of Process Parameters and Additional Heat Sources on Residual Stresses in Laser Cladding', *Journal of Thermal Spray Technology*, Vol. 16, No. 3, pp. 355-373, 2006
- [6] P. V. RF RIVINDAR REDDY, G. CHANDRA MOHAN REDDY, P. RADHAKRISHNAE PRASAD: 'A Review on Finite Element Simulations in Metal Forming', *International Journal of Modern Engineering Research*, Vol. 2, Issue 4, pp. 2326-2330, 2012
- [7] I. NEUBAUER: 'Verschweißen eines Umformteils mit einem additiv gefertigten Bauteil unter Berücksichtigung der Fertigungshistorie', *19th Simufact Round Table*, Marburg, 2018.
- [8] N. J. REDDY, K. D. GARTLING: 'The finite element method in heat transfer and fluid dynamics', CRC Press, 2001.
- [9] P. HAUPT: 'Continuum Mechanics and Theory of Materials', Springer, 2002
- [10] J. ALTENBACH and S. A. SACHAROV: 'Die Methode der finiten Elemente in der Festkörpermechanik', Hanser, 1982
- [11] H. PARISCH: 'Festkörper-Kontinuumsmechanik', Teubner, 2003

*intentionally blank page*

*intentionally blank page*

*intentionally blank page*



*intentionally blank page*

*intentionally blank page*

*intentionally blank page*

*intentionally blank page*

*intentionally blank page*

*intentionally blank page*

*intentionally blank page*

*intentionally blank page*



*intentionally blank page*

*intentionally blank page*

*intentionally blank page*

*intentionally blank page*

*intentionally blank page*

# EVALUATION OF TWO METHODS FOR WELDING DISTORTION SIMULATION

A. BAUMGARTNER\*, F. WIRNSPERGER\*\* and  
N. ENZINGER\*

\* Institute of Materials Science, Joining and Forming, Graz University of Technology, Austria  
\*\* Palfinger Europe GmbH, Salzburg, Austria,

DOI 10.3217/978-3-85125-615-4-20

## ABSTRACT

For manufacturers of heavy steel constructions, it is a major goal to minimize the number of required prototypes within the design process of welding assemblies. Distortion minimization of complex structures usually needs several tries until the best design, welding parameters and welding sequences can be defined.

ESI GmbH provides two different numerical simulations tools which can predict the distortion of welded structures. One of them is the initially introduced and more general purpose welding simulation package Sysweld®. It uses the transient method and thus allows calculations close to full physics on a global model. In this case thermo-mechanical metallurgical effects are coupled, therefore high quality meshes, and long calculation times are required compared to Weld Planner®, which is based on the shrinkage model. It requires less effort for meshing and can be computed very quickly. However, simplified models neglect some aspects like phase transformation.

The present work's objective is to figure out which of the two provided simulation tools is more applicable from a practical perspective of industrial heavy steel constructions engineers. Therefore, an exemplary welded structure of a loader crane boom, stiffener plate and console is investigated using both tools comparatively. Simulated distortions are validated against experimental results. Therefore, welding distortions are measured by means of 3D point measurement after welding experiments of the component under consideration. Based on the validated results the preferred method regarding accuracy and required effort for modelling and simulation costs is identified.

Keywords: welding simulation, transient method, shrinkage method, distortion measurement

## Nomenclature

$\vec{P}_1$	Vector containing coordinates of measuring points before welding experiments	$Jx$	Joint (x stands for the sequence number)
$\vec{P}_2$	Vector containing coordinates of measuring points after welding experiments	$x, y, z$	Cartesian coordinates
$\Delta\vec{P}_{1-2}$	Vector containing calculated differences of the coordinates of the measured points	$z +$	Positive distortion along z-axis
<i>HAZ</i>	Heat affected zone	$z -$	Negative distortion along z-axis
<i>DOF</i>	Degree of freedom	<i>JMAK</i>	Johnson-Mehl-Avrami-Kolmogoroff Model

### INTRODUCTION

To this day welding remains one of the most important joining technologies within steel industries. Especially when it comes to manufacturing of heavy and big structures the effort which is put into production and process optimization can be enormous [1], [2]. Often several prototypes and changes in the design are required until the best welding process can be defined. Among further challenges minimization of welding distortion is one of the most commonly tasks which becomes obvious. This is specifically an issue regarding big assemblies comprising a high number of joints since costs for an experimental analysis of different approaches are rising with the amount of material required and effort for carrying out. Years of experience are a decisive factor when it comes to determine the optimum.

Introducing the finite element method back in the 1950s a new technology appeared to hit all fields of engineering. Basically it did, but access to this technology has long been reserved for a selected group because high processing power was inaccessible to most engineers. Since the digital revolution this limitation has disappeared and finite element methods are applied to any field of science and engineering. But there is still a huge variance between scientific and applied use of different software tools. Usually the scientific user group applies simulations of very high quality for fundamental research. The exact description of observation in nature is a main objective. Apart from that there is an industrial user group which main objective is to receive quick results around application related tolerances. Although both user groups use the same method their requirements are completely different.

Applying these considerations on simulation of welding distortion another significant argument can be identified: even if processing power raised within the last years it is still a balancing act to apply simulations on big structures. Very fine meshes and high element quality is required within the area of the heat affected zone (HAZ), whereas coarse mesh is required at large structures to reduce the degree of freedom (DOF) which has a critical impact on the required computation time. There are various methods established to face this challenge like local global approach [3], adaptive mesh techniques [4], [5] or simplified methods for estimating welding shrinkage [6].

The present work reflects two different simulation approaches to estimate the distortion of a welded structure. First simulations were carried out using the transient method which allows consideration of almost any physical effect based on a number of different models [7]. A moving heat source model, for instance double ellipsoid heat source [8], is used to create the thermal cycle for each weld. The heat source is modeled based on welding process parameters and is described as a function in space and time. In addition to stability criteria, the maximum permissible time increment is limited by the movement of the heat source by half the length of the molten zone. At each time step the transient temperature field is calculated considering temperature dependent material properties. Finally the mechanical and metallurgical reaction of the structure is calculated by applying a coupling procedure on the thermal results of the transient simulation. The results of transient simulations include stresses, strains and the material properties after welding. Typical applications are detailed investigations on sub assemblies, critical loaded objects and validations. The software used to implement this model is Sysweld® provided by ESI GmbH. Secondly, a mechanical replacement model (shrinkage method) is applied to simulate the welding process based on a non physical approach. The proposed method is

based on the elasto-plastic shrinkage of material close to the weld joints. The overall shrinkage in the area of a joint is applied within one time increment. The whole welding process of an assembly is modeled by applying the shrinkage of each new joint within one single time step. Generally it is possible to apply the shrinkage of all joints within one single time step too. There is no heat source model required and material behaviour is reduced to elastic-plastic properties. The results of simulations based on the shrinkage model include distortions and global stress field. Common applications are preliminary investigations, minimisation of distortion on the basis of different clamping conditions and welding sequences and as well the simulation of large assemblies. The software used to implement this model is Weld Planner® provided also by ESI GmbH.

A representative sample geometry was designed to ensure the desired industrial context. Therefore an exemplary welded structure of a loader crane boom, stiffener plate and console were implemented. The material used for the samples was S355 J2G3 which is a low alloyed steel. Standard material properties provided by the software tools were used.

In order of a consolidated evaluation of the results within this work remarkable distortion at the upper side of the boom is discussed. A comparison of the results from simulation and experiment is made by applying of an intersection plane and the subsequent consideration of the intersection line between the distorted surface and the cutting plane.

Mechanical boundary conditions such as clamping conditions were applied identically for both simulations based on the welding experiment. For the experiment the boom pipe was fixed at the bottom with clamps at the front and rear end. For the simulations all degrees of freedom were locked (rigid boundary condition) within the described area. The area is highlighted in fig.3 for the transient simulation and fig.7 for the simulation using the shrinkage model. Thermal boundary conditions including initial temperature and boundary conditions for the heat source model were considered within the transient simulation only. The input data for these boundary and initial conditions were taken from measurements carried out during the experiments.

### WELDING EXPERIMENT

The welding experiments were carried out on a sample geometry which represents typical components within the manufacture of loader cranes shown below at fig.1. The distortion due to the welding procedure was calculated based on the results of two measurements at designated positions carried out before and after welding procedure. The results of these measurements were given by 3d point coordinates (x, y, z) for each position. Overall 174 measuring points were applied on the top surface of the boom, the plate and the rib.

To ensure clearly recognizable positions for the measuring points a grid was applied mechanically on the top surface of the boom pipe (A), the plate (B) and the rib (C). Additionally, reference points were added at the bottom surface of the boom. These reference points were necessary to detect the point of origin and orientate the coordinate system properly. Additionally, to the sample geometry, fig. 1 shows the welding sequences (J1, J2, J3, J4) and directions. After the plate was joined to the boom the rib was welded.



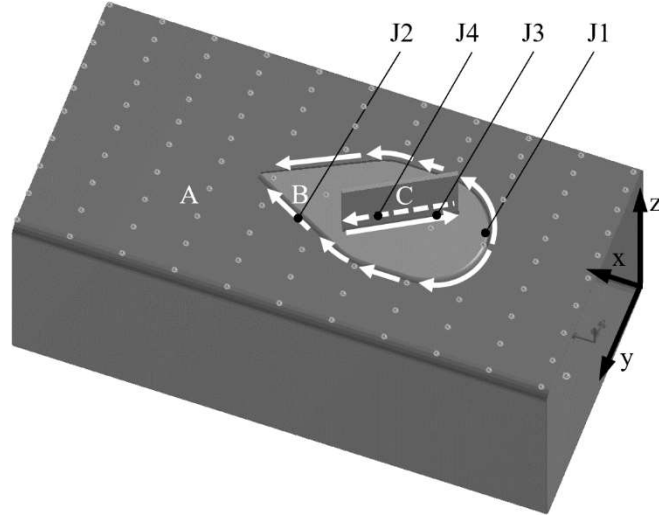


**Fig. 1** Geometry of the sample for the welding experiments. The number of the joints indicates the welding sequence and the white arrows the welding direction.

The distortion of the structure was calculated within an evaluation routine applying several steps to receive continuous surface plots based on the measured point clouds before and after the welding experiment.

First the datasets from the measurement system were organised in a structured way. Based on these clean datasets the transformation at each point was calculated. Therefore, the coordinates of the measuring points before ( $P_1$ ) and after ( $P_2$ ) welding were subtracted. In the formula below  $\vec{p}_i$  represents a vector containing the coordinates in the sequence shown. The first indices specify if the measurement was applied before or after welding and the second one is needed to identify each measuring point.

$$\Delta\vec{P}_{1-2} = \vec{P}_1 - \vec{P}_2 \quad (1)$$

$$\vec{P}_1 = [x_{1,1}, y_{1,1}, z_{1,1}, x_{1,2}, y_{1,2}, z_{1,2}, \dots, x_{1,i}, y_{1,i}, z_{1,i}]^T \quad (2)$$

$$\vec{P}_2 = [x_{2,1}, y_{2,1}, z_{2,1}, x_{2,2}, y_{2,2}, z_{2,2}, \dots, x_{2,i}, y_{2,i}, z_{2,i}]^T \quad (3)$$

Since significant changes were observed especially normal to the upper surface of the crane boom further processing of the data was limited to this direction. Therefore, the minor deviations in the x-y plane were not considered within the evaluation routine. The calculated distortions in z-coordinates were applied at the x-y coordinates of the dataset measured before welding [ $\vec{P}_1$ ].

$$\Delta\vec{P}_{1-2} = [x_{1,1}, y_{1,1}, \Delta z_{1-2}, x_{1,2}, y_{1,2}, \Delta z_{(1-2),i}, \dots, x_{1,i}, y_{1,i}, \Delta z_{(1-2),i}]^T \quad (4)$$

Based on these coordinates a linear interpolation algorithm was applied to obtain continuous transitions each point of the  $\Delta\vec{P}_{1-2}$  dataset. Finally, surface plots were generated

to visualise the changes due to the welding procedure. An example of these plots is shown on the left side in fig. 2. Overall six samples were welded within the experiments for comparison of the dispersion of the occurring distortion.

The figure presents the distortion in z direction which occurred at the top surface of the boom. At both ends of the boom positive distortion was observed whereas the area in the middle of the surface shows distortion in negative direction.

By applying a sectional plane at the middle of the surface along the x-axis an intersection line is defined. This graph represents the maximum distortion of the structure in a clear way and was used to compare the results of welding experiments and simulation.

Although constant welding parameters and boundary conditions were applied for all experiments and the general trend is comparable, the detailed distortion of the samples varied.

In Figure 2 the illustration on the right side shows the characteristic shape of four samples which represent the maximum and minimum distortion observed. Furthermore, the mean shape calculated from all six samples welded within the experiments is plotted.

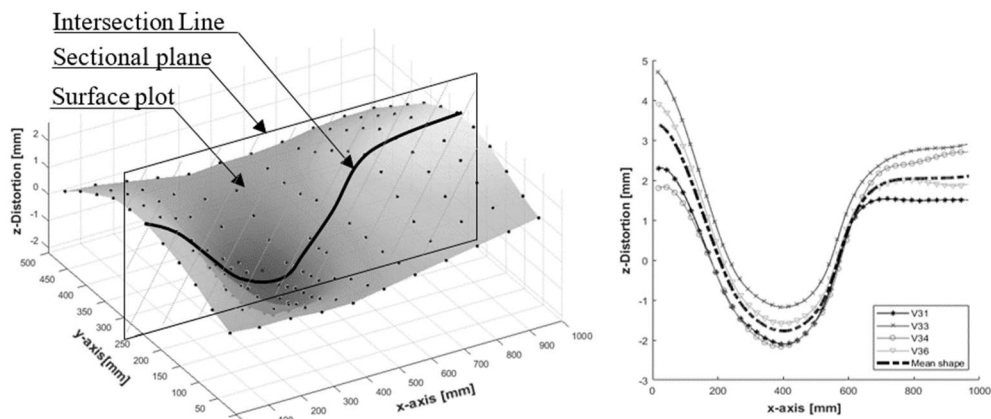


**Fig. 2** Left: Surface plot of the calculated distortion based on the measured data before and after the welding experiment. For further comparison a sectional plane was applied to obtain an intersection line. Right: Intersection lines of four different samples. The dashed line shows the mean shape of all six intersection lines calculated from the measurements of each welding experiment.

### TRANSIENT THERMO-METALLURGICAL SIMULATION

Based on the geometry designed for the sample production, a three-dimensional model of the structure was created using 3d solid elements. Attention was paid to high element density and element quality around the weld seam and the HAZ. Concurrently it has been considered that the number of elements of the overall model should be minimized to reduce the computation time. Therefore, in a designated distance to the HAZ a continuous transition to a coarser mesh structure was applied.

Fig. 3 gives an overview of the created mesh for the transient simulation in *Sysweld*. Overall the model included more than 219000 elements. The first detail A on the left side shows the mesh around the joints J3 and J4. Based on micrographs of this area the seam geometry was modelled. Below this detail the area of joints J1 and J2 is shown in detail B. Based on the clamping situation during the welding experiments rigid boundary conditions were applied to the highlighted elements at position (C).

For modelling the energy input a double elliptic heat source model [8] was applied using the database of *Sysweld*<sup>®</sup> [7]. Input parameters for the heat source comprise initial time and end time, welding velocity, estimated values for the geometry of the heat source, energy input, and efficiency. The welding trajectory was defined by selecting individual node points along the corresponding weld seam. For this purpose, an algorithm implemented in *Sysweld*<sup>®</sup> can be used which defines a continuous line along the element edges based on the definition of start, end and direction.

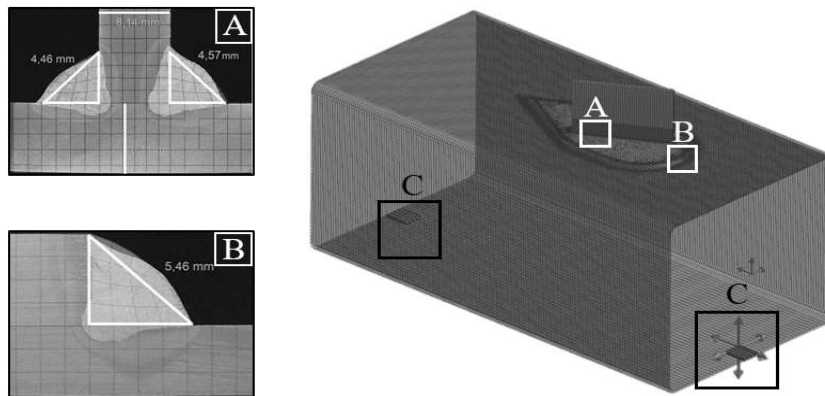


**Fig. 3** Finite element model for the transient simulation in Sysweld<sup>®</sup>. The details show certain areas of the mesh. Detail A: cross section of joints J3 and J4. Detail B cross section of joints J1 and J2. Position C: elements which contain boundary condition (rigid clamping condition).

The applied values for the heat source parameters were estimated from the welding experiments and micrographs of the samples and are represented in the table below

**Table 1** Parameters of the double elliptic heat source applied within the transient simulation

Joint	$t_{init}$	$t_{end}$	Velocity	Energy	Efficiency	Penetration	Width	Length
[ / ]	[s]	[s]	[cm/min]	[kW/cm]	[ / ]	[mm]	[mm]	[mm]
J1	0	95.5						
J2	107	203.0	30.4	10.5		5	9	18
J3	213	246.5			0.85			
J4	254	287.5	35.8	9		4.5	7	15

The same material (S355 J2G3) which was applied for manufacturing the samples for the welding experiments was used for the transient simulation. The material behaviour was modelled by using the material data supplied from *Sysweld*<sup>®</sup>. The material model takes into consideration six different phases of this low alloyed steel. The thermophysical properties (density, heat conductivity, specific heat) of the material are phase-, and temperature dependent. Young's modulus is considered temperature dependant whereas yield strength

and thermal strains are phase-, and temperature dependent. Ten different phase transformation reactions can be considered by applying JMAK- Model [9] and Koistinen Marburger law [10]. The behaviour of the material properties depending on phase and temperature is shown in figure 4.

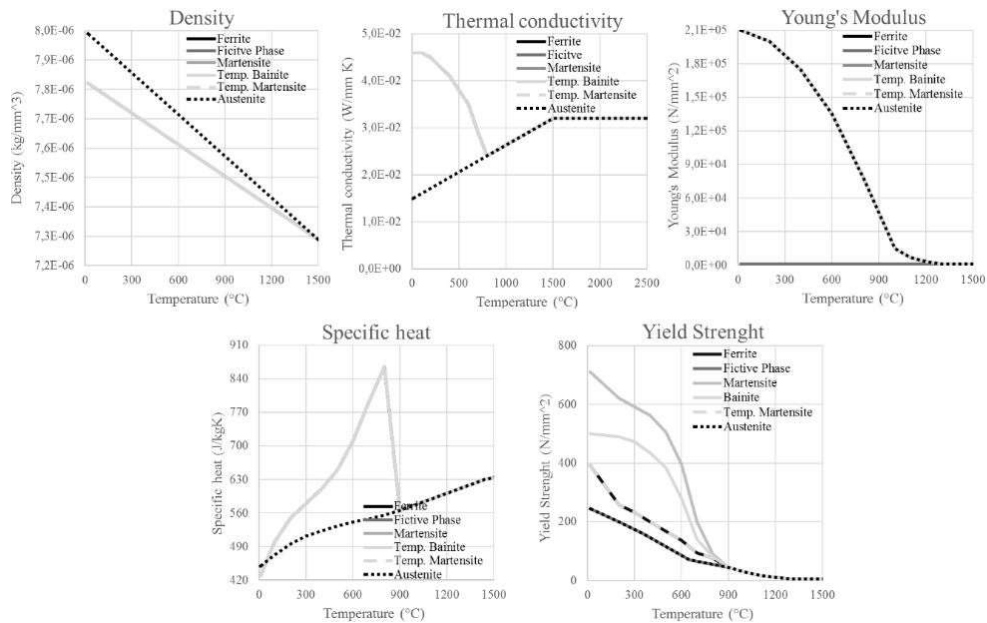


**Fig. 4** Material properties as a function of temperature and metallurgical phase. The fictive phase is used for simulation of the material deposit during welding.

The material deposit is modelled using the “chewing gum method”. An fictive phase is assigned to the weld bead at the start of the simulation. Once the temperature rises in a certain area due to the heat input of the moving heat source the fictive phase transforms to austenite. At this approach the simulation software and the metallurgical model apply activation of elements automatically.

In a first step the results of the transient simulation were verified by comparing the simulated temperature distribution with results from temperature measurements. Figure 5 shows the temperature profile of one measurement compared with the calculated thermal cycle at the same position (starting point of J1 and J2). Several measurements were carried out to compare thermal cycles at different positions.

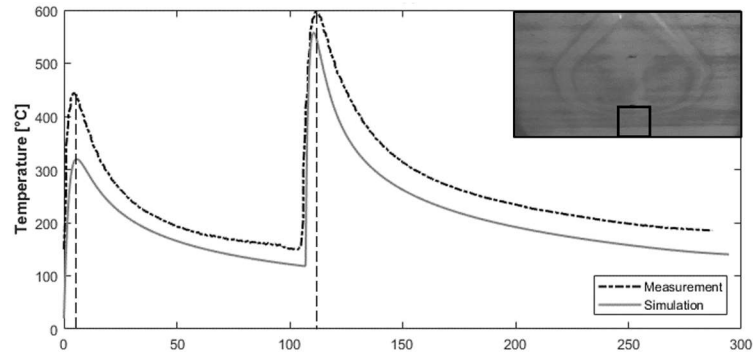


**Fig. 5** Comparison of the simulated and measured temperature profile. The position for this temperature measurement was underneath the starting point of the first two joints (J1, J2) which is marked at the picture on the right top of diagram.

Figure 5 shows that temperature peaks due to the joints J1 and J2. The simulation is almost exactly in time with the measured temperature profile. The maximum values reached by simulation and experiment show a difference of about 100°C at the first joint and almost the same maximum temperature at the second peak. These deviations can be attributed to a slightly different position of the measuring point from the evaluated nodal point. The result of the simulated temperature distribution was considered to be sufficiently accurate for further calculation of the mechanical behaviour. No further optimisation of the heat source model was applied.

After the verification of the temperature distribution the mechanical calculation was applied. Based on the results of each time step of the transient temperature field calculation the mechanical reaction of the structure was simulated.

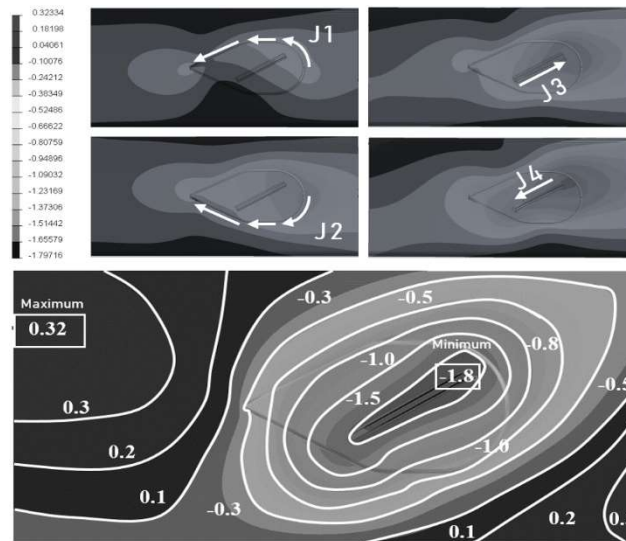


**Fig. 6** Calculated distortion after each weldment based on the transient simulation in *Sysweld*<sup>®</sup>.

Figure 6 shows on the top the developing distortion field step by step after each weldment. The illustration below shows the boom from top view. Areas of positive and negative distortion and the location of the maximum and minimum distortion are marked. Obviously similar effects are simulated like observed at the welding experiment. The open ends of the boom show positive distortion and the area around the joined plate and rib is distorted in the direction of the negative z-axis.

For final comparisons of the results of simulation an experiment the sectional plane introduced earlier was applied to the deformed structure and is discussed in fig. 9.

### SHRINKAGE MODEL

In the simplified method volume shrinkage is applied within an area around the weld seam. This area is defined by a parameter which represents the diameter of a virtual tube which is applied alongside the nodes of the welding trajectory. Details of the method applied in *Weld Planner*<sup>®</sup> are not available. At all elements of the structure within the tube the volume shrinkage is applied. With this approach the thermal dilation is substituted by a resulting strain neglecting the history [11]. Fig. 7 shows the virtual tube on the left bottom side.

For the simulation with the shrinkage model a mesh of the structure was created using 2d shell elements. In contrast to the meshing for the transient simulation no particular requirements were considered at the areas around the HAZ. The mesh was created by using automatic mesh functions and barley manual rework what allows a quick set up of the simulation model. Even the weld seam geometry was replaced by the shape of triangles.

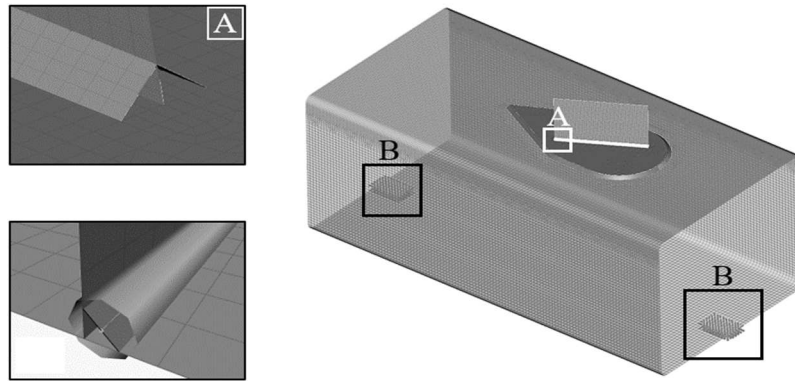
Only a few parameters were required to finish the simulation model setup. First the thickness of all components was entered. In a second step the material for the components and joints was defined. After that the diameter of the virtual tubes for each weld seam was entered. After the definition of the welding sequence the model setup was finished.

Table 2 sums up the required parameters for setting up the model based on the shrinkage method. The parameter “Bead Width” in table 2 represents the diameter of the tube representing the weld seam shrinkage area.

**Table 2** Model parameters for the simulation with the shrinkage method

Joint [ / ]	Bead Width [mm]	Thickness [kW/cm]	Sequence [ / ]	Material [ / ]
J1	11	5.5	1	S355J2G3
J2			2	
J3	9	4.5	3	
J4			4	

Figure 7 gives an overview of the created model for the simulation with the shrinkage method which includes appx. 60000 finite elements. Detail A on the left side of the illustration shows the area of the Joints J3 and J4. Below an example of the tube representing the weld seam is presented.



**Fig. 7** Finite element model for the simulation using the shrinkage model in *Weld Planner*<sup>®</sup>. The details show certain areas of the mesh. Detail A: cross section of joints J3 and J4. Detail B shows elements which contain boundary condition (rigid clamping condition). The last picture on the left side shows an example of the virtual tube which is applied at the joints.

The results of the simulation are presented in figure 8. At the top of the figure the developing distortion field is presented after each joint welded. Similar effects like in the transient simulation and the welding experiments can be observed. The detailed view below shows that the areas of positive and negative distortion are divided again. The negative distortion reaches its peak at the area of the joint plate and areas of positive distortion can be observed at the both ends of the tube.

Comparing the absolute values of the distortion it is remarkable that especially the positive distortion reaches higher values compared to the transient simulation.

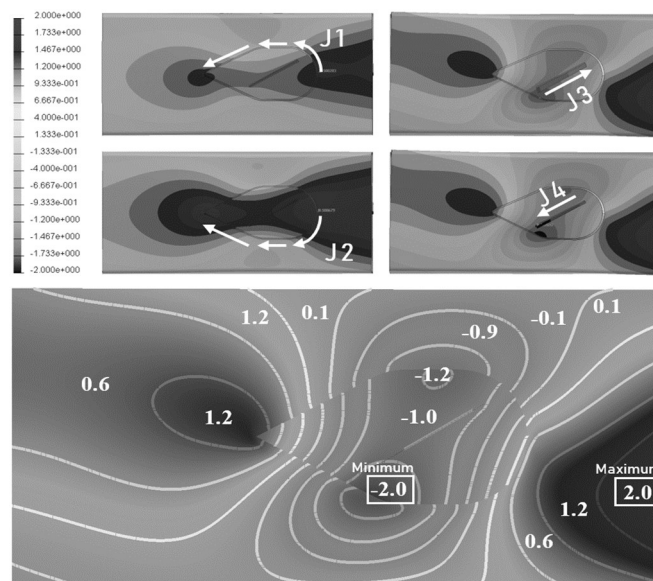


**Fig. 8** Calculated distortion after each weldment based on the simulation in *Weld Planner*<sup>®</sup> using the shrinkage method.

COMPARISON OF THE DISTORTION

Once the simulation with the transient model and the shrinkage method have been accomplished the results were compared with the results of the distortion measurements based on the experiment. Therefore, the intersection line of both simulation results and the results of the experiments were put into contrast. The 2d-representation of the distortion submits a clear way of comparison. The intersection lines of the simulations were created the same way as described before at the welding experiment (fig. 2).

Fig. 9 shows the distortion along the same path of all welding experiments and simulations accomplished. The six light grey curves represent the section lines of the six welded samples. Based on these lines an averaged line was calculated which represents the mean shape of the experiments – the scatter must be judged to be remarkable. *Weld Planner*<sup>®</sup> and *Sysweld*<sup>®</sup> simulation results are represented by the dashed and dash-dotted lines. The figure shows that the results from both simulations underestimate the magnitude of the positive distortion at the front and rear end of the boom, while the area of the joint plate achieves good agreement in all cases. Generally, the transient simulations results show almost no significant positive distortion whereas the results from the shrinkage method, especially at the front end of the boom reaches almost two millimetres.

For a better understanding of the results it is mandatory to mention that simulations in *Weld Planner*<sup>®</sup> have been performed several times due to the short calculation time required and adjustments of the model parameters led to an improvement of the results. This procedure was not performed for the *Sysweld*<sup>®</sup> simulation due to a high number of influencing parameters and the high calculation time. The results shown in fig. 9 represent the first shot of the transient simulation without performing any optimization on the model. To clarify the question of the deviation of the experiments a closer look is required. The absolute values at the front end of the boom differ up to three millimetres. This means that the fluctuation of the measured values reaches the dimension of the distortion itself.

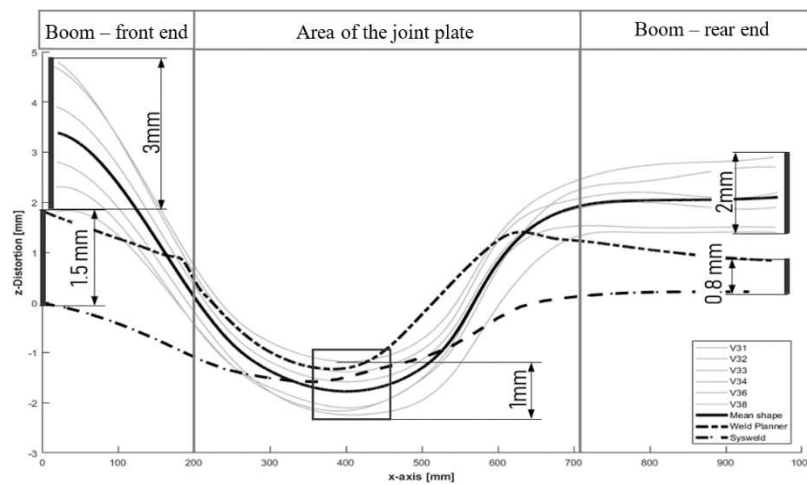


**Fig. 9** Two-dimensional representation of the distortion obtained by simulation and welding experiments.



Due to the fact the welding parameters and boundary conditions have been set constant for all experiments the reason for the difference of the results has to be a different one. A post processing of the measured data before the welding was done gives an evidence that the starting geometry of the samples differed already before the weldment was done. The bending process of the sheet metal to produce the booms for the samples obviously caused variations of the starting conditions for each sample. The influence of residual stresses related to earlier steps within the production process, limits of the tolerances and spring back effects manifests within these variations of the starting conditions.

APPLICABILITY IN PRODUCTION PLANNING

Beside the evaluation of the accuracy of the simulations achieved, the effort for modelling was captured qualitatively. Since the application of welding simulation as a tool for process and production planning in steel processing companies requires quick results and high flexibility the effort for modelling and applying changes on existing models is a basic requirement. Furthermore, the simulation should provide the opportunity to apply optimization calculations to figure out the best welding sequence. This requires short simulation times too. To ensure comparable results the modelling and simulation was implemented on the identical hardware.

Table 3 gives an overview of the effort required for geometry discretization, modelling, calculation time, memory requirements and preparation of the results. The effort for various adaptations or variant comparisons was summarized based on the experience gained in this work.

**Table 3** Effort for modelling and simulation from a qualitative point of view

Criteria	Transient simulation	Shrinkage Method
Discretisation of geometry	Using 3d-solid elements requires high effort for meshing critical areas like the HAZ in a proper way. Fine and coarse meshes must be manually combined	Based on 2d-shell elements the meshing can be applied using automatic meshing tools
Mesh adaption	If using 3d-solid elements changes usually cause additional effort.	If using 2d-shell elements changes can be applied easier.
Interval (time/step)	minimum 0,1935 s (auto adapted)	5 (steps)
DOF	691938	119696
Set up welding parameters	Applying welding wizards reduces the amount of work.	Only a few clicks are required
Calculation time	Generally high calculation times	Generally faster.
Appx. calculation time	250 h	20 min
Data storage requirements	Raw data of computation and result files can exceed significant amounts	Raw data of computation and result files are significant smaller
File size	120 GB	100 MB
Optimization of the welding sequence	Due to high computation times transient Method is not recommended	Optimization tool is already implemented
Post processing	Effort is strongly connected to the respective application	Effort is strongly connected to the respective application

### CONCLUSION

In this paper, two different methods of welding distortion simulation were compared against the results of measured distortion based on welding experiments. A transient simulation was applied using the software *Sysweld*<sup>®</sup> and the shrinkage method was implemented using the software *Weld Planner*<sup>®</sup>. The effort for modelling and simulating for both methods was shown and evaluation criteria were discussed on a qualitative basis.

The described variance of the starting conditions of the samples reflect the daily challenges of applying simulations on industrial use cases beyond ideal surrounding conditions. Each production step is influenced by upstream processes. Related to the welding processes the variance of the supplied metal sheets, sheet metal cutting, bending process can be examples. Not only the deviation of the geometry, but above all the state of stress and hardening of the material due to forming processes matters.

In addition, it can be deduced from the results that a transient simulation needs excellent models. Those are usually not obtained within one step. Rather, a continuous approach to reality is required until the desired degree of accuracy has been achieved.

Obviously, this fact is in direct contradiction with an application of this method for rapid estimation of distortion on large assemblies and its automated optimization. This is precisely the strength of the shrinkage method. It is therefore consistent that in a first step, the results from the simulation with *Weld Planner*<sup>®</sup> are closer to the measured values. The collected knowledge within this work can be summarised by following list:

- Effort for modelling of simulation is very different. Transient simulation requires excellent model quality to receive good results.
- Both methods basically enable the user to estimate welding distortion within the experimental scatter of results. Obviously different application areas are addressed by *Sysweld*<sup>®</sup> and *Weld Planner*<sup>®</sup>.
- Accuracy of both simulations is similar at the presented stage. Further improvement of the transient model probably enables simulations with higher accuracy but is not practical within an industrial application as a fast estimation tool.

In the context of using welding simulation software as a tool for production planning, the deviation of the geometry of the sample, of the ideal CAD geometry, which has been obtained, must be considered. There is a chance for improving the results of any simulation, regardless of the method chosen. Especially in the application of simulations in production planning, this problem needs to be solved. Manufacturers of simulation software are already moving in that direction and offering tools for the complete mapping of the production chain, from the clamping of the components to the forming and different joining techniques.

### REFERENCES

- [1] X. CHEN, Z. YANG and F. BRUST: "Modeling distortion and residual stress during welding: practical applications," *Woodhead Publishing Series in Welding and Other Joining Technologies*, pp. 225-263, 2055.
- [2] P. DONG, Z. CAO, J. HONG, J. ZHANG, F. BRUST, W. BELL and E. J. McDONALD: „Recent Progress In Analysis Of Residual Welding Stresses: Modeling of Weld Residual Stresses and Distortions: Computational Procedures and Applications,“ WRC 455 - Part 1, p. 38, 2000.
- [3] B. SOULOUMIAC, F. BOITOUT and J.-M. BERGHEAU: "A new local global approach for the modelling of welded steel component distortions," *Mathematical Modelling of Weld Phenomena 6*, January 2002.
- [4] Q. SHI, A. LU , H. ZHAO and A. WU: "Development and application of the adaptive mesh technique in the three-dimensional numerical simulation of the welding process," *Journal of Materials Processing Technology 121*, pp. 167-172, 2002.
- [5] H. RUNNEMALM and S. HYUN: "Three-dimensional welding analysis using an adaptive mesh scheme," *Computer methods in applied mechanics and engineering 189*, pp. 515-523, 2000.
- [6] J. LEE, H. SEO and H. CHUNG: "Efficient welding distortion analysis method for large welded structures," *Journal of Materials Processing Tech. 256*, pp. 36-50.
- [7] ESI Group©, Technical description of capabilities, ESI Group©, 2016.
- [8] J. GOLDAK, A. CHAKRAVARTI and M. BIBBY: "A Double Ellipsoid Finite Element Model for Welding Heat Sources," *Metallurgical Transactions*, vol. Volume 15 B, pp. 299-305, Juni 1984.
- [9] M. AVRAMI: "Kinetics of Phase Change. I General Theory," *The Journal of Chemical Physics*, no. 7, pp. 1103-1112, December 1939.
- [10] D. KOISTINEN and R. MARBURGER, "A general equation prescribing the extent of the austenite-martensite transformation in pure iron-carbon alloys and plain carbon steels," *Acta Metallurgica*, pp. 59-60, January 1959.
- [11] G. ESI: "SYSWELD® 2008 - Welding Simulation - Users Guide," ESI Group, 2007.

# SIMULATION OF WELDING RESIDUAL STRESSES – FROM THEORY TO PRACTICE

S. GKATZOGIANNIS\*, P. KNOEDEL\* and T. UMMENHOFER\*

\*Karlsruhe Institute of Technology, KIT Steel & Lightweight Structures - Research Center for Steel, Timber & Masonry, Otto-Ammann-Platz 1, 76131, Karlsruhe, Germany, stefanos.gkatzogiannis@kit.edu

DOI 10.3217/978-3-85125-615-4-21

## ABSTRACT

The present study reviews previous and new simulations of welding residual stresses with the finite element method. The influence of modelling mechanical boundary conditions, erroneous prediction of the weld heat source coefficient, the influence of microstructural changes in aluminium welds and the consideration of strain-rate sensitivity of steel are investigated. The results are analysed so that sound conclusions regarding the investigated factors, acting as recommendations for the practitioner, can be presented.

Keywords: Weld simulation, strain-rate dependency, boundary conditions, heat input, aluminum welding

---

### List of Notations

---

$f_r$	heat fraction deposited in the rear quadrant of Goldak's heat source (J)
$f_f$	heat fraction deposited in the front quadrant of Goldak's heat source (J)
$Q$	thermal power or energy input rate (Watt or J/s)
$C$	characteristic radius of flux distribution (m)
$v$	welding source travel (m/s)
$t$	time (s)
$\tau$	lag factor ("phase shift") needed to define the position of weld heat source source at time $t = 0$
$V$	voltage (V)
$I$	current of the weld metal arc (A)
$\eta$	weld metal arc efficiency (-)
$\rho$	density (Kg/m <sup>3</sup> )
$c$	specific heat (J/(kg K))
$T$	temperature (K)
$K_{xx}, K_{yy}, K_{zz}$	thermal conductivity in the element's x, y, and z directions (W/(m K))
$\dot{Q}$	heat generation rate per unit volume (W/m <sup>3</sup> )
$\alpha^{se}$	temperature dependent coefficient of thermal expansion
$T_{ref}$	reference temperature for thermal strains (°C)
$f_s(u)$	resisting force as a function of deformation (N)
$p(t)$	external transient loading (N)

## Mathematical Modelling of Weld Phenomena 12

$E$	Young's modulus (N/mm <sup>2</sup> )
$\nu$	Poisson's ratio (-)
$\sigma_e$	the von Mises effective stress (N/mm <sup>2</sup> )
$\dot{\epsilon}_{pl}$	equivalent plastic strain rate (-)
$\sigma$	yield stress at the investigated strain rate (N/mm <sup>2</sup> )
$\sigma_0$	static yield stress (N/mm <sup>2</sup> )
$\gamma$ and $m$	coefficients with no direct physical meaning characterizing the strain rate hardening behavior

---

### INTRODUCTION

The mathematical background for modelling welding phenomena exists since the 80's [1]. Simple FE models for academic purpose have been developed ever since [2]. Nevertheless, the increase of computational power during the last 2 decades allowed the creation of more sophisticated three-dimensional models for practical applications as well ([3], [4], [5], [6] etc.). This rapid increase in applications regarding weld simulation did not allow detailed documentation of the applied approaches. Despite the thorough existing theoretical background, the lack of established practical methods is profound.

Main interest of industrial applications lies in the calculation of welding residual stresses (WRS) and distortions with high preciseness but reduced computational effort [8]. For this purpose, an engineering approach, which is applicable to any commercial general purpose FE Software, takes into consideration microstructural changes and can be reproduced by a non-metallurgist for modelling various alloys requiring only basic knowledge of material science, was proposed in previous work by the authors of the present paper [3]. Use of this method, which was validated for single-pass welds, has enabled the investigation of factors, which influence significantly the simulated welding residual stresses, in all three fields of weld simulation: the thermal, the microstructural and the mechanical field.

Previous work of the authors has highlighted the significant practical aspects and the predominant factors of weld simulation that influence the calculated welding residual stresses. A review of this previous work, regarding the influence of mechanical boundary conditions [9], material models [10], [11], heat input parameters [12], along with new series of analyses regarding the influence of microstructural transformation in the case of aluminium welding, are presented in the current paper. Moreover, the background for an extension of the previously presented model [3] to multi-pass welds is outlined. The conclusions can work as a guide for the practitioner, in order to exclude effects during modelling and decrease in extension the computational effort, without reducing the required accuracy from an engineering point of view.

THEORETICAL BACKGROUND

MODELLING OF WELDING RESIDUAL STRESSES AND DISTORTION

Welding is a multiphysics problem, but simulation of WRS requires modelling only of some aspects of the welding process. The thermal behavior and possible microstructural changes are investigated along with the mechanical behavior of a component when WRS are under the scope. These three fields, which are presented in Fig. 1 are interacting bidirectionally with each other. Practical models, predicting the WRS with satisfying preciseness by only simulating the interaction of thermal on microstructural and mechanical behavior and of microstructural field on the mechanical behavior have been suggested [8] and developed [3]. The considered interactions are presented in Fig. 1. Ignoring the reverse influence of microstructural and mechanical behavior enables solution of the problem with a sequential unidirectionally coupled thermal–mechanical analysis [3].

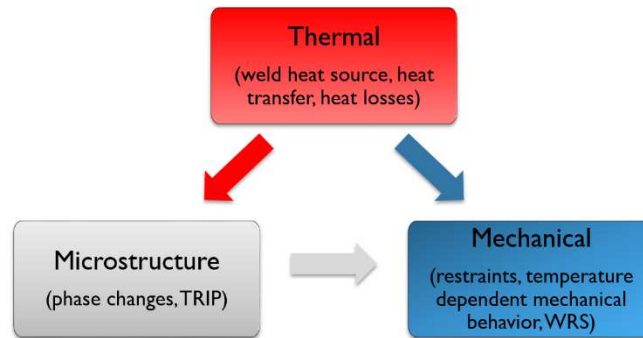


**Fig. 1** Investigated fields and respective interactions in an engineering approach for arc welding simulation, TRIP stands for transformed induced plasticity [3]

*Thermal modelling*

Thermal modelling tackles the problem of heat transfer. Simulation of the heat transfer inside the investigated component, the weld heat source and heat losses to the surrounding environment (boundary conditions) is required in this field. According to Goldak’s double ellipsoidal model, which is the state-of-the-art approach for modelling the weld heat source [13], the power density distribution inside front and rear quadrant are described by the following two equations respectively (Eqn. (1) and (2)):

$$q(x, y, z, t) = \frac{6\sqrt{3}f_f Q}{abc\pi\sqrt{\pi}} e^{-3x^2/a^2} e^{-3y^2/b^2} e^{-3[z+v(\tau-t)]^2/c^2} \quad (1)$$

and

$$q(x, y, z, t) = \frac{6\sqrt{3}f_r Q}{abc\pi\sqrt{\pi}} e^{-3x^2/a^2} e^{-3y^2/b^2} e^{-3[z+v(\tau-t)]^2/c^2}. \quad (2)$$

The effective energy input rate (thermal power, equal to the electric power of the arc minus the losses) is predicted according to the following Eqn. (3) [3]

$$Q = \eta VI. \quad (3)$$

Heat input  $h$  is calculated by dividing Eqn. (3) with the welding speed. Proposed values for the  $\eta$  coefficient for various weld types are proposed in [14]. Nevertheless, different values usually in a range of  $\pm 10\%$  for same welding types are found elsewhere (see [2] etc.). Combining the first thermodynamics law (conservation of energy) with Fourier's law for heat conduction and neglecting the fluid flow in the weld pool, the transient heat transfer Eqn. (4) which governs the heat transfer inside the component is calculated [15]:

$$\rho c \frac{\partial T}{\partial t} = \dot{Q}_G + \frac{\partial}{\partial x} \left( K_x \frac{\partial T}{\partial x} \right) + \frac{\partial}{\partial y} \left( K_y \frac{\partial T}{\partial y} \right) + \frac{\partial}{\partial z} \left( K_z \frac{\partial T}{\partial z} \right). \quad (4)$$

Heat losses are modelled according to Newton's law of cooling (Eqn. (5))

$$\frac{q}{A} = h_f (T_s - T_b). \quad (5)$$

A transient thermal analysis is carried out, whereby the temperature history of the nodes of the FE model are saved at each solution step.

#### *Microstructural modelling*

Various models have been proposed in the past, in order to predict the metallurgical transformations during a weld thermal cycle ([16], [17] etc.). A straightforward engineering approach, which was proposed by the authors of the present study [3], provided results with sufficient preciseness. The method is applicable for the simulation of various materials [9], [12], [10]. Main feature of the approach lies on the assignment of material models to the finite elements inside the fusion zone (FZ) and the heat-affected zone (HAZ) during cooling down based on predominant parameters of the thermal cycle, in order to simulate the modified mechanical behavior of the transformed microstructure. The considered parameters are the the maximum reached temperature inside a thermal cycle  $T_{\max}$ , the time needed for the temperature to drop from  $800\text{ }^\circ\text{C}$  to  $500\text{ }^\circ\text{C}$  during cooling down inside a thermal cycle  $t_{85}$ , and the austenitization time  $t_a$ , during which the temperature is above the austenitization temperature (Ac1) inside a thermal cycle.

In the case of single-pass butt-welds the austenitization time is similar in all areas around the weld [2], [3]. Austenitization time influences the proportion of the parent material, which is transformed to austenite during warm up and is subsequent to metallurgical transformations during cooling down. This proportion is as well influenced by the

maximum achieved temperature. The coupled influence of these two parameters on the proportion of the austenitized temperature, can be expressed only by the  $T_{max}$ , if the retardation effect is taken into consideration. When high heating rates and thus, short austenitization times, are present the temperature at which full austenitization is achieved ( $Ac_3$ ) is higher than the respective theoretically predicted value (for “static” slow warm up). This effect was firstly mentioned by Leblond [16] and was integrated to the weld modelling approach by the authors of the present paper [3] based on measurements of theoretical and real  $Ac_3$  found in [18]. During cooling down, the selection of material models for the austenitized proportion in each area of the weld, is based on predictions of the transformed microstructure according to continuous cooling transformation (CCT) diagram or assessment of microstructure through measurements. The process of selecting the respective material models is presented in Fig. 2.

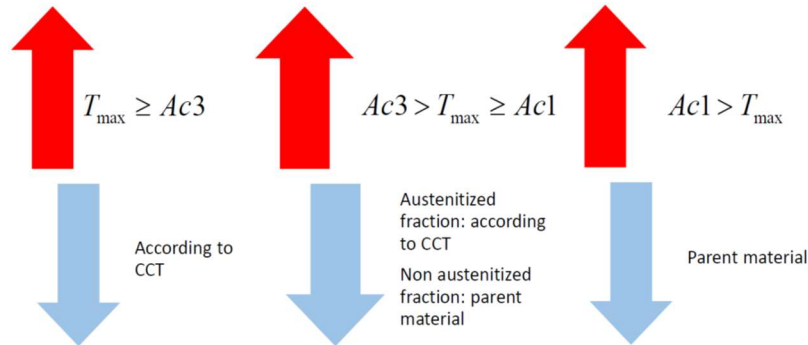


Fig. 2 Assumed microstructural transformations depending on  $T_{max}$  values [3]

The importance or negligibility of microstructural changes during modelling of ferritic or austenitic steels respectively has been confirmed in the past [3], [12]. Softening in the HAZ of aluminum alloys was as well successfully modelled in a previous study of the authors [10]. Three new models were assigned during cooling down, one of fully recrystallized material in the FZ and two of partially recrystallized microstructure in the HAZ (different levels of recrystallization). Nevertheless, a quantification of this influence on WRS is not known to the authors of the present study. The same problem arises as well when high strength steels are regarded. Liu et al. [19] and Lee and Chang [20] simulated weldments of ASTM A514 (yield strength of 717 MPa) with phase changes and a high strength carbon steel with yield strength of 790 MPa by neglecting them respectively.

However, the present approach has not yet been extended to the simulation of multi-pass welds. Material that lies within the boundaries of a single pass is being influenced from the subsequent weld passes. Therefore, a single consideration of  $T_{max}$  and  $t_{85}$  during the thermal cycle of the preceding weld pass is not sufficient for modelling precisely the material behavior after completion of the consecutive pass. Previous studies regarding simulation of multi-pass welds, which are known to the authors of the present paper, have been carried out either for cases, whereby phase transformations were negligible ([21], [22], [23], [24], [25]) or the validation of the applied models for multi-pass welding was carried out based on CCT diagrams ([26], [6]). In the latter case, special consideration has to be made, in order to properly model the influence of multi-pass welds, as CCT diagrams describe only the influence of a single thermal cycle on the parent material.



*Modelling of mechanical behaviour*

During modelling of the mechanical field, the nodal temperature history from the prior transient thermal analysis is applied as body force nodal loads (thermal strains  $\varepsilon_{th}$ ), which are calculated based on the temperature dependent coefficient of thermal expansion  $\alpha^{se}$  [15]

$$\varepsilon^{th} = \alpha^{se}(T) \cdot (T - T_{ref}) . \quad (6)$$

Solution takes place in a quasi-static structural analysis, whereby temperature dependent material parameters and the restraints applied to the real welded component are modelled [3]. Quasi-static structural analysis is governed by the following equation:

$$f_s(u) - p(t) = 0 . \quad (7)$$

Usually, components are clamped down during welding. Fixing of the respective nodes in the FE models is a common approach of modelling but deviates from physical restraining reality. An alternative approach applied elsewhere [9] is the use of linear spring elements, restraining the respective nodes (see Fig. 4). The free edge of the spring is then fixed parallel to its length direction. Therewith, only very small displacements are allowed, which coincides with the situation in real “clamping”.

In most cases, mechanical solution is based on classical theory of strain-rate independent plasticity [27]. Total mechanical strain is decomposed to elastic and plastic parts (Eqn. (8)).

$$\varepsilon_{tot}^{mech} = \varepsilon_{el} + \varepsilon_{pl} . \quad (8)$$

The stress  $\sigma$  is proportional to the elastic strain  $\varepsilon_{el}$  according to Hooke’s law for linear isotropic material behaviour, which is presented in terms of Young’s modulus and Poisson’s ratio and in index notation in the following equation (Eqn. (9)),

$$\varepsilon_{ij} = \frac{1}{E} (\sigma_{ij} - \nu(\sigma_{kk} \delta_{ij} - \sigma_{ij})) , \quad (9)$$

where  $\delta_{ij}$  is the Kronecker delta. Von Mises yield criterion (Eqn. (10))

$$f(\sigma, \sigma_y) = \sigma_e - \sigma_y = 0 , \quad (10)$$

is widely applied for metallic materials, where  $\sigma_e$  is the von Misses effective stress

$$\sigma_e = \sqrt{\frac{3}{2} \left( \sigma : s - \frac{1}{3} tr(\sigma)^2 \right)} . \quad (11)$$

Isotropic hardening is usually applied, during welding simulations, as theoretically, heating the material up to near melting temperature erases previous hardening history and the material deforms as virgin [23], [28]. Nevertheless, kinematic hardening provided better results elsewhere [9], [12]. In some cases, even mixed hardening models are proposed [28].

Lindgren [8] proposed that during weld simulation, when very high accuracy is required, strain-rate dependent plasticity should be considered, without providing though any information regarding the order of magnitude of the influence on calculated WRS. Previous analyses of the authors of the present paper have showed that in the heat affected zone (HAZ) and the fusion zone (FZ) of a 3-pass butt-weld, strain rates of up to  $0.122 \text{ s}^{-1}$  are present [11]. Although this value lies clearly lower than the classical dynamic cases such as modelling of ballistic tests or car crash simulation ( $100 \text{ s}^{-1}$ ), still clearly deviates from the static case ( $\dot{\epsilon} \rightarrow 0$ ). Several models have been proposed in the past for modelling of the strain-rate dependent behavior of steel. The following model proposed by Perzyna in 1966 [29] is appropriate for implicit FE simulations like in the present case (Eqn. 12)

$$\dot{\epsilon}_{pl} = \gamma \left( \frac{\sigma}{\sigma_0} - 1 \right)^{1/m} . \quad (12)$$

### REVIEWING THE INLUEFNCE OF INPUT PARAMETERS

Results from previous and new FE analyses, which were all carried out according to the above-described theoretical background, are presented in the current study in order to review specific aspects of weld simulation. FE commercial software ANSYS [15] was applied in all cases. Solid 8 node elements “solid 90” and “solid 180” were applied for the transient thermal and the static structural analyses respectively in all cases. Mesh element dimensions were 0.4 mm x 0.4 mm x 5 mm (width x height x length) in the FZ and the HAZ in all cases. The following aspects were investigated:

#### A: MODELLING OF MECHANICAL BOUNDARY CONDITIONS (BC)

A single-pass weld component of Swedish steel HT36 (equivalent to S355) with dimensions of 2000 mm x 1000 mm x 15 mm was simulated in [9] (component A in the present study). Geometry of the weld section is presented in Fig. 3. The component was welded with submerged-arc welding (three electrodes welding consecutively), an electric power of 98 kW and a welding speed of 25 mm/s (150 cm/min; 3.92 kJ/mm heat input). Applied material parameters are given in [3]. Clampers were modelled either by fixing the respective nodes in all directions or by applying linear spring elements with stiffness of  $10^6 \text{ N/mm}$  to all nodes in the clamped area in the longitudinal and transverse direction and fixing their vertical displacement. The results are compared with measurements for an identical component found elsewhere [2].

## Mathematical Modelling of Weld Phenomena 12

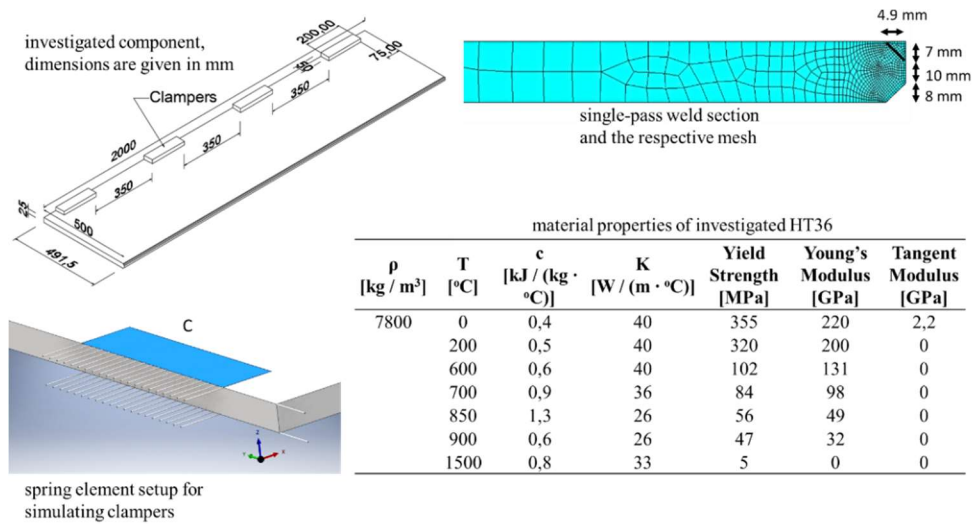


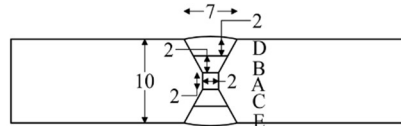
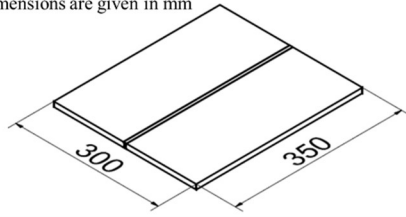
**Fig. 3** Investigated component A

### B: THERMAL INPUT AND WELDING SEQUENCE OF MULTI-PASS WELDS

Influence on the WRS, which can be caused by possible erroneous modelling of thermal heat input is investigated in [12]. The 5-pass X-grooved butt-weld with dimensions 300 mm x 300 mm x 10 mm by AISI 316L, which is presented in Fig. 4, was simulated (component B in the present study) and different cases of differentiating heat input were modelled. The component was initially considered to be welded with an electric power of 4.3 kW, a welding speed of 5 mm/s (30 cm/min; 0.86 kJ/mm heat input) and the welding sequence A-B-C-D-E. Applied material parameters are given in [13]. Heat input was changed by either increasing the welding speed, or reducing the energy input rate (see respective Table of Fig. 4). The results are reviewed from a different scope in the present study in order to estimate the possible error of calculated WRS under the assumption that an under- or overestimation of  $\pm 10\%$  of the weld heat source's efficiency has taken place.

# Mathematical Modelling of Weld Phenomena 12

investigated component,  
dimensions are given in mm



5-pass weld section and original welding sequence, dimensions are given in mm

material properties of AISI 316L

T [°C]	K [W / (m K)]	C [kJ / (kg K)]	$\rho$ [kg / m <sup>3</sup> ] x 10 <sup>6</sup> [-]	$\alpha$	Young's Modulus [GPa]	$\nu$ [-]
20	13,3	0,47	7966	15,2	195	0,267
400	19,4	0,55	7814	17,4	172	0,322
1000	27,5	0,676	7535	19,3	100	0,229
1420	31,9	0,765	7320	20,7	10	0,223
1460	320	0,765	7320	20,7	2	0,223
3000	320	0,765	7320	20,7	2	0,223

reviewed investigated cases found in [9]

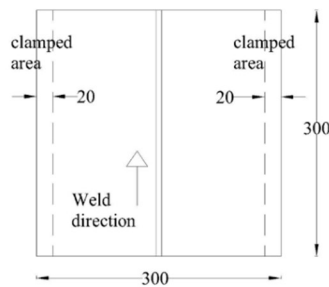
Model	Investigated variable
H1	initial welding parameters
V1	welding speed – 25 % reduced
V2	welding speed – 50 % reduced
Q1	energy input rate – 25 % increased
Q2	energy input rate – 50 % increased

Fig. 4 Investigated component B

## C: INFLUENCE OF MICROSTRUCTURAL CHANGES IN ALUMINIUM WELDING

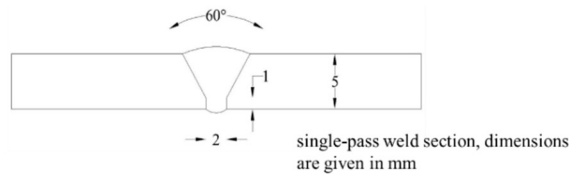
Previous numerical studies regarding welding of Aluminum alloy initially presented at [10], were repeated in the present study and in [30], by neglecting this time the metallurgical transformations, in order to evaluate qualitatively and quantitatively the influence of recrystallization in the HAZ of aluminum alloys on the simulated WRS. The single-pass V grooved component of EN AW-6060 with dimensions 300 mm x 300 mm x 5 mm, welded with an electric power of 3.1 kW and a welding speed of 10 mm/s (60 cm/min; 0.31 kJ/mm heat input), which is presented in Fig. 5 is modelled.

investigated component,  
dimensions are given in mm



material properties of EN AW 6060

Temperature [°C]	c [J/(kg K)]	K [W/(m K)]	Yield Strength [MPa]	Yield Strength (HAZ) [Mpa]
20	911	192	140	60
100	944	197	127	54,6
400	1067	218	9,7	4,3
655	1172	236	1	1
1000	1313	260		
1590	1555	301		
5000	2953	540		



single-pass weld section, dimensions are given in mm

Fig. 5 Investigated component C

## Mathematical Modelling of Weld Phenomena 12

### D: STRAIN-RATE DEPENDENCY OF WELDING RESIDUAL STRESSES

Numerical studies regarding single-pass butt-welding of a S355 component (component D) with dimensions 500 x 200 x 5, whose section and respective FE model is shown in Fig. 6, were repeated in [11], by taking into consideration this time the strain-rate dependency of the investigated material. Goal was the qualitative and quantitative evaluation the influence of strain-rate dependency on the simulated WRS. A single-pass V grooved component welded with an electric power of 7.934 kW and a welding speed of 6.7 mm/s (40 cm/min; 1.18 kJ/mm heat input) is modelled. Three different cases were considered, one strain-rate independent (BC) and two strain-rate dependent cases VA\_TM1 and VA\_TM2, whereby the strain-rate dependent material behavior was calibrated based on material data found in [31] and [32], [33] and [34] respectively.

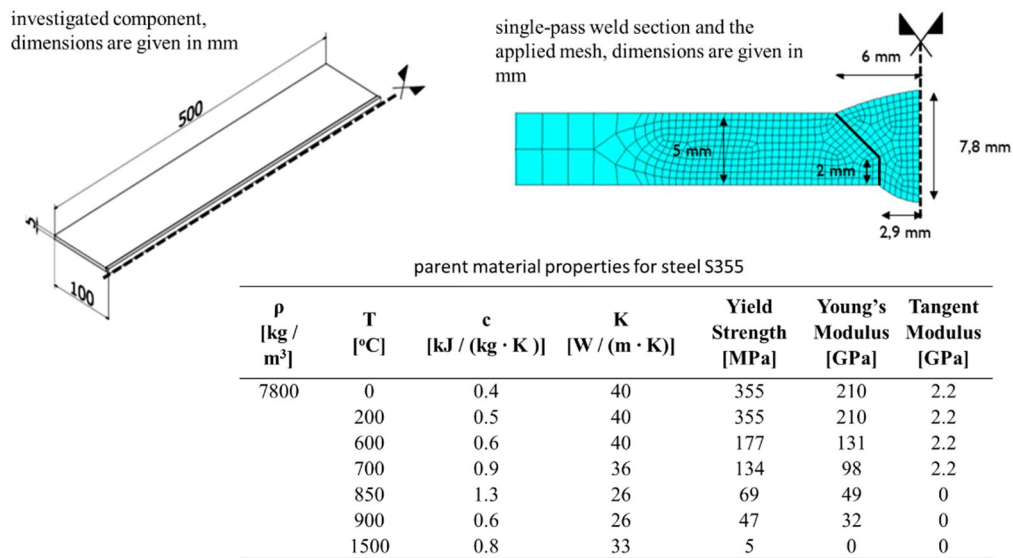


Fig. 6 Weld section and the applied FE mesh for component D

### A PROPOSAL FOR THE EXTENSION OF THE PRESENT MODEL TO MULTI-PASS WELDING AND HIGH STRENGTH STEELS

The present approach, as mentioned-above, is based on the use of CCT diagrams in order to predict the transformed microstructure after cooling-down of a single-pass butt-weld [3]. CCT diagrams have already been used for calibration of algorithms, which were applied for the simulation of multi-pass welds ([26], [6]). Nevertheless, extra aspects have to be considered so that the effect of consecutive passes to the microstructure of preceding passes can be caught by such an approach, as the CCT diagrams describe a single thermal cycle. In both of these cases there was a non negligible deviation between measured and simulated WRS, especially in the longitudinal direction (almost 200 MPa for [6], even higher for [26]). Moreover, in the case of high strength steels, CCT diagrams are usually not available

in literature although the research interest on these materials is increasing in the last years (see [35]).

With the present approach, in the case, whereby a CCT diagram is available, it can be assumed that succeeding weld passes carry on the austenitization of the boundary areas of previous passes, if there was no full austenitization, or that there is a reaustenitization of the previously fully-austenitized materials. In both cases it can be assumed as well that the investigated material's cooling down behaviour still can be described by the CCT diagram of the parent material despite the thermal treatment of the preceding passes.

An alternative approach would be the use of hardness measurements on the macro sections of welded components. This measurements could be applied either as a validation of the modelling approach based on the CCT diagrams validating the above-mentioned assignments or as direct input for the material behaviour of various areas of the weld section. The relation of hardness and yield strength of steel has been proven in several cases in the past and various equations have been proposed such as in [36] and [37]. Moreover, the hardness of the individual steel phases at room temperature as a function of the chemical composition can be analytically calculated [38]. Knowing the proportion of the metallurgical phases and the yield strength and hardness, it could be possible to calculate the proportion of phases at each area of the macro section based on the hardness measurements.

### RESULTS AND DISCUSSION

The calculated longitudinal WRS for the HT36 component A are presented in Fig. 6. "Meas." stands for measured WRS found in [2], while "Fixed" and "Springs" are referring to the respective applied modelling approach of BC. In both cases, tensile longitudinal stresses, higher than the nominal yield limit of the material at room temperature are met in the FZ and HAZ and compressive stresses in the areas away from the weld. In the case of modelling with spring elements, tensile stresses of even up to 700 MPa are met (yield strength in the weld area is higher than the nominal 355 MPa due to the phase changes taken place – increase of bainitic and martensitic phases), while for the fixed case the maximum tensile stress is not higher than 450 MPa. Although both approaches produce similar results qualitatively, the agreement of the spring model with the measurements inside the weld section is clearly better. Similar improvement due to use of spring elements was observed as well in the case of calculated transverse WRS [9]. Nevertheless, it seems that initial expectations that the fixed model, being stiffer, would produce higher WRS are not met. However, significant bending of the plate takes place and the interpretation of the results based on the simplified theoretical expectations is not valid anymore, as the profile stresses of Fig. 6 are measured on top surface of the plate. A more complex interpretation of the results taking into consideration the 3D effects should be made.

The calculated longitudinal WRS for the AISI 316L component B are presented in Fig. 7. Similar profiles of longitudinal WRS are calculated in all investigated cases (see Table 1). Tensile and compressive WRS are met near and away from the weld respectively. The increase of the heat input, either by increase of thermal power or reduction of welding speed, shifts down the calculated profile of WRS. Nevertheless, the largest deviation from the initial profile (H1) is met in the case of reduced welding speed down to 50 % (case V2),

which equals to an increase of heat input up to 100%. A difference of up to 150 MPa or 28 % between the peak tensile stresses of those two cases is observed. Similar but not so significant differentiation of the transverse WRS profiles was observed as well [13].

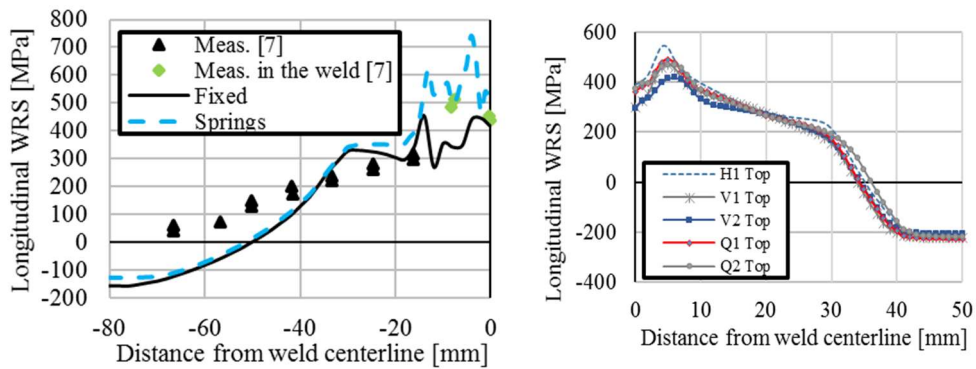


**Fig. 7** Longitudinal WRS – left: Component A (HT36) – right: Component B (316L), resulting WRS on the top of the component, for the investigated cases presented in Table 1

The calculated WRS for the EN AW 6060 component C are presented in Fig. 5 for the cases of taking into consideration and neglecting the recrystallization in the HAZ. In the case of the longitudinal WRS the calculated profile differs significantly, both qualitatively and quantitatively, near the weld. Neglecting the microstructural changes, leads to a lower calculated peak stress and a shift of this peak stress from the boundaries between HAZ and parent material in the middle of the component. The second peak stress met at the left part of the WRS profile, lies on the boundaries of the clamped area of the component. Stress increase is due to fixing of the respective nodes. In the case of the transverse WRS, neglecting recrystallization causes a shift up of the calculated profile of up to 100 MPa.

The calculated longitudinal and transverse WRS for the strain-rate independent and dependent cases are presented in Fig. 9 and Fig. 10 respectively. The rate independent investigated case BC exhibits very good agreement with the measured WRS. A significant deviation is observed only inside the weld section, a region where the robustness of measured WRS is questionable, due to technical reasons. The profiles from both rate dependent investigated cases are almost identical with each other but deviate significantly from the BC case, i.e. the rate-independent model. Regarding the profiles of the longitudinal WRS, deviations from 50 MPa up to 100 MPa between the strain-independent and the rate-dependent cases are observed at the region outside the weld section. Inside the weld section, the difference between the rate dependent and independent cases is almost negligible. Nevertheless, the rate independent model seems to exhibit slightly better agreement with the measured WRS, which in the region away from the boundaries of the weld lie between the curves of the calculated WRS from the rate independent and dependent cases. In the case of the transverse WRS, a significant difference between rate independent and dependent case was observed overall, with the largest deviation to be met at the weld toe, where a difference of 140 MPa is met. The rate independent model BC exhibited in this case an overall clearly better agreement with the measured WRS than the rate-dependent

models. Equilibrium seems not to be achieved, but this is acceptable as the presented WRS are calculated and measured on the top of the plate.

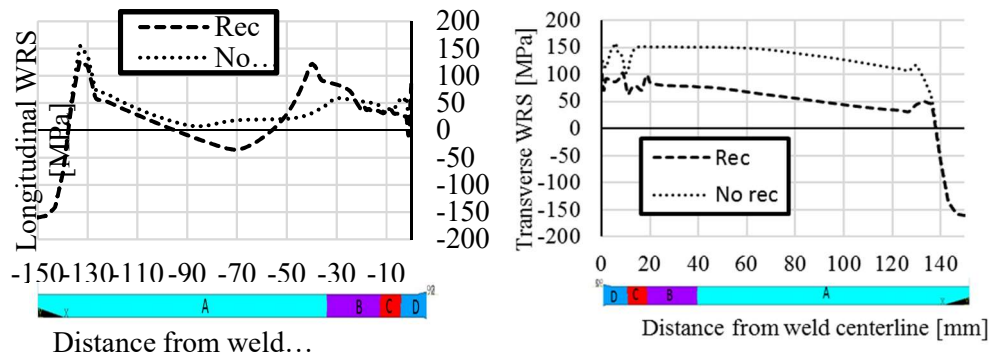


**Fig. 8** WRS of the alluminum component C with and without modelling of recrystilisation in the HAZ, collored areas of the component show modelling of the microstructural changes, A: parent material, B: HAZ 50 % recrystalized, C: HAZ 100 % recrystalized, D: FZ.

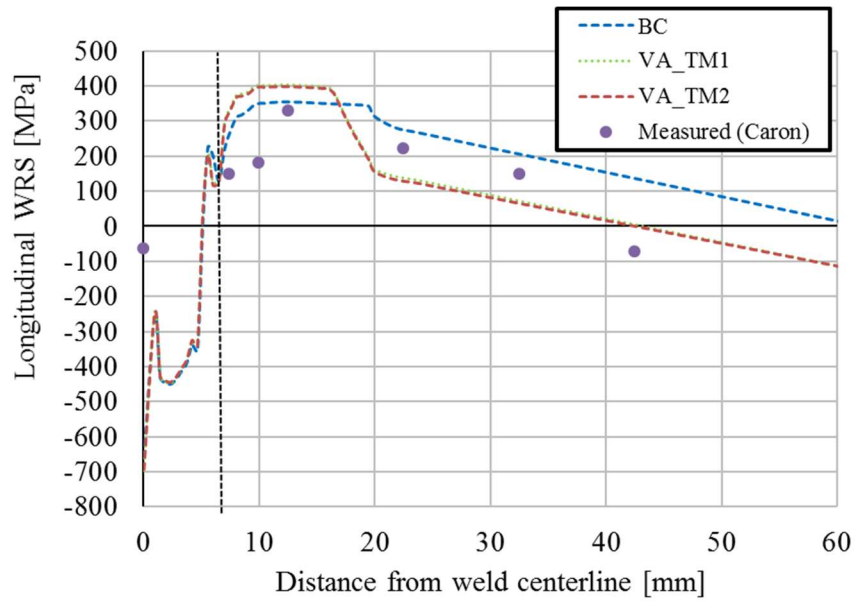


**Fig. 9** Results for component D – calculated and experimentally measured longitudinal WRS on the top of the plate (measured WRS found in [6]) – vertical broken line shows the limits of the weld area [11]



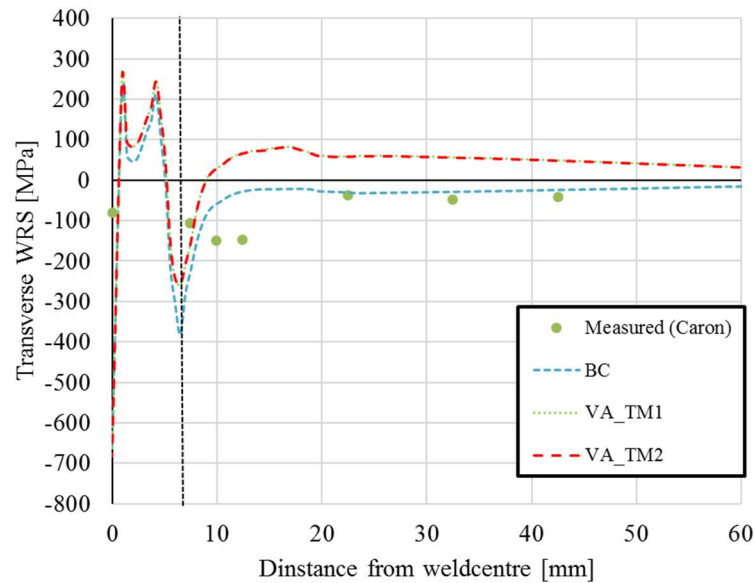


**Fig. 10** Results for component D – calculated and experimentally measured transverse WRS on the top of the plate (measured WRS found in [6]) – vertical broken line shows the limits of the weld area [11]

### CONCLUSIONS AND FUTURE WORK

The following conclusions were drawn, based on the above-presented results:

Applied approach for modelling of clampers during a weld simulation can have a significant effect on the calculated WRS, at least in the case of butt-welds. The use of spring elements for modelling the longitudinal and transverse restraints in the clamped area produces results that show better agreement with experimentally measured WRS. Moreover, as higher tensile WRS are calculated, this approach lies on the safe side. This modelling approach is therefore suggested for adoption in practical applications as well.

A possible erroneous modelling of the weld heat source could lead to an underestimation of the WRS and therefore non-conservative results. An increase of 100 % of the heat input led to a reduction of 28 % of the peak tensile stress (worst case scenario). Assuming a linear behavior, an overestimation of 10 % of the heat source coefficient would lead to an underestimation of 2.8 % of the peak tensile stresses. This deviation lies in the boundaries of the acceptable numerical error, of practical weld simulations ( $\pm 10\%$  [3]). Therefore, applying values for the weld metal arc efficiency from literature or previous measurements during the simulation of WRS, is considered valid.

Aluminum welding simulations neglecting the recrystallization in the HAZ, produce erroneous results. A lower longitudinal peak stress is calculated and is present at the middle of the component. Simulations considering the microstructural changes show that the peak stress is met on the boundaries of the HAZ, exhibiting a much more crucial case, regarding fatigue strength of the investigated component. Therefore, neglecting recrystallization in

the HAZ of aluminum weld during weld simulation is not conservative and should be avoided.

Applying strain rate dependent material models during a weld simulation produces significant deviation in the profiles of calculated WRS in comparison with the classical static material models. A deviation of up to 150 MPa was observed in the present case between rate independent and dependent cases. Therefore, strain rate dependency cannot be neglected during weld simulation when high accuracy is required. Nevertheless, the strain-rate independent case provided results with better agreement in the case of transverse WRS and this incompatibility has to be clarified.

The present method has been proven to provide accurate results with less computational effort and increased simplicity in comparison with previous modeling approaches for single pass-welds [3]. A validation of the above-mentioned extension for the case of multi-pass welds and high strength steels is therefore dictated. Comparison with measured WRS of real multi-pass welds has to be carried out and the effectiveness should be compared with other approaches [26], [6].

### ACKNOWLEDGEMENTS

The above presented work was carried out as a part of the framework of [39].

### REFERENCES

- [1] J. H. ARGYRIS, J. SJIMMAT AND K. J. WILLAM: 'Computational Aspects of Welding Stress Analysis', *Computer Methods in Applied Mechanics and Engineering*, Vol. 33, No. 1-3, pp. 635-665, 1982.
- [2] B. ANDERSSON: 'Thermal Stresses in a Submerged-Arc Welded Joint Considering Phase Transformations', *Trans. ASME*, Vol. 100, pp. 356-362, 1978.
- [3] P. KNOEDEL, S. GKATZOGIANNIS AND T. UMMENHOFER: 'Practical Aspects of Welding Residual Stress Simulation', *Journal of Constructional Steel Research*, Vol. 132, pp. 83-96, 2017.
- [4] P. DONG: 'Residual Stress Analyses of a Multi-Pass Girth Weld: 3-D Special Shell Versus Axisymmetric Models', *Journal of Pressure Vessel Technology*, Vol. 123, No. 2, pp. 207-213, 2001.
- [5] D. DENG AND H. MURAKAWA: 'Numerical simulation of temperature field and residual stress in multi-pass welds in stainless steel pipe and comparison with experimental measurements', *Computational Materials Science*, Vol. 37, pp. 269-277, 2006.
- [6] C. HEINZE, C. SCHWENK, M. RETHMEIER AND J. CARON: 'Numerical Sensitivity Analysis of Welding-Induced Residual Stress Depending on Variations in Continuous Cooling Transformation Behavior', *Front. Mater. Sci.*, Vol. 5, No. 2, pp. 168-178, 2011.
- [7] A. A. BHATTI, Z. BARSOU, H. MURAKAWA AND I. BARSOU: 'Influence of Thermo-Mechanical Material Properties of Different Steel Grades on Welding Residual Stresses and Angular Distortion', *Materials and Design*, Vol. 65, pp. 878-889, 2015.
- [8] L. E. LINDGREN: *Computational Welding Mechanics – Thermomechanical and Microstructural Simulations*, 1<sup>st</sup> Edition, Woodhead Publishing, Cambridge, England, 2007.
- [9] S. GKATZOGIANNIS, P. KNOEDEL AND T. UMMENHOFER: 'FE Welding Residual Stress Simulation – Influence of Boundary Conditions and Material Models', *EUROSTEEL 2017, September 13–15, 2017, Copenhagen, Denmark, Ernst & Sohn, CE/papers*, 2017.

- [10] P. KNOEDEL, S. GKATZOGIANNIS AND T. UMMENHOFER: 'FE Simulation of Residual Welding Stresses: Aluminum and Steel Structural Components', *Key Engineering Materials*, Vol. 710, pp. 268-274, 2016.
- [11] S. GKATZOGIANNIS, P. KNOEDEL AND T. UMMENHOFER: 'Strain-Rate Dependency of Simulated Welding Residual Stresses', *Journal of Material Performance and Engineering*, 2017.
- [12] S. GKATZOGIANNIS, P. KNOEDEL AND T. UMMENHOFER: 'Influence of Welding Parameters on the Welding Residual Stresses', *Proceedings of the VII International Conference on Coupled Problems in Science and Engineering, Rhodes Island, Greece, June 12 – 14*, pp. 767-778, 2017.
- [13] J. A. GOLDAK, A. CHAKRAVARTI AND M. BIBBY: 'A New Finite Element Model for Welding Heat Sources', *Metall. Trans. B*, Vol. 15, pp. 299-305, 1984.
- [14] J. N. DUPONT AND A. R. MARDER: 'Thermal Efficiency of Arc Welding Processes', *Weld. J.*, pp. 406-416, 1995.
- [15] ANSYS® Academic Research, Release 18.2, Help System, ANSYS, Inc., 2018.
- [16] J. B. LEBLOND AND J. DEVAUX: 'A New Kinetic Model for Anisothermal Metallurgical Transformations in Steels including Effect of Austenite Grain Size', *ACTA Metall.*, Vol. 32, pp. 137-146, 1984.
- [17] D. P. KOISTINEN AND R. E. MARBURGER: 'A General Equation Prescribing the Extent of the Austenite-Martensite', *ACTA Metall.*, Vol. 7, pp. 59-61, 1959.
- [18] M. Q. MACEDO, A. B. COTA AND F. G. DA S. ARAÚJO: 'The Kinetics of Austenite Formation at High Heating Rates', *Metal. E Mater.*, Vol. 64, pp. 163-167, 2011.
- [19] W. LIU, J. MA, F. KONG, S. LIU AND R. KOVACEVIC: 'Numerical Modeling and Experimental Verification of Residual Stress in Autogenous Laser Welding of High-Strength Steel', *Lasers Manuf. Mater. Process.* 2, pp. 24-42, 2015.
- [20] C. H. LEE AND K. H. CHANG: 'Prediction of Residual Stresses in High Strength Carbon Steel Pipe Weld Considering Solid-State Phase Transformation Effects', *Computers and Structures*, Vol. 89, pp. 256-265, 2015.
- [21] B. BRICKSTAD AND B. L. JOSEFSON: 'A Parametric Study of Residual Stresses in Multi-Pass Butt-Welded Stainless Steel Pipes', *International Journal of Pressure Vessels and Piping*, Vol. 75, pp. 11-25, 1998.
- [22] D. E. KATSAREAS, C. OHMS AND A. G. YOUTSOS: 'Finite Element Simulation of Welding in Pipes: A Sensitivity Analysis', *Proceedings of a Special Symposium held within the 16th European Conference of Fracture - ECF16, Alexandroupolis, Greece, 3-7 July, 2006*, pp. 15-26, 2006.
- [23] H. WOHLFAHRT, T. NITSCHKE-PAGEL, K. DILGER, D. SIEGELE, M. BRAND, J. SAKKIETTIBUTRA AND T. LOOSE: 'Residual Stress Calculations and Measurements - Review and Assessment of the IIR Round Robin Results', *Welding in the World*, Vol. 56, pp. 120-140, 2012.
- [24] S. NAKHODOCHI, A. SHOKUFAR, S. A. IRAJ AND B. G. THOMAS: 'Residual Stress Calculations and Measurements- Review and Assessment of the IIR Round Robin Results', *Journal of Pressure Vessel Technology*, Vol. 137, 2015.
- [25] C. K. LEE, S. P. CHIEW AND J. JIANG: '3D Residual Stress Modelling of Welded High Strength Steel Plate-to-Plate Joints', *Journal of Constructional Steel Research*, Vol. 84, pp. 94-104, 2013.
- [26] L. BÖRJESSON AND L. E. LINDGREN: 'Simulation of Multipass Welding With Simultaneous Computation of Material Properties', *Journal of Engineering Materials and Technology*, Vol. 123, pp. 106-111, 2001.
- [27] J. LUBLINER: 'Plasticity Theory', Dover Publications, 3<sup>d</sup> Edition, New York, USA, 2008.
- [28] J. MULLINS AND J. GUNNARS: 'Influence of Hardening Model on Weld Residual Stress Distribution', *Research Report 2009:16, Inspecta Technology AB*, Stockholm, Sweden, 2009.

- [29] P. PERZYNA: ‘Fundamental Problems in Viscoplasticity’, *Advances in Applied Mechanics*, Vol. 5, pp. 243-377, 1966.
- [30] S. GKATZOIANNIS, P. KNOEDEL AND T. UMMENHOFER: ‘Reviewing the Influence of Welding Setup on FE-simulated Welding Residual Stresses’, *Proceedings of the 10<sup>th</sup> European Conference on Residual Stresses - ECRS10, Leuven, Belgium, on 11-14 September, 2018.*, accepted for publication.
- [31] N. JONES: *Structural Impact*, 2<sup>nd</sup> Edition, Cambridge University Press, New York, USA, 2012.
- [32] D. FORNI, B. CHIAIA AND E. CADONI: ‘Strain Rate Behaviour in Tension of S355 Steel: Base for progressive collapse analysis’, *Engineering Structures*, Vol. 119, pp. 167-173, 2016.
- [33] M. KNOBLOCH, J. PAULI, M. FONTANA: ‘Influence of The Strain Rate on the Mechanical Properties of Mild Carbon Steel at Elevated Temperatures’, *Materials and Design*, Vol. 49, pp. 553-565, 2013.
- [34] D. FORNI, B. CHIAIA AND E. CADONI: ‘High Strain Rate Response of S355 at High Temperatures’, *Materials and Design*, Vol. 94, pp. 467-478, 2016.
- [35] J. SCHUBNEL, S. GKATZOIANNIS, M. FARAJIAN, P. KNOEDEL, T. LUKE AND T. UMMENHOFER: ‘*Rechnergestütztes Bewertungstool zum Nachweis der Lebensdauererlängerung von mit dem Hochfrequenz-Hämmerverfahren (HFMI) behandelten Schweißverbindungen aus hochfesten Stählen*’, Research Project DVS 09069 – IGF 19227 N, 2018 (in progress).
- [36] E. J. PAVLINA AND C.J. VAN TYNE: ‘Correlation of Yield Strength and Tensile Strength with Hardness for Steels’, *Journal of Materials Engineering and Performance*, Vol. 17, No. 6, pp. 888-893, 2008.
- [37] P. ZHANG, S. X. LI AND Z. F. ZHANG: ‘General Relationship Between Strength and Hardness’, *Materials Science and Engineering A*, Vol. 529, No. 6, pp. 62-73, 2011.
- [38] J. HILDEBRAND: ‘*Numerische Schweißsimulation: Bestimmung von Temperatur, Gefüge und Eigenspannung an Schweißverbindungen aus Stahl- und Glaswerkstoffen*’, Dissertation, Bauhaus-Universität Weimar, 2008.
- [39] S. GKATZOIANNIS: ‘*Finite Element Simulation of High Frequency Hammer Peening*’, Doctoral Thesis , KIT, Karlsruhe Institute of Technology, 2018 (in progress).



# RESIDUAL STRESS MEASUREMENTS AND MODEL VALIDATION OF SINGLE AND DOUBLE PULSE RESISTANCE SPOT WELDED ADVANCED HIGH STRENGTH STEEL

P. EFTEKHARIMILANI\*, H. GAO\*\*, R. M. HUIZENGA\*,  
E. M. VAN DER AA\*\*, M. AMIRTHALINGHAM\*\*\*,  
I. M. RICHARDSON\* and M. J. M. HERMANS\*

\*Delft University of Technology, Mekelweg 2, 2628 CD Delft, The Netherlands. Email: p.eftekharmilani@tudelft.nl

\*\*TATA Steel, 1970 CA IJmuiden, The Netherlands.

\*\*\* Department of Metallurgical and Materials Engineering, Indian Institute of Technology Madras, Chennai, India.

DOI 10.3217/978-3-85125-615-4-22

## ABSTRACT

Advanced high strength steels (AHSS) are increasingly used in automotive industry; thousands of resistance spot welds are applied to car body-in-white. High alloying levels of AHSS result in lower weldability. Residual stresses play an essential role on the formation of defects and the mechanical performance of the weld. An electrical-thermal-metallurgical-mechanical finite element model was constructed to simulate the temperature and stress distribution during single and double pulse resistance spot welding. The models are validated by ex-situ synchrotron X-ray diffraction stress measurements.

In this paper, single pulse and double pulse resistance spot welds were made on 1.3 mm thin sheets of a 3rd generation AHSS. Depth resolved stress measurements in two orthogonal directions were carried out using high-resolution powder diffraction at beamline ID22 of the European Synchrotron Research Facility. A monochromic 70 keV X-ray was used to record the d-spacing of (200) bcc planes in transmission mode. The strains were calculated from the shift in the d-spacing of the planes. The stresses were calculated by the biaxial Hook's law.

The numerical and experimental results show that the residual stresses in the weld nugget zone and the heat affected zone of the welds are tensile in nature, whereas the base material experiences compressive stresses. Lower residual stresses at the weld nugget and HAZ were obtained by applying a second current pulse. The simulated results show a good agreement with the residual stresses measured.

This study provides a better understanding of the stress distribution in resistance spot welds and allows prediction of stresses as a result of welding conditions applied.

Keywords: Residual stress measurement, synchrotron X-ray diffraction, depth resolved stress, finite element modelling, resistance spot welding, advanced high strength steel.

## INTRODUCTION TO THIS DOCUMENT

The continued development of Advanced High Strength Steels (AHSS) to combine high strength and formability with excellent crashworthiness behaviour for automotive vehicles

requires the investigation of weldability. The favourable properties of AHSS are obtained by appropriate design of the alloys to provide multi-phase microstructures.

The main method used to join sheet metals in the automotive industry is resistance spot welding (RSW), which is characterised by the low costs, high reliability, high operating speeds and suitability for automation [1, 2]. The carefully designed multi-phase microstructures of the parent material are destroyed in and around the weld by the thermal-mechanical cycle imposed during RSW.

Generally in RSW, there is a critical weld nugget size where the failure changes from an interfacial to a plug failure mode [3, 4]. However, in the newest generation of AHSS, even the largest weld nugget sizes have the tendency to show failure modes other than the desirable full plug failure when subjected to mechanical loading. Our previous work [5, 6] has shown that by applying double pulse welding schemes, the mechanical response of the welds has improved. It seems that the failure mode depends both on metallurgical effects and residual stress levels.

A typical RSW thermal cycle, mechanical and thermal constraints due to the electrode force in combination with a high heating and cooling rate introduce residual stresses within a resistance spot weld, which influence the mechanical properties of the welds. There is limited literature on residual stress investigation of spot welds. Florea et al. [7] reported results on residual stresses, obtained by neutron diffraction in spot welded aluminum alloys.

The exact stress levels and distribution in the spot welded area for the AHSS are not available, nor is the effectiveness of multiple thermal cycling, by double pulsed welding schemes, on stress redistribution or stress mitigation. High-energy synchrotron X-ray diffraction allows to obtain this data [8, 9], which is required to come to a better understanding of the failure mechanisms of spot welds.

In this paper, the constructed finite element model validated by measured residual stresses of single and double pulse resistance spot welds are presented. The model link welding conditions with the stress state of a spot weld, allowing to correlate the data with the mechanical behaviour of the welds.

### EXPERIMENTAL APPROACH

The material examined was a 3<sup>rd</sup> generation 1 GPa complex phase AHSS with a thickness of 1.3 mm applied in the automotive industry. The steel was received in a cold-rolled and galvanised condition (surface density of 50 gm<sup>-2</sup>). Material characteristics and composition are according to the VDA chemistry for 590Y980T-DH in the recently drafted VDA specifications [10], as listed in Table 1.

RSW was carried out on a SchlatterTM 50 Hz AC spot welding machine using F1-16-20-5.5 electrodes with a holding force of 4 kN and welding parameters, as described in the VDEh SEP1220-2 standard [11]. The selected welding parameters are based on the weld nugget growth analysis reported elsewhere [5, 6] and are indicated schematically in Fig. 1, showing the welding sequences for single pulse and double pulsing. A welded sample is shown in Fig. 2, schematically.

The stress measurements were carried out on the high-resolution powder diffraction beamline ID22 at the European Synchrotron Research Facility (ESRF) in Grenoble, France. A monochromatic 70 keV X-ray, providing a wavelength of 0.1771 Å with a focal spot size

of  $150 \times 50 \mu\text{m}^2$  at the sample position was used to record the diffraction patterns of ferrite {200} planes in transmission mode. An analyser crystal was placed between the sample and the detector. A point detector placed behind the sample scanned the  $2\theta$  diffraction angle of  $6.8^\circ$  to  $7.3^\circ$ . The experimental arrangement is shown in Fig. 3. Strain scanning was performed along the radius with the step size of  $300 \mu\text{m}$  with a resolution of about  $600 \mu\text{m}$ , at the depth of  $0.65 \text{ mm}$  (half of one plate thickness). The counting time per point was 10 min.

In order to measure the stress free d-spacing, samples with similar welding schedules were electro-discharged machined from the weld. In addition, some vertical slits at positions of weld centre, 1 mm, 3 mm, 5 mm and 7 mm were made to release the stresses even further. The slit depth and width were  $0.65 \text{ mm}$  and  $0.25 \text{ mm}$ , respectively.

**Table 1** Materials characteristics for the base material [10].

VDA 239-100 classification	Coating [g/m <sup>2</sup> ]	Proof strength (MPa)	Ultimate tensile strength (MPa)	Elongation at fracture L0 = 80 mm (%)	C (wt.%)	Mn +Cr+ Mo (wt.%)	Si+ Al (wt.%)
CR700Y980T-DH	GI (galvanised) (50/50)	700- 850	980- 1180	13	0.18- 0.22	1.8- 2.3	0.8- 1.2

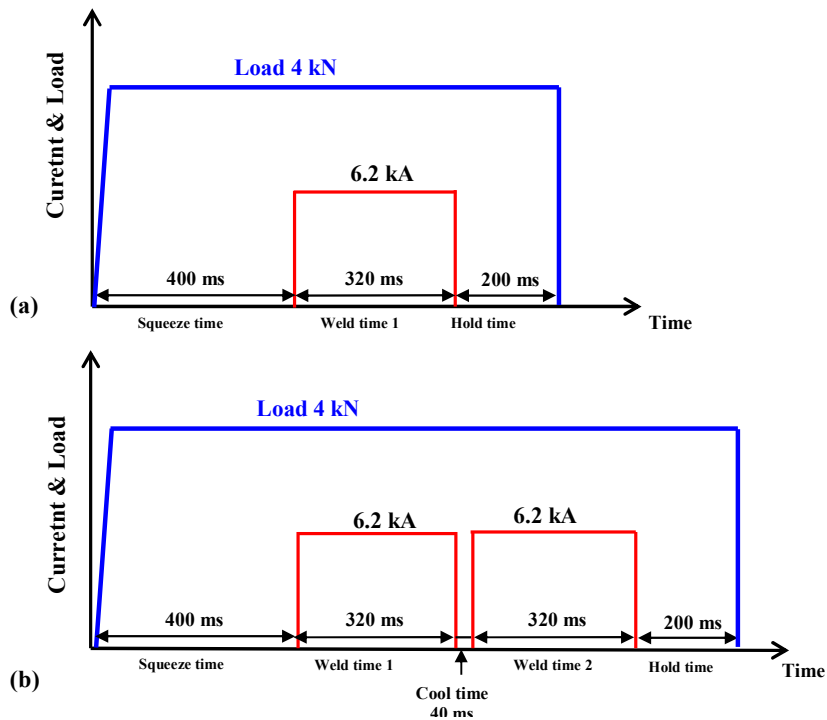


**Fig. 1** Welding parameters.



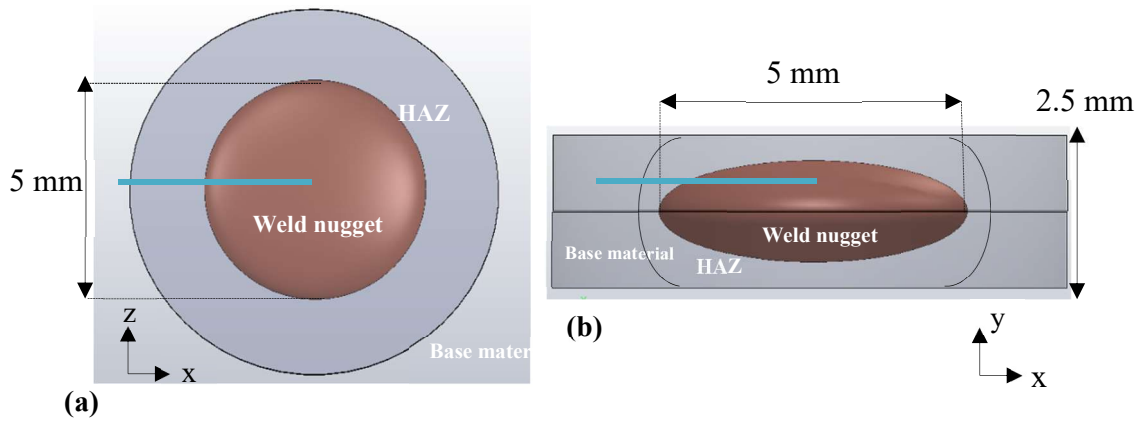


**Fig. 2** Schematic representation of a welded sample (a) top view and (b) side view, the dark shape represents the weld nugget. The straight lines indicate the positions at which residual stresses were measured.

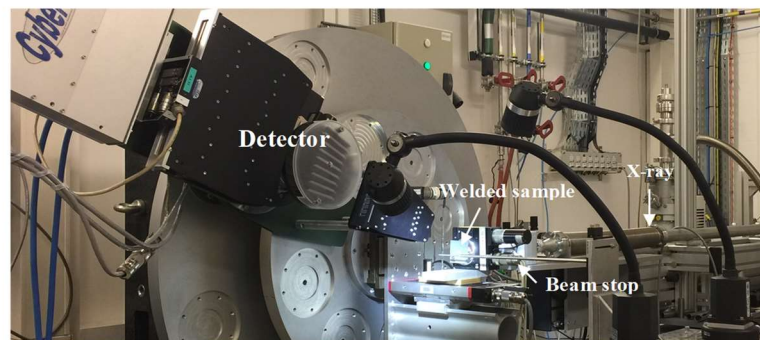
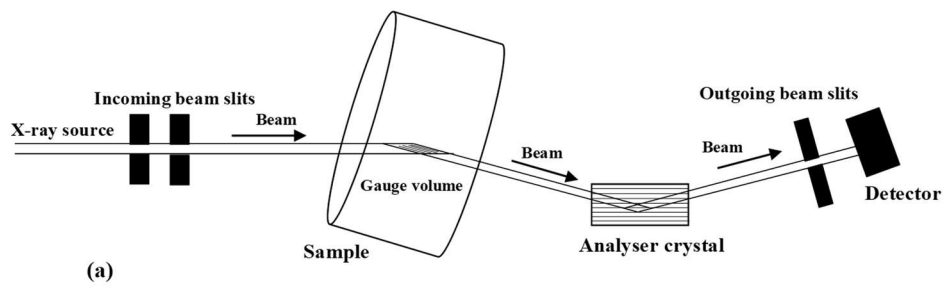


**Fig. 3** (a) Schematic and (b) experimental set-up for the synchrotron X-ray diffraction measurements

## Mathematical Modelling of Weld Phenomena 12

A pseudo-Voigt profile was used to fit the XRD measurements. Fig. 4 shows a typical peak fitting for the {200} bcc plane within the weld nugget, HAZ and the base material. For a fixed diffraction angle and a specific energy, the d-spacing for a certain plane be can be obtained from Bragg's law [12]. The strain ( $\varepsilon$ ) can be derived by (Eq. 1):

$$\varepsilon_i = \frac{(d_i - d_0)}{d_0} \quad (1)$$

The stress can be calculated by the biaxial Hooke's law (Eq. 2) using the diffraction elastic constant ( $E$ ) and Poisson ratio ( $\nu$ ) of the (200) planes, which are considered to be 169.3 GPa and 0.295, respectively [13].

$$\sigma_i = [\varepsilon_i + \nu\varepsilon_j] \left[ \frac{E}{1-\nu^2} \right] \quad (2)$$

The stress free lattice parameters of {200} bcc planes within weld nugget, HAZ and base material are 1.434 Å, 1.434 Å and 1.4354 Å, respectively. The strains were calculated using the stress free lattice parameter at the same zones for the selected plane.

The uncertainty in the induced strain from peak fitting is in the order of  $10^{-6}$ , and from the measurement itself is within 0.0002.

## Mathematical Modelling of Weld Phenomena 12

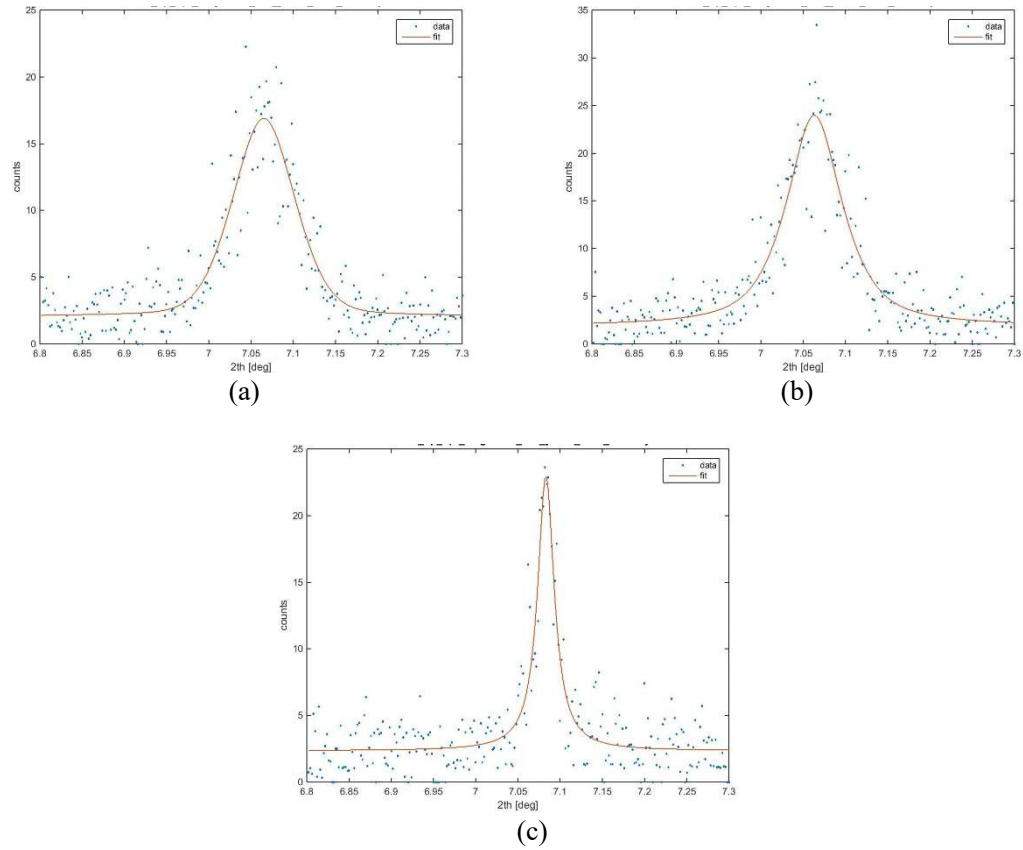


**Fig. 4** Typical peak fitting of {200} bcc for (a) weld nugget zone, (b) HAZ and (c) base material of a resistance spot weld.

### MODELLING APPROACH

A 3D finite-element (FE)-based electrical-thermal-metallurgical-mechanical model was developed to compare with the experimental results. After validation, the FE-model can be utilised for various spot welding conditions applied to this steel. The commercial software Simufact welding was used for this purpose. A sheet coupon with a dimension of 45 mm x 45 mm x 1.3 mm is created, meshed and assembled. A schematic representation of RSW and trends of electrical resistance and temperature in various components during welding is shown in Fig. 5. Considering both the bulk resistance and the contact resistance between each two adjacent components, it can be seen that copper electrodes have the lowest value of electrical resistance while the highest value is reached at the contact surface between the two metal sheets.

Material properties were calculated based on chemical composition in JMatPro and imported to the model. The temperature dependent material properties, such as thermal conductivity, specific heat capacity, Young's modulus, density, thermal expansion coefficient, electrical resistivity, flow stress and phase diagram are shown in Fig. 6(a-h). The initial room temperature, heat conduction and convection coefficients were defined to be 293 K, 30 W/K m<sup>2</sup> and 10 W/K m<sup>2</sup>. A reference point is set on the centre-bottom of the lower sheet in order to align the lower electrode. An external force of 4 kN is applied on the upper electrode perpendicular to the sheet surface. The current, time for squeeze, weld and hold are defined in accordance with SEP 1220-2 as shown in Fig. 1. A dynamic mesh refinement is applied to the sheets near the electrodes with a radius of 5 mm. One cubic element was splitted into eight. This model includes the physics of Joule heating, heat transfer, phase transformation and solid mechanics, from which evolution of temperature, phases and stress during resistant spot welding can be obtained.

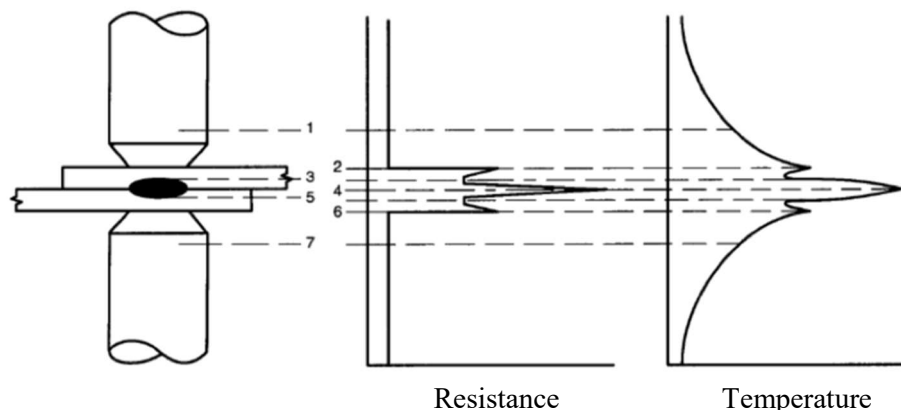


**Fig. 5** Schematic representation of RSW and various existing resistances as well as trends of electrical resistance and temperature in various components.

# Mathematical Modelling of Weld Phenomena 12

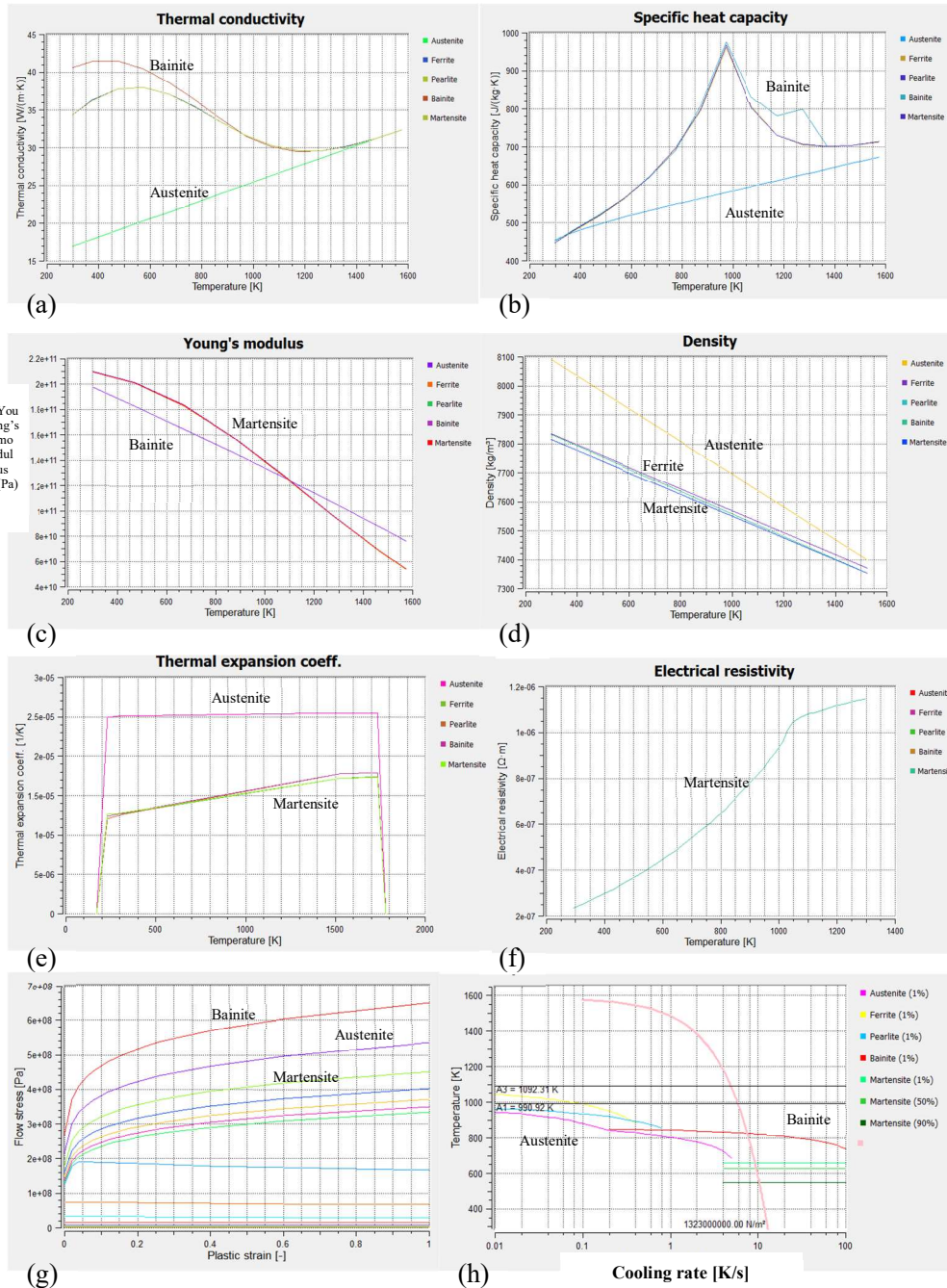


**Fig. 6** Temperature dependent material properties, (a) thermal conductivity, (b) specific heat capacity, (c) Young's modulus, (d) density, (e) thermal expansion coefficient, (f) electrical resistivity, (g) flow stress and (h) phase diagram (the pink line indicates a cooling rate of 100

### RESULTS AND DISCUSSION

Fig. 7 shows the comparison of simulated weld nugget and the cross section of a single pulse resistance weld. Good agreement was found between the simulated and experimental weld nugget size and shape.

The simulated phase evolution during welding and subsequent cooling at the area shown in Fig. 7 (black circle within the HAZ) is shown in Fig. 8. The base material microstructure consists of 80 vol.% bainite, 13 vol.% martensite and 7 vol.% ferrite. During welding, the microstructure becomes austenitic by heating and during cooling the martensitic transformation occurs and the final microstructure consists of 98 vol.% martensite. The retained austenite is 2 vol.% in the HAZ.

The simulated volume fractions of martensite within the weld nugget, HAZ and the base material of a spot weld are shown in Fig. 9. The result shows that the weld nugget is 98 vol.% martensitic and this is the same as the amount obtained from experimental analysis. Thus, there is a good agreement between the simulated and experimental results from the phase transformations point of view in resistance spot welding. It is also shown in Fig. 9, by moving from the weld nugget towards the base material that the volume fraction of martensite decreases.

The simulated residual stress fields in z-direction for a single pulse weld are shown in Fig. 10. As shown in Fig. 10a, the stresses are in tensile mode within the weld and the HAZ. The cross section of the stress field is shown in Fig. 10b. The stress value at the weld centre is about +450 MPa. The highest residual stress is predicted to be at the weld edge to be about +500 MPa. This can be attributed to the stress concentration due to the geometry and the interface between two sheets. Moving from the weld nugget and the HAZ to the base material, the residual stresses are decreasing and at the base material, compressive residual stresses are calculated. It can be seen that there are high tensile residual stresses at the electrode and sheet interface at the HAZ. The residual stresses at these areas can be in the order of +500 MPa.

The residual stress profile of the single pulse weld obtained with simulation and validated using experimental synchrotron data is shown in Fig. 11. There is reasonable agreement between the experimental and numerical results. The numerically calculated residual stress shows a value of about 450 MPa in tensile mode at the weld centre and by moving from the weld centre towards the HAZ, the residual stress initially decreases and then increases and with moving through the base material it decreases. A resistance spot weld exhibits a tensile stress in the weld nugget due to the fact that the molten nugget cools and contracts at the end of the weld cycle. The base material exhibits compressive residual stresses, so that equilibrium can be achieved in the work-piece.

The small deviation between measured and computed residual stress profiles as shown in Fig. 11, can be explained from two perspectives. One is from the input temperature dependent material properties and constraining assumptions in the model, and the other is the experimental error originating from the accuracies of the exact location definition of the weld centre during measurements, fitting of the XRD peaks and considering only the (200) ferrite planes.

## Mathematical Modelling of Weld Phenomena 12

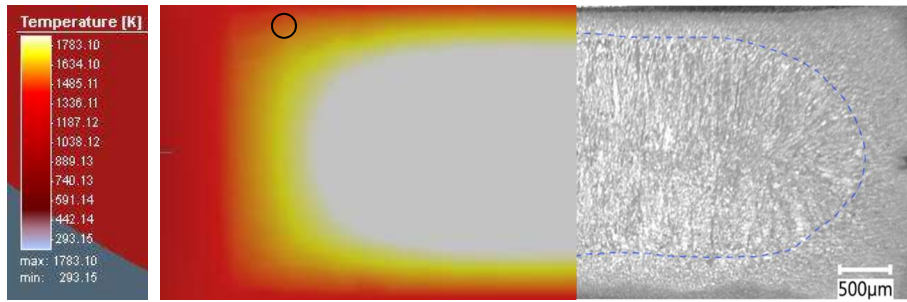


**Fig.7.** Comparison of simulated temperature profile at peak temperature and a cross section of a single pulse resistance spot weld. Black circle indicates the area within the HAZ, where the phase fractions of different phases during welding are extracted.

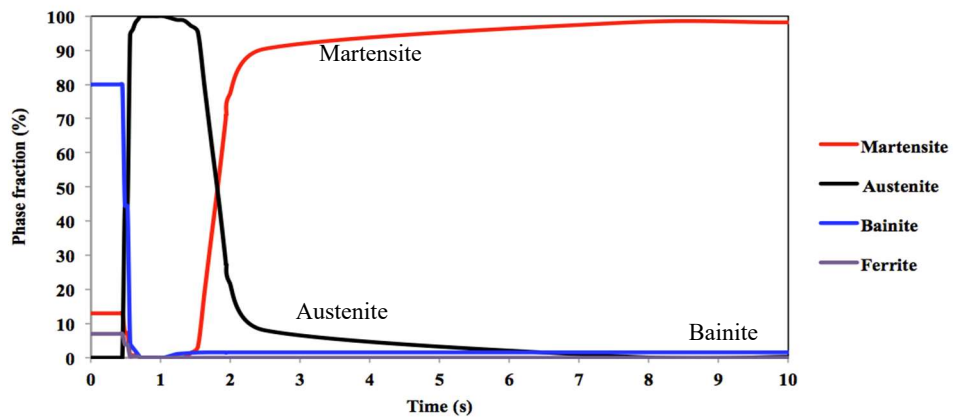


**Fig. 8.** Simulated phase fraction variation vs. time during RSW

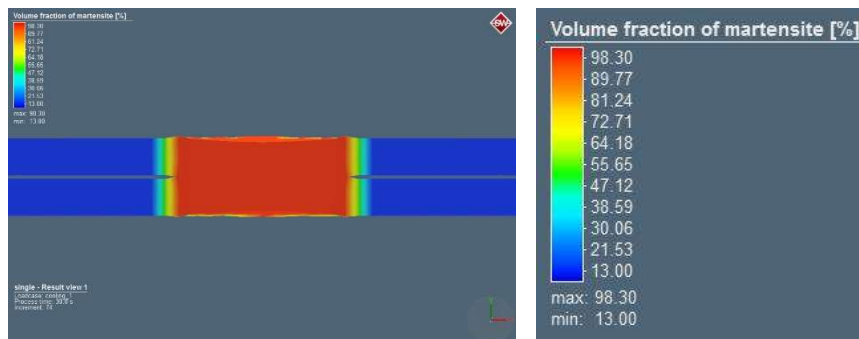


**Fig. 9.** Simulated volume fraction of martensite in a resistance spot weld.

## Mathematical Modelling of Weld Phenomena 12

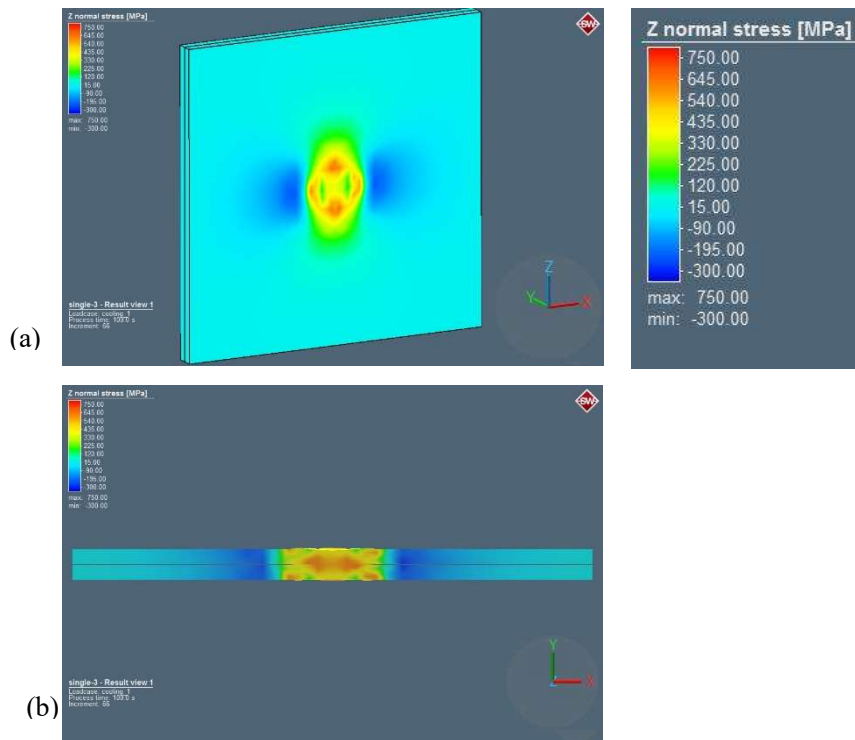


**Fig. 10** Simulated residual stress of a single pulse spot weld, (a) top view and (b) cross section view.

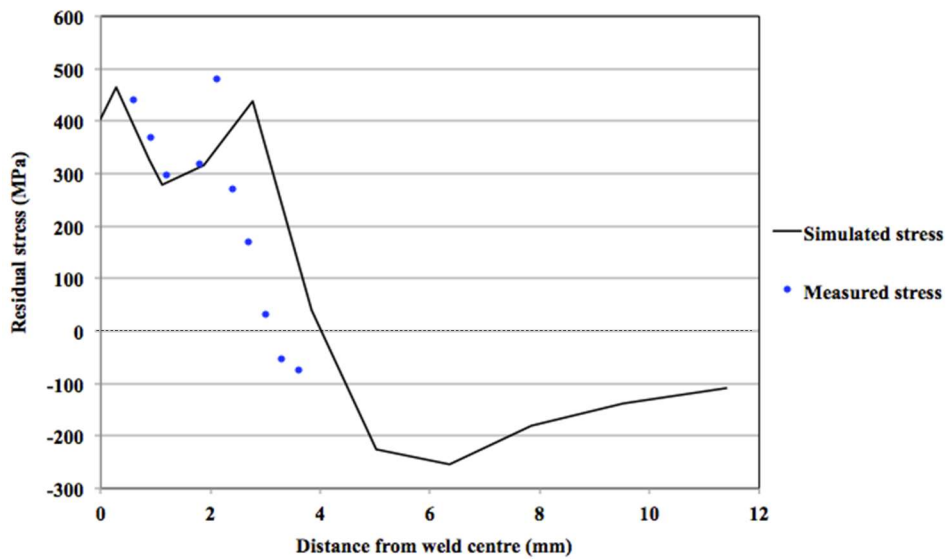


**Fig. 11** Comparison of simulated and measured residual stress of a single pulse spot weld.



The validated FE-based numerical model is used to predict the residual stresses in double pulse spot welds. The temperature profile for the double pulse weld is shown in Fig. 12. During applying the first current pulse, the same size of the weld nugget is observed (Fig. 12a) as for the single pulse condition (Fig. 7). During the inter-pulse time, solidification shrinkage and thermal contraction of the weld metal result in a slightly smaller nugget size than the first pulse nugget size (Fig. 12b). When the second current pulse is applied, the size of the weld nugget becomes slightly larger than that of the inter-pulse stage, but not as big as that from the first pulse (Fig. 12c). The smaller weld pool size during the second current pulse is related to the fact that the resistance between the two sheets has decreased due to the first weld nugget presence. A much smaller contact resistance results in less heat generation at the sheet interface in the second pulse.

The overviews of the simulated residual stress profiles of single and double pulse welds are shown in Fig. 13a and b, respectively. The simulated residual stresses are tensile in nature within the weld nugget and the HAZ of both the single and double pulse welds. In the base material (near the weld) the residual stresses are in compression mode in both welds. The residual stresses seem to be redistributed by double pulsing. The double pulse weld shows lower residual stresses at the weld centre. The calculated residual stress at the weld centre of a single pulse weld is about 450 MPa, however, in a double pulse weld is about 50 MPa. The residual stresses are calculated to be decreased at the weld nugget and the HAZ of the double pulse weld. The compressive stress at the base material (near the weld) of a single pulse weld is about -80 MPa whereas in a double pulse weld is about -20 MPa.

The simulation results suggest that by double pulsing, the residual stresses can be reduced in a resistance spot weld. Our previous results [5, 6] showed that a double pulse weld exhibits an improved failure mode, tension shear strength and elongation in comparison with a single pulse weld. The decline of the residual stress can play a major role in mechanical response improvement of a double pulse weld.

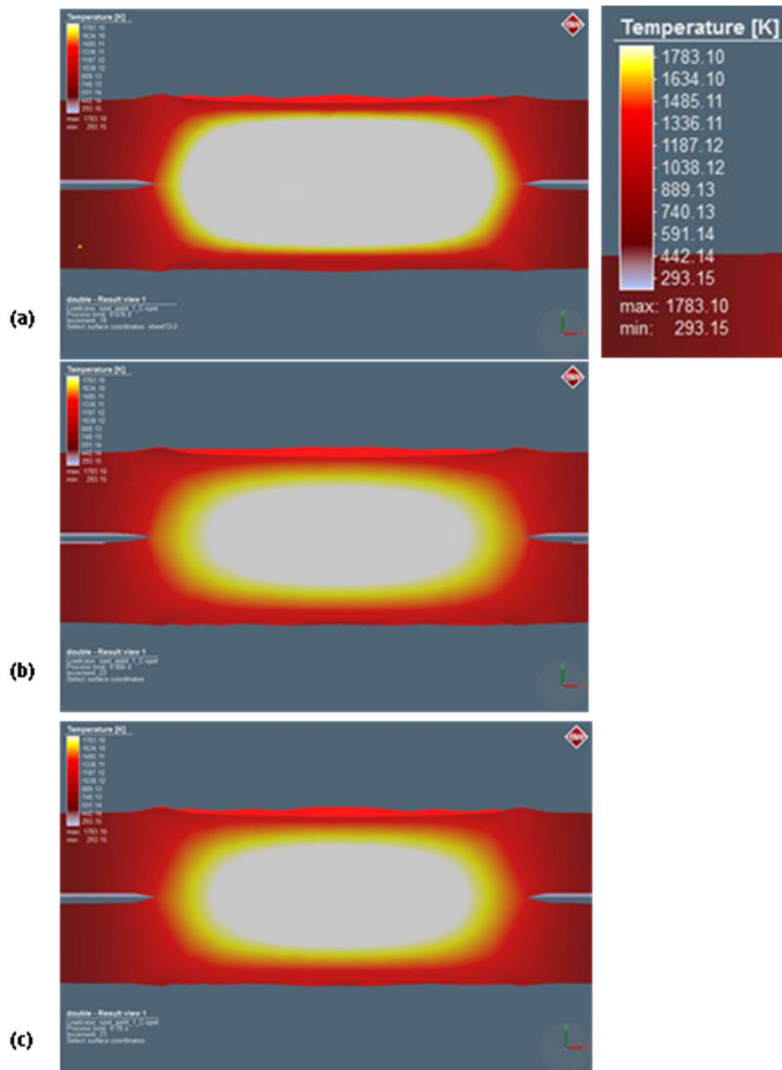


**Fig. 12** Simulated temperature profile during double pulse welding at the (a) peak temperature of the first current pulse, (b) at the end of the cooling time (40 ms cooling time between two pulses) and (c) peak temperature of the second current pulse.

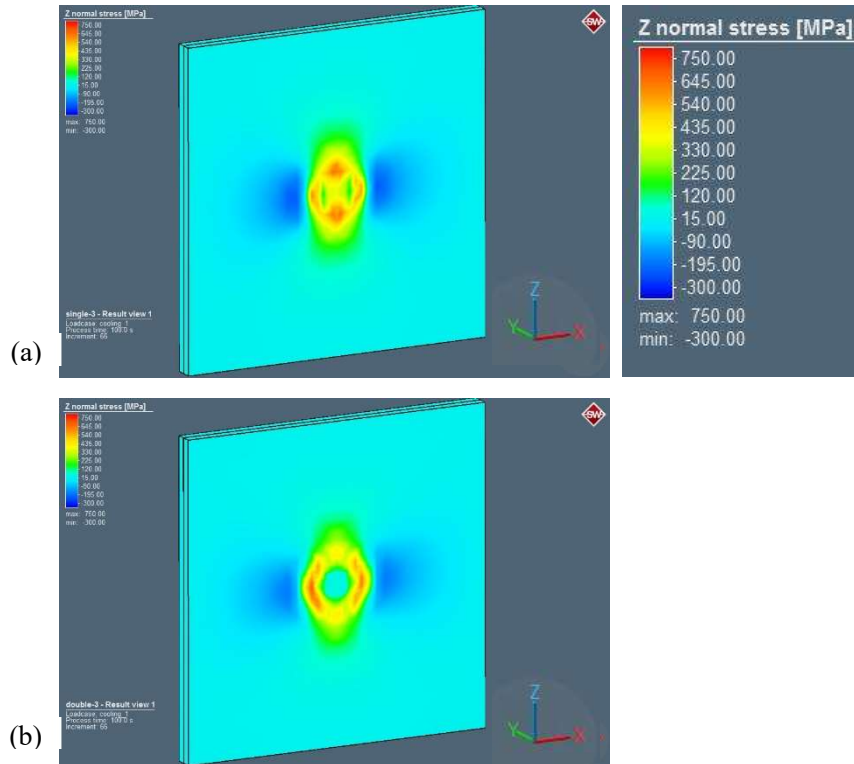


**Fig. 13** Simulated residual stress profiles of (a) single pulse weld and (b) double pulse weld.

## CONCLUSIONS

In summary, the residual stresses of a single pulse weld were simulated and verified using synchrotron X-ray diffraction data for the first time. The experimental and simulated results showed a tensile stress in the weld nugget due to the molten nugget cooling and contracting at the end of the weld cycle. The HAZ exhibited also a tensile stress mode due to the contraction. The base material showed compressive residual stresses near the weld, thus achieving the equilibrium in the work piece. Further from the weld, stresses are relatively low and nearly zero at the edge of the work piece. The residual stresses of a double pulse weld are expected to be lower than a single pulse weld. The validated FE-based numerical model can be used to ascertain the residual stresses in spot-welded AHSS.

## APPENDICES AND ACKNOWLEDGEMENTS

This research was carried out under project number F22.7.13507 in the framework of the Partnership Program of the Materials innovation institute M2i ([www.m2i.nl](http://www.m2i.nl)) and the Foundation of Fundamental Research on Matter (FOM) ([www.fom.nl](http://www.fom.nl)), which is part of the Netherlands Organisation for Scientific Research ([www.nwo.nl](http://www.nwo.nl)). The authors thank Tata Steel for delivering the materials. The authors would like to acknowledge ESRF for beamtime and thank the ID22 beamline team for their assistance. Mr. G. Agarwal and Mr. K. Goulas for their assistance during the experiments.

## REFERENCES

- [1] S.K. KHANNA, X. LONG: 'Residual stresses in resistance spot welded steel joints'. *Science and Technology of Welding and Joining*, Vol. 13(3), pp. 278–288, 2008.
- [2] S.S. NAYAK, Y. ZHOU, V.H. BALTAZAR HERNANDEZ: 'Resistance spot welding of dual-phase steels: heat affected zone softening and tensile properties'. *Proceedings of 9<sup>th</sup> International Conference on 'Trends in Welding Research'*, Chicago, USA, pp. 641–649, 2012.
- [3] M. POURANVARI, H.R. ASGARI, S.M. MOSAVIZADCH, ET AL: Effect of weld nugget size on overload failure mode of resistance spot welds. *Science and Technology of Welding and Joining*, Vol. 12(3), pp. 217–225, 2007.
- [4] Y.J. CHAO: 'Failure mode of spot welds: interfacial versus pullout'. *Science and Technology of Welding and Joining*, Vol. 8(2), pp. 133-137, 2003.
- [5] P. EFTEKHARIMILANI, E.M. VAN DER AA, M.J.M. HERMANS, I.M. RICHARDSON: 'The microstructural evolution and elemental distribution of a 3<sup>rd</sup> generation 1 GPa advanced high strength steel during double pulse resistance spot welding', *Welding in the World*, Vol. 61(4), pp. 691-701, 2017.
- [6] P. EFTEKHARIMILANI, E.M. VAN DER AA, M.J.M. HERMANS, I.M. RICHARDSON: 'Microstructural characterisation of double pulse resistance spot welded Advanced High Strength Steel', *Science and Technology of Welding and Joining*, Vol. 22(7), pp. 545-554, 2017.
- [7] R.S. FLOREA, ET AL.: *J Mat. Pro. Tech.*, Vol. 212, pp. 2358- 2370, 2012.
- [8] E.M. VAN DER AA: Local cooling during welding: prediction and control of residual stresses and distortion, thesis, Delft University of Technology, 2007.
- [9] M. PEEL, ET AL., *Acta Materialia*, Vol. 51, pp. 4791-4801, 2003.
- [10] VDA 239-100 Material specification: Sheet Steel for Cold Forming; 5 May 2016.
- [11] SEP 1220-2: Testing and documentation guideline for the joinability of thin sheet of steel-part 2: resistance spot welding. VDEh Standard; 2007 (Technical Report 08).
- [12] W.L. BRAGG: 'The Diffraction of Short Electromagnetic Waves by a Crystal', *Proceedings of the Cambridge Philosophical Society*, Vol. 17, pp. 43-57, 1913.
- [13] R.K. DUTTA, R.M. HUIZENGA, M. AMIRTHALINGAM, A. KING, H. GAO, M.J.M. HERMANS, I.M. RICHARDSON: 'In situ synchrotron diffraction studies on the temperature-dependent plane-specific elastic constants in a high-strength quenched and tempered structural steel', *Scripta Mater.*, pp. 187-190, 2013.
- [14] N.D. RAATH, ET AL., *Metallurgical and Materials Transactions A*, Vol. 51, pp. 4791-4801, 2003.



# NUMERICAL SIMULATION OF STRESS BEHAVIOR DURING SHOT PEENING

K. IKUSHIMA\*, Y. YAMADA\*, M. SHIBAHARA\*,  
S. NISHIKAWA\*\* and K. AKITA\*\*\*

*\*Osaka Prefecture University*

*\*\*Iwate University*

*\*\*\*Tokyo City University*

DOI 10.3217/978-3-85125-615-4-23

## ABSTRACT

Welding is widely used in the manufacture of steel structures. But welding causes residual tensile stress. Residual stresses due to welding may affect the initiation of fatigue cracks and stress corrosion cracking. These defects have significant effect on the integrity of products. In order to reduce or mitigate the tensile residual stress, surface treatment by peening has been proposed. To guarantee the safety of the products, it is important to evaluate the effect of peening on the surface stress in advance of fabrication. In this study, we proposed a method to predict the reduction of tensile residual stress due to shot peening using finite element method. The proposed method was applied to the analysis of Almen strip piece. In the analysis, the relation between the amount of shot projection and the arc height was discussed. In addition, the proposed method was also applied to the analysis of the shot-peened bead-on-plate specimen. As a result, we confirmed that the proposed method can quantitatively predict shot peening and it can analyse the effect of reduction of welding residual stress of tension by shot peening.

## INTRODUCTION

Welding is widely used to join members in the manufacture of steel structures, but it is known that strong tensile residual stress can be generated on the surface by welding [1-3]. Residual stress is considered to be one of the major cause of the initiation of fatigue crack and stress corrosion cracking (SCC). Those severe defects many influence the integrity of the structure. So, it is important to reduce or mitigate the residual tensile stress in the structure due to welding.

Various peening techniques using a laser, shot, water jet have been proposed in order to modify the tensile residual stress of the surface of welding construction [4-6]. In these peening methods, an impact force is applied to the surface of the target, and this generates an elongating plastic strain in the in-plane direction by a strong compressive force in the normal direction due to the impact. A compressive stress is introduced to the surface since the elongation is elastically restrained from the surrounding part. It is reported that peening is effective in improving the fatigue life [7] and preventing SCC [8] by modifying the stress state of the surface in such a process.

The strength and number of impacting load can influence the residual stress distribution after peening since the compressive stress is introduced by the impulsive load. So, the

residual stress distribution after peening was predicted in various reports [9-11]. In these reports, mechanical behavior under the collision of a shot is investigated using elastic plastic analysis. Since the dimension of shot is 1mm or smaller and the duration of collision of shot is several micro seconds, very high resolution for space and time is necessary to predict the collision of shot. So, the prediction of the residual stress distribution for the entire of the target is very difficult in the point of analysis scale. Furthermore, in order to discuss the effect of peening on the modification of an analysis method is proposed to welding residual stress, it is necessary to consider the residual stress generated by the welding. This will make the simulation more difficult.

On the other hand, to conduct a large scale analysis of welding mechanical problem, the authors have proposed the Idealized Explicit FEM (IEFEM) [12-13]. IEFEM is developed based on dynamic explicit FEM and realizes fast and highly accurate analysis by considering the convergence to the static equilibrium state. In addition, since this method is based on the dynamic explicit FEM, It has a high applicability to parallelization. It has been reported that much faster analysis than conventional methods can be achieved by introducing parallelization using a graphics processing unit (GPU). So an efficient analysis can be expected by using IEFEM and we have proposed an analysis system to analyze the residual stress after shot peening using Idealized Explicit FEM [14].

Therefore, in this study, in order to construct an analysis method, we extend the Idealized Explicit FEM to consider the dynamic effect due to the impact load. Next, a load model of the impact load due to the collision of a shot is also proposed. The validity of the proposed analysis method is investigated by applying the proposed method to the shot peening of the Almen strip pieces [15]. Finally, the influence of the amount of shot collision on residual stress distribution is investigated by applying the proposed method to the modification of the residual stress distribution in the bead-on welded plate by shot peening.

### ANALYSIS METHOD OF RESIDUAL STRESS DISTRIBUTION DURING SHOT PEENING

#### IDEALIZED EXPLICIT FEM CONSIDERING DYNAMIC EFFECT

In shot peening, 1 mm or smaller shots collide with the target surface numerous times and compressive stress is introduced. To predict the stress distribution under such a process, dynamic elastic plastic analyses with extremely high spatial resolution are necessary. Here, the proposed analysis system that can predict the residual stress distribution after shot peening by using the large-scale nonlinear mechanical analysis method named IEFEM [10], is briefly explained. The detailed formulations are found in the literature [12].

In dynamic elastic plastic analyses using IEFEM, the semi-discretized equation of motion by FEM is discretized for time by using Newmark's beta method and the linearized equation from the Newton-Raphson method. Equation (1) to (3) is defined as the fundamental equation:

$$[K_{eff}]^{(k)} \{\Delta U\} = \{F_{eff}\}^{(k)} \quad (1)$$

$$[K_{eff}] = \left( \frac{1}{\beta \Delta t^2} [M] + \frac{\gamma}{\beta \Delta t} [C] + [K] \right) \quad (2)$$

$$\{F_{eff}\} = \{F\}_{t+\Delta t} - [M]^{(k-1)} \{\ddot{U}\}_{t+\Delta t} [C]^{(k-1)} \{\dot{U}\}_{t+\Delta t} - {}^{(k-1)}\{Q\}_{t+\Delta t} \quad (3)$$

where,  $[K_{eff}]$ ,  $\{\Delta U\}$  and  $\{F_{eff}\}$  are the effective stiffness matrix, the displacement increment vector and the effective load vector,  $[M]$  and  $[C]$  are mass matrix and damping matrix,  $\{\ddot{U}\}_{t+\Delta t}$ ,  $\{\dot{U}\}_{t+\Delta t}$ ,  $\{Q\}_{t+\Delta t}$  and  $\{F\}_{t+\Delta t}$  are acceleration vector, velocity vector, internal force vector and load vector at time  $t+\Delta t$ , respectively. Upper left subscript ( $k$ ) of each term means the iteration count.

To apply the procedures of Idealized Explicit method, the following equation is assumed by adding virtual inertial term and damping term at virtual time  $\tau$  to Eq. (1).

$$[M_{dum}]\{\ddot{U}_{dum}\}_{\tau} + [C_{dum}]\{\dot{U}_{dum}\}_{\tau} + [K_{eff}]\{U_{dum}\}_{\tau} = \{F_{eff}\}_{\tau} \quad (4)$$

Discretizing Eq. (2) by the central difference and advancing the time steps until the virtual inertial term and the virtual damping term become negligibly small, that is, advancing the virtual time  $\tau$  in Eq. (4), enables the displacement vector to be obtained. The displacement vector obtained by advancing the virtual time  $\tau$  is used as a solution. By using these steps, it is expected that the same solution as that by solving Eq. (1) using the iteration method (Newton-Raphson method) can be obtained. The virtual mass matrix  $[M_{dum}]$  and the virtual damping matrix  $[C_{dum}]$  are utilized only to obtain the converged solution. The formulation of these matrices, which can reduce the number of time steps for convergence, are employed as shown in [8].

#### EQUIVALENT LOAD MODEL

A load on the collision of a shot is considered in the above dynamic elastic plastic analysis method based on IEFEM, and the analysis system of the mechanical behavior during shot peening is constructed. As shown in Fig. 1, the history of the load distribution during the collision of a shot is modeled as an equivalent load model [13], which is introduced as an external force. The equivalent load model is expressed as the product of the load distribution function defining the shape of the load distribution, and the load history function defining the amount of the colliding load as shown in the following equation:

$$P(\rho, \tau) = f(\rho, \tau) \cdot g(\tau) \quad (5)$$

where,  $\rho$ ,  $\tau$ ,  $P(\rho, \tau)$ ,  $f(\rho, \tau)$  and  $g(\tau)$  are defined as the normalized distance from the collision center, the normalized time from the beginning of collision, the load distribution history function, the load distribution function and load history function, respectively.  $\rho$  and  $\tau$  are defined as follows:

$$\rho = \frac{r}{r_0}, \quad \tau = \frac{t}{t_0} \quad (6)$$



## Mathematical Modelling of Weld Phenomena 12

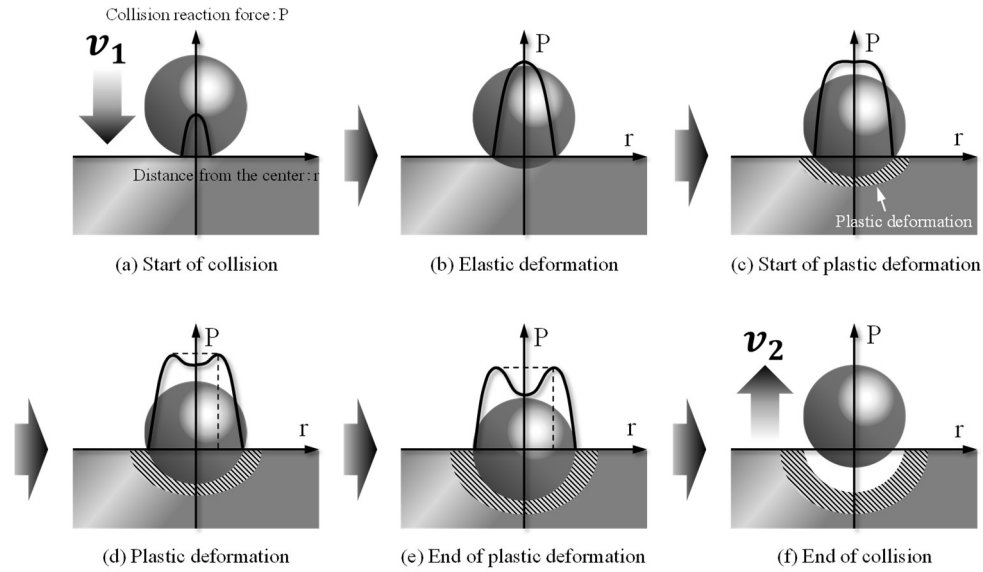


**Fig. 1** Schematic illustration of reactive force for each stage of shot collision.

where  $r$  and  $r_0$  are the distance from the collision center and the shot radius, and  $t$  and  $t_0$  are the time from the beginning of the collision and the duration of the collision, respectively. The load distribution function and the load history function are defined as the functions that can reproduce the reaction force distribution obtained by the analysis of the collision of a single shot considering contact[14].

### INDICATORS USED IN THE PROPOSED METHOD

The amount of the projected shot in shot peening is expressed by coverage in the Almen strip test. To simulate the Almen strip test, the corresponding index to the coverage in the numerical analysis is proposed. The definition formula of the coverage obtained by the experiment is shown in the following equation. The coverage means the area ratio of the shot collision area to the area of the shot collision surface. It is understood that it corresponds to the surface equivalent plastic strain ratio defined as follows;

$$Coverage = \frac{S}{A} \quad (coverage < 100\%) \quad (7)$$

Where  $A$  is the area of the target surface of shot projection and  $S$  is the area of the shot impression. After the coverage reaches 100%, the following definition is used.

$$Coverage = 100(\%) \times \frac{t}{t_{100\%}} \quad (coverage \geq 100\%) \quad (8)$$

Where  $t$  is shot projection time, and  $t_{100\%}$  is the time required for the coverage to reach 100%. Regarding the coverage, the coverage is 200% at the time when the shot projection

## Mathematical Modelling of Weld Phenomena 12

amount was doubled from the time required for the coverage of 100%, and the coverage is 300% when tripled.

Next, in order to clarify the relationship between the equivalent plastic strain on the target surface of the shot peening and the coverage in the proposed analysis system, the surface equivalent plastic strain rate  $C_v$  is defined as Eq. (9).

$$C_v = \frac{\bar{\varepsilon}_{surface}^p}{\bar{\varepsilon}_{single}^p} \quad (9)$$

$$\bar{\varepsilon}_{surface}^p = \frac{\int_{A_t} \bar{\varepsilon}^p dA}{\int_{A_t} dA} \quad (10)$$

$$\bar{\varepsilon}_{single}^p = \frac{\int_{A_s} \bar{\varepsilon}^p dS}{\int_{A_s} dA} \quad (11)$$

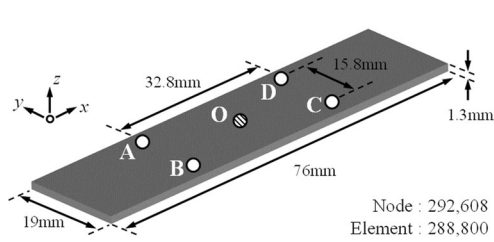
Here,  $\bar{\varepsilon}_{surface}^p$  is the average of the equivalent plastic strain on the target surface of shot peening, and  $\bar{\varepsilon}_{single}^p$  represents the average of equivalent plastic strain on the surface due to a single shot.  $A_s$  and  $A_t$  represents the impression area of a single shot and the target surface, respectively. The definition of  $C_v$  by Eqns. (9)-(11) is used for the  $C_v$  less than 1.0 (100%). For more than 1.0 of  $C_v$ ,  $C_v = t/t_{C_v=1.0}$  is used in the same way as the coverage. Here,  $t_{C_v=1.0}$  is the time required for  $C_v$  to reach 1.0.

## PERFORMANCE OF THE PROPOSED METHOD

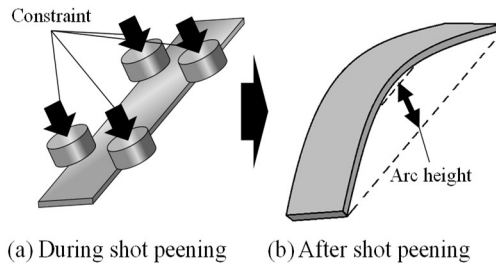
### ANALYSIS MODEL AND CONDITIONS

Figure 2 shows analysis model. The dimension of model is 76.0 mm in length, 19.0 mm in width, 1.3 mm in thickness, The model is meshed with 0.2 mm intervals in the longitudinal direction and the width direction and meshed with 0.1625mm intervals in the thickness direction. The material was assumed to be high speed steel (SKH51, JIS G4403:2006) for the specimen and SUS 304 for the shot. The material constants obtained by the tensile test is shown in Table 1. The diameter of the shot was set to 0.8mm, and the velocity of shot projection is set to be 30 mm/s. Fig. 3 shows the schematic diagram of the experimental procedure of the shot peening test using the Almen strip piece. In the analysis, shots were projected until the surface equivalent plastic strain rate  $C_v$  reached 500%. In the test using Almen strip piece, shot peening is carried out under the constraint as shown in Fig. 3.

## Mathematical Modelling of Weld Phenomena 12



**Fig. 2** Analysis model and measurement position of Arc height.



**Fig. 3** Schematic illustration of Experimental procedure of Almen strip.

**Table 1** Material constant of High-speed-steel and SUS304.

	High-speed-steel	SUS304
Density (kg/m <sup>3</sup> )	$7.92 \times 10^3$	$7.90 \times 10^3$
Young module (MPa)	201086	198500
Poisson ratio	0.300	0.294
Initial yield stress (MPa)	1450.0	288.0
Work hardning (MPa)	15485.0	1474.0

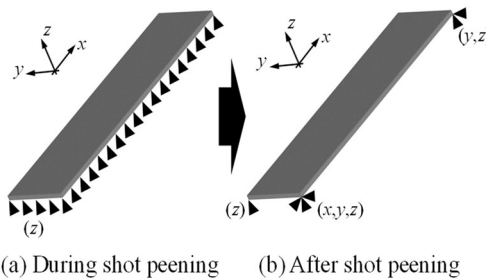


**Fig. 4** Schematic illustration of Analysis procedure of Almen strip.

After the shot peening, the constraint is released the arc height is measured. To simulate these procedures, the following procedure is adopted in the analysis. First, the analysis of shot peening is conducted under which the backside of the specimen is constrained in the out-of-plane direction during shot peening. And static analysis is conducted to determine the arc height. After that, the constraint is released. The arc height was calculated from the distance between the plane formed by points A, B, C and D and O point shown in Fig. 2.

### ANALYSIS ACCURACY

Fig. 5 shows the displacement distribution in the out-of-plane direction at the surface equivalent plastic strain rate  $C_v = 100, 300, \text{ and } 500 (\%)$ . From the figure, it can be confirmed that the displacement in the out-of-plane direction increases with the increase of the surface equivalent plastic strain rate  $C_v$ . Since the elongating plastic strain in the in-plane direction on the target surface due to the peening will cause the difference of the elongation between the back and front surface, a bending deformation in out-of-plane direction can occur. This can lead to the occurrence of the arc height.

Fig. 6 shows the relation between the arc height and the surface equivalent plastic strain rate  $C_v$  defined in analysis. The figure indicates that the increase of the arc height is large in the small  $C_v$  and that in the large  $C_v$  is small. The plastic deformation amount is small, the influence of work hardening is small because the influence of work hardening increases as the amount of plastic strain increases, Since the yield stress is also small, plastic deformation is likely to occur, but as the surface equivalent plastic strain rate  $C_v$  increases, the plastic deformation of the surface increases, so the effect of work hardening increases and the yield stress increases, so the amount of occurrence of plastic deformation becomes small, which is considered to be small. So, plastic deformation tends to occur because the

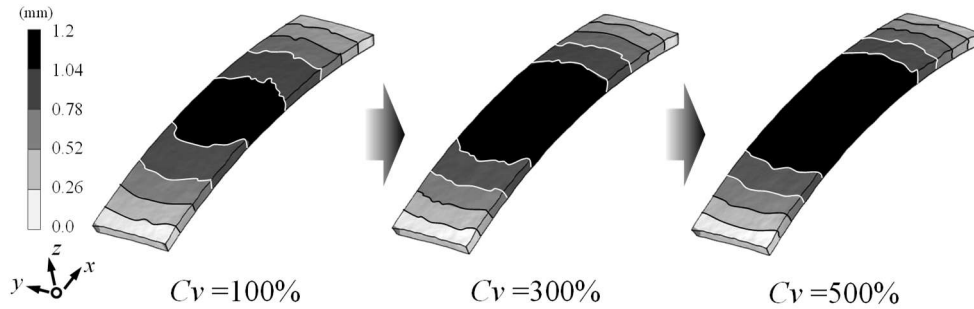


Fig. 5 Distribution of out-of plane deformation in each  $C_v$ .

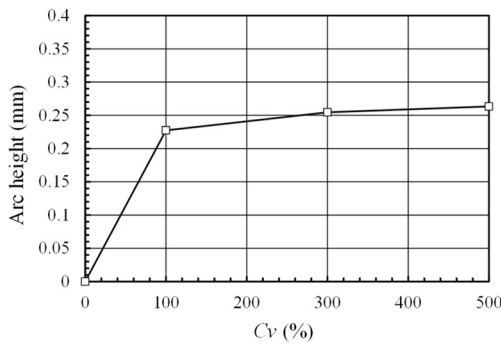


Fig. 6 Relation between  $C_v$  and Arc height by analysis.

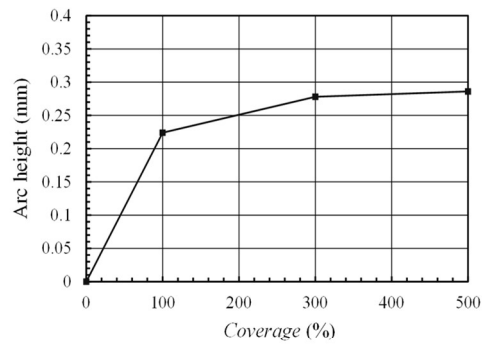


Fig. 7 Relation between coverage and Arc height by experiment.

yield stress is also small. However, as the surface equivalent plastic strain rate  $C_v$  increases, the plastic deformation of the surface increases, so the effect of work hardening increases and the yield stress increases. Therefore, it is considered that the amount of occurrence of plastic deformation becomes small.

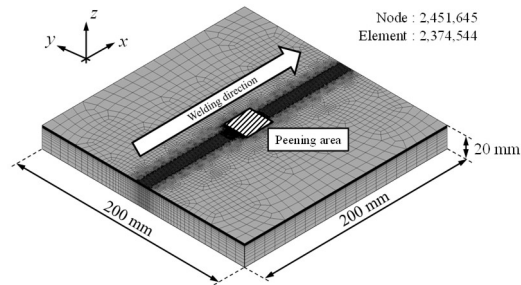
Fig. 7 shows the relation between the coverage and the arc height of the Almen strip piece obtained by the measurement. Comparing Figs. 6 and 7, it can be seen that the tendency of the arc height up to  $C_v$  and coverage are in good agreement; the increase of the arc height is large in small  $C_v$  and coverage, and that in large  $C_v$  and coverage is small. In addition, the amount of the arc height is in good agreement. As shown in the above

## Mathematical Modelling of Weld Phenomena 12

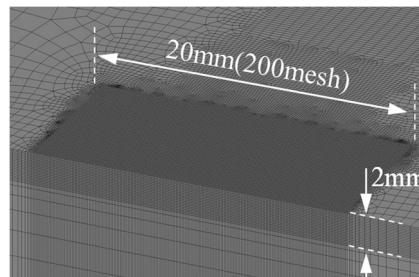
discussion, it is found that the relation between the proposed indicator  $C_v$  and the arc height can well reproduce that between the coverage and the arc height.

### APPLICATION TO BEAD-ON-PLATE JOINT

#### ANALYSIS MODEL



(a) Overall of analysis model.



(b) Zoomed view of peening area

Fig. 8 Analysis model.

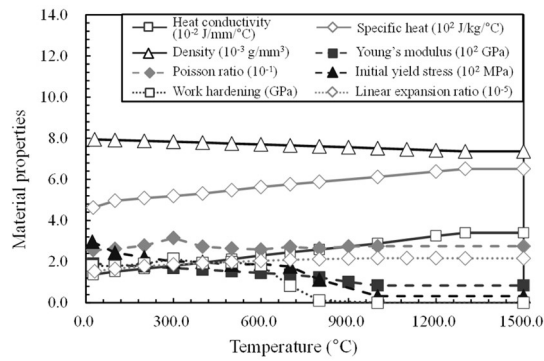


Fig. 9 Material properties of SUS316L.

In this chapter, the relaxation behavior of welding residual stress by shot peening is predicted. The proposed method is applied to the residual stress distribution of the bead-on-plate weld specimen. The analysis model is shown in Fig. 8 (a). The dimension of the model is 200mm in length, 200mm in width, 20mm in thickness. The number of nodes is 2,451,645, the number of elements is 2,374,544, and the number of degrees of freedom is 7,280,810. The material is assumed as SUS316L. The welding condition assumed in this analysis is as follows; the current is 180A, the voltage is 10V, speed is 3.33mm/s and the heat efficiency is 0.7. As shown in Fig. 8 (b), the 20 mm × 20 mm portion of the center of the model was defined as the collision area of the shot. The collision area was meshed with the interval of 0.1 mm in the welding line direction and the width direction. The assumed temperature dependence of material properties of SUS316L is shown in Fig. 9. The procedures of this analysis is as follows; first, welding residual stress is predicted using thermal elastic plastic analysis method based on IEFEM. And, the shot peening process is analyzed by the proposed analysis system and the modification of stress distribution due to shot peening is investigated. As the condition of peening, the material of the shot is assumed as SUS 304, and analysis is performed until the surface equivalent plastic strain rate  $C_v$  defined in the previous section reaches 150%.

ANALYSIS RESULTS

Figure 10 shows the residual stress distribution on the wide cross section along the welding line at the end of welding. Fig. 10 (a) shows the residual stress distribution in the direction

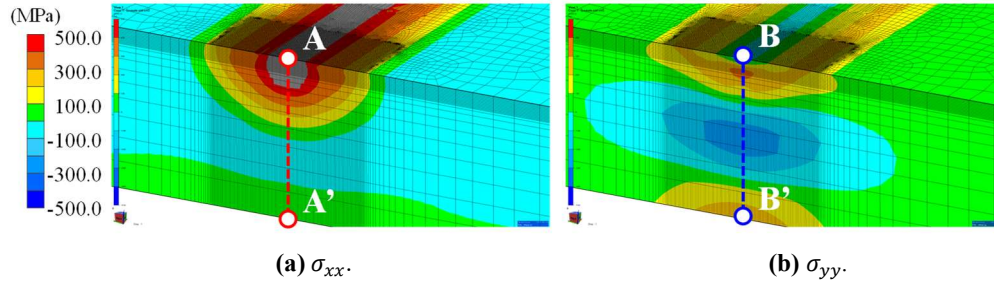


Fig. 10 Distribution of stress in  $x$  direction and  $y$  direction before peening.

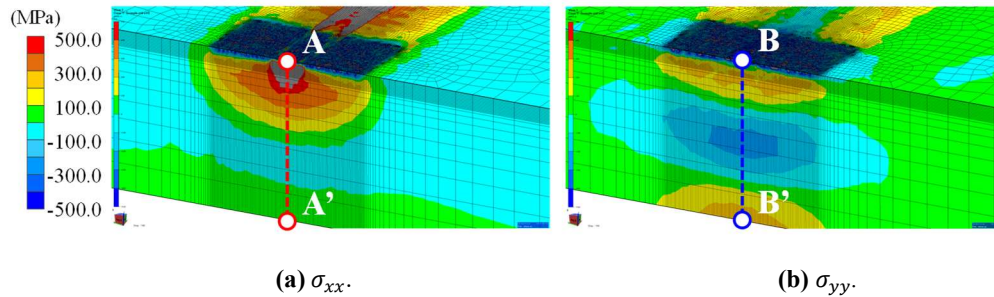
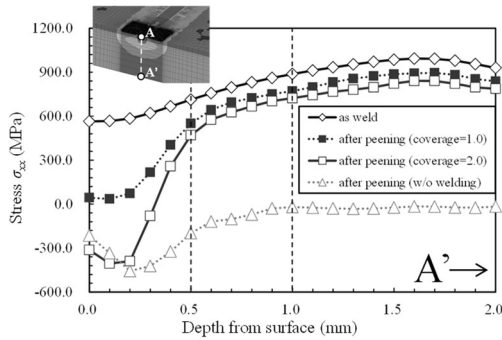


Fig. 11 Distribution of stress in  $x$  direction and  $y$  direction for after peening.

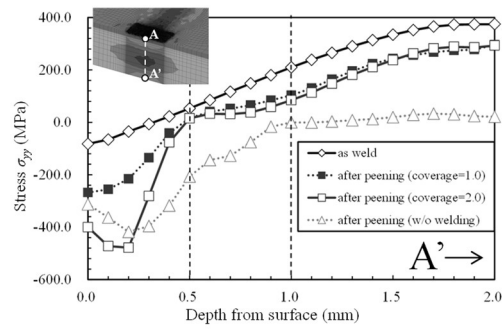
of the weld line, and Fig. 10 (b) shows the residual stress distribution in the direction perpendicular to the weld line. From Fig. 10 (a) and (b), it can be seen that strong tensile residual stress occurs particularly near the surface due to the welding. Fig. 11 shows the stress distribution after the shot peening on the same cross section as Fig. 10. Fig. 11 (a) shows the residual stress distribution in the weld line direction, and Fig. 11 (b) shows the residual stress distribution in the direction perpendicular to the weld line. From Figs. 10 and 11, it is found that the tensile residual stresses in both the welding line direction and the vertical direction to the welding line, changed to strong compressive residual stress especially on the target surface by the shot peening.

Fig. 12 shows the distribution of stress in weld line direction along line A-A'. In Fig. 12, diamonds with solid line indicates the as-weld stress. Squares with dotted line and squares with solid line show the stress in weld line direction at  $C_v=75\%$ ,  $150\%$ , respectively. In addition, triangles with dotted line shows these at  $C_v=150\%$  which considers no welding residual stress. From the figure, it is found that the difference between the stress distribution at as-weld and that at  $C_v=75\%$  is large and with the increase of coverage, the compressive

## Mathematical Modelling of Weld Phenomena 12



**Fig. 12** Distribution of residual stress in  $x$  direction for each coverage.



**Fig. 13** Distribution of residual stress in  $y$  direction for each coverage.

stress in peening region becomes larger. From the comparison of stress distribution between with and without welding residual stress at  $C_v=150\%$ , it is shown that the both stress distributions is similar in the peened region. Fig. 13 shows the distribution of stress in the vertical direction to the welding line along line A-A' in the same way as Fig. 12. From the figure, the same tendency as stress in welding direction is found: the compressive stress in the peening region becomes larger with the increase of coverage.

## CONCLUSIONS

In this research, to predict the effect of the modification of residual stress distribution due to shot peening, the authors proposed an analysis system and an indicator to quantitatively evaluation the effect of shot peening. In order to verify the validity of the proposed method, the arc height in the test using the Almen strip piece was compared by experiment and analysis. The proposed analysis system was also applied to the prediction of the modification of residual stress distribution in bead on plate model. As a result, the following results were obtained:

- From the analysis and experiment of the test using Almen strip pieces, it was confirmed that the arc height increase largely under small coverage, while the increase of arc height becomes small in large coverage both in the analysis and experiment. And it was also found that the proposed indicator  $C_v$  which corresponds to the coverage can well reproduce the relation between the coverage and the arc height.
- Shot peening to the Almen strip piece was analysed by the proposed method. As a result, it was confirmed that the arc height obtained by the experiment agrees well with those by the analysis. In addition, it was confirmed that the coverage in the experiment corresponding to each arc height and the  $C_v$  in the analysis also agree well. By using the surface equivalent plastic strain rate  $C_v$ , we confirmed that it can be arranged like the coverage obtained by the experiment.
- To analyse change due to shot peening of weld residual stress distribution, Idealized Explicit method FEM was applied to the analysis of residual stress at



bead on plate and applied development method to the obtained residual stress distribution. As a result, it was confirmed that there was a difference in stress change between  $C_v=75\%$  and  $150\%$ . The number of elements, the number of nodes and degrees of freedom of the model used for the above analysis were 2,374,544, 2,451,645, and 7,280,810 respectively.

### REFERENCES

- [1] A. OHTA, N. SUZUKI, Y. MAEDA: Unique fatigue threshold and growth properties of welded joints in a tensile residual stress field, *International Journal of Fatigue*, Vol.19, No.93 (1997), pp.303-310.
- [2] P. A. DESCHÈNES, J. LANTEIGNE, Y. VERREMAN, D. PAQUET, J. B. LÉVESQUE, M. BROCHU: A new experimental method to study the influence of welding residual stresses on fatigue crack propagation, *International Journal of Fatigue*, Vol.100, No.1 (2017), pp.444-452.
- [3] Z. LU, L. SHI, S. ZHU, Z. TANG, Y. JIANG: Effect of high energy shot peening pressure on the stress corrosion cracking of the weld joint of 304 austenitic stainless steel, *Materials Science and Engineering*, Vol.637, No.18 (2015), pp.170-174.
- [4] S. BAGHERIFARD, R. GHELICHI, M. GUAGLIANO: On the shot peening surface coverage and its assessment by means of finite element simulation: a critical review and some original developments, *Applied Surface Science*, Vol.259 (2012), pp.186-194.
- [5] Y. SANO, N. MUKAI, K. OKAZAKI, M. OBATA: Residual stress improvement in metal surface by underwater laser irradiation, *Nuclear Instruments and Methods in Physics Research Section B*, Vol.121 (1997), pp.432-436.
- [6] H. SOYAMA, O. TAKAKUWA: Enhancing the aggressive strength of a cavitating jet and its practical application, *Journal of Fluid Science and Technology*, Vol.6, No.4 (2011), pp.510-521.
- [7] J. SAKAMOTO, Y. LEE, S. CHEONG: Effect of surface flaw on fatigue strength of shot-peened medium-carbon steel, *Journal of Engineering Fracture Mechanics*, Vol. 133(2015), pp.99-111.
- [8] A. TELANG, A.S.GILL, S. TEYSSEYRE, S. R. MANNAVA, D. QIAN, V. K. VASUDEVAN: Effects of laser shock peening on SCC behavior of Alloy 600 in tetrathionate solution, *Journal of Collision Science*, Vol. 90(2015), pp.434-444 .
- [9] M. KLEMENZ, V. SCHULZE, I. ROHR, D. LOHE: Application of the FEM for the prediction of the surface layer characteristics after shot peening, *Journal of Materials Processing Technology*, Vol.209 (2009), pp.4093-4102.
- [10] M. KLEMENZ, V. SCHULZE, I. ROHR, D. LOHE: Application of the FEM for the prediction of the surface layer characteristics after shot peening, *Journal of Materials Processing Technology*, Vol.209 (2009), pp.4093-4102.
- [11] B. BHUVARAGHAN, S. M. SRINIVASAN, B. MAFFEO, R. D. MCCLAIN, Y. POTDAR, O. PRAKASH: Shot peening simulation using discrete and finite element method, *Advances in Engineering Software*, Vol.41 (2010), pp.1266-1276.
- [12] K. IKUSHIMA AND M. SHIBAHARA: Prediction of residual stresses in multi-pass welded joint using Idealized Explicit FEM accelerated by a GPU, *Computational Materials Science*, Vol.93 (2014), pp.62-67.
- [13] M. SHIBAHARA, H. SERIZAWA AND H. MURAKAWA: Finite element method for hot cracking using interface element (3rd report) - development of static-dynamic hybrid method, *Journal of Kansai Society of naval Architects Japan*, No.235 (2001), pp.161-169.
- [14] K. IKUSHIMA, M. SHIBAHARA, K. AKITA, H. SUZUKI, S. MOROOKA, S. NISHIKAWA, T. FURUKAWA: Numerical analysis of residual stress distribution on peening process, *Welding in the World*, VOL.61, No.3 (2017), pp.517-527.

## Mathematical Modelling of Weld Phenomena 12

- [15] O. UNAL: Optimization of shot peening parameters by response surface methodology, *Journal of Surface & Coatings Technology*, Vol. 305(2016), pp.99-109



# LASER BEAM WELDING OF STEEL- ALUMINUM JOINTS - INFLUENCE OF WELD METAL ELASTIC-PLASTIC PROPERTIES ON THE DISTORTIONS

A. EVDOKIMOV\*, R. OSSENBRINK\*, N. DOYNOV\* and  
V. MICHAILOV\*

*\*Brandenburg University of Technology Cottbus-Senftenberg*

*DOI 10.3217/978-3-85125-615-4-24*

## ABSTRACT

Great attention is focused nowadays on laser welding of dissimilar steel-aluminum joints in overlap configuration in key-hole mode. It was found that elastic-plastic properties of the weld metal exhibit strong difference to those of the base alloys and can be defined as a function of aluminum content in the weld metal. A developed Finite-Element simulation model allows prediction of the aluminum content as a function of welding parameters and subsequently the elastic-plastic properties of the weld metal as a function of the determined content. The main goal of the present study is to show the impact of the weld metal properties on welding distortions and residual stresses. For that purpose, a sensitivity analysis of the thermomechanical model was performed, where the distortions and residual stresses were computed as a function of welding parameters and therefore as a function of corresponding weld metal properties. The analysis showed that the influence of the weld metal is essential, and its properties should be taken into consideration in the models for better prediction accuracy.

Keywords: Laser welding, FEM, Distortions, Residual stresses, Dissimilar welding

## INTRODUCTION

The application of hybrid lightweight structures, which possess good mechanical properties and lower weight, offers enormous technical and economic potential. Combinations of aluminum and steel are particularly interesting for modern lightweight design concepts. The joining of dissimilar metals within hybrid structures is still a challenging task.

Lately, the attention of researchers has been attached to the thermal joining processes such as brazing–welding–brazing [1], laser welding in conduction mode [2] and key-hole laser welding [3–6] of St-Al joints. In this work the keyhole laser welding is considered. In works [3–9] the researchers concentrated mainly on optimization of the welding parameters to increase the global tensile strength of the joints and on an investigation of the weld quality with respect to the formation of Fe–Al intermetallic compounds. It was found that the intermetallic phases at the weld – aluminum boundary is the weak spot of the joint

which causes the fracture under subsequent loading. However intermetallic phases are formed on a micro level and therefore they do not affect another important issue such as distortions and residual stresses after welding.

It has been found that besides the formation of the IMC phases on the weld – aluminum boundary, the mechanical properties of the dissimilar weld metal itself undergo significant changes and differ strongly from properties of the both participating base metals. The authors [3–6] confirmed a strong increase in hardness and related this to the aluminum concentration in the weld. In the work [10] the weld metal was investigated with respect to its basic mechanical properties such as Young’s modulus, yield stress, and strain hardening exponent. It was revealed that the yield stress of the mixed weld metal is significantly higher than the yield stress of the participating base alloys, however, Young’s modulus and strain hardening exponent vary slightly with and remain almost on the same value as those of the steel. The weld dimensions are on the macro level and the strong changes in the mechanical properties of the weld metal can affect the overall behavior of the joint with respect to distortions and residual stresses. The method proposed in [10] for determination of the weld metal mechanical properties is time-consuming and required special equipment. Since mechanical properties of the mixed steel – aluminum weld metal can’t be quickly determined, the following aspect becomes important for the welding FE simulation models. It is necessary to investigate how the change in the mechanical properties due to the mixing of liquid steel and liquid aluminum in the weld pool affects the distortions and residual stresses after welding.

Therefore, the main goal of the present study is to show the impact of the dissimilar weld metal and its mechanical properties on a calculation of welding distortions and residual stresses. First, the comparison between the distortions and residual stresses calculated with and without consideration of the change in the weld metal mechanical properties was performed. Second, the influence of the basic mechanical properties and their variations on the distortions was demonstrated by performing the full factorial sensitivity analysis.

### VALIDATION OF THE FE MODEL

#### EXPERIMENTAL SETUP

Prior to the sensitivity analysis, the developed simulation model was validated. The validation took place on geometrically simple components. Instrumented laser beam welding of two metal sheets in steel on aluminum overlap configuration served as an initial set up (Fig. 1). The sheets for the trials were austenitic steel X5CrNi18-10 (1.4301) with 1.5 mm sheet thickness and hardenable 6082-T6 Al alloy of the same thickness. The sheets were fixed on both sides by the clamping claws so that the optical access to the lower surface for the displacements measurements was available. The displacements of the sheets were determined optically, based on stochastically distributed gray value patterns on the underside of the sample. No special pre-processing of the welding surfaces was done prior to the joining.

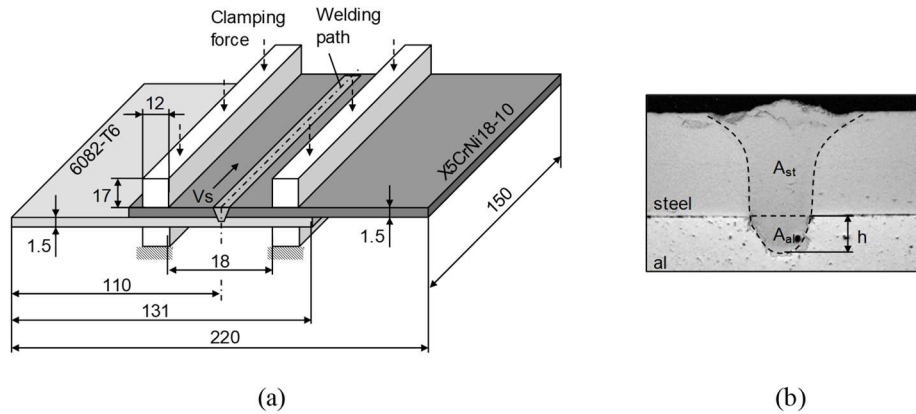
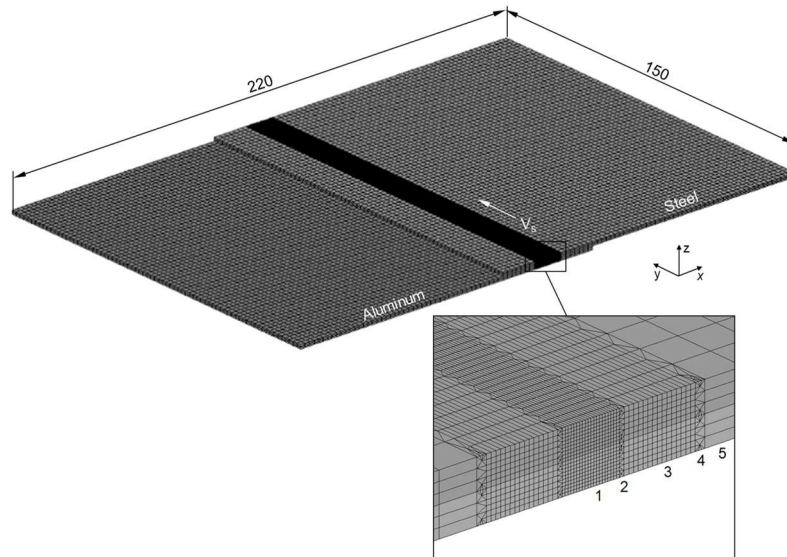


Fig. 1 Scheme of the welding (a), typical St-Al joint (b)

A disk laser was applied for the welding. The welding parameters were experimentally determined to obtain defect-free joint. The final parameters were set to laser power  $P = 3,75$  kW, welding velocity  $V_s = 4,8$  m/min. The selected welding parameters lead to stable process conditions. Two welding trials were performed in cooperation with Laser Zentrum Hannover e.V. (LZH). The cross section of the St-Al joint is shown in Fig. 1.  $h$  is the weld penetration depth, the ratio  $A_{st}/A_{al}$  defines the dilution.

#### FE MODEL

For the lap joints, the complete geometry of the plates must be considered, as there is no symmetry due to the different material properties and asymmetric configuration of the plates relative to the welding line. The meshing strategy is shown in Fig. 2. A coarse mesh was adopted for the region far from the weld area. The element type for thermal process analysis with FE-Code ANSYS® is the eight-node hexahedral element SOLID70 and the four-node surface contact elements CONTA 173 and TARGET 170 for modeling the overlap region (thermal and mechanical contact). The full model consists of approximately 210 000 nodes and 240 000 elements. Element size lengths in zone 1:  $0.15 \times 0.5 \times 0.15$ , in area 3:  $0.25 \times 1 \times 0.25$  and in the range 5:  $2 \times 2 \times 0.5$  mm. The transition areas 2 and 4 consists of pyramidal elements. The meshing strategy allows to save a CPU time, achieve high accuracy and get rid of bad shaped elements, which can be a source of the unconverged solution during the thermomechanical simulations. The material thermophysical properties can be found elsewhere [11]. The change in thermophysical properties of the weld metal due to the mixing in the weld pool was not considered for the thermal simulation. The heat losses into the ambient were considered as the heat exchange through convection and radiation under the assumption of distinct film coefficients for steel and aluminum. The special thermal contact between the plates was defined. With regard to details about the thermal model, readers can refer to [12].



**Fig. 2** Meshing of the FE model.

For the thermomechanical simulation, the ideal elastic plastic material model for steel, aluminum and weld metal was implemented. The steel and aluminum alloys were extensively examined in the work [11]. The properties of the dissimilar steel – aluminum welds were determined in the work [10]. The softening of the steel and aluminum in heat affected zone were considered as a function of maximal temperatures. The hardening of the weld metal due to the mixing was implemented as a function of the average aluminum concentration in the weld, which is calculated automatically after the temperature simulation, based on the ratio of melted steel and aluminum elements. The research [10] showed that the aluminum concentration and mechanical properties within the weld metal are quite homogeneous. Therefore, for the simulation, the homogeneous weld metal material model was assumed. The properties of the weld metal were taken from the study [10]. Yield stress  $\sigma = 950$  MPa, Young's modulus  $E = 200$  GPa. For the thermal expansion coefficient, a linear mixture is assumed, derived from the area fraction values presented in Fig. 1. The thermal expansion coefficient of the weld metal was assumed as a linear mixture, derived from the area fraction values. The user subroutine for an accurate description of the materials properties was implemented directly into the ANSYS code. Modeling of the clamping jaws and contact conditions between them and the sheets brings additional complexity to the model. It requires more computational time and often results in convergence problems. To avoid application of the contact elements the influence of the jaws was approximated with the spring elements. The nodes which belong to the area of contact between the jaws and the sheets, get the non-linear spring elements. The springs act in plane of the sheets and representing the friction forces. On the upper side the normal forces to these nodes represent the clamping force. On the underside the displacement on the nodes is blocked. The mechanical contact between plates was set to exclude the penetration of the sheets. The bonding temperature was set to the melting temperature of the aluminum alloy.

Transversal shrinkage ( $X$ ), longitudinal shrinkage ( $Y_{st}$ ,  $Y_{al}$ ) and out of plane distortion ( $Z_{st}$ ,  $Z_{al}$ ) (Fig. 3) were calculated and compared to the measured values. The results are summarized in Table 1. According to Table 1, the calculated and measured transverse and longitudinal shrinkage is in an excellent agreement. The deviation between the calculated and measured out of plane distortions  $Z_{st}$  and  $Z_{al}$  arise possibly due to the approximation of the jaws by the normal forces acting at nodes. It should be noted that the measured and calculated displacements are very small, and therefore some deviations can arise due to the inaccuracies of the measurements. In general, it can be concluded that the developed model allows the correct prediction of the distortions after welding.

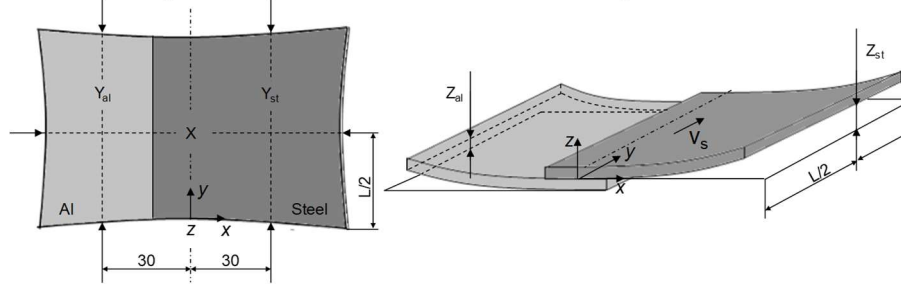


Fig. 3 Distortions of the lap joint.  $L$  is the length of the sheets.

Table 1 Validation of the model. Calculated and measured distortions (in mm)

Distortions (Fig. )	P= 3,75 kW, $V_s = 4,8$ m/min		
	Exp 1	Exp 2	FEM
Transverse shrinkage $X$	-0.04	-0.057	-0.0474
Longitudinal shrinkage of steel $Y_{st}$	-0.02	-0.01	-0.0187
Longitudinal shrinkage of aluminum $Y_{al}$	-0.03	-0.031	-0.027
Out of plane distortion of steel $Z_{st}$	0.25	0.32	0.45
Out of plane distortion of aluminum $Z_{al}$	0.44	0.54	0.78

### SENSITIVITY ANALYSIS

Sensitivity analysis aims to describe how much model output values are affected by changes in model input values. In this study the mechanical properties of the dissimilar steel – aluminum weld metal serve as the input parameters and the distortions as output responses. A full factorial design was chosen in the current work for the sensitivity study. Such an experiment allows the investigator to study the effect of each factor, as well as the effects of interactions between factors on the response variable. From the CPU point of view, the model was reduced to 50 mm in length (Fig. 4). For the sensitivity analysis, the longitudinal shrinkage  $Y_{st}$  and  $Y_{al}$  differ from the ones shown in Fig. 3.  $Y_{st}$  is the shrinkage along the welding line on the top and  $Y_{al}$  along the welding line on the bottom (Fig. 4). Transverse shrinkage  $X$  and out of plane distortions  $Z_{st}$  and  $Z_{al}$  are the same as presented in Fig. .



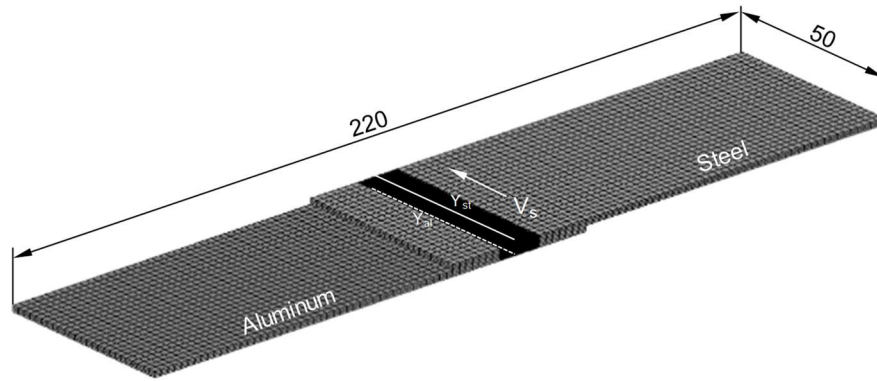


**Fig. 4** Reduced model for the sensitivity analysis.

The first step of the sensitivity analysis involves an identification of the important input variables and their suitable working range. Due to the ideal elastic plastic material model assumed for the simulation, the strain hardening exponent plays no role. The following parameters were considered as input parameters: yield stress  $\sigma_y$ , thermal strain coefficient  $\alpha$  and Young's modulus  $E$ . The input parameters were divided into discrete levels. The upper limit of a factor was coded as +1, the lower one was coded as -1. Simulation runs are made for all combinations of parameter levels. In the current study, three input parameters gives 8 simulations to be performed. The input parameters with their coded levels as well as the assumed properties of the real weld are listed in Table . The lower and upper values of the yield stress and Young's modulus were chosen based on the estimated accuracy of the indentation technique for the determination of the mechanical properties of the weld [10]. The lower level for the thermal expansion coefficient was chosen as the one of the steel and the upper limit was chosen as for the weld metal containing twice more aluminum than the real weld. A full factorial design contains all possible combinations of low/high levels for all the factors (Table 4).

**Table 2** Summary of the input parameters and their levels

Input variables	Code levels		Assumed properties of the real weld
	-1	+1	
Yield stress, MPa	800	1100	946
Thermal expansion coefficient, $10^6 k^{-1}$	18.3	19.9	19.12
Young's modulus, GPa	180	220	200

## RESULTS AND DISCUSSIONS

In Table 3 the calculated distortions with consideration of the weld metal mechanical properties (computation 1) is compared to the calculated ones, where the properties of the steel were assigned to the weld metal (computation 2). In brackets, the deviation from the reference value is shown for each type of distortion. The reference value implies the distortion when the mechanical properties of the weld are considered (computation 1). It is

obvious from Table 3, that the most affected response values (compared to the reference) are the longitudinal shrinkage  $Y_{st}$  and  $Y_{al}$ . However, it is important to note that the absolute values are extremely low. The relative deviation of the out of plane distortion  $Z_{st}$  and  $Z_{al}$  from the reference value is less, however, the absolute difference is higher and therefore this deviation can be crucial if the dimensions of the structure become larger. The results indicate that the implementation of the additional material model for the weld metal is important with respect to the distortions after welding and can't be neglected or approximated by assuming the properties of steel for the weld metal.

**Table 3** Comparison of the distortions calculated with and without consideration of the weld material model

Computation	Input parameters			Response values (in mm)				
	$\sigma$	$\alpha$	E	X	$Y_{st}$	$Y_{al}$	$Z_{st}$	$Z_{al}$
Weld model included (1)	946	19.12	200	-0.0430	-0.0126	-0.0167	0.537	0.712
Weld model excluded (2)	265	18.3	200	-0.0428 (-0.5 %)	-0.00887 (-29.6 %)	-0.00989 (-40.7 %)	0.566 (+5.4%)	0.72 (+1.1 %)

The distribution of the residual stresses along the path at the upper surface of the joint is shown in Fig. 5. It is clearly indicated that the higher stress concentration exists in the weld, especially the longitudinal stresses when the weld metal material model is included. The distribution of the residual stresses along the path at the bottom surface is presented in Fig. 6. The difference between computed residual stresses is not significant since the path does not cross the weld metal.

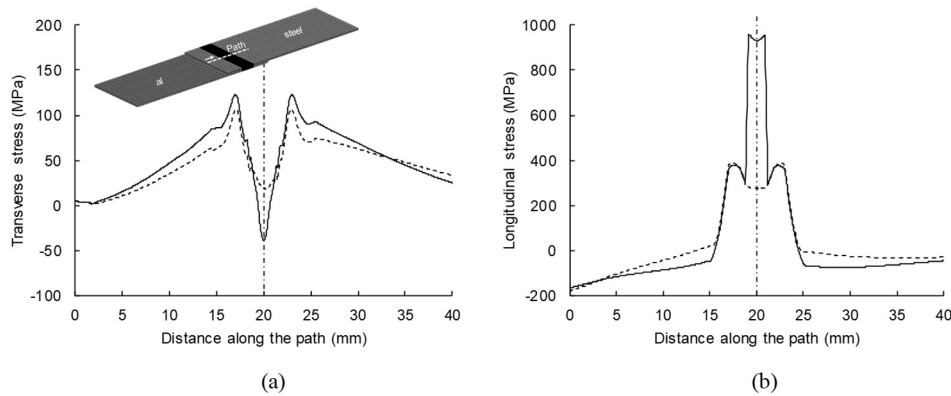


**Fig. 5** Stress distribution along the path at the top: transverse stress (a), longitudinal stress (b). Full lines correspond to the stress computed with the weld material model and the dashed lines without weld model.

## Mathematical Modelling of Weld Phenomena 12

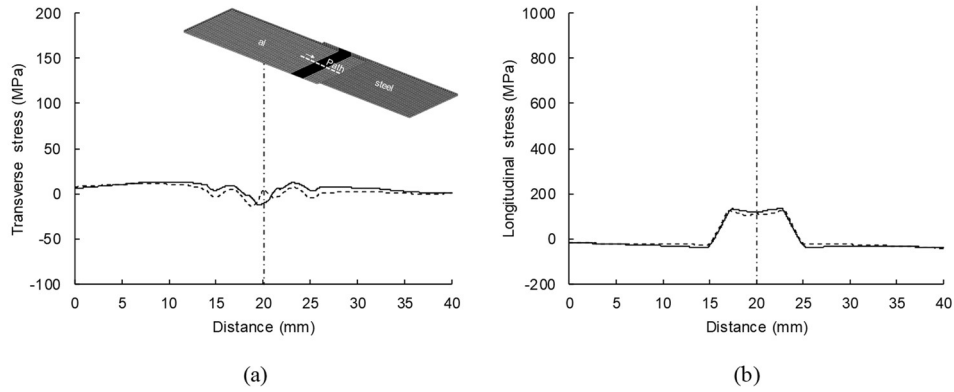


**Fig. 6** Stress distribution along the path at the bottom: transverse stress (a), longitudinal stress (b). Full lines correspond to the stress computed with the weld material model and the dashed lines without weld model.

The results of the sensitivity analysis are presented in Table 4. The analysis of the relations between input variables and transverse shrinkage  $X$  shows that the thermal expansion coefficient had the most significant effect; the yield stress had less effect; Young's modulus had the least effect and basically, the variation of this parameter within the defined boundaries does not affect the transverse shrinkage. For the longitudinal shrinkage  $Y_{st}$ , the analysis shows that the yield stress is the most significant parameter; the thermal expansion coefficient is less important; the change in the Young modulus can be neglected.

**Table 4** Results of the sensitivity analysis

#	Input parameters			Response values (in mm)				
	$\sigma$	$\alpha$	E	X	$Y_{st}$	$Y_{al}$	$Z_{st}$	$Z_{al}$
1	-1	-1	-1	-0.0426	-0.0088	-0.0160	0.540	0.724
2	-1	-1	+1	-0.0428	-0.00876	-0.0159	0.535	0.728
3	-1	+1	-1	-0.0477	-0.00671	-0.0158	0.587	0.768
4	-1	+1	+1	-0.0449	-0.00666	-0.0158	0.578	0.774
5	+1	-1	-1	-0.0411	-0.0186	-0.0170	0.504	0.654
6	+1	-1	+1	-0.0413	-0.0185	-0.0173	0.490	0.658
7	+1	+1	-1	-0.0432	-0.0165	-0.0170	0.545	0.697
8	+1	+1	+1	-0.0434	-0.0165	-0.0173	0.529	0.700

For the longitudinal shrinkage  $Y_{al}$ , the most significant parameters are the yield stress and the interaction of the yield stress and Young's modulus; Young's modulus itself and especially the thermal expansion coefficient of the weld metal do not affect the shrinkage  $Y_{al}$ . The out of plane distortions of the steel  $Z_{st}$  and aluminum  $Z_{al}$  sheets are affected mostly by the changes in the yield stress and thermal expansion coefficient; Young's modulus had less effect. Considering the distortions  $Z_{st}$  and  $Z_{al}$  the following observations can be made. In the dissimilar steel – aluminum lap joints, the increase in the yield stress of the weld

metal leads to the decrease of the distortions  $Z_{st}$  and  $Z_{at}$ . The increase of the thermal expansion coefficient of the weld metal results in the increase of the distortions. According to the obtained results, the calculation of the distortions is sensitive to the variations of the input parameters within the defined boundaries.

### CONCLUSION

In this study, the influence of the mechanical properties of the dissimilar steel – aluminum weld metal on the residual stresses and distortions after welding was analyzed. The following conclusions can be drawn:

- The change in the weld metal mechanical properties due to the mixing in the weld pool significantly affects the distortions and residual stresses after welding. The additional material model for the weld metal should be implemented in the simulations for a more accurate prediction.
- The distortions are sensitive to variations of the yield stress and the thermal expansion coefficient and less sensitive to variations of Young's modulus of the weld metal. Therefore, the accurate determination of yield stress and thermal expansion coefficient prior to simulation is necessary and Young's modulus can be approximated as those of steel.

### ACKNOWLEDGEMENT

This research has been funded by the German Federal Ministry of Education and Research in the Framework of the Photonic Research Germany under grant no. 13N12877.

### REFERENCES

- [1] J. LIU, S. JIANG, Y. SHI, Y. KUANG, G. HUANG, H. ZHANG: Laser fusion-brazing of aluminum alloy to galvanized steel with pure Al filler powder, *Opt. Laser Technol.* 66 (2015) 1–8. doi:10.1016/j.optlastec.2014.08.004.
- [2] S. MECO, L. COZZOLINO, S. GANGULY, S. WILLIAMS, N. MCPHERSON: Laser welding of steel to aluminium: Thermal modelling and joint strength analysis, *J. Mater. Process. Technol.* 247 (2017) 121–133. doi:10.1016/j.jmatprotec.2017.04.002.
- [3] G. SIERRA, P. PEYRE, F. DESCHAUX-BEAUME, D. STUART, G. FRAS: Steel to aluminium key-hole laser welding, *Mater. Sci. Eng. A.* 447 (2007) 197–208. doi:10.1016/j.msea.2006.10.106.
- [4] M.J. TORKAMANY, S. TAHAMTAN, J. SABBAGHZADEH: Dissimilar welding of carbon steel to 5754 aluminum alloy by Nd: YAG pulsed laser, *Mater. Des.* 31 (2010) 458–465. doi:10.1016/j.matdes.2009.05.046.
- [5] J. MA, M. HAROONI, B. CARLSON, R. KOVACEVIC: Dissimilar joining of galvanized high-strength steel to aluminum alloy in a zero-gap lap joint configuration by two-pass laser welding, *Mater. Des.* 58 (2014) 390–401. doi:10.1016/j.matdes.2014.01.046.
- [6] A. KOUADRI-DAVID: Study of metallurgic and mechanical properties of laser welded heterogeneous joints between DP600 galvanised steel and aluminium 6082, *Mater. Des.* 54

- (2014) 184–195. doi:10.1016/j.matdes.2013.07.093.
- [7] M.A. EZAZI, F. YUSOF, A.A.D. SARHAN, M.H.A. SHUKOR, M. FADZIL: Employment of fiber laser technology to weld austenitic stainless steel 304l with aluminum alloy 5083 using pre-placed activating flux, *Mater. Des.* 87 (2015) 105–123. doi:10.1016/j.matdes.2015.08.014.
- [8] J. YANG, Y.L. LI, H. ZHANG: Microstructure and mechanical properties of pulsed laser welded Al/steel dissimilar joint, *Trans. Nonferrous Met. Soc. China (English Ed.* 26 (2016) 994–1002. doi:10.1016/S1003-6326(16)64196-1.
- [9] L. CUI, B. CHEN, L. CHEN, D. HE: Dual beam laser keyhole welding of steel/aluminum lapped joints, *J. Mater. Process. Technol.* 256 (2018) 87–97. doi:10.1016/j.jmatprotec.2018.02.016.
- [10] A. EVDOKIMOV, A. OBROSOV, R. OSSENBRINK, S. WEIß, V. MICHAILOV: Mechanical Properties of Dissimilar Steel-Aluminum Welds, *Mater. Sci. Eng. A.* 722 (2018) 242–254. doi:10.1016/j.msea.2018.03.019.
- [11] R.O. ANTON EVDOKIMOV, KATRIN SPRINGER: *Simulationsmodelle für das 3D-Laserstrahlschweißen von Stahl/Aluminium Mischverbindungen*, 2018.
- [12] A. EVDOKIMOV, K. SPRINGER, N. DOYNOV, R. OSSENBRINK, V. MICHAILOV: Heat source model for laser beam welding of steel-aluminum lap joints, *Int. J. Adv. Manuf. Technol.* (2017). doi:10.1007/s00170-017-0569-6.

# **IV Cracking Phenomena and Hydrogen Effects**

*intentionally blank page*

*intentionally blank page*



*intentionally blank page*

*intentionally blank page*

*intentionally blank page*

*intentionally blank page*

*intentionally blank page*

*intentionally blank page*

*intentionally blank page*

*intentionally blank page*



*intentionally blank page*

*intentionally blank page*

*intentionally blank page*

*intentionally blank page*

*intentionally blank page*

*intentionally blank page*

*intentionally blank page*

*intentionally blank page*



*intentionally blank page*

*intentionally blank page*

*intentionally blank page*

*intentionally blank page*

*intentionally blank page*

# STUDY OF SOLIDIFICATION CRACKING IN ADVANCED HIGH STRENGTH AUTOMOTIVE STEELS

G. AGARWAL\*, H. GAO\*\*, M. AMIRTHALINGAM\*\*\*,  
I. M. RICHARDSON\* and M. J. M. HERMANS\*

\*Department of Materials Science and Engineering, Faculty of 3mE, Delft University of Technology, Mekelweg 2, 2628CD Delft, The Netherlands, G.Agarwal@tudelft.nl, I.M.Richardson@tudelft.nl, M.J.M.Hermans@tudelft.nl

\*\*Tata Steel, P.O. Box 10000, 1970 CA IJmuiden, The Netherlands, He.Gao@tatasteelurope.com

\*\*\*Department of Metallurgical and Materials Engineering, Indian Institute of Technology Madras, Chennai 600036, India, murugaiyan@iitm.ac.in

DOI 10.3217/978-3-85125-615-4-25

## ABSTRACT

Advanced high-strength steels (AHSS), which are increasingly used in the automotive industry, meet many functional requirements such as high strength and crash resistance. Some of these steels contain high amounts of alloying elements, which are required to achieve the necessary mechanical properties, but render these steels susceptible to weld solidification cracking. Weld solidification cracking results from the complex interplay between mechanical and metallurgical factors. Our recent work is focused on studying solidification cracking in dual phase (DP) and transformation induced plasticity (TRIP) steels using the following modeling and experimental strategies:

1. A finite element (FE) based model was constructed to simulate the dynamic thermal and mechanical conditions that prevail during bead-on-plate laser welding. To vary the restraint, laser welding was carried out on single sided clamped specimens at increasing distances from the free edge. In TRIP steel sheets, solidification cracking was observed when welding was carried out close to the free edge and at a certain minimum distance, no cracking was observed. For the no cracking condition, *in situ* strain evolution during laser welding was measured by means of digital image correlation to validate the strain from the FE-model. Subsequently, a phase field model was constructed using the validated thermal cycles from the FE-model to simulate the microstructural evolution at the tail of a weld pool, where primary dendrites coalesce at the weld centerline. From the phase field model, elemental segregation and stress concentration are used to explain the cracking susceptibility in TRIP and DP steels. For DP steel, both the experimental and modeling results indicate a higher resistance to solidification cracking.

2. A phase field model was constructed to simulate the directional solidification in TRIP and DP steels. The thermal cycle and temperature gradient were derived from the *in-situ* solidification experiments conducted using high temperature laser scanning confocal microscopy (HTLSCM). The model showed that longer and narrower interdendritic liquid channels exist in the case of TRIP steel. For the TRIP steel, both the phase field model and atom probe tomography revealed notable enrichment of phosphorus, which leads to a severe undercooling in the interdendritic region. In the presence of tensile stress, an opening at the interdendritic region is difficult to fill with the remaining liquid due to low permeability, resulting in solidification cracking.

The overall study shows that a combination of factors is responsible for the susceptibility of a material to solidification cracking. These include particularly mechanical restraint, solidification temperature range, solidification morphology, solute segregation and liquid feeding capability.

Keywords: Solidification Cracking, Hot Cracking, Steel, Laser Welding, Automotive, Advanced high strength steels (AHSS)

INTRODUCTION

The CO<sub>2</sub> emission regulation of passenger vehicles has become stringent in the last two decades and the target emission between 2020-2025 seems to converge globally [1] as can be seen in figure 1. One of the fundamental ways to achieve this target in the automotive industry is to reduce the overall weight of the vehicle. Naturally, reduction of weight should not compromise the vehicle performance and passenger safety. To meet this demand, new steels under the umbrella, Advanced High Strength Steels (AHSS) are being increasingly developed and put into use. These steels comprise on an average, 30-35 % of a typical car body (body in white) weight [2] and possess high strength, ductility and toughness. The increased strength and ductility allows the use of thinner gauge steels thus reducing the vehicle weight. AHSS are used in chassis components, B-pillars, crash boxes, engine cradles etc. [3].

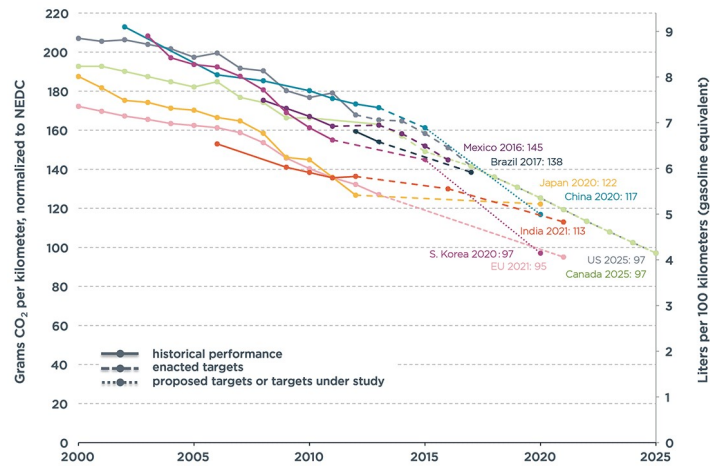


**Fig. 1** Passenger car CO<sub>2</sub> emission standard and fuel consumption, normalized to New European Driving Cycle (NEDC). The figure also indicates the proposed emission standard of various countries [1].

Apart from formability requirements in these steels, weldability of such steels is an important aspect. The higher content of alloying elements in some of the AHSS, required for achieving necessary mechanical properties, render them susceptible to solidification cracking during welding. Solidification cracking, also known as hot tearing or hot cracking in casting, occurs due to a complex interplay between mechanical and metallurgical conditions, that are generated during the weld thermal cycle. During weld metal solidification, columnar grains grow perpendicular to the fusion boundary since the temperature gradient here is at its steepest and accordingly the heat extraction is maximised. The solidifying dendrites meet at the weld centreline. The solidifying weld metal shrinks due to solidification shrinkage and thermal contraction. As solidification progresses, the

solid in the mushy zone begins to form a rigid network, *i.e.*, tensile strain is induced. If the deformation exceeds a certain threshold, separation of the dendrites at the grain boundary can occur. At the terminal stage of solidification, such an opening cannot be compensated by the remaining liquid due to both low permeability and high solid fraction [3–4]. As a result, solidification cracking occurs. Eskin *et al.* [6] in their review paper, elaborated existing hot tearing theories and models. These models are based on the existence of a critical stress, critical strain or critical strain rate criterion that leads to cracking. Katgerman [7] in his mathematical model considered stresses and insufficient feeding in the vulnerable temperature range to be the cause of hot cracking. Recent physical models from Rappaz *et al.* [8] and Kou [9] indicate that in the presence of local deformation, insufficient liquid feeding in the interdendritic or intergranular region results in cracking. Experiments by Coniglio *et al.* [10] also indicate that the presence of a critical strain rate is responsible for cracking. The mechanism of solidification cracking is still not properly understood [11], particularly experiments or models focussing on determining the physical mechanism leading to the separation of grains are lacking.

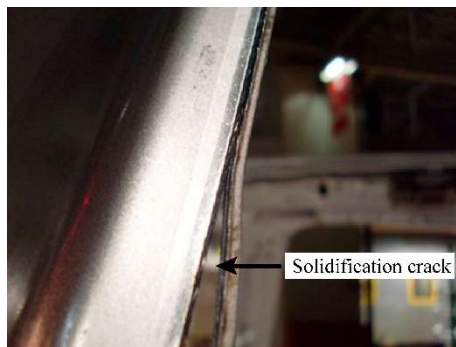


**Fig. 2** Solidification cracking in the B-pillar of a Volvo XC60 car body. With permission from [12].

In the assembly lines of car bodies, preformed parts are welded in a flange geometry and the width of the flange is reduced to decrease the weight of the car body. As reported by Omar [14], a typical car body has 40 m of weld flanges that are welded using resistance spot welding. Resistance spot welding requires 16 mm of flange width to fit the electrode system on either side [15]. The flange width can be minimised by using laser welding and can lead to an overall weight reduction of up to 30–40 kg [14]. However, below a critical distance from the flange edge, solidification cracking is often reported. For instance, it is reported [12] that solidification cracking can occur during laser welding of the B-pillar used in Volvo XC60 (figure 2). In order to test the resistance to solidification cracking in thin sheets, VDEh (German Steel Institute) has developed a self-restraint hot cracking test [13]. In this test, bead-on-plate laser welding is conducted on single sided clamped rectangular steel sheets. The starting position is set at a distance of 3 mm from the free edge with the welding direction inclined  $7^\circ$  to the edge. Crack length is used to assess the hot cracking susceptibility of various alloys. The test is of practical importance for overlap and flange welding geometries in order to minimise the flange width.

In the present work, solidification cracking was studied in two commercial automotive AHSS, *i.e.*, transformation induced plasticity (TRIP) and dual phase (DP) steels. These



steels are extensively used in automotive car bodies [16] and hence make a good case for the present study. The following two approaches were implemented:

- Laser bead-on-plate welding experiments were carried out on single sided clamped rectangular sheets, similar to the VDEh standard test. However, the welding direction was kept parallel to the free edge. In TRIP steel, solidification cracking was observed when welding was carried out close to the free edge and beyond a certain distance from the free edge, solidification cracking was not observed. A 3D finite-element (FE) sequential thermal-mechanical model of the laser welding was created. The thermal model was validated by the experiments using both the temperature measurements and weld bead size. The mechanical model was further validated using the experimentally measured transverse strain by the digital image correlation (DIC) technique [17]. Subsequently, a phase field model for solidification under laser welding conditions was created for both TRIP and DP steels. The boundary conditions were adopted from the FE-model. A pre-described global strain of 0.1 % magnitude was applied perpendicular to the weld centreline. The focus was on the solidification behaviour at the weld centreline behind the weld pool and particularly on the conditions that lead to the separation of grains. The approach is described schematically in figure 3.
- A phase field model was created to simulate the directional solidification in both steels using the thermal conditions from the experiments. In-situ solidification experiments were conducted using a high temperature laser scanning confocal microscope. A circular melt pool was formed at the centre of thin disks while the outer rim remained solid in order to provide the restraint. Solidification cracking was observed in the case of TRIP steel while the DP steel was observed to be resistant to solidification cracking.

The results are discussed pertaining to the effect of the solidification temperature range, the interdendritic segregation of phosphorus, liquid feeding tendency, dendrite coherency and the surrounding restraint on the solidification cracking susceptibility.

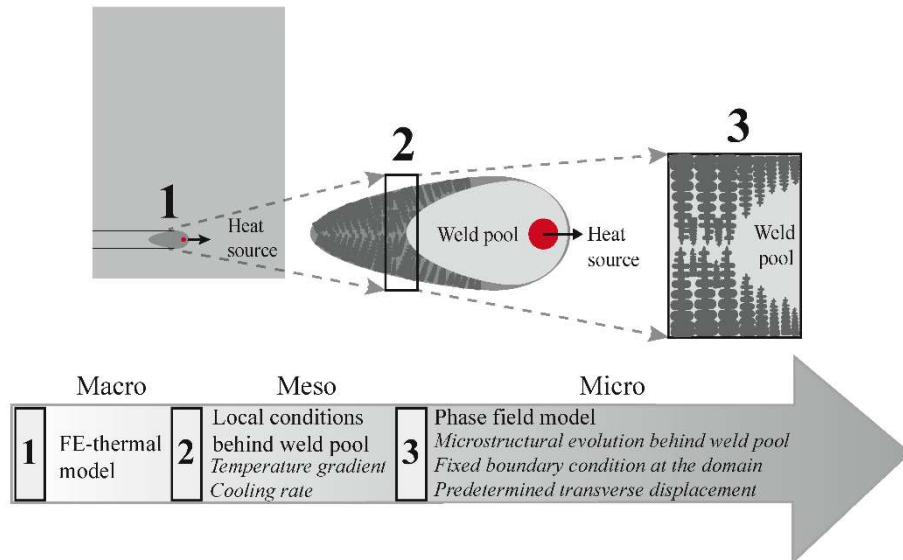


**Fig. 3** Schematic of the approach adopted in the present work. At first, a FE-thermal model of laser welding was created. The local thermal gradient behind the weld pool (from the FE-thermal model) along with the thermodynamic and mobility data from Thermo-Calc™ were used in the phase field model of solidification.

### EXPERIMENTAL SETUP

The composition of the steels used in this work is listed in Table 1. The experimental arrangement for the laser welding experiments is shown in figure 4. Laser bead-on-plate welding experiments were conducted using a 3 kW Nd:YAG laser in the keyhole mode. Specimens were kept at the focal point of the optical system and the laser spot size was 0.6 mm. A laser power of 1100 W and a welding speed of 10 mm s<sup>-1</sup> were used. Rectangular steel sheets with dimensions of 90 × 45 mm<sup>2</sup> and thickness of 1.25 mm were used. The starting position of the laser (Y ordinate) was varied from 5 mm to 13 mm with each increment being 2 mm. Each experiment was repeated five times. For the 13 mm case, temperature was measured at three locations (figure 4) using spot welded K-type thermocouples. Also, the displacement field during welding was measured using the digital image correlation (DIC) method. More details on the method can be found in our previous work [16–17].

The weld surface and cross section were prepared for optical microscopy using standard procedures. Etching was carried out using 4 % Picral and 2 % aqueous sodium metabisulfite [19]. The fracture surface was observed using a scanning electron microscope.

## Mathematical Modelling of Weld Phenomena 12

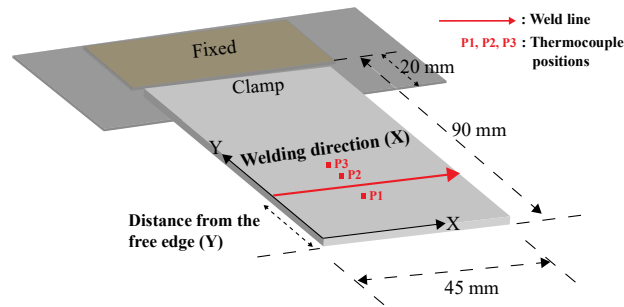


**Fig. 4** Schematic of the hot cracking test setup. The thermocouple positions are also indicated. P1 is 3 mm from the weld centreline (towards the free edge) and P2, P3 are 3 mm and 4.5 mm from the weld centreline (towards the constrained edge). Adapted from [17].

**Table 1** Composition of the steels used in this work.

Elements, wt.%	C	Mn	Al	Si	Cr	P	Fe
TRIP	0.19	1.63	1.1	0.35	0.019	0.089	bal.
DP	0.15	2.3	0.03	0.10	0.56	0.01	bal.

In-situ solidification experiments were conducted using high temperature laser scanning confocal microscopy. Circular disk-shaped specimens with a diameter 10 mm and a thickness 250  $\mu\text{m}$  were prepared. The sample was placed in an alumina crucible and was held by ceramic protrusions at the periphery of the crucible. The crucible was held in a platinum holder with a thermocouple spot-welded to it. The sample was placed at the upper focal point of a gold-plated ellipsoidal cavity and was heated by radiation using a 1.5 kW halogen lamp placed at the lower focal point. An inert atmosphere was maintained using high purity argon gas. A stable melt pool with a diameter of 3-3.5 mm was formed at the centre of the specimen while the outer rim remained solid. A cooling rate of 10  $\text{K s}^{-1}$  was applied until 1623 K using a PID controller, which controls the lamp power appropriately. The temperature at the platinum holder was recorded and concurrently images were acquired at a rate of 30 frames per second. More information on the technique and the setup can be found in references [3], [19–22].

### FINITE-ELEMENT (FE) MODEL

A 3D finite element (FE) sequential thermal mechanical model for the welding process was created using a commercial software, COMSOL<sup>TM</sup>. The heat balance during welding was simulated including the heat input, heat transfer and heat loss. A 3D conical Gaussian heat source as used by [24]–[26] was adopted to describe the laser beam heat input. The thermal history, *i.e.*, temperatures ( $T$ ) at ( $x, y, z$ ) were obtained by solving the following Fourier heat transfer equation using the temperature-dependent thermal properties of the material,

$$\frac{\partial}{\partial x}\left(k(T)\frac{\partial T}{\partial x}\right) + \frac{\partial}{\partial y}\left(k(T)\frac{\partial T}{\partial y}\right) + \frac{\partial}{\partial z}\left(k(T)\frac{\partial T}{\partial z}\right) + Q_v = \rho(T)C_p(T)\left(\frac{\partial T}{\partial t}\right) \quad (1)$$

Here,  $k(T)$  is the temperature dependent thermal conductivity,  $Q_v$  is the net volumetric heat flux from the heat source,  $\rho(T)$  is the temperature dependent density and  $C_p(T)$  is the temperature dependent specific heat.

The temperature dependent thermal and mechanical properties of the steel used in the present work were taken from the reference [18]. Latent heat, absorbed or released during melting (or solidification) is incorporated in the temperature dependent specific heat capacity. The latent heat absorbed during melting was related to the temperature-phase fraction data, obtained using Scheil-Gulliver solidification approximation. The thermal expansion coefficient during solidification is considered to be dependent on the amount of solid and liquid phases. The solidification temperature range, solid and liquid phase fraction data of the steel composition were obtained from a commercial thermodynamic software, Thermo-Calc<sup>TM</sup>. Quadratic elements with a minimum mesh size of  $0.3 \times 0.3 \text{ mm}^2$  and a thickness of 1 mm were used. The process efficiency of laser welding was assumed to be 40 % based on previous work of [27] on the same experimental arrangement. It is thus assumed that the heat losses due to convection and radiation in the keyhole are taken into account.

#### PHASE-FIELD (PF) MODEL

The phase field modelling approach applied in this study is based on our recent work [23], [28]. Figure 3 shows schematic of the methodology adopted in this work. The emphasis was on the microstructural evolution during solidification at the tail of the weld pool. For this, the local conditions like transient temperature profiles and thermal gradient were taken from the FE-model of laser welding. A commercial software, MICRESS<sup>TM</sup> based on the phase field approach for multiphase systems was employed. It utilises the thermodynamic (TCFE6) and mobility database (MOB2) from Thermo-Calc<sup>TM</sup>. A two dimensional grid of  $200 \times 300 \text{ }\mu\text{m}$  with a grid size of  $1 \text{ }\mu\text{m}$  was defined. The energy parameters for the phase interaction used in this simulation were taken from reference [29] and are listed in table 2. The initial concentration of the components was set to be the bulk composition in the liquid phase. One nucleus of  $\delta$ -ferrite was placed at the bottom and the top left corner of the computational domain. The radius of the nucleus was set to  $0.5 \text{ }\mu\text{m}$ . During solidification, the system underwent a liquid to solid reaction based on the local thermodynamic and chemical conditions. Only the cooling cycle behind the weld pool was considered.

For the thermal conditions, transient temperature profiles at the fusion boundaries from the FE model were applied to both edges of the domain. A thermal gradient was defined according to the temperature difference from the fusion to the weld centre line. The initial temperature at the bottom edge was given as the liquidus temperature. The boundary conditions for the phase and concentration were set to be symmetrical. The interface thickness was assumed to be  $3 \text{ }\mu\text{m}$ . The time evolution is calculated by a set of phase field equations deduced by the minimization of the free energy functional,

**Table 2** Energy parameters for liquid to  $\delta$ -ferrite phase interaction.

<b>Surface energy</b>	$1.6 \times 10^{-1} \text{ J/m}^2$
<b>Kinetic coefficient</b>	$7.3 \times 10^{-11} \text{ m}^4/(\text{J s})$
<b>Static anisotropy coefficient</b>	0.45
<b>Kinetic anisotropy coefficient</b>	0.3

$$\dot{\phi}_\alpha = \sum_\beta M_{\alpha\beta}(\vec{n})(\sigma_{\alpha\beta}^*(\vec{n})K_{\alpha\beta} + \frac{\pi}{\eta}\sqrt{\phi_\alpha\phi_\beta}\Delta G(\vec{c}, T)) \quad (2)$$

$$K_{\alpha\beta} = \phi_\beta \nabla^2 \phi_\alpha - \phi_\alpha \nabla^2 \phi_\beta + \left(\frac{\pi}{\eta}\right)^2 (\phi_\alpha - \phi_\beta) \quad (3)$$

where,  $\phi$  is a phase field parameter,  $\alpha$  indicates solid phase,  $\beta$  indicates liquid phase,  $\eta$  is the interface thickness,  $M_{\alpha\beta}$  is the mobility of the solid-liquid interface as a function of the interface orientation, described by the normal vector  $\vec{n}$ .  $\sigma_{\alpha\beta}^*$  is the anisotropic surface stiffness,  $K_{\alpha\beta}$  is related to the local curvature of the interface,  $\Delta G$  is the thermodynamic driving force as a function of temperature  $T$  and local chemical composition  $\vec{c}$ .

For the stress analysis, a fixed strain of 0.1 %, normal to the welding direction was applied to the phase field domain. A constant elastic modulus of 10 GPa for solid [30] and 1 GPa for liquid [10], [31] was used for both the steels. A thermal expansion coefficient of  $2.5 \times 10^{-5} \text{ K}^{-1}$  for the solid phase and  $3 \times 10^{-5} \text{ K}^{-1}$  for the liquid phase was employed.

A similar approach was adopted to simulate the directional solidification observed from the *in-situ* solidification experiments. TRIP steel composition, with and without P was considered (referred to as TRIP-No P). Cooling rate and thermal gradient were based on experimental results. Four nuclei of  $\delta$ -ferrite with an undercooling of 5 K were placed at the underside of the phase field domain. The size of the phase field domain was set to  $150 \times 200 \mu\text{m}$  with a grid size of  $2 \mu\text{m}$ . The stress in the solid phase due to solidification shrinkage and thermal contraction was calculated by fixing the boundaries of the domain. Elastic constant and thermal expansion coefficient of the solid and liquid phases were chosen as described previously.

## RESULTS

### LASER WELDING EXPERIMENTS

Solidification cracking was observed in the TRIP steel when welding was carried out close to the free edge ( $x = 5 \text{ mm}$  from the free edge). With the same welding parameters, the DP steel showed no signs of solidification cracking. Figures 5 (a-b) shows high-speed camera images taken during welding. A solidification crack at the weld centreline was observed to follow the heat source and complete fracture (figure 5 (b)) was observed when welding was carried out close to the free edge. Figure 5 (c) shows an optical macrograph revealing a

weld centreline crack. Figure 5 (d) shows a secondary electron micrograph of the fracture surface with dendritic morphology, a typical feature of solidification cracking [32].

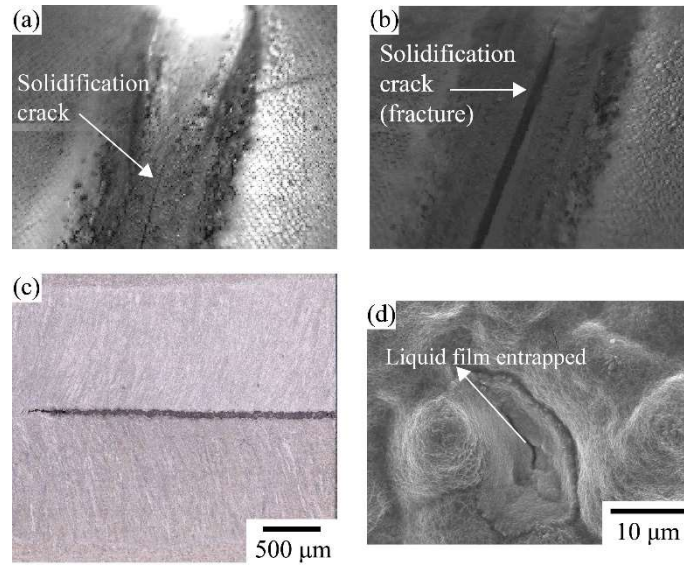


**Fig. 5** Laser bead-on-plate welding of TRIP steel sheets. (a) high speed camera image showing solidification crack following the heat source, (b) high speed camera image showing complete fracture, (c) an optical macrograph indicating centerline cracking in TRIP steel, (d) secondary electron micrograph of the fracture surface showing a dendritic morphology. Figures 5 (a) and (c) are taken from reference [23].

To vary the amount of restraint, the starting distance of welding from the free edge was increased. As the distance increased, the average crack length was found to decrease and when welding was carried out at a distance of 13 mm, no solidification cracking was observed. Figure 6 show the experimental and calculated thermal cycle at points P1, P2 and P3 respectively. A good agreement was found between the measured and calculated thermal cycles. Weld bead size was also found to be in good agreement with the thermal model. Subsequently, the temperature gradient and the cooling rate history, behind the weld pool, were extracted from the validated FE-thermal model. The extracted thermal profile was subsequently used in the phase field model.

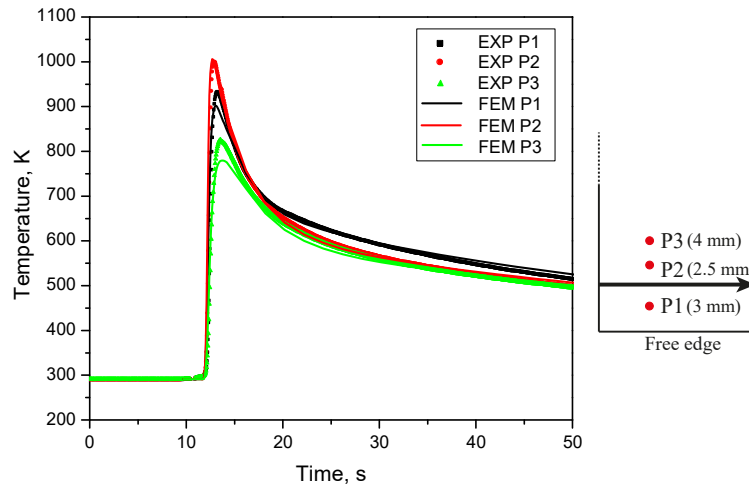


**Fig. 6** Experimental and calculated temperature cycles for the 13 mm case. The position of the points P1, P2 and P3 with respect to the weld centreline is also indicated. P1 is at a distance of 3 mm (towards free edge) while P2 and P3 are at 2.5 mm and 4 mm (towards the fixed edge).

#### IN-SITU SOLIDIFICATION EXPERIMENTS

Figure 7 (a) indicates the diameter of the weld pool achieved before the cooling cycle was started in the in-situ solidification experiment of TRIP steel. Figures 7 (b-f) show the solidification sequence of the TRIP steel. Due to a temperature gradient in the thickness direction, solidification was observed to occur from the underside of the specimen (figure 7 (c)). Solidification cracking was observed during the last stage of solidification (figures 7 (c-d)). Concurrently, isolated liquid droplets were also observed (figure 7 (d)) at low temperatures indicating the presence of strong undercooling. The complete extent of cracking is shown in the secondary electron micrograph taken after the experiment (figure 7 (a)). Under same conditions, solidification cracking was not observed in DP steel [23].

Based on the average solidification rate of the dendrites from the underside to the top, a thermal gradient of  $200 \text{ K mm}^{-1}$  was applied in the phase field model.

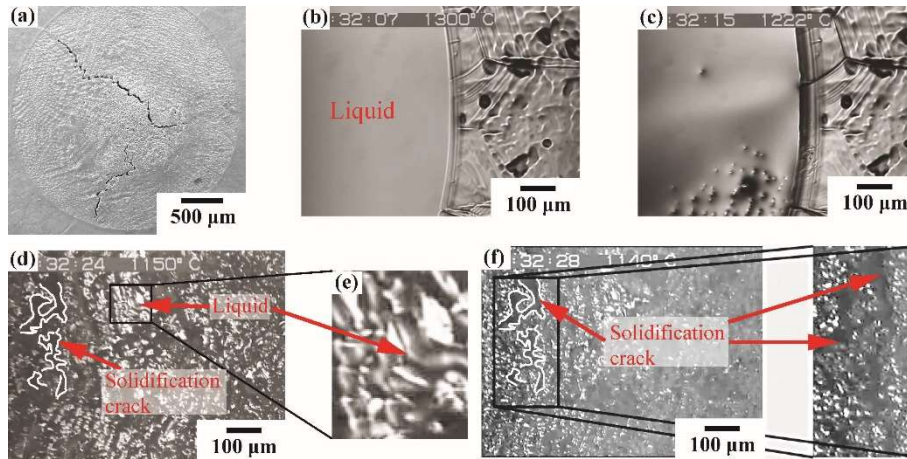


**Fig. 7** In-situ solidification experiments (a) secondary electron micrograph showing the extent of solidification cracking, (b-f) solidification images from the confocal microscope, (b) a circular melt pool at the centre of the specimen, (c) dendrites growing mostly from the bottom of the pool, (d-e) solidification crack and isolated liquid pockets, (f) solidification crack observed *in-situ* at the last stage of solidification. Temperature indicated in images (b-d) and (f) is measured at the periphery of the platinum specimen holder. Taken from reference [23].

#### PHASE FIELD MODELLING

Figures 8 (a) through (d) show the solidification sequence of  $\delta$ -ferrite columnar dendrites behind the weld pool in TRIP steel. Solidification begins at the fusion boundary with  $\delta$ -ferrite as the first solid phase (figure 8 (a)). As the heat source (or weld pool) moves further, solidification progresses and columnar dendrites impinge (or coalesce) at the weld centreline (figures 8 (b-c)). Note that due to the restriction of imposing thermal gradient only in the  $y$  direction, the direction of solidification is fixed, *i.e.*, perpendicular to the fusion boundary (domain boundary). Figure 8 (e) shows the solidification morphology in DP steel with approximately the same solid fraction as that of TRIP steel in figure 8 (c). The secondary arm dendritic structure is more prominent in TRIP steels. This is also evident from the microsegregation of phosphorous. Figures 8 (f) and (g) shows the P map in TRIP and DP steel. Note the scale difference in P due to nominal compositional difference of P in both the steels. Phosphorous microsegregation of more than two times the nominal composition exists in the case of TRIP steel.

Figure 8 (h) shows the normal stress map in TRIP steel at  $t = 0.011$  s. Stress distribution along the arrow as indicated in figure 8 (h) was extracted for both the steels and is shown in figure 9. A more prominent dip in stress at the grain boundaries exist in TRIP steel when compared with DP steel.



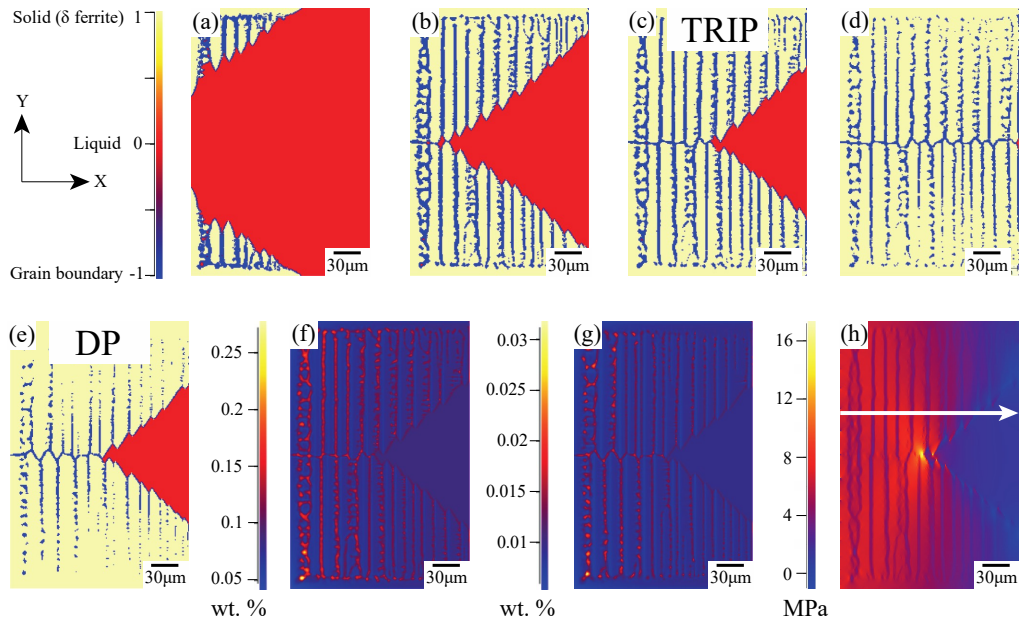


**Fig. 8** Phase field simulation of solidification behind the weld pool. (a) solidification starts at the fusion boundaries behind the weld pool in TRIP steel, (b) columnar dendrites of  $\delta$ -ferrite impinge at the centre at  $t=0.011$  s, (c) solidification continues as weld pool progresses further, (d) primary solidification ( $\delta$ -ferrite) is complete, (e) solidification structure of DP steel at  $t=0.01$  s, (f) P map in TRIP steel at  $t=0.011$  s, (g) P map in DP steel at  $t=0.01$  s, (h) normal stress map in TRIP steel at  $t=0.01$  s. An arrow is also marked along which the stress data is extracted for both the steels.

Figures 10 (a) and (b) show the solidification morphology/state in TRIP and TRIP-No P steel respectively. Solidification occurs at a faster rate in TRIP-No P steel, *i.e.*, without P. Also, long and narrow liquid channels exist in TRIP steel with P. Figure 10 (c) shows the P map in TRIP steel, indicating the presence of microsegregation. Microsegregation of P in the interdendritic/intercellular regions leads to undercooling. Figure 11 (a) shows the temperature *versus* solid fraction ( $f_s$ ) curves of TRIP and TRIP-No P steel based on equilibrium and the present phase field model. The phase field model also indicates the presence of strong undercooling in the interdendritic regions in the TRIP steel, in agreement with the experimental observations. Figures 11 (b) and (c) shows the tensile stress maps for both of the steels. Higher tensile stress (and concentration at the dendrite roots) exists in the TRIP steel.

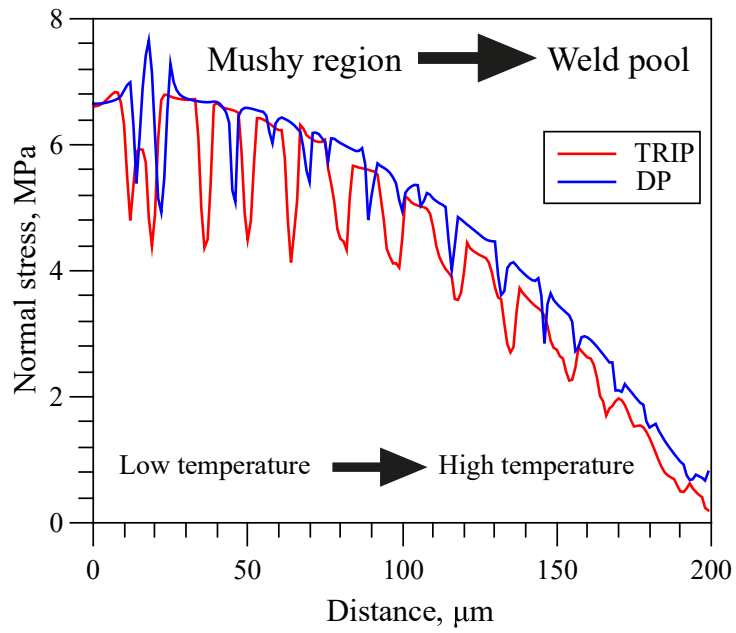


**Fig. 9** Normal stress distribution in TRIP and DP steel along the arrow indicated in figure 8 (h).

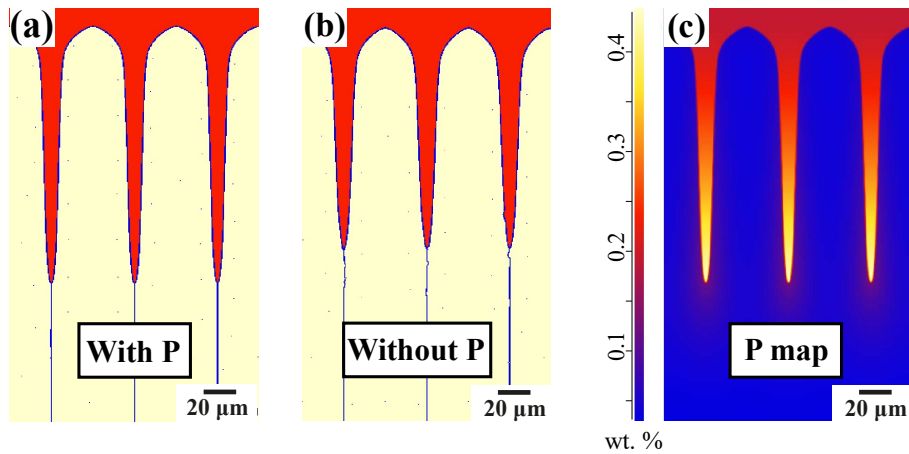


**Fig. 10** Phase field simulation showing liquid channel morphology and microsegregation. (a) TRIP steel composition, (b) TRIP-No P steel composition, (c) Phosphorus map in TRIP steel. Adapted from reference [23].

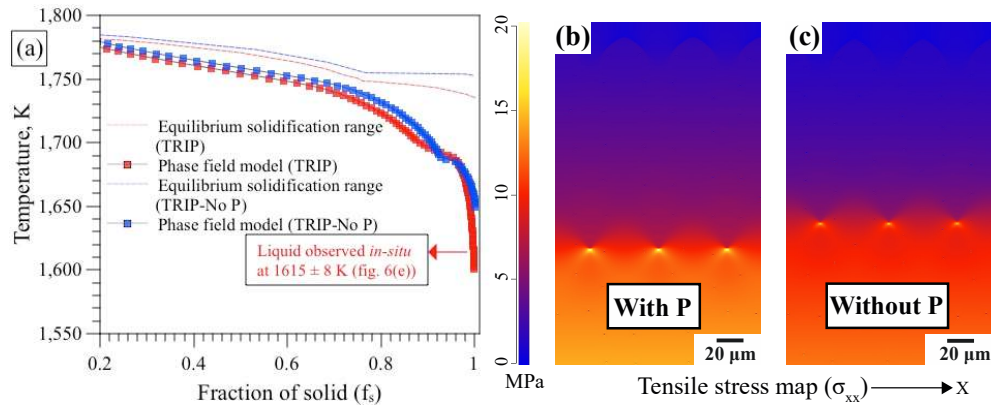


**Fig. 11** (a)  $T$  vs.  $f_s$  curves for the two steels from equilibrium phase diagram and phase field simulations, (b) and (c) tensile stress map in TRIP and TRIP-No P steel respectively. Taken from reference [23].

## DISCUSSION

Both the experimental and numerical approaches indicate a higher cracking susceptibility in TRIP steel than in the DP steel. Solidification cracking was not observed in the DP steel. The factors (or combination of factors) that affect cracking susceptibility are discussed below.

### SOLIDIFICATION TEMPERATURE RANGE

The equilibrium solidification temperature range of TRIP and DP steel composition is 50 K and 33 K respectively. In general, a wider solidification temperature range leads to a wider mushy region, which in turn increases the susceptibility to cracking [33]. The brittle temperature range (BTR), defined as the temperature range over which a material exhibits loss in ductility is also influenced by the material's solidification temperature range [33–34]. Phosphorus segregation in the TRIP steel leads to undercooling and widens the effective solidification temperature range. Experimental observation of liquid droplets at approximately 1615 K, as shown in figure 7 (e), means that an undercooling of more than 160 K existed during the solidification of the TRIP steel. Note that P in TRIP steel is intentionally added as it helps to retard cementite precipitation, partially replaces Si and provides solid solution strengthening [23]. The P content in DP steel was limited to 30 ppm and isolated liquid droplets at low temperature were not observed during solidification. Temperature *versus* solid fraction curves obtained from phase field simulation, as shown in figure 11 (a) also indicate that the presence of a comparatively large amount of P leads to significant undercooling. In our earlier study [23], atom probe tomography revealed that P content in the interdendritic region is as high as 0.29 wt. %.

### INTERDENDRITIC LIQUID FEEDING

Sufficient interdendritic liquid feeding is required to compensate for both the solidification shrinkage and thermal contraction. Darcy's law is often used to describe liquid flow in the mushy region. The law is given as [23]:

$$v_l f_l = -\frac{K \Delta P}{\mu Z} \quad (4)$$

here,  $v_l$  is the interdendritic fluid velocity,  $f_l$  is the fraction of liquid,  $K$  is the permeability of the solid network,  $\mu$  is the viscosity of the liquid,  $\Delta P$  is the pressure difference between the dendrite root and tip and  $Z$  is the channel length. Here,  $Z$  refers to the dendrite growth direction (figure 10). With the same solid fraction ( $f_s$ ), longer and narrower liquid channels exist in TRIP steel due to the microsegregation of P. Adequate liquid feeding is thus more difficult in TRIP steel than in DP steel. In our recent work, liquid feeding in the interdendritic regions was observed in DP steels [4], whereas, no liquid feeding and solidification cracking were observed in the TRIP steel under similar conditions.

### DENDRITIC COHERENCY

At high temperatures within the solidification temperature range, the amount of liquid is high and therefore the solidifying dendrites are surrounded by liquid. From a particular temperature or fraction of solid (dependent on the alloy), a rigid network is formed and the solid structure is able to transmit stresses. The solid network thus becomes coherent. When grain boundaries are involved, the intergranular coalescence temperature is generally low as compared with the intragranular coalescence temperature. This happens when the grain boundary energy ( $\gamma_{gb}$ ) is higher than twice the solid-liquid interface energy ( $\gamma_{sl}$ ) [36]. From the phase field results, secondary dendritic arms are more prevalent in the TRIP steel than in the DP steel. In addition, a higher P content also increases the secondary dendrite arm spacing. Thus, dendritic coherency in the TRIP steel is reached at a lower temperature compared to the case of DP steel. This is also evident from figures 8(c) and (e). Delayed coherency of the mushy zone in the TRIP steel increases the susceptibility to solidification cracking. The prominent dip in normal stress at the grain boundaries in the TRIP steel (figure 9) further indicates that liquid films tend to persist for a longer time in the TRIP steel. As a result, the solid network is rendered weak and stress is concentrated at the weld centerline, eventually leading to cracking. At the same time, the dendritic network in the DP steel is more coherent and therefore more resistant to cracking.

### RESTRAINT

Solidification cracking occurs when the local stress applied to a material is greater than the local strength. Even though TRIP steel is susceptible to solidification cracking, the mechanical restraint is low enough to prevent cracking when welding is carried out beyond a certain distance from the free edge. The reduction in mechanical restraint can therefore

improve the weldability of steels that are otherwise prone to solidification cracking. For example, in our recent work [18], a decrease in heat input led to a decrease in the critical distance beyond which no solidification cracking was observed.

PRESENT WORK IN RELATION WITH EXISTING PHYSICAL MODELS ON HOT CRACKING

A recent criterion of solidification cracking proposed by Kou [9] was applied to both the steels. According to the criterion, the susceptibility of solidification cracking is directly related to the  $|dT/d(f_s)^{1/2}|$ , near  $(f_s)^{1/2} = 1$ . Temperature *versus* solid fraction ( $f_s$ ) curves were obtained using Scheil-Gulliver solidification model. The steepness of the curve (figure 12) in the case of TRIP steel is twice that of DP steel. Therefore, TRIP steel is considered to be more susceptible to cracking.

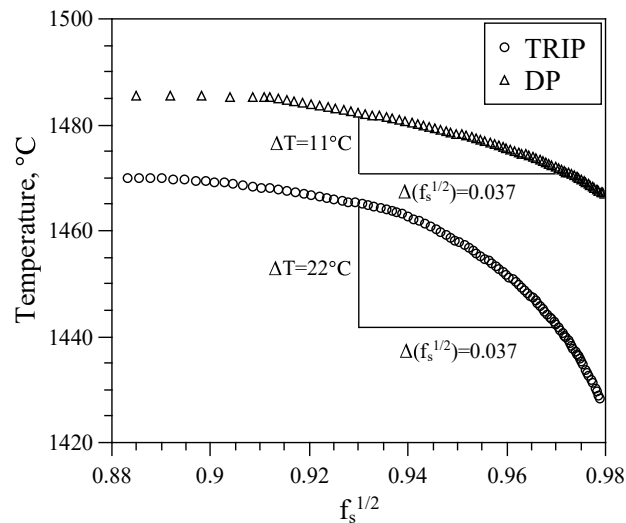


**Fig. 12** Prediction of cracking susceptibility using the Kou criterion [9]. Slope of  $T - (f_s)^{1/2}$  curves with  $f_s$  varying from 0.87 to 0.94 indicates higher crack susceptibility of TRIP steel.

The Rappaz-Drezet-Gremaud criterion [8] was also applied on these steels in our previous work [28]. The liquid pressure drop in the mushy zone is comprised of a pressure drop due to solidification shrinkage together with a thermal deformation term. A larger pressure drop in the liquid increases the susceptibility to cracking. The total pressure drop in the TRIP steel was found to be higher (941.2 kPa) than in the DP steel (10.2 kPa), indicating higher cracking susceptibility in the TRIP steel [28].

Both the criteria are found to be consistent with the cracking susceptibility of the two steels. In general, the applicability of these criteria depends on the accuracy with which the solidification curves can be predicted under welding conditions. Also, it is important to note that all the existing models provide an indication of susceptibility towards solidification cracking. Actual cracking behaviour depends on the welding conditions and in general needs to be determined experimentally. For instance, no solidification cracking was observed in either steel when welding was carried out beyond a certain distance from the

free edge, *i.e.*, restraint effect. The present work was focussed on the (local) governing/contributing factors that affect the solidification cracking susceptibility, using both experimental and modelling approaches. For instance, interdendritic liquid feeding was observed and quantified experimentally [4] and later on studied in relation to solidification cracking susceptibility using phase field solidification models [23], [28]. Solidification models also provided insights into the influence of dendritic coherency and solute segregation on solidification cracking, which is difficult to obtain experimentally.

### CONCLUSIONS

A detailed investigation of solidification cracking susceptibility in two common automotive AHSS was carried out by means of both experimental and numerical methods. A novel approach was adopted in which the dynamic thermal conditions behind the moving heat source were extracted from a validated FE-model and applied to a phase field solidification model. Solidification behaviour behind the weld pool was further studied pertaining to the factors, which affect cracking susceptibility. Solidification behaviour during *in-situ* experiments was also studied by means of a phase field model.

The observations from both the laser welding experiments and *in-situ* solidification experiments corroborate the results of phase field modelling. The following conclusions are drawn from the present study:

- The actual solidification temperature range is widened significantly by undercooling in the TRIP steel due to P segregation. A wider solidification temperature range leads to increased susceptibility towards solidification cracking. The solidification rate is faster in the DP steel than in the TRIP steel. In addition, a narrower solidification temperature range in the DP steel entails that the mushy regions spends less time in the crack vulnerable regime.
- Phosphorous microsegregation leads to longer and narrower liquid channels in the TRIP steel. Inadequate liquid feeding thus increases the likelihood of cracking in the TRIP steel.
- In the DP steel, the solid in the mushy region forms a coherent network at an early stage. As a result, it can effectively withstand transverse tensile strains. In the TRIP steel, a continuous network of liquid films persists at the grain boundaries until the latter stages of solidification. As a consequence, tensile strain is concentrated at the weld centreline, eventually leading to cracking.
- Cracking occurs if the threshold strength of a crack susceptible material is exceeded by the mechanical restraint. The amount of restraint affects the local strain and can lead to different cracking behaviour.

In future, solidification models considering interdendritic liquid feeding under welding conditions will be employed. These models will enable further understanding of the solidification cracking phenomena.

## ACKNOWLEDGEMENTS

This research was carried out under project numbers F22.8.13485a and F22.8.13485b in the framework of the Partnership Program of the Materials innovation institute M2i ([www.m2i.nl](http://www.m2i.nl)) and the Foundation for Fundamental Research on Matter (FOM) ([www.fom.nl](http://www.fom.nl)), which is part of the Netherlands Organisation for Scientific Research ([www.nwo.nl](http://www.nwo.nl)). The authors would like to thank the industrial partner in this project 'Tata Steel Nederland B.V.' for the financial support.

## REFERENCES

- [1] International Council on Clean Transportation. 'Global passenger vehicle standards (2014)'. Retrieved from <http://theicct.org/info-tools/global-passenger-vehicle-standards>.
- [2] S. KEELER, M. KIMCHI AND P. J. MCONEY: 'Advanced High-Strength Steels Application Guidelines', 2017.
- [3] C. LESCH, N. KWIATON AND F. B. KLOSE: 'Advanced High Strength Steels (AHSS) for Automotive Applications – Tailored Properties by Smart Microstructural Adjustments', *steel research international*, Vol. 88, No. 10, p. 1700210.
- [4] G. AGARWAL, M. AMIRTHALINGAM, S. C. MOON, R. J. DIPPENAAR, I. M. RICHARDSON AND M. J. M. HERMANS: 'Experimental evidence of liquid feeding during solidification of a steel', *Scripta Materialia*, Vol. 146, pp. 105–109, 2018.
- [5] M. RAPPAZ AND J. A. DANTZIG: *Solidification*, 1st ed. EFPL Press, 2009.
- [6] D. G. ESKIN AND L. KATGERMAN: 'A Quest for a New Hot Tearing Criterion', *Metallurgical and Materials Transactions A*, Vol. 38, No. 7, pp. 1511–1519, 2007.
- [7] L. KATGERMAN: 'A Mathematical Model for Hot Cracking of Aluminum Alloys During D.C. Casting', *JOM*, Vol. 34, No. 2, pp. 46–49, 1982.
- [8] M. RAPPAZ, J.-M. DREZET AND M. GREMAUD: 'A new hot-tearing criterion', *Metallurgical and Materials Transactions A: Physical Metallurgy and Materials Science*, Vol. 30, No. 2, pp. 449–455, 1999.
- [9] S. KOU: 'A criterion for cracking during solidification', *Acta Materialia*, Vol. 88, pp. 366–374, 2015.
- [10] N. CONIGLIO AND C. E. CROSS: 'Mechanisms for Solidification Crack Initiation and Growth in Aluminum Welding', *Metallurgical and Materials Transactions A*, Vol. 40, No. 11, pp. 2718–2728, 2009.
- [11] N. CONIGLIO AND C. E. CROSS: 'Initiation and growth mechanisms for weld solidification cracking', *International Materials Reviews*, Vol. 58, No. 7, pp. 375–397, 2013.
- [12] J. K. LARSSON: 'Avoidance of crack inducement when laser welding hot-formed car body components --- a variable analysis', *Physics Procedia*, Vol. 5, pp. 115–124, 2010.
- [13] VDEH: *SEP 1220-3 : Testing and Documentation Guideline for the Joinability of thin sheet of steel - Part 3: Laser beam welding*. 2011.
- [14] M. A. OMAR: 'Automotive Joining', in *The Automotive Body Manufacturing Systems and Processes*, Wiley-Blackwell, 2011, pp. 107–176.
- [15] K.-M. HONG AND Y. C. SHIN: 'Prospects of laser welding technology in the automotive industry: A review', *Journal of Materials Processing Technology*, Vol. 245, pp. 46–69, 2017.
- [16] T. B. HILDITCH, T. DE SOUZA AND P. D. HODGSON: 'Properties and automotive applications of advanced high-strength steels (AHSS)', in *Welding and Joining of Advanced High Strength Steels (AHSS)*, M. Shome and M. Tumuluru, Eds. Woodhead Publishing, 2015, pp. 9–28.
- [17] G. AGARWAL, H. GAO, M. AMIRTHALINGAM AND M. J. M. HERMANS: 'In-situ strain investigation during laser welding using digital image correlation and finite element based

- numerical simulation', *Science and Technology of Welding and Joining*, Vol. 23, No. 2, pp. 134–139, 2018.
- [18] H. GAO, G. AGARWAL, M. AMIRTHALINGAM, M. J. M. HERMANS AND I. M. RICHARDSON: 'Investigation on hot cracking during laser welding by means of experimental and numerical methods', *Welding in the World*, Vol. 62, No. 1, pp. 71–78, 2018.
- [19] A. K. DE, J. G. SPEER AND D. K. MATLOCK: 'Color tint-etching for multiphase steels', *Advanced Materials and Processes*, Vol. 161, No. 2, pp. 27–30, 2003.
- [20] M. REID, D. PHELAN AND R. DIPPENAAR: 'Concentric solidification for high temperature laser scanning confocal microscopy', *ISIJ International*, Vol. 44, No. 3, pp. 565–572, 2004.
- [21] S. GRIESSER AND R. DIPPENAAR: 'Enhanced Concentric Solidification Technique for High-Temperature Laser-Scanning Confocal Microscopy', *ISIJ Int.*, Vol. 54, No. 3, pp. 533–535, 2014.
- [22] S. GRIESSER, R. PIERER, M. REID AND R. DIPPENAAR: 'SolTrack: An automatic video processing software for in situ interface tracking', *Journal of Microscopy*, Vol. 248, No. 1, pp. 42–48, 2012.
- [23] G. AGARWAL, A. KUMAR, H. GAO, M. AMIRTHALINGAM, S. C. MOON, R. J. DIPPENAAR, I. M. RICHARDSON AND M. J. M. HERMANS: 'Study of Solidification Cracking in a Transformation-Induced Plasticity-Aided Steel', *Metallurgical and Materials Transactions A: Physical Metallurgy and Materials Science*, Vol. 49, No. 4, 2018.
- [24] N. SHANMUGAM, G. BUVANASHEKARAN, K. SANKARANARAYANASAMY AND S. R. KUMAR: 'A transient finite element simulation of the temperature and bead profiles of T-joint laser welds', *Materials and Design*, Vol. 31, No. 9, pp. 4528–4542, 2010.
- [25] J. MA, F. KONG AND R. KOVACEVIC: 'Finite-element thermal analysis of laser welding of galvanized high-strength steel in a zero-gap lap joint configuration and its experimental verification', *Materials and Design*, Vol. 36, pp. 348–358, 2012.
- [26] M. ZAIN-UL-ABDEIN, D. NELIAS, J.-F. JULLIEN AND D. DELOISON: 'Prediction of laser beam welding-induced distortions and residual stresses by numerical simulation for aeronautic application', *J. Mater. Process. Technol.*, Vol. 209, No. 6, pp. 2907–2917, 2009.
- [27] Y. PAN: *Laser welding of Zinc coated steel without pre-set gap*, TU Delft, 2011.
- [28] H. GAO, G. AGARWAL, M. AMIRTHALINGAM AND M. J. M. HERMANS: 'Hot cracking investigation during laser welding of high-strength steels with multi-scale modelling approach', *Science and Technology of Welding and Joining*, Vol. 23, No. 4, pp. 287–294, 2018.
- [29] M. AMIRTHALINGAM, E. M. VAN DER AA, C. KWAKERNAAK, M. J. M. HERMANS AND I. M. RICHARDSON: 'Elemental segregation during resistance spot welding of boron containing advanced high strength steels', *Weld. World*, Vol. 59, No. 5, pp. 743–755, 2015.
- [30] W.-Y. WANG, B. LIU AND V. KODUR: 'Effect of temperature on strength and elastic modulus of high-strength steel', *Journal of Materials in Civil Engineering*, Vol. 25, No. 2, pp. 174–182, 2013.
- [31] C. BORDREUIL AND A. NIEL: 'Modelling of hot cracking in welding with a cellular automaton combined with an intergranular fluid flow model', *Computational Materials Science*, Vol. 82, No. Supplement C, pp. 442–450, 2014.
- [32] T. SOYSAL AND S. KOU: 'A simple test for assessing solidification cracking susceptibility and checking validity of susceptibility prediction', *Acta Materialia*, Vol. 143, pp. 181–197, 2018.
- [33] S. KOU: 'Welding Metallurgy', in *Welding Metallurgy*, John Wiley & Sons, Inc., 2003.
- [34] C. E. CROSS: 'On the Origin of Weld Solidification Cracking', in *Hot Cracking Phenomena in Welds*, T. Böllinghaus and H. Herold, Eds. Springer Berlin Heidelberg, 2005, pp. 3–18.
- [35] J. C. LIPPOLD: *Welding Metallurgy and Weldability*. John Wiley & Sons, 2014.
- [36] N. WANG, S. MOKADEM, M. RAPPAZ AND W. KURZ: 'Solidification cracking of superalloy single- and bi-crystals', *Acta Materialia*, Vol. 52, No. 11, pp. 3173–3182, 2004.





# SIMULATION OF WELD SOLIDIFICATION CRACKING IN VARESTRAINT TESTS OF ALLOY 718

J. DRAXLER\*, J. EDBERG\*, J. ANDERSSON\*\* and  
L-E. LINDGREN\*

*\*Luleå University of Technology, 97187 Luleå, Sweden. Joar.Draxler@ltu.se, Jonas.Edberg@ltu.se, Lars-Erik.Lindgren@ltu.se*

*\*\*University West, 46132 Trollhättan, Sweden. Joel.Andersson@hv.se*

DOI 10.3217/978-3-85125-615-4-26

## ABSTRACT

Several nickel-based superalloys are susceptible to weld solidification cracking. Numerical simulation can be a powerful tool for optimizing the welding process such that solidification cracking can be avoided. In order to simulate the cracking, a crack model inspired by the RDG model is proposed. The model is based on a crack criterion that estimates the likelihood for a preexisting pore in a grain boundary liquid film to form a crack. The criterion depends on the thickness and the liquid pressure in the grain boundary liquid film, as well as the surface tension of the pore. The thickness of the liquid film is computed from the macroscopic mechanical strain field of an FE model with a double ellipsoidal heat source. A temperature-dependent length scale is used to partition the macroscopic strain to the liquid film. The liquid pressure in the film is evaluated using a combination of Poiseuille parallel plate flow and Darcy's law for porous flows. The Poiseuille flow is used for the part of the grain boundary liquid film that extends into the region with liquid fraction less than 0.1, while Darcy's law is used for the rest of the liquid film that extends into the regions with liquid fraction greater than 0.1. The proposed model was calibrated and evaluated in Varestraint tests of Alloy 718. Crack location, width, and orientation were all accurately predicted by the model.

Keywords: Solidification cracking, Hot cracking, Varestraint testing, Computational Welding Mechanics, Alloy 718

## INTRODUCTION

Several nickel-based superalloys are susceptible to weld hot cracking [1]. These cracks can act as sites for the initiation of fatigue and corrosion cracking. Weld hot cracking involves cracks that form during the solidification of the weld. It consists of two different types of cracking: solidification cracking (SC) and liquation cracking [2]. In this study, we only consider SC. SC forms in the fusion zone of the weld via fracture of liquid films. The liquid films are normally grain boundary liquid films (GBLFs). The crack formation depends on a complicated interplay between metallurgical, thermal, and mechanical factors [3].

Numerical simulation can be a powerful tool to study the susceptibility of a welding process to SC. In order to model the cracking, a model for the crack initiation is needed.

Several models have been developed, often for casting, wherein SC is also a problem and is referred to as hot tearing [4, 5]. However, most of these models suffer from one common shortcoming, in that they fail to address how the liquid is fractured [5]. One exception is the model by Rappaz, Drezet, and Gremaud (the RDG model) [6], which estimates the inter-dendritic liquid pressure drop to cavitation. Suyitno et al. [7] compared eight different hot cracking criteria in a simulation of DC casting of aluminum alloys and found that the RDG model best reproduced experimental trends. Nonetheless, this model is limited by some shortcomings. Rappaz has stated the two main approximations used [8]: first, the rheology of the mushy zone is not accurately accounted for; second, the localization of strains and feeding at grain boundaries is not considered. Coniglio et al. [9] pointed out a third shortcoming of the RDG model: cavitation as a liquid fracture mechanism is not likely to occur except at elevated levels of hydrogen content.

The second and third shortcomings have been addressed by Coniglio et al. [9]. Instead of assuming that strain is localized evenly between dendrites, as in the RDG model, they assumed it to be localized evenly between grains, and instead of assuming cavitation as the liquid fracture mechanism, they considered the cracking to originate from pore growth.

The assumption that cracking originates from pores agrees with recent in situ experiments. Puncreobutret et al. [10] performed in situ hot tensile tests of an Al-15 wt% Cu alloy. Using fast synchrotron X-ray microtomography, they observed that the cracking grew from pre-existing voids and internally nucleated voids. Aucott et al. [11] have studied Vastrestraint testing in situ with high-energy synchrotron X-ray microtomography of steel. In agreement with Puncreobutret, they also observed that the cracking was initiated from internal voids.

In this study, we present a model for weld SC that is inspired by the RDG model and the improvements made to this model by Coniglio. The model addresses all three aforementioned shortcomings of the RDG model to some degree. It was calibrated and evaluated in Vastrestraint tests of Alloy 718. Both crack location and crack width predicted by the model were in good agreement with experimental data.

MODEL DEVELOPMENT

The development of the model used for estimating the risk of SC in a given GBLF is presented below. First, the crack criterion is introduced, and then the method for computing the GBLF pressure, which is required to calculate the crack criterion, is presented.

PORE FRACTURE MODEL

As was discussed earlier recent in situ experiments have indicated that SC forms from voids that grow into cracks. In this study, we assume that SC initiates from small pores in GBLFs which then grow into cracks when the GBLF pressure drops and/or GBLF thickness increases due to tensile strain. We assume that for each point on the axis of a given GBLF, there is a pore that extends across the thickness of the GBLF and has the potential to grow into a crack. The nucleation of these pores is not considered; instead, the conditions for how such a pre-existing pore can grow into a SC is studied.

*Equilibrium pore shape*

To simplify the study of how a pore can grow into a crack, a GBLF with parallel solid-liquid interfaces was studied. In such a GBLF, a SC is assumed to form from a pre-existing gas capillary bridge which grows into a crack when the pressure and the thickness of the GBLF change (see Fig. 1). The capillary bridge is assumed to be rotationally symmetric about the  $z$ -axis and symmetric about the  $z = 0$  plane.

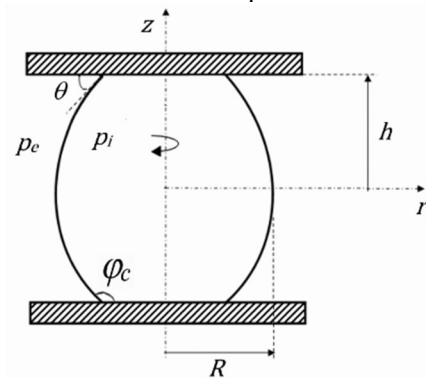


**Fig. 1** Coordinates used for describing the profile shape of the gas bridge.

Let  $r$  and  $z$  be the coordinates that trace out the profile of the pore, and let  $R$  be the radius of the pore at its equator (see Fig. 1). The equilibrium shape of the capillary bridge can be obtained from the Young-Laplace equation, which for the rotational symmetric bridge gives [12]:

$$z(\phi) = \int_{\pi/2}^{\phi} \frac{1 - p \cos^2(v)}{\sqrt{(p(\sin(v)-1)+1)(p(\sin(v)+1)-1)}} dv \tag{1}$$

where  $\phi$  is the dimensionless variable

$$\sin(\phi) = \frac{r}{R} \quad (2)$$

and  $p$  is the dimensionless capillary pressure

$$p = \frac{\sin(\phi_c)\sin(\theta)-1}{\sin^2(\phi_c)-1} \quad (3)$$

$\theta$  is the contact angle between the pore interface and the solid-liquid interface (see Fig. 1).  $\phi_c$  is the value of  $\phi$  at the solid-liquid interface, which can be determined by solving Eq. (1) for  $\phi$  when  $z$  is equal to half the GBLF thickness ( $h$ ). This can be done using a numerical root finder such as MATLAB's `fzero`.

By applying the ideal gas law, and again using the Young-Laplace equation, the external pore pressure ( $p_e$ ) can be obtained as a function of the dimensionless capillary pressure  $p$  (Eq. (3)), the pore radius  $R$ , and the volume of the pore  $V$  :

$$p_e = \frac{p_{i0}V_0}{V} - \frac{2\gamma_{gl}}{R}p \quad (4)$$

where  $\gamma_{gl}$  is the interfacial energy of the liquid-gas pore interface, and  $p_{i0}$  and  $V_0$  are the initial pressure and volume of the pre-existing pore. It is assumed that no gas diffuses to the pore during the solidification. By letting the pore radius  $R$  in Eq. (4) go to infinity, the external pore pressure becomes:

$$p_{e,\infty} = \lim_{R \rightarrow \infty} p_e = -\frac{\gamma_{gl}\cos(\theta)}{h} \quad (5)$$

How  $p_e$  varies with  $R$  for different values of  $p_{i0}$  is shown in Fig. 2a. The values  $h = 2.5 \mu\text{m}$ ,  $\gamma_{gl} = 1 \text{ J/m}^2$ ,  $\theta = 10^\circ$ , and  $R_0 = 2h$  were used in the plot. Here,  $R_0$  is the pore radius of the initial pre-existing pore. As can be seen in the figure, the external pressure required to keep the pore in equilibrium at its initial growth is highly dependent on  $p_{i0}$ . Fig. 2b shows how  $p_e$  varies with  $R$  for different values of  $h$ , using the same parameter values as in the Fig. 2a but with  $p_{i0} = 0$  bar. As can be seen in the figure, the pressure required for a large pore to be stable is highly dependent on the GBLF thickness. A large pore can be stable at a much lower pressure drop in a wide GBLF than in a narrow GBLF.

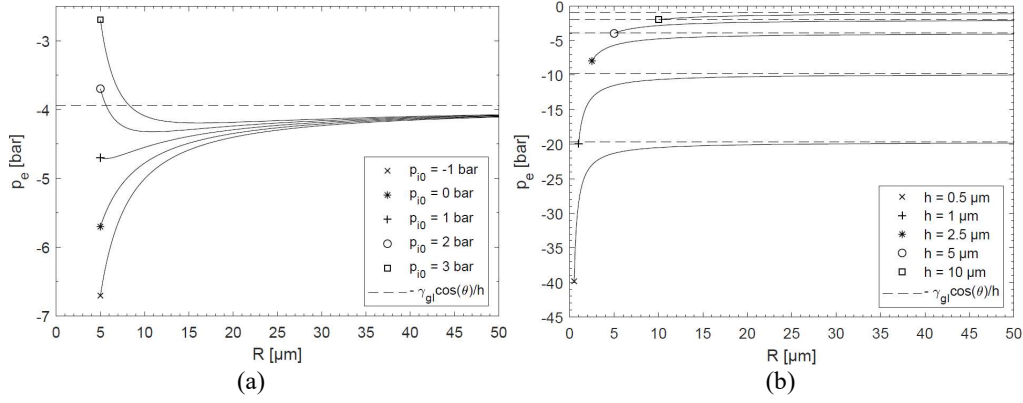


**Fig. 2**  $p_e$  as a function of  $R$  for: (a) different values of  $p_{i0}$ , (b) different values of  $h$ .

More details about derivations of the above equations and the influence of the different parameters on the relation between  $p_e$  and  $R$  can be found in [12].

### Crack criterion

From the relation between the radius and external pressure of a stable pore in a GBLF with parallel interfaces (Eq. (4)), it can be shown that the external pressure of a stable pore never exceeds  $p_{e,\infty}$  (Eq. (5)), unless the initial pore pressure and size are large. This can be used to construct a conservative pressure-based crack criterion for SC. We assume that a large stable pore in a GBLF can form as soon as the liquid pressure in the GBLF drops below  $p_{e,\infty}$ . A crack initiation index (CII) can then be defined as the ratio between the liquid pressure drop and the liquid pressure drop to  $p_{e,\infty}$ :

$$CII = \frac{p_{atm} - p}{p_{atm} - p_{e,\infty}} \quad (6)$$

where  $p_{atm}$  is the atmospheric pressure, and  $p$  is the liquid pressure in the GBLF, which is computed in the absence of the pore via the pressure model described below. A CII value larger than 1 indicates that crack initiation is predicted.

A CII value larger than 1 does not guarantee the formation of a permanent crack. For example, if the liquid pressure drop decreases, the surface tension of the pore can contract and close the pore. In this study, we consider the formation of a permanent crack to occur when the CII value is larger than 1 at the location of the solidus isotherm. If we assume that all the remaining liquid instantly solidifies at the solidus temperature, a crack that is passed by this isotherm can never be healed, and therefore becomes a permanent crack in the solid phase. Thus, SC is considered to occur in a GBLF if the CII value is larger than 1 at the terminal solidification location of the GBLF. The crack initiation length (CIL) can then be defined as the length along a GBLF where the CII value is larger than 1, as follows:

$$CIL = \int_{s_{ct}} ds \quad (7)$$

where  $s$  is a coordinate along the GBLF axis, which, for example, can be along the columnar grain growth direction in a TIG weld. The integration path  $s_{ci}$  is the part of the GBLF axis where the CII value is larger than 1 at the intersection with the solidus isotherm, as shown in Fig. 3.

We consider the CIL of a GBLF to be the part of the GBLF where a pore, if its initial size is large enough, can form a permanent crack in the solid phase. Thus, if a large enough pre-existing pore is located within this region of the GBLF, it is assumed to cause crack initiation.

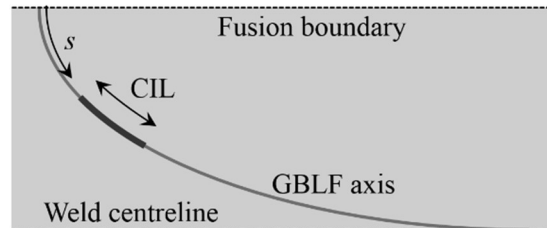


**Fig. 3** Schematic representation of the CIL of a GBLF. The welding direction is from left to right. The GBLF axis shown is located between columnar grains that extend from the fusion boundary and aligns with the weld centerline. The GBLF axis shown is located close the weld surface.

#### GBLF PRESSURE MODEL

In order to compute the susceptibility to cracking for a given GBLF using the criterion in Eq. (7), the liquid pressure and the thickness of the GBLF must be known. These quantities were estimated as follows.

#### *GBLF orientation*

To compute the liquid pressure in a given GBLF, the orientation and shape of the GBLF must be known. In this study, we only consider a fully columnar dendritic microstructure in the fusion zone, which can result from low welding speed with TIG welding [13]. In order to estimate the orientation of a GBLF in this microstructure, it was assumed that the columnar grains were always growing normal to the liquidus isotherm, with zero undercooling to solidification. This results in long curved grains that extend from the fusion boundary to the weld centerline. The axis of such a grain can be determined from [13]:

$$\frac{dr}{dt} = -\frac{1}{G_L^2} \frac{\partial T_L}{\partial t} \mathbf{G}_L \quad (8)$$

where  $\mathbf{r}(t)$  is the location of the grain tip,  $\mathbf{G}_L$  is the temperature gradient at the tip, and  $T_L$  is the liquidus temperature. The longitudinal axis of a GBLF was defined to be the same as the axis of an adjacent grain. By giving a point  $r_0$  on the axis, the GBLF axis was computed by integrating Eq. (8) with a fourth-order Runge-Kutta method (see Fig. 4). The temperature field required in the integration was obtained from post-processing of the FE

model of the weld process described below. As will be explained later, the transverse direction to a GBLF was defined as the direction of maximum strain rate, normal to its longitudinal axis.

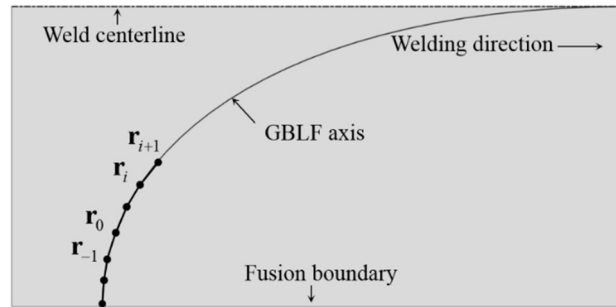


**Fig. 4** Schematic showing the procedure of integrating the longitudinal axis of a GBLF that passes the point  $r_0$ .

### *GBLF solidification*

The solidification of the liquid in the given GBLF was approximated with a multicomponent Scheil-Gulliver model. The undeformed GBLF is assumed to be bounded by columnar dendrites separated by the primary dendrite arm spacing  $\lambda_1$  (see Fig 5a). In order to simplify the modeling of the solidification process, the interfaces of the GBLF were assumed to be planar, separated by the undeformed GBLF thickness  $2h_0$  (see Fig. 5b) [14].

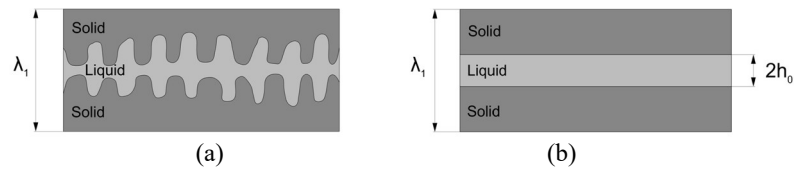


**Fig. 5** (a) Schematic representation of a GBLF with dendritic interfaces, (b) simplified GBLF with planar interfaces.

The undeformed half GBLF thickness ( $h_0$ ) can then be written as:

$$h_0 = \frac{\lambda_1}{2} (1 - f_s) \quad (9)$$

where  $f_s$  is the volume fraction of solid.  $f_s$  was determined for Alloy 718 with the thermodynamic software Thermo-Calc [14]. The resulting volume fraction of solid vs. temperature curve is shown in Fig 6.



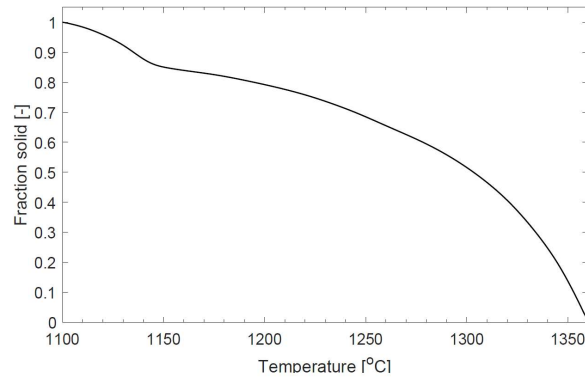


**Fig. 6** Volume fraction of solid of Alloy 718 as a function of temperature.

The primary dendrite arm spacing  $\lambda_1$  in Eq. (9) was computed from the following simple one-parameter expression [8,13]:

$$\lambda_1 = \frac{C_1}{(G_L)^{1/2}(R_L)^{1/4}} \quad (10)$$

where  $R_L$  is the solidification velocity at the grain tip and  $C_1$  is a calibration parameter.

The solidification speed  $v^*$  of the solid-liquid interface for the idealized GBLF shown in Fig. 5b can now be computed by the negative time-derivative of  $h_0$  (Eq. (9)), which gives:

$$v^* = \frac{\lambda_1}{2} \frac{df_s}{dT} \frac{dT}{dt} \quad (11)$$

where  $T$  is obtained from the FE model of the weld process. The liquid that remains when the temperature drops below the solidus temperature was assumed to solidify instantly.

#### *GBLF thickness*

During the solidification of the weld, thermal tensile strains can strongly localize in the weak GBLFs. The deformed GBLF thickness,  $2h$ , at an arbitrary location on the axis of the GBLF, was computed as follows. At the given location on the GBLF axis, all macroscopic mechanical strain normal to the axis that occurs during the infinitesimal time interval  $dt$  and within a region with diameter  $2h + l_0$  surrounding the GBLF axis, is assumed to localize in the GBLF (see Fig. 7). The length scale  $l_0$  represents the amount of surrounding solid phase of the GBLF that can carry tensile loads. The solid phase is assumed to be much stiffer than the liquid phase, such that all macroscopic mechanical strains localize in the GBLF. Let  $\epsilon_m$  be the macroscopic mechanical strain tensor obtained from the FE model of the weld process. Then the velocity of the solid-liquid interface of the GBLF can be written as (see Fig. 7):

$$\frac{dh}{dt} = \left(h + \frac{l_0}{2}\right) \frac{d\varepsilon_{\perp, \max}^m}{dt} - v^* \quad (12)$$

where  $v^*$  is the solidification velocity given by Eq. (11).  $\varepsilon_{\perp, \max}^m$  is the largest macroscopic mechanical strain rate in a plane normal to the axis of the GBLF, and is evaluated on the GBLF axis. Thus, the normal direction of the GBLF is assumed to be parallel to the direction of  $\varepsilon_{\perp, \max}^m$ .

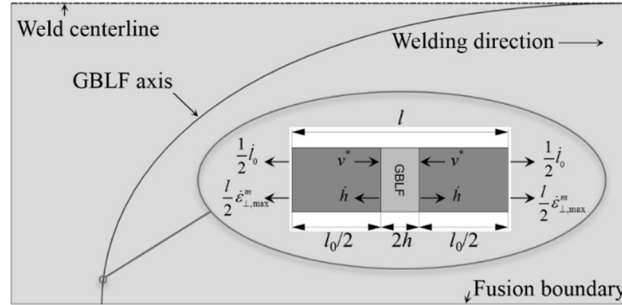


Fig. 7 Strain localization in a GBLF.

The strain partitioning length  $l_0$  depends on the coalescence and the interlocking of dendrites and grains. In this study,  $l_0$  was estimated from the temperature and the primary dendrite arm distances as follows. At the liquidus temperature  $T_l$ , there is no strain localization, and thus  $l_0 = 0$  at  $T_l$ . At the coherent temperature  $T_c$ , the dendrites of individual grains have started to coalesce, and therefore the dendritic structure can carry small tensile loads. In this case,  $l_0$  was assumed to have length equal to the width of the primary dendrite arm spacing. Below  $T_c$ , strains were assumed to localize between grain clusters. At the solidus temperature  $T_s$ ,  $l_0$  was assumed to have the same size as the grain clusters. The grain cluster size is not known, and was assumed to be proportional to the primary dendrite arm distance:

$$l_0(T_s) = C_2 \lambda_1 \quad (13)$$

where  $C_2$  is a parameter that is determined by inverse modeling [13,14]. At temperatures between  $T_s$ ,  $T_c$ , and  $T_l$ ,  $l_0$  was assumed to vary linearly. Fig. 8 show the values of  $l_0$  used in this study.

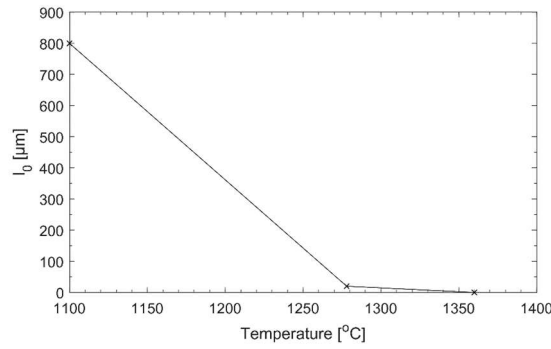


Fig. 8  $l_0$  as a function of temperature for Alloy 718.

### GBLF PRESSURE

By knowing the orientation, solidification velocity, and thickness of the GBLF from the above expressions, the liquid pressure in the GBLF can be computed as follows. The liquid flow in a GBLF is assumed to be in the direction of the GBLF axis. Moreover, the flow in a given GBLF is assumed to be confined solely to that GBLF, and thus no flow interactions with other GBLFs are considered. Taking the mass balance of an infinitesimally thin cross-section volume element of a given GBLF gives [13]:

$$\frac{d}{ds}(h\bar{v}) = -(1 + \beta)v^* - \frac{dh}{dt} \quad (14)$$

where  $\bar{v}$  is the average flow velocity,  $\beta$  is the solidification shrinkage factor, and  $s$  is a curved coordinate along the GBLF axis as shown in Fig. 3. For the part of the GBLF that extends into regions with liquid fraction below 0.1, a Poiseuille parallel plate flow is used, which gives:

$$\bar{v} = -\frac{h^2}{3\mu} \frac{dp}{ds}, \quad f_l \leq 0.1 \quad (15)$$

where  $\mu$  is the dynamic viscosity and  $p$  is the liquid pressure. For the rest of the GBLF, which extends into regions with liquid fraction greater than 0.1, the flow is assumed to be governed by Darcy's law for porous flows:

$$\bar{v} = -\frac{K_{\parallel}}{\mu f_l} \frac{dp}{ds}, \quad f_l > 0.1 \quad (16)$$

where  $K_{\parallel}$  is the longitudinal permeability of the columnar dendrite structure. The permeability relation developed by Heinrich and Poirier [15] for columnar dendritic structures is used:

$$K_{\parallel} = \begin{cases} 3.75 \times 10^{-4} f_l^2 d_1^2, & f_l \leq 0.65 \\ 2.05 \times 10^{-7} \left[ \frac{f_l}{1-f_l} \right]^{10.739} d_1^2, & 0.65 < f_l \leq 0.75 \\ 0.074 \left[ \log \left( \frac{1}{1-f_l} \right) - 1.49 \right. \\ \left. + 2(1-f_l) - 0.5(1-f_l)^2 \right] d_1^2, & 0.75 < f_l \leq 1.0 \end{cases} \quad (17)$$

where  $d_1$  is the spacing between the dendrites. In order to account for the increase in permeability at the GBLF that occurs when deformation is localized to the GBLF,  $d_1$  and  $f_l$  in Eq. (17) are replaced by [13]:

$$d_1^* = \lambda_1 + 2h - 2h_0 \quad (18)$$

and

$$f_l^* = 1 - \frac{\lambda_1^2(1-f_l)}{d_1^{*2}} \quad (19)$$

The pressure in the GBLF was obtained by integrating Eq. (14) twice along the axis of the GBLF, with  $\bar{v}$  given by Eqs. (15) and (16). The integrand was computed from the temperature and mechanical strain fields obtained from post-processing of the FE model of the weld process, evaluated at Lagrangian sample points on the GBLF axis. For a given time, the integration was performed between the intersections of the solidus and liquidus isotherms with the GBLF axis [13]. At the junction between the Poiseuille and Darcy flow regions, continuous pressure and flow were assured. In the integration of Eq. (14), the following two boundary conditions were used. At the liquidus isotherm, the liquid pressure was assumed to be equal to the atmospheric pressure. At the solidus isotherm, the pressure gradient was given by [13]:

$$\frac{dp}{ds} = \left( \frac{3\mu\beta}{h^2} \frac{ds}{dt} \right) \Big|_{s=s_{T_s}} \quad (20)$$

where  $ds/dt$  is the projected solidification velocity at the solidus temperature, in the direction of the GBLF axis. Eq. (20) corresponds to the pressure drop at the end of the GBLF due to the liquid flow caused by solidification-induced shrinkage of the remaining liquid at the end of the film.

The dynamic viscosity of Alloy 718 in the solidification interval was obtained from the software package JMatPro [14].

#### GAS-LIQUID INTERFACE ENERGY

To compute the CII value in Eq. (6), the factor  $\gamma_{gl} \cos \theta$  must be known. It is assumed that the solid phase is sufficiently wetted by the liquid phase, such that the contact angle is small. In this case,  $\cos \theta$  is approximately 1.

## Mathematical Modelling of Weld Phenomena 12

The surface tension of Alloy 718 has been measured by the oscillating drop method [14]. It varies linearly with temperature, in the temperature interval  $1350 < T < 1600$  °C, according to the function:

$$\gamma \text{ mNm}^{-1} = 1800 - 0.11(T - 1725^\circ\text{C}) \quad (21)$$

This equation was used to estimate  $\gamma_{gl}$ . The equation was assumed to be valid for extrapolation down to the solidus temperature.

### MATERIAL AND EXPERIMENTAL PROCEDURES

The SC model in this study was calibrated and evaluated with Vareststraint tests of Alloy 718. The tests are described below, along with some relevant properties of Alloy 718.

#### ALLOY 718

Alloy 718 is a high-strength, corrosion-resistant nickel-chromium alloy used between -250 and 700 °C. It was developed in the early 1960s and is used in a wide range of applications such as components for liquid fuel rockets, rings, casings, and various formed sheet metal parts for aircraft and land-based gas turbine engines, and in cryogenic tanks. It is the predominant nickel-iron-based superalloy, representing nearly half of the total quantity of superalloys used worldwide. Typical composition limits of Alloy 718 are shown in Table 1.

**Table 1** Chemical composition limits of Alloy 718 (wt%).

Ni	Fe	Cr	Nb	Mo	Ti	Al	Co	C	Mn	Si	P	S	B	Cu
50.00	Bal.	17.00	4.75	2.80	0.65	0.20	-	-	-	-	-	-	-	-
55.00	Bal.	21.00	5.50	3.30	1.15	0.80	-	0.08	0.35	0.35	0.015	0.015	0.006	0.30

The matrix consisting of approximately 50% nickel, 20% chromium, and 20% iron is strengthened primarily by the 5% niobium content. Niobium forms the main strengthening precipitate  $\gamma''$  ( $\text{Ni}_3\text{Nb}$ ). In an age-hardened condition, Alloy 718 contains approximately 20%  $\gamma''$  phase.

Alloy 718 is reported to be resistant to strain-age cracking, owing to the sluggish precipitation kinetics of its principal strengthening precipitate  $\gamma''$ . However, it is not free of weldability challenges, including SC.

## Mathematical Modelling of Weld Phenomena 12

### THE VARESTRAINT TEST

The Varestraint test was developed in the 1960s by Savage and Lundin at Rensselaer Polytechnic Institute. This test allows the study of the susceptibility of a specimen to hot cracking via a systematic procedure requiring only small and simple test specimens. The influences of the material, the welding process, and the constraint factors on the hot cracking behavior can be identified. The basic procedure is to rapidly apply an augmented strain during the welding of a plate. The amount of augmented strain  $\varepsilon_{aug}$  depends on the material thickness and the radius of the die block, according to the following equation:

$$\varepsilon_{aug} = \frac{t}{2R+t} \quad (22)$$

where  $t$  is the sample thickness and  $R$  is the radius of the die block. The bending is applied along the length of the weld made on the sample. The augmented strain can be varied simply by changing the die block radius.

### EXPERIMENTAL PROCEDURE

The derived model for SC was calibrated and evaluated using Varestraint tests. The test setup is shown in Fig. 9a. Figs. 9b and c show the test plate in the press before and after bending, respectively.

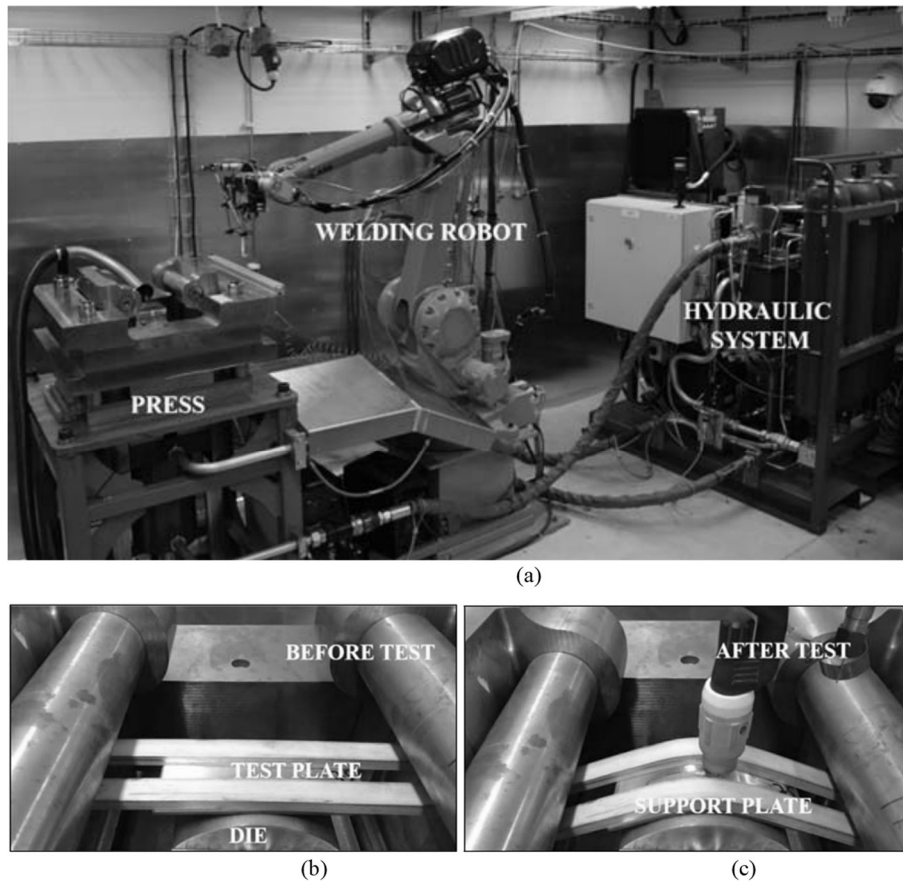


**Fig. 9** Vareststraint test equipment used in the experiments.

In the test, the plate is bent over the die block by vertical displacement of the rollers while the die block remains stationary. Support plates are used to reduce kinking of the test plate. All tests were performed on 3.2 mm-thick plates with dimensions of 60×150 mm. The dimensions of the support plates were 10×20×300 mm. The starting position of the weld was 40 mm from the contact point between the plate and the die block. The bending was initiated when the weld electrode passed over the apex of the die block (i.e., the contact point between the plate and die). Welding was continued for 5 s after bending was initiated. Autogenous TIG welding was used for the tests. The welding current was 70 A, with automatic voltage regulation. Based on an estimated voltage of 10 V, the weld power was 700 W. The welding speed was 1 mm/s and the stroke rate was 10 mm/s. The Vareststraint test parameters are summarized in Table 2.

**Table 2** Varestraint parameters.

Welding speed	1 mm/s
Welding current	70 A
Arc length	2 mm
Gas flow (Ar)	15 L/min
Weld length	40 mm
Weld offset	5 mm
Stroke rate	10 mm/s

Four different die block radii were used, resulting in 0.3%, 0.4%, 0.8%, and 1.1% augmented strains. The test plates underwent two different heat treatments prior to the welding: the first was solution annealing at 954 °C for 1 h, and the second consisted of solution annealing at 1050 °C for 3 h followed by furnace cooling to 954 °C, where it was held for 1 h. Table 3 shows the details of the Varestraint samples used in this study.

**Table 3** Sample parameters.

Sample #	Augmented strain (%)	Heat treatment
3	1.1	954 °C (1 h)
6	1.1	1054 °C (3 h) + 954 °C (1 h)
20	0.8	954 °C (1 h)
21	0.8	954 °C (1 h)
23	0.8	1054 °C (3 h) + 954 °C (1 h)
24	0.8	1054 °C (3 h) + 954 °C (1 h)
37	0.4	954 °C (1 h)
38	0.4	954 °C (1 h)
40	0.4	1054 °C (3 h) + 954 °C (1 h)
41	0.4	1054 °C (3 h) + 954 °C (1 h)
42	0.4	1054 °C (3 h) + 954 °C (1 h)
58	0.3	1054 °C (3 h) + 954 °C (1 h)

The location, length, and width of the surface cracks in the fusion zone were measured using a stereo microscope. No cracks were found in any of the samples with 0.3% and 0.4% augmented strains. Even though no cracks were found in the 0.4%-strain test samples, a strain of 0.4% was considered to be the threshold strain for crack initiation [14].

### FINITE ELEMENT MODEL

The temperature field and macroscopic mechanical strain fields are required in order to evaluate the SC model derived in this study. Both were obtained from coupled thermo-mechanical finite element models of Varestraint tests using the software MSC Marc. The FE models use a double ellipsoid heat source as the weld heat input. Thermophysical properties of the mushy zone in the FE models were obtained from mixture rules of the solid and liquid phases. Four different material models, each active in a different temperature range, were used to describe the inelastic behavior in the fusion zone and the partially melted zone in the FE models. Due to the symmetry at the weld centerline, only one half of the Varestraint test was modeled. In the region of the Varestraint test where SC occurs, an element size of approximately 100 μm was used in order to resolve the



temperature and strain fields. Fig. 10a shows the meshed model and Fig. 10b shows the fine mesh used in the crack-susceptible region. The FE model is described in more detail in [14].

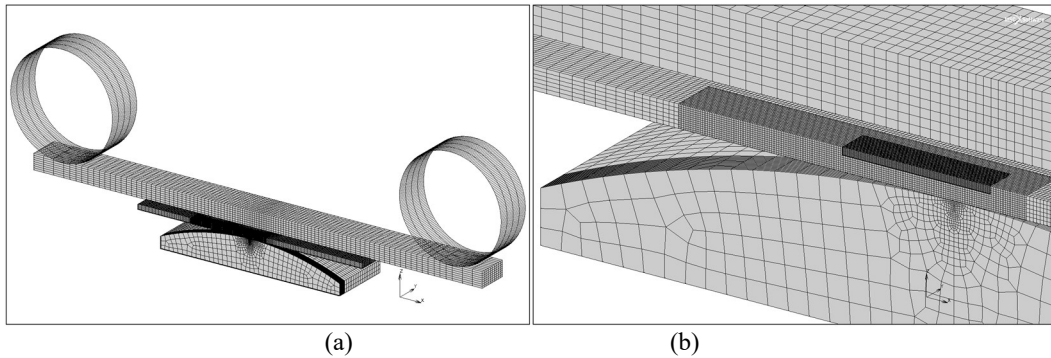


**Fig. 10** (a) Meshed half-symmetric part of the Varestraint test and (b) mesh used in the region where cracking occurred.

### RESULTS

The proposed SC model was calibrated in a Varestraint test with 0.4% augmented strain, and then validated on tests with 0.8% and 1.1% strains. All properties were evaluated on GBLF axes on the surfaces of the weld, separated from each other at the fusion boundary by approximately 1 mm. The evaluation was performed on the weld surface, as the susceptibility to cracking is considered to be highest at this area because the tensile strains from the bending are largest on the weld surface. It is also easier to evaluate experimental results on the weld surface, as no cutting is required. The x and y coordinates in the plots represent the distances from the weld start and the weld centerline, respectively. The welding direction was from left to right. When computing the GBLF pressure, the presence of the pore in the GBLF was not considered. The effect of surface interaction on the flow in GBLFs was not considered either; in other words, the evaluation was considered to have taken place close to the weld surface but not so close that it would be disturbed by the surface.

#### GBLF AXES

Fig. 11 shows the computed GBLF axes from Eq. (8), at the weld surface in a Varestraint test with 0.4% augmented strain. They are separated by 1 mm at the fusion boundary, and together cover the entire region where surface cracks occurred. For the leftmost axis, the locations of the sample points which were used to evaluate the temperature and mechanical strains using the FE model, are shown with crosses.

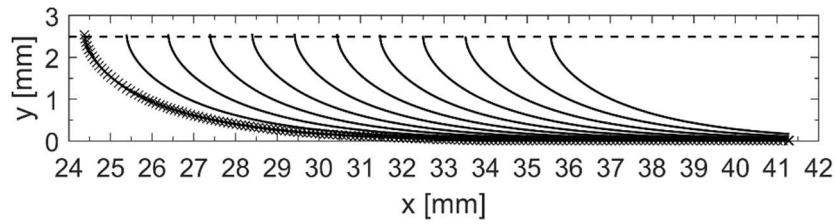


**Fig. 11** Computed GBLF axes at the weld surface in the Varestraint test with 0.4% augmented strain. The axes are separated by 1 mm at the fusion boundary. Only one half of the symmetric weld is shown.

#### CALIBRATION

In order to estimate the susceptibility of the sample to cracking, the parameters  $C_1$  and  $C_2$  must be calibrated.  $C_1$ , which is related to  $\lambda_1$  via Eq. (10), was calibrated such that the computed value agreed with the measured value at a location approximately 30 mm from the weld start, 1 mm from the fusion boundary, and 0.1 mm below the weld surface.  $C_2$  was calibrated such that a maximum CIL of 300  $\mu\text{m}$  was obtained for the 0.4%-strain test. As was previously mentioned, an augmented strain of 0.4% was considered to be the threshold value for crack initiation. More details of the calibration can be found in [14].

#### CIL

Fig. 12a shows the computed CIL for the 0.8%-strain tests, together with the crack locations in four experimental test specimens with the same strain. The computed CIL for the GBLF tracks shown covers all cracks found in the experiments. Most of the cracks were located 0.5 - 2 mm from the weld centerline. Interestingly, it is also this region that has the GBLFs with the highest CILs. It is also interesting to note that the crack orientations did not diverge too much from the GBLF axes, which indicates that the assumption that grain growth occurred in the direction normal to the liquidus isotherm was a fairly good approximation in this situation.

Fig. 12b shows the computed CILs for the 1.1%-strain test together with the crack locations in two test specimens with the same strain. The computed CIL for the GBLF tracks shown almost covers all cracks found in the experiments. Similarly to the result for the 0.8%-strain test, the majority of the cracks were located 0.5 - 2 mm from the weld centerline. Again, it is in this region that the model predicts the highest CILs. The agreement between the crack orientations and the GBLF axes in this test is fairly strong.

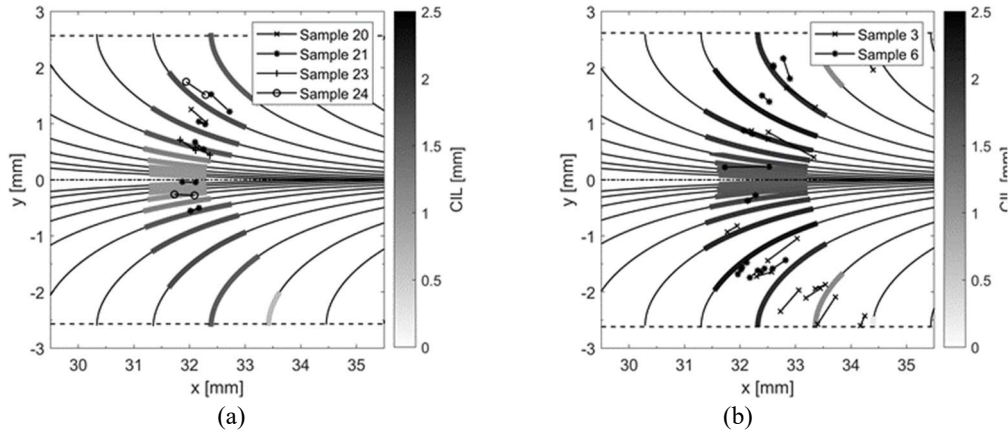
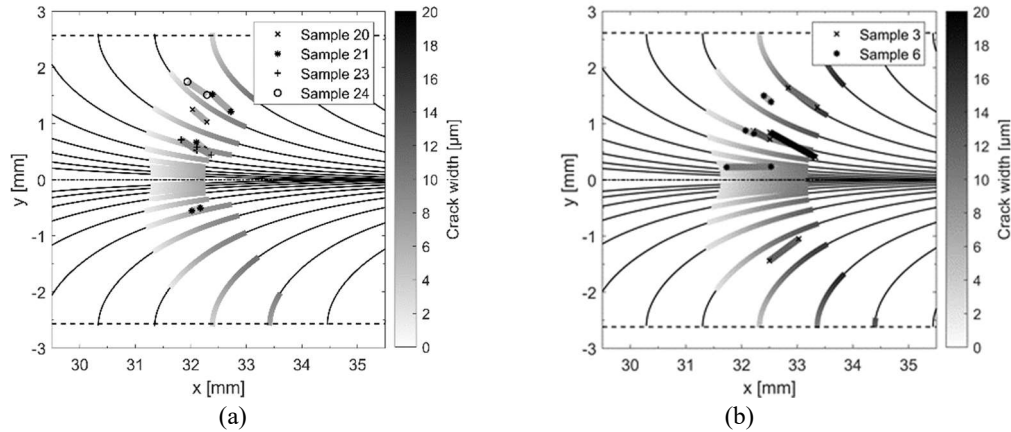


Fig. 12 CIL of (a) 0.8% and (b) 1.1% augmented strain tests.

### CRACK WIDTH

In order to evaluate the strain localization model used in this work, the crack widths predicted by the model were compared to those measured experimentally. The predicted crack width was computed as the GBLF thickness at the moment when the temperature dropped below the solidus temperature. Fig. 13a shows the computed and measured crack widths for the 0.8%-strain tests. The agreement between the computed and measured crack widths is pretty strong.

The agreement between the computed and measured crack widths is also fairly good for the 1.1%-strain test, which is shown in Fig. 13b. However, there is one crack, approximately 20  $\mu\text{m}$  wide, that is considerably larger than the rest of the cracks. The reason for this may be that deformation continued to localize in the crack at temperatures below the solidus temperature, a phenomenon which is not accounted for in the model. The strong agreement between the computed and measured crack widths is an indication that the strain localization model used in this experiment worked fairly well under these conditions.



**Fig. 13** Crack width in samples subjected to (a) 0.8% and (b) 1.1% augmented strain tests.

### CONCLUSIONS

Simulations of weld solidification cracking in Varestraint tests of Alloy 718 were performed, and good accuracy was achieved. The physical based crack criterion is capable of pinpointing the region where SC will occur. The strain localization model used in this work predicts crack widths that are in good agreement with experimental measurements. The computed orientations of the grain boundaries agree fairly well with the orientation of the intergranular cracks observed experimentally.

### ACKNOWLEDGEMENTS

The authors gratefully acknowledge financial support from the NFFP program operated by the Swedish Armed Forces, the Swedish Defense Material Administration, and the Swedish Governmental Agency for Innovation Systems (project numbers: 2013-01140 and 2017-04837). Senior lecturer Paul Åkerström at Luleå Technical University is also gratefully acknowledged for his invaluable support and guidance. Moreover, the authors sincerely thank Rosa Maria Pineda Huitron and Laetitia Lefevre from the Material Science Department at Luleå Technical University for their assistance in evaluating the experimental Varestraint tests.

### REFERENCES

- [1] LIPPOLD, JOHN C., SAMUEL D. KISER, AND JOHN N. DUPONT: *Welding metallurgy and weldability of nickel-base alloys*. John Wiley & Sons, 2011.
- [2] LIPPOLD, JOHN C: *Welding metallurgy and weldability: John Wiley & Sons, 2014*.
- [3] KOU, SINDO: *Welding metallurgy*. John Wiley & Sons, 2003.
- [4] ESKIN, D. G., AND L. KATGERMAN: *Mechanical properties in the semi-solid state and hot tearing of aluminum alloys*. *Progress in Materials Science* 49.5 (2004): 629-711.

- [5] CONIGLIO, N., AND C. E. CROSS: *Initiation and growth mechanisms for weld solidification cracking*. International Materials Reviews 58.7 (2013): 375-397.
- [6] RAPPAZ, M., J-M. DREZET, AND MET GREMAUD: *A new hot-tearing criterion*. Metallurgical and materials transactions A 30.2 (1999): 449-455.
- [7] SUYITNO, W. H., AND L. KATGERMAN: *Hot tearing criteria evaluation for direct-chill casting of an Al-4.5 pct Cu alloy*. Metal Mater Trans A 36.6 (2005): 1537-1546.
- [8] DANTZIG, JONATHAN A., AND MICHEL RAPPAZ: *Solidification*. EPFL press, 2009.
- [9] CONIGLIO, N., AND CARL EDWARD CROSS: *Mechanisms for solidification crack initiation and growth in aluminum welding*. Metallurgical and Materials Transactions A 40.11 (2009): 2718-2728.
- [10] PUNCREOBUTR, CHEDTHA, ET AL.: *Synchrotron tomographic characterization of damage evolution during aluminum alloy solidification*. Metallurgical and Materials Transactions A 44.12 (2013): 5389-5395.
- [11] AUCOTT, L., ET AL.: *Initiation and growth kinetics of solidification cracking during welding of steel*. Scientific reports 7 (2017): 40255.
- [12] JOAR DRAXLER, JONAS EDBERG, LARS-ERIK LINDGREN, JOEL ANDERSSON: *Simulation of Weld Solidification Cracking Part I: A Pore Based Crack Criterion*, Submitted for publication.
- [13] JOAR DRAXLER, JONAS EDBERG, LARS-ERIK LINDGREN, JOEL ANDERSSON: *Simulation of Weld Solidification Cracking Part II: A Model for Estimation of Grain Boundary Liquid Pressure*, Submitted for publication.
- [14] JOAR DRAXLER, JONAS EDBERG, LARS-ERIK LINDGREN, JOEL ANDERSSON: *Simulation of Weld Solidification Cracking Part III: Application to Varestraint tests of Alloy 718*, Submitted for publication.
- [15] HEINRICH, JUAN C., AND DAVID R. POIRIER: *Convection modeling in directional solidification*. Comptes Rendus Mecanique 332.5-6 (2004): 429-445.

# USE OF MODELLING TO CHARACTERIZE THE RISK OF HOT CRACKING IN AUSTENITIC STAINLESS STEELS DURING WELDING

G. TRAN VAN\*\*\*, D. CARRON\*\*, P. LE MASSON\*\*,  
J. STODOLNA\*\*\*, A. ANDRIEU\*\*\*, J. DELMAS\* and V. ROBIN\*

\*EDF R&D, Chatou, France

\*\*Univ. Bretagne Sud, UMR CNRS 6027, IRDL, F-56100, Lorient, France

\*\*\*EDF R&D, Renardières, France, vincent.robin@edf.fr

DOI 10.3217/978-3-85125-615-4-27

## ABSTRACT

Liquation cracking may occur in the heat affected zone (HAZ) during welding. Two factors influence this phenomenon: the tensile stresses generated during welding and the potential loss of ductility due to the presence of a liquid film at grain boundaries depending on their chemical composition.

Gleeble hot-ductility tests have been used to study the combined effect of boron content and holding time on ductility drop in the liquation temperature range of a 316L type austenitic stainless steel. It is shown that high boron contents and short holding times promote the loss of ductility in the liquation temperature range. Secondary ion mass spectrometry (SIMS) has been used to correlate mechanical results to boron distribution either at grain boundaries or in the bulk.

Other weldability tests have been performed to confirm the influence of boron content on hot cracking sensitivity of AISI 316L stainless steels. Results indicate that cracks appear on all specimens but at different strain levels. The higher boron content is, the more specimen exhibits tendency to hot cracking. Thanks to numerical modelling of these tests, a cracking criteria is proposed to quantify the risk of liquation cracking for different boron contents.

Keywords: Welding, Hot Cracking, Austenitic Stainless Steel, Boron

## INTRODUCTION

Many welded components of pressurized water reactors are made of austenitic stainless steels. During welding of these materials hot cracking due to solidification cracking and/or liquation cracking must be prevented. The influence of harmful elements as sulphur, phosphorus, boron, silicon, niobium and titanium on fully austenitic stainless steel cracking sensitivity is well documented [1][2][3]. With a very low solubility in austenite at high temperature and its tendency to form low melting eutectics with iron and nickel, boron has a particularly unfavourable influence on hot cracking resistance of austenitic stainless steel [1][3] and nickel-based superalloys [4][5][6][7]. Even at very low contents, boron favours

the phenomenon of heat-affected zone (HAZ) liquation cracking which occurs when both intergranular liquid films and sufficient strains are present. In nickel-based superalloys, this intergranular microfissuring phenomenon is associated with constitutional liquation of precipitates at grain boundaries [5][8][9] or grain boundary segregation of melting point depressant elements as boron [4][6][7]. As reported in literature [1], HAZ liquation cracking can also occur during welding of 18Cr-10Ni austenitic stainless steels due to the presence of intergranular austenite /  $(\text{FeCr})_2\text{B}$  eutectic phase with a low melting point of 1180°C [10][11]. During welding, the temperature in the HAZ can reach the melting temperature of this eutectic phase, which leads to the presence of a liquid phase at the grain boundaries. If the thermal stresses due to welding and self-restraint are sufficiently high, liquation intergranular cracks may appear in the HAZ close to the fusion zone.

To avoid the problem of HAZ liquation cracking, the specification of nuclear fabrication French code RCC-M requires the boron content to be less than or equal to 18 ppm for all of the austenitic stainless steels. However, for the steel of the type 321, the literature shows that there is no cracking if the boron content is less than 35 ppm [10][11]. To rule on the acceptability of these boron-alloyed products, it is essential to better characterize their hot cracking behaviour with respect to the boron content. In this work, Gleeble hot-ductility testing and Vareststraint and PVR [12] welding test were achieved to analyse the effect of boron content on hot cracking susceptibility in type 316L austenitic stainless steel. These tests were evaluated to confirm the underlying metallurgical mechanisms. The set of tests also shows that the threshold of 18 ppm is particularly severe for the studied alloy.

Finally, the simulation of the PVR type weldability tests allowed access to the local thermo-mechanical conditions that lead to grain decohesion in a HAZ sensitive to hot cracking. The proposed criteria for estimating the risk of cracking is based on a critical stress and a holding time which are two elements depending on the welding configuration and process. The elevation of the threshold on boron content of austenitic stainless steels can be ensured experimentally by classification of the risk of cracking according to the boron content from weldability tests or by simulation demonstration that the critical conditions in terms of stress and holding times are not reached in a given welding configuration.

### EXPERIMENTAL WORK

Seven AISI type 316L austenitic stainless steels were used in this study. Their chemical composition are shown in Table 1. Three of them, designated by the letters A, B and C, were industrially manufactured and have a boron content of  $2\pm 1$  ppm,  $19\pm 2$  ppm and  $31\pm 2$  ppm respectively. Four of them, designated by the letters D, E, F and G, were experimental alloys with identical composition than alloy C except for the boron content which was  $20\pm 2$  ppm,  $35\pm 3$  ppm,  $44\pm 4$  ppm and  $50\pm 4$  ppm respectively. Cast ingots of these alloys were prepared by UGITECH (Ugine, France) using vacuum induction melting and hot rolled to 11-mm-thick-plates at 1250°C. Experimental alloys were solution heat treated at 1050°C for 50 minutes and water quenched according to the common industrial process. Measurements of boron content was realized by inductively coupled plasma mass spectrometry (ICP-MS).

**Table 1** Chemical compositions of the 316L stainless steels (wt % except for boron content in ppm)

Steel	B (ppm)	C	Mn	Si	P	S	Cr	Ni	Mo	Co	Cu	Al	N
A	2±1	0.020	1.40	0.510	0.040	0.026	16.90	10.20	2.0	0.340	0.410	<0.004	0.074
B	19±2	0.014	1.40	0.400	0.030	0.029	16.70	10.10	2.0	0.130	0.480	0.010	0.042
C	31±2	0.018	1.58	0.513	0.027	0.001	16.95	10.05	2.06	0.084	0.105	-	0.048
D	20±2	0.019	1.56	0.540	0.031	0.0015	16.97	10.07	2.06	0.087	0.106	0.033	0.043
E	35±3	0.017	1.54	0.550	0.026	0.0014	16.87	10.04	2.06	0.082	0.108	0.033	0.051
F	44±4	0.016	1.59	0.540	0.027	0.0011	17.25	10.03	2.05	0.080	0.106	0.043	0.052
G	50±4	0.016	1.61	0.540	0.027	0.0017	17.03	10.08	2.06	0.082	0.107	0.035	0.050

A Gleeble 3500 thermo-mechanical simulator was used to achieve hot ductility tests in vacuum. Test specimens, of 6 mm in diameter and with a 16 mm free span between water-cooled grips, were heated according to a predetermined thermal cycle and fractured at temperatures between 1150°C and 1350°C by applying a tensile load with a stroke rate of 50 mm/s. After the test, fracture surfaces are examined using a scanning electron microscope JEOL JSM 6460-LV and ductility is determined in terms of the reduction in area by comparing final and initial section area of the broken specimen. On-heating and on-cooling tests were realized. For on-heating tests, the heating rate was 100°C/s and the influence of isothermal holding time before applying the tensile load at testing temperature was studied with holding time varying between 0.1 and 3s. For on-cooling tests, the heating rate was also 100°C/s and two peak temperatures of 1330°C and 1360°C were considered. Once the peak temperature was reached the specimen was subsequently cooled at 80°C/s before to be fractured after a holding time of 0.2s at testing temperature. For alloy F, the influence of the holding time on boron distribution was also characterized by Secondary-Ion Mass Spectrometry (SIMS) analysis. Prior to SIMS analysis, two thermal treatments identical to on-heating hot ductility thermal cycles with 0.1s and 2.5s holding time at 1220°C respectively, but with a cooling rate of the order of 300°C/s, were achieved into a LINSEIS quenching dilatometer (RITA). As received and heat treated F-alloy samples were electrolytically etched in 10% oxalic acid. SIMS analysis was then performed on a CAMECA IMS5F ion microscope using primary ion beam of O<sub>2</sub><sup>+</sup> (15kV acceleration voltage, 1 µA beam current). The negative secondary ions emitted from the surface were BO<sub>2</sub><sup>-</sup>. Varestraint and PVR tests were carried out on the materials D, E, F and G with 20 ppm, 35 ppm, 44 ppm and 50 ppm of boron content respectively. The dimensions of the Varestraint specimens were 200 × 60 × 7 mm. The dimensions of PVR specimens were 300 × 40 × 3 mm. The welding parameters of Varestraint and PVR tests, achieved with a single melt run with TIG welding, were kept constant and are shown in Table 2.



**Table 2** TIG welding parameters of the Varestraint and PVR tests

Parameters of Varestraint tests		Parameters of PVR tests	
Current	200A	Current	81A
Voltage	13V	Voltage	8.4V
Travel speed	2.33 mm/s	Travel speed	2.00 mm/s
Shielding gas	Argon	Shielding gas	Argon
Strain level (47 mm die block radius)	7%	Maximal stroke rate	20 mm/min

A part of the welding surface of F-specimen containing cracks were electrolytically etched using 10% oxalic to reveal the microstructure of grains, and then observed at the binocular.

## EXPERIMENTAL RESULTS

### GLEEBLE HOT-DUCTILITY TESTING AND HAZ LIQUATION CRACKING SUSCEPTIBILITY

On-heating and on-cooling Gleeble tests can be used to evaluate HAZ liquation cracking susceptibility [13][14]. The on-heating test consists of heating the specimen until a predetermined temperature, of holding at this temperature during a certain time and of fracturing the specimen by applying a tensile load with a constant stroke rate. When the testing temperature is raised, ductility may increase slightly then suddenly drop until it reaches almost zero at the nil ductility temperature (NDT). If low-melting point eutectics are present as grain-boundary precipitates or if segregation of impurities to grain boundaries reducing the melting temperature of the boundaries relative to the surrounding matrix has occurred, the increase in temperature leads the grain boundary to melt and the sudden drop in ductility occurs at lower temperature. In this case the ductility drop temperature is representative of the metallurgical degradation associated with grain boundary melting and NDT can then be considered as the temperature where a thin continuous liquid film coats the grain boundary surfaces. As the testing temperature is increased, the nil-strength temperature (NST) is reached where the amount of liquid is high enough that the boundaries are unable to accommodate any stress. On-cooling ductility tests are achieved typically with peak temperature between NDT and NST and the ductility recovery temperature (DRT) is determined when the alloy regains measurable ductility due to a sufficient solidification of the liquid formed during the heating cycle. Various criterion exist to interpret hot ductility tests for assessing HAZ liquation cracking susceptibility, the temperature range NST-DRT being the most widely utilized. Lin et al. [14] having noticed that this criteria may not be representative of HAZ liquation cracking that occurs close to the fusion boundary, had rather suggested a methodology to quantify a thermal-crack susceptible region (CSR) in the HAZ where liquation may occur. On heating and on-cooling CSR can be determined using the temperature range between NDT and the liquidus temperature and the temperature range between on-cooling peak temperature and DRT respectively.

*On-heating hot ductility tests*

As explained previously, the ductility drop with temperature highlighted by on-heating tests is a relevant information to evaluate HAZ liquation cracking susceptibility. In Fig. 1 the results of the on-heating tests achieved with the seven materials with a holding time of 1.0s at the testing temperature are compared. A noticeable difference exists between ductility evolution with temperature for high (F, G) and low and medium boron-level (A to E) alloys. To better highlight this behaviour, the ductility drop temperature was determined as the temperature where ductility decreases to 75% which corresponds to a reduction of one half of the diameter of the specimen. Fig. 2 shows the dependence of this temperature as a function of the boron content. At boron level lower or equal to 35 ppm, ductility drop temperature has an almost constant value around 1320°C. This temperature decreases abruptly if the boron content exceeds this value and then levels out around 1180°C for the alloys with 44 and 50 ppm boron content.

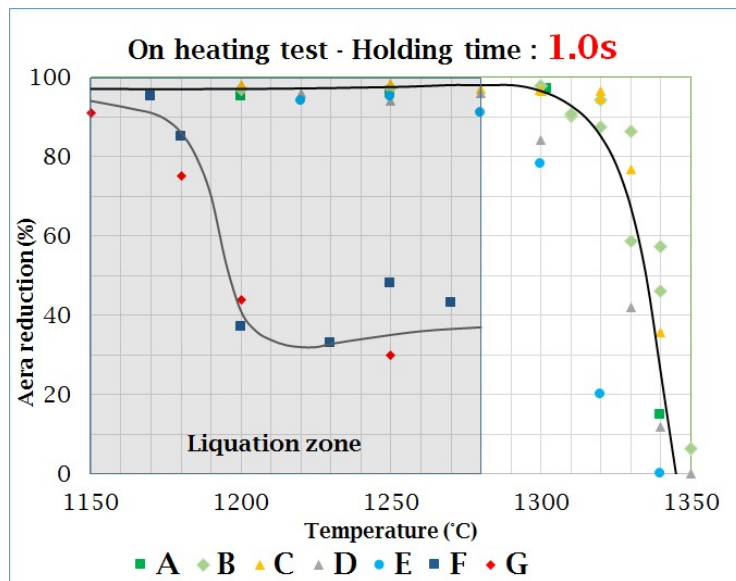


**Fig. 1:** Results of the on-heating tests with a holding time of 1.0s (A=2, B=19, C=31, D=20, E=35, F=44, G=50 ppm of boron respectively)

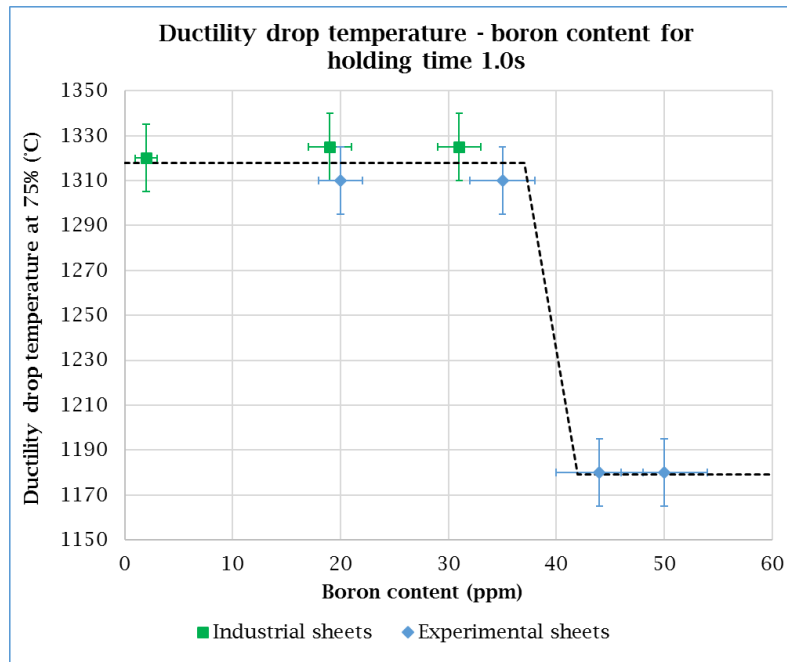


**Fig. 2:**Dependence of the ductility drop temperature with respect to boron content.

It is known that in austenitic stainless steel, because of the low solubility of boron in Fe-Cr-Ni alloys and the formation of boride-austenitic matrix low-melting eutectics at grain boundaries, boron has a detrimental effect on liquation susceptibility and thus lowers the ductility drop temperature even at low content [11][15]. Furthermore, due to non-equilibrium intergranular boron segregation occurring during the heat treatment cooling stage prior to welding, thin boron-enriched zone formation around grain boundary surface can also take place as shown in type 316L stainless steel [16]. As demonstrated for an Inconel alloy [7], it is also suggested a direct correlation between the amount of boron segregated at grain boundaries and the susceptibility to HAZ cracking once again because of the lower melting point of boron-enriched grain boundaries. In very low boron level type 321 and 316 stainless steels that do not experiment liquation cracking phenomena on welding, the ductility drop temperature is over 1300°C. Between 35 and 45 ppm of boron this temperature falls suddenly to 1280°C. At higher boron level, when intergranular boride eutectics were clearly identified, this temperature is around 1200°C [11]. The dependence of the ductility drop temperature with respect to boron content for the seven alloys tested in this study is thus consistent with the literature. When the holding time at the testing temperature is 1.0s, grain boundary melting must take place for boron level over 44 ppm with a ductility drop temperature around 1200°C that is close to the austenite-boride eutectic melting temperature. When intergranular boron enrichment is insufficient to promote grain boundary melting, i.e. when boron content is here under 35 ppm, the ductility drop temperature is over 1300°C and it is considered that the material has no risk of HAZ liquation cracking. The transition zone is between 35 and 44 ppm. The temperature range

where liquation may occur - i.e. “liquation zone” on Figure 1 - was defined between 1150 and 1280°C.

The literature [10] shows that increasing the holding time at on-heating testing temperature may reduce the risk of ductility drop into the liquation zone for type 321 stainless steels containing high boron content. Compared to welding it is similar to an increase of the magnitude of the heat input [16] since the higher the weld heat input the longer time the HAZ material spent at peak temperature. Therefore to confirm this effect, different welding representative holding times between 0.1 and 3s were considered for tests achieved on materials F (44 ppm) and G (50 ppm) that present the highest risk of HAZ liquation cracking.

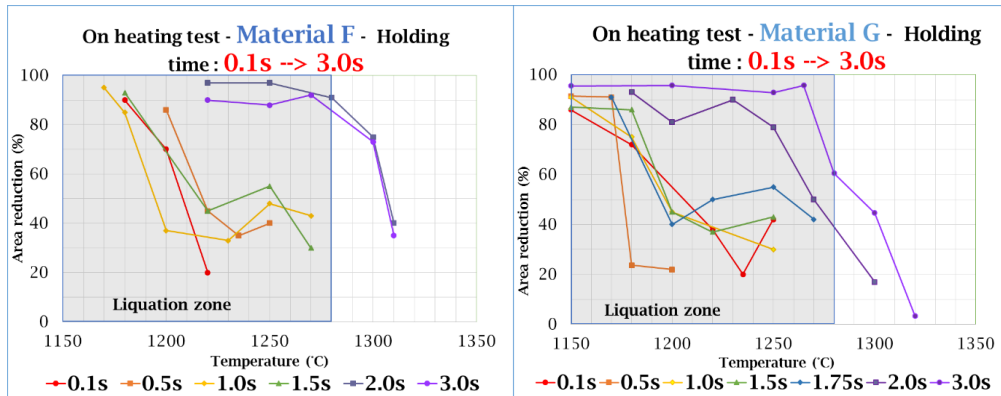


**Fig. 3:** Results of on-heating tests on two materials F (44 ppm B) and G (50 ppm B) with holding time from 0.1s to 3.0s.

It can be seen in Fig. 3 that the ductility drop temperature increases with increase in holding time for all of these two materials. This increase is abrupt with a holding time threshold between 1.5s and 2.0s. The ductility drop temperature for a holding time of 2.0s is actually much higher than that observed with 1.5s. Scanning electron microscopy (SEM) observation of the fracture surface of the F-specimens with 0.1s holding time confirms ductile failure in specimen tested at 1180°C (Fig. 4) and brittle intergranular failure in specimen tested at 1220°C (Fig. 5) that is consistent with a decrease of ductility with the testing temperature from 90% to 20% respectively. For comparison the fractograph of G-specimens tested at 1200°C with 0.5s (brittle failure mode, Fig. 6) and 3s (ductile failure mode, Fig. 7) are consistent with an increase of ductility with holding time from 22% to 96% respectively. Fracture surfaces show features that are consistent with SEM images obtained on 304B grade B boron-containing austenitic stainless steel hot ductility-tested specimens [13]. In particular intergranular mode of fracture is also found at a testing temperature around 1200°C. But one can note no clear evidence of large amount melted liquated film since the amount of boron in our alloys is largely lower than the 1.30 wt% boron content in 304B grade B austenitic stainless steel. Nevertheless small quantities of eutectic liquid coating the grain boundaries could be present given the rather smooth aspect of some grain boundaries appearing in Fig. 5 and Fig. 6.

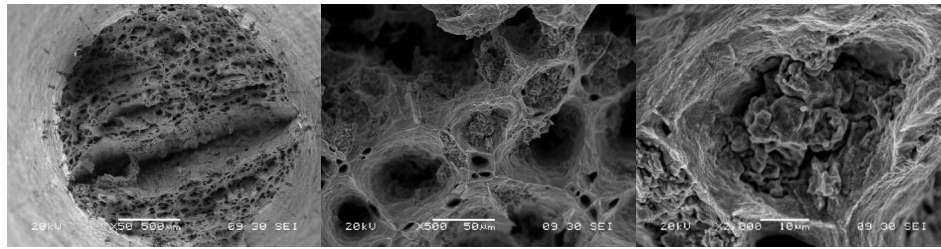


**Fig. 4:** SEM fractograph of Gleeble on-heating F-specimen tested at 1180°C with holding time of 0.1s.

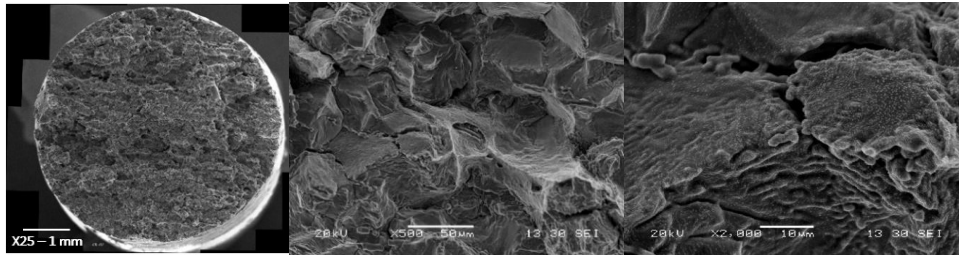


**Fig. 5:** SEM fractograph of Gleeble on-heating F-specimen tested at 1220°C with holding time of 0.1s.

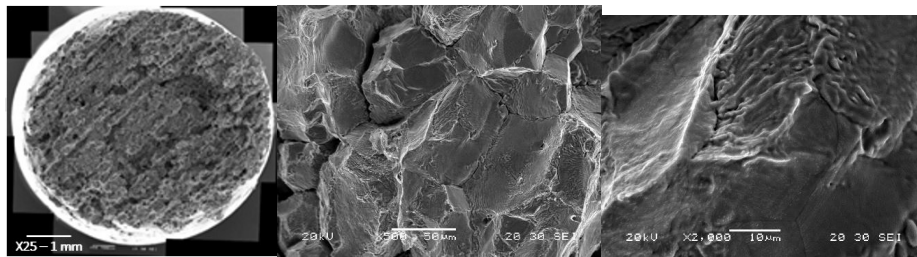


**Fig. 6:** SEM fractograph of Gleeble on-heating G-specimen tested at 1200°C with holding time of 0.5s.

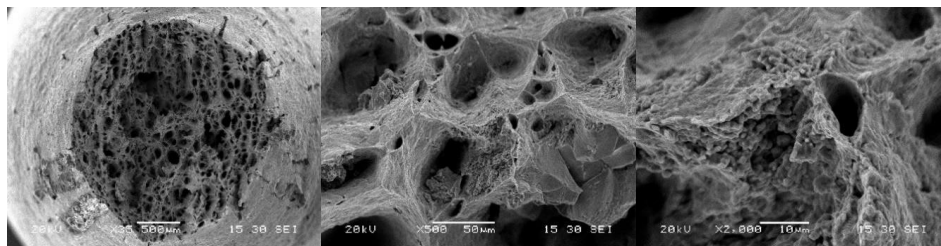


**Fig. 7:** SEM fractograph of Gleeble on-heating G-specimen tested at 1200°C with holding time of 3s.

To better understand the influence of the holding time at microstructural scale, thermal treatments with holding times 0.1s and 2.5s at 1220°C and the same thermal cycles than corresponding hot ductility tests were realised using a quenching dilatometer on material F. After the holding time, these samples were cooled to room temperature at 300°C/s in an attempt to freeze the microscopic structure and their boron distribution was characterized by SIMS analysis. The Figure 8 shows the results of SIMS analysis of the material F in the as received state and after two different heat treatments. Positions of boron appear in light on the pictures.

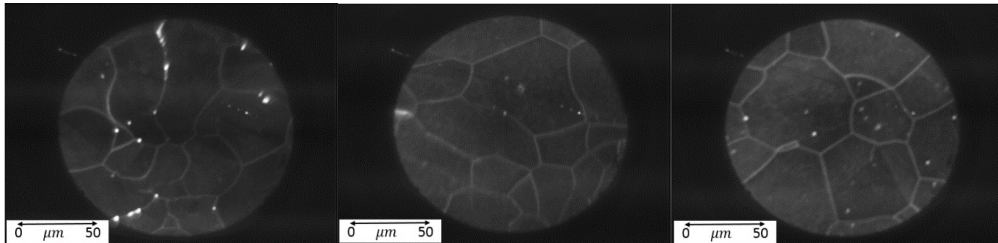


**Fig. 8:** Results of SIMS analysis of the material F: as-received (left), heat treatment at 1220°C with 0.1s of holding time (middle), and heat treatment at 1220°C with 2.5s of holding time (right).

In the as-received material, large intergranular borides that concentrate boron together with some boron segregation at grain boundaries are observed. After heat treatment at 1220°C, the boron concentration decreases but segregation still remains at the grain boundaries with no clear differences between the samples with 0.1 and 2.5s holding time. However, one can note that intragranular precipitates that are nearly absent after a holding time of 0.1s seem more present after a holding time of 2.5s. Since the SIMS analysis is not a quantitative analysis the boron concentration at grain boundaries of these two samples may nevertheless be different. Furthermore, even at a cooling rate of 300°C/s non-equilibrium grain boundary segregation may occur [17]. It is thus difficult to draw a conclusion on the microstructural origin of the increase of ductility drop temperature with holding time. However, it can be hypothesized that there is some boron diffusion from grain boundaries towards the austenitic matrix even during short holding times and that it becomes sufficient to prevent grain boundary melting after a few seconds.

### *On-cooling hot ductility tests*

Influence of boron content and holding time on ductility drop temperature were highlighted by the heating tests. However, liquation cracks appear the most often in HAZ during cooling because the stresses are in tension at this stage of the welding cycle. Gleeble on-cooling tests were thus achieved to complement on-heating tests. It consists of heating the sample to a peak temperature then cooling it to the test temperature and finally rapidly applying a tensile load without holding time to break the sample (Fig. 9). Chosen peak temperatures are  $T_{\text{peak}} = 1330^{\circ}\text{C}$  and  $T_{\text{peak}} = 1360^{\circ}\text{C}$ . In order to be able to compare with the results of

the on-heating tests, duration time over the testing temperature on heating was added with those on cooling that defined an equivalent holding time (Fig. 9, left). On-heating and on-cooling tests achieved at the same testing temperature and for the same holding /equivalent time were compared in Fig. 9 (right). A coherence between the on-heating and on-cooling results thus appears. During this equivalent time, in agreement with the literature, it is actually considered that boride eutectics stay liquid if temperature is over 1200°C. Thus, neglecting the variation of boron diffusion coefficient with the temperature, the same boron diffusion from grain boundaries towards the austenitic matrix must occur during the holding time for on-heating test or during the high-temperature excursion for on-cooling tests. Indeed, for the low temperature test achieved under 1260°C, the duration time is long and there is no risk of cracking. For the high temperature test, the duration time becomes shorter, ductility falls down and the risk of cracking increases.

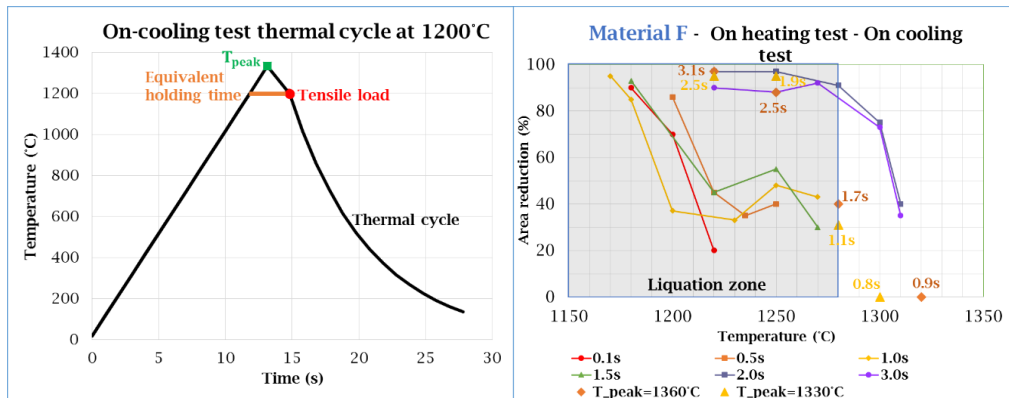


Fig. 9: Definition of an equivalent holding time for the on cooling test (left), comparison the results of the on heating test and the on cooling test (right).

#### WELDABILITY TESTS

Hot ductility testing permits to determine the sensibility of the material to the HAZ liquation cracking but does not take into account the thermal stress induced by welding operation. In order to approach as closely as possible, the real welding conditions Varestreint and PVR tests were achieved.

#### *Varestreint tests*

Varestreint test consists of making a weld line then of bending quickly the sheet when the welding passes the point of contact between the specimen and the mandrel torch [14][18][19]. Welding continues while the bending is applied. The strain is parallel to the welding direction. The welding surface is then examined. The extent of cracking observed is an indication of the sensitivity to hot-cracking. Fig. 10 shows the macrographs of welded sheets of D, E, F and G materials with 20 ppm, 35 ppm, 44 ppm and 50 ppm of boron

content respectively. Most of the cracks appearing in these macrographs are solidification cracks occurring into the fusion zone. A SEM image of one of these solidification cracks in F material is showed in Fig. 11 (left). Few cracks, which are hardly visible on the macrographs, are located near the fusion boundary. Cracking along grain boundaries is visible on SEM images of these latter (Fig. 11, right) which is coherent with liquation cracking phenomenon.

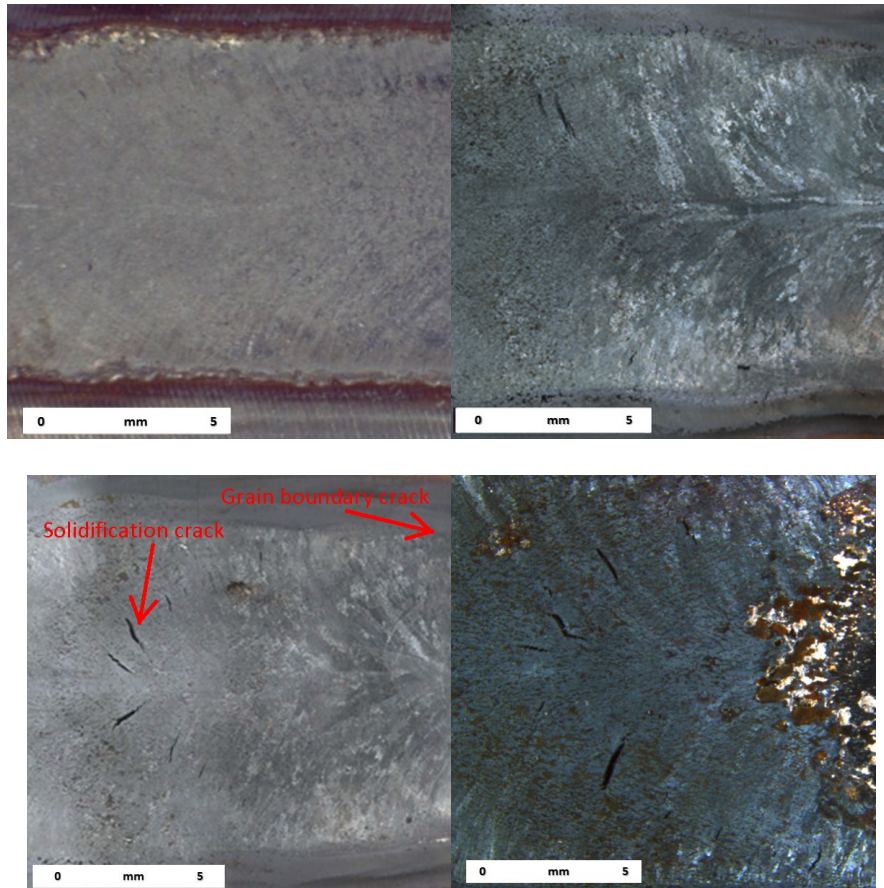


**Fig. 10:** Macrographs of welding surface of Vareststraint specimens: D (top, left); E (top, right); F (bottom, left); G (bottom, right). D=20, E=35, F=44, G=50 ppm of boron respectively.



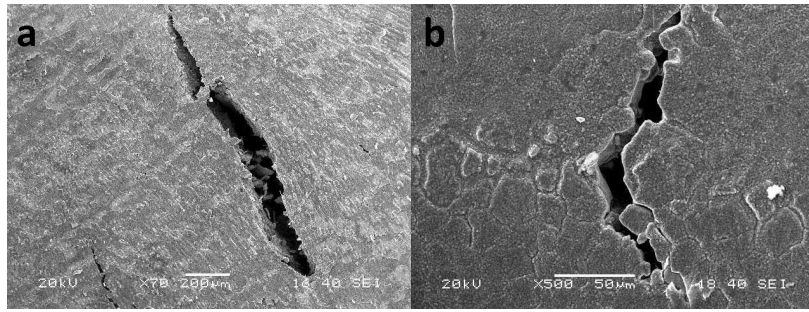


**Fig. 11:** SEM image of welding surface of F Varestraint specimen: a) solidification crack located close to the center of the fusion zone and b) grain boundary crack located near the fusion boundary.

Observation of specimen surface shows that the higher the boron content is, the more there are cracks. Even if grain boundary cracks are in the minority, high cracking sensibility of high boron content F and G stainless steels is confirmed. Few cracks appeared for E-specimen with 35 ppm of boron but with a deformation level of 7%, which is much higher than the real welding conditions for which strain level caused by thermal expansion is smaller than 2%.

*PVR tests*

PVR test consists of making a fusion line using bead-on-plate TIG-welding with argon shielding while the specimen is tensile loaded [19][20]. The welding torch moves with a constant speed while the strain rate increases from 0 to a maximal value with a constant acceleration (Figure 12). PVR tests were achieved on materials D, E, F and G.

The location of the first crack and those where the densities of cracks are 3 cracks/10mm and 9 cracks/10mm respectively were determined. Figure 13 shows the results obtained for each material.

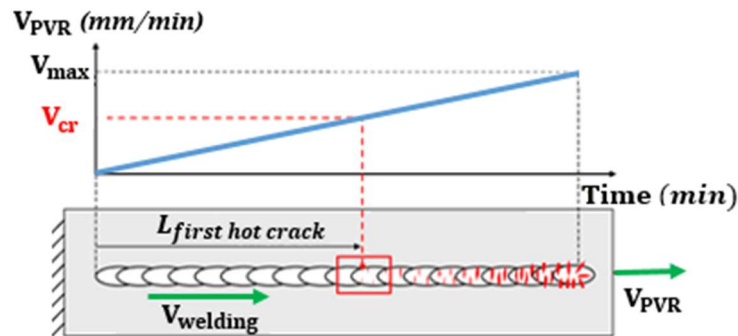


**Fig. 12:** Dependence of the ductility drop temperature with respect to boron content.

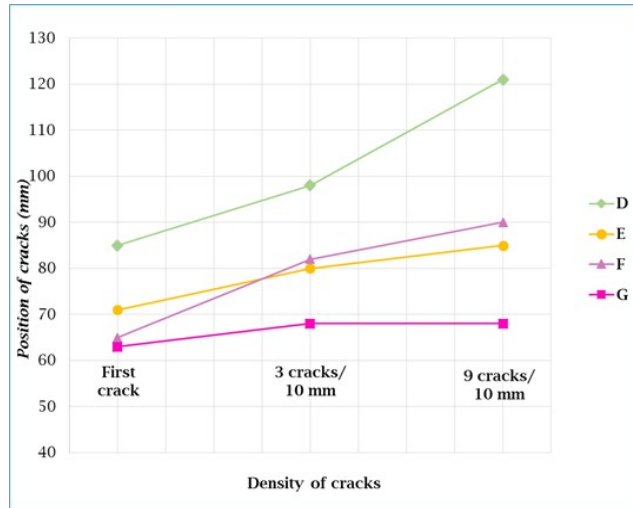


**Fig. 13:** Position of the first cracks for D, E, F and G materials in the PVR specimens. D=20, E=35, F=44, G=50 ppm of boron respectively.

The higher the boron content is, the earlier cracks appear. Therefore, the boron element has a negative effect on the cracking, even at a low content of 20 ppm (material D). However as for Varestraint tests, the direct surface observation did not allow to reveal grain boundary cracks. Thus a part of the welded surface of the F-specimen containing cracks was electrolytically etched to reveal the grain microstructure. Fig. 14 shows the results of this observation before and after the etching.

The cracks appear in the HAZ and are along grain boundaries, which is consistent with HAZ liquation cracking. As for Varestraint testing results', further analysis by transmission electron microscopy or X-ray microanalysis could be carried out to provide some evidence of liquated borides particles that would support this assumption. This experience was then repeated but at a depth of 0.5mm but no cracks were revealed (Fig. 15) highlighting the superficial character of cracking.

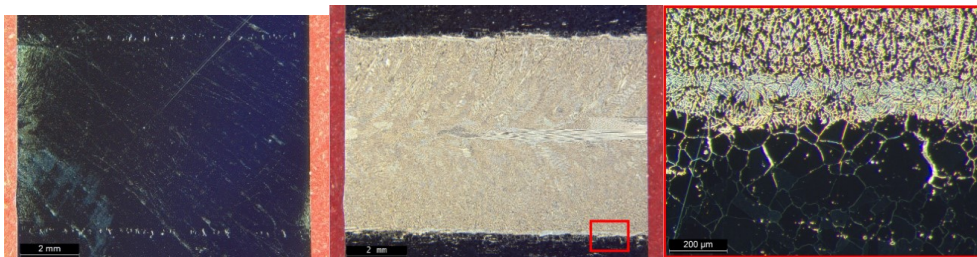


**Fig. 14:** Observation of a part of the welding surface of the PVR specimen F: before chemical attack (left) and after electrolytic etching (center and right).

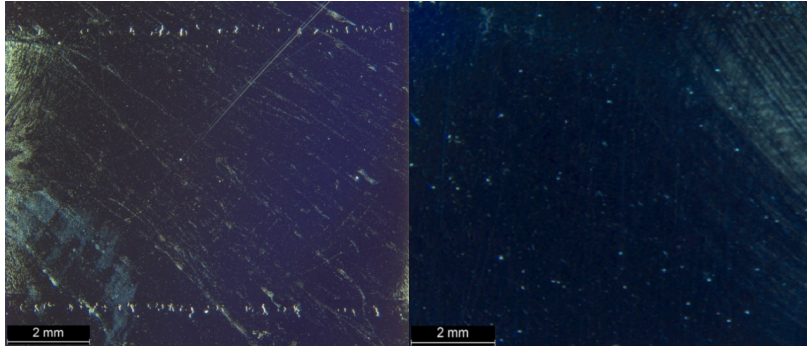


**Fig. 15:** Images at welding surface of PVR specimen F (left) and at depth of 0.5mm (right).

In the future, fracture surfaces could be obtained from Vareststraint or PVR specimens in order to be compared to the fracture surfaces from the Gleeble tests.

### NUMERICAL MODELLING OF WELDABILITY

#### GENERAL

Computational Welding Mechanics (CWM) provides access to physical quantities that are not accessible by other techniques for the purpose of understanding phenomena. These quantities can be treated qualitatively or quantitatively according to the objective and the level of modelling proposed. CWM generally relies on a three-dimensional model of the geometry discretized by finite elements to solve a thermal dependant problem thermal of solid mechanics. The thermal part of the analysis consists of solving the heat equation by modelling the energy input of the process with a mobile equivalent heat source. The parameters describing the spatial-temporal distribution of the heat source are based on the parameters of the welding process and they may be recalibrated with the help of experimental measurements. Thermo-mechanical coupling is achieved sequentially using the thermal history to solve the mechanical equilibrium at each time step while integrating the history effects according to an implicit scheme. An Elastic-Viscous-Plastic constitutive law (EVP) with mixed strain hardening is used to model the behaviour of the material between the ambient temperature and the solidus temperature. CWM was conducted with Code\_Aster software [21] in accordance with the recommendations of CEN ISO / TS 18166: 2015 [22].

In order to access local thermomechanical conditions leading to hot cracking by liquation, the modelling effort focuses on the implementation of a detailed model dedicated to the simulation of PVR tests. In fact, the PVR tests are more discriminating than the Vareststraint tests for treating the effect of boron on the weldability of the alloy.

*Heat transfers*

The heat input associated with the welding process is modeled by the equivalent heat source proposed by Goldak [23]. It is a double ellipsoid volumetric heat source whose intensity varies according to the position of the points with respect to the center of the source. This source moves at the speed of welding along the x axis. The function which describes the Goldak's source centered in  $(x_0 = 0, y_0 = 0, z_0 = 0)$  makes it possible to represent, in three dimensions, a source of heat with a Gaussian distribution of the power density. A generalized formula for the heat distribution is given in (1):

$$\begin{aligned} q_f(x, y, z) &= Q_f \exp\left(-\frac{3(x-x_0)^2}{a_f^2} - \frac{(y-y_0)^2}{b^2} - \frac{(z-z_0)^2}{c^2}\right) \text{ pour } x < x_0 \\ q_r(x, y, z) &= Q_r \exp\left(-\frac{3(x-x_0)^2}{a_r^2} - \frac{(y-y_0)^2}{b^2} - \frac{(z-z_0)^2}{c^2}\right) \text{ pour } x > x_0 \end{aligned} \quad (1)$$

In this case, it is assumed that the power transferred to the workpiece is given by  $\eta UI$  with  $\eta$  the efficiency of the process,  $U$  the voltage and  $I$  the current of the generator. During TIG welding, the coupling between the arc and the weld pool leads to an asymmetry of the power distribution. This effect can be taken into account by considering parameter  $Q_f$  and  $a_f$  for the "front" of the source and parameters  $Q_r$  and  $a_r$  for the "back" of the heat source (2). To reduce the number of parameters to adjust we can add some relationships between  $a_r$  and  $a_f$  and  $Q_r$  and  $Q_f$ . At each time step we must verify equation (2) over the workpiece domain  $\Omega$  :

$$\iiint (q_f + q_r) d\Omega = \eta UI \quad (2)$$

Based on the size of the molten zone measured experimentally and on the response of thermocouples positioned on a PVR specimen, an iterative identification procedure made it possible to obtain the heat source parameters by successively replaying the thermal simulation, the results of which are shown in Fig. 16.

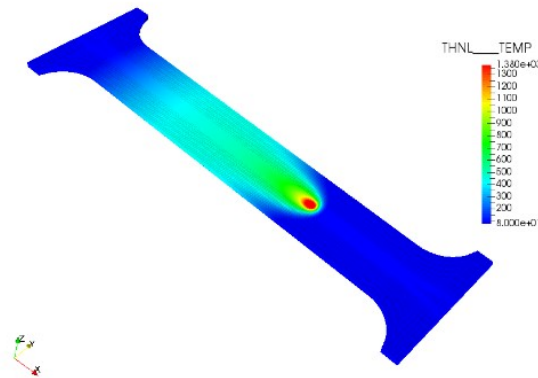


**Fig. 16:** Temperature field of the simulated PVR test at time 70 s.

*Mechanical analysis*

For the mechanical analysis, an elastoplastic law with mixed isotropic and kinematic hardening model and a Von Mises plasticity criteria have been used. Mechanical properties and thermal expansion varies with temperature. The phase transformation are not considered in the simulation as this material remains in a BCC crystal structure. Calculation is performed with small strains and displacements assumptions. The mixed isotropic–kinematic material hardening model was employed to produce the most representative material response to the cyclic thermo-mechanical loading imposed during welding. The model used is derived from Lemaitre-Chaboche model [24] with a tensor of kinematic non-linear hardening taking into account Bauschinger effect and cyclic hardening with plastic shakedown, a nonlinear isotropic hardening. Viscous effect are also considered. All the properties of material depend on the temperature. The model is called VISC\_CIN1\_CHAB in CODE\_ASTER [21]. The isotropic hardening component which defines the evolution of the yield surface,  $R(p)$ , where  $p$  is the cumulative plastic strain, is defined as follows (3):

$$R(p) = R_t + (R_0 - R_t)e^{-bp} \quad (3)$$

Where  $R_0$  and  $R_t$  are the yield stress at zero plastic strain, and the maximum yield surface size respectively.  $b$  defines the rate at which the size of the yield surface changes as plastic strain develops. The kinematic hardening component is defined as a combination of a kinematic term and a relaxation term. The kinematic hardening law is defined as follows (4):

$$\begin{aligned} \underline{\underline{X}} &= \frac{2}{3} C(p) \underline{\underline{\alpha}} \\ \underline{\underline{\dot{\alpha}}} &= \underline{\underline{\dot{\epsilon}}}_p - G(p) \underline{\underline{\dot{\epsilon}}}_p p \end{aligned} \quad (4)$$

Where  $C(p)$  and  $G(p)$  are material parameters that can depend on the cumulative plastic strain,  $\underline{\underline{\alpha}}$  is the back-stress tensor,  $\underline{\underline{\dot{\epsilon}}}_p$  is the equivalent plastic strain rate.

A Norton law is used to consider viscous effects (5):

$$\dot{p} = \left( \frac{\langle F \rangle}{K} \right)^N \quad \text{with} \quad F(\underline{\underline{\sigma}}, R, \underline{\underline{X}}) = \sqrt{\frac{3}{2} (\underline{\underline{\sigma}} - \underline{\underline{X}}) : (\underline{\underline{\sigma}} - \underline{\underline{X}})} - R(p) \quad (5)$$

Where  $\langle F \rangle$  is the positive part of  $F$  and  $\underline{\underline{\sigma}}$  the deviatoric part of the stress tensor.  $K$ ,  $N$  as well as parameters  $C(p)$ ,  $G(p)$  and  $b$  depend on the temperature. Table 3 gives the mechanical properties of the material proposed by LE [25] and adjusted to fit the load – displacement curve measured during the PVR test (see Fig. 17). The first crack appears for a displacement of 1.5 mm (material G, red region), and with material D (green region), the first crack appears for a displacement of 2.7 mm.

**Table 3** Elastic, Plastic and Viscous properties.

	E [MPa]	R <sub>0</sub> [MPa]	R <sub>1</sub> [MPa]	b	K [MPa]	N	C [MPa]	G
20°C	190000	60	120	8	151	24	30000	350
600°C	140000	10	80	8	150	12	24810	300

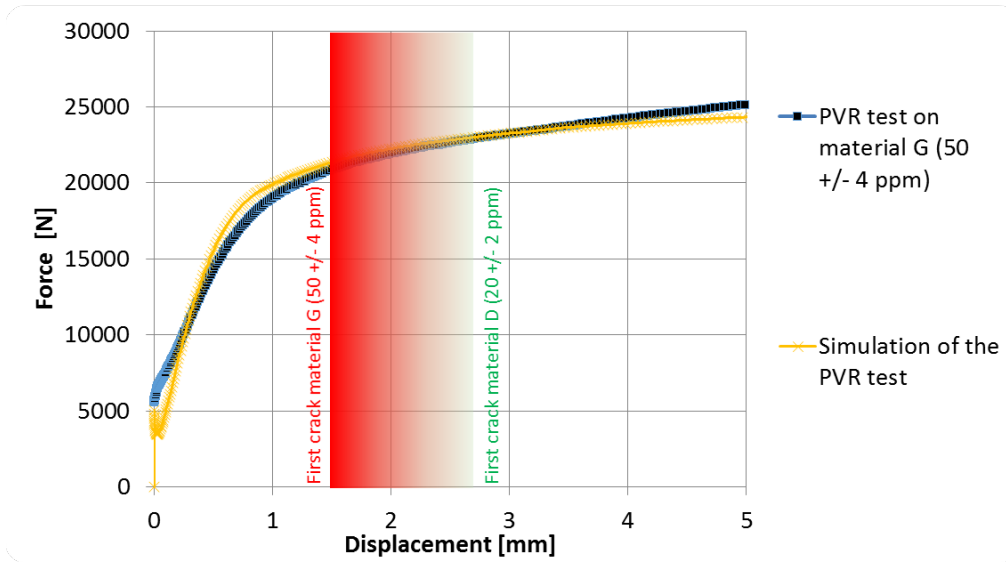


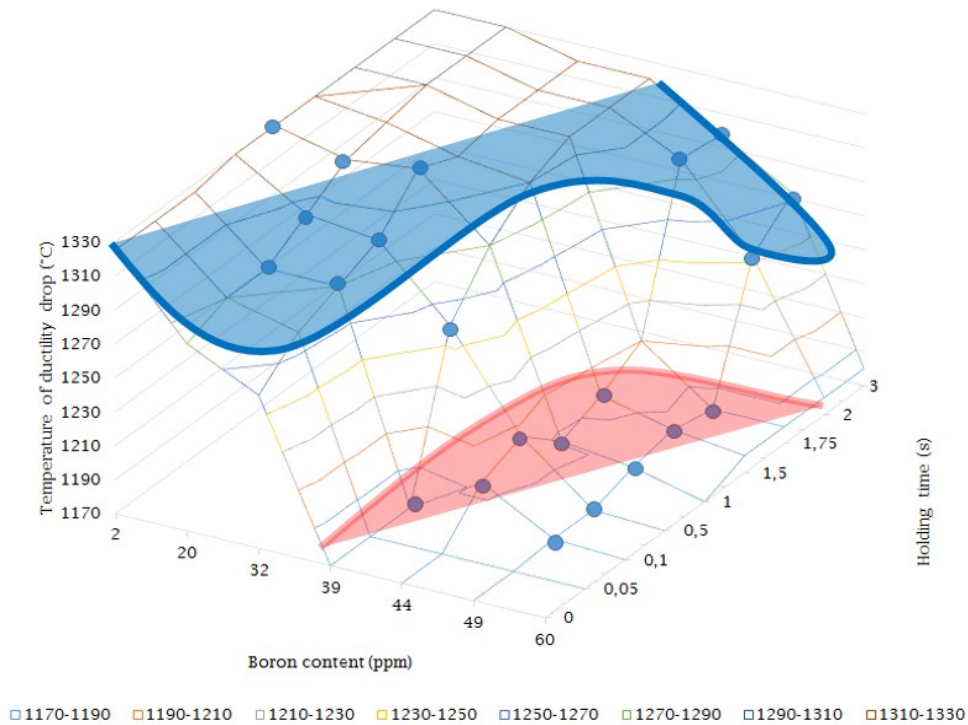
**Fig. 17:** Load-displacement curve for PVR test performed with material G. Comparison between measurements and simulation.

CRITERIA FOR THE ASSESSMENT OF HOT CRACKING RISK

Let us consider the two following experimental results: the sensitivity to the hot cracking by liquation determined by the hot ductility tests and the position of the first crack of the PVR test as a function of the boron content. The sensitivity to hot cracking by liquation is described by the surface response (see Fig. 18) derived from the hot ductility tests in a 3-dimensional space: boron content, ductility drop temperature and holding time.

## Mathematical Modelling of Weld Phenomena 12

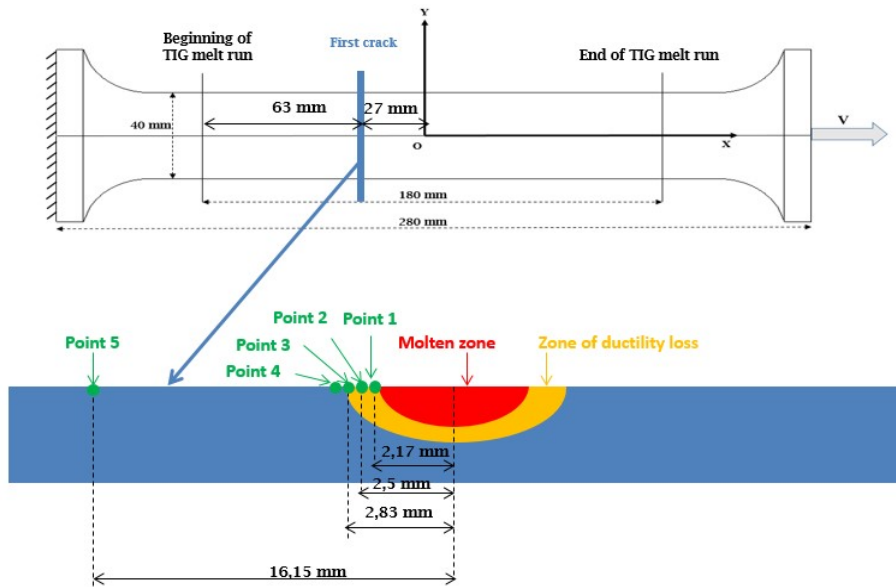
Ductility drop temperature vs. Boron content and holding time



**Fig. 18:** Surface response derived from the hot ductility tests: ductility drop temperature as a function of boron content and holding time.

Fig. 18 shows a transition in the evolution of material sensitivity versus boron content between 39 and 44 ppm. In fact, for boron contents below 39 ppm, the ductility drop temperature remains high and tends to increase with the holding time. Conversely, for boron contents above 39 ppm, the ductility drop temperature is low for holding times of less than 2 s. This temperature increases significantly for holding times greater than 2 s to reach values however lower than for alloys with low boron content. Fig. 13 shows the position of the first crack as well as the position for which the crack densities are 3 cracks / 10 mm and 9 cracks / 10 mm, depending on the boron content (cracks detected by liquid penetrant testing). These results make it possible to define the position of the first crack as a function of the boron content to be considered conservatively for the establishment of the criteria. For the boron content of 20 ppm, the first crack appears late at a distance of 85 mm. For the boron content of 35 ppm, the distance is 71 mm, for the highest contents, the distance is between 60 and 65 mm. The positions at 60 and 85 mm constitute the boundaries of an area in which the cracking conditions are met (boron content, holding time and ductility drop temperature). The fact that the PVR test is an external mechanical stress test allows to integrate an additional parameter which involves the level of stress applied to the zone of ductility drop. This level of stress is determined by the numerical simulation of the test. A tensile stress seems to be a sufficient condition to create liquation cracks because they make it possible to overcome the cohesive strength between two grain boundaries and the liquid

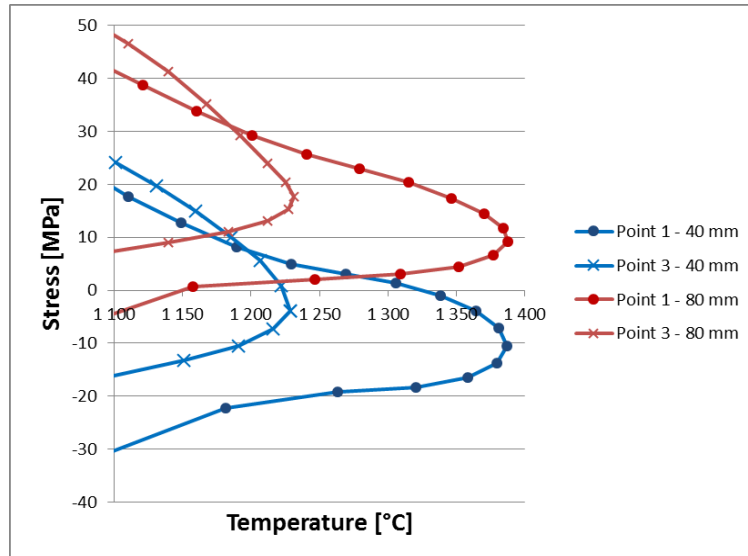
film. In the case of the PVR test, it is a uniaxial tension (in the tensile x direction of welding) and the cracks observed are perpendicular to this direction. Therefore, only the constraint component in this direction,  $\sigma_{xx}$ , is considered. This approach can be generalized in a real welding case considering the maximum principle stress. The simplest way to integrate this quantity into the criteria is to compare it with a threshold value. If the local value of the stress is greater than the threshold value, there is a risk of hot cracking. To determine this threshold stress, it is possible to post-process stress-temperature-time curves from the simulation results at different points in the HAZ of the model. The 3-dimensional stress-temperature-time curves extracted at different points in the specimen can be used for comparison with the experimental ductility drop characterizations. The points studied correspond to the position where the first cracks appear for each boron content (see Fig. 19).



**Fig. 19:** Position along the specimen and through the section where stress-temperature-time curves are post-processed to determine stress threshold.

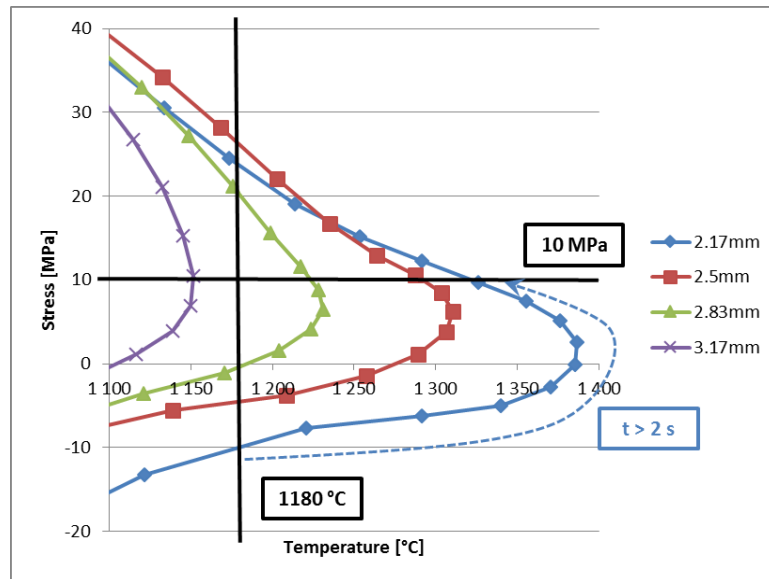
To facilitate the analysis, these curves are plotted in a two-dimensional stress - temperature space. Time is represented by markers on the curve. Fig. 20 shows an example for two points in the HAZ at the two positions 40 mm and 80 mm along the specimen, four points in total. The time between two markers is 0.25 s. It is possible to plot the evolution of the stress in the temperature range presenting a risk of ductility loss by liquation with a maximum temperature of the order of 1400°C for the point 1 close to the molten zone and 1200°C for point 3.





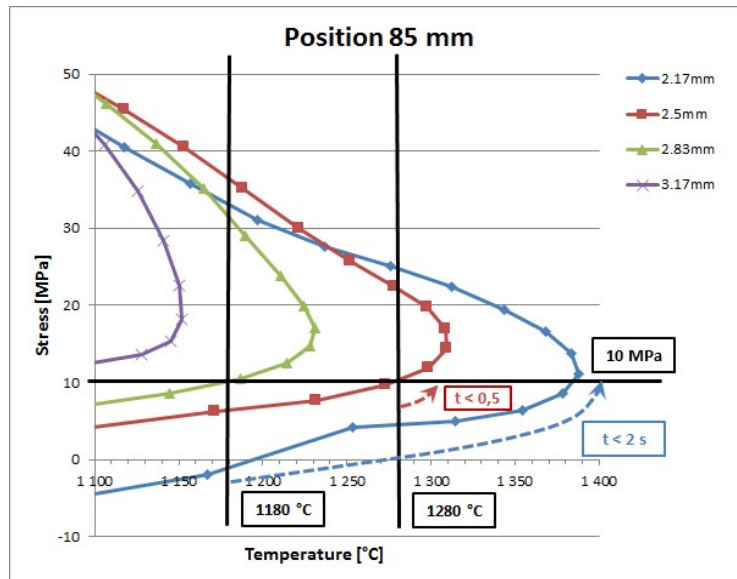
**Fig. 20:** Stress versus temperature curves at different locations along the specimen (40 and 80 mm from the fusion line start) and two positions in the HAZ (point 1 close to the molten zone and 3).

To determine a stress threshold below which the risk of hot cracking by liquation is null whatever the temperature, the holding time and the boron content are, it is necessary to base the analysis, in a conservative manner, on the test which shows a crack for the lowest stress. This is the PVR test conducted on the most sensitive to hot cracking material which contains 50 ppm of boron (material G). The ductility drop temperature measured for this boron content is of the order of 1180°C and the holding time necessary to recover its ductility is greater than 2 s. The position of the first crack for this test is 63 mm from the start of the melting line. Fig. 21 shows the evolution of the stress as a function of temperature at this position for several points in the HAZ. The threshold stress corresponds to the stress reached before the material recovers its ductility, after 2 s spent above the lowest ductility drop temperature. Conservatively, the lowest threshold stress level is obtained from the stress-temperature curve of the nearest point of the melted zone. The holding time above 1180 ° C is greater than 2 s (contains more than 8 intervals of 0.25 s) when the cooling stress reaches 10 MPa. The threshold stress value below which the risk of hot cracking by liquation is excluded is set at 10 MPa.



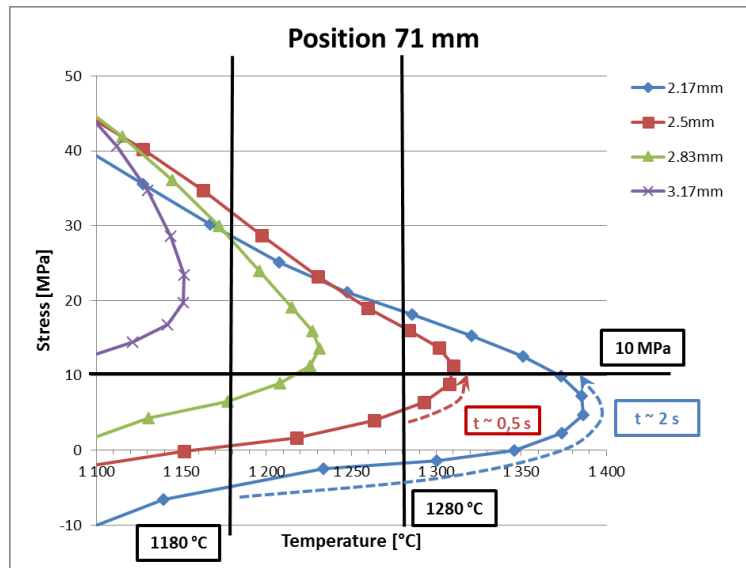
**Fig. 21:** Stress versus temperature curve at the 63 mm position of the first crack for the highest boron content (material G) for different points in the HAZ.

Fig. 22 allows to follow the evolution of the stress as a function of the temperature at the position of the first crack for the material least susceptible to cracking at different points of the HAZ, close to the molten zone. Holding times are relatively low to recover the ductility of the material for this boron content (material D containing 20 ppm boron). These holding times of order of 0.5 s are possible for points whose maximum reached temperature is close to the ductility drop temperature defined at 1280°C (point of the red curve in Fig. 22). This analysis makes it possible to confirm the presence of a point exceeding the threshold stress before its ductility is recovered and thus the presence of a crack at 85 mm for this material.



**Fig. 22:** Stress versus temperature curve at the 85 mm position of the first crack for the lowest boron content (material D); point 1 very close to the melted zone (blue curve), and point 2 which reaches the threshold stress for a low holding time low ( $<0.5$  s).

Fig. 23 allows to follow the evolution of the stress as a function of the temperature at the position of the first crack for the material E (35 ppm of boron content) which marks a transition with respect to the sensitivity to the loss of ductility (see Fig. 1, Fig. 2 and Fig. 18). The holding times are relatively low to recover the ductility for the material E. These holding times, of the order of 0.5 s, are possible for points whose maximum reached temperature is close to the temperature of ductility drop defined at 1280°C (red curve in Fig. 23). This analysis makes it possible to confirm the presence of a point exceeding the threshold stress before its ductility is recovered and thus the presence of a crack at 71 mm. For slightly higher boron content and a material whose ductility drop temperature approaching 1180°C, the holding time remains less than 2 s, which is consistent with the presence of liquation cracks observed in this area for material F.



**Fig. 23:** Stress versus temperature curves at the 71 mm position of the first crack for the 35 ppm grade (material E).

On the basis of these analyzes, the criteria for the assessment of liquation hot cracking risk for 316L austenitic stainless steel can be stated as follows: at positions where the maximum temperature reached is between 1150°C and 1350°C, only points with a maximum stress above 10 MPa during cooling present a risk of cracking:

- For materials with a boron content lower than 35 ppm, the risk becomes null if the holding time above 1280°C is greater than 0.5 s.
- For materials with a boron content greater than 35 ppm, the risk becomes null if the holding time above 1180°C is greater than 2 s.

### CONCLUSION

- The ductility drop temperature transition in type 316L steel occurs for a boron content between 35 ppm and 44 ppm. This is in agreement with the results of literature.
- The holding time at on-heating testing temperature increases the ductility drop temperature, so decreases the risk of HAZ liquation cracking. SIMS analysis are consistent with the hypothesis of boron diffusion from grain boundaries towards the austenitic matrix. Even a short holding times would be sufficient to prevent grain boundary melting.
- An equivalent time defined as the duration time over the testing temperature on heating in addition is considered to conduct on cooling test. A coherence between the on-cooling and on-heating results is found. For the low temperature test achieved under 1260°C, the duration time is long and there is no risk of cracking. For the high temperature tests, the duration time becomes shorter, ductility falls down and the risk of cracking increases.

## Mathematical Modelling of Weld Phenomena 12

- The Varestraint and PVR tests show that boron does have a negative impact on the hot cracking susceptibility: the higher the boron content, the more susceptible to hot cracking the steel is. Near the fusion zone boundary cracking along grain boundaries is visible on SEM images which is coherent with liquation cracking phenomenon.
- The experimental program has thus demonstrated that the 316L type of austenitic stainless steel studied does not exhibit weldability issues such as liquation hot cracking under the effect of the boron content if the boron content remains less than 35 ppm.
- The PVR test results are consistent with ductility test, they highlight the effect of boron content on the grain boundary crack susceptibility. The results of the PVR test and its simulation are used to determine a criteria for HAZ liquation cracking, taking into account of the boron content and the stress level.
- The proposed criteria states that for material with a boron content greater than 35 ppm, the risk is canceled if the holding time above 1180°C is greater than 2 s.
- The type 316L austenitic stainless steel do not highlight weldability issues such as boron assisted liquation cracking if the boron content remains below 35 ppm. In addition, real welding tests could be carried out to confirm this point. The degree of conservatism of the proposed criterion could thus be evaluated by simulation of these configuration, which would make it possible to release margins according to the welding configurations in order, for example, to relax the specification on the boron content in procurement procedures while securing the fabrications by increasing the holding times in the [1150°C – 1350°C] temperature range (preheating, welding energy ...).

## REFERENCES

- [1] E. FOLKHARD: *Welding metallurgy of stainless steels*, Springer-Verlag Wien, New York, 1988.
- [2] J.C. LIPPOLD: *Welding metallurgy and weldability*, John Wiley & Sons, Inc, 2014.
- [3] R.D. THOMAS JR.: 'HAZ cracking in thick sections of austenitic stainless steels - Part II', *Welding Journal*, 63(9), pp. 355s-368s, 1984.
- [4] X. HUANG, M. C. CHATURVEDI, N. L. RICHARDS AND J. JACKMAN: 'The effect of grain boundary segregation of boron in cast alloy 718 on HAZ microfissuring - a SIMS analysis', *Acta materiala*, 45 (8), pp. 3095-3107, 1997.
- [5] R.K. SIDHU, O.A. OJO AND M.C. CHATURVEDI: 'Microstructural response of directionally solidified René 80 superalloy to gas-tungsten arc welding', *Metallurgical and Materials Transactions*, 40A, pp. 150-162, 2009.
- [6] H. GUO, M.C. CHATURVEDI & N.L. RICHARDS: 'Effect of boron concentration and grain size on weld heat affected zone microfissuring in Inconel 718 base superalloys', *Science and Technology of Welding and Joining*, 4(4), pp. 257-264, 2013.
- [7] W. CHEN, M.C. CHATURVEDI AND N.L. RICHARDS: 'Effect of boron segregation at grain boundaries on heat-affected zone cracking in wrought Inconel 718', *Met. and Mat. Trans. A*, 32A, pp. 931-939, 2001.
- [8] O.A. OJO AND M.C. CHATURVEDI: 'Liquation microfissuring in the weld heat-affected zone of an overaged precipitation-hardened nickel-base superalloy', *Metallurgical and Materials Transactions*, 38A, pp. 356-369, 2007.

- [9] G. LI, X. LU, X. ZHU, J. HUANG, L. LIU AND Y. WU: ‘The Segregation and Liquation Crackings in the HAZ of Multipass Laser-Welded Joints for Nuclear Power Plants’, *Journal of Materials Engineering and Performance*, 26(8), 4083-4091, 2007.
- [10] G. ZACHARIE: ‘Influence du bore sur la résistance à la fissuration à chaud dans les zones affectées par le soudage et sur la tenue au fluage des aciers 18-10Ti’, *PhD dissertation*, Université de Paris-Sud, 1978.
- [11] J.R. DONATI, D. GUTTMANN AND G. ZACHARIE: ‘Influence de la teneur en bore sur la fissuration à chaud d’aciers 18-10’, *Revue de Metallurgie (Paris)*, 71(12), pp. 917-930, 1974.
- [12] ISO/TR 17641-3: ‘Destructive Tests On Welds In Metallic Materials - Hot Cracking Tests For Weldments - Arc Welding Processes’, 2005.
- [13] G. SRINIVASAN, M. DIVYA, C. R. DAS, S. K. ALBERT, A. K. BHADURRI, S. LAUF, S.TUBENRAUCH, A. KLENK (2015): ‘Weldability studies on borated stainless steel using Varestraint and Gleeble tests’, *Welding World*, 59, pp. 119-126, 2015.
- [14] W. LIN, J.C. LIPPOLD AND W.A. BAESLACK: ‘An evaluation of heat affected zone liquation cracking susceptibility Part I’, *Welding Journal*, 71(4), pp. 135s–153s, 1993.
- [15] R. BOUDOT AND G. ZACHARIE: ‘Influence de la teneur en bore sur la résistance à la fissuration à chaud dans les zones affectées par le soudage d’acier 18%Cr-12%Ni au molybdène en relation avec le mode d’élaboration’, *25ème Colloque de Metallurgie - Progrès Récents dans l’Elaboration des Métaux et Alliages, Conséquences sur leur Propriétés d’Emploi*, Saclay, 23-25 Juin 1982.
- [16] L. KARLSSON, H. NORDÉN AND H. ODELIUS: ‘Non-equilibrium grain boundary segregation of boron in austenitic stainless steel - I. Large scale segregation behavior’, *Acta metallurgica*, 36 (1), pp. 1-12, 1988.
- [17] L.O. OSOBA, Z. GAO AND O.A. OJO: ‘Physical and numerical simulations study of heat input dependence of HAZ cracking in nickel base superalloy IN 718’, *Journal of Metallurgical Engineering (ME)*, 2 (3), pp. 88-93, 2013.
- [18] C. D. LUNDIN ET AL. : ‘Hot ductility and hot cracking behaviour of Modified 316 Stainless Steels designed for high temperature service’, *Welding Journal*, 72(5), pp. 189s-200s, 1993.
- [19] T. KANNENGIESSER, K. BOELLINGHAUS : ‘Hot cracking test. An overview of present technologies and applications’, *Welding World*, 58(3), pp. 397-421, 2014.
- [20] G. TIRAND, C. PRIMAULT, V. ROBIN: ‘Sensibilité à la fissuration à chaud des alliages base nickel à haute teneur en chrome, High chromium nickel base alloys hot cracking susceptibility’, *Matériaux & Techniques*, 102(4), 403, pp. 1-5, 2014.
- [21] CODE\_ASTER, version 13.4, <https://www.code-aster.org/>, 2017
- [22] CEN ISO/TS 18166:2015, ‘Numerical welding simulation — Execution and documentation’, 2015.
- [23] J.A. GOLDAK, A. CHAKRAVARTI, J. BIBBY: ‘A new finite element model for welding heat sources’, *Metallurgical Transactions*, 15B, pp. 299-305, 1984.
- [24] J. LEMAITRE, J.L. CHABOCHE: ‘Mechanics of Solid Materials’, *Cambridge University Press*, 1990.
- [25] M. LE, ‘Approches expérimentale et numérique de la fissuration à chaud dans les soudures en acier inoxydable’, *PhD Thesis*, Université de Bretagne Sud, France, 2014.



# **V Solid State and Friction Stir Welding**





# 3D FINITE ELEMENT MODELING OF THE LINEAR FRICTION WELDING OF A BETA TITANIUM ALLOY

W. LI\*, Q. YE\*, X. WANG\*, X. YANG\* and T. MA\*

*\* State Key Laboratory of Solidification Processing, Shaanxi Key Laboratory of FrictionWelding Technologies, Northwestern Polytechnical University, Xi'an, 710072, Shaanxi, PR China, liwy@nwpu.edu.cn*

DOI 10.3217/978-3-85125-615-4-28

## ABSTRACT

In this study, a 3D numerical model for linear friction welding (LFW) of a metastable beta titanium alloy (Ti-8V-6Cr-4Mo-4Zr-3Al) with a rectangular cross-section was established and validated experimentally. The effects of welding time and oscillatory direction on the thermal profiles, burn-off rates and subsequent microstructures were investigated. The results showed that the interface temperature and width of the weld center zone (WCZ) decreased when the oscillation along the short edge of rectangle compared to that along the long edge. The temperature at the interface was quickly increased to 1000 °C at around 1s; and after 2s, the maximum interface temperature could be over 1052°C and the LFW process reached a quasi-steady state in which the plasticized metal was continuously extruded. With the increase of welding time, the thickness of plasticized layer at the interface decreased, and the grain size in WCZ first increased and then kept stable. The results confirm that the developed model is useful for welding design.

Keywords: linear friction welding; beta titanium alloy; finite element modeling; temperature field; microstructure

## INTRODUCTION

Linear friction welding (LFW) is an efficient manufacturing process which allows the solid-state joining or coalescence of non-axisymmetrical metals using frictional heat generated between two rubbing surfaces in a reciprocal motion [1-2]. One of the workpieces is held stationary, and the other one oscillates linearly under compressive forces without external heat and additional welding substance. Once sufficient heat has been generated, the relative movement is stopped and a forging force is applied [3]. The benefits of LFW over conventional welding methods are the absence of solidification defects, the ability of welding dissimilar metallic materials, low consumption, automation, high reproducibility, no production of fumes, short production time, and environmentally friendly [4-5]. It has been applied in very interesting studies of the transportation and especially in aerospace industries. For instance, a very successful application of the LFW process is regard to building up and repairing of aeroengine blisks [6]. As for the LFW process, several materials are considered, such as steels [7], aluminum alloys [8-9], superalloys [10], titanium alloys [11-12] and so on, but titanium alloys are the most concerned.

LFW is a complicated and strongly thermomechanically coupled physical process, and it is very difficult to study its nature merely by welding experiments. With the development of computer technology and numerical analysis, finite element modeling (FEM) has become a powerful and reliable technique for understanding what is happening during the rapidly evolving process [13-16]. For example, the previously developed models can predict the temperature history [17], stress fields [18], and flash morphology [13] within the welded parts. Different researchers have built two dimensional (2D) or three dimensional (3D) thermomechanically coupled models in Lagrangian or arbitrary Lagrangian–Eulerian (ALE) formulations using an implicit or explicit solver, and commercial softwares like DEFORM [13, 19], ABAQUS [20, 21], ANSYS [17] or FORGE [15] have been used. Grujicic et al. [22] developed the coupled thermo-mechanical 3D model for Ti64 by ABAQUS, with the modified Johnson-Cook material model, and calculated dynamic recrystallization from a custom material subroutine. Although there is some improvement in the temperature field, the size of the mesh is somewhat bulky compared with the workpiece size, so the flash morphology needs to be improved. The majority of the investigations into the LFW process about modeling and experiments were focused on characterizing the process inputs, namely the amplitude, frequency, applied force and burn-off. The effects of the workpiece geometry are often neglected. To the authors' knowledge, only a few journal publications specifically commented on the geometric effects; and most of them used machine data recorded during welding which was post-processed to determine the average heat flux over the initial phase. This was applied to a thermal model to predict the temperature distribution. After this, the single-body method was used to model the equilibrium phase and an inelastic heat fraction was specified to represent the amount of mechanical work converted to heat. Schroerer et al. [19] and McAndrew et al. [13] conducted the fully coupled thermo-mechanical analysis using the single-body modeling approach while applying the plane-strain condition to the 2D model, and experimentally validated 2D models were used to investigate the workpiece geometry effects on the material flow. The 3D model was considered by Sorina-Müller et al. [17] and McAndrew et al. [23], respectively. They provided insight into the effects of the workpiece geometry on the multi-directional material flow behavior of welds. Bilal Ahmad et al. [18] explored the 2D model by ABAQUS to investigate the influence of the oscillation direction on the residual stress.

The present paper reports on the development of a 3D LFW process model for joining Ti-8V-6Cr-4Mo-4Zr-3Al titanium alloy. The purpose of the article is to compare with other results and investigate the reasons why the workpiece geometry affects the process behavior. Some experiments are also carried out to validate the accuracy of the latest version of a process model.

### MODELING OF LFW

#### GEOMETRY AND MESHING

In order to build an efficient control method for LFW, a valid temperature prediction model needs to be established and many basic mechanics of this process need to be understood.

The 2D models are unable to express the flash from different direction and temperature field in the welding interface, thus the 3D model of the LFW process tested in this work was created using the software ABAQUS. Samples of the same rectangular cross-section but with two different oscillation directions (along long edge and short edge as shown in Fig. 1a and 1b, respectively), were chosen for the analysis.

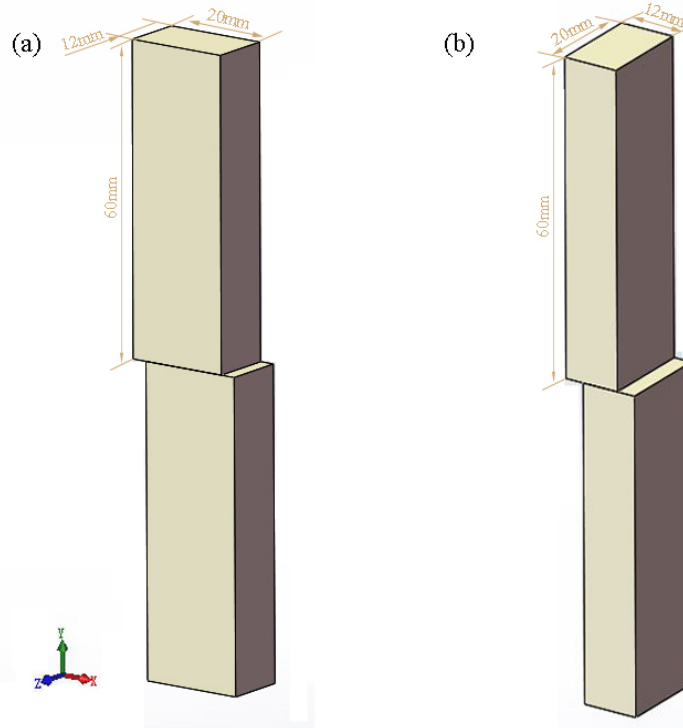


**Fig. 1** Workpiece dimensions with different oscillatory lengths: (a) 20mm and (b) 12mm

The detailed 3D model is shown in Fig. 2. Since the deformation and heat flow are considered to be approximately symmetric around the y-plane, only a half of the geometry was included. Instead, a rigid body having the same width as the specimen was used to model the welding interface and the friction process on account of a reasonable compromise between the computation cost and accuracy. The deformed body was divided into two regions, one region of 10mm containing the thermo-mechanically affected zone (TMAZ) and weld center zone (WCZ), therefore characterized by a fine structured mesh (meshing size of approximately 1mm) to predict the temperature accurately and another region of 50 mm with a coarse mesh to reduce the number of elements. The gradient meshes were adopted in TMAZ considering the computation efficiency and accuracy, and the mass scaling factor was set to 20000. The ALE adaptive meshing was adopted in the present paper to maintain a high-quality mesh throughout an analysis, even when large deformations occurred, by allowing the mesh to move independently of the material. The ALE adaptive meshing was used with a remeshing frequency of 1 and remeshing sweeps of 2 per increment. The meshing was conducted using the 8-node brick elements with coupled displacement and temperature, reduced integration, and hourglass control

(C3D8RT) which was based on thermo-mechanical coupling in the LFW process. The total numbers of nodes and elements of the model were 24716 and 22215, respectively.

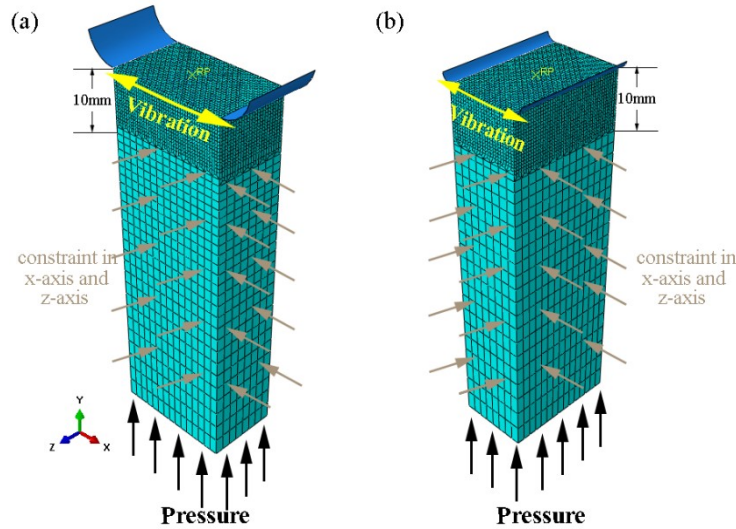
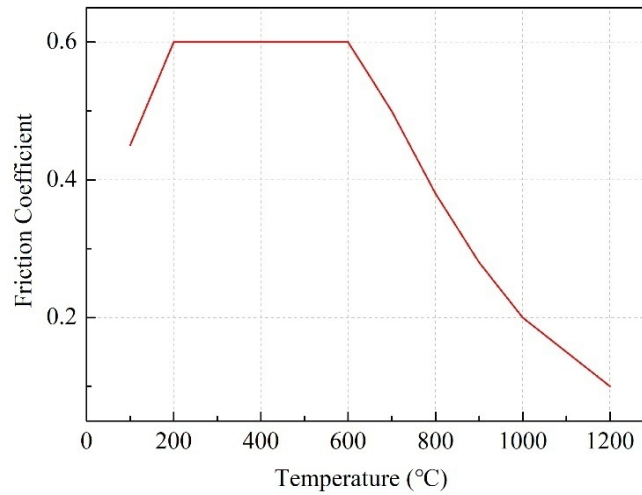


Fig. 2 Sketch of the 3D FEM model under different vibration lengths: (a) 20mm and (b) 12mm

#### BOUNDARY CONDITIONS

In the initial step, a uniform temperature of 25°C was applied to both samples. The temperature of the environment was also set to 25°C. As shown in Fig. 2, the lower 50mm region was only allowed to move in Y direction while constrained in X and Z directions. The rigid body was only allowed to move in X direction in a sinusoidal mode with a given amplitude and frequency. The type of interaction of the rigid surface and the top surface of the specimen was a surface-to-surface contact. In this study, the thermal radiation and convection coefficients between the workpiece and surroundings were set to 30W/(m<sup>2</sup>·°C), and the value of the contact thermal conductance between the workpiece and fixture was 1000W/(m<sup>2</sup>·°C). In the LFW process, the primary interaction occurs at the weld interface between workpieces; however, a secondary concern is the possible contact of weld flash with the sides of the body, here it was neglected. The interaction between the workpiece and rigid body was implemented by using the surface-to-surface contact formulation available in ABAQUS.

Due to difficulties in measurement of the friction coefficient, as evidenced by Vairis [24], and lack of available data in the literature, the temperature-dependent values in this study were hypothesized but in a reasonable range dependent on the interface temperature, which is shown in Fig. 3.



**Fig. 3** Temperature dependent friction coefficient of Ti-8V-6Cr-4Mo-4Zr-3Al

One of the important challenges about FEM-based LFW simulations is modeling the weld area because it needs a delicate compromise between accuracy and feasibility. According to Vairis and Frost [25-27], LFW is typically divided into four stages: initial, transition, equilibrium and deceleration (or forging) phases. Since the existing commercial software packages are not capable of joining separate meshes as required for the LFW process, the modeling was carried out for three distinct stages of process, dealing with (i) initial, (ii) transition, and (iii) equilibrium stages [26]. So the applied pressure was applied on the bottom surface of the deformed body during the welding process. The welding parameters, such as friction pressure, oscillation frequency, amplitude and welding time, are listed in Table 1.

**Table 1** Selected values for processing parameters

Pressure (MPa)	Frequency (Hz)	Amplitude (mm)	Welding time (s)
70	25	2	4

MATERIAL

The welds were performed on the forged Ti-8V-6Cr-4Mo-4Zr-3Al titanium alloy (nominal chemical composition is given in Table 2). To solve transient thermal problem, it is necessary to define thermal behavior of material; that is identified by specifying thermal conductivity and specific heat as temperature dependent. Since there is no available reports, these material properties were obtained by software JMatPro, as shown in Fig. 4.

**Table 2** Nominal chemical composition of Ti-8V-6Cr-4Mo-4Zr-3Al titanium alloy

Al	V	Cr	Mo	Zr	Fe
3.0~4.0	7.5~8.5	5.5~6.5	3.5~4.5	3.5~4.5	≤0.3
Si	C	N	H	O	Ti
≤0.10	≤0.05	≤0.03	≤0.015	≤0.12	Bal.

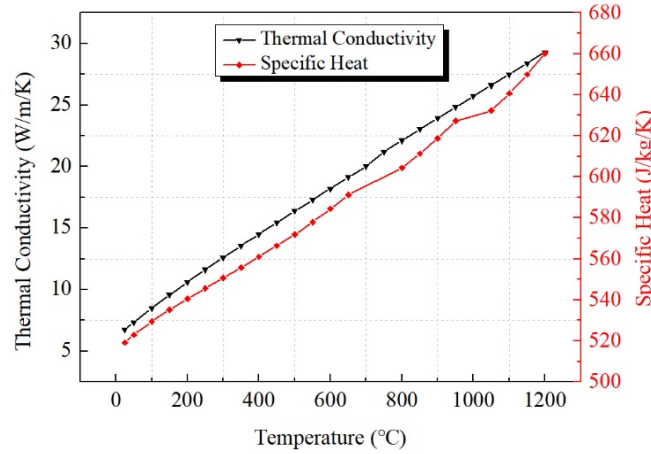


**Fig. 4** Thermal conductivity and specific heat of Ti-8V-6Cr-4Mo-4Zr-3Al as temperature dependent

The constitutive behavior of materials is usually expressed by a nonlinear equation, which is a relationship among flow stress, strain, strain rate and temperature. The inelastic behavior of the investigated alloy is assumed to be described by Johnson–Cook (JC) constitutive material model as follows [28]

$$\sigma = (A + B\varepsilon_p^n)[1 + C\ln(\dot{\varepsilon}^*)][1 - (T^*)^m] \quad (1)$$

where  $\sigma$  is the flow stress. A and B are the strain hardening parameters; C is a dimensionless strain rate strengthening coefficient; n and m are power exponents of the strain hardening and thermal softening terms;  $\varepsilon_p$  is the effective plastic strain.  $\dot{\varepsilon}^*$  is calculated by the expression  $\dot{\varepsilon}^* = \dot{\varepsilon}_p/\dot{\varepsilon}_0$ .  $\dot{\varepsilon}_p$  is the effective plastic strain rate.  $\dot{\varepsilon}_0$  is the reference plastic strain rate.  $\dot{\varepsilon}_0$  is normally selected as 1 S<sup>-1</sup>.  $T^*$  is a homologous temperature, which is expressed by the expression  $T^* = (T - T_r)/(T_m - T_r)$ .  $T_r$  and  $T_m$  are the reference temperature and the melting point, respectively. The room temperature was set as 25°C. The melting temperature was set as 1220°C. The JC material model parameters for Ti-8V-6Cr-4Mo-4Zr-3Al (A = 436.14 MPa, B = 90 MPa, n = 0.48, C = 0.552, m = 1.05,  $\dot{\varepsilon}_0 = 1$  S<sup>-1</sup>) were taken from our previous research for hot deformation behaviors.

## EXPERIMENTAL PROCEDURE

The experimental Ti-8V-6Cr-4Mo-4Zr-3Al workpieces dimensions used in this study are also displayed in Fig. 1. It is a kind of metastable beta titanium alloy, which consists of equiaxed beta grains, as shown in Fig. 5. The welding equipment used was the XMH-250 LFW machine developed in house by Northwestern Polytechnical University. The experimental conditions investigated in this work are displayed in Table 1. To investigate the correlation between microstructure change and temperature field during LFW, the LFW machine was stopped during the process cycle at specified times (1, 2 and 4 s) for the dimension of 20mm×12mm×60mm.

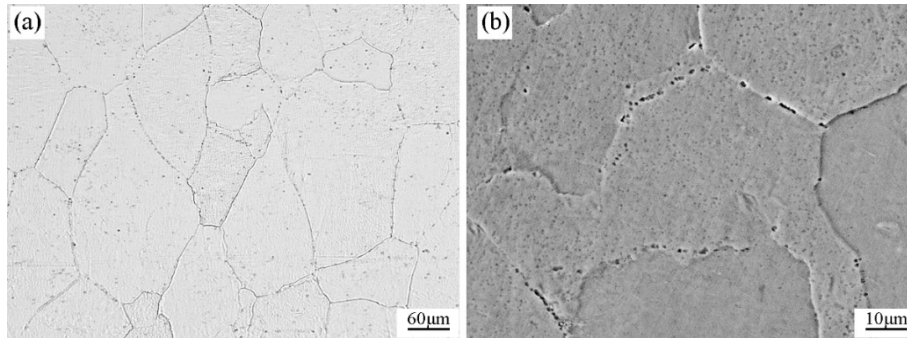


**Fig. 5** Microstructure of the Ti-8V-6Cr-4Mo-4Zr-3Al base metal: (a) OM and (b) SEM

Metallographic specimens were produced from the experiments, and they were sectioned and polished so that the center of the weld may be viewed in-plane to the direction of oscillation. The sectioned samples were mounted and then ground using 600, 1000, 2000 and 3000 silicon carbide grit papers. After grinding, the sectioned samples were polished using colloidal silica on a micro-cloth and etched using a solvent of 0.5 mL HF, 1.5 mL HNO<sub>3</sub>, 2 mL HCl and 96 mL distilled water. The metallographic samples were viewed under the optical microscope (OM) (OLYMPUS PMG3) to investigate the microstructure.

## RESULT AND DISCUSSION

### MODEL VERIFICATION

Fig. 6 shows the comparisons between simulated and experimental burn-off. It can be seen that there are some deviations between the experimental axial shortening values and simulation results. The changing trend of the two curves is consistent basically. The computed burn-off generally deviates less than 5% (in some rare instances up to 15%) from the experiment. The initial time that the two samples came into contact with each other is difficult to determine because the workpieces are not smooth entirely in the fact, but initial phase is neglected in the simulation. Therefore, burn-off increases persistently in the dash line curve.



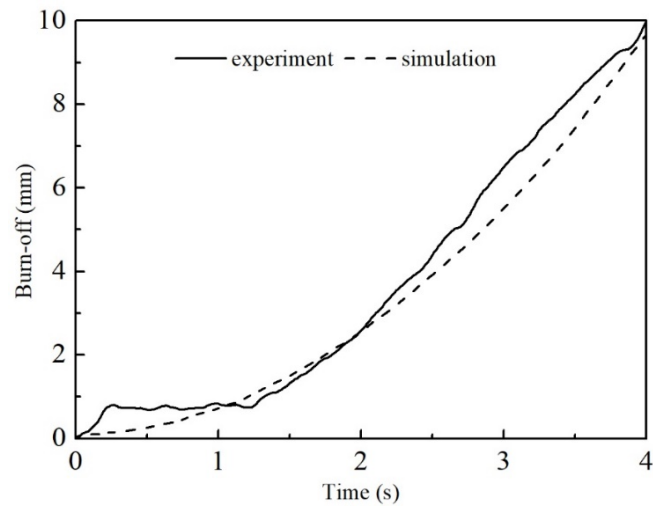


**Fig. 6** Calculated and experimental burn-off as a function of process time for 20mm of oscillatory direction

The result shows that the numerical model and the calculation method for deformation of material are proper and could be applied in further investigations.

#### TEMPERATURE FIELD

All simulations are carried out with the same initial and boundary conditions. Typical temperature distributions are shown in Fig. 7. When the welding process is finished, the interface is covered by high temperature metal, and flash is cooler than the interface. Fig. 8 shows the temperature distribution at the center vertical to the y axis. For an identical combination of process inputs, the models shows that the extent of the TMAZ decreases when the workpieces are oscillated along the shorter of the two interface contact dimensions, i.e. the 12mm dimension. This is because the material farther back from the interface was is much cooler in this weld. When this cooler material reaches the weld interface, it effectively cools the weld, producing a lower interface temperature (Fig.7), which is in agreement with the results of McAndrew et al. [13] and Schroeder et al. [19].

## Mathematical Modelling of Weld Phenomena 12

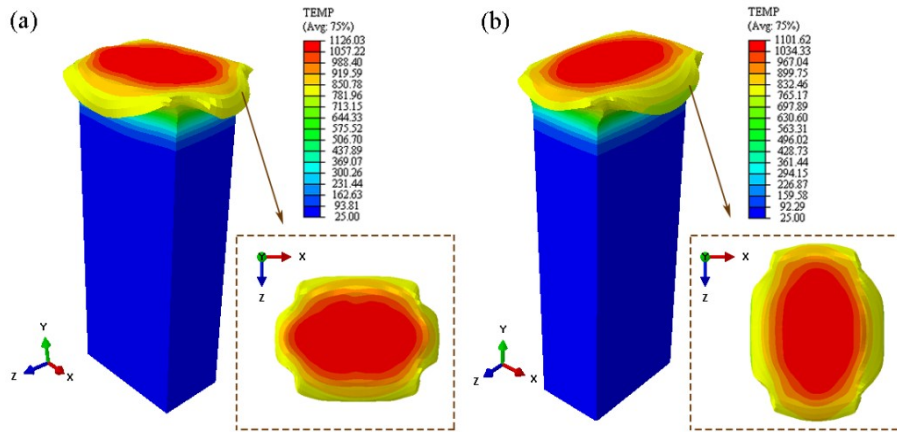


**Fig. 7** Temperature distribution in the rubbing interface when welding is finished: (a) the oscillation in the 20mm edge and (b) the oscillation in the 12mm edge

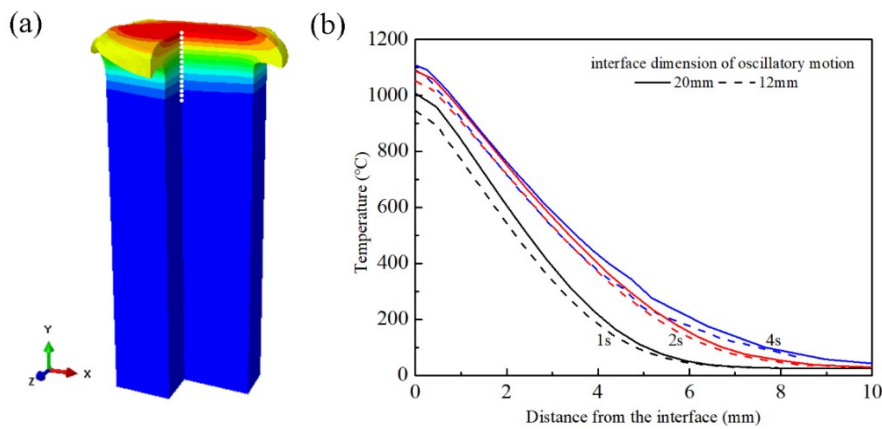


**Fig. 8** Thermal gradient recorded from the model: (a) data output from the model middle and (b) the temperature gradient at different welding times

The calculated temperature evolution at the center point is shown in Fig. 9. The temperature of interface center rises to  $1000^{\circ}\text{C}$  within 1s rapidly, and after 2s, the maximum interface temperature could be over  $1050^{\circ}\text{C}$ . For the long oscillatory length, i.e. 20mm, the temperature rises more rapidly at first, temperature rise rate is larger, and the time to reach the quasi-steady state is shorter. This is because that when a certain amplitude is applied, the long oscillatory length has less un-contact area between two workpieces, which leads to effective heat input increased, and interface temperature rises faster. Under the chosen welding conditions and geometries, it can be concluded from the calculations that no liquid phase exists during the welding process.

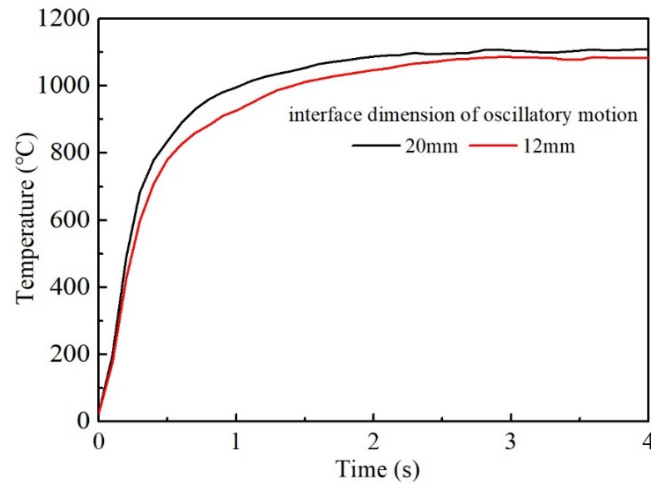


**Fig. 9** The calculated temperature evolution in the interface under two oscillation directions

#### BURN-OFF HISTORY

The time-dependent burn-off processes are shown in Fig. 10. Within the beginning 1.5 s, the burn-off is very small, the reason is that during this period, welding has not reached the quasi-steady state, and the temperature distribution of the interface is non-uniform, thus a few high temperature material cannot be expelled sufficiently. As friction continuing, the quasi-steady state is reached, thus the plasticity of interface material increases, then a layer of plastic metal at interface generates. Accordingly, the high-temperature plastic metal of the interface is extruded continuously to form flash, leading to burn-off to increase gradually. The burn-off rate is affected by the oscillatory length. Decreasing the oscillatory length of the workpiece caused the burn-off rate to increase, because the material at the WCZ has to be transported further to be extruded in the oscillation direction, and a reduction of the vibratory width removes a higher percentage of the total interface material with each cycle of oscillation before the steady state.

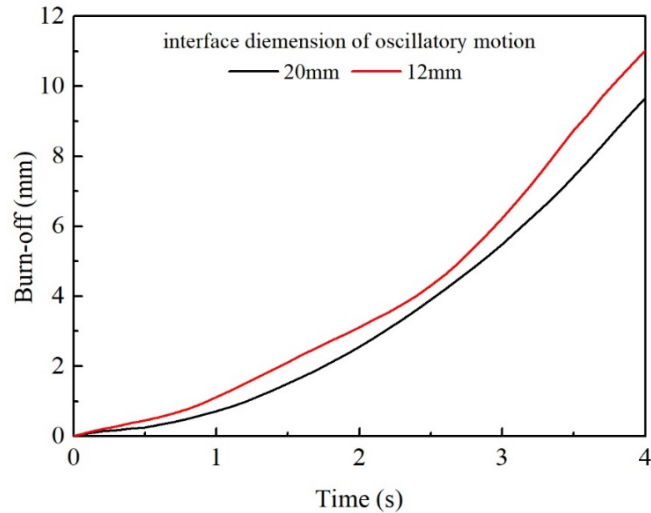


**Fig. 10** Calculated axial shortening (burn-off) for different oscillatory lengths

#### MICROSTRUCTURE ANALYSIS

The typical microstructures of LFWed Ti-8V-6Cr-4Mo-4Zr-3Al joint is shown in Fig. 11. There are fine equiaxed  $\beta$  phase grains in the WCZ (see Fig. 11b) with a size of 10-20 $\mu\text{m}$ , and the structure is not continuous. The welding process is characterized by severe plastic deformation, followed by fast cooling to room temperature. Moreover, the dynamic recrystallization can occur under the high temperature and the deformation, but short heating time restricts the grain growth. Further away from the weld line (starting from about 80 $\mu\text{m}$ , Fig. 11c), the microstructure shows evidence of severe plastic deformation during the welding process on both sides of the weld line, which is called TMAZ. The original grains are deformed heavily and re-oriented during the welding process in the direction of the friction motion and thus along the direction of material flow. The microstructure in the WCZ is different from that of the biphasic titanium alloy like Ti-6Al-4V, where is no martensite [29]. As  $\alpha$  phase is little, only dynamic recrystallization occurs without phase transformation, and the microstructure is similar to that of the high-temperature superalloy [30].

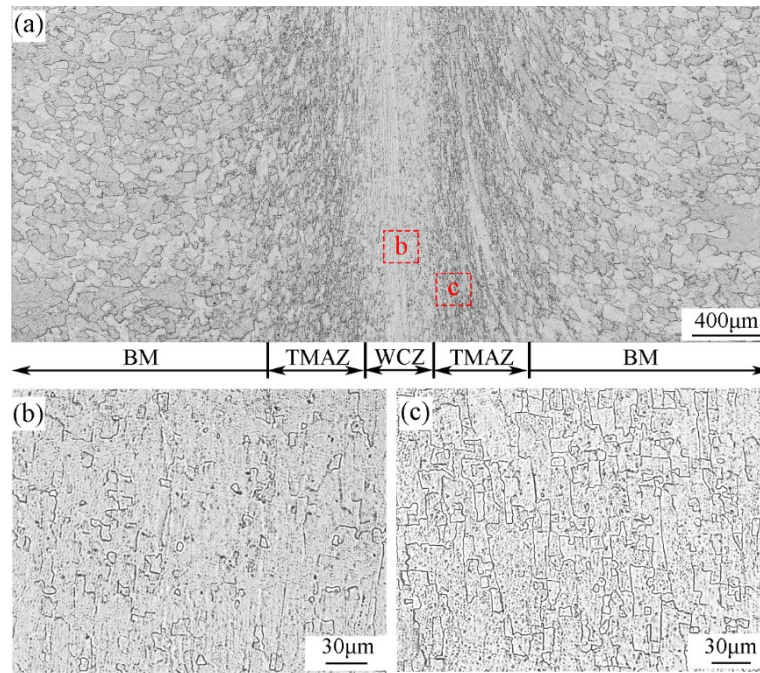


**Fig. 11** Typical microstructure of the LFWed Ti-8V-6Cr-4Mo-4Zr-3Al joint: (a) microstructure vertical to oscillatory direction, (b) high magnification of WCZ and (c) TMAZ

The cross-sectional microstructures under different welding times along the 20mm-oscillatory direction are shown in Fig. 12. When the welding time is 1s, the width of the WCZ is 555 $\mu\text{m}$ . As the welding goes on (about 2s), the width begins to decrease (233 $\mu\text{m}$ ), and finally the width tends to be stable (246 $\mu\text{m}$ ). Because the friction time is short, high-temperature region is small (Fig. 8), and heat input is insufficient to make thermoplastic metal cover the interface completely, thus only parts of the interface have been combined (see Fig. 12a), and a few of flash has been extruded. The accumulated heat is not taken away through the small flash, and could only be conducted along the vertical direction of the interface to the base metal. Therefore, the width of this weld is wider. As friction goes on, the welding process turns into the equilibrium stage, because heat accumulates progressively, thermoplastic metal of the interface continues to increase, then covers the entire interface completely, and is expelled from the interface to form a continuous, closed flash, finally, the width of welds decreases (see Fig. 12b). After the equilibrium stage is reached, the amount of the flash tends to be stable, and the WCZ width does not change, just like Fig. 12c.

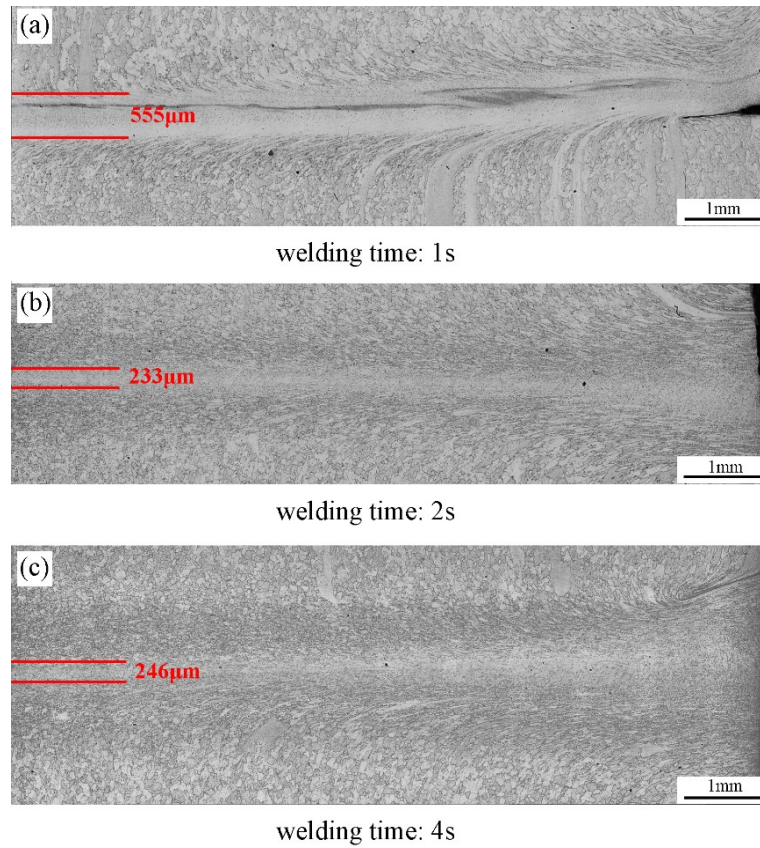


**Fig. 12** Overall views of linear friction welded Ti-8V-6Cr-4Mo-4Zr-3Al joints at different friction times: (a) 1s, (b) 2s, and (c) 4s

Fig. 13 is the microstructure of WCZ for different oscillatory directions. It figures that for the same combination of process inputs, the width of the WCZ appeared much narrower (about 200µm) that is produced with smaller oscillatory width (compare Fig. 13a and 13b), which is in agreement with Karadge et al. [9]. And the experimental values are consistent with the models (Fig. 8). The smaller oscillatory width has a greater burn-off rate, so the temperature gradient vertical to the friction direction is greater, and the deformed area is smaller.

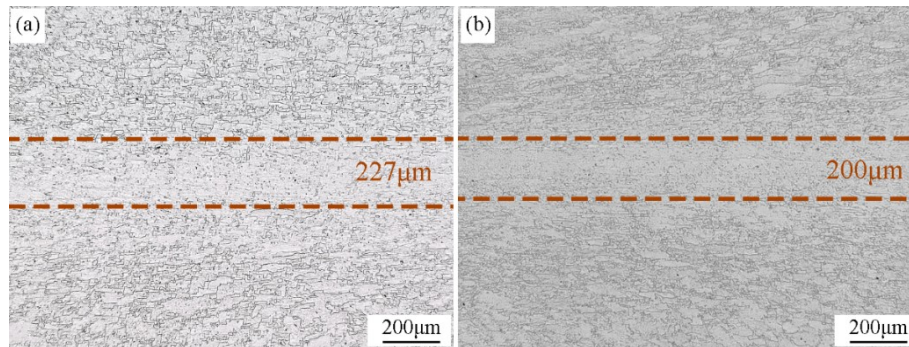


**Fig. 13** Experimental WCZ for: (a) the oscillation in the 20mm edge and (b) the oscillation in the 12mm edge

### CONCLUSIONS

The primary conclusions from this work are as follows:

- The 3D model predicts fairly well the LFW process compared to experimental results for the conditions investigated here.
- During the LFW process, the temperature in WCZ rises rapidly within 1s to about 1000 °C, high temperature area mainly concentrates in the center of interface. With welding continuing, high temperature area increases further, a large amount of the plastic metal is extruded to form larger flash. There are fine  $\beta$  phase grains instead of martensite in the WCZ.
- A reduction of the oscillatory width increases the steady-state burn-off rate. Furthermore, a reduction of the oscillatory width decreases the interface temperature, but increases the burn-off.
- Burn-off increases with the extension of the friction time, but the plastic metal layer thickness decreases at first and tends to be stable finally.

### ACKNOWLEDGEMENTS

The authors would like to acknowledge the financial support from the National Natural Science Foundation of China (No. 51675435). The project was supported by the fund of Key research and development plan (No.2016YFB1100104).

### REFERENCES

- [1] I. BHAMJI, M. PREUSS, P. L. THREADGILL, A. C. ADDISON: 'Solid state joining of metals by linear friction welding: a literature review', *Materials Science & Technology*, Vol. 27, No. 1, pp. 2-12, 2011.
- [2] A. MATEO: 'On the feasibility of blisk produced by linear friction welding', *Revista De Metalurgia*, Vol. 50, No. 3, pp. e023, 2014.

- [3] A. R. MCANDREW, P. A. COLEGROVE, C. BÜHR, B. C. D. FLIPO, A. VAIRIS: 'A literature review of ti-6al-4v linear friction welding', *Progress in Materials Science*, Vol. 92, pp. 225-257, 2018.
- [4] J. L. HUANG, N. WARNKEN, J. C. GEBELIN, M. STRANGWOOD, R. C. REED: 'On the mechanism of porosity formation during welding of titanium alloys', *Acta Materialia*, Vol. 60, No. 6-7, pp. 3215-3225, 2012.
- [5] C. PANWISAWAS, B. PERUMAL, R. M. WARD, N. TURNER, R. P. TURNER, J. W. BROOKS, H. C. BASOALTO: 'Keyhole formation and thermal fluid flow-induced porosity during laser fusion welding in titanium alloys: experimental and modelling', *Acta Materialia*, Vol. 126, pp. 251-263, 2016.
- [6] Y. GUO, T. JUNG, L. C. YU, H. LI, S. BRAY, P. BOWEN: 'Microstructure and microhardness of ti6246 linear friction weld', *Materials Science & Engineering A*, Vol. 562, No. 1, pp. 17-24, 2013.
- [7] T. J. MA, W. Y. LI, Q. Z. XU, Y. ZHANG, J. L. LI, S. Q. YANG, H. L. LIAO: 'Microstructure evolution and mechanical properties of linear friction welded 45 steel joint', *Advanced Engineering Materials*, Vol. 9, No. 8, pp. 703-707, 2010.
- [8] H. MOGAMI, T. MATSUDA, T. SANO, R. YOSHIDA, H. HORI, A. HIROSE: 'High-frequency linear friction welding of aluminum alloys', *Materials & Design*, Vol. 139, pp. 457-466, 2018.
- [9] G. BUFFA, M. CAMMALLERI, D. CAMPANELLA, U. L. COMMARE, L. FRATINI: 'Linear friction welding of dissimilar AA6082 and AA2011 aluminum alloys: microstructural characterization and design guidelines', *International Journal of Material Forming*, Vol. 10, No. 3, pp. 307-315, 2017.
- [10] T. J. MA, X. CHEN, W. Y. LI, X. W. YANG, Y. ZHANG, S. Q. YANG: 'Microstructure and mechanical property of linear friction welded nickel-based superalloy joint', *Materials & Design*, Vol. 89, pp. 85-93, 2016.
- [11] X. Y. WANG, W. Y. LI, T. J. MA, A. VAIRIS: 'Characterisation studies of linear friction welded titanium joints', *Materials & Design*, Vol. 116, pp. 115-126, 2017.
- [12] Y. GUO, M. M. ATTALLAH, Y. CHIU, H. LI, S. BRAY, P. BOWEN: 'Spatial variation of microtexture in linear friction welded Ti-6Al-4V', *Materials Characterization*, Vol. 127, pp. 342-347, 2017.
- [13] A. R. MCANDREW, P. A. COLEGROVE, A. C. ADDISON, B. C. D. FLIPO, M. J. RUSSELL, L. A. LEE: 'Modelling of the workpiece geometry effects on Ti-6Al-4V linear friction welds', *Materials & Design*, Vol. 87, No. 1, pp. 1087-1099, 2015.
- [14] P. S. EFFERTZ, F. FUCHS, N. ENZINGER: 'The influence of process parameters in linear friction welded 30CrNiMo8 small cross-section: a modelling approach', *Science and Technology of Welding and Joining*, (Published online), 2018.
- [15] R. TURNER, J. C. GEBELIN, R. M. WARD, R. C. REED: 'Linear friction welding of Ti-6Al-4V: modelling and validation', *Acta Materialia*, Vol. 59, No.10, pp. 3792-3803, 2011.
- [16] P. JEDRASIAK, H. R. SHERCLIFF, A. R. MCANDREW, P. A. COLEGROVE: 'Thermal modelling of linear friction welding', *Materials & Design*, Vol.156, pp.362-369, 2018.
- [17] J. SORINA-MÜLLER, M. RETTENMAYR, D. SCHNEEFELD, O. RODER, W. FRIED: 'FEM simulation of the linear friction welding of titanium alloys', *Computational Materials Science*, Vol. 48, No. 4, pp. 749-758, 2010.
- [18] C. BÜHR, B. AHMAD, P. A. COLEGROVE, A. R. MCANDREW, H. GUO, X. ZHANG: 'Prediction of residual stress within linear friction welds using a computationally efficient modelling approach', *Materials & Design*, Vol. 139, pp. 222-233, 2018.
- [19] F. SCHROEDER, R. M. WARD, R. P. TURNER, A. R. WALPOLE, M. M. ATTALLAH, J. C. GEBELIN, R. C. REED: 'Validation of a model of linear friction welding of ti6al4v by considering welds of different sizes', *Metallurgical & Materials Transactions B*, Vol. 46, No. 5, pp. 2326-2331, 2015.



- [20] W. LI, F. WANG, S. SHI, T. MA, J. LI, A. VAIRIS: '3D finite element analysis of the effect of process parameters on linear friction welding of mild steel', *Journal of Materials Engineering & Performance*, Vol. 23, No. 11, pp. 4010-4018, 2014.
- [21] W. LI, J. GUO, X. YANG, T. MA, A. VAIRIS: 'The effect of micro-swinging on joint formation in linear friction welding', *Journal of Engineering Science & Technology Review*, Vol. 7, No. 5, pp. 55-58, 2014.
- [22] M. GRUJICIC, G. ARAKERE, B. PANDURANGAN, C. F. YEN, B. A. CHEESEMAN: 'Process modeling of Ti-6Al-4V linear friction welding (LFW)', *Journal of Materials Engineering & Performance*, Vol. 21, No. 10, pp. 2011-2023, 2012.
- [23] A. R. MCANDREW, P. A. COLEGROVE, B. C. D. FLIPO, C. BÜHR: '3D modelling of Ti-6Al-4V linear friction welds', *Science and Technology of Welding and Joining*, Vol. 22, pp. 496-504, 2016.
- [24] A. VAIRIS: 'Investigation of frictional behaviour of various materials under sliding conditions', *European Journal of Mechanics - A/Solids*, Vol. 16, No. 6, pp. 929-945, 1997.
- [25] A. VAIRIS, M. FROST: 'On the extrusion stage of linear friction welding of Ti6Al4V', *Materials Science & Engineering A*, Vol. 271, No. 1-2, pp. 477-484, 1999.
- [26] A. VAIRIS, M. FROST: 'High frequency linear friction welding of a titanium alloy', *Wear*, Vol. 217, No. 1, pp. 117-131, 1998.
- [27] A. VAIRIS, M. FROST: 'Modelling the linear friction welding of titanium blocks', *Materials Science & Engineering A*, Vol. 292, No. 1, pp. 8-17, 2000.
- [28] G. R. JOHNSON, W. H. COOK: 'A constitutive model and data for metals subjected to large strains, high strain rates and high temperatures', *Proceedings of Seventh International Symposium on Ballistics*, The Hague, pp. 541-547, 1983.
- [29] Y. GUO, M. M. ATTALLAH, Y. CHUIA, H. LI, S. BRAY, P. BOWENA. 'Spatial variation of microtexture in linear friction welded Ti-6Al-4V', *Materials Characterization*, Vol. 127, No. 1, pp. 342-347, 2017.
- [30] X YANG, W LI, J LI, B XIAO, T MA, Z HUANG, J Guo. 'Finite element modeling of the linear friction welding of GH4169 superalloy', *Materials and Design*, Vol. 87, No. 1, pp. 215-230, 2015.

# ANALYSIS OF ACOUSTIC SOFTENING, HEAT AND MATERIAL FLOW IN ULTRASONIC VIBRATION ENHANCED FRICTION STIR WELDING

C. S. WU\*, L. SHI\* and J. CHEN\*

*\*Institute of Materials Joining, Shandong University, 250061 Jinan, Shandong, P.R. China*

DOI 10.3217/978-3-85125-615-4-29

## ABSTRACT

To improve the welding efficiency and lower the welding loads in friction stir welding (FSW), a process variant of conventional FSW, i.e., the ultrasonic vibration enhanced friction stir welding (UVEFSW), is developed. The experimentations show that UVEFSW not only increases the welding speed and decrease the weld load, but also improve the microstructure and mechanical properties of the joints. To understand the underlying physics in UVEFSW, a mathematical model is developed to analyze the interaction of the ultrasonic vibration with the plastically deformed material around the tool as well as the heat transfer and material flow phenomena in UVEFSW. It is found that the ultrasonic vibration enhances the material flow and the strain rate in the shear layer, but does not cause evident temperature increment. The assistant softening in the material around the tool is caused by the exerted ultrasonic vibration, i.e., acoustic softening. The numerical analysis results lay solid foundation to explain the process effectiveness and the UVEFSW process optimization.

Keywords: Ultrasonic vibration, friction stir welding, modelling, heat transfer, material flow

## INTRODUCTION

Friction stir welding process has been successful used for joining hard-to-weld aluminium alloys and for joining plates with different thickness or different materials [1]. As a solid state welding process, much less heat input is required for FSW, which leads to this process to be energy efficient, environment friendly, and versatile [2]. During FSW process, a non-consumable rotating tool with a specially designed pin and shoulder is inserted into the abutting edges of the workpieces to be joined and advancing along the abutting edges. Heat generated due to both friction and plastic deformation softened the material near the tool, thereafter, the softened material in front of the tool is transported to the trailing edge to form a joint behind the tool [3]. To generate enough heat energy to soften the material for the process, large rotational torque and plunge force are needed, so the welding equipment is large in volume, and complex clamping equipment is necessary [4]. These phenomena are particularly severe for welding of steel and titanium alloys [5]. In addition, the high

stress subjected by the tool pin causes rapid tool wear and premature tool failure which resulting in poor weld quality and high production cost [4,5]. Moreover, the high rotational torque and transverse force during FSW also limit the welding speed to a relatively low value [4]. To solve these problems, some assistant heat sources (induction heat, resistance heat, laser, plasma arc, etc.) have been used to preheat the workpiece near the tool [6-8]. However, the multiple thermal cycles would cause the increasing of the volume of heat-affected zone and make the precipitated phase of the aluminium alloys tend to grow in the weld nugget zone [9,10].

The application of ultrasonic energy to the plastic deformation of metal has been widely investigated [11-13]. It has been shown that superimposing ultrasonic vibration in metal forming can reduce the yield stress and flow stress, increase the processing speed and improve the product quality [11-13]. Ultrasonic energy is an assistant heat source of low power consumption and high efficiency which can reduce the deformation resistance of material [11]. Park has employed ultrasonic vibration to the FSW tool and found that by adding ultrasonic vibrations to FSW tool results in a better weld quality, less welding force needed and increasing of the tool life [10]. Amini et al. revealed that ultrasonic vibration can reduce downward force and welding force in FSW [14]. Ma et al. performed the studies on ultrasonic assisted FSW and found that superimposing ultrasonic vibration can improve the properties of the weld joint, refine the grain and reduce the residual stress in the weld [15]. Rostamiyan et al. studied ultrasonically assisted friction stir spot welding of AA6061, and found that superimposing ultrasonic vibration in friction stir spot welding can improve lap shear force and hardness [16]. Ahmadnia et al. conducted the ultrasonic-assisted friction stir welding of AA6061 joints to analyze the effects of process parameters on the mechanical and tribological properties of joints [17]. Wu's research group have developed the ultrasonic vibration enhanced FSW (UVEFSW) system which transmits ultrasonic vibration energy directly into the workpiece near the FSW tool [9,18]. Experimental results shown that this novel UVEFSW can enhance the plastic material flow, improve the weld quality, increase the welding speed and reduce the welding loads [9,18]. In all, by adding ultrasonic vibration energy to FSW can efficiently reduce the welding loads and the residual stress, improve the weld quality and enhance the plastic fluidity of the material near the tool. However, superimposing ultrasonic vibration energy in FSW increases the complexity of the process. In order to optimize the UVEFSW and make full use of the ultrasonic vibration energy in FSW, a fundamental knowledge of the effects of superimposing ultrasonic vibration energy in FSW on thermal process and plastic material flow should be required. A rigorous numerical model coupled with experimental validation is suitable for revealing the underlying physical mechanism of UVEFSW process.

In the past decades, numerous numerical models have been reported to simulate the material flow and heat transfer in conventional FSW [19-21], but few of them are related to ultrasonic assisted FSW process. Park has simulated the ultrasonic assisted FSW by impose sinusoidal horizontal ultrasonic vibration on the tip of the FSW tool and found that the downward force decreased with increasing the amplitude of ultrasonic vibration [10]. Lai et al. established a ultrasonic assisted FSW model by considering the longitudinal ultrasonic vibration of the FSW tool as an additive inertial force and found the ultrasonic vibration can provide additional heat energy to keep sufficient welding temperature at relatively higher welding speed [22]. However, these ultrasonic assisted FSW models have not considered the acoustic softening effect, i.e., ultrasonic energy can reduce the

deformation resistance of material [23-25]. Recently, Shi et al. [26-27] developed an integrated model, which take into consideration of the ultrasonic softening and preheating effect, to analyze the effects of superimposing ultrasonic vibration on FSW process.

In order to optimize the process and the relevant microstructure and mechanical properties of the joints, a fundamental knowledge of acoustic softening, heat and mass transfer during UVeFSW process should be required. In this paper, the integrated 3D numerical model is used for quantitatively analysing the acoustic softening, heat transfer and material flow in UVeFSW process. The variation of temperature fields, material flow velocity, strain rate and viscosity under the effect of ultrasonic vibration are quantitatively analyzed to get deep insight into the underling mechanism of UVeFSW process.

### EXPERIMENTAL DETAILS

Fig. 1 shows the experimental system for the self-developed ultrasonic vibration enhanced FSW (UVeFSW). The UVeFSW system can be divided into two main parts: a conventional FSW machine (FSW-3LM-003) and a self-designed device of ultrasonic vibration system. The ultrasonic vibration energy is directly transmitted into the workpiece by the sonotrode as shown in Fig. 1. Thus, the coupling of the ultrasonic energy with the friction and stirring action can produces an enhanced plastic material flow near the tool [9,18]. In this study, the ultrasonic system operates at a frequency ( $f$ ) of 20 kHz and the amplitude ( $\lambda$ ) of 40  $\mu\text{m}$  during the UVeFSW process. The maximum power of the ultrasonic system is 1200 W, while the efficient power during the process is about 300 W. The distance between the center of sonotrode and the FSW tool axis is 20 mm. The inclinations angle ( $\varphi$ , as shown in Fig. 2) of sonotrode with respect to the horizontal axis is 40°. The clamping force of the sonotrode is 300 N during the process.

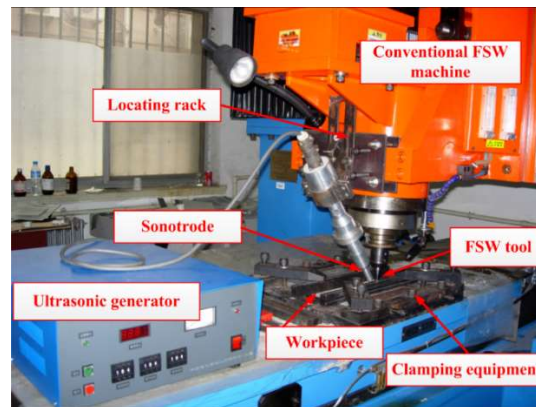


**Fig. 1** The ultrasonic vibration enhanced friction stir welding (UVeFSW) system.

**Table 1** Composition of workpiece material (AA2024-T3 Al alloy) (wt, pct)

Cu	Mg	Fe	Ni	Mn	Si	Ti	Zn	Al
4.58	1.59	0.25	<0.10	0.63	0.15	<0.10	0.20	Balance

Aluminum alloy AA2024-T3 plates (300 mm in length, 80 mm in width and 6 mm in thickness) were welded in a square butt joint configuration. Table 1 lists the compositions of the workpiece materials. The shoulder diameter is 15.0 mm. The diameters of the pin at the root and tip are 5.6 mm and 3.2 mm, respectively, and its length is 5.7 mm.

## MATHEMATICAL MODEL

### GOVERNING EQUATIONS

UVeFSW is a complex physical process which is consisted of fully-coupled heat generation, heat transfer, material flow and ultrasonic vibration energy transmission. Only the quasi-steady state (the welding period) is dealt with in this study. The plastic material during the UVeFSW is assumed to behave as an incompressible and single-phase non-Newtonian flow [28-31]. The geometrical model of UVeFSW process is shown in Fig. 2.

The conservation equations of mass and momentum are given as,

$$\frac{\partial \rho}{\partial t} + \nabla \cdot (\rho \vec{v}) = 0 \quad (1)$$

$$\frac{\partial(\rho \vec{v})}{\partial t} + \nabla \cdot (\rho \vec{v} \vec{v}) = -\nabla p + \nabla \cdot (\mu(\nabla \vec{v} + \nabla \vec{v}^T)) \quad (2)$$

where  $\rho$  is density,  $\vec{v}$  is material flow velocity,  $p$  is fluid pressure,  $\mu$  is viscosity. The energy conservation equation is given as,

$$\frac{\partial(\rho H)}{\partial t} + \nabla \cdot (\rho \vec{v} H) = \nabla \cdot (k \nabla T) + S_v \quad (3)$$

where  $H$  is enthalpy,  $k$  is thermal conductivity,  $T$  is temperature, and  $S_v$  is the viscous dissipation heat source due to plastic deformation near the tool in the shear zone [5].

Superimposing ultrasonic vibration in FSW, the ultrasonic vibration energy plays two important effects. One is acoustic softening effect, which would affect the dislocation evolution and subsequent reduce the yield stress and flow stress of the plastic deformed materials [32]. The other is the preheating effect due to the vibration friction heat originates from the relative motion between the vibratory sonotrode and the workpiece. In a thermo-fluid model, the fluid viscosity is key to predict the heat and mass transfer in the calculation domain. In the current simulation, the fluid viscosity is defined to be dependent on the temperature, strain rate and ultrasonic vibration energy density, which is proposed in reference [32]. The formulation of the fluid viscosity is given based on the visco-plasticity theory,

$$\mu = \frac{\bar{\sigma}}{3\dot{\epsilon}} \quad (4)$$

$$\bar{\sigma} = \frac{1}{\alpha} \ln \left\{ \left[ \frac{\bar{\epsilon}}{A} \exp \left( \frac{Q}{RT} - \frac{g_0 \mu_m b^3 \beta}{k_B T} \sqrt{\frac{ME}{\hat{\sigma}_{th}}} \right) \right]^{\frac{1}{n}} + \left[ 1 + \left[ \frac{\bar{\epsilon}}{A} \exp \left( \frac{Q}{RT} - \frac{g_0 \mu_m b^3 \beta}{k_B T} \sqrt{\frac{ME}{\hat{\sigma}_{th}}} \right) \right]^{\frac{1}{n}} \right]^{\frac{1}{2}} \right\} \quad (5)$$

where  $\bar{\sigma}$  is the flow stress,  $\bar{\epsilon}$  is the effective strain rate,  $Q$  is the activation energy,  $R$  is the gas constant, and  $\alpha$ ,  $A$ ,  $n$  are the material constants which represent the characteristics of base material [32].  $g_0$  is a pre-factor,  $\mu_m$  is the temperature-dependent shear modulus [33],  $b$  is the magnitude of Burgers vector,  $M$  is the Taylor factor,  $k_B$  is the Boltzmann's constant,  $E$  is the ultrasonic energy density which is calculated using the method proposed in reference [33],  $\hat{\sigma}_{th}$  is the thermal components of mechanical threshold stress,  $\beta$  is calibrated parameters for flow stress [32].

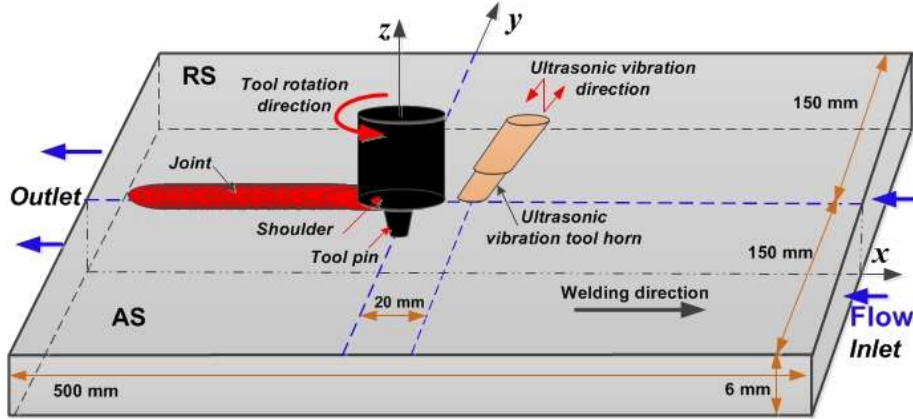


Fig. 2 Geometrical model of ultrasonic vibration enhanced friction stir welding (UVEFSW).

#### HEAT SOURCE MODEL

The heat source which takes into account the frictional heat at the FSW tool/workpiece contact interfaces as well as the shear plastic deformation heat has been used in this model. The interfacial contact shear stress is defined to be dependent on temperature, strain rate and ultrasonic energy density. Based on the von Mises yield criterion, the interfacial contact shear stress  $\tau_c$  and interfacial friction stress  $\tau_f$  at tool-workpiece interface can be expressed as [26]:

$$\tau_c = C_T \frac{\bar{\sigma}}{\sqrt{3}} \quad (6)$$

$$\tau_f = \mu_f P_N \quad (7)$$

where  $C_T$  is a temperature-dependent factor at a region near the melting point to prevent overprediction of temperature near the tool during FSW process [26],  $\mu_f$  is the frictional coefficient, and  $P_N$  is the normal pressure at the FSW tool/workpiece contact interface.

Thus, the heat generation rate at FSW tool/workpiece contact interface can be expressed as:

$$q = [\eta(1 - \delta)\tau_c + \beta_f \delta \tau_f] |\vec{v}_t + \vec{U}| \quad (8)$$

where  $\eta$  and  $\beta_f$  are the conversion efficiency of plastic deformation and friction heat, respectively.  $\delta$  is dimensionless slip rate [34].  $\vec{v}_t$  is the interfacial FSW tool velocity vector which is calculated by  $\vec{v}_t = \vec{\omega} \times \vec{r}$ , and  $\vec{\omega}$  is the rotation speed vector,  $\vec{r}$  is the radius vector, and  $\vec{U}$  is the welding speed vector.

The deformation heat in the shear zone is expressed as a volumetric heat source in the energy conservation equation, which is expressed as [4],

$$S_v = f_m \mu \Phi \quad (9)$$

where  $f_m$  is an constant,  $\Phi$  is a term related to the strain rate of the plastic deformation [4].

The preheating effect originates from the relative frictional sliding between the sonotrode and workpiece, which is considered as a frictional heat flux at the tip of the sonotrode in UVeFSW, is expressed as [26]:

$$q_u = \frac{4\lambda f \mu_c F_c \cos \varphi}{\pi R_h^2} \quad (10)$$

where  $\lambda$  and  $f$  are the amplitude and frequency of the ultrasonic, respectively.  $\mu_c$  is the constant frictional efficiency between sonotrode and workpiece,  $F_c$  is the clamping force of the sonotrode,  $R_h$  is the radius of the sonotrode at the contact interface with workpiece,  $\varphi$  is the tilt angle of the sonotrode.

#### BOUNDARY CONDITIONS

The heat dissipation at the top surface of the workpiece involves both convective and radiative heat losses and is expressed as [4-5]:

$$k \frac{\partial T}{\partial \vec{n}} = h_c (T_\infty - T) + \sigma_r \varepsilon_r (T_\infty^4 - T^4) \quad (11)$$

where  $h_c$  is the convective heat transfer coefficient,  $\sigma_r$  is the Stefan-Boltzmann constant,  $\varepsilon_r$  is the external emissivity, and  $T_\infty$  is the room temperature.

The bottom and side surfaces of the workpiece are contact to the backplate and clamping equipments. Thus, the boundary condition for heat exchange involves only convective heat transfer:

$$k \frac{\partial T}{\partial \vec{n}} = h_c (T_\infty - T) \quad (12)$$

At the FSW tool/workpiece contact interfaces, the heat flux boundary condition as following is applied [5],

$$k \frac{\partial T}{\partial \vec{n}} = \frac{\sqrt{(k\rho c_p)_w}}{\sqrt{(k\rho c_p)_w} + \sqrt{(k\rho c_p)_t}} q \quad (13)$$

where the subscripts  $w$  and  $t$  denote the workpiece and the tool, respectively.

The velocity boundary conditions at the tool-workpiece contact interfaces are expressed in terms of the rotation speed, the welding speed, the dimensionless slip rate and the radius vector as follows [4],

$$\vec{v} = (1 - \delta)\vec{\omega} \times \vec{r} + \vec{U} \quad (14)$$

The initial temperature of the material flow and the ambient temperature are assumed to be 300 K. Initially, the plastic material flows in and out of the inlet and outlet boundaries at the welding speed, respectively. The moving wall boundary condition is applied on the other boundaries away from the tool/workpiece contact interfaces. The effect of the threaded pin on material flow is considered as a boundary condition in this study. The thread leads to downward material flow velocity according to the rotation direction of the tool pin and the thread direction [5].

### SOLUTION METHOD

Numerical simulation of the process was performed using the computational fluid dynamics (CFD) code, Fluent, based on the governing equations and the boundary conditions as stated above. Conservation principles of mass, momentum and energy were calculated for the incompressible single-phase flow [28]. The calculations of the coupled temperature field and velocity field were performed by the Semi-Implicit Method for Pressure Linked Equations (SIMPLE) algorithms [35]. Second order upwind scheme was used for the discretization of the momentum equations and energy equation. Fig 3 shows the top view of the mesh system for finite volume calculations. Non-uniform grid system was used to discretize the calculation domain. Finer grids were chosen to describe the portion of the domain which encompasses severe material flow and heat generation near the tool and sonotrode, in order to resolve the plasticized material flow and heat convection. The computation was performed until the convergence criteria were reached.



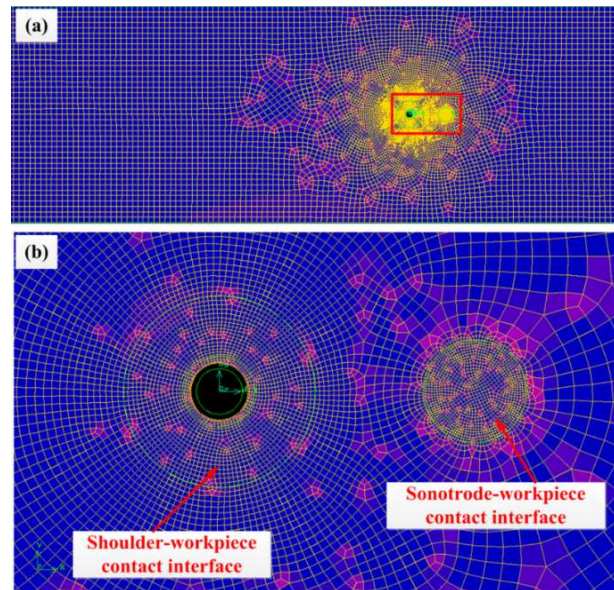


**Fig. 3** The mesh system in the simulation. (a) top view of the total workpiece, (b) local view of the mesh near the FSW tool and sonotrode-workpiece contact interface (enlarged of the red area in a).

## RESULTS AND DISCUSSION

Fig. 4 shows the monitoring locations on transverse cross-section. Three typical monitor locations near the tool are chosen to output the thermal history during welding process. One located below the tool axis at the bottom of the tool pin (i.e., location M0). The other two located at the top surface of the workpiece and 8.0 mm away from the weld line, with one at the AS (i.e., location M1) and the other at the RS (i.e., location M2).

Fig. 5 shows the calculated temperature fields of FSW and UVeFSW at the top surface of the workpiece and at  $z = 3.0$  (i.e., at the middle of the plate thickness) horizontal plane. It is revealed that the temperature distribution features of FSW and UVeFSW are approximately analogous. Due to superimposing of ultrasonic vibration, the isothermal of the same magnitude in UVeFSW are enlarged ahead of the FSW tool as shown in Fig. 5a and 5c. Fig. 6 shows the calculated temperature fields of the FSW and UVeFSW at transverse cross-section. It is shown that the temperature near the FSW tool in FSW is somehow higher than that in UVeFSW, while there are little temperature difference at about 10 mm away from the weld line.

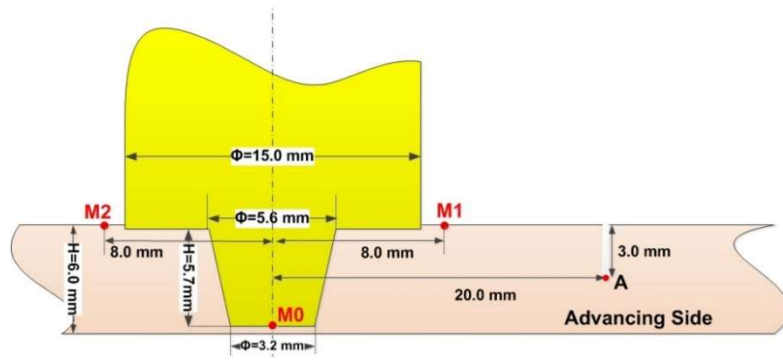


Fig. 4 Schematic figure of the monitoring locations (A, M0, M1 and M2) on transverse cross-section.

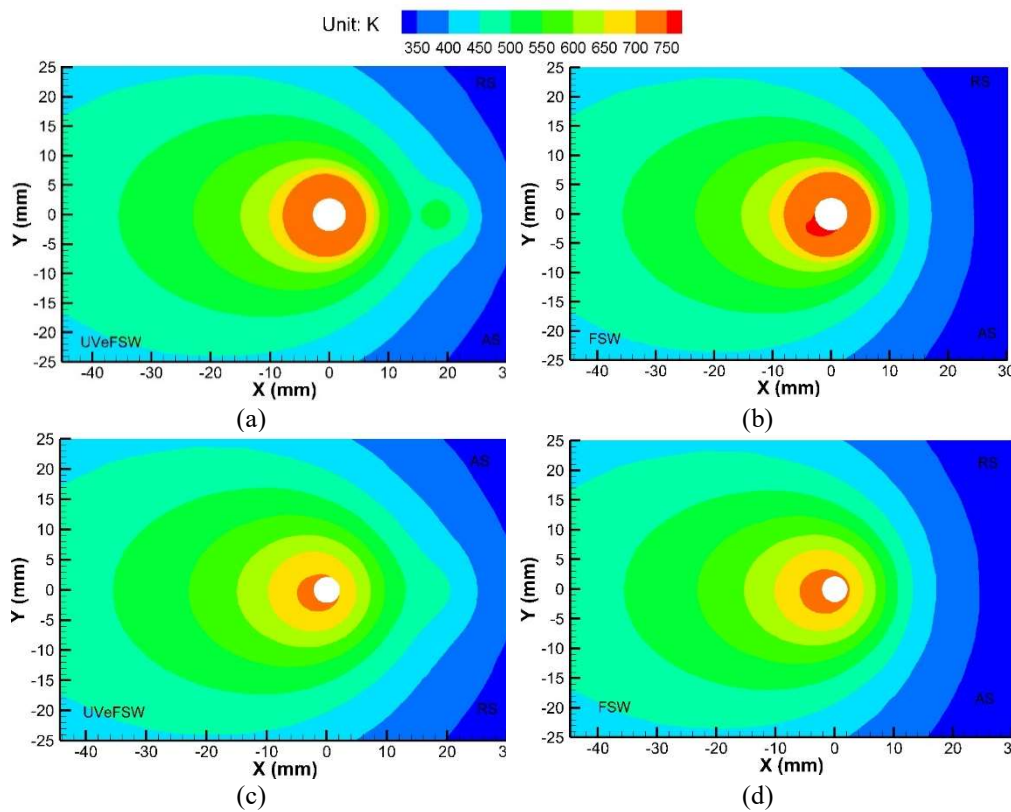
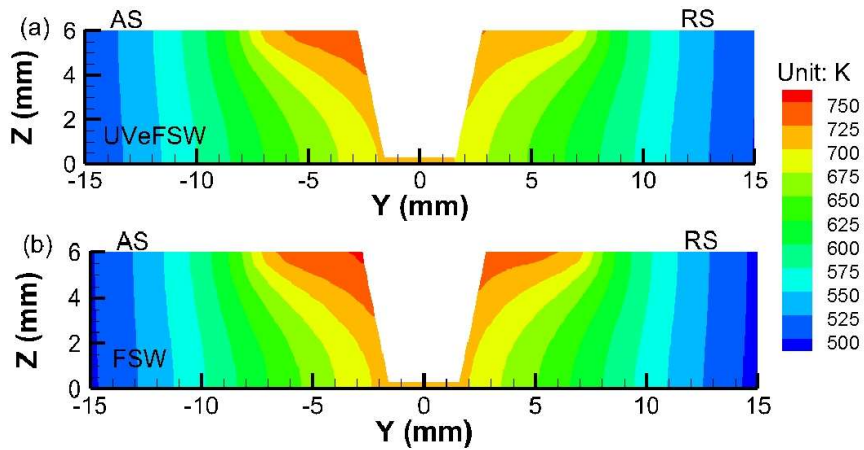
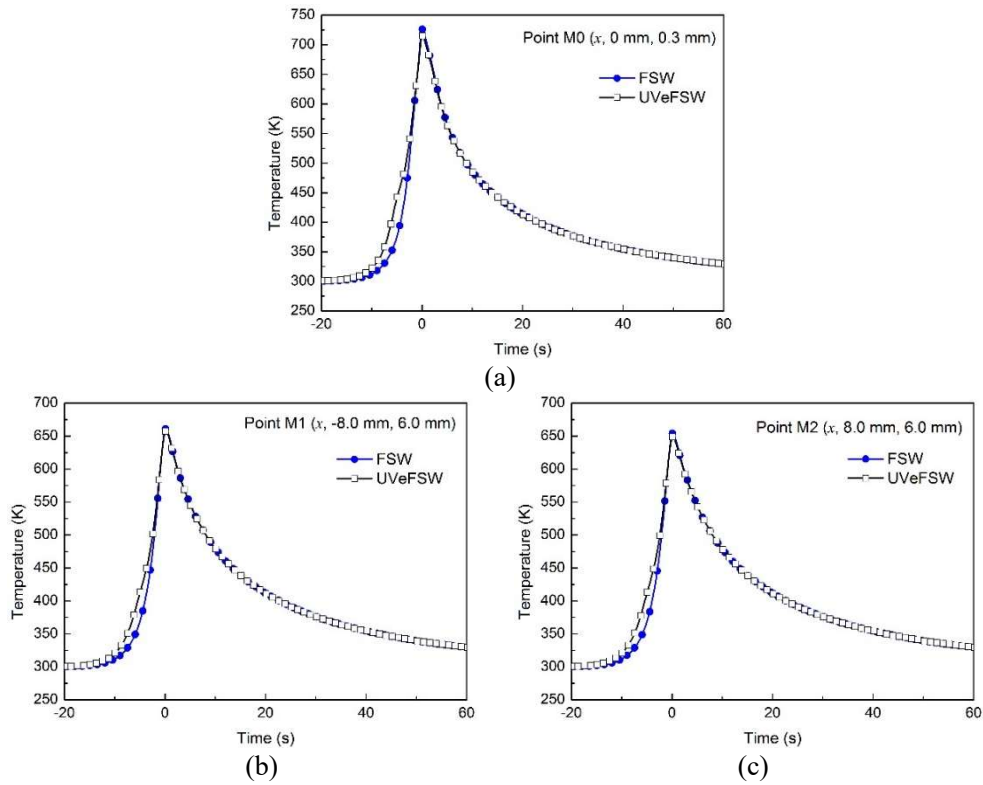


Fig. 5 Predicted temperature field at  $\omega = 600$  rpm,  $U = 240$  mm/min. (a) at the top surface of workpiece in UVeFSW; (b) at the top surface of workpiece in FSW; (c) at  $z = 3$  mm plane in UVeFSW; (d) at  $z = 3$  mm plane in FSW.



**Fig. 6** Predicted temperature field on transverse cross-section at  $\omega = 600$  rpm,  $U = 240$  mm/min. (a) UVeFSW; (b) FSW.

Fig. 7 shows the predicted thermal cycles at three typical locations (i.e., M0, M1 and M2 in Figure 4). It is seen that there is a preheating region near  $t = -5$  s (i.e., 20 mm prior to FSW tool axis where the sonotrode located). Fig. 8a shows that the temperature difference between UVeFSW and FSW at the preheating region (i.e., at  $t = -5$  s) is  $\sim 50$  K below the tool pin bottom (i.e., at location M0), while the temperature difference decreases to  $\sim 20$  K at 8.0 mm away from the weld line, as shown in Fig. 8b and 8c. However, there is little temperature difference between the peak temperature in UVeFSW and the one in FSW, the maximum temperature difference at the peak value of thermal cycles is less than 5 K as shown in Fig. 8. From Figs. 5-7, it is clearly shown that the temperature fields in FSW and UVeFSW are approximately analogous. The ultrasonic vibration in FSW does not significant change the process temperature in FSW. This is because on the one hand, the ultrasonic vibration preheats the workpiece at 20 mm before the FSW tool axis, on the other hand, the acoustic softening reduces the strength of plastic material near the tool which resulting in a lower plastic deformation heat generation in UVeFSW. As a result, superimposing ultrasonic vibration in FSW does not cause evident temperature increment.



**Fig. 7** The calculated thermal cycles in UVeFSW and FSW at  $\omega = 600$  rpm,  $U = 240$  mm/min. (a) Location M0; (b) Location M1; (c) Location M2.

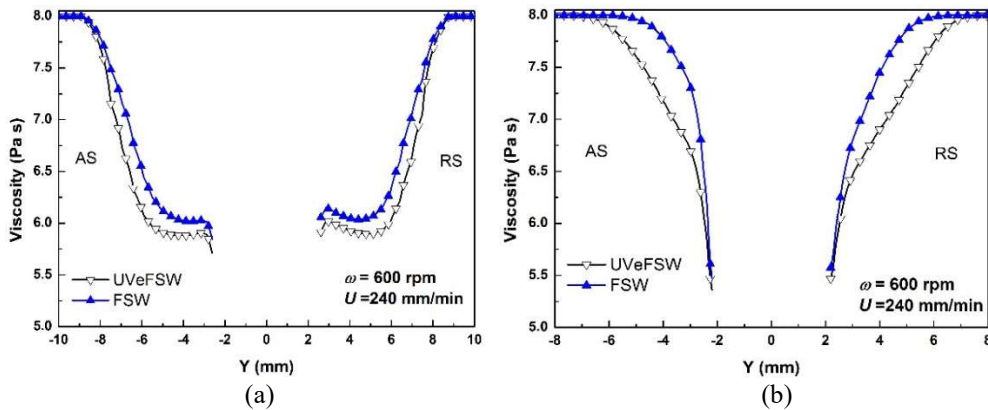


**Fig. 8** Variation of viscosity (a) at  $z = 5$  mm and (b) at  $z = 3$  mm horizontal planes in both UVeFSW and FSW (The viscosity value are represented in logarithm to the base 10).

The variation of viscosity near the tool are illustrated in Fig. 8. As pointed out in the literatures [36], the boundary of TMAZ could be obtained by the critical viscosity of  $2.5 \times 10^6$  Pa·s, because no significant plastic flow occurs above this critical value. Thus, the boundary of iso-viscosity of  $2.5 \times 10^6$  Pa·s is chosen as the TMAZ boundary as shown in

Fig. 9. Fig. 8 shows that viscosity in UVeFSW is lower than that in FSW, which resulting in a larger TMAZ in UVeFSW (as shown in Fig. 9). It indicates that superimposing ultrasonic vibration on FSW process can enlarge the TMAZ boundaries. This is because the ultrasonic vibration energy reduce the flow stress and the corresponding viscosity value near the tool. As a result, a larger volume of plastic materials near the tool are softened by the acoustic softening effect of the ultrasonic vibration energy which leads to a larger TMAZ in UVeFSW as shown in Fig. 9.

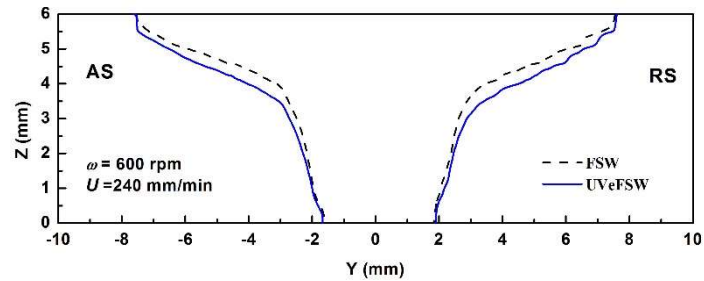


**Fig. 9** The calculated iso-viscosity line ( $2.5 \times 10^6$  Pa.s) in UVeFSW and FSW at transverse cross-section

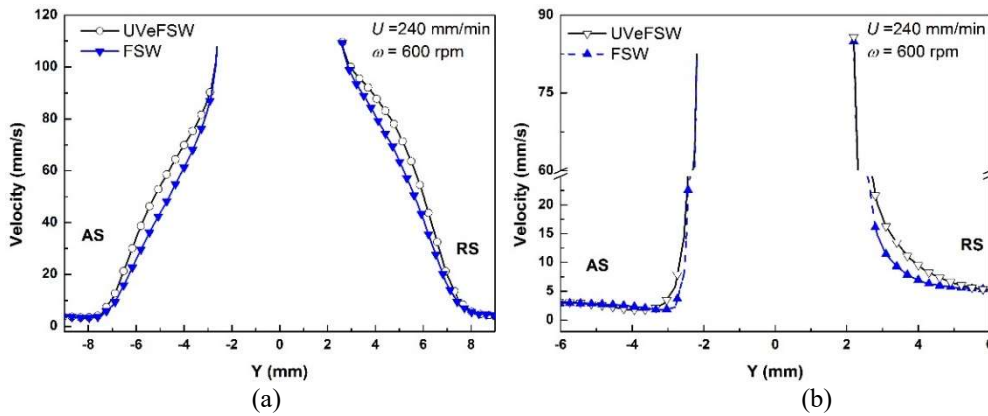


**Fig. 10** Variation of material flow velocity (a) at  $z = 5$  mm and (b) at  $z = 3$  mm horizontal planes in both UVeFSW and FSW.

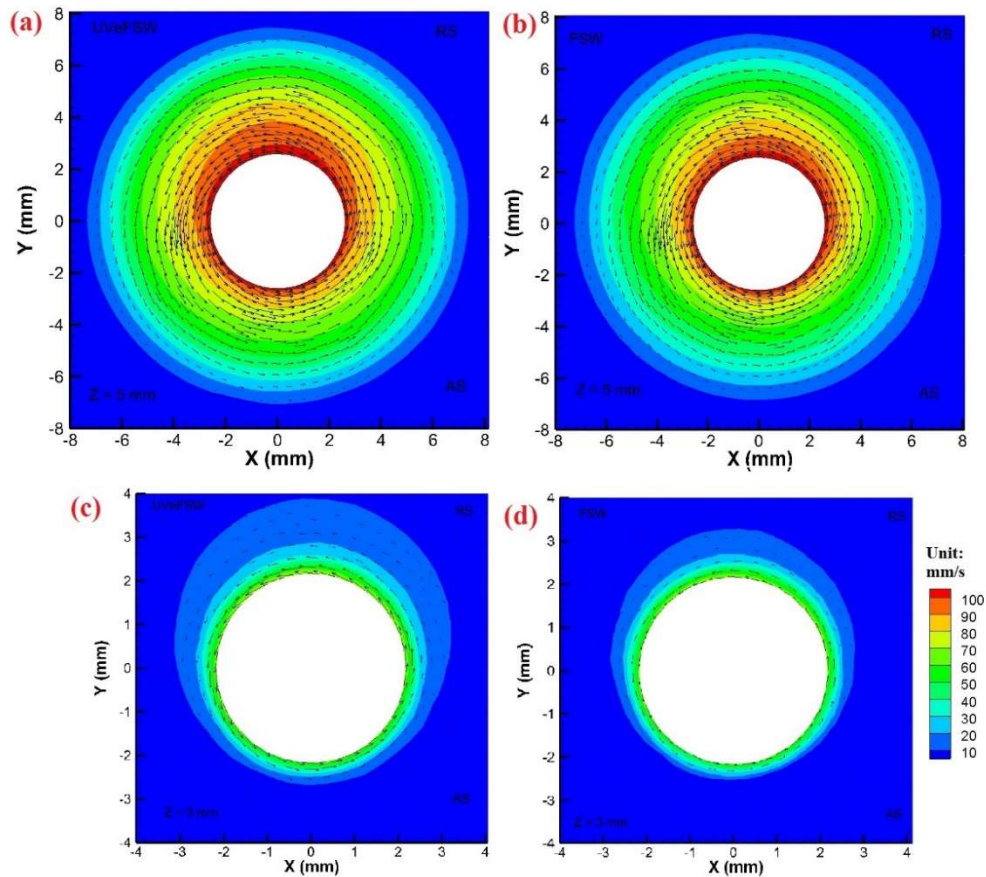


**Fig. 11** Material flow at different horizontal plane at  $\omega = 600$  rpm,  $U = 240$  mm/min. (a) at  $z = 5$  mm in UVeFSW; (b) at  $z = 5$  mm in FSW; (c) at  $z = 3$  mm in UVeFSW; (d) at  $z = 3$  mm in FSW.

Fig. 10 shows the variation of material flow velocity near the tool in both FSW and UVeFSW. It is clearly shown that the plastic material flow velocity adjacent to the FSW tool is identical in both FSW and UVeFSW. While away from the tool-workpiece interface (i.e., at about 3.0 mm from the weld line at  $z = 5.0$  mm horizontal plane as shown in Fig. 10a and at about 2.5 mm from the weld line at  $z = 3.0$  mm horizontal plane as shown in Fig. 10b), the plastic material flow velocity in UVeFSW is higher than that in FSW. Superimposing ultrasonic vibration in FSW could increase the material flow velocity, especially in the TMAZ. Fig. 11a through 11d illustrates the calculated material flow velocity and vector on horizontal planes at positions  $Z = 5$  and 3 mm from the bottom face, for both FSW and UVeFSW. The plastic material flows round the tool axis in all cases. The rotating flow region decreases with increasing depth, in other word with decreasing  $Z$ . This is because the influence of the shoulder decreases when the depth from the top surface increases. However, it can be clearly seen that the contours of the material flow with identical velocity are larger in UVeFSW than those in FSW. The acoustic softening in

UVeFSW leads to a lower viscosity which resulting in an enhancement of plastic material flow near the tool. In addition, the acoustic softening reduce the flow stress which leads to a lower plastic heat generation in UVeFSW and it offsets the preheating effects and resulting in less temperature increment. The exerting ultrasonic vibration can enhance the material flow and the strain rate in the shear layer, but does not cause evident temperature increment, which could be a reason for better mechanical properties of the joints in UVeFSW process.

To validate the model, the experimentally measured macro-sections of welds under welding conditions (800 rpm and 320 mm/min) in UVeFSW was obtained. It was used to compare the calculated TMAZ boundary. It can be found that both are in agreement with each other.



**Fig. 12** Comparison of the calculated and measured TMAZ profile in UVeFSW

### CONCLUSIONS

A three-dimensional model is developed to conduct the numerical simulation of the material flow and heat transfer in ultrasonic vibration enhanced friction stir welding (UVeFSW) process. Both the effects of ultrasonic softening and preheating are considered in the model. It is found that due to the acoustic softening effect of superimposed ultrasonic vibration energy, the thermo-mechanically affected zone (TMAZ) boundary predicted by iso-viscosity value in UVeFSW are larger than that in conventional FSW process. It reveals that superimposing ultrasonic vibration in FSW can enhance the material flow and the strain rate in the shear layer, but does not cause evident temperature increment. Ultrasonic softening is the mainly function of superimposing ultrasonic vibration in friction stir welding process, while the preheating effect is relatively small. UVeFSW process has great potential to improve the microstructure of joint and reduce the welding force.

### ACKNOWLEDGEMENTS

This research was supported by the National Natural Science Foundation of China (Grant No. 51475272).

### REFERENCES

- [1] P.L. THREADGILL, A.J. LEONARD, H.R. SHERCLIFF, P.J. WITHERS: 'Friction stir welding of aluminium alloys', *International Materials Reviews*, Vol. 54, No. 2, pp. 49-93, 2009.
- [2] R. MISHRA, Z.Y. MA: 'Friction stir welding and processing', *Materials Science and Engineering: R*, Vol. 50, No. 1-2, pp. 1-78, 2005.
- [3] R. NANDAN, T.S. DEBROY, H.K.D.H. BHADSHIA: 'Recent advances in friction-stir welding-process', weldment structure and properties', *Progress in Materials Science*, Vol. 53, pp. 980-1023, 2008.
- [4] A. ARORA, M. MEHTA, A. DE, T. DEBROY: 'Load bearing capacity of tool pin during friction stir welding', *The International Journal of Advanced Manufacturing Technology*, Vol. 61, No. 9-12, pp. 911-920, 2012.
- [5] G. CAM: 'Friction stir welded structural materials: beyond Al-alloys', *International Materials Reviews*, Vol. 56, No. 1, pp.1-48, 2011.
- [6] G. KOHN, Y. GREENBERG, I. MAKOVER, A. MUNITZ: 'Laser-assisted friction stir welding', *Welding Journal*, Vol. 81, No. 2, pp. 46-46, 2002.
- [7] J. LUO, W. CHEN, G. FU: 'Hybrid-heat effects on electrical-current aided friction stir welding of steel, and Al and Mg alloys', *Journal of Materials Processing Technology*, Vol. 214, No. 12, pp. 3002-3012, 2014.
- [8] A.H. LOTFI, S. NOUROUZI: 'Predictions of the optimized friction stir welding process parameters for joining AA7075-T6 aluminum alloy using preheating system', *The International Journal of Advanced Manufacturing Technology*, Vol. 73, No. 9-12, pp. 1117-1137, 2014.
- [9] X.C. LIU, C.S. WU, G.K. PADHY: 'Characterization of plastic deformation and material flow in ultrasonic vibration enhanced friction stir welding', *Scripta Materialia*, Vol. 102, pp. 95-98, 2015.
- [10] K. PARK: *Development and analysis of ultrasonic assisted friction stir welding process*. PhD Thesis, University of Michigan, 2009.
- [11] O. IZUMI, K. OYAMA, Y. SUZUKI: 'Effects of superimposed ultrasonic vibration on compressive deformation of metals', *Transactions of the Japan Institute of Metals*, Vol. 7, No. 3, pp. 162-167, 1966.
- [12] Y. DAUD, M. LUCAS, Z. HUANG: 'Modelling the effects of superimposed ultrasonic vibrations on tension and compression tests of aluminium', *Journal of Materials Processing Technology*, Vol. 186, No. 1, pp. 179-190, 2007.
- [13] A. SIDDIQ, T. EL SAYED: 'Ultrasonic-assisted manufacturing processes: Variational model and numerical simulations', *Ultrasonics*, Vol. 52, No. 4, pp. 521-529, 2012.
- [14] S. AMINI, M.R. AMIRI: 'Study of ultrasonic vibrations' effect on friction stir welding', *The International Journal of Advanced Manufacturing Technology*, Vol. 73, No. 1-4, pp. 127-135, 2014.
- [15] H.K. MA, D.Q. HE, J.S. LIU: 'Ultrasonically assisted friction stir welding of aluminium alloy 6061', *Science and Technology of Welding and Joining*, Vol. 20, No. 3, pp. 216-221, 2015.
- [16] Y. ROSTAMIYAN, A. SEIDANLOO, H. SOHRABPOOR, R. TEIMOURI: 'Experimental studies on ultrasonically assisted friction stir spot welding of AA6061', *Archives of Civil and Mechanical Engineering*, Vol. 15, No. 2, pp. 335-346, 2015.
- [17] M. AHMADNIA, A. SEIDANLOO, R. TEIMOURI, Y. ROSTAMIYAN, K.G. TITRASHI: 'Determining influence of ultrasonic-assisted friction stir welding parameters on mechanical and tribological properties of AA6061 joints', *The International Journal of Advanced Manufacturing Technology*, Vol. 78, No. 9-12, pp. 2009-2024, 2015.
- [18] Y.B. ZHONG, C.S. WU, G.K. PADHY: 'Effect of ultrasonic vibration on welding load, temperature and material flow in friction stir welding', *Journal of Materials Processing Technology*, Vol. 239, pp. 273-283, 2017.



- [19] X. HE, F. GU, A. BALL: 'A review of numerical analysis of friction stir welding', *Progress in Materials Science*, Vol. 65, pp. 1-66, 2014.
- [20] G. CHEN, Q. SHI, Y. LI, Y. SUN, Q. DAI, J. JIA, Y. ZHU, J. WU: 'Computational fluid dynamics studies on heat generation during friction stir welding of aluminum alloy', *Computational Materials Science*, 2013, 79: 540-546.
- [21] L. SHI, C.S. WU: 'Transient model of heat transfer and material flow at different stages of friction stir welding process', *Journal of Manufacturing Processes*, Vol. 25, pp. 323-339, 2017.
- [22] R.L. LAI, D.Q. HE, L.C. LIU, S.Y. YE, K.Y. YANG: 'A study of the temperature field during ultrasonic-assisted friction-stir welding', *The International Journal of Advanced Manufacturing Technology*, Vol. 73, No. 1-4, pp. 321-327, 2014.
- [23] J.C. HUNG, C. HUNG: 'The influence of ultrasonic-vibration on hot upsetting of aluminum alloy', *Ultrasonics*, Vol. 43, No. 8, pp. 692-698, 2005.
- [24] A. SIDDIQ, T. EL SAYED: 'Acoustic softening in metals during ultrasonic assisted deformation via CP-FEM', *Materials Letters*, Vol. 65, No. 2, pp. 356-359, 2011.
- [25] G.S. KELLY, S.G. ADVANI, J.W. GILLESPIE, T.A. BOGETTI: 'A model to characterize acoustic softening during ultrasonic consolidation', *Journal of Materials Processing Technology*, Vol. 213, No. 11, pp. 1835-1845, 2013.
- [26] L. SHI, C.S. WU, Z. SUN: 'An integrated model for analysing the effects of ultrasonic vibration on tool torque and thermal processes in friction stir welding', *Science and Technology of Welding and Joining*, Vol. 23, No. 5, pp. 365-379, 2018.
- [27] L. SHI, C.S. WU, S. GAO: 'Analysis of welding load reduction in ultrasonic vibration-enhanced friction stir welding', *The International Journal of Advanced Manufacturing Technology*, 2018. <https://doi.org/10.1007/s00170-018-2472-1>.
- [28] R. NANDAN, G.G. ROY, T. DEBROY: 'Three-dimensional heat and material flow during friction stir welding of mild steel', *Acta Materialia*, Vol. 55, No. 3, pp. 883-895, 2007.
- [29] H.H. CHO, S.T. HONG, J.H. ROH, H.S. CHOI, S.H. KANG, R.J. STEEL, H.N. HAN: 'Three-dimensional numerical and experimental investigation on friction stir welding processes of ferritic stainless steel', *Acta Materialia*, Vol. 61, No. 7, pp. 2649-2661, 2013.
- [30] L. SHI, C.S. WU, H.J. LIU: 'Numerical analysis of heat generation and temperature field in reverse dual-rotation friction stir welding', *The International Journal of Advanced Manufacturing Technology*, Vol. 74, No. 1-4, pp. 319-334, 2014.
- [31] A. ARORA, A. DE, T. DEBROY: 'Toward optimum friction stir welding tool shoulder diameter', *Scripta Materialia*, Vol. 64, No. 1, pp. 9-12, 2011.
- [32] L. SHI, C.S. WU, S. GAO, G.K. PADHY: 'Modified constitutive equation for use in modeling the ultrasonic vibration enhanced friction stir welding process', *Scripta Materialia*, Vol. 119, pp. 21-26, 2016.
- [33] L. SHI, C.S. WU, G.K. PADHY, S. GAO: 'Numerical simulation of ultrasonic field and its acoustoplastic influence on friction stir welding', *Materials & Design*, Vol. 104, pp. 102-115, 2016.
- [34] R. NANDAN, G.G. ROY, T. DEBROY: 'Numerical simulation of three-dimensional heat transfer and plastic flow during friction stir welding', *Metallurgical and Materials Transactions A*, Vol. 37, No. 4, pp. 1247-1259, 2006.
- [35] S.V. PATANKAR: '*Numerical Heat Transfer and Fluid Flow*', Hemisphere, Washington, D.C., USA. 1980.
- [36] L. SHI, C.S. WU, H.J. LIU: 'The effect of the welding parameters and tool size on the thermal process and tool torque in reverse dual-rotation friction stir welding', *International Journal of Machine Tools and Manufacture*, Vol. 91, pp. 1-11, 2015.

# THERMO-MECHANICAL MODEL OF THE FRICTION STIR WELDING PROCESS AND ITS APPLICATION FOR THE ALUMINIUM ALLOY AA5754

U. REISGEN\*, A. SCHIEBAHN\*, A. NAUMOV\*,  
A. MASLENNIKOV\* and V. EROFEEV\*\*

\* RWTH Aachen University, ISF-Welding and Joining Institute, 52062 Aachen, Germany, [schiebahn@isf.rwth-aachen.de](mailto:schiebahn@isf.rwth-aachen.de)

\*\* Tula State University, Welding department, 300012 Tula, Russian Federation, [va\\_erofeev@mail.ru](mailto:va_erofeev@mail.ru)

DOI 10.3217/978-3-85125-615-4-30

## ABSTRACT

A thermo-mechanical model of the FSW process for the investigation of the visco-plastic flows produced in the stir zone has been developed. It takes into account the frictional and volumetric heat sources. The input characteristics of the dynamic viscosity and shear stress for AA5754 were determined during specially designed FSW-alike experiments. The obtained distributions of the temperature, relative pressure, strain rate, viscous flow velocities, as well as the values of the longitudinal and transversal tool force components agree qualitatively with the literature data.

Keywords: friction stir welding (FSW), aluminium alloy AA5754, plastic deformation, finite difference method, experimental procedure, comparison

## INTRODUCTION

The FSW process is a variant of pressure welding and entails considerable plastic deformation. The process temperatures do not exceed 80% of the workpiece liquidus temperature [1, 2]. In friction stir welding a non-consumable rotating tool with a specially designed pin and shoulder is inserted into the abutting edges of workpieces to be joined and traversed along the line of the joint [3]. As the tool travels, heat is created by the contact friction between the shoulder, pin and the workpiece as well as by the plastic deformation of the material in the workpiece zone around the pin, where the material dwells in a visco-plastic condition – the stir zone (SZ). The plasticized material is stirred around the pin, forming behind a continuous weld seam.

The FSW process represents a combination of two tightly connected physical phenomena of mechanical and thermal treatment (friction, heat generation, and considerable visco-plastic metal flow), fig. 1.

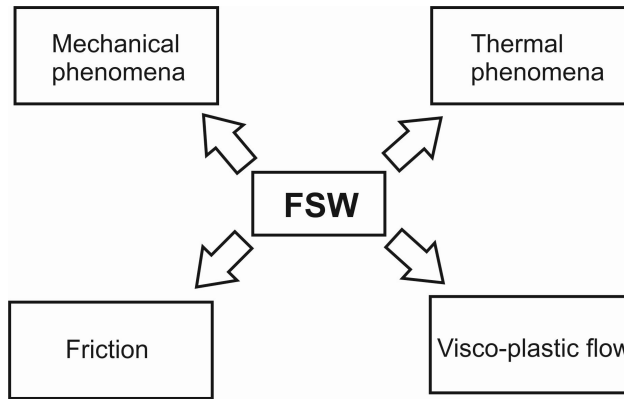


**Fig. 1** A scheme of interaction of mechanical and thermal phenomena in FSW.

The produced visco-plastic metal flows in the SZ influence, among others, the volumetric heat generation, thermal cycles in the workpiece metal, microstructure, mechanical properties and the final shape of the weld. These technological aspects are very important for producing sound welded joints [4]. Therefore, for a better understanding of the FSW process, one has to provide an analysis of the thermal and mechanical physical phenomena and their combined action on the primary internal characteristics of the FSW process i.e. heat generation, temperature distribution and viscous flow velocities in the SZ. It is planned to perform the investigation, among others, with the help of numerical modelling of the thermal and mechanical physical phenomena in the SZ on the basis of a thermo-mechanical model of the FSW process. For this purpose the model must be self-consistent and flexible to enhancement. It must consider the influence of main process parameters on the thermo-mechanical condition of the material in the SZ by means of computing the thermal, velocity and pressure fields.

The first studies were based on heat conduction, ignoring the plastic flow near the tool [5, 6]. Schmidt et al. [7] proposed a general analytical model for the heat generation during the FSW of 2024-T3 aluminium alloy. Friggard et al. [8] assumed that frictional heating at the tool shoulder-workpiece interface was entirely responsible for the heat generation during welding. Chao et al. [9] estimated the fraction of the heat generated at the tool-shoulder interface, being transported into the workpiece during the FSW of an aluminium alloy, considering the overall heat balance in the tool as well as in the workpiece with the usage of inverse modelling.

Seidel and Reynolds [10] developed a 2D fully coupled steady-state thermal model based on laminar, viscous and non-Newtonian flow around a circular cylinder. Moreover, they considered only one heat source in the form of viscous dissipation in the stirring zone, omitting the heat generation between the tool shoulder and the workpiece surface. Colegrove and Shercliff [11, 12] used a commercial software FLUENT to develop a 3D thermal and material flow model for the FSW of the AA7075 alloy. They used temperature-independent physical-mechanical properties of the alloy. Tutunchilar et al. [13] developed a valuable 3D Lagrangian finite element model by using the software DEFORM 3D for predicting the material flow in the FSW. The authors were able to show the material flow patterns in the center, advancing and retreating sides of the tool. The authors [14] provided a 2D FSW model, based on the smoothed particle hydrodynamics (SPH) with an assumption that effective viscosity depends only on temperature. Later this model was

improved by adding the Sellars-Tegart constitutive material law [15]. Despite the fact that large plastic deformation, defect formation and material mixing can be well captured by this method, the main its disadvantage is that to achieve the same accuracy as in the grid-based methods, the number of discretization points in SPH should be larger, the computational time and costs therefore increase [15].

One of the basic finite difference models of the FSW process was developed in the works [16, 17]. In the present paper, we have explicitly taken into consideration the frictional heat source in the contact between the tool shoulder and the workpiece surface. We present the visco-plastic flow of the metal around the pin in the stir zone as an incompressible viscous fluid flow. Internal friction between the layers of the plasticized metal causes the volumetric heat generation. At high strain rates, typical for the FSW conditions, the metals undergo work hardening, the rate of which is equivalent to the dynamic viscosity. This circumstance allows us to consider the metal, dwelling at pressures exceeding its yield stress, as a viscous fluid. The values of the dynamic viscosity and shear stress were obtained from a series of FSW-alike experiments. Hence, metal in the stir zone is treated as a highly viscous non-Newtonian fluid, with its dynamic viscosity dependent on both the temperature and the strain rate.

### PROBLEM STATEMENT

The objective of the present work was a numerical investigation of the thermal and mechanical physical phenomena, accompanying FSW, as well as their combined influence on the primary internal characteristics of the FSW process i.e. heat generation, temperature distribution and visco-plastic flow velocities in the SZ. The object for the investigation was a typical FSW system, consisting of a workpiece (butt joint 1.5+1.5 mm made of the aluminium alloy AA5754), anvil (AA6082, thickness 20.0 mm), and a working tool with a threadless pin in a form of a truncated cone, fig. 2.

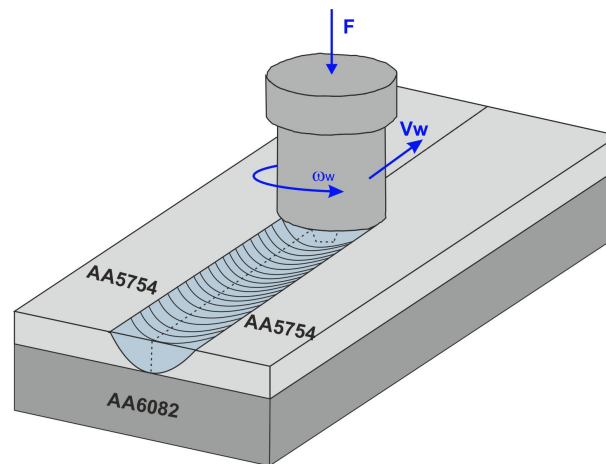


**Fig. 2** The FSW scene, being used for the modelling (schematic).

### COORDINATE SYSTEM, MODELLING SPACE

As the FSW process involves a circular motion of both the tool and visco-plastic flow around the tool pin, we have chosen a cylindrical coordinate system in the Eulerian formulation with the vertical axis coinciding with the tool rotation axis, fig. 3.

The modelling space comprises a few modelling zones differing with their physical properties:  $W_1, W_2$  is the workpiece metal (further, during the text a unified designation for both sheets is used –  $W$ , as the metal of both sheets is the same);  $P$  is the workpiece metal in the plastic condition (stir zone);  $P_w$  is the weld seam metal;  $T_p$  is the tool metal;  $B$  is the anvil;  $A$  is the air.

The coordinates of these zones are beforehand unknown and determined with accordance to the tool geometry and the interface boundaries  $W \cap T_p, W \cap B, W \cap A, T_p \cap A$  (where the symbol  $\cap$  means the intersection of the corresponding zones). The location of the SZ relative to the workpiece metal  $W - W \cap P$  is also unknown in advance and defined during the solution of the model equations.

The dimensions of the modelling finite difference mesh are determined in dependence on the sizes of the workpiece. In the  $Z$ -direction (mesh index  $k$ ) it was accepted that  $dz=S/15$  ( $S$  is the workpiece thickness). In the angular direction (mesh index  $j$ ) the step  $d\varphi=2\pi/60=\pi/30$ . In the radial direction (mesh index  $i$ ), the step was taken variable and increasing with moving away from the pin surface as:  $r_i=1.1r_{i-1}$ . The dimensions of the computational mesh ( $i_{\max} \times j_{\max} \times k_{\max}$ ) are  $36 \times 60 \times 15$ .

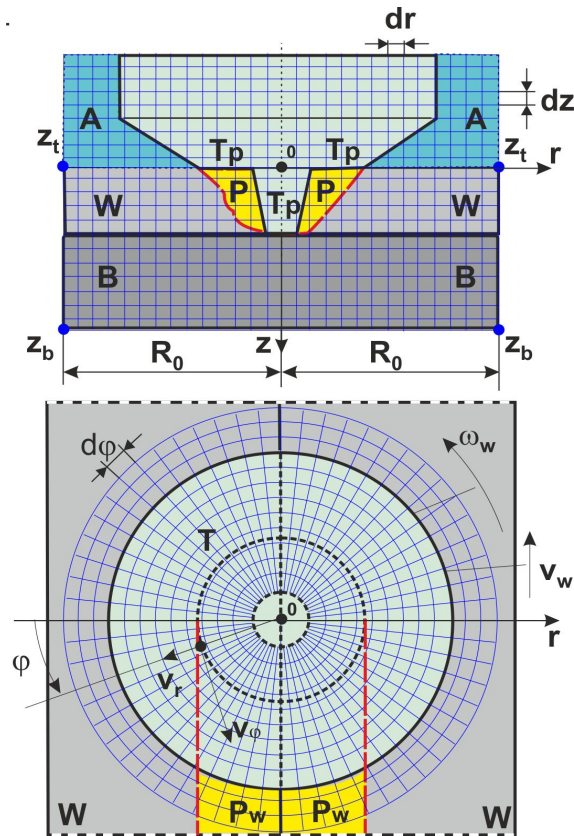


Fig. 3 Schematic representation of the structure of the modelling space.

## BASIC MODEL EQUATIONS

### ENERGY CONSERVATION EQUATION

During the FSW process, the two main sources generate the heat energy: the first source is the contact friction between the surfaces of the tool shoulder and workpiece, the second one is the plastic deformation process in the bulk of the SZ [18]. The produced heat energy redistributes with the help of heat conduction and flow of the visco-plastic metal around the pin. These phenomena are described by the energy conservation equation in the following non-stationary formulation

$$\frac{\partial H}{\partial t} + \text{div}(\rho \vec{v} H) = \text{div}(\lambda \text{grad} T) + q_{\Sigma} \quad (1)$$

where  $H$  is the temperature-dependent specific enthalpy;  $\rho$  is the density;  $\vec{v}$  is the velocity vector of the substance;  $\lambda$  is the temperature-dependent thermal conductivity;  $T$  is the temperature;  $q_{\Sigma}$  is the total heat generation rate.

The boundary conditions for Eq. 1 applied are as follows (see fig. 3)

$$\begin{aligned} \frac{\partial T}{\partial r} &= 0, \quad r = R_0, \\ -\lambda \frac{\partial T}{\partial z} &= q_{sh}, \quad z = z_t, \quad r \in [r_s \dots r_{ss}], \quad q_{sh} = \pi \omega_w \sigma_{cont} \frac{2}{3} (r_{ss}^3 - r_s^3) dz, \\ \lambda \frac{\partial T}{\partial z} &= \tilde{\epsilon} \sigma_0 (T^4 - T_0^4) + \alpha_t (T - T_0), \quad z = z_t, \quad r \in [r_{ss} \dots R_0], \\ \frac{\partial T}{\partial z} &= 0, \quad z = z_b, \end{aligned} \quad (2)$$

where  $\tilde{\epsilon}$  is the emissivity factor;  $q_{sh}$  is the heat input from the tool shoulder surface;  $\sigma_0$  is the Stefan-Boltzmann constant;  $T_0$  is the environment temperature;  $\alpha_t$  is the convective heat transfer coefficient.

The temperature-dependent thermo-physical properties of the metal at the different modelling zones depend on the location of the considered point to one of the modelling zones (see fig. 3) as follows

$$\begin{aligned} \lambda &= \begin{cases} \lambda_w(T) & \text{for } r, \varphi, z \in W, P_w \\ \lambda_p(T) & \text{for } r, \varphi, z \in P, P_w \\ \lambda_B(T) & \text{for } r, \varphi, z \in B \end{cases} \\ H &= \begin{cases} H_w(T) & \text{for } r, \varphi, z \in W, P_w \\ H_p(T) & \text{for } r, \varphi, z \in P, P_w \\ H_B(T) & \text{for } r, \varphi, z \in B \end{cases} \end{aligned} \quad (3)$$

Internal friction in the SZ initiates a volumetric heat source [19]

$$\begin{aligned} q_{in} &= \tau_T(T, \dot{\epsilon}) \dot{\epsilon}, \\ \dot{\epsilon} &= \sqrt{\frac{2}{3} \left( \left( \frac{\partial v_r}{\partial r} \right)^2 + \left( \frac{1}{r} \frac{\partial v_\varphi}{\partial r} + \frac{v_r}{r} \right)^2 + \left( \frac{\partial v_z}{\partial z} \right)^2 + \right.} \\ &\quad \left. \frac{1}{2} \left( r \frac{\partial (v_\varphi/r)}{\partial r} + \frac{1}{r} \frac{\partial v_r}{\partial \varphi} \right)^2 + \frac{1}{2} \left( \frac{\partial v_z}{\partial r} + \frac{\partial v_r}{\partial z} \right)^2 + \frac{1}{2} \left( \frac{\partial v_\varphi}{\partial z} + \frac{1}{r} \frac{\partial v_z}{\partial \varphi} \right)^2 \right) \end{aligned} \quad (4)$$

where  $\tau_T(T, \dot{\epsilon})$  is the temperature-and-strain-rate dependent shear yield strength;  $\dot{\epsilon}$  is effective the strain rate in the SZ;  $(v_r(r, \varphi, z), v_\varphi(r, \varphi, z), v_z(r, \varphi, z)) \in P$  are the components of the flow velocity vector  $\vec{v}$ .

The authors [20, 21] applied the concept of describing the tool geometry with cylindrical and taper pin configurations. Taking into account this concept, the heat source from the contact friction between the pin surface and workpiece is given as, fig. 4.

$$q_{cont} = \pi \omega_w \sigma_{cont} \left( \frac{1}{2} (r_s^2 + r_e^2) \frac{z_b}{\cos(\alpha)} + \frac{2}{3} r_e^3 \right), \quad (5)$$

where the contact stress  $\sigma_{cont}$  depends on the contact conditions at the interface tool surface-SZ and in general form can be written as [20]

$$\sigma_{cont} = \delta \tau_T(T, \dot{\epsilon}) + (1 - \delta) \mu p_{cont} = \delta \tau_T(T, \dot{\epsilon}) + (1 - \delta) \mu \frac{F}{S_{cont}},$$

where  $\sigma_{cont}$  is the contact stress;  $\delta$  is the contact state variable (1 – sticking condition, 0 – slipping condition, in the model it was taken 0.65);  $\mu$  is the coefficient of contact friction was set in modelling to 0.35-0.40;  $\alpha$  is the pin angle;  $F$  is the axial force;  $S_{cont}$  is the contact area being determined as follows

$$S_{cont} = \begin{cases} \pi r^2, r \in [0 \dots r_e] \\ r d\varphi dz \sin(\alpha), r \in [r_e \dots r_s] \end{cases}.$$

Hence, the total heat input in Eq. 1 is  $q_\Sigma = q_{in} + q_{cont}$ .

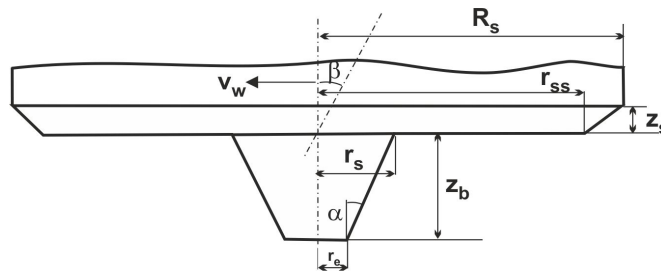


**Fig. 4** Schematic tool geometry being used for the modelling:  $R_s = 11.0$  mm,  $r_{ss} = 4.0$  mm,  $r_s = 1.7$  mm,  $z_s = 12.0$  mm,  $z_b = 1.1$  mm,  $r_e = 1.5$  mm,  $\alpha = 10^\circ$ ,  $\beta = 0^\circ$ .



## NAVIER-STOKES EQUATION

The plastic flow velocities are determined from solving the Navier-Stokes equation written in the form

$$\frac{\partial v_r}{\partial t} + \text{div}(v_r \vec{v}) = \frac{1}{\rho} \left( -\frac{\partial p}{\partial r} + \eta \left( \frac{\partial^2 v_r}{\partial r^2} + \frac{\partial^2 v_r}{(r \partial \varphi)^2} + \frac{\partial^2 v_r}{\partial z^2} \right) \right), \quad (6)$$

$$\frac{\partial v_\varphi}{\partial t} + \text{div}(v_\varphi \vec{v}) = \frac{1}{\rho} \left( -\frac{\partial p}{r \partial \varphi} + \eta \left( \frac{\partial^2 v_\varphi}{\partial r^2} + \frac{\partial^2 v_\varphi}{(r \partial \varphi)^2} + \frac{\partial^2 v_\varphi}{\partial z^2} \right) \right), \quad (7)$$

$$\frac{\partial v_z}{\partial t} + \text{div}(v_z \vec{v}) = \frac{1}{\rho} \left( -\frac{\partial p}{\partial z} + \eta \left( \frac{\partial^2 v_z}{\partial r^2} + \frac{\partial^2 v_z}{(r \partial \varphi)^2} + \frac{\partial^2 v_z}{\partial z^2} \right) \right), \quad (8)$$

$$\frac{\partial v_\varphi}{r \partial \varphi} + \frac{1}{r} \frac{\partial(r v_r)}{\partial r} + \frac{\partial v_z}{\partial z} = 0, \quad (9)$$

where  $p$  is the pressure in the SZ, determined with the help of the continuity equation (9);  $\eta = \eta(T, \dot{\epsilon})$  is the temperature-and-strain-rate dependent dynamic viscosity.

At the boundary surface  $P \cap W$  (see fig. 3), separating the stir zone from the rest of the workpiece metal, it was taken in the Eulerian reference frame

$$v_r = -v_w \sin(\varphi), v_\varphi = v_w \cos(\varphi), v_z = 0 \quad (10)$$

At the boundary surface  $P \cap T_p$  separating the plastic strain zone and the pin metal, the flow velocity components are determined by the tool geometry (see fig. 3) and given as follows

$$\vec{v} = \begin{cases} \tilde{v}_r = -v_w \sin(\varphi) & \text{for } r \in [r_e \dots r_{ss}], \\ \tilde{v}_\varphi = \omega_w \frac{r}{r_{ss}} \delta - v_w \cos(\varphi) & \text{for } r \in [r_e \dots r_{ss}], \\ \tilde{v}_z = 0 & \text{for } r \in [r_e \dots r_{ss}], \end{cases} \quad (11)$$

where  $\tilde{v}_r, \tilde{v}_\varphi, \tilde{v}_z$  are the radial, tangent and axial velocity components at the tool surface.

## DETERMINATION OF THE STIR ZONE BOUNDARY

We applied the von Mises criterion for determining the stir zone boundary. The coordinates of the SZ are calculated through the following variation procedure

## Mathematical Modelling of Weld Phenomena 12

$$3\tau_{P \cap W}^2 + (p + p_N)^2 \xrightarrow{P \cap W = \text{var}} \sigma_T^2, \quad (12)$$

where  $\tau_{P \cap W}$  is the shear stress produced by the flow at the boundary;  $p_N$  is the axial pressure from the tool;  $p$  is the dynamic pressure being obtained from solving the equations (6-9);  $\sigma_T$  is the yield strength.

The value of the shear stress at the boundary  $P \cap W$  is calculated as

$$\tau_{P \cap W} = \eta \cdot \text{grad} \vec{v}. \quad (13)$$

The axial pressure  $p_N$  is defined from solving the following integral equation

$$\iint_S \max(p_N, \tau_T) dS \xrightarrow{p_N = \text{var}} F, \quad (14)$$

describing the equilibrium condition between the axial force  $F$  and the pressure  $p_N$  within the contact working area  $S$  between the tool and the workpiece.

### TOOL FORCES AND TORQUE

The longitudinal  $F_l$  and transversal  $F_t$  components of the total force acting on the tool depend on the distribution of the pressure in the SZ

$$F_l = \int_S p(r, \varphi, z) \cos \tilde{\varphi} dS; \quad F_t = \int_S p(r, \varphi, z) \sin \tilde{\varphi} dS, \quad (15)$$

where  $p(r, \varphi, z)$  is the distribution of the pressure at the work contact area of the pin surface  $S$ ;  $\tilde{\varphi}$  is the current angle between the normal to the pin surface and the welding direction.

The tool torque is determined by the heat generation power in the SZ

$$M_p = \frac{1}{\omega_w} \int_{V_p} q_\Sigma dV_p, \quad (16)$$

where  $q_\Sigma$  is the total heat generation rate in the SZ;  $V_p$  is the volume of the SZ.

MATERIAL PROPERTIES

All the temperature dependencies, needed for simulation, namely the heat conduction, enthalpy for the alloys AA5754 and AA6082 were received with the help of the program JMatPro® in the temperature range 20 °C – solidus temperature for AA5754 (about 600 °C) based on their chemical compound [22]; the reference yield strength for AA5754 is also taken from [22] fig. 5. The temperature and strain rate dependent dynamic viscosity and flow shear stress for AA5754 are derived from a series of special spot-FSW trials [16] (see below). As the metal of the stir zone in the model is considered as an incompressible viscous fluid (AA5754), its density is taken as temperature independent and constant at 20 °C – 2.67 g/cm<sup>3</sup>.

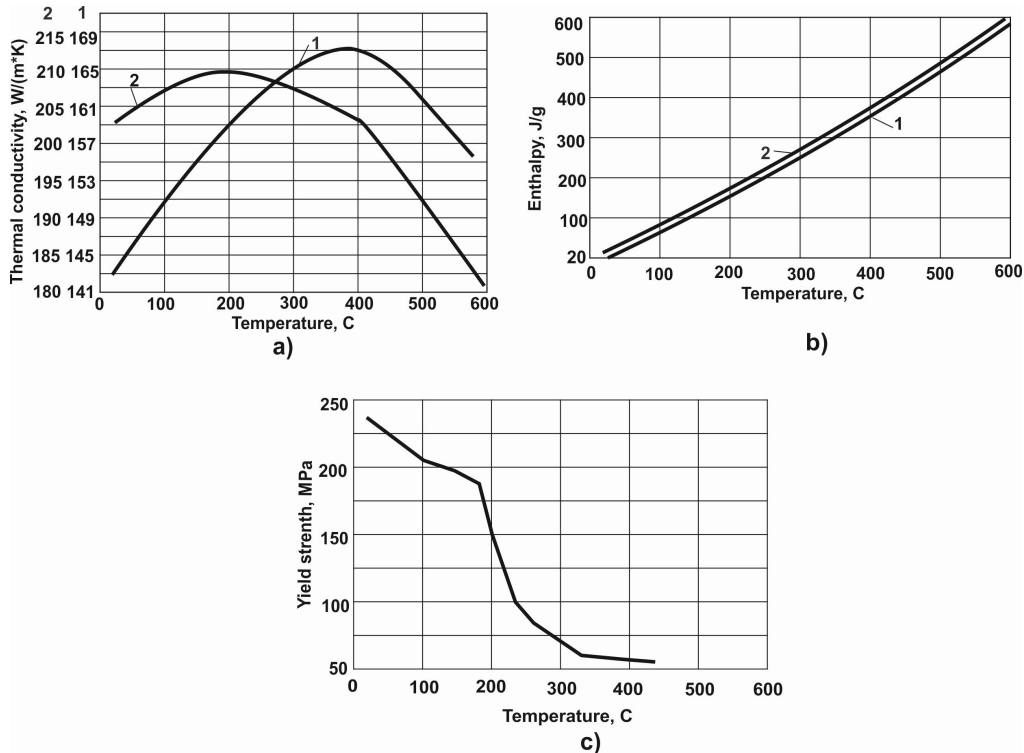


Fig. 5 Thermophysical properties for AA5754 (1) and AA6082 (2) (a, b); the reference yield strength for AA5754 (c).

The dynamic viscosity (or the coefficient of the internal friction) is equivalent to the hardening rate at deformation

$$\eta(T, \dot{\epsilon}) = k_{\epsilon} \frac{\bar{\tau}(T, \dot{\epsilon})}{\dot{\epsilon} + \dot{\epsilon}_0}, \quad (17)$$

where  $k_{\dot{\epsilon}}$  is the empirical coefficient;  $\tilde{\tau}(T, \dot{\epsilon})$  is the shear stress flow in dependence on the temperature  $T$  and strain rate  $\dot{\epsilon}$ ;  $\dot{\epsilon}_0$  is the parameter accounting for hardening strain rate of the alloy at its deformation in the conditions of FSW.

The strain properties are described by the dependence of the flow shear yield strength on the temperature  $T$  and the strain rate  $\dot{\epsilon}$

$$\tilde{\tau}(T, \dot{\epsilon}) = \tau(T, 0) \left( 1 + k_1 \frac{\dot{\epsilon}}{\dot{\epsilon}_0 + \dot{\epsilon}} \right), \quad (18)$$

where  $k_0$  is the coefficient takes into account the difference between  $\tilde{\tau}(T, \dot{\epsilon})$  in the conditions of FSW and  $\tau(T, 0)$ ;  $\tau(T, 0)$  is the temperature dependence of the shear yield strength at  $\dot{\epsilon} = 0$ ; the coefficient  $k_l$  accounts for the work hardening of the alloy.

The values of the coefficients for AA5754  $\dot{\epsilon}_0 = 200 \text{ 1/s}$ ,  $k_l = 0.9$ ,  $k_{\dot{\epsilon}} = 0.35$  were calculated, using the basic experimental methodology for determining the mechanical characteristics adapted from [16]. The reference shear yield strength is defined by a

theoretical relationship  $\tau(T, 0) = \frac{1}{\sqrt{3}} \sigma(T, 0)$  [19].

#### METHOD AND ALGORITHM OF NUMERICAL SOLUTION

We used the finite difference method for the numerical solution of the model equations. The program code was written in the object-oriented environment Embarcadero Delphi 2010. During the solution procedure, the methodology of successive iterations was applied until achievement of a quasi-stationary condition in the position of the SZ, as well as in the distributions of the flow velocities, heat generation, temperature and pressure. Table 1 represents the structure of the algorithm.

**Table 1** The algorithm of the numerical solution of the model equations

Input of the initial data: alloy, workpiece thickness, tool dimensions, angular velocity, welding speed, axial force
Reading thermophysical and reference mechanical properties from a database
Initial conditions on temperature, pressure, flow velocities and strain rate
Time-iterative loop $t=1..t_{max}$
Calculation of the enthalpy, heat conduction and shear yield stress
Calculation of the heat generation power
Solution of the Navier-Stokes equations with boundary conditions.
Consequent calculation of pressure, flow velocity and strain rate distributions
Solution of the energy equation and calculation of the temperature distribution
Variation procedure for specifying the boundaries of the SZ $P \cap W$
( $t_{k+1}=t_k+1$ ) until a quasi-stationary condition of the temperature and sizes of the SZ is reached
Output of the modelling results

RESULTS AND DISCUSSION

SOME MODELLING RESULTS

The modelling results were obtained for a butt aluminium workpiece (AA5754, thickness 1.5+1.5 mm) with the tool depicted in fig. 4. The welding conditions were those as specified in table 2. The modelling results are presented in a form of weld macrosections, torque values as well as distributions and graphs:

- temperature distribution  $T(r, \varphi, z)$  (fig. 6, trial N6 from table 2);
- relative pressure and strain rate  $(p + p_N)/p, \dot{\epsilon}$  (fig. 7, 8, trial N6 from table 2);
- components of the flow velocity vector  $v_r, v_\varphi, v_z$  (fig. 9, trial N6 from table 2);
- dependence of the tool torque and force components  $F_l$  and  $F_t$  on  $\omega_w$  (fig. 10, a, b);
- dependence of the tool torque and force components  $F_l$  and  $F_t$  on  $v_w$  (fig. 10, c, d).

**Table 2** Welding conditions for the modelling and experiment

N	Welding conditions	Experimental weld macrosection (a)*	Modelled weld macrosection (b)*
1,a,b	$v_w = 0.05$ m/min $\omega_w = 1000$ r/min $F = 14$ kN	$S_{exp} = 5.6$ mm <sup>2</sup> $M_{exp} = 7.50$ N*m	$S_{mod} = 6.0$ mm <sup>2</sup> ; $M_{mod} = 8.5$ N*m;
2,a,b	$v_w = 0.08$ m/min $\omega_w = 1750$ r/min $F = 14$ kN	$S_{exp} = 4.8$ mm <sup>2</sup> $M_{exp} = 7.20$ N*m	$S_{mod} = 5.2$ mm <sup>2</sup> ; $M_{mod} = 8.00$ N*m;
3,a,b	$v_w = 0.10$ m/min $\omega_w = 2000$ r/min $F = 14$ kN	$S_{exp} = 4.6$ mm <sup>2</sup> $M_{exp} = 6.99$ N*m	$S_{mod} = 4.9$ mm <sup>2</sup> ; $M_{mod} = 7.49$ N*m;
4,a,b	$v_w = 0.15$ m/min $\omega_w = 2000$ r/min $F = 14$ kN	$S_{exp} = 4.9$ mm <sup>2</sup> $M_{exp} = 7.20$ N*m	$S_{mod} = 4.7$ mm <sup>2</sup> ; $M_{mod} = 7.51$ N*m;
5,a,b	$v_w = 0.20$ m/min $\omega_w = 2750$ r/min $F = 12$ kN	$S_{exp} = 4.5$ mm <sup>2</sup> $M_{exp} = 6.48$ N*m	$S_{mod} = 4.2$ mm <sup>2</sup> ; $M_{mod} = 6.80$ N*m;
6,a,b	$v_w = 0.25$ m/min $\omega_w = 3000$ r/min $F = 10$ kN	$S_{exp} = 4.1$ mm <sup>2</sup> $M_{exp} = 6.10$ N*m	$S_{mod} = 4.0$ mm <sup>2</sup> ; $M_{mod} = 6.25$ N*m;

\* $S_{exp}, M_{exp}$  – area of the SZ on the experimental weld macrosection and torque;  $S_{mod}, M_{mod}$  – area of the SZ on the modelled weld macrosection and torque; Plunge depth = 1.1 mm. Butt joints (1.5 + 1.5 mm)

The modelling results show that the distributions of temperature (see fig. 6), relative pressure (see fig. 7), strain rate (see fig. 8) and viscous flow velocities (see fig. 9) have an asymmetric form relative to the tool longitudinal axis and welded joint surface. This asymmetrical form originates from the superposition of the translational and rotational welding velocities.

The gradients of the viscous flow govern the distribution of the strain rate and temperature. The maximum values of these distributions take place close to the workpiece surface in the contact with the tool and coincide in their shape, as the rate of the heat generation is proportional to the strain rate (see fig. 6, 8). The maximum of the relative pressure is, on contrary, displaced relative to the weld joint line against the tool rotation direction. It is explained by the fact that the metal in the zone of the lower temperatures possesses higher strength and therefore produces higher mechanical resistance (relative pressure) to the mass flow.

The motion of the tool surface, the pressure distribution and the form of the SZ defines the distribution of the metal viscous flow in the SZ.

The radial component of the viscous flow  $v_r$  (see fig. 9 a) is mainly determined by the translational welding speed, i.e. by the flow of the viscous metal around the pin. Therefore, the metal in front of the pin moves back from the pin surface. Correspondingly, the metal behind the pin moves towards the pin rear surface.

The tangent component  $v_\phi$  (see fig. 9 b) arises from the tool rotational motion. Its asymmetrical distribution is explained by the different values of the pressure and distances from the pin surface to the boundary of the SZ. The tangent component  $v_\phi$  reaches its maximum values near the pin and shoulder surfaces in the direction of rotation.

Despite the use of the threadless pin, the axial component of the flow velocity  $v_z$  arises in the SZ, which stems from the asymmetrical shape of the SZ and appearance of the axial pressure. The values  $v_z$  are relatively small compared to the angular and radial ones. Moreover, the axial velocity rise with an increase in the  $v_w$  and fall down with an increase in the  $\omega_w$ . The viscous metal moves down in front of the pin, reaching maximum values at the end of the pin. Correspondingly, behind the pin, the viscous metal flows upwards. The obtained results agree qualitatively with the literature data [19, 24].

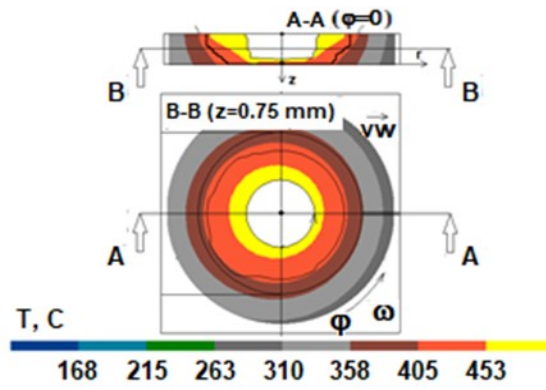


Fig. 6 Temperature distribution.

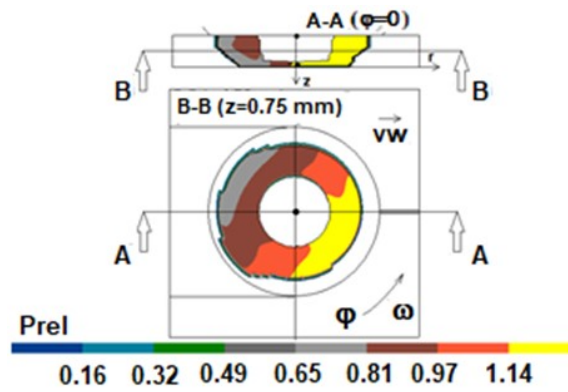


Fig. 7 Distribution of the relative pressure in the stir zone.

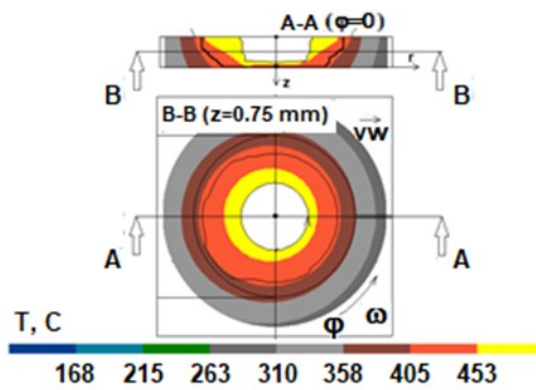


Fig. 8 Distribution of the strain rate in the stir zone.

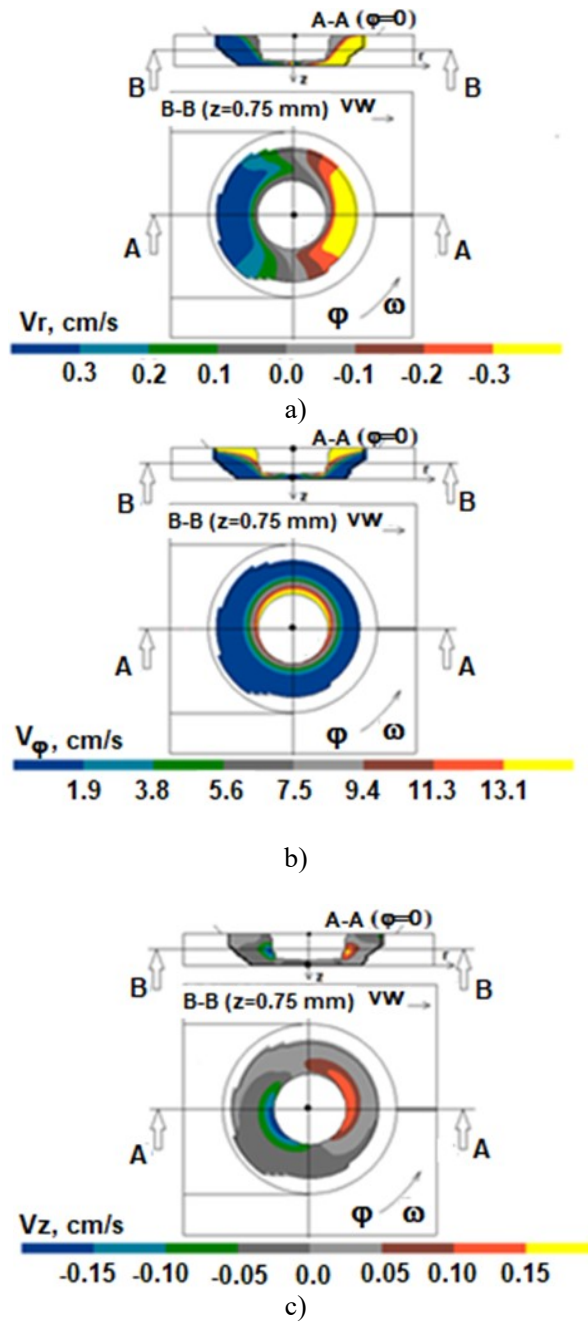
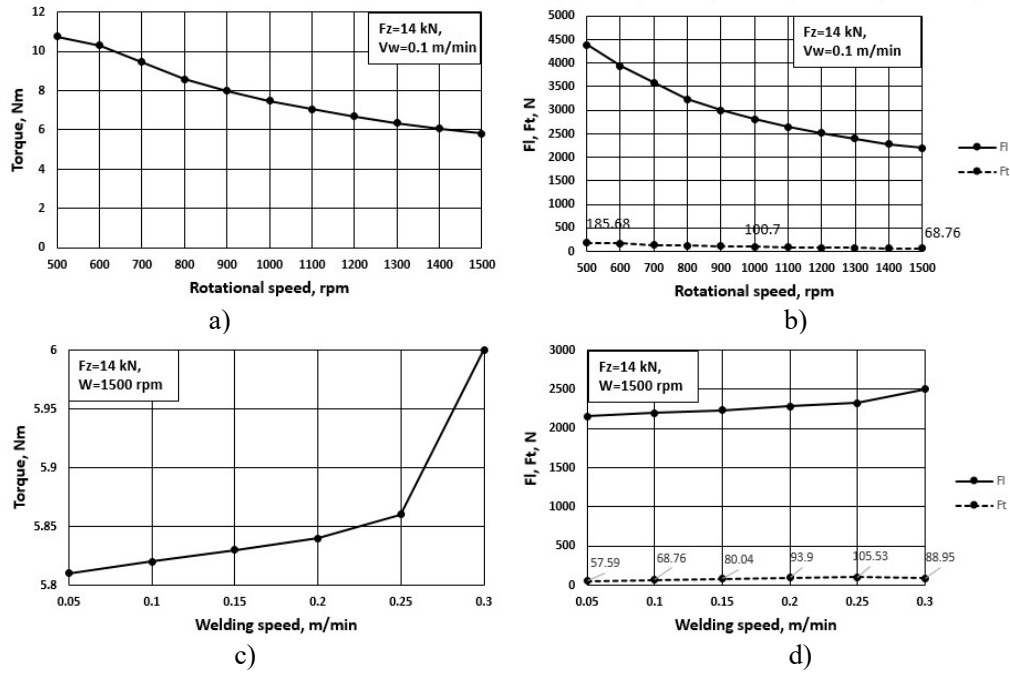


Fig. 9 Distributions of the components of the flow velocity vector: radial  $v_r$  (a), tangent  $v_\phi$  (b), axial  $v_z$  (c).



## Mathematical Modelling of Weld Phenomena 12



**Fig. 10** Graphs of the influence of the rotational (a, b) and welding speed (c, d) on the torque  $M$  and force components  $F_i, F_t$ .

The model reproduces qualitatively correct the trend in the influence of the rotational and welding speed on the torque and tool force components (see fig. 10), which corresponds to the literature data ([25], for example). Particularly, an increase in the rotational speed causes an increase in the power of the heat generation. The temperature of the metal rises and its strength decreases. Therefore, the power for the rotation (torque  $M$ ) and translation (forces  $F_i, F_t$ ) of the tool becomes less. On the contrary, an increase in the welding (translational) speed causes an increase in the torque and the tool force components ( $F_i, F_t$ ).

### COMPARISON WITH THE EXPERIMENTS

The experimental macrosections were also produced in order to compare the area of the SZ with the corresponding calculated values, fig. 11 (the welding conditions are those from table 2). A scatter plot depicting the experimental values versus the calculated ones, fig. 12-13, presents a comparison of the SZ shapes on the transversal weld macrosections as well as the corresponding torque values.

## Mathematical Modelling of Weld Phenomena 12

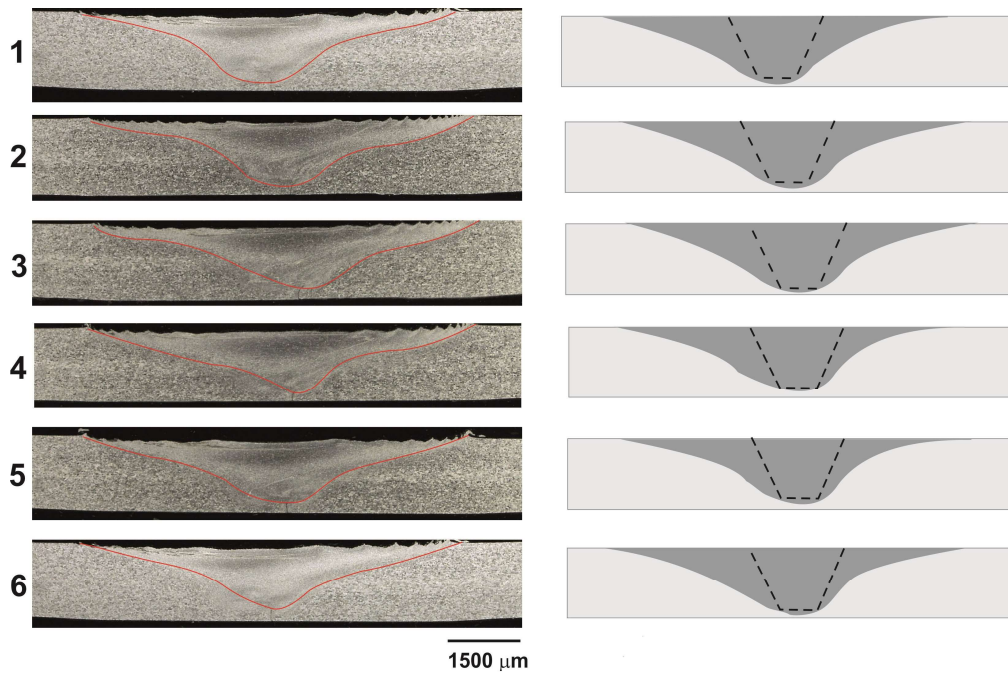


**Fig. 11** Comparison between the experimental (left part) and modelled (right part, outlined and scaled) weld macrosections.

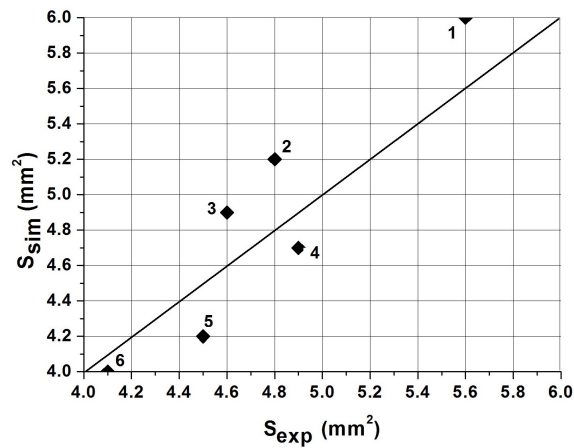


**Fig. 12** Scatter plot of the calculated values (vertical axis) of the stir zone area relative to the experimental data (horizontal axis).

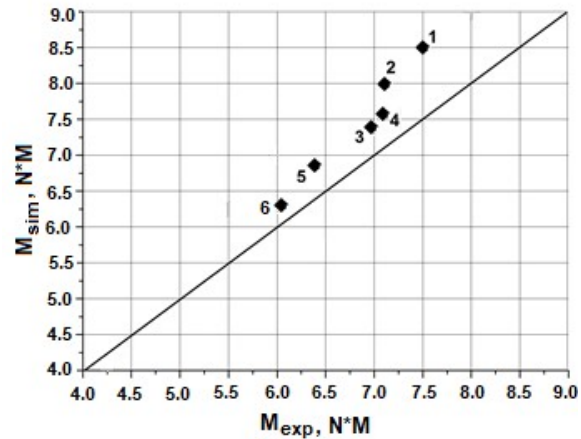


**Fig. 13** Scatter plot of the calculated values (vertical axis) of the torque relative to the experimental data (horizontal axis).

The comparison showed that the model satisfactorily reproduces the influence of the main welding conditions on the stir zone shape.

The location of the SZ boundary line is influenced by the distribution of the pressure in the SZ (axial from the tool and kinematic from the tool motion and rotation) as well as by the yield stress of the metal of the SZ. The latter is particularly temperature dependent. Therefore, the observed discordance could be explained by an inaccuracy in the values of the mechanical characteristics of the workpiece metal (AA5754), which requires the conduction of additional and modified mechanical tests [16] together with supplementary measurements of torque and thermo-cycles in a broader range of the process parameters.

#### ACKNOWLEDGEMENTS

The authors would like to thank the German research society (DFG) for the support in conducting the work (Project RE 2755/50 “Investigation of the voids formation process in friction stir welding by numerical modeling and experiment on the basis of a Stress-condition hypothesis”).

#### REFERENCES

- [1] THOMAS W.M, NICHOLAS E.D, NEEDHAM J.C, MURCH M.G, TEMPLE-SMITH P, DAWES C.J.: ‘Friction stir butt welding’, *International Patent Application No. PCT/GB92/02203*, 1991.
- [2] MORAITIS G. A., LABEAS G. N.: ‘Investigation of friction stir welding process with emphasis on calculation of heat generated due to material stirring’, *Science and Technology of Welding and Joining*, Vol. 15, pp. 177-184, 2010.
- [3] GEMME F., VERREMAN Y., DUBOURG L., JAHAZI M.: ‘Numerical analysis of the dwell phase in friction stir welding and comparison with experimental data’, *Mater Sci Eng A*, 527:4152–60. DOI: 10.116/j.msea.2010.03.026.
- [4] XIAOCONG H., FENGSHOU G., BALL A.: ‘A review of numerical analysis of friction stir welding’, *Progress in Materials Science*, Vol. 65, pp. 1-66, 2014.

- [5] RUSSELL, M.J., SHERCLIFF H.R.: 'Analytical Modeling of Friction Stir Welding', *Prec., INALCO '98: 7th Intl. Conf.: Joints in Aluminum*, Cambridge, UK, 16 April 1998, Vol.2, pp. 185-195.
- [6] GOULD J.E., Z. FENG.: 'Heat flow model for friction stir welding of aluminum alloys'. *J. Mater. Process. Manuf. Sci.* 1998, 7, pp. 185-194.
- [7] SCHMIDT H., HATTEL J.: 'An analytical model for the heat generation in friction stir welding', *Modelling Simul. Mater. Sci. Eng.*, 12 (2004), pp. 143-157.
- [8] FRIGAARD Ø., GRONG Ø., MIDLING O.T.: 'A Process Model for Friction Stir Welding of Age Hardening Aluminium Alloys', *Metall. Mater. Trans A.* May 2001; 32 (5), pp. 1189-1200.
- [9] CHAO Y.J., QI X., TANG W.: 'Heat transfer in friction stir welding: experimental and numerical studies', *ASME J. Manuf. Sci. Eng.* 125 (2003), pp.138-145.
- [10] SEIDEL T.U., REYNOLDS A.P.: 'Two-dimensional friction stir welding process model based on fluid mechanics', *Sci. Technol. Weld. Join.*, 2003, 8(3), pp. 175-183.
- [11] COLEGROVE P.A., SHERCLIFF H.R.: 'Development of Trivex friction stir welding tool. Part 2 – three-dimensional flow modelling', *Science and Technology of Welding and Joining*, 2004, Vol. 9, No. 4, pp. 352-361.
- [12] COLEGROVE P.A., SHERCLIFF H.R.: '3-Dimensional CFD modelling of flow round a threaded friction stir welding tool profile', *J. Mater. Process. Technol.*, 2005, 169, (2), pp. 320-327.
- [13] TUTUNCHILAR S., HAGHPANAHI M., BESHARATI GIVI M.K., et al.: 'Simulation of material flow in friction stir processing of a cast Al–Si alloy', *Mater. Des.* 2012; 40, pp. 415-426.
- [14] TARTAKOVSKIY A., GRANT G., SUN X., KHALEEL M.: 'Modeling of friction stir welding (FSW) process with smooth particle hydrodynamics (SPH)'. *In: SAE 2006 World Congress, Detroit, USA.*
- [15] PAN W.X., LI D.S., TARTAKOVSKY A.M., AHZI S., KHRAISHEH M., KHALEEL M.: 'A new smoothed particle hydrodynamics non-Newtonian model for friction stir welding: process modeling and simulation of microstructure evolution in a magnesium alloy', *Int. J. Plast.*, 2013, 48, pp. 189-204.
- [16] HENNEBÖHLE U.: 'Verifizierung und Bewertung eines thermischen Simulationsmodells des Rührreibschweißprozesses', *Aachen: Shaker*, 2008.
- [17] EROFEEV V., MASLENNIKOV A.: 'Fiziko-matematicheskaya model svarki treniem s peremeshivaniem [Physical and mathematical model of the friction stir welding process]', *Izvestiya Tul'skogo gosudarstvennogo universiteta (Technicheskie nauki)*, Vol. 10, pp. 64-73, 2013 [in Russian].
- [18] MISHRA R.S., DE P.S., KUMAR N.: 'Friction stir welding and processing', *Science and engineering, Springer*, Vol. 16-17, 2014.
- [19] NANDAN R., ROY G.G., DEBROY T.: 'Numerical simulation of three-dimensional heat transfer and plastic flow during friction stir welding', *Metallurgical and Materials transactions A*, Vol. 37A, pp. 1247-1259, 2006.
- [20] SCHMIDT H., HATTEL J., WERT J.: 'An analytical model for the heat generation in friction stir welding', *Model. Simul. Mater. Sci. Eng.*, Vol. 12, pp. 143-157, 2004.
- [21] VIJAY SHIVAJI GADAKH, KUMAR ADEPU: 'Heat generation model for taper cylindrical pin profile in FSW', *J. Mater. Res. Technol.*, 2(4), pp. 370-375, 2013.
- [22] DEMIRAY Y., KAVAKLIOGLU Z.B., Y. YUCEL: 'A study on thermo-mechanical behaviour of AA5754 alloy (tread and plain sheet) produced by twin-roll casting', *Acta Physica Polonica A*, Vol. 127, pp. 1097-1099, 2015.
- [23] BOOSTER R.E.: 'Handbook of lubrication', *CRC Press LLC*, pp. 46-47, 1983.
- [24] GRUJICIC M., ARAKERE G, YALAVARTHY H.V. et al.: 'Modeling of AA5083 material-microstructure evolution during butt friction-stir welding', *Journal of Materials Engineering and Performance*, Vol. 19(5), pp. 672-684, 2010.

- [25] SHAHI P., BARMOUZ M.: 'Force and torque in friction stir welding', *Advances in Friction Stir Welding and Processing*. Elsevier Limited, DOI: 10.1533/9780857094551.459, pp. 459-498, 2014.

# DEVELOPMENT OF A MODEL TO INVESTIGATE THE INTERACTION BETWEEN PROCESS AND MACHINE TOOL AND THE RESULTING DYNAMICS OF FRICTION STIR WELDING

F. PANZER\*, M. WERZ\*\* and S. WEIHE\*\*

*\* Institute for Materials Testing, Materials Science and Strength of Materials (IMWF), University of Stuttgart, Germany,  
Orcid Id 0000-0003-1179-6190, Florian.Panzer@imwf.uni-stuttgart.de*

*\*\* Materials Testing Institute (MPA) University of Stuttgart, Germany*

DOI 10.3217/978-3-85125-615-4-31

## ABSTRACT

Friction Stir Welding (FSW) is a solid state joining process where the process and the machine tool used for welding are in direct interaction with each other. This mechanical coupling means that the influence of the machine tool cannot be neglected when investigating FSW: Welds produced on different machines while keeping welding parameters and materials constant are known to show different properties. It is furthermore known that the process forces of FSW have a periodic nature. The reasons for this periodicity, however, are not fully understood yet. It is assumed that properties, like out-of-round-deviations of the spindle, the tool geometry or the stiffness of different machine parts in interaction with the welded material, lead to the characteristics of the FSW forces. Since the welding forces can presumably be employed for online process monitoring, a deeper understanding for the underlying reasons is necessary. In order to investigate this interaction of material and machine as well as the resulting dynamics, a finite element model containing both FSW process and machine, is developed in this work. The process is modeled using the coupled Eulerian-Lagrangian finite-element-formulation. The large strains and strain rates occurring during FSW make it necessary to use an Eulerian formulation for the material to avoid mesh distortion. The ability of the Eulerian formulation to describe the material flow, including free surfaces, furthermore provides the possibility to analyze the formation of volumetric welding defects, which severely reduce the strength of the welds. The tool is modeled using lagrangian elements, a contact is employed to couple the eulerian and lagrangian domains with each other. The machine is modeled in a simplified way using discrete spring elements. The developed model is validated in a first step with welding experiments that were conducted at the IMWF. Second, the model is employed to investigate the interaction between process and machine and therefore the dynamics of FSW. By varying the parameters of the model, the effects, which contribute significantly to the periodic dynamics of FSW, are identified. A simplified 2d-model is employed additionally to analyze the material flow during welding. Another focus lies on the correlation of the process forces and the tool trajectory with defect formation mechanisms. It is shown how flaws in the weld like voids or excessive flash correlate with saliences in the force measurements. These results can not only be employed for monitoring systems but also to improve existing or develop completely new process control strategies.

# Mathematical Modelling of Weld Phenomena 12

Keywords: friction stir welding; process dynamics; process-machine interaction; finite elements; coupled euler-lagrangian method; process forces; online process monitoring

## INTRODUCTION

Friction stir welding (FSW) is a solid state joining process invented 1991 at The Welding Institute (TWI) [1] that is especially suited to join aluminium alloys [2]. A rotating tool consisting of shoulder and pin is plunged into the parts which are to be welded. The friction between tool and material as well as friction in the material itself results in a heating and plasticizing of the parts. After a short dwell time, the tool is moved along the seam line where the combination of rotation and translation of the tool creates the weld. Since no melting of the materials occurs, the resulting weld properties are, especially for aluminium alloys, superior to fusion welding methods. Additionally, it is possible to join dissimilar materials like for example aluminium and steel [3].

The interaction of material and tool during friction stir welding results in process forces as schematically shown in Fig. 1. A force  $F_z$  is necessary to plunge the tool into the materials and maintain the welding position. A torque  $M_z$  is needed to maintain a steady rotational speed. The feed motion during welding results in a force  $F_x$ , additionally, a force  $F_y$  perpendicular to the welding direction occurs.

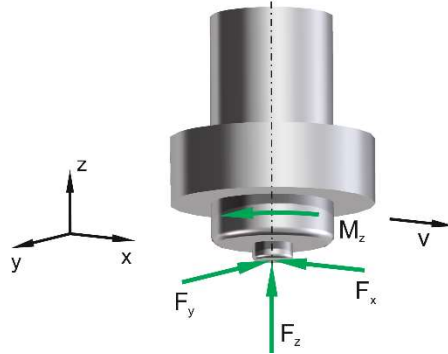


**Fig. 1** Friction stir welding forces

## PROBLEM STATEMENT

The friction stir welding forces have, as shown in Fig. 2, a static part which is superimposed by dynamic effects. Additionally, the friction stir welds show a characteristically banded structure as depicted in Fig. 3. The reasons leading to these periodic force and weld characteristics are not fully understood yet. A variety of theories trying to explain the reasons for the dynamics of friction stir welding exist, however, a systematic investigation still needs to be carried out. The welding force feedback data can presumably be used for the process monitoring of friction stir welding. However, a better understanding of the correlation between the forces and defect formation mechanisms still needs to be gained.

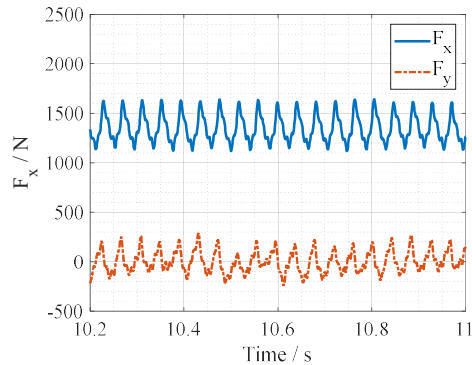


**Fig. 2** Example for friction stir welding forces from experiments



**Fig. 3** Banded structure of a friction stir weld

### OBJECTIVES

The objective of this paper is to gain a better understanding of the dynamics of friction stir welding, i.e., the forces, tool trajectory and resulting weld structure by using a finite element analysis.

To allow a systematic investigation of the friction stir welding dynamics, five hypotheses covering the whole process-machine-system, not only an isolated view of the process, were developed at the IMWF and MPA [4]. Each hypothesis covers a phenomenon that can result in dynamic effects.

In order to investigate which hypotheses, i.e. which effects, contribute significantly to the dynamics of friction stir welding, two finite element models are used.

- A 3d-model is used to complete the main task of the work, i.e. to analyze the welding forces and influence of the machine on the process.
- A geometrically more abstract and simplified 2d-model with a finer mesh is used to analyze the weld formation in vicinity of the pin.

Both models only differ in the geometric setup and mesh size, the simulation methodology is the same for both models.

The 3d-finite element model, as shown in [5], contains the process as well as relevant parts of the machine tool. Starting from a baseline variant, the model is modified to trigger the effects described in the hypotheses intentionally. The comparison of the different model variants shows the reasons for the force characteristics. Additionally, the influence of the machine on the welding results is analyzed. Furthermore, the model is employed to analyze correlations between welding defects and the force responses. This analysis is supported by the results gained from the previous investigations regarding the hypotheses.

The simplified model is used in addition to the process-machine-model in order to observe the material flow in the vicinity of the tool in more detail. A stronger abstraction of the geometry makes it possible to use a finer mesh which is necessary to resolve the material flow patterns.

Compared to experimental procedures, the finite element models offers the advantage that boundary conditions can be prescribed. In this way, features that do not exist in



experimental environments, like perfectly rigid bearings or tools without any geometrical deviations, can be realized. Furthermore, the weld formation can be observed easily compared to experiments, i.e. a deeper understanding for the underlying mechanisms can be gained.

### LITERATURE REVIEW

This chapter gives a short overview over relevant literature.

#### PROCESS FORCES AND MATERIAL FLOW

As will briefly be shown in this chapter, different theories trying to explain the periodic properties of the friction stir welding forces as well as the banded weld structure exist. A more extensive literature review on the matter can for example be found in [4].

A periodic friction condition between tool and material is postulated in [6] to be the reason for the periodicity of axial force and torque. The authors of [7] list discontinuous movements of dislocations as cause for the periodicity of the torque. In [8] and [9], the dynamic forces of FSW and the banded structure of the welds are explained to result from the interaction of an out-of-round tool movement with the welded material. Analogously, the elliptical motion of the tool in the material resulting from an eccentricity of the tool is stated in [10] to lead to the periodic force properties and banded weld structure of FSW. The elliptical motion of the tool is described to be the result of out-of-round deviations of spindle and tool combined with the flexibility of the machine. The material transport is claimed in [11] to deliver contributions to the periodic parts of the FSW forces in addition to the force parts caused by the interaction of elliptical tool movement and welded material. The tool geometry, more precisely the number of flats on the pin, is found in [12] and [13] to influence the dynamic properties of the FSW forces. Compared to other works, an out-of-round tool movement is not taken into account.

As shown, there are different theories trying to explain the force properties. A thorough investigation, however, still needs to be carried out. What is needed most, is a simulative approach where boundary conditions can be prescribed and, compared to experiments, no unaccounted effects can occur.

A visualization of the material flow during friction stir welding using experimental techniques is difficult. One approach is to use marker materials as presented in [14] and [15]. Another approach is to weld different alloys with each other as shown in [16]. A disadvantage of the experimental techniques using markers or different materials is that the material flow cannot be observed in situ, all analyses have to be done after welding. In [17], welding experiments were done with plasticine instead of metal, in [18], a transparent, visco-plastic material was welded instead of metal. The usage of these alternative materials allows a better observation of the process, however, a comparison of material behavior and especially welding parameters with metals may prove difficult. While no explanations for

## Mathematical Modelling of Weld Phenomena 12

the periodicity of the welds are provided in [14] and [16], the tool eccentricity is listed in [15] and [17] as main reason for the banded structure.

As for the friction stir welding forces, the need for a model to investigate and observe the material flow during friction stir welding is obvious. Again, the possibility to modify and prescribe boundary conditions is important to identify reasons for the friction stir welding dynamics.

### PROCESS MONITORING

The analysis of the frequencies of the FSW forces is used in [13], [19] and [20] for online process monitoring applications. Signs found for welds with flaws are the appearance of frequencies smaller than the rotational frequency of the tool as well as the appearance of multiples thereof. Explanations why certain frequencies are dominant when defects occur are scarcely provided. The two presented models offer a way to analyze the formation of welding defects and find possible explanations for the correlations between force patterns and defects.

### INFLUENCE OF MACHINE ON FRICTION STIR WELDING RESULTS

Mentioned works take the influence of the machine on the welding results only little into account. However, as Fig. 4 shows, the machine has an effect on the welding results. Although identical welding parameters and same aluminium alloys were used, welds manufactured on different machines look distinctly different. In [21] it is assumed that the stiffness of the machine influences the welding results, however, a thorough investigation of the matter was not done. The presented 3d-model offers a way to investigate the influence of machine properties on the welding results without the modification of machine tools or the need to use different machine tools for welding.

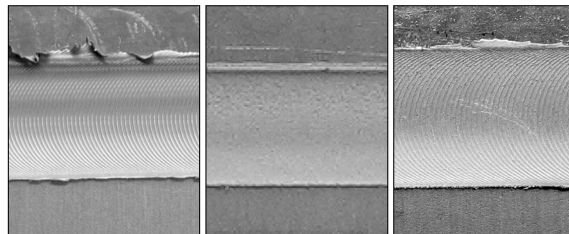


**Fig. 4** Friction stir welds using same FSW parameters and alloys manufactured on different machines [21]

### NUMERICAL SIMULATION OF FRICTION STIR WELDING

The numerical simulation of friction stir welding has been dealt with in a large number of publications. An extensive review can for example be found in [22]. In the following,

references are given for a few works with different modelling approaches towards friction stir welding.

In [23], a computational fluid dynamics (CFD) approach is employed to simulate FSW. A drawback using this approach is that the material behavior can only be modeled as a fluid, but not as a solid. A semi-analytical model that is solved numerically to predict material flow as well as the temperature and slip distribution is presented in [24]. Additionally, a material model suited especially for the simulation of FSW is developed. In [25], FSW is modelled using the Arbitrary Lagrangian-Eulerian (ALE) Finite Element method. This formulation allows a movement of the mesh independent of the material, giving the possibility of adaptive meshing. The large deformations occurring during FSW however reveal the limits of the ALE approach. A relatively new approach to simulate FSW is the Coupled Eulerian-Lagrangian Finite Element method as also used in this work. This approach can cope with the large deformations that occur during FSW and allows the simulation of the welding process including the formation of volumetric defects as well as the calculation of process forces as for example shown in [26] and [27]. A 2d-model using the CEL-method to investigate the material flow during friction stir welding with trigonal pins is developed in [28]. Another possibility to cope with the large deformations is the use of meshfree methods like smoothed particle hydrodynamics (SPH). As shown in [29] or [30], this approach can be used to simulate FSW. An advantage of the SPH formulation is the possibility of parallelization on graphic cards. In [11], a model containing process as well as machine is presented. While the machine is represented numerically with finite elements, the process is modelled using an empirical force model. Using this approach, the impact of welding forces on the machine can be investigated, however, the influence of the machine on welding results cannot be analyzed.

### HYPOTHESES

In order to guarantee a systematic investigation of the dynamics of friction stir welding, the following hypotheses were developed at the IMWF and MPA based on literature review and own experimental results [4] [5]. Each hypothesis covers a phenomenon that can lead to dynamic effects. The whole system consisting of friction stir welding process and machine is considered.

**Hypothesis 1:** Excitation through imbalance. Production tolerances lead to uneven mass distributions. This in return leads to dynamic forces.

**Hypothesis 2:** Excitation through the process. The motion of the tool in the material creates reaction forces. The characteristics of the forces depend on the material properties and the state of the material. When the rotational axis of the spindle and tool does not coincide with the theoretical perfect axis for example, the forced out-of-round motion of the tool in the material causes reaction forces with dynamic properties.

**Hypothesis 3:** Excitation through the tool geometry. Besides tools with circular pins, tools with other pin shapes like e.g. quadratic or triangular are used. The variation of the cross sectional area over time causes forces with dynamic properties. As described before, the forces depend on the material and its state.

**Hypothesis 4:** Excitation through the drive train of the machine. Motor, gearbox and spindle build a mechanical system where vibrations can occur at certain rotational speeds.

**Hypothesis 5:** In order to produce sound FSW-welds, relatively high axial forces are necessary. The axial forces in combination with the compliance of the machine and the feed motion lead to slip-stick-like effects: The reaction force of the process acts against the feed motion of the machine, i.e. a process-dependent threshold value must be reached in order to enable a feed motion. The compliance of the machine, influenced by the axial force, acts like a spring between process and feed force. Until the spring is loaded, the tool does not move. When the threshold value is reached, a motion is suddenly possible. These slip-stick-like effects cause vibrations when the process-dependent threshold force is suddenly overcome and results in an impulse-like excitation. As mentioned in hypotheses 2 and 3, the forces depend on the material properties and its state.

The focus of investigations in this work lies on the first three hypotheses. Hypothesis 4 and 5 will be investigated in future works.

### MODEL SETUP

As described in the introduction, two different models are used in this work. Both models are set up and solved with Abaqus/Explicit 6.14-3.

The models differ in the geometric setup and mesh size, but not the simulation methodology. The first model is a 3-dimensional model of the process and parts of the machine which is set up according to an available experimental environment. This allows a validation of the model by comparison of calculated and measured forces. A drawback of the model is the need to use a relatively coarse mesh for the welded material in order to achieve reasonable simulation times. The coarse mesh does not allow the analysis of the weld formation in detail. The focus of the model is therefore the analysis of the forces as well as the tool trajectory. Additionally, the 3d-model can be used to investigate the influence of machine properties on the welding process.

In order to be able to investigate the influence of the tool trajectory on the weld formation, a second, simplified 2d-model of the friction stir welding process is used. The usage of strong simplifications allows the use of a finer mesh, however, the calculated forces cannot be compared anymore to the experimental results. The model has therefore more of a supportive character in this work to get qualitative results.

Both models use the same governing equations and description for the material behavior as stated in the next chapter. The differences in the geometry, mesh size and boundary conditions between the two models are described in the following chapters.

### GOVERNING EQUATIONS AND MATERIAL BEHAVIOR

In both model versions, the Coupled Eulerian-Lagrangian (CEL) approach is used to cope with the large deformations that occur during friction stir welding in the material. The mass, momentum and energy conservation equations can be written in the eulerian framework using spatial time derivatives as shown in equations (1) - (3) [27]:

$$\frac{\partial \rho}{\partial t} + \nabla \cdot (\rho v) = 0, \quad (1)$$

$$\frac{\partial \rho v}{\partial t} + \nabla \cdot (\rho v \otimes v) = \nabla \cdot \boldsymbol{\sigma} + \rho \mathbf{b}, \quad (2)$$

$$\frac{\partial e}{\partial t} + \nabla \cdot (ev) = \boldsymbol{\sigma} : \mathbf{D}, \quad (3)$$

with the material velocity  $v$ , the density  $\rho$ , the Cauchy stress  $\boldsymbol{\sigma}$ , the vector of body forces  $\mathbf{b}$ , the strain energy  $e$  and the velocity strain  $\mathbf{D}$ . Details on the eulerian formulation, the solution procedure of the governing equations, numerical implementation and contact formulation can be found in [31] and [32].

The usage of eulerian elements for the material avoids mesh distortions which would occur with lagrangian elements. All other parts like the tool, spindle or bearing rings, can be modeled using lagrangian elements. Eulerian linear solid elements with 8 nodes, thermal coupling, reduced integration and hourglass control (EC3D8RT) are used to mesh the material, while the other parts are meshed with lagrangian linear solid elements with also 8 nodes, thermal coupling, reduced integration and hourglass control (C3D8RT). All lagrangian parts are constrained to be rigid bodies in order to save computational costs. Since these parts deform very little compared to the welded sheets, this simplification is justified. In order for thermal contact properties as described below to work, the temperature degree of freedom of the lagrangian parts is not constrained.

The coupling between eulerian and lagrangian domain is realized using a general contact which is available in Abaqus. The Coulomb friction law which relates the frictional shear stress  $\tau$  with the contact pressure  $p$  at the interface as stated in equation (4) is used.

$$\tau = \mu \cdot p \quad (4)$$

A constant friction coefficient of  $\mu = 0.3$  is employed. This value is in accordance with other works [10]. The production of frictional heat through friction between tool and material is taken into account with the “gap heat generation” option of Abaqus. With this option, a fraction of dissipated sliding friction energy can be included as heat source in the analysis. The heat  $q_f$  is calculated using the slip rate  $\dot{\gamma}$  as stated in equation (5) [33]. The default fraction value of  $\eta_f = 1.0$  is used in all analyses.

$$q_f = \eta_f \cdot \tau \cdot \dot{\gamma} \quad (5)$$

The material behavior of the welded aluminum sheets is described using the Johnson-Cook material model [34] which expresses the von Mises flow stress as a function of strain, strain rate and temperature as shown in equation (6):

$$\sigma_y = \left( A + B \cdot \varepsilon_{pl}^n \right) \left( 1 + C \cdot \ln \frac{\dot{\varepsilon}_{pl}}{\dot{\varepsilon}_0} \right) \left( 1 - \left( \frac{T - T_{ref}}{T_m - T_{ref}} \right)^m \right), \quad (6)$$

with the equivalent plastic strain  $\varepsilon_{pl}$ , the equivalent plastic strain rate  $\dot{\varepsilon}_{pl}$ , the normalizing strain rate  $\dot{\varepsilon}_0$ , the material solidus temperature  $T_m$  and the reference temperature  $T_{ref}$ .  $A$ ,  $B$ ,  $C$ ,  $n$  and  $m$  are the material model constants.

Due to the dependency on strain, strain rate and temperature, the model is suited for simulations of FSW, for this reason it is also used by other researchers [26] [27]. All simulations in this work were conducted with Johnson-Cook parameters from [10] for EN AW 6061 T6 as listed in Table 1. In Table 2, additionally needed material parameters can be found.

**Table 1** Johnson-Cook parameters for EN AW 6061 T6 [10]

<b>A</b>	<b>B</b>	<b>n</b>	<b>m</b>	<b>C</b>
291 MPa	113 MPa	0.42	1.43	0.006

**Table 2** Additional material parameters

	<b>Density</b>	<b>Young's Modulus</b>	<b>Poisson's Ratio</b>	<b>Thermal Conductivity</b>	<b>Specific Heat</b>
Aluminum	2700 kg/m <sup>3</sup>	70000 MPa	0.33	190 W/(mK)	900 J/(kgK)
Steel	7800 kg/m <sup>3</sup>	210000 MPa	0.3	50 W/(mK)	460 J/(kgK)

In friction stir welding, heat is also produced by internal friction in the material itself, not only by the friction between tool and material [35]. The “inelastic heat-fraction” option of Abaqus allows the inclusion of inelastic energy dissipation as heat source  $q_{pl}$  in the analysis as stated in equation (7) [33]. The default fraction value of  $\eta_{pl} = 0.9$  is used.

$$q_{pl} = \eta_{pl} \cdot \sigma : \dot{\varepsilon}_{pl} \quad (7)$$

#### MODEL FOR THE ANALYSIS OF WELDING FORCES AND THE INFLUENCE OF THE MACHINE

The first model, the process-machine-model, consists, as shown in Fig. 5, of the welded sheets, the tool as well as the spindle and the bearings of the machine. The dimensions of the spindle are taken from an ESAB Legio 3ST dedicated FSW machine, which is available at the IMWF respectively MPA for research purposes. The tool used for welding has dimensions as shown in Fig. 6, the welded aluminum sheets have a thickness of 2 mm. In order to capture phenomena like the formation of flash, the thickness of the eulerian mesh is chosen twice the thickness of the sheets. The material is assigned in form of the sheets to the eulerian mesh at the beginning of the simulation.

The stiffness of the bearings is modeled using linear spring elements that connect the bearing rings with the spindle, as schematically shown in Fig. 7. Each bearing is represented

by four springs to model the behavior in the lateral x- and y-direction. A spring in the axial z-direction in the lower bearing represents the axial stiffness of the bearings.

The welding parameters can be found in Table 3 and are applied as boundary conditions as described in the following. The rotational speed is applied on spindle and tool whereas the boundary conditions for feed speed and heel plunge depth are applied on the bearing rings. The coupling of bearing rings and spindle with the spring elements results in the motion and positioning of the tool. In 0.5 seconds, the tool is plunged into the material realizing the heel plunge depth through the proper plunge feed speed. After a dwell time of 0.5 seconds, the feed speed is applied and two seconds of welding are simulated. In order to realize the tool tilt angle, the whole assembly is rotated. The welded sheets are fixed at the bottom. This is achieved by prescribing a velocity boundary condition of zero in the z-direction. Likewise, the material is prevented from flowing out of the eulerian domain by prescribing a velocity of zero at the edges of the plates in the respective x- and y-directions.

The relatively long simulation time span of 3 seconds for the explicit analysis results in long computation times: About 23 days are needed for one run with 8 cores of an Intel® Xeon® E5-2650 CPU and 128 GB of RAM. In order to speed up the calculations and conduct the presented amount of simulation runs in a reasonable time frame, the density of the material was artificially changed. The time step size of an explicit simulation with solid elements is given by equation (8) [36]:

$$\Delta t = \frac{L_e}{\sqrt{\frac{E \cdot (1-\nu)}{(1+\nu) \cdot (1-2 \cdot \nu) \cdot \rho}}} \quad (8)$$

with the characteristic length  $L_e$  of the element, the Young's modulus  $E$ , the Poisson's ratio  $\nu$  and the density of the material  $\rho$ . The denominator is the sound speed of the material. The time step size is determined by the size of elements and the density of the materials. A certain mesh size is necessary to discretize the problem in a satisfying level of detail, i.e. the mesh size cannot be chosen at random. For the calculation of welding forces, a mesh size of 0.5 mm is necessary, for the analysis of the weld formation, a finer mesh is needed. The density however can be set deliberately to any value by the user. Through scaling of the density, a larger time step size and therefore a shorter simulation time can be realized. In this work, a scaling factor of  $10^4$  is used which reduces the simulation time from 23 days to about half a day. Since the specific heat is dependent on the mass, cf. Table 2, it must be scaled as well. The scaling is a massive change and it must therefore be ensured that the simulation results can still be used to investigate the presented problem. The impact of the mass scaling is shown in the next chapter.

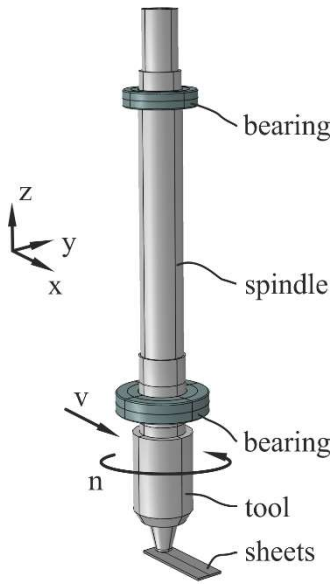


Fig. 5 Process-machine-model

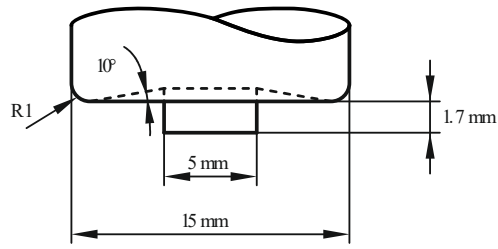


Fig. 6 Tool dimensions

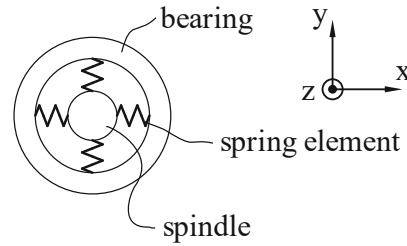


Fig. 7 Schematic of bearing modelling

Table 3 Friction stir welding parameters

Rotational speed	Feed speed	Heel plunge depth	Tilt angle
1500 1/min	1500 mm/min	0.2 mm	1 °

In order to investigate which effects contribute in which amount to the dynamics of friction stir welding, the model is modified. The modifications are done to intentionally trigger the effects described in the hypotheses. The influence of an uneven mass distribution (hypothesis 1) is examined by adding a point mass  $m_p$  at the edge of the tool with a distance  $r$  from the rotational axis as shown in Fig. 8 a. To analyze the impact of an out-of-round tool movement (hypothesis 2), the pin of the tool is moved a distance  $d$  from the rotational axis to an eccentric position as shown in Fig. 8 b. Different pin geometries, namely cylindrical, triangular and quadrangular, as shown in Fig. 8 c, are used to investigate hypothesis 3. As mentioned above are hypothesis 4 and hypothesis 5 not part of the investigations, therefore, no model modifications are needed.

In order to separate effects from welding process and machine, simulations are carried out where no welding is done. This is achieved through a deactivation of the general contact.

All other model properties were kept the same with values as described above. To calculate the frequency responses of the forces, only the welding stage but not the plunging and dwelling phase was taken into account. A sampling rate of 1000 Hz was used for all outputs, additionally an anti-aliasing filter was applied.



## Mathematical Modelling of Weld Phenomena 12

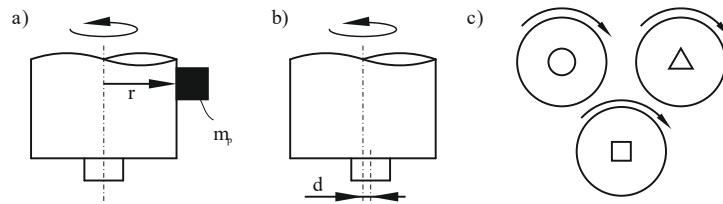


**Fig. 8** Modifications of the process-machine-model to trigger effects of hypotheses

Despite the mass scaling, a mesh size of 0.5 mm is needed with the process-machine-model to reach reasonable computational costs. This mesh size is sufficient to investigate the welding forces, for the investigation of the weld formation in detail however, a finer mesh is necessary. Out of this reason, a simplified 2d-model similar to the one presented in [28] is employed additionally.

### MODEL FOR THE INVESTIGATION OF WELD FORMATION AND MATERIAL FLOW IN DETAIL

The simplified model consists, as shown in Fig. 9, of two welded sheets and a cylinder representing the pin of the tool. The boundary conditions for the rotational speed of the tool as well as feed speed are directly applied on the cylinder representing the pin of the tool.

Only ten revolutions of the tool are simulated. This strong abstraction of the geometry reduces the model size and allows the usage of a much finer element size of 0.1 mm for the eulerian mesh of the material. The CEL-method as implemented in Abaqus does not allow the user to set up two-dimensional models. For this reason, one layer of EC3D8RT elements is used and velocity boundary conditions, as described above, are used to keep the material from flowing out of the eulerian room in all three directions. To this point, no stiffness elements are included. All other properties of the 2d-model are similar to the process-machine-model as described above.

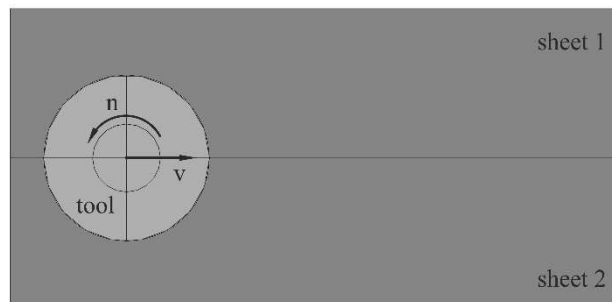


**Fig. 9** 2d-model of friction stir welding

### VALIDATION

In order to investigate the impact of the mass scaling, simulation results are compared to experimental data. Welding experiments where EN AW 6111 T6 sheets were joined using the ESAB Legio 3ST dedicated FSW machine were done at the IMWF and MPA. As shown

in Table 4, the mechanical properties of EN AW 6111 T6 are similar to those of EN AW 6061 T6.

**Table 4** Mechanical properties of EN AW 6061 T6 and EN AW 6111 T6

	Yield strength $R_{p0,2}$	Ultimate tensile strength $R_m$	Total strain at maximum load $A_{gt}$
EN AW 6061 T6 [10]	291 MPa	317 MPa	9.4 %
EN AW 6111 T6 (own tensile tests)	292 MPa	335 MPa	11 %

In the simulations, the heel plunge depth was prescribed in order to achieve a similar plunge depth of the tool between all simulations. The welding experiments were done force-controlled with an axial force  $F_z$  of 6000 N, resulting in an approximately similar heel plunge depth as in the simulations. The other welding parameters, the tool geometry and the sheet thickness were the same as in the model. During welding, the force in welding direction  $F_x$ , the force perpendicular to the welding direction  $F_y$  and the torque around the rotational axis  $M_z$  were measured using a rotating dynamometer called Spike by the company pro-micron.

In addition to the experiments, a simulation without mass scaling was conducted for comparison. All in this chapter presented results were obtained using a model without described modifications and with rigid bearings.

In Fig. 10, the force in welding direction  $F_x$  obtained from the simulation without mass scaling, from the simulation with the aforementioned factor for mass scaling of  $10^4$  as well as from the experiment are shown over a time frame of 0.5 seconds during steady state of welding. Fig. 11 shows the results in the frequency domain.

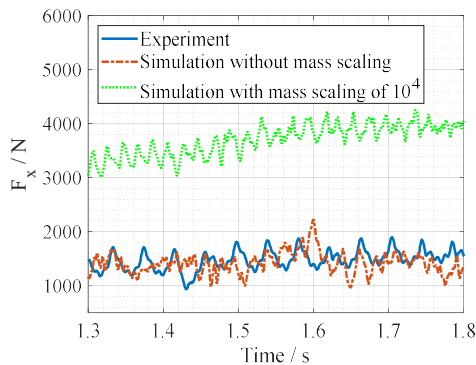


**Fig. 10** Comparison of experiment and simulation in time domain for  $F_x$

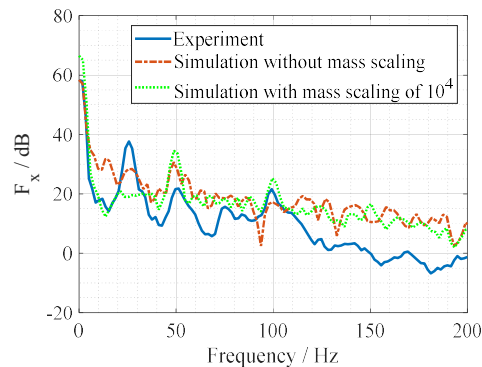


**Fig. 11** Comparison of experiment and simulation in frequency domain for  $F_x$

In the time domain, the results of the simulation without mass scaling are in good accordance with the measurements from the experiment. In the frequency domain it can be seen that the mean values are approximately the same, however, differences can be seen in the dynamic parts. This can be expected since the dynamic forces are part of the investigations conducted in this work. The force calculated with a mass scaling factor of  $10^4$  is higher since the higher density results in a higher mass of the material that is being

extruded during welding. The mean value of the force is about 2.7 times higher when mass scaling is used. This is significantly less than the height of the mass scaling factor of  $10^4$ . An explanation for this circumstance is that only a small amount of material is transported by the tool. This also accounts for the only small differences regarding the height of the amplitudes of the dynamic forces for most frequencies. A larger difference between the two simulations can be seen in the frequency domain at 25 Hz, which is the rotational speed. As will be shown in the next chapters, the peak at this frequency is largely influenced by the modifications of the model, the differences here can be accepted. The results for the torque  $M_z$ , see Fig. 24 and Fig. 25 in the appendix, show similar trends.

Looking at the results it can be concluded that the model can be used to calculate the process forces occurring during friction stir welding. The artificial mass scaling leads to an increase of the process forces, however, general trends are preserved. Through a comparison of the results of different simulations with each other, the reasons for the periodic dynamics of FSW can be identified. It must however be kept in mind that with the employed mass scaling, no absolute, quantitative values can be obtained.

The 2d-model has the purpose to get a deeper understanding of the mechanism of the weld formation in a qualitative way and not to calculate welding forces, therefore, no validation is done for this model. The strong simplifications of the 2d-model would make a validation difficult since welding experiments cannot be set up in the same way.

### RESULTS

In this chapter, the results obtained from the simulations are presented. First, the investigations regarding the first three hypotheses through the modifications of the model are shown. It is furthermore shown how the results change with a change of machine properties, i.e. the spring stiffness of the bearings. Additionally, the 2d-model is employed to analyze the weld formation. Second, correlations between process forces and welding defects are shown using the 3d-model. Mass scaling as described above was used in all presented simulations. The friction stir welding parameters as listed in Table 3 were used if not stated otherwise. Parts of the results can also be found in [5].

#### EXCITATION THROUGH IMBALANCE

In Fig. 12, the force in welding direction  $F_x$  is shown in the frequency domain for the unmodified model without imbalance, for a model with an added imbalance mass of 0.1 kg and for a simulation with an added imbalance mass of 1 kg. As first step, the bearings were defined as rigid. Peaks can be seen at multiples of the rotational speed used for welding which is 25 Hz, cf. Table 3. In Table 5 it is listed at which frequencies peaks occur with which amplitudes. In all three model variants, notable peaks occur at 50 Hz, 100 Hz and 150 Hz. Peaks at 25 Hz are only present in the modified models, a significant amplitude occurs only with an imbalance mass of 1 kg. The results for different imbalance masses and flexible bearings with a chosen stiffness of  $5 \cdot 10^6$  N/mm can be seen in Fig. 13. A dominant peak that can be attributed to the bearing stiffness can be seen at 380 Hz. The influence of the bearing stiffness on dynamic force parts with frequencies being multiples of the

rotational speed is very small, the amplitudes have almost the same height as in the model with rigid bearings, compare also Table 5.

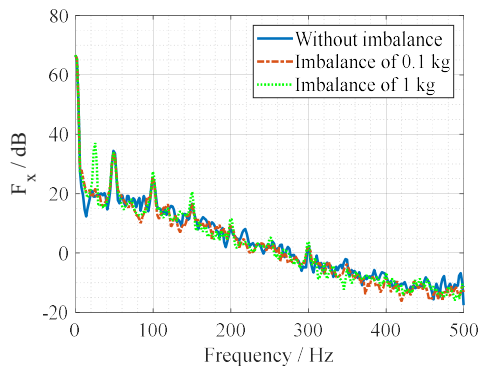


**Fig. 12** Force  $F_x$  in frequency domain for different imbalances with rigid bearings

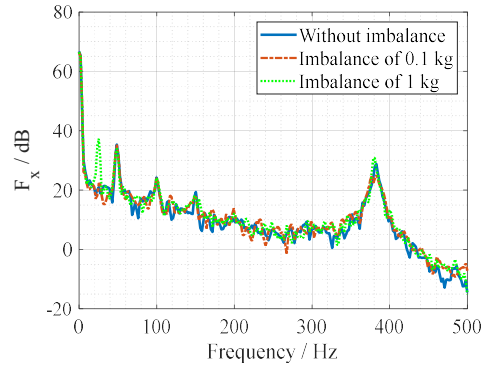


**Fig. 13** Force  $F_x$  in frequency domain for different imbalances with flexible bearings

The force in feed direction  $F_x$  in the frequency domain without welding, i.e. without the influence of the process, for the two different imbalance masses with flexible bearings is shown in Fig. 14. Peaks are present at 25 Hz, 185 Hz and 380 Hz. The peak at the rotational speed is caused by the imbalance mass while the other two peaks can be attributed to the stiffness. A comparison with the simulation with friction stir welding process, Fig. 13 or Table 5, shows that the amplitudes at 25 Hz are approximately the same for the imbalance of 1 kg. This means that the imbalance mass mostly influences the height of the excitation, not the interaction between process and machine. Different amplitudes between welding and no welding at 25 Hz can be seen for the smaller imbalance mass of 0.1 kg. It must however be noted that the peak is barely visible in Fig. 12 respectively Fig. 13, i.e. it may be superimposed by ground level noise.

In Fig. 14, no further dominant peaks can be seen at multiples of the rotational speed, it is therefore concluded that these are caused by the process. The damping introduced into the system through the process may be the reason for the difference of amplitudes at 380 Hz respectively 185 Hz when comparing welding with no welding.

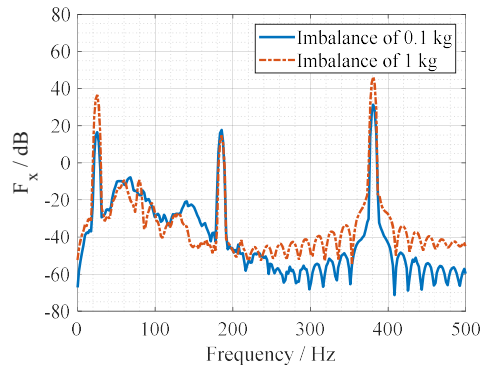


**Fig. 14** Force  $F_x$  in frequency domain for different imbalances without welding with flexible bearings

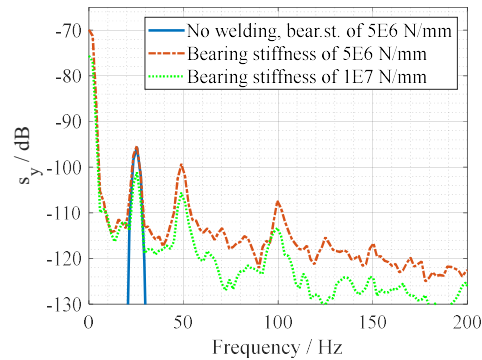


**Fig. 15** Deflection of spindle  $s_y$  without and with welding process with an imbalance of 1 kg

While the simulations show almost no influence of the bearing stiffness, even when comparing rigid with flexible bearings, on the height of the force amplitudes at multiples of the rotational speed, an influence is visible regarding the deflection of the tool. In Fig. 15, the deflection of the spindle without and with welding process for the y-direction with a stiffness of  $5 \cdot 10^6$  N/mm and an imbalance of 1 kg each is shown. In addition, the deflection with welding is shown for an imbalance of 1 kg, but a higher stiffness of  $1 \cdot 10^7$  N/mm. Again, a peak occurs at 25 Hz for all scenarios, while peaks at 50 Hz and 100 Hz can only be seen with friction stir welding process. As for the Force  $F_x$ , the amplitudes at 25 Hz are almost identical for the stiffness of  $5 \cdot 10^6$  N/mm with and without welding. A comparison of the amplitudes between the two different bearing stiffness however shows a difference: The higher stiffness leads to smaller spindle deflections. It can furthermore be seen that the deflection of the spindle during welding has a static part which does not occur without welding. A reason for this could be the differences in the material states between advancing and retreating side of the friction stir weld. The advancing side of the weld is the side where the direction of tool rotation coincides with the welding direction. The retreating side is the side where direction of tool rotation and welding direction are opposite.

### EXCITATION THROUGH THE PROCESS

The results regarding the second hypothesis can be found in Table 5, where the heights of the amplitudes at various frequencies for different simulations are listed. Simulations #8 and #9 as well as #11 and #12 show that for both simulated pin offsets peaks occur at the rotational frequency and multiples thereof. Compared to the first hypothesis, more peaks, for example at 75 Hz and 125 Hz, appear. A higher amplitude compared to the excitation through imbalance can especially be noticed at 25 Hz. Simulations #10 and #13 show the results for the two different pin offsets without welding. A peak occurs at 25 Hz since the pin offset introduces an imbalance into the system. A comparison between the simulations with welding process and without, for example #12 and #13, shows a clear difference in the

amplitudes at 25 Hz. This means that the interaction between process and eccentric tool has a significant contribution to the dynamics of friction stir welding. Dynamic force parts are caused by the forced eccentric motion of the tool in the material which occur in addition to the dynamic force parts introduced by the pin offset imbalance. The interaction between process and material causes higher amplitudes than the imbalances. As shown above, peaks at harmonics of the rotational frequency occur only with the welding process.

Again, only little differences occur between the models with rigid and flexible bearings (#8 and #9 respectively #11 and #12 in Table 5) when looking at peaks being multiples of the rotational speed. This can also be seen in Fig. 16, where the results for a pin offset of 0.2 mm, but different bearing stiffness of  $1 \cdot 10^6$  N/mm,  $5 \cdot 10^6$  N/mm and  $1 \cdot 10^7$  N/mm are shown. The peaks at 25 Hz, 50 Hz and 75 Hz show almost the same amplitudes. The change of stiffness values has its main impact in a shifting of the right peak to higher frequencies for the higher stiffness value and to lower frequencies for the lower stiffness value.

In all simulations where the FSW process is included, a dominant peak is present independent of the bearing stiffness or other modifications of the model at 50 Hz, i.e. twice the rotational speed. The material transport during FSW is identified in [11] to lead to dynamic forces with twice the frequency of the rotational speed. In Fig. 17, the force  $F_x$  is shown for three simulations with rigid bearings and without modifications, but with three different rotational speeds. Peaks occur at 50 Hz and 100 Hz in all three variants independent of the rotational frequency, which is in contradiction to the aforementioned theory. One explanation could be unaccounted numerical effects, another one the excitation of unaccounted eigenfrequencies of the system. A distinctive peak is present at 80 Hz with a rotational speed of 40 1/s and a small peak is present at 26 Hz in the simulation with 13 1/s as rotational speed. A clear separation of effects, e.g. numerical influences from physical phenomena like material transport must be achieved in future investigations. In order to do so, the 2d-model will be employed. As will be shown in the following, the 2d-model provides a way to visualize and understand the material flow during friction stir welding.

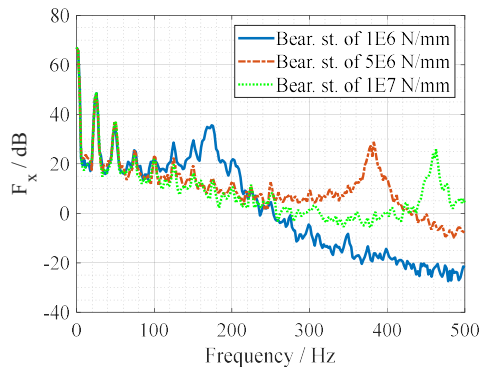


**Fig. 16** Force  $F_x$  in frequency domain for different bearing stiffness with pin offset of 0.2 mm

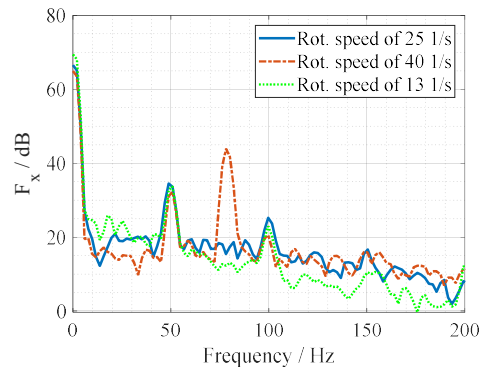


**Fig. 17** Force  $F_x$  in frequency domain for different rotational speeds with rigid bearings

## Mathematical Modelling of Weld Phenomena 12

**Table 5** Comparison of amplitudes of peaks of force  $F_x$  in dB at harmonics of rotational speed for various simulations (bearing stiffness if not rigid:  $5 \cdot 10^6$  N/mm)

#	Hypothesis									
	With process?/Flexible bearings?	25 Hz	50 Hz	75 Hz	100 Hz	125 Hz	150 Hz	300 Hz	350 Hz	425 Hz
1	Yes/No (Baseline model)	-	34.5	-	25.2	-	16.7	2.4	-	-
2	1 (0.1 kg) Yes/No (Fig. 12)	21.7	34.0	-	25.4	-	16.7	2.3	-	-
3	1 (0.1 kg) Yes/Yes (Fig. 13)	22.3	35.3	-	24.1	-	17.8	-	-	-
4	1 (0.1 kg) No/Yes (Fig. 14)	16.6	-	-	-	-	-	-	-	-
5	1 (1 kg) Yes/No (Fig. 12)	37.1	33.8	-	27.4	-	20.6	3.4	-	-
6	1 (1 kg) Yes/Yes (Fig. 13)	37.3	34.0	-	24.1	-	17.8	-	-	-
7	1 (1 kg) No/Yes (Fig. 14)	36.6	-	-	-	-	-	-	-	-
8	2 (0.03 mm) Yes/No	27.6	34.4	22.7	23.1	14.1	19.0	-	-	-
9	2 (0.03 mm) Yes/Yes	27.8	35.5	22.9	24.3	15.7	17.0	9.7	-	-
10	2 (0.03 mm) No/Yes	17.2	-	-	-	-	-	-	-	-
11	2 (0.2 mm) Yes/No	48.7	36.4	24.2	21.8	22.2	15.1	1.9	0.8	-
12	2 (0.2 mm) Yes/Yes	48.1	36.7	25.4	23.0	22.5	19.3	9.4	-	-
13	2 (0.2 mm) No/Yes	27.3	-	-	-	-	-	-	-	-
14	3 (tri.) Yes/Yes	39.0	33.8	32.8	19.6	21.4	26.9	19.5	26.6	18.1
15	3 (quad.) Yes/Yes	18.4	34.6	-	39.3	-	16.7	20.3	29.4	-

In Fig. 18, the results from three simulations with different pin offsets using a mass scaling factor of  $10^6$  are shown. The contour plot shows the eulerian volume fraction (EVF)

of the two different aluminum sheets. The EVF is a value between 0 and 1 and gives the amount of the respective material that is present in an eulerian element, i.e. the material flow of the two sheets caused by the welding process can be visualized. After two or three rotations the process has stabilized and is stationary. While no mixing of the sheets can be seen without pin offset, a banded structure results for both pin offsets. With the larger offset, more material mixing occurs and a slightly different weld geometry results. Without tool offset, material from the lower plate (red) is continuously transported around the tool and deposited behind it. The width of the layer of material that is sheared around the pin does not change. With tool offset, a more batch-wise material transport around the tool takes place. The off-center motion results in a varying width of the material layer moving around the tool. In combination with the varying feed speed, this allows material of the upper plate (blue) to be drawn in behind the tool resulting in the banded structure of the friction stir weld. The distance between the bands is equal to the weld pitch, i.e. the tool advance per revolution of 1 mm. The banded structure is also visible when looking at the plastic strain resulting from the welding process, cf. Fig. 26 in the appendix. No periodic properties however are visible in the temperature distribution as shown in Fig. 27 in the appendix. To the knowledge of the authors no friction stir welds without banded structure exist. It can therefore be assumed that in real-world applications, at least a small off-center motion of the tool must always be present.

The need for the fine mesh of the 2d-model to investigate the material flow is evident from Fig. 28 in the appendix. When using a coarse mesh of 0.5 mm, the weld formation cannot be resolved. A comparison of the force  $F_x$  calculated with the 2d-model with fine and coarse mesh, Fig. 29 in the appendix, shows only little differences. Compared to the 3d-model (Fig. 10), however, the force levels are completely different. A comparison with experimental measured forces is not possible with the 2d-model. One property the two curves (Fig. 16 and Fig. 29) have in common is the dominance of 25 Hz in the dynamic parts of the force when a tool offset is present. This shows that the 2d-model can at least in a qualitative way give information on the dynamic force parts.

More investigations using the 2d-model will be conducted in the future. Especially needed are analyses where the influence of the machine stiffness on the tool trajectory and resulting weld formation is investigated in more detail.



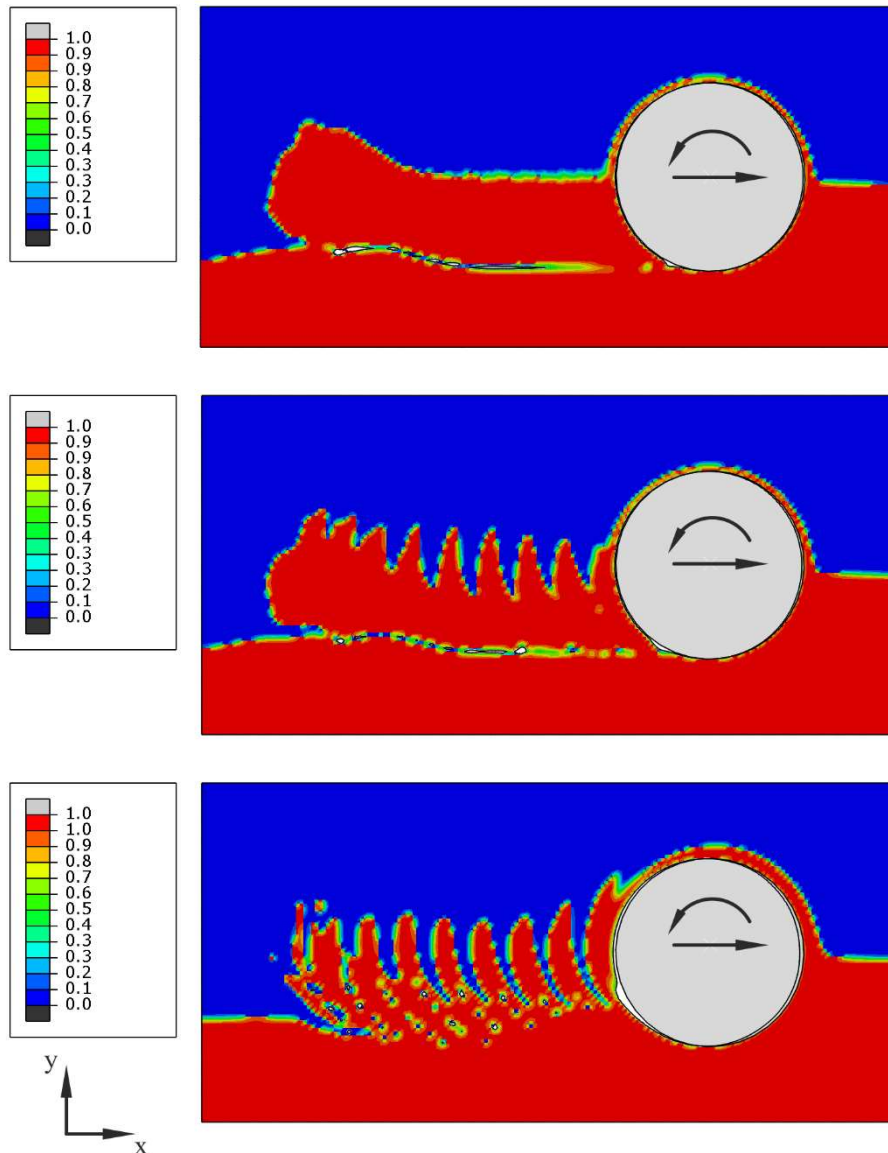


**Fig. 18** Results (eulerian volume fraction) of 2d-model without pin offset (top), with an offset of 0.03 mm (middle) and an offset of 0.2 mm (bottom)

### EXCITATION THROUGH THE TOOL GEOMETRY

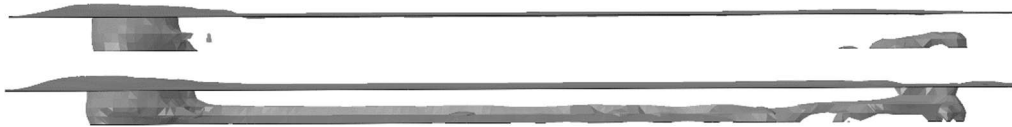
The results for different pin shapes with flexible bearings are also listed in Table 5 under simulations #14 and #15. As for the two hypotheses before, peaks can be found at harmonics of the rotational speed. Compared to the other simulations, notable peaks can also be found at frequencies above 200 Hz. While the triangular pin shows a notable peak at 75 Hz, the quadrangular pin shows a notable peak at 100 Hz. These multiples of the rotational frequency correlate with the number of sides of the respective pin. The strong excitations, especially at higher frequencies, can be attributed to the used pin shapes (Fig. 8 c) which deviate strongly from the circular shape. For other tool shapes, e.g. pins with only small flats on the sides, smaller excitations can be expected.

### CORRELATION OF WELDING DEFECTS AND PROCESS FORCES

In this chapter, two small examples of correlations between FSW defects and welding forces are shown. Additionally, it is demonstrated that the insights from above presented investigations must be considered when developing process monitoring applications based on force feedback data.

#### *Tunnel defect*

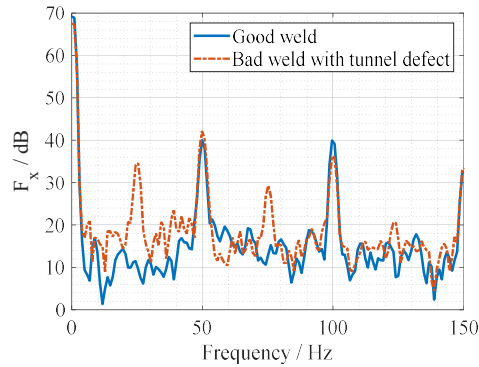
In Fig. 19, the results from two simulations with two different heel plunge depths are shown. All other welding parameters, material data and boundary conditions were the same. The unmodified baseline model was used, i.e. no dynamic defects were triggered intentionally. The simulation allows a view below the surface of the welded sheets where free surfaces are depicted in grey, allowing a visualization of volumetric defects. Only a small volumetric defect can be seen at beginning of the first weld. The second weld on the contrary shows a tunnel defect on the advancing side along the complete length of the weld caused by the insufficient heel plunge depth of the tool.



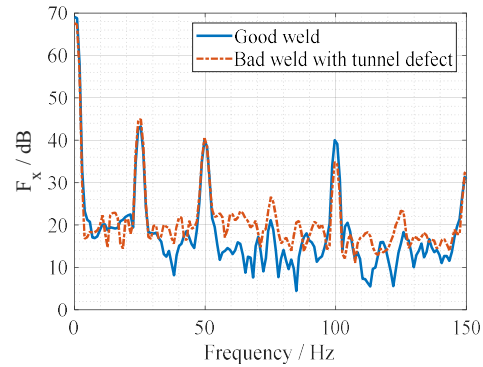
**Fig. 19** Simulation of friction stir welds without and with tunnel defect

Fig. 20 shows the frequency domain plot of the force in welding direction  $F_x$  for both welds. Peaks can be seen at 50 Hz and 100 Hz for both welds, however, only the bad weld shows peaks at 25 Hz, 75 Hz and 125 Hz. Taking these results alone, it could be suggested that welds with tunnel defects can be identified using the occurrence of these peaks. However, only when using the model it can be guaranteed that no additional dynamic effects occur. As shown in the chapters before, frequencies being multiples of the rotational speed are caused by imbalance masses, pin offsets or different tool geometries. These effects superimpose the peaks at 25 Hz, 75 Hz and 125 Hz, which indicate the tunnel defect. This in return results in difficulties identifying the bad welds. A solution to that problem

may lie in the comparison of the height of amplitudes at 25 Hz and 75 Hz, i.e. at the first and third harmonic. Fig. 21 shows the force  $F_x$  for a good and bad weld with tunnel defect, this time with an offset of the tool in both cases. The difference between the two curves is as expected much smaller. The peak at 25 Hz is dominated by the effects of the tool offset resulting in almost identical amplitudes. The impact of the tool offset is less strong at 75 Hz, resulting in different amplitudes. Taking the ratio of the amplitudes at these two frequencies, a criteria for welds with tunnel defects may be defined.



**Fig. 20** Force  $F_x$  in frequency domain for weld without and with tunnel defect, no offset of tool

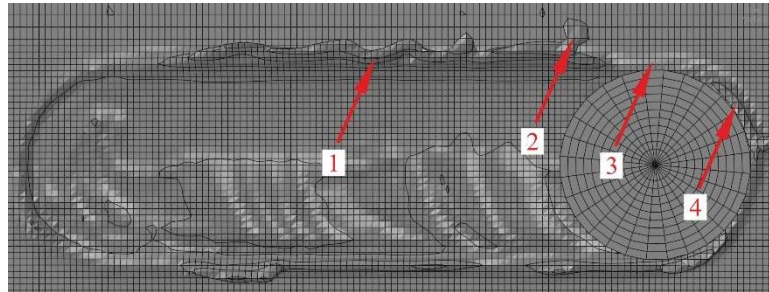


**Fig. 21** Force  $F_x$  in frequency domain for weld without and with tunnel defect, with offset of tool

The same methodology is used in [20] to identify welds with volumetric defects. A ratio of 0.2 between the force amplitudes in welding direction at first and third harmonic of the rotational speed is identified as reliable indicator for volumetric defects with the given experimental setup. The force measurements are additionally used to predict the size of the volumetric defects. The peak at the third harmonic is explained to be caused by the interaction of the three flats of the tool pin with the volumetric defect. Similar trends are found in this work, although a cylindrical pin was used. This shows that further analyses regarding the relation between volumetric defect formation and welding forces are necessary. One way could be the usage of the 2d-model.

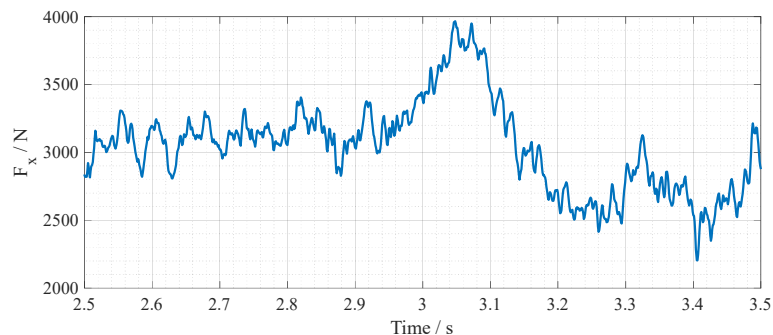
## *Flash formation*

Fig. 22 shows a simulation with strong flash formation caused by a high heel plunge depth. The corresponding force  $F_x$  in the time domain for a time frame of 1 second is shown in Fig. 23.



**Fig. 22** Simulation with flash formation

At the beginning of the weld, flash is continuously formed as indicated (1) in Fig. 22. A relatively steady force level can be seen between 2.5 s and 3 s for this part of the weld in Fig. 23. A larger part of flash is then formed at position (2) and sheared off at position (3). A corresponding peak occurs in the force signal at 3 s, followed by a drop of the force below the initial level at 3.2 s. New flash is formed at position (4) which is accompanied by a rise of the force at the end of the shown time frame. In the frequency domain, no signs could be found indicating the flash formation. The showed correlation could probably be used for monitoring systems. However, it must be known what the force level for a weld without flash looks like. Furthermore, it must be considered that other reasons like the machine stiffness or a change of the heel plunge depth due to thickness variations can also lead to a change of force level. Difficulties will most likely arise in the separation of the different effects.



**Fig. 23** Force  $F_x$  in time domain for weld with flash formation

### SUMMARY AND OUTLOOK

In this work, a finite element model analysis was used to investigate the dynamics of friction stir welding. A systematic variation of the 3d-model was done to verify postulated hypotheses regarding the causes of the FSW dynamics. The 2d-model was used to get additional information on the material flow in the weld.

- Frequencies occurring in the forces are the rotational speed of the tool and its harmonics as well as frequencies which can be attributed to the bearing stiffness. Multiples of the rotational speed can only be seen with welding process, but not without. The frequency of the rotation speed itself, i.e. the first harmonic, is only visible in the modified models.
- The addition of imbalance masses (hypothesis 1) leads to an amplification of the rotational frequency and multiples thereof. The first harmonic is affected most. It is found that the height of amplitudes is almost exclusively influenced by the imbalance mass, but not the interaction of process and tool.
- Tools with pin offset (hypothesis 2) also result in an excitation of the rotational speed and its harmonics. As for the first hypothesis, the pin offset has the strongest impact on the first harmonic. In contrast to the imbalance masses, the interaction of process and out-of-round tool movement is identified as the main reason for the amplification of the frequencies. The forced motion delivers the main contribution to the dynamic force parts while the imbalance introduced through the tool offset only has a minor influence.
- Pin geometries other than cylindrical (hypothesis 3) again result in an excitation of the spindle frequencies and multiples. While a dominant peak is visible at the third harmonic for a triangular pin, a dominant peak can be seen at the fourth harmonic for a quadrangular pin. An excitation is visible over a broader range of frequencies compared to hypothesis 1 and 2.
- Dominant peaks at frequencies which are no multiples of the rotational speed are caused by the stiffness of the bearings. Only a small influence of the stiffness on the force amplitudes being multiples of the rotational frequency can be seen. However, an impact on the tool trajectory is visible: For lower stiffness values, the deflection of spindle and tool gets larger.
- Peaks are visible at 50 Hz and 100 Hz in all simulations, even when the rotational speed is changed. Further analyses are needed to identify if numerical reasons or not yet understood physical phenomena play a role.
- The 2d-model predicts the formation of the characteristic banded structure of friction stir welds for cylindrical pins only for the case when the tool performs an out-of-round movement. A weld without banded structure is only obtained for simulations without tool offset.

The simulations show that correlations between welding defects and welding forces exist and that an identification of defects using force feedback data is principally possible. Tunnel defects may be identified using the ratio of the force amplitudes at first and third harmonic of the spindle frequency. Changes in the force level in the time domain can be employed to identify flash formation. Problems may arise when it comes to a robust implementation of the monitoring systems. Since it must be known how the welding forces look like for a

good weld, it is very likely that a calibration towards the specific environment, i.e. welding machine, tool, parameters and material has to be done for each application.

When comparing the experimental data, Fig. 11, with the forces obtained from the process-machine-model, it can be seen that the results from the simulation with a pin offset of 0.2 mm (Fig. 16) show the best reflection of the overall appearance of the frequency spectrum. The results obtained with the 2d-model regarding the weld structure support that the tool offset plays an important role. The identification of the out-of-round tool movement as main reason for force characteristics and banded weld structure is in accordance with literature [8] [9] [10].

Further work to be done in the future includes simulations without mass scaling to get quantitative results. Simulations superimposing the dynamic effects, especially tool runout and pin geometry, should be carried out. Furthermore, the model needs to be enhanced with additional stiffness elements that represent structural components of the machine. With the enhanced model, the fourth and fifth hypothesis can be investigated. A better understanding of the relation between machine stiffness, tool trajectory and weld formation has to be gained to explain effects as shown in Fig. 4. To do so, the 2d-model can be employed. More investigations to identify numerical influences, for example with varying mesh sizes or different sheet geometries need to be carried out. To get more information for monitoring systems, more simulations with different tool designs and different welding parameters that result in welds with defects have to be done. Another aspect worth looking into is if a possibility exists to couple both finite element model variants.

### ACKNOWLEDGEMENTS

The authors would like to thank the German Research Foundation (Deutsche Forschungsgemeinschaft DFG) for providing funding for the presented research work in scope of the project “Entwicklung eines experimentell gestützten Rührreißschweißmodells zur Festigkeitsvorhersage von Mischverbindungen am Beispiel von Aluminium-Stahl-Verbindungen” (SCHM 746/182-1).

APPENDIX

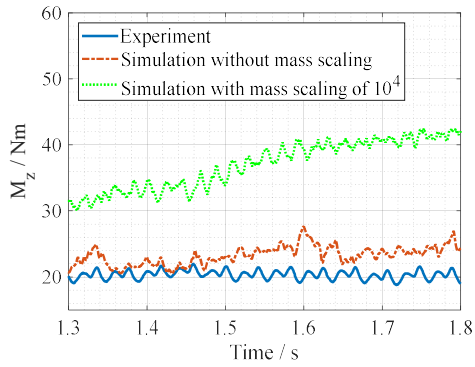


**Fig. 24** Comparison of experiment and simulation in time domain for  $M_z$

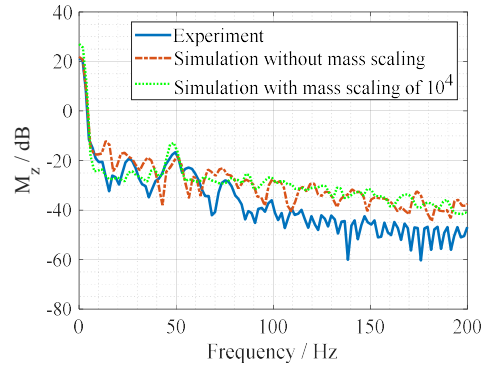


**Fig. 25** Comparison of experiment and simulation in frequency domain for  $M_z$

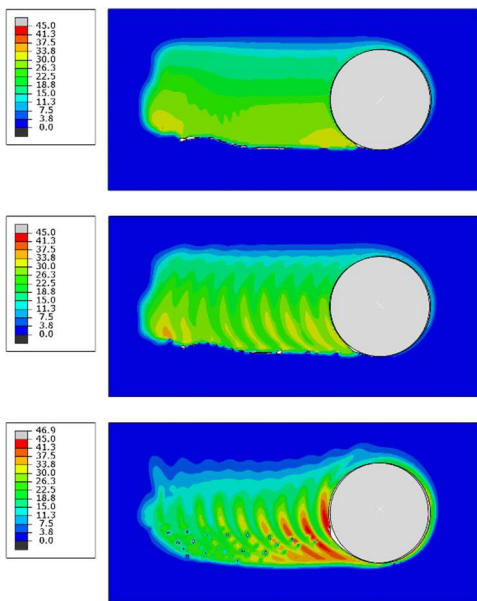


**Fig. 26** Results (volume fraction weighted average equivalent plastic strain) of 2d-model without pin offset (top), with an offset of 0.03 mm (middle) and an offset of 0.2 mm (bottom)

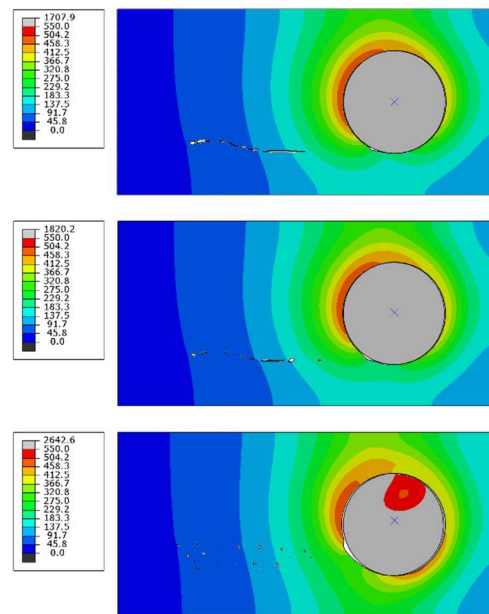


**Fig. 27** Results (temperature) of 2d-model without pin offset (top), with an offset of 0.03 mm (middle) and an offset of 0.2 mm (bottom)

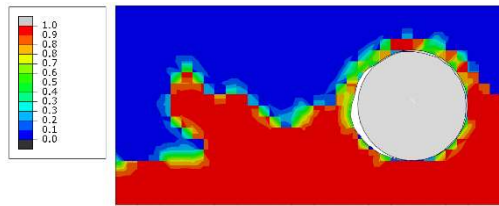


**Fig. 28** Results (eulerian volume fraction) of 2d-model with coarse mesh and pin offset of 0.2 mm

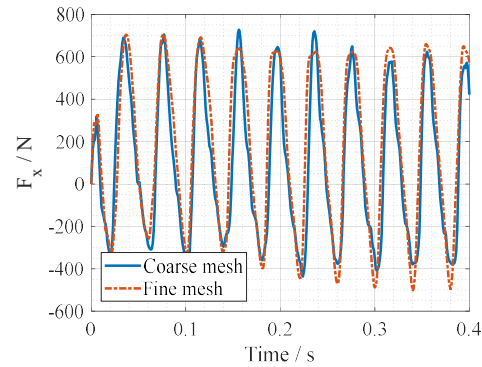


**Fig. 29** Force  $F_x$  in time domain for 2d-model with fine and coarse mesh and a pin offset of 0.2 mm

## REFERENCES

- [1] W. THOMAS, E. NICHOLAS, J. NEEDHAM, M. MURCH, P. TEMPLESMITH, AND C. DAWES, ‘Great Britain Patent G.B. Patent Application No. 9125978.8’, 1991.
- [2] A. K. LAKSHMINARAYANAN, V. BALASUBRAMANIAN, AND K. ELANGOVA, ‘Effect of welding processes on tensile properties of AA6061 aluminium alloy joints’, *Int. J. Adv. Manuf. Technol.*, vol. 40, no. 3–4, pp. 286–296, 2009.
- [3] M. WERZ AND M. SEIDENFUB, ‘High-Strength Friction Stir Welds for Joining Aluminum and Steel with Dissimilar Sheet Thicknesses’, in *11th International Symposium on Friction Stir Welding, Cambridge*, 2016.
- [4] F. PANZER, M. WERZ, AND S. WEIHE, ‘Experimental investigation of the friction stir welding dynamics of 6000 series aluminum alloys’, *Prod. Eng.*, vol. 12, no. 5, pp. 667–677, 2018.
- [5] F. PANZER, M. WERZ, AND S. WEIHE, ‘Analysis of the oscillating process forces of friction stir welding using finite elements’, in *12th International Symposium on Friction Stir Welding, Chicoutimi*, 2018.
- [6] J. W. QIAN, J. L. LI, J. T. XIONG, F. S. ZHANG, W. Y. LI, AND X. LIN, ‘Periodic variation of torque and its relations to interfacial sticking and slipping during friction stir welding’, *Sci. Technol. Weld. Join.*, vol. 17, no. 4, pp. 338–341, 2012.
- [7] J. T. XIONG *ET AL.*, ‘Characterisation of periodic variation in torque occurred in friction stir welding process’, *Sci. Technol. Weld. Join.*, vol. 19, no. 4, pp. 350–354, 2014.
- [8] J. H. YAN, M. A. SUTTON, AND A. P. REYNOLDS, ‘Processing and banding in AA2524 and AA2024 friction stir welding’, *Sci. Technol. Weld. Join.*, vol. 12, no. 5, pp. 390–401, 2007.
- [9] R. FONDA, A. REYNOLDS, C. R. FENG, K. KNIPLING, AND D. ROWENHORST, ‘Material flow in friction stir welds’, *Metall. Mater. Trans. A Phys. Metall. Mater. Sci.*, vol. 44, no. 1, pp. 337–344, 2013.
- [10] M. HOFELD, ‘Experimentelle, analytische und numerische Untersuchungen des Rührreibschweißprozesses’, Universität Stuttgart, 2016.
- [11] M. F. ZAEH AND P. GEBHARD, ‘Dynamical behaviour of machine tools during friction stir welding’, *Prod. Eng.*, vol. 4, no. 6, pp. 615–624, 2010.



- [12] A. SHRIVASTAVA, M. ZINN, N. A. DUFFIE, N. J. FERRIER, C. B. SMITH, AND F. E. PFEFFERKORN, ‘Analysis of Force Transients during Friction Stir Welding’, *43rd Proc. North Am. Manuf. Res.*, vol. XXX, pp. 1–10, 2015.
- [13] A. SHRIVASTAVA ET AL., ‘Physics-based process model approach for detecting discontinuity during friction stir welding’, *Int. J. Adv. Manuf. Technol.*, vol. 79, no. 1–4, pp. 605–614, 2015.
- [14] W. Y. LI, J. F. LI, Z. H. ZHANG, D. L. GAO, AND Y. J. CHAO, ‘Metal Flow during Friction Stir Welding of 7075-T651 Aluminum Alloy’, *Exp. Mech.*, vol. 53, no. 9, pp. 1573–1582, 2013.
- [15] F. C. LIU AND T. W. NELSON, ‘In-situ material flow pattern around probe during friction stir welding of austenitic stainless steel’, *Mater. Des.*, vol. 110, pp. 354–364, 2016.
- [16] X. C. LIU, Y. F. SUN, Y. MORISADA, AND H. FUJII, ‘Dynamics of rotational flow in friction stir welding of aluminium alloys’, *J. Mater. Process. Technol.*, vol. 252, no. October 2017, pp. 643–651, 2018.
- [17] F. GRATECAP, M. GIRARD, S. MARYA, AND G. RACINEUX, ‘Exploring material flow in friction stir welding: Tool eccentricity and formation of banded structures’, *Int. J. Mater. Form.*, vol. 5, no. 2, pp. 99–107, 2012.
- [18] R. KUMAR, V. PANCHOLI, AND R. P. BHARTI, ‘Material flow visualization and determination of strain rate during friction stir welding’, *J. Mater. Process. Technol.*, vol. 255, pp. 470–476, 2018.
- [19] E. BOLDSAIKHAN, E. CORWIN, A. LOGAR, J. MCGOUGH, AND W. ARBEGAST, ‘Detecting Wormholes in Friction Stir Welds from Welding Feedback Data’, in *42nd Midwest Instruction and Computing Symposium*, 2009.
- [20] A. SHRIVASTAVA, M. ZINN, N. A. DUFFIE, N. J. FERRIER, C. B. SMITH, AND F. E. PFEFFERKORN, ‘Force measurement-based discontinuity detection during friction stir welding’, *J. Manuf. Process.*, vol. 26, pp. 113–121, 2017.
- [21] TECHNISCHE UNIVERSITÄT ILMENAU AND UNIVERSITÄT STUTTGART, ‘Untersuchungen zur Übertragbarkeit der Prozessparameter auf Anlagen unterschiedlicher Bauart beim Herstellen von Tailored Blanks auf geschlossener Bahn mittels Rührreibschweißen’, *Forschungsvorhaben AiF-Nr. 14572 N / DVS-Nr. 05.034*, 2007.
- [22] X. HE, F. GU, AND A. BALL, ‘A review of numerical analysis of friction stir welding’, *Prog. Mater. Sci.*, vol. 65, pp. 1–66, 2014.
- [23] Y. ZHU, G. CHEN, Q. CHEN, G. ZHANG, AND Q. SHI, ‘Simulation of material plastic flow driven by non-uniform friction force during friction stir welding and related defect prediction’, *Mater. Des.*, vol. 108, pp. 400–410, 2016.
- [24] M. WERZ AND M. SEIDENFUB, ‘Semi-analytical 1D strain-rate based friction stir welding model for predicting material flow, temperature distribution and slip’, *Math. Model. Weld Phenom.*, vol. 11, 2016.
- [25] H. SCHMIDT AND J. HATTEL, ‘A local model for the thermomechanical conditions in friction stir welding’, *Model. Simul. Mater. Sci. Eng.*, vol. 13, no. 1, pp. 77–93, 2005.
- [26] F. AL-BADOUR, N. MERAH, A. SHUAIB, AND A. BAZOUNE, ‘Coupled Eulerian Lagrangian finite element modeling of friction stir welding processes’, *J. Mater. Process. Technol.*, vol. 213, no. 8, pp. 1433–1439, 2013.
- [27] Z. ZHU, M. WANG, H. ZHANG, X. ZHANG, T. YU, AND Z. WU, ‘A Finite Element Model to Simulate Defect Formation during Friction Stir Welding’, *Metals (Basel)*, vol. 7, no. 7, p. 256, 2017.
- [28] A. TONGNE, C. DESRAYAUD, M. JAHAZI, AND E. FEULVARCH, ‘On material flow in Friction Stir Welded Al alloys’, *J. Mater. Process. Technol.*, vol. 239, pp. 284–296, 2017.

- [29] W. PAN, D. LI, A. M. TARTAKOVSKY, S. AHZI, M. KHRAISHEH, AND M. KHALEEL, 'A new smoothed particle hydrodynamics non-Newtonian model for friction stir welding: Process modeling and simulation of microstructure evolution in a magnesium alloy', *Int. J. Plast.*, vol. 48, pp. 189–204, 2013.
- [30] K. FRASER, L. ST-GEORGES, AND L. I. KISS, 'Meshfree simulation of the entire FSW process on the GPU', *11th Int. Symp. Frict. stir Weld.*, no. May, p. 15, 2016.
- [31] D. J. BENSON, 'A mixture theory for contact in multi-material Eulerian formulations', *Comput. Methods Appl. Mech. Eng.*, vol. 140, pp. 59–86, 1997.
- [32] D. J. BENSON AND S. OKAZAWA, 'Contact in a multi-material Eulerian finite element formulation', *Comput. Methods Appl. Mech. Eng.*, vol. 193, no. 39–41 SPEC. ISS., pp. 4277–4298, 2004.
- [33] DASSAULT SYSTÈMES, 'Abaqus theory manual 6.10', 2010.
- [34] G. R. JOHNSON AND W. H. COOK, 'A constitutive model and data for metals subjected to large strains, high strain rates and high temperatures', *Proc. 7th Int. Symp. Ballist.*, vol. 21, 1983.
- [35] H. SCHMIDT, J. HATTEL, AND J. WERT, 'An analytical model for the heat generation in friction stir welding', *Model. Simul. Mater. Sci. Eng.*, vol. 12, no. 1, pp. 143–157, 2003.
- [36] LIVERMORE SOFTWARE TECHNOLOGY CORPORATION, 'LS-DYNA Theory manual', 2006.



# ADVANCES IN NUMERICAL MODELLING OF LINEAR FRICTION WELDED HIGH STRENGTH STEEL CHAINS

P. S. EFFERTZ\*, F. FUCHS\*\* and N. ENZINGER\*

*\*Institute of Materials Science, Joining and Forming, Graz University of Technology, Kopernikusgasse 24/I, 8010 Graz, Austria*

*\*\*pewag Austria GmbH, Mariazeller Straße 143, 8605 Kapfenberg, Austria*

DOI 10.3217/978-3-85125-615-4-32

## ABSTRACT

The linear friction welding process is an innovative solid state joining technology enabling high quality joints in chains, thus competing with the currently in use flash butt welding (FBW) process, with none of the drawbacks related to fusion welding processes. Modelling has proven to be an indispensable tool in LFW, providing necessary insight to the process due to its rapid nature. Furthermore, no need of expensive infrastructure, welding experiments and subsequent testing is necessary. In this article, the current status of understanding and development in LFW of chains is presented via 2D and 3D models carried out in the commercial software DEFORM. The pre-processing steps are thoroughly described in terms of meshing characteristics, energy input analysis, boundary conditions, amongst others. As a result, various process outputs are presented, such as temperature evolution, flash morphology, material flow behaviour, and stress analysis. Experimental validation was carried out to assess the quality of the models. The models were able to predict the thermal evolution in the vicinity of the weld interface, as well as reproduce the phenomena behind flash formation and material flow. Finally, an outlook on numerical simulation of the process applied to chain welding is presented.

Keywords: Linear friction welding; chain welding, DEFORM; numerical simulation;

## INTRODUCTION

Flash butt welding (FBW) is the process of preference regarding chain welding [1]. However, it is not without its drawbacks since FBW is a fusion process. Therefore, welding defects related to fusion joining processes such as, slug residues, porosity, segregation or hot cracking are prone to appear [1], [2]. To overcome the shortcomings related to FBW, linear friction welding has been a subject of research in chain welding over the recent years, since it provides very clean and reproducible welds, comprising exceptional mechanical properties [3].

Linear friction welding (LFW) is a solid-state joining process in which a stationary part is forced against another that is reciprocating in a linear manner to generate frictional heat [4], [5]. Heat, along with the axial compressive forces applied perpendicular to the weld interface, results in material deformation and plasticization. Most of the plasticized material is removed from the weld through the flash, due to the combined action of applied force

and reciprocating movement. Surface oxides and other asperities are expelled from the interface, producing a clean joint. This results in a loss of length of the overall component. Towards the end of the process the parts are forged together with some plasticized material remaining at the weld line [6].

Although the process is continuous, LFW can be split into four phases [7], [8].

In the **initial phase** the two surfaces are brought into contact under external load. Interaction between the surface asperities occurs, thus generating heat due to friction. The asperities soften and deform, increasing the true contact area between the two workpieces. In this phase, negligible axial shortening (burn-off) perpendicular to the oscillation direction is observed.

In the **transition phase** the material plasticizes and becomes viscous, causing the true contact area to increase until total surface contact is established. Heat from the interface is conducted to its vicinity, plasticizing more material, and burn-off starts to occur as a result of the expulsion of viscous material.

At this point, the force, thermal profile and burn-off reach a quasi-steady-state condition and significant burn-off occurs through the rapid expulsion of viscous material through the interface. This phase is referred to as the **equilibrium phase**.

Finally, during the deceleration phase the motion is ceased in a quick, however progressive manner, to ensure alignment between the workpieces. At that time the axial force is increased to forge the two components together, which gives this phase its name: **forge phase**.

Computational modelling came a long way over the past few years, especially regarding Ti64 for aerospace applications, and more recently 30CrNiMo8 steel in the chain industry. It has proven to be an indispensable tool to give insight to the LFW process, which would not be possible with experiments alone [9], [10]. Various authors developed 2D [4], [9], [11]–[13] and 3D [14]–[18] computational models in order to predict various welding outputs, such as thermal fields [10], [13], [19], [20], flash morphology and formation rates [9], [14], [19], [21], residual stresses, strain rates [9] and microstructural characterization [22].

This paper aims to describe the numerical modelling advances within the scope of linear friction welded steel chains, by combining the advantages of 2D and 3D FEA efforts to evaluate and predict the intervening physical quantities of the process, such as temperature distribution, flash formation and shortening, and stress fields.

## EXPERIMENTAL PROCEDURE

### MATERIAL AND EQUIPMENT

The material used in the present study is a medium carbon 30CrNiMo8 high strength steel. The nominal chemical composition and mechanical properties at room temperature are given in table 1 and 2, respectively.

Dropforged half chain links were used with a cross-sectional width and height of 22 mm and 24 mm, respectively. Figure 1 illustrates the geometry of the used chain parts.

The main process parameters in LFW are the amplitude of oscillation, frequency of oscillation, and applied load during the friction and forging stages [23]. According to figure 1 the reciprocating movement is consistent with the x-direction, whereas the friction and forging load are applied along the y-direction.

**Table 1** Chemical composition of 30CrNiMo8 (wt%) [24].

Elem.	C	Si	Mn	Cr	Mo	Ni	Fe
%	0.30	0.30	0.50	2.00	0.35	2.00	Bal.

**Table 2** Mechanical properties of 30CrNiMo8 at room temperature.

$E$ (GPa)	$YS\sigma_y$ (MPa)	UTS (MPa)	$\epsilon$ (%)
210	1050	1250	9

The combination of parameters yielding the best mechanical properties was already optimized in previous investigations [3]. Hence, solely one combination is considered in the present study. Due to confidentiality reasons, the welding parameters are not presented.

The welds were carried out in a prototype machine, which is fully instrumented and allows the measurement of both normal and in-plane forces as well as displacements during the process.

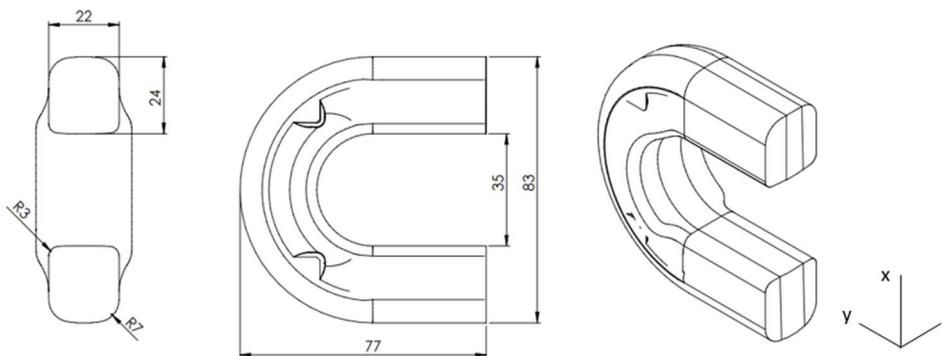


**Fig. 1** Technical drawing of the used half chain link to be welded.

To characterize the weld and geometry of the flash, light optical microscope (LOM) was used to compare with the results yielded by the numerical model. The sample welded with the aforementioned best parameter combination was embedded in cold resin, ground using SiC paper from 120 grit to 4000, and polished with a diamond suspension 3 and 1  $\mu\text{m}$ . Finally, the sample was etched using Nital 5%.

To validate the thermal evolution of the developed models, thermocouple measurements were carried out. To that end, three  $\text{Ø}0.3$  mm K-type thermocouples were installed, equally distanced from one another, placed at 3.6 mm, 4.0 mm and 4.8 mm from the interface. To fit the thermocouples, one of the links was cut in half and three  $\text{Ø}2.5$  mm channels were

milled perpendicular to the oscillation direction to accommodate the wiring. The thermocouple terminals were soldered at the desired position. Finally, the two halves were joined together and locally TIG welded as far away as possible from the weld interface, to avoid subjecting regions around the interface to thermal cycle and ensure their alignment throughout the process.

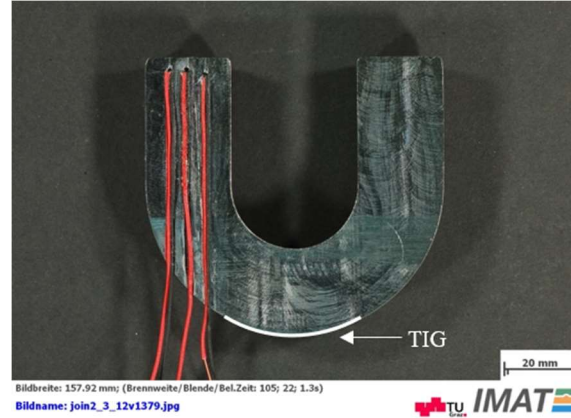


**Fig. 2** Macrograph with the positioning of the thermocouples: 3.6 mm (left), 4.0 mm (centre) and 4.8 mm (right) from the interface. The tack welding position is indicated by the white line [25].

### WELD ENERGY

Determining the energy given to the welding interface is of utmost importance to account for the friction component during the initial phase of the process. To that end, a similar approach to the one reported by Ofem et al. [26] is used, provided the fact that the machine is fully instrumented.

Using the recordings of in-plane load and displacement recorded by the machine, the energy input can be obtained. However, the load cell does not measure the in-plane load directly at the sample but rather between the clamping and servo-hydraulic system, as depicted schematically if figure 3. The instantaneous heat flux at the interface can be computed by,

$$\dot{q}'' = \frac{F_{\text{int}}^{\text{net}}(t)v(t)}{A(t)} \quad (1)$$

Where  $F_{\text{int}}^{\text{net}}(t)$ ,  $v(t)$  and  $A(t)$  is the in-plane load, velocity at the interface and contact area between the half links, at a particular time step, respectively. Applying free body analysis to the system presented in figure 3, the load in the interface can be computed by,

## Mathematical Modelling of Weld Phenomena 12

$$F_{int}^{net} = F_{int}^{total} - Ma \quad (2)$$

Notwithstanding, the mass  $M$  of the oscillatory clamping system is unknown. Hence, the LFW machine was subjected to an unloaded run to account for the inertial movement and internal friction of the tooling system  $F_{int}^0$ . The load registered was then subtracted from the results obtained when the machine is loaded with a sample and equation 2 reduces to the following,

$$F_{int}^{net} = F_{int}^{total} - F_{int}^0 \quad (3)$$

The preceding analysis requires an estimate of the velocity. This can be achieved numerically since the position at discrete values in time is known. Thus, the central finite difference is used for the first order derivative [27],

$$v(t) = \frac{|x_{t+\Delta t} - x_{t-\Delta t}|}{2\Delta t} \quad (4)$$

Where  $x_{t+\Delta t}$  and  $x_{t-\Delta t}$  denote the position at a previous and future time step;  $\Delta t$  stands for the time step size.

Finally, the total energy applied at the interface during a certain phase can be obtained as a result of the integration of equation over the phase duration  $t_{ph}$ .

$$E_{ph} = \int_0^{t_{ph}} \dot{q} A(t) dt \quad (5)$$

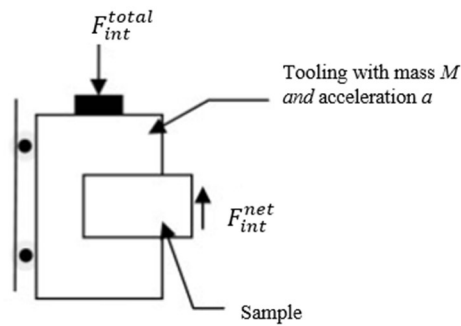


**Fig. 3** Schematic diagram of the oscillating clamping system of an LFW machine [26].



### MODELLING APPROACH

Numerical modelling of linear friction welded chains was conducted using finite element analysis (FEA) commercial software DEFORM-2D/3D 11.1 SP1. Similar to what is reported by McAndrew et al. [11], the “single-body” approach is used in both 2D and 3D models. Therefore, the numerical approach was divided into two models: purely thermal model and a coupled thermo-mechanical model. The first model represents the heating by friction in the initial phase of the process, thus serving as an initial thermal boundary condition for the thermo-mechanical model. This latter model accounts for the plastic deformation in the equilibrium phase. The mathematical formulation of the problem in hand is described in Annex A.

Unlike other studies, the initial phase during chain welding has considerable plastic deformation and is traduced in approximately 2 mm of burn-off, as reported in [25]. This has to do with the fact that the interfaces of the chains are not flat. However, deformation from the initial phase was not considered in this modelling approach. This assumption proved to be reliable, however it has to be considered during the evaluation. The models were ran until a burn-off of approximately 3 mm, which represent the total upset in the equilibrium phase.

### MATERIAL MODEL

To describe the material behaviour in the 2D and 3D models, the tabular format provided by DEFORM software was used, due to its versatility and ability to represent any material. Temperature dependent thermal conductivity and heat capacity were obtained experimentally.

The material flow stress is given as a function of strain, strain-rate and temperature [28].

$$\bar{\sigma} = f(\bar{\varepsilon}, \dot{\bar{\varepsilon}}, T) \quad (6)$$

Stress-strain curves were obtained for temperatures, strains and strain-rates up to 1400°C, 4 and 1000 s<sup>-1</sup>, respectively. Gleeble 3800 was used to characterize material flow stresses at low strain-rates and JmatPro for estimating the values at high strain rates [29]. Logarithmic interpolation was considered whenever the models surpass the defined flow stress data.

### MESH CHARACTERISTICS

In LFW most of the heat generation and plastic deformation throughout the process occurs along the weld interface. Thus for the 2D purely thermal model, an average element size of 0.2 mm was used within a 4 mm band around the interface. Outside this region, the element size was increased. The mesh of the thermo-mechanical model is obtained by merging and mirroring the purely thermal model along the interface. The mesh appearance is illustrated in figure 4(a)

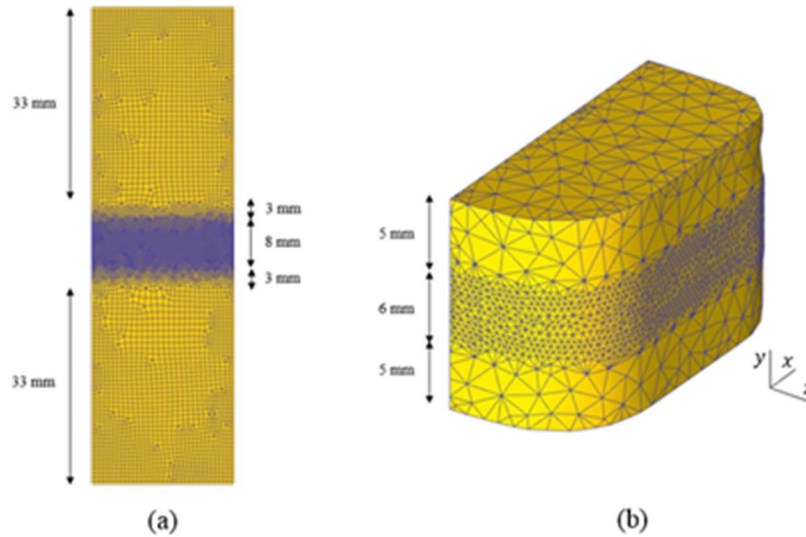


**Fig. 4** Illustration of the mesh used for the thermo-mechanical models: (a) 2D model and (b) 3D model.

The 3D purely thermal and thermo-mechanical models were discretized using 4-node tetrahedral elements, which besides fitting better the geometry, are more stable for problems dealing with high deformations. Again, the mesh was refined in the areas of interest such as in the vicinity of the welding interface. Hence for the purely thermal model a width band with 3 mm close to the interface was considered, using elements with an average size of 0.5 mm. Similar element sizes were used by Gao et al. [17] and Pashazadesh et al. [30] when modelling friction stir spot and friction stir welding, respectively. The approach described in the 2D model was also carried out to the 3D one. Hence, the mesh used on the thermo-mechanical model is a result of mirror merging the purely thermal model at the interface, and is illustrated in figure 4 (b).

#### THERMAL MODELS

The thermal models account for the effect of frictional heat during the initial phase of the process. The developed 2D and 3D models are analogous, modelled with a single plastic workpiece, although differing slightly in the way heat input is applied at the interface.

In either models the heat flux is computed using equation presented in the section “Weld energy”. As reported in [11], a uniform heat flux ( $\dot{q}$ ) was applied across most of the interface and only linearly reduced to 50% of this value from a distance away from the edge, corresponding to the amplitude. This reduction represents the effect of the oscillatory movement, where the offset between the workpieces means a lower heat input in the regions of the edges (see figure 5(a)).

## Mathematical Modelling of Weld Phenomena 12

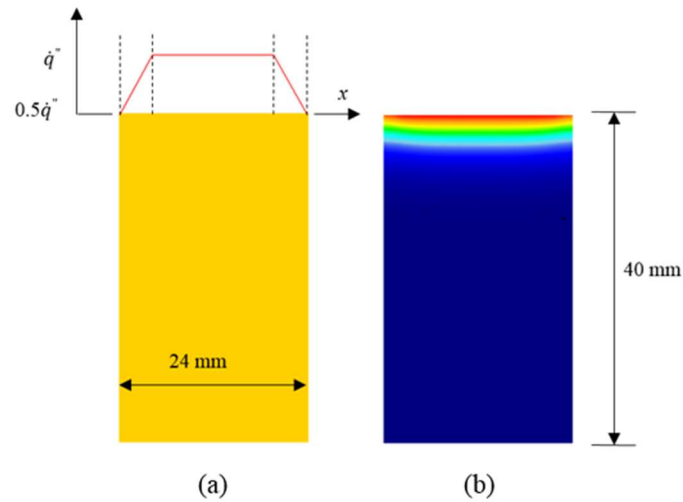


**Fig. 5** 2D thermal model: (a) applied heat flux profile; and (b) thermal profile generated at the end of the initial phase [25].

Regarding the 3D thermal model, the heat flux was not linearly reduced away from the edges, corresponding to the amplitude (a), as reported in the 2D model. Instead, a single step approach was used, where 50% of the value of  $(\dot{q}'')$  was used for half the amplitude near the edges. In order to maintain the mean energy due to contact/no-contact condition, 100% of  $(\dot{q}'')$  was considered for the remaining half of the amplitude value. Thus, the heat flux was applied as illustrated in Figure 6(a).

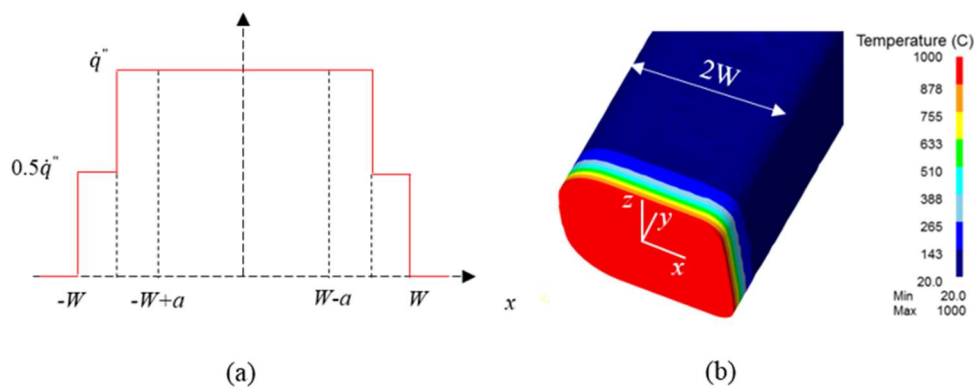


**Fig. 6** 3D thermal model: (a) applied heat flux profile; and (b) thermal profile generated at the end of the initial phase [31]

Emissivity was kept at default setting in both models, hence 0.7. The convective heat transference between the workpiece and the surroundings assumed to be  $20 \text{ W}/(\text{m}^2\text{K})$ . Bulk and medium temperatures were set to  $20 \text{ }^\circ\text{C}$ .

A simplification to the thermal model was made by not assuming the influence of the rounded edges in the overall interfacial contact throughout the process, hence the same heat flux profile was used in every point in the direction perpendicular to oscillating movement. The model was ran until a process time of 1.5s was reached, which corresponds to the end on the initial phase.

### THERMO-MECHANICAL MODELS

The 2D thermo-mechanical was set up using a plastic workpiece and two rigid dies, illustrated in figure 7(a). Plain strain condition was assumed, as the dimension of the chain perpendicular to the oscillatory movement (22 mm) can be considered to be “much larger” than the material regions under viscoplastic condition ( $\sim 3\text{mm}$ ). Additionally, the amount of material being extruded in the direction perpendicular to the reciprocating movement is comparatively lower. The model focuses on a small portion of the chain link, to reduce the number of elements employed and consequently computational time. The temperature profile obtained from the thermal model described in the previous section was mapped onto the plastic workpiece. The reciprocating movement and axial load is attributed to the upper and lower dies, respectively.

The 3D thermo-mechanical setup is analogous to 2D, apart from the fact that in the lower die the registered data of burn-off movement is used rather than load, as shown in figure 7(b). This approach enables the possibility to exploit the advantages of the Conjugate Gradient Solver, which, according to the DEFORM users' manual, computationally more advantageous in terms of reduction of simulation time and storage.

Due to the symmetry of the process not only in relation to the interface but also the  $y$  direction, half of the deformable workpiece was used to reduce computational effort even further.

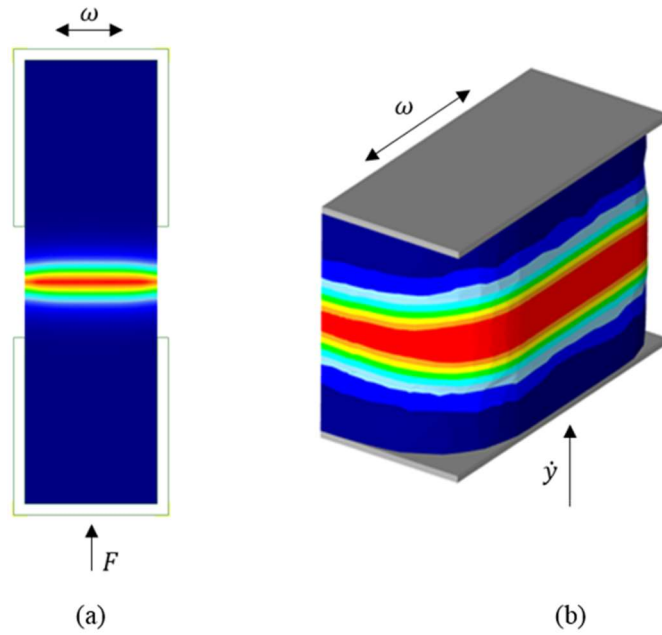


**Fig. 7** Thermo-mechanical model showing a plastic single workpiece with a mapped thermal profile and applied boundary conditions: (a) 2D model; and (b) 3D model.

## RESULTS AND DISCUSSION

### THERMAL ANALYSIS

The thermal histories were recorded every 0.5 s at the corresponding upset position to assess the adequacy of the developed models, as presented in figure 8. The predicted temperatures are presented until the end of the equilibrium phase.

For the thermocouple closest to the interface, good agreement was obtained when compared to the predicted temperatures, as shown in figure 8(a). From  $t = 1$  s to  $t = 2.5$  s, the 3D model overestimated the temperature, and a maximum temperature difference of approximately  $100^{\circ}\text{C}$  registered at the beginning of the equilibrium phase ( $t = 1.5$  s).

## Mathematical Modelling of Weld Phenomena 12

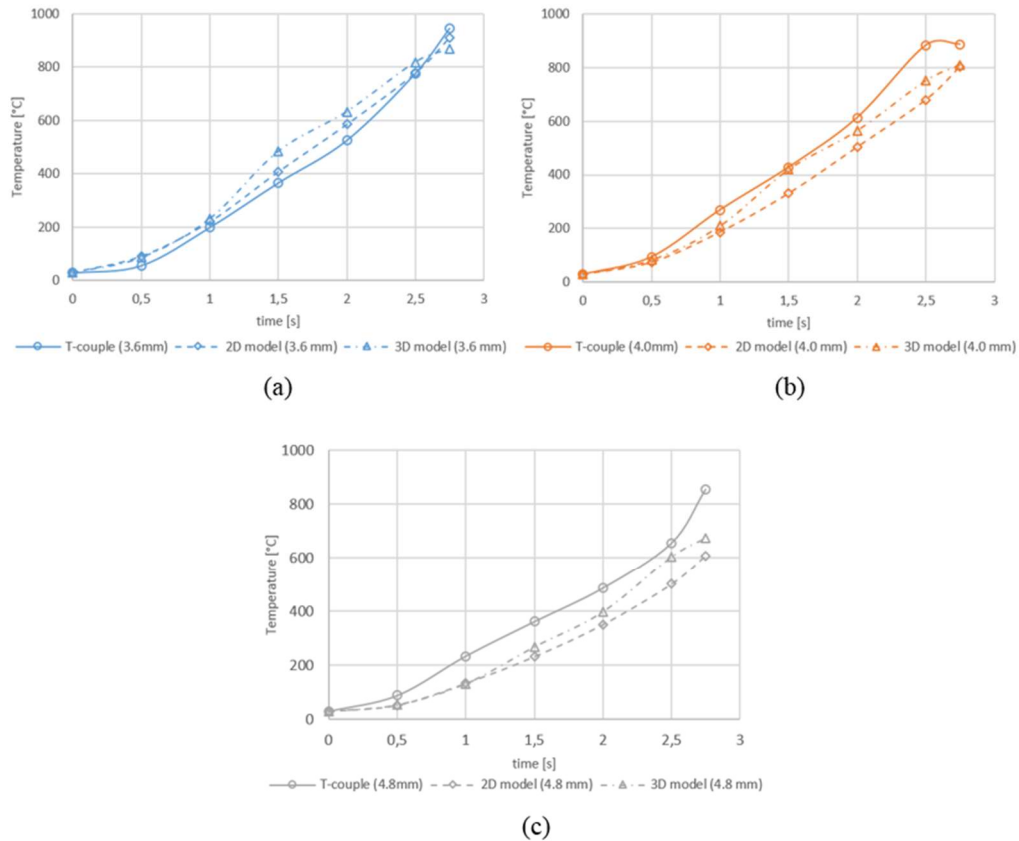


**Fig. 8** Comparison of the thermal histories between experiment and models: (a) 3.6 mm; (b) 4.0 mm; and (c) 4.8 mm.

Adequate results were also obtained between the thermocouple initially at 4.0 mm and the models. Both models underestimated the temperature at  $t = 2.5$  s. Worth mentioning is the fact that this particular thermocouple registered higher temperatures than the one closest to the interface. Although the thermocouples are mounted on the stationary part of the chain, they are under high cyclic stress due to the reciprocating movement and in-plane load. It is believed that the thermocouple did indeed move as a result, registering a higher temperature.

Finally, the highest discrepancy is acknowledged in the thermocouple furthest from the interface. However, the 3D model was able to predict more accurately the temperatures throughout the process, despite the differences at the end of the equilibrium phase.

### FLASH FORMATION

The morphology and formation of the flash is directly related to the mechanisms driving the plastic deformation. Thus, the viscous material is expelled according to two main

mechanisms: (i) the axial load steadily extruding the viscous hot layer of material from between the workpieces; and (ii) the oscillatory motion dragging material from the weld line in each stroke of the oscillation. The prevailing effect is linked to the process parameters used, namely amplitude. Thus (i) is associated with low amplitudes, whereas (ii) with high amplitudes. Furthermore, larger oscillation amplitudes produces larger ripples in the flash. The rippling effect is a result of the interaction between viscoplastic material and vertical surface of the workpiece. The vertical surface therefore drags the viscoplastic material during the reciprocating movement, creating a distinct ripple [9].

In the present case the amplitude value is not high enough to shear the viscous material. Hence, mechanism (i) occurs and the extruded material remains in constant contact with the upper and lower workpiece during oscillation. Also, the thermal profile is wide enough to accommodate the difference in strain rates, and flow stresses associated, between the interface and material being sheared by the edge. As a result, a smooth flash without rippling is formed. Figure 9 depicts the comparison between the experimental and modelling results for the flash morphology.

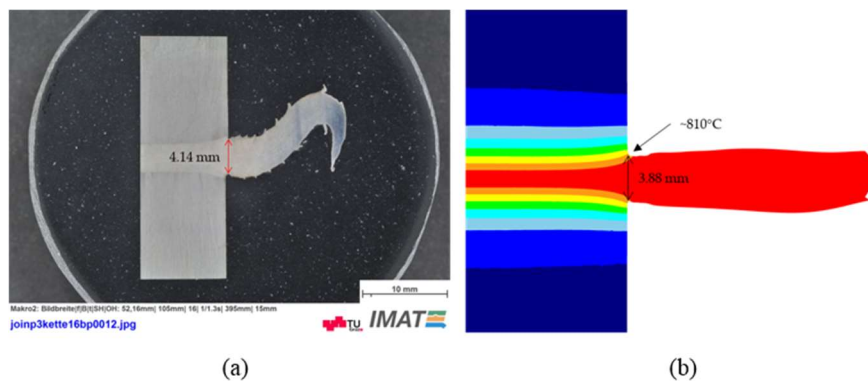


**Fig. 9** Flash morphology comparison between the (a) experimental and (b) modelled flash.

The experimental flash is characterized by a smooth surface regardless of the small rippling which has not been reproduced by the model, since the element size used is not small enough to capture these features.

Moreover, the predicted flash shows a rounded edge, in contrast with the sharp edge obtained in the experiment. This difference can be explained by the geometric properties of the chain links, as they are not completely flat as shown in figure 10. As a result, in the initial phase of the process this translates in higher pressure and local heat input, consequently plasticizing locally the material in the interface.

The flash deflects upwards and downwards with the reciprocating movement, reaching its maximum height when the amplitude is at its maximum value. At a certain length, the flash contacts the tooling, causing it to bend as shown in figure 9(a). This behaviour was not observed in the model since there is no tooling interacting with the flash.

A relatively good agreement was obtained for the flash extrusion thickness, with 4.14 mm and 3.88 mm for the experiment and model, respectively. This difference might be due

to model related assumptions, such as meshing characteristics, heat input data; and material related, like flow stress and heat conductivity data.

Worthy of note, the model showed that the boundary temperature between flash formation and negligible material flow is approximately 810°C, as shown in figure 9(b). This temperature corresponds to the Ac3 temperature of this material.

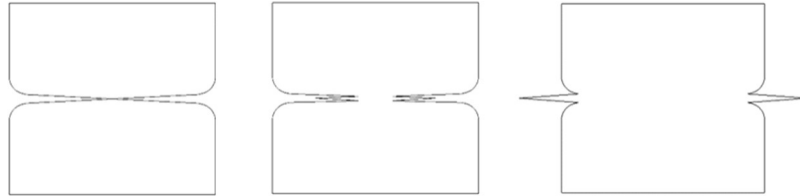


**Fig. 10** Schematic representation of the evolution of the flash formation at the interface of the chain.

Analogous to the 2D flash formation, the extruded material remains in constant contact with the upper and lower parts of the workpiece during the oscillation movement, which characterizes welds with low amplitude, unable to promote shearing. The 3D model is invaluable to understand the multi directional material flow behaviour of the process, and figure 11 shows the morphology of the flash mirrored in the z-direction at different time steps.

Figure 11(a) shows the flash appearance in the early stages of the process. Also, until approximately  $t = 0.35$  s, the flash distorts severely upwards and downwards with the oscillating movement. However, at a certain point despite the flipping movement of the flash, a preferential flow towards the moving part is acknowledged and is shown in figure 11(b). This tendency might be related due to the constant constraints imposed on the flash by self-contact and tooling contact, promoting local shearing on the base of the flash, which coupled with the pressure increase at high amplitudes redirects the flash to the moving side. Furthermore, the deflection of the flash might also be a product of the tooling effect entitled “micro-swinging”. Hence, the moving part of the chain does not move rigidly in the oscillation direction, but has a micro-swing relative to the oscillation plane instead. According to Li et al. [32] micro-swinging has a significant effect of the extrusion manner, as the swinging part ends up digging into the other promoting deflection of the flash from its centre point. On the other hand, negligible effect on the interface temperature at the centre of the weld. This phenomena can also observed in the experimental flash, according to the figure 9(a). Notice that the flash near to the extrusion zone also diverts upwards.



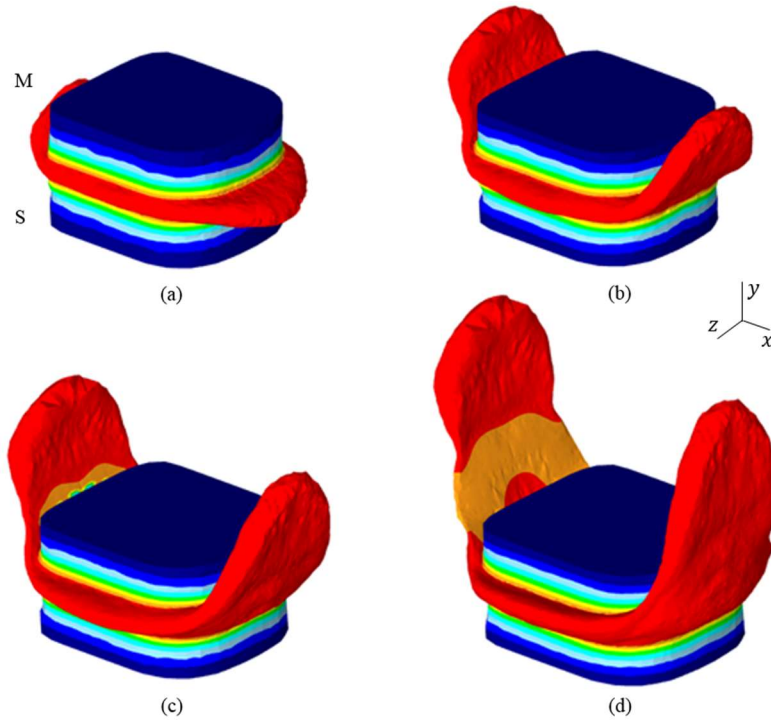


**Fig. 11** Appearance of the formed flash through different time steps: (a)  $t = 0.25$  s; (b)  $t = 0.50$  s; (c)  $t = 0.75$  s; and (d)  $t = 0.90$  s. ‘S’ and ‘M’ denote the stationary and moving components, respectively.

A further consequence of the flash extrusion evolution has to do with the self-contact observed at a certain point of the simulation process as the flash contacts the workpiece. As a result, conduction heat transfer occurs locally, causing the uneven cooling of the flash as shown in figure 11(c). Moreover, by the end of the equilibrium phase  $t = 0.90$  s illustrated in figure 11(d), one can intuitively acknowledge that the flash further away from the extrusion zone is locally colder when compared to other regions due to convection and the influence of conduction from earlier stages.

#### *Partial unbonding*

The partial unbonding phenomena was observed in the developed 3D model at low burn-off values, as depicted in figure 12. This particularity was also reported by McAndrew et al. [33] and Addison [34], and is known to compromise mechanical properties, ultimately leaving a notch that acts as a crack propagation site. Unbonding was observed solely in the corners of the cross-section with lower radii, suggesting that there might be a critical radius at which partial unbonding is prone to occur. Nonetheless, as the model progressed the heat provided to these regions provided by the flash and interface due to conduction, caused the corners to soften and plastically deform, thus resulting in a defect free bond.

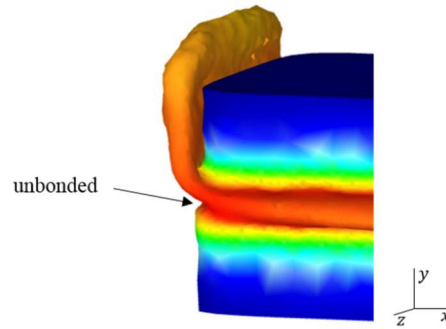


Fig. 12 FEA appearance of partial unbonding at the interface [31].

#### BURN-OFF ANALYSIS

The interest in studying and predicting the rate of material expelled as flash is of great importance, as it is related to the upsetting process. To that end, a burn-off analysis was solely carried out to the 2D model since it is load controlled, whereas the 3D model is stroke controlled. Hence, in the latter case makes no sense to study the burn-off rate.

To evaluate the burn-off throughout the process, point tracking was used, as shown in figure 13 specified by  $P_1$ . The model predicted a linear axial shortening, typical of the LFW process in the equilibrium phase, where quasi-steady state conditions are achieved in steel. Figure 14 relates the burn-off as a function of time for the experiment and model. A comparable result is acknowledged, with an experimental and predicted burn-off rate of 3.08 mm/s and 3.13 mm/s, respectively. Despite the good agreement, it is clear that in the initial instants of the equilibrium phase the model does not upset in the same rate as experimentally, which suggests that the prescribed interface temperature resulting from the purely thermal model is low. Hence, the material flow until 0.25 s was underestimated. Steady state burn-off is observed throughout the remainder of the equilibrium phase and comparable upset was reached between model and experiment.

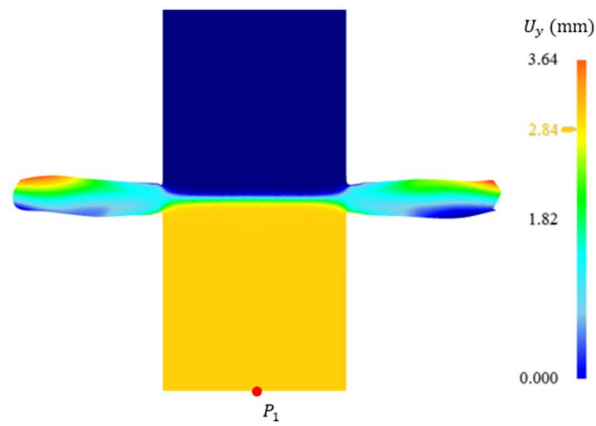


Fig. 13 2D FEA axial displacement with point tracking  $P_1$ .

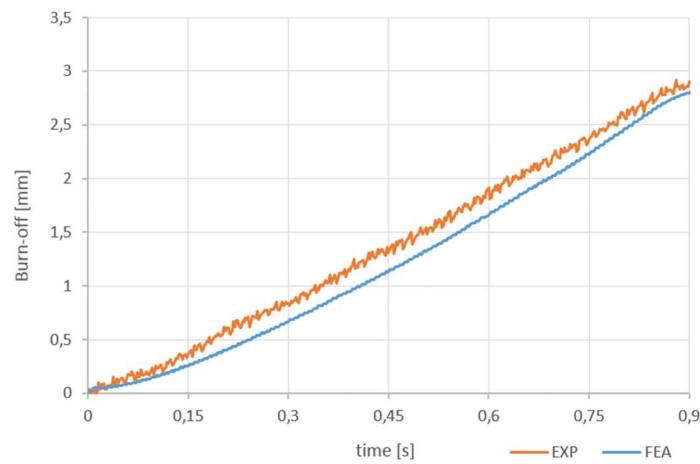


Fig. 14 Comparison between experimental and predicted burn-off histories.

## CONCLUSIONS

A summary of the main findings and advances in LFW of chains, followed by an outlook for further research within this subject, is presented in this section. This should allow the reader to appreciate the benefits of numerical modelling in LFW process for joining 30CrNiMo8 high strength steel chains, envisioning further process development and exploitation.

### SUMMARY

This paper describes the use of 2D and 3D modelling approaches to evaluate and predict the intervening physical quantities of the LFW process when joining 30CrNiMo8 high strength steel half chain links. The key findings and advances are listed below:

- Comparable results were obtained with thermocouple measurements and FE models. Nonetheless, a slight temperature offset was acknowledged for the setting furthest from the interface. In all situations, the temperature predicted by the 3D model is slightly higher than the 2D model.
- A 2D and 3D finite element modelling for the LFW of 30CrNiMo8 high strength steel chains has been formulated, using an optimized welding parameter combination, in order to predict the thermal and mechanical characteristics. This was achieved by means of a purely thermal and thermo-mechanical model. A very good agreement between reality and model was achieved without application of a single fit parameter.
- For either models, the flash showed a smooth morphology which is in accordance with experimental observation apart from the slight rippling effect observed in the experiment. This smooth pattern in the simulation is related to low process parameters which yield low energy input.
- The local plasticization of the material due to the uneven surface of the experimental interface meant that the morphology of edges between experimental and predicted flash did not match perfectly.
- The mechanism that prevails for the set of parameters in this study, is dictated by the forging load, steadily extruding viscous material from the interface.
- Partial unbonding phenomena was observed via the 3D model, solely in the corners of the cross-section with lower radii, suggesting that there might be a critical radius at which partial unbonding can occur. However, unbonding proved not to be an issue as the process heat input is high enough. Partial unbonding was only observed for low burn-off values.
- The 2D model predicted a linear axial shortening, typical of the LFW process in the equilibrium phase, where quasi-steady state conditions are achieved. Very good agreement was obtained with an experimental and predicted burn-off rate of 3.08 mm/s and 3.13 mm/s, respectively.

### OUTLOOK

Despite the recent advances in modelling and comprehending the linear friction welding process applied to chains, there are still several knowledge gaps that need to be tackled. Some of which are:

- Residual stress analysis: modelling can be used to predict the impact of the processing conditions, such as the workpiece geometry, amplitude, frequency, axial load, on the formation and magnitude of residual stresses in linear friction welds. Figure shows some preliminary results on residual stresses after cooling and before PWHT. However, the next step is to validate the obtained results.

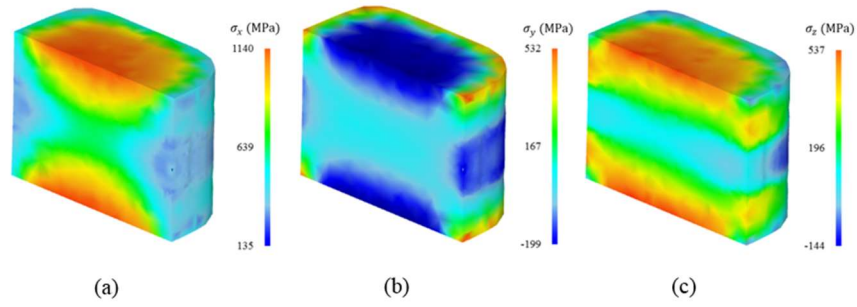


**Fig. 15** FEA results for residual stresses: (a)  $\sigma_x$ ; (b)  $\sigma_y$ ; and (c)  $\sigma_z$ .

- **Microstructure modelling:** Models could be used to investigate the impact of the processing conditions on the microstructure evolution. This would allow for the effects of the processing conditions on different phases, average grain size and their spatial distribution [35].
- **Influence of interface geometry:** Most of the modelling effort has been put into planar interface geometries. However, the influence of the interface geometry (e.g. bevels angles) on LFW chains should be assessed and optimized to reduce flash formation and ultimately curtail the amount of scrap generated during production.

### ACKNOWLEDGEMENTS

The authors gratefully acknowledge the financial support of this work by the project JOIN. The K-Project Network of Excellence for Joining Technologies JOIN is fostered in the frame of COMET – Competence Centers for Excellent Technologies by BMVIT, BMWFJ, FFG, Land Oberösterreich, Land Steiermark, SFG and ZIT. The program COMET is handled by FFG.

### ANNEX A. MATHEMATICAL FORMULATION

The thermal analysis is governed by the diffusion equation with thermo-mechanical heat source term given by equation [36].

$$\rho c_p \dot{T} = (kT_{,i})_{,i} + \eta \sigma_{ij} \dot{\epsilon}_{ij} \quad (7)$$

Where  $c_p$  is the specific heat capacity,  $k$  the thermal conductivity,  $\sigma_{ij}$  the stress tensor and  $\dot{\epsilon}_{ij}$  is the strain rate tensor. The terms  $\rho c_p \dot{T}$  and  $(kT_{,i})_{,i}$  represent the internal energy and heat transfer rates, respectively. “ $i$ ” denotes the differentiation in  $i$ . The energy balance can be rewritten in the variational form as [37]:

$$\int_V kT_{,i}\delta T_{,i} + \int_V \rho c_p \dot{T} dV - \int_S q_n \delta T dS - \int_V \eta \sigma_{ij} \dot{\epsilon}_{ij} \delta T dS = 0 \quad (8)$$

where  $q_n$  is the heat flux over surface  $S$ . The term  $\eta$  is related to the fraction of mechanical work that is converted into heat, which in the case of the purely thermal model is not considered, as no plastic deformation is considered. In this case equation 7 reduces to:

$$\int_V kT_{,i}\delta T_{,i} + \int_V \rho c_p \dot{T} dV - \int_S q_n \delta T dS \quad (9)$$

It is, however, taken into account in the thermo-mechanical model and assumed to be  $\eta = 0.9$ . The fraction of remainder plastic deformation energy is associated with changes in dislocation density, (sub-)grain boundary generation and migration, and phase transformation and evolution [30].

In an FE framework, the energy balance can be discretized into:

$$[C]\{\dot{T}\} + [K]\{T\} = \{Q\} \quad (10)$$

where  $[C]$  is the heat capacity matrix,  $[K]$  the conductivity matrix,  $\{Q\}$  the vector accounting for all thermal sources in the system,  $\{T\}$  and  $\{\dot{T}\}$  are the nodal temperature and temperature rate vectors, respectively.

The temperature rate at the beginning of a time increment can be obtained according to equation 10.

$$\{\dot{T}\}_i = [C]^{-1} (\{Q\} - [K]\{T\}_i) \quad (11)$$

DEFORM uses an implicit dynamic procedure designed for metal forming processes. Thus, the temperature equation can be given as [38], [39]:

$$\{T\}_{i+1} = \{T\}_i + \Delta t \left( (1 - \beta) \{\dot{T}\}_i + \beta \{\dot{T}\}_{i+1} \right) \quad (12)$$

Where  $\beta$  specifies the forward integration coefficient for temperature integration over time, and varies between 0 and 1. The default value of 0.75 is adequate for most simulations [28].

Regarding the mechanical analysis, rigid-viscoplastic finite element approach was considered using the variational principle.

The rigid-viscoplastic material is an idealization of an actual one, by neglecting the elastic response. The rigid viscoplastic material, which was introduced for the analytical convenience, simplifies the solution process with less demanding computational procedure. Moreover, it seems that the idealization offers excellent solution accuracies due to the negligible effects of elastic response at large strain in the actual material. Hence, this

simplification is especially suitable for metal forming analysis at high temperatures, in which LFW is included [40].

The variational approach requires that among admissible velocities  $u_i$  that satisfy the conditions of compatibility and incompressibility, as well as velocity boundary conditions, the actual solution gives the following functional a stationary value [41]:

$$\pi = \int_V E(\dot{\epsilon}_{ij}) dV - \int_{S_F} F_i u_i dS \quad (13)$$

where  $F_i$  represents surface tractions, and  $E(\dot{\epsilon}_{ij})$  is the work function expressed by [42]:

$$E(\dot{\epsilon}) = \int_0^{\dot{\epsilon}} \bar{\sigma} d\dot{\epsilon} \quad (14)$$

where  $\bar{\sigma}$  is the effective stress, and  $\dot{\epsilon}$  is the effective strain-rate. The solution of the original boundary-value problem is then obtained from the solution of the dual variational problem, where the first-order variation of the functional vanishes, namely,

$$\delta\pi = \int_V \bar{\sigma} \delta\dot{\epsilon} dV - \int_{S_F} F_i \delta u_i dS = 0 \quad (15)$$

with  $\bar{\sigma} = \bar{\sigma}(\bar{\epsilon}, \dot{\epsilon})$  for rigid-viscoplastic materials. The incompressibility constraint on admissible velocity fields is removed by introducing a penalized form of the incompressibility in the variation of the functional. Therefore, the actual velocity field is determined from the stationary value of the variation as follows [15],

$$\delta\pi = \int_V \bar{\sigma} \delta\dot{\epsilon} dV + K \int_V \dot{\epsilon}_v \delta\dot{\epsilon}_v - \int_{S_F} F_i \delta u_i dS = 0 \quad (16)$$

where  $K$  is the penalty constant, which should be a large positive value for incompressibility; and  $\dot{\epsilon}_v = \dot{\epsilon}_{ii}$  is the volumetric strain-rate [41].

## REFERENCES

- [1] K. MUCIC, N. ENZINGER, AND F. FUCHS, "Linear Friction Welding of High Strength Chains," *Trends Weld. Res. Proc. 9th Int. Conf.*, pp. 752–756, 2013.
- [2] C. ÇETINKAYA AND U. ARABACI, "Flash butt welding application on 16MnCr5 chain steel and investigations of mechanical properties," *Mater. Des.*, vol. 27, no. 10, pp. 1187–1195, 2006.
- [3] K. MUCIC, F. FUCHS, AND N. ENZINGER, "Process optimization for linear friction welding of high strength chain," in *EUROJOIN Conference*, 2012, pp. 157–166.

- [4] X. SONG, M. XIE, F. HOFMANN, T. S. JUN, T. CONNOLLEY, C. REINHARD, R. C. ATWOOD, L. CONNOR, M. DRAKOPOULOS, S. HARDING, AND A. M. KORSUNSKY, “Residual stresses in Linear Friction Welding of aluminium alloys,” *Mater. Des.*, vol. 50, pp. 360–369, 2013.
- [5] I. BHAMJI, M. PREUSS, P. L. L. THREADGILL, AND A. C. C. ADDISON, “Solid state joining of metals by linear friction welding: a literature review,” *Mater. Sci. Technol.*, vol. 27, no. 1, pp. 2–12, 2011.
- [6] I. BHAMJI, M. PREUSS, R. J. MOAT, P. L. THREADGILL, AND A. C. ADDISON, “Linear friction welding of aluminium to magnesium,” *Sci. Technol. Weld. Join.*, vol. 17, no. 5, pp. 368–374, 2012.
- [7] A. VAIRIS AND M. FROST, “On the extrusion stage of linear friction welding of Ti 6Al 4V,” *Mater. Sci. Eng. A*, vol. 271, no. 1–2, pp. 477–484, 1999.
- [8] A. VAIRIS AND M. FROST, “High frequency linear friction welding of a titanium alloy,” *Wear*, vol. 217, no. 1, pp. 117–131, 1998.
- [9] R. TURNER, J. C. GEBELIN, R. M. WARD, AND R. C. REED, “Linear friction welding of Ti-6Al-4V: Modelling and validation,” *Acta Mater.*, vol. 59, no. 10, pp. 3792–3803, 2011.
- [10] A. R. MCANDREW, P. A. COLEGROVE, A. C. ADDISON, B. C. D. FLIPO, AND M. J. RUSSELL, “Energy and Force Analysis of Ti-6Al-4V Linear Friction Welds for Computational Modeling Input and Validation Data,” *Metall. Mater. Trans. A Phys. Metall. Mater. Sci.*, vol. 45, no. 13, pp. 6118–6128, 2014.
- [11] A. R. MCANDREW, P. A. COLEGROVE, A. C. ADDISON, B. C. D. FLIPO, AND M. J. RUSSELL, “Modelling the influence of the process inputs on the removal of surface contaminants from Ti-6Al-4V linear friction welds,” *Mater. Des.*, vol. 66, no. PA, pp. 183–195, 2015.
- [12] A. VAIRIS AND M. FROST, “Modelling the linear friction welding of titanium blocks,” *Mater. Sci. Eng. A*, vol. 292, no. 1, pp. 8–17, 2000.
- [13] W.-Y. LI, T. MA, AND J. LI, “Numerical simulation of linear friction welding of titanium alloy: Effects of processing parameters,” *Mater. Des.*, vol. 31, no. 3, pp. 1497–1507, 2010.
- [14] J. SORINA-MÜLLER, M. RETTENMAYR, D. SCHNEEFELD, O. RODER, AND W. FRIED, “FEM simulation of the linear friction welding of titanium alloys,” *Comput. Mater. Sci.*, vol. 48, no. 4, pp. 749–758, 2010.
- [15] G. BUFFA, M. CAMMALLERI, D. CAMPANELLA, AND L. FRATINI, “Shear coefficient determination in linear friction welding of aluminum alloys,” *Mater. Des.*, vol. 82, pp. 238–246, 2015.
- [16] Y. MAO, L. KE, F. LIU, Q. LIU, C. HUANG, AND L. XING, “Effect of tool pin eccentricity on microstructure and mechanical properties in friction stir welded 7075 aluminum alloy thick plate,” *Mater. Des.*, vol. 62, pp. 334–343, 2014.
- [17] Z. GAO, J. T. NIU, F. KRUMPHALS, N. ENZINGER, S. MITSCHKE, AND C. SOMMITSCH, “FE modelling of microstructure evolution during friction stir spot welding in AA6082-T6,” *Weld. World*, vol. 57, no. 6, pp. 895–902, 2013.
- [18] W. LI, F. WANG, S. SHI, T. MA, J. LI, AND A. VAIRIS, “3D Finite Element Analysis of the Effect of Process Parameters on Linear Friction Welding of Mild Steel,” *J. Mater. Eng. Perform.*, vol. 23, no. 11, pp. 4010–4018, 2014.
- [19] E. CERETTI, L. FRATINI, C. GIARDINI, AND D. LA SPISA, “Numerical modelling of the linear friction welding process,” *Int. J. Mater. Form.*, vol. 3, no. SUPPL. 1, pp. 1015–1018, 2010.
- [20] R. TURNER, R. M. WARD, R. MARCH, AND R. C. REED, “The magnitude and origin of residual stress in Ti-6Al-4V linear friction welds: An investigation by validated numerical modeling,” *Metall. Mater. Trans. B Process Metall. Mater. Process. Sci.*, vol.



- 43, no. 1, pp. 186–197, 2012.
- [21] F. SCHROEDER, R. M. WARD, R. P. TURNER, M. M. ATTALLAH, J. GEBELIN, AND R. C. REED, “Linear friction welding of titanium alloys for aeroengine applications: modelling and validation,” *9th Int. Conf. Trends Weld. Res.*, no. January, pp. 886 – 892, 2012.
- [22] M. GRUJICIC, R. YAVARI, J. S. SNIPES, S. RAMASWAMI, C. F. YEN, AND B. A. CHEESEMAN, “Linear friction welding process model for carpenter custom 465 precipitation-hardened martensitic stainless steel,” *J. Mater. Eng. Perform.*, vol. 23, no. 6, pp. 2182–2198, 2014.
- [23] M. MAALEKIAN, “Friction welding - critical assessment of literature,” *Sci. Technol. Weld. Join.*, vol. 12, no. 8, pp. 738–759, 2007.
- [24] BÖHLER, “Heat Treatable Steel Böhler V145.”
- [25] P. S. EFFERTZ, F. FUCHS, AND N. ENZINGER, “Modelling the flash formation of linear friction welded 30CrNiMo8 high strength steel chains,” *Int. J. Adv. Manuf. Technol.*, 2017.
- [26] U. U. OFEM, P. A. COLEGROVE, A. ADDISON, AND M. J. RUSSELL, “Energy and force analysis of linear friction welds in medium carbon steel,” *Sci. Technol. Weld. Join.*, vol. 15, no. 6, pp. 479–485, 2010.
- [27] E. KREYSZIG, *Advanced Engineering Mathematics: Maple Computer Guide*, 8th ed. New York, NY, USA: John Wiley & Sons, Inc., 2000.
- [28] SFTC, “DEFORM v11.1 SP1 System Documentation.” .
- [29] M. STUMMER, “Eigenschaften von 30CrNiMo8 für die Simulation,” TU Graz, 2014.
- [30] H. PASHAZADEH, J. TEIMOURNEZHAD, AND A. MASOUMI, “Numerical investigation on the mechanical, thermal, metallurgical and material flow characteristics in friction stir welding of copper sheets with experimental verification,” *Mater. Des.*, vol. 55, no. March, pp. 619–632, 2014.
- [31] P. EFFERTZ, F. FUCHS, AND N. ENZINGER, “3D Modelling of Flash Formation in Linear Friction Welded 30CrNiMo8 Steel Chain,” *Metals (Basel)*, vol. 7, no. 10, p. 449, 2017.
- [32] W. LI, J. GUO, X. YANG, T. MA, AND A. VAIRIS, “The effect of micro-swinging on joint formation in linear friction welding,” *J. Eng. Sci. Technol. Rev.*, vol. 7, no. 5, pp. 55–58, 2014.
- [33] A. R. MCANDREW, P. A. COLEGROVE, B. C. D. FLIPO, AND C. BÜHR, “3D modelling of Ti-6Al-4V linear friction welds,” *Sci. Technol. Weld. Join.*, no. December, pp. 1–9, 2016.
- [34] A. C. ADDISON, “Linear friction welding information for production engineering,” *TWI Industrial Member Report Summary*, vol. 961, TWI, Granta Park, UK, 2010.
- [35] A. R. MCANDREW, P. A. COLEGROVE, C. BÜHR, B. C. D. FLIPO, AND A. VAIRIS, “A literature review of Ti-6Al-4V linear friction welding,” *Prog. Mater. Sci.*, vol. 92, no. October, pp. 225–257, 2018.
- [36] H. SCHMIDT AND J. HATTEL, “A local model for the thermomechanical conditions in friction stir welding,” *Model. Simul. Mater. Sci. Eng.*, vol. 13, no. 1, pp. 77–93, 2005.
- [37] L. YANG, “Modelling of the Inertia Welding of Inconel 718,” *Dep. Metall. Mater.*, no. January, p. 160, 2010.
- [38] J. S. SUN, K. H. LEE, AND H. P. LEE, “Comparison of implicit and explicit finite element methods for dynamic problems,” *J. Mater. Process. Technol.*, vol. 105, no. 1–2, pp. 110–118, 2000.
- [39] T. J. R. HUGHES, *The Finite Element Method: Linear Static and Dynamic Finite Element Analysis (Dover Civil and Mechanical Engineering)*. Dover Publications, 2000.
- [40] S. I. OH, “Finite element analysis of metal forming processes with arbitrarily shaped dies,” *Int. J. Mech. Sci.*, vol. 24, no. 8, pp. 479–493, 1982.
- [41] S. KOBAYASHI, S.-I. OH, AND T. ALTAN, “Metal forming and the finite element method ,”

## Mathematical Modelling of Weld Phenomena 12

- vol. 4 . Oxford Univ. Press , New York, NY [u.a.] , 1989.
- [42] R. HILL, "New horizons in the mechanics of solids," *J. Mech. Phys. Solids*, vol. 5, pp. 66–74, 1956.

*intentionally blank page*

*intentionally blank page*

*intentionally blank page*

*intentionally blank page*

*intentionally blank page*

*intentionally blank page*



*intentionally blank page*

*intentionally blank page*

*intentionally blank page*

*intentionally blank page*

*intentionally blank page*

*intentionally blank page*

*intentionally blank page*

# A PROPOSAL FOR THERMAL COMPUTATIONAL MODEL FOR API 5L-X80 STEEL FRICTION STIR WELDS BASED ON THERMOCOUPLES MEASUREMENTS

G. G. DE SOUSA\*, M. MONTOYA\*, N. BOUCHONNEAU\*,  
T. F. C. HERMENEGILDO\* and T. F. A. SANTOS\*

*\*Universidade Federal de Pernambuco, Av. da Arquitetura, s/n, Post Code: 50740-550, Recife, Brazil,  
<https://orcid.org/0000-0003-2273-0760>, \* [tiago.felipe@ufpe.br](mailto:tiago.felipe@ufpe.br)*

DOI 10.3217/978-3-85125-615-4-33

## ABSTRACT

This work aims to validate a computational model suitable for predicting temperature distribution of API 5L-X80 steel welded joints manufactured by Friction Stir Welding. The model was verified through comparative analysis between experimental data and a computational model generated from a commercial finite element method software. The testing data was acquired by temperature measurements, using thermocouples positioned equally spaced along a workpiece plate of 12 mm thick during the welding process. The experiment was conducted with two different sets of heat inputs and rotational pin speeds: a joint with heat input of 1.69 KJ.mm<sup>-1</sup> and 300 rpm (cold joint), and the other with a heat input of 1.91 KJ.mm<sup>-1</sup> and 500 rpm (hot joint). Temperature data was processed and used to preview the material's thermal cycle. The computational model was developed using the COMSOL Multiphysics® software, as the heat source was considered stationary in a Eulerian model. The model was calibrated for both joints and comparison between measured temperatures with thermocouples results have showed significant similarities when the maximum simulated thermal cycles and the experimental temperature data are compared. The thermal model was also used to predict maximum temperatures the thermal history for points of the welded region where is physically impossible to perform experimental temperature measurements due to the presence of the pin and the tool's shoulder.

Keywords: Friction Stir Welding, Computational Modelling, API 5L-X80 Steel Joints

## INTRODUCTION

Friction stir welding (FSW) is a solid-state welding and joining process, developed and patented by The Welding Institute (TWI) in 1991 [1]. This manufacturing process has been successfully conducted in aluminum, titanium, copper, zinc and lead alloys. Advantages in employing FSW, among others, are: joints with superior mechanical properties due to dynamic re-crystallization and minor distortions in the workpiece [2], leading to a less damaging manufacturing process and stable union of the joint; an environmentally harmless process, producing few machining waste and requiring minimum or no surface cleaning.



Recently, the attention of shipbuilding industries and petrochemical producers was drawn towards the feasibility of friction stir welding high temperature alloys such as steels stainless steels and High Strength Low Alloy (HSLA) steels [3-5]. HSLA steels such as the API 5L-X80 are more suitable to pipeline and offshore construction owing to a combination of suitable microstructure and strength, making this type of material more adequate for oil and gas pipelines [6,7]. These steels are characterized by low carbon content, which results in higher tenacity in the HAZ after welding processes, and by the presence of alloying elements, such as Nb, V, Ti, Cr, Mo, Ni and B [8].

The API 5L-X80 used in this study has a carbon equivalent (C.E) of 0,17 following the API 1104 standard [9]. This provides a good weldability index for this material and the possibility of application in a future industrial production line using FSW. The increasing necessity for a FSW computational model, in order to provide an understanding of the thermal phenomena of X80 welding joints manufactured by this process, was the driving force for this work. The adequate microstructure, which allows high structural commitment depends on welding thermal cycles whichever the process, but specially friction stir welding that combines high degree of deformation and elevated temperature. Due to this fact, this work focuses on validating a computational thermal model proposed to preview temperature distribution and thermal cycles in the advancing side of API 5L-X80 steel welds manufactured by FSW. Computational pure thermal models are some of the accessible approach to predict thermal cycles in FSW. They provide a practical and straightforward perception of the heat distribution along the welding line [10]. In this work, the advancing side was chosen owing to be a major concern regarding the nugget integrity, where a zone of high hardness tends to appear at high cooling rates [11].

**Table 1** The API 5L-X80 steel chemical composition used in this study (wt%)

C	Nb	Al	Mn	V	Si	B	Cu
0,05	0,066	0,035	1,76	0,025	0,17	0,03	0,02
P	S	Cr	Ni	Ti	N	Ca	Mo
0,016	0,002	0,15	0,02	0,016	0,0059	0,003	0,20

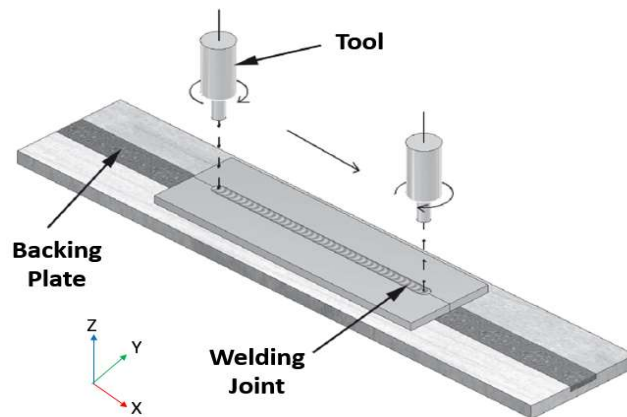


**Fig. 1** Schematics of the FSW process showing the tool's shoulder moving along the joint, adapted from Santos *et al.* [12].

EXPERIMENTAL PROCEDURE

WELDING AND THERMAL HISTORY ACQUISITION

The welded joints were produced from two X80 plates of  $110 \times 400 \times 12$  mm, which were placed in a ceramic backing plate and butt welded along their largest dimension, resulting in weld of 380 mm in length, as illustrated in Fig. 1. Due to the dimensional limitations of the PCBN pin's length (5.7 mm) ceramic tool used, the joints were manufactured by two welding passes, one on each side of the plate. After the welding procedure, the PCBN tool's structural integrity was visually verified, neither wear nor broken fragments were found on the pin and shoulder surface. To measure the thermal history at specific locations, an experimental setup was developed with eight K type thermocouples attached to both sides of the joint, positioned at 2 mm below the surface of the plate. During the welding procedure temperature measurements were carried out with these thermocouples positioned along the workpiece, at distances of 6, 8, 10 and 12 mm from the welding line. Fig. 2 has the detailed arrangement of the thermocouples used during the welding procedure. Although there are minor reports regarding the estimation of energy imposed in the FSW process, the heat input was calculated by the following equation:

$$HI = \left( \frac{\omega \cdot M}{1000 \cdot u_{welding}} \right) \cdot \eta \quad (1)$$

The welding procedure was conducted with a set of parameters leading to a lower heat input of  $1.69 \text{ kJ.mm}^{-1}$  (cold joint), and a greater heat input of  $1.91 \text{ kJ.mm}^{-1}$  (hot joint). Values of tool's translational speed ( $u$ ), rotational speed ( $\omega$ ) and the input torque ( $M$ ) were calculated and acquired by experimental data and are shown in Table 2. The acquisition data from the input parameters used in the FSW process was recorded and analyzed to measure maximum temperatures and to generate thermal cycles for each joint.

**Table 2** FSW Experimental parameters – Hot Joint and Cold Joint

Weld Joint	Heat Input [kJ.mm <sup>-1</sup> ]	$u$ - Welding Speed [m.s <sup>-1</sup> ]	$\omega$ - Rotational Speed [rpm]	$F$ - Axial Force [kN]
Hot	1.91	1.67	500	35.8
Cold	1.69	2.00	300	29.8

## Mathematical Modelling of Weld Phenomena 12

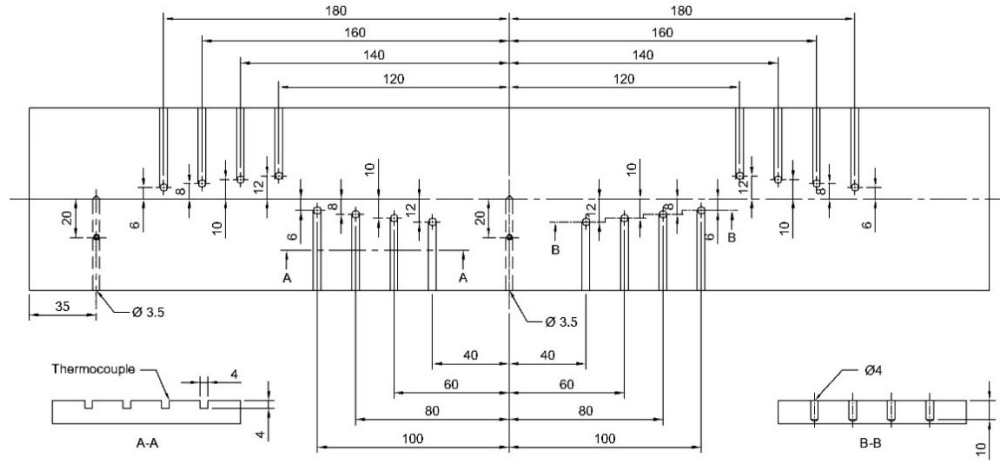


**Fig. 2** Thermocouple arrangement used during the FSW experimental setup.

### COMPUTATIONAL THERMAL MODELLING

A computational thermal model was developed using the COMSOL Multiphysics® heat transfer module. Being previously calibrated, the model is proposed to preview temperature distribution and thermal history in the advancing side of the welds at positions/distances from the welding line where is physically/extremely difficult to conduct temperature measurements by thermocouples due to the presence of the pin and shoulder. In order to reduce the processing time of the computational calculations the model geometry is considered to be symmetric along the welding line, and thus half of the joint was modelled and enmeshed. More details can be found in Fig. 3.

The following equation defines the heat transfer in the plate, with the above assumption:

$$\nabla(-k \cdot \nabla T) = Q - \rho \cdot C_p \cdot u \cdot \nabla T \quad (2)$$

The stationary heat source, with a 90% efficiency ( $\eta = 0.90$ ) [13], was modelled based on previous works of Song and Kovacevic [14] and Schmidt and Hattel [10], in which a flat shoulder, with no tilt angle, contributes to a surface heat flux (purely frictional) and the pin shares a volumetric heat contribution. The tool was modelled having a conical pin with the following dimensions:  $R_p = 5$  mm,  $R_{tip} = 1.8$  mm  $H_p = 5.7$  mm being the pin's radius, the pin's tip radius and the pin's height. The pin's heat contribution is considered to be:

$$Q_{pin} = \left( \frac{f_{pin} \cdot M \cdot \omega}{V_{pin}} \right) \cdot \eta \quad (3)$$

## Mathematical Modelling of Weld Phenomena 12

In the pin's equation the  $f_{pin}$  is the factor related to the percentage heat generation from the pin and estimated to be  $\approx 20\%$  according to Colegrove [15],  $\omega$  is the tool's rotational speed ( $\text{rev min}^{-1}$ ), and  $M$  is the average torque measured in welding ( $\text{Nm s}^{-1}$ ).

The shoulder geometry was modelled as:  $R_{shoulder} = 12.0$  mm and  $H_{shoulder} = 5.7$  mm. The total heat expression at the shoulder/workpiece interface can be defined by:

$$Q_{shoulder} = \omega \cdot r \left[ (1 - \delta) \mu \cdot \tau_{friction} + \delta \cdot \tau_{yield} \right] \cdot \eta \quad (4)$$

In this equation:  $r$  is the radial distance from the tool's center axis to the tool's shoulder,  $\mu$  is friction coefficient,  $\tau_{friction}$  is the forging pressure related to the applied normal force, and  $\delta$  is the contact variable which balances the heat generated by plastic deformation ( $\tau_{yield}$ ) and by friction ( $\tau_{friction}$ ). In this work we assume the contact condition ( $\tau_{contact}$ ) being independent of temperature, strain rate and also being in equilibrium with the pressure distribution ( $\tau_{friction}$ ), leading to a value of  $\delta = 0$ . This previous assumption leads to a sliding condition:

$$Q_{shoulder} = (1 - f_{pin}) \cdot \omega \cdot r \cdot \mu \cdot \tau_{friction}, \quad \tau_{friction} = \frac{F_N}{A_s} \quad (5)$$

In which  $F_N$  is the forging pressure, and  $A_s$  is the shoulder's surface area. The friction coefficient is considered to be variable during the welding, to simplify a value of  $\mu = 0,4$  was chosen as used by [14]

The FSW is, innately, a solid-state manufacturing process, with the workpiece reaching 70 - 90% its melting point or solidus temperature [15, 16]. To transport this fact to the current model a calibration was done by comparing simulated temperatures with temperatures registered by the thermocouple at 8 mm from the welding line. At this distance one can assume/infer/presume there was no interference from the tool in measured temperatures by the thermocouple. A step condition was inserted limiting the maximum temperature reached by the model, as made by [14] setting the heat flux to zero when the temperature reaches values greater than  $T_{solidus}$  of the workpiece [17].

$$Q_{shoulder}(r, T) = \begin{cases} Q_{shoulder}, & \text{if } T < T_{solidus} \\ 0, & \text{if } T \geq T_{solidus} \end{cases} \quad (6)$$

At such high temperatures, radiation cannot be neglected and it is brought to the model with insertion of an emissivity coefficient  $\varepsilon = 0,3$  applied all over the workpiece surface and the tool.

$$q_{totalloss} = \sigma \cdot \varepsilon (T_{env}^4 - T^4) + h \cdot (T_{env} - T) \quad (7)$$

The heat losses in the model were defined as general outflux and where applied all over the upside and the downside of the workpiece. In the above equation.  $\varepsilon$  is the surface emissivity of the tool and the workpiece,  $\sigma$  is the Stefan-Boltzmann constant,  $T_{env}$  is the environment temperature and  $h$  refer to the convective coefficients associated with the surfaces present in the model (surface of the workpiece and the exposed area of the tool).

## Mathematical Modelling of Weld Phenomena 12

The convective coefficients at the upper surface and at the downside of the workpiece were estimated to be  $h_{upside} = 10 \text{ W m}^{-2}\text{K}^{-1}$  e  $h_{downside} = 100 \text{ W m}^{-2}\text{K}^{-1}$ . The backing plate has its conductive coefficient lumped into a general convective coefficient with different values,  $h_{backing-cold} = 600 \text{ W m}^{-2}\text{K}^{-1}$  for the cold joint and  $h_{backing-hot} = 200 \text{ W m}^{-2}\text{K}^{-1}$  for the hot joint. [18,19]. These values were considered once taking the forging pressure  $F_N$  related influence on the gap conductance between the workpiece and the backing plate [14,18,19]. As for the tool, values of a lateral and top coefficients were considered  $h_{shoulder-lateral} = 15 \text{ W m}^{-2}\text{K}^{-1}$  and  $h_{shoulder-top} = 20 \text{ W m}^{-2}\text{K}^{-1}$ , respectively regarding convective and conductive heat losses due to high temperature values achieved by the tool material.

**Table 3** API 5L-X80 thermophysical properties. Adapted from Rocha *et al* [20].

Temperature [°C]	Thermal Conductivity [W m <sup>-1</sup> °C <sup>-1</sup> ]	Specific Heat [J kg <sup>-1</sup> °C <sup>-1</sup> ]
0	51.062	571.235
100	510.62	571.235
200	47.324	571.235
300	43.840	571.235
400	40.424	614.841
500	29.634	686.617
550	33.546	730.831
600	26.461	780.774
650	18.019	868.623
700	14.874	977.691
750	11.386	841.431
800	14.735	790.265
900	14.735	608.333
1200	14.735	681.529

The steel's density was considered to be constant, with a value of  $\rho = 7860 \text{ kg m}^{-3}$ . The alloy's thermophysical properties were implemented in the workpiece according to data provided by the work of Rocha *et al* [20] and shown in the Table 3.

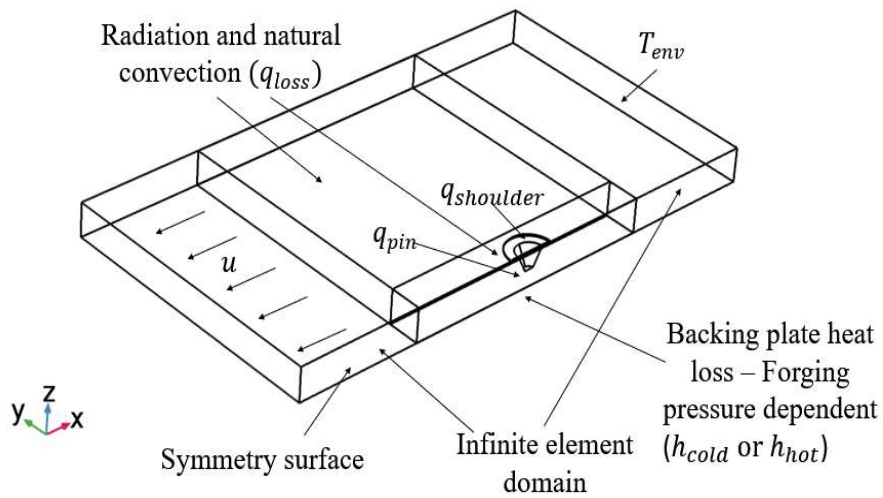


Fig. 3 The model geometry with a reduced size illustrating zones and considerations.

The material used for the tool, Polycrystalline Boron Cubic Nitride (PCBN), had to be implemented as a new material in the program library with the data from Table 4. This material must withstand high temperatures and be chemically inert. The final enmeshed geometry was composed of 25 125 tetrahedral elements and 52274 DOFs detailed in Fig. 4.

Table 4 PCBN termophysical properties [13]

Density [Kg.m <sup>-3</sup> ]	Thermal Conductivity [W m <sup>-1</sup> °C <sup>-1</sup> ]	Specific Heat [J kg <sup>-1</sup> °C <sup>-1</sup> ]
3120	130	1966

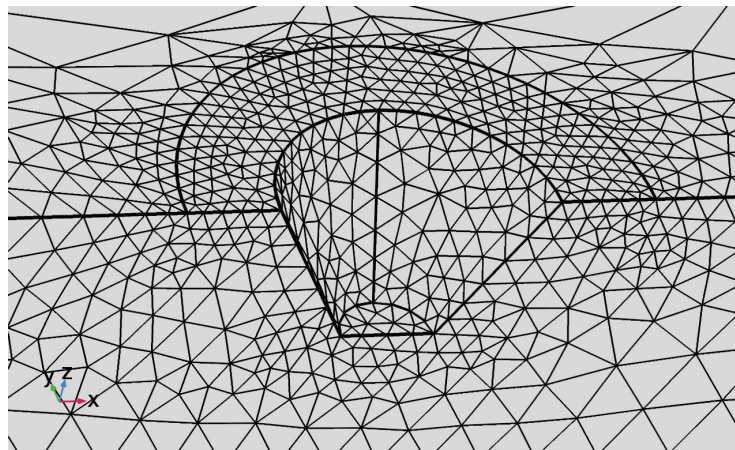


Fig. 4 Detailed meshed geometry of the tool and the workpiece with tetrahedral mesh elements.

RESULTS AND DISCUSSION

The model was verified and validated through comparative analysis between experimental data and simulated results for both joints. The maximum temperature values estimated by the model at the closest thermocouple was 992 °C for the hot joint and 873 °C for the cold joint. The simulated curves had a considerable agreement with the experimental values for maximum values as well as cooling rates.

**Table 5** Comparison between the simulated and experimental temperatures for the advancing side of welds, at different distances from the welding line – Hot Joint and Cold Joint.

Weld Joint	6 mm	8 mm	10 mm	12 mm
Hot	989 °C	913 °C	815 °C	567 °C
Hot-Simulated	992 °C	915 °C	805 °C	676 °C
Cold	880 °C	794 °C	753 °C	510 °C
Cold-Simulated	873 °C	793 °C	673 °C	566 °C

**Table 6** Simulated temperature for neighboring distances of the welding line.

Weld Joint	0 mm	2 mm	4 mm
Hot-Simulated	1222 °C	1215 °C	1159 °C
Cold-Simulated	1114 °C	1106 °C	1041 °C

The simulated and experimental maximum temperatures for the advancing side of both joints are shown in Table 5.

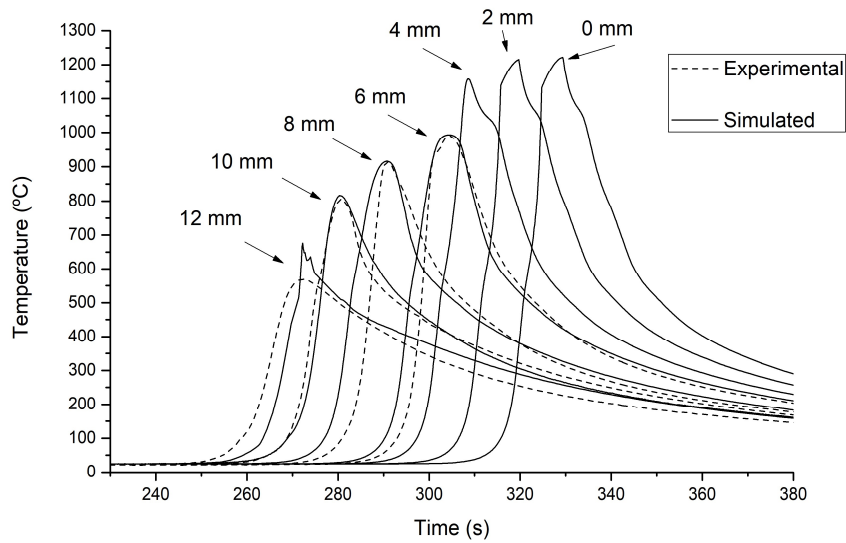


**Fig. 5** Comparative graphic showing simulated and experimental thermal cycles of FSW considering a hot joint.

For the cold joint thermal cycles represented in Fig. 7, it can be recognized from that the experimental data curve for the 6 mm thermocouple is slightly altered. As this thermocouple was next to the tool zone this shift might represent a disruption in temperature acquisition during the welding, caused by the sudden contact with the tool. This fact can be reassured by the style of the simulated temperature curve for 4 mm, 2 mm and 0 mm, in which one can notice the different shape of the slope for simulated thermal cycles in regions situated around the pin. The simulated temperatures for the cold joint in Table 5 still helps to preview what would have been the correct values for the experimental temperatures, had the tool not touched the thermocouples.

Temperatures simulated for the welding line are slightly lower for the cold joint, as shown in Fig. 7. This can be justified by a lower heat input, leading to greater cooling rates imposed during welding. An overall precise temperature prediction was achieved for both simulations. The exceptions are the thermal cycles for thermocouples situated at 12 mm from the welding line, where the maximum simulated temperatures are slightly overpredicted. The “spike-like” curve of the last simulated temperature can be justified due to temperature data acquisition from the tool’s edge, measuring temperatures coming from a transition zone (shoulder/workpiece) of the model. These differences concerning simulated and measured temperatures might also be due to simplifications of the current thermal model, which ignores the heat contribution by the material flow around the tool [21]. As proposed by Schmidt and Hattel [22], a pure thermal model is capable of predict the non-uniform thermomechanical conditions in the shear region to a certain degree. Furthermore, if one assumes an equilibrium of contact pressure and its temperature independence, one is not accounting for the plastic heat dissipation contribution. This fact has a direct influence on temperature prediction for external zones of the weld, as can be seen in the major difference for the last thermocouples in both conditions.

For simulated temperatures much closer to welding line (at 0, 2 and 4 mm), the model had a reliable agreement with both conditions, as can be noted in Table 6. As expected, simulated temperatures in this region were higher for the hottest condition than for the cold condition. The surface maximum temperature computed for both conditions can be view in Fig. 6 and Fig. 8. Both are located right behind the tool along the welding line, having a value of 1235 °C for the hot joint and 1140 °C for the cold joint. These values share a position similarity with the work of Santos *et al.* [21], in which maximum surface temperatures were simulated and can be found in the trailing side of the tool. In Table 6, higher values of simulated temperatures at 0 mm in both conditions are in agreement with the location, as maximum temperatures are generally measured along the welding line and are located in the proximities of the shoulder region [22]. The simulated values are also in agreement with previous works, since FSW of low carbon steel and stainless steel is likely to provide joints with extreme temperatures, ranging from 1000 °C in the TMAZ to 1300 °C in the SZ welding line. [23].



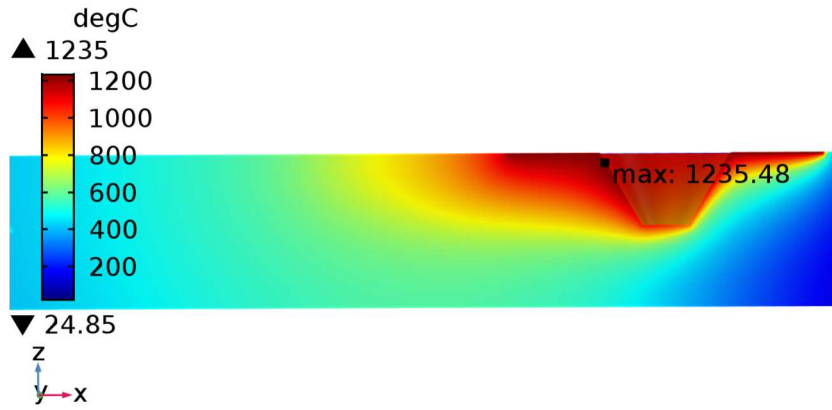


**Fig. 6** Simulation result of FSW considering a hot joint, showing the location of maximum temperature on the workpiece surface.

Multiple works [19,22,24] have credited the differences between simulated and experimental temperatures on the difficulty of finding a definite experimental convective coefficient for the workpiece/backing plate interface. Schmidt and Hattel [22] concluded that one can obtain a reasonable agreement with minor adjusts in these convective values.

The usage of a backing plate during the FSW procedure allows the X-80 welding joint to be more thermally isolated and to receive higher normal forces (forging pressures), as concluded by Santos *et al* [12]. This is also proposed in the current thermal model, as the adopted values for the convective coefficient values are distinct for best fitting with the experimental data and also are considered dependent from the forging pressure.

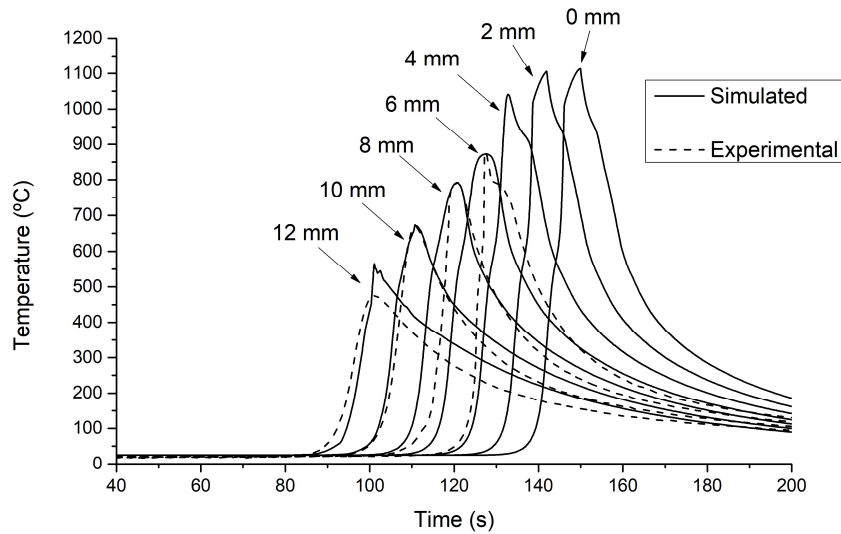


**Fig. 7** Comparative graphic showing simulated and experimental thermal cycles of FSW considering a cold joint.

This work also allows a good correlation with the work of Hermenegildo *et al.* [3], which has found a remarkable microstructure variation for the advancing sides of both welding conditions. The computational model simulated that temperatures of the workpiece around the tool's vicinity reached values higher than the  $A_{r3}$  temperature ( $A_{r3} = 735$  °C).

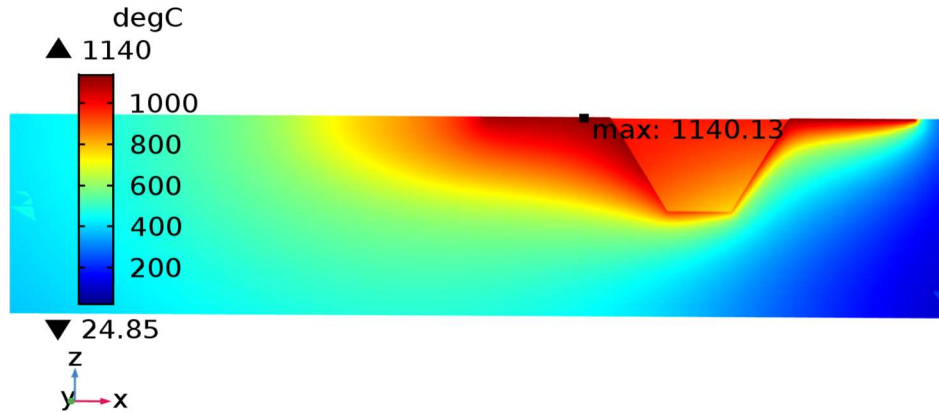


**Fig. 8** Simulation result of FSW considering a cold joint, showing the location of maximum temperature on the workpiece surface.

As proposed in Fig. 9 for the hot joint, simulated temperatures within the hard zone of the welding line (at 0, 2 and 4 mm) are superior than the recrystallization temperature ( $T_{nr}$ ) estimated for this material by the same authors ( $T_{nr} = 899$  °C) [3], which, coupled with a lower cooling rate ( $21.4$  °C.s<sup>-1</sup>) than that of cold joint ( $31.0$  °C.s<sup>-1</sup>) would lead to a growth in austenite grain around the nugget zone, and eventually, the presence of martensite in this region, at the advancing side. As previous works of Santos *et al.* [25] have shown for comparable welding conditions, in the stir zone the hot joint presented CTOD values below the minimum requirements for offshore applications (DNV-OS-101 standards), whereas for the cold joint the CTOD values were higher. This confirms the potential of this work to estimate temperatures and to analyze welding conditions which are critical for the mechanical performance of the joints.

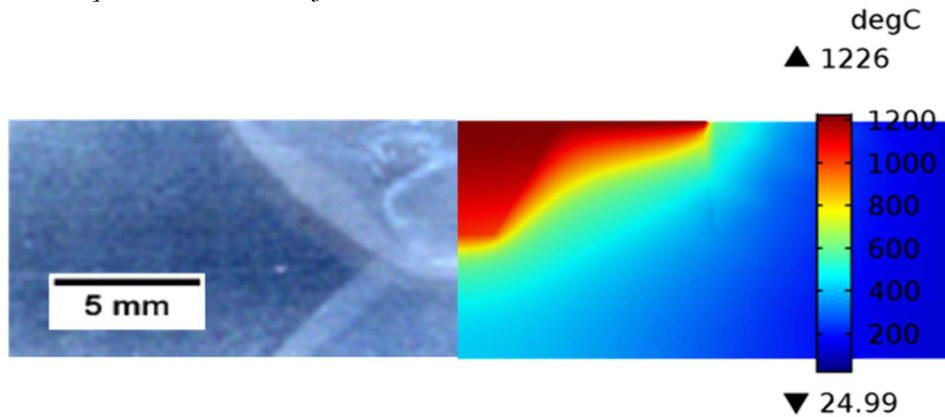


**Fig. 9** Comparative image between the tool and micrograph from the welding, considering a hot joint. Adapted from Hermenegildo *et al.* [3]

### CONCLUSION

The current work is an approach to preview temperatures and thermal cycles for different and multivariable welding conditions of API 5L-X80 weld joints of FSW. Considering the difficulty of finding accurate values for the convective coefficients related to the backing plate contact, the thermal model showed a consistent agreement with the experimental values of temperature and with maximum temperatures predicted for the proximities of the welding line. Furthermore, the intrinsic complexity of the FSW experimental setup presented an extra challenge for the feasibility of this model. The simulation helped previewing temperatures in a case where the tool interfered in the temperature acquisition. The model also took minor time to process the computational data, becoming a rapid and straightforward approach to study and understand the thermal phenomena occurring in the FSW of the API 5L-X80.

A correlation with the material's microstructure obtained in previous works can be drawn, once the simulated thermal cycles showed slight differences for maximum temperatures in the tool vicinity. Additionally, the model managed to confirm that peak temperatures in the hot joint were greater than the material's recrystallization temperature, which contributes to martensite formation. This leads to an improved understanding of FSW thermal cycles and its association with the material mechanical properties. It is also pointed out the current work with a mechanical model as the thermocouples located at 12 mm from the welding line have shown divergent values for the maximum temperature.

A coupling model which simultaneously treats complementary contributions of both shearing and frictional, offering a complete computational approach to the FSW processing of API 5L-X80 welds is also in progress.

### ACKNOWLEDGMENTS

The authors would like to acknowledge financial support of Brazilian science agencies CAPES, FACEPE, and CNPq.

### REFERENCES

- [1] M. W. THOMAS, E. D. NICHOLAS, J. C. NEEDHAM, M. G. MURCH, P. TEMPLESMITH, C. J. DAWES: 'Friction Stir Butt Welding', *GB Patent Application No. 9125978.8*, December, 1991; *US Patent Application No. 5460317*, October, 1995.
- [2] A. SURESH BABU and C. DEVANATHAN: 'An Overview of Friction Stir Welding', *International Journal of research In Mechanical Engineering & Technology*, Vol. 3, No. 2, pp. 259-265, 2013.
- [3] T. F. C. HERMENEGILDO, T. F. A. SANTOS, E. A. TORRES, C. R. M. AFONSO, A. J. RAMIREZ: 'Microstructural Evolution of HSLA ISO 3183 X80M (API 5L X80) Friction Stir Welded Joints', *Metals and Materials International*, Vol. 24, No 5, pp. 1120-1132, 2018.
- [4] J. A. AVILA, J. RODRIGUEZ, P. R. MEI, A. J. RAMIREZ: 'Microstructure and fracture toughness of multipass friction stir welded joints of API-5L-X80 steel plates', *Materials Science and Engineering: A*, Vol. 673, No. 15, pp. 257-265, 2016.

- [5] M. ABBASI, T. W. NELSON and CARL D. SORENSEN: ‘Analysis of variant selection in friction-stir-processed high-strength low-alloy steels’, *Journal of Applied Crystallography*, Vol. 46, No 3, pp. 716-725, 2013.
- [6] M. WITEK: ‘Possibilities of Using X80, X100, X120 High-Strength Steels for Onshore Gas Transmission Pipelines’, *Journal of natural gas science and engineering*, Vol. 27, Part 1, No. 48, pp. 374–384, 2015.
- [7] L. WEI and T. W. NELSON, ‘Influence of heat input on post weld microstructure and mechanical properties of friction stir welded HSLA-65 steel’, *Materials Science and Engineering: A*, Vol. 556, No. 7, pp. 51-59, 2012.
- [8] J. JANOVEC, M. TAKAHASHI, T. KURODA, K. IKEUCHI: ‘Microstructural and mechanical aspects of tempered ICCGHAZ of SQV-2A low alloy steel weld’, *ISIJ International*, Vol. 40, Suppl. S44-S48, 2000.
- [9] AMERICAN PETROLEUM INSTITUTE: ‘*Welding of Pipelines and Related Facilities, API Standard 1104*’ 20th Edition, 2005.
- [10] H. SCHIMDT AND J. HATTEL: ‘Modelling heat flow around tool probe in friction stir welding’, microstructure, and properties”, *Science and Technology of Welding and Joining*. Vol. 10, No. 2, pp. 176-186, 2005.
- [11] T. W. NELSON, S.A. ROSE, J. MATER: ‘Controlling hard zone formation in friction stir processed HSLA steel’, *Journal of Materials Processing Technology*, Vol. 231, No. 8, pp. 66–74, 2016.
- [12] T. F. A. SANTOS, E. A. TORRES, T. F.C. HERMENEGILDO, A. J. RAMIREZ: ‘Development of ceramic backing for friction stir welding and processing’ *Welding International*, Vol. 30, No. 5, pp. 338-347, 2016.
- [13] H. CHOI; S. HONG; J. ROH; H. CHOI; S. H. KANG; R. J. STEEL; H. N. HAN: ‘Three-dimensional numerical and experimental investigation on friction stir welding processes of ferritic stainless steel’, *Acta Materialia*, Vol. 61, No. 7, pp. 2649-2661, 2013.
- [14] M. SONG, R. KOVACEVIC: ‘Thermal modeling of friction stir welding in a moving coordinate system and its validation’, *International Journal of Machine Tools and Manufacture*, Vol. 43, No. 6, pp. 605 – 615, 2003.
- [15] P. COLEGROVE, M. PAINTER, D. GRAHAM and T. MILLER: ‘3-dimensional flow and thermal modeling of the friction stir welding process’, *The 2nd International Symposium on Friction stir welding*, 2, pp. 1–11, 2000.
- [16] Y. J. CHAO, X. QI, W. TANG: ‘Heat transfer in friction stir welding experimental and numerical studies’, *Journal of Manufacturing Science and Engineering*, Vol.125, No. 1, pp. 138-145, 2003.
- [17] M. B. SANTILLANA: ‘Thermo-mechanical properties and cracking during solidification of thin slab cast steel’, *doctoral thesis*, Technische Universiteit Delft, 2013.
- [18] A. SIMAR, J. LECOMTE-BECKERS, T. PARDOEN, B. MEESTER: ‘Effect of boundary conditions and heat source distribution on temperature distribution in friction stir welding’, *Science and Technology of Welding & Joining*, Vol. 11, No. 2, pp. 170-177, 2006.
- [19] M. Z. H. KHANDKAR, J. A. KHAN, A. P. REYNOLDS: ‘Prediction of temperature distribution and thermal history during friction stir welding: Input torque-based model’, *Science and Technology of Welding & Joining*, Vol. 8, No. 3, pp. 165-174, 2003.
- [20] E. J. F. ROCHA, T.S. ANTONINO, P.B. GUIMARAES, R. A. S. FERREIRA, J. M. A. BARBOSA, J. ROHATGI: ‘Modeling of the temperature field generated by the deposition of weld bead on a steel butt joint by FEM techniques and thermographic images’, *Material Research, São Carlos*, Vol. 21, No. 3, e20160796, 2018.
- [21] T. F. A. SANTOS, H. S. IDAGAWA, A. J. RAMIREZ: ‘Thermal history in UNS S32205 duplex stainless steel friction stir welds’, *Science and Technology of Welding and Joining*. Vol. 19. No. 2. pp. 150-156, 2014.
- [22] H. N. B. SCHMIDT and H. J. HATTEL: ‘Thermal modelling of friction stir welding’, *Scripta Materialia*, Vol. 58, No. 5, pp. 332-337, 2008.

## Mathematical Modelling of Weld Phenomena 12

- [23] M. MATSUSHITA, Y. KITANI, R. IKEDA, S. ENDO, H. FUJII: 'Microstructure and Toughness of Friction Stir Weld of Thick Structural Steel', *ISIJ International*, Vol. 52, No. 7, pp. 1335–1341, 2012.
- [24] R. NANDAN, T. DEBROY, H. K. D. H. BHADESHIA: 'Recent advances in friction-stir welding – process, weldment structure and properties', *Progress in Materials Science*, Vol. 53, No. 6, pp. 980-1023, 2008.
- [25] T. F. A. SANTOS, T. F. C. HERMENEGILDO, R. R. MARINHO, M. T. P. PAES, A. J. RAMIREZ: 'Fracture toughness of ISO 3183 X80M (API 5L X80) steel friction stir welds', *Engineering Fracture Mechanics*, Vol. 77, No. 15, pp. 2937-2945, 2010.

# INFLUENCE OF THE PROBE GEOMETRICAL FEATURES ON THE STRESS CONDITION OF THE TOOL DURING FRICTION STIR WELDING

I. GOLUBEV<sup>\*\*\*</sup>, M. WEIGL<sup>\*</sup> and V. MICHAÏLOV<sup>\*\*</sup>

*\*Grenzbach Maschinenbau GmbH, 86663 Asbach-Bäumenheim, Hamlar, Germany, Iurii.Golubev@grenzbach.com*

*\*\*Brandenburg University of Technology (BTU) Cottbus-Senftenberg, 03046 Cottbus, Germany*

DOI 10.3217/978-3-85125-615-4-34

## ABSTRACT

The objective of the present paper is to investigate the effect of the tool probe features on the stress condition of the tool in friction stir welding (FSW). The friction stir welding of an Al 6082 T6 alloy was performed to provide validation data for numerical models of the process. The developed earlier 3D thermal model was improved in order to collect the data about workpiece material strength and heat generation at the probe/workpiece interface during FSW. These data were used as a boundary conditions in models for temperature in the welding tool and stress condition of the tool. Influence of temperature and tool probe features such as flat depth, thread root radius and probe root radius, on stress condition of FSW tool at different angular position was defined.

Keywords: Friction Stir Welding, Aluminum Alloys, Numerical Simulation, Stress Analysis, Probe Geometry

## INTRODUCTION

Friction stir welding (FSW) is the solid-state joining technique invented in 1991 by TWI. The FSW method have a number of advantages over conventional methods of fusion welding such as no solidification cracks, low distortion and low residual stresses in the workpiece. However, the method has some disadvantages. One of the main disadvantages is the slower welding speed of the process compared to the competing welding processes.

An increase of the welding speed can result in insufficient material flow around the tool probe leading to the defects formation such as void or lack of fill [1-2]. Numerous researchers tried to enhance the material flow through the improvement of the tool probe geometry [3-15]. They used various outer shape of the probe [9-10, 13], thread [3-8, 11-13, 15] and addition of machined flats or flutes on the tool probe [3-6, 12, 14-15]. Thomas et al. [3] concluded that the existence of thread and flutes aids material flow because of swept ratio increase. It is this ratio of the 'dynamic volume' of the tool to the static volume of the

tool that is important in providing an adequate flow path. Fujii et al. [6] showed that a profiled tool probe can provide a sound weld even at a relative high welding speed.

The welding tool is heavily loaded during FSW process due to high temperature gradient [8-16] and interaction of the tool surfaces with workpiece material. The tool probe geometrical features enhancing the material flow can become the weak points leading to the earlier tool breakage. Some researchers [3, 15] calculated numerically the stresses in the FSW tools under the same loading conditions to compare the tools of different designs. Thomas et al. [3] applied uniform pressure loads to the faces of the tool to create pure torsion, pure bending and combination of the two loading modes. Reza-E-Rabby [15] defined the stress distributions in the FSW tool by applying experimentally measured loads to the faces of the tool probe and determined that the maximum von Mises stress is observed at a point where there is full thread depth closest to the tool shank. The pressure load distributed over the tool surfaces is influenced by the temperature-dependent flow stress of the workpiece material. Experimental measurements of the temperature in the weld nugget are difficult to achieve, but numerical simulation enables to determine the temperature and, therefore, the material flow stress and pressure load.

The objective of the present work is to develop the model that predicts the stresses in the FSW tool from the mechanical and thermal properties of the tool and workpiece materials, the tool and workpiece dimensions and the process parameters. The temperature data is collected to enable model to be validated. The developed model is used to investigate the influence of the probe geometrical features on the stress condition of the welding tool. Furthermore, a new welding tool with improved probe geometry is proposed.

## EXPERIMENTAL PROCEDURE

### MATERIAL

In this work plates of 6082 – T6 aluminium alloy with the dimensions  $300 \times 75 \times 3$  mm have been welded with FSW. The chemical composition and mechanical properties of the aluminium alloy used in the experiments are given in Table 1 and Table 2, respectively.

**Table 1** Nominal chemical composition of the workpiece material AA 6082 T6

Si	Fe	Cu	Mn	Mg	Al
0.89	0.4	0.31	0.4	1.18	Bal.

**Table 2** Mechanical properties of the workpiece material AA 6082 T6

Ultimate tensile strength, MPa	Yield strength, MPa	Elongation, %
323	256,8	6,3

# Mathematical Modelling of Weld Phenomena 12

## WELDING TRIALS

Temperature measurements were carried out during FSW using thermocouples placed on the top surface of the weld plates to validate the calculated results. To ensure repeatability, three welds were successfully replicated, showing nearly identical temperature histories. Figure 1 shows the thermocouples position during the FSW process.

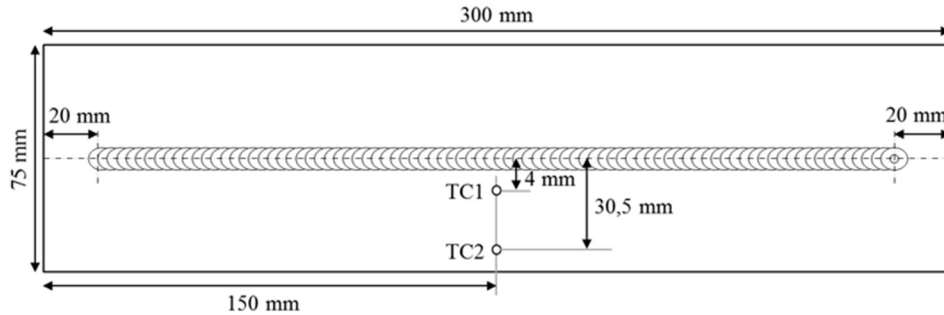


**Fig. 1** Thermocouples position

The experiments were carried out on a force-controlled robotic FSW system by Grenzebach Maschinenbau GmbH (Germany) employed with a heavy-duty robot KUKA KR5000 and a specially designed spindle for rotational speeds up to 14000 rpm. For the FSW process a conventional welding tool made of WC-10Co alloy was used. The welding tool consisted of a threaded tapered probe with a 3 mm root diameter, 2,2 mm tip diameter and a 2,3 mm length and a flat shoulder with a 5,5 mm diameter. The welding tool features were three flats with depth of 0,3 mm, thread with thread root radius of 0,14 mm and probe root radius of 0,3 mm. The rotational speed, traverse speed, axial force and tilt angle were set to the constant values of 2500 RPM, 1000 mm/min, 3 kN and 3° respectively.

## MODELLING OF FRICTION STIR WELDING

### THERMAL MODELLING

The thermal modelling process is divided into two steps. The first step is the calculation of the temperature in the workpiece and total heat generation at the tool/workpiece interface by using 3-dimensional finite element model with the analytical heat source model moving along the weld line. The second step is the 3-dimensional finite element model uses calculated heat generation at the tool/workpiece interface as boundary condition for the calculation of the temperature distribution in the welding tool.

The calculation of the temperature in the welding tool were performed for 7 welding tools having different geometrical features such as flat depth, probe root radius and thread root radius. The varied geometrical features are shown in Table 3.



**Table 3** Varied geometrical features

Flat depth, mm	Probe root radius, mm	Thread radius, mm
0,25	0,2	0,14
0,3	0,3	0,16
0,35	0,35	0,18

In this work, it is assumed that change of the probe geometrical features has no significant influence on the heat generation at the tool/workpiece interface and temperature in the weld nugget. Hence, the heat generation calculated in the first model for the initial welding tool is used for the calculation of the temperature distribution in all welding tools.

*Analytical heat source model*

The heat source model is the distribution of the local heat generations at the contact interface between the welding tool and workpiece. The local heat generation at the interface segment is given by

$$q = \tau_{contact} \omega r \quad (1)$$

where  $\omega$  is the angular velocity,  $r$  is the distance from the interface segment to the rotational axis and  $\tau$  is the contact shear stress at the contact interface equals the yield shear stress  $\tau_{yield}$  and can be converted from experimentally measured yield stress data using the following expression

$$\tau_{contact} = \tau_{yield} = \frac{\sigma_{yield}}{\sqrt{3}} \quad (2)$$

where  $\sigma_{yield}$  is the yield stress depending on the temperature of the workpiece material at the contact interface.

By integration the equation (1) over the shoulder, probe side and probe tip surfaces are found total heat generations at the shoulder  $Q_{shoulder}$ , probe side  $Q_{probe\ side}$  and probe tip  $Q_{probe\ tip}$  respectively. The total heat generation over the entire contact interface between the welding tool and workpiece is given by

$$Q_{total} = Q_{shoulder} + Q_{probe\ side} + Q_{probe\ tip} \quad (3)$$

The heat generated at the contact interface flows into the both the welding tool and the workpiece. The thermal efficiency  $\eta$  describes how much heat is conducted into the workpiece itself compared to the total heat generation  $Q_{total}$ . The heat conducted in the workpiece  $Q_{workpiece}$  is given by

$$Q_{workpiece} = \eta Q_{total} \quad (4)$$

The heat conducted in the welding tool is given by

$$Q_{tool} = (1 - \eta)Q_{total} \quad (5)$$

The thermal efficiency can be calculated by using thermophysical properties of the workpiece and tool materials [Chen, Feng 2016], i.e.

$$\eta = \frac{\sqrt{(\lambda\rho C_p)_W}}{\sqrt{(\lambda\rho C_p)_W + (\lambda\rho C_p)_T}} \quad (6)$$

Where  $\lambda$  is the thermal conductivity,  $\rho$  is the density,  $C_p$  is the heat capacity, the subscripts W and T denote the workpiece and tool, respectively.

*Finite element model for the temperature and heat generation*

Figure 2 shows the finite element model for the temperature in the workpiece and the total heat generation at the tool/workpiece interface.

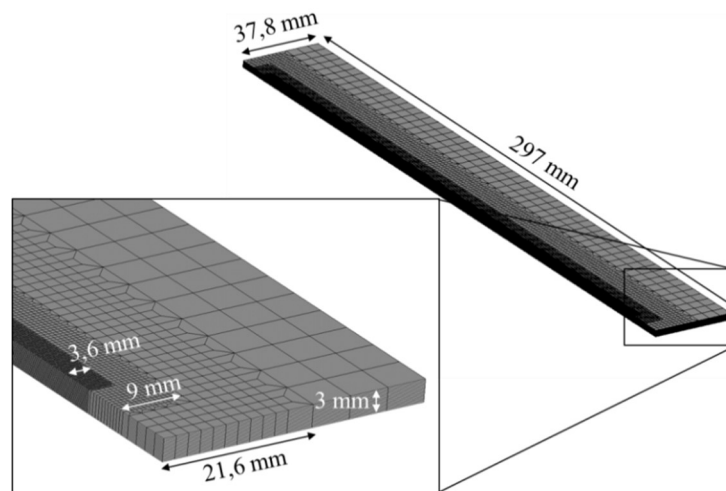


**Fig. 2** Finite element model for the temperature and heat generation

In this work, it is assumed that two plates are welded symmetrically and the heat generation is symmetrical about the welding line. Thus only one plate is modelled. The welding tool and backing plate are not included in the calculation to limit the number of the geometries that are enmeshed and save computational resources. Enmeshed model consists of 642590 hexahedral elements with a single degree of freedom, temperature. The mesh

density is varied over the width of the workpiece model. The higher mesh density is near the welding line where the higher temperature gradient is expected.

The effect of the backing plate is taken into account due to application of a temperature-dependent equivalent heat transfer coefficient at the bottom surface of the workpiece  $h_{bp}$  given in Table 4. The welding tool is modelled by applying of the heat flux to the contact interface between the tool and workpiece. The heat flux is described by equation (1) requiring temperature-dependent yield shear stress data given in Table 5. Convective heat loss to the air is applied at the top and side surfaces of the workpiece using a temperature-dependent convective heat transfer coefficient  $\alpha_{tool}$  given in Table 6.

**Table 4** Equivalent heat transfer coefficient,  $^{\circ}\text{C} / \times 10^{-5} \text{ W mm}^{-2} \text{ K}^{-1}$

20	40	50	100	200	500
3,9	4,9	7,7	8,5	11	65

**Table 5** Yield shear stress data,  $^{\circ}\text{C} / \text{MPa}$

20	100	200	300	370	420	500	630
158	150	130	58	29	12	6	0

**Table 6** Convective heat transfer coefficient,  $^{\circ}\text{C} / \times 10^{-5} \text{ W mm}^{-2} \text{ K}^{-1}$

20	100	200	300	400	500
2,5	2,722	3,143	3,729	4,508	5,511

*Finite element model for the temperature in the welding tool*

Figure 3 illustrates the geometrical model and boundary conditions of the model for the temperature distribution in the welding tool.

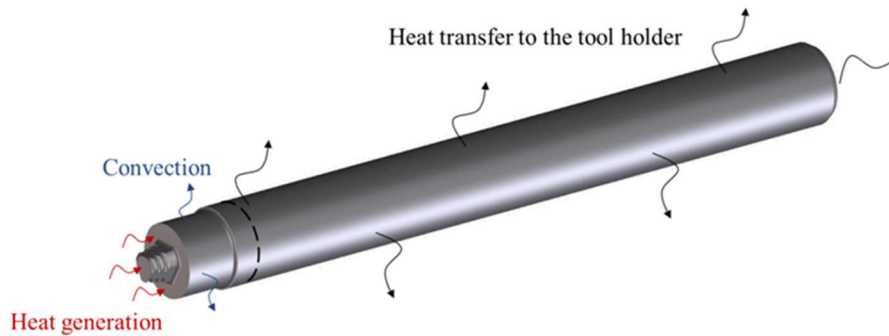


**Fig. 3** Schematic illustration of boundary conditions for the thermal analysis of the welding tool

For the thermal characteristics of the considered WC-10Co alloy, the following values were utilized: thermal conductivity  $\lambda = 0,11 \text{ W mm}^{-1} \text{ K}^{-1}$ , density  $\rho = 14,5 \text{ g cm}^{-3}$  and thermal capacity  $c = 0,134 \text{ J g}^{-1} \text{ K}^{-1}$ . The heat loss is realized through the convection to the air and heat transfer to the tool holder from the shank surfaces. Convective heat transfer coefficient  $\alpha_{tool} = 25 \times 10^{-6} \text{ W mm}^{-2} \text{ K}^{-1}$  was applied at the shank surface between the tool shoulder and dotted line as shown in Figure 3. The effect of the tool holder was taken into account due to application of an equivalent heat transfer coefficient  $h_{th} = 10^{-3} \text{ W mm}^{-2} \text{ K}^{-1}$  at the shank surface in contact with the tool holder (above the dotted line).

The geometrical models of 7 welding tools were enmeshed with the mesh density varied over the height of the tool model. The higher mesh density was at the tool probe and shoulder where the higher temperature gradient is expected. The smallest element edge length was 0,04 mm.

The total heat generation at the shoulder and tool probe surfaces was defined in the first model for temperature in the workpiece. The fraction of the total heat conducted into the FSW tool was calculated by equation (5).

MODELLING OF THE STRESSES IN THE TOOL

The modelling process of stresses in the welding tool is also divided into two steps. The first step is a structural analysis evaluating stresses due to temperature distribution in the welding tool. The second step is the model uses thermal stresses as initial condition for the model when subjected to a load due to interaction with the workpiece material.

The calculation of the stresses in the welding tool were also performed for 7 welding tools having different geometrical features.

*Thermal-stress analysis*

Figure 4 illustrates the geometrical model and boundary conditions for the thermal-stress analysis.

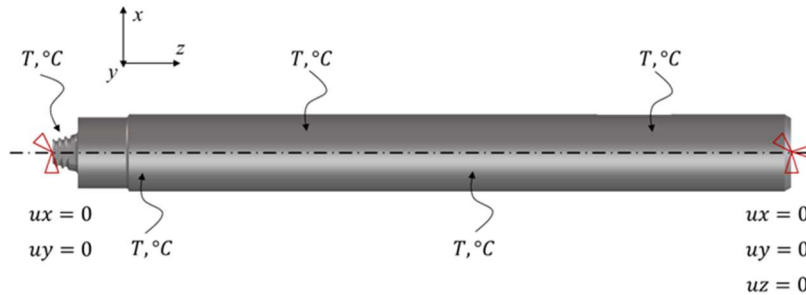


**Fig. 4** Schematic illustration of the boundary conditions for the thermal stress analysis

The following characteristics of WC-10Co alloy were used in the numerical model for stresses: coefficient of thermal expansion  $\alpha = 5,5 \times 10^{-6} \text{ } ^\circ\text{C}^{-1}$ , Young's modulus  $E = 580$

GPa and Poisson ratio  $\nu = 0,3$ . The results of the model for the temperature distribution in the welding tool are converted to a temperature load for the thermal-stress analysis of the welding tool.

*Stress analysis*

Interaction of the welding tool with the workpiece material results in reaction forces that the tool experiences during the FSW process. While the rotation of the welding tool causes the torsional forces at the entire tool/workpiece contact interface, the tool traverse affects the traverse forces acting on the leading side of the tool probe, as shown in Figure 5.

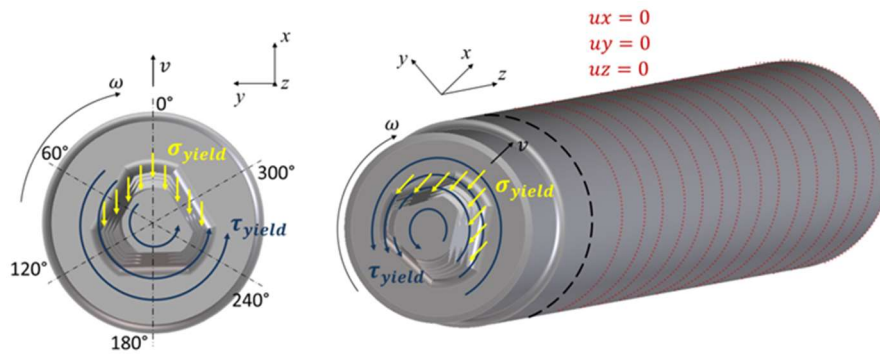


**Fig. 5** Schematic illustration of the boundary conditions for the stress analysis in the tool

The plastic deformation of shear layer contacting the welding tool is the necessary condition for the successful weld. Hence, the traverse and torsional forces can be represented as pressure corresponding to workpiece material yield strength and shear yield strength respectively. The yield strength and shear yield strength of the workpiece material depend on the temperature and can be defined by means of calculation results of the model for the temperature in the workpiece described before.

The tool probe is not axisymmetric because of helical nature of the thread. Hence, it is necessary to load the tool probe from different direction in order to define the weak angular position. Six different orientations were chosen, as shown in Figure 5.

RESULTS AND DISCUSSIONS

HEAT INPUTS AND TEMPERATURE DISTRIBUTION

Figure 6 shows the comparison between numerically estimated and experimentally measured temperature cycles on the top surface of the workpiece during FSW.

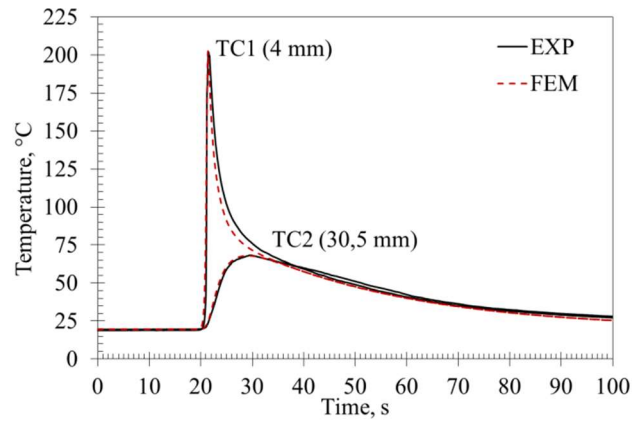


**Fig. 6** Comparison between numerical and experimental temperature cycles

The computed temperature cycles are in good agreements with the experimental measurements. Therefore the model can be used to calculate the heat generation at the tool/workpiece interface and temperature in the weld nugget.

The calculated heat generations at different tool surfaces conducted in the workpiece and conducted in the welding tool are given in Table 7.

**Table 7** Calculated heat generations at different tool surfaces during steady-state FSW

Heat generation	Shoulder	Probe side	Probe tip
<b>Total, W</b>	312,5	182,5	32,5
<b>Workpiece, W</b>	287,5	167,9	29,9
<b>Tool, W</b>	25	14,6	2,6

The calculated heat generation over the entire contact interface between the welding tool and workpiece is found to be 527,5 W. The most of the heat (59 %) is generated at the shoulder/workpiece interface, while the heat fractions of 35 % and 6 % are generated at the probe conical side and probe tip respectively.

Figure 7 shows the calculated temperature distribution in the workpiece during the steady-state FSW process.

Since most of the heat is generated at the shoulder/workpiece interface, the workpiece temperature decreases from the tool shoulder to the probe tip. It is also observed that the workpiece temperature under the leading side of the welding tool is lower than under the tool trailing side because of welding tool traverse. The temperature of the workpiece material being in contact with the welding tool is found to be not uniform. Hence the pressure loads distributed over the tool surfaces is not uniform. The calculated maximum temperature of 421 °C is observed on the workpiece top surface under the trailing side of the tool shoulder. The calculated lowest temperature of 296 °C is observed on the leading edge of the tool probe tip.

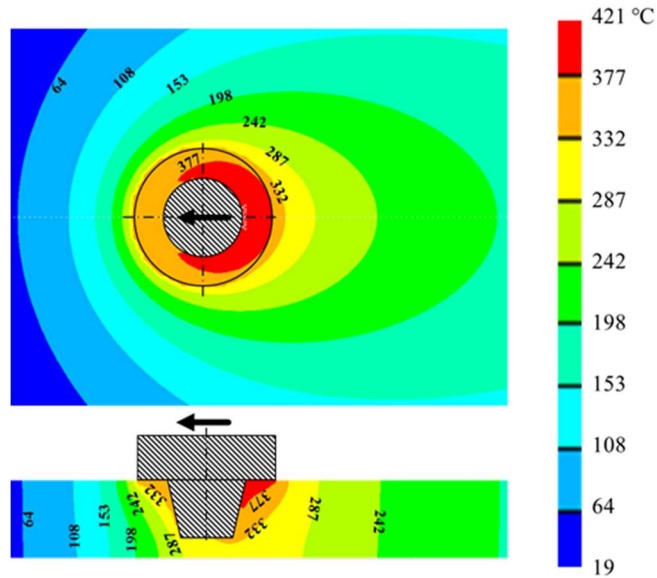


**Fig. 7** Temperature distribution in the workpiece during steady-state FSW

Figure 8 shows the calculated temperature distribution in the initial welding tool with flat depth of 0,3 mm, probe root radius of 0,3 mm and thread root radius of 0,14 mm during the steady-state FSW process.

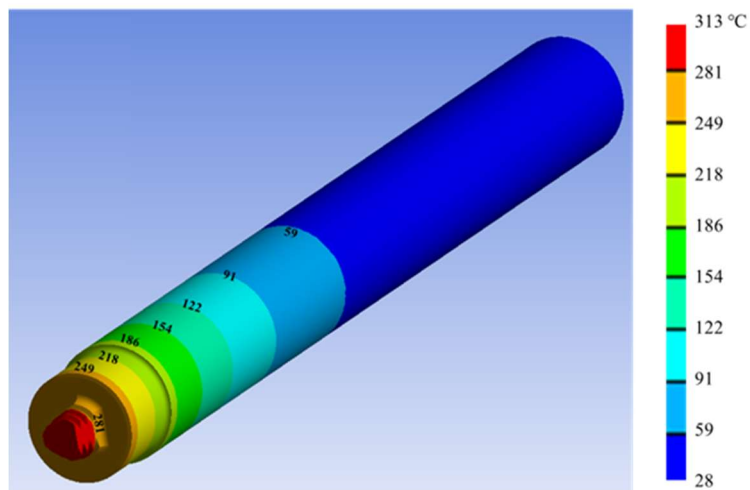


**Fig. 8** Temperature distribution in the welding tool of initial geometry

The temperature distributions in the FSW tool is not uniform over the welding tool height. The temperature decreases from probe tip to the end face of the tool shank because of heat generation on the tool probe and shoulder and high heat transfer from the tool shank

## Mathematical Modelling of Weld Phenomena 12

surfaces to the tool holder. The calculated maximum temperature of 313 °C is observed on the tool probe tip. The minimum temperature of 28 °C is observed on the end edge of the tool shank. The lowest temperature of the tool surface being in contact with the workpiece is found to be 254 °C.

### STRESS CONDITION OF THE TOOL

Figure 9 shows the calculated thermal stresses in the initial welding tool with flat depth of 0,3 mm, probe root radius of 0,3 mm and thread root radius of 0,14 mm during the steady-state FSW process.

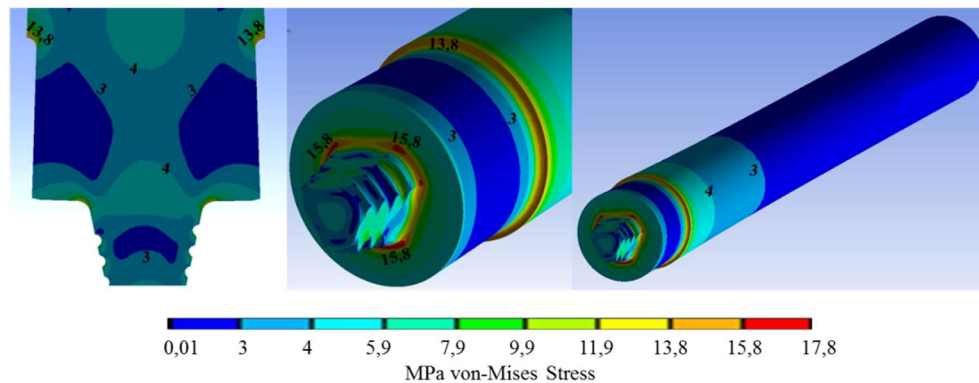


**Fig. 9** Thermal stresses in the welding tool of initial geometry

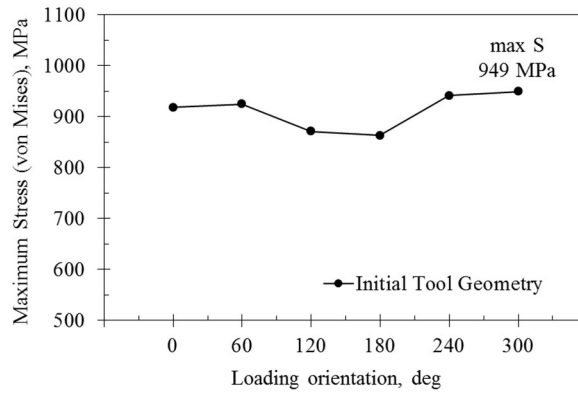
The calculated maximum stress of 17,8 MPa is observed at the probe root. Since the maximum stress due temperature distribution is found to be much less than the tool material strength, the welding tool breakage cannot be caused by thermal stress only.

Figure 10 shows influence of the tool angular position on maximum von Mises stress resulted by combination of temperature load and interaction with the workpiece material.

The angular position of 300 deg. is found to be the critical orientation having maximum stress of 949 MPa. Hence the welding tool fracture at the angular position of 300 deg. is expected. The lowest maximum stress of 864 MPa is observed at the tool angular position of 180 deg. The weak point is observed on the thread root being closest to the tool shoulder at the advancing side for all loading orientation.



## Mathematical Modelling of Weld Phenomena 12



**Fig. 10** Maximum stress for different loading orientation of welding tool

The stress distributions in the welding tool of initial geometry at the angular position of 300 deg. is shown in Figure 11.

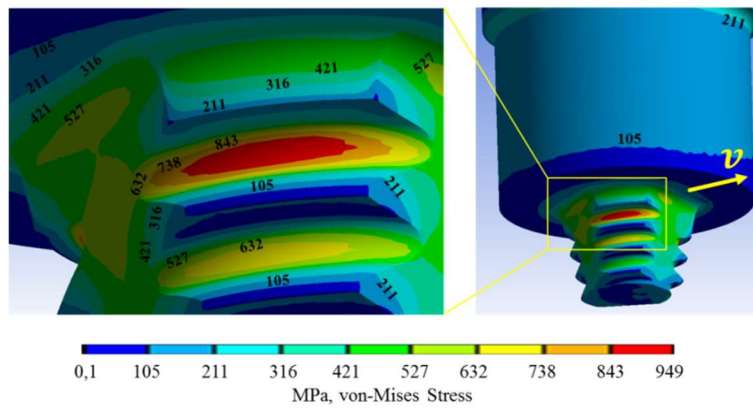


**Fig. 11** Stress distributions of initial welding tool at the angular position of 300 deg

The probe conical surface can be divided into six surfaces, three threaded and three flat surfaces. The higher thread is found to weak point for each threaded surface while probe root is found to be weak point for each flat surface. The fracture line can be drawn by connection of the weak points defined on the each surface.

### INFLUENCE OF THE PROBE FEATURES ON THE STRESS CONDITION

Figure 12 shows the calculated maximum stress for the welding tools with different flat depth.

## Mathematical Modelling of Weld Phenomena 12

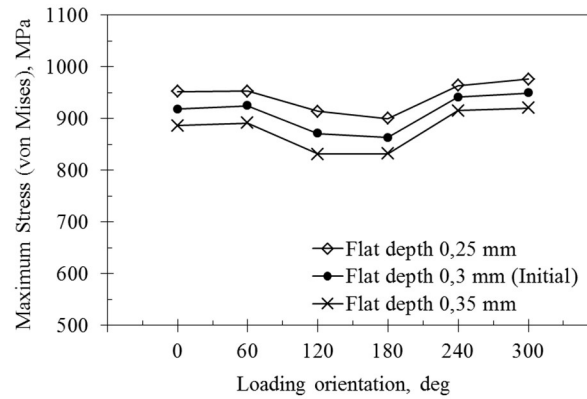


**Fig. 12** Influence of flat depth on the stress condition of the welding tool

An increase of the flat depth does not result in the change of the critical orientation. It is observed that increase of the flat depth leads to decrease of maximum stress due to decrease of threaded probe surface being a weak point. Moreover, the flat depth increase causes the increase of the swept ratio and therefore enhances the material flow. However, it is expected that further increase of flat depth can result in increase of maximum stress because of decrease of probe cross-sectional area.

Figure 13 shows the calculated maximum stress for the welding tools with different probe root radius.

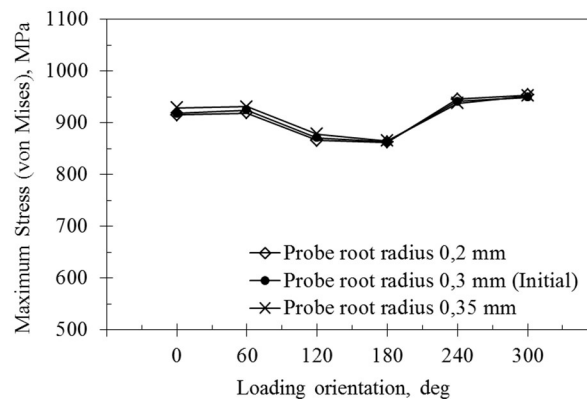


**Fig. 13** Influence of probe root radius on the stress condition of the welding tool

Since the weak point is on the thread root, the change of probe root radius has no significant influence on the maximum stress. However decrease of probe root radius results in increase of the stress on the probe root. Hence too small probe root radius can become a weak point and changes the critical orientation of the welding tool.

Figure 14 shows the calculated maximum stress for the welding tools with different thread root radius.

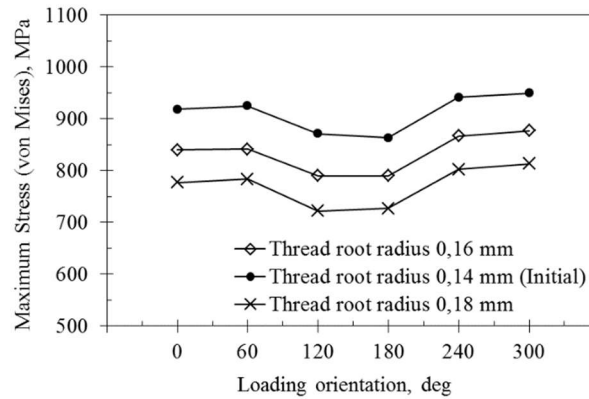


Fig. 14 Influence of thread root radius on the stress condition of the welding tool

An increase of thread root radius does not cause the change of the critical orientation. It is observed that increase of thread root radius results in decrease of maximum stress. Increase of thread root radius causes the decrease of the swept ratio and can lead to insufficient stirring of the workpiece material and therefore weld imperfections (lack of fill).

### CONCLUSIONS

A numerical FE model was developed to simulate the stresses in the FSW tool from the mechanical and thermal properties of the tool and workpiece materials, the tool and workpiece dimensions and the process parameters. The model takes into account temperature gradient in the welding tool and not uniform pressure distribution at the tool surfaces. The experimental measurements of process forces and torque are not required.

The model was used to investigate the influence of tool probe geometrical features on the stress condition of the welding tool. The following conclusions can be drawn from the investigation:

The temperature gradient in the welding tool during the FSW has no significant influence on the tool stress condition because of too low maximum thermal stress.

The weak point for each angular position is the highest thread root at the advancing side.

It is expected that the fracture line will go through the higher threads at the threaded probe surfaces and the probe roots at the flat surfaces.

An increase of flat depth results in decrease of maximum stress due to decrease of threaded probe surfaces.

Change of probe root radius has no significant influence on the maximum stress. However decrease of probe root radius causes the increase of stress on the probe root. Hence too small probe root radius can become a weak point.

An increase of thread root radius results in decrease of maximum stress.

It is suggested the combination of higher flat depth with increased thread root radius to decrease the maximum stress.

### REFERENCES

- [1] A. J. LEONARD and S. A. LOCKYER: 'Flows in friction stir welds', *Proc. Of the 4<sup>th</sup> International Conference on Friction Stir Welding*, Park City, Utah, USA, 2003.
- [2] Y. G. KIM, H. FUJII, T. TSUMURA, T. KOMAZAKI and K. NAKATA: 'Three defect types in friction stir welding of aluminium die casting alloy', *Material Science and Engineering A*, Vol. 415, pp. 250-254, 2006.
- [3] W. M. THOMAS, E. D. NICHOLAS and S. D. SMITH: 'Friction stir welding – tool developments', *TMS Annual Meeting*, New Orleans, Louisiana, USA, 2001.
- [4] S. W. KALLEE, E. D. NICHOLAS and W. M. THOMAS: 'Friction stir welding – invention, innovations and applications', *INALCO 2001 8<sup>th</sup> International Conference on Joints in Aluminium*, Munich, Germany, 2001.
- [5] R. ZETTLER, S. LOMOLINO, J. F. DOS SANTOS, T. DONATH, F. BECKMANN, T. LIPMANN and D. LOHWASSER: 'A study of material flow in FSW of AA2014-T351 and AA6065-T4 alloys', *Proc. 5<sup>th</sup> International Conference on Friction Stir Welding*, Metz, France, 2004.
- [6] H. FUJII, L. CUI, M. MAEDA and K. NOGI: 'Effect of tool shape on mechanical properties and microstructure of friction stir welded aluminium alloys', *Material Science and Engineering A*, Vol. 419, pp. 25-31, 2006.
- [7] MD. REZA-E-RABBY and A. P. REYNOLDS: 'Effect of tool pin thread form on friction stir weldability of different aluminium alloys', *Procedia Engineering*, Vol. 90, pp. 637-642, 2014.
- [8] N. DIALAMI, M. CERVERA, M. CHIUMENTI, A. SEGATORI and W. OSIKOWICZ: 'Experimental Validation of an FSW Model with an Enhanced Friction Low: Application to a Threaded Cylindrical Pin Tool', *Metals*, Vol. 7, No. 491, 2017.
- [9] M. A. HUSSAIN, N. Z. KHAN, A. N. SIDDIQUEE and Z. A. KHAN: 'Effect of different tool pin profiles on the joint quality of friction stir welded AA6063', *Materials Today: Proceedings*, Vol. 5, pp. 4175-4182, 2018.
- [10] P. GOEL, A. N. SIDDIQUEE, N. Z. KHAN, M. A. HUSSAIN, Z. A. KHAN, M. H. ABIDI and A. AL-AHMARI: 'Investigation on the Effect of Tool Pin Profiles on Mechanical and Microstructural Properties of Friction Stir Butt and Scarf Welded Aluminium Alloy 6063', *Metals*, Vol. 8, No. 74, 2018.
- [11] G. CHEN, H. LI, G. WANG, Z. GUO, S. ZHANG, Q. DAI, X. WANG, G. ZHANG and Q. SHI: 'Effect of pin thread on the in-process material flow behaviour during friction stir welding: A computational fluid dynamics study', *International Journal of Machine Tools and Manufacture*, Vol. 124, pp. 12-21, 2018.
- [12] MD. REZA-E-RABBY, W. TANG and A. P. REYNOLDS: 'Effect of tool pin features on process response variables during friction stir welding of dissimilar aluminium alloys', *Science and Technology of Welding and Joining*, Vol. 20, No. 5, pp. 425-432, 2015.
- [13] F. Y. ISUPOV, A. A. NAUMOV, O. V. PANCHENKO, L. A. ZHABREV and A. A. POPOVICH: 'Comparative analysis of the mechanical properties of aluminium alloys welded joints obtained by friction stir welding', *Proc. Material Science and Technology Conference and Exhibition 2018*, In press.
- [14] P. A. COLEGROVE and H. R. SHERCLIFF: 'Two-dimensional CFD modelling of flow round profiled FSW tooling', *Science and Technology of Welding and Joining*, Vol. 9, No. 6, pp. 483-492, 2004.
- [15] MD. REZA-E-RABBY: *Quantification of the effect of tool geometric features on aspects of friction stir welding*, Ph. D. Thesis, College of Engineering and Computing, University of South Carolina, 2015.
- [16] M. ASSIDI, L. FOURMENT, S. GUERDOUX and T. NELSON: 'Friction model for friction stir welding process simulation: Calibrations from welding experiments', *International Journal of Machine Tools and Manufacture*, Vol. 50, pp. 143-155, 2010.



# MODELLING APPROACH TO THE MICROSTRUCTURE EVOLUTION IN COMMERCIALY PURE ALUMINIUM DURING THE RFW PROCESS

E. HEPPNER\* and E. WOSCHKE\*\*

*\*Institute of Mechanics, Otto-von-Guericke University of Magdeburg, 39106 Magdeburg, Germany, eric.heppner@ovgu.de*

*\*\*Institute of Mechanics, Otto-von-Guericke University of Magdeburg, 39106 Magdeburg, Germany,  
elmar.woschke@ovgu.de*

DOI 10.3217/978-3-85125-615-4-35

## ABSTRACT

The rotary friction welding (RFW) is nowadays a well-established joining technique since it is highly productive, entirely repeatable, and very economical. It belongs to the solid-state fusing methods allowing the combination of similar and for a wide spectrum of dissimilar materials. Commonly combined are aluminium and steel materials to manufacture high quality lightweight structures with excellent technological properties. Due to the fact that the welding temperature does not exceed the material's melt temperature, microstructural transformations only appear caused by the heating and cooling rate and the amount of plastic deformation. Aluminium alloys in particular show a pronounced change in microstructure as a consequence of dynamic recrystallization evoked by the high degree of plastic deformation. The purposes of this paper is to present a modelling approach to the microstructure evolution in commercially pure aluminium, for aluminium to steel friction welded joints. The main motivation therein is the consistent prediction of the recrystallization rate of different layers in the process affected zone for an improved understanding of microstructural evolution during the RFW process.

Keywords: rotary friction welding, aluminium, steel, dissimilar materials, microstructure modelling, welding simulation

## INTRODUCTION

Present-day research in the field of product development are increasingly focused on the efficient use of energy and raw material resources. In the light of this, the design principle of consistent lightweight construction is gaining more and more importance. One possible approach is the targeted exploitation of technological properties of different materials in hybrid structures. The objective is always to continuously improve the product properties in terms of functional performance, safety and frequency, as well as to reduce the use of resources and energy consumption. Depending on their field of application, in the automotive and transport industry, tool and fixture construction and in the aerospace

industry, hybrid structures often consist of combinations of metallic materials with aluminium alloys.

Against this background, a considerable number of established joining methods can only be used to a limited extent. Either they do not take into account the differences in material's behaviour in the manufacturing process (e.g. different melting temperatures referring to fusion welding) or they greatly increase the effort for the joining operation by adding additional joining elements (e.g. by riveting or screwing). Due to this fact, joining techniques based on plastic deformation, like the rotary friction welding (RFW), are particularly advantageous. It allows the joining of similar and dissimilar materials without passing the material's melt temperature and without using any filler material or inert gas. Further benefits are the short manufacturing cycling time, the high joint quality and the good automatization potential.

In the RFW, commonly rotationally symmetrical workpieces are welded by using the frictional heat and the axial pressure. Fig. 1 illustrates the general setup wherein one part (A) is static and the other part (B) is rotating and pressed on producing the frictional heat in the contact area. The determining process parameters thereby are the axial force ( $F$ ), the axial shift ( $s$ ) and the rotary speed ( $n$ ).

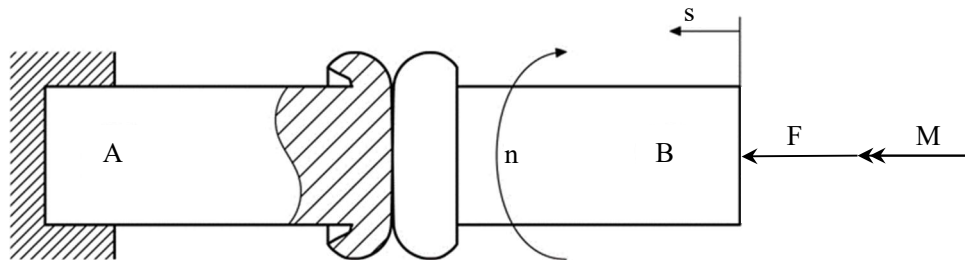


**Fig. 1** General structure of the rotary friction welding process [1]

The usual procedure consists of two fundamental process stages being the rubbing (I) and the forging stage (II) whose characteristics are strongly link to the type of machine drive (directly or fly wheel driven). The decisive difference between these two variants is related to the rotation speed curve of the spindle (Fig. 2). In fly wheel friction welding, the rotary speed is applied and decelerated in a self-regulated manner depending on stored energy by the inertia of the fly wheel. By contrast, in the direct driven friction welding process it is done by a continuously driven engine. Hence, these variants are known as inertia friction welding (IFW) and direct driven friction welding (DDFW).

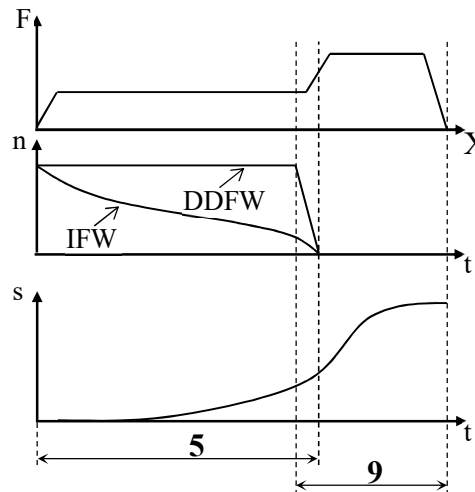


Fig. 2 Parameter regime of the IFW process in contrast to the DDFW process [1]

Concerning interfacial material bond, it can be stated that its creation is based on solid-state reactions in the contact area between the different former separated substance systems of the involved welding materials. The required activation energy thereby is provided by the frictional heat and supported by the elastoplastic deformation of the underlying material. In order to enable the substance systems interaction it is necessary to replace all contaminants and oxide layers out of the interface. This is accomplished during the material's deformation the rubbing and forging stages while they are first cracked and afterwards spread out into the resulting flash. With respect to the interdiffusion process it has to be emphasized that its occurrence is an attendant phenomenon of the material bonding during the welding procedure leading to new intermediate material layers. These layers are the result of the changes of the chemical composition in the contact area and mainly consist of intermetallic compounds.

Due to the fact that the welding temperature does not exceed the material's melt temperature, micro-structural transformations only appear caused by the heating and cooling rate and the degree of severe plastic deformation. With this in mind, aluminium to steel friction welded joints were analysed with respect to their microstructure after the welding procedure. Several studies [2–4] indicated that only the aluminium material undergoes a pronounced change in microstructure due to the fact of lack any deformation on the steel side. According to the location on the aluminium side an increase of the dynamic recrystallization volume from the unaffected base material to the contact area was recognized.

Against this background, this paper is presenting an ansatz to simulate the dynamic recrystallization in commercially pure aluminium during the RFW process based on an Avrami-type equation. Further scenarios, such as precipitation and strain hardening or coarsening, are purposely not modelled. On the one hand, these microstructural transformations do not occur in commercially aluminium (precipitation hardening) and on the other hand, they do not take place during the RFW process (strain hardening and coarsening).

Since, the passed welding temperatures and degree of plastic deformation are required, it is essential to map the thermal and deformation cycles itself through a RFW process



simulation. Nevertheless, the process simulation is completely independent from the microstructure simulation and serves exclusively to determine the state variables (temperature and degree of deformation history) for the Avrami equation.

The outline of this paper is as following: First of all, the derivation of the microstructure evolution equation and its computational treatment is shown in common with an introduction to the RFW process modelling ansatz. Later, the simulation results are displayed corresponding with their related experimental data analysis. Finally, the results are summarized up and an outlook for the further actions is given.

### THEORETICAL BACKGROUND AND METHODOLOGY

#### MICROSTRUCTURE MODELLING

Starting point for basically description of phase transition or structural transformation phenomena in solids under isothermal and unstressed conditions is the general Johnson-Mehl-Avrami-Kolmogorow equation, commonly known as Avrami equation. Hence, it is used to model the static recrystallization in aluminium alloys shown by [5]

$$\chi = 1 - \exp(-\alpha t^\beta). \quad (1)$$

Therein are  $\chi$  the recrystallization volume fraction,  $\alpha$  the overall rate constant and  $\beta$  the Avrami exponent. Generally  $\alpha$  and  $\beta$  are temperature dependent and have to be experimentally estimated. Due to the conditional limitations [6] consistently modified this evolution equation to describe also the dynamic recrystallization by taking the part of the plastic strain  $\varepsilon$  instead of the time

$$\chi = 1 - \exp(-\alpha \varepsilon^\beta). \quad (2)$$

Various investigations [7,8] confirmed its validity for different aluminium alloys whereas it has to stated that this approach is only phenomenologically justified and needs to be reviewed for the considered case. With this in mind, the correctness will be discussed later. In this paper a further modification is made with the purpose to consider also non-isothermal and non-steady-state conditions. For that reason, Eqn. (2) was derived in time and subsequently the plastic strain was eliminated by employing the recrystallization volume fraction

$$\dot{\chi} = \alpha \beta (1 - \chi) \left( \frac{-\ln(1 - \chi)}{\alpha} \right)^{\frac{\beta-1}{\beta}} \dot{\varepsilon}. \quad (3)$$

The resulting differential equation is no more limited to isothermal and steady-state conditions. Its computational integration can be done by the Runge-Kutta procedure, for instance. Here, the applied strain rate  $\dot{\varepsilon}$  is related to a 1D problem, hence it can easily be estimated by the direct time derivation of the plastic strain. In case of 3D problems like the

FRW process, the von-Mises equation can be used under the assumption of volume constancy. Therefore, the symmetric part of deformation rate gradient tensor  $\mathbf{D}$  is adopted

$$\dot{\varepsilon} = \sqrt{\frac{2}{3} \mathbf{D} \cdot \mathbf{D}} \quad (4)$$

as well as the deformation gradient tensor  $\mathbf{F}$

$$\mathbf{D} = \frac{1}{2} (\dot{\mathbf{F}} \cdot \mathbf{F}^{-1} + \mathbf{F}^{-T} \cdot \dot{\mathbf{F}}^T). \quad (5)$$

#### THERMAL AND DEFORMATION CYCLE MODELLING

First attempts of modelling the RFW process can be dated back to the mid 1990's by [9] and followed later by [10–13] always with the purpose of developing a robust simulation tool to be capable to understand and improve the welding process. Nowadays, a new modelling approach from [14] gain more and more attention caused by its computational time efficiency, high robustness and stability. In view of these benefits, this modelling approach is also used here. In the following a few comments to the general procedure and to the main governing equations are given. Due to the fact, that the RFW process is a deformation with temperature coupled problem, two essential differential equations have to be solve. One is related to the description of the motion of continua. At this point, it is represented in its weak form by the principle of virtual power

$$\int_B \delta \mathbf{v} \cdot \ddot{\mathbf{x}} \rho dV = \int_B \delta \mathbf{v} \cdot \mathbf{b} \rho dV + \int_B \delta \mathbf{v} \cdot \text{div}(\boldsymbol{\sigma}) dV. \quad (6)$$

Here, the acceleration is depicted by  $\ddot{\mathbf{x}}$ ,  $\mathbf{b}$  is related to the inner body forces,  $\boldsymbol{\sigma}$  is the Cauchy stress tensor and  $\rho$  describes the mass density. The other equation concerns to the heat conduction in the welding components and is mapped in its weak form by the principle of virtual temperature

$$\int_B \delta \theta c \dot{\theta} \rho dV = \int_B \delta \theta r \rho dV - \int_B \delta \theta \text{div}(\mathbf{q}) dV + \int_B \delta \theta \boldsymbol{\sigma} \cdot \mathbf{D} dV. \quad (7)$$

Incidentally,  $\theta$  expresses the absolute temperature,  $\boldsymbol{\sigma} \cdot \mathbf{D}$  is the dissipation energy of the inner stresses,  $\mathbf{q}$  represents the heat flux and  $r$  is the mass specific heat source term. Both initial value problems are solved by the help of the finite element method and the use of a penalty contact formulation. Further details concerning the modelling of the friction or the environmental modelling can be seen in [14].

Another issue in the RFW modelling affects the material deformation behaviour. The most challenging part therein is to cover the large elastoplastic deformation over the entire welding temperature range with simultaneous consideration of the immense changes in the rate of deformation. The main innovation in [14] is the use of an advanced Carreau fluid model to describe the material behaviour during the process. As a consequence, the Cauchy

stress is just a function of the current deformation rate gradient tensor, the temperature and the von-Mises strain rate

$$\boldsymbol{\sigma} = \mu_B \operatorname{tr}(\mathbf{D}) \mathbf{I} + 2\mu(\dot{\boldsymbol{\epsilon}}, \theta) \operatorname{dev}(\mathbf{D}). \quad (8)$$

The advantages of this formulation in contrast to others are its improved approximation of the stress-strain rate relation in the higher temperature ranges and the better tangibility of the material parameters. The employed shear viscosity  $\mu(\theta, \dot{\boldsymbol{\epsilon}})$  is derived from a Norton-Bailey power law

$$\mu(\dot{\boldsymbol{\epsilon}}, \theta) = \left[ 1 + \left( \left( \frac{\sigma_0(\theta)}{3\mu_0 \dot{\boldsymbol{\epsilon}}_0} \right)^{\frac{n}{1-n}} \frac{\dot{\boldsymbol{\epsilon}}}{\dot{\boldsymbol{\epsilon}}_0} \right)^2 \right]^{\frac{1-n}{2n}} (\mu_0 - \mu_\infty) + \mu_\infty. \quad (9)$$

Wherein, the temperature-dependant exponent  $n(\theta)$  is consistently assessed by the assumption that all isothermal viscosity-strain rate curves finally intersect in the same point. Fig. 3 illustrates the regime of isothermal viscosity-strain rate curves for this Carreau fluid formulation.

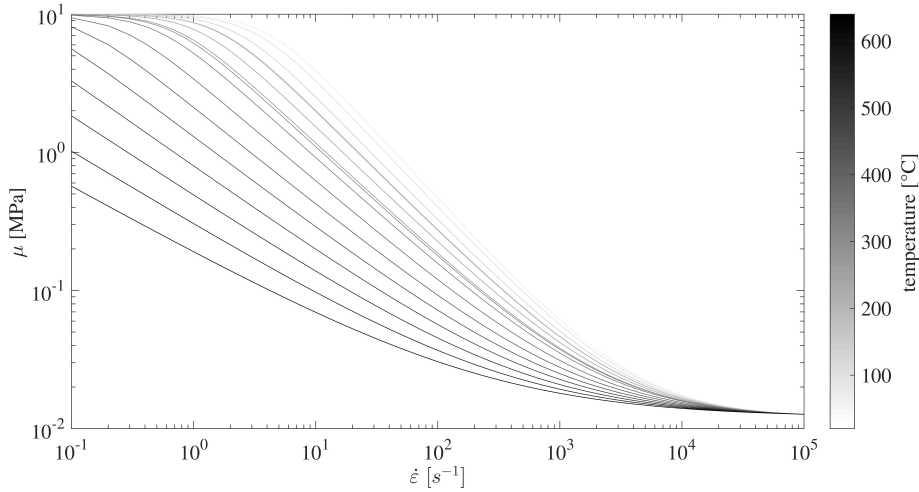


**Fig. 3** Regime of isothermal viscosity-strain rate curves

The introduced saturation parameters  $\mu_0$  and  $\mu_\infty$  in Eqn. (9) are applied for a better computational tangibility of various singularities arising in cases of  $\dot{\boldsymbol{\epsilon}} \rightarrow 0$ ,  $\dot{\boldsymbol{\epsilon}} \rightarrow \infty$  and  $\theta \geq \theta_M$ . Whereas, the adopted bulk viscosity linked to the spherical part of the Cauchy stress tensor in Eqn. (8) is in order to preserve the volume constancy and acts in this way like a Lagrange multiplier. The reference strain rate  $\dot{\boldsymbol{\epsilon}}_0$  and the reference flow stress  $\sigma_0(\theta)$  in Eqn. (8) arisen from Norton-Bailey power law are material specific constants. Additional detailed information regarding the local and temporal discretization, the finite element formulation and the meshing respectively the remeshing procedure, can be found in [14].

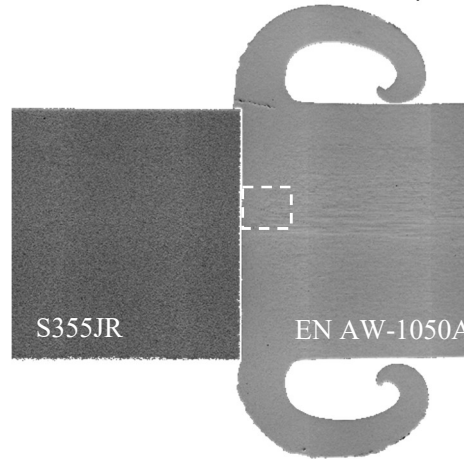
EXPERIMENTAL AND SIMULATION RESULTS

This section is demonstrating the potential and the performance of the aforementioned simulation methodology for the microstructural evolution in commercially pure aluminium during the RFW process. The focus lies on the qualitative prediction of the dynamic recrystallized volume fraction according to the location from the contact area to the unaffected base material. For that purpose, a commercially pure aluminium (EN AW-1050A) to structural steel (S355JR) direct driven friction welded joint was analysed. The used process parameterization set is displayed in Table 1.

**Table 1** Process parameterization

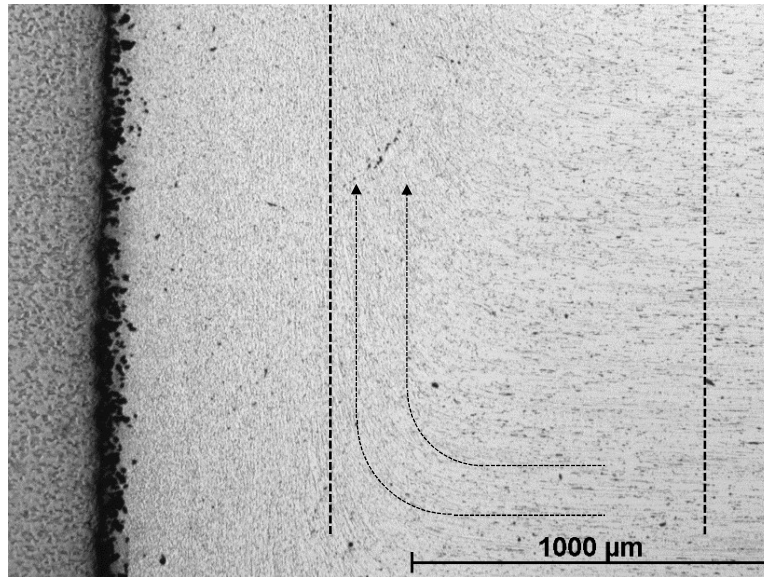
friction pressure	forging pressure	friction time	forging time	rotary speed
[MPa]	[MPa]	[s]	[s]	[min <sup>-1</sup> ]
20	60	1	3	7500

Since, only the aluminium underwent a relevant change in microstructure, the examination of the steel side was neglected. Fig. 4 shows the cross-section of the weld pointing out the investigation area for the microstructural analysis.



**Fig. 4** Cross-section of the weld displaying the investigation area

In accordance with [15], Fig. 5 represents two different layers with microstructural transformations, commonly known as, dynamically recrystallized zone (DRX) and thermo-mechanically affected zone (TMAZ). The microstructure study offers fully recrystallized fine and equiaxed grains in the DRX immediately after the interface. Followed by partially dynamically recrystallized grains plus redirected unaffected grains in the TMAZ. The reason for that is based on the material flow from the inner to the outer body during the manufacturing process and effects in this way a turn round of the former axial-directed grains to the radial direction (exemplified by two arrows in Fig. 5). Furthermore, the analysis of the base material (BS) expectedly displays an unaffected microstructure due to the lack of thermal and plastic deformation. In agree with [15], these results are typically observed for aluminium to steel friction welded joints.



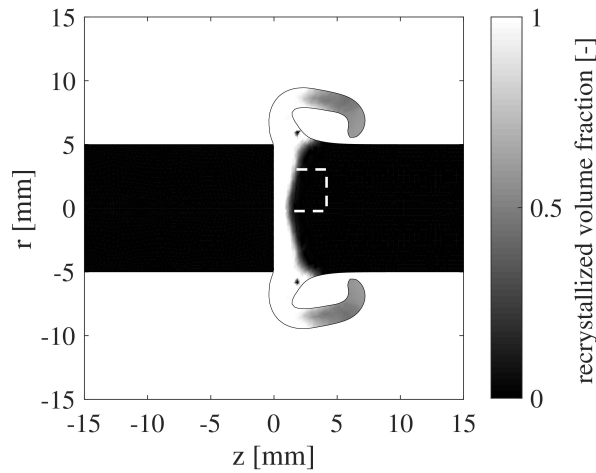
**Fig. 5** Optical microstructure taken from near-centre region

Table 2 lists the measured mean grain sizes corresponding to their appearance in these zones.

**Table 2** Process parameterization

<b>DRX</b> [ $\mu\text{m}$ ]	<b>TMAZ</b> [ $\mu\text{m}$ ]	<b>BS</b> [ $\mu\text{m}$ ]
7	11-45	73

As a consequence of the microstructural study, every individual zone indicates a distinctive percentage of dynamically recrystallized volume being  $\chi = 1$  for the DRX,  $0 < \chi < 1$  for the TMAZ and  $\chi = 0$  for the base material. Nevertheless, it has to be stated that an exact experimental estimation of the range of every single zone is quiet difficult due to the fact that the transition into each other is flowing. With this in mind, here is just a qualitatively comparison of the dynamically recrystallized volume fraction between the model and the experiment done. Fig. 6 illustrates the computational results of the microstructural evolution based on the previous described modelling method and clarifies the area of experimental investigation (Fig. 6).



**Fig. 6** Regime of the dynamically recrystallized volume fraction

All in all, it can be stated that a qualitatively good agreement with the experimental investigation is achieved. The simulation maps the regime of microstructural transformation from the unaffected base material to the DRX quite well. However, the expanse of TMAZ is only insufficiently mapped and indicates a very narrow transition between the DRX and the BS unlike it was observed by the microscopic analysis (Fig. 5). One reason for this concerns the lack of knowledge of the exact material specific parameters  $\alpha$  and  $\beta$  for the related von-Mises strain rates and temperatures. Here, these data have been estimated using the method described in [8] with the help of the tensile test data from [16]. Another reason is related to the exact computation of the required temperatures and the von-Mises strain rates, commonly known as state variables, mapped by the process simulation for the entire welding procedure. Fig. 7 and Fig. 8 display exemplary the temperature and the von-Mises strain rate immediately after the rubbing stage at  $t = 1.5$  s.

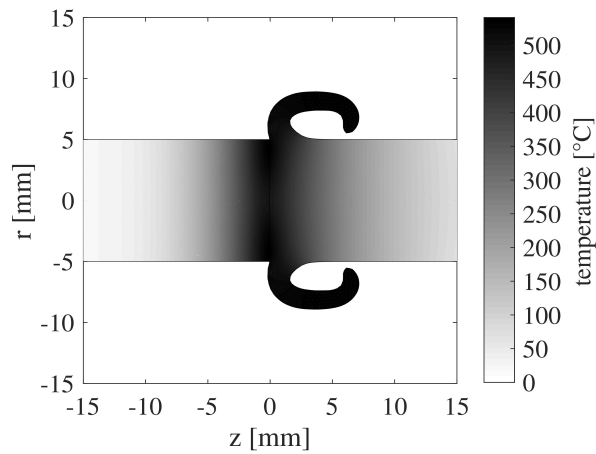


**Fig. 7** Temperature immediately after the rubbing stage at  $t = 1.5$  s

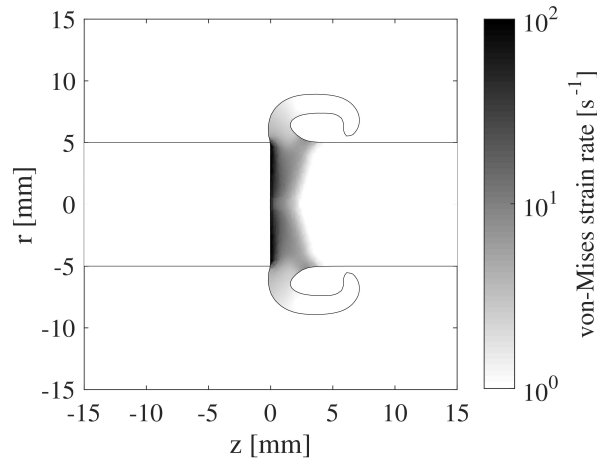


**Fig. 8** von Mises strain rate immediately after the rubbing stage at  $t = 1.5$  s

Basically, there are almost no satisfying possibilities to determine these state variables during the process experimentally. Therefore, no direct comparison between the process simulation results and reality can be made. For this reason, other options must be used to validate the simulation. [14] pointed out that the agreement of the flash evolution between the simulation and the experiment is an excellent indicator for the simulation quality and thus also for validity of the corresponding state variables. Fig. 9 illustrates the comparison of the flash evolution between the model and experiment for the analysed joint.

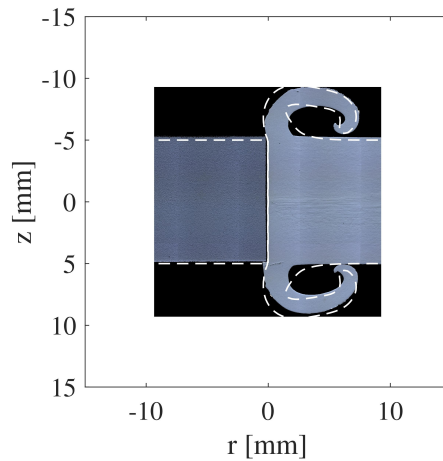


**Fig. 9** Comparison of the simulated and the experimental obtained flash at the end of the forging stage

Despite some small deviations in the flash evolution, it can be assumed that the mapping of the process and the related state variables is not the cause for the differences in the microstructure simulation. Rather, it has to be worked on a better estimation of the material specific parameter for the modified Avrami equation to achieve an even better approximation.

CONCLUSION

In the current paper, a modelling ansatz for the microstructural evolution in commercially pure aluminium was represented. The main purpose therein was the simulation of the dynamic recrystallization due to its dominating rule during the RFW process. Therefore, the generally Avrami equation was modified in order to consider dynamic recrystallization for non-isothermal and non-steady-state conditions. The obtained results indicate a qualitatively good agreement with the experimental investigation. Benefits of this model are the proper estimation of the dynamic recrystallized volume fraction and by the means of a mixing rule the determination of the resulting grain size.

REFERENCES

- [1] D. SCHMICKER, K. NAUMENKO, AND J. STRACKELJAN, “A robust simulation of Direct Drive Friction Welding with a modified Carreau fluid constitutive model,” *Computer Methods in Applied Mechanics and Engineering*, vol. 265, pp. 186–194, 2013.
- [2] M. SAHIN AND C. MISIRLI, “Mechanical and Metalurgical Properties of Friction Welded Aluminium Joints,” in *Pure 7000 Alloys: Microstructure, Heat Treatments and Hot Working*, P. Leo and E. Cerri, Eds., INTECH Open Access Publisher, 2012.
- [3] M. YILMAZ, M. ÇÖL, AND M. ACET, “Interface properties of aluminum/steel friction-welded components,” *Materials Characterization*, vol. 49, no. 5, pp. 421–429, 2002.
- [4] M. ASHFAQ, N. SAJJA, H. KHALID RAFI et al., “Improving Strength of Stainless Steel/Aluminum Alloy Friction Welds by Modifying Faying Surface Design,” *Journal of Materials Engineering and Performance*, vol. 22, no. 2, pp. 376–383, 2013.
- [5] M. AVRAMI, “Kinetics of Phase Change. I. General Theory” *Journal of Chemical Physics*, vol. 7, no. 12, pp. 1103–1112, 1939.
- [6] Q. GUO-ZHENG, “Characterization for Dynamic Recrystallization Kinetics Based on Stress-Strain Curves,” in *Recrystallization Processes Involving Iron Oxides in Natural Environments and In Vitro*, N. Taitel-Goldman, Ed., INTECH Open Access Publisher, 2013.
- [7] K. HUANG AND R. E. LOGÉ, “A review of dynamic recrystallization phenomena in metallic materials,” *Materials & Design*, vol. 111, pp. 548–574, 2016.
- [8] Y.-B. HE, Q.-L. PAN, Q. CHEN et al., “Modeling of strain hardening and dynamic recrystallization of ZK60 magnesium alloy during hot deformation,” *Transactions of Nonferrous Metals Society of China*, vol. 22, no. 2, pp. 246–254, 2012.
- [9] V. K. STOKES AND A. J. POSLINSKI, “Effects of variable viscosity on the steady melting of thermoplastics during spin welding,” *Polymer Engineering and Science*, vol. 35, no. 5, pp. 441–459, 1995.
- [10] L. D’ALVISE, E. MASSONI, AND S. J. WALLØE, “Finite element modelling of the inertia friction welding process between dissimilar materials,” *Journal of Materials Processing Technology*, 125-126, pp. 387–391, 2002.
- [11] A. MOAL AND E. MASSONI, “Finite element simulation of the inertia welding of two similar parts,” *Engineering Computations*, vol. 12, no. 6, pp. 497–512, 1995.
- [12] G. J. BENDZSAK, T. H. NORTH, AND Z. LI, “Numerical model for steady-state flow in friction welding,” *Acta Materialia*, vol. 45, no. 4, pp. 1735–1745, 1997.



- [13] L. WANG, M. PREUSS, P. J. WITHERS et al., “Energy-input-based finite-element process modeling of inertia welding,” *Metallurgical and Materials Transactions B*, vol. 36, no. 4, pp. 513–523, 2005.
- [14] D. SCHMICKER, *A holistic approach on the simulation of rotary friction welding*, Dissertation, Fakultät für Maschinenbau; epubli GmbH, 2015.
- [15] M. ASHFAQ AND K. J. RAO, “Comparing bond formation mechanism between similar and dissimilar aluminium alloy friction welds,” *Materials Science and Technology*, vol. 30, no. 3, pp. 329–338, 2014.
- [16] E. DOEGE, H. MEYER-NOLKEMPER, AND I. SAEED, *Fließkurvenatlas metallischer Werkstoffe: Mit Fließkurven für 73 Werkstoffe und einer grundlegenden Einführung*, Hanser, München, 1986.

## **VI Special Joining Processes**

*intentionally blank page*

*intentionally blank page*

*intentionally blank page*

*intentionally blank page*

*intentionally blank page*

*intentionally blank page*



*intentionally blank page*

*intentionally blank page*

*intentionally blank page*

*intentionally blank page*

*intentionally blank page*

*intentionally blank page*

*intentionally blank page*

*intentionally blank page*



*intentionally blank page*

*intentionally blank page*

*intentionally blank page*

# ELECTRICAL CONTACT RESISTANCE MODEL FOR ALUMINUM RESISTANCE SPOT WELDING

M. PIOTT\*, A. WERBER\*, L. SCHLEUSS\*\*, N. DOYNOV\*\*,  
R. OSSENBRINK\*\* and V. G. MICHAILOV\*\*

*\*Daimler AG, Sindelfingen, Germany*

*\*\*Department of Joining and Welding Technology, Brandenburg University of Technology, Cottbus-Senftenberg, Germany*

DOI 10.3217/978-3-85125-615-4-36

## ABSTRACT

Resistance spot welding is one of the most important welding processes for joining sheet metal parts in automotive industry. In the process of resistance spot welding electrical contact resistance is of critical importance. The process involves mechanical, electrical and thermal interactions and is dominated by Joule heating, generated at faying surfaces and electrode-sheet-interface. Especially for aluminum alloys, due to small bulk resistance and oxide layer, most of heat is generated at the interfaces.

Up to today, barely numerical models for the dynamic contact resistance of aluminum have been published. In this work, a model for contact resistance of aluminum alloys is presented. The model describes the dynamic contact resistance as a function of pressure and temperature.

Therefore, an experimental study was designed to determine the dynamic behavior of the contact resistance. Two sheets of aluminum alloy AA5182 were joined by resistance spot welding with variation of electrode force and current. In order to determine the apparent contact resistance, current and voltage differences between sheet-sheet and electrode-sheet were measured.

A coupled thermal-electrical-mechanical FE-model with temperature-dependent material properties was used to simulate the experiments. Calculated contact resistances and nugget diameters were compared to the measured ones in order to calibrate the contact resistance model and to validate the simulation.

Experimentally measured resistances and nugget diameters are in good accordance with numerical results. The dynamic contact resistance can be calculated by the deployed model with reasonable accuracy.

## INTRODUCTION

Today, resistance spot welding (RSW) is one of the most frequently used joining processes in the body in white shop due to high ability for automation, low cost and short cycle time [1–3]. The required heat of the welding process is generated by Joule heating. The RSW process can be structured in the four process steps displayed in Fig. 1. First, a force is applied on the electrodes and two or more metal sheets are pressed together. In the second step, an electric current through the workpieces is applied and heat is generated by Joule heating, dependent on the distribution of bulk and contact resistances. With increasing temperature, material is softening and a molten nugget forms, when the temperature of the faying surface reaches the melting point of material. After switching off current, the nugget

solidifies under pressure and joins the sheets together. In the last step, electrode force is released and the electrodes are removed.

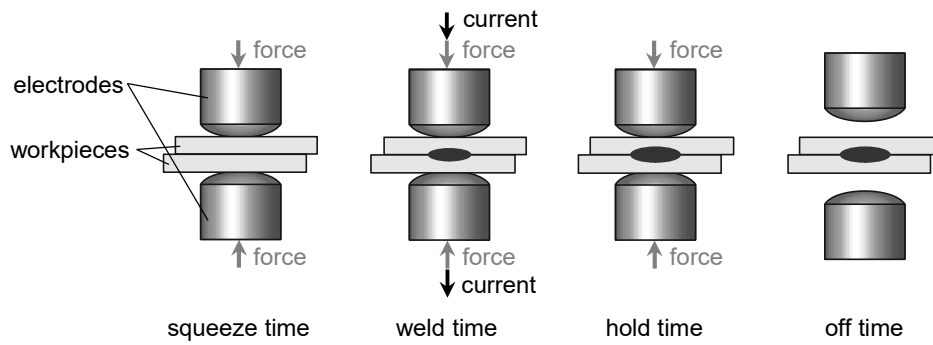


Fig. 1 Process steps of resistance spot welding

In order to save weight and reduce emissions, more light metal alloys, especially aluminum alloys, are utilized in the automotive industry [4, 5]. With the growing demand of aluminum, the need for integration of aluminum resistance spot welding increases. The welding behavior of aluminum is different from steel, which is already well integrated in the body in white shop. Higher currents and shorter process times are required for RSW of aluminum, due to higher electrical and thermal conductivity [6]. Furthermore, the rapidly forming oxide layer of aluminum significantly increases contact resistance and heat generation, which causes rapid electrode cap degradation [2]. Prerequisite of an extended integration of RSW of aluminum alloys into the body in white shop is an improved understanding of influencing parameters and inter-dependencies. Thereby process parameters and the machine setup can be optimized.

Fig. 2 shows the two kinds of resistances in RSW: contact and bulk resistance. The contact resistance appears at electrode-sheet and sheet-sheet interfaces ( $R_2$ ,  $R_4$  and  $R_6$ ) and the bulk resistances in workpieces ( $R_3$  and  $R_5$ ) and electrodes ( $R_1$  and  $R_7$ ) [7].

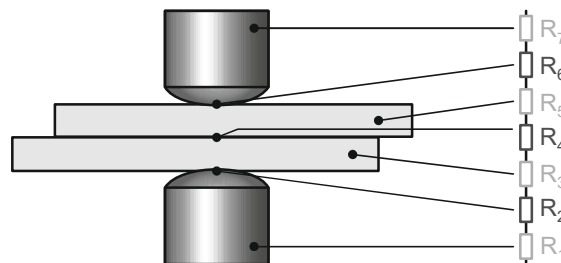


Fig. 2 Electrical resistances in resistance spot welding

The bulk resistance of aluminum alloys and copper increases with temperature. Due to low bulk resistances of aluminum and copper, RSW process of aluminum alloys is strongly influenced by contact resistances, depending on pressure, temperature and surface conditions of the interfaces. Additionally, aluminum alloys form an oxide layer, which is significantly increasing contact resistance. For a robust process, an uniform oxide layer is important. Therefore, aluminum suppliers use special surface treatments to create stable

and uniform oxide layers. Further conditions influencing the contact resistance are surface roughness, lubricants, contaminants and adhesives.

There are many different models for contact resistance in literature. Basics of electrical contacts were studied by Holm [8]. There, it was assumed, that the real contact area is only part of the apparent contact area due to surface roughness. As a result, Holm divided the contact resistance into constriction and film resistance. The constriction resistance represents the constriction of current flow due to surface roughness, see Fig. 3. Thus, the conducting real contact area is always smaller than the apparent contact area. According to Holm, the constriction resistance  $R_c$  depends on the bulk resistivity  $\rho_{el}$  and the radius of a circular contact spot  $a$ :

$$R_c = \frac{\rho_{el}}{2a} \quad (1)$$

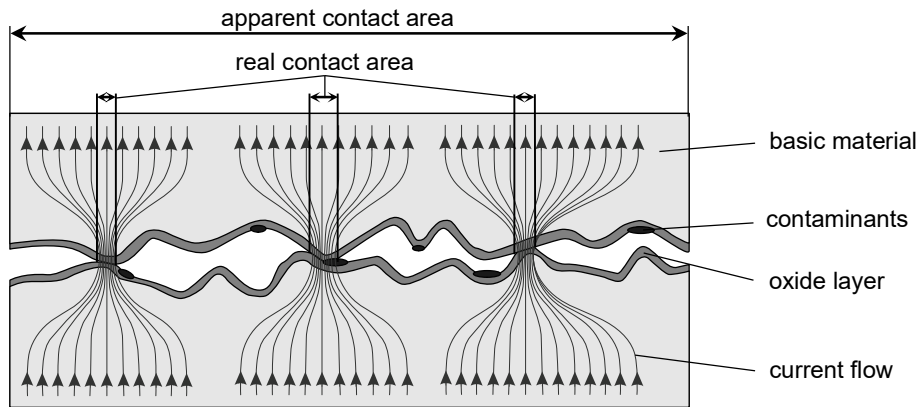


Fig. 3 Surface morphology of electrical contact of aluminum surfaces based on [9]

Metallic surfaces are generally contaminated with an insulating or poorly conducting film layer or residues of lubricant, which influence the conducting contact area and increase contact resistance [10]. Especially aluminum alloys exhibit a rapidly forming oxide layer that is highly increasing contact resistance as film resistance [2].

By generation of heat due to Joule heating in RSW process, contact surface is changing. Increasing temperature of contact asperities result in a thermal expansion, which leads to film rupturing. High loads and high currents can yield to further ruptures of the film. Real contact area increases with growing temperatures due to material softening. Additionally, bulk resistance of contacting materials is increasing with temperature. These effects are superimposed and dynamic. Thus, separating bulk and contact resistance in experiments is not possible.

There are different possibilities to characterize the temperature and pressure dependent behavior of the contact resistance. In situ measurements determine the dynamic behavior of the absolute resistance during RSW-process. Thus, separating bulk and contact resistance in in situ measurements is not possible, because the temperature and pressure distribution in the contact interface is unknown and very dynamic. Therefore, numerical simulation can be used to determine contact resistance inversely [11, 12]. In ex situ measurements the geometry and the conditions of contact interface are simplified in order to control temperature and pressure of contact interface [13–16]. Thus, the specific contact resistance

can be determined, but this method cannot reproduce the dynamically changing contact area and contact conditions during RSW-processes.

In literature, several analytical models of contact resistance have been published. Holm presented a formula for clean contacts based on contact load and material hardness [8]. Other researchers suggested models, which describe the constriction resistance dependent on surface roughness, like Greenwood and Williamson [17, 18]. These models usually rely on surface parameters, which are difficult to determine. Zhang describes contact resistance as a function of flow stress, pressure, bulk resistivity of materials and film resistivity [19]. Popov presented a model for clean contacts, which depends on material bulk resistivity and surface roughness [20]. Kaars published a simple contact resistance model for aluminized steel, where contact resistance is a combination of pressure and temperature dependent functions [12].

In summary, several models for contact resistance are published, but they are usually limited to clean contact faces or rely on parameters, which are difficult to determine. Further, many models describe the behavior of contact resistance for steel and cannot be directly transferred to aluminum alloys.

The current investigation focuses on RSW of aluminum alloy AA5182, which is well integrated in the body in white shop. A model for dynamic contact resistance, depending on contact pressure and temperature, is presented. It considers coupled thermal-electrical-mechanical FE-formulation. To calibrate the model, experiments were carried out, joining two sheets by RSW with variation of electrode force and current. A direct measurement of contact resistances in experiments is not possible. Thus, coupled thermal-electrical-mechanical FE-simulations are carried out to analyze the RSW process. By measuring current and voltage differences between sheets as well as electrode and sheet, the apparent contact resistances, which contain contact and bulk resistances, can be evaluated. FE-simulations with temperature-dependent properties are performed to develop and calibrate a contact resistance model by simulation of the experiments. The FE-model gets validated by comparison of experimental and simulated nugget dimensions.

### EXPERIMENTAL SETUP

The experimental setup is developed to determine resistance curves and to calibrate the model for electrical contact resistance with numerical simulations. Therefore, welding experiments are carried out with two samples of aluminum sheets with same thickness in each case. The dimensions of the sheets are 80 mm × 50 mm with a thickness of 0.85 mm and 1.5 mm, respectively. Sheet material is aluminum alloy AA5182 with a Ti-Zr based conversion layer and lubricant. These workpieces are joined with electrode caps of type ISO 5821-A0-16-20-100 and material CuCr1Zr (ISO 5182-A2/2) by one single spot, Fig. 4.

## Mathematical Modelling of Weld Phenomena 12

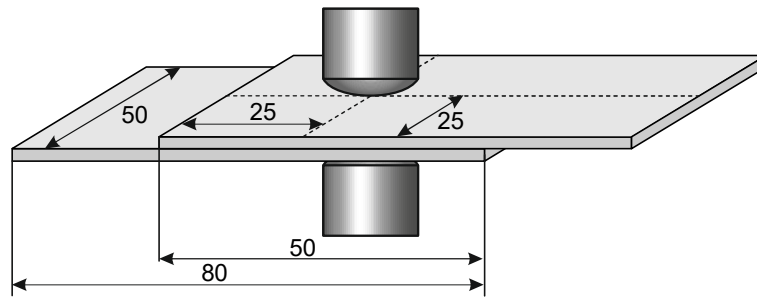


**Fig. 4** Experimental setup

The applied welding current was DC, delivered by an inverter power source clocked with 1 kHz. Two different welding current programs were applied. First current program uses a preheating current of 8 kA and a slope up to the main welding current of 27 kA. The second program has a slope of 50 ms with increasing current from zero to 25 kA. Afterwards, the current is constant for 100 ms. In both programs, electrode force is set constant to 3 kN, 4 kN or 5 kN. Electrode force was applied pneumatically. For each force and current program, five experiments were performed. The electrode forces and current programs are visualized in Fig. 5 and parameter sets are summarized in Table 1.

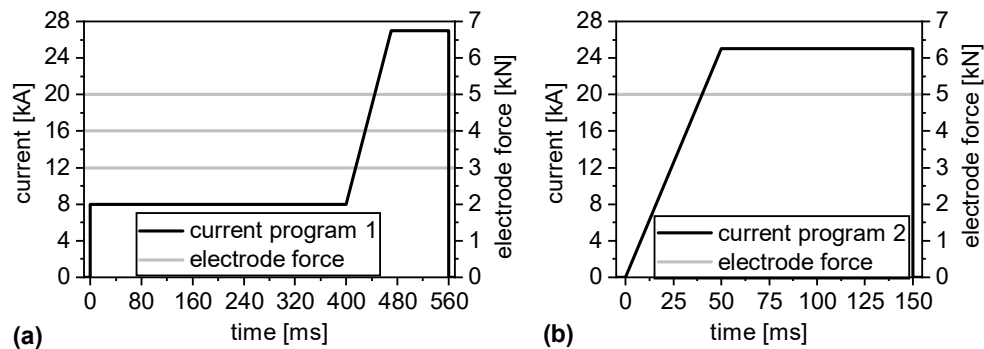


**Fig. 5** Process conditions for experiments: (a) electrode forces with current program 1 and (b) electrode force with current program 2

**Table 1** Sets of parameters in experiments

Set	Sheet thickness [mm]	Current program	Preheating current [kA]	Main current [kA]	Electrode force [kN]
1	0.85	1	8	27	5
2	0.85	1	8	27	4
3	0.85	1	8	27	3
4	0.85	2	-	25	5
5	1.5	1	8	27	5

In order to determine electrical resistances during RSW, the electrical voltage differences between lower electrode and lower sheet, upper sheet and upper electrode were measured. Voltages at sheets were tapped with clamps and a copper wire was soldered onto each



electrode. Additionally the voltage difference between the electrodes was measured twice for verification of measurement. Furthermore, the current flow was measured by a Rogowski coil and electrode force was measured by strain gauges, which have been calibrated before. Fig. 6 shows the experimental setup. The experimental resistances between sheet-sheet ( $R_2'$ ) and between electrode-sheet ( $R_1'$  and  $R_3'$ ) can be determined by equ. (2).

$$R' = \frac{\Delta U}{I} \quad (2)$$

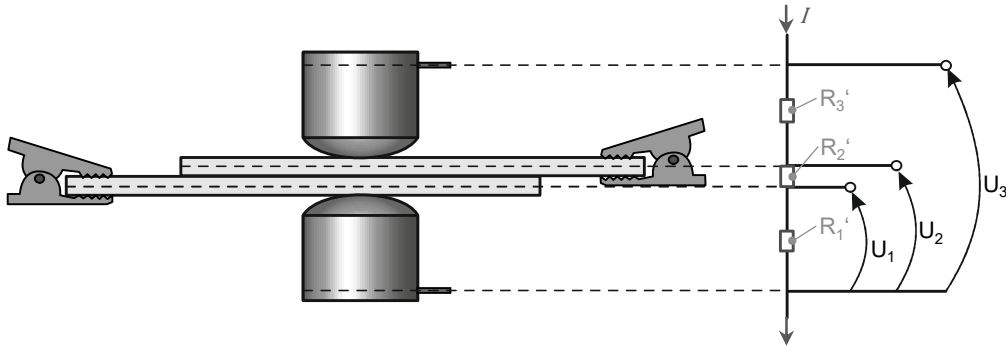


Fig. 6 Measurement of potentials and resistances

#### FINITE ELEMENT MODEL FOR ALUMINUM SPOT WELDING

RSW is a complex process with interactions of mechanical, electrical and thermal phenomena. So a coupled thermal-electrical-mechanical FE-model is set up to consider the essential effects of the welding process. For the numerical simulation, the problem formulation is separated in three sequentially coupled fields: a mechanical, a thermal and an electrical. This chapter gives a short introduction into the used FE-model.

A simplified model is used for FE-simulations, with respect to axial symmetry. Fig. 7 shows the geometry with initial and boundary conditions. The magnitude of initial and boundary conditions of the FE-model are summarized in Table 2.

Table 2 Initial and boundary conditions of FE-simulation

Parameter	Unit	Magnitude
Initial electrode temperature $T_{0,E}$	°C	20
Initial sheet temperature $T_{0,S}$	°C	25
Cooling water temperature $T_W$	°C	20
Ambient temperature $T_{Amb}$	°C	25
Convective heat transfer coefficient $\alpha_A$	W/(m <sup>2</sup> K)	25

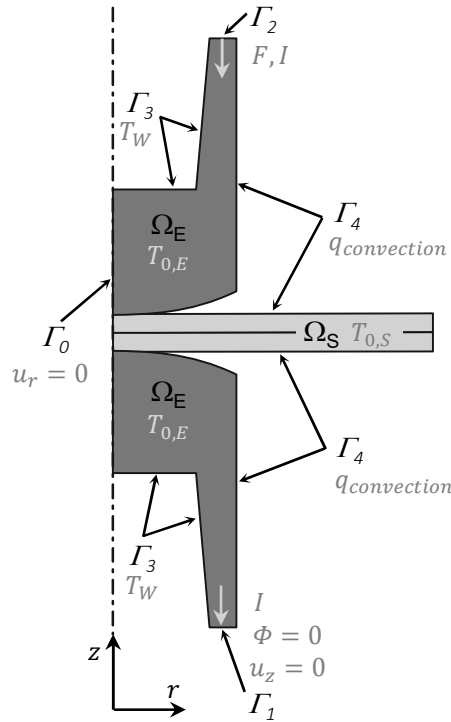


Fig. 7 Initial and boundary conditions

By neglecting inductive effects, the static electrical field is characterized by Ohm's law according to:

$$\mathbf{J} = \frac{1}{\rho_{el}} \mathbf{E} = -\frac{1}{\rho_{el}} \nabla \Phi \quad (3)$$

where  $J$  denotes the current density,  $E$  designates the electrical field,  $\rho_{el}$  is the electrical bulk resistivity of material and  $\Phi$  is the electrical potential. The electrical potential on surface  $\Gamma_1$  is zero as shown in equ. (4) and the electrical current through surfaces  $\Gamma_1$  and  $\Gamma_2$  is defined by the applied welding current  $I$ , which is directed towards  $y$ -axis. The other surfaces are considered to be insulating.

$$\Phi = 0 \quad (\text{boundary } \Gamma_1) \quad (4)$$

Heat generation in RSW is dominated by Joule heating, which is caused by current flow. The increase of temperature yields to a heat conduction problem. The transient heat conduction is described by linear Fourier's law with internal heat source as heat generations per unit volume. The Joule heating per unit volume  $q_J$  depends on resistivity of material  $\rho_{el}$  and current density  $J$  according to equ. (5). The effect of liquid flow in the molten nugget is neglected, due to small size of nugget weld pool and short welding time [21].

$$q_J = \rho_{el} J^2 \quad (5)$$

The thermal initial conditions for electrodes and sheets ( $\Omega_E$  and  $\Omega_S$ ) are equal to initial temperature  $T_0$ , as shown in equ. (6). The thermal boundary condition on surface  $\Gamma_3$  is defined equal to the temperature of the cooling water  $T_W$  (equ. (7)) and a convective heat flux rate  $q_{convection}$  is applied at surface  $\Gamma_4$  according to equ. (8), where  $\alpha_A$  denotes the convective heat transfer coefficient,  $T$  is the surface temperature and  $T_{Amb}$  is the ambient temperature. The other surfaces are considered adiabatic.

$$T_{initial} = T_0 \quad (\text{domain } \Omega_E \text{ and } \Omega_S) \quad (6)$$

$$T = T_W \quad (\text{boundary } \Gamma_3) \quad (7)$$

$$q_{convection} = \alpha_A (T - T_{Amb}) \quad (\text{boundary } \Gamma_4) \quad (8)$$

The mechanical problem considers small deformations. The material behavior is described by constitutive linear momentum balance equation, relating the stress to imposed strain due to electrode force and thermal strain. The thermal strain results from calculated transient temperature field, considering linear isotropic expansion coefficient. The electrode force  $F$  is applied as a set of traction boundary condition at boundary  $\Gamma_2$ . A displacement boundary condition is defined on all points of boundary  $\Gamma_1$ , where the displacement component  $u_z$  is set to zero:

$$uz u_z = 0 \quad (\text{boundary } \Gamma_1) \quad (9)$$

The displacement boundary condition  $u_r$  results from axial symmetry and is applied on all nodes of  $\Gamma_0$ :

$$ur u_r = 0 \quad (\text{boundary } \Gamma_0) \quad (10)$$

In the FE-model of RSW, the electrodes are modeled elastic and sheets are defined elastoplastic with isotropic hardening using the von Mises yield criterion. The governing equation for elastic behavior in incremental form is shown in equ. (11).  $\{d\sigma\}$  denotes the stress increment,  $\{d\varepsilon^e\}$  is the elastic strain increment and  $[D]$  is the elastic matrix.

$$\{d\sigma\} = [D]\{d\varepsilon^e\} \quad (11)$$

Plastic deformation starts, when the von Mises equivalent stress  $\bar{\sigma}$  reaches the flow stress of the elastoplastic material  $\sigma_F$ , according to equ. (12). The associated plastic strain can be calculated by equ. (13) and equ. (14).  $\mathbf{S}$  denotes the deviatoric stress tensor,  $\dot{\boldsymbol{\varepsilon}}^p$  is the plastic strain rate and  $\dot{\bar{\varepsilon}}^p$  is the equivalent plastic strain rate.

$$\bar{\sigma} = \sqrt{\frac{3}{2} \mathbf{S}^T \mathbf{S}} \leq \sigma_F \quad (12)$$

$$\dot{\bar{\varepsilon}}^p = \sqrt{\frac{2}{3} \dot{\boldsymbol{\varepsilon}}^p{}^T \dot{\boldsymbol{\varepsilon}}^p} \quad (13)$$

$$\dot{\boldsymbol{\varepsilon}}^p = \frac{3}{2} \frac{\dot{\boldsymbol{\varepsilon}}^p}{\bar{\sigma}} \mathbf{S} \quad (14)$$

Material properties of the elastoplastic material model are defined as nonlinear functions of temperature up to melting temperature, like presented in [22]. Electrical resistivity, thermal properties, density and flow curves of AA5182 are based on experiments ranging from room temperature to 500 °C. Thermal data above 500 °C is extrapolated and Young's modulus as well as Poisson's ratio are based on data generated by software JMatPro®. Furthermore, phase change is taken into account by latent heat. The material properties of AA5182 at room temperature are shown in Table 3.

**Table 3** Material properties of aluminum alloy AA5182 at room temperature

Yield Stress	Young's Modulus	Poisson's Ratio	Density	Electrical Resistivity	Specific Heat	Thermal Conductivity	Thermal Expansion
MPa	MPa	-	g/cm <sup>3</sup>	μΩ m	J/(kg K)	W/(m K)	-
155	70000	0.33	2.62	0.06	926	110	24·10 <sup>-6</sup>

In order to simulate RSW, a model of the dynamic behavior of contact resistance at faying interface and electrode-sheet interface is required. In the following, an approach for contact resistance, considering the elementary effects of RSW, is described.

The dynamic absolute contact resistance  $R$  is connected to specific contact resistance  $r(p, T)$  and apparent contact area  $A$  according to equ. (15).

$$R = r p, T A R = \frac{r(p, T)}{A} \quad (15)$$

Assuming that the specific contact resistance is a function of pressure and temperature. Effects of pressure and temperature are assumed to be independent. Effects of time are neglected. Thus, the contact resistance  $r(p, T)$  can be described as:

$$r p, T = r_0 f(T) g(p) \quad (16)$$

where  $r_0$  is a basic contact resistance,  $f(T)$  and  $g(p)$  are functions of temperature and pressure, respectively. The basic contact resistance depends on the interface (electrode-sheet or sheet-sheet), the conducted materials and surface morphology (passivation, oxide layer, lubricant, surface roughness and contaminants).

Based on literature [8, 19, 12, 16], the function of pressure is defined as:

$$g(p) = \left( \frac{p_k}{p + p_k} \right)^n \quad (17)$$

wherein  $p$  is the contact pressure and  $p_k$  is a constant to avoid numerical instabilities for a contact pressure equal to zero. The pressure exponent  $n$  gets determined by simulations.

In many contact resistance models, the temperature dependency of contact resistance is considered by hardness or flow stress of materials. To obtain a more universal model, the

temperature function is defined by a nonlinear curve, which gets investigated iteratively by simulations.

### RESULTS AND DISCUSSION

The measured current and electrode forces have little difference compared to the machine settings (Fig. 5). Fig. 8 shows examples of measured data for current program 1. Electrode force shows small increase at current slope due to high thermal expansion, which can not be compensated by the control of the welding gun. Further, the measured current has some differences due to the current control of the welding gun. In order to include these effects in FE-simulation, measured current curves and electrode forces are used in simulation. Experiments with splashes are excluded from evaluation.

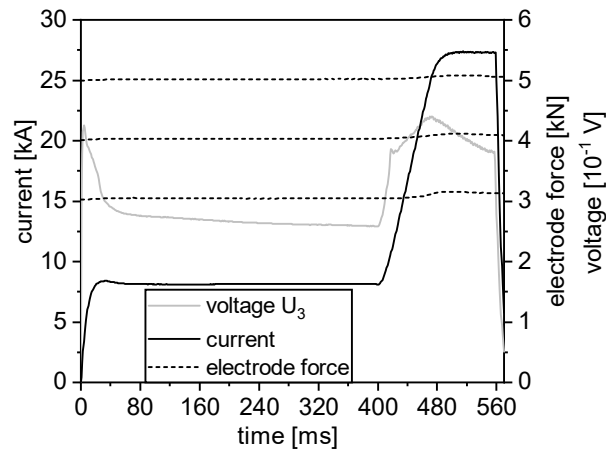


**Fig. 8** Examples of measured current, voltage and electrode force at current program 1

### CALIBRATION OF CONTACT RESISTANCE MODEL

In order to calibrate the contact resistance model, measured curves of apparent contact resistances for sheet-sheet and electrode-sheet are used. Resistances are determined by the recorded voltage differences and currents. All measured apparent contact resistance curves have the maximum resistance at the beginning, due to the smallest real contact area and lowest temperature, visualized in Fig. 9 and Fig. 10. The contact resistance is rapidly decreasing due to an increasing amount and deformation of asperities with temperature, which are influencing the contact constriction resistance [10]. Regarding contact resistance, there is a difference in the behavior of current program 1 and current program 2. The preheating current of program 1 yields to a nearly constant resistance, see Fig. 9. With increasing current up to the main welding current, the resistance is falling to a minimum. In contrast, the measured resistance of current program 2 in Fig. 10 is steadily decreasing to an almost constant level. The comparison of simulated and measured results shows a qualitative good accuracy. Up to 25 ms process time, the simulated resistance is smaller

than the measured ones. This error is assumed to be tolerable, because current and generated Joule heating is small.

For calibration of contact resistance model, parameters of presented contact resistance model are optimized by numerical simulations to fit of measured curves. First, boundary conditions of temperature function are defined. The value of temperature function at room temperature was set to one and the value of zero was applied at melting temperature of aluminum. Values of steadily decreasing temperature function between room temperature and melting temperature, parameters  $r_0$  and  $n$  of equ. (16) and equ. (17) are determined by simulation.

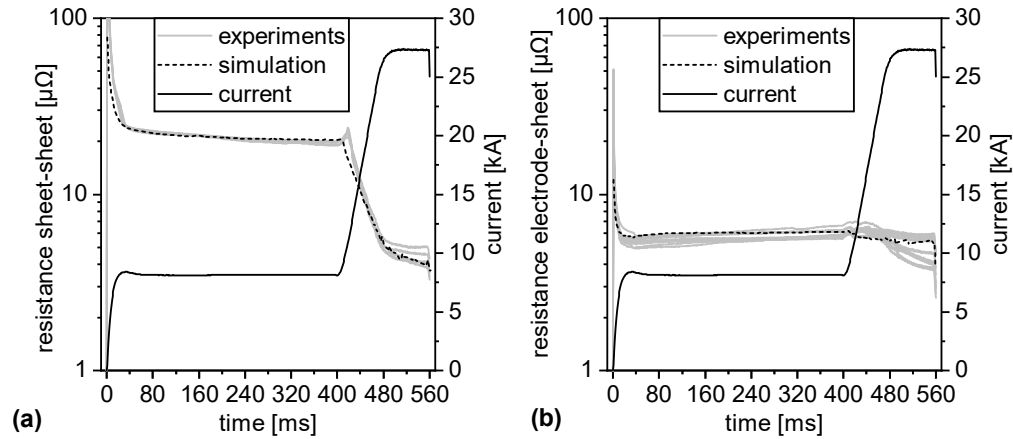


**Fig. 9** Experimental apparent contact resistance curves between (a) sheet-sheet and (b) electrode-sheet with electrode force 5 kN, current program 1 and sheet thickness 0.85 mm

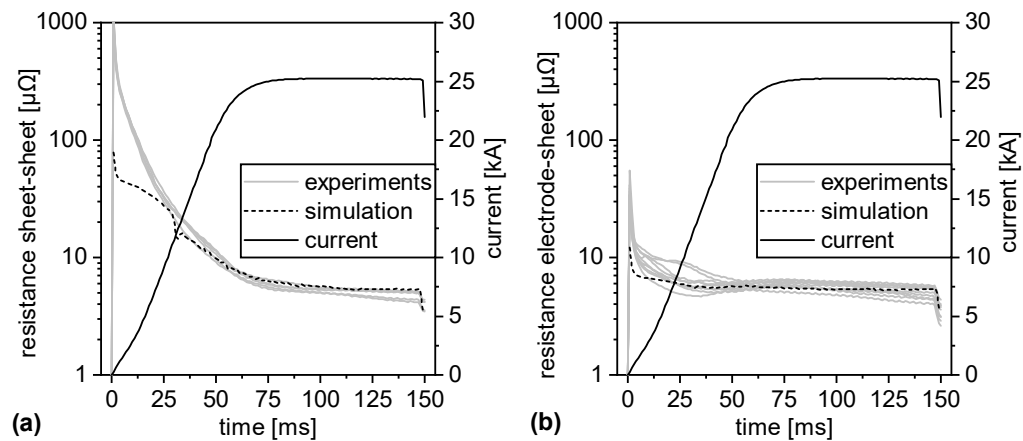


**Fig. 10** Experimental apparent contact resistance curves between (a) sheet-sheet and (b) electrode-sheet with electrode force 5 kN, current program 2 and sheet thickness 0.85 mm

The results of simulative calibration of the dynamic contact resistance model for AA5182 are shown in Fig. 11. Further parameters of the model are summarized in Table 4. Thus, pressure exponent  $n$  is determined to be 1/3 and the corrective term is set to 0.001 GPa, considering pressure  $p$  in GPa. The temperature dependent function is

decreasing from one at room temperature to zero at melting temperature. Further, a drop of temperature function can be seen between 400 °C and 450 °C. The basic contact resistance of electrode-sheet interface is much smaller than basic resistance of sheet-sheet interface, see Table 4. Reason for this effect could be the rupturing of aluminum oxide layer at electrode-sheet interface due to electrode hardness, high electrode forces and electrode radius. In all presented results of FE-simulations, the described dynamic contact resistance model is used.

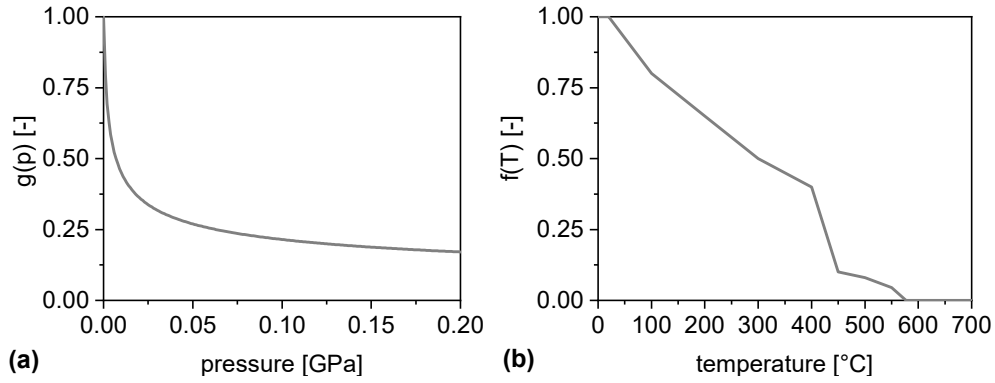


**Fig. 11** Functions of the contact resistance model: (a) pressure and (b) temperature

**Table 4** Parameter of contact resistance model for the sheets with thickness 0.85 mm

Parameter	Unit	Magnitude
$r_0$ (electrode-sheet)	$\mu\Omega \text{ mm}^2$	50
$r_0$ (sheet-sheet)	$\mu\Omega \text{ mm}^2$	3 650
$n$	-	1/3
$p_k$	GPa	0.001

In experiment, only the apparent contact resistance can be measured. By recording voltages and currents, measured resistances are always a combination of contact resistance and bulk resistances of materials between the taps. In contrast, FE-simulation enables the determination of real contact resistance. Fig. 12 visualizes the calculated contact resistance. Further, bulk resistance, which depends on material bulk resistivity and the conducted are, is shown. Up to the slope time, the apparent resistance at the faying surface is dominated by contact resistance for current program 1. Afterwards, the contact resistance is breaking down, due to melting process. At electrode-sheet interface, the apparent contact resistance is dominated by bulk resistance.

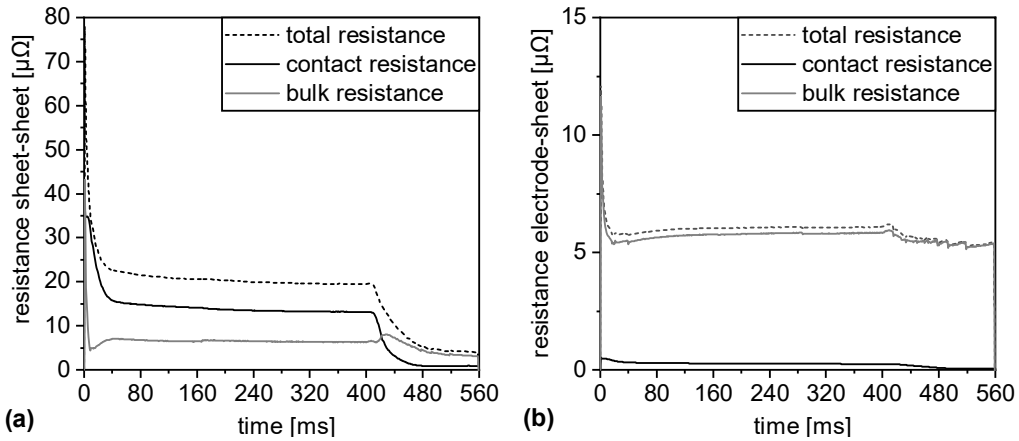


**Fig. 12** Calculated total, contact and bulk resistances with electrode force 5 kN, current program 1 and sheet thickness 0.85 mm for (a) sheet-sheet interface and (b) electrode-sheet interface

Heat generation due to Joule heating is shown in Fig. 13 for current program 1, electrode force of 5 kN and sheet thickness 0.85 mm. Most heat (about 1080 J in experiments and 1043 J in simulation) is generated at sheet-sheet interface caused by contact and bulk resistances. In contrast, Joule heating at electrode-sheet (about 586 J in experiment and 617 J in simulation) is smaller for electrode force of 5 kN. Generated heat caused by contact resistance is about 534 J at faying interface and Joule heating due to contact resistance at electrode-sheet interface is essentially smaller (about 14 J).

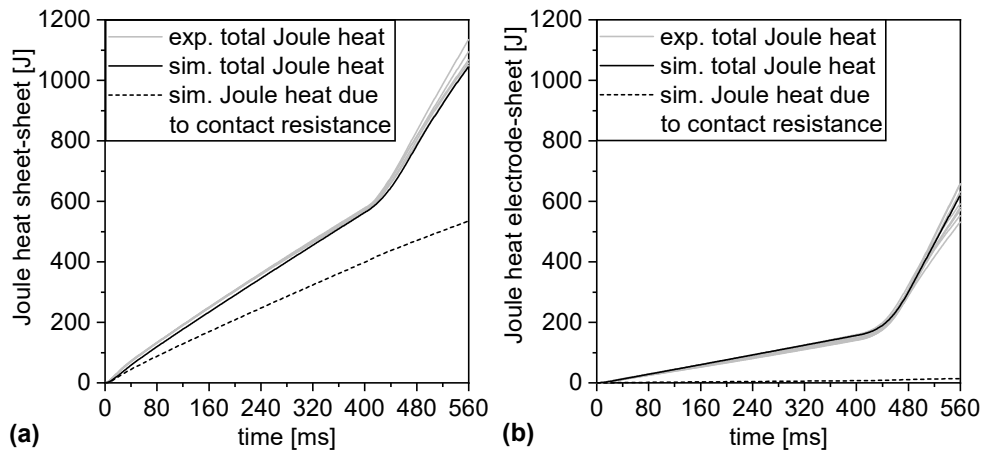


**Fig. 13** Measured and simulated Joule heat with electrode force 5 kN, current program 1 and sheet thickness 0.85 mm for (a) sheet-sheet interface and (b) electrode-sheet interface

In order to determine the deviation between measured and simulated results, total heat generated by Joule heating at faying interface and electrode-sheet interface are compared in Fig. 14 and Fig. 15, respectively. The resulting averaged deviation for generated Joule heating between calculated and mean measured heat is about 3% for faying interface and



## Mathematical Modelling of Weld Phenomena 12

about 5% for electrode-sheet interface. Thus, the results of FE-simulation are matching experiments with a high accuracy.

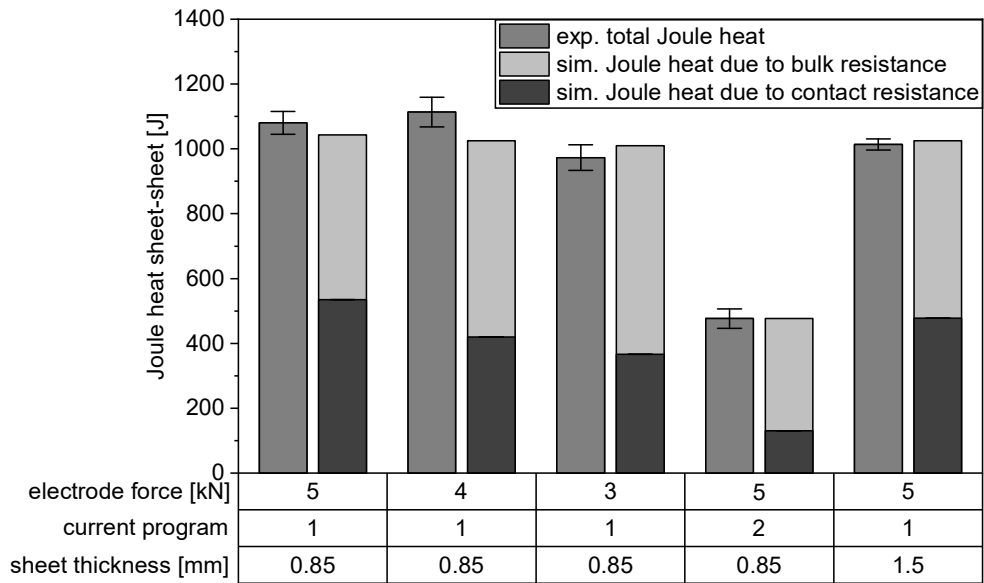


**Fig. 14** Measured und calculated Joule heat at faying interface

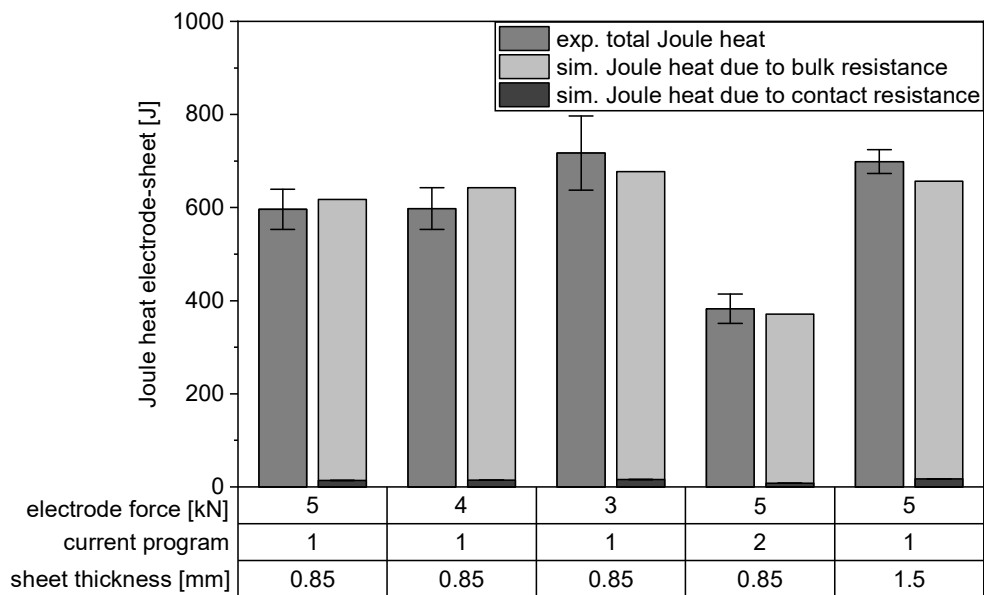


**Fig. 15** Measured und calculated Joule heat at electrode-sheet interface

VALIDATION OF FE-MODEL

For validation of the developed FE-model and the contact resistance model, calculated and measured nugget dimensions are compared in Fig. 16. Therein, measured weld diameters are compared to simulated nugget diameters due to asymmetric nuggets. By decreasing electrode force from 5 kN to 3 kN, mean weld diameter is growing from 4.0 mm to 6.5 mm for sheet thickness 0.85 mm. Mean weld diameter of 4.5 mm at current program 2 is greater than the one of current program 1, although the main current is 2 kA less. The increasing sheet thickness to 1.5 mm yields to bigger nuggets. In experiments the weld diameter grows to 5.0 mm. With a mean discrepancy of about 4% between mean weld diameters and calculated nugget diameters, the simulative results are in good accordance to the measured results. Thus, the accuracy of the FE-model is acceptable.

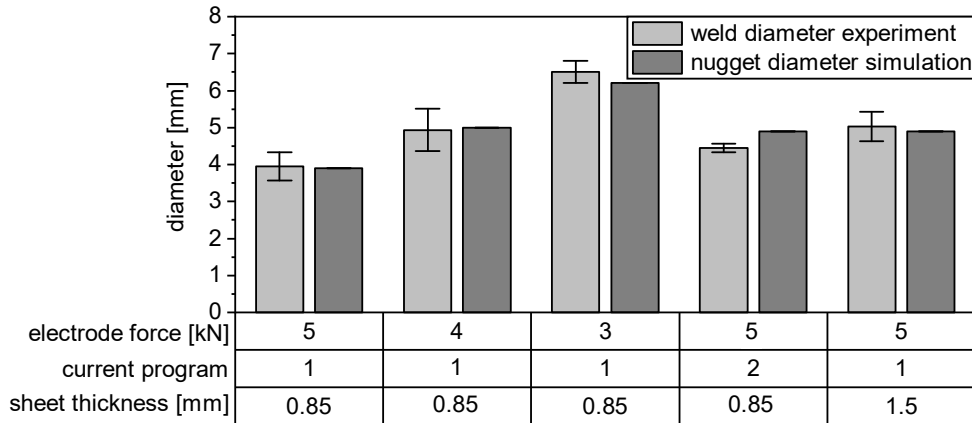


Fig. 16 Comparison of measured weld diameter and simulated nugget diameter

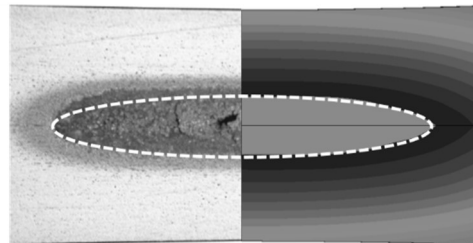


Fig. 17 Comparison of simulated and measured nugget geometry with electrode force 5 kN, current program 1 and sheet thickness 1.5 mm

Fig. 17 visualizes measured and calculated nugget geometry for electrode force of 5 kN, current program 1 and sheet thickness 1.5 mm. The isothermals are used to determine the geometry of the nugget by reaching melting temperature. Both, experimental and calculated nugget diameter are about 4.9 mm. Fig. 17 indicates that the experimental nugget penetration is higher to the direction of the anode-side electrode, which is located at the top. This phenomenon can be explained by Peltier effect, which is not considered in the numerical simulation. Though, the nugget thicknesses are comparable. Thus, the predicted nugget is matching well with the physical nugget profile, which indicates that the FE-model has a good accuracy.

### SUMMARY AND CONCLUSION

In this article, the resistance spot welding process of aluminum, which is dominated by Joule heating at faying surface, has been investigated. The main focus was to develop an approach for contact resistance, which has been proved feasible to model the behavior of contact resistance in the RSW process of aluminum alloy AA5182, which is frequently used in automotive body in white shop. For this purpose, an experimental setup was developed in order to analyze the behavior of the apparent contact resistances in RSW process. A coupled thermal-electrical-mechanical FE-model was successfully used to determine apparent contact resistances as well as the resulting nugget geometry of the experiments.

In the first step, FE-simulations with temperature-dependent elastoplastic material properties for the aluminum sheets were used to calibrate the contact resistance model using measured resistance curves with respect to temperature and pressure dependent effects. Therefore, currents and voltage differences were measured in experiments by variation of applied current, electrode force and sheet thickness. The contact resistance model was fitted to match with measured resistances and is valid for sheet-sheet interface and electrode-sheet interface. Afterwards, in order to determine the accuracy of the calibrated contact resistance model, the heat generated by Joule heating at electrode-sheet and sheet-sheet interface was analyzed. As result, the averaged deviation between calculated and mean measured Joule heating amounts 3% for faying interface and about 5% for electrode-sheet interface. Hence, the obtained results of FE-simulation with the contact resistance model are reproducing experiments with good accuracy.

Further, the presented thermal-electrical-mechanical FE-model was validated. Therefore, the measured experimental nugget dimensions were compared to calculated ones. As result, calculated nugget diameters are matching with experimental weld diameter with a small averaged deviation of 4%, which represents good accordance.

In summary, the presented contact resistance model can reproduce the behavior of the contact resistance in RSW of aluminum alloy AA5182 with the essential effects and interactions. Thus, the thermal-electrical-mechanical FE-simulations are in good accordance to the experimental results.

In future, higher electrode forces and currents should be investigated. Moreover, other surface conditions and their effects on contact resistance should be analyzed. Also, sensitivity studies of the temperature dependent material properties need to be examined.

### REFERENCES

- [1] D. H. PHILLIPS: '*Welding engineering. An introduction*', John Wiley & Sons Ltd., 2016.
- [2] S. M. MANLADAN, F. YUSOF, S. RAMESH, M. FADZIL, Z. LUO and S. AO: 'A review on resistance spot welding of aluminum alloys', *The International Journal of Advanced Manufacturing Technology*, pp. 605–634, 2017.
- [3] U. DILTHEY: '*Schweißtechnische Fertigungsverfahren 1. Schweiß- und Schneidtechnologien*', Springer-Verlag Berlin Heidelberg, Berlin Heidelberg, 3. edition, 2006.

- [4] Ducker Worldwide: 'Aluminum Content in North American Light Vehicles 2016 to 2028', 2017. Online available at: [http://www.drivealuminum.org/wp-content/uploads/2017/10/Ducker-Public\\_FINAL.pdf](http://www.drivealuminum.org/wp-content/uploads/2017/10/Ducker-Public_FINAL.pdf), proved: 2018/06/18.
- [5] S. DAS: 'Life Cycle Energy and Environmental Assessment of Aluminum-Intensive Vehicle Design', *SAE International Journal of Materials and Manufacturing* 7(3), pp. 588–595, 2014.
- [6] M. KIMCHI and D. H. PHILLIPS: 'Resistance spot welding. Fundamentals and applications for the automotive industry', Morgan & Claypool Publishers, San Rafael, California, 2017.
- [7] M. J. GREITMANN, O. VOLZ and H.-J. WINK: 'Untersuchungen zum Übergangswiderstand an blanken und beschichteten Stahlblechen', *Schweißen und Schneiden* 56 Heft 1, 2004.
- [8] R. HOLM: 'Electric contacts. Theory and application', Springer-Verlag, Berlin, New York, 4. completely rewritten edition, 1967.
- [9] S. TIMSIT: 'Electrical contact resistance: properties of stationary interfaces', Electrical Contacts - 1998. Proceedings of the Forty-Fourth IEEE Holm Conference on Electrical Contacts. Arlington, VA, USA, pp. 1–19, 1998.
- [10] E. VINARICKY, K. H. SCHRÖDER and J. WEISER: 'Elektrische Kontakte, Werkstoffe und Anwendungen. Grundlagen, Technologien, Prüfverfahren', Springer Vieweg, Berlin Heidelberg, 3. edition, 2016.
- [11] M. Galler: 'Investigation of interfacial contact condition during resistance spot welding of automobile sheet steel', Graz, Technische Universität GrazDissertation, 2011.
- [12] J. KAARS, P. MAYR and K. KOPPE: 'Simple transition resistance model for spot welding simulation of aluminized AHSS', *Mathematical modelling of weld phenomena 11*, edited by C. Sommitsch, N. Enzinger and P. Mayr, Verlag der Technischen Universität Graz, pp. 685–702, 2016.
- [13] P. Rogeon, P. Carre, J. Costa, G. Sibilia, G. Saindrenan: 'Characterization of electrical contact conditions in spot welding assemblies', *Journal of materials processing technology* 195, 2008.
- [14] S. S. M. VOGLER: 'Electrical contact resistance under high loads and elevated temperatures', *Welding Journal* 72 (6), 231s–238s, 1993.
- [15] Q. Song, W. Zhang, N. Bay: 'An experimental study determines the electrical contact resistance in resistance welding', *Welding Journal* 84, 2005.
- [16] S. S. BABU, M. L. SANTELLA, Z. FENG, B. W. RIEMER and J. W. COHRON: 'Empirical model of effects of pressure and temperature on electrical contact resistance of metals', *Science and Technology of Welding and Joining*, pp. 126–132, 2013.
- [17] J. A. GREENWOOD: 'Constriction resistance and the real area of contact', *British Journal of Applied Physics* 17, pp. 1621–1632, 1966.
- [18] J. A. GREENWOOD and J. B. P. WILLIAMSON: 'Contact of nominally flat surfaces', *Proceedings of the Royal Society of London, Series A, Mathematical and Physical Sciences* Vol. 293, No. 1442, pp. 300–319, 1966.
- [19] W. ZHANG: 'Design and Implementation of Software for Resistance Welding Process Simulations', SAE Technical Paper 2003-01-0978, 2003.
- [20] V. L. POPOV: 'Kontaktmechanik und Reibung. Von der Nanotribologie bis zur Erdbebendynamik', 3. edition, 2015.

- [21] J. A. KHAN, L. XU, Y.-J. CHAO and K. BROACH: 'Numerical Simulation of Resistance Spot Welding Process', *Numerical Heat Transfer, Part A: Applications*, pp. 425–446, 2000.
- [22] R. OSSENBRINK and V. MICHAÏLOV: 'Thermomechanical Numerical Simulation with the Maximum Temperature Austenisation Cooling Time Model (STAAZ)', *Mathematical modelling of weld phenomena 8*, edited by H. Cerjak, Verlag der Technischen Universität Graz, pp. 357–372, 2007.

# WELDABILITY OF A DISSYMMETRIC ASSEMBLY WITH A VERY THIN SHEET DURING RESISTANCE SPOT WELDING

J. QUEVAL\*, E. GESLAIN\*, P. ROGEON\*, T. PIERRE\*,  
C. POUVREAU\*, L. CRETTEUR\*\* and S. MARIE\*\*\*

*\*Université Bretagne Sud, IRDL, CNRS FRE 3744, Lorient, France*

*\*\* ArcelorMittal Global R&D, Montataire, France*

*\*\*\* Transvalor S.A., Mougins, France*

DOI 10.3217/978-3-85125-615-4-37

## ABSTRACT

In automotive industry, to simultaneously impact safety and light weighting for reducing energy consumption, new families of high strength steel have been introduced in the design of body in white. Some combinations of dissimilar sheets, including a very thin sheet, cause weldability problems and difficulties to the optimization of the process parameters setting. Thanks to the progress achieved in numerical and computer engineering fields, modelling and numerical simulation is a relevant approach, to understand the difficulties encountered during resistance spot welding of these assemblies, and to search solutions to improve the weldability. This work aims at the improvement of the weldability of a dissymmetric combination of three dissimilar sheets: a very thin (0.57 mm) zinc coated low carbon steel sheet, a thick (1.47 mm) zinc coated advanced high strength steel sheet, and a thick (1.2 mm) aluminum-silicon coated press hardened sheet.

A numerical axisymmetric 2D Electro-Thermo-Mechanical model developed with the software FORGE® is used to improve the knowledge about the mechanisms which influence the nugget formation and growth, and its penetration inside the cover thin sheet. Experimental evolutions of thermal and electrical contact resistances evolutions, at electrode/sheet and sheet/sheet interfaces, strongly dependent of coatings properties, are embedded in the model and considered dependent on contact temperature and normal stress. The contact radius evolutions, involving the normal contact stresses and the current density distributions in the assembly, are calculated during squeezing, welding, and forging stages.

The model is consistent with several experimental observations (nugget size, contact radii, dynamic resistance) issued from welding tests. Thanks to this model, the important effect of the interfacial mechanisms on the formation and the growth of the molten pool have been highlighted. Furthermore, the influence of the process parameters (current, force) and of the curvature radius of the rounded tip electrodes on the penetration of the welding pool into the thin sheet have been investigated.

Keywords: Resistance spot welding, interface, numerical modeling, contact resistance, physics coupling

## INTRODUCTION

In automotive industry, light weighting of automobiles is one of the principal engines for innovation for reducing the energy consumption. ArcelorMittal, the world leader in the

production of steel works to develop new steels, stronger in order ensure the security inside the vehicle and meet the same specifications with thinner steel sheets.

A body in white is composed by different grade of steels and their position depends on their mechanical properties, duties. In some part of the body in white, it can be necessary to assemble three dissimilar sheets by resistance spot welding (RSW). These combinations create very dissymmetric assemblies that raise problems of weldability with difficulties to grip the thin sheet with the two others, as mentioned by Nielsen [1] or by Kaars [2]. In the case of this study, the assembly (Fig. 2) is made by:

- a zinc coated low carbon steel (LCS) sheet (AM54 – 0.57 mm in depth)
- a zinc coated advanced high strength steel (AHSS) sheet (DP600 – 1.47 mm in depth)
- an Aluminum-Silicon (Al-Si) coated press hardened steel (PHS) sheet (Usibor® – 1.2 mm in depth)

The purpose of this study is to understand the source of the difficulties met during the RSW of this assembly. It is about the identification of the parameters that influence the formation and the development of the molten pool and the penetration of the nugget in the thin sheet. Solutions to improve the grip of the thin sheet could be given. This study is realized through a numerical approach using the software Forge®. A specific attention is given to the interfacial phenomena.

First, the model is validated, comparing numerical and experimental results obtained from welding tests [3]. Then, it is used here mainly to highlight the main mechanisms which influence the formation and the development of the nugget inside the dissymmetric assembly.

### MATERIAL AND METHODS

The results of the experimental welding tests used here for the comparison with numerical results are performed by using a GYSPOT MFDC welding machine developed for automotive body repair [16]. Rounded tip electrodes (ISO 5821-A0-13-18-32) with diameter 13 mm and curvature radius 32 mm are used (Fig.1).



**Fig. 1** Reference electrodes type A0-13-18-32 – diameter 13mm, curvature radius 32mm

The welding process parameters imposed are the electrical current ( $I=8500$  A), the load ( $F=4000$  N) and the welding time ( $t=350$  ms). To highlight the formation and growth of the nugget in the dissymmetric combination studied here, several interrupted welding tests are performed in the range [80 ms -350 ms].

## Mathematical Modelling of Weld Phenomena 12

The voltage between the two electrodes is registered at the frequency of 1 kHz with a numerical recorder SEFRAM (DAS1400) (Fig. 7).

The experimental contact radii at the two electrode/sheet (E/S) interfaces are measured firstly at the end of the clamping stage, with pressure-sensitive paper Prescale® (Fig. 8). Secondly, they are also measured after the cooling stage, from interrupted welds, with an optical profilometer Altimet (Altisurf 500 with the probe CM300) (Fig. 8). The irreversible marks on the surface of the sheets after the electrode indentation are assumed circular.

The experimental value of the final thickness ( $e_A$ ) of the assembly ( $2.75 \pm 0.05$  mm) is measured from the macrograph corresponding to the total welding time (350 ms) (Fig.9).

The main sizes of the nugget (global thickness ( $e_N$ ), radius at S1/S2 interface ( $r_{N1}$ ), radius at S2/S3 interface ( $r_{N2}$ ), penetration inside the thin sheet ( $p$ )) are measured from the macrographs at different interrupted times (Figs. 12-15) by using the software ImageJ®. The precision is related to the pixel size ( $\pm 50 \mu\text{m}$ ).

### NUMERICAL MODEL

#### GEOMETRY AND MESH

Due to the revolution geometry of the electrodes, the geometry of the model can be assumed 2D-axisymmetric. The coatings of the sheets are taken into account through interfacial properties in the contact conditions, and so they are not integrated in the geometry.  $e_1 = 0.54$  mm,  $e_2 = 1.45$  mm, and  $e_3 = 1.14$  mm are respectively the thickness values of the sheets AM54, DP600 and Usibor® respectively.

The initial mesh of the assembly (Fig. 2) is achieved by using linear triangular elements. The size of an element is defined by the average length of its edges. At the proximity of the contact zones, the average size is 0.1 mm. In the zones where the variation of the physical phenomena and the gradients should be high, average size is 0.25mm. Elsewhere the average size is 0.4 mm.

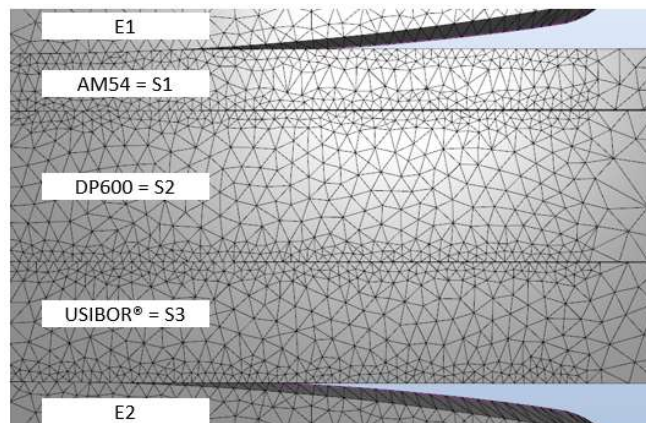


Fig. 2 Initial mesh of the assembly



The criterion for activating the remeshing is automatic and is based on the increasing of the deformation between two remeshing operations. The remeshing is activated after a maximum deformation of 100 %.

### GOVERNING EQUATIONS

Based on some similar recent numerical works ([4], [5], [6]), the model developed here takes into account the main phenomena involved in the process (electrical, thermal, mechanical) with their coupling occurring inside the material and along the interfaces. The metallurgical transformations in the steels are not explicitly taken into consideration in this model. Only the austenitic transformation during heating is implicitly taken into consideration in the evolution of the physical properties and mechanical behavior with the temperature. The transformations during the cooling are not correctly modeled, but their effect concern, principally, the residual stresses [7], which are not in the focus of this study. The effect of the magneto-hydro-dynamic (MHD) phenomenon that are susceptible to occur inside the molten nugget are supposed negligible and are not taken into consideration, according to Wan [6], Wang [5], or Raoelison [4], but in contradiction with Wei ([8], [9]) or Li [10]. However, in the MHD model developed by Wei ([8], [9]) the contact radii are assumed constant. This numerical approach is not suitable in our configuration where convex tip electrodes promote indentation inside the sheets and will induce the increase of the contact radii as a consequence.

The electrical problem consists of solving the equation of electrical current conservation in stationary condition:

$$\text{div}(\vec{J}) = 0 \quad (1)$$

With  $J$  (A/m<sup>2</sup>) the current density. According to Ohm's law:

$$\text{div}(\sigma^{el}(T)\overrightarrow{\text{grad}}(V)) = 0 \quad (2)$$

With  $V$  (Volt) the electrical potential and  $\sigma^{el}(T)$ ( $\Omega.m$ )<sup>-1</sup> the electrical conductivity. The evolutions of the electrical conductivity of the different steels and copper alloy (CuCrZr) of the electrodes come from previous work [3], [11] and [12].

The governing equation for the transient thermal analysis is given by the energy balance:

$$\rho^{vol} \frac{\partial H(T)}{\partial t} = \text{div}(\lambda(T)\overrightarrow{\text{grad}}(T)) + Q \quad (3)$$

Equation in which one, the heat generation by Joule effect is expressed as follows :

$$Q = \overrightarrow{\text{grad}}^T(V)\sigma^{el}(T)\overrightarrow{\text{grad}}(V) \quad (4)$$

Where  $T$ (K),  $\rho^{vol}$  ( $kg.m^{-3}$ ),  $H$  ( $J.kg^{-1}$ ),  $\lambda$ ( $W.m^{-1}.K^{-1}$ ), et  $Q$  ( $W.m^{-3}$ ) denotes respectively the temperature, the mass per unit of volume, the enthalpy per unit of mass and

the internal heat generation by Joule effect. The thermophysical properties of the steels and CuCrZr alloy come from previous work [3], [11] and [12].

The mechanical analysis consists in solving the equilibrium equation :

$$\text{div}(\vec{\sigma}) = -\rho f \quad (5)$$

With  $\sigma$  the stress tensor,  $\rho$  the mass density and  $f$  the force.

During the welding, the temperatures inside the sheets vary in a large range of temperature, from the ambient temperature to high temperatures higher than the liquidus temperature (1535°C). To calculate the strains, a good description of the behaviors of the material at high temperature is needed [7]. Near the melting temperature, sheets become sensitive to the strain rate. The description of the viscoplastic behavior of steels has been input in data tables. The work-hardening curves at different strain rates from  $10^{-3}$  to  $10^3 \text{ s}^{-1}$  and at different temperatures from 20 °C to 1600 °C are given for each steel. The material data for the sheets are given by the software JMatPro® which allows the calculation of the thermophysical and mechanical properties of the steels from their chemical composition. For CuCrZr alloy, plastic behavior has been assumed [11].

The tensor of the strain rates can be decomposed into a reversible part corresponding to the thermoelastic strains and an irreversible part corresponding to viscoplastic strains.

$$\dot{\epsilon} = \epsilon_{rev} + \epsilon_{vp} = \epsilon_{th} + \epsilon_{el} + \epsilon_{vp} \quad (6)$$

The equivalent load stress  $\sigma_{eq}$  (6), for dense materials only depends on the second invariant  $J_2$  (8) of the stress deviator tensor:

$$\sigma_{eq} = \sqrt{\frac{3}{2}J_2} \quad (7)$$

$$J_2 = \frac{1}{2}s^2 = \frac{1}{2}\text{tr}(s \cdot s) \quad (8)$$

$$s = \sigma - \frac{1}{3}\text{tr}(\sigma)I \quad (9)$$

The criterion of plasticity  $f_c$  permit to define the domain of the stress space within which one all the deformations generated are elastic deformations (reversible). In the case of the viscoplasticity with a threshold  $\sigma_y$  and isotropic hardening  $R$ , it corresponds to the von Mises criterion:

$$f_c = \sigma_{eq} - (\sigma_y + R) \quad (10)$$

## BOUNDARY CONDITIONS

Specific boundary conditions are applied during each stage, squeezing, welding, and forging (Fig. 3):

- During squeezing, welding, and forging a mechanical load ( $F=4000\text{ N}$ ) is applied on the upper electrode,
- During welding, electric current is imposed on upper electrode ( $I=8500\text{ A}$ ), and ground ( $V=0$ ) on the lower electrode.
- During welding and forging, water convective exchanges are imposed inside the electrode holes, and air radiative and convective exchanges are imposed on the surfaces of the sheets and electrodes.

The process parameters values are those used during the experimental test taken as reference for this study [3].

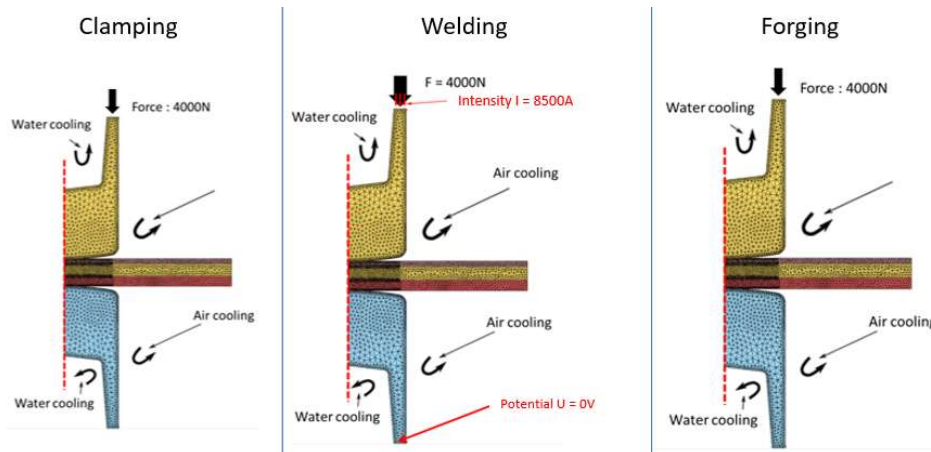


**Fig. 3** Boundary conditions applied on the model corresponding to the welding conditions

## CONTACT CONDITIONS

Due to their curvature radius, electrode tips indent inside the sheets during the welding stage. Furthermore, an important thermal dilatation of sheets occurs, due to the high temperature reached inside the assembly. Consequently, contact conditions change at macroscopic scale.

In fact, the apparent electrode/sheet (E/S) contact area increases during the welding time, and the current density in the assembly and the contact pressure at the interfaces decreases, as a consequence. For the mechanical contact modelling, sliding conditions are assumed for the whole E/S and sheet/sheet (S/S) interfaces.

At the microscopic scale, due to the imperfections of the contact surfaces (surface roughness, chemical pollutants), the interfaces are not perfect and a contact resistance opposes to the current and heat flow. The electrical and thermal contact resistances (respectively ECR and TCR at E/S and S/S interfaces are taken into account through 3 contact parameters (ECR, TCR,  $\alpha$ ) [12]. The electro-thermal contact conditions are

considered purely resistive. The power generation by Joule Effect  $\phi$  inside the ECR, crossed by the current density  $J$ , ( $\phi = ECR \cdot J^2$  (W/m<sup>2</sup>)), is spread over the two surfaces in contact, thanks to a partition coefficient ( $\alpha$ ) imposed to 0.5 outside the thermal contact resistance TCR ([13], [14]).

MATERIALS DATA

The differences between physical and mechanical properties of the sheets contribute strongly to the dissymmetry of the studied assembly (Table 1, Fig. 4). For example, higher resistivity and lower solidus temperature for the two thicker sheets will promote the efficiency of the Joule heating and the earlier initiation of nugget inside Usibor® and DP600, respectively. Furthermore, the lower mechanical strength of the thin sheet AM54 will enhance the indentation of the rounded tip electrode during the welding stage with the decrease of the current density and then of the Joule heating inside the thin sheet as a consequence.

**Table 1** Thermo-physical and mechanical properties of the sheets at ambient temperature (293K) [3]

Nom	Thermo-physical properties at 293 K				Melting temperature T <sub>solidus</sub> (°C)	Mechanical properties at 293 K	
	Density (kg.m <sup>-3</sup> )	Heat capacity (J.kg <sup>-1</sup> .K <sup>-1</sup> )	Thermal conductivity (W.m <sup>-1</sup> .K <sup>-1</sup> )	Electrical resistivity (μΩ.m)		Re (MPa)	Rm (MPa)
<b>AM54</b>	7750	446	66.1	0.12	1531	180	315
<b>DP600</b>	7790	447	42.2	0.27	1480	383	626
<b>Usibor</b>	7940	452	38.6	0.24	1456	1100	1500

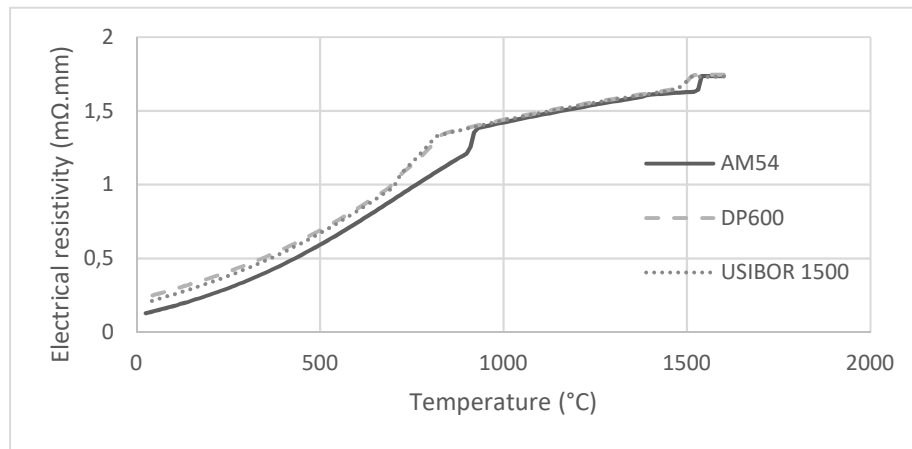


**Fig. 4** Electrical resistivity evolutions of the steel sheets [3]

In several RSW numerical models [9], [5], [15], the ECR are calculated through correlations or phenomenological laws and the TCR are issued from the ECR by using

Wiedmann-Franz law. On the contrary, in this model, concerning the interfacial properties for the E/S and sheet/sheet (S/S) contacts, the evolution of the thermal and electrical contact resistances, TCR and ECR, have been characterized on a specific device [16] in function of the pressure and the temperature (Fig. 5, Fig. 6). Due to the plastic deformations of the asperities, the evolution of the ECR and TCR are irreversible in function of the pressure and the temperature. The bulk resistances of the coatings are directly embedded in the values of the contact resistances. Due to the specific properties of the Al-Si coating (lower conductivity, higher hardness and roughness [16], [3]) comparatively to the zinc coating, the contact resistances (ECR(S2/S3), ECR(S3/E2)) for the two interfaces with the Usibor® sheet are higher (Fig. 5, Fig. 6). In this study, the contact resistances are implemented in the numerical model but their irreversibility in function of the temperature and the pressure is not yet taken into consideration.

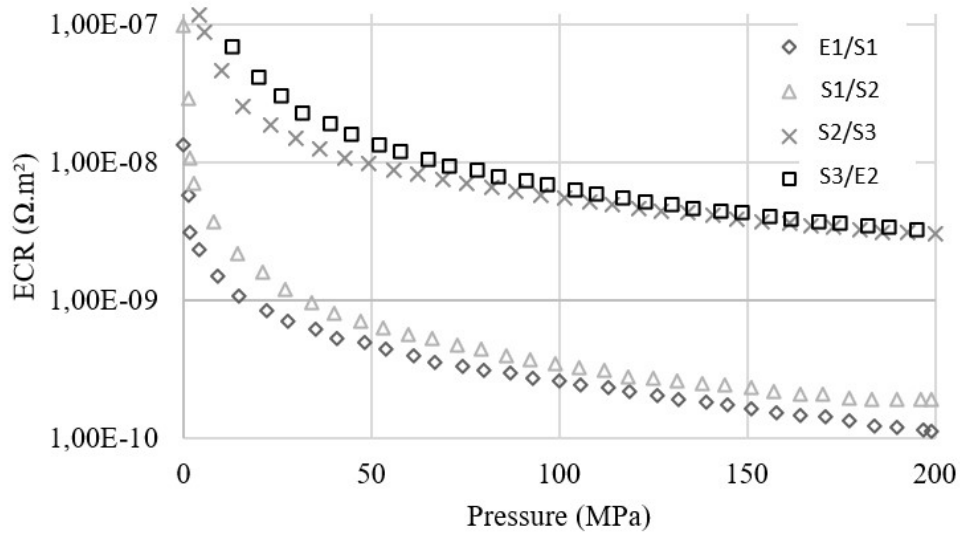


**Fig. 5** Experimental evolutions of the ECR for each interface versus the contact pressure P at ambient temperature

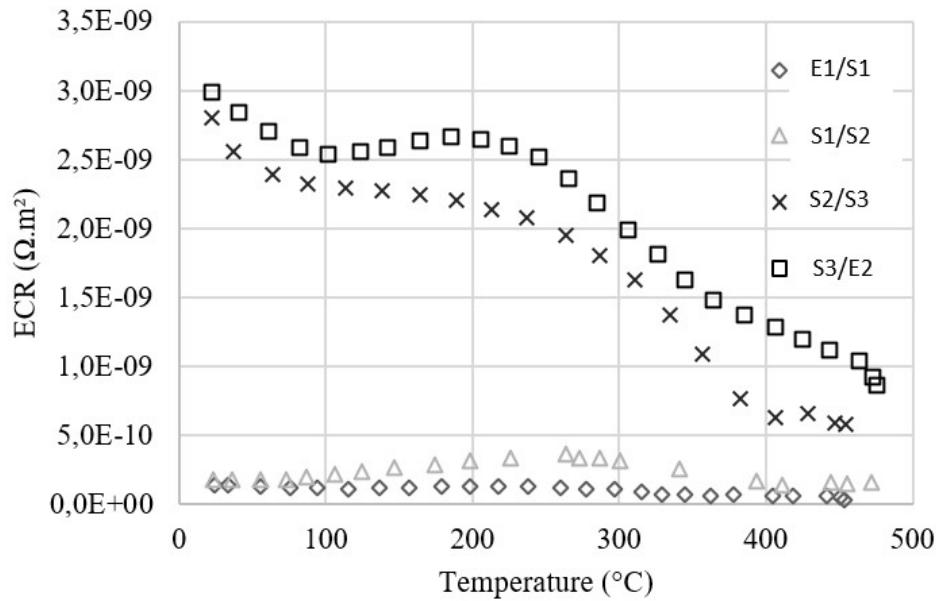


Fig. 6 Experimental evolutions of the ECR for each interface versus the temperature at 200MPa

## RESULTS AND ANALYSIS

### VOLTAGE BETWEEN THE ELECTRODES

The voltage depends on the electrical current evolution imposed (Fig. 7) and on the electrical resistance of the assembly which varies with the electrical contact resistances, the electrical resistivity of the sheets, the thickness of the sheets, and with the contact radii.

In both experimental and numerical evolutions, a peak of voltage is obtained slightly after that the electrical current reaches its maximal value (Fig. 7). If the evolutions of the numerical and experimental upper electrode voltage are really in good accordance until 40 ms, however, after 40 ms, the numerical curves present a jump of the potential not observed experimentally (Fig. 7). It may be due to the reversibility of the electrical contact resistances assumed in the model. The calculated values of ECR(S3/E2) in the model increase between 40 and 80 ms when the contact pressure decreases with the electrode indentation (Fig. 20). In fact, ECR values should remain constant or decrease due to irreversible contact phenomena. After 150 ms the numerical and experimental curves become in good accordance again.

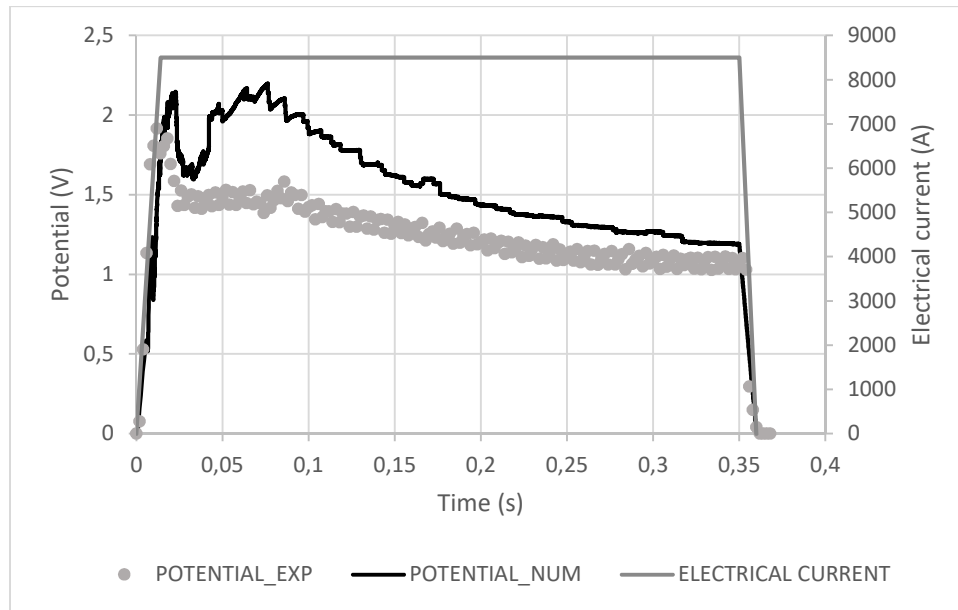
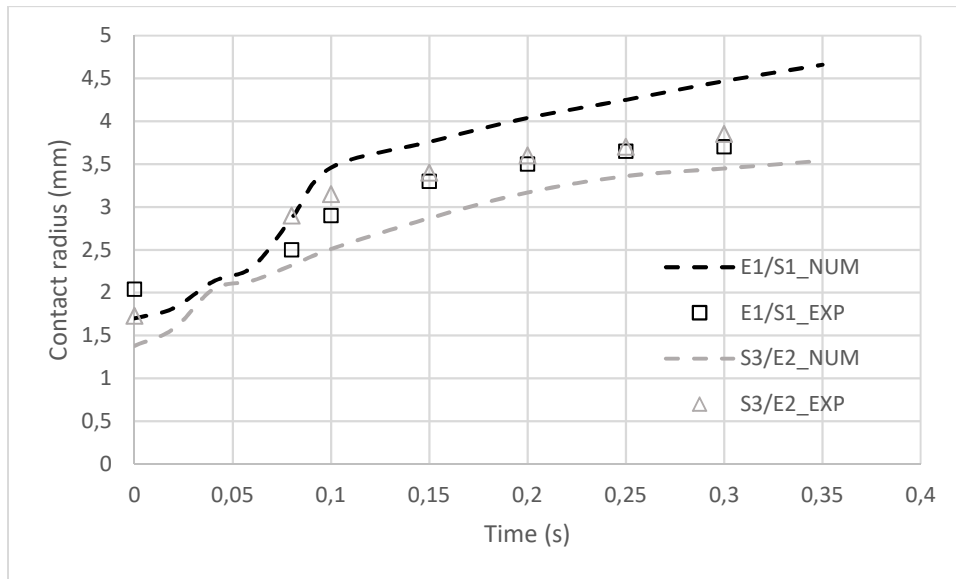


Fig. 7 Numerical and experimental voltage evolutions and electrical current profile.

STRAINS OF THE ASSEMBLY, CONTACT RADII AND THICKNESS

At the end of the clamping stage, the experimental contact radii measured with pressure-sensitive paper Prescale® appear 0.5mm higher for the S3/E2 contact and 0.5mm lower for the E1/S1 contact than the numerical values (Fig. 8). The measurement technique with ink-laden microbeads may overestimate the values-of the radii [3] and explains the observed discrepancies. During the welding stage, at the interface E1/S1, the evolution of the measured and calculated radii intersects around 80ms, then diverge after (Fig. 8). The numerical radii calculated are higher than the experimental radii measured. For the interface S3/E2, the calculated values of the contact radii are lower than the experimental ones for the whole welding time (Fig. 8). The causes of the discrepancies may be probably multifactorial such as, the comparison between experimental values at room temperature and numerical values at hot temperature, the experimental errors, and the relevance of the mechanical behavior laws for the sheets at high temperature. Despite the differences, the dynamic of the evolutions of the E/S contact radii obtained by the numerical model are rather similar to values issue from experimental tests.



**Fig. 8** Comparison between numerical and experimental contact radii evolutions for the two E/S interfaces

The assembly of three sheets also meets a variation of its thickness  $e$  ( $e = e_1 + e_2 + e_3$ ) during the process. Two antagonist forces are responsible of this variation:

- The squeezing load applied by the electrodes which induces the indentation of the rounded tip electrodes inside the sheets
- The thermal dilatation of the materials

The thickness increases during the first part of the welding step ( $0 \rightarrow 190 \text{ ms}$ ) (Fig. 9), due to the important temperature rise in the assembly. During this period of time the heat production by Joule effect is largely higher than the thermal losses, because of the electrical contact resistance effects and because of the small contact areas which induce high current density values in the assembly. The indentation of the electrode tips inside the sheets begins, but the evolution of the thickness is mostly driven by the thermal dilatation. The molten pool size also increases quickly in thickness until around 200 ms (Fig. 13).

For a time greater than 190 ms the thickness of the assembly decreases. Indentation of electrode tips inside the sheets become the prevalent factor, due to the softening of the sheets with the strong heating in the first moment.

When the welding current is interrupted after 350 ms, the thickness decreases continuously, mainly due to the thermal shrinkage, during the forging stage till 860 ms and during the air-cooling stage (duration of the cooling stage : 120s).



## Mathematical Modelling of Weld Phenomena 12

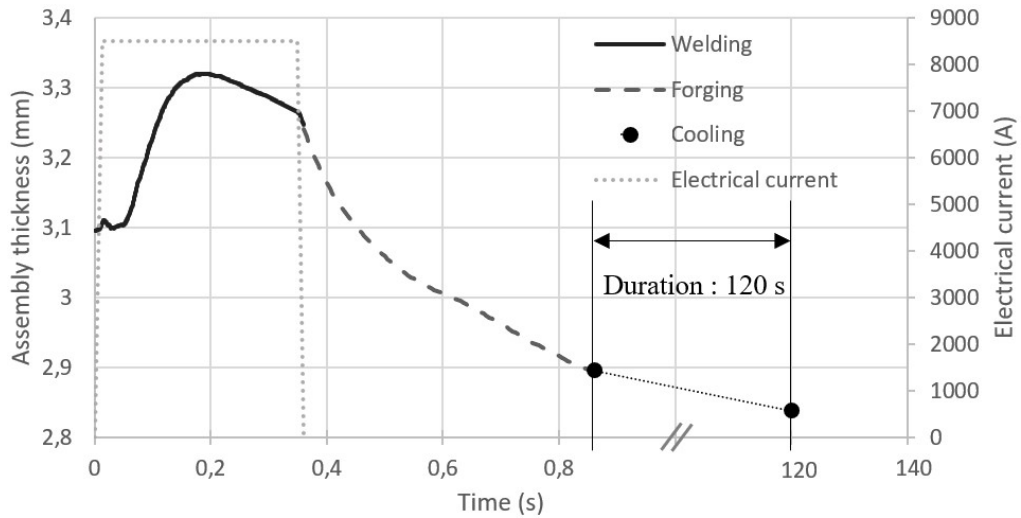


**Fig. 9** Evolution of the assembly thickness

### RADIUS AND THICKNESS OF THE MOLTEN POOL, PENETRATION IN THE THIN SHEET

The computed shapes of the nugget appear in a relatively good accordance with experimental ones for different interrupted times 80 ms, 150 ms, 300 ms (Fig. 10). However, the sizes cannot be compared directly. In effect, the numerical nugget boundary, which corresponds during the welding stage to the isotherm 1535 °C, is observed at high temperature when thermal dilatation is important (Fig. 9). On the contrary, the experimental solidified nugget is obtained after thermal shrinkage at ambient temperature. So only the experimental and numerical localization and dynamic evolution of the nugget can be compared.

## Mathematical Modelling of Weld Phenomena 12

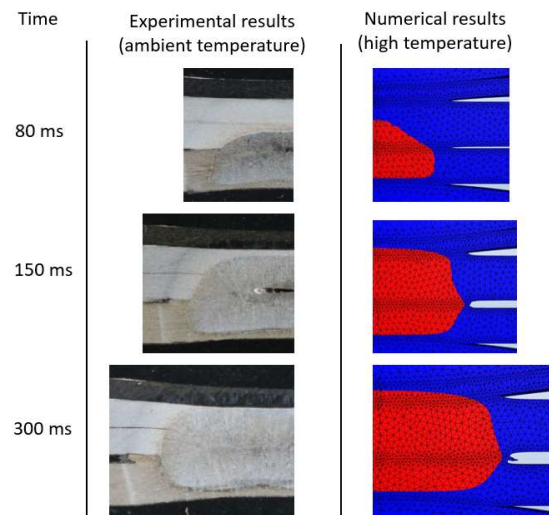


**Fig. 10** Comparison of the localization and the shape of the numerical molten pool (high temperature) and the experimental nugget (ambient temperature)

The calculations show that the molten nugget appears inside the Usibor® plate around 40 ms (Fig. 11) at the opposite of the thin sheet. After it develops quickly in thickness inside the DP600 and towards the AM54 thin sheet (Fig. 11). The origin is linked to the huge contact resistances at interfaces with the Usibor® sheet which initiate overheating at these interfaces and locate the hot spot within the Usibor® sheet (Fig. 19).

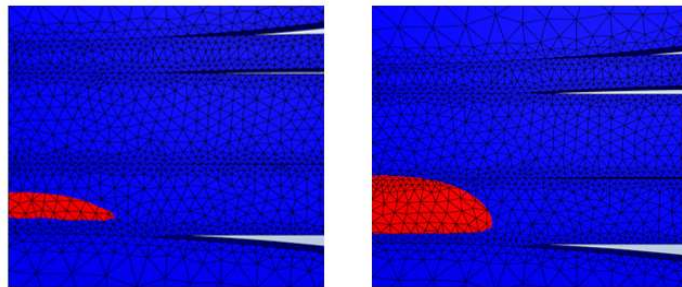


**Fig. 11** Localization and shape of the molten pool at 40ms and 60ms

In this section, the numerical and experimental dimensions of the nugget are compared more precisely (thickness  $e_N$ , radii ( $r_{N1}$   $r_{N2}$ ), penetration in the thin sheet  $p$ ) (Fig. 12).

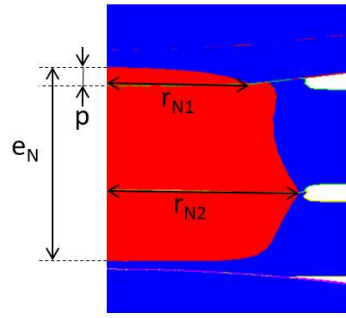


**Fig. 12** Dimensions of the nugget:  $e_N$  (thickness),  $r_{N2}$  (radius at the interface S2/S3),  $r_{N1}$  (radius at the interface S1/S2),  $p$  (penetration inside the thin sheet).

The numerical and experimental evolutions of the thickness of the molten pool present similar dynamics (Fig. 13). The thickness increases quickly, then meets a maximum around 200 ms, and decreases slowly until the electrical current is cut off at the end of the welding at 350 ms. The numerical values, taking into account the strong thermal dilatation of the molten pool, are logically higher than the experimental values measured at ambient temperature after cooling of the assembly. The numerical thickness values obtained after forging stage from 3 interrupted points (80 ms, 150 ms, 300 ms) are logically nearer (Fig. 13).

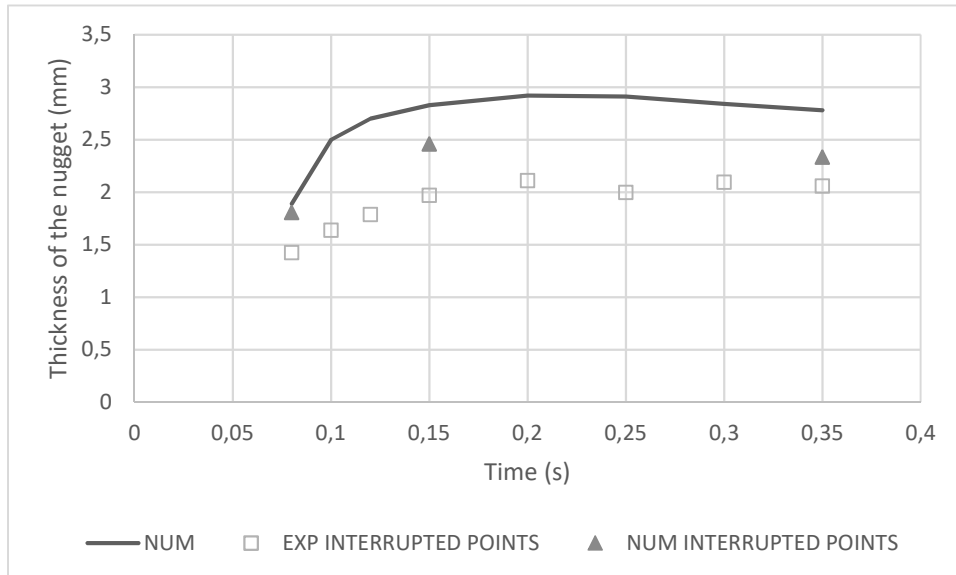


**Fig. 13** Evolution of the depth of the molten pool (during the welding) and the nugget (after cooling)

The thickness evolution of the molten pool is driven by the equilibrium between the heating by Joule effect, at the interfaces ( $ECR \cdot J^2$  ( $W/m^2$ )) and inside the sheets ( $1/\sigma \cdot J^2$  ( $W/m^3$ )), and the heat losses mainly by conduction through the electrodes. Indeed, until the values of the contact radii (Fig. 8) remain sufficiently low, heating is dominant and the

nugget thickness increases quickly. After 200 ms when the contact radii reach high values with the indentation of the electrode tips inside the sheets, the current density drops causing a decrease of the power heating and the heat losses increase and become prevalent. Consequently, the nugget thickness regresses slightly.

Furthermore, the evolutions of the numerical and experimental nugget  $r_{N2}$  are in pretty good adequacy (Fig. 14), by taken into consideration the preceding remarks on the potential causes of distortions.

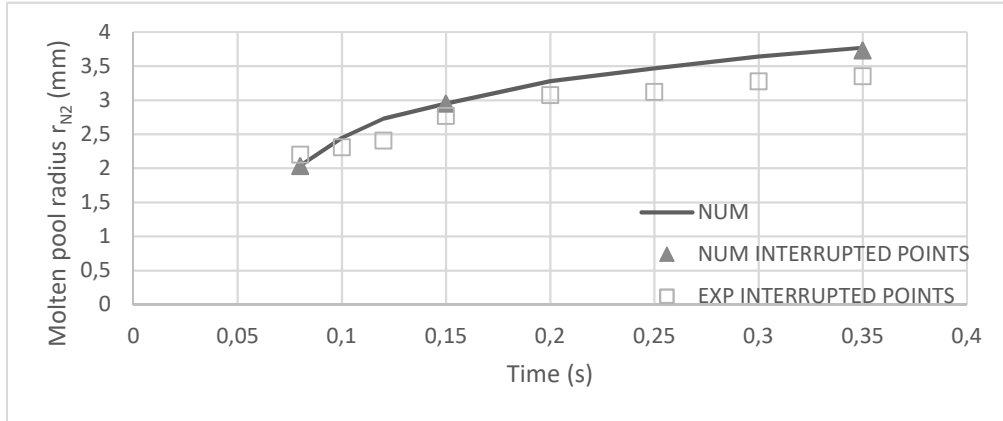


**Fig. 14** Comparison between experimental nugget radius and numerical molten pool radius during welding stage

The penetration of the molten pool inside the AM54 sheet reaches a maximal value 0.34 mm at 200 ms (Fig. 15) and decreases slightly after. The experimental value 0.14 mm measured after the end of the cooling stage is significantly lower, which indicates that the numerical molten pool thickness is certainly overestimated. The radius  $r_{N1}$  of the molten pool at the contact E1/S1 increases continuously during the welding stage and reaches 3 mm.

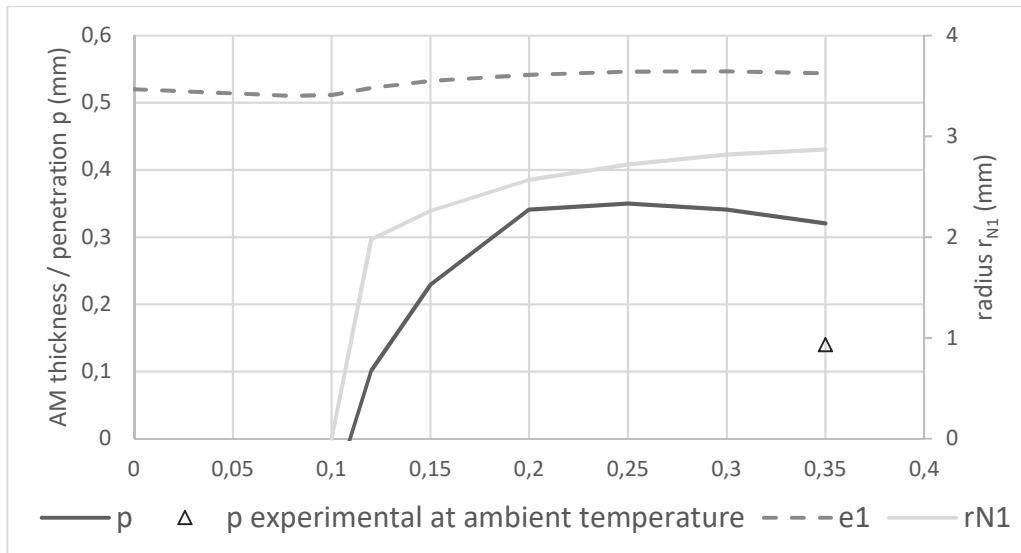
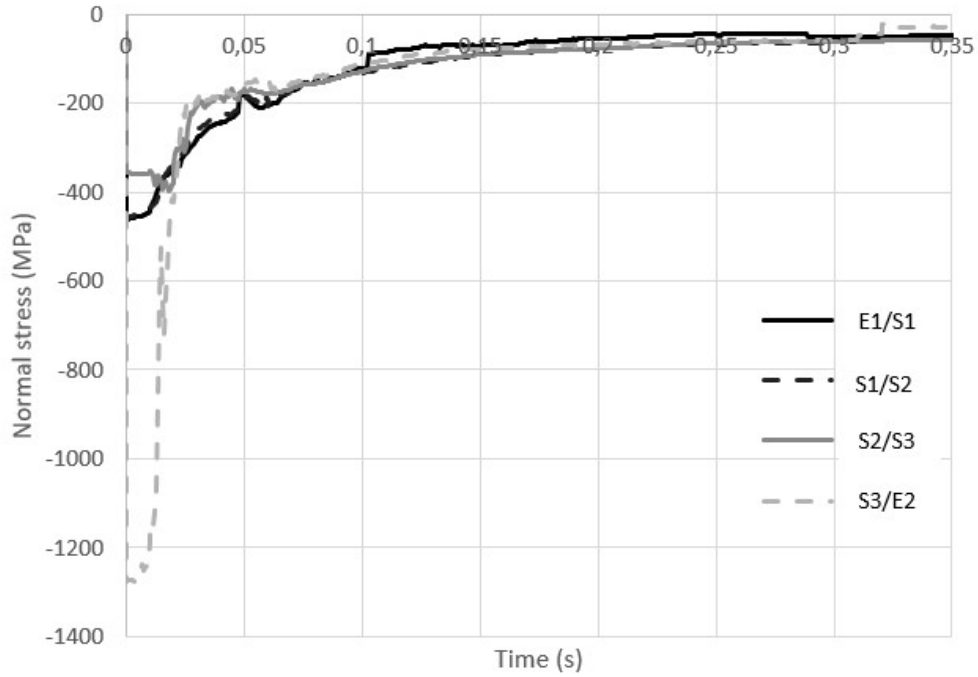


Fig. 15 Penetration of the molten pool inside the LCS sheet and thickness of the LCS sheet.

ELECTRO-THERMO-MECHANICAL COUPLING PHENOMENA AT CONTACTS

The normal stress at the different interfaces present different initial values and vary strongly in function of the time (Fig. 16) with the indentation of the electrode tips inside the sheets. The maximal values of the normal stress are calculated after the squeezing stage. When the indentation increases, a drop of the normal stress is observed, and the evolutions at the different interfaces become similar. The drop is particularly important for the S3/E2 contact. After  $t = 60$  ms, the normal stresses at each contact are similar and continue to decrease slowly during the welding.



**Fig. 16** Normal stress calculated at the central axis on each interface

Furthermore, the spatial distributions of the normal stress are not uniform, and the values are higher at the extremity of the contact zone (-400 MPa) versus (-160 MPa) along the contact axis (Fig. 17).

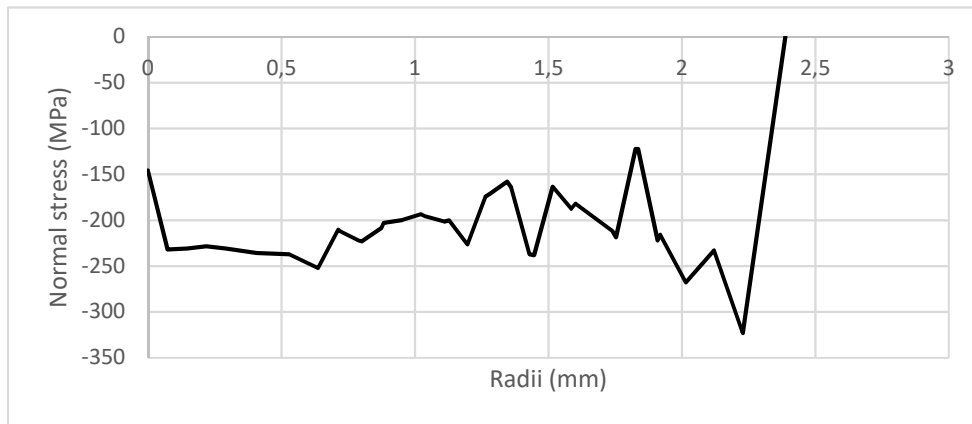


**Fig. 17** Spatial distribution of the normal stress along the S3/E2 interface at a time  $t=80\text{ms}$

The axisymmetric geometry of the electrodes provides a non-uniform current density distribution on the contact zones, with a peak at the extremity of the contact zones (Fig. 18).

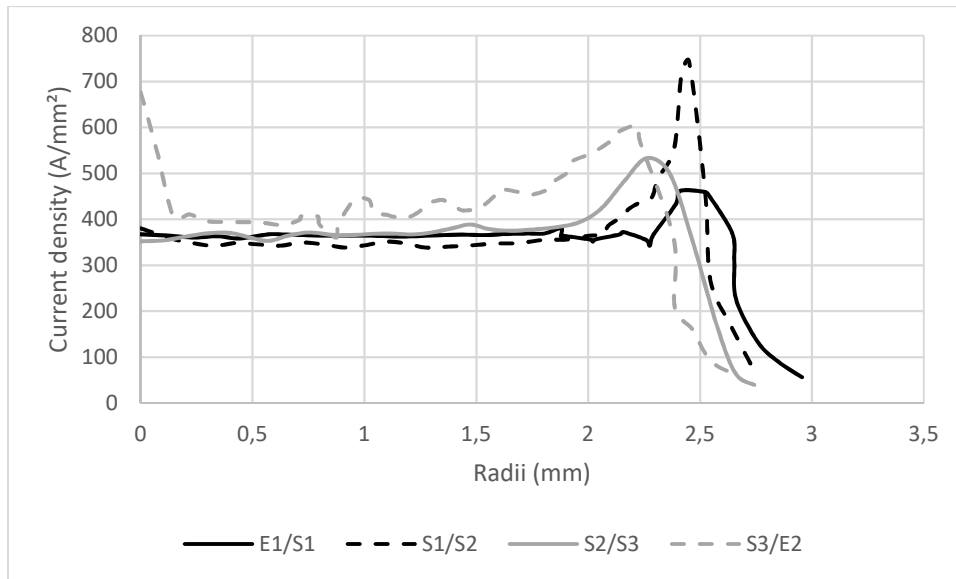


**Fig. 18** Repartition of the current density along the interfaces ( $J$  ( $A/mm^2$ )) at  $t=80$  ms

Consequently non-uniform power heating and non-uniform temperature distribution are expected (Fig. 19 and Fig. 22). At the first moment of the welding stage, a peak of temperature is calculated at the periphery of the S3/E2 contact zone, in good adequacy with observations by infrared camera [3] [16] (Fig. 19).

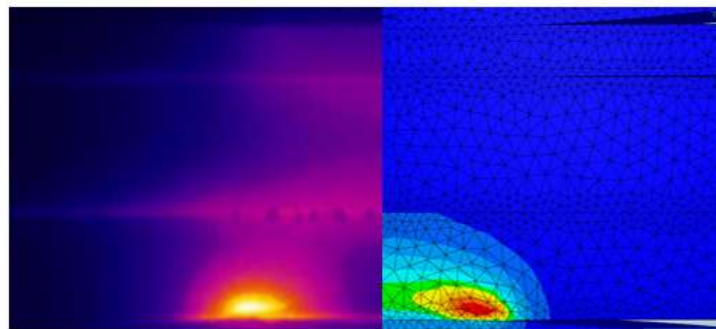


**Fig. 19** Peak temperature at the periphery of S3/E2 interface in the first moments

With the non-uniformity of the contact pressure and of the contact temperature along the interface, the values of the contact resistances ECR and TCR are also non-uniform and are lower at the periphery of the contact zones where the contact temperature and the normal stresses are the highest. In the model, the contact resistances ECR and TCR could artificially increase when the contact temperature or the normal stress decrease. This is the case at the interface (S3/E2) between the Usibor® sheet and the lower electrode, where the electrical contact resistance increases with the drop of the normal stress at this interface (Fig. 20), while the contact temperature remains relatively low and inferior to the melting point of the Al-Si coating (around  $1000$  °C) [17] (Fig. 22). This phenomenon is not

observable at the interface S2/S3 (Fig. 21) because the contact temperature increases quickly over the melting temperature of the Al-Si coating.

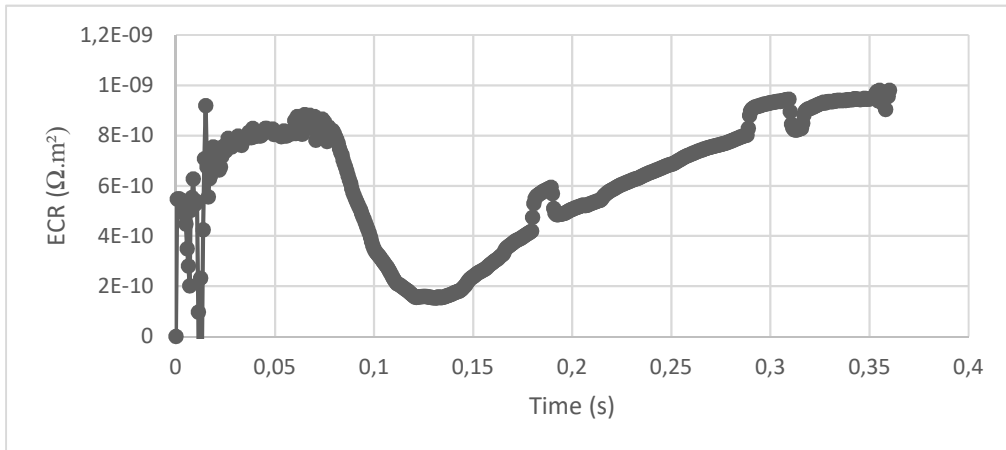


Fig. 20 Electrical contact resistance at central axis on the interface S3/E2

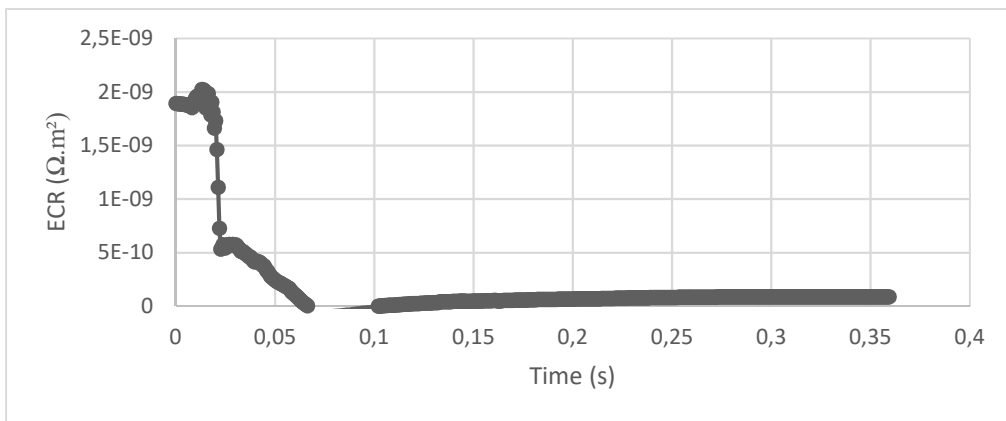
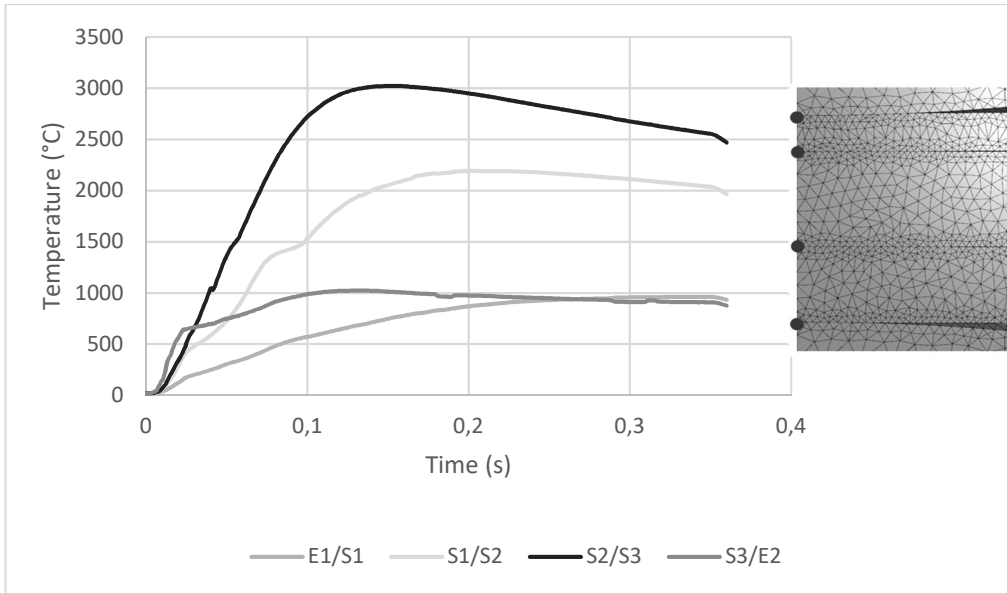


Fig. 21 Electrical contact resistance at central axis on the interface S2/S3





**Fig. 22** Contact temperature calculated along central axis at each interface

The values of the ECR(P,T) at S3/E2 interfaces increase in the model between 30 ms and 80 ms (Fig. 20), because of the reversible contact conditions assumed in the model. In fact, when the contact radii increase the contact pressure decreases and the numerical ECR values increase. On the contrary, at the S2/S3 interface, the ECR decrease (Fig. 21), despite the decrease of the contact pressure, because the temperature rise is largely higher at this interface (Fig. 22). The artificial increase of the ECR(P,T) at the interface S3/E2 could probably explain in a great part, the abnormal overheating obtained numerically in the assembly, with the over-estimated size of the nugget (Fig. 10) and with the non realistic temperature ( $T > 3000$  °C) reached in the molten pool (Fig. 22), and the jump observed on the numerical voltage evolution (Fig. 7). Moreover, in the model, the MHD phenomena are neglected. It could also explain the high abnormal temperatures reached in the molten pool.

## CONCLUSION

In this study, achieved in partnership with ArcelorMittal, a numerical model has been developed using the software Forge® to simulate the resistance spot welding of a 3 dissimilar sheets assembly, including a very thin sheet. The aim is to give a better understanding of the difficulties encountered to succeed the weldability of the thin sheet.

The good adequacy found between numerical and experimental results, concerning the E/S contact radii, the size of the nugget with the penetration inside the thin sheet and the voltage between electrodes, proves the reliability of the model and the suitability of the software Forge® to simulate the RSW process. The huge electrical and thermal contact resistances at the two interfaces with the Usibor sheet, because of the Al-Si coating, promote the initiation of the nugget inside this sheet, far from the thin sheet. The growing of the nugget in thickness and the penetration inside the thin sheet appear in the first

moment of the welding stage, till the contact radii become too important with indentation of rounded tip electrodes inside the sheets. After the nugget progresses only in diameter at the two S/S interfaces till the end of welding stage.

Due to the complex spatio-temporal contact conditions, with the non-uniform distributions of the normal-stress, of the current density, and of the contact temperature, a great attention should be paid to the modelling of the contact conditions. To improve the numerical model, irreversibility laws for the contact resistances should be imbedded and optimization of the extrapolation of the mechanical behavior laws at high temperature for the steels could be assessed.

### REFERENCES

- [1] C. V. NIELSEN, K. S. FRIIS, W. ZHANG, N. BAY: ‘Three-Sheet Spot Welding of Advanced High-Strength Steels’, *Welding Journal* 90, pp. 32s-40s, 2011.
- [2] J. KAARS, P. MAYR, K. KOPPE: ‘Simple transition resistance model for spot welding simulation of aluminized AHSS’, *Math. Model. Weld Phenom* 11, pp. 32s-40s, 2016.
- [3] E. GESLAIN: *Soudage par résistance des tôles fines revêtues : formation du noyau dans un assemblage de trois tôles*, thesis, Université de Bretagne Sud, 2018.
- [4] R. RAOELISON, A. FUENTES, C. POUVREAU, P. ROGEON, P. CARRE, F. DECHALOTTE: ‘Modeling and numerical simulation of the resistance spot welding of zinc coated steel sheets using rounded tip electrode: analysis of required conditions’, *Appl. Math. Model* 38, pp. 2505-2521, 2014.
- [5] J. WANG, H. P. WANG, F. LU, B. E. CARLSON, D. R. SIGLER: ‘Analysis of Al-steel resistance spot welding process by developing a fully coupled multi-physics simulation model’, *International Journal of Heat and Mass Transfer* 89, pp. 1061–1072, 2015.
- [6] ZIXUAN WAN, HUI-PING WANG, MIN WANG, BLAIR E. CARLSON, DAVID R. SIGLER, ‘Numerical simulation of resistance spot welding of Al to zinc-coated steel with improved representation of contact interactions’, *International Journal of Heat and Mass Transfer* 101, pp. 749–763, 2016.
- [7] J.M . BERGHEAU: ‘Modélisation numérique des procédés de soudage’, *Techniques de l’ingénieur*, 2004.
- [8] P.S. WEI, S.C. WANG, M.S. LIN, ‘Transport phenomena during resistance spot welding’, *J. Heat Transfer* 118, pp. 762–773, 1996.
- [9] P.S. WEI, T.H. WU : ‘Electrical contact resistance effect on resistance spot welding’, *International Journal of Heat and Mass Transfer* 55, pp. 3316-3324, 2012.
- [10] Y. LI, Z. LUO, Y. BAI, S. S. AO: ‘Investigation of induced magnetic force on liquid nugget during resistance spot welding’, *Sci. Technol. Weld. Join.* 18-4, pp. 329–336, 2013.
- [11] E. GAUTHIER: *Etude expérimentale et numérique de la dégradation cyclique des électrodes en CuCrZr lors du soudage par résistance par point*, thesis, Université de Bretagne Sud, 2014.
- [12] G. SIBILIA: *Modélisation du soudage par point : Influence des conditions interfaciales sur le procédé*, thesis, Ecole Polytechnique de l’Université de Nantes, 2003.
- [13] G. LE MEUR, G. BOROUGA AND B. BARDON: ‘Microscopic analysis of interfacial electrothermal phenomena – Definition of a heat generation factor’, *International Journal of Heat and Mass Transfer* 49, pp. 387-401, 2006.
- [14] P. ROGEON, R. N. RAOELISON, P. CARRE AND F. DECHALOTTE: ‘A Microscopic Approach to Determine Electrothermal Contact Conditions During Resistance Spot Welding Process’, *J. Heat Transfer*, vol 131, pp. 022101-1 – 022101-11, 2009.

- [15] S. BABU, M. SANTELLA, Z. FENG, B. RIEMER, J. COHRON, 'Empirical model of effects of pressure and temperature on electrical contact resistance of metals', *Sci. Technol. Weld. Joining* 6 (3), pp. 126–132, 2001.
- [16] E. GESLAIN, P. ROGEON, T. PIERRE, C. POUVREAU AND L. CRETTEUR: 'Coating effects on contact conditions in resistance spot weldability', *Journal of Materials Processing Tech.* 253, pp. 160-167, 2018.
- [17] M. SUEHIRO, K. KUSUMI, T. MIYAKOSHI, J. MAKI AND M. OHGAMI: 'Properties of Aluminium-coated Steels for Hot-forming', *Nippon Steel Technical Report* 88, pp. 16-21, 2003.

# OVERHEATING INDUCED BY AL-SI COATING DURING SPOT WELDING OF A DISSYMMETRICAL THREE SHEETS ASSEMBLY

E. GESLAIN\*, P. ROGEON\*, T. PIERRE\*, C. POUVREAU\* and  
L. CRETTEUR\*\*

\* *Université Bretagne Sud, IRDL, UMR CNRS 6027, Lorient, France*

\*\* *ArcelorMittal Global R&D, Montataire, France*

DOI 10.3217/978-3-85125-615-4-38

## ABSTRACT

In automotive industry, the lightweight of body in white is a challenge to meet environmental standards. Where some car manufacturers favour lighter materials, steel is always more economical and easy to assemble by resistance welding. Thus, the tendency is to reduce the thickness of cover sheets and use advanced high strength steel in better position for the structure. The press-hardened steels (of hot-pressed forming steel) are also a key of lightweight. The manufacturing of the body in white requires various combinations of different steel sheets that can induce weldability issues when using resistance spot welding process.

This work aims at understanding the mechanisms that influence the initiation and the growing of the nugget in a specific combination with three dissimilar coated steel sheets. The stack-up includes a very thin (0.57 mm) zinc coated low carbon steel sheet, a thick (1.47 mm) zinc coated advanced high strength steel sheet, and a thick (1.2 mm) aluminum-silicon coated press hardened steel sheet. The aluminum-silicon coating is transformed during hot stamping process and becomes more resistive.

A numerical 2D axisymmetric electro-thermal model developed with COMSOL Multiphysics® is used here to improve the knowledge of the thermal phenomena occurring during the first times of the welding stage. Specific attention is paid to the contact conditions at both macroscopic and microscopic scales. Contact radii evolutions issued from experimental observations are considered in the model. Thermal and electrical contact resistances evolutions experimentally measured versus stress and temperature are also considered in the model.

The model is consistent with several experimental observations issued from infrared images and voltage between the electrodes. It confirms the intense heating observed by infrared camera at the level of the two interfaces with the PHS sheet, because of the high contact resistances induced by the aluminum-silicon coating. Consequently, the nugget appears quickly inside the PHS sheet.

Keywords: resistance spot welding, contact resistances, infrared thermography

## INTRODUCTION

Advanced high strength steels are developed to gain weight and safety on new vehicles for automotive application. Steel sheets tend to become thinner to follow the environmental goals by reducing the weight of material. The resistance spot welding (RSW) process is largely optimized to join assemblies with similar steel sheets but difficulties could happen with dissymmetrical assemblies: the ones combining different sheets with different thicknesses, different steel grades, and different coatings. This work deals with the understanding of the mechanisms that influence the overheating observed at the beginning of welding of a very dissymmetrical assembly of three steel sheets. The stack-up includes a very thin zinc coated low carbon steel (LCS) sheet, a zinc coated advanced high strength steel (AHSS) sheet, and a press hardened steel (PHS) with Al-Si coating. By applying standard RSW conditions, there is a high probability that the thin LCS sheet will not be welded. An attempt to understand the effect of the contact conditions on the initial heats through numerical and experimental approaches is proposed in this article. An electro-thermal model is used here for the numerical simulation of the phenomena during the first 50 ms of welding.

Recent works already mention weldability problems when joining by RSW three sheet assemblies combining a thin mild steel sheet and high strength steel thicker sheets [1], [2]. The use of different material combinations with different coatings, and different sheet thicknesses in the three layers complicates drastically the weldability of the combinations of steel sheets. The authors report difficulties to find the right operating conditions to encourage the nugget development toward the thin sheet. Nielsen et al. find that the thin sheet is dominantly welded to the thicker by bonding diffusion [1]. Huda et al. were particularly interested by three-sheet stacks with a thick Al-Si coated steel (AL-HPF) sheet [2]. They show from macrographs that significant heating occurs at the interfaces of the Al-Si coated sheet, placed at the centre of the three-sheet stack. This coating appears to have an important role in the heating process.

Several relevant works [3]–[8] have already highlighted through numerical approaches the importance of contact conditions in the case of dissimilar assemblies. The nature of the coating on the sheets influences mainly the contact conditions. With galvanized steel sheets, electrical contact resistance at the faying interface is strongly reduced compared to the case with non-coated sheets [9]. Füssel et al. [10] have used a specific welding device to observe by infrared (IR) camera the development of the nugget inside sheets stack. The method consists in squeezing and welding the border of the steel sheets stack with half electrodes to open the welding area and provide to the camera with an observation angle. They have compared heating development filmed by IR camera and obtained by numerical simulations.

We have designed an experimental apparatus to reproduce a RSW operation and to allow observation of heating process by IR camera. A finite element model has been developed with COMSOL Multiphysics®. It is a coupled electro-thermal model with contact radii evolution. An important work has been done concerning the modelling of the contact conditions.

Half-spot IR images are compared with numerical simulation in the first milliseconds of welding to link higher contact resistance with faster heating. Numerical voltage calculated between electrodes are also confronted to measurements.

EXPERIMENTAL WORK

MATERIAL

The welding tests are achieved with a GYSPOT® medium frequency direct current welding machine developed for automotive body repair. A structure has been designed to maintain the welding gun in a horizontal position and the IR camera above in a vertical position (Fig. 1).

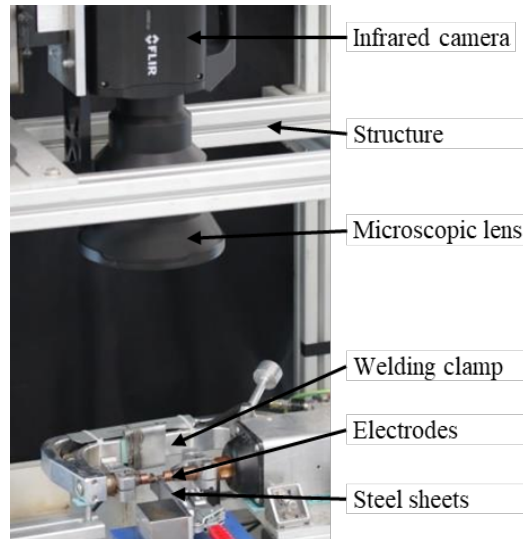


**Fig. 1** Specific welding device with the IR camera to observe the welding area.

Welding electrodes are in copper-chromium-zirconium alloy with a 32 mm contact radius and a 13 mm diameter. They are milled on 6 mm depth at the half of diameter (Fig. 2). The support of electrodes is water-cooled.

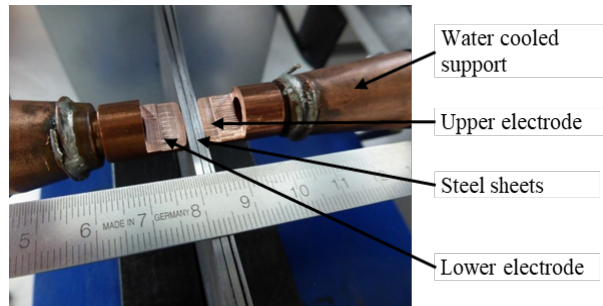


**Fig. 2** Half-electrodes squeezed at the stack border of steel sheets.

The IR camera used for the observations is a MW FLIR X6580sc. A microscopic lens with high focal length (300 mm) centres the map only on steel sheets between the electrodes (9.6 mm x 7.68 mm). Temperature measurements, with emissivity evolution, have been achieved on the same device and presented elsewhere [11]. The temperature range is from

## Mathematical Modelling of Weld Phenomena 12

20 °C to 600 °C for blackbody temperature. Three integration times are needed to operate on the whole temperature range. Therefore, the effective frequency is 220 Hz, and that corresponds to one image each 4.545 ms with a map at 640 x 256 pitches.

The dissimilar assembly of three-steel sheets considered here is presented in table 1. The combination includes a very thin LCS sheet of 0.57 mm thickness, a 1.47 mm AHSS sheet and a 1.2 mm PHS sheet. The LCS and the AHSS sheets are coated by galvanization. The PHS has an Al-Si coating to resist to hot stamped conditions. More details on this coating are given by Saha *et al.* [12].

**Table 1** Stack-up details.

Position	Name	Type	Thickness (mm)	Coating
upper	AM54	LCS	0.57	zinc (10 µm)
center	DP600	AHSS	1.47	zinc (10 µm)
lower	Usibor®1500	PHS	1.2	Al-Si (30 µm)

### EXPERIMENTS

To maintain an equivalent current density and contact pressure during half-spot welding, the intensity and the load are split by two ( $I = 4.5$  kA and  $F = 2$  kN), comparatively to the parameters used during classic spot weld configuration ( $I = 9$  kA and  $F = 4$  kN). During the welding time, the current is measured with an electrical shunt and the voltage between electrodes too (Fig. 3).

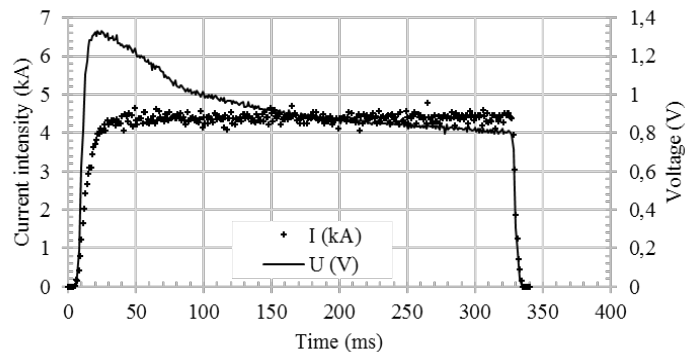


**Fig. 3** Experimental current intensity and voltage in half-spot welding.

On the first IR image (Fig. 4), the two electrodes, the three-steel sheets and the four interfaces can be identified.

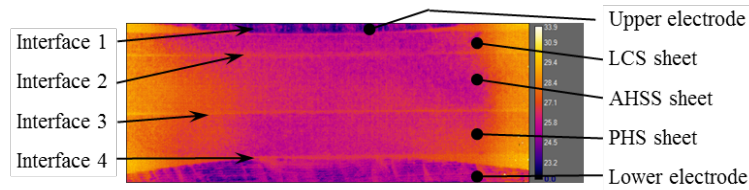


Fig. 4 Initial IR image at  $t = 0$  ms.

The IR camera recording is synchronised with current and voltage measurements through a numerical data recorder. The vertical dashed red lines in Fig. 5 represent the times for the different recorded images in Fig. 6.

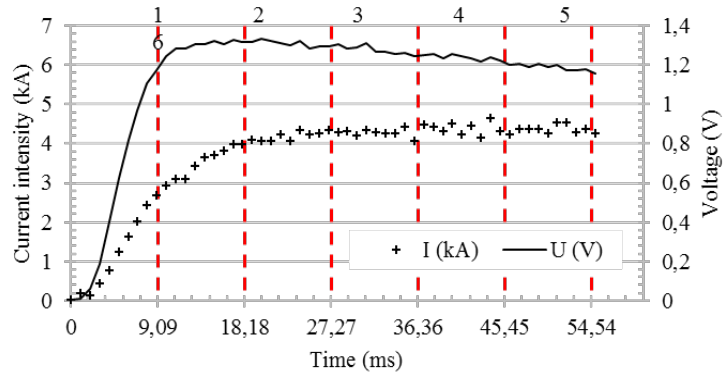


Fig. 5 Current intensity and voltage versus time for six IR images.

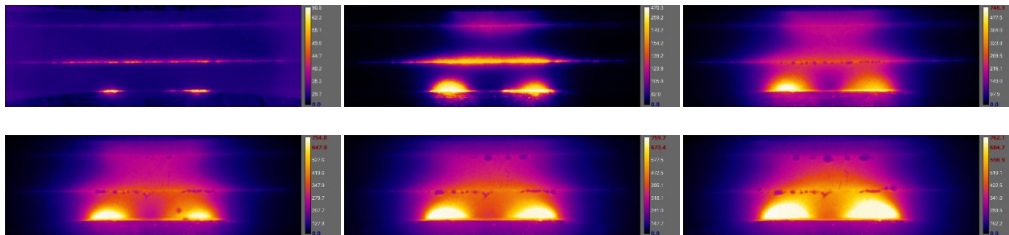


Fig. 6 IR images at different times.

On the IR images, the interfaces 3 and 4 (Fig. 4) from either side of PHS sheet that react from 9.09 ms appear clearly. The fusion of zinc coating appears with small coolest drops at the interface. The drops are visible at 27.273 ms between AHSS and PHS sheets and at 36.364 ms between LCS and AHSS sheets.

The heating at the interface 4 between PHS sheet and electrode is localised on the external of the contact. This is due to the non-uniform current density distribution in revolution geometry providing higher current density at the extremities of the contact area.



## NUMERICAL SIMULATION

### NUMERICAL MODEL

The numerical model is a coupled electro-thermal finite element model with a 2D axisymmetric geometry. The governing equation for the electrical problem is the current density conservation:

$$\text{div } \overset{\frown}{J} = 0 \quad (1)$$

where  $J (A \cdot m^{-2})$  is the current density calculated according to:

$$\overset{\frown}{J} = -\sigma \cdot \nabla V \quad (2)$$

where  $\sigma (S \cdot m^{-1})$  is the electrical conductivity.

The heat generation due to Joule effect is calculated with:

$$Q_J = \frac{1}{\sigma} J^2 = \sigma \cdot (\nabla V)^2 \quad (3)$$

The governing equation for thermal problem is the following heat equation:

$$\rho c \frac{\partial T}{\partial t} = \nabla \cdot (k \nabla T) + Q_J \quad (4)$$

where  $T (K)$  is temperature,  $t (s)$  is time and  $k (W \cdot m^{-1} \cdot K^{-1})$ ,  $\rho (kg \cdot m^{-3})$  and  $c (J \cdot kg^{-1} \cdot K^{-1})$  are respectively the thermal conductivity, the density and the specific heat of materials. The latent heat of change phase is taken into account with equivalent specific heat.

For the electrical boundary conditions, the current density  $J$  is imposed at the top of the upper electrode with the current value  $I$  measured in half-spot welding multiplied by two. The potential  $0 V$  is imposed at the bottom of the lower electrode. For the thermal boundary conditions, exchanges with the environment are assumed negligible and therefore adiabatic conditions are considered.

The mesh is composed of triangular quadratic elements (Fig.7). The maximum size of the elements is imposed: 50  $\mu m$  at the interfaces, 100  $\mu m$  in steel sheets between electrodes and 1 mm for the rest of the geometry.

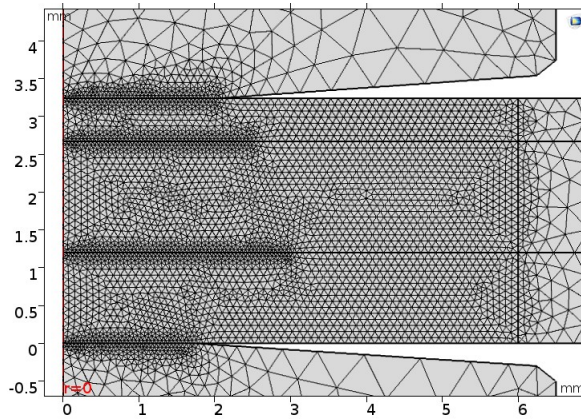


Fig. 7 Meshing in the interest areas.

### CONTACT CONDITIONS

Due to indentation of the rounded tip electrodes inside the sheets, the contact radii at electrode-sheet (E/S) and sheet-sheet (S/S) interfaces increase during the welding stage. Without a coupled mechanical analysis, the contact radii evolutions cannot be calculated directly by the electro-thermal model. The deformations of the sheets induced mainly by thermal dilatation and indentation of electrodes neither. In our electro-thermal model, contact radii of each interfaces are imposed during 10 ms before to evolve. We assume dilatation and indentation phenomena are negligible before 50 ms.

Measurements of the two E/S contact radii evolutions have been achieved after the squeezing stage and at different interrupted welding times [13] ( Fig. 8).

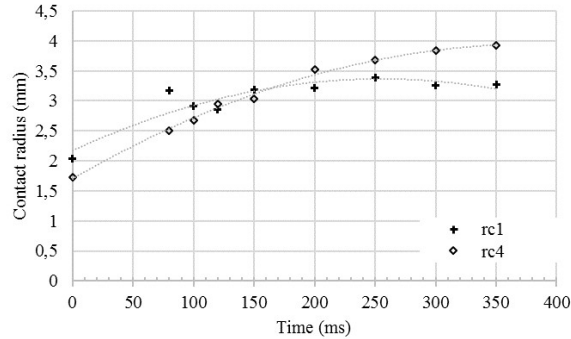


Fig. 8 Experimental evolutions of the electrode-sheet contact radii.

The evolution of E/S contact radii could be represented by a polynomial law (5.1) and (5.2), which are used to calculate  $rc_1$  and  $rc_4$  at 0 ms, 10 ms, 20 ms, 30 ms, 40 ms, and 50 ms.

$$rc_1 = -1.85 \times 10^{-5} t^2 + 9.41 \times 10^{-3} t + 2.04 \quad (5.1)$$

## Mathematical Modelling of Weld Phenomena 12

$$rc_4 = -1.52 \times 10^{-5} t^2 + 1.17 \times 10^{-2} t + 1.73 \quad (5.2)$$

Initial S/S contact radii are respectively 2.52 mm and 3.03 mm, but we have no mean to measure these values until 50 ms. From the initial measurements of S/T contact radii, we assume the ratio between  $rc_1$  and  $rc_2$  and,  $rc_3$  and  $rc_4$  are constant until 50 ms:

$$rc_2 = 1.25 rc_1 \quad (5.3)$$

$$rc_3 = 1.80 rc_4 \quad (5.4)$$

We obtain the evolution of contact radii each 10 ms following the graph presented in Fig. 9.

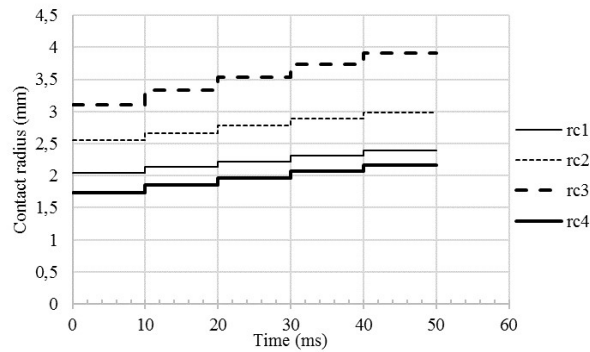


**Fig. 9** Contact radii evolutions imposed in the model.

The electrical contact resistances (ECR) and thermal contact resistances (TCR) encountered in this very dissymmetrical stack-up have been measured versus pressure and temperature on a specific device (Fig. 10).

## Mathematical Modelling of Weld Phenomena 12

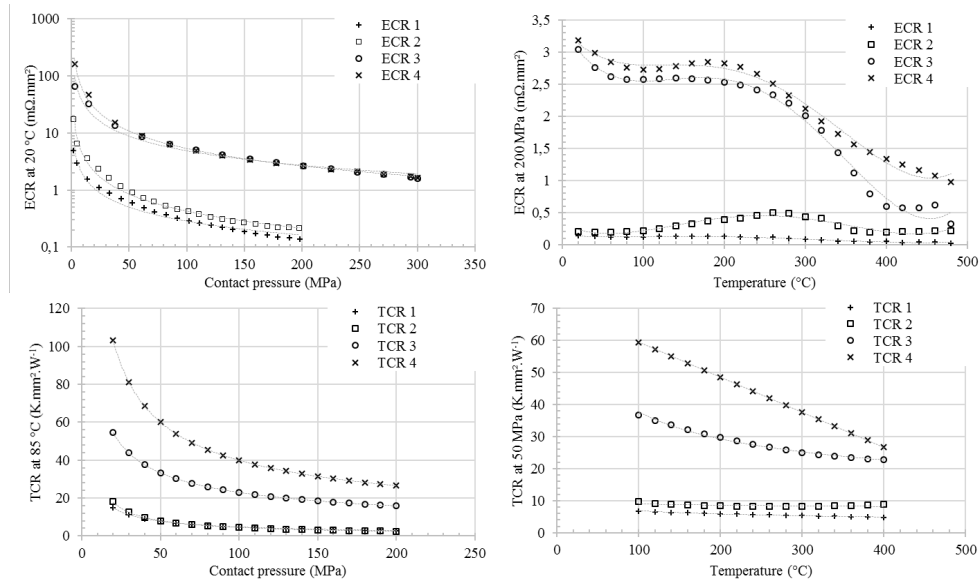


**Fig. 10** Electrical and thermal contact resistances evolutions measured on a specific device versus contact pressure and temperature [13], [14].

The contact resistances could be separated in two groups: the zinc coated interfaces and the aluminized interfaces. The intermetallic components formed during the heat treatment of PHS sheet by diffusion of iron in aluminum-silicon (Al-Si) contribute to increase drastically the electrical resistivity of the coating. The resistance of the Al-Si layer is included in the contact resistance values [14].

To be embedded properly in the model, experimental evolutions should be fitted with a phenomenological law. We suppose ECR and TCR evolutions follow a law with separable variables as Srikanwong [15]:

$$ECR(p_c, T_c) = f(T_c) g(p_c) \quad (6.1)$$

$$TCR(p_c, T_c) = f'(T_c) g'(p_c) \quad (6.2)$$

Measurements versus contact pressure at room temperature allowed defining a law for  $g(p_c)$  and  $g'(p_c)$  as a power function of contact pressure:

$$g(p_c) = R_0 p_c^{-n} \quad (7.1)$$

$$g'(p_c) = R_0' p_c^{-n'} \quad (7.2)$$

With the coefficients  $n$  and  $n'$  close to 1, we assume we can calculate the ECR and TCR evolutions at the contact pressure  $p_c$  from the reference pressure  $p_{ref}$  (8.1 and 8.2).

$$ECR(p_c, T_c) = ECR(p_{ref}, T_c) \frac{p_{ref}}{p_c} \quad (8.1)$$

$$TCR(p_c, T_c) = TCR(p_{ref}, T_c) \frac{p_{ref}}{p_c} \quad (8.2)$$

The contact pressure and the correction pressure ratio are automatically calculated from the contact radii. Furthermore, the contact resistances evolutions for the aluminized interfaces have been extrapolated at high temperature, until the fusion temperature (1 000 °C) of the Al-Si layer (Fig. 11).

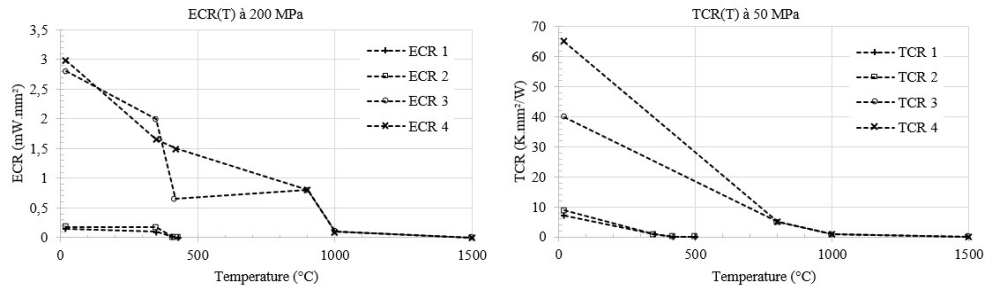


**Fig. 11** Extrapolation of the electrical and thermal contact resistances evolution versus temperature at reference pressure for the aluminized interfaces.

## RESULTS AND DISCUSS

The calculation time takes 10 min with a standard desktop computer (Intel® Core™ i3-3120M and 8 Go RAM) and less than 5 min with a calculation computer.

Fig. 12 presents the numerical temperature distribution, which is similar to the experimental observations done by IR thermography (Fig 6). The first hot areas are localised on either side of PHS sheet where is Al-Si coating. The red arrows represent the heat flux and their size is proportional to the energy quantity transmitted by conduction. Isothermal lines of coating fusion temperature are drawn in black. They correspond to 420 °C and 1 000 °C for zinc and Al-Si after heat treatment respectively. The white line represents the fusion zone as the isothermal 1 460 °C line.

## Mathematical Modelling of Weld Phenomena 12

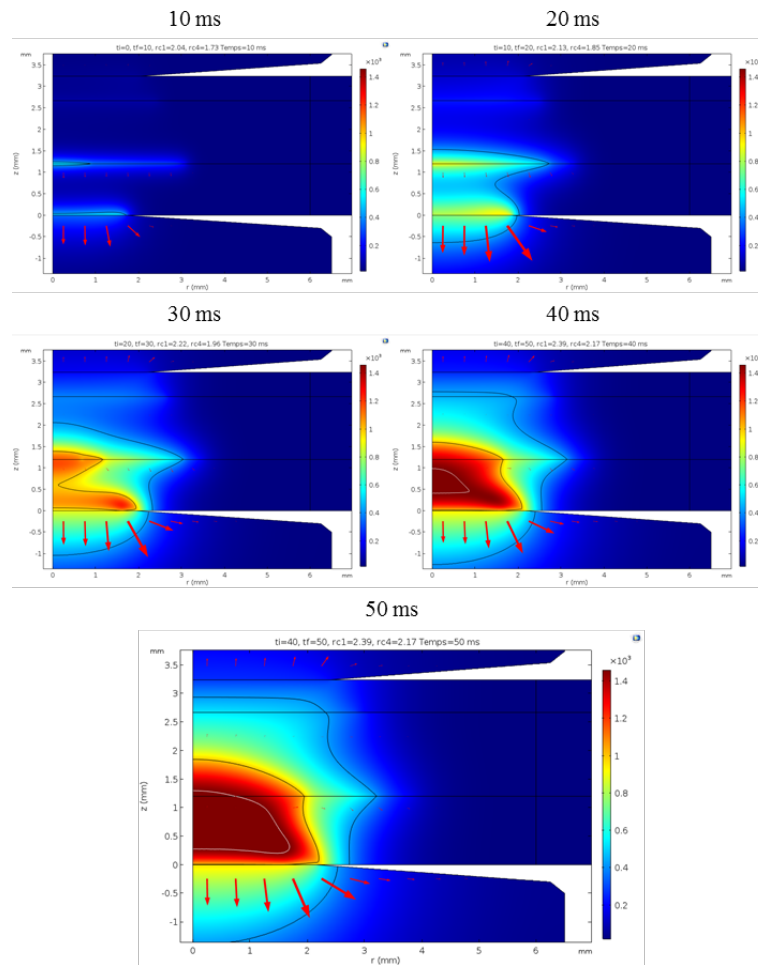


**Fig. 12** Temperature distribution from numerical simulation each 10 ms.

The temperature is heterogeneous on the interfaces. On the fourth interface (PHS/Electrode), the hottest point is at the extremity of contact where the current density is higher (Fig. 13). On the third one (AHSS/PHS), the hottest point is on the  $z$ -axis probably because of lower heat losses at this location.

Unlike experimental observations, a fusion zone is present in the PHS sheet at 40 ms. In half-spot configuration, a large part of energy is lost through the free area by radiation, which contributes to reduce the temperature and delays the melting of sheets.

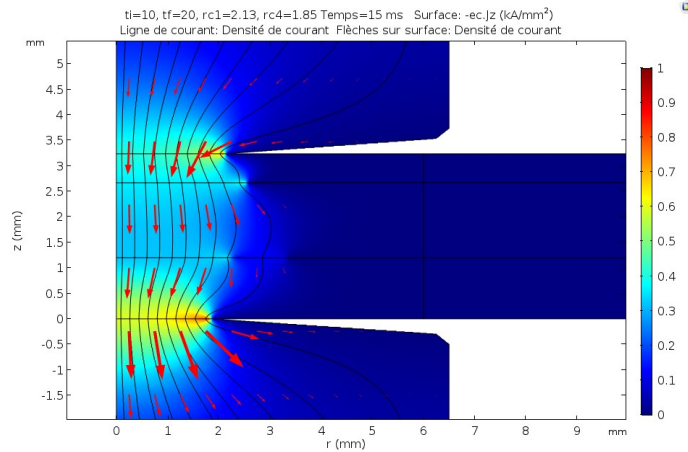


**Fig. 13** Current density distribution at 15 ms.

On the IR image at 36 ms, some drops appear at LCS/AHSS interface (Fig.14). They correspond to zinc coating fusion and give information on the contact temperature. On the equivalent numerical temperature repartition, we find the isotherm at  $420^{\circ}\text{C}$  at the same interface and at the same moment.

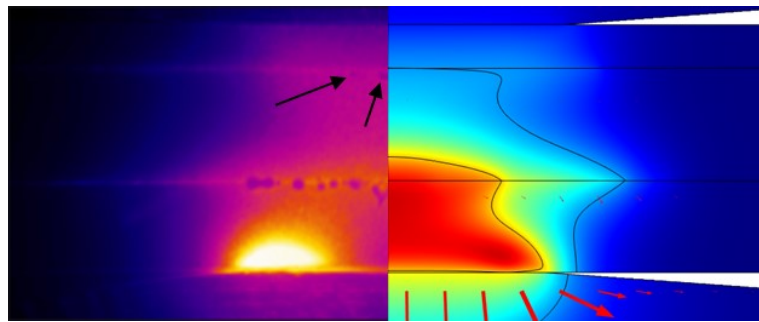


**Fig. 14** Comparison between infrared image and numerical simulation at 36 ms.

Even if the model cannot be used beyond 50 ms, the comparison between the experimental nugget at 80 ms and the numerical simulation at 50 ms give similarities (Fig. 15). Firstly, the distance between the fusion zone and the lower electrode is equal. This distance is driven by the cooling of nugget by the electrode. The numerical values of contact areas and of thermal contact resistances are of the same order of magnitude than the experimental ones. Secondly, the shape and the size of the fusion zone and the heat affected zone are consistent between numerical simulation and experimental macrograph.

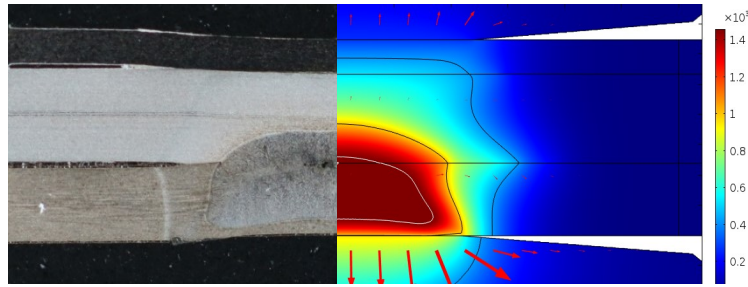


**Fig. 15** Comparison between macrographic image at 80 ms and numerical temperature distribution at 50 ms.

The contact temperature on the z-axis is presented in Fig. 16. It can be seen that the zinc fusion temperature as the interface 2 is reached at 36 ms as already observed in Fig. 14. The contact temperatures  $T_{c1}$  and  $T_{c2}$  slowly increase, while  $T_{c3}$  and  $T_{c4}$  reach 800 °C in 16 ms and 21 ms, respectively. The temperature  $T_{c4}$  is saturated at 1 000 °C due to the cooling of the electrodes. The heating speed are reported in Table 2.

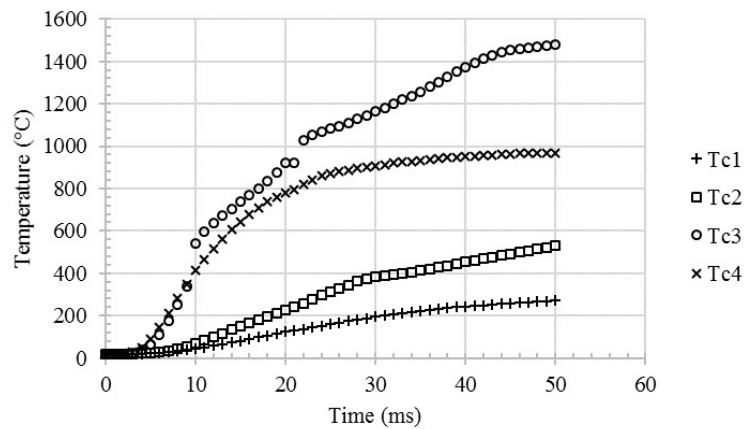


**Fig. 16** Contact temperatures versus time on the symmetrical axis.

**Table 2** Heating speed of contact temperatures in °C/ms.

$T_{c1}$	$T_{c2}$	$T_{c3}$	$T_{c4}$
7	16	94 – 35 – 19	55

The three values for the  $T_{c3}$  correspond to the three stages seen Fig. 16, respectively, on the ranges [5 ms – 11 ms], [10 ms – 19 ms] and [22 ms – 40 ms]. The heating speed at the interface between AHSS and PHS has been measured by IR thermography [11]. The experimental value, 40 °C/ms, is very close to the value obtain with the numerical model in the range [10 ms – 19 ms] where 35 °C/ms is calculated (Table 2).

Finally, the numerical voltage between the electrodes could be compared with the experimental one. It permits to assess the coherence of the contact radii and the electrical



contact resistances. Fig. 17 presents the experimental and the numerical voltage between the two electrodes. The curves are very close until 8 ms then the simulation gives weaker values until 20 ms. The change of slope occurs before the change of contact radius. It seems like the difference comes from the electrical contact resistance, which had a lower value.

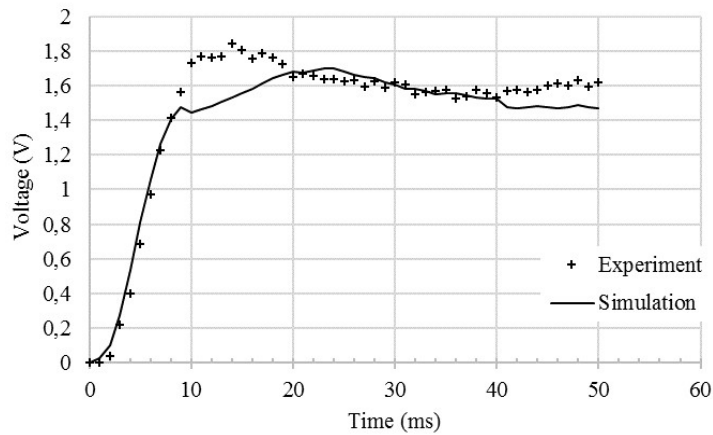


Fig. 17 Experimental and numerical voltage between electrodes.

### CONCLUSION AND PROSPECT

The evolution of contact radii in the first 50 ms show a lot of information during the initial heating that occurs in the resistance spot welding process in the presence of a PHS sheet with Al-Si coating in hot stamped conditions. In a stack-up including a very thin zinc coated Low Carbon Steel sheet, a zinc coated Advanced High Strength Steel sheet, and an Al-Si coated Press Hardened Steel of 0.57 mm, 1.47 mm, and 1.2 mm thicknesses, respectively, the initial overheating occurs on either side of PHS sheet. The melted area initiates directly in the Al-Si coated sheet then grows toward the top of the assembly.

The simply electro-thermal model developed in this study permits in 10 min of calculation time to identify the causes of overheating. The Al-Si coating is very resistive after the heat treatment for hot stamping. The current density is also a key parameter and the difference of contact radius at two electrode-sheet contacts focusses the heating on the side of the hardest sheet.

Several models of resistance spot welding include mechanical calculation at the expense of calculation time. But in the first 50 ms, dilatation phenomena are negligible, and the contact radii can be imposed from some experimental investigations.

This model can be adapted to other assemblies and with other coatings. However, new experimental characterization of contact resistance would be necessary even if the experimental temperature measurements by infrared camera allows to validate the models.

REFERENCES

- [1] C. V. NIELSEN, K. S. FRIIS, W. ZHANG, AND N. BAY: ‘Three-Sheet Spot Welding of Advanced High-Strength Steels’, *Welding Research*, vol. 90, February, pp. 32s–40s, 2011.
- [2] N. HUDA AND Y. PARK: ‘Weldability Evaluation and Nugget Formation Mechanism in Three Sheets Spot Welding of High Strength Steels’, *Welding Research, Proceedings of the 9th International Conference*, Chicago, Illinois, USA, pp. 680–684, 2012.
- [3] J. A. KHAN, L. XU, AND Y. J. CHAO: ‘Prediction of nugget development during resistance spot welding using coupled thermal–electrical–mechanical model’, *Science and Technology of Welding and Joining*, vol. 4, no. 4, pp. 201–207, 1999.
- [4] S. S. BABU, M. L. SANTELLA, Z. FENG, B. W. RIEMER, AND J. W. COHRON: ‘Empirical model of effects of pressure and temperature on electrical contact resistance of metals’, *Science and Technology of Welding and Joining*, vol. 6, no. 3, pp.126–132, 2001.
- [5] E. FEULVARCH, V. ROBIN, AND J. M. BERGHEAU: ‘Resistance spot welding simulation: A general finite element formulation of electrothermal contact conditions’, *Journal of Materials Processing Technology*, vol. 153–154, no. 1–3, pp. 436–441, 2004.
- [6] P. S. WEI AND T. H. WU: ‘Electrical contact resistance effect on resistance spot welding’, *International Journal of Heat and Mass Transfer*, vol. 55, no. 11–12, pp. 3316–3324, 2012.
- [7] R. N. RAOELISON, A. FUENTES, P. ROGEON, P. CARRÉ, T. LOULOU, D. CARRON, AND F. DECHALOTTE: ‘Contact conditions on nugget development during resistance spot welding of Zn coated steel sheets using rounded tip electrodes’, *Journal of Materials Processing Technology*, vol. 212, no. 8, pp. 1663–1669, 2012.
- [8] R. N. RAOELISON, A. FUENTES, C. POUVREAU, P. ROGEON, P. CARRÉ, AND F. DECHALOTTE: ‘Modeling and numerical simulation of the resistance spot welding of zinc coated steel sheets using rounded tip electrode: Analysis of required conditions’, *Appl. Math. Model.*, vol. 38, no. 9–10, pp. 2505–2521, 2014.
- [9] P. ROGEON, P. CARRÉ, J. COSTA, G. SIBILIA, AND G. SAINDRENAN: ‘Characterization of electrical contact conditions in spot welding assemblies’, *Journal of Materials Processing Technology*, vol. 195, no. 1–3, pp. 117–124, 2008.
- [10] U. FÜSSEL, V. WESLING, A. VOIGT, AND E. C. KLAGES: ‘Visualisierung der Temperaturentwicklung in der Schweißzone einschließlich der Schweißelektroden über den gesamten zeitlichen Verlauf eines Punktschweißprozesses’, *Schweißen und Schneiden*, vol. 64, pp. 634–642, 2012.
- [11] E. GESLAIN, T. PIERRE, P. ROGEON, C. POUVREAU, AND L. CRETTEUR: ‘Contact temperature measurement by infrared thermography during resistance spot welding process’, *QIRT*, Berlin, 2018.
- [12] D. C. SAHA, C. W. JI, AND Y. D. PARK: ‘Coating behaviour and nugget formation during resistance welding of hot forming steels’, *Science and Technology of Welding and Joining*, vol. 20, no. 8, pp. 708–720, 2015.
- [13] E. GESLAIN: *Soudage par résistance des tôles fines revêtues : formation du noyau dans un assemblage de trois tôles*, thesis, Université Bretagne Sud, 2018.
- [14] E. GESLAIN, P. ROGEON, T. PIERRE, C. POUVREAU, AND L. CRETTEUR, “Coating effects on contact conditions in resistance spot weldability,” *Journal of Materials Processing Technology*, vol. 253, pp. 160–167, 2018.
- [15] C. SRIKUNWONG : *Modélisation du procédé de soudage par points*, thesis, Ecole des Mines de Paris, 2005.



# ADVANCING SPOT WELDING PROCESS ASSESSMENT

J. KAARS\*, P. MAYR\*\* and K. KOPPE\*\*\*

\*Chemnitz University of Technology, Germany, ORCID 0000-0002-0037-3400, jonny.kaars@mb.tu-chemnitz.de

\*\*Chemnitz University of Technology, Germany, ORCID 0000-0003-2530-4644, peter.mayr@mb.tu-chemnitz.de

\*\*\*Anhalt University of Applied Sciences, 06366 Koethen/Anhalt, Germany, kurt.koppe@hs-anhalt.de

DOI 10.3217/978-3-85125-615-4-39

## ABSTRACT

Resistance spot welding still is one of the most important techniques for joining sheet material. Ongoing developments such as new material grades, coating technologies and process controls generate new challenges for the process. In order to overcome those challenges, numerical process simulation is an important tool in order to develop new welding strategies. Conventional simulation approaches only evaluate basic parameters like nugget diameter, temperature profiles and basic electrical parameters. Although evaluation of these parameters is very important to compare the model to experimental data, it does not do the true evaluation possibilities of numerical models justice.

For the first time, new mathematical methods are presented in this work, which allow the computation of comprehensive parameters like electric potentials, effective temperatures, true electrical resistances and heat contributions as well as mechanical parameters from finite element simulation. Exemplary results of the approach on the example of a spot weld on martensitic 22MnB5 steel are discussed. Among these, for the first time, the quantitative curve of dynamic efficiency of the spot welding process is presented.

Keywords: spot welding, finite element analysis, contact, energy balance

## INTRODUCTION

Resistance spot welding (RSW) is perhaps the most important technique for economically joining sheet metal under industrial conditions. Although the process is well-researched, new materials, coatings and methods of process control still create challenges. Two peculiarities characterize RSW: First, the joining heat is generated in the parts to be joined itself, resulting in a strong dependency of the weld heat on material properties of sheets and electrodes. Second, the welding process is covered by the electrodes and the sheets, leaving only external quantities like electrode voltage and –travel accessible to measurements. The difficult relation between welding heat and process conditions in combination with the little measureable data available often makes it hard to further elaborate on the release of the welding heat in terms of location and magnitude. This also holds true even if multiphysical finite-element analyses (FEA) on the process are performed and validated with experiments. The reason is, that conventional FEA computes a spatial distribution of displacement, temperature and electric potential for a number of timesteps, but does not provide preprocessed information on how the temperature distribution evolved. This task

is left to the engineer analysing the data computed. Therefore, unexpected observations on nugget formation in certain welding configurations are often hard to understand and verify.

It is the goal of this work, to provide mathematical methods for further pre-processing of FEA results on RSW. For the first time, this allows enhanced process assessment by means of FEA. The focus lies on deduction of information relevant for the spot welding process from an engineering point-of-view out of the comprehensive amount of spatial data computed with FEA.

### DATA ACQUISITION FOR PROCESS ANALYSIS

#### PRELIMINARIES AND DEFINITIONS

Fig. 1 defines the entirety of mechanical and electrical process quantities accessible to measurement in RSW, along with their location.

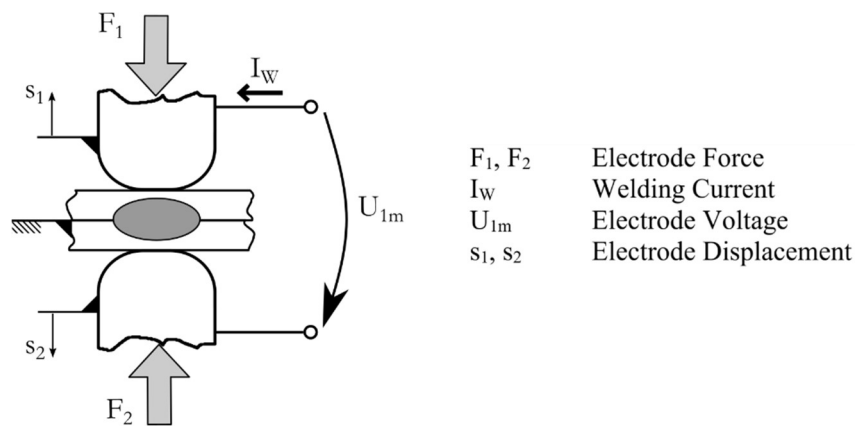


**Fig. 1** Process quantities in resistance spot welding.

Usually, the welding current  $I_w$  is the main process quantity being adjusted by the machine control. The electrode voltage  $U_{1m}$  is the result of the electrical resistance of the weld. It is often recorded for monitoring purposes [1], [2]. While the sheets are clamped together by the electrode forces  $F_1$  and  $F_2$ , thermal expansion and softening of the sheets cause a dynamic displacement  $s_1$  and  $s_2$  of the electrodes. The displacement can be used to monitor the process as well, especially to detect splash. In an industrial environment the displacement is difficult to measure, therefore the electrode voltage is preferred in most cases. Each of the quantities needs to be understood as a strong function of time.

The mechanical contact make between sheets and electrodes as well as between the sheets is the most important aspect of a resistance weld, as it defines most of the other quantities. An overview of the situation is given in Fig. 2.

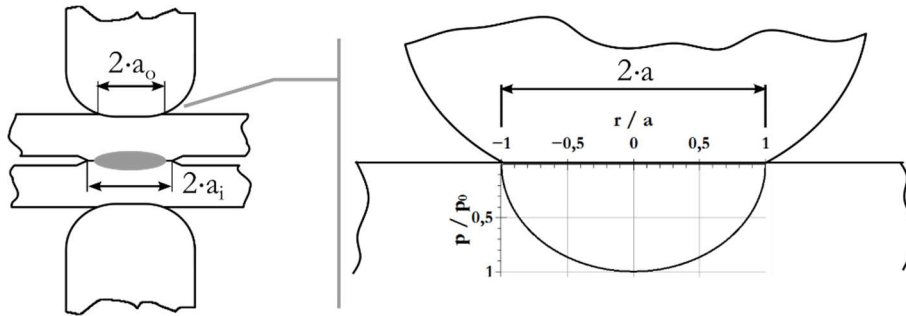


**Fig. 2** Mechanical contacts at the weld with an example of the uneven contact pressure distribution according to Hertz' [3] theory.

Therein, the contact radii  $a_i$  of the inner contact and  $a_o$  of the outer contact as introduced by [4] are defined at the weld. That means, the contact area is assumed to be a perfect circle. This will hold true as long as the electrodes are axisymmetric and positioned roughly perpendicular to the sheet surface, i.e. in most practical cases.

In Fig. 2, a representation to scale of the contact pressure distribution at the contact is shown as well. It is important to note, that just like the contact pressure depicted, other quantities at the contact like temperature or electric potential are a more or less strong function of the contact radius as well. In circumferential direction of the contact, the quantities are constant, due to axisymmetry.

The electrical situation during formation of the weld is rather involved, as the electric resistance at the weld needs to be divided into several parts [5]: The bulk resistance of the material and the transition resistance at the contacts. Fig. 3 defines detailed denotations for the resistances and corresponding electric potentials, as well as their localisation.

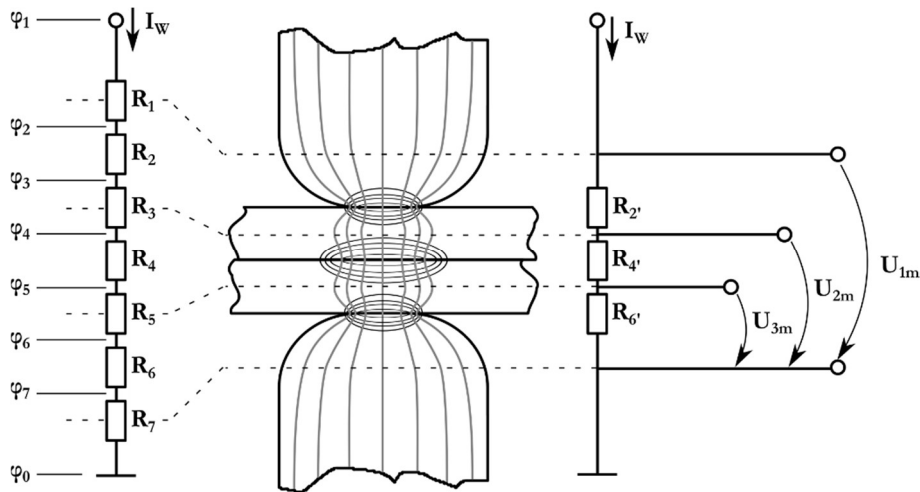


**Fig. 3** Definition and location of electrical quantities at the weld, left: true potentials and partial resistances, right: measurable voltages and resistances; illustration by Kaars et al. [6] current flowlines and potential isolines based on Gengenbach [7].

In Fig. 3 on the right, the three partial voltages and their corresponding resistances being measurable during welding are shown. On the left side, the true partial potentials of the

weld and their corresponding resistances are outlined. The dashed lines in between both represent the connection true and measurable resistances and especially their physical location at the weld. The respective true resistance is a

$$\textit{transition resistance for } R_i \quad i \in \{2, 4, 6\} \tag{1}$$

and

$$\textit{bulk resistance for } R_i \quad i \in \{1, 3, 5, 7\} \tag{2}$$

The measureable resistances are composed out of the true resistances by

$$R_i' = R_i + \chi \cdot (R_{i-1}(T) + R_{i+1}(T)) \quad i \in \{2, 4, 6\} \tag{3}$$

with  $\chi$  being an unknown number fulfilling  $0 < \chi < 1$ . Each of the true resistances will significantly change its magnitude during the welding process, especially the transition resistance. Most of the dynamic resistance change is driven by temperature [8–11], with the underlying effects being rather complicated. With respect to the scope of this work, the reader shall be pointed to [5], [12], [13] for more details. However, it is important to note, that the resistances are a strong function of time during welding.

Fig. 3 and equation (3) also prove, that it is not possible to determine the true resistance portions, and therefore their respective heat contributions to the weld, by measurements alone. In the following, the enumeration used in Fig. 3, left portion, will also be used to denote other quantities conjoined to the respective locations at the weld.

According to the German Standard DVS 2902-1 [14], a significant part of the total weld heat input is distributed into electrodes and surrounding sheet material, while heat dissipation to the surroundings by radiation and convection can be neglected. The standard states, that in many cases only 10 % of the total heat contributes to the formation of the melt.

A more comprehensive description of the heat flows at the weld is defined in Fig. 4. Therein, the composition of the total welding heat out of its portions, distinguished by heat sources and heat sinks is visualized.

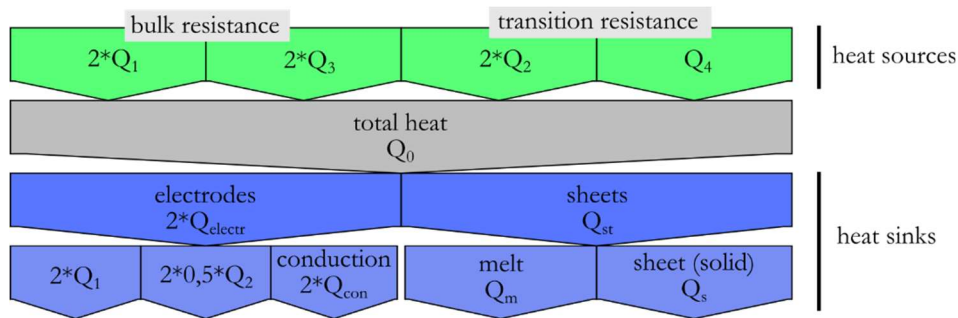


Fig. 4 Definition of the energy flow in a spot weld by heat sources and sinks.

The denomination of the heat sources in Fig. 4 is in accordance with the true resistances  $R_i$  in Fig. 3. Moreover, the heat sinks at the weld are divided by their locations, namely electrodes and sheets. The electrode heat  $Q_{electr}$  is composed out of heat from its bulk resistance  $Q_1$ , half of the transition resistance heat  $Q_2$  and heat conducted into the electrode

from the hot sheet  $Q_{con}$ . Depending on the algebraic sign of  $Q_{con}$ , the formulation theoretically also allows heating of the sheets by bulk heat from the electrodes. This approach is sometimes used to weld low resistance materials such as copper by using high resistance tungsten or molybdenum electrodes [15]. The heat in the sheets is divided into two portions, one being the melt heat  $Q_m$  being stored in the molten zone of the joint, the other being the heat  $Q_s$  increasing the temperature of the surrounding sheets. As the melt heat eventually is a portion of the total heat, the description in Fig. 3 is of great relevance for process analysis. By evaluating the different heat portions, one can gather information on where the heat dominantly forming the joint comes from, or why the heat produced does not create a sufficient nugget.

The RSW process features a peculiarity: As soon as the nugget is formed, the melt is exposed to significant hydrostatic pressure caused by the electrode force. Also, this same electrode force causes the unmolten portion of the sheets at the inner contact to be pressed to each other strongly enough in order to ensure secure enclosure of the high-pressure melt. Sometimes this mechanism of melt enclosure fails, resulting in the melt being expelled out of the weld. This event is known as weld splash or expulsion and is the most important process limit in RSW [16]. In literature, the mechanism of melt enclosure is disputed. Some authors assume that expulsions occur as soon as the molten zone grows larger than the inner contact [17], [18], Broda [19] presumed that excessive melt pressure due to melt evaporation is responsible for the expulsion. Senkara et al. [20] proposed the only mathematical model for splashes available to date. The model assumes splash, as soon as the effective force of the expanding nugget has grown larger than the electrode force. In Fig. 5, a graphical summary of the mechanism of nugget enclosure by contact pressure of the outer contact  $p_o$ , with  $p_{e,fl}$  being the hydraulic nugget pressure, is shown.

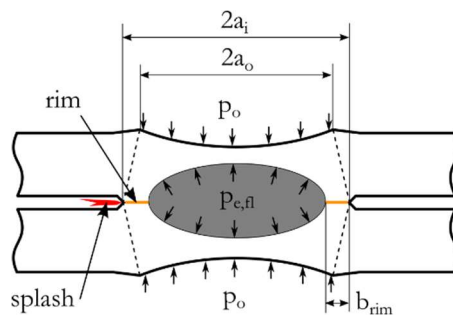


Fig. 5: Enclosure of melt in the spot welding process.

#### MATHEMATICS OF DATA ACQUISITION

The contact pressure distribution outlined in Fig. 2 is processed to determine the actual contact radii in the FEA: A routine implemented in the postprocessing code evaluates the location of the contact node at which the pressure switches to about zero, starting from the symmetry axis. The contact radii of electrodes and sheets are the most important input quantities for further data processing, as will be shown in the following paragraphs. Of course during the welding process, the contact radii will significantly change their



magnitude, as the sheets will thermally expand and subsequently soften because of the welding heat. This effect is correctly included by the routine, as always the actual contact pressure distribution for the respective timestep is considered for contact radius detection.

Given a quantity  $g(r)$  in  $0 \leq r \leq a$ , also cf. Fig. 2, the space spanned by the curve in the axisymmetric domain can be understood as a volume with the boundaries

$$0 \leq r \leq a \quad \wedge \quad 0 \leq g \leq g(r) \quad (4)$$

According to Guldins second rule [21], the volume of this body of revolution is

$$G = \iint_{(A)} g(r) dA = 2\pi \int_0^a g(r) \cdot r dr \quad (5)$$

Assumed  $g(r)$  for example would represent the contact pressure, then  $G$  would be the contact force. As the effective magnitude  $g_e$  of  $g(r)$  has to have the same physical effect as the unevenly distributed quantity,  $g_e$  must fulfil the expression

$$2\pi \int_0^a g_e \cdot r dr = 2\pi \int_0^a g(r) \cdot r dr \quad (6)$$

which after some transformation yields

$$g_e = \frac{2}{a^2} \int_0^a g(r) \cdot r dr \quad (7)$$

However, in FEA the quantity  $g(r)$  will never be given as a mathematical function, but as discrete numbers on the respective nodes. For this reason, the integration must be carried out numerically. The approach can also be pictured as a summation of the volumes of a number of hollow cylinders. Equation (5) then can be approximated by

$$G = \sum_{i=1}^n G_i \quad (8)$$

$$G_i = 2\pi \cdot \frac{r_i+r_{i-1}}{2} \cdot \frac{g(r_i)+g(r_{i-1})}{2} \cdot (r_i - r_{i-1}) \quad (9)$$

wherein  $r_n = a$ . Accordingly, the required effective magnitude is written as

$$g_e = \frac{2}{a^2} \cdot \sum_{i=1}^n \left( \frac{r_i+r_{i-1}}{2} \cdot \frac{g(r_i)+g(r_{i-1})}{2} \cdot (r_i - r_{i-1}) \right) \quad (10)$$

Expression (10) was implemented into the FEA code to compute the effective magnitude of various quantities in the contact areas, for example effective electric potential, effective pressure and effective temperature. In order to compute the heat content of the molten zone of the sheets, another integration is necessary: At first, all elements whose coldest node of the temperature  $T_n$  fulfils the condition  $T_n \geq T_m$  are selected.  $T_m$  is set by the user fulfilling

$$T_{sol} \leq T_m \leq T_{liq} \quad (11)$$

## Mathematical Modelling of Weld Phenomena 12

where  $T_{sol}$  is the onset and  $T_{liq}$  the end of the sheet materials melting interval. Based on the average temperature  $\bar{T}_i$  of the respective element, the heat of the molten zone is written as

$$Q_m = \sum_{i=1}^k (V_i \cdot h(\bar{T}_i)) \quad (12)$$

wherein  $V_i$  represents the element volume and  $h(\bar{T}_i)$  the specific enthalpy density. Because of the selection approach excluding partially molten elements, the procedure yields the lower limit of the melt heat, but can be slightly adjusted by selection of the melting temperature  $T_m$  according to (11).

The criterion (11) was also used in order to detect the nugget diameter in each timestep of the solution. Provided that the inner contact is closed and at least one node in the model supersedes  $T_m$ , a postprocessing routine was used to evaluate the nugget diameter. The routine detects the location where the nodal temperature in the inner contact is smaller than  $T_m$  for the first time, starting from the symmetry axis.

### COMPUTATION OF ENGINEERING DATA

Based on the effective magnitude as described in the preceding section, the effective electric potential  $\varphi_i$  is computed out of the electric potential distribution in each contact surface. This effective potential is the most important prerequisite for caloric considerations at the weld, as it is necessary in order to compute the true resistance contributions at the weld by using the expressions

$$R_i = (\varphi_i - \varphi_{i+1})/I_w \quad 1 \leq i \leq 6 \quad (13)$$

$$R_7 = \varphi_7/I_w \quad (14)$$

$$R_0 = \varphi_1/I_w \quad (15)$$

Based on those  $R_i$ , the heat contributions to the weld result from

$$Q_i = \int_{t_0}^{t_1} R_i(t) \cdot I_w(t)^2 dt \quad 0 \leq i \leq 7 \quad (16)$$

for a welding time from  $t_0$  to  $t_1$ . Furthermore, the heat transported across the electrode-sheet contact  $Q_{con}$  is computed using expression (9). The local contact heat flow across each contact element therein is considered as  $g(r)$  accordingly. Based on these caloric data, the process efficiency can be determined as well. In literature, the terms effective efficiency [22], melt efficiency [23], [24] and process efficiency [24] are defined. Only the effective  $\eta_{eff}$  and melt efficiency  $\eta_m$  shall be discussed here. They are defined as follows:

$$\eta_{eff} = Q_{st}/Q_0 \quad (17)$$

$$\eta_m = Q_m/(\eta_{eff} Q_0) \quad (18)$$

Of course, other quantities like local and total electric power, specific transition resistance, effective contact pressure and temperature and many more can be derived using

the data and methods explained above. The latter, along with the electrode heat as defined in Fig. 4, are particularly useful for the evaluation of electrode wear. For the sake of length of this work, these continuative topics shall not be further discussed.

### FEA MODEL AND VERIFICATION

With respect to the scope of this work only a brief overview of the model and the experimental conditions used to verify it will be given. The reader shall be pointed to [6], [25–27] for more details. Also, results on the true resistances  $R_i$  can be examined in [6].

The FEA model employed for the analysis presented in this work was set up in ANSYS v19, using an axisymmetric model geometry. The elements use a second-order ansatz and have structural, thermal and electrical degrees of freedom. A brief overview over the boundary conditions applied and mesh used is given in Fig. 6. At the inner and outer contacts the model uses the transition resistance model introduced by Kaars et al. [25]. All material properties of the sheets are implemented as functions of temperature up to the melting point.

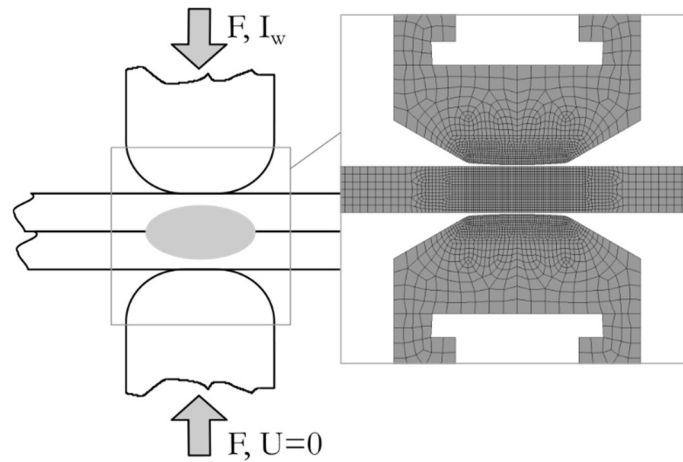


**Fig. 6:** FEA model, major boundary conditions and mesh.

The FEA was set up to represent welding of two sheets of 1.5 mm martensitic 22MnB5 steel with aluminium-silicon coating AS150. In both, experiments and FEA, a welding force of 6 kN and a welding current up to 6.6 kA were applied.

In welding experiments with an instrumented RSW gun, a data basis was obtained to validate the FEA. Furthermore, the dynamic curve of the resistance  $R_{1m}$  was recorded and the result afterwards compared to the computed curve from the FEA. Overall, a very good agreement between both was observed. The reader shall be pointed to [6] for details, more verifying results are presented in the following section. Additionally, the dynamic contact radii and nugget diameter of FEA and experiment were recorded and compared. In order to obtain the data from the experiment, the welding process was prematurely interrupted at certain points. Afterwards, the radius of the electrode indentation  $a_o$  was measured using a

microscope Zeiss Axiovert 200. The weld was then mechanically broken open to reveal the nugget and inner contact area, whose radii  $r_p$  and  $a_i$  were then measured as well.

RESULTS REVIEW AND DISCUSSION

In Fig. 7, the computed and measured results of contact radii and nugget radius are presented. In the contact radii curves, the onset of welding current flow is indicated by a steep decline of both contact radii, especially at the inner contact. The reason for this is the thermal expansion of the sheets in the vicinity of the contacts. As the welding time progresses, the heated sheets begin to soften, which causes the electrodes to sink into the sheets, along with increasing contact radii. It can be readily seen, that the measured values for the contact radii are in good conformity with the computed ones.

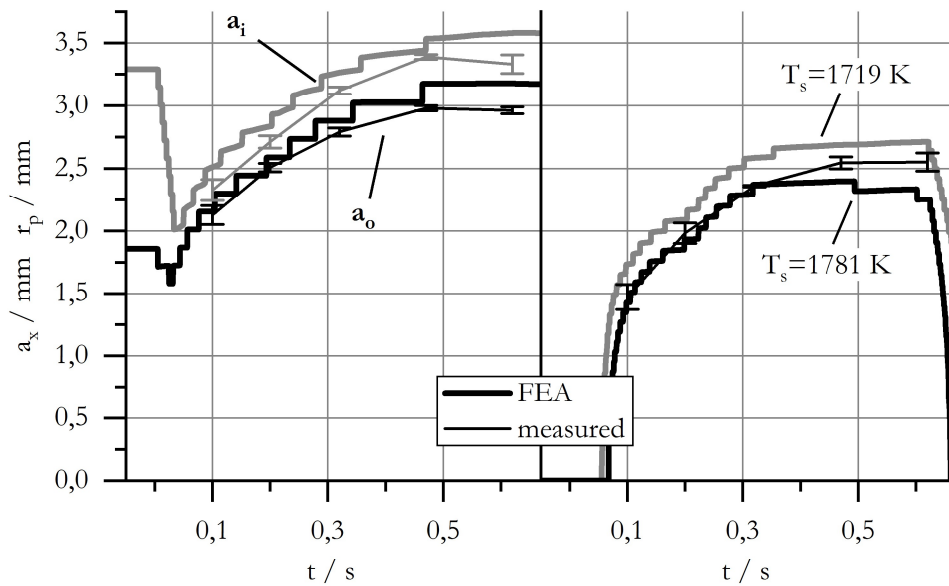


Fig. 7: Comparison of computed and measured dynamic contact radii  $a_x$  and nugget radius  $r_p$ .

The nugget radius depicted in the right half of the diagram is divided into two curves. At the welded joint, one cannot distinguish for sure at which temperature  $T_m$  in the mushy zone with  $T_{sol} \leq T_m \leq T_{liq}$  the sheets actually formed a sound joint. But in the FEA, a definition needs to be made, at which minimum temperature the joint is considered welded. For this reason, the nugget growth curves are depicted for both limits of the mushy zone. As it can be seen, the deviation between both is small, the measured curve lies well in between. As the dynamic resistance curve of the model conformed very well with the experiments as well, cf. preceding section, the FEA model is considered to be accurate.

In Fig. 8, the distribution of the total welding energy on the individual contributors of the heat sources as well as the heat sinks according to Fig. 4 is shown. It can be seen that the major part of heat generation of about 60 % takes place in the bulk material of the sheets.

## Mathematical Modelling of Weld Phenomena 12

The electrode material only contributes roughly 5 %. This is interesting because it also means that about 35 % of the welding heat is released by transition resistances, of which the major part of 30 % is attributed to the outer contacts. About 70 % of the welding heat remains in the electrodes when the weld is finished, with the heat transported into the electrodes by conduction being by far the largest contributor to that amount. About 15 % of the total welding heat in the electrodes is appropriated to the electrical contacts. Obviously, the contact heat distributes itself in equal portions among both contact partners. Only 5 % of the total welding heat are used to form the nugget, while 25 % are used to heat up the sheets around the weld.

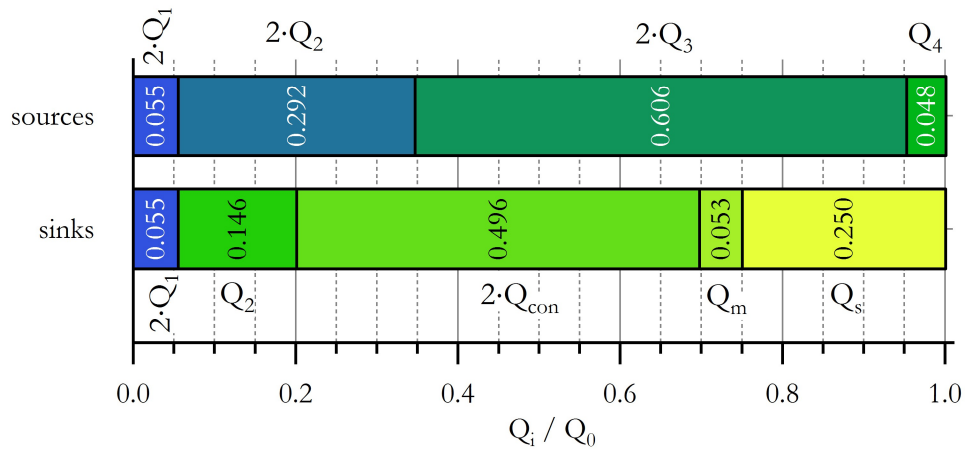


**Fig. 8:** Relative energy balance at the end of the welding cycle, separated by heat sources and sinks.

The utilization of welding heat for the joint formation can be better observed by evaluating the process efficiencies. Those are depicted in Fig. 9, along with the welding current. It can be seen, that the effective efficiency has its maximum of about 55 % at the very beginning of current flow and from then on decreases to about 30 % at the end of the welding cycle.

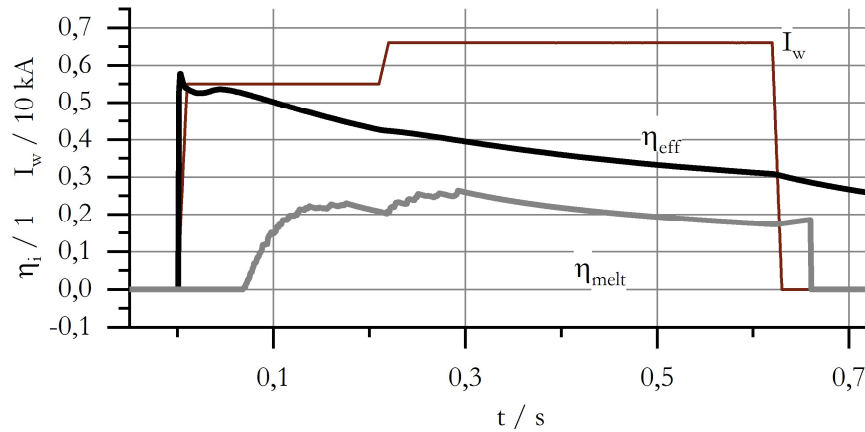


**Fig. 9:** Dynamic process and melt efficiency of the weld.

The melt efficiency on the contrary has its maximum of about 25 % after about 300 ms after the onset of current flow and decreases to about 18 % towards the end of the welding cycle. These observations have very important consequences: They prove the common assumption, that spot welding is more efficient in terms of relative heat being input into the sheets when the duration of current flow is short [14]. But moreover, they show that a certain duration of current flow exists, at which the energy is utilized best for joint formation. In this case, this happens after about 300 ms of current flow. This instant also coincides with the moment, where nugget formation is practically completed, cf. Fig. 7. Arbitrarily prolonging the welding process over this “optimal welding time” will only decrease efficiency, but not form any more melt volume. Of course, prolonged welding can be advisable for metallurgical reasons in several cases nonetheless.

In Fig. 10, detailed information on the mechanical situation at the inner contact is presented. While therein  $T_{e,rim}$  is the effective temperature of the solid rim around the nugget,  $b_{rim}$  is the width of the latter, also cf. Fig. 5. Additionally, the hydraulic force exerted by the nugget  $F_{fl}$  is displayed as relative portion of the total contact force at the inner contact. Accordingly,  $p_{e,rim}$ ,  $p_{e,fl}$  and  $p_{e,i}$  are the effective contact pressures of rim, nugget and inner contact in total. Per definition, data on rim and nugget does not exist before the first melt is formed. It can be readily seen, that during the process the rim temperature has a nearly constant temperature of about 200 K below the  $A_4$  point of the sheets. The width of the rim has two maxima of about 2 mm at the end and beginning of the process, while a minimum of about 1 mm exists in the middle of the process. In the same instant where the rim is most narrow, the hydraulic force has its maximum of about 50 % of the inner contact force. The effective pressures all have a maximum at the beginning and from then on decrease hyperbolically. At all times, the fluid pressure in the nugget is the largest pressure, the pressure in the rim the smallest. The effective total pressure lies well in between.

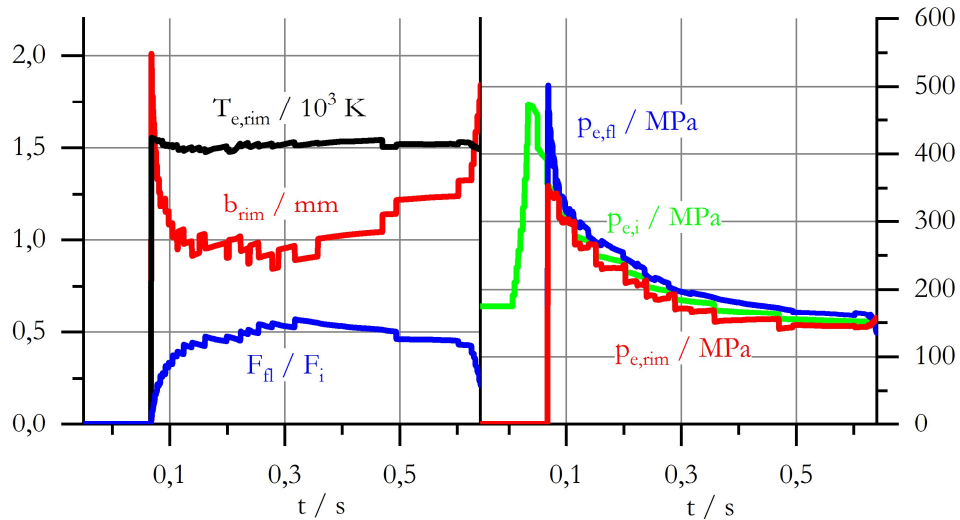


**Fig. 10:** Dynamic quantities characterizing the enclosure of melt in resistance spot welding.

In Fig. 11, the contact pressure distribution at both contacts of the weld during various stages of the process is displayed. It can be seen, that at both contacts, the contact pressure initially is distributed according to Hertz' theory, cf. Fig. 2. With progress of welding time, the pressure distributions become more and more flattened, especially at the inner contact. At the outer contact, a local maximum of contact pressure forms towards the end of the welding cycle.

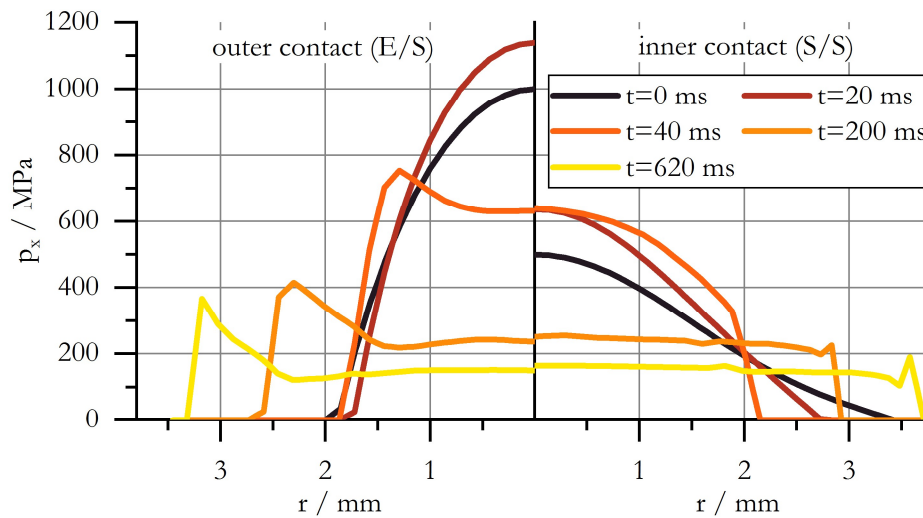


**Fig. 11:** Contact pressure distribution at the outer (left) and inner (right) contact of the weld during various stages of the welding process.

These information are very important in order to understand the effects responsible for the data in Fig. 10: As the weld advances and the nugget is formed, the sheets soften and

subsequently melt, causing the contact pressure distributions to flatten. This effect is equal to a mechanical representation the effective pressure computation in the contact zone. As a result, the hydraulic pressure in the nugget must be greater than that of the rim at any times, because the hydraulic pressure represents the integration of the high-pressure zone in the middle of the contact. The effective pressure of the contact in total must lie in between that of the melt and that of the rim. This is exactly what is visible in Fig. 10. Fig. 10 also proves, that the width of the rim is not constant at all. Moreover, the conjunction of nugget diameter, rim width and hydraulic melt pressure results in the magnitude of the hydraulic melt force.

These observations have some very important consequences: At first, they prove that a melt pressure greater than that of the rim does not result in a splash, as the rim pressure is the smallest, the melt pressure the greatest pressure at the inner contact at any times anyway. At the very beginning of melting, a melt pressure equal to the maximum contact pressure is present, from that point on the melt pressure can only decrease. Secondly, the hydraulic force of the melt can never exceed the inner contact force, as long as a rim exists. In case of total melting of the rim, the relative hydraulic force would be one. Of course melting of the rim would result in a splash anyway. That means, that splashes can't be a result of the hydraulic force getting larger than the electrode force.

### CONCLUSIONS

The FEA model presented has been proven capable of accurately computing the nugget diameter as well as the contact radii of an exemplary weld of martensitic steel. Methods have been introduced, to extend the assessment of the computed data by important process parameters such as resistances, energies, efficiencies as well as mechanical pressures and forces. The method is extendable to other potential quantities of interest.

For the first time, a comprehensive quantitative energy balance of the spot welding process for heat sources as well as heat sinks has been computed using the methods outlined. Additionally, the dynamic curve of effective and melt efficiency have been computed for the first time.

The data suggests, that an optimal duration of current flow in resistance spot welding may exist. Furthermore, the computed parameters proved, that the hydraulic pressure in the nugget is larger than that of the surrounding rim at any time. That means, that increased nugget pressure as assumed in literature can't be a reason for welding splashes. This indirectly also means, that the force exerted by the molten nugget will never exceed the electrode force.

### REFERENCES

- [1] N., N.: *Untersuchung innovativer Geräte zur Qualitätssicherung beim Widerstandspunktschweißen* (Forschungsbericht Nr. AiF-13.568N). München: SLV München, 2005
- [2] MIRO, URAN: *Qualitätsüberwachung beim Widerstandspunktschweißen mittels mehrparametrischer Analyse*. Berlin, Technische Universität Berlin, Dissertation, 2004



- [3] HERTZ, HEINRICH: Über die Berührung fester elastischer Körper. In: *Journal of Engineering Materials and Technology* Bd. 92 (1881)
- [4] HOLM, RAGNAR: *Die technische Physik der elektrischen Kontakte*. 1. Aufl. Berlin : Springer-Verlag, 1941
- [5] BRUNST, WALTER: *Das elektrische Widerstandsschweißen*. 1. Aufl. Berlin : Springer-Verlag, 1952
- [6] KAARS, J. ; KOPPE, K. ; GEORGI, W. ; MAYR, P.: Transition resistance of 22MnB5+AS150— experimental results and their numerical application. In: *Welding in the World* (2017)
- [7] GENGEBACH, O.: Untersuchungen über die Stromverteilung, den Wärmefluss und die Temperaturverteilung in der Umgebung von Widerstandsschweißpunkten. In: *Schweißtechnik* Bd. 45 (1965)
- [8] ROGEON, P. ; CARRE, P. ; COSTA, J. ; SIBILIA, G. ; SAINDRENAN, G.: Characterization of electrical contact conditions in spot welding assemblies. In: *Journal of Materials Processing Technology* Bd. 195 (2008), Nr. 1–3
- [9] RAOELISON, R.N. ; FUENTES, A. ; POUVREAU, C. ; ROGEON, PH. ; CARRÉ, P. ; DECHALOTTE, F.: Modeling and numerical simulation of the resistance spot welding of zinc coated steel sheets using rounded tip electrode: Analysis of required conditions. In: *Applied Mathematical Modelling* Bd. 38 (2014), Nr. 9–10
- [10] ESHRAGHI, MOHSEN ; TSCHOPP, MARK A. ; ASLE ZAEEM, MOHSEN ; FELICELLI, SERGIO D.: Effect of resistance spot welding parameters on weld pool properties in a DP600 dual-phase steel: A parametric study using thermomechanically-coupled finite element analysis. In: *Materials & Design* Bd. 56 (2014)
- [11] GESLAIN, EDOUARD ; ROGEON, PHILIPPE ; PIERRE, THOMAS ; POUVREAU, CÉDRIC ; CRETTEUR, LAURENT: Coating effects on contact conditions in resistance spot weldability. In: *Journal of Materials Processing Technology* Bd. 253 (2018)
- [12] HOLM, RAGNAR: *Electric Contacts - Theory and Application*. 4. Aufl. : Springer-Verlag, 1967. — 3. Reprint der 4. Aufl. von 1967
- [13] JOHNSON, K.L.: *Contact Mechanics*. Cambridge : Cambridge University Press, 1987. — Ninth Printing 2003
- [14] DVS-MERKBLATT 2902-1: *Widerstandspunktschweißen von Stählen bis 3mm Einzeldicke - Übersicht*
- [15] N., N.: *Schweißen von Kupfer und Kupferlegierungen* (Informationsschrift) : Deutsches Kupferinstitut, 2009
- [16] NORM DIN EN ISO 14327: *Widerstandsschweißen - Verfahren für das Bestimmen des Schweißbereichsdiagramms für das Widerstandspunkt-, Buckel- und Rollennahtschweißen*, 2004
- [17] SHEN, J. ; ZHANG, Y. S. ; LAI, X. M.: Influence of initial gap on weld expulsion in resistance spot welding of dual phase steel. In: *Science and Technology of Welding and Joining* Bd. 15 (2010), Nr. 5
- [18] NIELSEN, CHRIS VALENTIN: *Genzbedingung für die Spritzerentstehung*. Aachen, SWANTEC Software and Engineering ApS, pers. Mitteilung, 2013
- [19] BRODA, TOBIAS: Pulsierender Gleichstrom für Blechdickenkombinationen. In: *16. Kolloquium Widerstandsschweißen und alternative Verfahren*. Halle/Saale, 2014
- [20] SENKARA, J. ; ZHANG, H. ; HU, S. J.: Expulsion Prediction in Resistance Spot Welding. In: *Welding Journal* (2004), Nr. 04
- [21] PAPULA, LOTHAR: *Mathematik für Ingenieure und Naturwissenschaftler, Studium*. Bd. 2. 12. Wiesbaden : Vieweg + Teubner, 2009
- [22] SCHELLHASE, MARTIN: *Der Schweißlichtbogen – ein technologisches Werkzeug*. Berlin : Verlag Technik, 1985
- [23] RYKALIN, NIKOLAJ: *Berechnung der Wärmevorgänge beim Schweißen*. Bd. 3. Berlin : Verlag Technik, 1957

- [24] CHANG, CHIN-LUNG: *Berechnung der Schmelzbadgeometrie beim Laserstrahlschweißen mit Mehrfokustechnik*. Stuttgart, Universität Stuttgart, Dissertation, 2000
- [25] KAARS, JONNY ; MAYR, PETER ; KOPPE, KURT: Simple Transition Resistance Model for Spot Welding Simulation of aluminized AHSS. In: *Mathematical Modeling of Weld Phenomena*. Bd. 11, 2016 — ISBN 978-3-85125-490-7
- [26] KAARS, JONNY ; MAYR, PETER ; KOPPE, KURT: Generalized dynamic transition resistance in spot welding of aluminized 22MnB5. In: *Materials and Design* Bd. 106 (2016)
- [27] KAARS, JONNY ; MAYR, PETER ; KOPPE, KURT: Dynamic apparent transition resistance data in spot welding of aluminized 22MnB5. In: *Data in Brief* Bd. 8 (2016)



MULTIPHYSICS FINITE ELEMENT  
SIMULATION OF RESISTANCE SPOT  
WELDING TO EVALUATE LIQUID METAL  
EMBRITTEMENT IN ADVANCED HIGH  
STRENGTH STEELS

K. M. PRABITZ \*, W. ECKER\*, M. BORCHERT\*,  
T. ANTRETTNER\*\*, H. SCHUBERT\*\*\*, B. HILPERT\*\*\*,  
M. GRUBER\*\*\*\* and R. SIERLINGER\*\*\*\*

\* *Materials Center Leoben Forschung GmbH, Roseggerstraße 12, 8700 Leoben, Austria*

\*\* *Chair of Mechanics, Montanuniversität Leoben, Franz Josef-Straße 18, Austria*

\*\*\* *Daimler AG, 710 Sindelfingen, Germany*

\*\*\*\* *voestalpine Stahl GmbH, voestalpine-Straße 3, 4020 Linz*

DOI 10.3217/978-3-85125-615-4-40

ABSTRACT

Advanced high strength steels (AHSS) open new possibilities in lightweight design in the automotive industry. However the risk of liquid metal embrittlement (LME) of modern zinc coated advanced high strength & high ductility steels (AHSS HD) during resistance spot welding (RSW) is a limiting factor for the use of such steels in the cars body in white. The goal of this work is to evaluate and exclude this risk for the high ductility dual phase steel DP1200HD. In the RSW process two electrodes are pressed to similar or dissimilar metal sheets, which are heated and joined by means of Joule heating. An experimental RSW study of similar two-sheet stack ups of DP1200HD showed zinc induced LME for certain welding conditions. Commonly trial and error testing is applied to determine proper welding conditions in order to increase the spot weld quality and to decrease LME. To avoid this extensive testing and to better understand the effect of the local physical conditions on the formation of LME a finite element model of the RSW process has been developed. This multi-physical model couples electrical, thermal, mechanical and metallurgical effects and provides local quantities for current density, temperature, strains, stresses and phase compositions. In addition a damage parameter for LME has been developed based on experimental findings and the local mechanical quantities from the simulations. The simulation results have been validated against experimental RSW tests.

Keywords: resistant spot welding, finite element simulation, advance high strength steels, liquid metal embrittlement

## INTRODUCTION

Safe and lightweight construction in automotive has become a driving factor of material development. Advanced high strength steels with high ductility (AHSS) open up new possibilities for lightweight design and, hence, fuel and emission reduction. In cars body in white these steels as well as their joints have to show a high crashworthiness. In this study a dual phase steel with high ductility (DP1200HD) was investigated. Modern dual phase steels are unalloyed steels with high ultimate tensile strength and a martensitic and ferritic microstructure.

A preferred joining method of thin steel sheets in automotive is resistance spot welding (RSW) [1]. RSW represents a quick and reliable joining technique that is also highly automatable. As seen in figure 1 two electrodes clamp the metal sheets together. In the next step a defined electrode force  $F$  is applied and after that the welding current  $I$  passes through the electrodes and metal sheets. In the centre between the sheets the temperature rises due to Joule heating. The heating takes mainly place between the sheets, because there electrical resistance is at this interface about ten times larger than between sheet and electrode. A molten pool of metal also called nugget develops and connects the sheets. After the current is switched off the force is kept constant for a defined time while the nugget solidifies.

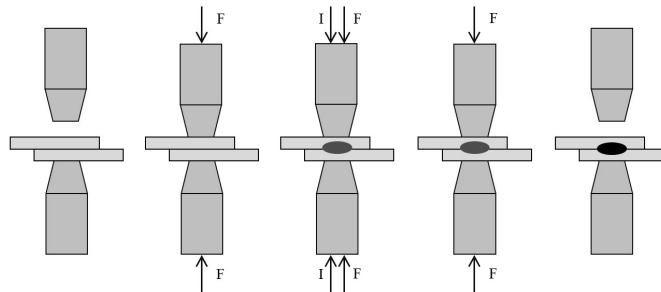


**Fig. 1** Scheme of the different steps in resistance spot welding process including the force and current application

Resistance spot welding with bare steel sheets is a quick and reliable process. However, in the particular case considered here zinc is used as cathodic surface protection of the steel sheets. Zinc coating is applied via an electrogalvanizing process and a thin layer of about  $10\ \mu\text{m}$  is deposited.

Electrogalvanized DP1200HD has high potential as a new high strength material for car bodies in white. However, when introducing new materials the whole processing has to be taken into account and adapted to the new material.

Under specific conditions, electrogalvanized steels tend to show liquid metal embrittlement (LME) in the spot weld during RSW. LME describes the drastic loss of tensile ductility of an otherwise ductile metal. DP1200HD shows as a high strength steels a higher susceptibility to LME than low or medium strengths steels, which has to be investigated properly in order to adapt the welding process and, hence, to guarantee a satisfying welding result. The main reasons for LME are on the one hand that zinc remarkably decreases the bulk and grain boundary cohesion [2] in many metals, including steel [3], and on the other hand that the liquid zinc state and its very high wettability leads to high zinc mobility. Since the phase state of zinc and the zinc diffusivity in steels are

depending on temperature, the temperature is an important factor in LME [4-5]. For LME cracking a minimum threshold stress has to be present. These cracks nucleate at surfaces wetted with liquid zinc [6] and cause brittle cracking [7-8]. Liquid metal, stress and high temperatures therefore count as main influences to LME in a susceptible material. In RSW a local temperature of 700°C has been found as critical threshold for LME cracking [9] although in general LME might also occur at lower temperatures.

The main welding parameters with an impact on LME cracking are electrode force, welding time and welding current because these process parameters have the highest influence on the local temperature and stress state. To find process parameters that avoid LME cracking two different approaches are possible. In the first approach the welding parameters are identified by means of extensive RSW testing. In this case a large number of tests has to be conducted and the local conditions remain unknown and, hence, a deeper understanding of the governing mechanisms and local driving forces is not possible. The second approach is based on a validated finite element based RSW simulation, which has the advantage that less testing is needed, the local effects can be investigated and radically new process concepts can be easily evaluated. In the literature a number of different finite element modelling approaches with different model complexities are reported [10-12]. Many of these models have in common that the effects stemming from phase transformation are neglected and a proper LME cracking criterion has never been described. In the current paper a multi-physical finite element model considering phase transformation effects was developed in order to calculate current densities, temperature fields, stresses, phase transformation and furthermore to estimate the local LME risk by a first very simple damage indicator. The aim of this paper is to describe the novel and due to the consideration of phase transformation more complete modelling approach for the first time. The approach is demonstrated using pre-existing data and shows reasonable results.

### EXPERIMENTAL

Extensive spot weld tests were realised to investigate nugget formation, nugget size, penetration depth, heat affected zone (HAZ) and LME cracking. The process parameters welding current, welding time, electrode force and holding time were systematically varied. To investigate the influence of the zinc coating comparable experiments for coated and uncoated steel sheets were carried out. For these tests, a Nimak pedestal welder with a Matuschek controller and C-shaped calliper was used. Two 1.6 mm thick metal sheets were stacked and placed unconstrained between the electrodes on a table. Dome shaped and water cooled copper-chromium alloy electrodes of the type F1-16-20-6 were used. The welding process was started manually and the sample was removed after cooling down to room temperature.

Figure 2 shows the characteristic zones of a typical spot weld. In the centre of the spot weld a nugget, also called fusion zone (FZ), formed where the material was melted and re-solidified. This zone mechanically connects the two steel sheets. The nugget is surrounded by the upper-critical HAZ, where the material was austenitized. The next zone is the sub-critical HAZ, where only an annealing of the initial microstructure without phase transformation took place. This zone is followed by the unaffected base material (BM). Due

to the material characteristics of the investigated DP1200HD the HAZ and FZ consists mainly of martensite and the BM consists of martensite and ferrite.

The LME cracks can be grouped in three types that all occur in the upper-critical HAZ: Type one forms from the surface of the sheets at the boundary of the indentation, type two forms at the surface directly underneath the electrode near its axis and the third type forms at the boundary of the nugget between the two sheets, see Figure 2. Cracks of type one are most common and can easily exceed a length of 100  $\mu\text{m}$ . The type two cracks are typically small and uncritical. The type three cracks are rare, but might also reach higher crack lengths. In the micrograph in Figure 2 cracks of all types can be found. The largest type one cracks reach 170  $\mu\text{m}$ , the type two cracks 30  $\mu\text{m}$  and the type three cracks 220 $\mu\text{m}$ .

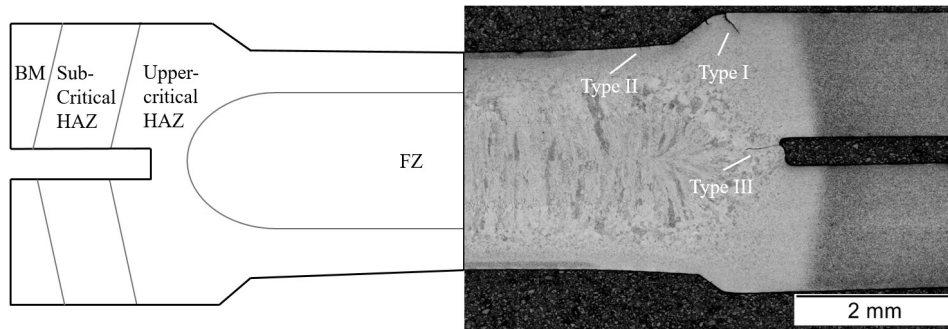


**Fig. 2** left: schematic representation of different regions in a spot weld; right: corresponding microstructure of sample D

For this work four exemplary chosen weld conditions as listed in Table 1 are compared to the results of the simulation.

**Table 1** List of applied welding conditions of the spot welds exemplarily investigated in the present paper.

Sample	Electrode force [kN]	Welding current [kA]	Welding time [ms]	Holding time [ms]
A	4.5	5.2	380	300
B	4.5	6.9	380	300
C	4.5	5.2	760	300
D	4.5	6.9	760	300

## MODELLING

The present model was developed using the commercial finite element software package Abaqus Version 2017 [12]. Modeling the RSW process is a complex multi-physics problem [13]. Figure 3 shows the different phenomena and their interactions taking place in RSW. The built-in models in Abaqus cover the electrical, thermal and mechanical part of the problem, but the phase transformation related evolution laws were implemented using a set of user defined subroutines.

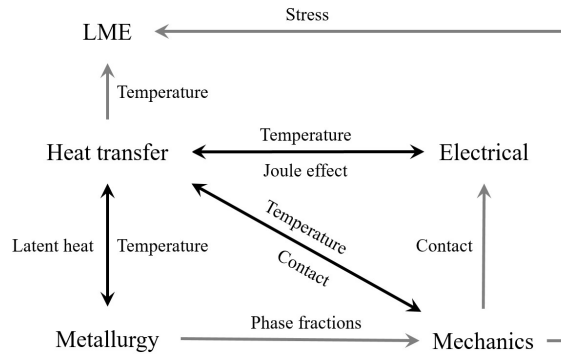


**Fig. 3** Interaction of electrical, thermal, mechanical, metallurgical modules and LME damage parameter [14]

The electrical current between the electrodes lead to Joule heating of the steel sheets in between. The electrical contact resistivities at the interfaces between the two zinc coated steel sheets and between the electrodes and the zinc coated steel as well as the temperature dependence of the resistivities are of great importance for the local heat generation. In the current state of the project most material data such as the electrical conductivity [14] are taken from literature on DP1000 material [15]. For the heat transfer problem in the steel sheet measured temperature dependent thermo-physical properties were used. With increasing temperature the material undergoes in the upper-critical HAZ and the FZ a phase transformation from the initial microstructure to austenite. Furthermore, in the FZ the material melts. During cooling, the affected material first re-solidifies and later on transforms to a martensitic microstructure. In case of the diffusive phase transformations and the melting the Johnson-Mehl-Avrami-Kolmogorov approach [16] was applied. The martensitic phase transformation follows a Koistinen-Marburger relation [17]. For all phase transformations the latent heat is considered by means of a body heat source and the transformation induced plasticity (TRIP) is modelled using Leblond's model [18]. The latent heat for the solid-solid phase transformations were experimentally measured. Missing material data such as temperature dependent Young's modulus, temperature dependent flow curves, thermal expansion coefficients and the parameters of the TRIP model, which has yet to be measured for the investigated DP1200, are taken from literature on a DP1000 steel [19]. Additionally, a first and very simple indicator for assessing the local LME risk has been developed. It ranges from 0 (i.e. no risk) to 1 (i.e. certain LME damage). This simple LME indicator gets non-zero if the local temperature at the investigated material point is above the for the investigated material class typical 700°C [7] and if at the same time and location tensile stresses are acting [7][9]. A third necessary condition for LME is the presence of zinc, which was respected by the fact that only surface elements can undergo LME crack initiation. For the same reason further LME crack extension is only possible if the investigated material point is connected to an already damaged position.

The model consists of the two electrodes and two steel sheets of 1.6 mm thickness. Since the zinc coating is very thin compared to the sheet thickness it is not modelled as a physical entity in the FE model. Nevertheless, the effect of the coating is respected in the contact conditions between the electrode and the sheet as well as between the two sheets.

As long as no lateral forces e.g. from the clamping act the RSW process can treated as an axial-symmetric problem. Since Abaqus only supports 3D elements for coupled electric,



thermal and mechanical problems, a 3D wedge model with an opening angle of  $3^\circ$  and axial-symmetric boundary conditions was built. Thermal, electrical and structural coupled elements of the type Q3D8 are assigned to the whole model except the element row near the axis of the model where Q3D6 wedge elements were used for geometrical reasons. The model consists of approximately 5000 elements. In the relevant zone near the zinc coated surfaces a mesh with an element height of 0.04 mm and an aspect ratio of 2:1 was assigned.

Different boundary conditions need to be assigned to the model. In order to suppress any displacement in axial-direction in the model the degrees of freedom of the nodes at the bottom surface of the lower electrode were fixed. The initial temperature of the whole model was set to  $25^\circ\text{C}$  and a fixed potential of 0V was defined for the bottom of the lower electrode. The welding force and the welding current were applied to the top of the upper electrode. The water cooled inside of the electrodes was modelled using a convection boundary condition with a heat transfer coefficient of  $7.5\text{ mW}/(\text{mm}^2\text{ K})$  and a sink temperature of  $25^\circ\text{C}$ . For the heat exchange between the zinc coated sheet surfaces to the environment an ambient temperature of  $25^\circ\text{C}$  and surface radiation with an emissivity of 0.2 [20] was used. The mechanical, thermal and electrical contact conditions between sheet/sheet and electrode/sheet play an important role on the Joule heating and thus on the entire solution. The contact properties for electrical conductivity and thermal conductivity were specified as a function of the temperature and the contact clearance based on literature [14][21]. When clearance reaches 0.1 percent of the element height of the sheets, conductivity is set to zero. The temperature dependency of contact conditions plays an important role for the formation and the shape of the FZ.

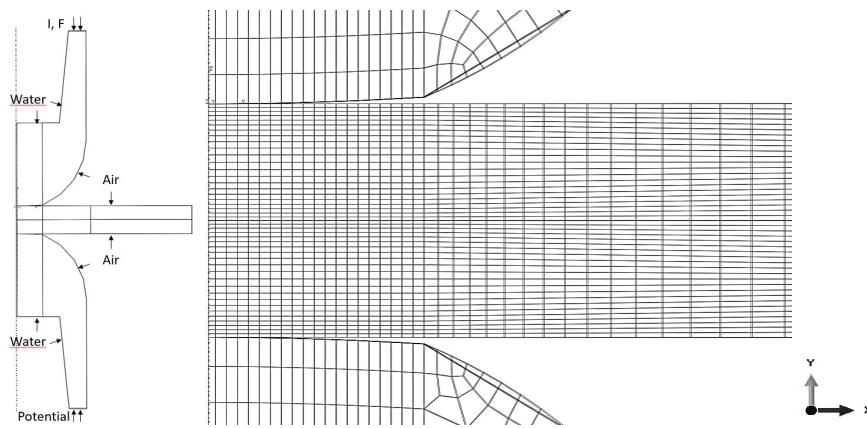


**Fig. 4** left: whole RSW model with symmetry axis; right: mesh in the spot welding zone

The simulation is segmented in four different steps: In Step 1 the contact between the electrodes and the sheets is established by a small displacement controlled movement of the upper electrode. In step 2 the full mechanical load is applied. In step 3 the current is introduced while the mechanical load is kept constant. Finally, in step 4 the current is set to zero again but the welding force is kept constant until the end of the step.

### RESULTS

The model allows to calculate a great variety of different results such as current density distributions, temperature fields, phase fields, stresses, strains and a first and simple LME cracking risk indicator. In Figure 5 the different temperature fields for the four investigated RSW cases are compared to the micrographs of real weld spots. The upper limit of the scale was set to 1500 °C, which is about the temperature where the material should be melted and the lower limit is set to 700 °C which is approximately the austenitization temperature. Hence, the upper limit corresponds roughly to the limit line of the FZ and the lower limit to the limit line of the upper-critical HAZ. The simulated shape of the FZ and the upper-critical HAZ and the qualitative tendencies between the different RSW cases agree quite well with the experimental findings, but the calculated temperatures seem to be too low or the assumed austenitization temperature is too low in this rapid heating case. This is also obvious judging from the penetration depth of the electrode, which is much bigger in the experiment than in the simulations. This is most likely due to the lack of reliable material data and missing information on the contact conditions at the current stage of the project. Due to less generated heat in the model, plastic conditions do not change as much as in the experiments and therefore the penetration depth is lower. The presented model describes the overall phenomena and trends quite well although the material data and LME risk indicator need further improvement. This is part in the ongoing work and will be presented in future works focusing not so much on modelling but on material and process aspects.

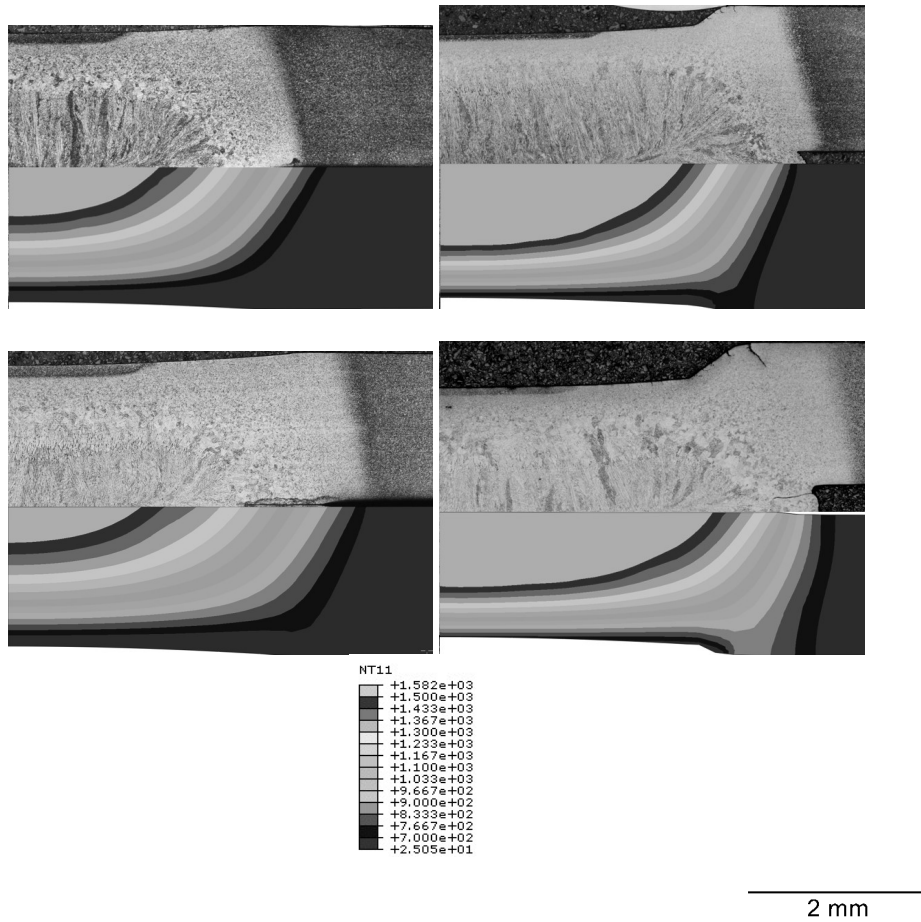


**Fig. 5** Comparison of the calculated temperature distribution with micrographs of different welding conditions (top: A – B, bottom: C - D)

In Figure 6 the micrograph of the spot weld D with the harshest RSW conditions is compared to a FZ indicator, describing the area where the material was melted, to an upper-critical HAZ indicator, describing the area where the material was austenitized but not melted, and to the LME risk indicator. The calculated upper-critical HAZ zone fits for this case quite well to the micrograph but the simulated FZ is again a little too small. The LME risk indicator shows the most critical area at the shoulder of the electrode's penetration depth and represents the critical zones in general already very well. It is important to point out that LME is naturally not only a function of temperature and stress, but also of the presence of zinc. Consequently, any LME risk indicator values below the zinc coated surface only make sense if a LME surface crack penetrates that far into the sheet. Also the risk indicator describes the surface damage with crack initiation and propagation risk.

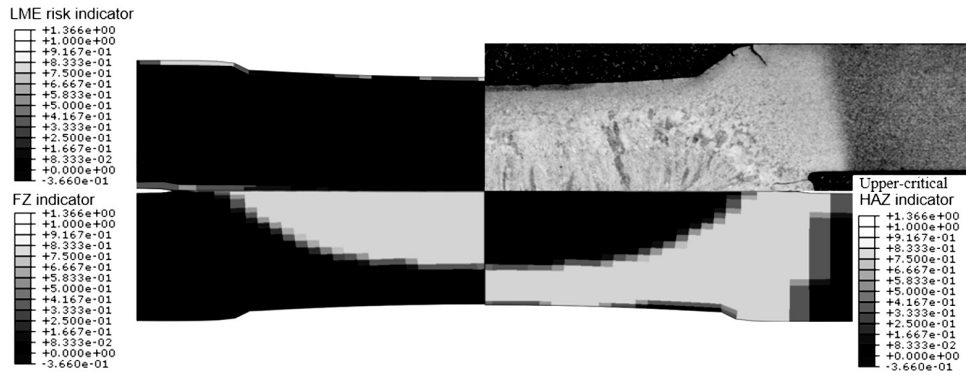


**Fig. 6** Calculated LME damage parameter and calculated FZ and upper-critical HAZ indicator compared to a micrograph of spot weld D

### CONCLUSIONS AND OUTLOOK

A promising multiphysics finite element model for calculating quantities like current densities, temperature fields, stress distribution and taking phase transformation into account, was set up. All necessary model equations to consider phase transformation and its related effects were implemented. The model of the investigated two-sheet DP1200 spot welds gives qualitatively correct results. However, in order to achieve quantitatively reliable results the calculations using material data mostly taken from literature on the similar steel grade DP1000 have to be repeated with measured data on DP1200. Another important value which has to be determined from instrumented spot welding tests is the electrical contact conductance that has a high impact on the temperature distribution and hence on all other results as well due to the strong interdependencies of the relevant physical phenomena.

Additionally to the fully coupled multiphysics model, a first and very simple LME cracking risk indicator was implemented. It already allows reasonable predictions of the critical zones. In a next step this LME damage indicator will be further elaborated and validated against extensive RSW testing.

The long term goal is to provide a validated and quantitatively accurate model that predicts the metallurgical and mechanical state as well as the LME cracking of spot welds. This model will then be utilized to develop new low LME RSW processes.

### ACKNOWLEDGEMENTS

The authors gratefully acknowledge the financial support under the scope of the COMET program within the K2 Center “Integrated Computational Material, Process and Product Engineering (IC-MPPE)” (Project No 859480). This program is supported by the Austrian Federal Ministries for Transport, Innovation and Technology (BMVIT) and for Digital and Economic Affairs (BMDW), represented by the Austrian research funding association (FFG), and the federal states of Styria, Upper Austria and Tyrol.

REFERENCES

- [1] E. TOLF, J HEDEGARD., E. MELANDER: Surface breaking cracks in resistance spot welds of dual phase steels with electrogalvanized and hot dip zinc coating. *Science and Technology of Welding and Joining* vol. 18 no. 1 25-31, Maney, 2012.
- [2] K.D. BAUER, M. TODOROVA, K. HINGERL, J. NEUGEBAUER: A first principles investigation of zinc induced embrittlement at grain boundaries in bcc iron, *Acta Mater.* 90 (2015) 69–76. doi:10.1016/j.actamat.2015.02.018.
- [3] G. JUNG, I. S. WOO, W. S SUH, S. J. KIM: Liquid Zn Assisted Embrittlement of Advanced High Strength Steels with Different Microstructures. *Met. Mater. Int.*, Vol. 22, No. 2 (2016), pp. 187-195, KIM and Springer, 2015.
- [4] R. ASHIRI, M. SHAMANIAN, H. R. SALIMIJAZI, M. A. HAQUE, J. H. BAE, C. W. JI, K. G. CHIN, Y. D.PARK: Liquid metal embrittlement-free welds of Zn-coated twinning induced plasticity steels. *Scripta Materialia* 109 (2015) 6-10, Elsevier Ltd., 2015.
- [5] C. BEAL, X. KLEBER, D. FABREGUEA, M. BOUZEKRI: Liquid zinc embrittlement of twinning-induced plasticity steel. *Scripta Materialia* 66 (2012) 1030-1033, Acta Materialia Inc. Published by Elsevier Ltd., 2012.
- [6] P.J.L. FERNANDES, D.R.H. JONES, The effects of microstructure on crack initiation in liquid- metal environments, *Engineering Failure Analysis*, Vol. 4, No. 3, 1997, pp. 195-204
- [7] C. BEAL: Mechanical behaviour of a new automotive high manganese TWIP steel in the presence of liquid zinc. C. Beal, INSA de Lyon, tous droits reserves, 2012.
- [8] G. K. KIM, I. J. KIM, J. S. KIM, Y. I. CHUNG, D. Y. CHOI: Evaluation of Surface Crack in Resistance Spot Welds of Zn-Coated Steel. *Materials Transactions*, Vol. 55, No. 1 (2014) pp. 171 to 175, The Japan Institute of Metals and Materials, 2013.
- [9] R. ASHIRI, M. A. HAQUE, C. W. JI, M. SHAMANIAN, H. R. SALIMIJAZI, Y. D. PARK: Supercritical area and critical nugget diameter for liquid metal embrittlement of Zn-coated twinning induced plasticity steels. *Scripta Materialia* 114 (2016) 41-47, Acta Materialia Inc. Published by Elsevier Ltd., 2015.
- [10] H. MOSHAYEDI, I. SATTARI-FAR: Resistance spot welding and the effects of welding time and current on residual stresses. *J. Mater. Process. Technol.* 214, 2545–2552, 2014.
- [11] Y. LEE, H. JEONG, K. PARK, Y. KIM, J. CHO: Development of numerical analysis model for resistance spot welding of automotive steel. *J. Mech. Sci. Technol.* 31, 3455–3464, 2017.
- [12] Dassault Systemes. (2018, July 5). Abaqus Unified FEA – Simulia. Retrieved from <https://www.3ds.com/de/produkte-und-services/simulia/produkte/abaqus/aktuelle-version/>
- [13] T. KOBAYASHI, Y. MIHARA: Numerical Simulation of Nugget Formation in Spot Welding. 1–15, *Mechanical Design & Analysis Corporation*, 2014.
- [14] M. ESHRAGHI, M. A. TSCHOPP, M. ASLE ZAEEM, S. D. FELICELLI: Effect of resistance spot welding parameters on weld pool properties in a DP600 dual-phase steel: A parametric study using thermomechanically-coupled finite element analysis. *Mater. Des.* 56, 387–397, 2014.
- [15] X. LI, L. WANG, L. YANG, J. WANG, K. LI: Modeling of temperature field and pool formation during linear laser welding of DP1000 steel. *J. Mater. Process. Technol.* 214, 1844–1851, 2014.
- [16] M. AVRAMI: Kinetics of phase change. I: General theory. *J. Chem. Phys.* 7, 1103–1112, 1939.
- [17] D. P. KOISTINEN, R. E. MARBURGER: A general equation prescribing the extent of the austenite-martensite transformation in pure iron-carbon alloys and plain carbon steels. *Acta Metall.* 7, 59–60, 1959.

- [18] J.B. LEBLOND, J. DEVAUX, J.C. DEVAUX: Mathematical modelling of transformation plasticity in steels. I: Case of ideal-plastic phases, *International Journal of Plasticity*, 5, 551-572, 1989
- [19] M. KIČIN: Diploma thesis. Experimentelle Ermittlung thermisch- mechanischer Eigenschaften von verzinktem DP1000 Stahl als Input Dateien fuer die Simulation des Widerstandspunktschweissens, Austria, Graz: Technical University of Graz, 4/2011
- [20] MIKRON INSTRUMENT COMPANY. Table of Emissivity of Various Surfaces. 1–13, 2014. doi:[http://www-eng.lbl.gov/~dw/projects/DW4229\\_LHC\\_detector\\_analysis/calculations/emissivity2.pdf](http://www-eng.lbl.gov/~dw/projects/DW4229_LHC_detector_analysis/calculations/emissivity2.pdf)
- [21] M. IYOTA ET AL.: The effect of martensitic transformation on residual stress in resistance spot welded high-strength steel sheets. *J. Alloys Compd.* 577, S684–S689, 2013.



# MAGNETIC PULSE WELDING OF TUBULAR PARTS - PROCESS MODELING

R. SHOTRI\* and A. DE\*

*\*Indian Institute of Technology, Bombay, Mumbai, India ( e-mail address –rishabhshotri@gmail.com, amit@iitb.ac.in)*

DOI 10.3217/978-3-85125-615-4-41

## ABSTRACT

Joining of metallic tubes by fusion welding processes has remained critical due to distortion and dimensional inaccuracy of the joint. Magnetic pulse welding (MPW) facilitates joining of overlapping tubes by controlled plastic deformation under the action of a short electromagnetic impulse without bulk melting of workpiece materials. Thus, MPW can be an efficient recourse for joining of circular sections. However, the short duration and high amplitude electromagnetic forces impose significant challenge to real-time monitoring of MPW. In contrast, computer-based models can provide an opportunity to realize the causative effect of the key process variables on the joint structure and quality quickly and economically. An attempt is therefore presented in this investigation to develop and test a finite element method based numerical model for MPW process with a focus to realize the nature of the magnetic field and electromagnetic forces that facilitates plastic deformation and joining between the flyer and the target tubes. The effect of key process variables is also tested with experimentally measured results reported in independent literature.

Keywords: (Magnetic pulse welding, inductor coil geometry, high strain rate plastic deformation, tube welding)

## INTRODUCTION

MPW involves joining of overlapping metallic tubes by the action of an electromagnetic (EM) force, which is generated by applying a high amplitude discharge potential to a shaped inductor coil for a short duration, e.g. a few microseconds. The EM force compels the overlapping region to undergo plastic deformation resulting in a solid state joint with a wavy interface and without any melting. The discharge current, pulse frequency, coil geometry, stand-off distance between the parts and the air gap between the coil and the outer tube, referred to as the flyer tube, influence the rate and extent of plastic deformation, and affect the joint quality.

Although MPW is an established joining process, the complex process mechanism and limited availability of the commercial MPW set-ups have restricted widespread experimental studies. Raoelison et al. [1] studied the effect of discharge voltage and the stand-off distance in MPW of 25 mm diameter aluminium (AA6060T6) tubes. They found the optimum ranges of the discharge voltage and the stand-off distance as 6.5 kV to 7.5 kV, and 1.5 mm to 4.0 mm, respectively. Yu et. al. [2] used MPW to join sheets of dissimilar alloys such as AA1060 and Q235 steel using multi-turn coil. The width of the overlapping region was found as a critical parameter to ensure the joint quality. Faes et al. [3] employed



multi-turn coils with field shaper to join thick copper tubes with brass rods. They reported an increase in the EM force on the flyer tube with increase in the overlapping width between the field shaper and the coil. Coil design parameters influence the MPW process significantly and has attracted attention of the researchers. Mishra et al. [4] showed that multi-turn coils with rectangular shaped windings yielded stronger EM force and better joint quality compared to circular shaped windings in MPW of aluminium tubes. Uhlmann et al. [5] used an aluminium field shaper inside a multi-turn copper solenoid coil to augment the EM force.

Although real-time monitoring has helped to understand the causative effect of the operating variables on weld joint structure and quality in several processes, the short duration and high amplitude EM field pose critical challenge to real-time monitoring of MPW. In contrast, computer-based models with coupled electromagnetic and mechanical analyses can provide a better understanding of the evolution of joint interface morphology, structure and property in MPW as function of process variables efficiently. We present here an attempt to simulate MPW through numerical process model based on fundamental relations. In particular, MPW of tubular parts using a solenoid winding coil with field shaper is analysed and tested with corresponding experimentally measured results reported in independent literature.

### NUMERICAL INVESTIGATION

MPW of a typical tubular assembly with an axisymmetric multi-turn solenoid inductor coil and a field shaper [Fig. 1] is modelled using finite element method. The two tubes are separated by a standoff distance with an oblique overlapping arrangement as shown in Fig. 1. The outer (flyer) tube and the field shaper are separated by a radial gap that controls the diffusion of the magnetic field. Table 1 provides the ranges of the overlapping width and the radial gap that are considered here. A damped sinusoidal discharge current is considered with peak pulses in the range of 100 kA to 200 kA and pulse frequency in the range of 15 kHz to 25 kHz.

**Table 1** Range of processing conditions considered for analysis

Legend	Unit	Value/Range
$I$ (Peak current)	kA	100, 150, 200
$f$ (Pulse frequency)	kHz	15, 20, 25
$\tau$ (Damping coefficient)	$s^{-1}$	1/15000
$r$ (Radial gap)	mm	0.8, 1, 1.25, 1.5, 2, 2.5
$L$ (Overlapping width)	mm	10, 13, 15, 18, 20
Flyer tube material	aluminium, copper, titanium, and AISI 1010 steel	
Inner (target) tube material	aluminium and AISI 1010 steel	

## Mathematical Modelling of Weld Phenomena 12

### NUMERICAL MODELING OF MAGNETIC PULSE PHENOMENON

The damped sinusoidal nature of the current associated with the high amplitude discharge potential in MPW can be expressed as [6]

$$I = I_0 e^{(-t/\tau)} \sin(\omega t) \quad (1)$$

where  $I_0$  is the peak discharge current from the capacitor bank,  $t$  is the time of discharge,  $\omega$  is the frequency (in radians) of the discharge current pulse and  $\tau$  is the damping coefficient. The resulting EM field can be evaluated following the Maxwell's governing equation as [7,8]

$$\frac{1}{\mu\sigma} \nabla^2 H = \frac{\partial H}{\partial t} \quad (2)$$

where  $H$  is the magnetic field intensity,  $\mu$  is the magnetic permeability and  $\sigma$  is the electrical conductivity. Equation (1) is also referred to as the diffusion equation that further relates the transient magnetic field and the induced eddy current as

$$J = \nabla \times H = \nabla \times (\mu B) = \nabla \times \mu(\nabla \times A) \quad (3)$$

where  $J$  is the current density,  $B$  is the magnetic flux density and  $A$  is the magnetic vector potential. The EM force distribution is further obtained as

$$\mathbf{F} = \mathbf{J} \times \mathbf{B} \quad (4)$$

where  $\mathbf{F}$ ,  $\mathbf{J}$  and  $\mathbf{B}$  refer respectively to EM force, current density and magnetic flux vectors. Figure 1 presents the solution domain and the applied boundary conditions for the modelling calculations. The boundary conditions can be listed as follows [9].

- Nil magnetic vector potential ( $A = 0$ ) over the specified boundary of the solenoid coil,
- Normal component of magnetic flux density vector is continuous along the specified boundary and given as  $\mathbf{a}_n \cdot (\mathbf{B}_1 - \mathbf{B}_2) = 0$  with  $\mathbf{a}_n$  as unit vector normal to the surface.
- Tangential component of magnetic field vector is discontinuous along the specified boundary and expressed as  $\mathbf{a}_n \times (\mathbf{B}_1 - \mathbf{B}_2) = \mathbf{J}_s$  with  $\mathbf{J}_s$  as the surface current density vector.

The transient electromagnetic analysis is undertaken using the commercial finite element software, ANSYS (16) with PLANE233 elements and the magnetic vector potential ( $A_z$ ) as the nodal degree of freedom. The current density ( $J$ ) is applied as an element body load. Table 2 presents the material properties used in the modeling calculations.

**Table 2** Material properties considered in modeling calculations

Material	Relative magnetic permeability ( $\mu$ )	Conductivity ( $\sigma$ ), S/m
Copper (Coil windings, field shaper and flyer tube)	0.99	$58 \times 10^6$
Aluminium (Flyer and target tube)	1.0	$38 \times 10^6$
Steel (Flyer and target tube)	Estimated from B-H curve [Fig. A1]	$2 \times 10^6$
Titanium (Flyer tube)	1.0	$1.82 \times 10^6$
Air (Surrounding region)	1	0

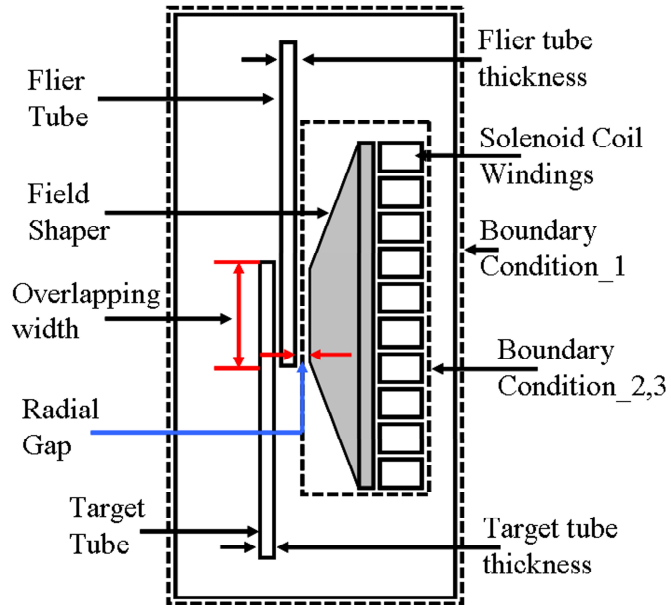
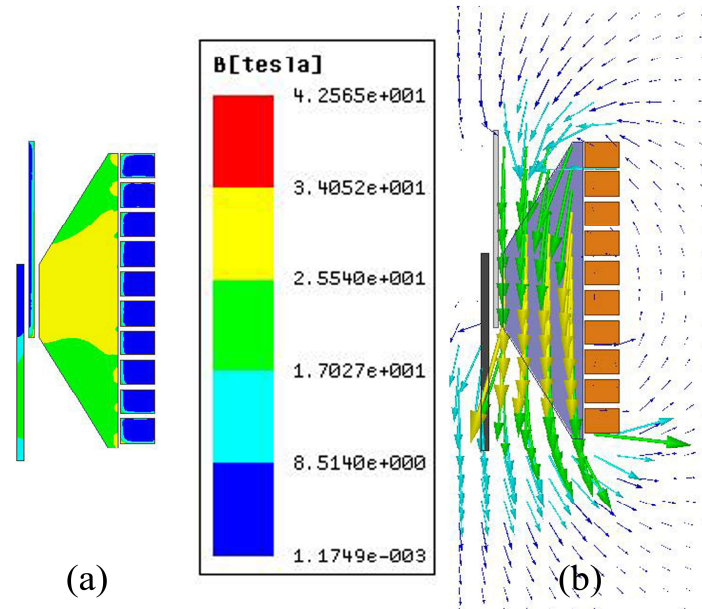


**Fig. 1** Schematic assembly of MPW coil with coil design parameters and the boundary conditions.

## RESULTS AND DISCUSSIONS

Fig. 2 shows the computed results of magnetic field ( $B$ ) distribution over an aluminium flyer tube of 1 mm thickness at a time instant of  $11 \mu\text{s}$  for a peak discharge current of 200 kA. The magnetic field is tangential through the radial gap, which in turn induces the eddy current over the flyer tube surface. The concentration of magnetic field vectors increases towards the interacting region of field shaper and the flyer tube surface [Fig. 2 (b)]. The maximum EM force with the aluminium flyer tube was obtained around 68 kN. In contrast, the computed results with a AISI 1010 flyer tube provided the maximum

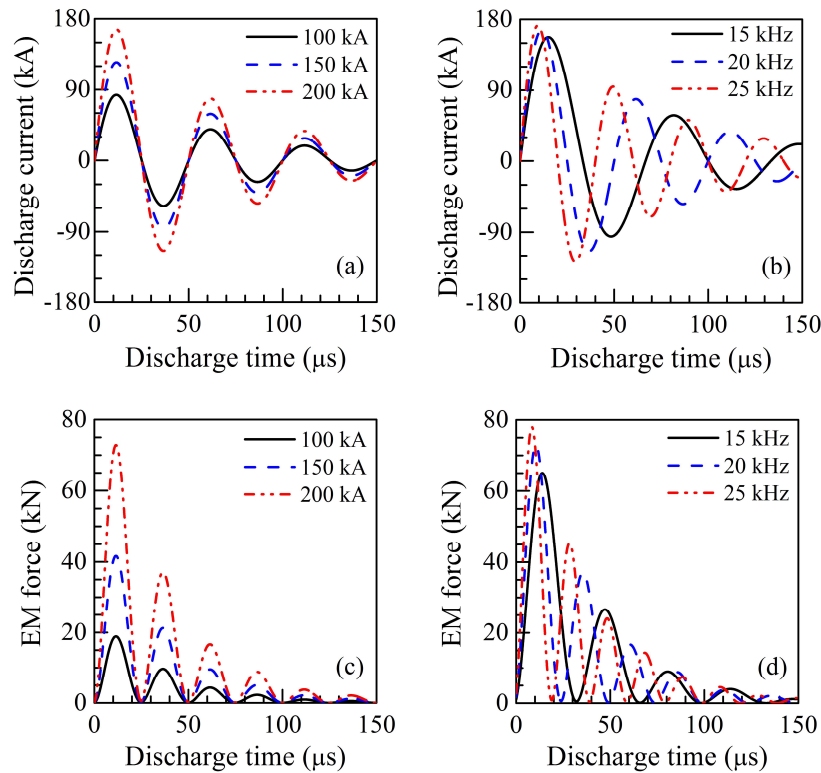
magnetic field and the corresponding EM force as 38 T and 40 kN, respectively with the same processing conditions and the tube dimensions. Thus, the magnetic field and the EM force are influenced both by the flyer tube material and the radial gap parameter. Yu et al. [2] reported a typical EM force of 6.2 kN in MPW of aluminium flyer tube to a steel target tube ( $\sim 1$  mm wall thickness) for a peak discharge current of 90 kA and radial gap of 1.2 mm. The smaller EM force computed by these authors is attributed to the lower magnitude of the peak discharge current.



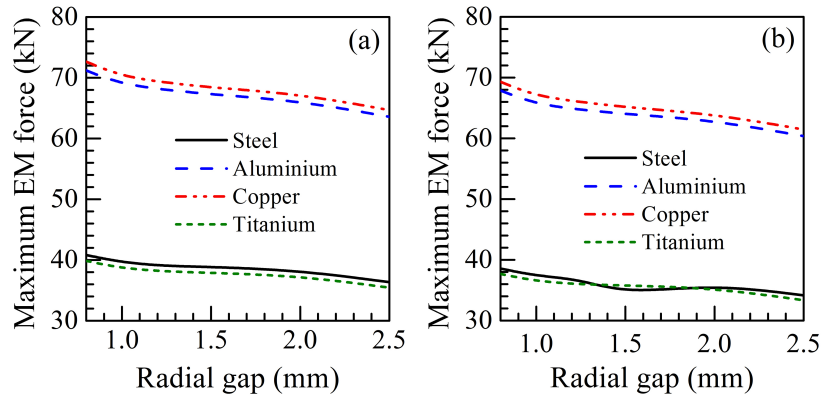
**Fig. 2** Computed magnetic field,  $B$ , at a timeduration of  $30 \mu\text{s}$ : (a) isocontours, (b) vectorial representation. Input conditions: discharge current with a 200 kA peak value, pulse frequency 20 kHz, damping factor  $1/15000 \text{ s}^{-1}$ , aluminium flyer tube with 1 mm wall thickness and AISI 1010 steel inner target tube with 1.5 mm thickness. Radial gap between flyer and coil is 1 mm.

Fig. 3 shows the computed results of transient current flow and the corresponding EM force in MPW with a aluminium flyer tube for different combinations of peak pulse and its frequency of the discharge current. The current and EM force attain the maximum quickly within the first half cycle of the total duration, and their magnitudes increase with rise in the peak pulse of the applied discharge current [Fig. 3(a, c)]. Increase in pulse frequency of the discharge potential also enhance the peak current and EM force with both reaching faster to the corresponding maximum values as shown in Figs 3(b) and (d). The higher pulse frequency reduces the depth of penetration of the magnetic field into the flyer tube thickness thereby providing more concentration of induced eddy current over the surface and greater EM force. Guglielmetti et al. [10] showed a similar increase in the EM force with increase in the pulse frequency [from 3 kHz to 18 kHz] of the discharge potential in MPW of aluminium alloys.

Fig. 4 shows the effect of radial gap on the computed values of the maximum EM force for different combinations of flyer and target tube materials. The maximum EM force over the flyer tube reduces with increase in the radial gap that is attributed to the sparser magnetic field with decreasing intensity at higher radial gaps. For example, the maximum EM force reduces from 72 kN to 64 kN with increase in the radial gap from 0.8 mm to 2.5 mm in MPW of a copper flyer tube with a steel target tube as shown in Fig. 4(a). With all the conditions remaining the same, use of a titanium flyer tube reduces the range of the maximum EM force from 40 kN to 35 kN [Fig. 4(a)] as the electrical conductivity of titanium is much lower compare to that of copper. A comparison of Figs 4(a) and (b) further shows the effect of the target tube material on the EM force for a range of radial gaps. For a radial gap of 0.8 mm and an aluminium flyer tube, the maximum EM force increases from around 67 kN to 71 kN as the target tube material is changed from aluminium to steel [Figs 4(a, b)]. This is attributed to higher magnetic permeability and lower electrical conductivity of steel that has reduced the density of its surface eddy current. As a result, there is lesser interference on the resulting magnetic field over the flyer tube. Shim et al. [11] also reported a decrease in EM pressure from 39 MPa to 16 MPa as the radial gap was increased from 0.76 mm to 6 mm in MPW of 1.5 mm thick aluminium flyer tube with copper target tubes using a single turn solenoid coil.



**Fig. 3** Influence of peak current and frequency of the damped sinusoidal applied current pulse on the computed magnitude and nature of discharge current and EM forces in MPW with an aluminium flyer tube of wall-thickness 1 mm and radial gap of 1 mm with the coil assembly inside an air region at 150 mm offset along both x- and y- axis respectively.



**Fig. 4** Effect of radial gap on the computed values of EM force for various combinations of flyer and (a) AISI 1010 steel and (b) aluminium target tube materials. Process conditions considered: discharge potential with a peak current of 200 kA, pulse frequency 20 kHz, time duration 30  $\mu$ s and damping factor of  $1/15000$   $s^{-1}$ . The overlapping width and tube thickness were 15 mm and 1.5 mm, respectively.

Fig. 5 shows the effect of overlapping width on the computed values of the maximum EM force for different combinations of flyer and target tube materials. The maximum EM force over the flyer tube decreases with increase in the overlapping width that is attributed to the higher area of EM field distribution. The maximum EM force reduces from around 80 kN to 60 kN with increase in the overlapping width from 10 mm to 20 mm for MPW of an aluminium flyer tube with a steel target tube [Fig. 5(a)]. In contrast, use of a titanium flyer tube reduces the range of maximum EM force from 45 kN to 34 kN that is attributed to lower electrical conductivity of titanium in comparison to aluminium alloys. A comparison of Figs 5(a) and (b) shows the effect of the target tube material on the EM force for a range of overlapping widths. For an overlapping width of 15 mm and a copper flyer tube, the maximum EM force increases from 67 kN to 71 kN as the target tube material is changed from aluminium to steel [Figs 5(a, b)]. This is also attributed to the higher permeability and lower conductivity of steel compared to copper resulting in reduced interference with the magnetic field over the flyer tube when the target tube is of steel. In MPW of aluminium to steel tubes using a single turn solenoid coil, Lorentz et al. [12] observed optimal weld joint condition for overlapping widths of 4 mm to 8 mm. They reported multi-directional and uneven weld propagation for overlapping width higher than half of the width of the coil, although no quantitative analysis based on EM force was provided.

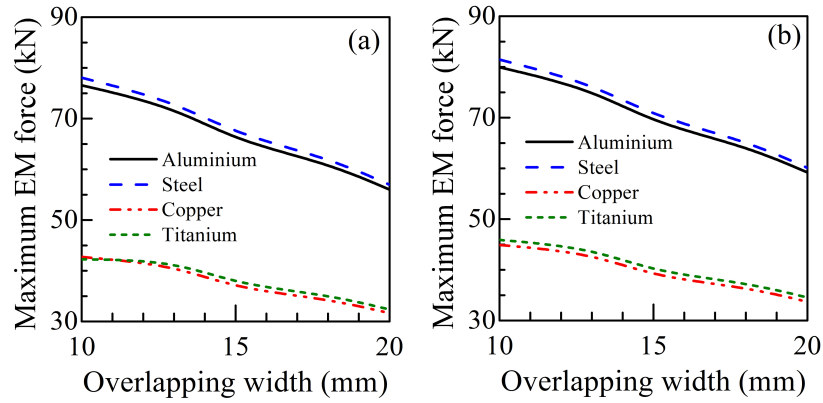


**Fig. 5** Effect of overlapping width on the computed values of EM force for various combinations of flyer and (a) aluminium and (b) AISI steel target tube materials. Process conditions considered: discharge potential with a peak current of 200 kA, pulse frequency 20 kHz, time duration 30  $\mu$ s and damping factor of  $1/15000 \text{ s}^{-1}$ . The radial gap and tube thickness were 1 mm and 1.5 mm, respectively.

### CONCLUSIONS

A numerical model to simulate the underlying transient phenomena in MPW of tubular parts with circular cross-section is developed using finite element method. The model is utilized to examine the effect of key processing variables on the nature and magnitude of magnetic field intensity and EM force for various combinations of flyer and target tube materials that are topical in nature for MPW application. Increase in the radial gap between the coil and the flyer tube was found to result in a sparser magnetic field with reduced magnitude of EM force. In contrast, increase in the overlapping width between the flyer and the target tubes reduces the maximum EM force. Magnetic permeability and electrical conductivity of the tube materials are found to influence the magnetic field intensity and resulting EM force significantly for a given applied discharge potential.

## APPENDICES

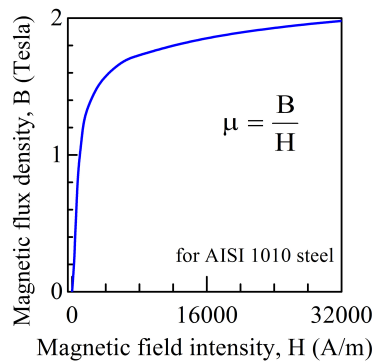


Fig. A.1 Non-linear B-H curve used to assign magnetic permeability of steel.

## REFERENCES

- [1] R. N. RAOELISON, N. BUIRON, M. RACHIK, D. HAYE and G. FRANZ: 'Efficient welding conditions in magnetic pulse welding', *Journal of Manufacturing Process* Vol. 14, pp. 372-377, 2012.
- [2] H. YU and Y. TONG: 'Magnetic pulse welding of aluminium to steel using uniform pressure electromagnetic actuator', *International Journal of Advance Manufacturing Technology*, Vol. 91, pp. 2257 - 2265, 2016.
- [3] K. FAES, T. BAATEN, W. DE WAELE and N. DEBROUX: 'Joining of copper to brass using magnetic pulse welding', *International Conference of High Speed Forming*, Vol. 4, pp. 84-96, 2010.
- [4] S. MISHRA, S. K. KUMAR, K. SAGAR, M. MEENA, and A. SHYAM: '40 kJ magnetic pulse welding system for expansion welding of aluminium 6061 tube', *Journal of Materials Processing Technology*, 240, pp. 168-175, 2017.
- [5] E. UHLMANN, A. ZIEFLE, C. KONIG and L. PRASOL: 'Coupled FEM- simulation of magnetic pulse welding for non-symmetric applications', *International Conference on High Speed Forming*, Vol. 5, pp. 303-314, 2012.
- [6] M. KIMCHI, H. SHAO, W. CHENG and P. KRISHNASWAMY 'Magnetic pulse welding aluminium tubes to steel bar' *Welding in the World*, Vol. 48, pp. 19-22, 2004.
- [7] M. V. K. CHARI and S. J. SALON: 'Numerical Method in Electromagnetism' *Academic Press*, 2000.
- [8] M. N. O. SADIKU and S. V. KULKARNI: 'Principle of Electromagnetics', *Oxford University Press*, Vol. 6, 2015.
- [9] NPTEL: 'Boundary conditions for electromagnetic field', *Electromagnetic Fields nptel.ac.in*, 2009.



- [10]A. GUIGLIEMMETTI, N. BURION, D. MARCEAU, M. RACHIK and C. VOLAT: 'Modelling of tubes magnetic pulse welding', *Conf. on Engineering Systems Design and Analysis*, Vol. 11, pp. 1-12, 2012.
- [11]J. Y. SHIM, B. Y. KANG, I. S. KIM, M. J. KANG, D. H. PARK and I. J. KIM: ' A study on distributions of electromagnetic force of the dissimilar metal joining in MPW using FEM' *Advance Materials Research*, Vol. 83-86, pp. 214-221, 2009.
- [12]A. LORENZ , J. LUEG-ALTHOFF, J. BELLMAN, G. GOBEL, C. WEDDLING, E. BEYER and A. E. TEKKAYA : 'Workpiece positioning during magnetic pulse welding of aluminium-steel joints', *Welding Research*, Vol. 95, pp. 101-106, 2016.

# CFD SIMULATION OF PARTICLE MOVEMENT DURING ATMOSPHERIC PLASMA SPRAYING

M. STUMMER\* and N. ENZINGER\*

*\*Graz University of Technology, Institute of Materials Science, Joining and Forming, maximilian.stummer@tugraz.at*

DOI 10.3217/978-3-85125-615-4-42

## ABSTRACT

Atmospheric Plasma Spraying (APS) is a powder based coating process with versatile applications in terms of functional layers like corrosion, wear resistant or thermal barrier coatings. However, the fundamental process interactions cannot fully be described and understood experimentally. Therefore, a supportive CFD model was carried out by use of ANSYS 19.0. In detail, the CFD model consists of direct coupled electromagnetic and hydrodynamic formalisms. The particle behaviour was described by a simple multiphase reaction routine. Based on the CFD model, the resulting temperature field and the particle behaviour can be investigated. Especially, the particle trajectory, which represents the particle dwell time in the plasma stream, is of special interest for the final APS coating. Therefore, the description of a stable heat source is of major priority. This work shows a promising approach to evaluate the above mentioned particle and plasma properties, supported by a systematic parameter investigation. The obtained and experimental validated data can be used for a better process understanding as well as for further process optimisation.

Keywords: Atmospheric Plasma Spraying, APS, Simulation of Thermal Spraying, CFD simulation of particle movement, Process optimisation due to numerical simulation, Particle movement, Particle tracking

## INTRODUCTION

Thermal spraying processes share about 35% of all world-wide used functional coating technologies. Especially, industrial applications (chemical industry and engineering) led to an overall invested capital of 3.1 billion USD of thermal spraying with a mean growing rate of 12% p.a. [1]. Atmospheric Plasma Spraying (APS) is part of these thermal spraying processes and is distinguished by high flexibility and high deposition rates. Due to parameter management and suitable process gases and torch properties, various material types, like ceramics or high-melting metals can be processed. This leads to a variety of applications, which have been published in literature [2-4]. However, due to many parameter interactions, an accurate extrapolation of known parameter sets for introducing new materials is not possible. Therefore, a transient CFD simulation is a promising approach to highlight parameter interactions and investigate the APS process in more detail.

The scope of this work is a CFD based description of particle movement in correlation to parameter dependent quantity fields. This numerical method can be used for better process understanding and process optimisation. Especially, the layer morphology, which

## Mathematical Modelling of Weld Phenomena 12

is directly linked to particle inflight reactions, can be further improved by CFD based parameter management. The CFD Simulation consist of three main components:

- Material data
- Torch geometry (mesh)
- MHD model, using Electric Potential Method

### MATERIAL DATA

Precise material data is crucial to describe physical interaction due to numerical simulation. In case of APS, three different material data sets were carried out and are directly influencing the numerical results:

- Process gas properties and environment
- Material data of the solid compounds
- Powder material

Pure Argon is used as plasma and particle carrier gas. Therefore, chemical properties like molar mass and physical properties like electric or thermal conductivity, heat capacity and viscosity were set up as a function of temperature and pressure. The gas data was provided by [5] in 100K steps from 300K to 30,000K. These wide ranged parameter windows form the foundation for the plasma arc (PA) simulation. The mixture of plasma gas and environment (air at 25°C) was also considered in the simulation model by a scalar material mixture model.

The material data for all solid parts made from copper, tungsten and steel were extracted from the internal material database of ANSYS 19.0. Due to the overall low process temperatures (ideal cooling), no additional temperature dependence material data was considered.

The powder material is described by idealised particle Gauß-distribution. The material data, such as the powder melting or sublimation temperatures, were assumed to be constant. This approximation can be applied due to the interaction of high energy densities (Plasma arc) and small particle diameters of max. 80µm, which lead to a fast phase transformation (<0.5ms). Pure zinc particles with a mean particle size according to Figure 1a) were used for CFD Simulation. Figure 1 shows an idealized particle size distribution (red dashed line) and spherical Zn particles, observed by SEM investigation. The spherical shape was implemented into the CFD Simulation by introducing a mass point with specific properties like diameter, mass and phase transition temperature.

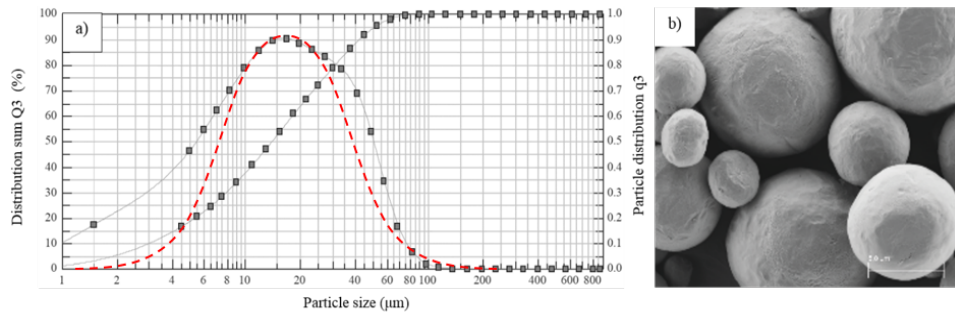


**Fig. 1** a) Real particle size distribution of Zn powder. The red dashed line represents the idealized particle distribution, which was used for CFD Simulation b) SEM image of spherical shaped Zn particles

### MESHING

The torch geometry was defined by use of CAD input data. Therefore, a full 3D mesh of the non-symmetrical Plasma torch (PT) with a total number of approximately 8 mil. elements was set-up. Due to complex body geometries, tetrahedral cell types were used. Regions of interests (ROI) and interfaces (IF) were systematically refined with a tetragonal element size of  $<0.2\text{mm}$ . To save computational time, the particular mesh size of ROIs and IF was increased stepwise by a factor of 1.3 using cylindrical coordinates. To describe the predominant molecular viscosity of a fluid flow at wall near regions and its interaction perpendicular to the wall surface [6], the local mesh was adapted (Fig. 2), whereby 3 mesh layers were applied parallel to the solid wall. The mesh quality was tested in terms of orthogonality, expansion and skewness by an internal software routine.

The final mesh consists of following solid and fluid components (IDs)

- Torch body (solid)
- Anode and cathode (solid)
- Supporting geometries (solid)
- Insulations (solid)
- Ambient (fluid)
- Main plasma gas flow channel and particle inlets (fluid)

Interface connections (e.g. Cathode – plasma gas flow channel) are considered by interface coupling during pre-processing. Therefore, both interfaces are selected manually and certain interface models (element connection, heat transfer,...) are taken into account. Figure 2 shows an example of mesh refining (ROI) and mesh adaption in a wall near region, which is crucial to generate the electric field and improves the convergence during iteration.

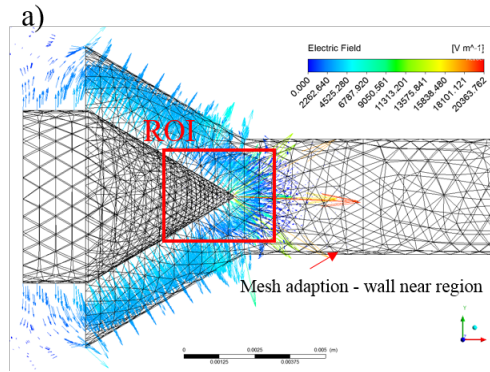


**Fig. 2** Detail view of the cathodic near region. Mesh refining at the cathode tip, the interface and the flow channel (ROI). Mesh adaption in wall near region to display the boundary layer

## MODELLING

To describe the particles' behaviour related to different physical influencing factors, a Computer Fluid Dynamics Simulation (CFD) is one possible approach. To define movement of complex particle flows mathematically, different numerical models are used to solve the partial non-linear differential equations. In case of APS the iterative solution of Navier-Stokes (momentum, heat and mass) and Maxwell equations (electromagnetic potentials) is the main goal during processing.

### ELECTROMAGNETIC POTENTIAL

Physical effects like fluid flow, electricity, magnetism or turbulence, which are influencing the particle track, must be considered. Therefore, these interactions can be described by Electric Potential Method (EPM). Here, the current density is used to solve the electric potential equation by use of Ohm's law. The electric field  $\vec{E}$  can be expressed as

$$\vec{E} = -\nabla\varphi - \frac{\partial\vec{A}}{\partial t} \quad (1)$$

Whereby  $\frac{\partial\vec{A}}{\partial t}$  describes the change of vector potential over time and  $\varphi$  equals a scalar electric potential. For a static electric field the combined approach using Ohm's law and Maxwell equations can be expressed by the current density  $\vec{j}$

$$\vec{j} = \sigma(-\nabla\varphi + (\vec{U} \times \vec{B}_0)) \quad (2)$$

$\vec{U}$  ... fluid velocity field  
 $\vec{B}_0$  ... external imposed magnetic field

## Mathematical Modelling of Weld Phenomena 12

By applying a boundary condition for the electric potential  $\varphi$  and the principle of energy charge conservation  $\nabla * \vec{j} = 0$ , the basic equation to describe the electric potential can be written as

$$\nabla^2 \varphi = \Delta * (\vec{U} \times \vec{B}_0) \quad (3)$$

The mathematic description of the electric potential (3) and the electric current density (Equation 2) can be used for magneto-hydrodynamic (MHD) coupling in a next step. By introducing additional terms to fluid momentum and energy equations, such as additional Lorentz Forces ( $\vec{F} = \vec{j} \times \vec{B}$ ) and Joule heating ( $\vec{Q} = \frac{1}{\sigma} \vec{j} \times \vec{j}$ ), the interactions of charged particles in an electromagnetic field can be calculated. Consequently, this approach can be used to describe the interactions of particles with a discrete charge density, particle velocity and a resulting Lorentz Force within a turbulent fluid flow.

### TURBULENCE

The  $k$ - $\varepsilon$ -model is a standard model to describe turbulent fluid flows with good accuracy and computational time [7]. The model itself is based on the eddy viscosity model, which describes the Reynold stresses by the phenomenon of molecular shear stresses. It describes the effect of different mechanisms (transport, diffusion, convection, dissipation,...) on the change of kinetic energy [8]. The turbulence model approach can be calculated as

$$\mu_t = \rho * c_\mu * \frac{k^2}{\varepsilon} \quad (4)$$

Where  $k$  represents the turbulent kinetic energy,  $\varepsilon$  the turbulent dissipation rate,  $c_\mu$  is an empiric constant (value = 0.09) and  $\rho$  the density. The accuracy of the model in wall near regions is significantly reduced, due to dominance of molecular viscosity in those regions. Consequently, a dimensionless wall shear stress velocity  $u_r$  can be calculated, which is dependent of the dimensionless wall distance  $y^+$  according to equation

$$y^+ = \frac{y * u_r}{\vartheta} \quad (5)$$

Where  $\vartheta$  is the fluid viscosity and  $y$  the wall distance. This wall function increases the accuracy of MHD coupling, and consequently improves the quality of final results.

### PARTICLE INTERACTIONS

The interactions of acting particles are assumed by a set of mathematical models. The drag forces and the gas-particle were utilized by Schiller-Naumann model, which describes the interaction of primary and secondary phases of an Eulerian multiphase calculation. The rate of energy transfer ( $Q_{pq}$ ) was assumed as a function of temperature difference (6). The heat transfer coefficient is related to the Nusselt number  $Nu_p$ , which is calculated by Ranz-

Marshall correlation [9], [10]. This leads to the basic equation of the volumetric rate of energy transfer between 2 phases:  $p$  and  $q$ .

$$Q_{pq} = h_{pq}(Nu_p, \kappa, dp) * \Delta T(p, q) \quad (6)$$

Where  $h_{pq}$  is volumetric heat transfer coefficient between 2 different phases  $p$  and  $q$ .  $\kappa$  is the thermal conductivity and  $dp$  is the characteristic length. The elastic particle collision was described by Sommerfeld model, which is a stochastic model of two “virtual” collision partners.

All previously described models and the combination of energy, mass and transport equations complements the MHD model, which can now be used for a transient APS investigation.

## RESULTS AND DISCUSSION

To describe the particle movement during the APS process, information about present physical quantities like pressure, temperature, velocity and turbulences is mandatory. The torch and the cathode is ideally cooled, which results in a 300K boundary condition at PT shell elements. Using the previously explained MHD model, transient quantities can be calculated.

### TRANSIENT PHYSICAL QUANTITIES

In a first step, a defined parameter window for a steady-state calculations was set up. Table 1 shows the main variable parameters, which were used for the steady-state calculations, but also for further transient investigations. The steady-state result files were used as initial condition for the subsequent transient calculations. Especially, the interaction of inserted electric power and the particle size is of main interest.

**Table 1** Investigated variable parameter window; Constant parameters: electric voltage, process gas flow (Argon), particle mass flow, working distance and particle carrier gas flow (Argon)

Parameters	Lower limit	Upper limit
Electric current (A)	60	200
Mean particle diameter ( $\mu\text{m}$ )	5	50

Due to fast particle speeds of  $>200\text{m/s}$  [1] (Fig. 3b), the total simulation time is fixed with 200ms and  $\Delta t=0.2\text{ms}$ . Figure 3 shows some representative examples using parameter set 2 (100A, 25 $\mu\text{m}$ ) after 200ms.

However, parameter interactions were investigated in a previous work [11], but could also be confirmed by the MHD Simulation model within the investigated parameter window. As a result, the electric current was determined as the main influencing parameter concerning changing temperature and velocity fields, as well as particle properties. The

parameter dependent, transient particle properties (Fig. 3c) can now be used to describe particle movement.

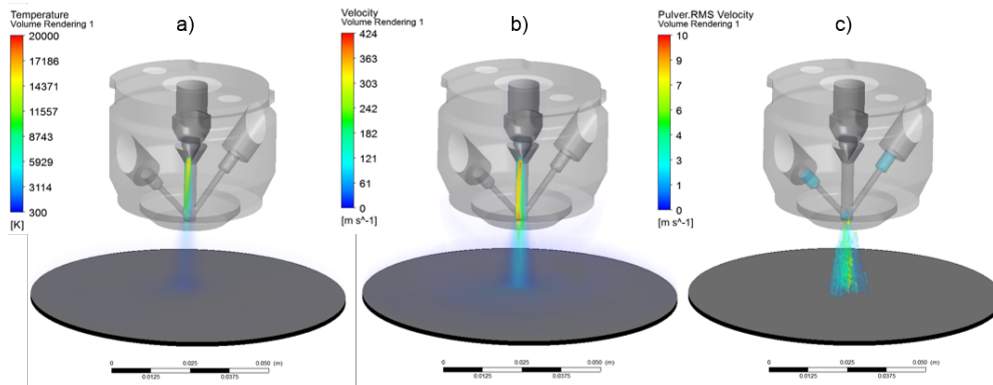


**Fig. 3** Exemplary global results of transient physical quantities after 0.2s a) Plasma arc temperature, b) process gas speed, and c) powder flow speed

### PARTICLE MOVEMENT

Based on the transient calculation of Gauß-distributed particle flows, single particles can now be traced and the particle movement can be investigated. Therefore, a random particle, which suffers elastic particle-particle and particle-wall interactions as well as physical interactions of turbulent fluid flows, is traced and recorded during post-processing. Figure 4a) shows 2 examples of particle movement at the interfacial area of powder inlet and main flow channel. Figure 4b) shows the resulting transient velocity vectors at the powder inlet and main flow channel interface.

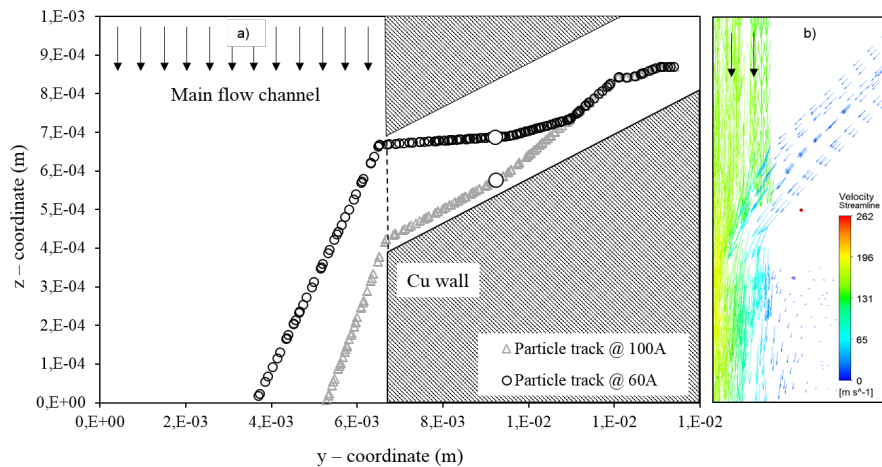


**Fig. 4** a) Transient particle track of one representative particle using different parameter sets b) Vector plot of the local velocity field using standard parameters (100A)



Due to different primary currents the particle track differs. By increasing the electric current two main effects take place. First, the local gas velocity (main flow channel) increases, which leads to more pronounced velocity-vector orientation in z-coordinate direction and respectively a reduction of the particle dwell time. Second, due to higher plasma temperatures, the resulting particle temperature increases. However, these combined effects are influencing the particle movement, and consequently correlate with the inflight particle properties. As a result, various physical properties can be investigated: e.g. the particle phase fraction (Zn).

PARTICLE PHASE FRACTION

The calculated particle track gives insight about important coating related phenomena. Especially, the correlation of the particle travel path and the phase state of the tracked particle is of main interest for the APS process and the final APS coating. Therefore, a Liquid2Solid (L2S) subroutine was implemented in the MHD model, in order to calculate the liquid particle fractions as a function of process dependant transient physical quantities, e.g. particle velocity, mass flow rate, temperature field and pressure. The foundation of the simple L2S subroutine is the definition of different phase transformation points. As mentioned above, a constant melting temperature of  $T_m=692.45K$  can be assumed for all Zn particles. This melting temperature represents the main phase transition point during particle movement. Other phase transformations like particle agglomeration, solidification and sublimation were neglected in the L2S routine.

A typical application for APS is the local deposition of Zn based corrosion resistance coatings onto steel sheets. Therefore, a combined approach of an experimental parameter investigation and CFD Simulation is one possibility to improve the Zn coating properties. Table 2 shows 4 representative parameter sets.

**Table 2** Investigated parameter sets. Const. parameters: Working distance=30mm, Powder mass flow=5g/min, Particle carrier gas flow=5l/min, Powder material=Zn

	Electric current (A)	Plasma gas flow (l/min)	Particle size (µm)
Parameter set 1	60	10	5
Parameter set 2	200	10	5
Parameter set 3	200	10	50
Parameter set 4	80	12	25

Figure 5 shows the correlation of the phase fraction of a random Zn particle and the calculated particle travel path for all specific parameter sets.

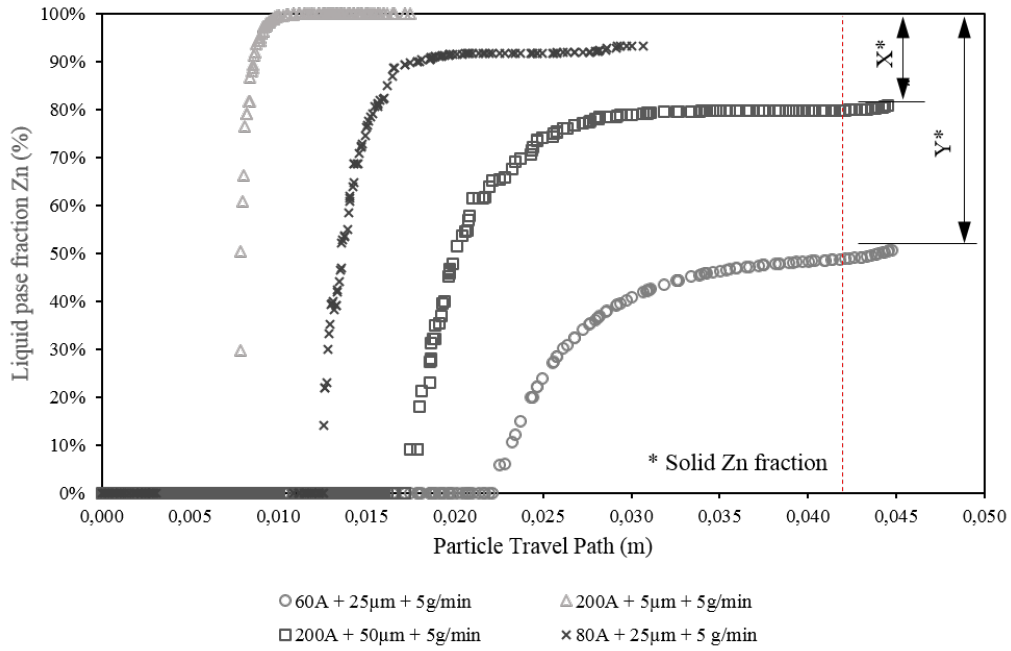


**Fig. 5** Correlation of the tracked particle path and the phase fraction of Zinc. Different parameter set were investigated by experiment and simulation; Red dashed line represents the shortest possible particle track, due to PT geometry

However, while one base criteria for homogenous APS coatings is the liquid phase fraction should be near 100%, the remaining solid fraction of Zn particles ( $X^*$  and  $Y^*$ ) can be calculated during particle flight. Liquid Zn droplets lead to a more pronounced splat formation and to more compact APS coatings respectively [12]. Representative cross sections of the deposited APS coatings were investigated by light optical microscopy (LOM).

Figure 6a) shows typical irregularities like void formation, increased porosity, irregular coating thicknesses and a decrease of inter-particle adhesion forces. These irregularities occurred predominantly near semi-molten particle boundaries, due to incorrect process parameter setting. Figure 6 b) shows a representative cross section of the Zn coating, which was deposited using a MHD computed parameter set (parameter set 4). As a result, predominant solid particles could be avoided and the amount of irregularities could be significantly reduced.

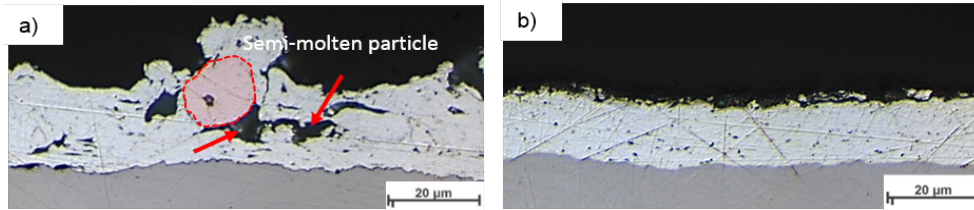


**Fig. 6** LOM investigation of two representative cross sections of a Zn layer on a steel substrate  
a) Local void formation of particle near region and irregular surface morphology, due to semi-molten particles – Parameter set 1 b) Zn coating deposited with parameter set 4

### SUMMARY AND CONCLUSION

The present, physical based MHD simulation model can be used for optimising the deposition process. First, transient physical quantities like temperature, velocity or pressure were calculated. These quantities give an insight about parameter interactions and physical loads during APS, depending on the PT geometry. Second, these quantities act as an initial condition for the subsequent particle track calculation. Therefore, one random particle is tracked during its' flight through the powder inlets and the main flow channels, interacting with the previously described physical quantity fields. As a result, the particle track for each involving particle could be calculated. Third, the interaction of particle moving and particle phase fraction (Zn) was investigated.

The MHD Simulation of the APS process led to some interesting findings:

- The combined approach of particle movement simulation and the implemented S2L routine allows process and parameter optimisation. Therefore, the liquid phase fraction of a particle, which correlates with splat formation, can be calculated. As a result, a reduction of semi molten particles within the Zn coating could be achieved by use of the MHD simulation model. Consequently, the amount of irregularities could be significantly reduced, which could also be confirmed by experimental investigation.
- The simulation model can be used to investigate and validate new powder materials. Here, the prediction of the coating morphology and the deposition efficiency are in the main focus. The simulation results correlate with the microscopic analyses.
- The numerical simulation can be used to improve the PT or cathode design. Here, the formation of transient temperature fields and the resulting particle movement is of major interest.

### ACKNOWLEDGEMENTS

The K Project Network of Excellence for Metal JOINing is fostered in the frame of COMET – Competence Centers for Excellent Technologies by BMWWF, BMVIT, FFG, Upper Austria, Styria, Tirol and SFG. The program COMET is handled by FFG. The plasma torch CAD data and the experimental validation of the simulation model was provided by Inocon Technologie GmbH, Austria. Special thanks to CFX Berlin, Germany for material data and CFD support.

### REFERENCES

- [1] R. HEIMANN: '*Plasma Spray Coating*', Weinheim Wiley-VCH Verlag-GmbH & CoKG, 2008.
- [2] P. ERNST AND G. BARBEZAT: '*Thermal spray applications in powertrain contribute to the saving of energy and material resources*', Surf. Coatings Technology, vol. 202, pp. 4428–4431, 2008.
- [3] P. FAUCHAIS: '*Understanding plasma spraying*', Journal of Physics D: Applied Physics, vol. 37, no. 9. 2004.
- [4] C. J. LI AND B. SUN: '*Microstructure and property of micro-plasma-sprayed Cu coating*', Mater. Sci. Eng. A, vol. 379, pp. 92–101, 2004.
- [5] CFX BERLIN: '[Online]. Available: <https://www.cfx-berlin.de/>. [Accessed: 18-Jul-2018].
- [6] S. ROBINSON: '*Coherent Motions in the Turbulent Boundary Layer*', Annu. Rev. Fluid Mech., 1991.
- [7] B. MOHAMMADI AND O. PIRONNEAU: '*Analysis of the K-Epsilon Turbulence Model*', Res. Appl. Math., 1994.
- [8] B. E. LAUNDER AND D. B. SPALDING: '*The numerical computation of turbulent flows*', Comput. Methods Appl. Mech. Eng., 1974.
- [9] W. E. RANZ AND W. R. MARSHALL: '*Evaporation from drops. Parts I & II.*', Chem. Eng. Progr, 1952.
- [10] A. AISSA, M. ABDELOUAHAB, A. NOUREDDINE, M. EL GANAOUI AND B. PATEYRON: '*Ranz and Marshall Correlations limits on heat flow between a sphere and its surrounding gas at high temperature*', Therm. Sci., 2015.
- [11] M. STUMMER, T. EICHINGER, P. STÖGMÜLLER AND N. ENZINGER: '*Improving the wetting behaviour of steel substrates by use of Atmospheric Pressure Plasma*', Int. J. Mech. Eng. Autom., vol. 3, pp. 482–490, 2016.
- [12] P. FAUCHAIS, V. RAT, J. F. COUDERT, R. ETCHART-SALAS AND G. MONTAVON: '*Operating parameters for suspension and solution plasma-spray coating*', Surf. Coatings Technol., vol. 202, pp. 4309–4317, 2008.



# **VII Modelling Tools and Computer Programs**



# CORRELATING LARGE SETS OF EXPERIMENTAL DATA WITH HIGH RESOLUTION COMPUTATIONAL WELD MECHANICS MODELS

J. GOLDAK\*, M. MARTINEZ\*\*, S. TCHERNOV\*, H. NIMROUZI\*,  
J. ZHOU\*, D. K. AIDUN\*\* and H. EISAZADEH\*\*\*

*\*Goldak Technologies Inc., 3745 Revelstoke Dr., Ottawa, ON, K1V 7C2, Canada.*

*\*\*Clarkson University, Department of Mechanical and Aeronautical Engineering, 8 Clarkson Av, Potsdam, NY, 13699, USA,  
mmartine@clarkson.edu*

*\*\*\*Mechanical Engineering Technology, Old Dominion University, 108B Kaufman Hall, Norfolk, VA 23529, USA*

DOI 10.3217/978-3-85125-615-4-43

## ABSTRACT

The validity of 3D transient computer models to predict the mechanics of welds is judged by correlating predictions made by the computer model with data acquired from experiments, i.e., correlating virtual and real data. The authors suspect that by far the greatest uncertainty in the predictions from these computational models has been due to the sparsity in the available experimental data on material properties and the welding process itself. The goal of this paper is to present a few examples that demonstrate how large sets of experimental data provided by recent developments in sensor technology and data acquisition systems such as distributed fiber optic temperature and strain sensing optical fiber, in addition to full field and transient data such as thermographic and Digital Image Correlation (DIC) cameras can be correlated with predictions from VrWeld, a computer model for computational weld mechanics. A fiber optic system using Rayleigh backscattering is used to measure temperature and strain with a spatial resolution of 0.65 mm at a data acquisition rate of 10 Hz but it could be as high as 250 Hz. The experimental data has noise that must be filtered. To correlate the virtual data the 3D transient Computational Weld Mechanics (CWM) models had to use time steps smaller than 1 second and element size less than 1 mm. With this data, one can correlate the clocks for the experiment and the computer model. In addition, one can run Design of Experiments (DOEs) to correlate material properties such as temperature dependent thermal conductivity and boundary conditions such as convection coefficients. Some of the challenges in synchronizing real and virtual data in space and time are discussed.

Keywords: Transient Welding Analysis, Digital Image Correlation, Thermography of Welds, Computational Welding Models.

## INTRODUCTION

The objective of this study was to provide an example of the correlation between modern experimental methods and a current computer model of welds, i.e., to estimate the uncertainty in the validation of one particular current computer model - VrWeld. The



approach is to correlate as much experimental data, particularly transient, full field experimental data, as we can afford to collect with as much 3D transient full field virtual data as we can afford to compute. We do not seek the value of a binary decision of whether the computer model is valid or not valid. Rather we seek measures of the correlation between each type of real and virtual data. Because the physical and virtual experiments use different clocks and different coordinate frames, one of the first challenges is to synchronize the physical and virtual clocks and physical and virtual spatial coordinate frames.

### DESIGN OF THE EXPERIMENT

Our study is divided into five sections: (i) a description of a 3D transient computer weld model; (ii) a detailed explanation on the synchronization of the clock data for different experimental data sets and the computer model; (iii) an optimization Design of Experiment (DOE) study to compute estimates of the sensitivity of parameters in the computational model; (iv) a transient analysis result section which discusses the correlation of real and virtual DIC data; (v) a discussion and conclusion section.

Our study made use of an A36  $300 \times 300 \times 6.35$  mm steel plate. A 90-degree V-groove weld joint runs the length of the plate on the symmetry plane. The welding process was a manual GTAW with 1/16-inch ER 70S2 filler metal added. The arc was 180 amps and 15 volts. A 50/50 mixture of argon and helium shielding gas at 30 CFM was used. The plate was fixed in the vertical plane. The weld was made upward (3G position). The weld length was 270 mm; the total time for the weld was 280 seconds. Data was gathered for a total time of 30 minutes from the start of welding in order to capture the behavior during cool-down after the weld was complete.

Fig. 1 shows the setup used for this study. As seen in this figure the front of the plate was instrumented with a fiber optic sensor connected to a Rayleigh backscattering system from Luna Technologies [1]. Also seen in the test setup, the back of the plate was painted with very high temperature paint with a speckle pattern which allowed for acquisition of the strain distribution in situ during the welding process using a VIC-3D Digital Image Correlation System [2]. A fan was also placed blowing room temperature air towards the back of the plate. This was required in order to avoid heat buildup in the air between the plate and the camera. Furthermore, the plate was clamped to a portrait fixture which allowed the authors to rotate the specimen to specific orientation. In this study the plate was set to approximately 90 degrees from the base of the table.

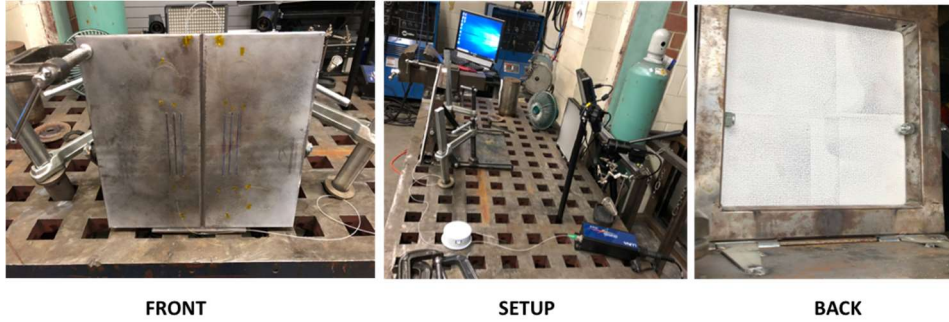


Fig. 1 Experimental Setup.

### TRANSIENT 3D COMPUTER MODEL OF WELD

The weld heat source model is based on models proposed by Ohji et al. [3] and Sudnik [4]. The weld heat source model is a 3D transient Eulerian formulation that solves the conservation of energy, mass and momentum with a Gaussian pressure distribution, thermal flux distribution and mass flux distribution from the arc. The effects of surface tension and gravity were included. Patterns for weave welds with weave amplitude and dwell times are supported in the model. Melting, solidification and the evolution of microstructure were modelled. This heat source model predicts the weld shape and size. This is in sharp contrast to the distributed power density that is often called the double ellipsoid heat source model that requires the weld pool shape and size be known experimentally [5].

The conservation of energy in spatial coordinates is solved using a semi-Lagrange method:

$$\rho \frac{dh}{dt} - \nabla \cdot \mathbf{q} + Q = 0 \quad (1)$$

Where,  $\rho$  is density,  $h$  is specific enthalpy,  $\mathbf{q}$  is thermal flux and  $Q$  is power per unit volume. The specific heat and thermal conductivity are functions of temperature and phase fractions. The transient transformations of austenite to ferrite, pearlite, bainite and martensite and the grain growth of austenite were computed in the model.

The quasi-static conservation of momentum in spatial coordinates was solved using a semi-Lagrange method.

$$\nabla \cdot \boldsymbol{\sigma} + \mathbf{g} = 0 \quad (2)$$

and

$$\Delta p = \gamma \left( \frac{1}{R_1} + \frac{1}{R_2} \right) \quad (3)$$

Where,  $\boldsymbol{\sigma}$  is the Cauchy stress,  $\mathbf{g}$  is the acceleration due to gravity,  $\Delta p$  is the pressure drop across the liquid-plasma interface,  $\gamma$  is the surface tension and  $1/R_1$ ,  $1/R_2$  are the

## Mathematical Modelling of Weld Phenomena 12

principal curvatures at a point on the liquid surface. The inertial force and Marangoni forces are neglected in this model.

The conservation of mass is enforced as a constraint such that the mass flow in the wire,  $\pi r_{\text{wire}}^2 v_{\text{wire}} = A_{\text{filler}} v_{\text{weld}}$  where  $r_{\text{wire}}$  is the radius of the wire,  $v_{\text{wire}}$  is the wire speed,  $v_{\text{weld}}$  is the weld speed and  $A_{\text{filler}}$  is the cross-sectional area of the filler metal. Weld pool model requires all parameters of most weld procedures plus additional parameters such as surface tension and arc pressure that are not usually included in weld procedure data sheet.

### INPUTS TO THE VRWELD MODEL

The VRWeld heat source model required input of the power needed to perform the weld. Thus, the video captured during the actual weld process of the welding station which displayed the instantaneous voltage and current was transformed into a graph of current and voltage vs. time as shown in Fig. 2.

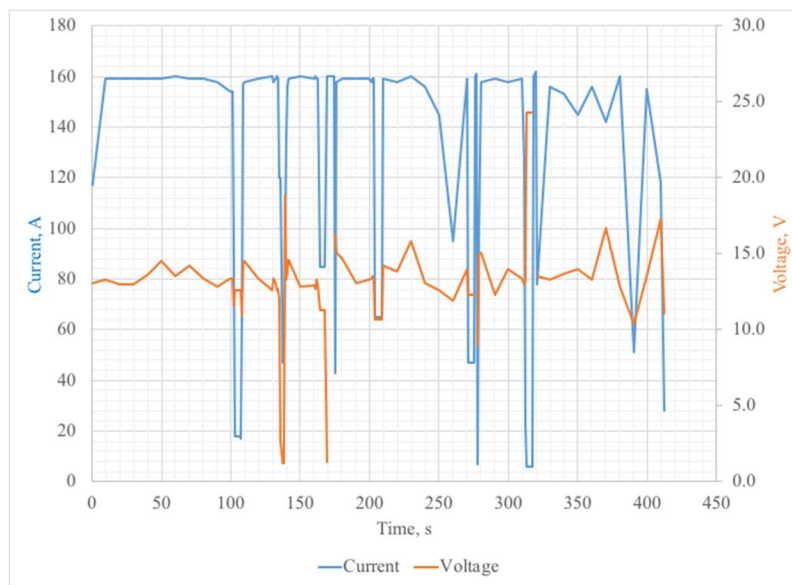


**Fig. 2** Voltage and Current vs. Time during the welding process.

The power input causes burn-through on the backside of the plate. Fig. 3, relates the virtual burn-through and the real burn-through shown. The width of the virtual burn-through in the left image and the width of the real burn-through in the photograph on the right are both close to 8 mm. This comparison is indicative that weld pool model parameters have generated a weld pool shape that agrees well with the observed data. This real data is very important because it provides a constraint that the weld pool model design parameters must satisfy.

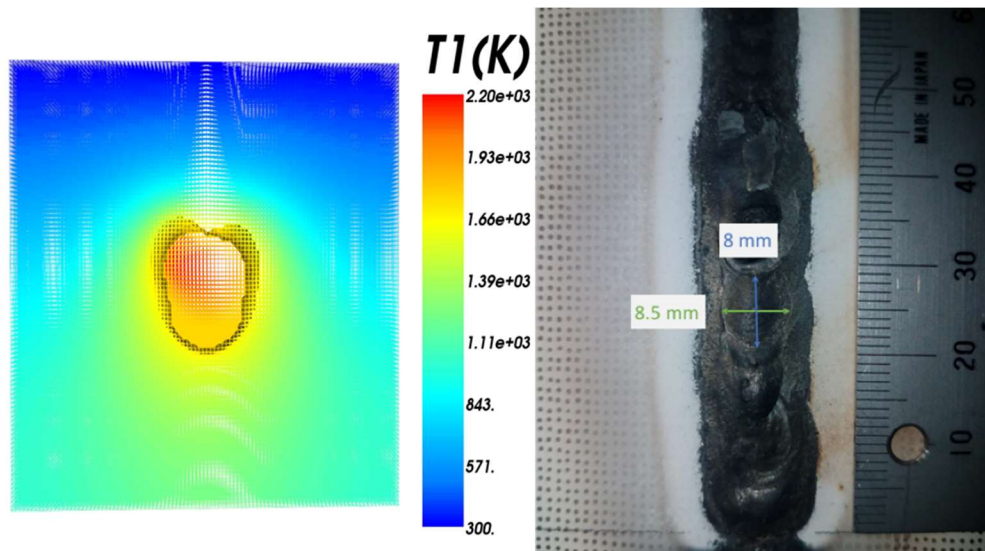


**Fig. 3** The left image shows iso-surfaces of the temperature 5 degrees above and below the melting point on the bottom surface at time 45 seconds. The right image shows the burn through on the bottom of the plate after the weld had cooled. Both predicted and measured burn-through are approximately 8.5 mm.

In addition, the burn-through, the VrWeld model accounts for the weaving motion performed by the welder during the welding process. This is an important input parameter in the model due to the manual nature of the welding process being considered in this study. Fig. 4 shows some of the results of the VrWeld model, each row of images has one image with a left weave and a right weave. The top row is 6 seconds after the start of the weld. The second row is about 15 seconds after the weld started, while the last row is approximately 45 seconds after the weld started. If computer vision data was available, it would provide a strong constraint that the design parameters the weld pool model should satisfy, e.g., arc pressure distribution and surface tension. The weld pool model used a Gaussian arc pressure distribution with parameters for the integral and width of the Gaussian function.

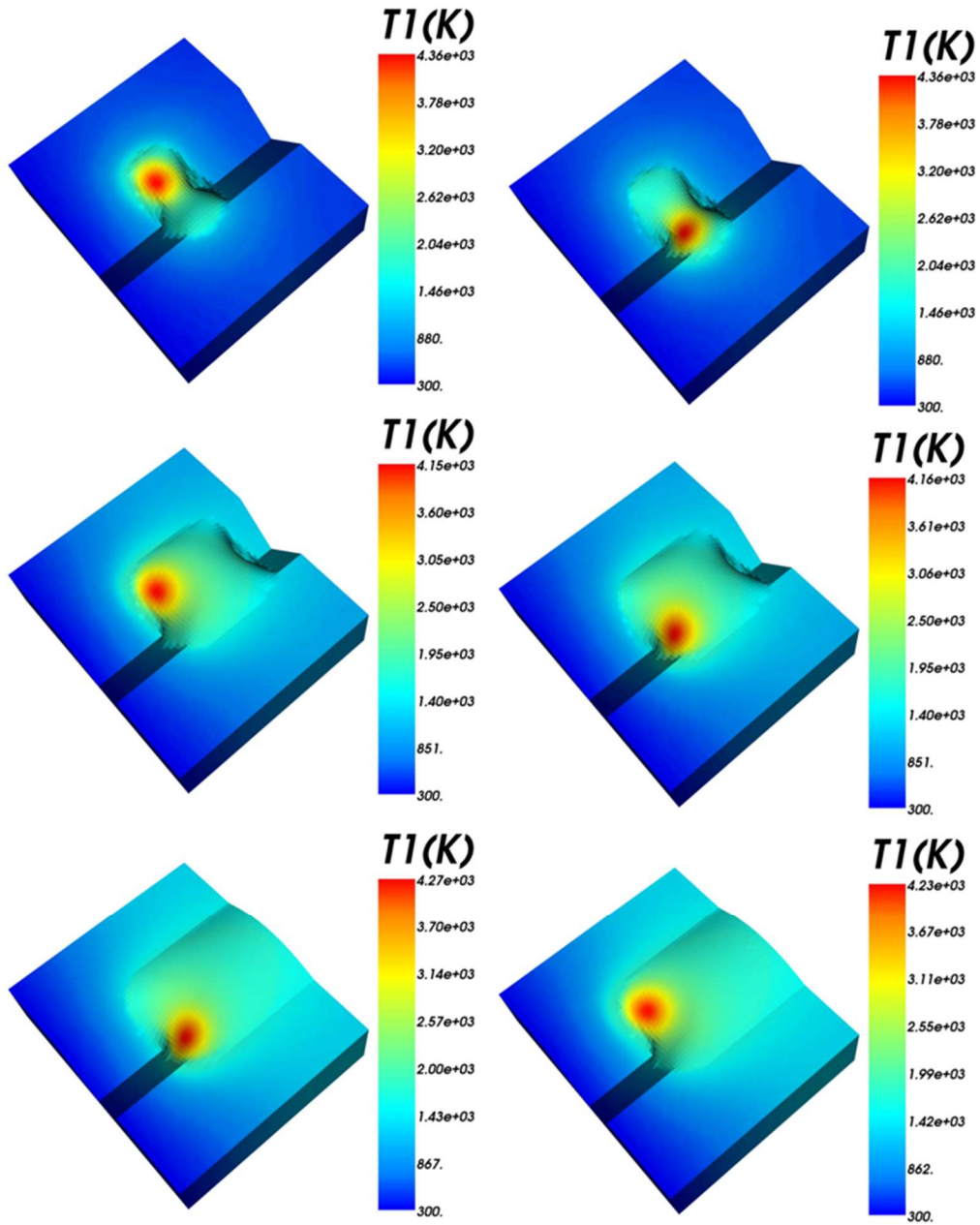


**Fig. 4** The image of the weld pool surface is shown for a sequence of time steps. The color represents the temperature in °K.

PHASE TRANSFORMATION

An important outcome of the VrWeld model is the coupling of the temperature fields to material phase transformation models. Fig. 5 shows the isosurfaces for the temperature 5°K below the melting temperature in blue and 5°K above the melting point in red. The region between the isosurfaces in front of the weld pool is melting. The region between the isosurfaces behind the weld pool is solidifying.

In Fig. 6, the top right image shows isosurfaces for phase fraction austenite of 0.05 and 0.95. The region between the outer two isosurfaces shows where fraction of austenite and ferrite-pearlite is increasing or decreasing. The region between the inner two isosurfaces is where austenite and liquid phases are increasing or decreasing. These images are at time 14 and 14.5 seconds after the start of the weld, respectively. We have ignored the delta ferrite phase in this model.

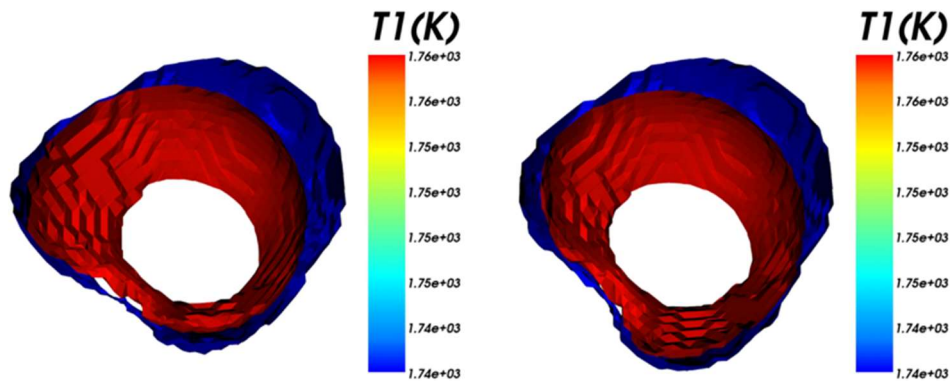


Fig. 5: The top left image shows the isotherms for temperatures 10 °K above and below the melting temperature.

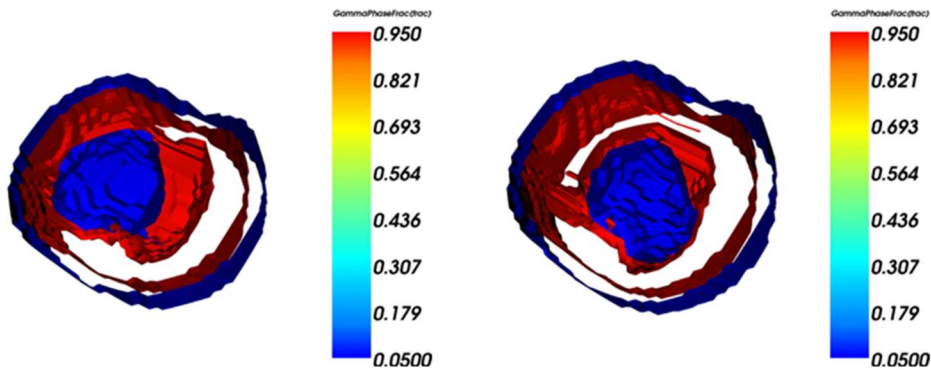
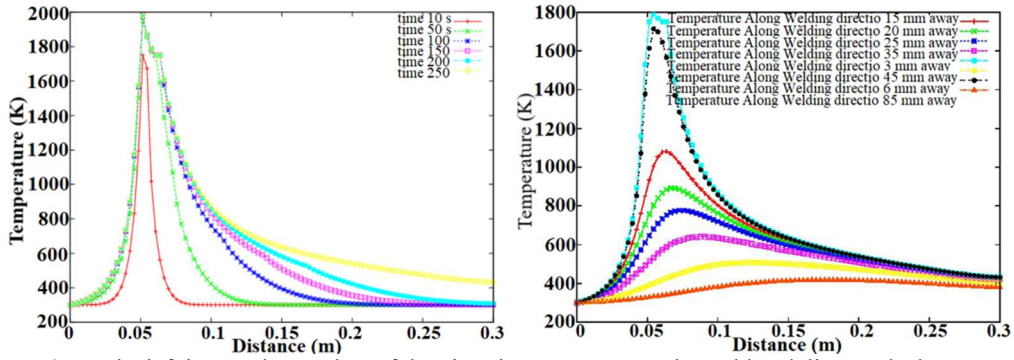


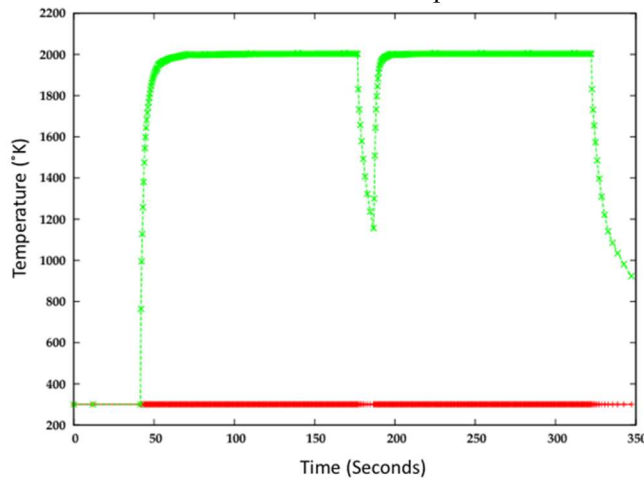
Fig. 6: Iso-Surfaces of the 0.05 and 0.95 fraction of the austenite phase are shown at time 14 seconds in the left image and 14.5 seconds in the right image

Fig. 7 shows virtual temperature data, however it is important to note that this data has not yet been correlated to real temperature data.



**Fig. 7** The left image shows plots of the virtual temperature on the weld path line on the bottom surface for a sequence of time steps in the weld. The right image shows virtual temperatures at an instant of time on lines on the bottom surface of the plate at increasing distances from the weld path.

Fig. 7 shows the temperature profile along the weld line, while the same figure on the right shows the temperature profiles on the bottom or back surface offset from the weld line. As shown in Fig. 7, the approximate zero slopes near the peak are the mushy zone for melting in front of and for solidification behind the weld pool. These straight sections at the high temperature values for the two plot is due to the phase changes. During the phase change the enthalpy changes however temperature is kept constant. The right image shows plots of the virtual temperature at an instant of time on lines parallel to the weld path line at different transverse distances from the weld path. Note that the high frequency temperature oscillations near the 1800°K peak that are thought to be due to weaving. Note that the oscillations decay with distance from the weld and cannot be seen in line plots with lower peak temperatures that are farther from the weld path.



**Fig. 8** The minimum and maximum temperatures in each time step in the virtual analysis.

Note the decay in maximum temperature near 200 seconds shown in Fig. 8. It corresponds to the time when the welder stops welding to change his filler metal wire.

SYNCHRONIZING CLOCKS FOR REAL AND VIRTUAL THERMAL DATA

The first virtual analysis was run with values of parameters claimed to be correct for the real welding experiment. The four sensor systems; DIC, Voltage-current, Fiber optic and FLIR Thermographic data acquisition systems, have independent clocks. The virtual model must synchronize the virtual clock with the four real clocks. We first assume that each of these clocks keeps perfect time in the sense that they would each measure the length of one hour exactly. Then N-1 offset times are computed to synchronize the N clocks.

Clocks for real and virtual thermocouples with similar locations in the real and virtual plate can be synchronized by correlating peak times for thermocouples with similar locations in the real and virtual plate. The time a thermal sensor detects peak temperatures for a given weld pass depends on its position with respect to the weld path. A local coordinate system is defined such that  $w$  is the distance along the weld path,  $u$  is the distance in the plane of the plate transverse to the weld path, and the  $v$ -coordinate is the distance through the thickness of the plate. The clock for the data acquisition instruments is started a few seconds before the arc is struck. As the arc travels along the weld path, heat diffuses transverse to the arc. The time to diffuse from the weld pool to the thermal sensor is sensitive to the  $(u,v,w)$  coordinates of the real and virtual temperature sensor.

In order to correlate the peak times of each real and virtual thermal sensor, Eq. 4 is solved for the following regression:

$$\begin{bmatrix} 1 & w_1 & u_1 & w_1^2 & w_1 d_1 & d_1^2 \\ 1 & w_2 & u_2 & w_2^2 & w_2 d_2 & d_2^2 \\ \vdots & \vdots & \vdots & \vdots & \vdots & \vdots \\ 1 & w_n & u_n & w_n^2 & w_n d_n & d_n^2 \end{bmatrix} \begin{bmatrix} a_0 \\ a_1 \\ \vdots \\ a_6 \end{bmatrix} = \begin{bmatrix} \Delta t_1 \\ \Delta t_2 \\ \vdots \\ \Delta t_n \end{bmatrix} \quad (4)$$

The matrix for the least square problem has one row for each thermal sensor that has the values  $(1, w, d, w^2, wd, d^2)$  where  $(w, d)$  are the coordinates of the thermal sensor where  $w$  is the distance along weld path from the weld path start point and  $d$  is the distance from the weld path for this thermocouple (TC). The real and virtual sensors are assumed to have the same  $(u,v,w)$  coordinates. This is an assumption that the location of the real sensor is known exactly. The  $n^{\text{th}}$  component of the right hand side vector has the value of the difference in the peak times for the  $n^{\text{th}}$  real and virtual thermal sensor located at  $(u_n, v_n, w_n)$ .

In addition,  $(u_i, w_i)$  are the  $(u,w)$  coordinates of the  $i^{\text{th}}$  thermal sensor. The parameter  $a_0$  is a measure of the average difference in the time between the real and virtual sensor reaches its peak temperature. While, the parameter  $a_1$  is a measure of the difference in the time that each pair of real and virtual thermal sensors reaches their peak temperatures as a function of distance parallel to the weld path. The parameter  $a_2$  is a measure of the difference in the time that each thermal sensor reaches its peak temperature as a function of distance normal to the weld path.  $\Delta t_n$  is the difference in time that real and virtual thermal sensor pair  $n$  located at  $(u_n, v_n, w_n)$  reach their peak temperatures.



### DESIGN OF EXPERIMENT TO OPTIMIZE PARAMETERS IN THE COMPUTER MODEL

The first virtual model is idealized to model parameters of a constant speed, constant weld power with constant weave pattern. This idealization is not imposed by the computer model, it is imposed by the limitations of the information provided before correlating virtual data with data obtained from the sensors in the real experiment.

If the clocks and spatial coordinate frames were perfectly synchronized and if the virtual experiment perfectly replicated the real experiment, the difference in peak times would be zero. The first goal was to compute the start time for the virtual clock that minimizes the sum of squares of the difference in peak times of the pairs of real and virtual sensors  $\sum_{i=1}^n \Delta t_i^2$ . This was done shifting the start time of the virtual clock using the regression analysis shown in Eq. 4.

This correlation is done by running a Design of Experiment (DOE) analysis to minimize an objective function with a Design Matrix. Each design variable is one column in the DOE matrix and each row of the DOE matrix is one virtual experiment. One could also run multiple real and virtual experiments that solves the 3D transient weld pool model and 3D transient thermal analysis, where each row corresponds to an associated pair of a real and virtual experiments. Each design variable can have a specified lower bound, upper bound, minimum and maximum increment and a proposed initial guess.

The DOE matrix has one column for each design variable and one row for each numerical experiment. To optimize the weld speed, the DOE matrix has one design variable, the weld speed. The DOE matrix specifies an upper bound and a lower bound for each design variable. The usual objective function is to minimize the sum of squares of differences between real and virtual observables variables that are usually called design variables. To optimize virtual weld speed, the objective function minimizes a sum of squares of the difference in peak times of the real and virtual sensor  $\sum_{i=1}^n \Delta t_i^2$ , i.e., the weld speed that minimizes this objective function is computed.

A stochastic analysis with a kriging algorithm [6] is then used to compute a surrogate model for the design space for the virtual trials that have been completed. The number of virtual experiments to be run in each sub-set of trials is specified. If the number of trial sets has not reached its specified limit and if the allowed resources such as computing time have not been exceeded, a new set of virtual trials will be run until the limit is reached. This surrogate model contains estimates of the optimal value of each virtual design variable to minimize the sum of squares of differences between real and virtual observables or design variables. It can also evaluate the sensitivity of each design with respect to the objective function.

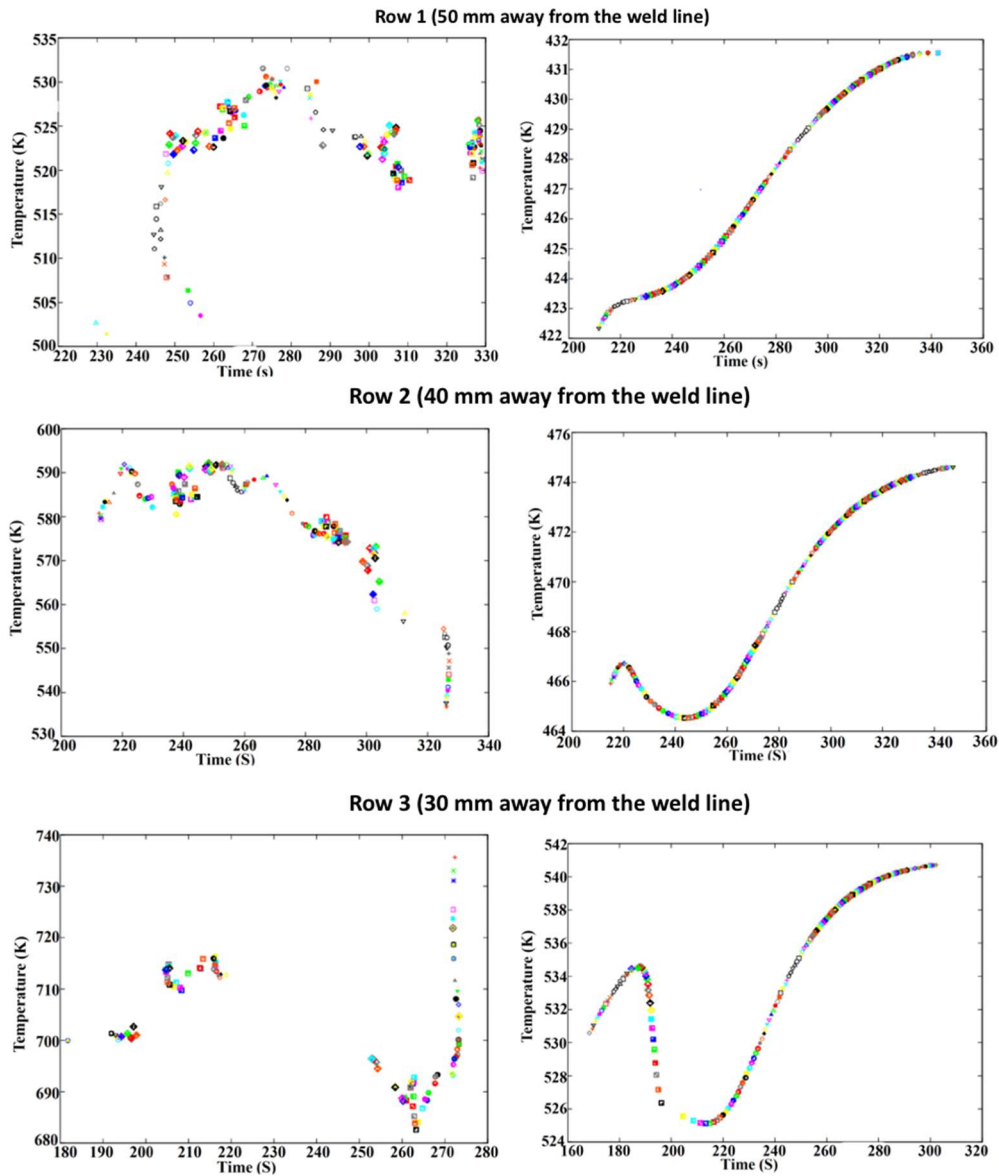
The second goal was to compute a virtual weld speed to minimize the difference in peak times. In the early stages of correlating real and virtual data, the virtual weld model uses a constant weld speed that is viewed as the average weld speed. Of course, this is an approximation as the speed of a manual weld is not really constant as the welder moves the

electrode to control the weld pool. If the virtual weld speed is slower than the average real weld speed, then virtual peak times for thermal sensor data near the start of the weld will be earlier than the peak times for the real thermal sensors, and peak times for thermal sensors near the end of the weld will be later than the peak times for the real thermal sensors. This assumes the weld speed is constant. In this case the real thermal sensor data was captured using the distributed fiber optic sensor. This system allows for capturing temperature data every 0.65 mm along the fiber length, thus creating an array of thermocouples longitudinal to the weld path.

If the weld speed varied as a function of time, as it does in manual welds, it would be desirable to include such variations in the analysis. Much of the difference is thought to be because of differences between the real and virtual local weld speed and local weld power as shown in Fig. 9. It is important to note that this figure correlates real and virtual data.

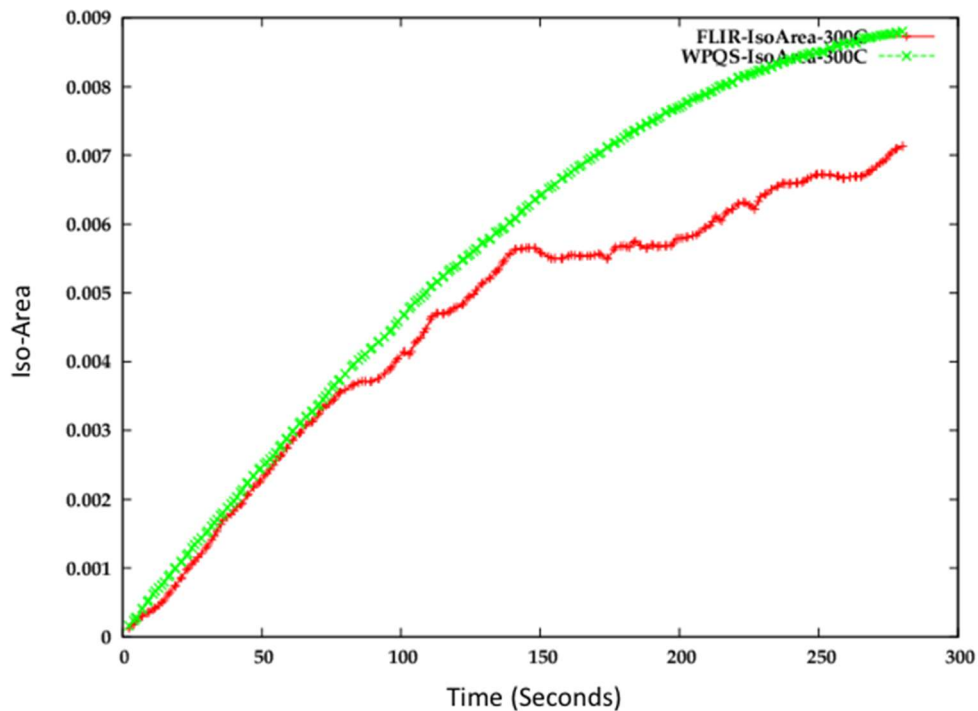
To optimize the virtual weld speed, a kriging analysis was run in which the objective function minimizes the sum of squares of the difference in peak times of the real and virtual sensor  $\sum_{i=1}^n \Delta t_i^2$ .

After the virtual clock and the real clock have been synchronized and differences in weld speed have been minimized, the values in the parameters for the virtual weld power, and convection coefficient are optimized. This is done by minimizing differences in the shape of the temperature peak for each pair of real and virtual thermal sensors. The convection coefficient and ambient temperature is most sensitive to thermal sensors far from the weld pool and during cool-down after the weld has been completed. The temperature peaks in sensors near the weld are sensitive to weld power distribution and to errors in the location of the thermal sensors and the lateral position of the weld pool as a function of time. If the temperature gradient at time  $t$  at a thermal sensor is 100 degrees per mm, then an error in position of 1 mm could generate an error in temperature of 100 degrees at time  $t$ .



**Fig. 9** The left images shows the real peak temperatures for the fiber data at 50, 40 and 30 mm from the weld path. The right images show the corresponding virtual peak temperatures.

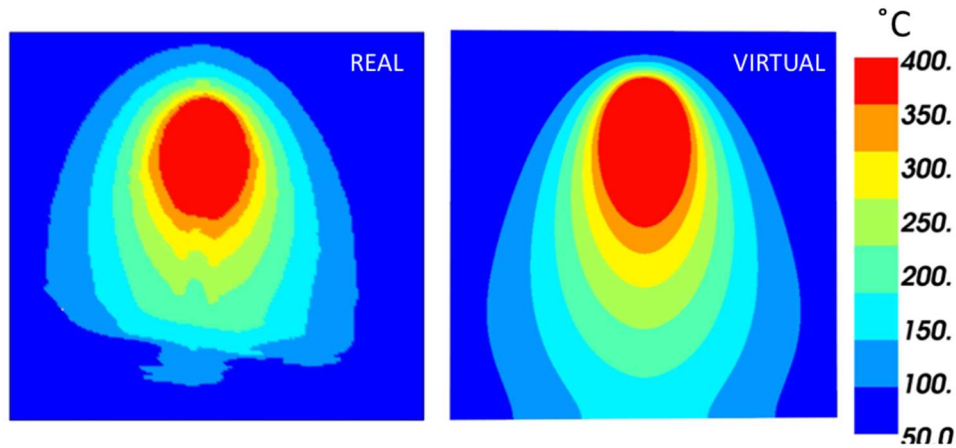
In addition to the fiber optic sensor data, a FLIR One Pro thermographic camera was used in this study. The real and virtual isotherms for temperatures of 100, 200, 300 and 400°C are computed. The difference in the area of each real and virtual isotherm at each discrete time step was calculated as shown in Fig. 10.



**Fig. 10** The red curve is the area in units of  $m^2$  of the  $300^\circ C$  isotherm computed from the thermographic data vs time. The green curve shows the area of the  $300^\circ C$  isotherm vs time computed by VrWeld. The x-axis shows time in seconds.

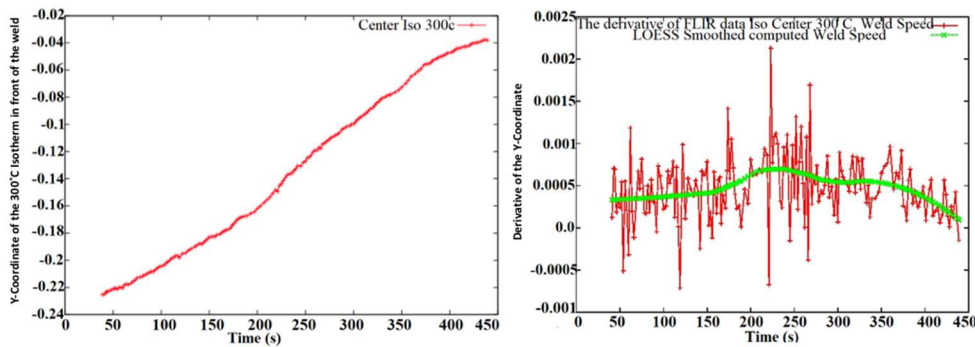
As seen in Fig. 10, after 75 seconds the VrWeld model and real data deviate, this suggests that the power distribution or the power in the real weld was reduced in the last half of the weld. This figure correlates real thermographic data with virtual thermographic data from the VrWeld model.

Fig. 11, shows the actual comparison at one of the time steps between the VrWeld model and those captured by the FLIR One Pro thermographic data. These images have different camera positions and the perspectives are different. The difference in the shapes of the tails of the isotherm presents an opportunity to study why they differ. Possible causes may include differences in microstructure, phase transformations and differences in material properties of the filler metal and base metal.



**Fig. 11** The left image shows isotherms captured by the thermographic camera at 45 seconds. The right image shows virtual isotherms computed by VrWeld at 45 seconds.

As seen in Fig. 12, the red curve in the right image shows the derivative of the curve in the left image with respect to time. The green curve is the red curve filtered to reduce high frequency fluctuations. The green curve is an estimate of the weld speed as a function of time in units of m/s. As such the right image provides the instantaneous weld speed, the green curve shows the smoothed curve. Based on the results obtained from the thermography data shown in Fig. 12, an average of 0.5 mm/s weld speed was estimated.



**Fig. 12** The left image shows the longitudinal or y-coordinate of the 300 °C isotherm captured by the thermographic camera as a function of time. The right picture shows the derivative of the left picture with respect to the time. The red curve is raw values of the derivative. The green curve shows filtered data.

### TRANSIENT THERMAL STRESS ANALYSIS

Digital Image Correlation (DIC) is an experimental technique used to measure transient displacement or deformation fields. From the measured displacement fields, strain fields can be computed. In contrast, FEM computes a strain field based on displacements computed by a computer model. The essential difference between DIC and FEM is DIC

measures a displacement field by using stereo cameras to measure the deformation of a speckle pattern while FEM solves integral equations to compute the transient displacement in a mesh.

One of the drawbacks with DIC, is its inability to correlate displacement close to the weld pool. We set DIC values to zero at points for which the DIC cannot correlate the deformation of the speckle pattern. We use this as a surrogate transient fiducial mark to correlate real and virtual displacements as described in Fig. 13.

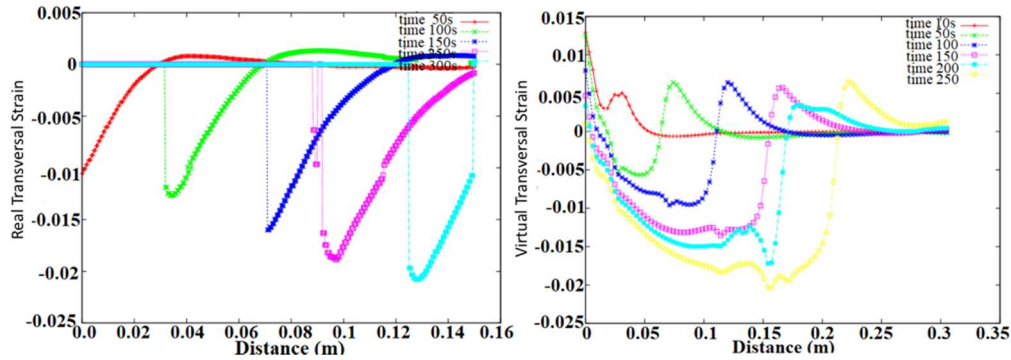


**Fig. 13** The left image shows line plots from DIC data for transverse strain at five different times during the weld. The lines are parallel to the weld joint on the bottom surface of the plate. The lines for DIC data ends when the real deformation exceeds the DIC software’s capability to correlate image data. The right image shows the corresponding line plots for the virtual DIC data.

As observed in Fig. 13, due to the inability of the DIC to cross correlate the strain near the passing of the weld pool, the values of strain are set to zero. As such the comparison between the virtual and DIC strain should be focused solely on the peaks and the decay away from the weld pool. Fig. 13 on the right is taken from the virtual DIC data set, as such the VrWeld allows for the computation of the strain along all locations of the finite element mesh.

### WELD INTERRUPTION FOR FILLER ROD EXCHANGE

Fig. 14 and Fig.15, show the transversal and longitudinal strains captured by the DIC system during the interruption of the weld in order to perform an exchange of the filler rod. As seen in these two figures a complex formation of both transversal and longitudinal strains develops during this process as described next:

- Immediately prior to extinguishing the weld arc. The transversal strain (Fig. 14) above the liquid weld pool is found to be  $-13,599 \mu\epsilon$  in compression, while on the left (west) side of the weld pool it is  $+8,918 \mu\epsilon$ . This combination of strains indicates the pry open nature of the weld pool on the material as its being welded. The compressive region on top of the weld pool is caused by the tensile strain on

## Mathematical Modelling of Weld Phenomena 12

the side of the weld pool. The longitudinal strain readings at the same locations (Fig. 15) with respect to the welding pool are  $+3,488 \mu\epsilon$  and  $+5,029 \mu\epsilon$  in tension.

- When the arc is switched off, a cooling of the weld pool initiates immediately followed by a solidification on the back side as captured by the DIC cameras. Transversal strain (Fig. 14) readings drop to  $-15,352 \mu\epsilon$  in the compression region just in front of the weld pool followed by a tensile region reaching  $+874 \mu\epsilon$  further up on the plate. In contrast, the longitudinal strain (Fig. 15) right above the weld pool is in the order  $+4,794 \mu\epsilon$  in tension.
- Liquid weld pool solidifies on the back side. Transversal compressive region (Fig. 14) becomes more compressed (strain value of  $-16,771 \mu\epsilon$ ) while the longitudinal strain at the same location is measured to be  $+5,493 \mu\epsilon$  (Fig. 15).
- Weld arc is back on, the material is liquefied. The strain in transversal compressive region drops further to  $-19,457 \mu\epsilon$  while in the tensile region above drops to  $+128 \mu\epsilon$  (Fig. 14). Longitudinal strain above weld pool  $+6,652 \mu\epsilon$  (Fig. 15).

It is interesting to see through this process how the exchange of a filler rod increases the local compressive transversal strain by almost  $-5858 \mu\epsilon$  in front of the weld pool. It is also important to note that the vertical nature of the weld causes an increase in this compressive local transversal strain from the beginning to the end of the weld. The longitudinal local strain in front of the local weld pool also suffers an increase of approximately  $3164 \mu\epsilon$  in tension due to the filler rod exchange. This is a significant increase in both transversal and longitudinal strain near the weld pool every time the welder is required to exchange the filler rod.

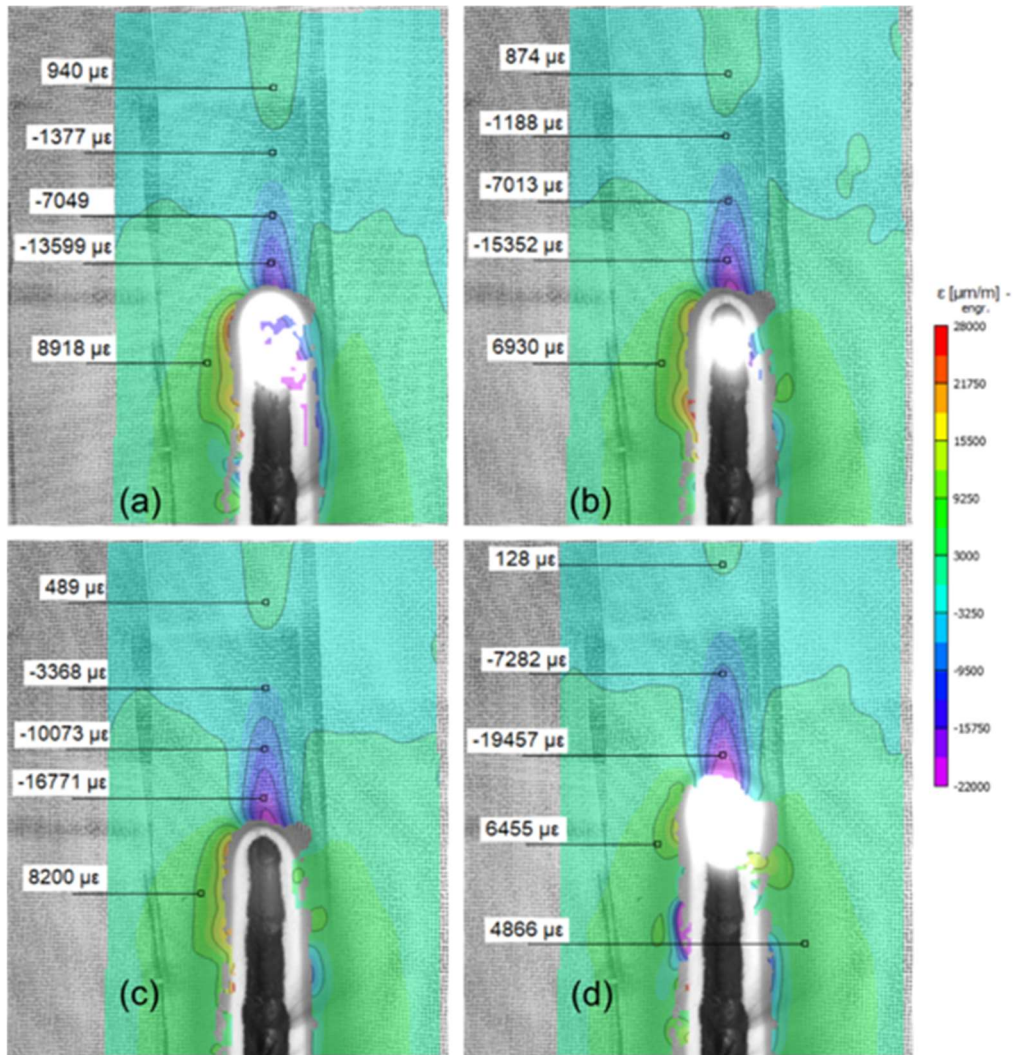


**Fig. 14** Transversal strain measurement during the process of switching the filler rod: (a) prior to switching off the weld torch, (b) while the weld torch is fully switched off, (c) liquid weld pool on the back side of the plate, (d) weld torch back on.



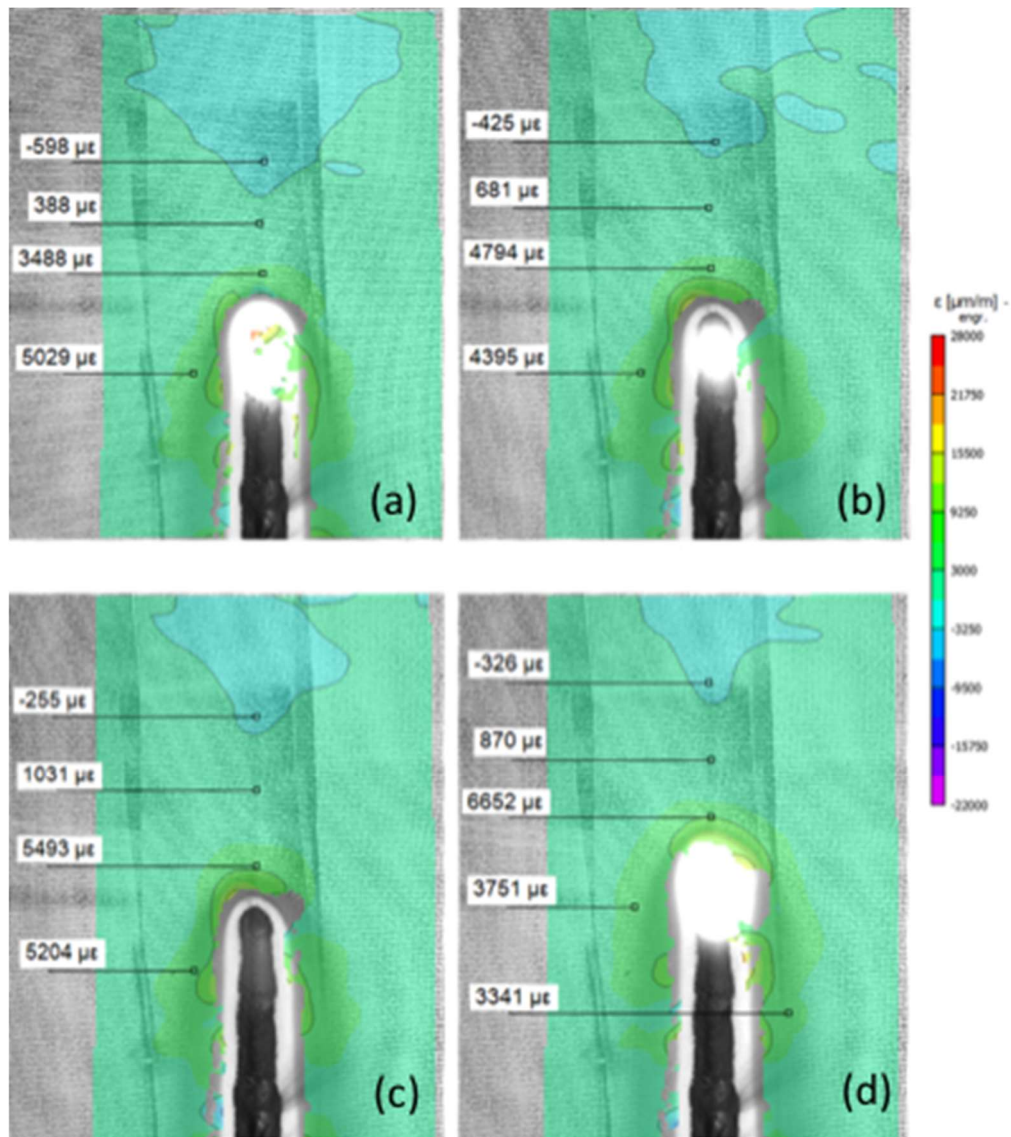


**Fig. 15** Longitudinal (y-axis) strain readings during the process of switching the filler rod: a) right before switching the weld torch off, b) weld torch switched off, c) liquid weld pool solidified on the back side, d) weld torch back on.

A one to one comparison of transversal and or longitudinal strains of the experimental data set and the VrWeld model are presented in Fig. 16 and Fig. 17. The left image Fig. 16 shows the experimental transversal strain along the back of the plate. The right image shows the equivalent transversal strain results computed by the VrWeld model. The experimental data does not show data at the core of the weld pool, as in these locations the DIC speckle pattern is fully burned through. The results are shown for three-time steps, after, before and at time step for which the weld pool passes through. It is interesting to observe that the

change in transverse strain away from the weld pool is consistent with that of the VrWeld model. Variation and lack of symmetry in the experimental data are believed to be attributed to the changes in the weaving pattern of the welder and the inability of the DIC to compute strain in the proximity of the weld pool. The uncertainty in the peaks in the experimental data on either side of flat blue line for zero strain is high because the high temperatures from the weld pool destroyed the speckle pattern. Thus, DIC is computing the peaks with incomplete speckle patterns.

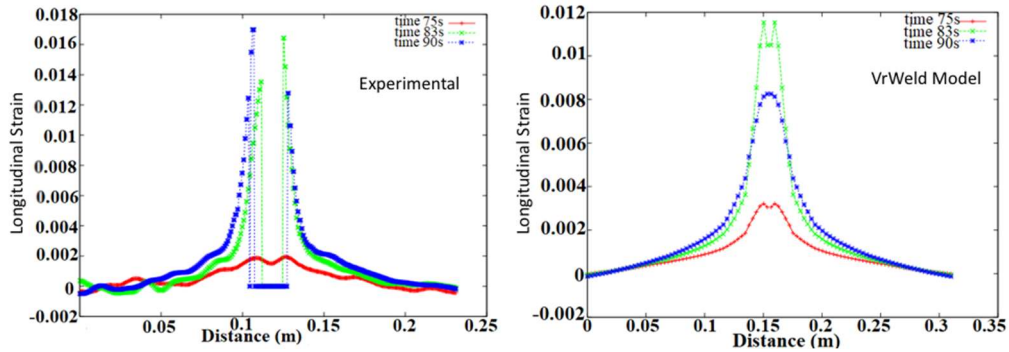


Fig. 16 Transversal strain comparison between the experimental (left) and VrWeld model (right) at 75, 83 and 90 seconds along a line  $y=7.5\text{mm}$  from the bottom edge of the plate.

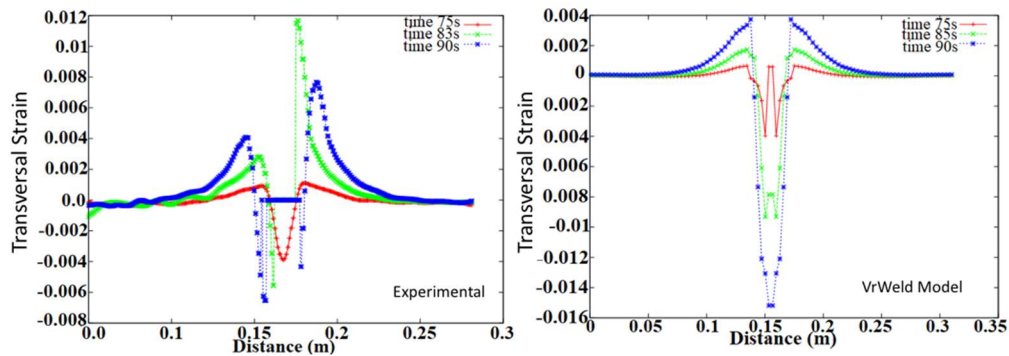


Fig. 17 Longitudinal strain comparison between the experimental (left) and VrWeld model (right) at 75, 83 and 90 seconds along a line  $y=7.5\text{mm}$  from the bottom edge of the plate.

Fig. 17 shows the experimental and VrWeld longitudinal strain along the transvers direction on the back of the plate. The left figure shows the experimental results while the right image shows the virtual data of the computed longitudinal strain distribution. Both experimental and VrWeld longitudinal strains show very good agreement. The longitudinal strain has less variations translating into a more symmetrical distribution of strain along the 3 different time steps.

### COMPUTING TIMES AND USER TIMES

The computing times for these analyses using a single core Intel I7 processor with an Nvidia GPU for the weld pool model was 325 seconds with 36K 8-node brick FEM elements; VrWeld thermal analysis with 16,400 FEM elements took 319 seconds; 730 seconds for VrWeld stress solver 16,400 FEM elements. None of the correlations between real and virtual data took more than 2000 seconds. In contrast the DIC data file size was 24.4 Gb. The fiber data file size was 1.09 Gb.

### SUMMARY AND CONCLUSIONS

Experimental data from a single pass GTIG manual weld in an A36 steel plate was gathered from four types of sensors, thermographic camera, fiber optic with Rayleigh back scattering, DIC displacement and strain sensors and voltage-current. This experimental data has been correlated with a 3D transient parametric computer model, VrWeld, that computes transient 3D temperature, microstructure, displacement, strain and stress. Both the experimental data and the virtual data have limited resolution in space and time and both have errors with respect to some expected ground truth for the real weld. In the authors' opinion, the correlation shows that the computer model has the potential to provide useful predictions for the design and optimization of welds and welded structures.

The most important lesson learned in this study is that as the accuracy, spatial resolution and temporal resolution of the sensor systems and the computer model increase, it becomes ever more important to synchronize the real and virtual clocks and the real and virtual spatial coordinate systems. The clock of each sensor system should not be set to zero at the start of an experiment. The clock of each sensor system should be set to Greenwich Mean Time. Also each sensor for spatial data should have fiducial marks that enable to the spatial coordinate system to computed for each set of spatial data.

The methods that were developed for synchronizing the real and virtual clocks and particularly the coordinate frames have been described. This is an essential part of correlating real and virtual data. In this study, the various sensor data systems had separate clocks. A data acquisition sensor that synchronized all sensor clocks in real time would be an improvement.

For example, adding at least four infrared LEDs fixed to the plate that could be captured by the thermographic camera is one possibility. The thermographic camera was hand held. A camera fixed in space would reduce camera motion. Although a thermographic camera that could record temperatures above 400°C would provide additional data, we were pleasantly surprised by the data this camera provided. Since the area of the 300°C isotherm was 10 mm<sup>2</sup> while the total area of the plate was 9x10<sup>4</sup> mm<sup>2</sup> (300 mm by 300 mm), as such the area not sampled by the FLIR camera represents less than 0.01% (10/9x10<sup>4</sup>) of the total area of the plate. Thus, 99.99% of the plate was sampled by the FLIR camera. Because the fields for temperatures below 400°C are very smooth and have low frequency modes, it is not essential to have a high-resolution camera. We could fit a polynomial to virtual

temperatures below 400°C. We would expect that the polynomial would be a low degree polynomial.

For each real thermal sensor, a set of 9 virtual thermal sensor's in the pattern of a 9-node quadrilateral FEM element and the centroid of the pattern the position specified for the real thermal sensor could be made. The quad edge length could be chosen to approximate the probable error in the position of the real thermal sensor. Then at a later stage of synchronizing real and virtual thermal sensors, one could choose the virtual real thermal sensor in the pattern that best matched the data for the real thermal sensor or interpolate data in the virtual pattern to estimate error in the position of the real thermocouple.

A global optimal design of experiment algorithm has been used with various objective functions that measure the difference between real and virtual data to optimize some of the parameters in the computer model for a parametric design space. To the author's knowledge, our demonstration of the correlation of transient space-time data from four sensor systems with a 3D parametric computer model of the weld is novel. In other research areas this might be called Data Fusion or Data Analytics, Deep Learning or artificial neural networks. They are all based on standard mathematics of statistics.

To the author's knowledge, this is the first demonstration of a local 3D transient Eulerian Ohjii-Sudnik weld pool model that is coupled with a microstructure solver. To the author's knowledge, this is the first publication of a 3D transient weld pool model that supports weave weld patterns. The solver for this weld pool model was then coupled with Lagrangian thermal and stress global solvers to compute transient 3D temperature, microstructure, displacement, stress and strain fields. As part of future work, we plan a detailed correlation between real and virtual microstructure evolution. It would be useful to use computer vision to measure the transient 3D geometry of the weld pool surface. This would enable one to define objective functions to optimize the design parameters for this weld pool model such as surface tension and arc pressure distribution.

The challenge of working with a manual weld is that the local weld speed, and transverse oscillations of the arc as a function of time are not known. Nevertheless, from both thermographic data and the DIC data, it was possible to estimate the actual local weld speed as a function of time. The uncertainty in the local weld speed would be expected to be less of a problem with welds made with a robot. However, because it is the reality of manual welds and because manual welds are an important welding technology it is important to study manual welds.

While [7] focusses on verification and validation of the computer models in computation weld mechanics, this study suggests that it is equally important to assess the accuracy of experimental data.

R.D. Rasch et al. in [8] wrote "Optimal research design implies that the objective of the investigation is determined in detail before the experiment or survey is carried out and that the precision requirements for the type of analysis planned for the data using the chosen statistical model are formulated and that all possible things which would have a negative

influence on the research work or could bias or disturb the results are considered. This all makes work, takes time, and is much more difficult than simply starting with the practical investigation and formulating the objective of the study after the data have been collected and then seeing the reliability the results have. Another reason that design methods are not used as much as they could or should be is that the designs are spread throughout a huge number of articles and books and they are sometimes not easy for the experimenter to understand.”

The authors did not achieve this goal, but we did make progress toward this goal.

### REFERENCES

- [1] Website: [www.lunainc.com](http://www.lunainc.com), last accessed July 18-2018.
- [2] Website: [www.correlatedsolutions.com](http://www.correlatedsolutions.com), last accessed July 18-2018.
- [3] T. OHJI, T. MATSUTANI, F. MIYASKA and Y. HIRATA, *A mathematical model for circumferential GTA welding of pipe*, IIW Doc. 212-892-96.
- [4] W. SUDNIK, D. RADAJ, W. EROFREW, *Validation of computerized simulation of welding processes*, *Mathematical Modelling of Weld Phenomena 4*, Editors H. Cerjak, H. K. D. H. Bhadeshia,
- [5] J. A. GOLDAK, A. CHAKRAVARTI and M. J. BIBBY, *A New Finite Element Model for Welding Heat Sources*, *Trans. AIME.*, Vol. 15B, June 1984, pp. 299-305.
- [6] JONES, D.R., SCHONLAU, M. AND WELCH W.J. (1998). *Efficient global optimization of expensive black-box functions*. *Journal of Global Optimization*, 13, 455-492.
- [7] *Guide for Verification and Validation in Computation Weld Mechanics 1st Edition*, AWS A9.5:2013 An American National Standard Approved by the American National Standards Institute October 30, 2012.
- [8] R.D. RASCH, J. PILZ, R. VERDOOREN, A. GEBHARDT, *Optimal Experimental Design with R*, *Chapman and Hall*, 2011.

# INVESTIGATION OF THE INFLUENCE OF THE WELDING SPEED AND CURRENT ON THE PARAMETERS OF THE ADAPTIVE FUNCTION

M. B. NASIRI\*, A. PUTZ\* and N. ENZINGER\*

*\* Institute of Materials Science, Joining and Forming, Graz University of Technology, Graz 8010, Austria, Email:  
Mohammad.nasiri@tugraz.at*

DOI 10.3217/978-3-85125-615-4-44

## ABSTRACT

The adaptive function developed by authors allows direct correlation between welding circumstances and temperature distribution using limited experimental data including weld pool dimensions and temperature at some arbitrary points. This paper intends to investigate the effects of welding speed and welding current on the parameters of the adaptive function. GTAW with various welding speeds and various welding currents was applied on duplex stainless steel plates. According to the experimental data, the parameters of the adaptive function were expressed as a function of welding speed and weld pool dimensions. To show the effectiveness of the new method, Rosenthal model and FEM were employed to simulate the conducted welding and the accuracy of the predicted result rather than the measured temperature were estimated by relative error. The results show that the adaptive function method is more accurate than the FEM and Rosenthal approach in all studied cases.

Keywords: Welding Simulation, Heat Flow, Analytical Solution, Partial Differential Equation, FEM

## INTRODUCTION

Modelling and simulation of the thermal cycle and the subsequent mechanical behaviours have been investigated for more than 80 years. Analytical, numerical and empirical approaches have been employed to solve the heat flow problem in welding [1]. However, the proposed solutions have shown an only limited success. Analytical solutions such as Rosenthal solution are limited by accuracy [2] and numerical solutions are computationally expensive [3]. The adaptive function method (AFM) is based on a mathematical 3D function which can be adjusted using experimental data and it can be used to solve the partial differential equation of any moving heat source with high accuracy and low computation cost [4]. The parameters of the adaptive function are directly determined by temperature measurement and no information about material properties, phase transformation, and heat source parameters are required [4]. Therefore, the adaptive function method is able to overcome the obstacles of inaccuracy and computation cost. This paper intends to study the dependency of the parameters of the adaptive function to the welding speed and welding current and make a correlation between them.

EXPERIMENTAL SETUP

A Gas Tungsten Arc Welding (GTAW) process using argon as shielding gas with various welding speed and welding current given in Table 1 was applied on duplex stainless steel plates with the dimensions given in Table 2 and chemical composition given in Table 3. Tests No. 1-4 were conducted with a same welding current of 150A; and welding speed varies from 7 to 12cm/min. The welding speed was constant for test series No. 2, 5-8 and in this series the welding current differs from 125 to 175 A. The welding parameters of test No. 7 and 8 are same as test No. 5 and 2 respectively but in these cases, the temperature of the bottom surface of the plate were measured instead of the top surface. Experimental data including weld pool dimension and temperatures measured at specified points were extracted to be used in modelling. The temperature history of points at positions shown in Fig. 1, were measured by type K thermocouples (0.3 mm in diameter). After welding the width (W), depth (D), rear tail ( $L_r$ ) and front radius ( $L_f$ ) of the weld pool were measured on the samples and are presented in Table 4. Fig. 2 shows the macrograph of the weld bead of the test No. 6.

**Table 1** Parameters of the welding process at the constant welding voltage of 14V

Test No.	Welding current (A)	Speed (cm/min)
1	150	7
2		8.4
3		10
4		12
5	125	8.4
6	175	
7	125	
8	150	

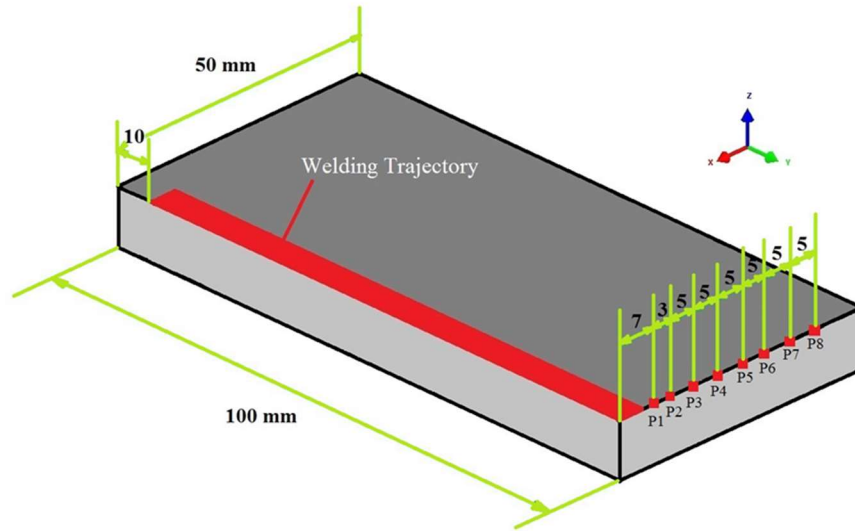
**Table 2** Dimensions of the welding plate

Plate size (mm)		
Width	length	thickness
100	200	10

## Mathematical Modelling of Weld Phenomena 12

**Table 3** Chemical composition of the duplex stainless steel 1.4462 plates

Element	C	Mn	P	S	Si	Cu	Cr	Ni	Mo	Nb	N
Weight %	0.026	1.9	0.02	0.007	0.67	0.47	23	5.5	3	0.5	0.2



**Fig. 1** Schematic of a quarter of the welding plate and the position of the thermocouples which are all in one line

**Table 4** Weld pool dimensions (mm)

Test No.	W	L <sub>f</sub>	L <sub>r</sub>	D
1	4.6	3.8	8.5	2.1
2	4.3	3.3	7.4	1.9
3	4.0	2.8	6.2	1.7
4	3.7	2.3	5.2	1.5
5	3.8	2.8	5.4	1.7
6	5.2	3.8	9.6	2.1
7	3.8	2.8	5.4	1.7
8	4.3	3.3	7.4	1.9



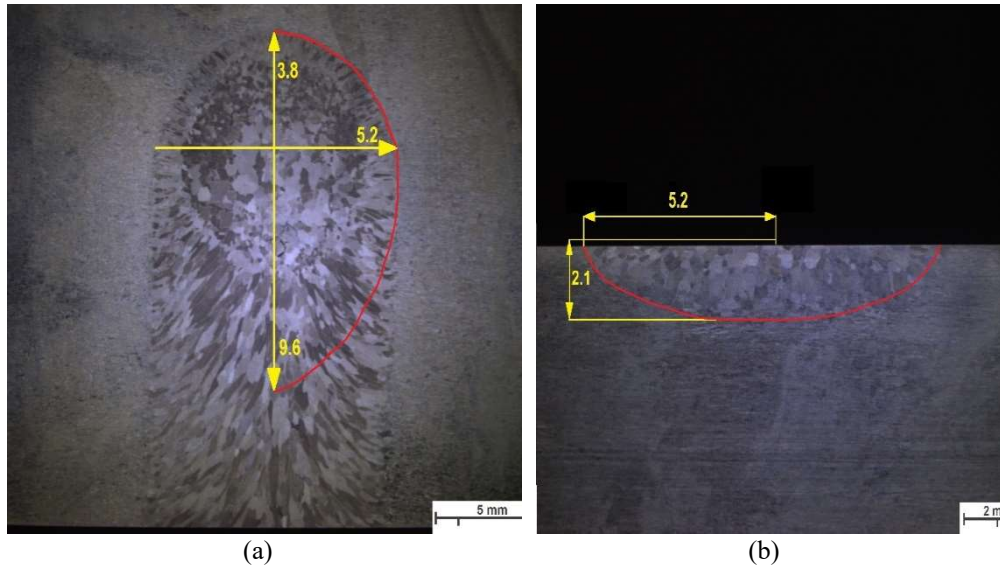


Fig. 2 Macrograph of the bead of the test No.6 (a) upper view (b) cross section

### MODELING METHODS

The conducted welding tests were simulated by Rosenthal's model and FEM beside the AFM to examine the accuracy of the available methods in different welding cases.

#### ROSENTHAL METHOD

The theory of heat conduction that was developed by Fourier and applied to a moving heat sources by Rosenthal [5] is the most popular and simplified analytical method used to calculate the thermal history of welds. The quasi-steady state solution of Rosenthal using the transformation presented by Eq. 1 for a semi-infinite plate expresses temperature as a function of the position and constant physical properties of the material (Eq. 2) when the point heat source moves along the y-axis. A Matlab routine was developed to calculate the temperature field based on Rosenthal's model. The constant thermo-physical properties of duplex stainless steel were considered according to the Table 5 and the arc thermal efficiency of GTAW was considered to be 0.7 [6].

$$\xi = y - vt \quad (1)$$

$$T = T_0 + \frac{Q}{2\pi kR} e^{\left(-\frac{\rho cv}{2k}(R+\xi)\right)} \quad (2)$$

$$R = \sqrt{x^2 + \xi^2 + z^2} \quad (3)$$

**Table 5** Material properties of Duplex stainless steel at room temperature [7], [8]

Heat capacity (J/kg °C)	Density (kg/m <sup>2</sup> )	Conductivity(J/m)	Melting Point(°C)
495	7990	15	1400

By considering the quasi-steady state condition, the measured temperature history (time-temperature) of a point can be converted into a spatial temperature distribution along the y-axis (y-temperature) using Eq. 1. Accordingly, the temperature distribution along the y-axis at 7, 10, 15, 20, 25, 30, 35 and, 40mm away from the centreline, were calculated according to the recorded temperatures at points P1- P8 (Fig. 1). Fig. 3 shows the result of Rosenthal model for upper surface along with calculated and measured fusion line in x-y cross-sections and the relative errors based on the measured temperature [4]. According to the result, the accuracy of Rosenthal’s model is low in the prediction of the weld pool size and the relative error of calculated temperature is between 37-53% in the case of test No.1.

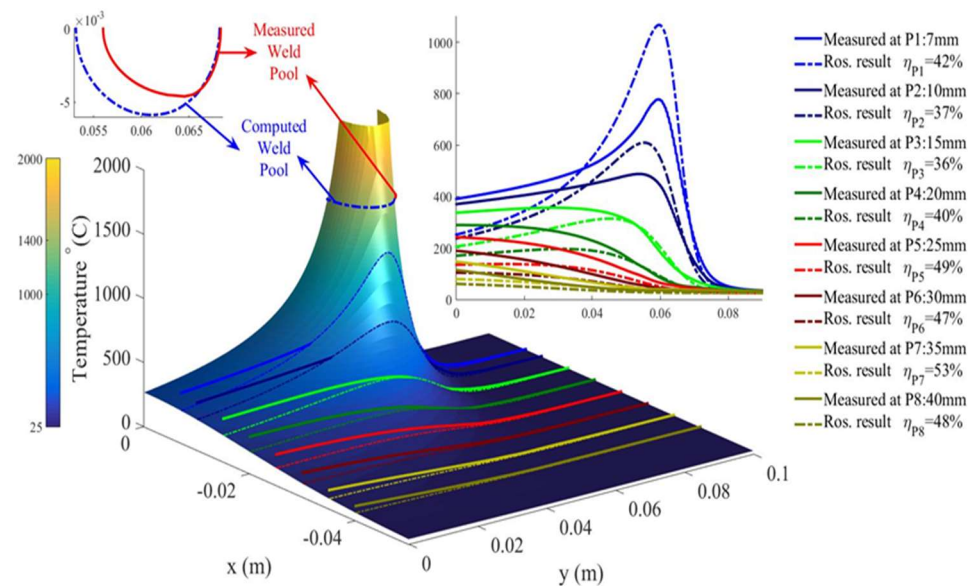


**Fig. 3** Temperature distribution on the upper surface of the plate as calculated with the Rosenthal equation for test No. 1(welding speed 7 cm/min, welding current 150A)

FINITE ELEMENT METHOD (FEM)

The thermal fields and the weld pool dimensions of the bead on plate gas tungsten arc welding have been investigated by using SYSWELD, a software package that can be used to conduct numerical analyses of welding processes. The minimum mesh size was

considered 0.5 mm for elements close to the welding trajectory, and 8 mm mesh size was considered as the maximum at the edges of the plate as shown in Fig. 4. The parameters of the double ellipsoidal heat source model are presented in Table 6 and the arc efficiency considered to be 0.7 [6]. The material properties considered to be temperature dependent according to the SYSWELD database. The initial temperature was set at 25°C and heat losses due to convection and radiation were taken into account using SYSWELD database for natural air cooling medium [9].

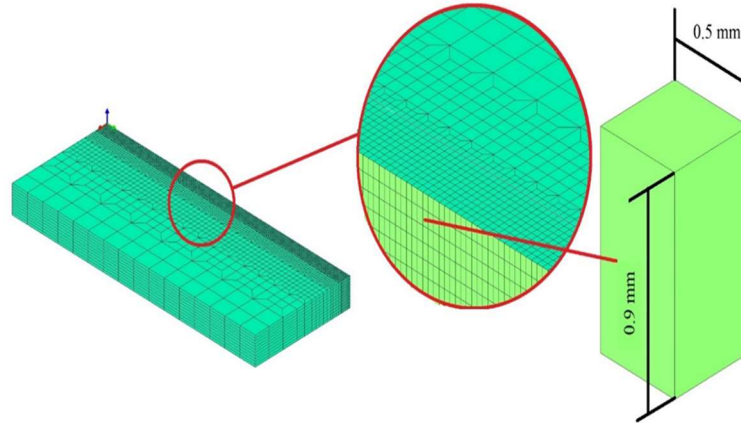
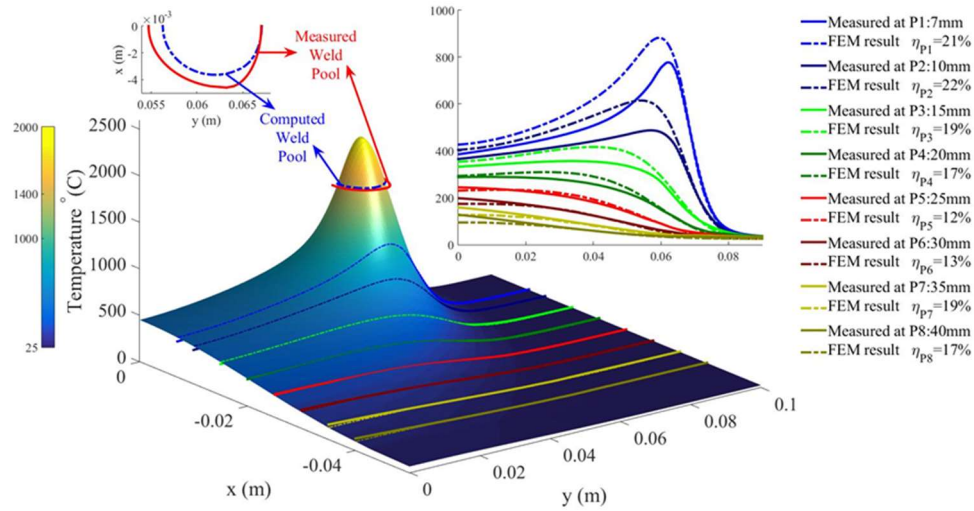


Fig. 4 Half of the FEM model

Table 6 Double ellipsoidal heat source parameters (Goldak's model) [9], [10]

Test No.	Width ( $2 \times a_w$ ) (mm)	Length ( $b_{hf} + b_{hr}$ ) (mm)	Penetration ( $c_w$ ) (mm)	Length Ratio ( $\frac{b_{hf}}{b_{hr}}$ )	Energy per length ( $\frac{I}{mm}$ )
1	8.28	11.07	1.98		
2	7.74	9.63	1.71	0.45	1470
3	7.2	8.1	1.53		
4	6.75	6.75	1.35		
5	6.84	7.38	1.53	0.5	1225
6	9	11.92	1.98	0.38	1715
7	6.84	7.38	1.53	0.5	1225
8	7.74	9.63	1.71	0.45	1470

Fig. 5 shows the result of the FEM simulation of test No. 1 on the upper surface and compares the experimental data with the computed result. The relative error of the FEM, in this case, is 12-22% that shows the FEM is almost 58-67% more accurate than the Rosenthal's approach.



**Fig. 5** Temperature distribution on the upper surface of the plate of test No. 1 as calculated with the FEM (welding speed 7 cm/min, welding current 150A)

ADAPTIVE FUNCTION METHOD

The rigid formulation of Eq. 2 does not allow for changes in such a way, that the result can be matched to the measured temperature. The material properties and arc thermal efficiency are just the parameters of the Rosenthal's equations that can be manipulated to increase the accuracy of the Rosenthal's solution. However, the different values of those parameters may improve local accuracy at a point but may destroy accuracy in other places and therefore several researchers tried to modify the Rosenthal's equations which shows limited success [2], [11], [12], [13], [14], and [15]. In the case of the FEM method, the accuracy might increase by considering more accurate heat source model, material properties or boundary conditions which are required more computational and experimental works. High accuracy in the weld pool and its adjacent area can be obtained using a suitable heat source model or manipulating the parameters of the heat source model by trial and error [16]. The material properties which are used in FEM require considering the deconvergence effect of sharp changes in material properties which inhibits accuracy improvement of the FEM [17]. The principle of the adaptive function method is based on a function which can be matched to the measured temperature by determining some limited parameters directly by using experimental data. In fact, the adaptive function method proposes that instead of dealing with mathematical models of the physical phenomena which occur in welding, we can consider the cumulative effects of those phenomena which appear in the form of temperature distribution and weld pool dimensions. The adaptive function is developed by manipulating the Rosenthal equation so that the calculated fusion line coincides with the measurement. Accordingly, the term R (Eq. 3) in the Rosenthal's equation which is the mathematical equation of a sphere is replaced by the equation of an ellipsoid. To coincide with the temperature distribution in the rest of the welding sample with the reality a

modification function is proposed which adjusts the temperature gradient along the main axis. The proposed adaptive function is as follows [4]:

$$T = T_0 + \frac{1}{R_p} e^{(-B(R+y))} \quad (4)$$

$$R_p = \sqrt{\left(f\left(\frac{x}{W}\right) \times \frac{x}{a_m}\right)^2 + \left(f\left(\frac{\xi}{L_f}\right) \times \frac{\xi}{b_m}\right)^2 + \left(f\left(\frac{z}{D}\right) \times \frac{z}{c_m}\right)^2 + d_m^2} \quad ; \xi \geq 0 \quad (5)$$

$$R_p = \sqrt{\left(f\left(\frac{x}{W}\right) \times \frac{x}{a_m}\right)^2 + \left(f\left(\frac{\xi}{L_r}\right) \times \frac{\xi}{b_m}\right)^2 + \left(f\left(\frac{z}{D}\right) \times \frac{z}{c_m}\right)^2 + d_m^2} \quad ; \xi < 0 \quad (6)$$

$$f(\omega) = \left(M\omega^2 - M\sqrt{\omega^2 + 1}\right)^N \quad (7)$$

The parameters of the adaptive function including  $a_m$ ,  $b_m$  and  $c_m$  cause the adaptive function to match the real fusion line. The parameter  $d_m$  removes the singularity in the origin of the moving heat source, and it is the main factor which determines the maximum temperature at the origin (centre of the heat source) [4]. By considering the weld pool dimensions and an estimated maximum temperature  $T_{max}$  from the experiment, the optimum values of the parameters are determined so that the calculated fusion line coincides with the measurement [4].

The term  $\frac{k}{\rho c}$  in Eq. 2 is heat diffusivity which is a temperature-dependent material property in the solid state, while the heat diffusivity in the weld pool strongly depends on the mass transfer. Since it is not possible to consider the temperature dependency of the physical properties and the mass transfer with an analytical equation, the term  $\frac{\rho c}{2k}v$  is substituted by a constant value of B as a function of welding speed which is considered to be a parameter of the adaptive function.

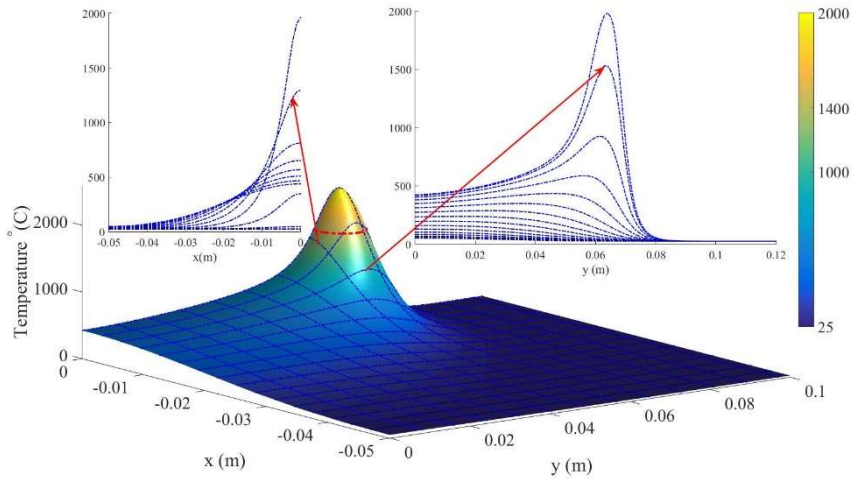
$$B = \frac{\rho c}{2k}v \quad (8)$$

The modification function  $f$  is a function of dimensionless parameter of  $\omega$  which changes the scale from a length unit (m) to the scale of the weld pool dimensions. In order to avoid changing the melting isotherm, the modification function  $f(\omega)$  is always 1 everywhere along the fusion line, which is defined by Eq. 9.

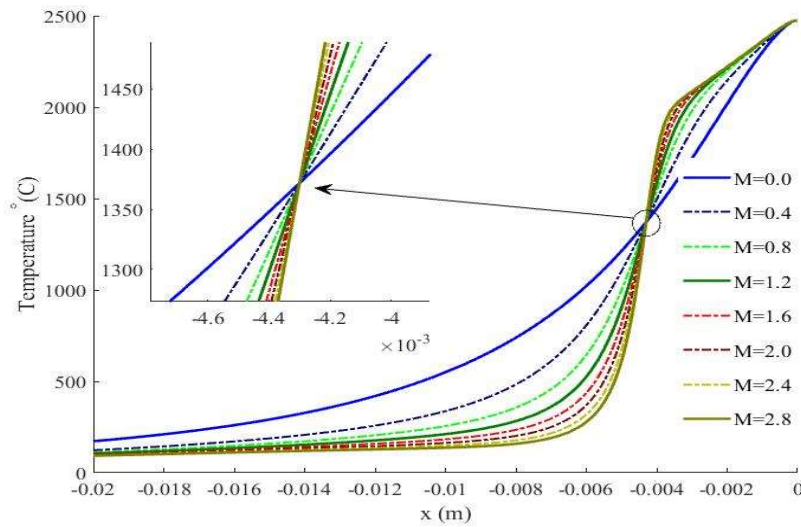
$$\omega_x = \frac{x}{W} ; \omega_{\xi f} = \frac{\xi}{L_f} ; \omega_{\xi r} = \frac{\xi}{L_r} ; \omega_z = \frac{z}{D} \quad (9)$$

Fig. 6 shows the result of the FEM for the upper surface of the sample of test No.2. As shown in Fig. 6, welding temperature curves in any cross section parallel to the main axis, have a special waveform shape. The M and N as parameters of the modification function provide the flexibility so that the proposed adaptive function (Eq. 4) could reproduce this waveform curve. According to the Eq. 7 parameter M mainly control the slope of temperature in the fusion line where  $\omega$  is 1 Fig. 7 and Fig. 8 show the temperature curve along y-axis and x-axis on the upper surface of the plate of test No.2 with different values of M. As shown in Fig. 7 and Fig. 8 by changing the values of M temperature gradient can

be changed in the fusion line while the weld pool size and the maximum temperature do not change [4].



**Fig. 6** Temperature distribution on the upper surface of the plate of test No.2 as calculated with the FEM and waveform curve cross section parallel to the x and y-axis



**Fig. 7** Effect of parameter M on temperature curve along the x-axis at point  $\xi=0$  on the upper surface of welding sample of the test No. 2

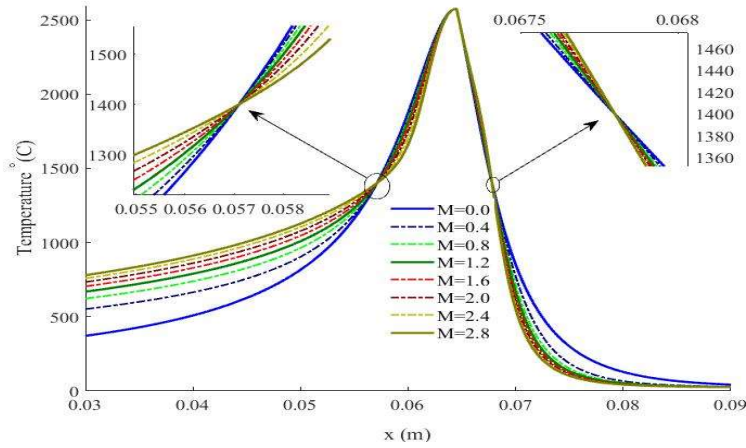


**Fig. 8** Effect of parameter M on temperature curve along the y-axis at point x=0 on the upper surface of welding sample of the test No. 2

The temperature gradient can also be controlled by N in each direction of heat flow. For instance, as shown in Fig. 9, the temperature gradient of the rear part of the temperature curve changes by changing the N parameter in this direction ( $N_{yr}$ ). The flexibility of the adaptive function to get matched to any curve with such configuration is provided by the parameters of the modification function (M,  $N_x$ ,  $N_{yf}$ ,  $N_{yr}$ , and  $N_z$ ) each of which particularly affects a certain part of the temperature curve [4].

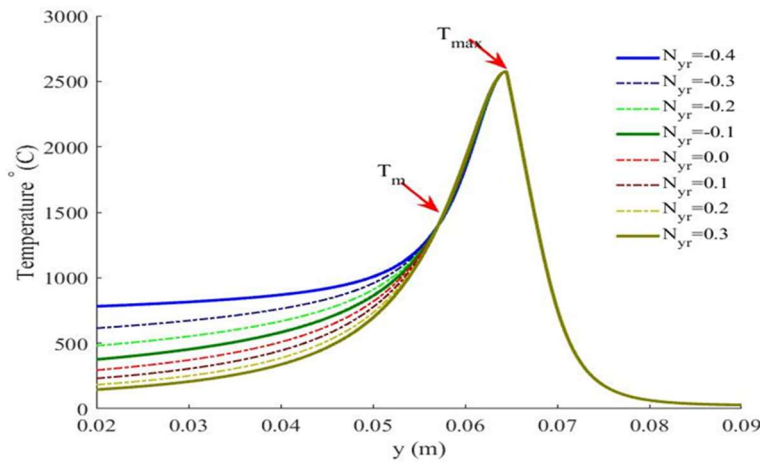


**Fig. 9** effect of parameter  $N_{yr}$  on temperature curve along the y-axis at point x=0 on the upper surface of welding sample of the test No. 2

ESTIMATION OF THE PARAMETERS OF THE ADAPTIVE FUNCTION

The parameters of the adaptive function are classified into adaptive function parameters including  $a_m, b_m, c_m, d_m$  and B and parameters of the modification function including M,  $N_x, N_{yf}, N_{yr}$  and  $N_z$ . According to Eq. 8, the parameter B is a function of the heat diffusivity and welding speed. Since the heat diffusivity is a temperature dependent and it is not possible to consider variable material properties in an analytical solution, an optimum constant value is considered for the heat diffusivity of each welding material based on the estimated maximum temperature (Tmax) [4]. The parameters of  $a_m, b_m, c_m, d_m$  are determined according to the weld pool dimensions using Eq. 4. To compensate for the discrepancies between the results of the adaptive function and measured temperature, the parameters of the modification function are adjusted in such a way that the computation error is reduced. The M parameter is assumed to be constant and therefore the parameters of  $N_x, N_{yf}, N_{yr}$ , and  $N_z$  can vary by the dimensionless parameter of  $\omega$ . A MatLab routine developed to estimate the optimum values of the parameters of the modification function according to the measured temperature in such a way that the computation error is reduced. The computation error is the relative error of the calculated temperature compared to the measured temperature based on a method proposed in [4]. Table 7 presents the constant parameters of the adaptive function for tests No.1-8. The maximum temperature of 2500 °C was assumed at the origin of the moving coordinate system and accordingly the estimated value of  $\frac{\rho c}{2k}$  is  $7571 S/m^2$  and thus, the parameter B changes in accordance with the welding speed ( $v$ ). The accuracy of the result of the adaptive function shows low sensitivity to the values of  $N_z$  and  $N_{yf}$ . Therefore, an optimum constant values were estimated for  $N_z$  and  $N_{yf}$ .

**Table 7** Parameters of the adaptive function for test No. 1-8

Test No.	$a_m$	$b_m$	$c_m$	$d_m \times 10^{-4}$	$B = \frac{\rho c}{2k} v$ ( $1/m$ )	M	$N_z$	$N_{yf}$
1	11.45	14.06	4.35	4.03	53.5			
2	11.02	12.09	3.71	3.92	63.6			
3	10.71	10.06	3.33	3.86	75.7			
4	11.23	8.51	3.27	3.96	90.8			
5	9.34	8.91	3.03	3.99		0.45	-0.44	0.45
6	14.13	15.69	4.44	3.94				
7	9.34	8.91	3.03	3.99	63.6			
8	11.02	12.09	3.71	3.92				

Fig. 10 shows the estimated  $N_x$  as a function of  $\omega_x$ . As shown in Fig. 10 by increasing  $\omega_x$ , the parameter  $N_x$  decreases. Eq. 10 is a proposed extrapolation function of  $N_x$  according to the  $\omega_x$ . Fig. 11 shows the estimated values of  $N_{yr}$  as a function of  $\omega_x$  and rear tail of the weld pool ( $L_r$ ). Eq. 11 is a linear extrapolation function for  $N_{yr}$ .

$$N_x(\omega_x) = \frac{4.3}{\omega_x^2 + 0.61} + 0.015 \tag{10}$$

$$N_{yr}(\omega_x, L_r) = -4.7\omega_x \times L_r + 0.02\omega_x + 4.4L_r - 0.24 \tag{11}$$



## Mathematical Modelling of Weld Phenomena 12

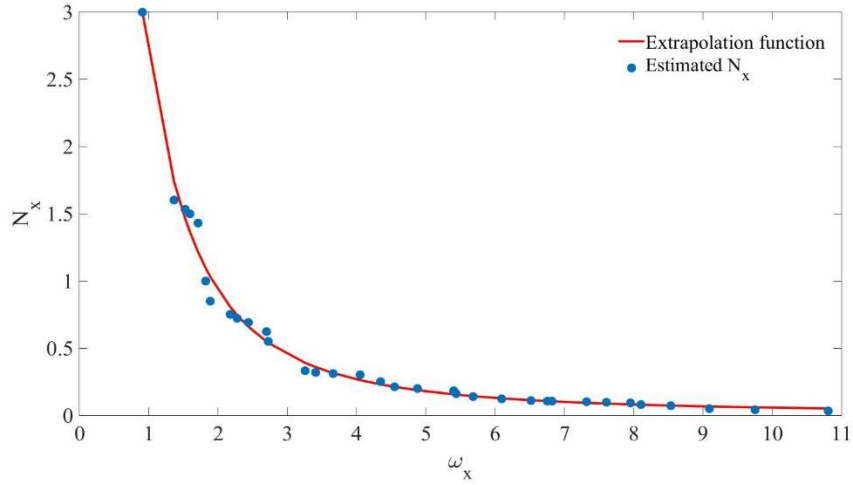


**Fig. 10** Estimated  $N_x$  for test No. 1-4 as a function of  $\omega_x$  and extrapolation function result (Eq. 10)

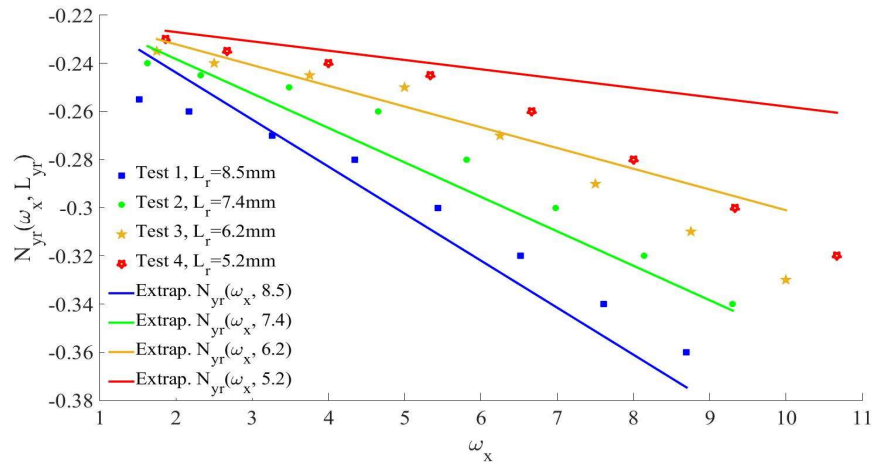
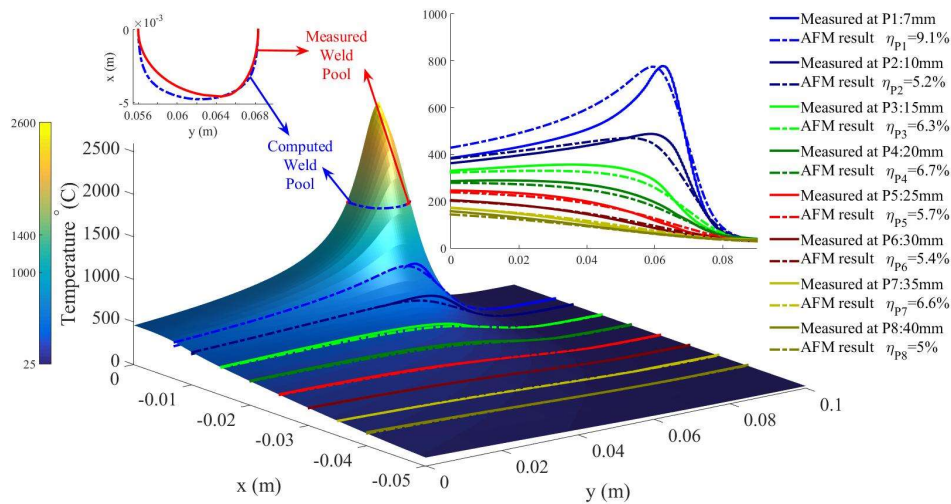


**Fig. 11** Estimated  $N_{yr}$  for test No. 1-4 as a function of  $\omega_x$  and  $L_r$  and extrapolation function result (Eq. 11)

ADAPTIVE FUNCTION RESULTS

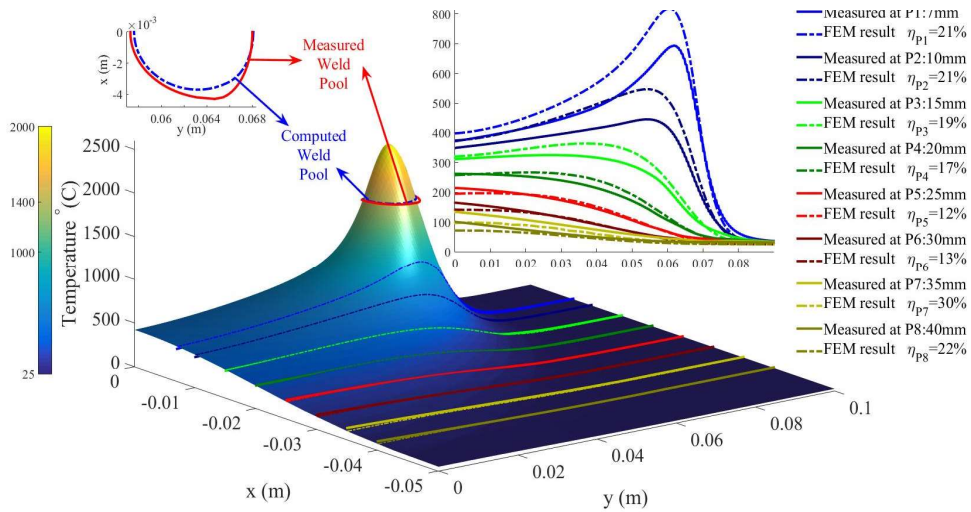
RESULTS OF THE ADAPTIVE FUNCTION METHOD

Fig. 12 shows the temperature distribution on the upper surface of the welding plate of test No.1 calculated by the adaptive function. As shown in Fig. 12 the calculated fusion line by the adaptive function method matches to the measured fusion line quite well. The relative error of the calculated temperature rather than the measured temperature is between 5-9% while the relative error of the FEM in the case of the test No. 1 (Fig. 3) is 12-22% which shows almost 60% improvement. Fig. 13 and 14 show the temperature distribution on the upper surface of the plate of test No.2 calculated by FEM and adaptive function respectively. In the case of the test No. 2, the relative error of the adaptive function is less than 8% and the relative error of the FEM is more than 12%. It is worth noting that the computation cost including computation time, verification and data provisioning in case of the adaptive function is much less than the FEM which discussed in reference [4] with detail.



**Fig. 12** Temperature distribution on the upper surface of the welding sample of test No. 1 as calculated with the adaptive function approach (welding speed 7 cm/min, welding current 150A)

## Mathematical Modelling of Weld Phenomena 12



**Fig. 13** Temperature distribution on the upper surface of the welding sample of test No. 2 as calculated with the FEM (welding speed: 8.4 cm/min, welding current: 150A)

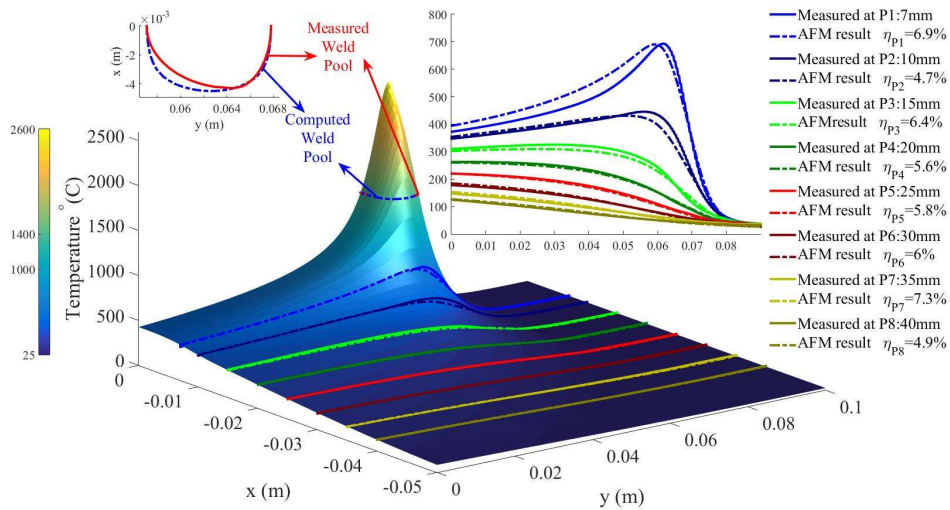


**Fig. 14** Temperature distribution on the upper surface of the welding sample of test No. 2 as calculated with the adaptive function approach (welding speed:8.4 cm/min, welding current:150A)

# Mathematical Modelling of Weld Phenomena 12

## WELDING SPEED EFFECT

Fig. 15-18 show the measured and calculated time-temperature curves at point 1-8 for tests No. 1-4. According to the Table 1, the welding speed for test No.1-4 are 7, 8.4, and 10 and, 12cm/min respectively, therefore the parameter B changes accordingly (Table 7). The constant parameters given in Table 7 and Eq. 10 and 11 were used as the parameters of the adaptive function. The overall relative error of 5.3, 4.9, 5.1, and 5.1% were calculated for tests No. 1-4 respectively which shows high accuracy of the adaptive function in different welding speed. As shown in Fig. 19 by increasing welding speed, heat input decreases and thus, the peak temperature decreases at the same measuring points.

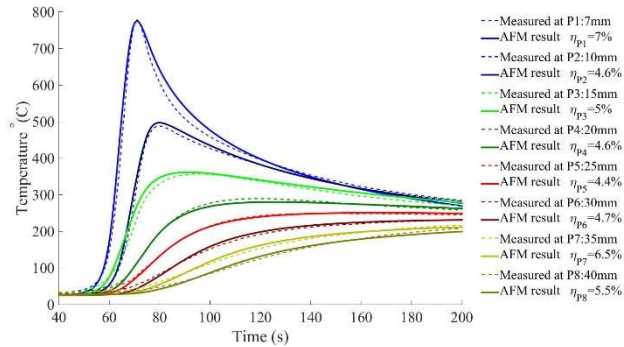


**Fig. 15** Time-temperature curve measured and calculated by the adaptive function for test No.1 (speed: 7 cm/min)

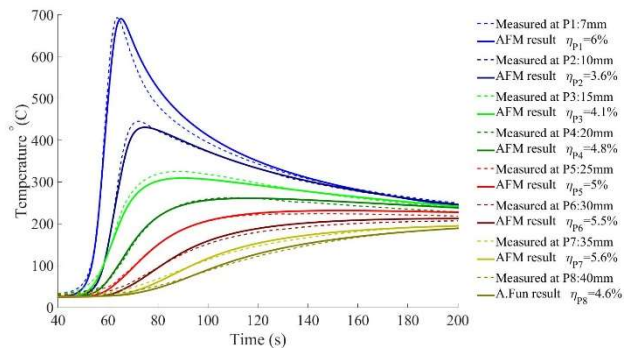


**Fig. 16** Time-temperature curve measured and calculated by the adaptive function for test No.2 (speed: 8.4 cm/min)

## Mathematical Modelling of Weld Phenomena 12

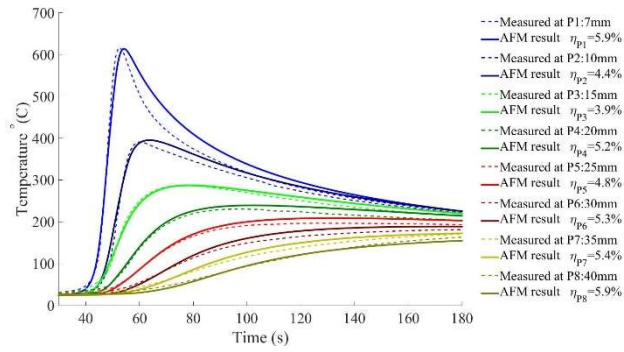


**Fig. 17** Time-temperature curve measured and calculated by the adaptive function for test No.3 (speed: 10 cm/min)

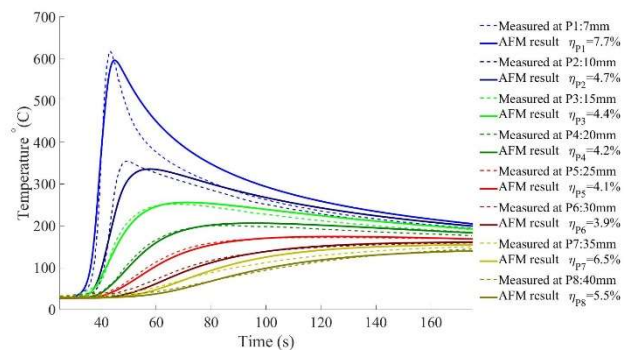


**Fig. 18** Time-temperature curve measured and calculated by the adaptive function for test No.4 (speed 12 cm/min)

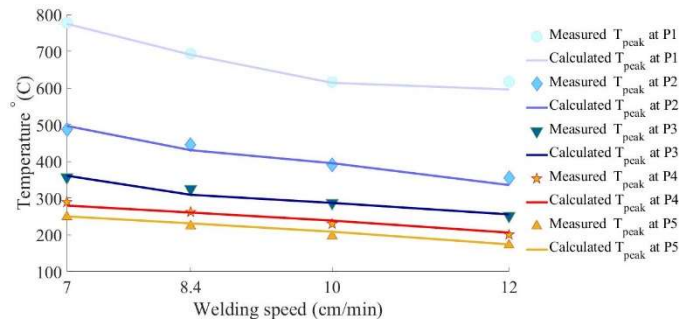


**Fig. 19** Peak temperature of P1-P5 as a function of welding speed

# Mathematical Modelling of Weld Phenomena 12

## WELDING CURRENT EFFECT

Fig. 20 and Fig. 21 show the measured and calculated time-temperature curves at point 1-8 for tests No. 5 and 6 with welding speed of  $8.4 \frac{cm}{min}$  and welding current of 125 and 175 A. The welding speed of test No. 2 is also  $8.4 \frac{cm}{min}$  while the welding current is 150 A. As shown in Fig. 20, Fig. 16 and Fig. 21 the adaptive function is able to predict temperature with a high accuracy of 5% using the constant parameters given Table 7 and Eq. 10 and 11 as extrapolation functions of  $N_x$  and  $N_{yr}$ . As shown in Fig. 22 by increasing welding current, heat input increases and thus, the weld pool dimensions and peak temperature decrease at the same measuring points.

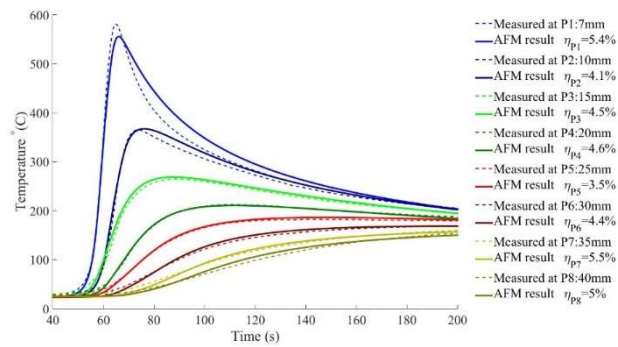


**Fig. 20** Time-temperature curves measured and calculated by the adaptive function for test No.5 (welding current 125A)

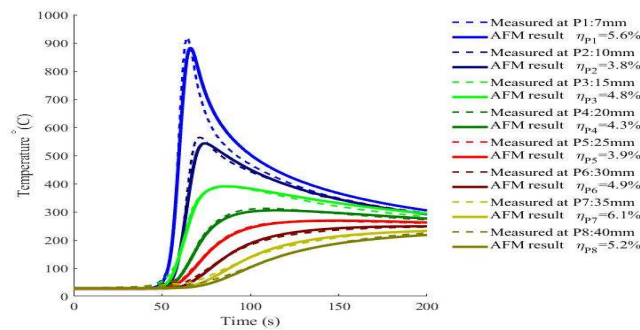


**Fig. 21** Time-temperature curves measured and calculated by the adaptive function for test No. 6 (welding current 175A)

## Mathematical Modelling of Weld Phenomena 12

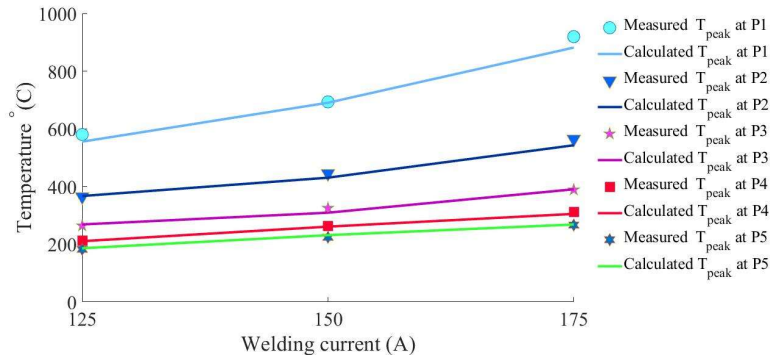


**Fig. 22** Peak temperature of P1-P5 as a function of welding current

Fig. 23 and 24 show the result of the adaptive function for test No.7 and 8. The welding parameters of test No.7 and 8 are the same as test No. 5 and 2 respectively but the temperature measurement has been done on the bottom surface. The result indicates that a constant value of  $N_z$  equal to -0.44 provides a good agreement between the adaptive function and measured temperature.

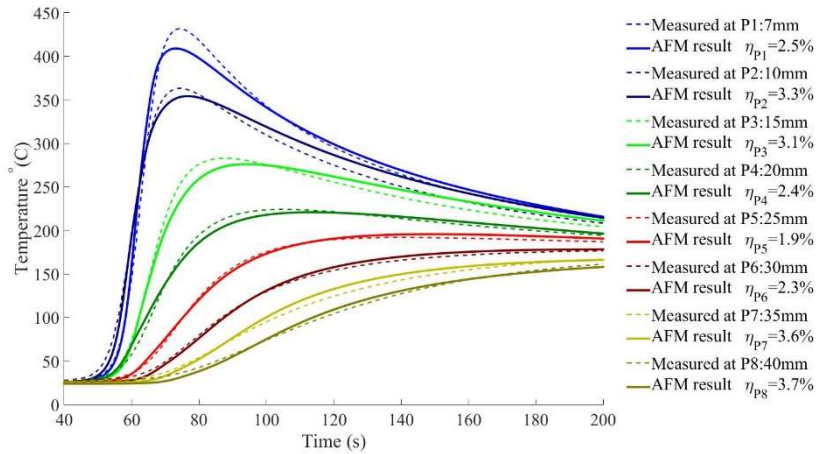


**Fig. 23** Time-temperature curves measured and calculated by the adaptive function for test No.7 (welding current 125A), thermocouples installed on the beneath of the plate

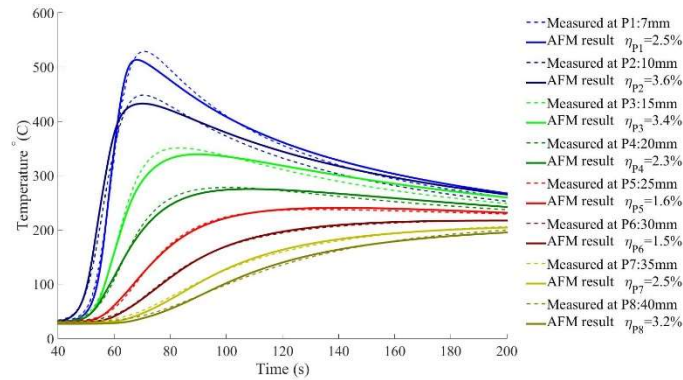


**Fig. 24** Time-temperature curves measured and calculated by the adaptive function for test No.8 (welding current 150A), thermocouples installed on the beneath of the plate

### CONCLUSION

In this paper, the new analytical model called “adaptive function method” (AFM) was applied to study the welding temperature distribution in different welding circumstances and a correlation between welding circumstance and the parameters of the adaptive function was developed. The heat flow problem in welding with various welding current and speed were solved by Rosenthal’s method, FEM, and the adaptive function method and the accuracy of the models compared. The results can be summarized as follows:

- The accuracy of the adaptive function is much higher than the other methods in all studied cases. The relative error of the adaptive function is almost 5% which is not comparable with FEM and Rosenthal’s approach.
- The parameters of the adaptive function are expressed as a function of a dimensionless parameter of  $\omega$  and  $L_{yr}$  (the rear tail of the weld pool). The weld pool dimension and dimensionless parameter can be expressed as a function of welding speed and current.

The adaptive function method is an effective solution to heat flow problem in welding with the most accurate result and low computation cost. Accordingly, the following advantages of the adaptive function method are expected:

- Since temperature calculation does not require meshing, the calculated temperature gradient helps us to develop an automatic adaptive meshing algorithm to apply in the mechanical simulation of welding.
- The parameters of the adaptive function are directly determined by temperature measurement and no information about material properties, phase transformation, and heat source parameters are required.



### REFERENCES

- [1] K. MASUBUCHI, Heat flow in weldments, in: *Anal. Welded Struct.*, Elsevier, 1980: pp. 60–87.
- [2] T.W. EAGAR, N.S. TSAI, Temperature fields produced by traveling distributed heat sources, *Weld. J.* 62 (1983) 346–355.
- [3] L.-E. LINDGREN, Finite Element Modeling and Simulation of Welding Part 1 :, *J. Therm. Stress.* 24 (2012) 141–192.
- [4] M.B. NASIRI, N. ENZINGER, Powerful analytical solution to heat flow problem in welding, *Int. J. Therm. Sci.* 135 (2019) 601–612. doi:10.1016/j.ijthermalsci.2018.08.003.
- [5] D. ROSENTHAL, The Theory of Moving Source of Heat and its Application to Metal Transfer, *ASME Trans.* 43 (1946) 849–866.
- [6] M.B. NASIRI, M. BEHZADINEJAD, H. LATIFI, J. MARTIKAINEN, Investigation on the influence of various welding parameters on the arc thermal efficiency of the GTAW process by calorimetric method, *J. Mech. Sci. Technol.* 28 (2014). doi:10.1007/s12206-014-0736-8.
- [7] W. ZHANG, T. DEBROY, T.A. PALMER, J.W. ELMER, Modeling of ferrite formation in a duplex stainless steel weld considering non-uniform starting microstructure, *Acta Mater.* 53 (2005) 4441–4453.
- [8] J.J. DEL COZ DÍAZ, P. MENÉNDEZ RODRÍGUEZ, P.J. GARCÍA NIETO, D. CASTRO-FRESNO, Comparative analysis of TIG welding distortions between austenitic and duplex stainless steels by FEM, *Appl. Therm. Eng.* 30 (2010) 2448–2459.
- [9] SYSTUS 2017: Reference Analysis Manual, ESI Group., 2017.
- [10] J. GOLDAK, A. CHAKRAVARTI, M. BIBBY, A new finite element model for welding heat sources, *Metall. Trans. B.* 15 (1984) 299–305.
- [11] C.M. ADAMS JR, Cooling rates and peak temperatures in fusion welding, *Weld. J.* 37 (1958) 210s–215s.
- [12] N. CHRISTENSEN, V. DAVIES, K. GJERMUNDSEN, Distribution of temperatures in arc welding, *Br. Weld. J.* 12 (1965) 54–75.
- [13] R. KOMANDURI, Z.B. HOU, Thermal analysis of the arc welding process: Part I. General solutions, *Metall. Mater. Trans. B.* 31 (2000) 1353–1370.
- [14] N.T. NGUYEN, A. OHTA, K. MATSUOKA, N. SUZUKI, Y. MAEDA, Analytical Solutions for Transient Temperature of Semi-Infinite Body Subjected to 3-D Moving Heat Sources, *Weld. Res. Suppl. I* (1999) 265–274.
- [15] S.K. JEONG, H.S. CHO, An analytical solution to predict the transient temperature distribution in fillet arc welds, *Weld. Journal-Including Weld. Res. Suppl.* 76 (1997) 223s.
- [16] A.S. AZAR, S.K. AS, O.M. AKSELSEN, Determination of welding heat source parameters from actual bead shape, *Comput. Mater. Sci.* 54 (2012) 176–182.
- [17] L.-E. LINDGREN, Finite Element Modeling and Simulation of Welding. Part 2: Improved Material Modeling, *J. Therm. Stress.* 24 (2001) 195–231.

PREDICTION OF GRAIN BOUNDARY  
EVOLUTION IN AN TITANIUM ALLOY  
SUBSTRATE USING A NOVEL PHASE FIELD  
MODEL COUPLED WITH A SEMI-  
ANALYTICAL THERMAL SOLUTION

T. F. FLINT\*, Q. XIONG\* Y. L. SUN\*, A. N. VASILEIOU\*,  
M. C. SMITH\* and J. A. FRANCIS\*

*\* Dalton Nuclear Institute, The University of Manchester, Manchester M13 9PL, UK  
Corresponding Author - Thomas.flint@manchester.ac.uk (Orcid: 0000-0002-0615-8621)*

DOI 10.3217/978-3-85125-615-4-45

ABSTRACT

Grain boundary migration in the presence of concentrated sources of heat is a complex process that has a considerable impact on resultant material properties. The large thermal gradients generated during welding cause grain boundaries to migrate in order to minimise the total free energy of the system. It is important to consider both the thermal gradient driving force, as well as the local curvature driving force of the grain boundaries which both play a significant role in the evolution of the micro-structure in the weld region. In this work a multi-phase field model is used to predict the grain boundary evolution in a Ti6Al4V substrate subjected to a heat source representative of the electron beam (EB) welding process. While numerical simulations incorporating the mass transfer and complex flow dynamics associated with high energy density welding processes are favourable in that they consider the physical processes occurring in the weld explicitly, they are also extremely computationally expensive. As such, the thermal field, on which the phase field model is dependent, is computed using a semi-analytical solution technique. In this approach the complicated flow dynamics of the EB process are represented as a four-quadrant volumetric heat source, the recently published DEC heat source which has shown to be a good thermal representation of EB processes. Using a Green's function approach, the time and position dependent thermal field is obtained for this DEC heat source in motion is found, free from numerical errors. Predicted grain size distributions are presented for various energy inputs and conclusions drawn based on the applied driving forces, captured in the phase field model

Keywords: Phase Field; High Energy Density; Analytical Solution; Grain Boundary Migration; Thermal Gradient

INTRODUCTION

Grain boundaries in alloy systems migrate in response to driving forces acting upon them, in such a manner as to minimise the total free energy in the entire system [14, 13]. The

resultant micro structure has strong effects on the physical properties and may favourably or adversely affect material performance and is therefore of great academic and industrial interest [5, 9, 7]. Recently, the effect of thermal gradient and curvature driving forces has been studied for an isotropic micro structure. It has been shown that the thermal gradient driving force is an important factor in determining the coarsening behaviour local to high energy density sources of heat, as are present in advanced manufacturing processes [5]. The thermal field induced in a domain may be calculated using a full thermal fluid dynamics approach; where the complex heat and mass transfer involved in the EB welding process was fully resolved and the physics fully captured for the most accurate prediction of the thermal fields and their spatial gradients [12]. While the thermal fluid dynamics approach is preferred, the computational cost is high. In this respect it is beneficial to use a semi-analytical solution procedure to calculate the thermal fields.

In this semi-analytical approach, the complex flow dynamics of the molten and vaporised substrate material is represented as a volumetric heat flux distribution. The most representative volumetric heat source model for high energy density welding processes is the double ellipsoidal conical (DEC) heat source model which was recently proposed [3]. With this approach the momentum equations are not explicitly solved, and the complex physics of the process is captured in the heat flux model. This semi-analytical approach has shown to be promising in the limiting case where the component geometry is orthogonal [2, 6]. Recently a semi-analytical solution was computed for the (DEC) heat source model using a Green's function approach and the method of images for construction of Dirichlet and/or Neumann boundary conditions [4]. The nature of the Greens function approach for the construction of the semi-analytical solution enables multiple heat sources to be considered. This ensures that the typical 'bugle' type fusion profile in EB welds is achieved [4]. A major advantage of the semi-analytical solution approach is that the entire domain of the weld under consideration need not be considered to compute the temperature history at a given set of points, this is attractive for the investigation of micro structural behaviour, due to complex thermal histories, at specific locations.

In this work the semi-analytical approach is used for the computationally efficient, yet physically justified, calculation of the thermal field induced in a Ti6Al4V substrate due to the application of a high energy density beam of electrons causing melting and vaporisation. The micro structural evolution in the substrate is predicted using a multi-phase field model considering boundary curvature and thermal gradient driving forces at grain interfaces. The computational domain for the simulations is placed in the heat affected zone (HAZ) of the Ti6Al4V substrate such that no state change is considered in the metallic substrate. The effect of welding travel speed on micro-structural evolution is investigated with conclusions drawn based on the physical justification of the chosen multi-phase field model.

### SOLUTION APPROACH

To predict the evolution of the temperature field due to a complex heat source and the evolution of the micro structure that this thermal field initiates; appropriate physical models and numerical techniques must be used. The multi-phase field model has been chosen for the simulation of the micro structural evolution as it is able to physically resolve important thermodynamic driving forces at the grain boundaries that determine migration behaviour.

The semi-analytical solution approach for the computation of the transient temperature fields has been chosen due to the unparalleled computational efficiency the approach offers, and the generation of a thermal field free from spatial numerical discretisation errors.

MULTI-PHASE FIELD MODEL

To predict the micro structural behaviour of the material under consideration a physics-based model, such as the phase-field model, should be used. This type of model incorporates various driving forces into the free energy functional of the system and can accurately predict the micro structural behaviour due to complex thermal fields. The velocity,  $v$ , of a migrating grain boundary is given as the superposition of the curvature driving pressure,  $F_c$ , and the thermal gradient driving pressure,  $F_t$  as shown in Equation 1

$$v = m(F_t + F_c) = m\left(\frac{\Delta S 2\lambda \nabla T}{\Omega} - \sigma \kappa\right) \quad (1)$$

where  $m$  is the GB mobility,  $\kappa$  is the local curvature,  $\Delta S$  is the entropy difference between the GB and the crystal which is approximately equal to the melting entropy,  $2\lambda$  is the GB width,  $T$  is the temperature and  $\Omega$  is the molar volume of the material and  $\sigma$  is the GB energy. [10, 7, 1]. In this work  $T$  is computed using the semi-analytical approach due to the application of a DEC heat flux in the heat equation. The evolution equation for the PF is then given by Equation 2

$$\frac{\partial \varphi_n}{\partial t} = \frac{2M_\varphi}{s} \sum_{p \neq n}^N s_p s_n \left( \frac{\delta F}{\delta \varphi_n} - \frac{\delta F}{\delta \varphi_p} \right) \quad (2)$$

where  $M_\varphi$  is the isotropic PF mobility [10, 14], and has the form  $M_\varphi = m\sigma/\epsilon^2 = \pi^2 m/16\xi$ . The parameters  $S$  and  $s$  are used to define the sum of the number of coexisting phases and a step function per phase respectively.  $m$  is strongly temperature dependent and is often assumed to follow an Arrhenius-type relationship as shown in Equation 3.

$$m = m_0 e^{-Q/k_B T} \quad (3)$$

The variation in the free energy density due to the GB curvature and thermal gradient driving forces is given by Equation 4

$$\frac{\delta F}{\delta \varphi_n} = \sum_{m \neq n}^N \left( \frac{\epsilon^2}{2} \nabla^2 \varphi_m + \omega \varphi_m - \frac{\mu}{2} \nabla \varphi_m \cdot \nabla T \right) \quad (4)$$

where  $\epsilon$  is the gradient energy coefficient,  $T$  is the temperature,  $\mu$  is the temperature gradient energy coefficient, and  $\omega$  is the height of the parabolic potential with a double obstacle [5, 10]. The parameters  $\epsilon$ ,  $\omega$ ,  $\mu$  and  $M_\varphi$  have definite relationships with the GB energy,  $\sigma$ , PF boundary width,  $2\xi$ , boundary entropy difference,  $\Delta S$ , GB width,  $2\lambda$ , alloy molar volume,  $\Omega$ , and mobility  $m$  of a GB.  $Q$  is the activation energy for the GB under consideration,  $m_0$  is a pre-exponential constant and  $k_B$  is the Boltzmann constant.

SEMI-ANALYTICAL SOLUTION FOR THE TRANSIENT TEMPERATURE FIELD

The semi-analytical computation of the temperature field induced by a DEC volumetric heat flux model is performed using a Laplace transform approach as well as the method of images (MOI) to generate analytical expressions for the heat kernels in the spatial dimensions before the final numerical temporal integration is performed [4, 3]. For a 3D domain with insulating boundary conditions on all faces except a Dirichlet boundary condition on the  $x=B$  face the three-dimensional Green's function may be found by multiplying the appropriate 1D functions and is shown in Equation 5

$$G = \sum_{n=-\infty}^{\infty} \left\{ \begin{aligned} & (-1)^n \frac{e^{-\frac{(2nB+x-x')^2}{4\alpha(t-t')} + e^{-\frac{(2nB+x+x')^2}{4\alpha(t-t')}}}{\sqrt{4\pi\alpha(t-t')}} \times \\ & \frac{e^{-\frac{(2nD+y-y')^2}{4\alpha(t-t')} + e^{-\frac{(2nD+y+y')^2}{4\alpha(t-t')}}}{\sqrt{4\pi(t-t')}} \times \\ & \frac{e^{-\frac{(2nL+z-z')^2}{4\alpha(t-t')} + e^{-\frac{(2nL+z+z')^2}{4\alpha(t-t')}}}{\sqrt{4\pi(t-t')}} \end{aligned} \right\} \quad (5)$$

where  $\alpha = \frac{k}{\rho c_p}$  is the thermal diffusivity;  $k$  is the thermal conductivity,  $\rho$  is the mass density and  $c_p$  is the specific heat at constant pressure respectively. The temperature variation induced at a point with co-ordinates  $(x,y,z)$  at a time  $t$ , by an instantaneous heat pulse of magnitude  $q(x',y',z',t')$  is then  $\frac{1}{\rho c_p} q(x',y',z',t') G(x,x',y,y',z,z',t,t')$ . The temperature increment at point  $(x,y,z,t)$  is given by the integral over time as shown in Equation 6

$$\frac{1}{\rho c_p} \times \int_0^t q(x',y',z',t') G(x,x',y,y',z,z',t,t') dt' \quad (6)$$

The temperature increase at any point and time,  $t$ , due to a volumetric heat source  $q(x',y',z',t')$  is given by Equation 7

$$\Delta T_{(x,y,z,t)} = \frac{1}{\rho c_p} \times \int_0^t \int_0^L \int_0^D \int_0^B q(x',y',z',t') G(x,x',y,y',z,z',t,t') dx' dy' dz' dt' \quad (7)$$

Here  $q(x',y',z',t')$  represents the DEC heat source distribution as shown in Figure 1, where a surface of constant power density is displayed, and the spatial parameters of the heat source are shown. The functional form of the DEC distribution is fully described elsewhere [3].

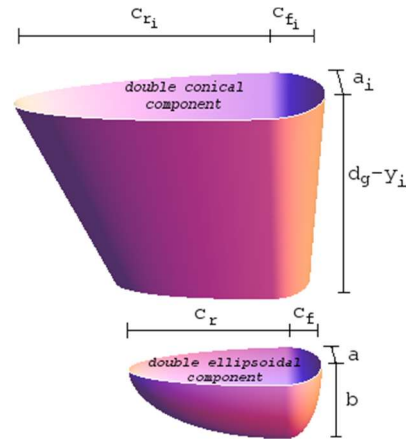


**Fig. 1** A schematic representation of the double ellipsoidal conical heat source model showing the spatial parameters

The transient thermal field induced in the finite domain due to the DEC heat source distribution is computed by summing the contributions from the four quadrants of the DEC heat source according to Equation 8 where the spatial integration's have been performed after collecting the dimensional components. The minutia of the computation of the semi-analytical thermal solution is detailed elsewhere, including the spatial heat kernels BX, DX and LX [4, 3].

$$\Delta T_{(x,y,z,t)} = \frac{1}{\rho c_p} \times \int_0^t \left\{ \begin{aligned} &(Q_{0_{c_r}} B_T D_{T_c} L_{T_r}) + (Q_{0_{c_f}} B_T D_{T_c} L_{T_f}) + \\ &(Q_{0_{D_r}} B_T D_{T_e} L_{T_r}) + (Q_{0_{D_f}} B_T D_{T_e} L_{T_f}) \end{aligned} \right\} dt' \quad (8)$$

In the semi-analytical approach, multiple heat sources may be applied. In approaches where momentum and mass transfer effects are neglected, typically the predicted fusion zone profiles are not appropriate due to neglecting surface flow effects. To compensate for this a small surface heat source may be added to represent the thermal contribution due to the mass and heat transfer due to this flow at the surface [4]. The thermal contribution from the surface Gaussian distribution is computed according to Equation 9, where  $a$  is the radius of the surface Gaussian distribution, and  $f$  is the heat fraction apportioned to the surface distribution.

$$\frac{6f\sqrt{3}P}{\rho c_p a^3 \pi \sqrt{\pi}} \times \int_0^t B_T D_{T_e}(a_g=0) \left( L_{T_r}(c_r=a) + L_{T_f}(c_f=a) \right) dt' \quad (9)$$

where  $P$  is the power of the electron beam heat source, generally taken as the product of the current, voltage and efficiency of the source. The temperature at any point within the finite domain is given by the sum of Equation 8 and Equation 9. Figure 2 shows the computed temperature field and spatial derivatives for an arbitrary EB welding geometry as the heat source model is at peak intensity through the cross section. The temperature and

spatial derivatives are then used in the phase field model to determine the evolution behavior of the order parameters  $\varphi_n$ .

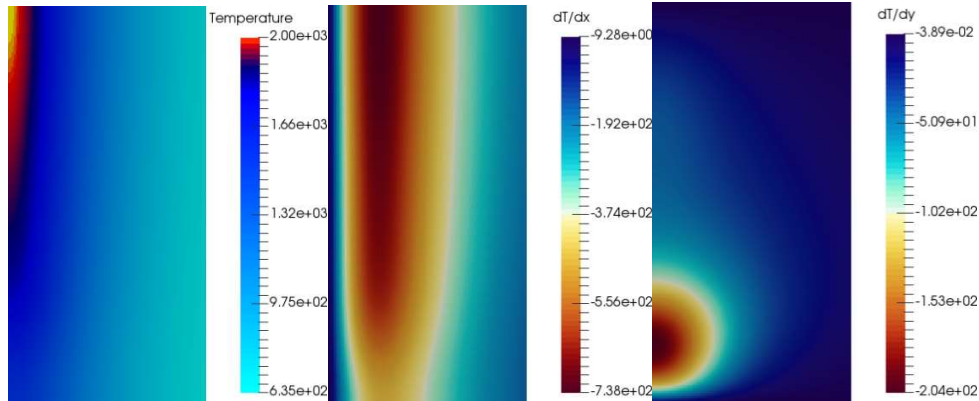


**Fig. 2** Representative temperature field as computed by Equations 8 and 9 and spatial derivatives that are used in the multi-phase field analysis of the micro-structural evolution.

### RESULTS AND DISCUSSION

In this work, initially a small numerical study was performed to investigate the effects of the phase field interface width on the boundary migration velocity for a linear boundary in a constant thermal gradient. Once an appropriate width had been determined, the effect of welding travel speed on microstructural evolution was investigated for a two-dimensional region in the HAZ of a Ti6Al4V substrate.

#### SINGLE LINEAR BOUNDARY IN A CONSTANT THERMAL GRADIENT

A key parameter in the phase field model is the boundary width,  $2\xi$ , this has a strong influence on the response of the boundaries to applied driving forces. To determine an appropriate value a small numerical study was performed to determine the optimum value of the phase field width. The remaining parameters used in the phase field simulation are shown in Table 1 [8].

**Table 1** Values and units of the parameters used in the multi-phase field simulations

Parameter	Value
$\sigma(kg\ s^{-2})$	0.81
$\Omega(mm^3mol^{-1})$	$100.3 \times 10^3$
$\Delta S(kg\ mm^2\ s^{-1}K^{-1}mol^{-1})$	$152.9 \times 10^6$
$Q(eV)$	1.0
$2\lambda(nm)$	5.0
$m_0(mm^2kg^{-1}\ s)$	178.0
$\alpha(mm^2\ s^{-1})$	7.06

For various values of  $\xi$ , the velocity of the migrating PF boundary was found, for the same inter-facial energy. Figure 3 shows how the PF velocity tended to the analytically determined velocity, deduced from Equation 1, with  $\kappa=0$  as is the case for a linear boundary, in a thermal gradient of  $93.9 \times 10^6\ Km^{-1}$ .

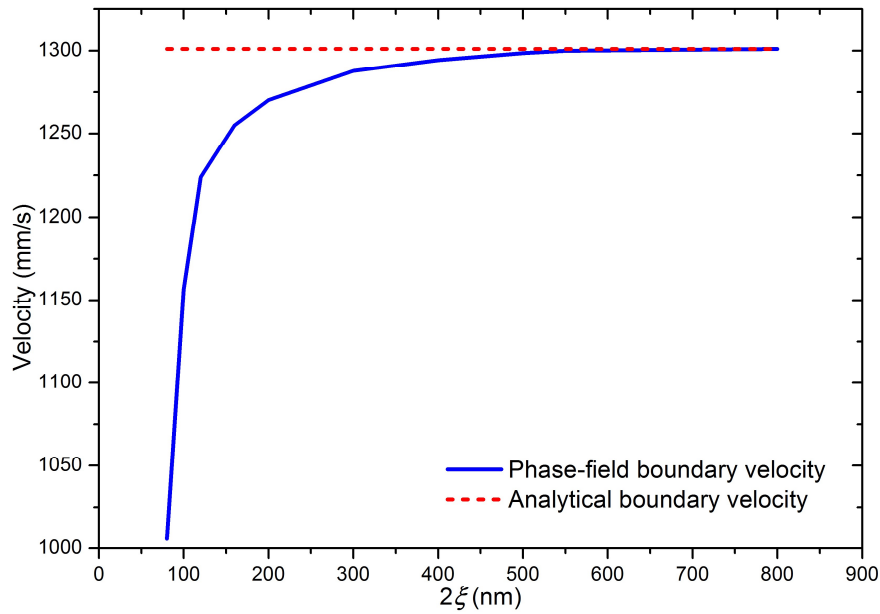


**Fig. 3** Velocity of a linear boundary in a constant thermal gradient, as a function of the phase field width parameter. The analytical velocity of a linear boundary normal to this temperature gradient is shown by the red dashed line.

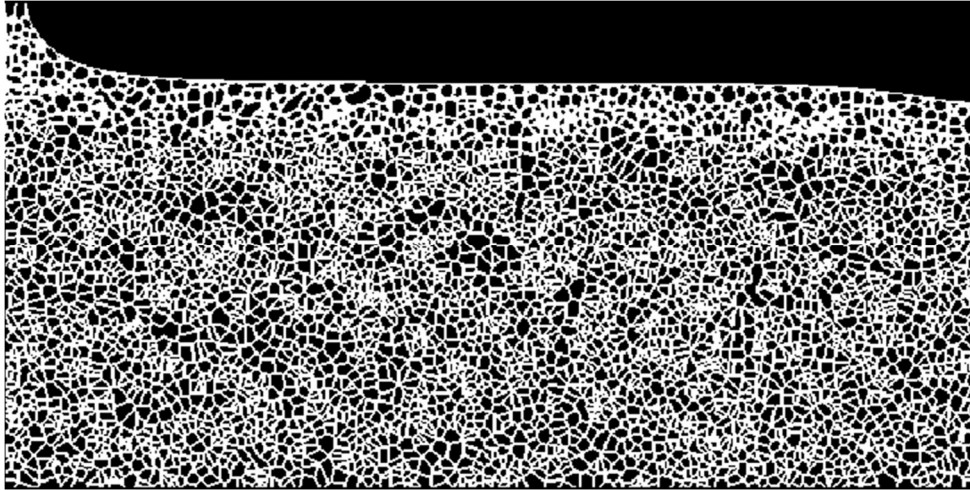


A boundary width of  $2\xi = 80$  nm, corresponding to 4 calculation points in the simulation domain, resulted in a PF boundary velocity of  $1005.7 \text{ mm s}^{-1}$ , an error of 22.70% with respect to the analytical boundary velocity of  $1301.1 \text{ mm s}^{-1}$ . A boundary width of 300 nm resulted in a PF velocity of  $1287.8 \text{ mm s}^{-1}$ , an error of 1.08%. As the number of cells that the PF boundary spans is increased, the accuracy of the PF simulation increases, as can be seen from Figure 3 $\uparrow$ . This single GB simulation was used to determine the value of the width parameter,  $2\xi$ , for the subsequent GB network simulations; boundary widths were chosen such that the PF boundaries spanned a minimum of 10 cells.

### THE EFFECT OF WELDING SPEED ON MICROSTRUCTURAL DEVELOPMENT

With the PF model parameters defined the behaviour of a Ti6Al4V substrate subjected to a DEC heat source was considered. A Ti6Al4V plate with dimensions 170mm in the x-direction, 1mm in the y-direction and 300mm in the z-direction was considered. The heat source travelled along the  $x=85\text{mm}$  plane, the heat source applied normal to the  $y=0$  surface such that the heat source intensity decreased as the distance into the domain increased. The remaining thermal modelling parameters for the semi-analytical solution are the spatial heat flux parameters and the heat source power. The heat source power,  $P$ , has a value of 120W. The heat source shape parameters are:  $a = a_i = 0.3\text{mm}$ ,  $b = 0.2\text{mm}$ ,  $c_r = c_{r_i} = 4.0\text{mm}$ ,  $c_f = c_{f_i} = 1.0\text{mm}$  and  $b_g = 85.0\text{mm}$ . The fraction of heat in the surface Gaussian distribution,  $f$ , used was 0.04. The radius of the surface Gaussian component is 0.25mm.

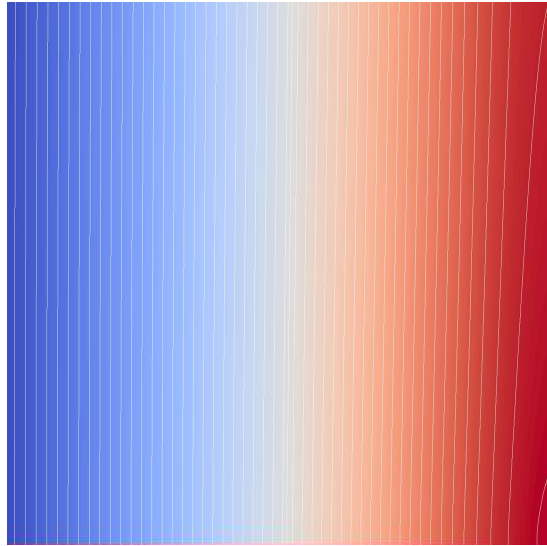
While this work focuses on the grain structure evolution in the HAZ, where no state change occurs, it is interesting to observe the spatial extent of the molten phase within the Ti6Al4V substrate due to the DEC heat source model. Figure 4 shows the cross section through the welding axis for the case under consideration as the heat source is at peak intensity. Above the solidus temperature the phase field variables have assigned a random orientation. The solidus interface is then clearly visible in the phase field domain with the typical 'bugle' type profile typically seen in high energy density welding scenarios. As can be seen in Figure 4 the grains immediately adjacent to the solid-liquid interface have begun to coarsen due to the strong thermal gradients and curvature driving forces. Away from the heat source location there has been negligible grain coarsening due to the relatively low temperature and the nature of the relation between mobility and temperature.



**Fig. 4** Cross-section through the welding axis as the DEC heat source traverses the computational domain

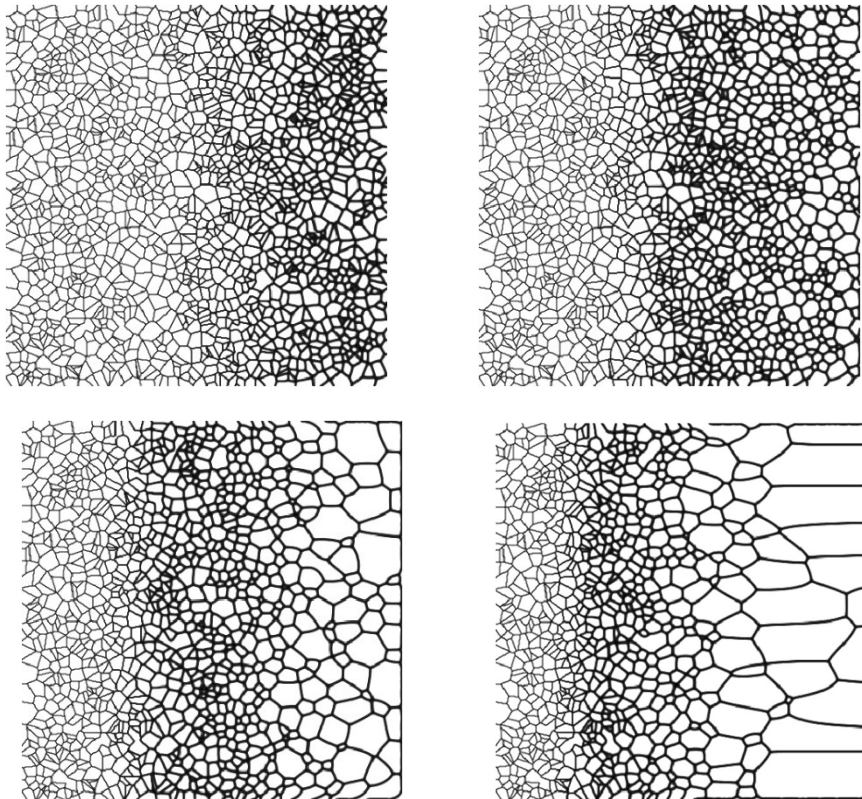
A theoretical investigation was performed on a Ti6Al4V substrate subjected to a DEC heat source representative of an EB welding process. The evolution of the micro structure was simulated immediately adjacent to the fusion zone for the duration of the heat source application. Therefore, no consideration of state change in the metallic grains is considered. Figure 5 shows the iso-thermal lines in the heat affected zone considered, as the heat source traverses, for an arbitrary time. To investigate the effect of welding heat source travel speed on microstructural development, a heat source as described was applied to the substrate with a travel speed of 3.33 m/s and a slightly higher speed of 5.0 m/s. The phase field simulation domain considered was a square of side 0.5mm, initialised with 1600 grains at  $t=0s$ , representative of the grain size observed in Ti6Al4V alloy systems.

The grain boundaries tend to migrate up the temperature gradient and normal to these lines, if the spatial thermal gradients are of high enough magnitude to be dominant over the curvature driving forces. As the thermal field evolves, the iso-thermal lines migrate and therefore the thermal gradient driving force is a strong function of time.



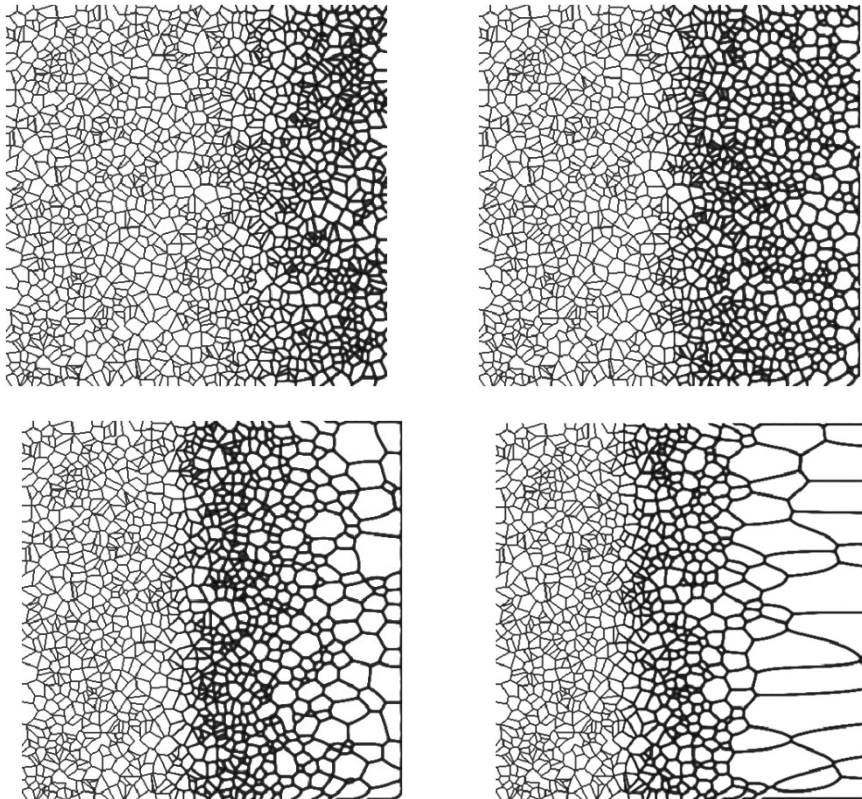
**Fig. 5** Time dependent temperature field for an arbitrary time. As the temperature field evolves, as too do the thermal gradients and therefore the magnitude and direction of the thermal gradient driving force

Figure 6 shows the resultant micro structure in the HAZ for the 3.33m/s speed, while Figure 7 shows the same section of the micro structure after the application of the heat source with at velocity of 5.0m/s, at various times after the heat source reaches peak intensity in the considered domain. Both figures show the evolution in the x-z plane perpendicular to the heat source travel direction. The heat source was located at some distance to the east in the chosen cross section as shown in Figure 5.



**Fig. 6** Evolution of temperature field in the heat affected zone of a full penetration EB weld in Ti6Al4V due to the application of a DEC heat source with surface Gaussian component, at a travel speed of  $3.33 \text{ m s}^{-1}$ . The images correspond to a cross section through the HAZ perpendicular to the heat source travel vector at  $1.375 \times 10^{-4} \text{ s}$ ,  $1.375 \times 10^{-3} \text{ s}$ ,  $1.375 \times 10^{-2} \text{ s}$  and  $1.375 \times 10^{-1} \text{ s}$  respectively after the DEC heat flux reaches peak intensity.

The thermal gradient driving force on the right of the sub-figures, where the spatial thermal gradients are largest, has a considerable effect on the development of a columnar grain structure, as can be seen in Figure 6. The lower travel speed of the heat source for the same P deposits more energy into the substrate and means that the average temperature of the domain is higher than in the higher travel speed case. The higher average temperature and steep thermal gradients leads to considerable coarsening and boundary migration towards the hotter region of the domain.



**Fig. 7** Evolution of temperature field in the heat affected zone of a full penetration EB weld in Ti6Al4V due to the application of a DEC heat source with surface Gaussian component, at a travel speed of  $5.0 \text{ m s}^{-1}$ . The images correspond to a cross section through the HAZ perpendicular to the heat source travel vector at  $1.375 \times 10^{-4} \text{ s}$ ,  $1.375 \times 10^{-3} \text{ s}$ ,  $1.375 \times 10^{-2} \text{ s}$  and  $1.375 \times 10^{-1} \text{ s}$  respectively after the DEC heat flux reaches peak intensity.

In the higher travel velocity case as shown in Figure 7 the temperature on the boundary farthest away from the heat source location doesn't reach as high a magnitude; as such the mobility of the boundaries is lower due to the Arrhenius dependence of the mobility with temperature. There is still considerable boundary migration and coarsening towards the hotter region of the domain. However, comparing Figures 6 and 7 at  $1.375 \times 10^{-1} \text{ s}$  after the heat source traversed the plane, more coarsening occurred and the extent of the HAZ is greater in the slower case. This agrees with the expected microstructural behaviour.

## CONCLUSIONS

While the semi-analytical solution procedure is computationally efficient, the fundamental physics is not solved, and as such the approach is only valid in a limited number of cases. The use of a full-thermal fluid solution procedure for the computation of the transient thermal field ensures the entire physics including the complex heat and mass transfer within advanced manufacturing processes are captured and therefore the thermal solutions these approaches generate are much more accurate and not limited to certain cases. That said the

semi-analytical solution procedure is valid in the case of EB welding where significant material is not ablated.

The utilisation of a semi-analytical solution procedure for the computation of transient thermal fields, representative of the EB welding process, coupled with a multi-phase field framework for the prediction of micro-structural evolution permits grain structure evolution near strong thermal gradients to be investigated. The effect of the thermal gradient driving force and the temperature dependent grain boundary mobility leads to the generation of columnar type grains that are oriented towards the heat source travel axis, as the thermal gradient driving force magnitude in these regions is comparable if not greater than the curvature driving force magnitude.

The effect of heat source travel speed is investigated. The higher travel speed results in a lower temperature domain on average and therefore for the same locations the boundary mobility is generally lower and the overall grain size smaller as the boundaries are not as mobile on average. The higher travel speed therefore results in a narrower heat affected zone.

### ACKNOWLEDGEMENTS

The work presented in this manuscript is supported by the Engineering and Physical Sciences Research Council (EPSRC) under the “An integrated (ICME) approach to multiscale modelling of the fabrication and joining of powder processed parts” grant EP/P005284/1 and the NNUMAN programme grant in nuclear manufacturing (Grant No. EP/J021172/1).

### REFERENCES

- [1] XIAN-MING BAI, YONGFENG ZHANG, MICHAEL R. TONKS: “*Testing thermal gradient driving force for grain boundary migration using molecular dynamics simulations*”, *Acta Materialia*, pp. 95—106, 2015.
- [2] ANA P FERNANDES, PRISCILA F B SOUSA, VALERIO L BORGES, GILMAR GUIMARAES: “*Use of 3D transient analytical solution based on Greens function to reduce computational time in inverse heat conduction problems*”, *Applied Mathematical Modelling*, pp. 4040—4049, 2010.
- [3] T.F. FLINT, J.A. FRANCIS, M.C. SMITH, J. BALAKRISHNAN: “*Extension of the double-ellipsoidal heat source model to narrow-groove and keyhole weld configurations*”, *Journal of Materials Processing Technology*, pp. 123—135, 2017.
- [4] T.F. FLINT, J.A. FRANCIS, M.C. SMITH, VASILEIOU A.N.: “*Semi-analytical solutions for the transient temperature fields induced by a moving heat source in an orthogonal domain*”, *International Journal of Thermal Sciences*, pp. 140—150, 2018.
- [5] T.F. FLINT, C. PANWISAWAS, Y. SOVANI, M.C. SMITH, H.C. BASOALTO: “*Prediction of grain structure evolution during rapid solidification of high energy density beam induced remelting*”, *Materials & Design*, pp. 200—210, 2018.
- [6] THOMAS F FLINT, JOHN A FRANCIS, JOHN R YATES: “*Analytical solutions of the transient thermal field induced in finite bodies with insulating and convective boundary conditions subjected to a welding heat source*”, *Conference Proceedings: SMIRT 22, San Francisco*, 2013.
- [7] GUNTER GOTSTEIN, LASAR S SHVINDLERMAN: *Grain boundary migration in metals: thermodynamics, kinetics, applications*. CRC press, 2009.

- [8] Y HUANG, F J HUMPHREYS: “*Measurements of grain boundary mobility during recrystallization of a single-phase aluminium alloy*”, *Acta Materialia*, pp. 2259—2268, 1999.
- [9] HYUN-KYU KIM, SEONG GYOON KIM, WEIPING DONG, INGO STEINBACH, BYEONG-JOO LEE: “*Phase-field modeling for 3D grain growth based on a grain boundary energy database*”, *Modelling and Simulation in Materials Science and Engineering*, pp. 34004, 2014
- [10] SEONG GYOON KIM, DONG IK KIM, WON TAE KIM, YONG BUM PARK: “*Computer simulations of two-dimensional and three-dimensional ideal grain growth*”, *Physical Review E - Statistical, Nonlinear, and Soft Matter Physics*, pp. 1—14, 2006.
- [11] MATTHIAS MILTZER: “*Phase field modeling of microstructure evolution in steels*”, *Current Opinion in Solid State and Materials Science*, pp. 106—115, 2011.
- [12] CHINNAPAT PANWISAWAS, YOGESH SOVANI, RICHARD P TURNER, JEFFERY W BROOKS, HECTOR C BASOALTO, ISABELLE CHOQUET: “*Modelling of thermal fluid dynamics for fusion welding*”, *Journal of Materials Processing Technology*, pp. —, 2017.
- [13] I STEINBACH, M APEL: “*Multi phase field model for solid state transformation with elastic strain*”, *Physica D: Nonlinear Phenomena*, pp. 153—160, 2006.
- [14] I STEINBACH, F PEZZOLLA: “*A generalized field method for multiphase transformations using interface fields*”, *Physica D: Nonlinear Phenomena*, pp. 385—393, 1999.
- [15] B B VYNOKUR: “*Influence of alloying on the free energy of austenitic grain boundaries in steel*”, *Materials Science*, pp. 448—455, 1996.

# EXPERIMENTAL VALIDATION OF A SIMPLIFIED WELDING SIMULATION APPROACH FOR FATIGUE ASSESSMENTS

N. FRIEDRICH\* and S. EHLERS\*

*\*Hamburg University of Technology (Institute for Ship Structural Design and Analysis, 21073, Hamburg, Germany,  
nils.friedrich@tuhh.de)*

DOI 10.3217/978-3-85125-615-4-46

## ABSTRACT

The paper presents the application of a simplified approach for numerical welding simulations and its validation by means of residual stress measurements. The aim of the presented work is to provide a practical calculation method for welding residual stresses to assess their influence on the fatigue strength of welded structures. Welding simulations are relatively complex while their reliability is often uncertain. On the other hand, residual stress measurements frequently show wide scatter. The paper motivates the use of a simplified approach without calibration by experimental data, as it is applicable for fore- and hindcasting of residual stresses during the design phase or for failure analysis. The simulations are divided into a transient thermal analysis followed by a mechanical analysis. A simple prescribed temperature heat source with uniform temperatures is used to apply the welding energy. The results are validated with residual stress measurements by X-ray diffraction and hole drilling on three welded geometries: longitudinal stiffeners, K-butt welds and a structure-like component.

Keywords: simplified welding simulation; residual stress prediction; uniform temperature distribution; experimental validation; residual stress measurement; longitudinal stiffener; multilayer weld.

## INTRODUCTION

Direct consideration of welding residual stresses in engineering applications is still limited. Measurements are complex and not always possible. Welding simulations often do not prove very efficient considering modelling and computation effort opposed to accuracy and reliability of the results. On the one hand, non-linear simulations with a high temporary resolution will require long calculation times depending on the model size, load step number and computational capacities. On the other hand, modelling and setting up the simulation will require effort. This includes the calibration of the heat input in the thermal part of the analysis which is often considered a pre-requisite for reliable residual stress and distortion results [1]. It usually involves measuring temperatures during welding and taking macrographs from the weld cross-section. Simulation parameters are then iteratively adapted in order to match the calculated temperature distributions with the acquired experimental data. Although this procedure, applied e.g. in [1-5], seems straightforward, when it comes to detail, differences may be observed in the practical execution. Sometimes



peak temperatures are compared or the focus lays on the trend of the temperature curve after a few seconds of cooling. Distances from the weld at which temperatures are compared may vary significantly and for small distances it may be hard to accurately measure and transfer it to an idealized weld shape in the model. The molten weld bead in the macrograph or the heat affected zone may be matched with the respective isotherm from the simulation. The shape of the weld may be modelled in different detail. Different importance may be given to the element size close to the weld to be fine enough to capture the steep gradients in temperature (and in residual stresses as well). These none exclusive parameters will to some extent influence the outcome of the heat source calibration.

In [1] a bench mark study on uncertainties in welding simulations is presented and the importance of an accurate calibration is pointed out. But how relevant is a correct heat input really for the resulting residuals stresses? Does a careful and (apparently) accurate calibration guarantee reliable simulation results? Despite of being laborious, the need for experimental data limits the applicability of a simulation. Such calibration procedure is not practical during the design phase, when measurements are not yet be possible, or for the assessment of existing structures for which such data is not available. Simplified simulation approaches without calibration may be less accurate, but perhaps accurate enough for applications such as fatigue assessments affected by other parameters, which are often rough estimates only.

According to Goldak and Akhlaghi [6] the best heat source model to choose depends on how accurately the heat source should be modelled, on the objective of the modelling and on what information is available. To predict distortions and residual stresses in low alloy steel structures accurate temperatures below 600 to 800°C are described to be most important. Simplified simulation approaches for multilayer welds were studied in [5]. It was found that geometrical simplification of the modelled weld shape can produce good results in terms of residual stresses while reducing simulation times. Whereas, approaches aiming to reduce the number of calculated load steps (e.g. application of thermal cycles or lumping of weld passes) may produce poor results compared to transient simulations.

In [7] the authors adopted a simplified welding simulation procedure for metal active gas welding renouncing on experimental calibration to assess residual stresses in small-scale specimens for fatigue investigations. Instead of using an equivalent heat source with a volumetric power density distribution (e.g. according to [8]), a prescribed temperature heat source [6] with a uniform temperature on the weld cross section has been applied in a transient thermal analysis. In [7] the simulation approach was applied to a multilayer K-butt weld and the influence of different simulation parameters has been investigated. The aim of the present paper is to transfer the approach to the weld geometry of a longitudinal stiffener and to validate it by residual stress measurements on three different geometries including small-scale specimens and a structure-like component.

The objective is to provide a simulation procedure to calculate residual stresses and consider them in the fatigue assessment of welded structures. It should be applicable also if no detailed data of the welding process is available. For fatigue assessments residual stresses transversal to the weld, at the weld toe are most important as possible cracks will initiate here.

## SIMULATION APPROACH

### GENERAL PROCEDURE

The applied finite element simulation approach consists of a transient thermal analysis followed by a nonlinear structural analysis. A uniform temperature distribution is applied to the weld cross-section and moved along the weld, instead of using a volumetric heat source with a power density distribution (Fig. 1). Prescribed temperature heat sources are described in [6] and have been applied e.g. in [9-10]. The procedure used in the present paper was described in [7] and will be summarized shortly in the following.

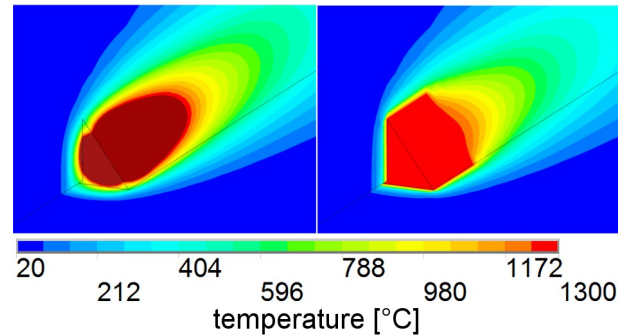


**Fig. 1** Volumetric heat source (left) and uniform temperature (right) applied on a fillet weld [7].

In the thermal analysis a temperature of 1300°C is applied to a short section of the simulated weld. At each time step, this section is moved by the assumed welding speed of 7.8 mm/s. The time step size is 0.5 seconds, respectively 0.25 seconds for portions of the weld closest to the investigated region e.g. for fatigue assessments. Elements of the simulated welds are deactivated at the beginning of the simulation and are activated as the temperature is applied to them. For each time step the temperature distribution in the model is calculated considering radiation and convection on its surfaces according to the analytical formulas given in [11].

In the structural analysis the same time steps as before are calculated. The temperature distributions from the thermal analysis are applied as loads to calculate residual stresses and distortions. Effects of phase transformation are considered by using two different curves for the thermal expansion coefficient for heating and cooling on the weld elements. The curve used for cooling showing an expansion between 400 and 500°C. The yield strength is reduced in the same temperature interval to account for transformation-induced plasticity (TRIP).

### PARAMETER VARIATION

The simulations are performed without calibration by experimental data. Therefore, a variation of the simulation parameters was performed to verify if and how they may affect

## Mathematical Modelling of Weld Phenomena 12

simulation results. In [7] this was done for a multilayer cruciform joint. As a result, it was found that a variation of the applied temperature or the assumed welding speed (i.e. of the heat input) did not significantly affect the resulting transversal residual stresses in front of the weld.

In the following the simulation approach described above was applied to the model of a longitudinal stiffener. Simulation parameters were varied to assess the influence for this particular weld geometry.

### *FE-Model*

Modelling and simulation were done using the finite element (FE) software ANSYS Mechanical 15.0. The model of a small-scale specimen with a longitudinal stiffener used for the parameter variation is shown in Fig. 2. It consists of 8 node solid elements. Elements size was 0.25 mm in front of the weld toe at the end of the stiffener and coarser on the rest of the model. Temperature-dependent material data for S355 steel from [12] was used assuming kinematic hardening. The young's modulus was increased to 215 GPa to improve the stability of the simulations. Constrains were applied to three nodes only to avoid rigid body motion.

It was assumed that the welding starts and ends at half length of the stiffener.

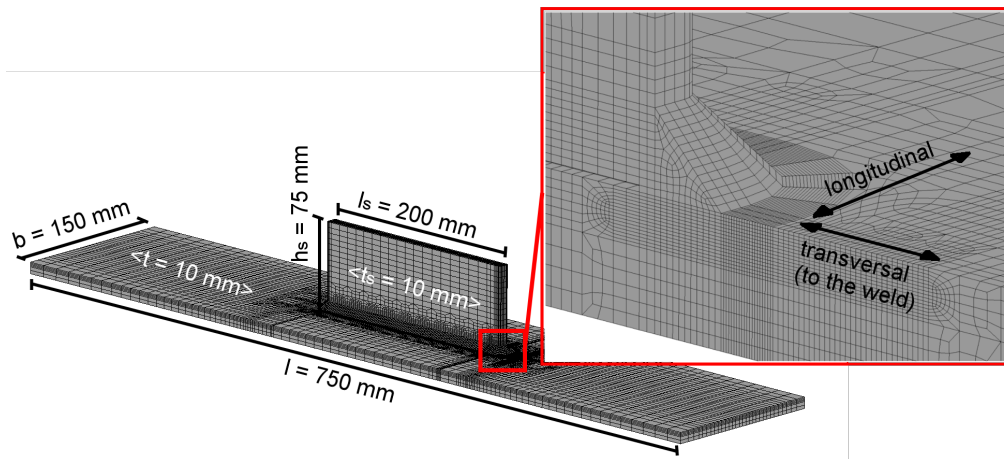


**Fig. 2** Dimensions of the fe-model and definition of directions with respect to the weld at the end of the stiffener.

### *Applied temperature*

The temperature applied to the weld cross-section was varied between 1000 and 1500°C. The resulting residual stresses in front of the weld toe at the end of the stiffener are shown in Fig. 3. The directions transversal and longitudinal are referred to the weld at the end of the stiffener as defined in Fig. 2. For temperatures of 1400°C and more the cut-off

temperature above which the elements are deactivated had to be below 1200°C in order to run the simulations. In the diagram this is indicated by a dashed line.

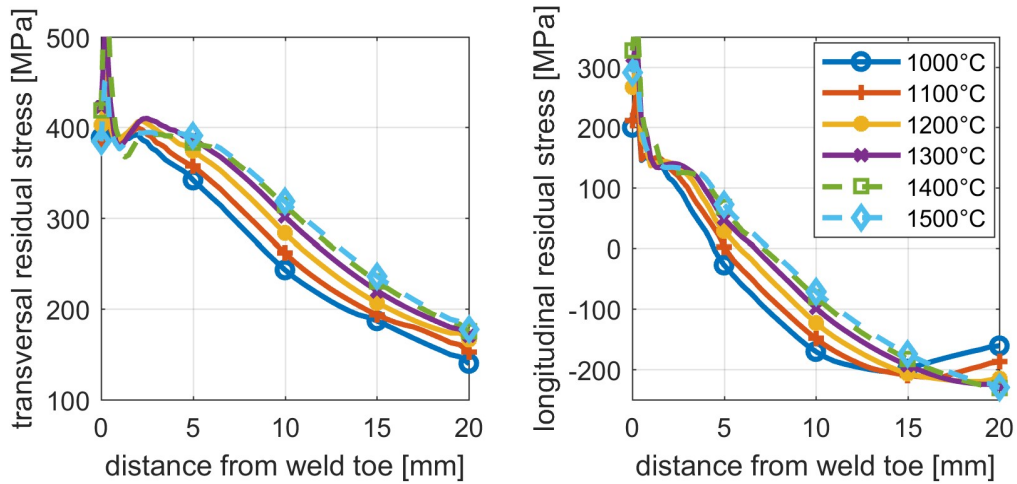


**Fig. 3** Calculated residual stress depending on the temperature applied to the weld elements (dashed line: cut-off temperature lower than applied temperature).

The curves for both directions (transversal and longitudinal) show a steep increment on the first element from the weld toe. At the weld toe, the elements of the weld are activated as they cool below the applied temperature while the adjacent elements are always active. At the moment of the activation, large deflections can occur in the neighbouring elements, which at that point present elevated temperatures themselves and thus low stiffness. This may cause a peak in the resulting residual stresses at the first node in front of the weld toe. Moreover, the weld toe is not modelled with a radius and thus shows a sharp notch. This represents a singularity in the FE-model, which will cause an unrealistic stress concentration at the weld toe. The residual stress values on the first elements, up to approximately 1 mm from the weld toe, should therefore not be evaluated and will not be considered in the following.

Neglecting the peak at the first node from the weld toe, transversal residual stresses reach a value of about 400 MPa some millimetres from the weld with decreasing tendency towards the weld toe. In longitudinal direction values of approximately 150 MPa are reached. With increasing temperatures, the curves become wider and the residual stresses decrease farther from the weld.

All in all, the residual stress curves and the highest values in front of the weld differ only little depending on the applied temperature. This is in agreement with the findings for the cruciform joint in [7]. For the following simulations a temperature of 1300°C was applied.

*Throat thickness*

The throat thickness of the weld was varied between 3.0 and 6.5 mm. With an increasing weld cross section more thermal energy is applied to the model and thus the heated volume undergoing shrinkage during cooling is larger. The resulting residual stresses in front of the weld toe at the end of the stiffener are shown in Fig. 4.

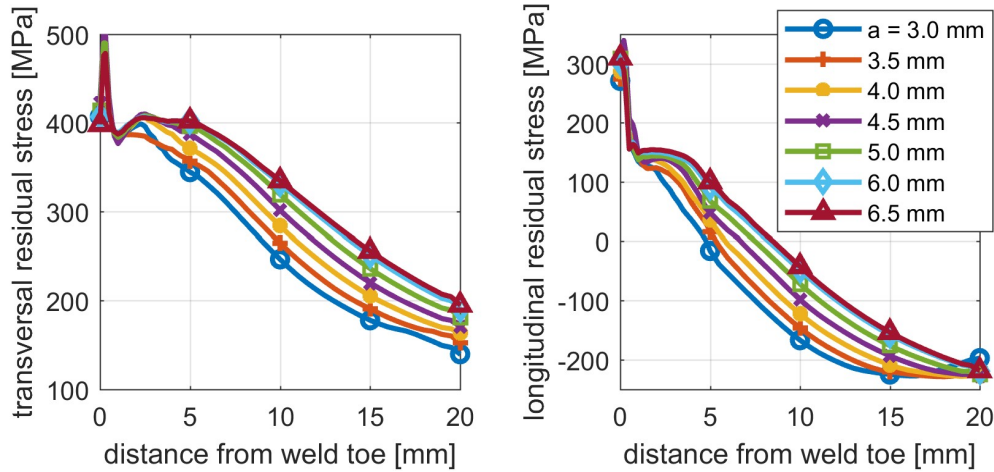


**Fig. 4** Calculated residual stress depending on the throat thickness  $A$ .

Analogue to the results with varied temperatures, the curves become wider and the residual stresses decrease farther from the weld as the throat thickness increases. The highest values reached in front of the weld differ only little depending on the throat thickness. For the following simulations a throat thickness of 4.5 mm was applied.

*Phase transformation temperature interval*

As described in section 2.1 phase transformation is considered by using two different curves for the thermal expansion coefficient for heating and cooling. On all weld elements the same curve is used for cooling, independently of the reached peak temperature and cooling time. The temperature interval in which the phase transformation and thus a volume expansion is assumed during cooling was varied between 300 and 700°C. The resulting residual stresses are shown in Fig. 5. The results include those from simulations without phase transformation (with straightened thermal expansion curve as for an austenitic steel) and with the same thermal expansion curve as for heating (austenite phase transformation between 700 and 900°C). The assumed temperature interval for phase transformation shows no influence on the calculated residual stresses in front of the weld. As described above, it was not possible to evaluate the simulation results at the weld toe.

For the following simulations phase transformation during cooling was assumed between 400 and 500°C. According to experimental results in [13] this should be a realistic range and has yielded satisfying results for a K-butt weld in [7].

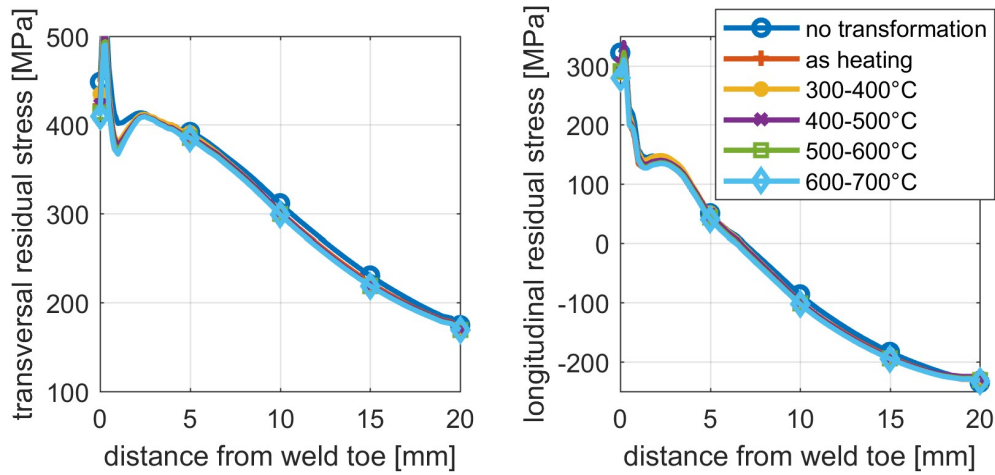


**Fig. 5** Calculated residual stress without phase transformation and depending on the temperature interval for phase transformation.

### *Yield strength*

The yield strength was varied between 385 and 470 MPa. Temperature dependent material data, including stress-strain curves, for S355 was taken from [12]. At room temperature these showed a yield strength of approximately 385 MPa. Tensile tests (at room temperature) were performed on steel of grade A36 and S460 showing yield strengths of 430 and 470 MPa, respectively. Stress-strain curves for elevated temperatures of the S355 were adapted by scaling the yield strength with the ratio of yield strengths at room temperature. The elastic-plastic zone was scaled by the ratio of the difference between yield limit and tensile strength. All other material properties, including young's modulus, were kept the same for all simulations. The resulting residual stresses are shown in Fig. 6. In transversal direction the maximum reached residual stresses increases with the yield strength of the material.

For the following simulations material properties of the S355 were assumed.

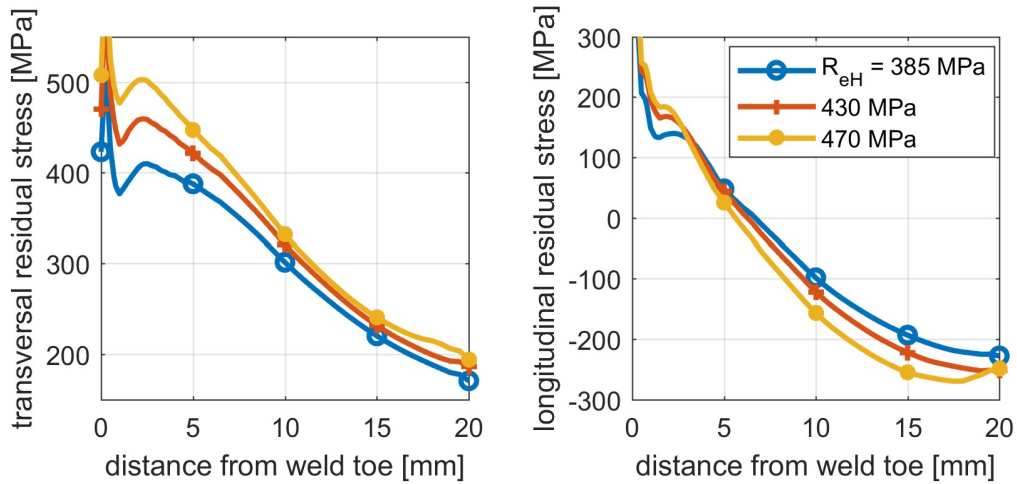


Fig. 6 Calculated residual stress depending on the yield strength  $r_{eH}$ .

### EXPERIMENTAL VALIDATION

To validate the simulation results the calculated residual stresses were compared to measurements on three different welded geometries:

- Small-scale specimen with a longitudinal stiffener
- Small-scale specimen with a multilayer K-butt weld
- Large-scale component including a multilayer cruciform joint and a longitudinal stiffener.

#### LONGITUDINAL STIFFENER

The geometry of the longitudinal stiffener specimens is shown in Fig. 7. The specimens were made of steel S355J2+N. The base plates were cut from a 10 mm plate using a band saw. Tensile tests gave the following values: yield strength  $R_{p0.2} = 370$  MPa; tensile strength  $R_m = 543$  MPa; Young's modulus  $E = 201$  GPa. Flat bars 40x10 (S355) were used for the stiffeners. Manual metal active gas (MAG) welding was applied. Welding started at the left end of the stiffener (referred to Fig. 7). Welding current was 250 A and voltage 29 V. During welding the ends of the specimens were fixed on a square tube 80x80x3.5 by screw clamps to reduce distortion. The clamps were removed after the specimens had cooled below 100°C (measured by infrared thermometer). To allow hole drilling measurements close to the weld toe, on a number of specimens the right end of the stiffener was cut at a 45° angle before welding (see Fig. 7). According to simulations, residual stresses in the base plate should have been the same as in specimens with straight stiffeners.

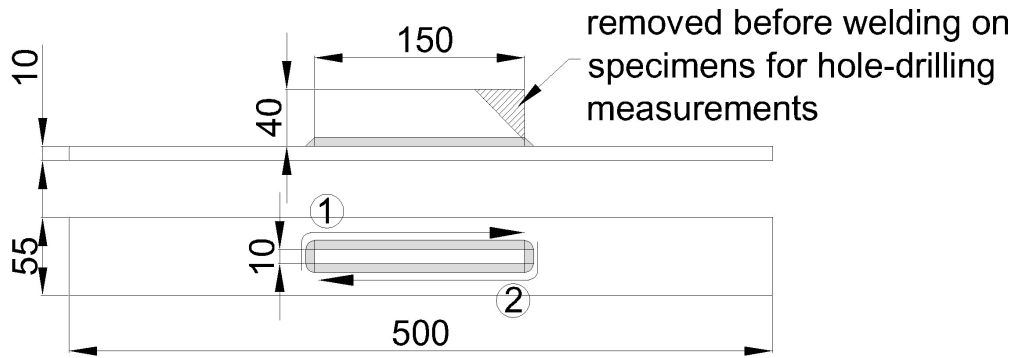


Fig. 7 Longitudinal stiffener specimens, welding sequence indicated by ① and ②.

Residual stress measurements by the hole drilling method were done on three specimens. The measurements were done at the right end of the stiffener. The holes were distributed leaving at least 4 mm in between and so that they do not shadow each other with respect to the stiffener. Strain gauge rosettes of Type A according to ASTM E837 [14] were applied, respectively Type B when closer than 5 mm to the weld. The drill diameter was 1.6 mm. The drilling depth 1 mm. Depth increments were 0.01 mm up to a depth of 0.1 mm and then 0.05 mm. Fig. 8 shows exemplarily the residual stresses over the hole depth measured on a specimen at two different distances from the weld toe. The residual stress curves over depth were calculated by the integral method [15]. Furthermore, values according to ASTM E837-13 assuming a uniform residual stress distribution up to 1 mm depth are plotted. Transversal residual stresses show a steep increment on the first 0.1 mm and then stabilize on a value slightly higher than the result assuming a uniform distribution. The residual stress assessment close to the surface is sensitive to inaccuracies. Residual stresses may be underestimated due to uncertainties in the determination of the “zero” position where the cutter touches the specimen surface [14, 16] or a smaller hole diameter than measured at the end of drilling. The evaluation of the uniform residual stress distribution is less prone to errors and typically more accurate [16].

Further measurements were done by X-ray diffraction on three specimens. The measurements were executed by the Institute of Joining and Welding (ifs), TU Braunschweig. The X-ray measurements were performed on the centreline of the specimen.

The residual stresses measured by hole drilling and X-ray diffraction are compared to the simulation results in Fig. 9. Specimens 16 and 19 used for the X-ray measurements had a straight stiffener, specimen 5 had a bevelled stiffener (compare Fig. 7) as the specimens for hole drilling. When comparing the results of both measuring methods it has to be considered, that the measuring depth of the X-ray diffraction is approximately 5  $\mu\text{m}$ , while the hole drilling measurements were evaluated over a depth of 1 mm. The results in Fig. 8 indicate that the transversal residual stresses increase on the first 0.1 mm from the surface. The specimens presented a rolling skin. For the hole drilling measurements the surface had to be slightly grinded with sandpaper in order to assure a proper installation of the strain gauge rosettes. Still, the results obtained with both methods are in good agreement beyond 5 mm from the weld. Closer to the weld, where welding residual stresses are expected to dominate over those resulting from the production or surface treatment of the plate,



transversal residual stresses show different trends. While the hole drilling results increase to over 300 MPa, the X-ray values show a maximum of about 200 MPa and decrease towards the weld. In the heat affected zone close to the weld material properties may differ from those of the base material. The accuracy of hole drilling measurements close to the weld may be affected by the vicinity to a step feature (the weld), the use of Type B strain gauge rosettes and residual stresses of more than 70% of yield strength [16]. On X-ray measurements close to the weld the measuring spot of 1-2 mm will in part cover weld material. Furthermore, measurements in transversal direction are limited to  $\Psi$ -angles of the same sign. These not ideal measuring conditions may have affected the results obtained with both methods. To what extent, cannot be definitely said without further investigations.

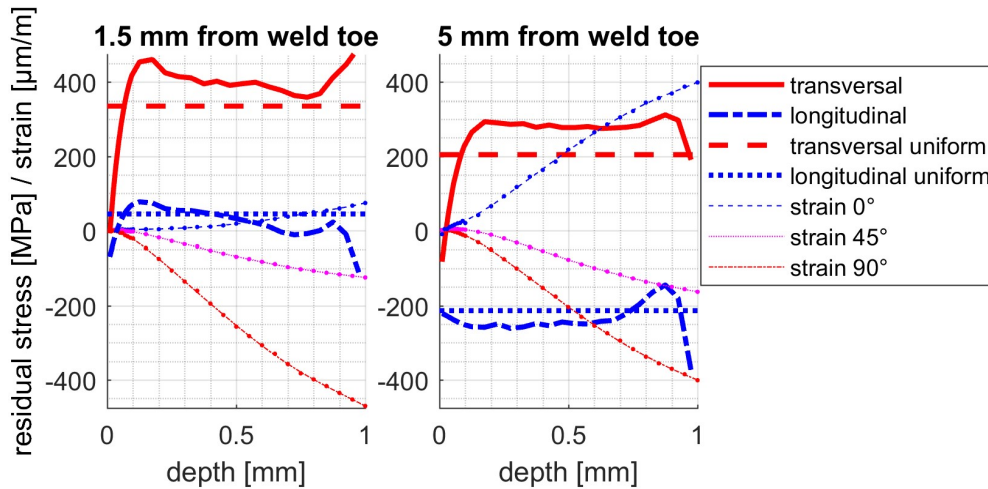


**Fig. 8** Residual stresses measured by hole drilling (specimen 1). Strains refer to their orientation relative to the weld ( $0^\circ \triangleq$  longitudinal).

In the simulation the mechanical boundary conditions were simplified by restraining the displacement in vertical direction at the ends of the model and relieving these restraints in the last load step, at room temperature. As mentioned in section 2.2.2, the calculated residual stresses should not be evaluated on the first 1 mm from the weld toe because of the singularity in the FE model. In both directions simulation results lay close to the hole drilling measurements. Both curves show an offset of about 2 mm compared to the measurements. This may indicate that too much energy was put into the model (compare Fig. 3 and Fig. 4).

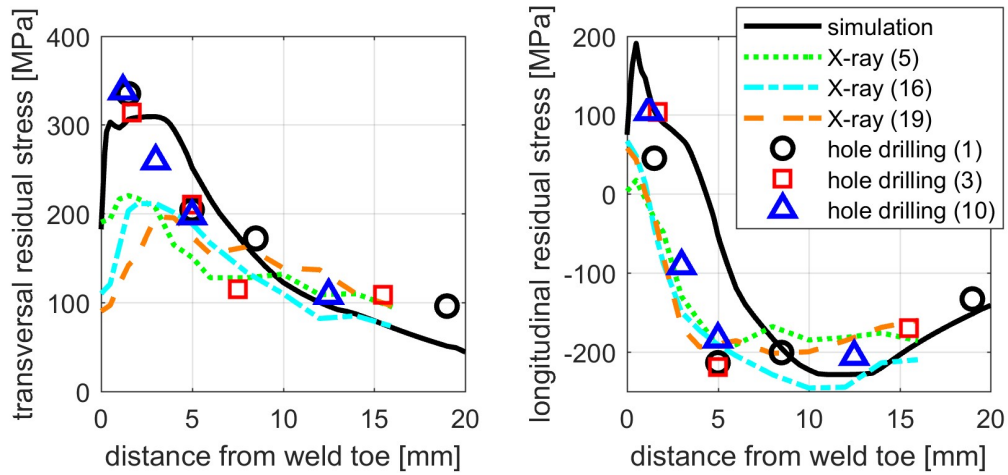


**Fig. 9** Calculated and measured residual stresses (numbers in brackets indicate the specimen number).

K-BUTT WELD

Small-scale specimens with a K-butt weld between two plates of different thicknesses have been investigated in [7]. The dimensions of the geometry are shown in Fig. 10. A 10 mm plate was welded to a 25 mm plate using six weld passes as shown in the detail. Five specimens have been cut out of each plate using a band saw. Steel of grade S355J2C+N was used. Tensile tests of the 10 mm plate gave the following values: yield strength  $R_{eH} = 394$  MPa; tensile strength  $R_m = 524$  MPa; Young's modulus  $E = 204$  GPa.

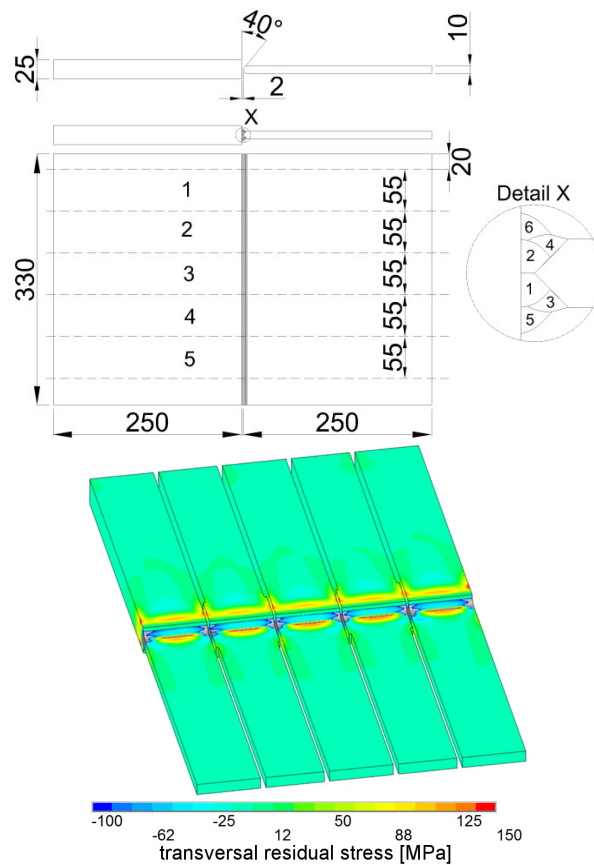


**Fig. 10** K-butt specimens (left) and calculated residual stresses (right) [7].

Welding simulations were performed with the approach described above. To simulate the cutting of the specimens the elements between the specimens were deactivated after cooling to room temperature. The resulting transversal residual stress distribution after cutting is plotted in Fig. 10 (right).

In Fig. 11 the calculated residual stresses on the upper side of the specimens are compared to measurements by X-ray diffraction and hole drilling. Measurements were performed on several specimens indicated in the legend of Fig. 11 by the number of the plate and of the specimen (1 to 5 according to Fig. 10). As mentioned in section 3.1 the X-ray diffraction and hole drilling methods have different measuring depths. Compared to the longitudinal stiffeners the X-ray measurements show a larger scatter. Measurements on specimen 23-5 are in agreement with the hole drilling results, the other two curves indicate lower values. The five curves for the simulation show the results on the five specimens cut out of one plate. Transversal residual stresses lay within the scatter of the hole drilling measurements up to 5 mm from the weld toe and slightly above it beyond this distance. Two of the X-ray measurements lay about 100 MPa below the simulation results. The third (specimen 23-5) shows values in the range of the hole drilling measurements and simulations up to 7 mm from the weld.

In longitudinal direction the simulation results follow the trend of the hole drilling measurements and the highest of the X-ray measurements (specimen 23-5) overestimating them by about 100 MPa.

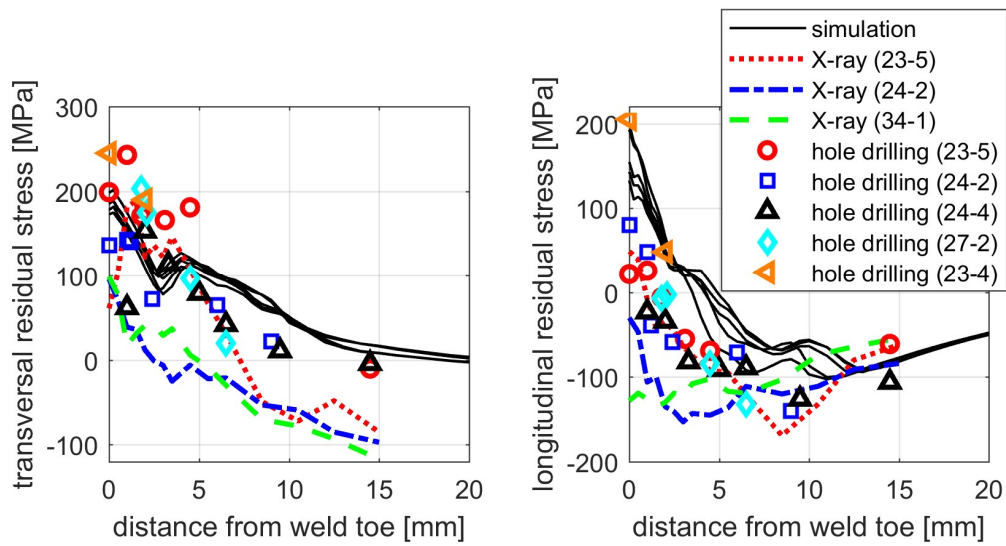


**Fig. 11** Calculated and measured residual stresses on the upper side of the k-butt weld specimens (numbers in brackets indicate the specimen number) [7].

LARGE-SCALE COMPONENT

In [17] residual stresses on structure-like components have been investigated. The investigated geometry is shown in Fig. 12. It included a cruciform joint and a longitudinal stiffener as shown in the detail (Fig. 12, right). The plate thickness was 20 mm for the girder and 16 mm for the stiffener. In the welding sequence the right stiffener and the right side of the cruciform joint (detail in Fig. 12) were welded last. The applied steel was of shipbuilding grade A36 with a yield strength of  $R_{eH} = 430$  MPa and tensile strength  $R_m = 555$  MPa (determined in tensile tests of the 20 mm material).

## Mathematical Modelling of Weld Phenomena 12

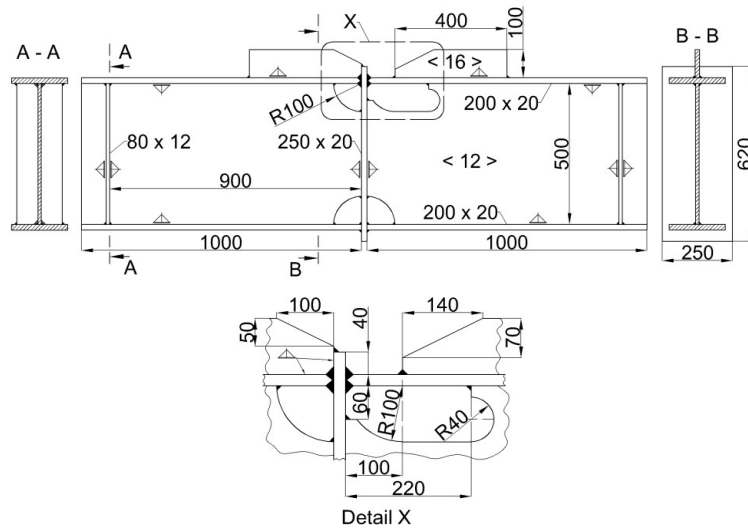


**Fig. 12** Dimensions of the large-scale component [17].

Residual stresses were measured by X-ray diffraction at ifs, TU Braunschweig. Fig. 13 shows the results from two specimens along with the corresponding calculated residual stresses. The measurements were performed at the centreline of the specimens between the cruciform joint and the longitudinal stiffener. The indicated distance refers to the weld toe of the cruciform joint. The weld toe of the longitudinal stiffener is located at the right side of the diagrams (at 75 mm). Simulation and measurement results for two specimens are shown. On specimen M3 the cruciform joint was welded with a total of 10 weld passes, on specimen M4 with 15. On the latter specimen the last weld beads were applied on top of the weld, a few millimetres from the weld toe at the horizontal girder (comparable to weld pass 6 in the detail of Fig. 10). In this manner two different residual stress distributions were achieved. Whereas on specimen M3 transversal residual stresses decrease to zero at the cruciform joint (left side of the diagram), on specimen M4 they rise to about 200 MPa.

The simulations were performed with the procedure describe above. Stress-strain curves with a yield strength of 430 MPa at room temperature, as on the actual specimens, were used. For higher temperatures the curves have been scaled as described in section 2.2.5. Welding speeds were determined based on thermocouple measurements prior to perform the simulations, these values were used for the simulations: 7.1 mm/s on the side of the longitudinal stiffener and 10 mm/s at its end; between 5.3 and 8.3 mm/s for the cruciform joint in specimen M3 and 7.8 mm/s in specimen M4. As shown in [7] the applied welding speed does not significantly influence the resulting residual stresses. In [18] it was observed for the cruciform joint that the residual stresses calculated on the plate surface depend mostly on the last applied weld beads. It is therefore assumed that a fixed welding speed (7.8 mm/s) would have resulted in the same residual stress distributions.

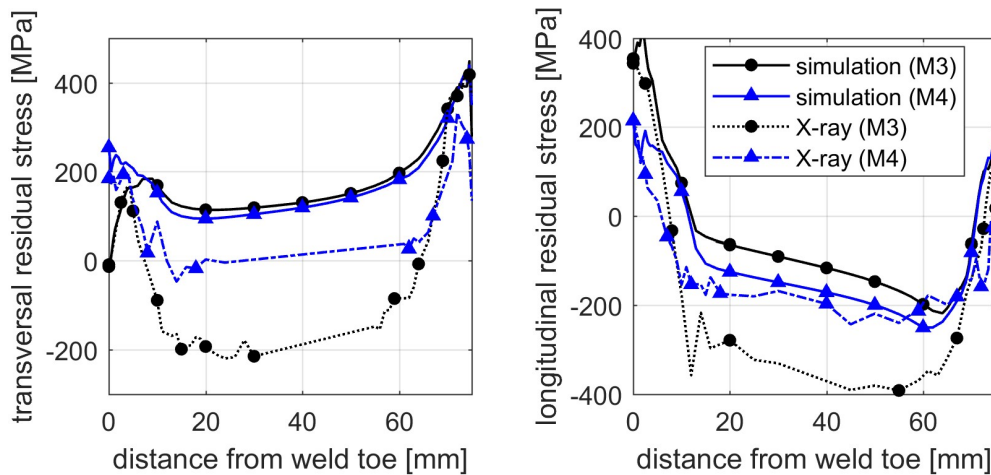


**Fig. 13** Calculated and measured residual stresses between cruciform Joint (distance = 0 mm) and longitudinal stiffener (distance = 75 mm) (M3 and M4 indicate specimen number according to [17]).

The comparison of the simulation results to the measurements (Fig. 13) shows a relatively good agreement at the ends of the measuring path (up to 5 mm from both welds) and a large difference in the middle (5 to 70 mm). This was due to compressive residual stresses up to -300 MPa on the plate surface resulting from blast cleaning. Specimen M4 had been stress relieved before welding and these compressive residual stresses were reduced to -50 MPa. In the zones heated by the welds the residual stresses present in the plate were relieved and the welding residual stresses prevailed.

## CONCLUSIONS

A welding simulation approach for metal active gas welding using a uniform temperature heat source without calibration and a simplified consideration of phase transformation was applied to a longitudinal stiffener. Simulation parameters were varied to show their influence on the calculated residual stresses. Simulation results and residual stress measurements on three different welded geometries were compared for validation.

The following is concluded from the results:

- With the applied simulation approach a variation in heat input does not significantly affect the amount of residual stresses calculated on the plate surface at a longitudinal stiffener. No influence of the temperature interval for phase transformation during cooling was observed. The variation of yield strength did affect the resulting residual stresses. If the objective are the residual stresses in front of the weld, for this particular weld geometry, the heat input appears to be of less importance than mechanical material properties.
- Residual stress measurements by X-ray diffraction and holed drilling showed large differences. Especially on the longitudinal stiffener transversal residual stresses measured by X-ray diffraction were lower than the hole drilling results.

- The calculated residual stresses lay within the scatter of the hole drilling measurements. On the small-scale specimens the values were about 100 MPa higher than the X-ray diffraction measurements. Different residual stress distributions due to the changed weld pass arrangement at the cruciform joint of the large-scale component could be determined by the simulations.
- Based on the results, the presented simulation approach appears suitable to predict residual stresses from MAG welding in low alloy steels at least qualitatively ( $\pm 100$  MPa). This applies only to residual stresses on the plate surface in front of the weld. Residual stress distributions over the plate thickness or distortions have not been verified. Considering the uncertainties in the measurements, this result seems acceptable.

### ACKNOWLEDGEMENTS

The presented research was funded by the Deutsche Forschungsgemeinschaft (DFG, German Research Foundation) – EH 485/4-1.

### REFERENCES

- [1] J.-D. CAPRACE, G. FU, J. F. CARRARA, H. REMES, S. B. SHIN: ‘A benchmark study of uncertainty in welding simulation’, *Marine Structures*, Vol. 56, pp. 69-84, 2017.
- [2] L.-E. LINDGREN: *Computational welding mechanics - Thermomechanical and microstructural simulations*, Woodhead Publishing in Materials, Cambridge, 2007.
- [3] C. HEINZE, C. SCHWENK, M. RETHMEIER: ‘Effect of heat source configuration on the result quality of numerical calculation of welding-induced distortion’, *Simulation Modelling Practice and Theory*, Vol. 20, pp. 112-123, 2012.
- [4] A. BELITZKI, C. MARDER, A. HUISSEL, M. F. ZAEH: ‘Automated heat source calibration for the numerical simulation of laser beam welded components’, *Prod. Eng. Res. Devel.*, Vol. 10, pp. 129-136, 2016.
- [5] J. KLASSEN: *Beitrag zur vereinfachten Eigenspannungsberechnung von Mehrlagenschweißverbindungen [Contribution to simplified residual stress calculations for multilayer welds, in German]*, dissertation, TU-Braunschweig, 2018.
- [6] J. A. GOLDAK AND M. AKHLAGHI: *Computational welding mechanics*, Springer, New York, 2005.
- [7] N. FRIEDRICH AND S. EHLERS: ‘A simplified welding simulation approach used to design a fatigue test specimen containing residual stresses’, *Ship Technology Research*, to be published 2018.
- [8] J. GOLDAK, A. CHAKRAVARTI, M. BIBBY: ‘A new finite element model for welding heat sources’, *Metallurgical Transactions B*, Vol. 15, pp. 299-305, 1984.
- [9] J. B. ROELEN, F. MALTRUD, J. LU: ‘Determination of residual stresses in submerged arc multipass welds by means of numerical simulation and comparison with experimental measurements’, *Welding in the World*, Vol. 33, No. 3, pp. 152-159, 1994.
- [10] L.-E. LINDGREN, H. RUNNEMALM, M. O. NÄSTRÖM: ‘Simulation of multipass welding of a thick plate’, *Int. J. for Numerical Methods in Engineering*, Vol. 44, No. 9, pp. 1301-1316, 1999.
- [11] VEREIN DEUTSCHER INGENIEURE, EDITOR: *VDI heat atlas. 2nd ed.*, Springer, Berlin, 2010.

- [12] M. WICHERS: *Schweißen unter einachsiger, zyklischer Beanspruchung – Experimentelle und numerische Untersuchungen [Welding under uniaxial cyclic loads – Experimental and numerical research, in German]*, dissertation, TU-Braunschweig, 2006.
- [13] K. DILGER AND T. WELTERS, EDITORS: *Schlussbericht zum BMBF-Verbundprojekt SST – Schweißsimulationstool [Report to the BMBF-project SST – welding simulation tool, in German]*, Shaker Verlag, Aachen, 2006.
- [14] ASTM E837-13a. *Standard test method for determining residual stresses by the hole-drilling strain-gage method*, ASTM International, West Conshohocken (PA), 2013.
- [15] G. SCHAJER: ‘Measurement of non-uniform residual stresses using the hole drilling method’, *J. of Engineering Materials and Technology*, Vol. 110, No. 4, Part I pp. 338-343, Part II pp. 344-349, 1988.
- [16] G. S. SCHAJER, EDITOR: *Practical residual stress measurement methods*, Wiley, Chichester (UK), 2013.
- [17] J. KLASSEN, N. FRIEDRICH, W. FRICKE, T. NITSCHKE-PAGEL, K. DILGER: ‘Influence of residual stresses on fatigue strength of large scale welded assembly joints’, *Welding in the World*, Vol. 61, pp. 361-374, 2017.
- [18] J. KLASSEN, N. FRIEDRICH, W. FRICKE, T. NITSCHKE-PAGEL, K. DILGER: *Entwicklung von Methodiken zur Bewertung von Eigenspannungen an Montagestößen bei Stahl-Großstrukturen. AiF-Schlussbericht. IGF-Vorhaben 17652N [Development of methods for evaluation of residual stresses in assembly joints of large steel structures. AiF-report. IGF-project 17652N, in German]*, 2016.





# REAL-TIME WELDING SIMULATION FOR EDUCATION

O. MOKROV\*, M. SIMON\*, A. SCHMIDT\*, U. REISGEN\*,  
A. BEHMEL\*\*, J. MARTIN\*\*, A. BECIROVIC\*\*\* and  
D. RUDOLPH\*\*\*\*

*\*Institut für Schweißtechnik und Fügetechnik der RWTH Aachen University, 52062 Aachen, Germany*

*\*\*Institute of Design & Communication der FH JOANNEUM Gesellschaft mbH, 8020 Graz, Austria*

*\*\*\*Fronius International GmbH, 4600 Wels-Thalheim, Austria*

*\*\*\*\*AUDI AG, Neckarsulm, Germany*

DOI 10.3217/978-3-85125-615-4-47

## ABSTRACT

Virtual reality training systems are state-of-the-art technology in welding education and are mainly meant to teach the manual skills needed for proper welding. In combination with computational numerical welding process simulation such systems can also be used to investigate the influence of different welding parameters on close-to-reality welding results. In this work, a virtual welding training system has been combined with physical welding process simulation algorithms that are optimised for near-real-time calculations and thereby enable a trainee to visualise and learn the influence of different welding parameters in a fast and cost-efficient way.

Keywords: Arc Welding, Visualization, Weld Pool, Education, Modelling

## INTRODUCTION AND MOTIVIATION

Virtual Reality Training Systems are well known and well established in many different disciplines. One example are Flight Simulation Training Systems. In welding education, such systems are state-of-the-art when it comes to learn the manual skills needed for proper welding. In combination with computational numerical welding process simulation, it is possible to enhance such Virtual Reality Training Systems and therefore to enable a trainee to visualize and learn the influence of different welding parameters in a fast and cost-efficient way. To our knowledge, there is no virtual welding training system available currently that combines the advantages of virtual environments and physically calculated welding results into one system.

The use of computational simulation methods based on physical models for the investigation of arc welding processes is an established engineering method [1,2]. It is an efficient way to find necessary welding parameters, especially for tasks that exceed usual or well-known requirements. However, numerical welding process simulation has a trade-off between calculation time and result accuracy. The calculation of half a second of welding with high physical accuracy can easily take several weeks, even on a high-performance computing system [3].

To overcome these restraints regarding the usage of numerical welding simulation algorithms within Virtual Reality Training Systems, a research project has been executed that focused on the solution of the following challenges:

- Based on the welding simulation algorithms programmed for the SimWeld® platform [4] the simulation models have to be enhanced to allow transient calculation for the process simulation of manual GMA welding.
- For real-time simulations and visualizations in a virtual reality framework a framerate of at least 25 Hz is mandatory. An extensive acceleration of the transient numerical welding simulation algorithms is necessary to allow the computation in or near real-time.
- Based on the virtual welding training system Fronius Virtual Welding® a visualization module for the simulation results has to be designed and implemented.
- These two software systems have to be coupled to interact in a way that minimizes delays.

This article summarizes the results of the research project.

### INITIAL STEADY STATE MODEL OF GMA WELDING IN SIMWELD®

Since 2001 the simulation group of the Welding and Joining Institute of RWTH Aachen University (ISF) has been carrying out research on arc welding processes to formulate physical models that, after being implemented into software (SimWeld® – Welding Process Simulation Software [5-7]), allow to calculate weld seam geometry and heat input and distribution within a few minutes on a standard personal computer. This kind of simulation is referred to as welding process simulation [8], which covers a macroscopic area of the construction component (welding and heat affected zone without material transformations) with a considered time interval between a few milliseconds and a few seconds.

The model architecture of the steady-state simulation algorithms implemented in SimWeld® is shown in Fig. 1: based on the given welding parameters, material properties and power source control algorithms, in the first part of the simulation, the Wire Drop Arc Model is calculating an average heat and mass input as well as an arc pressure distribution for a defined welding time. This result then serves as an input parameter for the Weld Pool and Seam Formation model and the Heat Flow model: The former one calculates the weld pool and seam geometry while the latter one calculates the heat flow within the complete macroscopic area of the work-piece.

With this model implementation the calculation of one simulation iteration that covers all three models takes about 5 minutes on a common office PC, which is much less time compared to other welding process simulation algorithms [3]. This is solely possible, because fluid flows as well as magneto-hydrodynamic effects in the weld pool and arc area are not included in the calculation directly but in the form of simplified compensation algorithms.

However, even this rather quick calculation is by far not fast enough to be applied in a virtual reality welding training system, where the trainee has to get a prompt response to his actions in order to benefit from this system. At the same time, the model architecture

has to be modified in a way that it allows transient calculations to provide results for manual welding, where the welding velocity, the torch angles and the torch distance are irregular in comparison to robotic welding and even small corrections of the trainee by moving the torch backwards have to be considered. Therefore, the initial steady-state version of SimWeld® was used only as a starting point for the development of a fast transient calculation with the aim of eventually achieving real-time performance.

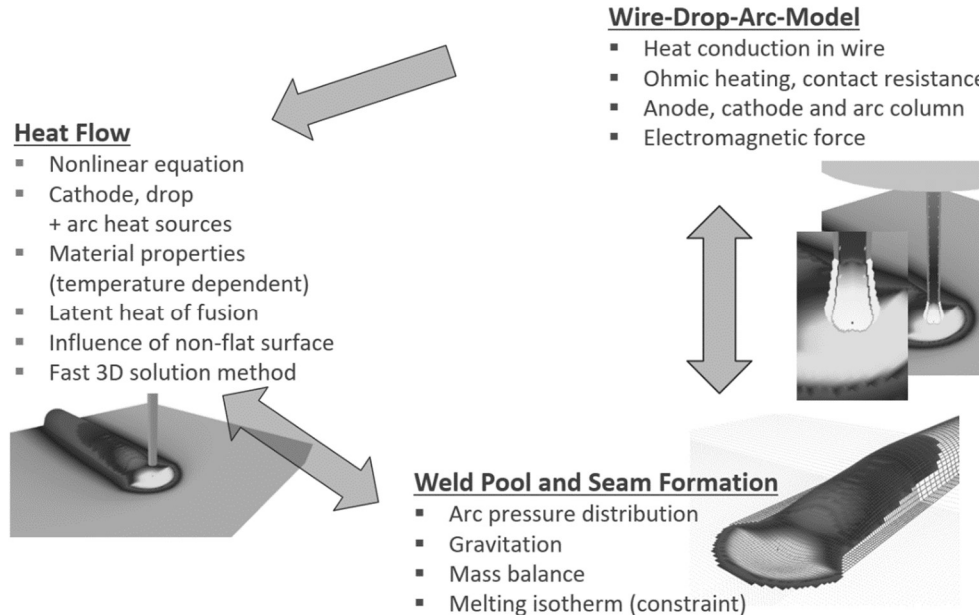


**Fig. 1** Physical models implemented in SimWeld® and their interactions

### A TRANSIENT SIMULATION MODEL OF GMA WELDING FOR REAL-TIME PROCESS SIMULATION

The transient model architecture that was developed is based on the steady-state algorithms of SimWeld® but allows the transient execution of the GMA welding process simulation. The base Wire Drop Arc Model in Fig. 1 is already transient and able to simulate the heat- and droplet mass transfers to the weld pool. Nevertheless, it was necessary to add the reaction of the electrical circuit on the variable stick-out to the model. In the main simulation loop, each iteration covers a time of 0.04 s. The first step in each iteration is the execution of the Wire Drop Arc Model that includes an inner loop where each iteration covers 0.1 ms. This model is able to react on current pulses and short circuits. For a simulated time of 0.04 s it generates the following average results: voltage, heat input of the arc cathode energy as well as heat, mass and velocity of the droplet.

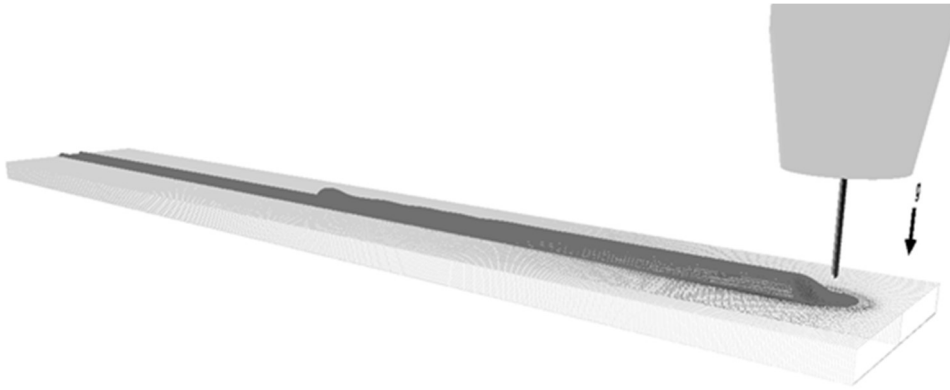


**Fig. 2** Example of the result of a transient Simulation in SimWeld®

These average results are used as input parameters for both other sub-models in the main loop iteration. First of all, the tentative top surface of the weld pool from the previous main loop iteration will be modified proportionally to the droplet mass. In a second step, the distributions of cathode heat input and droplets effect, which are functions of wire speed, current and voltage of the arc and melting front location, are calculated. Then, these distributions are modified according to the torch position and the torch angles in relation to the weld pool, to be used subsequently as input parameters in the heat transfer computation of the weld pool and HAZ. The last step in the main loop iteration is the calculation of the modifications of the weld pool surface that maintain a balance of pressures, taking into account: surface tension, mass balance in the weld pool, gravitation and pressure of the arc. An underlying assumption here is that the transient effects of the changes during the period of 0.04 s are negligible. The results of this simulation procedure are shown in Fig. 2, where it can also be seen that the initial and the end of the transient weld were retrieved in the simulation.

In parallel to the development of a transient simulation model of GMA welding the model structure was modified to allow a significant speedup in calculation time with the aim to reach a frequency of 25 simulation iterations per second. As a first step to this goal, a prototype has been developed, which allowed the determination of the calculation time for one simulation iteration and the fraction of this time for each model in SimWeld®.

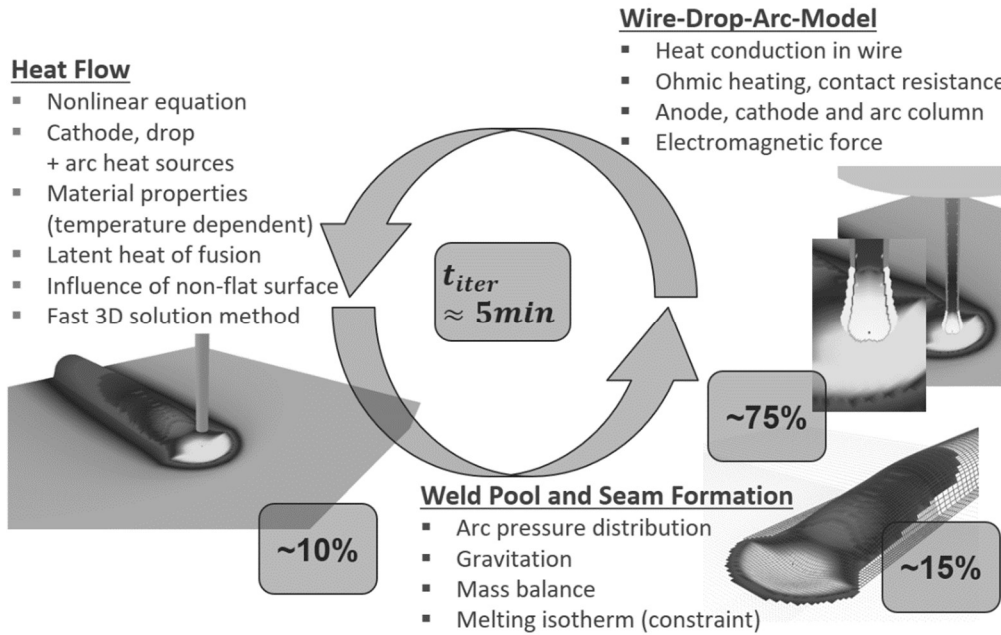


**Fig. 3** Calculation time for one steady-state iteration of all physical models as well as the according fraction of calculation time for each model before the speed up and restructuring of the algorithms

The result based on simulations with a regular office PC is shown in Fig. 3: The overall calculation time for one iteration is about five minutes, where the Wire Drop Arc Model takes about 75 %, the Weld Pool and Seam Formation Model 15 % and the Heat Flow Model 10 % of the calculation time. Further investigations have shown that 80 % of the calculation time within the Wire Drop Arc Model were needed for the calculation of the heat transfer. The transient sub-models were reduced in dimensions from 2D to 1D:

- wire electrode heating
- electrode metal melting
- droplet formation
- droplets transfer to melting pool
- electric arc plasma area

The sub-model of Weld Pool and Seam Formation has been restricted in two iteration loops: first with fast convergence and coarse results and second with slow convergence and fine results. All non-linear effects are neglected during each time step and only taken into account between two succeeding time steps. Additionally, the calculation area of the Heat Flow sub-model has been limited to an area that covers the molten zone as closely as possible. Outside of this area, a different concept is used, see Fig. 6. The temperature dependent material properties are pre-calculated.

The result of restructuring the simulation models and accelerating the algorithms lead to a significantly reduced simulation time of less than 1 s per iteration (Fig. 4), which means an acceleration by factor of 300. This is a remarkable result although it does not fulfil the

requirement of 40 ms per iteration for real-time simulations and visualizations in a virtual reality framework.

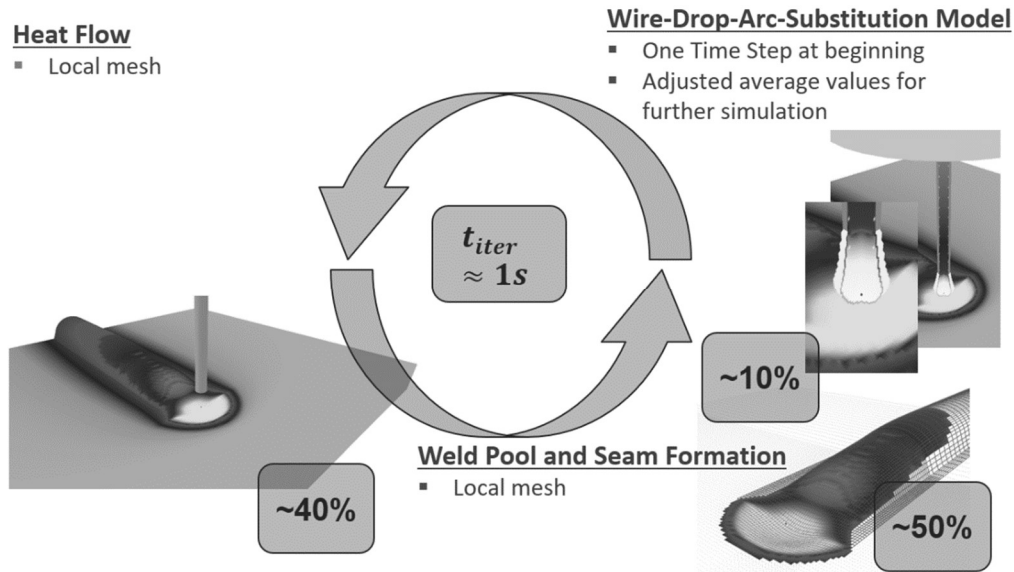


**Fig. 4** Calculation time for one transient iteration of all physical models as well as the according fraction of calculation time for each model after the speed up and restructuring of the algorithms

### IMPROVEMENTS OF THE HEAT INPUT DISTRIBUTION IN THE ARC CATHODE AREA

In the GMA welding process, an arc plasma burns between the work piece (cathode) and the melting wire electrode (anode). For the prediction of the weld seam geometry the calculation of the temperature fields is necessary. The conversion of electrical energy of the arc to heat energy to the materials of the cathode and the anode happens in thin layers of the arc adjacent to the material boundaries. In GMA process simulation, the distribution of the generated heat flux is usually described as a 2D Gaussian distribution that is applied to the weld pool (Fig. 5 - left).

Current results of fundamental research regarding the cathode area of GMA welding processes show that further improvements concerning the accuracy of the simulation results can be reached by a more detailed description of the physical processes in the cathode area. Although in this project, one main objective is the acceleration of the simulation algorithms, the new heat flux distribution in the cathode area can be assumed as a simplified consideration, to counteract the loss of accuracy caused by the simplifications that were made to reach the main objective.

In [9] it has been shown that a different heat input distribution appears (Fig. 5 - right) when taking into account effects of evaporation, as a reduction of the probability of an elementary cathode spot by evaporation is hypothesized. Therefore, the effects of

evaporation not only on heat transfer but also on heat generation in the cathode region were taken into account. In order to achieve real-time calculation, this model cannot be used directly. An additional algorithm was developed to consider a distribution of the resulting heat flux, which resembles the physically in depth result. Therefore, a shape-matched distribution of the resulting heat flux will be used in the accelerated model. This represents a reasonable trade-off between calculation time and physical depth description.

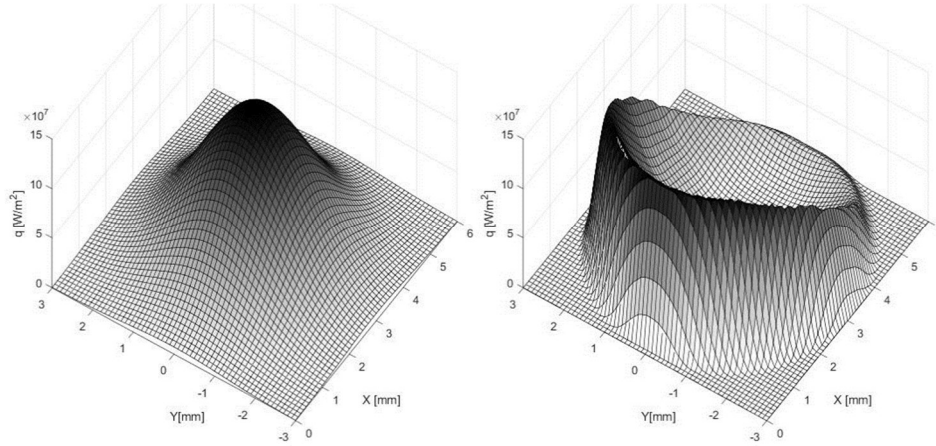


**Fig. 5** Heat energy distribution in the cathode area: left – Gaussian distribution; right – distribution modified by evaporation

### ALGORITHM FOR REAL-TIME GMA WELDING PROCESS SIMULATION

The described model modifications are the fundamental parts to reach the goal of a real-time welding process simulation software for educational purposes. This fundamental part can be used only with an algorithm that allows a fast and appropriate transient simulation for the usage in a Virtual Welding Training System.

Such an algorithm was developed based on the simulation algorithm of SimWeld®. Additionally a concept of dual local/global calculation is used: the heat transfer model consist of two simulation areas (Fig. 6). For each area a model of transient heat transfer was formulated. The first, local area is a free boundary condition area with the free surface of the weld pool. The second, global area includes the local area and is used for heat transfer calculation only.



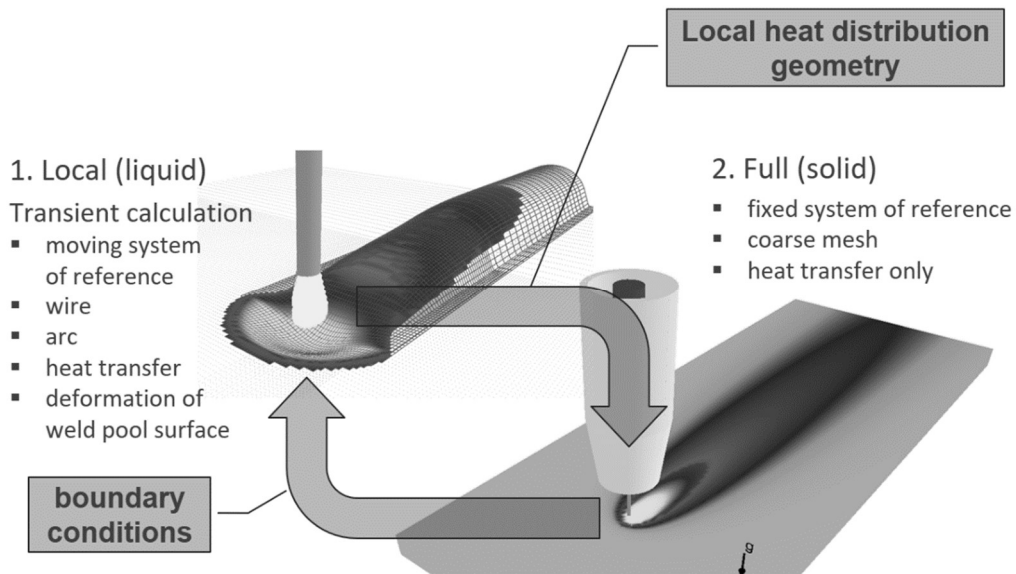


**Fig. 6** Local/Global Calculation

Within the framework of this concept, the calculation is divided into two stages and accordingly into two calculation meshes. In the first step, the transient local calculation is performed in a moving reference frame according to the torch position. A fine mesh in this step allows to calculate the processes in the wire, in the arc, the heat transfer in the melt pool and HAZ as well as the formation of the melt pool surface with acceptable accuracy. The sub-model of the surface formation of the weld seam is adapted to the transient boundary condition and to the other sub-models. These modifications allow a simulation in transient mode with an erratically moving torch in the local mesh, which is usually the case in manual welding. In the second step, the heat input of the first step is used for calculation of the global heat transfer across the entire work piece in a fixed reference frame and a relatively coarse mesh.

### COMPARISON OF SIMULATED AND EXPERIMENTAL RESULTS

The implemented simulation algorithms that are described above are designed to allow a fast calculation to be used in a virtual reality educational environment with the goal of allowing the trainee to benefit from physically based virtual welding results. For this purpose, in the trade-off-system of calculation time and result accuracy the balance was tilted in favour of a short calculation time over a high accuracy of the simulation result: the goal is that the general tendencies in the simulation were in sufficiently realistic accordance with the results of the actual weld. This approach is supported further by the argument that, when considering that many cross sections will be calculated in the transient simulation, the errors of each of the calculations will average out over a larger time interval.

To provide this goal, the simulation results have to be compared with experimental data. For this reason, welding experiments have been executed including transient measurement of current and voltage as well as cross-sections of the weld seam.

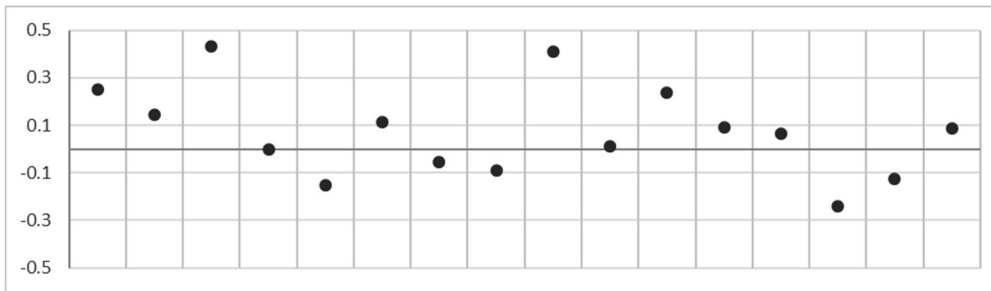


**Fig. 7** Normalized deviation of experimental and simulated weld seam area (positive means overestimated seam area in simulation, negative means underestimated)

The comparison of the experimental and the simulated results shows that the normalized area deviation between experimental and simulated results is between -0.24 and +0.44 (Fig. 7) as well as that the deviation of the heat input is between -10 % and +10 % (Fig. 8)

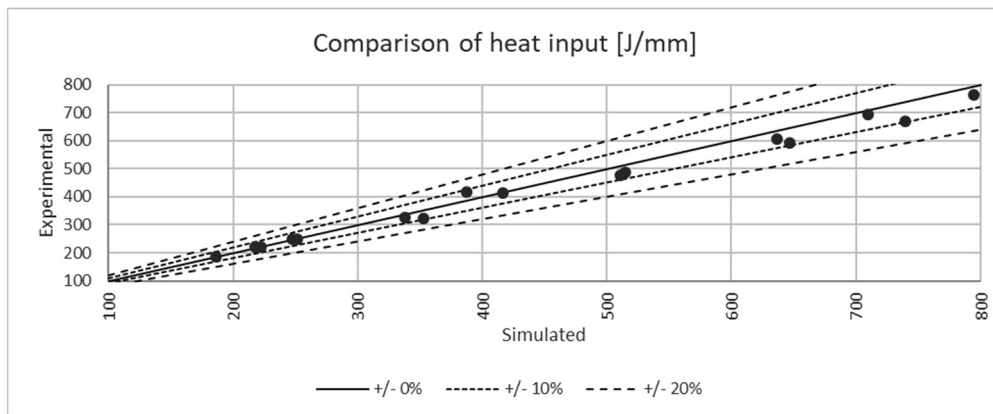


**Fig. 8** Comparison of experimental and simulated heat input in J/mm, taking into account an efficiency factor of approx. 80 %

### COMBINED VIRTUAL REALITY TRAINING SYSTEM AND PHYSICAL WELDING PROCESS SIMULATION

To connect the virtual reality training system and the numerical welding simulation models, an interface for the two systems has been defined. Therefore the approach of dynamic linked libraries was followed where the Fronius Virtual Welding® system uses a specially implemented SimWeld® DLL to provide the simulation results.

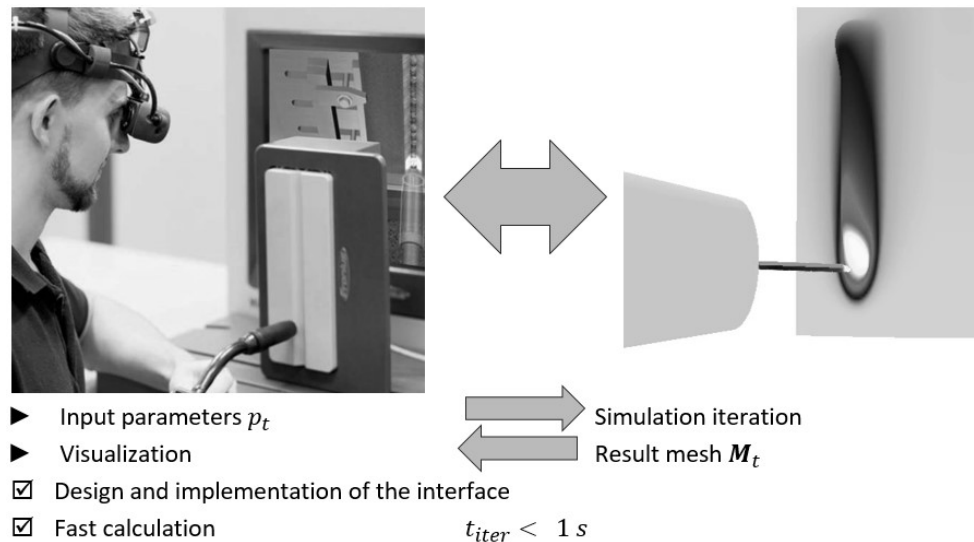


**Fig. 9** Interaction of Fronius Virtual Welding® (left) and SimWeld® DLL (right)

Fig. 9 demonstrates the basic workflow: The user uses the virtual reality platform to define the basic welding parameters and to start the training. In the background these parameters are transferred to the simulation algorithms and the simulation is initialized. During the training the current torch position and angle are transferred from the virtual reality training system to the simulation algorithms where in background the simulation of each time step is executed and its results are cached. After the training has ended, the user can check his training results based on the simulated welding results in a playback view.

The central part of the interface regarding the result visualization in 3D is a mesh that allows the transfer and display of the simulated temperature and geometry information of the weld bead, the weld seam and the work-piece. This mesh is extracted from the simulation results for each simulated time step. To reduce the amount of data, only modified nodes are stored. However, during the testing phase it became clear that the amount of data is too high to be kept in primary storage, so therefore it was decided to store the data in secondary storage and to load it on demand in the playback and analyse view.

Additionally to the 3D results for each time step the following results are provided to allow the virtual training system to determine the quality of the trainees welding results: 2D cross-section of the weld seam including seam area, seam width, reinforcement thickness and penetration depth.

## RESULT VISUALIZATION IN FRONIUS VIRTUAL WELDING

Since 2005 Fronius International GmbH together with FH JOANNEUM Gesellschaft mbH is developing a virtual welding training system (Fronius Virtual Welding®) for different welding processes (including GMA) which uses a qualitative weld seam simulation that is not based on numerical welding simulation algorithms.

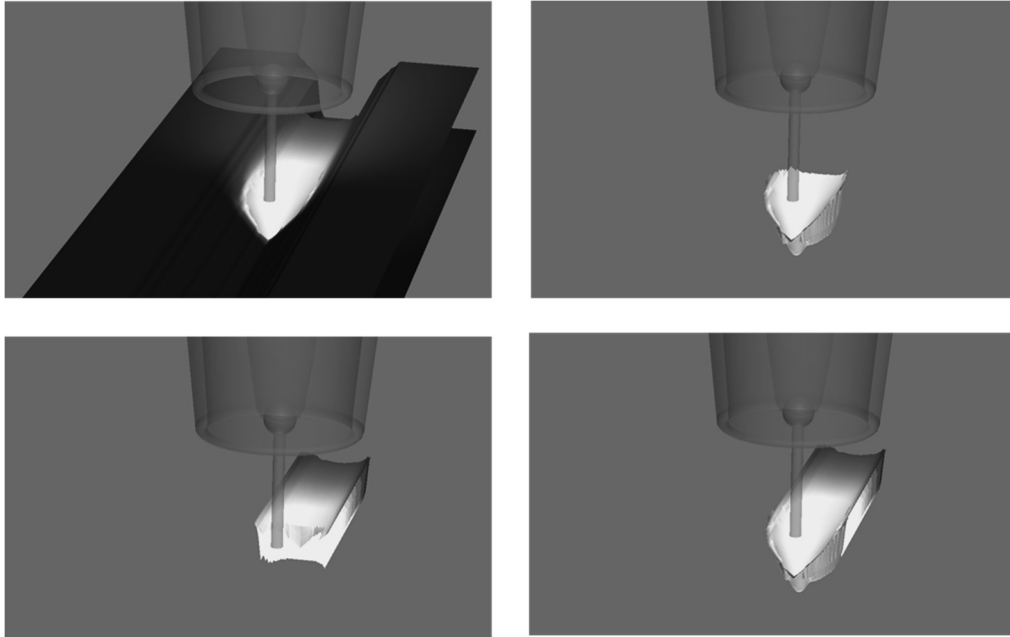


**Fig. 10** 3D visualization of numerical simulation results calculated by SimWeld® DLL (Top left: overall results, top right: weld bead only, bottom left: weld seam only, bottom right: combined weld bead and weld seam)

To visualize the results of the numerical welding simulation the training system had to be extended by an analysis module that on the one hand shows the calculated weld seam geometry (Fig. 10) and on the other hand visualizes several welding parameters (stick-out, travel and work angle) in an intuitive user interface. The user interface also includes a view of a virtual slice across the weld seam and allows the user to move its view along the weld seam. Fig. 11 shows a screenshot of the analysis module.



**Fig. 11** Screenshot of the analysis module as implemented in the Fronius Virtual Welding® training system

### CONCLUSION AND OUTLOOK

Based on our understandings regarding the GMA welding process including the current fundamental research results, a simplified but physics based model for numerical welding process simulation has been developed for usage in a virtual reality training system.

This model consists of a transient architecture that is implemented in highly efficient algorithms. This evolution of the SimWeld® model allows a reduction of the calculation time of one iteration from five minutes to less than one second. Further acceleration of the heat transfer calculation can be achieved for example with the Galerkin-Method. Additionally, the next generation of SimWeld® will be based on the newly developed transient architecture, also in cases where simulation time is not a critical condition and slower but more accurate algorithms can be used.

The losses in accuracy due to the extensive reduction of the physical models have been addressed by a calibration of the compensation models based on experimental results. Furthermore, with the consideration of a newly developed model for the heat flux distribution in the cathode area a further improvement in the understanding of the dominating physics has been applied, as well.

For real-time simulations and visualizations in a virtual reality framework, a framerate of at least 25 Hz is mandatory. Currently, this can be achieved only by using high-end computer hardware. The current training system runs on regular PCs and therefore the acceleration of the numerical simulation was not yet able to perform at the desired

framerate. Nevertheless, it is a great benefit for the trainee to have the possibility of an in-depth analysis of the training results very shortly after the training.

The project showed that it is possible to integrate a numerical welding process simulation into the Fronius Virtual Welding® training system. In a next step the prototype implementation will be further refined with the goal to provide it to users of the system in the future.

### ACKNOWLEDGEMENTS

The K-Project Network of Excellence for Metal JOINing is fostered in the frame of COMET - Competence Centers for Excellent Technologies by BMWFW, BMVIT, FFG, Land Oberösterreich, Land Steiermark, Land Tirol and SFG. The programme COMET is handled by FFG.

### REFERENCES

- [1] U. REISGEN, O. MOKROV, E. ROSSITER ET AL.: 'Welding process simulation for the calculation of an equivalent heat source', *Mathematical Modelling of Weld Phenomena 9*, Verlag der Technischen Universität Graz, pp. 927-940, ISBN 978-3-85125-127-2, 2010.
- [2] T. LOOSE, O. MOKROV, A. SCHARFF, U. REISGEN: 'Prediction of weld quality with expanded welding process analysis by SimWeld and WeldWare for GMA welding', *Mathematical Modelling of Weld Phenomena 11*, Verlag der Technischen Universität Graz, pp. 205-212, 2016.
- [3] U. REISGEN, M. SCHLESER, O. MOKROV, A. ZABIROV, U. FÜSSEL, M. SCHNICK, M. HERTEL, S. JAECKEL.: 'Modellierung und Visualisierung der MSG-Lichtbogenprozesse', *Schweißen und Schneiden 64*, DVS Media, Düsseldorf, pp. 166 – 174, 2012.
- [4] T. LOOSE, O. MOKROV: 'SimWeld® and DynaWeld Software tools to setup simulation models for the analysis of welded structures with LS-DYNA', *European LS-DYNA Conference, Würzburg*, 15.-17.6.2015, Stuttgart: Dynamore GmbH, S. 145-146.
- [5] O. MOKROV, V. PAVLIK, V., U. DILTHEY: 'Analyses of Thermo-Electrical Process and Electrode Metal Transfer During Gas-Metal-Arc Welding with the Aid of Numerical Modelling.' *Math. Mod. Inf. Techn. Weld. Relat. Pro., Paton Electric Welding Institute*, Kiev, Ukraine, pp.250-257, 2006
- [6] V. PAVLYK, O. MOKROV, U. DILTHEY: 'Heat Source Modelling in GMA-Welding and its integration in Stress-Strain Analysis'. *Mathematical Modelling of Weld Phenomena 8*, Verlag der Technischen Universität Graz, pp.801-818, ISBN 978-3-902465-69-6, 2007.
- [7] T. LOOSE: SimWeld® [online]: 'SimWeld® - Prozeßsimulation für das MSG Schweißen', Wössingen, Ingenieurbüro Loose, available online: <http://www.simweld.net>, 18.09.2018
- [8] D. RADAJ, 'Schweißprozesssimulation: Grundlagen und Anwendungen', Düsseldorf: Verl. für Schweißen und verwandte Verfahren DVS-Verl, 1999.
- [9] O. MOKROV, M. SIMON, A. SCHIEBAHN, U. REISGEN: 'Evaporation-determined Model for Cathodic Heating in GMA Welding'. Proceedings of the XXII<sup>nd</sup> International Conference on Gas Discharges and Their Applications 2<sup>nd</sup>-7<sup>th</sup> September 2018 Novi Sad, Serbia Vol. 1, Beograd: SANU 2018 (Beograd Planeta print), pp. 87-90, ISBN 978-86-7025-781-8, 2018.



# ASYMPTOTICS AND BLENDING IN THE MODELING OF WELDING

Y. WANG\*, Y. LU\*, M. GRAMS\*, A. CESARO\* and P. MENDEZ\*

*\*University of Alberta, University of Alberta, Canada; pmendez@ualberta.ca*

DOI 10.3217/978-3-85125-615-4-48

## ABSTRACT

Important welding questions are often easy to ask and difficult to answer. For example, the question "what is the width of the weld?" is essential for understanding the strength of a weld, but it is currently answered through trial and error, or through sophisticated numerical modeling. In this work, it is proposed that there is a third approach based on a deep understanding of physics, and a basic command of mathematics. From the point of view of the practitioner, the answer can be approximated using formula, tables, and graphs of great generality. In this approach, the aspect of interest of the weld is reduced to its minimal representation, neglecting all secondary physical phenomenon. Mathematically, this corresponds to an asymptotic regime. In contrast with other asymptotic techniques such as perturbation analysis, in the proposed methodology, blending techniques are applied. The advantage of these blending techniques is that they approach the exact solutions (typically within a few percentage points) but involve only a few constants that are suitable to be transmitted in print. Much of the existing work on heat transfer outside welding is summarized in this form, but the approach has not been applied to welding yet. Some welding problems are outside the range of standard blending techniques, and an extension of the techniques will be discussed. The application of this approach will also be discussed using the width of the weld and other related problems.

Keywords: Heat transfer, Asymptotics, Blending, Scaling, Modeling

## INTRODUCTION

The complexity of an engineering problem can be decomposed into the complexity of its physics, which can be assessed by the number of parameters related to the physics of the problem, and the complexity of its geometry, given by the number of parameters necessary to capture the shape of the problem [1]. In the field of welding, the geometry of welding processes (e.g. bead geometry and joint preparation) is generally not complex; however, the large number of parameters relative to relevant physics such as heat and mass transfer, fluid dynamics, electromagnetism, thermodynamics, as well as their tight coupling make welding very difficult to understand at intuitive level and more complex than most other engineering fields.

Typically, there are three approaches to analyze welding problems: trial and error (making a prototype), numerical simulation and design rules. Trial and error is the most common and reliable way in welding procedure development as it is capable of producing the reality with complex geometries and provides direct measurements from experiments. However, case-by-case results of specific processes are difficult to be synthesized for the



next trial or extended to new operating parameters. The horizontal axis in Fig. 1 is the cost of making a prototype and the vertical axis represents the total cost.

Sophisticated computer simulations are cost effective in the fields such as aerospace and nuclear industry where the prototype is time-consuming and expensive to make. In welding, running a weld may cost on the order of one to thousand dollars and within this range of cost, making a prototype or trial and error usually costs much less money than developing or implementing a comprehensive simulation. Numerical models excel at dealing with the complexity of geometries, but implementing multicoupled physics is often challenging.

Design rules (the red horizontal line in Fig. 1) can significantly lower costs, and enable a design approach to welding procedures which are usually done by trial and error. Typically, the design rules can be expressed in the form of simple formulae and correction factors. The simple formulae are the asymptotic solutions to ideal case and their correction factors are developed to capture the departures from the ideal cases.

Instead of considering every point in the space-time domain, the target of the design rules is to predict the characteristic values such as a maximum velocity, or maximum temperature. The concept of characteristic values was discussed in detail in [2] to normalize the governing equations into proper magnitudes and it is typically chosen as the maximum absolute value of the function of interest. Asymptotic analysis and blending do not present convergence problems and they are well suited for multiphysics problems.

The use of design rules can provide guidelines for follow-up tests and significantly reduce the money and effort put in the trial and error stage. There are very few of these design rules in the field of welding; for example, the practical question "what is the resulting width of a weld bead by a given set of parameters" is difficult to be answered quickly within the existing knowledge.

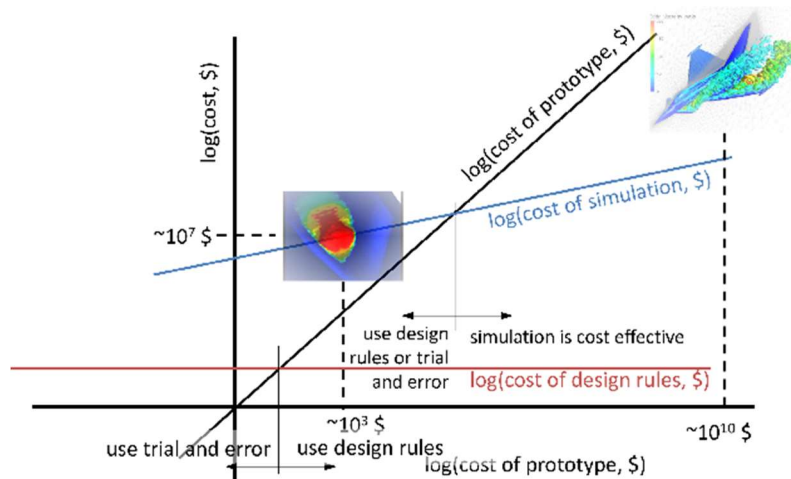


**Fig. 1** Costs of simulation, prototypes, and design rules. For the aerospace industry, a prototype is much more expensive than simulations. For welding, a prototype is often cheaper than simulations, resulting in trial-and-error approaches. Design rules are much less expensive than simulations, and should enable a design approach where it is seldom done currently.

Expressions in explicit form which are general, accurate, easy-to-calculate are convenient for transmission and amenable to be used by practitioners in industry. This

paper proposes a systematic methodology based on asymptotics and blending techniques to develop a set of formulae in standardized form (asymptotics and correction factors) that can predict (or estimate reasonably) important weld properties valid for general welding procedures with different alloys, process conditions and operating parameters. The predictions sought would target the size of the weld pool, heating and cooling rates, melting efficiencies, etc., such that they could be coupled with metallurgical and performance models.

The systematic methodology advocated here to obtain engineering formulas of interest can be roughly summarized as a six-step procedure call the Minimal Representation and Correction Factors (MRCF) [3]. MRCF considers the dominant phenomena and the deviations from the ideal case using the exact analytical solutions, experimental measurements or results from numerical models. Once a complex multicoupled problem is minimally represented by its dominant mechanisms, explicit, closed-form expressions can be developed.

Blending techniques will be applied to extend the asymptotic solutions to the whole domain of dimensionless groups capturing the characteristic values of interest. Blending has been widely applied in many disciplines such as heat transfer [4, 5], including moving heat sources [6], mass transfer [7], and fluid dynamics [8]. With blending, correction factors can be rigorously derived to capture the deviation from asymptotic behavior and define the validity of the asymptotics. Blending techniques and their extension are the main focus of this paper.

### MRCF: MINIMAL REPRESENTATION AND CORRECTION FACTOR

The approach presented here for asymptotic analysis of engineering problems is the Minimal Representation and Correction Factor (MRCF). It was first proposed in [3] and has been successfully implemented to construct general expressions for thermal characteristics of moving heat sources in [6, 9]. The MRCF approach consists of the following six steps:

- List all physics considered relevant
- Identify dominant factors
- Solve approximate problem considering only dominant factors (Minimal Representation)
- Check for self-consistency
- Compare predictions to "reality"
- Create correction factors

The minimal representation of a problem corresponds to the formulation of the problem with parameters such that all secondary phenomena become negligible. There are various techniques for obtaining the minimal representation. They can be roughly divided into manual and computational techniques. Manual Asymptotics include "Informed" Dimensional Analysis: generate dimensionless groups based on knowledge about system [10-15], Inspectional Analysis: dimensionless groups from normalized equations[16-19],

Order of Magnitude/Balancing Techniques [20-22]. Computational Asymptotics include Statistical analysis/data mining[23-25], and analysis of the Governing equations[2, 3, 26].

The MRCF is an iterative approach of identifying dominant phenomena and solve the simple solutions of this minimal represented problem by considering only dominant factors and characteristic values of the simplified problem can be addressed by asymptotics to capture the behavior of the system for combinations of parameters that result in the same dominant phenomena (which is called a Regime). Thus, a multicoupled complex problem will be decomposed into its minimal representation of the dominant mechanisms. The dominant factors are typically unknown and need ingenuity and expertise to make a reasonable postulation. The advantage of the MRCF is that this iterative process transverses all possible choice of dominant factors and self-consistency is checked for the obtained results to assure the neglected phenomenon are secondary. Departure from the reality caused by the neglect of secondary phenomenon will be accounted by the correction factors, which capture the deviation from the ideal solutions. Correction factors can be calibrated with experimental numerical results to account for secondary phenomena not considered explicitly.

### IMPORTANT CONCEPTS AND NOTATION IN MRCF

Because of the complexity of the concepts involved in MRCF, careful notation is essential. We will call here  $\{U\}$  the set of dependent variables with elements  $u(\{X\}, \{P\})$ , where  $\{X\}$  is the set of independent variables, and  $\{P\}$  is the set of problem parameters.

When the parameters of an engineering problem change, the resulting characteristic values will be influenced even if the independent variables remain unchanged. Thus, the set of problem parameters  $\{P\}$  is also included as arguments of the solution functions. Accordingly,  $u_c$  represents the characteristic value of  $u(\{X\}, \{P\})$ .

For the sake of greater generality, normalization will be applied to transform relevant variables into dimensionless form and thus, results in different units or from different operating parameters can be generalized and compared within the same scale. The magnitude  $\hat{u}_{c,i}$  is the asymptotic behavior of  $u_c(\{P\})$  in Regime  $i$  (e.g. Regime I, Regime II) where the value of the dimensionless groups based on parameters is asymptotically large or small. Very often, the asymptotic behavior has power-law dependence on the dimensionless groups.

In normalized form,  $u^*(\{X^*\}, \{\Pi\})$  is the dimensionless dependent variable where  $\{X^*\}$  is the set of normalized independent variables, and  $\{\Pi\}$  is a set of independent dimensionless groups based only on the problem parameters.  $u_c^*(\{\Pi\})$  is the characteristic value of  $u^*(\{X^*\}, \{\Pi\})$ . Similarly,  $\hat{u}_{c,i}^*(\{\Pi\})$  is the asymptotic behavior of  $u_c^*(\{\Pi\})$  in Regime  $i$  (often in the form of a power law).

Dimensional analysis indicates that a problem can be captured by a set of  $n$  dimensionless groups, where  $n = m - k$ ,  $m$  is the number of independent physical magnitudes involved in the problem, and  $k$  is the set of independent reference units of the problem [27]. Typically, the functional dependence between the characteristic value targeted ( $u_c$ ) and the dimensionless groups is monotonic, thus the number of regimes is two per dimensionless group (close to zero, and close to infinity, then the number of regimes  $n_r$  is:

$$n_r = 2^n \quad (1)$$

### FOUNDATIONS OF BLENDING TECHNIQUES

Blending is the general description of a family of techniques of interpolation between two asymptotic solutions. In this work, the focus is on techniques that use a very small number of parameters (typically one or two). The advantage is that they are very easy to communicate and implement. Surprisingly, in many practical cases these techniques have a very small error (typically few percentage points) against the exact solution they are interpolating.

The oldest technique of interest for this work was first described by Acrivos [28, 29] for the rate of heat and mass transfer in several laminar boundary layer flows and was later extended and generalized by Churchill and Usagi [30, 31] as the CUE (Churchill-Usagi equation).

In this work we will use the notation  $\mathcal{B}$  to represent the blending of asymptotics  $\widehat{u}_{c,i}^* (\{\Pi\})$ , corresponding to regime  $i$  (Regime I, Regime II, etc.) using the set of blending parameters  $\{B\}$ , thus:

$$u_c^* (\{\Pi\}) \approx \widehat{u}_c^{*+} (\{\Pi\}) = \mathcal{B}(\widehat{u}_{c,I}^* (\{\Pi\}), \widehat{u}_{c,II}^* (\{\Pi\}), \widehat{u}_{c,III}^* (\{\Pi\}) \dots \{B\}) \quad (2)$$

where the symbol  $\widehat{\phantom{x}}$  indicates that the magnitude is an asymptotic approximation and the  $^+$  superscript represents the improvement over the asymptotics after blending.

There are several approaches to determine the set of blending constants  $\{B\}$  and the minimax optimum procedure [6] applied in this paper is used to determine the optimum set of blending constants which minimizes the maximum error defined as:

$$\text{Maxerror} = \max_{\Pi} \left[ \ln \frac{\widehat{u}_c^{*+} (\{\Pi\})}{u_c^* (\{\Pi\})} \right] \quad (3)$$

where  $u_c^* (\{\Pi\})$  is the target dimensionless characteristic value, which can be an exact analytical solution, experimental measurements or numerical simulation results. The maximum value is explored over the whole domain of  $\{\Pi\}$ , and the minimum is explored over the blending parameters  $\{B\}$ .

Eqn. (3) has the advantage of revealing the comparable magnitudes for large errors and it is equivalent to the definition of relative error when the error is small. The set of blending constants  $\{B\}$  needs be determined only once for each blending function.

One essential property of the blending function  $\mathcal{B}$  is that it shares the asymptotic behavior of the original function:

$$u_c^* (\{\Pi\}) \rightarrow \widehat{u}_{c,i}^* (\{\Pi\}) \quad \text{when} \{\Pi\} \rightarrow \{\Pi\}_i \quad (\text{Regime } i)$$

DEVELOPMENT OF CORRECTION FACTORS

Based on the blending of Eqn. (1), correction factors can be established for each asymptotic regime to capture the departure of the blended approximation from asymptotic behavior. In dimensionless form:

$$u_c^* (\{\Pi\}) \approx \widehat{u}_{c,i}^+ (\{\Pi\}) = \widehat{u}_{c,i}^* (\{\Pi\}) \mathcal{B} \left( \frac{\widehat{u}_{c,I}^* (\{\Pi\})}{\widehat{u}_{c,i}^* (\{\Pi\})}, \frac{\widehat{u}_{c,II}^* (\{\Pi\})}{\widehat{u}_{c,i}^* (\{\Pi\})}, \frac{\widehat{u}_{c,III}^* (\{\Pi\})}{\widehat{u}_{c,i}^* (\{\Pi\})} \dots \{B\} \right) \\ = \widehat{u}_{c,i}^* f_{u_{c,i}} (\Pi) \quad \text{for Regime } i \quad (4)$$

and its dimensional counterpart:

$$u_c (\{\Pi\}) \approx \widehat{u}_{c,i}^+ (\{\Pi\}) = \widehat{u}_{c,i} (\{\Pi\}) \mathcal{B} \left( \frac{\widehat{u}_{c,I} (\{\Pi\})}{\widehat{u}_{c,i} (\{\Pi\})}, \frac{\widehat{u}_{c,II} (\{\Pi\})}{\widehat{u}_{c,i} (\{\Pi\})}, \frac{\widehat{u}_{c,III} (\{\Pi\})}{\widehat{u}_{c,i} (\{\Pi\})} \dots \{B\} \right) \\ = \widehat{u}_{c,i} f_{u_{c,i}} (\Pi) \quad \text{for Regime } i \quad (5)$$

where the  $i^{\text{th}}$  term inside the correction factor is equal to 1 and the set of blending constants  $\{B\}$  is the same as in Eqn. (2) and  $f_{u_{c,i}} (\Pi)$  is a shorthand notation for the blending function that leads to correction factors. In the shorthand notation, the set of blending parameters is not stated explicitly, but it is present.

As the blending function  $\mathcal{B}$  maintains the asymptotic behavior of the original function, the value of the correction factor  $f_{u_{c,i}} (\Pi)$  tends to the value of 1 or at the same order as 1 in its corresponding Regime  $i$ :

$$f_{u_{c,i}} (\Pi) \rightarrow 1 \quad \text{when } \{\Pi\} \rightarrow \{\Pi\}_i \quad (\text{Regime } i)$$

Eqn. (4) and Eqn. (5) capture the deviation of the blended approximation from the asymptotic behavior. These equations can also be used to determine the range of validity of the asymptotic equations for a given acceptable error, and can also be used to account for systematic errors from the mathematical treatment of the asymptotics, or random errors from the physics caused by neglected secondary phenomenon. The correction factors developed are explicit and can typically be calculated with a handheld calculator or a spreadsheet.

1D BLENDING

When the target function depends on only one dimensionless group, the system has two asymptotic regimes (Eqn. (1)). Thus, according to Eqn. (4):

$$u_c^* (\{\Pi\}) \approx \widehat{u}_c^+ (\{\Pi\}) = \mathcal{B} (\widehat{u}_{c,I}^* (\{\Pi\}), \widehat{u}_{c,II}^* (\{\Pi\}), \{B\}) \quad (6)$$

Blending in 1D (when blending depends on only one dimensionless group) is the simplest case and the basis of the extension of blending to more complex scenarios. Standard 1D blending was treated in [28-31]; however, these studies could not account for

the case when the asymptotes did not cross. Also, the standard blending technique can result in high errors when the functions involved are not power laws.

STANDARD 1D BLENDING

In the case where the two asymptotic solutions are known and intersect with each other only once, the two asymptotes can be blended with only one blending constant (in this case  $\{B\} = \{n\}$ ):

$$u_c^* (\{\Pi\}) \approx \widehat{u}_c^+ (\{\Pi\}) = [\widehat{u}_{c,I}^* (\{\Pi\})^n + \widehat{u}_{c,II}^* (\{\Pi\})^n]^{\frac{1}{n}} \quad (7)$$

where the optimal value of  $n$  needs to be determined only once for each blending function. A sufficient (more restrictive than necessary) condition to permit the use of Eqn. (7) is that the target function is monotonous on its dependence on the dimensionless group. A vast number of engineering problems have an asymptotic behavior in the form of power laws. Eqn. (7) can also be used to create the correction factors  $f_{u_{c,I}} (\Pi)$  (based on asymptotic in Regime I) and  $f_{u_{c,II}} (\Pi)$  (based on asymptotic in Regime II) as follows:

$$f_{u_{c,I}} (\Pi) = \mathcal{B} \left( 1, \frac{\widehat{u}_{c,II}^* (\{\Pi\})}{\widehat{u}_{c,I}^* (\{\Pi\})}, n \right) = \left\{ 1 + \left[ \frac{\widehat{u}_{c,II}^* (\{\Pi\})}{\widehat{u}_{c,I}^* (\{\Pi\})} \right]^n \right\}^{\frac{1}{n}} \quad (8)$$

$$f_{u_{c,II}} (\Pi) = \mathcal{B} \left( \frac{\widehat{u}_{c,I}^* (\{\Pi\})}{\widehat{u}_{c,II}^* (\{\Pi\})}, 1, n \right) = \left\{ 1 + \left[ \frac{\widehat{u}_{c,I}^* (\{\Pi\})}{\widehat{u}_{c,II}^* (\{\Pi\})} \right]^n \right\}^{-\frac{1}{n}} \quad (9)$$

Eqn. (8) and Eqn. (9) are exactly equivalent and they capture the difference between the blended approximation and different starting asymptotic expressions. They tend to the exact value of 1 in their corresponding limits for all finite values of  $n$ . The value of  $n$  for Eqn. (8) and Eqn. (9) are the same as for Eqn. (7).

Standard 1D blending provides a new paradigm to obtain a general solution over the whole domain in terms of simple, known, limiting solutions with minimal degree of explicit empiricism, which is typically caused by the additional introduction of the blending constants  $\{B\}$ . Eqn. (7) is a canonical expression for the formulation of correlating equations and has the advantage of simplicity, generality, inherent accuracy, and convergence to theoretical solutions in the limits. Nevertheless, it must be applied with an understanding of its restrictions. It can not represent processes with irregular transition in the non-asymptotic part and Eqn. (7) only applies for the situation where asymptotes in the limiting regimes have a single intersection. What's more, the asymptotic solutions must be free of singularities because the existence of singularity will persist and disrupt the prediction even though the singularity occurs outside asserted range of the asymptote [30, 31].

1D BLENDING OF NON-CROSSING ASYMPTOTICS

Eqn. (7) is not applicable for non-crossing asymptotics. For any finite positive value of  $n$ , the blended result will always be the asymptotic of larger magnitude and the smaller asymptotic would be chosen as the approximation for any negative value  $n$ .

A modified blending technique is proposed here to extend the applicability of Eqn. (7), by applying a factor  $\exp(a\Pi^b)$  to either of the asymptotes to force the two asymptotics to have a single intersection. This approach is useful for asymptotic behavior weaker than exponential; for example, it can not be used in the case such as a  $\Gamma$  function. The 1D blending function for non-crossing asymptotics has the following expression:

$$u_c^*({\Pi}) \approx \widehat{u}_c^+({\Pi}) = \mathcal{B}(\widehat{u}_{c,I}^*({\Pi}), \widehat{u}_{c,II}^*({\Pi}), \{n, a, b\}) \\ = \{\widehat{u}_{c,I}^*({\Pi})^n + [\widehat{u}_{c,II}^*({\Pi}) \exp(a\Pi^b)]^n\}^{\frac{1}{n}} \quad (10)$$

where in this case,  $\{B\} = \{n, a, b\}$ .

The reason of choosing exponential function as the form of modification factor is due to its simplicity and that its dependence on the dimensionless group is stronger than any power law or other common functional relationships in engineering design. The sign of the coefficient  $a$  determines the type of the modification factor: when  $a > 0$ , the modification factor is always larger than 1 while for  $a < 0$ , the modification factor  $\exp(a\Pi^b)$  varies within the interval of  $(0,1]$ . Both the sign and the magnitude of  $b$  matter as the modification factor has increasing dependence on the independent variable for  $ab > 0$  while for the case of  $ab < 0$ , it decreases as the independent variable increases. An appropriate magnitude of  $b$  should be chosen to ensure the modified asymptote intersects the other. With a suitable selection of the blending constants  $\{n, a, b\}$ , the modified asymptote still maintains its asymptotic behavior, while the exponential term changes its intermediate behavior such that the two asymptotes intersect. A similar approach was made in [7] to obtain a general correlation of three functions, with the applied modification factor using  $b = 1$ .

1D BLENDING OF CONSTANT ASYMPTOTICS

Many phenomena demonstrate the asymptotic behavior of two limiting solutions of different constant values, for example, in the field of welding, the maximum hardness of the heat affected zone [32, 33] and in heat transfer, the temperature distribution of a slab heated on both surfaces at different constant temperatures. Although the treatment of non-crossing asymptotes could apply to constant asymptotics, a specific treatment of this particular problem results in convenient solutions of smaller complexity.

The following three blending functions are explored:

$$u_c^*({\Pi}_1) \approx \widehat{u}_c^+({\Pi}_1) = \mathcal{B}(\widehat{u}_{c,I}^*, \widehat{u}_{c,II}^*, \{a_1, b_1\}) \\ = \widehat{u}_{c,I}^* + \frac{\widehat{u}_{c,II}^* - \widehat{u}_{c,I}^*}{2} \left( 1 + \frac{1 - a_1{\Pi}_1^{b_1}}{1 + a_1{\Pi}_1^{b_1}} \right) \quad (11)$$

$$\begin{aligned}
 u_c^*({\Pi}_2) &\approx \widehat{u}_c^+({\Pi}_2) = \mathcal{B}(\widehat{u}_{c,I}^*, \widehat{u}_{c,II}^*, \{a_2, b_2\}) \\
 &= \widehat{u}_{c,I}^* + \frac{\widehat{u}_{c,II}^* - \widehat{u}_{c,I}^*}{2} [1 + \tanh(a_2{\Pi}_2 + b_2)]
 \end{aligned} \tag{12}$$

$$\begin{aligned}
 u_c^*({\Pi}_3) &\approx \widehat{u}_c^+({\Pi}_3) = \mathcal{B}(\widehat{u}_{c,I}^*, \widehat{u}_{c,II}^*, \{a_3, b_3\}) \\
 &= \widehat{u}_{c,I}^* + \frac{\widehat{u}_{c,II}^* - \widehat{u}_{c,I}^*}{2} \left[ 1 + \frac{2}{\pi} \arctan(a_3{\Pi}_3 + b_3) \right]
 \end{aligned} \tag{13}$$

where  $\Pi_1, \Pi_2, \Pi_3$  represents three different blending expressions, not implying multi-variable dependence, and  $\{a_1, b_1\}, \{a_2, b_2\}, \{a_3, b_3\}$  are the corresponding sets of blending constants. Eqn. (11)-(13) converge to exact asymptotics in both regimes for all finite values of  $\{a, b\}$ . Eqn. (11) is consistent with the correlation method proposed by Churchill [31] when only limiting values are known by replacing the constant asymptotic behavior of either regime with a postulated functional dependence (typically power functions) and then blending the constructed function with constant asymptotic in the other regime with a blending exponent  $n$ . Eqn. (11) is the special case with  $n = 1$ . Eqn. (11) and Eqn. (12) are essentially equivalent with the transformation of variables:  $\Pi_2 = -\frac{1}{2}\ln(\Pi_1)$ ,  $a_2 = -\frac{1}{2}b_1$  and  $b_2 = -\frac{1}{2}\ln(a_1)$ .

The two blending constants  $\{a, b\}$  capture the two degrees-of-freedom of the functional behavior after blending: the location of the midpoint  $u_c^*(\Pi) = (\widehat{u}_{c,I}^* + \widehat{u}_{c,II}^*)/2$  and the slope of tangent at the midpoint,  $\frac{d\widehat{u}_c^+({\Pi})}{d{\Pi}}$ , which represents the steepness of the transformation between the two asymptotics.

The differences in the form of the three blending expressions make them applicable for different scenarios. The main difference between Eqn. (11) and Eqn. (12) is the domain, which is  $(0, \infty)$  of Eqn. (11), and  $(-\infty, \infty)$  of Eqn. (12). Eqn. (12) and Eqn. (13) share the same domain of  $(-\infty, \infty)$  and but the curvature is different, with the same slope at the value of 1 and the same location of midpoint, Eqn. (13) is less sharp than Eqn. (12) as shown in Fig. 2.



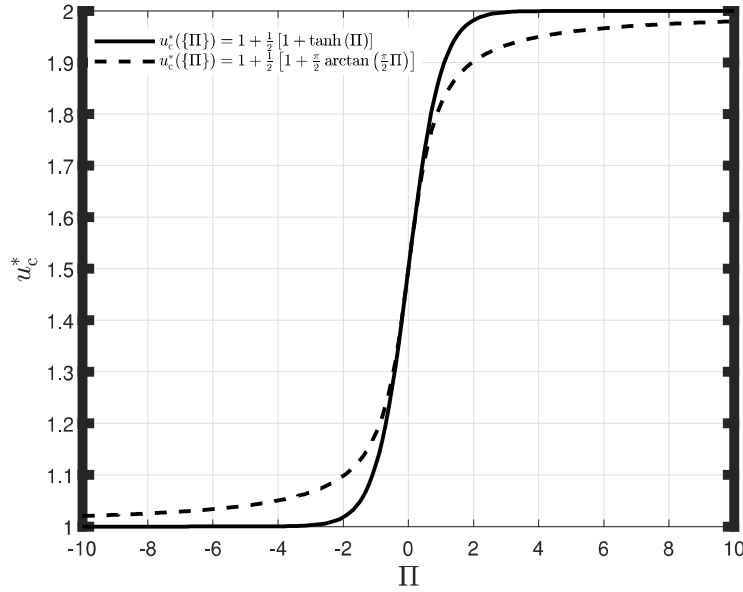


**Fig. 2** Comparison between Eqn. (12) and Eqn. (13). The solid line is  $u_c^*({\Pi}) = 1 + \frac{1}{2}[1 + \tanh(\Pi)]$ , and the dash line represents  $u_c^*({\Pi}) = 1 + \frac{1}{2}\left[1 + \frac{\pi}{2} \arctan\left(\frac{\pi}{2}\Pi\right)\right]$ . Two constant asymptotics are 1 and 2. The center point  $\Pi = 0$  and its slope is the same for both functions but the dash line is less steep than the solid line.

ASYMPTOTES WITH CHANGES IN THE SIGN

The blending techniques proposed require that all asymptotes are positive over the whole domain; however, in some cases the asymptotic function might be negative outside its range of asymptotic validity. For example, when the asymptotic behavior towards infinity is logarithmic (e.g.  $\widehat{u}_c^*({\Pi}) = \ln \Pi$  as  $\Pi \rightarrow \infty$ ), the asymptotic tends to minus infinity as  $\Pi$  tends to zero, which is invalid for the techniques proposed. One possible solution in this case is replacing the asymptote  $\ln \Pi$  with  $\ln(1 + \Pi)$ , such that asymptotic behavior keeps unaffected as  $\ln(1 + \Pi) \approx \ln(\Pi)$ , when  $\Pi \rightarrow \infty$  and the modified expression is always positive over the whole domain of  $(0, \infty)$ .

ADDITION OF INTERMEDIATE TERMS

The blending function Eqn. (7) guarantees the limiting solutions in asymptotic regions and estimates values of the intermediate region by optimization of the blending constant  $n$ . For power-law functions, this approach is simple and accurate; however, when the functions to be blended are not power-laws, such as logarithmic or exponential functions, Eqn. (7) converges very slowly towards small errors. When convergence is slow, the blending error

is small at unrealistically large or small orders of magnitude. An alternative approach is proposed here to deal with these functions while preserving simplicity and accuracy. To improve the accuracy of estimation in the intermediate regime, an additive term  $G(\Pi)$  can be introduced as:

$$u_c^*(\{\Pi\}) \approx \widehat{u}_c^+(\{\Pi\}) = [\widehat{u}_{c,I}^*(\{\Pi\})^n + \widehat{u}_{c,II}^*(\{\Pi\})^n + G(\Pi)^n]^{\frac{1}{n}} \quad (14)$$

where the choice of  $G(\Pi)$  is flexible as long as it does not change the asymptotic behavior, i.e., for the case of  $n > 0$ ,  $G(\Pi) \ll \widehat{u}_{c,I}^*(\{\Pi\})$  as  $\Pi \rightarrow \infty$ , and  $G(\Pi) \ll \widehat{u}_{c,II}^*(\{\Pi\})$  as  $\Pi \rightarrow 0$ . Although the blended result could be more accurate with a sophisticated  $G(\Pi)$ , the format of  $G(\Pi)$  should be as simple as possible to minimize the number of involved blending constants.

The added term can be interpreted as the departure between normal blending equation and the exact value of the intermediate regime, or the "asymptote" of the intermediate regime.

As the absolute value of blending constant  $n$  is typically of the order of magnitude of 1, it is reasonable to set the blending parameter  $n = \pm 1$  to reduce the number of optimization variables to two. These variables can be optimized by the proposed minimax optimum procedure of minimizing the maximum error defined in Eqn. (3). The sign of  $n$  is chosen based on the asymptotic solutions. When both asymptotes are the lower bounds in their corresponding regimes,  $n = 1$  while the dependent variable,  $u_c^*(\{\Pi\})$ , has a decreasing power of  $\Pi$ ,  $n = -1$ .

For the case of two power asymptotes, the additive term can be chosen in the form of power law as  $G(\Pi) = a\Pi^b$ , with blending constants  $\{B\} = \{a, b, \pm 1\}$ . Denoting the two power asymptotes as  $\widehat{u}_{c,I}^*(\{\Pi\}) = c_I\Pi^{d_I}$  and  $\widehat{u}_{c,II}^*(\{\Pi\}) = c_{II}\Pi^{d_{II}}$ , the exponent of the additive term  $b$  has to be set between  $d_I$  and  $d_{II}$  to make sure  $G(\Pi)$  is negligible in the asymptotic regions. It is not clear in what cases this approach is more accurate than Eqn. (7). One obvious difference is that this approach needs to optimize two variables instead of one.

For the case of logarithmic asymptotes (e.g.  $\widehat{u}_{c,II}^*(\{\Pi\}) = \ln \Pi$ ),  $G(\Pi) = a\Pi^b$  fails in maintaining asymptotic behavior, because  $\ln \Pi$  is always smaller than power laws when  $\Pi$  tends to infinity, no matter the value of exponent. In this case, additive term  $G(\Pi)$  can be expressed in the fractional form as  $G(\Pi) = a\Pi/(b + \Pi)$  instead with blending constants  $\{B\} = \{a, b, \pm 1\}$ , such that the additive term can be smaller than the logarithmic asymptote in the limiting regime when  $\Pi \rightarrow \infty$ .

#### AN EXTENSION OF 1D BLENDING: PARAMETRIC 1D BLENDING

Some problems involve multiple dimensionless groups, so they are not 1D blending problems. However, when the some dimensionless groups have a reduced range of variation, they can be considered as another parameter in the blending problem, as opposed to another dimensionless group to be blended. For example, solid mechanics problems involve the dimensionless parameter  $\nu$  (Poisson's ratio), which is seldom far from 0.3 for

most engineering materials. In this case, it is convenient to consider  $\nu$  as a constant instead of performing blending over unrealistic values.

This approach is especially valuable when the dimensionless groups that can be considered as parameters is such that blending can be reduced to 1D.

### CHALLENGES BEYOND 1D BLENDING

The 1D blending describes many engineering problems concerning to one independent variable with much rigor and elegance, however, in some cases, the secondary factors play a significant role and are not negligible indeed, for example, welding on a plate of medium thickness[34, 35], or where the size of a Gaussian distributed heat source can not be neglected [36]. It is necessary to develop a series of practical and systematic 2D blending methods on the basis of current 1D blending theory.

In normalized form, 2D blending problem can be defined as  $u_c^*(\Pi_1, \Pi_2)$ , where  $u_c^*$  is the target characteristic value dependent on two dimensionless variables  $\{\Pi\} = \{\Pi_1, \Pi_2\}$ . The 2D blending problem can also be addressed with an equivalent expression in implicit form:  $F(u_c^*, \{\Pi\}) = F(u_c^*, \Pi_1, \Pi_2) = 0$ , which could be one equation or a group of equations associated with problem parameters. The general strategy to construct 2D blending is to decompose the 2D blending problem into several 1D blending branches, where 1D blending theory is well-developed, and then combine the solved 1D blending equation of each branch to assemble the solution to 2D problem.

Asymptotes in 2D problems are typically derived with limitation theorems, but the limitation theorems of two variable or multi-variable functions are much more complex than functions of single dependence. The complexity includes but not restrict to the division of limiting regimes, different types of asymptotics, relationship between double limits and iterated limits, and so on. The decomposition of 2D blending into 1D blending problems and the assembly of 2D blending solution based on 1D blending functions have high demand on mathematical skills and are never trivial. The simplest case of 2D blending is that the target function  $u_c^*(\Pi_1, \Pi_2)$  is assumed variable separable over its entire domain, which means  $u_c^*(\Pi_1, \Pi_2) = \nu(\Pi_1) \cdot w(\Pi_2)$ , and the 2D blending could be directly split into two 1D blending functions of  $\nu(\Pi_1)$  and  $w(\Pi_2)$ . Thus the assembled 2D blending is in form of the product of both 1D blending equation  $\widehat{u}_c^+(\Pi_1, \Pi_2) = \widehat{\nu}^+(\Pi_1) \cdot \widehat{w}^+(\Pi_2)$ , where  $\widehat{\nu}^+(\Pi_1)$   $\widehat{w}^+(\Pi_2)$  are relatively simple and easily tractable with in 1D blending theory proposed in this paper. Systematic 2D blending methods to obtain general estimation of the target characteristic value in terms of asymptotics and correction factors with high accuracy are the focus of current research.

### CASE STUDIES

Four case studies are be presented to demonstrate the application of MRCF approach. Target characteristic values of interest are expressed in terms of asymptotics (simple case solutions in the extreme cases) and the type of the blending approach for each case will be identified and applied to generate correction factors in explicit form.

### CASE A: ESTIMATION OF MAXIMUM BEAD WIDTH BASED ON ROSENTHAL 3D MODEL

Step 1: List all physics considered relevant

Relevant physics involved in the shape of the weld pool include heat transfer, heat dissipation on the surface to the environment, convective flow, the effects of fluid dynamics and so on. It is impossible to list all relevant mechanisms but the dominant phenomenon and the best practice is to list typical and essentially relevant approximations, which can be suggested by published papers and experimental observations.

Step 2: Identify dominant factors

For the case of the maximum bead width, the dominant mechanism is postulated as heat transfer via conduction and the classic Rosenthal 3D model [37, 38] was utilized to calculate thermal characteristics which assumes the heat source as a point moving with constant velocity in a straight line on the surface of the semi-infinite base materials with constant thermal properties. Heat dissipation on the mental surface, convective flow, and the effects of fluid dynamics are neglected as secondary phenomenon. This Rosenthal 3D model assumes the heat source as a infinitely small point (which is actually not), and considers everything as solid by neglecting the effect of fluid dynamics and phase changes. What' more, it only focuses on the conduction within the solid base metal and the advection due to the relative motion between heat source and the substrate without considering the effects of convective heat transfer in the molten metal and heat dissipation to the external environment (convection and radiation). Due to the huge simplifications, this idealized model with the assumption of identifying pure conduction as the most dominant phenomena and the obtained estimations must check self-consistency which will be discussed in step 4.

Step 3: Solve approximate problem considering only dominant factors (Minimal Representation)

Starting from the Fourier's law and the boundary conditions of the moving system, the simplified problem has been solved in [6] and the obtained analytical solution of the temperature field has the following expression:

$$T(x, y, z) = T_0 + \frac{q}{2\pi kr} \exp\left[-\frac{U}{2\alpha}(r + x)\right] \quad (15)$$

where  $q$  is the net thermal power absorbed by the base material,  $k$  is the thermal conductivity of the base material, and  $T_0$  is the temperature of the substrate far from the heat source or the preheat temperature. In welding, the power  $q$  is estimated as the product of nominal power of the heat source and its thermal efficiency.

Eqn. (15) provides the value of temperature for each point in the domain with a singularity at  $r = 0$ , which is the location of the point heat source and the temperature value there is infinite. It is the theoretical solution of the temperature field as a function of position to the simplified welding problem by considering conduction as the dominant mechanism. However, in practical applications, temperatures of interest always appear as known conditions, for example, melting temperature and the  $A_1$ ,  $A_3$  where phase transformations typical occur are readily known beforehand. Characteristic values which capture the essence of thermal history such as maximum bead width and the location where it occurs are unknown and difficult to obtain.

In this idealized model, dependent variable is the temperature  $\{U\} = \{T\}$ , and there are three spatial independent variables  $\{X\} = \{x, y, z\}$ , and five parameters  $\{P\} = \{T_0, q, k, U, \alpha\}$ . The characteristic value of interest is the maximum isotherm width:  $u_c(\{P\}) = y_{\max}$ . After normalization and dimensional analysis of Eqn. (15), the conclusion is that if we denote the temperature value of the isotherm under consideration as  $T = T_c$ , the dimensionless characteristic values associated with  $T = T_c$  depend only on one dimensionless group (more details can be found in [6]): The Rykalin number (Ry), first proposed by Fuerschbach [39] and has the following expression in terms of parameters:

$$Ry = \frac{qU}{4\pi k\alpha(T_c - T_0)} \quad (16)$$

where the constant of  $1/4\pi$  is added to simplify the final expressions detailed below.

All dimensionless characteristic values associated with an isotherm  $T = T_c$  can be captured with functions depending only on Ry, thus the set of independent dimensionless groups based only on parameters turns into  $\{\Pi\} = \{Ry\}$  and the dimensionless characteristic value  $u_c^*(\{\Pi\}) = y_{\max}^*(\{\Pi\})$  can be expressed with sole dependence on Ry as  $y_{\max}^*(Ry)$ . As Ry is the only one dimensionless group necessary to capture all characteristic values, the number of asymptotic regimes is given by  $2^1 = 2$  and they are Regime I, corresponding to large values of Ry ("fast heat source" where advection dominates over conduction), and Regime II, corresponding to small values of Ry ("slow heat source" with heat transfer dominated by conduction) and the two asymptotics can be represented as  $\widehat{u}_{c,I}^*(\{\Pi\}) = \widehat{y}_{\max I}^*(Ry)$  and  $\widehat{u}_{c,II}^*(\{\Pi\}) = \widehat{y}_{\max II}^*(Ry)$ , respectively. These asymptotic regimes yield simple expressions for the characteristic values, usually in the form of power laws. Asymptotic analysis of Eqn. (15) yields the following two asymptotics of the dimensionless maximum isotherm width dependent only on Ry [6]:

$$\widehat{y}_{\max I}^*(Ry) = \sqrt{\frac{2Ry}{e}} \quad \text{for Regime I (fast)} \quad (17)$$

$$\widehat{y}_{\max II}^*(Ry) = Ry \quad \text{for Regime II (slow)} \quad (18)$$

Step 4: Check for self-consistency

As Eqn. (15) comes directly from the postulated model, the validity of calculations based on Eqn. (15) (Eqn. (17) and Eqn. (18)) will remain in the limit of the validity of this model itself. The self-consistency of this idealized model has been accomplished by comparison with experiments as it is impossible to prove the accuracy of the Rosenthal 3D model from the mathematical point of view. Christensen in the 1960s has done a series of experiments to test the validity of this Rosenthal 3D model [16] of different operating parameters and materials. It has shown that despite of the great simplifications, the model by considering conduction and advection as the dominant phenomena can still generate reasonable results for points far away from the heat source at temperatures below the melting temperature.

Step 5: Compare predictions to "reality"

Eqn. (17) and Eqn. (18) are less accurate for intermediate values ( $Ry=O(1)$ ). As the obtained two asymptotics are in the form of power laws, Standard 1D Blending method is

applicable for this case. For the non-asymptotic region, simple and accurate expression can be obtained with Eqn. (7).

Substitute Eqn. (17) and Eqn. (18) into Eqn. (7), the blended function of the maximum isotherm width in dimensionless form is obtained:

$$y^*_{\max}(\text{Ry}) \approx \widehat{y}^*_{\max}(\text{Ry}) = \left[ \widehat{y}^*_{\text{ma}_I}(\text{Ry})^n + \widehat{y}^*_{\text{ma}_{II}}(\text{Ry})^n \right]^{\frac{1}{n}} \quad (19)$$

The optimal blending constant  $n$  was determined using a minimax approach with two nested optimizations as detailed in [6]. With Rosenthal 3D model and the resulting temperature field, the "reality" used here to calibrate the deviations from the idealized behavior is the maximum value of the isotherm width calculated from Eqn. (15) numerically. When  $n$  is equal to -1.7312, the maximum error over the whole domain of  $\text{Ry}$  is less than 0.7236%.

Step 6: Create correction factors

Substituting the two asymptotics  $\widehat{u}^*_{c,I}(\{\Pi\}) = \widehat{y}^*_{\text{ma}_I}(\text{Ry})$  and  $\widehat{u}^*_{c,II}(\{\Pi\}) = \widehat{y}^*_{\text{ma}_{II}}(\text{Ry})$  into Eqn. (8) and Eqn. (9), the following expression for the correction factors are obtained:

$$f_{y_{\max}}(\text{Ry}) = \left[ 1 + \left( \sqrt{\frac{e\text{Ry}}{2}} \right)^{\pm n} \right]^{\frac{1}{n}} \quad \begin{array}{l} \text{+for Regime I (fast)} \\ \text{-for Regime II (slow)} \end{array} \quad (20)$$

where the exponent  $+n$  corresponds to Regime I, and  $-n$  corresponds to Regime II. The minimax error is always smaller than 0.7236% at the optimal value of  $n=-1.7312$ .

Correction factors based on both asymptotics are plotted in Fig. 3 and the reflected symmetry are consistent with Eqn. (20) as expected. They can also be used to check the validity of both asymptotics. The intersection of the correction factors,  $\text{Ry}_c = 0.7359$ , can be considered as the rough divider of the two asymptotic regions: Regime I, Regime II and the intermediate region (the vicinity of  $\text{Ry}_c$ ) where the typically the maximum departure occurs.

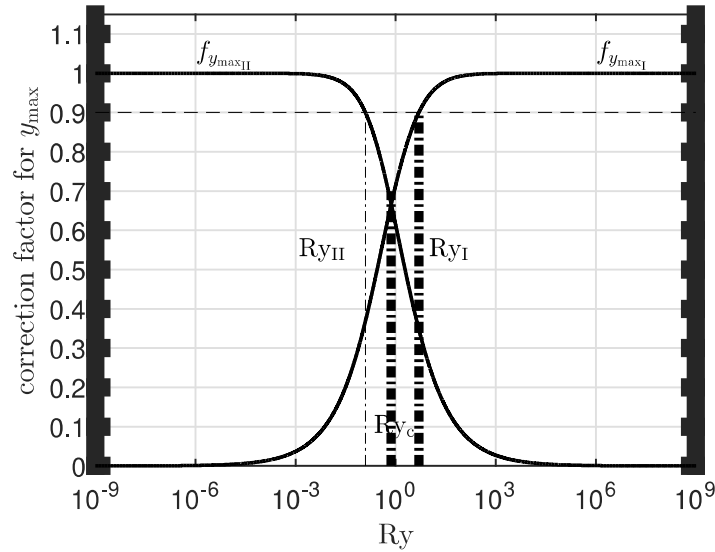
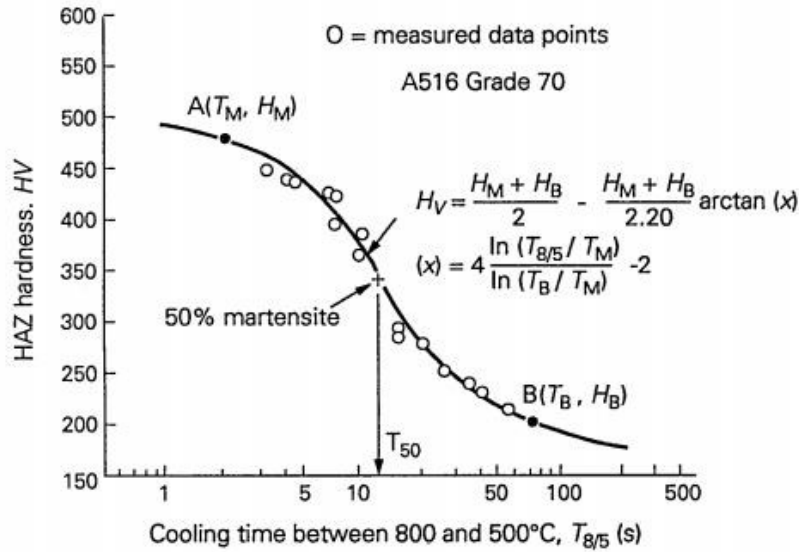


Fig. 3 Correction factors for maximum isotherm width  $y_{max}$  [6]

CASE B: PREDICTIONS OF THE MAXIMUM HARDNESS OF THE HAZ

One of the major challenges in welding industry is predicting the maximum hardness of the heat affected zone that depends the chemical composition and the welding parameters. During the 1970s and the 1980s, many empirical models (based on statistical regression of experimental data) was proposed to address this problem [33, 40]. Although each proposed model is different, they all treat the problematic with a similar nature using asymptotic values to obtain a hardness value as a function of the cooling rate.

Basically, the hardness of a specific point on heat affected zone depends on the present microstructures and their volume fraction. At the same time, the type and amount of each microstructure is a function of the thermal history and chemical composition. In the case, the characteristic value of interest is the the maximum hardness of the HAZ, many variables can be discarded as the assumptions are made. For example, austenitization peak temperature, which plays an important role on the kinetics of austenite decomposition, can be assumed to be equal for all cases by considering that the maximum hardness will be found adjacent to the fusion line where the peak temperature is maximum, very close to the fusion temperature (i.e in the coarse grain heat affected zone). By making this simplification, hardness can be written down as a function of the cooling rate at 700 °C (or cooling time,  $t_{8/5}$ ), and the nominal chemical composition of the welded plate.



**Fig. 4** Characteristic hardness in HAZ as a function of cooling time between 800 °C and 500 °C [33]

One clear example of using asymptotes to address this problem is given by the Yurioka's model [33] and a proposed Continuous Cooling Transformation Structure Hardness (CCTSH) curve is represented in Fig. 4. In this case, the maximum hardness in HAZ depends only on the cooling time between 800 °C and 500 °C. With only one dependence on the cooling time, there are in total two regimes and the characteristic points given by the hardness upper ( $H_M$ ) and lower limits ( $H_B$ ) and their characteristic times are used to develop an equation able to predict the hardness value for any time between  $\tau_M$  and  $\tau_B$ .

Upper and lower hardness asymptotes are easy to picture when this problem is addressed, if the different possible microstructures are considered. The upper limit is directly related with the hardness of the martensite, which means  $\hat{u}_{c,II} = H_M$ . No other microstructure is harder than the fresh martensite obtained from cooling from the austenite region with cooling rates higher than a critical value  $\tau_M$ . On the other hand, the lower limit it can be quite more complicated to picture, since different criteria used depends on the author. However, the main idea resides on using a lower limit,  $\hat{u}_{c,I} = H_B$ , that represents a microstructure with no martensite,  $\tau_B$ . After the formulation of the two limiting constant hardness values empirically, a blended expression in the form of Equation 13 was proposed:

$$HV = \frac{H_M + H_B}{2} - \frac{H_M - H_B}{2.2} \arctan x \quad (21)$$

where  $x$  is defined as:

$$x(\text{rad}) = 4 \frac{\log \frac{t_{8/5}}{\tau_M}}{\log \frac{t_B}{\tau_M}} - 2$$



It is important to remark that, when blending two constant asymptotics (point A and B in Fig. 4), Eqn. (13) must be applied with a understanding of its applicable scope as for cooling times that are not between  $\tau_M$  and  $\tau_B$ , Eqn. (21) is not applicable. As it was mentioned before, Eqn. (11) and Eqn. (12) can also be applied for this case and there are many other types of functions proposed by different authors.

### CASE C: THERMAL STRESS FIELD IN THE VICINITY OF A MOVING POINT HEAT SOURCE

Step 1: List all physics considered relevant

The thermal stress field produced by non-uniform temperature field surrounding a moving point heat source is of significant interest in welding research due to the implications for the size and magnitude of the residual stress field. This example will focus on estimation of the thermal stresses produced by a moving heat source in a thin-plate (i.e. 2D material). The characteristic values ( $u_c$ ) which are of primary interest in the analysis of thermal stresses are the longitudinal stress ( $\sigma_{x,c}$ ) and transverse stress ( $\sigma_{y,c}$ ) produced by some critical temperature change ( $\Delta T_c$ ). The dimensionless form ( $u_c^* = \{\sigma_x^*, \sigma_y^*\}$ ) of the characteristic values is obtained by normalizing with respect to the product of the elastic modulus ( $E$ ), coefficient of thermal expansion ( $a$ ), and critical temperature change ( $\Delta T_c$ ):

$$\{u_c^*\} = \{\sigma_{x,c}^*, \sigma_{y,c}^*\} = \{\sigma_{x,c}/(Ea\Delta T_c), \sigma_{y,c}/(Ea\Delta T_c)\}$$

The mathematical formulation for the thermal stress field in a 2D plane composed of a homogeneous, isotropic, linear elastic material involves a total of six dependent variables, three independent variables and six fixed parameters. The dependent variables are:

$$\{U\} = \{\varepsilon_x, \varepsilon_y, \gamma_{xy}, \sigma_x, \sigma_y, \tau_{xy}\}$$

which represent the  $x$ ,  $y$ , and shear components of the strain and stress fields; the independent variables are:

$$\{X\} = \{\Delta T, x, y\}$$

where  $\Delta T$  is the temperature field at a given location ( $x,y$ ) in a 2D cartesian plane; and the parameters are:

$$\{P\} = \{\Delta T_c, x_c, y_c, E, G, a\}$$

where  $\Delta T_c$  is some characteristic temperature change,  $x_c$  is the maximum length of the characteristic temperature isotherm,  $y_c$  is the maximum width of the characteristic temperature isotherm,  $G$  is the shear modulus of the material,  $E$  is the elastic modulus of the material, and  $a$  is the linear coefficient of thermal expansion.

Step 2: Identify dominant factors

Applying the Buckingham  $\Pi$  theory, it is found that there can only be exactly two independent dimensionless groups in this analysis. Any 2 dimensionless groups that form an independent set may be selected. In this example, the dimensionless parameters are chosen as:

$$\{\Pi\} = \{E/G, x_c/y_c\}$$

---

by convention stresses/strains oriented parallel to the heat source movement (i.e.  $x$  direction) are termed longitudinal, and stresses/strains oriented perpendicular to heat source movement (i.e.  $y$  direction) are referred to as transverse

where  $E/G$  is the ratio of the elastic modulus to shear modulus which can be equivalently expressed in terms of the Poisson's ratio ( $\nu$ ) as  $E/G = 2(1 + \nu)$  and  $x_c/y_c = A_R$  defined as the aspect ratio of the critical isotherm  $\Delta T_c$ .

Note that in this example, since there are two dimensionless groups ( $G/E$  and  $A_R$ ), there will be four asymptotic regimes:

- Regime I:  $A_R \rightarrow \infty, E/G \rightarrow 0$
- Regime II:  $A_R \rightarrow 1, E/G \rightarrow 0$
- Regime III:  $A_R \rightarrow \infty, E/G \rightarrow \infty$
- Regime IV:  $A_R \rightarrow 1, E/G \rightarrow \infty$

Note that the lower asymptotic value of the aspect ratio  $A_R$  is 1, which corresponds to a perfectly circular temperature isotherm (i.e. an infinitely slow or stationary heat source).

For all isotropic materials it is necessary that  $-1 \leq \nu \leq 0.5$ [41], which constrains the allowable range of the modulus ratio to  $0 \leq E/G \leq 3$ . For all commonly welded metallic materials, Poisson's ratio is approximately  $\nu = 0.3$  and the modulus ratio is approximately  $E/G = 2.6$ . Since for all practical problems, the modulus ratio is relatively small, the Regime I, and Regime II are of practical interest.

Step 3: Solve approximate problem considering only dominant factors (Minimal Representation)

The asymptotic solutions for the dimensionless stresses in Regime I are [42]:

$$\begin{aligned}\widehat{\sigma}_{x,c,I}^* &= 1 \\ \widehat{\sigma}_{y,c,I}^* &= 1/A_R^2\end{aligned}$$

and the corresponding dimensional stress values are:

$$\begin{aligned}\hat{\sigma}_{x,c,I} &= aE\Delta T_c \\ \hat{\sigma}_{y,c,I} &= aE\Delta T_c/A_R^2\end{aligned}$$

Analytical expressions for the asymptotic solutions of the dimensionless stresses in Regime II is the subject of an ongoing study, but these expressions will have the general form:

$$\begin{aligned}\widehat{\sigma}_{x,c,II}^* &= \widehat{\sigma}_{x,c,II}^*({A_R, \nu}) \\ \widehat{\sigma}_{y,c,II}^* &= \widehat{\sigma}_{y,c,II}^*({A_R, \nu})\end{aligned}$$

Step 4: Check for self-consistency

For single-pass full-penetration welding of plain carbon and low-alloy steel, the aspect ratio is expected to vary between 2-20 depending on the welding process. Although the asymptotic equations may provide reasonable estimates in some of these cases, it is clearly an issue of practical interest necessary to obtain estimates of the characteristic stresses at intermediate values of the aspect ratio. The asymptotic blending technique provides a powerful and convenient method to develop a closed form equation for estimating the stresses at these intermediate values.

Step 5 and 6: Compare predictions to "reality" and create correction factors

In this case, the standard approach for 1D asymptotic blending may be applied with only one minor modification. Although the asymptotic solutions in Regime I depend on only  $A_R$ , this will not necessarily be the case in Regime II. If the asymptotic expressions in Regime II are found to depend on the value of Poisson's ratio, it will be necessary to

optimize the value of the set of blending constants  $\{B\}$  over a range of typical values of  $\nu$  (ex. 0.25-0.35) using Parametric 1D blending. In this case, the value of  $\nu$  is treated as a parameter and the optimization for the 1D blending coefficients is evaluated in the 2D space defined by  $1 < A_R < \infty$  and  $\nu$  is around the value of 0.3. The 1D parametric blending technique provides a simple and powerful alternative to full 2D blending in 2-parameter systems where the range of one parameter is relatively restricted.

Although significant challenges are associated with obtaining experimental measurements of thermal stresses, the "reality" for the critical stress at a selection of intermediate values used in the optimization may be readily obtained from finite-element analysis (FEA). A limited number of experimental measurements may then be performed to validate the final solution and aid in the development of additional correction factors for secondary effects.

#### CASE D: MAXIMUM TEMPERATURE IN FRICTION STIR WELDING (FSW)

Step 1: List all physics considered relevant

Relevant physics involved in FSW are the plastic flow near the pin and the generated heat, heat conduction into the base material, heat loss to the environment, inertial factors, kinematics and forces related in the deformation and so on.

Step 2: Identify dominant factors

For the case of FSW, the dominant factors are identified as the heat diffusion in a localized soft layer in [1, 43]. Four groups of competing phenomena are considered: heat diffusion vs. heat advection, kinematics of rotational flow vs. translational flow, thickness of the soft shear layer vs. the radius of the pin and the peak temperature jump caused by shoulder vs. the contribution of plastic area around the pin. Among the four groups, dominant factors are identified as the heat diffusion, rotational flow, thickness of the shear layer and the dominance of the pin on peak temperature. Self consistency will be check for the secondary factors in step 4 by comparing the obtained expression for maximum temperature against experiments published in literature.

Step 3: Solve approximate problem considering only dominant factors (Minimal Representation)

The problem is greatly simplified to its minimal representation by considering only dominant factors listed above. Target characteristic value is the maximum temperature developed during process can be expressed as  $u_c = T_s$  and asymptotics obtained have the following form[43]:

$$\hat{T}_s = T_0 + \Delta T_m \left[ \frac{3}{2} \frac{\eta_s}{AB\Delta T_m} \left( \frac{\eta K_0}{\Delta T_0} \right)^{n-1} \left( \frac{\alpha^2 \tau_R}{k} \right)^n \omega^{n+1} \right]^{\frac{1}{2}} \quad (22)$$

where  $T_s$  is the maximum temperature achieved at the pin-shear layer interface,  $T_0$  is the temperature at the interface between shear layer and the base plate,  $\Delta T_m = T_m - T_0$  and  $T_m$  is the melting temperature of the substrate,  $\eta_s$  is the efficiency which considers mechanical energy converted into heat, excluding the mechanical energy accumulated in the form of dislocations,  $A$  is the constant of constitutive behavior of the alloy and  $\eta$  is the total

efficiency of the process, accounts for energy stored in the form of dislocations in the shear layer and heat lost to the tool,  $K_0$  is the Modified Bessel function of second kind and 0 order,  $\Delta T_0 = T_0 - T_\infty$ ,  $a$  is the pin radius,  $\tau_R$  is the reference shear stress of the alloy,  $k$  is the thermal conductivity of the alloy at  $T_0$  and  $\omega$  is the angular velocity of rotation of the pin.

Step 4: Check for self-consistency

All predictions based on the minimally represented problem must be checked for self-consistency. For the case of FSW, Eqn. (22) evaluated by comparing the effect of assumed secondary factors on the accuracy of the estimation. The relative magnitude of selected secondary factors can be represented by its value to that of the dominant factors. In this way, a value of 1 indicates that the secondary factor is of similar magnitude than the dominant factor. Very small values on the horizontal axis correspond to the self-consistent regime, while high values correspond to inconsistent cases in which the factors considered secondary are actually larger than the dominant factors. There are four independent dimensionless groups that characterize the secondary phenomena  $\{\Pi\} = \{Pe, V/\omega\hat{\delta}, \hat{\delta}/a, (T_p - T_\infty)/(T_s^+ - T_\infty)\}$

Step 5: Compare predictions to "reality"

Eqn. (22) must be validated through comparisons with reality. In summary, three factors considered secondary (advective heat transfer, pin translation on maximum temperature and shoulder heat input on the peak temperature in FSW) have been proved indeed secondary for the vast majority of cases in [1, 43], and that for those valid cases, Eqn. (22) predicts the proper order of magnitude and dependence on process parameters. However, the approximation by considering the shear layer thickness on peak temperature as secondary phenomena is not always valid and correction factor for the estimation of maximum temperature are necessary. The 4D blending problem can be simplified into Parametric Blending of one dependence:  $\{\Pi\} = \{Pe, V/\omega\hat{\delta}, \hat{\delta}/a, (T_p - T_\infty/T_s^+ - T_\infty)\} \approx \{\hat{\delta}/a\}$

Step 6: Create correction factors

In this FSW case, systematic errors in the math and physics can be accounted for by the correction factor in Standard 1D blending form with blending constants  $\{B\} = \{C_1, C_2, C_3\}$ :

$$f_T^+ = C_1 \left( 1 + C_2 \frac{\hat{\delta}}{a} \right)^{C_3}$$

Blending constant  $C_1$  takes care of the systematic error in the mathematics while  $C_2$  and  $C_3$  are used to account the secondary phenomena for best accuracy. When  $C_1=0.764$ ,  $C_2=0.259$ , and  $C_3=-0.857$ , optimal match between Eqn. (22) and the published experimental values has been achieved with 12% standard deviation.

## CONCLUSIONS

Design rules in the form of a simple formula (asymptotic behavior of the simplified problem by considering only dominant mechanisms) and correction factors which capture the deviation from the ideal cases are proposed. This approach is of much help to solve complex multiphysics problems such as welding and is based on a six-step framework we termed Minimal Representation and Correction Factor (MRCF). The formulation of the design

rules makes it convenient to couple them to represent multi-coupled phenomena and embed them in numerical models and control systems. It is shown through examples that the technique of blending has wide applicability for correlating experimental or numerical data or theoretical values for processes with known asymptotic solutions.

The proposed blending theory extends the applicability of standard blending approaches to obtain general, accurate and explicit expressions in terms of known asymptotic solutions and blending constants determined with a systematic optimization procedure. The blending expressions are also used to develop correction factors that capture the deviations from ideal cases.

Blending is also useful in summarizing isolated experimental results and numerical data from simulation. The general and systematic formulation can be extended to other multi-coupled phenomena besides welding.

APPENDIX: NOTATION

**Table 1** Notation

<b>Symbols</b>	<b>Description</b>
<b>Variables</b>	
$a$	Blending constant
$b$	Blending constant
$f$	Correction factors
$k$	Number of independent reference units
$m$	Number of independent physical magnitudes
$n$	Blending exponent
$n_r$	Number of regimes
$u$	Dependent variable and related function
$v$	Variable separated function of $u$
$w$	Variable separated function of $u$
$B$	Blending constants
$F$	Implicit Function
$P$	Problem parameter
$X$	Independent variable
$U$	Dependent variable
$\Pi$	Independent dimensionless groups
$B$	Blending functions
<b>Superscripts</b>	
*	Normalized value
$\hat{\phantom{x}}$	Asymptotic behavior
+	Blended approximation
<b>Subscripts</b>	
I	Corresponding to Regime I
II	Corresponding to Regime II
III	Corresponding to Regime III
i	Regime i
c	Characteristic values
<b>Others</b>	
{...}	Set

### REFERENCES

- [1] K. TELLO, U. DUMAN, and P. MENDEZ, ‘Scaling Laws for the Welding Arc, Weld Penetration and Friction Stir Welding’, in *Trends in Welding Research, Proceedings of the 8th International Conference*, pp. 172–181, 2009.
- [2] P. F. MENDEZ, ‘Characteristic Values in the Scaling of Differential Equations in Engineering’, *Journal of Applied Mechanics*, vol. 77, no. 6, p. 061017, 2010.
- [3] P. F. MENDEZ, K. E. TELLO, and S. S. GAJAPATHI, ‘Generalization and Communication of Welding Simulations and Experiments Using Scaling Analysis’, in *9th International Conference on Trends in Welding Research*, vol. 1, (Chicago, Illinois, USA), pp. 249–258, ASM International, 2012.
- [4] S. W. CHURCHILL and H. H. CHU, ‘Correlating Equations for Laminar and Turbulent Free Convection From a Vertical Plate’, *International Journal of Heat and Mass Transfer*, vol. 18, no. 11, pp. 1323–1329, 1975.
- [5] S. W. CHURCHILL, ‘Comprehensive Correlating Equations For Heat, Mass and Momentum Transfer in Fully Developed Flow in Smooth Tubes’, *Industrial & Engineering Chemistry Fundamentals*, vol. 16, no. 1, pp. 109–116, 1977.
- [6] P. F. MENDEZ, Y. LU, and Y. WANG, ‘Scaling Analysis of a Moving Point Heat Source in Steady- State on a Semi-Infinite Solid’, *Journal of Heat Transfer*, vol. 140, no. 8, p. 081301, 2018.
- [7] P. S. FEDKIW and J. NEWMAN, ‘Mass-Transfer Coefficients in Packed Beds at Very Low Reynolds Numbers’, *International Journal of Heat and Mass Transfer*, vol. 25, no. 7, pp. 935–943, 1982.
- [8] F. DURST, S. RAY, B. ÜNSAL, and O. A. BAYOUMI, ‘The Development Lengths of Laminar Pipe and Channel Flows’, *Journal of Fluids Engineering*, vol. 127, no. 6, pp. 1154–1160, 2005.
- [9] G. WOOD, S. A. ISLAM, and P. F. MENDEZ, ‘Calibrated Expressions for Welding and Their Application to Isotherm Width in a Thick Plate’, *Soldagem & Inspeção*, vol. 19, no. 3, pp. 212–220, 2014.
- [10] G. G. ROY, R. NANDAN, and T. DEBROY, ‘Dimensionless Correlation to Estimate Peak Temperature during Friction Stir Welding’, *Science and Technology of Welding and Joining*, vol. 11, no. 5, pp. 606–608, 2006.
- [11] P. E. MURRAY and A. SCOTTI, ‘Depth of Penetration in Gas Metal Arc Welding’, *Science and Technology of Welding and Joining*, vol. 4, no. 2, pp. 112–117, 1999.
- [12] P. E. MURRAY, ‘Stability of Droplets in Gas Metal Arc Welding’, *Science and Technology of Welding and Joining*, vol. 5, no. 4, pp. 221–226, 2000.
- [13] P. E. MURRAY, ‘Selecting Parameters for GMAW Using Dimensional Analysis’, *Welding Journal*, vol. 81, no. 7, pp. 125–131, 2002.
- [14] P. W. FUERSCHBACH and G. A. KNOROVSKY, ‘A Study of Melting Efficiency in Plasma Arc and Gas Tungsten Arc Welding’, *Welding Journal, Research Supplement*, vol. 70, no. 11, pp. 287–297, 1991.
- [15] P. W. FUERSCHBACH, ‘Measurement and Prediction of Energy Transfer Efficiency in Laser Beam Welding’, *Welding Journal, Research Supplement*, vol. 75, no. 1, pp. 24–34, 1996.
- [16] N. CHRISTENSEN, DAVIES, V. DE L., and K. GJERMUNDSEN, ‘Distribution of Temperatures in Arc Welding’, *British Welding Journal*, vol. 12, no. 2, pp. 54–75, 1965.
- [17] A. ROBERT and T. DEBROY, ‘Geometry of Laser Spot Welds from Dimensionless Numbers’, *Metallurgical and Materials Transactions B*, vol. 32, no. 5, pp. 941–947, 2001.
- [18] X. HE, P. W. FUERSCHBACH, and T. DEBROY, ‘Heat Transfer and Fluid Flow during Laser Spot Welding of 304 Stainless Steel’, *Journal of Physics D: Applied Physics*, vol. 36, no. 12, pp. 1388–1398, 2003.

- [19] W. ZHANG, C. H. KIM, and T. DEBROY, 'Heat and Fluid Flow in Complex Joints during Gas Metal Arc Welding ? Part I : Numerical Model of Fillet Welding', *Journal of Applied Physics*, vol. 95, no. 9, pp. 5210–5219, 2004.
- [20] W. B. KRANTZ, *Scaling Analysis in Modeling Transport and Reaction Processes: A Systematic Approach to Model Building and the Art of Approximation*. New York: John Wiley & Sons, 2007.
- [21] A. BEJAN, *Convection Heat Transfer*. Hoboken, New Jersey: John Wiley & Sons, Inc., 2013.
- [22] J. A. DANTZIG and C. L. TUCKER, *Modeling in Materials Processing*. Cambridge, England: Cambridge University Press, 2001.
- [23] P. F. MENDEZ and F. ORDÓÑEZ, 'Scaling Laws from Statistical Data and Dimensional Analysis', *Journal of Applied Mechanics*, vol. 72, no. 5, pp. 648–657, 2005.
- [24] P. F. MENDEZ, R. FURRER, R. FORD, and F. ORDÓÑEZ, 'Scaling Laws as a Tool of Materials Informatics', *JOM*, vol. 60, no. 3, pp. 60–66, 2008.
- [25] K. RAJAN, C. SUH, and P. F. MENDEZ, 'Principal Component Analysis and Dimensional Analysis as Materials Informatics Tools to Reduce Dimensionality in Materials Science and Engineering', *Statistical Analysis and Data Mining*, vol. 1, no. 6, pp. 362–371, 2009.
- [26] K. M.-K. YIP, 'Model Simplification by Asymptotic Order of Magnitude Reasoning', *Artificial Intelligence*, vol. 80, no. 2, pp. 309–348, 1996.
- [27] E. BUCKINGHAM, 'On Physically Similar Systems; Illustrations of the Use of Dimensional Equations', *Physical Review*, vol. 4, pp. 345–376, Oct. 1914.
- [28] A. ACRIVOS, 'A Rapid Method for Estimating the Shear Stress and the Separation Point in Laminar Incompressible Boundary-Layer Flows', *Journal of the Aero/Space Sciences*, vol. 27, no. 4, pp. 314–315, 1960.
- [29] A. ACRIVOS, 'On the Solution of the Convection Equation in Laminar Boundary Layer Flows', *Chemical Engineering Science*, vol. 17, no. 6, pp. 457–465, 1962.
- [30] S. W. CHURCHILL and R. USAGI, 'A General Expression for the Correlation of Rates of Transfer and Other Phenomena', *AIChE Journal*, vol. 18, no. 6, pp. 1121–1128, 1972.
- [31] S. W. CHURCHILL and R. USAGI, 'A Standardized Procedure for the Production of Correlations in the Form of a Common Empirical Equation', *Industrial & Engineering Chemistry Fundamentals*, vol. 13, no. 1, pp. 39–44, 1974.
- [32] Y. ARATA, K. NISHIGUCHI, T. OHJI, and N. KOHSAI, 'Weldability Concept on Hardness Prediction (Materials, Metallurgy, Weldability)', *Transactions of JWRI*, vol. 8, no. 1, pp. 43–52, 1979.
- [33] N. YURIOKA, O. MAKOTO, K. TADASHI, and C. HARRY, 'Prediction of HAZ Hardness of Transformable Steels', *Metal Construction*, vol. 19, no. 4, pp. 217R–223R, 1987.
- [34] O. R. MYHR and Ø. GRONG, 'Dimensionless Maps for Heat Flow Analyses in Fusion Welding', *Acta Metallurgica Et Materialia*, vol. 38, no. 3, pp. 449–460, 1990.
- [35] K. POORHAYDARI, B. M. PATCHETT, and D. G. IVEY, 'Estimation of Cooling Rate in the Welding of Plates with Intermediate Thickness', *Welding Journal*, vol. 84, no. 10, pp. 149–s–155–s, 2005.
- [36] T. W. EAGAR and N. S. TSAI, 'Temperature Fields Produced by Traveling Distributed Heat Sources', *Welding Journal*, vol. 62, no. 12, pp. 346–355, 1983.
- [37] D. ROSENTHAL, 'Mathematical Theory of Heat Distribution During Welding and Cutting', *The Welding Journal*, vol. 20, no. 5, pp. 220–234, 1941.
- [38] D. ROSENTHAL, 'The Theory of Moving Sources of Heat and Its Application to Metal Treatments', *Transactions of the A.S.M.E.*, vol. 68, pp. 849–866, 1946.
- [39] P. W. FUERSCHBACH and G. R. EISLER, 'Determination of Material Properties for Welding Models by Means of Arc Weld Experiments', in *6th Intl. Trends in Welding Research*, (Pine Mountain, Georgia), 2002.



- [40] T. KASUYA and N. YURIOKA, 'Prediction of Welding Thermal History by a Comprehensive Solution', *Welding Journal, Research Supplement*, vol. 72, no. 3, pp. 107–s–115–s, 1993.
- [41] G. GREAVES, A. GREER, R. LAKES, and T. ROUXEL, 'Poisson's ratio and modern materials', *Nat Mater*, vol. 10, no. 11, pp. 823–837, 2011.
- [42] M. GRAMS and P. MENDEZ, 'Quantification of root pass residual stresses in pipeline girth welds', in *Fabtech/AWS Annual Meeting*, Nov 6-9, 2017. Chicago, IL.
- [43] P. F. MENDEZ, K. E. TELLO, and T. J. LIENERT, 'Scaling of Coupled Heat Transfer and Plastic Deformation around the Pin in Friction Stir Welding', *Acta Materialia*, vol. 58, no. 18, pp. 6012–6026, 2010.

# PROCESS SIMULATION OF TIG WELDING FOR THE DEVELOPMENT OF AN AUTOMATIC ROBOT TORCH THROUGH HEAT PIPE – HEAD COOLING SYSTEM

K. ALALUSS\* and P. MAYR\*\*

*\*Steinbeis Innovation Centre Intelligent Functional Materials, Welding and Joining Techniques, Implementation, 01099 Dresden – Germany, e-mail: khaled.alaluss@stw.de*

*\*\* Institute of Joining and Assembly Chemnitz University of Technology, 09126 Chemnitz – Germany, e-mail: schweisstech@mb.tu-chemnitz.de*

DOI 10.3217/978-3-85125-615-4-49

## ABSTRACT

Modern robot welding torches for arc welding are equipped with interchangeable neck systems. Generally, in TIG welding torches, the transfer powers to the electrode and the heat dissipation from the electrode occur just through the clamping area. The clamping geometry is usually formed in a ring. Therefore, a high resistance is generated between electrode and clamping system. This system suffers from power losses as well as limited heat dissipation. Furthermore, with this system, torch head setting needs tools and consumes a relatively long time. By developing of a non-linear thermo-flow-mechanical / magneto-hydro-dynamic (MHD) FE-model, using CFX ANSYS program, a novel robotic-TIG welding torch with an interchangeable head system and heat dissipation (heat pipe) was innovated. Depending on the predefined process parameters, the resulting thermo-physical heat output effects the torch-head design were investigated and analyzed then taken into account in the design process. The influences of the welding parameters such as current, shielding gas quantity on the torch design were determined through FE calculations. This determination process was connected to the design of the torch cooling system (heat pipe). The temperature distribution and its behavior at arc contour, shielding gas nozzle, and heat pipe body within the heat output range was determined. As well as, the distribution of flow gas velocity through the arc region and its behavior within the heat output range was determined. The use of a four heat pipes cooling system is sufficient for the maximum predefined power. The designed gas supply channels system gives efficient, functioning, and error-free gas flow results during the welding process. At maximum power range, the maximum calculated temperature at the shielding gas nozzle and at heat pipe – (tube body) is  $\leq 350$  K. Furthermore, the simulation results show the effect of arc focusing due to the shielding gas flow as well as the effect of increasing the welding current on the arc dynamics and their geometric shape. The performed simulation process shows a good alignment between the calculations and the experiments. Finally, a robotic TIG torch with high-quality performance and easy interchangeable torch's component was innovated and constructed, as well as high weld quality was achieved.

Keywords: Automatic TIG robot welding torch, Process simulation, Heat pipe cooling,

LIST OF SYMBOLS

B	[T = V s m <sup>-2</sup> ]	electromagnetic field
c	[J kg <sup>-1</sup> K <sup>-1</sup> ]	heat capacity
D <sub>a</sub>	[m <sup>2</sup> s <sup>-1</sup> ]	ambipolar diffusion coefficient
D <sub>e</sub>	[m <sup>2</sup> s <sup>-1</sup> ]	electron diffusion coefficient
e n	[1 C = 1 A s]	electron flux
FE	-	finite-element
f <sub>s</sub>	[N]	single forces in arc region
f <sub>L</sub>	[N]	Lorentz force
J	[A m <sup>-2</sup> ]	electric current density
h	[J kg <sup>-1</sup> ]	specific enthalpy
N <sub>e</sub>	[m <sup>-3</sup> ]	electron number density
N <sub>0</sub>	[m <sup>-3</sup> ]	neutral atom density number
p	[Pa]	pressure
q	[J mm <sup>-2</sup> s <sup>-1</sup> ]	heat flux
Q	[J s <sup>-1</sup> ]	thermal energy
S	[V]	electric potential
S <sub>He</sub>	[J]	energy value at the cathode
S <sub>He</sub>	[m <sup>-3</sup> ]	emitting electrons
S <sub>Hi</sub>	[J = C kg <sup>-1</sup> ]	impact of ions
S <sub>RH</sub>	[Ω]	resistive heating
T	[K]	temperature
α	[W m <sup>-2</sup> K <sup>-1</sup> ]	heat transfer coefficient
η	[m <sup>-2</sup> s <sup>-1</sup> ]	diffusion coefficient
$\dot{V}_{\text{Shielding gas}}$	[l min <sup>-1</sup> ]	shielding gas flow
$\dot{m}$	[l min <sup>-1</sup> ]	mass flow rate
ε	[W m <sup>-3</sup> sr]	emission coefficient
γ <sub>e</sub>	[S m <sup>-1</sup> ]	electrical conductivity
λ	[W m <sup>-1</sup> K <sup>-1</sup> ]	thermal conductivity
λ <sub>m</sub>	[m]	diffusion length
μ <sub>0</sub>	[T m A <sup>-1</sup> ]	magnetic permeability
v	[m s <sup>-1</sup> ]	velocity
η	[N s m <sup>-2</sup> ]	dynamic viscosity
Φ	[J C <sup>-1</sup> ]	electron diffusion
φ	[V]	electric current potential
ρ	[kg m <sup>-3</sup> ]	density
ω	[m s <sup>-1</sup> ]	electron drift

INTRODUCTION

Modern automatic robot welding torches for arc welding are equipped with interchangeable neck systems. Nowadays, in TIG welding torches, the tungsten electrodes are inserted from the back of the torch to fix it annularly in a clamping sleeve using a collet system. The

current transfer to the electrode while the heat dissipation from the electrode takes place exclusively via the clamping point. The geometry of the clamping system is designed as a clamping ring. This causes a high resistance between electrode and clamping system. This leads to a loss of power and lowering of the heat dissipation. Furthermore, with this clamping system, electrode distance to the component cannot be set without tools, and the torch head adjustment is very time-consuming. The exchange systems that are used for automatic/robot-TIG welding torches are constructed in the following technical versions: Short head design with tungsten electrode in "stick form"; and the long design (similar to hand torches) with long tungsten electrodes [1-3].

In the robotic TIG welding process, to achieve an exact arc positioning at the specific welding location, technical specifications are provided to the torch head and its changing system. These are constant heat dissipation in the torch head area, rapid replacement of wear parts, especially the cathode, reproducible replacement of the welding torch heads and rapid coupling of the process media (welding current, shielding gas and torch cooling system). The aim of this work is the development of an innovative TIG robotic welding torch with an adaptive changing system that can easily enable a reliable changing of TIG welding torch heads. This leads to achieving the following technical advantages:

- Provide the simplicity of the exchangeable module regard to reproducible fit and interchangeability,
- High positioning accuracy of welding position and wire feed location, and
- Integration of a closed heat transport system – heat dissipation – heat pipe with minimum installation space.

A heat pipe is a component in which the heat can be transported very efficiently from one place to another. The physical effect is used to convert enormously high amounts of energy during the evaporation and condensation of liquids. The characteristics of a heat pipe are the use of evaporation enthalpy, the high heat transfer capacity at low-temperature differences, the effective thermal conductivity, and the diverse geometric design [4, 5]. Within the framework of the flow-thermomechanical - magneto-hydrodynamic (MHD) FE simulation model, the required knowledge of process behavior and its thermo-physical – flow-mechanical effects for a reliable torch head design are determined. This allowed to design the torch part geometries that can suit materials, achieve an optimum cooling system of the heat-pipe torch head with a high cooling capacity, and improve the separation between the process media (inert gas, cooling medium) and the welding current. By using FE simulation, a design solution with an optimized physical functional principle for the technical and constructive design of the torch part geometries as well as cooling and the process gas supply is developed and optimized.

## Mathematical Modelling of Weld Phenomena 12

### FLUID AND THERMO MECHANICAL / MAGNETO-HYDRO-DYNAMIC MODELING TO SIMULATE THE TIG WELDING PROCESS

#### INPUT DATA FOR PROCESS SIMULATION

The temperature-dependent materials properties (tungsten, copper, and argon gas, etc.) that are used in the simulation process were taken from literature [6-10] or extracted directly from the simulation program library. These were provided as temperature dependent functions for the software calculations. The electrical and thermal conductivity of the gas was further extended as a Gaussian function with a normal distribution and implemented in the model data. Pure argon was used as the shielding gas. The following material data was also used:

- Density,
- Specific heat capacity, enthalpy,
- dynamic viscosity,
- Thermal and electrical conductivity,
- Emitted radiation: net emission model,
- Radiation properties and heat transfer coefficient,
- Binary diffusion coefficient.

The torch part geometries that are required for the model were extracted from a previously developed CAD model. With this model, the finite element network model was integrated for all model domains and interfaces. The necessary welding data were determined using experimental investigations and then integrated into the FE model.

#### MODEL DEVELOPMENT – MODEL DETAILS

By means of mathematical and numerical modeling of thermophysical, fluid mechanical process sequences in TIG arc welding, a detailed process analysis to capture and describe the heat balance and the resulting thermophysical effects of the TIG welding process can be performed. The resulting process knowledge makes it possible to develop a fundamental understanding of the processes involved taking into account the TIG process characteristics. This understanding enables for the efficient technical development and design of a functioning TIG welding torch. An exact knowledge of the processes in the TIG arc and a detailed description of the energy flow into the torch environment greatly contribute to a load adapted torch design and a faultless construction. The modeling of the arc was performed with the aid of the magneto hydro dynamic (MHD) equation system. This is understood as a combination of the conservation equations of mass, impulse and energy from fluid mechanics with the Maxwell equations of electromagnetics. The used Maxwell equations are shown below.

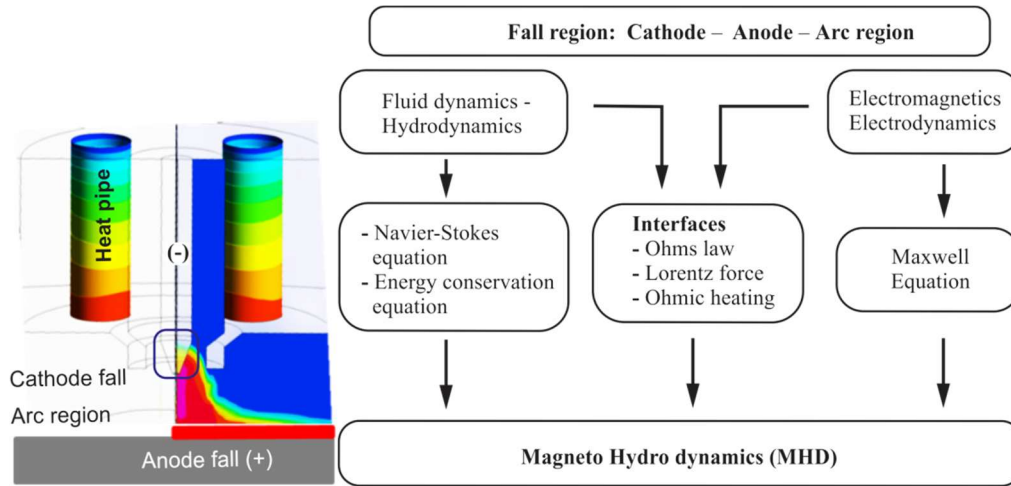


Fig. 1 TIG arc – MHD model

In the MHD, the electrical and magnetic properties of the liquid are described by the electrical conductivity ( $\gamma$ ) and the magnetic permeability ( $\mu_0$ ) respectively. Mostly external electrical field and the shielding gas flowing through the magnetic field, which allows the current to flow. The magnetic field results from the superposition of external and self-generated fields. The fundamental equations of electromagnetism are the Maxwell equations. It is used in the MHD model to calculate the electric current density and the magnetic field. For a stationary discharge, the preservation formula is valid, taking into account the quasi-neutrality [8-12]:

$$\text{div } \vec{j} = 0 \quad (1)$$

The current density follows from the generalized Ohms law. The induced field strengths and the Hall field are negligible compared to the field strength in the TIG arc. Thus Ohm's law applies as:

$$\vec{j} = -\gamma \text{grad } \Phi + \vec{j}_B \quad (2)$$

The magnetic potential ( $\vec{A}$ ) is described by permeability ( $\mu_0$ ) and current density ( $\vec{j}$ ):

$$\text{div}(\text{grad } \vec{A}) = -\mu_0 \cdot \vec{j} \quad (3)$$

and the magnetic field can be calculated with:

$$\begin{aligned} \vec{B} &= \text{rot } \vec{A} \\ \vec{B} &= \vec{B}_0 + \vec{B}_I \end{aligned} \quad (4)$$

The simulation of the arc welding process can thus be carried out by the coupling of computational fluid dynamics with the other physical effects, in particular, the coupling of the individual electromagnetic effects such as electric charges, magnetic dipoles, electromagnetic fields, and forces. In the case of hydrodynamics and electromagnetism, the current that flows through a flowing conductive fluid is formulated as follows:

$$\vec{j}_B = \gamma \vec{u} \times \vec{B} \quad (5)$$

In a TIG arc, the electric gas discharge takes place as a result of the sufficiently large electric potential between the cathode (tungsten electrode) and the anode (workpiece), then the electric current flows through a partially thermally ionized gas. Due to the high electrical current density and resistance heating, the necessary temperature to maintain the arc is generated. The limitation of the conductive cross-section of the TIG arc stabilizes the resulting gas discharge. The electrical gas discharges can be divided into three characteristic voltage-drop ranges. These voltage-drop ranges are the cathode and anode drop ranges as well as the voltage drop across the arc region. In contrast to the arc range, the transitions of the arc range to the anode or cathode (drop ranges) cannot be described with LTG boundary conditions. This is due to the too low plasma temperature in this range. At the interface between the arc and the electrodes, the gas temperature is less than 7000 K. Thus, assuming LTG characteristics, the electrical conductivity is too low for the carrier transport to be realized. Instead, the mechanisms of charge carrier transport is characterized by electron and ion diffusion, which are influenced by electron emission at the cathode as well as recombination effects of the charge carriers. Modeling of these effects is very complex, and it can be realized through the consideration of electron diffusion due to ambipolar diffusion, or during the magnification of the grid elements on the electrode. In the drop ranges, the model of Lowke and Sansonnes [15] is used, which is based on the comprehensive simulation of effects in the arc and drop ranges. This allows for the TIG welding process to have self-consistent physical modeling of the arc approach and the energy input to the electrode. The diffusion of electrons is considered using a general electron transport equation (6). This includes the ambipolar diffusion, the term considering recombination, the electron drift ( $\alpha$ ) and the cathode as an electron source and the anode as an electron sink. The model is based on the electron balance equation:

$$\frac{\partial N_e}{\partial t} = \text{div } D_a \text{ grad } D_e (N_0 G - N_e^2) + \alpha \varpi N_e + S_e \quad (6)$$

where ( $N_e$ ) is the electron number density, ( $D_a$ ) the ambipolar diffusion coefficient, ( $D_e$ ) the electron-ion recombination coefficient, and ( $N_0$ ) the neutral atom number density according to [15]. The thermal ionization term ( $G$ ) = ( $N_e$ )<sup>2</sup> /  $N_0$  is defined by the diffusion model and in this equation  $N$  represents the given density ( $N$ ). The current flow is defined by the electrical conductivity ( $\gamma_e$ ) of the electrons and the electron diffusion ( $\Phi$ ). In order to avoid zero values for the number of electrons at the anode surface, the electron absorption rate was defined as  $N_e = D_e N_e / \lambda_m$ , with ( $D_e$ ) as the electron diffusion coefficient, and ( $\lambda_m$ )

as the diffusion wavelength. For the conservation equation of the electric current, the following Poisson equation was used:

$$\sigma \text{grad } \Phi = eD_e \text{grad } N_e \quad (7)$$

Thus, resulting from [15] a higher electrical conductivity with an increase of the electron concentration in the near-electrode regions is given in the following:

$$\gamma = en_e \mu_e = \frac{e^2 n^2}{m_e \nu_{th} (n_i A Q_{ei} + n_0 B Q_{e0})} \quad (8)$$

The representative electron concentration at the cathode is calculated through the flow of electrons, the product of the unit charge, and the electrons thermal velocity. The electron flow is calculated by the Richardson equation for doped tungsten electrodes. The energy input to the cathode ( $S_{Hc}$ ) is derived from the sum of the heating by impacting ions ( $S_{Hi}$ ), the cooling by the emitted electrons ( $S_{He}$ ) and the radiation emission rate.

$$S_{HC} = S_{Hi} + S_{He} - \varepsilon \delta_{SB} T_k^4 \quad (9)$$

With:

$$S_{He} = j_e \Phi_w \quad (10)$$

$$S_{Hi} = j_i (U_i - \Phi_w) \quad (11)$$

$$j_i = j_i (j_{ges} - j_i) \quad (12)$$

The calculation of the electron current density is based on the Richardson's equation for thermal emission. The work function of a doped tungsten electrode ( $\text{La}_2\text{O}_3$ ), according to [15] has to be considered in the heat sink. The doping of the tungsten electrode increases the number of emitted electrons. For the cathode and anode constant radiation emission factors, a ( $\varepsilon = 0.5$ ) are considered. At the anode, the charge carrier transport takes place with electrons. This applies to the input energy in the anode surface (workpiece):

$$S_{HA} = j_{\Phi A} - \varepsilon \delta_{SB} T_k^4 \quad (13)$$

The calculation of heat transfer at the electrodes is carried out by the flow solver incorporated in ANSYS CFX. As shielding gas for the TIG welding, pure argon is used. Furthermore, the material properties calculated in [6-10, 13-17], and net emission coefficient of the radiation is used. By implementing a diffusion model, it is possible to calculate the temperature field and pressure gradients. According to the MHD model, the basic equations of fluid dynamics, the Navier-Stokes equations, are to be used for the



numerical simulation. These equations embody a system of nonlinear partial differential equations of 2nd order, consisting of mass conservation, impulse conservation, and energy conservation equations. From Newton's second law the conservation of momentum is derived. The temporal change of impulse is equal to the sum of the forces acting on the volume element.

$$\frac{\partial (\vec{u})}{\partial t} + \vec{u} \cdot \text{grad} (\vec{u}) = -\frac{1}{\rho} \text{grad} (\vec{\rho}) + \frac{\eta}{\rho} \Delta (\vec{u}) + \vec{f}_S \quad (14)$$

Furthermore, (t) represents the time, ( $\vec{u}$ ) the velocity vector, ( $\eta$ ) diffusion coefficient, ( $\rho$ ) the pressure and ( $\vec{f}_S$ ) the force vectors in the individual TIG arc region. The individual forces in the arc region can be described through the Cartesian coordinate system and in the equation terms. These forces include the force resulting from the pressure gradient, the frictional force due to shear forces, and the body force. The Lorentz force is implemented using the MHD model and thus applies:

$$\vec{f}_L = \vec{J} \times \vec{B} \quad (15)$$

Here the vectorial quantities are the electric current density and the magnetic field. The heat transfer to the outside is carried out by heat conduction. The enthalpy equation from the first law of thermodynamics describes the heat transfer in an open system with a slowly flowing fluid:

$$\frac{\partial H}{\partial t} + \text{div} (\rho \cdot H \cdot \vec{u}) = \text{div} (\kappa \cdot \text{grad} (T)) + \frac{\partial \rho}{\partial t} - S_{rad} + S_h \quad (16)$$

Where (H) is the enthalpy, (t) the time, (T) the temperature, ( $\rho$ ) the density, ( $\vec{u}$ ) the vector of the velocity components, ( $\kappa$ ) the thermal conductivity and ( $S_{rad}$ ,  $S_h$ ) the resistance heating in the radial and vertical directions. Here, the net emission of radiation and the resistance heating are taken into account. In the arc phase, the electromagnetics with applied voltage and current is produced through an imposed electric potential, a magnetic field, the Lorentz force, and resistance heating. The resistance heating is the main heating mechanism of the arc region, while the major cooling mechanism is radiation. The Lorentz-force is responsible for a reduction of the arc region volume and thereby an increase in velocity and pressure in the arc region axis.

In summary, it can be said that these physical effects occur in the TIG arc region, the material melting region, and the current flow region. Their magnitude and intensity depend mostly on TIG welding parameters and arc composition in the cathode region. By using the magneto-hydro-dynamic calculation model, taken into account the drop region mechanisms, as well as the TIG arc and its physical effects. The TIG arc and its physical effects can be described in detail by using the aforementioned equations. In addition to the implementation of the additional equations, also the grid to adapt this model approach is

required. In this case to gradient of the electrons correct mapping concentration, very fine grid resolution is necessary.

### MODEL GEOMETRY FORMATION – DEFINITION OF PROCESS CONSTRAINTS

Figure 2 shows the developed, procedural FE-simulation model based on the created CAD model. Due to the symmetry of the design, only half of the geometry of the torch head was modeled. The FE-model geometries and domains were developed using hexahedral 3D node elements and a fine FE mesh, as seen in Figure 2. This geometry includes the torch base body, the electrode as a cathode, gas nozzle for shield gas supply, Heat pipe area – domain for cooling, the workpiece as the anode, and the flow regions of shield gas and the arc area, as shown in Figure 2a-c.

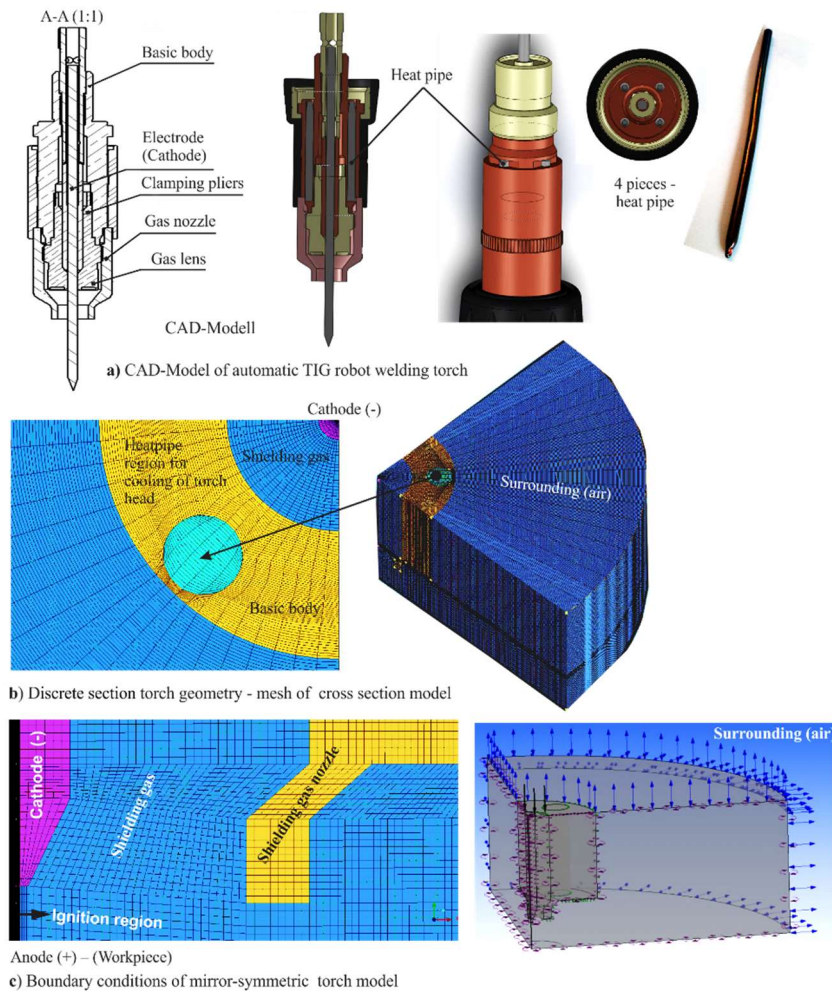


**Fig. 2** Meshed model of the axially symmetric torch construction and definition of process boundary conditions

The required temperature-dependent material properties and the welding parameters were provided and incorporated into the FE-model. The selected materials were tungsten for the electrode, copper for the main body as well as, the heat pipe – region, and pure argon as a shielding gas. Overall, an axially symmetric, thermal fluidic simulation model was developed, in which the heavily stressed torch parts were meshed with a higher density. With the higher mesh density, it was possible to overcome the difficulties that arise from the high temperature, arc pressure, and flow velocity. Distribution gradients in those regions under high stress and strong nonlinearities that arise from the temperature-dependent material properties and predefined thermal boundary condition and conduction condition, i.e. (thermal radiation, convection, junction, and flowing gas) that are defined by the FE-model.

With the completion of the meshing of the modeled torch head and the definition of temperature dependent material properties, the characteristics of the torch part geometry and process media such as gases and air and the contact surfaces of the FE model were set to the defined fluids and integrated at the participating torch geometry surfaces. The defined interfaces between the solid areas and the contacted fluids were defined by adiabatic boundary conditions. It is further determined that the shielding gas flows in the gas nozzle at a constant flow rate, which is a linear function of time. Under the use of mathematical equations (which are described above in detail), the information that necessary for the FE-model thermal boundary and transition conditions are defined for the TIG welding process and then incorporated into the model. These boundary conditions include thermal radiation, thermal conduction, heat transfer through heat pipe (cooling of the torch head), the process gas, and the surrounding air. The arc ignition took place under the action of the current flow and the shielding gas (argon) at temperatures above  $\sim 7000$  K is partially ionized. At this temperature, the discharge process takes place and starts the argon gas partially to ionize. Due to the thermal effect of the temperature, the gas is partially ionized and extended, depending on their ionization energy. On the basis of an artificial energy that is defined by the manipulation of the electrical conductivity, over a Gaussian bell curve with an exponential function in a defined local coordinate system, within the region between the cathode and the anode, the required gas partially ionization temperature was reached at about  $\sim 7000$  K for ignition of the arc. From the arc properties advantage, radiation levels have been formulated as a temperature dependent net emission within the mathematical model. This allows solving the, already described, MHD equation system for the existing temperature and flow distributions in the arc, cathode, and workpiece area within the structured FE model.

Furthermore, it is necessary for the energy conservation, to define interfaces, constraints in terms of flowing gas, electric charges and their potential, and the magnetic field and the vector potential. Thus, the resulting heat transfer is based on the defined processes. In addition, the device constraints can be determined. The outer boundary conditions shown in Table 1 were used for the TIG welding – FE model. To avoid collisions of the gas particles with the geometry surfaces at the gas flow region also to avoid a more rapid drop in temperature in the region of the base body, the process starting temperature is set to  $T = 300$  K and a modeling of process and material-dependent temperature transfer from the solid body to its surrounding was performed. Using the defined material and process constraints and the necessary mechanisms for the shielding gas flow, the drop ranges of cathode, anode, arc region, and heat distribution for the shown FE model were modeled

## Mathematical Modelling of Weld Phenomena 12

procedurally and integrated iteratively. With a defined maximum torch electrical performance ( $I = 200 \text{ A}$ ) extensive transient FE-simulations were conducted, and taking into account the:

- Temperature-dependent material properties of auxiliary and torch materials,
- Current density and the electric potential (welding current and voltage)
- Shielding gas flow and its effects,
- Heat transfer to the torch part geometries and cooling effects – heat pipe – heat transfer, predefined boundary and transition conditions.

**Table 1:** Boundary conditions for the FE Model

Region	Type	T [K]	Process gas / rel. pressure	Current density (j)	Electric potential ( $\phi$ )	Magnetic potential
Inlet – Fluid shielding gas	Inlet	300	$\dot{m}_{SG} * P$	$\frac{\partial \phi}{\partial n} = 0$	$\frac{\partial A_x}{\partial n} = \frac{\partial A_y}{\partial n} = \frac{\partial A_z}{\partial n} = 0$	
Inlet – Cooling heat pipe	Inlet	300	-	-	$\frac{\partial A_x}{\partial n} = \frac{\partial A_y}{\partial n} = \frac{\partial A_z}{\partial n} = 0$	
Shielding gas nozzle Top	Wall	300	0	-	$\frac{\partial A_x}{\partial n} = \frac{\partial A_y}{\partial n} = \frac{\partial A_z}{\partial n} = 0$	
Cathode – Section	Section	300	-	j	$\frac{\partial A_x}{\partial n} = \frac{\partial A_y}{\partial n} = \frac{\partial A_z}{\partial n} = 0$	
Fluid – Cathode	Interface	flux	-	flux	flux	
Fluid – Shielding gas nozzle	Interface	flux	-	$\frac{\partial \phi}{\partial n} = 0$	flux	
Fluid – Workpiece	Interface	flux	-	flux	flux	
Opening atmosphere	opening	300	P0	-	0	
Workpiece – Bottom	Interface	$\frac{\partial T}{\partial n} = 0$	0	0	$\frac{\partial A_x}{\partial n} = \frac{\partial A_y}{\partial n} = \frac{\partial A_z}{\partial n} = 0$	
Workpiece – Wall	Wall	300 K	0	$\phi_S$	$A_x = A_y = A_z = 0$	

The technical and design suggestions for the torch parts design with respect to the cooling, shield gas supply, and the construction of a functional TIG welding torch, a prototype was derived and iteratively optimized. In this case, the possible thermomechanical loads on the torch functional parts under the influence of the gas flow, the current density, the electric potential and the arc pressure due to the electromagnetic effect were determined. As a basis for the simulation, the following geometric parameters and geometrical structure were defined:

- electrode diameter:  $d_E = 2.4 \text{ mm}$ ,
- electrode grinding angles:  $\alpha_E = 20^\circ$ ,
- 4 x heat pipe diameter:  $d_P = 2.6 \times 60 \text{ mm}$ ,
- gas nozzle – bowed pipe diameter:  $d_P = 8.50 - 14.0 \text{ mm}$ .

### FE CALCULATION RESULTS

#### CURRENT DENSITY, ELECTRICAL POTENTIAL, TEMPERATURE FIELD DISTRIBUTION, ARC PRESSURE, SHIELD GAS FLOW AND PARTICLE VELOCITY

Under the defined TIG welding process boundary conditions and by using the thermo-mechanical / magneto-hydrodynamic FE model, the temperature distributions and their resulting physical effects in the TIG arc area and the torch parts were determined and analyzed. The individual images in Figure 3 show the distribution of the calculated arc and gas nozzle temperatures, the current density, the arc pressure, and the resulting temperatures at the torch cooling system – heat pipe and the flow velocity. The calculations were carried out using process parameters of  $I = 100$  A, shielding gas flow rate =  $12 \text{ l min}^{-1}$  under the influence of the torch cooling system (heat pipe). It was noticeable that the calculated maximum arc temperature  $T = 17330$  K on the arc axis is directly below the tungsten cathode. At the area of the gas nozzle, the arc cross-section is expanded so that a typical open TIG arc bell is formed. This expands rapidly below the nozzle, which leads to a high heat flow within the anode area. The Lorentz force is the cause of an arc flow that determines the dynamic pressure at the workpiece surface. Consequently, the reduction of the arc pressure is caused due to increasing the thermal gas conductivity. It can also be seen that the maximum calculated temperature at the lower edge of the gas nozzle was  $T = 320$  K, which corresponds well to the defined conditions for the torch cooling. This result guarantees a stable welding process under the defined torch cooling system – heat pipe tube.

Furthermore, Figure 3 shows the calculation results of the distribution and intensity of the current density, the arc pressure (dynamic pressure), and the flow velocity of the particles within the arc and the anode area (workpiece). Here the discharge regions are different in temperature, velocity, and potential gradients. In the area of the nozzle, the arc is characterized by a relatively high voltage fall and a high mean temperature of  $17330$  K. A maximum flow velocity of  $v = 200 \text{ m s}^{-1}$  at the arc core was determined. The high outflow velocity from the nozzle is due to the associated thermal gas expansion and continuity conditions of the mass flow. However, the maximum speed is calculated under the gas nozzle in the area of the arc axis. This is due to the Lorentz force of the electromagnetic field, which cause arc projection at the cathode and it is to be regarded, as the dominant cause for the suction of external shielding gas directly under the gas nozzle. This effect causes an increase in velocity that leads to arc expansion under the gas nozzle.

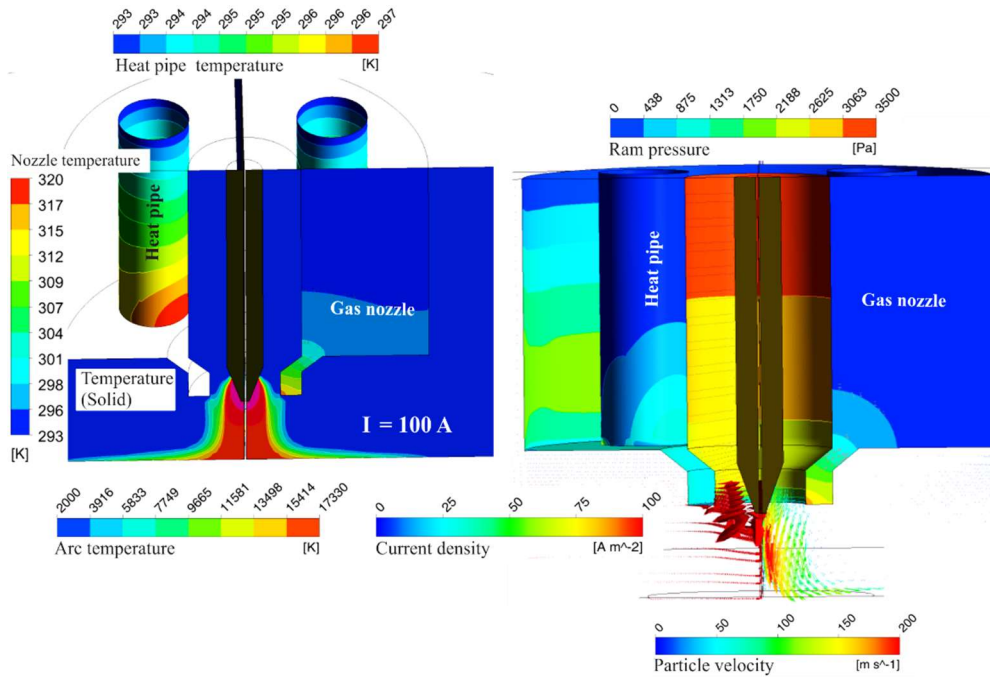
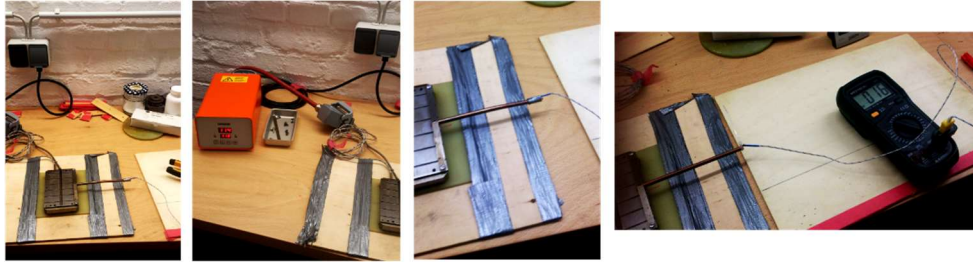


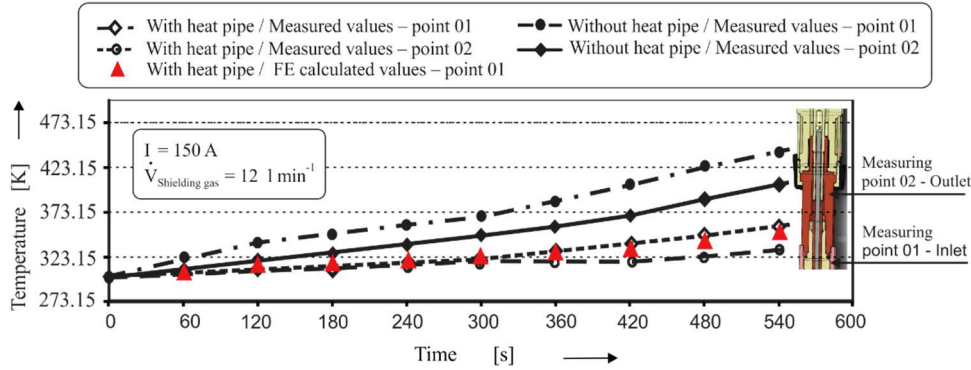
**Fig. 3** Calculation results: TIG arc temperature, current density, ram pressure and flow particle velocity

#### VERIFICATION OF FE MODEL BY PRACTICAL EXPERIMENTS

For an optimal technical-constructive design of the heat pipe cooling system in the torch head, temperature measurements were carried out to determine the heat dissipation at the heat pipe as shown in Figure 5a. Using the test system (thermocouples attached to the heat pipe with a control device) as shown in Figure 5a, the measured temperatures show that the heat generated flows error-free from the hot areas to the colder areas. The flow rate depends on the pipe cross-section as well as pipe material thermal coefficient of conductivity. Thus, the technical function ability of the heat pipe was clearly demonstrated.



a) Direct measurement of heat dissipation through heat pipe



b) Measurement results of heat dissipation through heat pipe during TIG welding process

**Fig. 4** Comparison of the calculated and measured of heat pipe temperatures during the welding process by means of attached thermocouples

Furthermore, with and without the heat pipe, under the predefined welding parameters (welding current value:  $I = 150 \text{ A}$ , shielding gas:  $12 \text{ l min}^{-1}$ ), the thermal and fluid mechanical influencing variables of cooling effects in the torch head up to a welding time of 540 seconds were examined, see Figure 5b. Thermocouples were installed on the outer surfaces of the torch's head gas-nozzle, also in the cooling parts of the heat pipe that are attached to the torch head. The results were applied for verification of the FE simulation model and verification of the heat pipe function during the welding process. The torch's head temperature measurements without heat pipe tubes show the larger difference compared to the temperature measurement by using heat pipe cooling. It is noticeable here that higher temperatures were recorded without the heat pipe. Especially at the lower edge of the gas nozzle, the temperature reached up to 438.15 K, while the measured temperatures with heat pipe are less than 361.15 K. Furthermore, the measured temperatures agreed with the simulation results. The maximum temperature measured at the gas nozzle – lower edge of the "highly loaded temperature range" was 361.15 K, while the maximum FE-calculated temperature is 350.15 K. The difference is  $< 10 \%$ . Thus, it was shown that the designed heat pipe principle for torch head cooling works technically well and can be considered as optimally for a torch head cooling system. These comparisons also showed the validity of the FE-model and the developed torch concept, as well as the selected materials, are well suited for the design of the torch model and its process-related requirements.

PROCESS PARAMETERS INFLUENCE – INVESTIGATION TO OPTIMIZE THE TORCH COOLING AND GAS SYSTEM

To determine the influence of the variation of the welding current and shielding gas quantity on the cooling system efficiency, FE-calculations were performed for the torch including torch-cooling system – heat pipe. Also, the influence of different welding currents  $I = 75$ ;  $150$  A and shielding gas flow rate of  $= 12 \text{ l min}^{-1}$  on the arc formation and its physical attribute were investigated. The simulations and evaluations regarding heat pipe cooled torch, heat dissipation, and flows conditions of the shielding gas were performed. Figures 5 and 6 summarize the influences of the process parameters on the arc formation and its intensity.

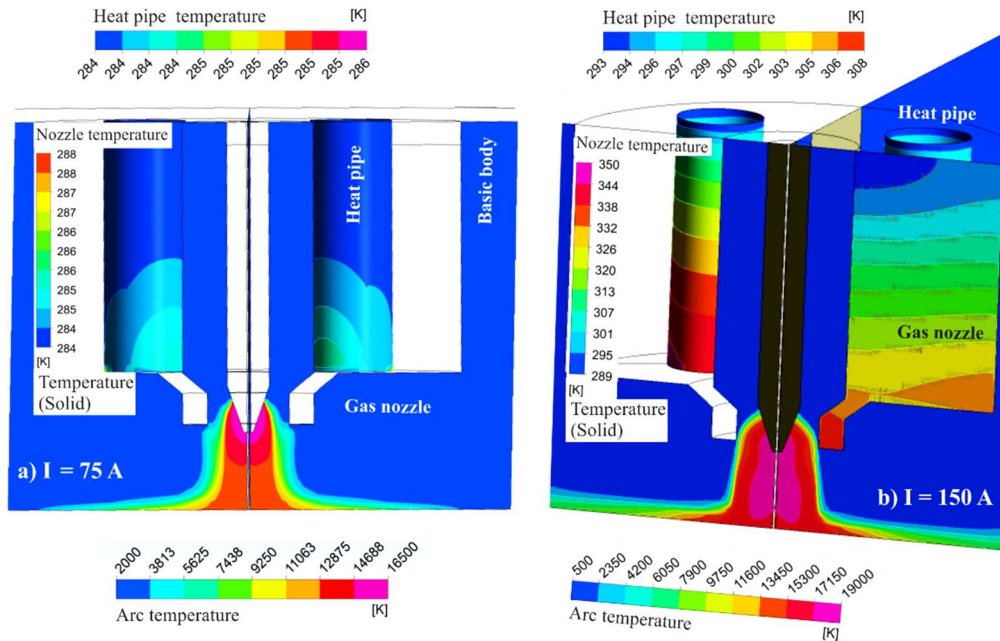


**Fig. 5:** Calculation results: TIG arc, gas nozzle temperature und heat pipe temperature: a)  $I = 75$  A, b)  $I = 150$  A;  $\dot{V}_{\text{shielding gas}} = 12.0 \text{ l min}^{-1}$

The results of the individual figures 5 and 6 show the calculated temperature distribution in the area of the arc, the gas nozzle, and the heat pipe cooling area. Furthermore, the distribution of the flow velocity of the particles from the arc cross-section to the anode area is shown. This shows that the current fields and particles velocity simulations are functioning well. In addition, results show the protective gas supply is uniform through the torch's head channels and cross-sections.



## Mathematical Modelling of Weld Phenomena 12

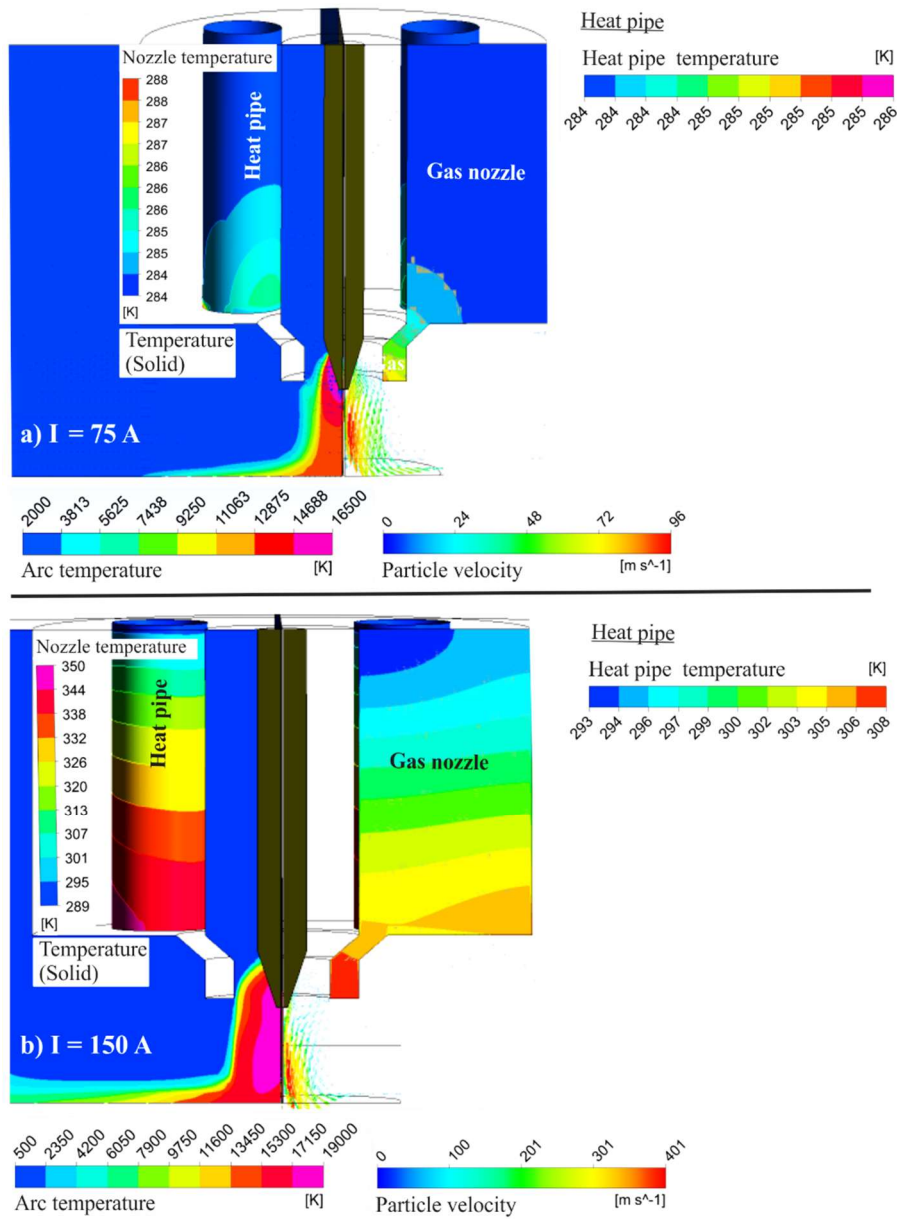


**Fig. 6** Calculation Results: TIG arc temperature, nozzle, heat pipe temperature and flow velocity: **a)**  $I = 75$  A, **b)**  $I = 150$  A;  $\dot{V}_{\text{Shielding gas}} = 12 \text{ l min}^{-1}$

Furthermore, the calculation results show that the maximum temperatures recorded at the lower edge of the gas nozzle reached up to 350 K. However, at the heat pipe cooling area, the temperature reached up to 308 K at a welding current of  $I = 150$  A. These correspond to temperatures of  $T = 350$  K at the lower edge of the gas nozzle, at the heat pipe cooling area respectively. Thus, the determined parameters fulfill the necessary

cooling capacity for the construction of the automatic robotic-TIG welding torch. Furthermore, the individual images in Figures 5 and 6 show that the temperature of the arc increased from 16500 K to 19000 K as the welding current increased. Increasing of the introduced energy into the arc leads to partial increasing ionization of the shielding gas. As a result, the arc becomes more intense. However, the higher current also leads to a stronger expansion of the TIG arc and therefore leads to a stronger increase of heat radiation in the anode area. At a constant gas flow rate, an increase of electrical potential, current leads to increasing of the arc forces, which increases the magnetic field strength and the arc pressure to  $P = 7500 \text{ Pa}$  and the flow velocity to  $v = 401 \text{ m s}^{-1}$  at the arc core. The reason for that is an increased degree of ionization of the shielding gas. Due to the temperature increase, the proportion of thermal plasma in the shielding gas area increases during the TIG process, as well as its speed, see Figure 6 and Table 2.

**Table 2:** Influence of welding current change on arc formation and its physical effects

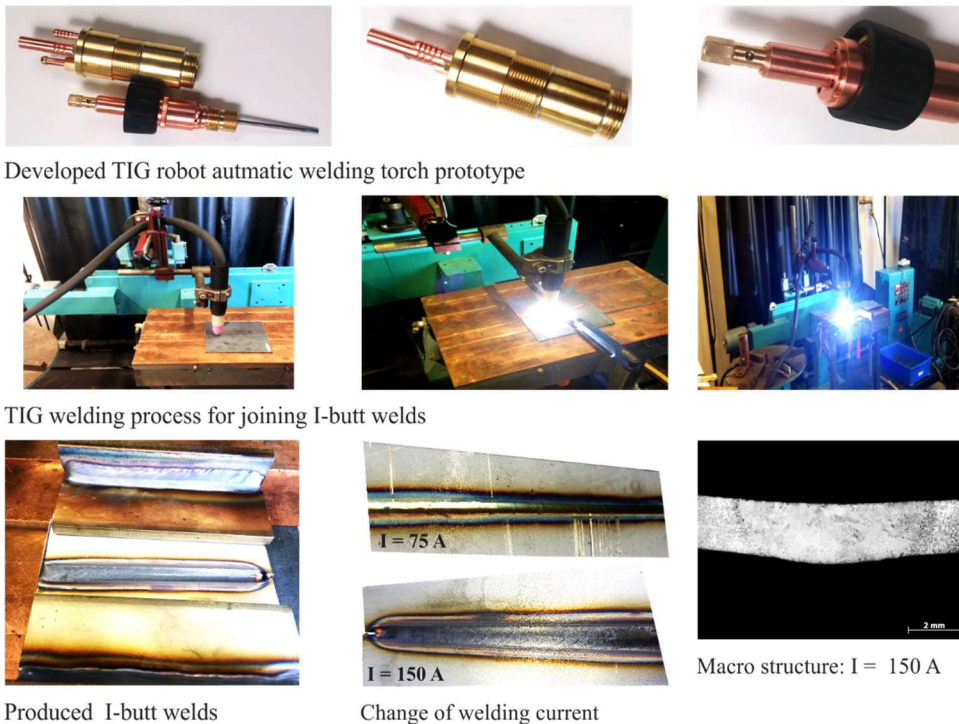
Current [A]	Max. arc temperature [K]	Max. temperature at the bottom of gas nozzle [K]	Max. temperature at the bottom of heat pipe [K]	Max. arc Pressure [Pa]	Max. flow velocity [m s <sup>-1</sup> ]
75	16500	288	285	2100	96
100	17330	320	297	3500	200
150	19000	350	308	7500	401

The individual images in Figure 6 and Table 2 show the influence of the change in welding current on the behavior and magnitude of the flow velocity and arc pressure. By increasing welding current, the flow velocity, and the arc pressure are rapidly increased. Therefore, a flow rate of  $v = 401 \text{ m s}^{-1}$  and a maximum pressure of  $P = 7500 \text{ Pa}$  were recorded in the arc core at an increased current of 150 A. When the current increase from 75 A to 150 A, the flow velocity, as well as the arc pressure, increased approximately four times. Based on the simulation results, it is confirmed that the physical arc effects such as arc pressure, current density, electromagnetic fields, and flow velocity increase their intensities were the current is increased. This shows, that in the automated robotic TIG torch, the required reproducibility, interchangeability, positioning accuracy, and faster replacement of torch-head parts, can be realized without errors by using the heat pipe cooling system.

Now, it is possible in automatic-TIG welding torches, which supplied with torch head changing systems to perform welding at higher energy and higher heat input. It is noticeable that the designed cooling principle ‘heat pipe’ for the torch-head cooling system works well. Four heat pipes are sufficient for the predefined torch electrical performance of  $I = 200 \text{ A}$ .

USE OF THE RESULTS FOR CONSTRUCTION OF AN AUTOMATIC TIG  
ROBOT TORCH WITH HEAT PIPE – COOLING SYSTEM

Figure 7 shows a prototype of the automatic-TIG robot welding torch-head with an exchangeable-head system and heat dissipation (heat pipe tube) torch head cooling system. This prototype was designed according to the defined torch electrical performance of  $I = 200$  A. With this prototype, component joints were welded under realistic working conditions. The evaluation of the torch prototype was carried out through producing welds under various welding conditions using various process parameters. The torch was tested and evaluated for gas tightness and ignition. The ignition process run smoothly and without any problems. Furthermore, by using this welding torch prototype, high-quality welded joints with defined properties can be produced. The welded joints quality shows high reproducibility.



Developed TIG robot autmatic welding torch prototype

TIG welding process for joining I-butt welds

Produced I-butt welds

Change of welding current

Macro structure:  $I = 150$  A

**Fig. 7** Developed automatic robotic TIG welding torch prototype

Figure 7 shows the welding tests that were carried out for the torch prototype to produce butt joints using different process parameters. The test results show reproducible, good weld quality, reliable process stability, and easy torch handling. The quality of the welds depends on the process parameters. The performance of the developed automatic robotic TIG-welding torch and its exchangeable head system, as well as its cooling system, was successfully proven.

### CONCLUSION FORM THE SIMULATION RESULTS

From the analysis of the simulation results, a new physical operating principle based on the heat dissipation (heat pipe) was derived to design an optimized heat balance for a TIG torch head, which can be used for the design of a functional automatic TIG robotic torch head with its interchangeable head system. The flow-mechanical/MHD model was used to investigate the arc formation and its attribute during automatic TIG robot welding. The physical processes during TIG welding were analyzed and characterized with different process parameters as well as temperature-dependent material properties. Therefore, it was possible to design a torch-head with its defined dimensions, using a heat pipe torch-head cooling system. In addition, the interactions between individual process parameters and the physical effects during the welding process were analyzed, in order to avoid design failures, and creation of a stable, functionally reliable TIG-robotic torch. This leads to the following conclusions:

- Arc characteristic such as formation, intensity, temperature, and flow gas dynamic can be influenced by process parameters.
- The difference between the calculations and the measurements in gas nozzle temperature equal to  $< 10\%$ . This indicates the practical application potential of the FE- model.
- The investigated torch cooling system and the gas flow cross-sections corresponded to the defined torch head design.
- The suitability of the construction of the automatic-robotic TIG welding torch including its exchangeable head system and heat dissipation (heat pipe), was proven through the production of butt joints component.

### REFERENCES

- [1] H.-J. FAHRENWALDT, V. SCHULER: *Praxiswissen Schweißtechnik, Werkstoffe, Prozesse, Fertigung*. 2. überarbeitete und erweiterte Auflage, Springer Vieweg, Wiesbaden, 2009. – ISBN: 978-3-87155-970-9.
- [2] K.-J. MATTHES, W. SCHNEIDER: *‘Schweißen von metallischen Konstruktionswerkstoffen’*, 5.; neu bearbeitete Auflage Fachbuchverlag Leipzig in Carl Hanser Verlag, München, 2012. – ISBN: 978-3-446-42073-1.
- [3] J. P. SCHULZ: *TIG-Process with dual shield Intermediate process between TIG and plasma arc welding, Wdg. In World*, 24 (1986), H. 11/12, pp. 248/58.
- [4] A. BEJAN, D. A. KRAUS: *Heat Transfer Handbook*. Wiley & Sons, Hoboken NJ 2003, ISBN 0-471-39015-1.
- [5] T.P. GOTTER: *Principles and Prospects of Micro Heat Pipes, Proc. 5th Int. Heat Pipe Conf, Tsukuba, 1984* – Japan Technology & Economics Center Inc., Vol. 1.
- [6] Y. S. TOULOUKIAN: *‘Thermophysical Properties of Matter (14 vol.)’*, New York, 1979 ff.
- [7] Committee AIH. ASM International v2, *‘Properties and selection-nonferrous alloys and special-purpose materials’*, 10<sup>th</sup> ed. OH: metals park 1990. – ISBN 0-87170-378-5.
- [8] K. ALALUSS: *‘Modelbildung und Simulation des Plasma-Schweißens zur Entwicklung innovativer Schweißbrenner – Modeling and simulation of plasma welding for the development of innovative welding torches’*, Habilitation, Technische Universität Chemnitz 2017.

- [9] K. ALALUSS, G. BÜRKNER, P. MAYR: *Process simulation of plasma-arc welding for the development of an orbital plasma arc welding torch*, 11<sup>th</sup> International Seminar Numerical Analysis of Weldability, Mathematical Modelling of Welding Phenomena 11 (2016), pp. 23/42, printed bound Styria Print GmbH, Gratkorn, Austria 2016, – ISBN 978-3-85125-490-7.
- [10] K. ALALUSS, G. BÜRKNER, P. MAYR: *Simulation of micro-plasma powder deposition for advanced welding torch design*, 10<sup>th</sup> International Seminar Numerical Analysis of Weldability, Mathematical Modelling of Welding Phenomena 10, Graz – Seggau, pp. 705 - 722, printed bound Styria Print GmbH, Gratkorn, Austria 2013. – ISBN 978-3-85125-293-4.
- [11] M. SCHNICK, M., U. FÜSSEL, J. ZSCHETZSCHE: *Strömungsmessung und Simulation von Lichtbogen- und Plasmaprozessen.*, Aachen, GST 2006.
- [12] S. ROSE, U. FÜSSEL, M. SCHNICK: *‘Modellierung des dynamischen Lichtbogenverhaltens unter Nutzung experimenteller Daten’*. DVS-Berichte Band 275. S. 545 – 553, DVS-Verlag, Düsseldorf 2011. – ISBN: 978-3-87155-267-0.
- [13] L. SANAONNEN, L.; J. HAIDAR; J. LOWKE: *‘Prediction of properties of free burning arcs including effects of ambipolar diffusion’*, J. Phys. D: Appl. Phys., Vol. 33, pp. 148 – 157, 2000.
- [14] C E MOORE: *‘Atomic Energy Levels Circular 467’*, vol 2 (Washington DC: US National Bureau of Standards), 1952.
- [15] J. J. LOWKE, M. TANAKA: *‘LTE-diffusion approximation for arc calculations’*, J. Phys. D: Appl. Phys. 39 (2006) 3634–3643.
- [16] A B MURPHY: *‘Diffusion in equilibrium mixtures of ionized gas’*, Phys. Rev. E 48, 3594 – 3603, 2003.
- [17] Lago, F.; Gonzales, J.J.; Freton, P.; Gleizes, A.: *A numerical modelling of an electric arc and its interaction with the anode: Part 1. The two-dimensional model*. Journal of Physics D: Applied Physics, Vol. 37, pp.883-897, 2004.

# EVAPORATION-DETERMINED MODEL FOR ARC HEAT INPUT IN THE CATHODE AREA BY GMA WELDING

O. MOKROV\*, M. SIMON\*, A. SCHIEBAHN\* and U. REISGEN\*

*\*RWTH Aachen University, ISF – Welding and Joining Institute, 52062 Aachen, Germany, simon@isf.rwth-aachen.de*

*DOI 10.3217/978-3-85125-615-4-50*

## ABSTRACT

The most used approaches for the modelling of the heat input in GMA welding process simulation usually assume an axisymmetrical Gaussian distributed heat flux in the cathode region, whereas it has been suggested that the attachment region of the arc to the cathode consists of several highly mobile elemental cathode spots. It is assumed, that the processes in each mobile spot are not stable, but are strongly influenced by the evaporation from the workpiece. Their existence is therefore transient and outside of equilibrium. To calculate the heat input in this area, a concept has been developed on the basis of a cellular automaton method, which allows to calculate the resulting heat flux distribution. At the core of this concept is a simplified model for the elementary cathode spot, which delivers the heat flux and the current density, while taking into account effects of evaporation, which are characteristic for the real GMA welding process.

The cellular automaton consists of a grid, whose size is related to the typical size of the cathode spot, taken from literature. The random motion of the spots is simulated according to a probability distribution, which is dependent on the potential heat release of each cathode spot to the cathode surface and therefore also the cathode surface temperature. The number of spots is counted to satisfy a „fuzzy“ current continuity. Additionally a condition is implemented to take into account the state of the arc area.

In a next step this model will be coupled to a weld pool calculation.

Keywords: GMA, cathode, evaporation, heat flux, current density

## INTRODUCTION

The gas metal arc welding (GMAW) is used widely in the industry due to its high reliability and productivity. However, as it is a complex phenomenon involving many interacting physical mechanisms, the development of the understanding of the process in detail is still ongoing. To further this understanding, the method of computer simulation is increasingly used. Welding simulation can be distinguished into three areas, following Radaj [1], and this work is concerned with a part of process simulation, where the accurate prediction of shape and size of the weld pool, according to the welding process parameters, is attempted. The phenomena that need to be taken into account include the resistance of the cables and the wire electrode, the droplet formation and detachment, the arc including heat transfer, melting and solidification enthalpies and heat conduction within the work piece. For the magneto-hydrodynamic calculation of the weld pool the most sensitive boundary condition

is that of the cathode layer, together with the effects of the heated molten droplets. In the recent works [2], [3], the cathodic heat flux is treated as a fixed Gaussian function, following [4], however in this work a model is presented to determine a new distribution.

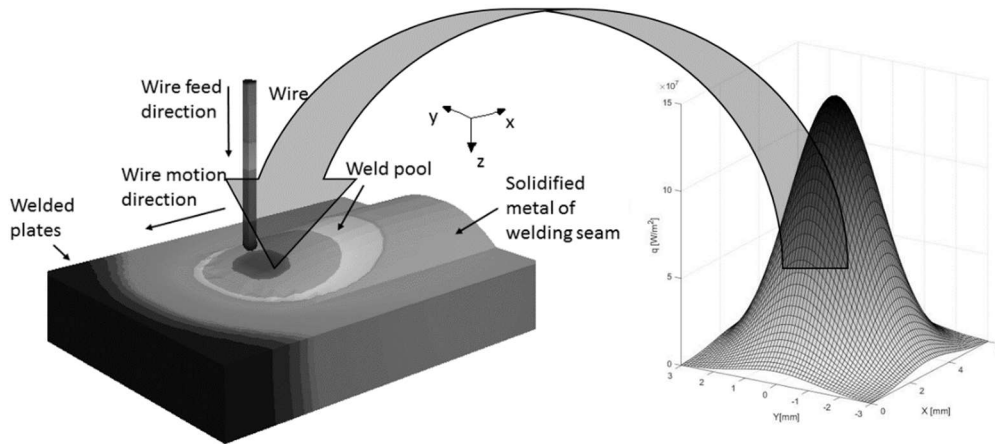


**Fig. 1** Gaussian distribution, as usually used as cathode heat source in GMA weld pool calculation.

### PROBLEM STATEMENT

It has been observed that the cathode region in an arc discharge consists of multiple highly mobile cathode spots (CS) on the weld pool [5]. The exact dynamic of the CS have so far remained unclear due to their very small spatio-temporal dimensions and the description of their properties still represents a field of active research. On a solid cathode, it is observed, that in an absence of an external magnetic field the spots seem to follow a quasi-stochastic random walk [6], which justifies the assumption of a Gaussian distribution (Figure 1) as a fair first approach. However it has been shown in experiments, that the CS follow a different distribution on a molten cathode [7], where it seems like they tend to avoid the center, where the hottest temperatures occur. In the present work, the authors present a concept to relate the cathode spot probability to the cathode surface temperature, by an evaporation-dependent model for the heat flux of the elementary cathode spot. In a second step this model will be used to calculate new heat flux and current density distributions which can be considered to be dependent on evaporation. The model of the elementary cathode spot is based on descriptions of the cathode layer found in the literature, although it uses an original approach to describe the ion current density, assuming a non-linear ionization process which is treated as a black box. This allows to match the current density to the empirically observed high current densities on non-refractory materials, which cannot be explained by thermionic emission, as is the case in refractory materials like tungsten. Additionally it assumes a strong damping effect to the ion current density, due to evaporation.

MODEL DESCRIPTION

MODEL OF ELEMENTARY CATHODE SPOT

The main phenomena which were considered to contribute to the net heat flux are the following: Heat gains by ion bombardment  $q_{ion}$  and back diffused electrons  $q_{ebd}$  and heat losses by thermionic emission  $q_{em}$ , evaporation  $q_{evap}$ , heat conduction  $q_{cond}$  and radiation  $q_{rad}$ . In order to calculate these, the current densities of thermionic electrons, ions and back-diffused electrons need to be known.

$$q_{CS} = q_{cond} = q_{ion} + q_{ebd} - q_{evap} - q_{em} - q_{rad} \quad (1)$$

The external parameters for the Model were  $d_{sheath} = 10^{-8}$  m;  $U_D = 10$  V, the thickness of the cathode sheath and the voltage drop, according to [8]. The heavy particle temperature  $T_h$  is assumed to equal the surface temperature of the wall  $T_w$  due to thermalization with evaporated atoms.

$$T_h = T_w \quad (2)$$

The electron temperature in the plasma is estimated by

$$T_e = \frac{(e \cdot U_D + k_B \cdot T_w - e \cdot E_{ion})}{3/2 \cdot k_B} \quad (3)$$

with  $k_B$  Boltzmann constant,  $e$  electron charge and  $E_{ion} = 7.9$  eV ionization energy of iron vapor.

The effective work function was taken as

$$A_{eff} = A - \Delta A \quad (4)$$

with  $A = 4.5$  eV being the work function for iron and

$$\Delta A = \sqrt{\frac{e \cdot U_D}{4\pi\epsilon_0 d_{sheath}}} \quad (5)$$

the lowering of the work function [9], with  $\epsilon_0$  the vacuum permittivity.

The thermionic electron current is calculated according to the Richardson-Schottky relation [10]

$$j_{em} = e \frac{4\pi k_B^2 m_e}{h^3} T_w^2 \cdot \exp\left(-\frac{A - \Delta A}{k_B T_w}\right) \quad (6)$$

with  $m_e$  electron mass,  $h$  Planck constant. The ion current is calculated as



$$j_{ion} = \left( j_{em} \cdot \exp\left(-\frac{P_{vap}^2}{P_{atm}^2}\right) \right)^{1.6} \quad (7)$$

The exponent of 1.6 is chosen to match the total current density found by Meysats [11] of  $j_{CS} = 1 - 3 \cdot 10^{12}$  A/m<sup>2</sup>, with  $P_{vap}$  the pressure of vaporized material Eqn. (7) taken from [12],  $P_{atm}$  the atmospheric pressure,  $T_b = 3134$  K the boiling temperature of iron,  $H_{vap} = 347 \cdot 10^3$   $\left[\frac{J}{mol}\right]$  the molar heat of vaporization of iron and  $R$  the gas constant.

$$P_{vap} = P_{atm} \cdot \exp\left[\frac{-H_{vap}}{R} \left(\frac{1}{T_w} - \frac{1}{T_b}\right)\right] \quad (8)$$

The back-diffused current is estimated as

$$j_{ebd} = (j_{em} + j_{ion})/2 \cdot \exp\left(-\frac{eU_D}{kT_e}\right) \quad (9)$$

The total current is therefore given as

$$j_{CS} = 2j_{ion} - j_{ebd} + j_{em} \quad (10)$$

The corresponding heat fluxes are given as

$$\begin{aligned} q_{ion} &= \frac{j_{ion}}{e} \left[ k_B \left( 2T_h + \frac{ZT_e}{2} - 2T_w \right) + ZeU_D + E_{ion} - ZA_{eff} \right] \\ &\approx \frac{j_{ion}}{e} \left[ k_B \frac{T_e}{2} + eU_D + E_{ion} - A_{eff} \right] \end{aligned} \quad (11)$$

following [8], with  $Z=1$ , considering only the first ionization for simplification.

$$q_{ebd} = \frac{j_{ebd}}{e} (2kT_e + A_{eff}) \quad (12)$$

according to [8].

$$q_{em} = \frac{j_{em}}{e} (2kT_w + A_{eff}) \quad (13)$$

according to [8].

$$q_{evap} = J_{vap} H_{vap} / M_{iron} \quad (14)$$

following [12], with  $M_{iron}$  the molar mass of iron and

$$J_{vap} = \left( \frac{m_M}{2\pi k_B T_w} \right)^{1/2} P_{vap} \quad (15)$$

the flux of evaporated particles in diffusive mode according to [13].

$$q_{rad} = \varepsilon\sigma T_w^4 \tag{16}$$

according to [14], with  $\varepsilon\sigma = 5.670367 \cdot 10^8 \text{ J}/(\text{s} \cdot \text{m}^2 \cdot \text{K}^4)$  the Stefan-Boltzmann constant.

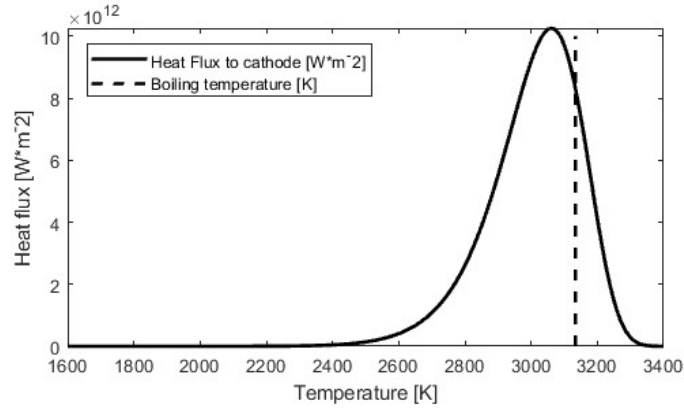


Fig. 2 Dependence of heat flux on surface temperature.

The proposed model states a relationship between the surface temperature and the expected heat flux as well as the current density in case of a cathode spot, see Figure 2 and Figure 3.

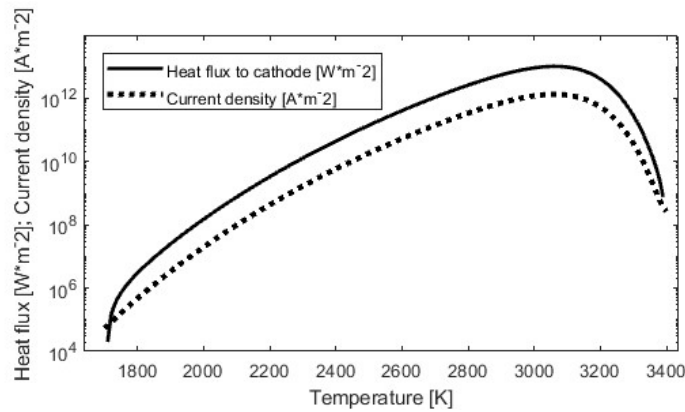


Fig. 3 Dependence of heat flux and current density on surface temperature in logarithmic scale.

#### MODEL OF CATHODE SPOT DISTRIBUTION

Assuming a initial temperature field  $T_{0,w}(x, y)$  (Figure 4) of a fully developed weld pool surface, a new distribution of CS is selected by sampling locations of single CS without replacement according to a probability  $P(x, y)$ . The probability at each location is chosen to be directly proportional to the possibly generated heat flux, convoluted with a Super-Gauss function to take into account the influence of distance of the anode tip to the cathode, favoring a spot close to the center below the torch  $(x_0, y_0)$ , with  $r_x = 3 \cdot 10^{-3} \text{ m}$ ,  $r_y = 3 \cdot$

## Mathematical Modelling of Weld Phenomena 12

$10^{-3}$  m,  $x_0 = 3 \cdot 10^{-3}$  m and  $y_0 = 0 \cdot 10^{-3}$  m. Here  $k = 3/(r_x r_y)$  is a geometrical parameter, which influences the spreading, similar to a standard deviation.

$$P_{abs}(x, y) = q_{spot}(T_w(x, y)) \cdot \exp(-k((x-x_0)^2 + (y-y_0)^2)) \quad (17)$$

$$P(x, y) = \frac{P_{abs}(x, y)}{\int P_{abs}(x, y) dx dy} \quad (18)$$

The grid size is chosen according to the assumed diameter of the CS of  $\Delta x = 5 \mu\text{m}$  and the time step is chosen as  $\Delta t = 5 \cdot 10^{-8}$  s following [10] and [5], giving an approximate speed of the CS of  $v_{CS} = 10^2$  m/s.

Initially a number of CS is generated on the grid, until the total current surpasses a fixed value  $I = 180$  A. If the total current is higher than the fixed value of  $I$ , the number of CS will be reduced in the next time step, picking according to the inverse probability inherent to each CS, until the total current falls below the fixed value again, and so on, therefore satisfying a “fuzzy” current continuity condition.

If the spot is not removed it will move around the grid in the next time step in random direction, only taking into account the probability at its adjacent fields, which is convoluted with a small Gaussian again to take into account the longer distance to diagonal grid-cells  $f_{diagonal} = 0.0751$ ,  $f_{straight} = 0.1238$ .

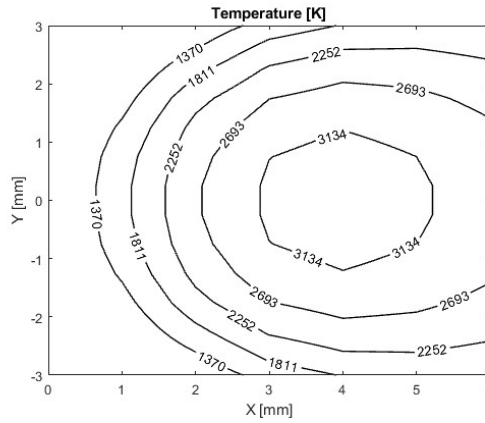


**Fig. 4** Initial temperature field.

At each location where a spot resides  $(x_{CS}, y_{CS})$  the local temperature modification of the surface is treated in a very simplified way. A local temperature gain  $\Delta T(x, y, t)$  is added to the surface temperature field  $T_w(x, y)$  according to a strongly simplifying assumption of transient heat transfer of a point explosion in a homogenous semi-infinite solid.

$$\Delta T(x, y, t) = \frac{H_0(t)}{(4\pi\alpha t)^{3/2} \rho C_p} \cdot \exp\left(-\frac{(x-x_{CS})^2}{4\alpha t} - \frac{(y-y_{CS})^2}{4\alpha t}\right) \quad (19)$$

where  $H_0$  is the amount of energy,  $\alpha = \kappa\rho C_p$  the thermal diffusivity,  $\kappa$  the thermal conductivity,  $\rho$  the density and  $C_p$  the heat capacity, taken from [15], not taking into account the actual local temperature, but assuming a fixed temperature of  $T_\alpha = 2450$  K everywhere.



After a calculation time of 76 h  $10^5$  iterations have been processed, therefore a simulation time of  $5 \cdot 10^{-3}$  s has been calculated. The total average current was  $I = 181.3$  A. The total electrical power was  $P = I \cdot U_D = 1.813$  kW, from that a total of  $P_{\text{Heat}} = 1.358$  kW have been transferred to the cathode, not accounting for the 20% losses from Eqn. (20).

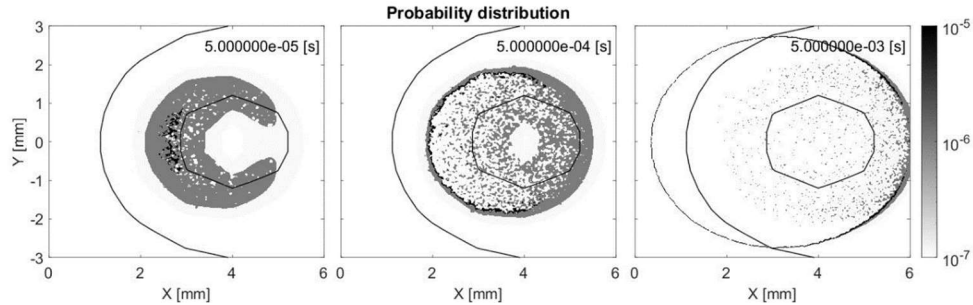


**Fig. 6** Resulting probability distribution, for time  $5 \cdot 10^{-2}$ ,  $5 \cdot 10^{-1}$ , 5 ms. The isolines of the liquidus and boiling temperature are overlaid.

Figure 6 presents the evolution of the probability distribution. It becomes apparent that the cathode spots modify the probability distribution locally, resulting in a very high concentration of the probability on a fine line at the front towards the welding direction.

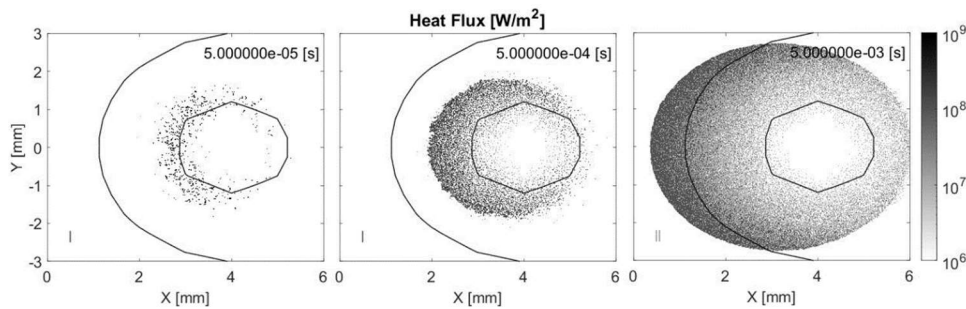


**Fig. 7** Resulting heat flux distribution, for time  $5 \cdot 10^{-2}$ ,  $5 \cdot 10^{-1}$ , 5 ms. The isolines of the liquidus and boiling temperature are overlaid, as well as an indication for the distance traveled by the torch in the lower left corner.

In Figure 7 the resulting heat flux distribution is presented. The welding direction is from right to left. It becomes apparent, that a sickle shape of the heat flux distribution is present with an emphasis towards the melting front. As the movement of the torch has not been taken into account, an arrow was placed in the figures (lower left) to indicate the movement of the plate according to time-scale and grid resolution, assuming a welding speed of 80 cm/min. The distance traveled by the torch after 5 ms equals  $d = 6.67 \cdot 10^{-4}$  m.

## Mathematical Modelling of Weld Phenomena 12

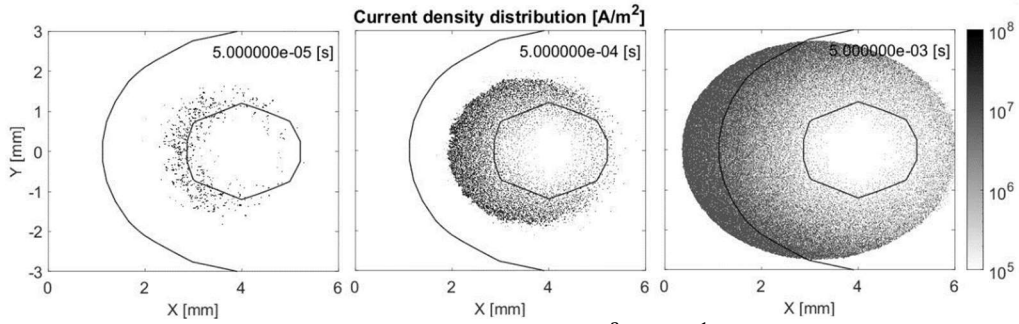


**Fig. 8** Resulting heat flux distribution, for time  $5 \cdot 10^{-2}$ ,  $5 \cdot 10^{-1}$ , 5 ms. The isolines of the liquidus and boiling temperature are overlaid.

As the distribution reflects the locations of the CS, the distribution of the current density in Figures 8 follow the distribution of the heat flux, however with values about one order of magnitude lower, as expected from the model (Figure 3).

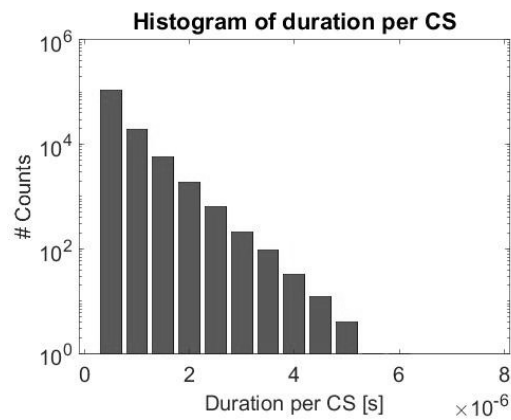


**Fig. 9** Semi-logarithmic histogram of the duration of a CS in intervals of  $50 \cdot 10^{-8}$  [s].

Besides this, the combined model also allows some statistical statements about the duration of a CS (Figure 9) as well as the current per CS (Figure 10). Single the cathode spots lasted up to  $6 \cdot 10^{-6}$  s after  $5 \cdot 10^{-3}$  s simulated time. In Figure 10 it can be seen, that the substantial part of the cathode spots carry a current of more than  $6 \cdot 10^{-3}$  A, which is lower than the stated possible minimum of current per cathode spot 0.1 A in [16]. The maximum current per CS was  $I_{CS,max} = 33.4$  A.

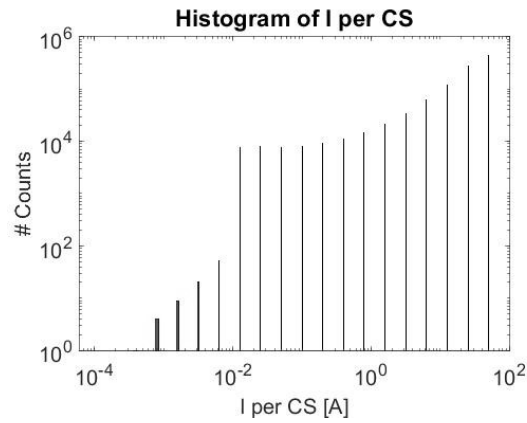


Fig. 10 Logarithmic histogram of current  $I$  per CS.

### DISCUSSION

The presented model allows the calculation of new cathodic heat flux (Figure 7) and current density distributions to replace the widely used Gaussian approximation (Figure 1), taking into account evaporation. However, there are several drawbacks, which need to be addressed.

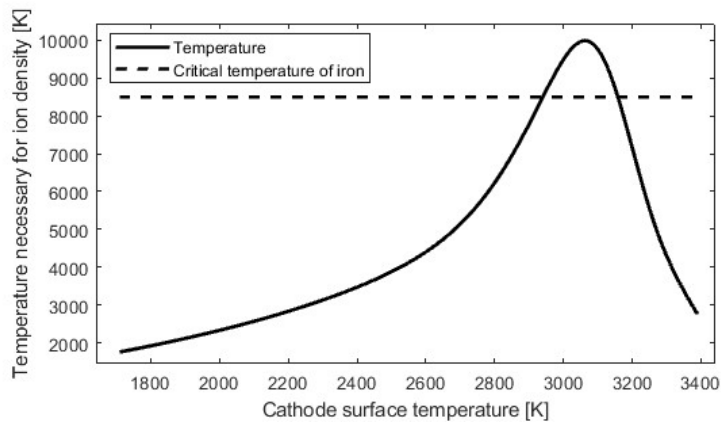
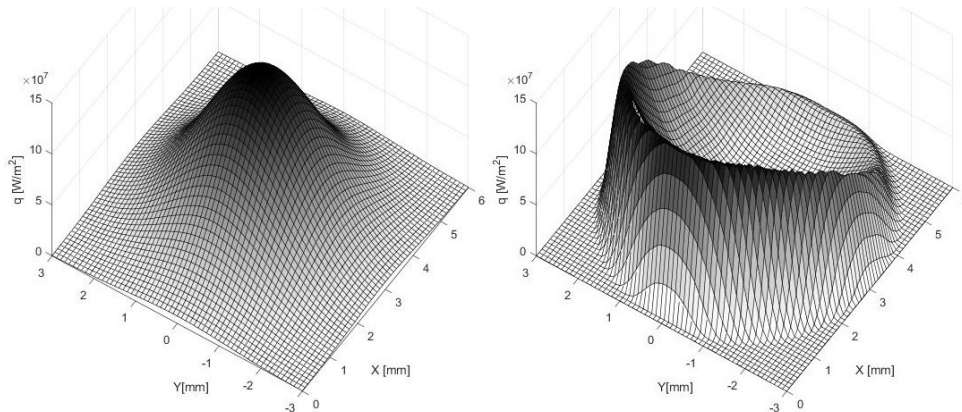


Fig. 11 Relationship between surface temperature and temperature necessary to bring forward evaporation pressure to generate the required ion densities.

The ionic current density generation is still treated as a black box and calibrated to match a semi-empirical value found for the vacuum arc. Also the presence of oxides is not considered. It should be also noted that the necessary for the ion density is much higher than the pressure generated by evaporation at that temperature (Figure 11). However, even though it seems unphysical, the cause might be found in the micro-dynamics of the CS.

Another weakness lies in the model for cathode spot distribution, as the heat transfer statement is very simplified. It assumes only an analytical expression of thermal point explosions in an isothermal, semi-infinite half space with a fixed heat flux and an additional

losses, at each cathode spot location. However, this flaw is not critical and can be overcome, even if it would slow down the calculation by a considerable amount. However, as a first approach the feasibility and structure of such model could be shown.



**Fig. 12** Comparison between Gaussian distribution with  $P = 1.358$  kW, and new resulting heat flux distribution, for time 5 ms as a smoothed, interpolated 3D- surface.

Another uncertainty lies in the Gauss-function, which is multiplied with the heat flux to give the local probability of the CS in Eqn. (17). As the arc pressure suppresses the liquid, and as the droplet-transfer process also has an influence on the shape of the surface, there could be effects by the electric field that have not been taken into account. In addition, the influence of the arc plasma has been neglected as well. However, it is assumed that the displayed tendencies of the distribution might be modified but not suppressed. It can be followed from the new distribution that, since the electric field within the arc column is mostly axisymmetric and concentrated at the center in the metal vapor core, a strong change of direction of the field lines must occur at the cathode, causing great deviations of Lorentz-force, which will have a strong influence on the weld pool hydrodynamics.

The hypothesis, that the cathode area in GMA welding should be treated as highly dependent on evaporation has been thoroughly studied and a novel model for the distribution of heat flux and current density has been suggested. Although there are still some open questions, the suggested model represents a continued development of the assumption of an axisymmetric Gaussian distribution and the results have been successfully used in a fast, near real-time calculation of the weld seam, in a strongly reduced form.

### ACKNOWLEDGEMENT

This work was carried out with the financial support of the Collaborative Research Centre SFB1120 (DFG (Deutsche Forschungs-gemeinschaft), Sonderforschungsbereich) "Precision Melt Engineering" at RWTH Aachen University and the K-Projekt of Excellence for Metal JOINing. The K-Project Network of Excellence for Metal JOINing is fostered in the frame of COMET - Competence Centers for Excellent Technologies by BMWFW, BMVIT, FFG, Land Oberösterreich, Land Steiermark, Land Tirol and SFG. The



programme COMET is handled by FFG. For the sponsorship and the support, we wish to express our sincere gratitude.

### REFERENCES

- [1] D. RADAJ: *Schweissprozesssimulation – Grundlagen und Anwendung*, DVS-VERL., DÜSSELDORF, 1999.
- [2] M.H. CHO ET AL.: *Simulation of Weld Pool Dynamics in the Stationary Pulsed Gas Metal Arc Welding Process and Final Weld Shape*. *Welding Journal supplement*. 12:271s-283s, 2006.
- [3] M.H. CHO ET AL.: *Simulations of weld pool dynamics in V-groove GTA AND GMA WELDING*. *WELD WORLD*. 57:223-233, 2013.
- [4] N. RYKALIN: *Berechnung der Wärmevergänge beim Schweißen*. VEB Verlag Technik, Berlin, 1957.
- [5] B. JÜTTNER: *Cathode spots of electric arcs*. *Journal of Physics D: Applied Physics*, 34:R103-R123, 2001.
- [6] E. HANTZSCHE ET AL.: *On the random walk of arc cathode spots in vacuum*. *Journal of Physics D: Applied Physics*, 16:L173-L179, 1983.
- [7] T. YUJI ET AL.: *Observation of the Behavior of Cathode Spots in AC Tungsten Inert Gas Welding on Aluminum Plate*. *Quarterly Journal of the Japan Welding Society*, Vol. 33, No. 2: 135s-138s, 2015.
- [8] M. S. BENOLOV AND A. MAROTTA: *A model of the cathode region of atmospheric pressure arcs*. *Journal of Physics D: Applied Physics*, 28:1869-1882, 1995.
- [9] L. PEKKER: *A Sheath Collision Model with Thermionic Electron Emission and the Schottky Correction Factor for Work Function of Wall Material*, *Plasma Chemistry and Plasma Processing*, 37:825-840, 2017.
- [10] F. CAYLA ET AL.: *Arc/Cathode Interaction Model*, *IEEE Transactions on Plasma Science*, 36:1944-1954, 2008.
- [11] G. A. MESYATS AND I. V. UIMANOV: *2D semiempirical model of the formation of an elementary crater on the cathode of a vacuum arc*, 27th International Symposium on Discharges and Electrical Insulation in Vacuum (ISDEIV), Suzhou, 1:1-4, 2016.
- [12] A. B. MURPHY: *The effects of metal vapour in arc welding*, *Journal of Physics D: Applied Physics*, 43:424001 32pp, 2010.
- [13] M. S. BENOLOV ET AL.: *Vaporization of a solid surface in an ambient gas*, *Journal of Physics D: Applied Physics*, 34:1993-1999, 2001.
- [14] M. S. BENOLOV: *Understanding and modelling plasma–electrode interaction in high-pressure arc discharges: a review*, *Journal of Physics D: Applied Physics*, 41:144001 31pp, 2008.
- [15] B. WILTHAN ET AL.: *Thermal Diffusivity and Thermal Conductivity of Five Different Steel Alloys in the Solid and Liquid Phases*, *International Journal of Thermophysics*, 36:2259–2272, 2015.
- [16] A. FRIDMAN: *Plasma Chemistry*, Cambridge University Press, Cambridge 2008.

POTENTIALS OF THE ALE-METHOD FOR  
MODELING PLASTICS WELDING  
PROCESSES, IN PARTICULAR FOR THE  
QUASI-SIMULTANEOUS LASER  
TRANSMISSION WELDING

A. SCHMAILZL\*, S. HÜNTELMANN\*, T. LOOSE\*\*,  
J. KÄSBAUER\*, F. MAIWALD\* and S. HIERL\*

*\*Ostbayerische Technische Hochschule Regensburg, Galgenbergstraße 30, D-93053 Regensburg, Germany*

*\*\*DYNAWELD GmbH & Co.KG, Herdweg 13, D-75045 Wössingen,, Germany*

DOI 10.3217/978-3-85125-615-4-51

ABSTRACT

The Arbitrary-Lagrangian-Eulerian-Method (ALE-Method) offers the possibility to model the quasi-simultaneous laser transmission welding of plastics, in which a squeeze-flow of molten plastic occurs. It is of great interest to get a deeper understanding of the fluid-structure-interactions in the welding zone, since the occurring squeeze-flow transports heated material out of the joining zone, causing a temperature decrease inside. In addition, the numerical modelling offers the possibility to investigate the flow conditions in the joining zone. The aim of this article is to show the potentials of the ALE-Method to simulate the quasi-simultaneous laser transmission welding with the commercially available software LS-DYNA. The central challenge is to realize a bi-directional thermo-mechanically coupled simulation, which considers the comparatively high thermal expansion and calculates the interactions of solid and melted plastic correctly. Finally, the potentials of the ALE element formulations for the mathematical description of welding processes are shown, especially for those with a squeeze-flow.

Keywords: Arbitrary-Lagrangian-Eulerian, squeeze-flow, plastics welding, laser transmission welding, friction welding, stud welding

INTRODUCTION

Laser transmission welding is an established joining technique for thermoplastics and used in many industrial sectors, such as automotive or electronics industry. The two joining partners are clamped in an overlap and irradiated along the weld trajectory with a high feed rate ( $v > 0.5$  m/s) for several scan repetitions (see Fig. 1 top left).

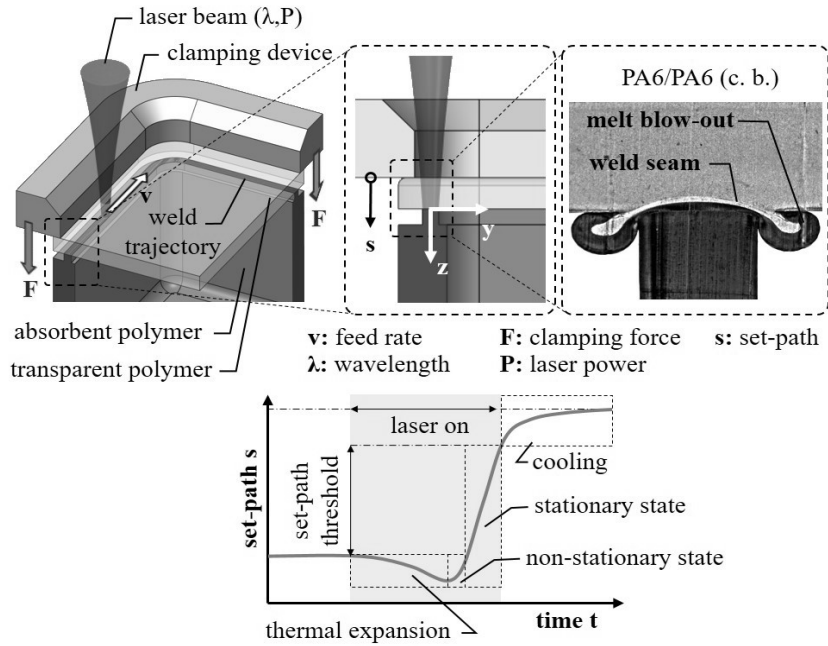


**Fig. 1** Principle of quasi-simultaneous laser transmission welding: a typical geometry with a clamping device (top left), a thin-cut of a typical weld (top right) as well as a sketch of the measured set-path with the process states (bottom).

The laser radiation is mainly transmitted through the upper and absorbed by the below placed joining partner close to the interface, since this one is filled with carbon black (c.b.). As far as the joining partners are in contact, heat is transferred via heat conduction, which also causes the melting of the upper joining partner. Typically, the movement of the clamping device is measured during welding and named as set-path ( $s$ ). Immediately in the beginning, thermal expansion occurs, which leads to negative data of the set-path (see Fig. 1, bottom). By performing further scan repetitions, the material is more and more softened, which leads to a squeeze-flow of the material, as soon as the stiffness of the material falls below a critical softening level. Later on, a continuous squeeze-flow is seen, and the set-path shows a linear course (see Fig. 1, bottom). The laser is switched off, until a predefined set-path threshold is reached, leading to cooling of the weld, which is seen in a digressive progression of the set-path. A typical joining zone of a PA6/PA6-weld with the weld seam and the melt blow-out is seen in a thin-cut in Fig. 1 (top right).

It is expected that the joint strength depends on the squeeze-flow conditions in the interface, as also seen in hot plate welding [1]. By measuring the velocity of the squeeze-flow, using tracer particles and x-ray radiation, it is found out by FARGAS RIBAS [2], that high joint strengths are achieved, if the squeeze-flow velocity in the centre of the weld is nearly equal to the one nearby the melt blow-out. Since the herein shown measurement does not allow the investigation of the interaction between temperature field and squeeze-flow velocity, it is of great interest to build up a thermo-mechanically coupled process model, in order to get a deeper process knowledge.

The squeeze-flow leads to large deformations in the simulation, whereby finite elements get highly distorted. For this reason, the entire process cannot be computed properly by

using a standard Lagrangian element formulation, as seen in previous studies [3]. This issue can be bypassed by employing an element formulation that bases on the Arbitrary-Lagrangian-Eulerian-Method (ALE).

By using ALE, each time-step is divided in a Lagrangian step and an advection cycle. In each Lagrangian step the mesh follows the deformation of the material. In the advection cycle, the mesh is transferred to a spatially fixed mesh by using an Eulerian technique. In the upcoming Lagrangian step the deformation of the material is calculated using a better mesh compared to simulations without a remapped mesh. By this, high element distortions, which are leading to a cancellation of the computation, can be avoided [4].

In this paper the element formulations Multi-Material-ALE (MMALE) and Single-Material-ALE with Void (SMALE-WV) are used to model the quasi-simultaneous laser transmission welding process. As an outlook, the potentials of the ALE-Method for modelling other welding processes are discussed.

### PROCESS MODELLING USING MULTI-MATERIAL-ALE

In the following, two process models with Multi-Material-ALE formulation (MMALE) are described exemplarily for a typical quasi-simultaneous welding and compared with each other, in order to demonstrate the capabilities of the process models.

#### PROCESS MODEL WITH SOLID AND FLUID PARTS

In general, the MMALE allows the usage of multiple solid and fluid material models in one coherent ALE mesh. By this, the interaction of solid and fluid parts can be simulated, correctly. Thus, it offers the possibility to model the quasi-simultaneous laser transmission welding at a certain time, at which a specific proportion of solid and a fluid material phase is already given. The flow conditions as well as the shape of the resulting melt blow-out can be investigated.

In order to divide the joining partner in fluid and solid parts, a thermal simulation is performed beforehand, using ANSYS. The shape of the fluid material-phase is marked by the computed isotherm of the melting temperature, which can be extracted at a specific time. Due to the high feed rate, 2D Finite-Elements are used, since the temperature does not vary significantly in feed direction, as seen in previous studies [3]. The absorbed radiation, which is equal to a volumetric heat, is implemented in the analysis using Eqn. (1):

$$Q(y,z,t) = \frac{\beta \cdot \alpha \cdot P}{\pi \cdot d^2} \cdot \exp \left( -\alpha \cdot z - \beta \cdot \frac{(x_0 - v \cdot t)^2 + y^2}{d^2} \right) \quad (1)$$

In this formula  $Q$  is the local heat generation rate ( $\text{W}/\text{mm}^3$ ),  $P$  the total power of the laser (W),  $\alpha$  the absorption coefficient of the material ( $1/\text{mm}$ ),  $d$  the laser beam diameter (mm),  $x_0$  the starting position of the laser (mm) and  $v$  the feed rate (mm/s).

One scan repetition of the laser is modelled in two steps. In the first step, the temperature field is calculated by considering the volumetric heat. In the second step only the heat transfer by heat conduction is calculated. This procedure is repeated alternately, until a

simulation-time of 2.3 s is reached. At this time, it is known from the set-path course of the welding, that the stationary process state is reached. That is why this simulation time is chosen. The resulting temperature field is then used to model the shape of the solid and the fluid phase, since the melting temperature correlates with the change of solid to fluid behaviour (see Fig. 2). Thus, the below placed joining partner as well as the upper joining partner are separated into different parts. For each joining partner a solid and a fluid part is modelled, according to the precomputed temperature field (see Fig. 2).

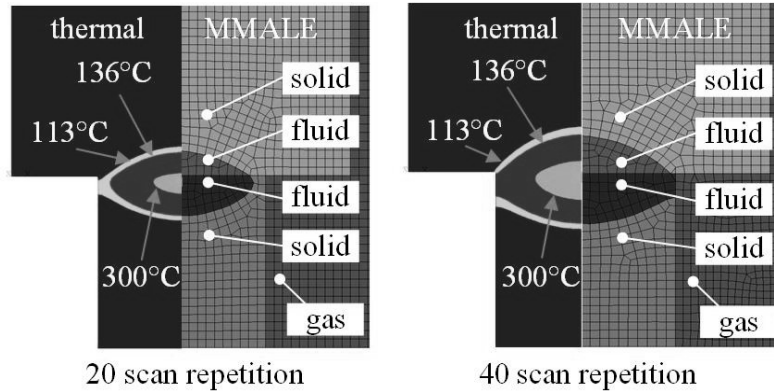


**Fig. 2** Precomputed temperature field using ANSYS and the MMALE-Model with fluid and solid parts at two different scan repetitions (left and right).

The ambient air in the surrounding is modelled as a gas using \*MAT\_NULL. Since contact definitions between parts are not supported using the MMALE formulation in LS-DYNA [5], the only way to connect the parts is to merge the coincident nodes of all parts. A rigid body is used to implement the clamping force on the top side of the upper joining partner. The viscosity of each fluid part is extracted from literature. The solid parts are modelled using a simple elastic material model.

Fig. 3 shows the local velocity of the melt flow in the horizontal direction. The melt flow is more and more squeezed out with increasing simulation-time (see Fig. 3, bottom). The computation of an equilibrium-state, at which the deformation does not further increase would be ideal, but cannot be realized since an explicit solver has to be used. Hence, the simulation-time does not correspond with the physical time. By comparing the shape of the squeeze-flow with a thin-cut of the welding, a good match is seen.

In the beginning, mainly material of the below placed joining partner is squeezed out (Fig. 3, bottom left). Later on, melt of the upper joining partner is also squeezed out (Fig. 3, bottom right). In general, the fluid fraction of the below placed joining partner nearby the melt blow-out is significantly bigger compared to the one in the upper joining partner. By this, the squeezed out volume per time is much bigger in the below placed joining partner compared to the upper one. This seems to be realistic, since in quasi-simultaneous laser transmission welding the highest velocity is very close to the interface of the joining zone, since there are high temperatures. The squeeze-flow of the upper and the below placed joining partner are sticking together, once they get into touch, which is caused by adhesion forces. By this, the melt flow of the below placed joining partner is flowing around the one of the upper joining partner. This effect is also seen in the simulation results, even though

the fluid parts are assigned with one single viscosity, which is not temperature-dependent (see Fig. 3, right).

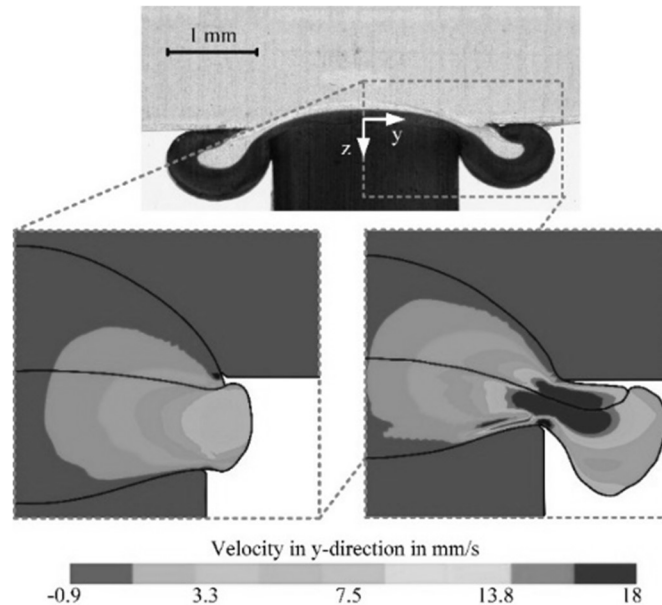


**Fig. 3** Thin-cut of a weld (top) and the velocity in y-direction in early (bottom left) and later stage of analysis (bottom right), both computed in an Multi-Material-ALE simulation.

By using a MMALE simulation with predefined fluid and solid parts, the resulting shape of the melt blow out can be analysed in dependence of the used process parameters. However, a distinct disadvantage is that the material properties are approximated roughly by defining parts as either solid or fluid. Additionally, there is no coupling from the mechanical to the thermal analysis and the simulation-time only reproduces a fraction of the whole welding process.

### PROCESS MODEL WITH TIME-DEPENDENT TEMPERATURE DISTRIBUTION

In order to compute the entire welding process more accurately, the time-dependent temperature distribution must be considered. By this, the time-dependent temperature field has to be implemented as a boundary condition using time-dependent temperature data. Here, the joining partners are modelled as two parts, which are described with a thermo-elastic material model. The geometry of the fluid and the solid material-phase is not user-defined, but derived by the model itself, using the already mentioned precomputed temperature field as a boundary condition.

Compared to the before mentioned MMALE-model with predefined solid and fluid parts, it can be observed, that a smooth transition between solid and fluid material-phase is realized, which is a better approximation of the real conditions during welding.

Since in Multi-Material-ALE a Finite-Element can contain material of multiple parts, the predefined temperature is allocated to the material of both joining partners. The implementation of a thermal analysis in the MMALE-model would require, that every node has to store several temperatures for the different parts. Currently, LS-DYNA only allows the calculation of one temperature per node, by which a bi-directional thermo-mechanically coupled simulation cannot be realized<sup>3</sup>.

### PROCESS MODELLING USING SINGLE-MATERIAL-ALE WITH VOID

The Single-Material-ALE with void (SMALE-WV) is a special type of the Multi-Material ALE-Method, which only allows the use of one material model for ALE parts. Like in an ordinary Multi-Material formulation, Finite-Elements can be partially filled. The empty space within elements is defined as void, which does not interact with the material. Thereby, one Finite-Element can contain material and void. To obtain a proper thermal and mechanical behaviour of the joining partners in solid and fluid phase, a nonlinear thermal and a temperature dependent nonlinear mechanical material model are chosen.

### COMPUTATION AND IMPLEMENTATION OF THE HEAT GENERATION RATE

For the mechanical simulation using ALE, only an explicit solver can be used, whereas for the thermal simulation an implicit solver is used. Thus, the applicable time steps between thermal and mechanical analysis differ significantly. The movement of the laser in quasi-simultaneous welding produces a time-dependent heat generation. Caused by the high feed rate of the laser beam, small time steps have to be used when implementing a time-dependent load.

To achieve a correct heat generation rate, which is independent from the thermal time step, an energy equivalent volumetric heat generation rate is computed by integrating Eqn. (1) over time, and refer it to a time  $t_p$ , in which the laser beam is guided once along the trajectory, coming to Eqn. (2).

$$Q_{eqv}(y,z) = \frac{1}{t_p} \int_0^{t_p} Q(y,z,t) dt \quad (2)$$

Using an equivalent volumetric heat generation rate in the simulation means that the entire weld trajectory is heated continuously and simultaneously. Since Eqn. (1) can be divided in a time-dependent and a time-independent term (see Eqn. (3))

$$Q(y,z,t) = \underbrace{\frac{8 \cdot \alpha \cdot P}{\pi \cdot d^2} \cdot \exp\left(-\alpha \cdot z - 8 \cdot \frac{y^2}{d^2}\right)}_{\text{time-independent}} \cdot \underbrace{\exp\left(-8 \cdot \frac{(x_0 - v \cdot t)^2}{d^2}\right)}_{\text{time-dependent}} \quad (3)$$

, Eqn. (2) can be simplified, leading to Eqn. (4)

---

<sup>3</sup> According to a statement of LSTC Inc.

## Mathematical Modelling of Weld Phenomena 12

$$Q_{eqv}(y,z,t) = \underbrace{\frac{\beta \cdot \alpha \cdot P}{\pi \cdot d^2} \cdot \exp\left(-\alpha \cdot z - \beta \cdot \frac{y^2}{d^2}\right)}_{\text{time-independent}} \cdot \underbrace{\frac{1}{t_p} \int_0^{t_p} \exp\left(-\beta \cdot \frac{(x_0 - v \cdot t)^2}{d^2}\right) dt}_{\text{time-dependent}} \quad (4)$$

, which is a combination of Eqn. (2) and Eqn. (3). The time-dependent term is named as equivalency factor  $\gamma$  and can be solved separately by computing Eqn. (5).

$$\gamma = \frac{1}{t_p} \cdot \int_0^{t_p} \exp\left(-\beta \cdot \frac{(x_0 - v \cdot t)^2}{d^2}\right) dt \quad (5)$$

Since no analytic antiderivative for this term exists, it has to be solved by numerically or symbolically methods.

### VERIFICATION OF THE THERMO-MECHANICAL COUPLING

Because the laser beam is larger than the width of the absorbent joining partner, the melt flow which leaves the joining zone is also heated during welding. By using SMALE-WV, the thermal energy is transported with the squeeze-flow, whereby the heating is taken into account. To check this, a T-joint geometry with an initial temperature of 150 °C in a square formed section is predefined (see Fig. 4, left).

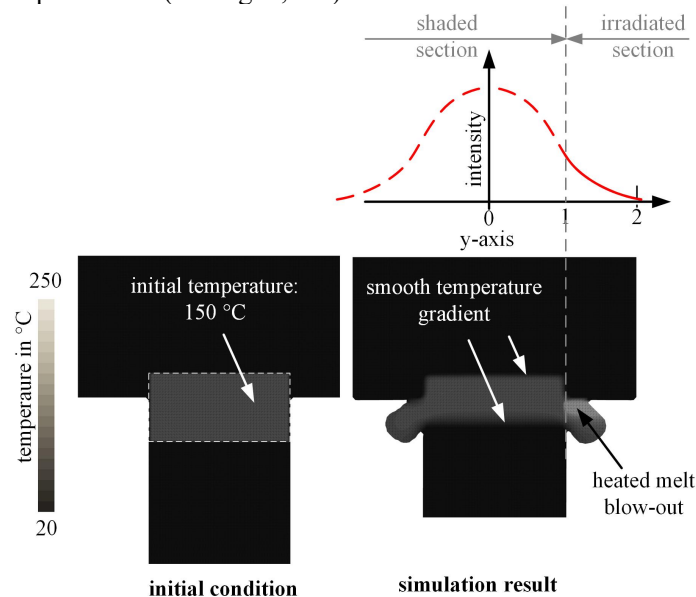


**Fig. 4** Temperature field of a T-joint geometry with an initial temperature of 150 °C in a square formed section and 20 °C in the surrounding (left) as well as the resulting temperature field after the melt is squeezed out of the joining zone and heated on the right-sided melt blow-out (right).

The thermo-mechanically coupled simulation is solved, whereby a typical clamping force and a heat generation only on the right-sided melt blow-out is applied (see Fig. 4,



right). In reality this would mean, that the rest of the joining zone is shaded, as can be seen on the solid and dashed line of the intensity distribution (see Fig. 4, top right).

The melt flow is squeezed out of the joining zone and again heated outside of the initial geometry (see Fig. 4, right). Also the steep gradient on the boundary of the initially assigned temperature is smoothed due to heat conduction (see Fig. 4, right). In conclusion it can be stated, that a bi-directional coupling is realized.

COMPARISON BETWEEN COMPUTED AND MEASURED DATA

In order to verify the process model, the measured set-path progression is used for a comparison with the computed deformation. Fig. 5 shows the measured set-path ( $s$ ) for a welding with typical process parameter settings in comparison to the computed deformation. The characteristic course in the three process states (non-stationary, stationary and cooling) are also reproduced in the simulation. At first, the set-path is reaching a negative value, caused by the thermal expansion. With increasing irradiation time the material nearby the joining zone is more and more softened until it is squeezed out, which corresponds with a positive progression of the set-path. The typical linear trend of the set-path is represented as well as the decreasing course in the cooling state, in which the laser is switched off.

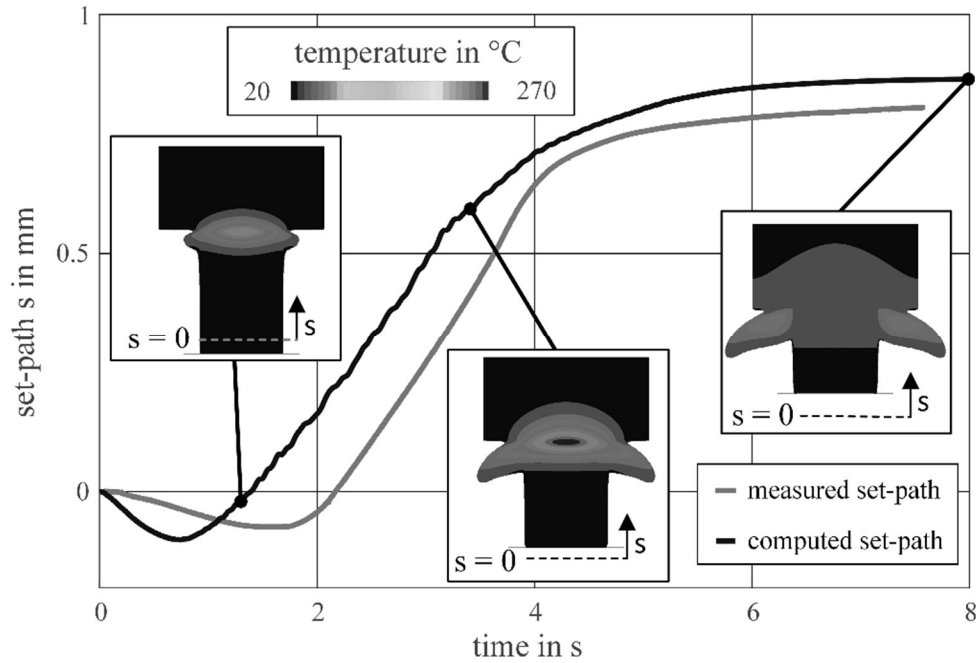


**Fig. 5** Comparison of the measured set-path during quasi-simultaneous laser transmission welding with the computed deformation using Single-Material-ALE with Void.

Since the coincident nodes of both parts have to be merged, no separation between the joining partners is allowed. However, previous studies (see Ref. [6]) show, that gaps between the joining partners arise. This is caused by a higher thermal expansion in the centre of the welding, compared to the boundary. Since no separation between the joining partners is allowed by using SMALE-WV, tensile stresses appear in the contact zone and prevent the gap from opening. As a consequence, more heat will be transferred from the below placed joining partner to the upper joining partner using SMALE-WV compared to the real welding, caused by the larger contact area. This effect might be negligible, if the intensity distribution in the joining zone is quite homogenous, whereby almost no significant gap area exists.

It is seen in thin-cuts (see Fig. 3), that the squeeze-flow is concentrated very close to the joining interface, which is not reproduced in SMALE-WV as realistic as in Multi-Material-ALE, as seen by comparing the shape of the melt blow-out in Fig. 3 and Fig. 5. This is also mainly caused by merging coincident nodes.

Nevertheless, all process states are reproduced properly using SMALE-WV, since a bi-directional coupling can be realized in contrast to MMALE. This makes the SMALE-WV to a promising tool for investigations concerning temperature field, flow condition and residual stresses.

### POTENTIALS OF THE ALE-METHOD TO MODEL WELDING PROCESSES

In some welding processes for metals (e.g aluminium or steel) the same deformation is seen like in quasi-simultaneous laser transmission welding of thermoplastics. For instance, stud welding, friction welding or flash welding are welding processes where also material is heated and squeezed out during welding. If the commonly used Finite-Element-Method with standard Lagrangian element formulation is applied to model these processes, the deformation of the mesh is inherently limited by the simulation technique itself, as it is demonstrated for friction welding in Ref. [7]. As a result, the shape of the welding bulge does not fit to the real shape very well, as reported by PETROPOULOS et. al [8]. Especially for stud welding the subsidence of the bolt in the molten pool of the component is of interest (see Ref. [9, 10]), but actually not modelled in a sufficient accuracy by using the Finite-Element-Method.

Using the Arbitrary-Lagrangian-Eulerian element formulation, which is commercially still available, one can overcome the limitations caused by high distortion of the mesh, which makes it to a promising tool for modelling welding processes in which a squeeze-flow of molten material occurs.

### SUMMARY

Modelling the squeeze-flow of molten material in quasi-simultaneous laser transmission welding is crucial, in order to realize a process model with a high accuracy. However, the Finite-Element-Method with standard Lagrangian element formulation restricts the process modelling, since the mesh is highly distorted as far as a squeeze-flow occurs, which leads to a cancellation of the simulation. By using the Arbitrary-Lagrangian-Eulerian element

formulation, these limitations are no longer given. In this paper the so called Multi-Material-ALE (MMALE) and the Single-Material-ALE with void (SMALE-WV) are used to model the quasi-simultaneous laser transmission welding. It is found that by using both techniques, the squeeze-flow can be analysed. The MMALE is restricted to a uni-directional thermo-mechanically coupling, whereas the SMALE-WV allows the realization of a bi-directional coupling. This means, that the initial temperature of the melt is transported by the squeeze-flow and can be reduced by heat conduction or increased again by an absorbed laser radiation. A verification study has shown, that the typical process states, indicated by the course of the set-path, are also seen in the computed deformation.

In an upcoming step the simulation has to be validated on several process parameter settings, in order to evaluate a suitable material model and parameterize it precisely. The aim is to compute the temperature field, the deformation as well as the residual stresses and link it to the joint strength, in order to identify the best process parameter setting. Since in many welding processes a squeeze-flow of molten material is also seen, the ALE-Method is found to be a promising technique to model such welding processes.

### ACKNOWLEDGEMENT

The authors want to thank the European Union for funding the research project “THECOS-Thermoplastic Composite Structures” in the program INTERREG V-A.

### REFERENCES

- [1] H. POTENTE: *Fügen von Kunststoffen: Grundlagen, Verfahren, Anwendung*, München, Hanser, 2004.
- [2] M. FARGAS RIBAS: *Erweiterung des Prozessverständnisses für das Laserdurchstrahlschweißen von Thermoplasten durch Analyse der Schmelzbaddynamik*, Dissertation, Hannover, 2012.
- [3] A. SCHMAILZL and S. HIERL: ‘Rechenzeitoptimierte Temperaturfeldberechnung beim quasisimultanen Laser-Durchstrahlschweißen’, *ANSYS Conference & 33th CADFEM Users' Meeting – ACUM*, pp. 1-15, Grafing, Darmstadt, 2015.
- [4] M. SOULI and D. J. BENSON: *Arbitrary Lagrangian-Eulerian and Fluid-Structure Interaction. Numerical Simulation*, London, Wiley, 2010.
- [5] LIVERMORE SOFTWARE TECHNOLOGY CORPORATION: *LS-DYNA® KEYWORD USER'S MANUAL*, Livermore Software Technology Corporation, Livermore, California, 2016.
- [6] A. SCHMAILZL, B. GEIBLER, F. MAIWALD, T. LAUMER, M. SCHMIDT and S. HIERL, ‘Transformation of Weld Seam Geometry in Laser Transmission Welding by Using an Additional Integrated Thulium Fiber Laser’, *Lasers in Manufacturing*, disk, pp. 1-10, Munich, 2017.
- [7] D. SCHMICKER: *A holistic approach on the simulation of rotary friction welding*, Dissertation, Magdeburg, 2015.
- [8] A. PETROPOULOS, M. MÜLLER, ‘Anwendung kommerzieller Schweißsimulationssoftware für das Rotationsreißschweißen’, *Simulationsforum Schweißen und Wärmebehandlung Weimar 2013*, Weimar, 2013, pp. 1131-1148.
- [9] H. SOLTANZADEH, J. HILDEBRAND, M. KRAUS and M. ASADI, ‘A reliable modelling of thermal, microstructure, and stress in arc stud welding joints and effect on fatigue strength’, *Ce/papers 2017*, Vol. 1, No. 2-3, pp. 453-460, 2017.

## Mathematical Modelling of Weld Phenomena 12

- [10] N. HYNES, P. NAGARAJ, R. PALANICHAMY, CAK ARUMUGHAM and J. SUJANA, 'Numerical Simulation of Heat Flow in Friction Stud Welding of Dissimilar Metals.', *Arabian Journal of Science and Engineering*, Vol. 39, No. 4, pp. 3217-24.



# **VIII Additive Manufacturing**



IMPROVEMENT OF NUMERICAL  
SIMULATION MODEL SETUP AND  
CALCULATION TIME IN ADDITIVE  
MANUFACTURING-LASER-METAL-  
DEPOSITION COMPONENTS WITH AN  
ADVANCED MODELLING STRATEGY

M. BIEGLER\*, P. KHAZAN\*\*, M. GATZEN\*\* and  
M. RETHMEIER\*‘\*\*\*

\* *Fraunhofer Institute of Production Systems and Design Technology (IPK), 10587 Berlin, Germany,  
email: max.biegler@ipk.fraunhofer.de*

\*\**Simufact engineering GmbH, 21079 Hamburg, Germany*

\*\*\* *Federal Institute of Materials Research and Testing (BAM), 12205 Berlin, Germany*

DOI 10.3217/978-3-85125-615-4-52

ABSTRACT

Rapid localized heating and cooling during additive manufacturing using laser deposition method (LMD) lead to loss of dimensional accuracy as well as cracking of built parts. Finite-Element welding simulations allow prediction of geometrical deviations and accumulated residual stresses as well as their optimization before conducting experiments. Due to the great length of stacked welds, calculation times for fully transient thermomechanical simulations are currently long, the calculation stability suffers from the high number of contact bodies in the model and the modelling effort is high, as the geometries need to be sliced and positioned layer-wise.

In this contribution, an integrated modelling approach is demonstrated for a thin-walled LMD component made from 30 layers of 1.4404 (316L) stainless steel: Instead of the layer-by-layer modelling strategy commonly found in the literature, the whole component mesh is kept in one piece and the fully transient, layer-by-layer material deposition is implemented via element sets. In contrast to prior simulations, nonlinear contact between the layers does not have to be considered, significantly decreasing calculation times. The calculated distortions are compared to recently published, in-situ digital image correlation (DIC) measurements as well as numerical simulations conducted with the established layer-wise modelling strategy to judge result quality. Finally, the improvement in calculation time and ease-of-use is compared between both modelling approaches and conclusions regarding future usage for industrial-scale components are drawn.

Keywords: Additive Manufacturing, Laser metal deposition, Calculation time, Distortion simulation, Directed energy deposition, Efficient modelling



### INTRODUCTION

Recently, additive manufacturing (AM) techniques have gained widespread attention in the industry. Laser Metal Deposition (LMD) is an AM technique that allows the build-up of 3-dimensional geometries by locally stacking wire- or powder-feedstock welds onto a substrate [1]. A broad range of materials can be processed, including titanium alloys and stainless steel [2] as well as nickel super alloys [3]. During the process, the pre-existing and already-deposited materials are repeatedly heated and cooled as multiple layers are stacked. The periodic reheating leads to complex effects such as inhomogeneous thermal strains, local re-melting, multiple phase transformations and annealing. When producing industrial-scale AM-LMD parts like excavator arms [4] or turbine housings [5], the build needs to be set up experimentally and iterated a number of times because of the interlocking nonlinear effects. For instance, welding parameters, path planning and pause times need to be optimized experimentally – with each build taking machine- and personnel-time – before a satisfactory result quality can be achieved.

Numerical simulations have the capacity to decrease the experimental effort for build-planning, parameter search and distortion reduction in AM-LMD by substituting experimental trials with virtual tests. To qualify numerical simulation tools for industrial practice, difficulties regarding long calculation times and the availability of reference measurements for validation of the model need to be overcome.

In a recent study by the authors [6] and studies from the literature for distortion prediction [5, 7, 8] and stress prediction [9, 10], fully transient FE analyses were compared to experimental results in LMD and good agreement between simulation and experiment was reported. With the predictive capabilities of numerical approaches regarding temperature flow, stress development and distortion-prediction being well-documented, further emphasis needs to be directed towards the reduction of the modelling effort and long calculation times. The high calculation times in AM originate from the comparatively long welding times and the need to resolve their transient evolution in order to predict the process. In addition, layer-wise, nonlinear contact needs to be calculated in each increment, leading to high computational cost especially for large models. Although the computational time is a key factor in the introduction of LMD simulation into industrial practice, they are rarely discussed in-detail in the literature:

Heigel et al. [11] and Denlinger et al. [7] use the CUBIC solver especially developed for additive manufacturing in their LMD simulation studies and find good agreement between the simulations and experiments. Utilizing a computational weld mechanics (CWM) approach they do not detail the calculation times or modelling efforts arising from stacking of single layer welds for their wall builds. Salonitis et al. [12] heated each layer simultaneously in their simulation of a LMD hollow cylinder. Presumably, this simplification is implemented to reduce the transient increments necessary for the simulation but the gains in process time were not evaluated in their publication. Marimuthu et al. [13] simulated the substrate distortion in an aero-engine component. They approximated the transient heat input by dividing the part into 954 subsections that were heated individually and instantaneously at the times corresponding to the process. The resulting transient temperature field was then used to conduct an uncoupled mechanical simulation. By neglecting the fully transient heat source movement, they were able to reduce calculation times by 80% to 7 h but the effect on result quality of the simplification

is not discussed. A similar approach was utilized by Papadakis et al. [5] for a cylindrical engine-case: The authors substituted the deposition path by introducing an equivalent heat quantity as thermal load on a whole layer and reduced the model by utilizing its symmetry. The geometry they investigated was too large to conduct fully transient simulations, so that the loss-of-accuracy of their simplification could not be addressed.

In powder bed additive manufacturing, where the length of weld paths is even longer than in LMD, a number of studies exist that focus on efficient modelling to reduce calculation time: Plotkowski et al. [14] described a semi-analytical approach to rapidly calculate the heat distribution in electron beam melting. Li et al. [15] used a multiscale model that predicted temperature flow on a micro-scale, mapped it to a layer hatch model in meso-scale for the body heat flux and finally calculated the macro-scale part distortions and residual stresses from the temperature flow. Afazov et al. [16] predicted the distortion of an industrial-scale selective laser melting (SLM) component by solving the heat input analytically and grouping it together for a set number of layers. The distortion due to the heat input for these layers is then calculated on the macro-scale part in a mechanical simulation. This approach is also used in commercial softwares like Simufact Additive.

Denlinger et al. [17] conducted a fully transient structural welding simulation to calculate base plate distortion for a SLM cube. In order to reduce the computation times, dynamic mesh coarsening was used to reduce the element count by roughly 98 % for the top layer. Irwin et al. [18] proposed longer heat sources to reduce the amount of increments needed to model additive manufacturing. They showed that the simplification of the heat input in SLM simulations does not significantly reduce the result quality because the speed of heat flow is in a similar order of magnitude as the laser scanning velocity.

In comparison to selective laser melting, where model simplifications in heat input and techniques to reduce calculation times are established in the literature, little published data exists for LMD. Due to the differences in scanning speed and the more localized heat input in LMD, formulations established for SLM cannot be readily transferred [19]. Hence, this work aims to increase the knowledge in LMD simulations by investigating ways to improve the calculation time while keeping the fully transient simulation approach. In contrast to the layer-by-layer approach commonly found in the literature [5, 6], the component is meshed in one piece and the layer-wise element activation is implemented via element handles. The calculated distortions are compared to in-situ validation experiments to ensure that the changed models do not introduce additional error.

## METHODS

### SIMULATION MODEL

The model for this investigation is comprised of a baseplate and a thin-walled AM-LMD geometry that represents a turbine blade. The baseplate has a dimension of 100x100x6 mm<sup>3</sup>. The blade is generated layer-wise with 1.4404 stainless steel powder (Fig. 1 (a)). According to a previous study reported in [6], each layer is considered to have a square shaped cross section of 1.2 mm width and 0.6 mm height (Fig. 1 (b)). Hence the deposit is considered as flat. The material properties (see also [6]) are temperature dependent, changes in

microstructure due to multiple heating cycles, however, are neglected. The density and Poisson's ratio are constant. The weld pool is modelled as a low-stiffness solid and the occurrence of weld pool dynamics is neglected.

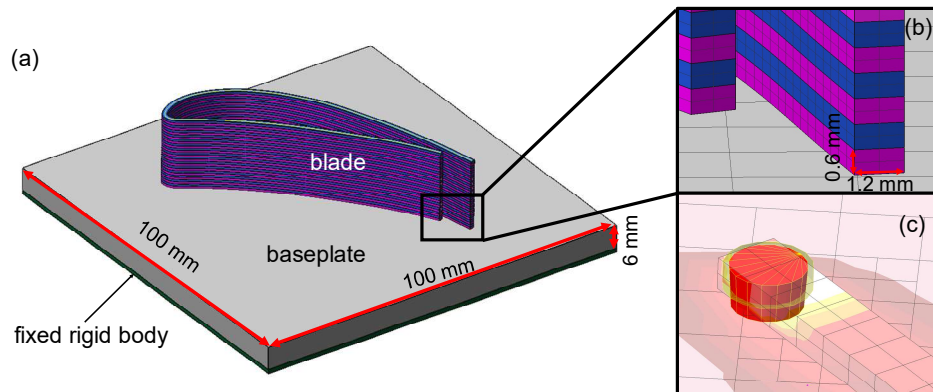


**Fig. 1:** Numerical model of the AM-LMD process. (a) Model geometry with baseplate (grey) and AM-LMD blade geometry made with 30 layers (blue/purple). A fixed rigid body (green) is glued to the lower surface of the baseplate to constrain movement. (b) The cross section of each layer has a simplified rectangular shape. The blade is modelled with individual bodies (and meshes) for each layer. (c) Heat input is modelled with a three-dimensional conically shaped volume heat source that moves transiently along the weld path (see also [6]).

The model was set up in the commercial FEA structural welding software Simufact Welding utilizing the direct FEA-solver sfMARC. The governing differential equations for the thermal and mechanical analysis are given in detail in [6]. A thermo-mechanically coupled transient simulation is considered using three-dimensional equivalent heat sources that move along a predefined path (Fig. 1 (c)). The so-called quiet-element method is used to model the molten powder addition by activating elements transiently on the basis of the moving source. With this approach the thermal and mechanical properties of the a-priori defined deposit geometry are drastically scaled down at the beginning of the simulation (quiet state) before getting “activated” by the propagating heat source via an element-birth formulation. The activation is done in two steps: a virtual activation box surrounding the heat source geometry activates the quiet elements and their nodes thermally once they get inside the box. Mechanical properties are then scaled up to full stiffness after the nodal temperature has reached melting temperature again after cooling down from a higher temperature.

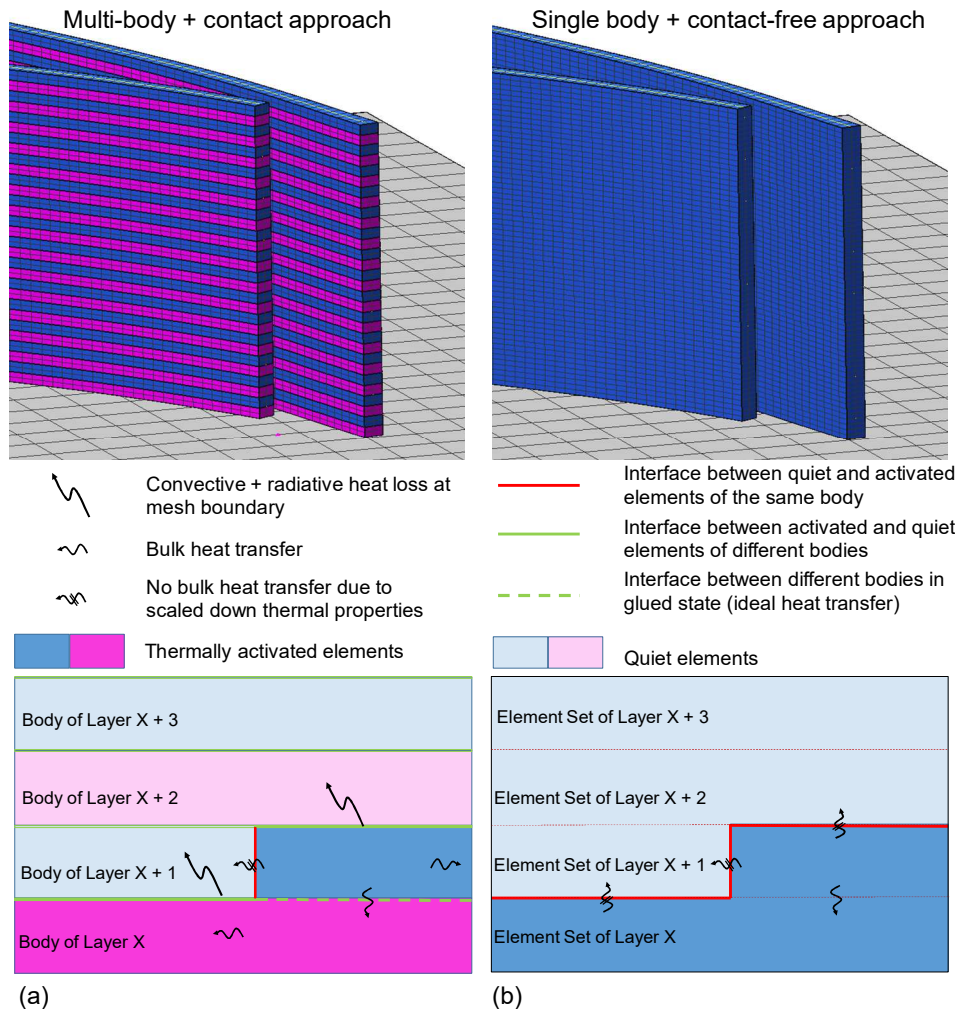


**Fig. 2:** Handling of thermal properties in multi-body and single body approach. (a) multi-body + contact approach: radiative and convective heat loss between activated and quiet elements is handled with boundary conditions. (b) single body + contact-free approach: No heat loss considered between the layers. Energy transfer between activated and quiet elements is neglected due to scaled down thermal conductivity and only takes place at outside surfaces.

For this study, two different ways of handling the deposited material and its mesh in a structural welding simulation of a LMD process has been investigated. A common and often successfully applied technique is to stack up separate deposit bodies each with individual meshes layer-by-layer (Fig 2 (a)). This way, the model consists of a high number of separate deformable bodies. This enables the possibility to attach surface boundary conditions and contact properties between each body and to safely control the activation of quiet elements for each individual weld seam body. Radiative and convective heat loss can be considered at interfaces between activated and quiet elements.

Handling each weld seam, as well as the components, as individual deformable bodies has generally been proven to be a good method to cover certain structural behaviors in

typical seam welding applications such as the opening of gaps. However, non-linear contact calculation is an additional computational step in the FEM solution procedure and it gets more demanding the more complex the contact situation is. This is generally true for every FEM solver. With a very high number of different contacts, the solution procedure takes longer and the calculation usually becomes slower. Due to the huge number of layers in real-life LMD applications together with the sheer length of the weld seam up to many meters, this approach is potentially not the most practical for industrial-scaled components.

Therefore, as a second approach, a single body and contact-less modelling approach has been tested in this study. Instead of using separate bodies for each layer, the entire LMD geometry is merged into one congruent mesh (Fig. 2 (b)). This aims for reducing the numerical effort of contact calculation leaving only the contact between baseplate and the first layer of the LMD geometry. Mechanical and thermal exchange between layers is, however, no longer controlled by surface boundary conditions but entirely handled via the quiet element method. This means, that radiative and convective heat loss at the top surface of each layer (except for the topmost one) is generally neglected. In addition, the layer-wise activation of quiet elements has to be handled by defining element sets to distinguish the different layers for both the heat input and the element-birth procedure.

For this investigation four different blade, made out of 10, 20, 30 and 40 layers are simulated with both methods (multi-body and single-body approach) to compare calculation times. In addition, the result accuracy in terms of distortion behavior is investigated by comparing the displacements of the 30-layer blades with experimental measurements. Simulation is performed on a 64GB Windows machine with 2 Intel Xeon® E5-2640 v3 (@ 2.66 GHz) CPUs. The calculations are done in parallel on 15 cores (without the use of Hyper threading) using sfMARC's domain decomposition method (DDM) and shared memory parallelisation (SMP). The calculation was split into 5 domains with 3 cores used in parallel for each domain.

### EXPERIMENTAL PROCEDURE

To evaluate the result quality of the developed modelling approaches, in-situ reference measurements were conducted using digital image correlation (DIC). A curved, thin-walled AM-LMD geometry was deposited from 1.4404 stainless steel powder onto a 100x100x6 mm<sup>3</sup> 1.4404 substrate plate with the same setup used in [6]. In brief, a coaxial powder nozzle welded single tracks onto one another with 400 W laser beam power, 0.6 mm spot diameter and 7.5 g/min of powder flow. The sample geometry was the curved outline of a turbine blade (Fig. 3 (b)-(c)). 20 tracks were welded on top of one another with 30s pause time between layers and a bi-directional strategy, resulting in a wall-thickness of 1.2 mm and a height of 12.4 mm. Then the process was stopped to apply the stochastic pattern required for DIC measurements. Subsequently, 10 additional layers were deposited, while measuring in-situ displacements with the commercial 3D DIC system GOM Aramis 4m. In the optical measurements, the bright process light was blocked with narrow bandpass optical filters, suppressing all wavelengths except 810 nm ± 22.5 nm. A defocused, monochromatic laser was used to illuminate the sample with 808 nm light so that the sample was sufficiently bright for the measurements [20]. The measurement setup is sketched around an in-situ frame in Fig 3 (a).

To validate the phenomenological heat source, temperature measurements were conducted with the same parameters used in the final experiments. Three thermocouples Type K were micro-welded on the substrate and a single track was welded next to them. After welding, the relative position of the thermocouples to the weld track was measured in a photograph and a cross section perpendicular to the weld was made.

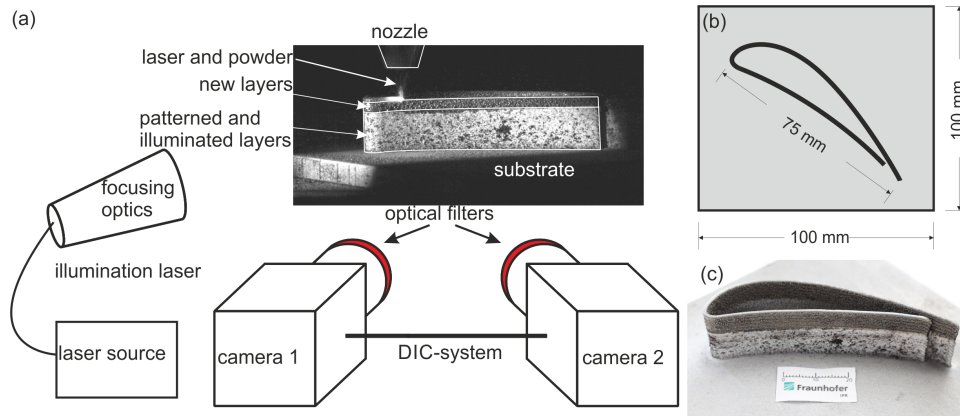


**Fig. 3:** Experimental setup, altered with permission from [6]. (a) In-situ image captured by the DIC-system is shown with the two cameras, optical filters and illumination laser sketched in their respective position. (b) Top-down view of the investigated, arbitrarily curved geometry. (c) Photograph taken after the process. The lower layers are patterned for the DIC measurements and the upper layers were added during the measurement.

## RESULTS AND DISCUSSION

### TEMPERATURE INPUT CALIBRATION

As the heat input and heat flow during manufacturing are the driving force behind distortions and residual stresses, it needs to be modelled to match the real heat input in the experiments as closely as possible. In CWM, the heat input is simplified with a phenomenological heat source and a calibration against experimental temperature measurements needs to be conducted.

The results for the thermal calibration are depicted in Fig. 4 (a), showing a very good agreement between the measured and simulated temperature development. Both the heat input – visible in the peaks – and the thermal conduction and thermal boundaries – visible in the cooling rates respectively – match well for an energy absorption efficiency of 60 % and a convective cooling of 35 W/m<sup>2</sup>K. In addition, the extent of the molten zone is compared between experimental cross section and the numerical results with good agreement in Fig. 4 (b). In Fig. 4 (c), the experimental melt pool taken from a DIC image and the simulated molten zone are compared. As effects from molten metal are neglected in CWM, the shapes do not match completely but the extent of the molten volumes match closely. With these results, the heat input is considered to match the experiments and will be used as an input in the mechanical model.

## Mathematical Modelling of Weld Phenomena 12

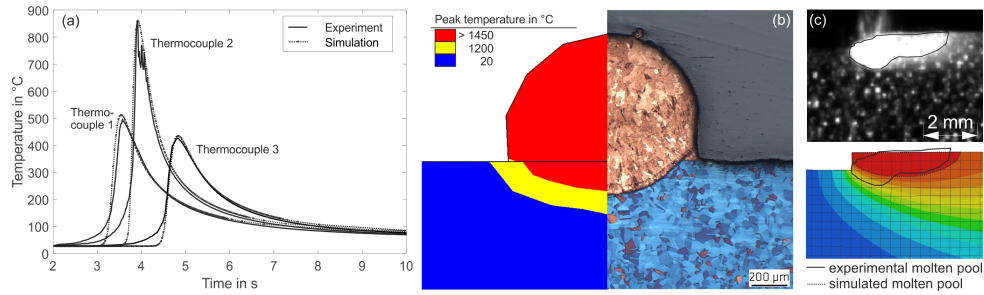


**Fig. 4:** Results of the heat input calibration, altered with permission from [6]. (a) The comparison between simulated and experimental temperature measurements shows good agreement. The simulated and experimental cross sections are compared in (b) with the molten area in the simulation image and the cross-section showing good agreement. In (c), the molten pool geometry from the DIC images is compared with the calculated molten zone.

### SIMULATION RESULTS

In Fig. 5, the simulated distortions in x-, y- and z-direction for a 30-layer blade are depicted after cooling down to room temperature for both modelling approaches. Both methods give almost similar distortion result, however, slight differences can be observed for the x-distortion, especially around the very top of the blade structure.

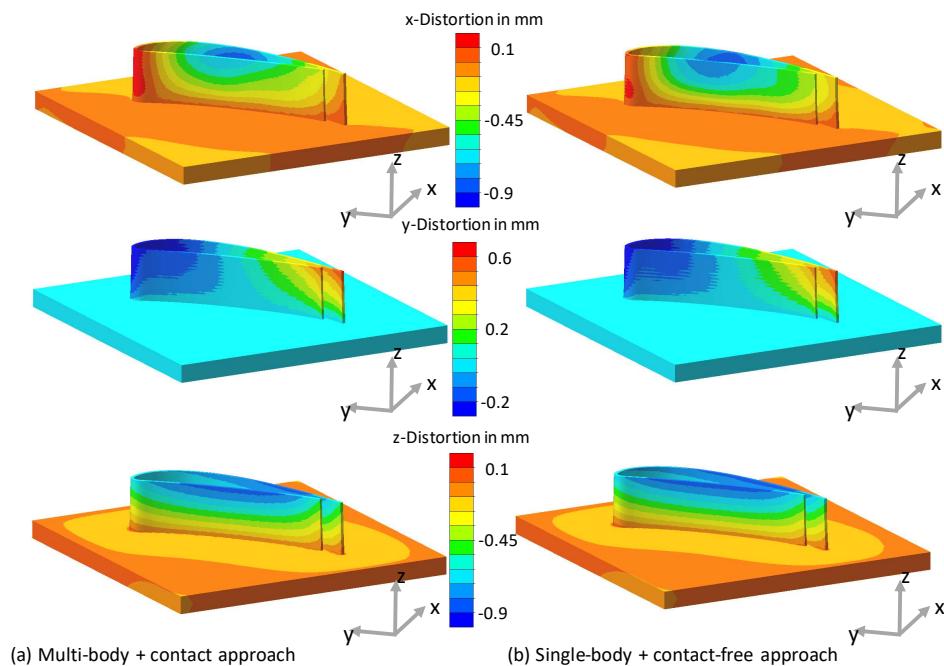


**Fig. 5:** Comparison of total displacement after simulation of a 30-layer blade for multi-body vs. single body approach.

In order to check the level of agreement more quantitatively and to evaluate the general accuracy of the simulation compared to experimental measurements, the out-of-plane distortion at six specific points is tracked over time and compared to the DIC measurements. The results are plotted in Fig. 6 for the out-of-plane distortions. The typical saw-tooth behaviour common in additive manufacturing can be observed in the experimental and simulated out-of-plane displacements. Only at P6, the transient movement is not as pronounced, presumably due to the relative proximity of the point to the rigid tip. In general, the simulation results are in good quantitative agreement with the DIC measurement and coincide closely with one-another. By trend, both simulation results tend to slightly underestimate the out-of-plane distortion at P1, P2, P3 and P6, while somewhat overestimating it in P4. The slight errors between simulation and experiments are likely due to the simplifications introduced in the simulation: Especially the orthotropic grain structure arising from multiple re-heating of the materials is not considered [6] and effects like stress relaxation and creep are neglected. More importantly for the argument presented in this work, there is little to no difference in the predicted distortions between both simulation approaches. Hence, the newly-developed contact-free approach does not introduce unforeseen errors.

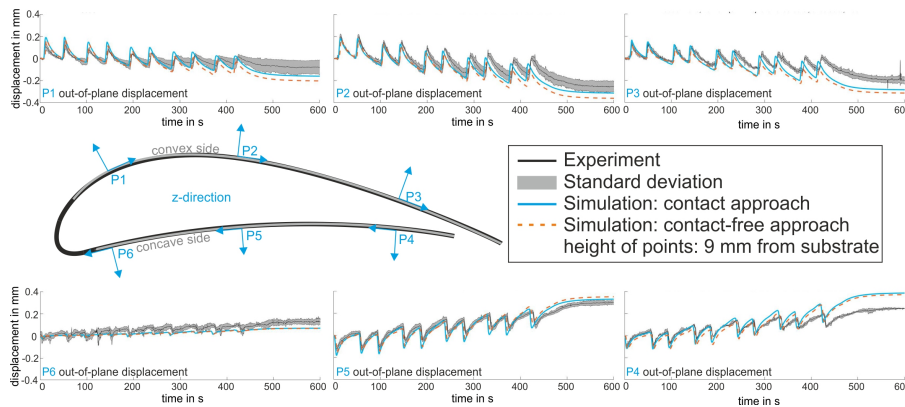


**Fig. 6:** Out-of-plane distortion vs. time at six distinct measure points at a height of 9 mm above the substrate for both simulation approaches and the DIC measurements (including standard deviation).

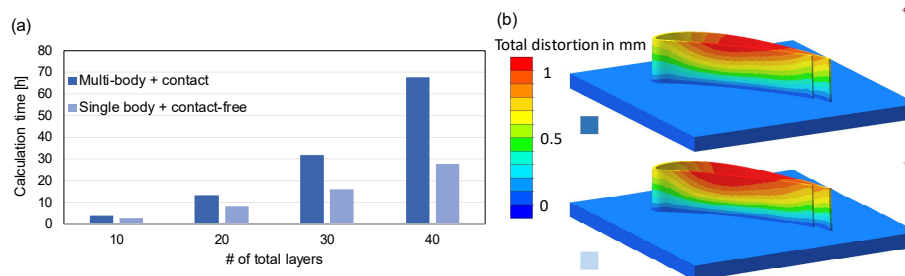


**Fig. 7:** (a) Comparison of calculation times (Wall time) on a 64 GB Intel Xeon® CPU E5-2640 v3 (@ 2.66 GHz) machine with the sfMARC solver. Multi-body vs. single body approach for 10, 20, 30 and 40 layers. (b) Comparison of total displacement after simulation of a 30-layer blade for multi-body vs. single body approach.



While the results of both simulation approaches are in good agreement with the experimental observation, the calculation times are very different. Fig. 7 gives an overview of the calculation times (Wall time) for blades with 10, 20, 30 and 40 layers of deposited material.

The comparison clearly depicts the advantages of a single-body, contact-free calculation approach to model the deposit. As expected the benefit increases with increasing total number of layers. Even for this relatively small model (compared a real industrial-scaled component) the calculation time for 30 layers is less than half of the multi-body simulation. Hence, the hypothesis that the contact-calculation is responsible for a large portion of the calculation time in the multi-body simulation approach is validated. Upon removal of the contacts, the calculation times improve significantly and the neglect of convective and emissive cooling at the top interface has little influence on the result quality for the investigated thin-walled part.

Especially with thick-walled LMD parts, the correct modelling of the cooling needs to be assessed in future works: For the thin-walled component, the side surfaces are far larger than the top surfaces and the heat loss is largely realized through them. In a thick-walled part, on the other hand, the top surface is larger and has an increased influence on the cooling; as this surface is part of the single-component in the contact-free approach, the heat loss to the surroundings might be underestimated for intermediate layers.

Although the calculation times were significantly improved with the new approach, they are still a major issue for large parts: In Fig. 7a, doubling the model size from 10 to 20 layers (1.5 m weld length to 3 m weld length) increases the calculation time by 300 % from 2.7 h to 8.3 h for the contact-less model. Adding another 10 layers, totalling in 4.5 m weld length, increases the calculation time by another 200 %. This hints at an almost exponential growth that might be problematic for investigating real-life parts with hundreds of layers. But with the in-situ distortion measurement results presented in [6] and in this work, future model improvements and simplifications can be easily tested for their validity.

Finally, the ease of modelling between both strategies can be compared. In the multi-body contact approach, each layer geometry and weld path need to be defined and positioned individually and manually in the FE software. This approach requires expert users and is prone to mistakes. In the contact-less approach, the whole part is meshed at once with mesh densities corresponding to the experimental layer thickness and imported into the FE pre-processor. The manual positioning of individual layers is no longer required but the weld paths and element sets still need to be defined by hand. In the long run, especially for industrial-scale parts, the model generation needs to be automated further. The ease-of-use can be improved especially by coupling the FE software with computer-aided manufacturing (CAM) tools for path planning and meshing tools to define the element sets.

## CONCLUSION

A novel modelling strategy for additive manufacturing laser-metal-deposition was presented to reduce the calculation times arising from long weld paths in transient simulations. It relies on a contact-less approach that minimizes nonlinear contact calculations by defining element sets for material activation. It was shown that the new

approach does not significantly change the result quality while improving calculation times by over 50 %.

### ACKNOWLEDGEMENTS

Fraunhofer IPK (Biegler and Rethmeier) is funded through the IGF-project 18737N of the research association Forschungsvereinigung Stahlanwendung e.V. (FOSTA), Sohnstraße 65, 40237 Düsseldorf, through the AiF within the program of the promotion of the industrial joint research (IGF) by the Federal Ministry for Economic Affairs and Energy based on a resolution of the Deutsche Bundestag.

The contribution of Simufact engineering GmbH (Gatzen and Khazan) is funded through the BMBF-project 03ZZ0210J “Zwanzig20 – Additiv-Generative Fertigung – Verbundvorhaben: ImProVe; TP10: Entwicklung Simulationstool“ by the German Federal Ministry of Education and Research.

### REFERENCES

- [1] W. E. FRAZIER, “Metal Additive Manufacturing: A Review,” *J. of Materi Eng and Perform*, vol. 23, no. 6, pp. 1917–1928, 2014.
- [2] B. GRAF, A. GUMENYUK, M. RETHMEIER, “Laser Metal Deposition as Repair Technology for Stainless Steel and Titanium Alloys,” *Physics Procedia*, vol. 39, pp. 376–381, 2012.
- [3] J. C. HEIGEL, P. MICHALERIS, T. A. PALMER, “In situ monitoring and characterization of distortion during laser cladding of Inconel® 625,” *Journal of Materials Processing Technology*, vol. 220, pp. 135–145, 2015.
- [4] S. SIMUNOVIC, A. NYCZ, M. NOAKES, C. CHIN, V. OANCEA, “Metal Big Area Additive Manufacturing: Process Modeling and Validation,” *NAFEMS World Congress 2017*, 2017.
- [5] L. PAPADAKIS AND C. HAUSER, “Experimental and computational appraisal of the shape accuracy of a thin-walled virole aero-engine casing manufactured by means of laser metal deposition,” *Prod. Eng. Res. Devel.*, vol. 11, no. 4-5, pp. 389–399, 2017.
- [6] M. BIEGLER, B. GRAF, M. RETHMEIER, “In-situ distortions in LMD additive manufacturing walls can be measured with digital image correlation and predicted using numerical simulations,” *Additive Manufacturing*, vol. 20, pp. 101–110, 2018.
- [7] E. R. DENLINGER, J. C. HEIGEL, P. MICHALERIS, “Residual stress and distortion modeling of electron beam direct manufacturing Ti-6Al-4V,” *Proceedings of the Institution of Mechanical Engineers, Part B: Journal of Engineering Manufacture*, vol. 229, no. 10, pp. 1803–1813, 2014.
- [8] A. J. DUNBAR, E. R. DENLINGER, M. F. GOUGE, P. MICHALERIS, “Experimental validation of finite element modeling for laser powder bed fusion deformation,” *Additive Manufacturing*, vol. 12, pp. 108–120, 2016.
- [9] Z. WANG, E. DENLINGER, P. MICHALERIS, A. D. STOICA, D. MA, A. M. BEESE, “Residual stress mapping in Inconel 625 fabricated through additive manufacturing: Method for neutron diffraction measurements to validate thermomechanical model predictions,” *Materials & Design*, vol. 113, pp. 169–177, 2017.
- [10] T. MUKHERJEE, W. ZHANG, T. DEBROY, “An improved prediction of residual stresses and distortion in additive manufacturing,” *Computational Materials Science*, vol. 126, pp. 360–372, 2017.

- [11] J. C. HEIGEL, P. MICHALERIS, E. W. REUTZEL, “Thermo-mechanical model development and validation of directed energy deposition additive manufacturing of Ti-6Al-4V,” *Additive Manufacturing*, vol. 5, pp. 9–19, 2015.
- [12] K. SALONITIS, L. D’ALVISE, B. SCHOINORITIS, D. CHANTZIS, “Additive manufacturing and post-processing simulation: Laser cladding followed by high speed machining,” *Int J Adv Manuf Technol*, vol. 85, no. 9-12, pp. 2401–2411, 2016.
- [13] S. MARIMUTHU, D. CLARK, J. ALLEN, AM KAMARA, P. MATIVENGA, L. LI, R. SCUDAMORE, “Finite element modelling of substrate thermal distortion in direct laser additive manufacture of an aero-engine component,” *Proceedings of the Institution of Mechanical Engineers, Part C: Journal of Mechanical Engineering Science*, vol. 227, no. 9, pp. 1987–1999, 2012.
- [14] A. PLOTKOWSKI, M. M. KIRKA, S. S. BABU, “Verification and validation of a rapid heat transfer calculation methodology for transient melt pool solidification conditions in powder bed metal additive manufacturing,” *Additive Manufacturing*, vol. 18, pp. 256–268, 2017.
- [15] C. LI, J. F. LIU, X. Y. FANG, Y. B. GUO, “Efficient predictive model of part distortion and residual stress in selective laser melting,” *Additive Manufacturing*, vol. 17, pp. 157–168, 2017.
- [16] S. AFAZOV, W. A.D. DENMARK, B. LAZARO TORALLES, A. HOLLOWAY, A. YAGHI, “Distortion prediction and compensation in selective laser melting,” *Additive Manufacturing*, vol. 17, pp. 15–22, 2017.
- [17] E. R. DENLINGER, M. GOUGE, J. IRWIN, P. MICHALERIS, “Thermomechanical model development and in situ experimental validation of the Laser Powder-Bed Fusion process,” *Additive Manufacturing*, vol. 16, pp. 73–80, 2017.
- [18] J. IRWIN AND P. MICHALERIS, “A Line Heat Input Model for Additive Manufacturing,” *J. Manuf. Sci. Eng.*, vol. 138, no. 11, p. 111004, 2016.
- [19] T. MUKHERJEE, V. MANVATKAR, A. DE, T. DEBROY, “Dimensionless numbers in additive manufacturing,” *J. Appl. Phys.*, vol. 121, no. 6, p. 64904, 2017.
- [20] N. BAKIR, A. GUMENYUK, M. RETHMEIER, “Investigation of solidification cracking susceptibility during laser beam welding using an in-situ observation technique,” *Science and Technology of Welding and Joining*, vol. 3, pp. 234–240, 2017.

# INFLUENCE OF THE FIRST WELD BEAD ON STRAIN AND STRESS STATES IN WIRE+ARC ADDITIVE MANUFACTURING

C. CAMBON\*, I. BENDAOU\*, S. ROUQUETTE\* and  
F. SOULIE\*

*\*LMGC, Univ. Montpellier, CNRS, Montpellier, France*

*DOI 10.3217/978-3-85125-615-4-53*

## ABSTRACT

WAAM (Wire+Arc Additive Manufacturing) allows manufacturing mechanical components by adding successive layers of molten metallic wire using electrical arc. The WAAM process, compared to other processes using metallic powders, presents some advantages such as: high deposition rate (2-4kg/hour), manufacturing of large scales components and cheaper industrial installations. WAAM is then an interesting candidate for manufacturing components often CNC machined. However, the main disadvantages of this process are: high surface roughness requiring a post machining, strains and stresses states generated during the deposition process [1]. A better understanding of the relation between the welding parameters and the state of stresses can contribute to minimize residual stresses, eventually in relation with a deposition strategy [2]. As a first approach, the effects of the first deposition of molten metal on the base plate is investigated. This work focuses on finite element method, based on Code Aster solver, with a nonlinear thermo-mechanical model. Concerning the thermal aspects, the GMAW heat input is modeled by a Gaussian distribution [3]. The temperature fields are used to solve the mechanical problem. The material behavior laws are assumed to be elastoplastic with different hardening configurations: no hardening, linear isotropic or kinematic hardening and non-linear isotropic hardening. Based on the results from these elastoplastic models, the influence of the hardening is presented.

Key-words: WAAM process, GMAW, Thermo-mechanical modeling, Residual stresses, Hardening

## INTRODUCTION

Almost one century ago, in 1920, R. Baker patented a technique for manufacturing decorative objects in a similar way to the WAAM one [4]. Nowadays, WAAM technology has greatly improved to the point that metal manufacturers have a growing interest in this revolutionary manufacturing process. However, despite some interesting advantages, WAAM application fields still remain little diversified or limited to prototyping level. Indeed, WAAM manufactured parts can present structural defects partly due to the residual stresses resulting of the deposition thermal cycles. These residual stresses also contribute in the generation of significant distortions which may lead to inaccurate deformed parts. An example of this problem is given in figure 1. This sample was manufactured in our lab with sixteen layers of G3Si1 steel [5]. The deformation of the baseplate is mainly due to

thermal effect. It appears from the first layer and the maximal out-of-plane displacement of the base plate edges can be up to 5 mm.

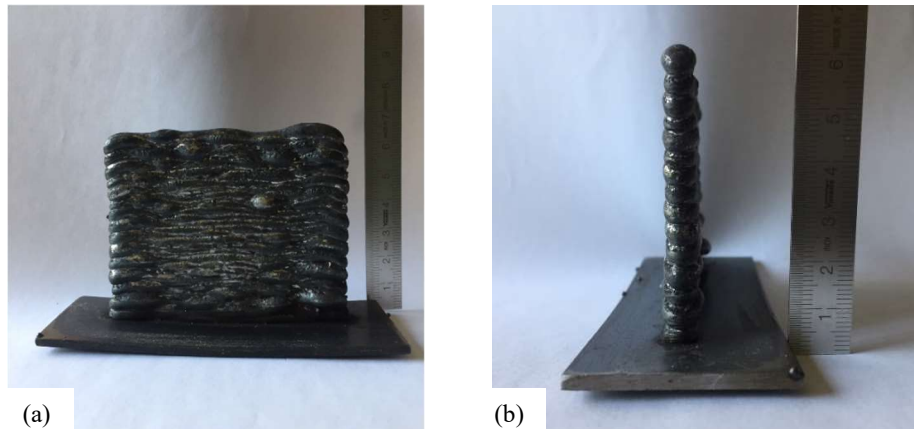


**Fig. 1** WAAM sample obtained with CMT process in LMGC facility. The thickness of the baseplate is 3 mm and 16 layers of G3Si1 steel were used to manufacture the sample: (a) front view, (b) side view.

The main objective of this scientific research is to understand residual stresses induced by WAAM process in order to lower it [6]. A Finite Element Analysis (FEA) associated to an experimental procedure are set up to get both distortions and residual stresses state. The present analysis is based on a thermomechanical weak coupling which considers only the influence of the thermal loading on the mechanical phenomena. The analysis is performed in two sequential steps. First, a thermal simulation is run in order to determine the temperature field generated by the welding torch. Secondly, this temperature field is used as an input data for the mechanical calculation of stress and strain states.

The numerical analysis is performed on a Stainless Steel (SS) 316L plate modelled in 2D under plane stress assumption (100 mm / 60 mm). The thermo-mechanical simulation is done with SalomeMeca software (Code Aster). The thermomechanical model is described in the first part of this work. Then, the results obtained at the end of each numerical analysis are presented. Finally, the influence of the hardening (linear, non-linear, isotropic, kinematic) on the numerical results, residual stresses and distortions, is discussed.

### MODELLING

The WAAM technology uses a GMAW (Gas Metal Arc Welding) process for the deposition of metallic wire. GMAW is an electric arc-based welding process [7]. The heat generated from the electric arc allows melting the metallic wire. Modelling completely this process is extremely complicated as it involves electromagnetic, fluid flow (in the molten metal pool), heat transfers, metallurgical transformations and mechanical phenomena. The driving physic is the heat generated by the electrical arc. This study is limited to the effect of the deposition thermal cycle on the generation of strain and stress states in both the deposit and plate. Indeed, this process generates high thermally-induced residual stresses causing the formation of residual stresses and distortions. Neither metallurgical

transformations are taken into consideration as the latent heat of phase change is generally smaller than the latent heat of fusion nor the effect of microstructure changes on the residual stresses that is assumed to be secondary.

A thorough thermal approach should include the arc plasma heat transfers and molten metal flows in the weld pool [8]. The weld pool surface is subjected to the action of arc pressure, gravity and surface tension and it is assumed to be in a static equilibrium. The effect of electromagnetic forces is neglected as the welding intensity is below 200 A [9]. The convection effects in the molten pool is considered by increasing the thermal conductivity value. An equivalent heat source is used for modelling the heat transfer between the arc plasma and the metallic work piece. Finally, half part of the work piece is considered since the weld is symmetrical along the joint centerline.

### GENERAL ASSUMPTIONS

The thermal and mechanical studies have been performed under the following assumptions:

- 2D geometry with symmetry axis,
- heat conduction transfer with temperature dependent thermophysical properties,
- Lagrangian reference coordinate system with a moving heat source,
- a Gaussian mathematical expression describes the heat source,
- the convection effect in the weld pool is modelled with an increased value of thermal conductivity,
- the mechanical problem is solved once the thermal analysis has been done (weak coupling),
- material mechanical properties are also temperature dependent,
- no metallurgical transformations,
- 2D plane stress assumption,
- no transverse displacement along the symmetry axis ( $Ox$ ) and no displacement (in both directions) along the ( $Oy$ ) axis at  $x=0$  mm (see Fig. 2),
- the two other boundaries are condition-free.

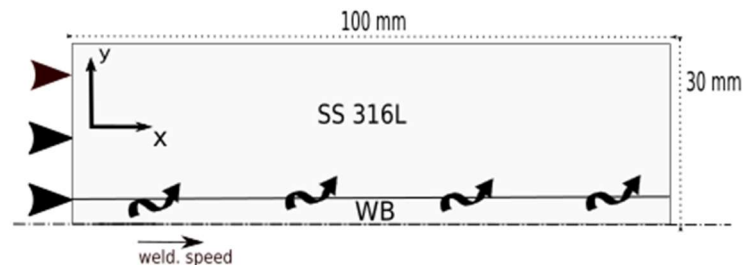


**Fig. 2** Studied geometry: a thin plate of size 100 x 30 x 3 mm with prescribed displacements on its left (black triangles).

## Mathematical Modelling of Weld Phenomena 12

### HEAT CONDUCTION AND THERMOPHYSICAL PROPERTIES

Let's consider a domain  $\Omega$  defined by the top plate face. The considered geometry is 2-Dimensional as the plate thickness is lower than the two other dimensions. The heat transfer through the thickness is neglected. The plate is scanned with a mobile heat source (GMAW torch) on its center so half part of the domain is investigated. A Lagrangian reference coordinate system  $(O,x,y)$  is defined from a corner of the domain on the symmetry axis. The applied thermal loading  $Q$  is a heat source defined with a Gaussian mathematical formulation (Eqn. (3)). The temperature field  $T(x,y,t)$  is the solution of equation system defined with the heat conduction equation with no internal heat production (Eqn. (1)), associated boundary conditions and initial condition (Eqn. (2)).

$$\rho(T)c_p(T) \frac{\partial T}{\partial t} = \lambda(T) \nabla^2(T) + Q \quad (1)$$

Where

$\rho$  is the density ( $\text{kg m}^{-3}$ ),

$c_p$  is the specific heat ( $\text{J kg}^{-1} \text{K}^{-1}$ ),

$\lambda$  is the thermal conductivity ( $\text{W m}^{-1} \text{K}^{-1}$ ) and,

$Q$  is the heat source ( $\text{W m}^{-2}$ ).

This nonlinear second-order PDE (Partial Differential Equation) cannot be solved uniquely without defining the boundary conditions and an initial condition. The associated boundary and initial conditions are:

$$-\lambda \frac{\partial T}{\partial n} = h(T - T_0) + \varepsilon \sigma (T^4 - T_0^4) + q(x,y,t) \quad (2)$$

Where

$n$  is the outside normal,

$q$  is the surface source ( $\text{W m}^{-2}$ ),

$h$  is the convective exchange coefficient ( $\text{W m}^{-2} \text{K}^{-1}$ ),

$\sigma$  is the Stefan-Boltzman constant ( $\sigma = 5.68 \cdot 10^8 \text{ J K}^{-4} \text{ m}^{-2} \text{ s}^{-1}$ ),

$\varepsilon$  is the metal emissivity and,

$T_0$  is the ambient temperature (K) considered as initial condition  $T(x,y,t=t_0) = T_0$ .

The absorbed heat (from the electric arc) is modelled with an equivalent heat source described with a Gaussian mathematical expression as follows:

$$q(x,y,t) = \frac{3\eta UI}{\pi R_0 e} \exp\left(-3 \frac{(x-x_0 - V_s t)^2 + y^2}{R_0^2}\right) \quad (3)$$

Where

$\eta$  is the process efficiency,

$U$  is the welding voltage (V),

$I$  is the welding intensity (A),

$R_0$  is the Gaussian distribution of the heat source (m),

$e$  is the thickness of the plate (m) and,

$V_s$  is the welding velocity ( $\text{m s}^{-1}$ ).

The thermophysical properties of SS 316L are assumed to be temperature dependent (see Table 2 in appendices) The enthalpy formulation is employed to solve the heat equation problem.

SalomeMeca software offers the possibility of using an enthalpic formulation for the heat conduction equation. The enthalpy function  $\beta(T)$  is defined as the product of the density  $\rho$  with the specific heat  $C_p$ . The enthalpic formulation is especially useful when important amount of latent heat is considered such as fusion phenomena. The enthalpic formulation provides a smoother and monotonic temperature dependent variable than the specific heat  $C_p$  which exhibits an important peak nearby the temperature of fusion. This huge change in  $C_p$  values is generally the cause of either numerical convergence problems or the latent heat of fusion is not considered according the chosen time step of the simulation. The enthalpy function is defined as follows:

$$\beta(T) = \int_{T_0}^T \rho C_p(u) du \tag{4}$$

Let's remember that the thermal conductivity is multiplied by 2 in the molten pool. This value is set to  $60 \text{ W}\cdot\text{m}^{-1}\text{K}^{-1}$  as it is shown in table 1. This numerical artifice is often used to reproduce the convection in the molten pool in order to get a suitable weld pool length.

The temperature range of fusion for the SS 316L is fixed to occur between  $1400^\circ\text{C}$  and  $1500^\circ\text{C}$  with a latent heat value of  $2.0 \cdot 10^9 \text{ J}\cdot\text{m}^{-3}$ [10]. The enthalpy curve for the SS 316L is presented in Fig. 3.

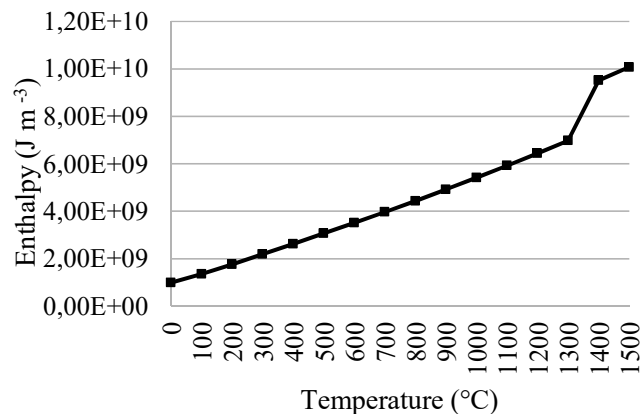


Fig. 3 Evolution of the Enthalpy with regards to the temperature for SS 316L.

#### MECHANICAL MODEL

A transient mechanical analysis is performed in order to calculate the strain and stress responses to the thermal cycle previously presented. Let's remember that the thermal analysis results are used as thermal loading into the mechanical analysis. The thermal and



mechanical analysis are performed in a one-way manner (weak coupling). A nonlinear static solver is used. The material behavior law is assumed to be elastoplastic. The influence of viscous phenomena is neglected. Four different types of hardening are investigated in order to observe their effect on the final strain and stress fields:

- Linear isotropic hardening
- Non-linear isotropic hardening
- Zero hardening (perfectly elastoplastic)
- Linear kinematic hardening

All these analyses are run under large deformations assumption with the "PETIT\_REAC" solver of SalomeMeca/Code\_Aster software. "PETIT\_REAC" solver is based on a geometry update (position of nodes) at each Newton iteration. So, several geometry updates are performed for each time step of the mechanical calculation. Apart this geometry update, the solver works like for the small deformations [11] [12]. The "PETIT\_REAC" solver is well suited for large deformations if rotation motions are small, the elastic strain is lower than the plastic strain, the material behavior law is isotropic and for smaller Newton iterations.

### *Governing equations*

At each time step, the mechanical problem must verify the equilibrium equation:

$$\text{div}(\sigma) + f_{\text{volume}} = 0. \quad (5)$$

Furthermore, under small deformations hypothesis, the strain tensor is defined according to the displacements:

$$\Delta \varepsilon = \frac{1}{2} (\nabla_{\Omega_i}(\Delta u) + \nabla_{\Omega_i}^T(\Delta u)), \quad (6)$$

With  $\Omega_i$  the updated configuration.

Under the assumption of small strains and considering an elastoplastic model, the strains decomposition at any time is formulated as follows:

$$\varepsilon(t) = \varepsilon^e(t) + \varepsilon^{\text{th}}(t) + \varepsilon^p(t), \quad (7)$$

With

$$\varepsilon^e(t) = A^{-1}(T(t))\sigma(t), \quad (8)$$

And

$$\varepsilon^{\text{th}}(t) = \alpha(T(t))(T(t) - T_{\text{ref}})\text{Id}. \quad (9)$$

## Mathematical Modelling of Weld Phenomena 12

A is the elasticity tensor which depends on the temperature at time  $t$ . The coefficient  $\alpha$  is the average coefficient of thermal expansion depending in terms of a reference temperature  $T_{ref}$  for which the thermal expansion is zero.

Finally, the discretized relation is:

$$\Delta\varepsilon = \Delta\varepsilon^p + \Delta(A^{-1}\sigma) + \Delta\varepsilon^{th} \quad (10)$$

### *Mechanical properties*

The mechanical analysis is strongly nonlinear due to both the transient thermal loading and the temperature dependence of the SS 316L mechanical properties. SS 316L yield strength and Young modulus decrease with the increase of temperature as it is shown in Table 2 and Fig. 13 in appendices. In order to cancel the stress in the molten pool, both yield strength and Young modulus have been fixed to low values (beyond  $T=1400^\circ\text{C}$ ).

Moreover, in order to cancel the cumulative plastic strains in the molten pool, a multiplicative function describing the hardening restoration is defined as follow [14]:

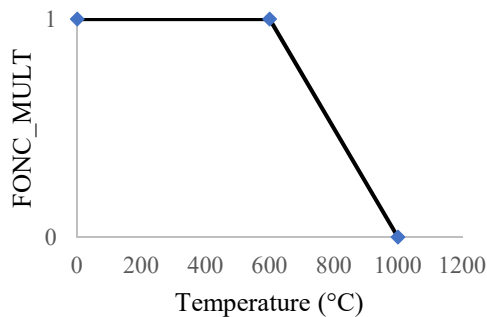


**Fig. 4** Multiplicative function of hardening restoration for SS 316L.

### *Boundary Conditions*

The plate is fixed on one side along the (Oy) direction as it is shown in Fig. 5 (full black triangles). All the nodes have a prescribed displacement in both x and y direction ( $DX=0$  and  $DY=0$ ). Furthermore, the welding line, (Ox direction), has prescribed displacement in the y direction ( $DY=0$ ) in order to satisfy the symmetry condition.

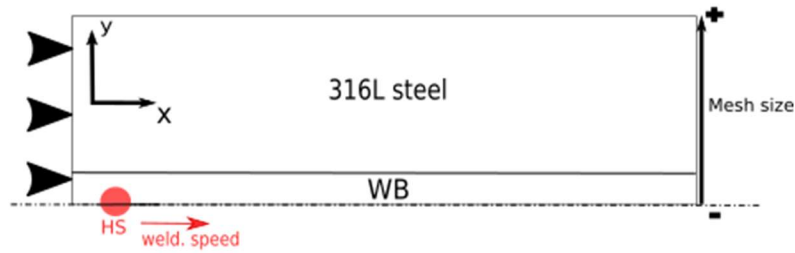


Fig. 5 Mechanical boundary conditions.

## RESULTS AND DISCUSSION

### CALCULATED TEMPERATURE FIELD

The average electric parameters are  $U=12$  V;  $I=120$  A. The process efficiency is fixed to  $\eta=0.8$  as it is classical for a GMAW process. The welding speed is set to  $V_s=5$  mm  $s^{-1}$ . The last parameters which are required in the Gaussian heat flux expression are chosen equal to  $R_0=3$  mm for the Gaussian distribution and  $e=3$  mm for the plate thickness. The Gaussian radius was roughly estimated in order to get a weld pool half-width of about 2 mm as observed experimentally. The total simulation duration is about 36.8 s defined as 0.8 s for the initiation followed of 16 s for the heat flux to scan the 80 mm of the plate and 20 s of cooling. The meshgrid used for the thermal simulation consists in 12090 quadrangle elements defined with 11546 nodes. The minimum element size is 0.2 mm in the weld bead and increases progressively far from the weld bead zone. The calculation is performed with a direct solver. The total CPU time consumed is 3725 s (~1h) for a time step of 0.04 s with a smaller time step of 0.008 s at the initiation of the heat source. The results of the thermal simulation are presented in Fig. 6 and 7.

In Fig. 6, the calculated temperature field is presented at time  $t=8$  s. The shape of the molten pool is delimited with the black line corresponding to the isotherm  $T=1400^\circ\text{C}$ . The molten pool exhibits a classic elongated shape. Its dimensions are 5 mm long by 2 mm half-width. The part of the plate in front of the source is not yet affected by the heating and it remains equal to the initial temperature. The thermal gradient in front of the heat source is important as it is commonly observed in welding experiment. This is due to the low thermal diffusivity (ratio  $\lambda / (\rho \cdot C_p)$ ) of SS 316L which takes values between  $3,89 \times 10^{-6}$   $\text{m}^2 \text{s}^{-1}$  to  $5,64 \times 10^{-6}$   $\text{m}^2 \text{s}^{-1}$  between  $20^\circ\text{C}$  and  $1200^\circ\text{C}$ . The heat propagates slower than the heat source motion so a high thermal gradient is produced in front of the heat source. At the rear of the heat source, the heat propagates towards the width by conduction. The boundary located at  $x=0$  mm is slightly heated by conduction as the heat source started 10 mm further. A maximum temperature of  $1790^\circ\text{C}$  is reached inside the molten pool. The isotherm defining the weld pool shape exhibits a perpendicular tangential derivative on the symmetry axis. This behaviour is due to the symmetry condition imposed on this boundary (homogenous Neumann condition). The computation of Biot number ( $Bi = h \cdot L / \lambda$  with  $h$  the convective exchange coefficient,  $L$  is a characteristic length and  $\lambda$  is the thermal conductivity) leads to a value between 0,003 and 0,0015 in the temperature range  $20^\circ\text{C}$ - $1200^\circ\text{C}$  (with  $h=15$  W

## Mathematical Modelling of Weld Phenomena 12

$\text{m}^{-2} \text{K}^{-1}$  and  $L$  is equal to the plate thickness). For Biot values inferior to 0.1, it can be assumed that the temperature field is almost the same through the plate thickness.

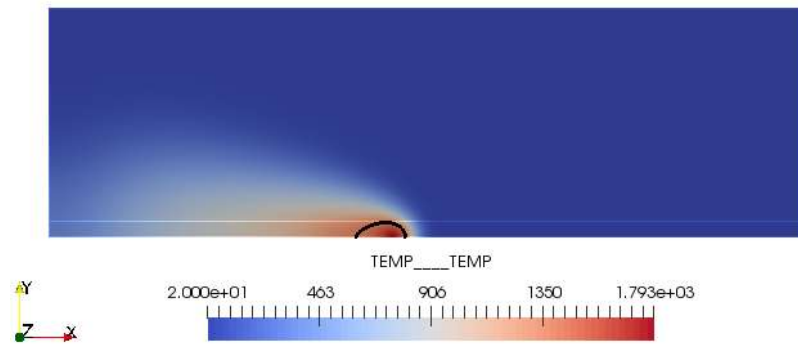


**Fig. 6** Temperature field ( $^{\circ}\text{C}$ ) at time  $t=8$  s. The weld pool shape is defined by the melting isotherm  $T_f=1400^{\circ}\text{C}$  (black line).

The temporal evolution of the temperature at time  $t=8$  s on the symmetry axis (see Fig. 7.a) is reported in Fig. 7.b. The temperature history is divided in four parts. Firstly, the temperature remains equal to the initial condition till the heat source comes over its position. Secondly, the heating rate increases hugely, about  $1275^{\circ}\text{C s}^{-1}$ , as the temperature rises from  $20^{\circ}\text{C}$  to  $1790^{\circ}\text{C}$  in about 1.5 s. Then the material cools down quickly from  $1790^{\circ}\text{C}$  to  $1400^{\circ}\text{C}$  with a cooling rate similar to the heating rate. At  $1400^{\circ}\text{C}$ , the cooling rate slows down to  $80^{\circ}\text{C s}^{-1}$ . This is due to the release of the latent heat of fusion. Once the material is totally solidified, the cooling rate decreases from  $200^{\circ}\text{C s}^{-1}$  (at  $t\sim 11.5$  s) to  $10^{\circ}\text{C s}^{-1}$  at the end of the computation ( $t\sim 37$  s). The plate has not reached the room temperature after 20 s of heat flux extinction. The average temperature of the plate is between  $400^{\circ}\text{C}$  and  $500^{\circ}\text{C}$  after 20 s of cooling time. At a cooling rate of  $10^{\circ}\text{C s}^{-1}$ , it would take 40 to 50 more seconds to reach the room temperature. Experimentally, it is extremely difficult to get thermal data inside the weld pool and its vicinity. Nevertheless, the weld pool shape and temperature field are in good agreement with some data found in the literature [15].

## Mathematical Modelling of Weld Phenomena 12

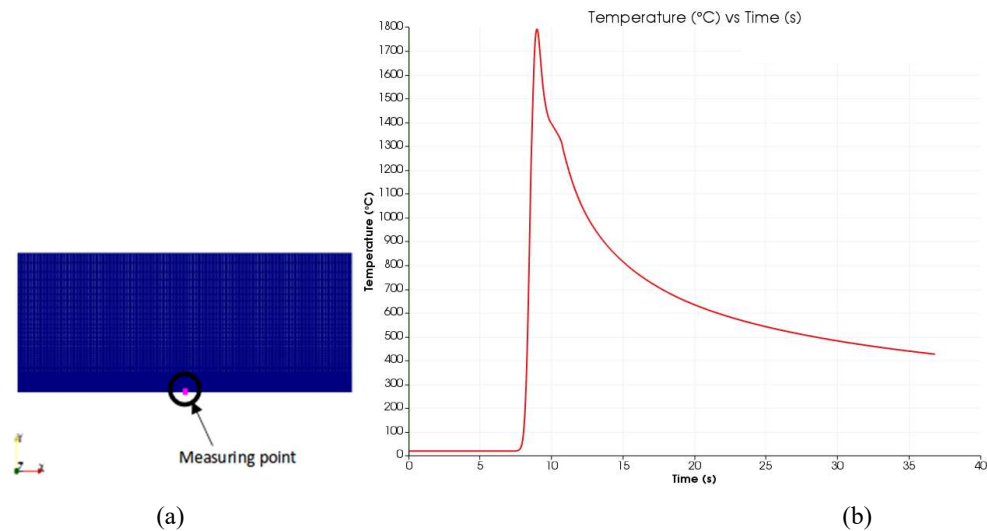


**Fig. 7** Time evolution of the temperature (b) for an arbitrary point on the symmetry axis (a).

This temperature results are used in the mechanical computation in order to predict the residual stresses generated by the heat flux passage. The effect of this thermal cycle on the residual stresses is presented in the next section.

### STRESS FIELDS

For the mechanical computation, the mesh is composed by 7290 quadrangle elements and 6946 nodes. Like the thermal analysis, a mesh refinement is made in the weld bead zone with a mesh element size of 0.2 mm. The computation is performed with a direct solver. The CPU time consumed for each analysis is nearly the same, about 40 000 s (~11 h) for a time step of  $5 \cdot 10^{-4}$  s.

The longitudinal stress field and evolution along the longitudinal and transverse directions are presented respectively in Fig. 9, 10, 11 and 12. The presented results in Fig. 9, 11 and 12 is obtained at the final time of the mechanical computation then after 20 s of cooling. Fig. 10 presents the longitudinal stress evolution at time  $t=8$  s along two longitudinal axis L1 and L2 (see Fig. 8) respectively situated at 1mm and 10 mm from symmetry axis (Ox). Let's remember that the SS 316L is supposed to be elastoplastic with hardening. Four hardening cases have been investigated: perfectly plastic, linear isotropic, nonlinear isotropic and linear kinematic.

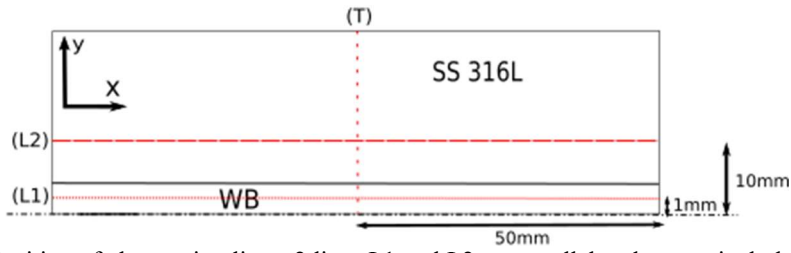


**Fig. 8** Position of observation lines: 2 lines L1 and L2 are parallel and respectively located at 1 mm and 10 mm from the symmetry axis (Ox). The third line L3 is located at  $y=50$  mm and perpendicular to the symmetry axis (Ox).

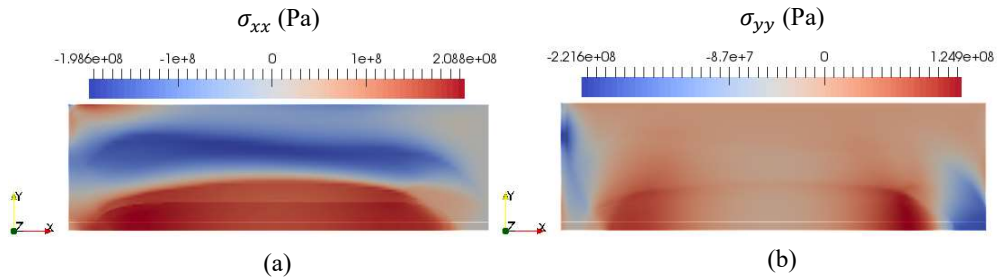


**Fig. 9** Longitudinal stress ( $\sigma_{xx}$  for (a)) and transverse stress ( $\sigma_{yy}$  for (b)) fields at  $t=t_{\text{final}}$  ( $\sim 37$  s) under elastoplastic behavior with linear isotropic hardening (Pa).

The longitudinal stress ( $\sigma_{xx}$ ) field is tensile between the starting and ending points of the weld path as we can see in Fig. 9.a. The longitudinal stress has a homogenous value along the weld bead (around +200 MPa). This longitudinal stress field has a classic distribution. Inside the molten pool, the stress must be equal to zero as it is observed experimentally (a numerical artifact cancels the stress when the temperature is greater than  $1400^{\circ}\text{C}$ ). Thus, during the solidification, the material shrinkage leads to tensile stress at the back of the weld pool as we can see in Fig. 9.a.

Transverse stress ( $\sigma_{yy}$ ) is tensile in the domain defined by the weld bead and heat affected zone. The transverse stress is equal to zero on the free lateral boundary ( $y=30$  mm). Another edge effect is visible on the fixed boundary ( $x=0$  mm); the transverse stress is under compression due to the condition of prescribed displacements in both directions.

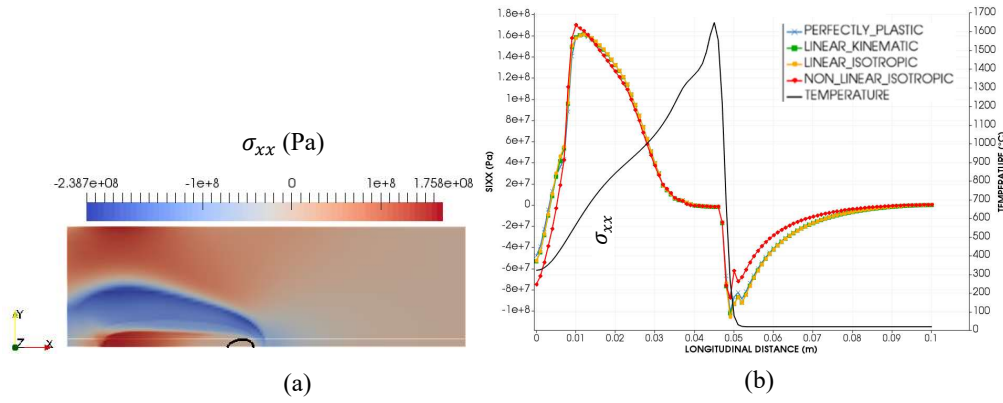


**Fig. 10** At  $t=8$  s, along L1: (a) Longitudinal stresses ( $\sigma_{xx}$ ) field at  $t=8$  s. (b): Evolution of the longitudinal stresses ( $\sigma_{xx}$ ) for four hardening configurations (left vertical axis in Pa) and temperature distribution (right vertical axis in °C).

Fig. 10.a and 10.b present the longitudinal stress field when the heat source is located at  $x \sim 50$  mm ( $t \sim 8$  s). The evolution of longitudinal stress along L1 line is presented as well as the temperature history. In front of the heat source ( $x > 50$  mm), the zone is under compression due to dilatation effects because of the high temperature difference in few millimeters. The temperature rises suddenly from  $20^\circ\text{C}$  to  $1700^\circ\text{C}$ . The stress values are equal to zero inside the molten pool because the cut-off temperature imposed on the material properties for canceling the stress ( $T_{\text{cut-off}} = 1400^\circ\text{C}$ ). Once the temperature, at the back of the heat source, goes below  $T_{\text{cut-off}}$ , the longitudinal stress goes from 0 MPa to reach 150-160 MPa. At  $x=10$  mm, the longitudinal stress has not yet reached its maximum value as shown in Fig. 11.b (about 220 MPa at  $t=t_{\text{final}}$ ).

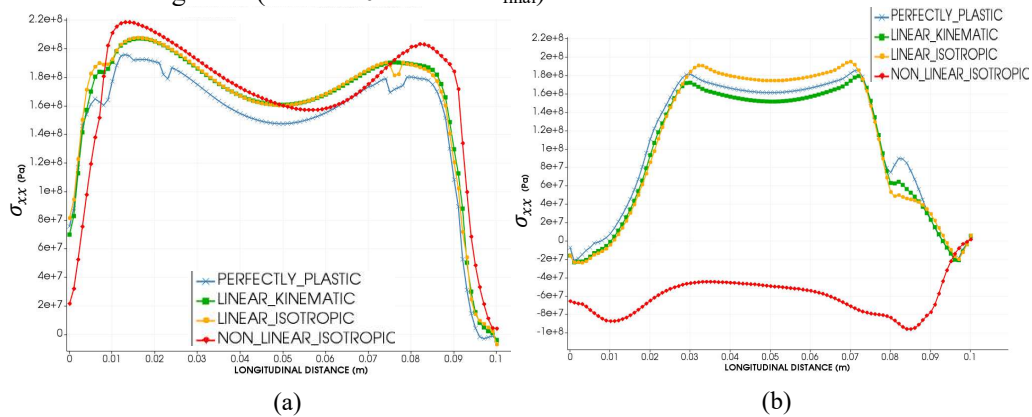


**Fig. 11** Evolution of longitudinal residual stress ( $\sigma_{xx}$ ) along L1 line (a) and L2 line (b) parallel to the weld bead and located respectively at 1 mm and 10 mm from the symmetry axis.

As mentioned for the longitudinal stress field, the longitudinal stress is cancelled on the free boundary, at  $x=100$  mm. The longitudinal stress is slightly tensile on the fixed boundary ( $x=0$  mm) because of the boundary condition applied here: no displacement in both directions, see Fig. 11.a. The longitudinal stress reaches two peaks values ( $\sim 220$  MPa)

at the beginning of weld path ( $x=10$  mm) and at its end at  $x=90$  mm this is due to the plate stiffness before the starting and after the ending points. The minimum value is reached at the plate middle with 160 MPa. At 10 mm from the symmetry axis, the longitudinal stress is still tensile and high with a homogenous value of 160 MPa between  $30 \text{ mm} < x < 80 \text{ mm}$ , Fig. 11.b. All the studied hardening led to the same residual stress field and longitudinal distribution except for the nonlinear isotropic hardening case. The nonlinear isotropic hardening led to a narrower tensile zone for the longitudinal stress. Fig. 12.a shows that the longitudinal stress is tensile (about 160 MPa) over 6-7 mm before decreasing and reaching a minimum value of -140 MPa at 12-13 mm from symmetry axis. The three other cases: perfectly plastic, linear isotropic and kinematic hardening led to a wider tensile zone, till 12 from symmetry axis and the minimum value is -200 MPa and it is reached about 20 mm from symmetry axis. The thermal loading is the same for the four studied cases. It seems that the nonlinear isotropic hardening leads to a narrower tensile zone (for  $\sigma_{xx}$ ) and the compressive value is lower as well.

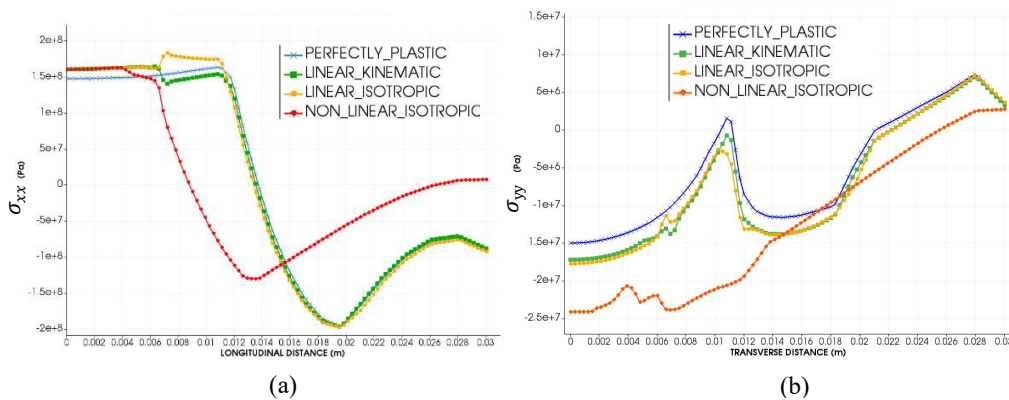


**Fig. 12** Evolution of longitudinal residual stress  $\sigma_{xx}$  (a) and transverse residual stress  $\sigma_{yy}$  (b) along a transverse line to the weld bead and located at  $x=50$  mm.

Fig. 12.a presents a classical longitudinal stress distribution along a perpendicular direction to welding path. The weld bead and heat affected zones are tensile followed to a compression zone with a peak value of -200 MPa. As the plate width is quite narrow, this compressive longitudinal stress remains quite high with a value of about -100 MPa on the lateral boundary ( $y=30$  mm). The calculated transverse stress at the plate middle ( $y=50$ mm) is more than 10 times lower than the longitudinal one. At this position of the weld bead, the stress field looks like an uniaxial loading as it is shown in Fig. 9.b. The transverse stress is high at the beginning and end of the weld bead probably due to the plate stiffness. The  $\sigma_{xx}$  and  $\sigma_{yy}$  residual stresses fields along transverse axis are in accordance with strain gauges and neutron diffraction measurements [16].



CONCLUSION AND PROSPECTS

A thermo-mechanical analysis was conducted in order to appreciate the stress distribution induced by WAAM process. As a first approach, only the first weld bead is considered to evaluate the level of distortion and residual stresses that could affect the WAAM process during the successive deposition. The thermo-mechanical simulations were done with SalomeMeca software (Code Aster). The thermo-mechanical model is elastoplastic type with different hardening configurations (linear, non-linear, isotropic, kinematic).

The magnitude and distribution of residual stresses are very similar for all the types of hardening, both on longitudinal and transverse sections. Only the non-linear hardening presents some discrepancies.

The obtained differences are probably due to the nonlinear mechanical management by the solver. Nevertheless, the global behavior and the maximal values of stresses are nearly the same for all the hardening configurations.

The management of several layers deposition for thermomechanical analysis is in progress. It will be carried out in relation with an experimental study conducted in similar conditions. The experimental data obtained in our lab facility are both thermal data (temperature histories with thermocouples) and mechanical data (displacements and strains).

APPENDICES AND ACKNOWLEDGEMENTS

**Table 1** Thermophysical properties of SS 316L [13].

Temperature (°C)	Conductivity ( $W m^{-1} K^{-1}$ )	Enthalpy ( $J m^{-3}$ )
0		9.8310 <sup>8</sup>
20	14	
100	15.2	1.36 10 <sup>9</sup>
200	16.6	1.76 10 <sup>9</sup>
300	17.9	2.19 10 <sup>9</sup>
400	19	2.62 10 <sup>9</sup>
500	20.6	3.06 10 <sup>9</sup>
600	21.8	3.51 10 <sup>9</sup>
700	23.1	3.96 10 <sup>9</sup>
800	24.3	4.43 10 <sup>9</sup>
900	26	4.92 10 <sup>9</sup>
1000	27.3	5.42 10 <sup>9</sup>
1100		5.92 10 <sup>9</sup>
1200	29.9	6.44 10 <sup>9</sup>
1300		6.97 10 <sup>9</sup>
1400	60.0	9.51 10 <sup>9</sup>
1500		1.01 10 <sup>10</sup>

## Mathematical Modelling of Weld Phenomena 12

**Table 2** Mechanical properties of SS 316L [13].

Temperature (°C)	Young Modulus E (10 <sup>6</sup> Pa)	Yield Strength R <sub>e</sub> (10 <sup>6</sup> Pa)	Coefficient of thermal expansion α (10 <sup>-5</sup> )	Tangent modulus of elasticity E <sub>T</sub> (10 <sup>6</sup> Pa)
20	197 000	287	1.55	2400
100	191 500	237	1.60	
200	184 000	198		
300	176 500	172	1.71	
400	168 000	157	1.75	
500	160 000	151		
600	151 500	145	1.84	
700	142 500	136	1.87	2400
800	130 000	127	1.90	2350
900	108 000	115		1500
1000	81 500	79	1.94	800
1100	32 000	38		725
1200	7 400	24		150
1300		18		10
1400		2	1.96	

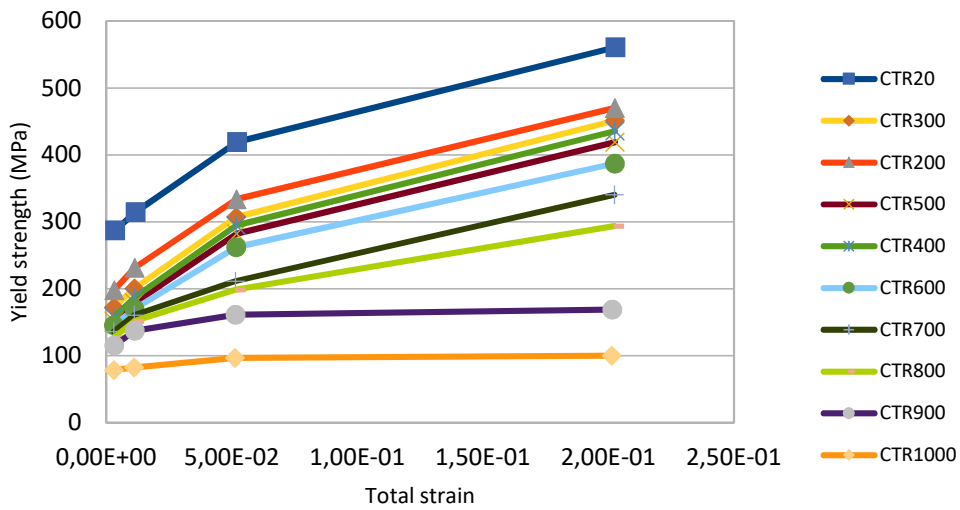


**Fig. 13** Traction curves of SS 316L [13].

### REFERENCES

- [1] D. DING, Z. PAN, D. CUIURI, H. LI: 'Wire-feed additive manufacturing of metal components: technologies, developments and future interests', *The International Journal of Advanced Manufacturing Technology* 81, University of Wollongong Northfield Ave, pp. 465-481, 2015.
- [2] T. MUKHERJEE, W. ZHANG, T. DEBROY: 'An improved prediction of residual stresses and distortion in additive manufacturing', *Computational Materials Science* 126, The Pennsylvania State University, pp. 360-372, 2017.
- [3] F. MONTEVECCHI, G. VENTURINI, A. SCIPPA, G. CAMPATELLI.: 'Finite Element modelling of Wire -Arc-Additive-Manufacturing process', *Procedia CIRP* 55, University of Firenze, pp. 109-114, 2016.
- [4] R. BAKER: 'Method of Making Decorative Articles', *US Patent 1533,300*, filed November 12, 1920, patented 14<sup>th</sup> April, 1925.
- [5] L. CORONA GALVAN : *Prototypage rapide de pièces en acier : étude du dépôt de matière et d'énergie lors de la fusion à l'arc d'un fil par le procédé MIG-CMT*, thesis, University of Montpellier, 2018
- [6] L.D. COZZOLINO, H.E. COULES, P.A. COLEGROVE, S. WEN: 'Investigation of post-weld rolling methods to reduce residual stress and distortion', *Journal of Materials Processing Technology* 247, Cranfield University, pp. 234-256, 2017.
- [7] J-P. PLANCKAERT : *Modélisation du soudage MIG/MAG en mode short-arc*, thesis, Henri Poincaré University, 2008.
- [8] M.C. NGUYEN : *Modélisation et simulation multiphysique du bain de fusion en soudage à l'arc TIG*, thesis, Ecole polytechnique universitaire de Marseille, 2015.
- [9] S. ROKHLIN, A. GUU: 'A study of arc force, pool depression, and weld penetration during gas tungsten arc welding', *Welding Journal* 72:8, The Ohio State University, pp. 381-390, 1993
- [10] F.X TISSOT : *Etude phénoménologique et modélisation du comportement du bain de fusion en soudage TIG en vue d'une application au contrôle du procédé*, thesis, University of Aix-Marseille I
- [11] D. HABOUSSA : 'Intégration des relations de comportement élasto-plastique de Von Mises', *Code\_Aster Documentation*, R5.03.02, 2005
- [12] E. LORENTZ: 'Modelling elasto (visco) plastic with isotropic work hardening in great deformations', *Code\_Aster Documentation*, R5.03.21, 2013
- [13] L. DEPRADEUX : *Simulation numérique du soudage-acier 316L Validation sur cas tests de complexité croissante*, thesis, L'Institut National des Sciences Appliquées de Lyon, 2004
- [14] S. HENDILI : 'HSNV140 - Thermo-plasticité avec restauration d'écrouissage : essai de dilatométrie bloquée', *Code\_Aster Documentation*, V7.22.140, 2016
- [15] H. SCHOPP, A. SPERL, R. KOSAKOV, G. GOTT, D. UHRLANDT, G. WILHELM: 'Temperature and emissivity determination of liquid steel S235', *Journal of Physics D: Applied Physics* 45, INP-Greifswald, 9pp, 2012
- [16] H.E. COULES, L.D. COZZOLINO, P. COLEGROVE, S. GANGULY, S. WEN, T. PIRLING: 'Residual strain measurement for arc welding and localised high-pressure rolling using resistance gauges and neutron diffraction', *Journal of Strain Analysis for Engineering Design* 47, University of Bristol, pp. 576-586, 2012

# NEW APPROACH FOR FAST NUMERICAL PREDICTION OF RESIDUAL STRESS AND DISTORTION OF AM PARTS FROM STEELS WITH PHASE TRANSFORMATIONS

M. SCHÄNZEL\*, A. ILIN\* and V. PLOSHIKHIN\*\*

*\*Corporate Sector Research and Advance Engineering Robert Bosch GmbH, 71272 Renningen, Germany,  
michael.schaenzel@de.bosch.com*

*\*\*Airbus endowed chair for Integrative Simulation and Engineering of Materials and Processes  
University of Bremen, 28359 Bremen, Germany*

DOI 10.3217/978-3-85125-615-4-54

## ABSTRACT

Selective Laser Melting (SLM) is a promising additive manufacturing technology for production of complex and highly individual parts on short lead time request. Pre-processing assisted by numerical simulation can reduce defects which occur during construction and manufacturing and hence increase the quality of the parts and the efficiency of this technology. Especially the inherent strain method [1] is common and well suited for the fast numerical prediction and optimization of residual stresses and distortion of AM-parts. A major disadvantage of this method is the restriction to austenitic steels without phase transformations in the solid state during the process. The inherent strain method has only a limited validity for martensitic steels because the effects of phase transformations are not taken into account. However, an increasing number of materials to be processed requires a detailed numerical forecast also for martensitic steels to guarantee high quality parts.

This research work introduces an extension of the inherent strain method for the consideration of martensitic phase transformations during SLM-process. A multiscale approach, based on a coupled nonlinear thermo-mechanical finite element analysis and the further development of the inherent strain method combined with a new calibration procedure is proposed. It is demonstrated, that the developed approach can be effectively used for the forecast of structure distortions. The presented approach opens the way for the optimization of the additive manufacturing technology towards a defect-free manufacturing process.

Keywords: Selective laser melting, residual stresses, finite element analysis, phase transformation

## INTRODUCTION

The economical production of highly individual products and complex parts requires innovative manufacturing technologies like the selective laser melting. This layer-based additive manufacturing technology becomes more common and relevant in various industrial branches like aerospace and automotive industries. Especially for these industries with growing fields of application a clear understanding of the process is crucial to achieve

a high process stability and reproducibility. In this case the numerical simulation can be used to develop a deeper understanding of the process.

For the beneficial application of the simulation in the production and development work efficient models with less calculation effort but nevertheless high accuracy are essential. In the area of selective laser melting especially the so called inherent strain method is a powerful tool for the fast prediction of distortion [1-2], residual stress as well as the cracking occurrence [3].

The method is based on the observations of Ueda [4-6] that the characteristic distribution of the permanent strains occurring in the weld area is directly related to the residual stresses. Ueda used an elastic analysis in which the occurring permanent strains are replaced by equivalent distributed loads to predict the residual stress. The method was successfully applied to large welding structures [7-12]. In Ref. [13] the so called 'Mechanical Process Equivalent' method is introduced for the determination of large structure distortions after welding process. As a further development this technique has been adapted for the selective laser melting [1-2] for the realization of the fast prediction of distortion and residual stress in AM parts using the finite element analysis.

However, the current state of the art of the inherent strain method in the case of SLM has been developed for stainless steels without phase transformations. If phase transformations occur in the process, the material behavior and condition of residual stress and strain can change entirely. This fact is shown in Fig. 1 with two standard cantilever beam specimen build-ups with equal process parameters but different materials. The cantilever built from austenitic steel 1.4404 (AISI 316L) shows an upward distortion after the process and cutting off the supports while the one from martensitic steel 1.4057 (AISI 431) shows a downward distortion. This material behaviour cannot be modelled numerically with the current inherent strain method, which makes simulation-supported pre-processing of the SLM process difficult.

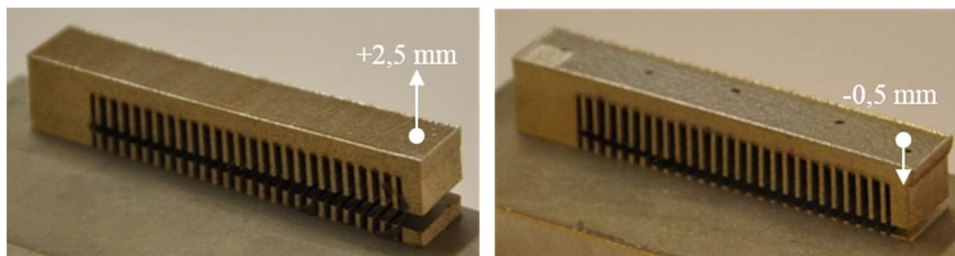


**Fig. 1** Distorted cantilever of austenitic steel 1.4404 (left) and martensitic steel 1.4057 (right) built with same process parameters

A new approach of the inherent strain method for the consideration of the phase transformation related influence on the material behaviour is presented in this research work. The advanced inherent strain method allows the prediction of process related residual stresses and distortion even for martensitic steels.

Fundamental knowledge about the effects of phase transformation has been gained based on a non-linear thermo-mechanical macroscale FEM simulation, including a phase transformations model, in combination with high temperature experiments. A fast

calibration procedure is introduced for the new model with higher complexity. Validation with experiments at different temperatures confirms the advanced method.

### NON-LINEAR MACRO SIMULATION MODEL

#### THERMO-MECHANICAL SIMULATION

The used sequentially coupled thermo-mechanical simulation model is based on the ‘effective meshing’ and ‘adaptive heat source’ model in reference to [14]. For the thermal analysis a full three-dimensional model is used. The plane or area of interest in this model is sufficiently fine meshed. The dimensions of the Goldak heat source [15] changes its dimension adaptively in correlation to the mesh density. This enables a physically plausible thermal modelling of the full geometry with a realistic temperature profile in the area of interest with a minimized calculation effort. The coupled mechanical simulation consists of a plane stress model of the plane of interest. Fig. 2 visualize the thermal three- and the mechanical two-dimensional model with temperature load.

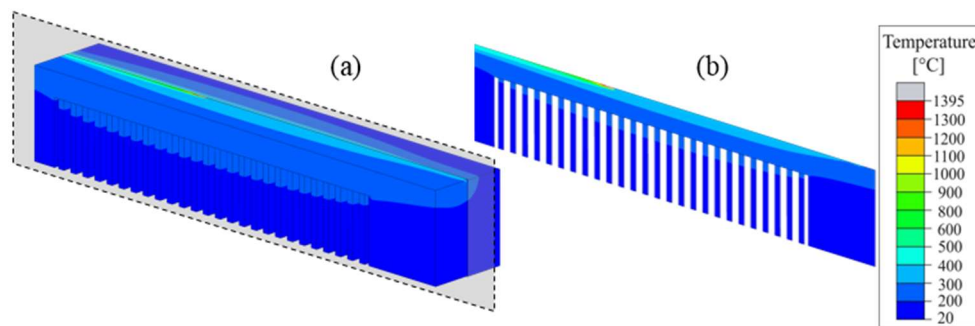


**Fig. 2** Three-dimensional thermal (a) and two-dimensional mechanical model of the plane of interest (b)

The simulation of all scanning vectors as well as the intercooling during the coating process returns the realistic temperature profile and cooling rates. The information is essential for the calculation of the accurate mechanical behavior and is the input for the integrated phase transformation model. In the phase transformation model the austenitisation during the heating of the material is implemented as a linear transformation between the  $A_{c1}$  and  $A_{c3}$  temperatures, which are extracted from the TTT diagram and dilatometer experiments, see Fig. 3. In the cooling stage the transformation to martensitic phase begins at the martensitic start temperature  $M_s$  and is finished when reaching the finish temperature  $M_f$ . Between  $M_s$  and  $M_f$  the transformation is calculated based on the model of Koistinen and Marburger [16], see Eqn. (1). Variable  $V_\gamma$  represents the volume fraction of the retained austenite and  $T_q$  the cooling temperature reached during quenching. This formula neglects the cooling rate, which also can have an influence on the transformations.

## Mathematical Modelling of Weld Phenomena 12

Because of the high cooling rates in the SLM process this simplification appears reasonable, see cooling profile in Fig. 3.

$$V_\gamma = \exp[-1.10 * 10^{-2}(M_s - T_q)] \quad (1)$$

To determine the phase transformation temperatures, dilatometer experiments are performed as well as calculations of material properties with the JMatPro [17] software. Based on this data the specific transformation temperatures are defined. In Fig. 4 are contrasted the experimental and JMatPro data with the simulation result of the numerical reproduction of the dilatometer experiment using the developed phase transformation model. The calculated proportions of the present phases were used in the mechanical material model to define phase-dependent material properties.

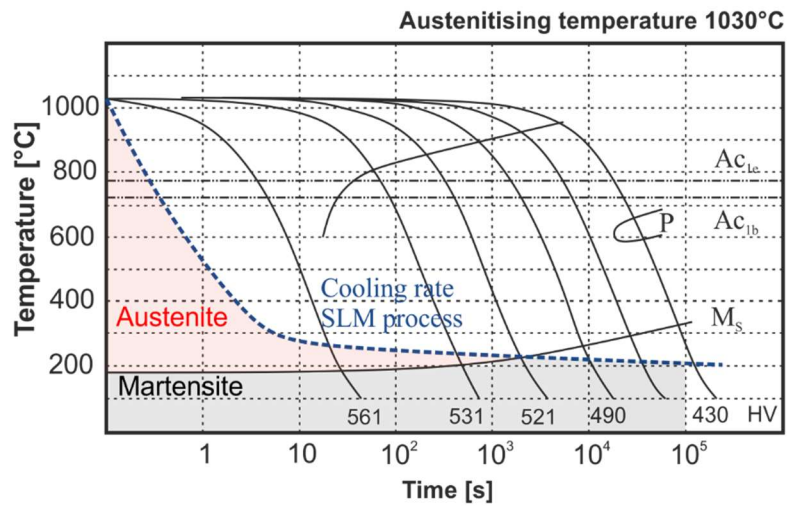


**Fig. 3** TTT diagram of martensitic steel 1.4057 (AISI 431) [18] and cooling profile SLM process

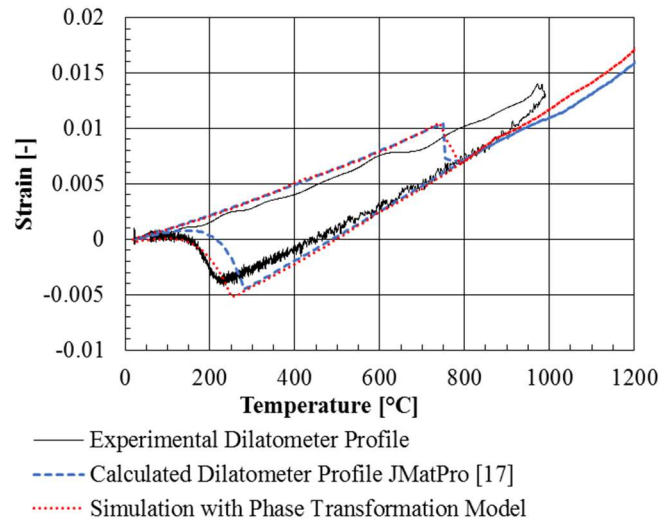


**Fig. 4** Dilatometer experiment with 1.4057, calculated profile with JMatPro [17] and numerical reproduction with developed phase transformation model

RESULTS

The thermo-mechanical simulation has been used for a numerical reproduction of the cantilever build-up. The results of the calculated stress condition after the build-up are presented in Fig. 5. The numerical simulations are performed with the ABAQUS 2017 solver [19]. The austenite steel sample shows high deformation of the part after separating the support as a result of the tensile stresses on the top layers. The martensitic sample have only a low stress and distortion level.

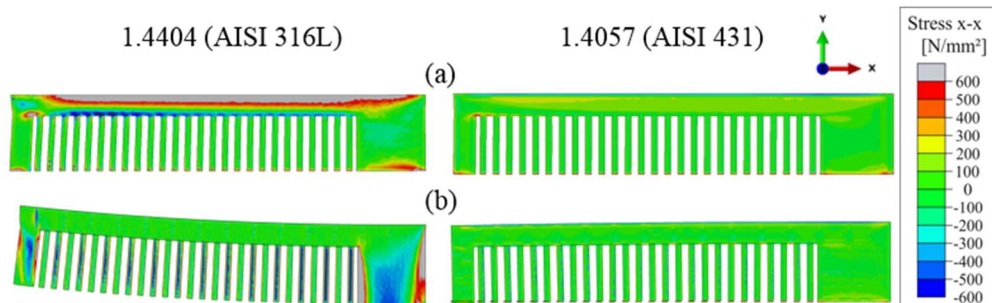


**Fig. 5** Contour plot of residual stress after build-up (a) and with separated support structure (b)

For the validation of the model parameter settings with 350 W and 600 W laser power have been investigated. The experimental measured and the numerical calculated distortions are compared in Fig. 6. The results show a close correlation and a similar behaviour even for different parameters.



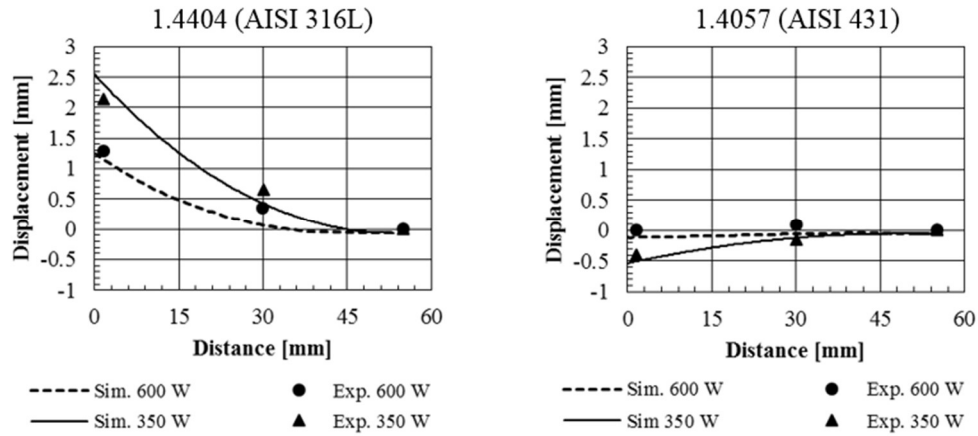


**Fig. 6** Experimental and numerical results of the upward displacement of the cantilever specimen after separating the support structures

An explanation of the different distortion behaviour is presented in the calculation results of the phase transformation. In Fig. 7 are visualized the contour plots of the calculated phase states at the end of the heat transfer in the last layer. The 1.4404 steel is completely austenitic. Only the upper layer of 1.4057 is austenitic while the lower layers are martensitic. For the experimental build-up as well as the numerical reproduction the ground plate are heated to 200 °C. This temperature is almost reached during the intermediate cooling after every scanning step because of the high cooling rates. The martensite start temperature  $M_s$  of 1.4057 is quite above the pre-heating temperature of 200 °C, see Fig. 3. Consequently a layer wise transformation from austenitic to martensitic phase after each layer takes place for the martensitic steel.

There is a change of the face-centered cubic crystal structure to the body-centered tetragonal crystal structure during the transformation from austenitic to martensitic phase. The phase transformation results in an increase of the volume, like the dilatometer profiles in Fig. 4 visualizes. As a result the 1.4057 steel shows a compensation of the thermal shrinkage by the layer-wise phase transformation and the accompanied increase of the volume. The austenitic 1.4404 steel does not have this compensation effect which is why thermal shrinkage leads to the high tensile stresses and high distortion.

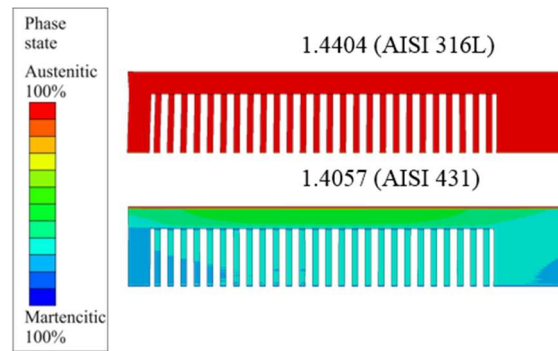


**Fig. 7** Volume fractions of austenite and martensite after scanning

As a conclusion the stress and strain condition of martensitic steels after build-up is strongly influenced by the phase transformation. The shrinkage strain of the material can be fully compensated if the process is characterized by a layer-wise transformation back from austenite to martensite. Numerical simulations of the build-up with a heating temperature of 300 °C during the process show an increased distortion of the 1.4057, similar to the 1.4404 material. In this case the  $M_s$  temperature and pre-heating temperature are almost identical. The transformation takes place in deeper layers or the whole part remains in austenitic phase until the process is completely finished. The missing layer-wise compensation of the shrinkage results in significant higher distortions.

## EXPERIMENTAL WORK

### HIGH-TEMPERATURE TESTING

For the investigation of the layer-wise shrinkage compensation thesis different cantilever build-ups were performed with another martensitic chrome steel. It is intended to evaluate if a high temperature influences the transformations and thus the distortion. This steel has a temperature interval for phase transformation between 200 °C and 300 °C. Because a high temperature build-up is quite costly, the preliminary studies were performed with standard SLM Solution 280 HL system with a 200 °C heating system. To reach higher temperatures the part is built on thin support walls to disturb heat dissipation and force an overheating of the component, see Fig. 8. When looking at the surfaces of the components, different surface colors becomes visible. The overheated sample looks dark discolored like an overhanging area. It could not be clarified directly whether these are tempering effects, but the color is a direct indicator for high process temperatures as the later performed high temperature build-ups show.

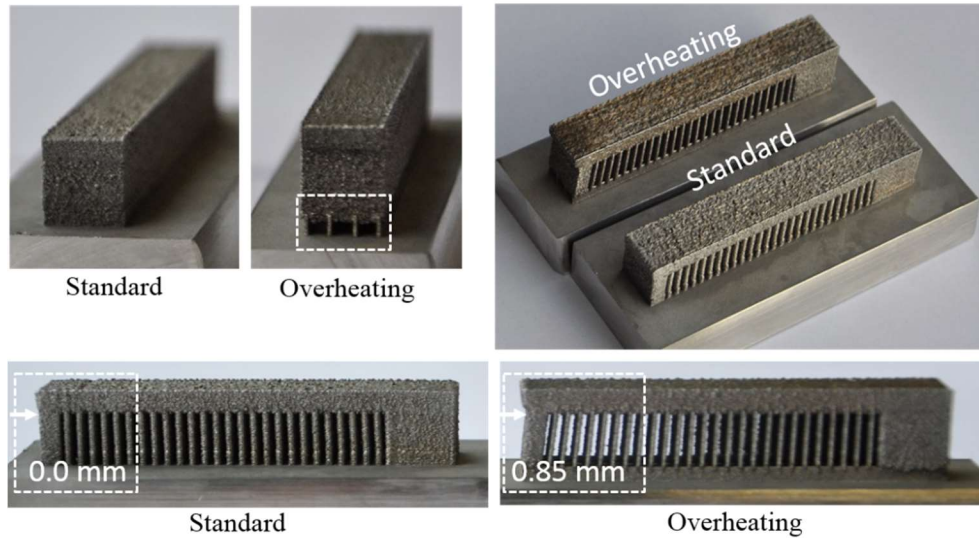


**Fig. 8** Cantilever specimen made of martensitic chrome steel. Different support structures were used to enforce heat accumulation due to disturbed heat conduction

Remarkable is the different distortion level of the samples. Even though the same material and parameters are used, the overheated sample shows a significant higher distortion. It is assumed that the degradation of the heat conduction leads to a heat accumulation of the sample almost above 300 °C and therefore above  $M_s$  temperature. The higher process temperatures prevent a layer-wise transformation as the standard sample indicates. As a result the overheated sample shows high distortion due to the not compensated shrinkage. Fig. 9 visualizes the measured upward displacement after separating the supports. Deviation of the distortion behavior can be observed.

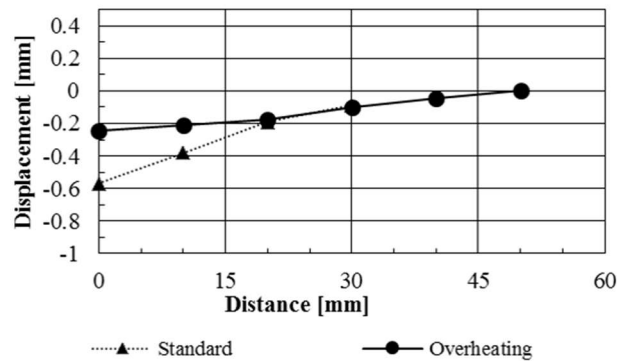


**Fig. 9** Measured upward displacement of the martensitic chrome steel cantilever samples

In order to compare the observed behaviour to the 1.4057 martensitic steel, further tests are performed with a SLM Solution 280 HL machine with a heating system until 650 °C. Samples are built with same parameters at pre-heating temperatures of 150 °C, 350 °C, 450 °C and 650 °C, see Fig. 10.

## Mathematical Modelling of Weld Phenomena 12

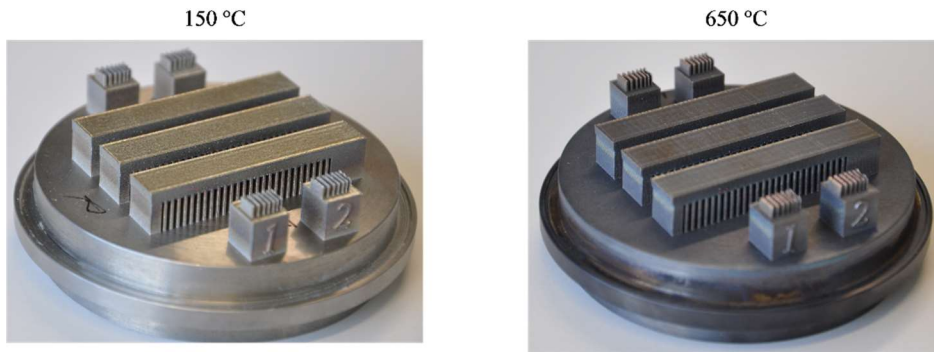


**Fig. 10** Cantilever specimen of 1.4057 built with different pre-heating temperatures and different colored surfaces

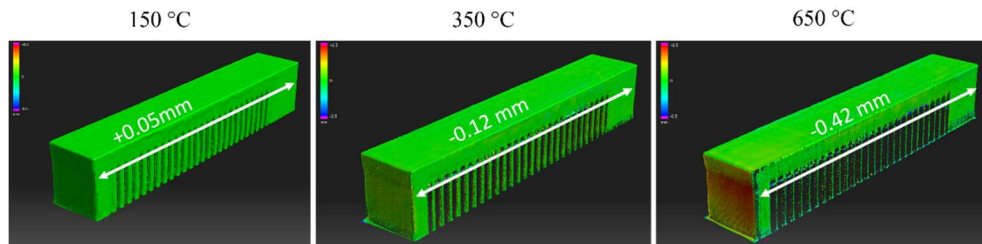


**Fig. 11** 3D-scanning results of cantilever specimen of 1.4057 with color map of the deviation to the reference geometry for different pre-heating temperatures

A three-dimensional scanning system is used for measuring and visualization of the distortion level, shown in Fig. 11. The 150 °C sample reveals a minimum distortion. With an increase of the temperature an increase of the shrinkage can be observed: The measurements of the longitudinal and upward displacement is represented in Fig. 12.

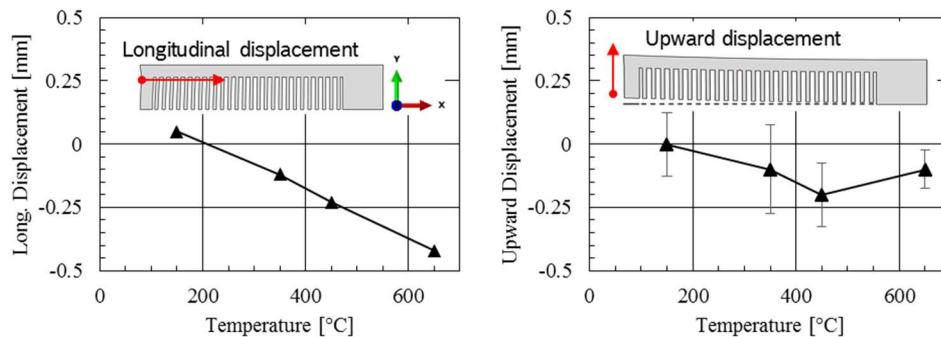


**Fig. 12** Distortion measurements of 1.4057 samples for different pre-heating temperatures

## HIGH-TEMPERATURE MATERIAL BEHAVIOUR

For a clear understanding of the material behavior of the martensitic steel 1.4057 next to the dilatometer experiments, tensile test at different temperature are performed on Gleeble machine [20], see Fig. 13. The specimens are pre-heated to 1350 °C close to solidus temperature for the complete austenitization. During cooling, the temperature is held at the respective temperature level and the tensile test is performed. The results show a significant decreased flow stress even at 200 °C. For the components these results indicate a significant reduction of the high stress peaks in the process caused by plastic deformation. Furthermore the events in lower temperatures ranges are of significant importance. That clarifies the influence of the phase transformation which occur in exactly this range.

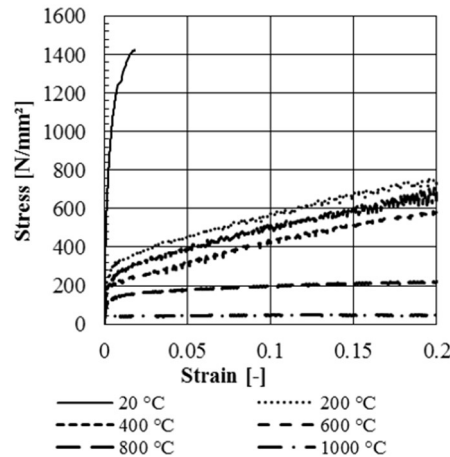


Fig. 13 Temperature dependent stress-strain properties of 1.4057 martensitic steel

## DISCUSSION

The experimental investigation with the cantilevers build-ups using different process temperatures confirms the thesis based on the macro simulation result. Higher temperature lead to a reduced effect of the layer-wise shrinkage compensation. It is assumed that the increased pre-heating temperature in combination with the heat accumulation caused by the laser power prevent the material from cooling down. The upper layers stay above  $M_s$  temperature and therefore in austenite phase. The transformation back to martensitic phase occurs later in the process with a layer delay. It is assumed that there is a dependency of the layer delay of the transformation to the process parameter as well as the pre-heating temperature. On average, the layer delay for the entire component is expected to remain constant if the heat transfer to the base plate is reasonably good due to sufficient amount of support structures.

NEW APPROACH FOR FAST SIMULATION CONSIDERING PHASE TRANSFORMATION

STATE OF THE SCIENCE

The new approach presented in this research work is based on the mechanical static FEM process model for the fast estimation of residual stresses and strains, also known as inherent strain method, introduced by [1-2].

A layer-wise finite element model is used to apply the inherent strain method on the additive manufacturing process. The build-up process is modeled by a layer-wise adding of the elements and the applying of the inherent strain tensor. The load of the strain tensor is modeled as a volume strain boundary condition. The simulation is performed at room temperature. The inherent strain tensor  $\varepsilon^{inh}$  represents the material condition in terms of the remaining plastic strain caused by the solidification and shrinkage process and is defined after Eqn. (2). In Eqn. (2),  $\varepsilon^t$  denotes the total strain,  $\varepsilon^E$  the elastic strain,  $\varepsilon^{pl}$  the plastic strain,  $\varepsilon^{pt}$  and  $\varepsilon^{cr}$  the transformation and creep strain. For simplification it is assumed, that after the process the thermal strain is equal to zero as well as the creep strain. In the current state of the science method also the transformation strain is neglected and set to zero, that finally the inherent strains  $\varepsilon^{inh}$  are the remaining plastic strains.

$$\varepsilon^{in} = \begin{pmatrix} \varepsilon_{xx} \\ \varepsilon_{yy} \\ \varepsilon_{zz} \\ \varepsilon_{xy} \\ \varepsilon_{yz} \\ \varepsilon_{zx} \end{pmatrix} = \varepsilon^t - \varepsilon^E = \varepsilon^{the} + \varepsilon^{pl} + \varepsilon^{pt} + \varepsilon^{cr} = \varepsilon^{pl} \quad (2)$$

The strain tensor  $\varepsilon^{in}$  can be calibrated for the specific process parameters of the build-up to be investigated. The calibration of the tensor is performed by the iterative comparison between the displacement of an experimental built standard cantilever beam and the calculated displacement by the numerical reproduction. The results of the inherent strain method show to some extent a dependency on the layer thickness and mesh, as well as the assigned strain and material [2]. An overview of the method is shown in Table 1.

**Table 1** Overview of the state of the science inherent strain method

Load application	Standard case	Applied material properties
Layer wise	$\varepsilon^{inh} = \begin{pmatrix} \varepsilon_x \\ \varepsilon_y \\ \varepsilon_z \end{pmatrix} = \varepsilon^{scan} (T_L \rightarrow T_{Rt})$ to be calibrated	Room temperature $T_{Rt}$

The main disadvantage of the state of the science inherent strain method is not considering the phase transformation strain  $\varepsilon^{pt}$ . Also the applied temperature is not taken into account which can lead to larger deviations at high temperatures. Therefore the method is only valid for austenitic steels and the applicability for martensitic steels is not given.

To ensure a reliable numerical prediction of the distortions for martensitic steels the phase transformation strain  $\varepsilon^{pt}$  have to be considered. The results of the thermo-mechanical simulation demonstrated the temporal occurrence of the phase transformation as the major influence on the mechanical behaviour. Even at pre-heating temperatures above  $M_s$  temperature a delayed transformation could be observed where only austenitic structure should be present. It is assumed that the heat convection with inert gas on the top surface and the heat conduction to the powder prevent a constant pre-heating temperature in the entire part and cause temperatures below pre-heating temperature. Hence, the process can be divided into three different cases in dependency of the pre-heating temperature, see Fig. 14. Case one represents a layer wise transformation for a pre-heating temperature that is significantly lower than the  $M_s$  temperature. In the second case, the heat accumulation supported by higher pre-heating temperature leads to a layer delay  $dn$  of the martensitic transformation. The third case is characterized by temperature field significant above the  $M_s$  temperature throughout the entire process as a result of a high pre-heating temperature. In this case, the phase transformation took place only at the end of the process during the final cooling of the component.

1. Layer wise transformation    2. Transformation with delay  $dn$     3. Post process transformation

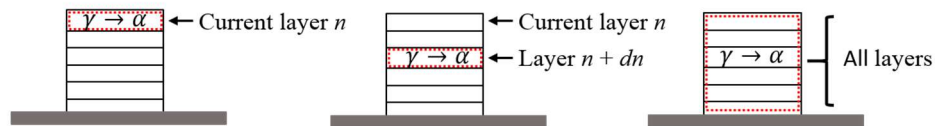


**Fig. 14** Different cases for the sequence of phase transformation during the process in martensitic steels

In a first model the inherent strain method has been extended by the additional phase transformation strain tensor  $\varepsilon^{pt}$ . The tensor  $\varepsilon^{pt}$  represents the increasing of the volume caused by the change of the lattice structure and is based on the dilatometer experiments, defined in Eqn. 3.

$$\varepsilon^{pt} = \begin{pmatrix} \varepsilon_x^{pt} \\ \varepsilon_y^{pt} \\ \varepsilon_z^{pt} \end{pmatrix} = 0.00325 \quad (3)$$

The application of the strain tensor  $\varepsilon^{pt}$  is taken place with a layer delay  $dn$  in parallel to the application of the standard inherent strain tensor  $\varepsilon^{in}$  in the current layer. A numerical series of tests were performed with a setup of  $\varepsilon^{in} = -0.003$  and a variation of the layer delay  $dn$  from 0 to 6. The results are shown in Fig. 15. The analysis shows that although the total amount of the applied strain is zero and both strains have the same size, the distortion can vary widely in dependency of the delay  $dn$ . Significant variables that characterize the process are the distortions in longitudinal direction before separating the support and the upward distortion after as already stated in the experimental investigations.

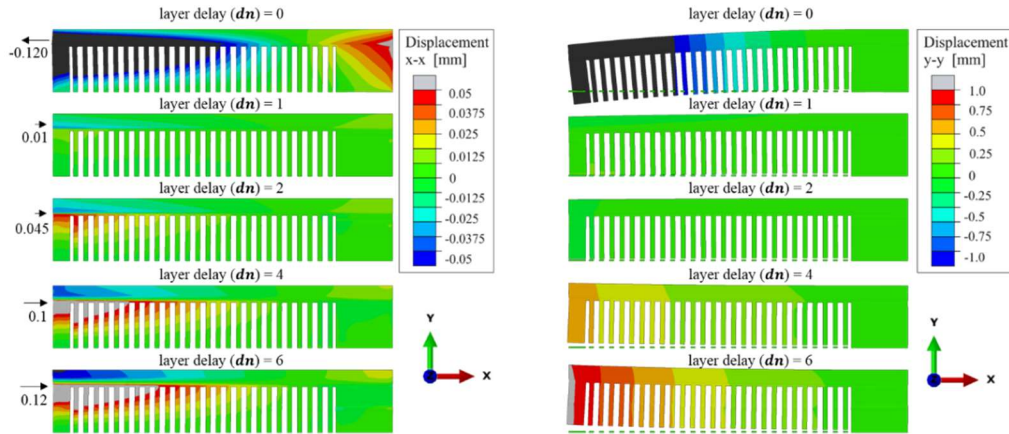


**Fig. 15** Numerical analysis of an extended inherent strain method with regard to a layer delayed volume increase due to martensitic phase transformation. Contour plots of distortion in x-direction before separating support (left) and distortion in y-direction after (right)

The numerical analysis was performed with the use of room temperature material properties. Exceeds the delay  $dn$  five layers, an upward displacement could be found. Because this is contrary to the experimental result is assumed that the high yield stress at room temperature prevent a plastic deformation of the material and thus the reduction of stress peaks. As a consequence, temperature-dependent flow curves are introduced in the model.

For another improvement of the quality of the results the strain tensor  $\varepsilon^{inh}$  is divided into different strain tensors  $\varepsilon^{scan}$  and  $\varepsilon^{cool}$ . The tensor  $\varepsilon^{scan}$  represents the layer-wise shrinkage due to the intermediate cooling from solidification temperature  $T_L$  to pre-heating temperature  $T_{Bt}$ . The tensor  $\varepsilon^{cool}$  denotes the shrinkage strain caused by the final cooling from pre-heating temperature to room temperature  $T_{Rt}$ .

Table 2 shows an overview of the final developed simulation procedure with three calculation steps. It is also listed which temperature the material properties are applied in the respective step.

**Table 2** Overview of the new approach of the inherent strain method for martensitic steels

Load application	New Approach	Applied material properties
Layer wise	Step 1: $\varepsilon^{scan} (T_L \rightarrow T_{Bt}) = \begin{pmatrix} \varepsilon_x \\ \varepsilon_y \\ \varepsilon_z \end{pmatrix}$ <i>to be calibrated</i>	Pre-heating temperature $T_{Bt}$
With layer delay ( $dn$ ) <i>to be calibrated</i>	Step 2: $\varepsilon^{pt}$ <i>to be calculated/ measured</i>	Pre-heating temperature $T_{Bt}$
Post process	Step 3: $T_{Bt} > T_{Mf} : \varepsilon^{cool1} (T_{Pt} \rightarrow T_{Rt})$ $T_{Bt} < T_{Mf} : \varepsilon^{cool2} (T_{Bt} \rightarrow T_{Rt})$ <i>to be calculated</i>	Room temperature $T_{Rt}$



## Mathematical Modelling of Weld Phenomena 12

The application of the new approach requires the following parameters to be known: The strain tensors  $\varepsilon^{scan}$ ,  $\varepsilon^{pt}$  and  $\varepsilon^{cool}$  as well as the delay  $dn$ . Those parameters can be classified in ones which have to be calibrated and ones which can be calculate or measured. Dilatometer experiment or a numerical reproduction are used to determine  $\varepsilon^{pt}$ . A numerical Satoh test modelling [21] is used to calculate the post process shrinkage  $\varepsilon^{cool}$ , see Fig. 16. A further distinction is made here whether the pre-heating temperature is above or lower than the middle phase transformation temperature  $T_{pt}$ .

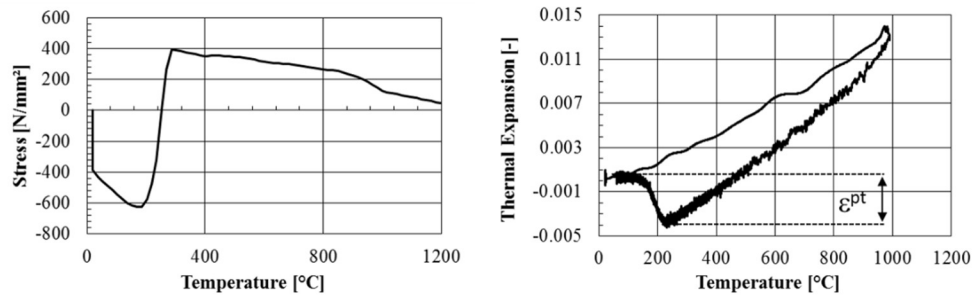


**Fig. 16** Satoh test modelling for calculation of  $\varepsilon^{cool}$  and dilatometer curve to determine  $\varepsilon^{pt}$

For the definition of the tensor  $\varepsilon^{scan}$  and the delay  $dn$  an iterative experimental calibration is used with a numerical reproduction in analogy to the state of the art method. In addition the longitudinal shrinkage  $U_{x-x}$  is measured before separating the supports as a second input variable for the calibration, next to the upward displacement  $U_{y-y}$ , see Fig. 17. With the two input variables it is possible to determine the missing parameters iteratively.

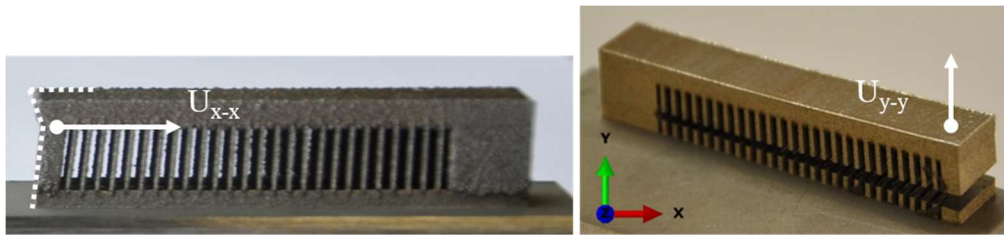


**Fig. 17** Definition of calibration input variables: Longitudinal shrinkage  $U_{x-x}$  (left) before separating and upward displacement  $U_{y-y}$  (right) after separating the support structures

In order to reduce the manual calibration effort, which can already time consuming with two parameters, an automated calibration is implemented, see Fig. 18. The calibration procedure is structured in a pre-processing stage and a parameter calibration stage.

## Mathematical Modelling of Weld Phenomena 12

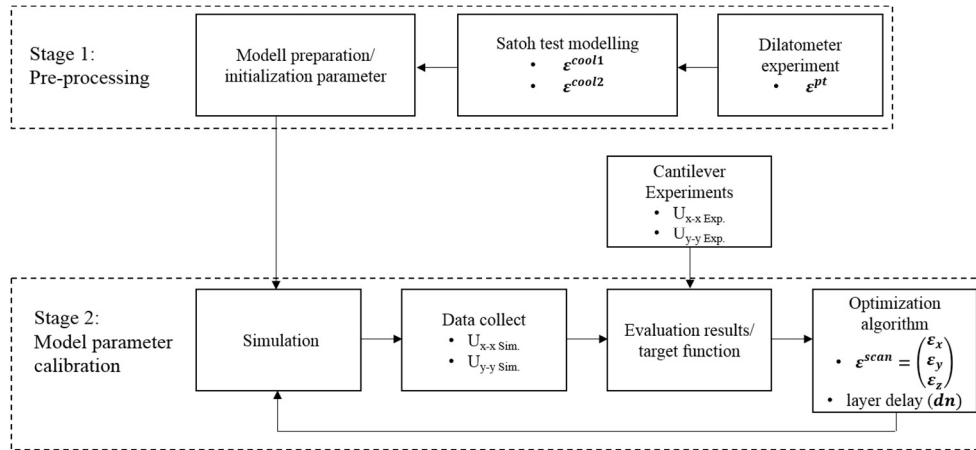


**Fig. 18** Visualization of the calibration procedure of the model parameters

Optimization algorithms are used for the iteratively calibration to reduce the calculation effort. In Eqn. 4 is shown the optimization problem, which have to be minimized to find the best solution for the tensor  $\epsilon^{scan}$  and the delay  $dn$  with the best agreement between simulation and experiment.

$$\arg \min f(\epsilon^{inh scan}, dn) = \arg \min |U_{Exp} - U_{Sim}| \quad (4)$$

Investigations of the fitness landscape have shown that the optimization problem can be of high complexity and multiple local minima can exist. In order to find best solution and therefore the global minimum, it is proposed to use hybrid optimization algorithm. Those optimization algorithm use a combined search existing of an “exploration” and “exploitation” part. In a first step is fulfilled a global search to explore the solution area. In a following step the promising optima is identified. In Fig. 19 is shown a contour plot of the fitness landscape for the optimization problem of the 150 °C pre-heating calibration with different local minima.

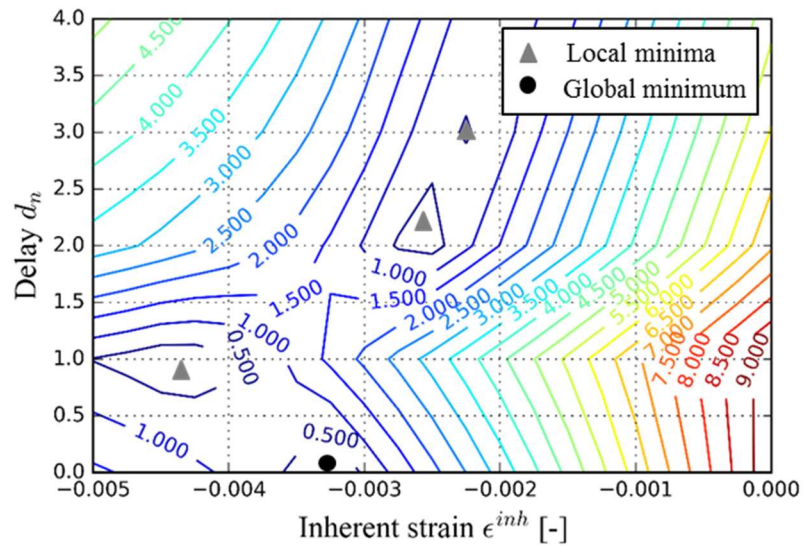


Fig. 19 Visualization of the fitness landscape  $f(\epsilon^{in\_scan}, dn)$  with different local minima

### SIMULATION RESULTS

In order to validate the developed approach over a wide temperature range, the cantilever build-ups at different pre-heating temperatures are repeated numerically. Table 3 lists the calibrated and applied parameters of the model for the different temperature levels. It can be stated that the strain tensor  $\epsilon^{scan}$  decreases with an increasing temperature. This observation is reasonable because the temperature interval from solidification to construction temperature  $T_L \rightarrow T_{Bt}$  is reduced relevant and therefore the shrinkage strain tensor  $\epsilon^{scan}$ . The delay  $dn$  of the transformation increases with an increase of the pre-heating temperature. However, the calibration showed that even for the 650 °C sample the third case could not be determined, classified in Fig. 14 and characterized with a complete post process phase transformation. The calibration however confirmed the increase in delay for higher temperatures. Because of the absence of temperature monitoring systems, the surface temperature in the process could not be determined experimentally. It is assumed, that the pre-heating system was unable to maintain the desired pre-heating temperatures with an increase in height of the specimen.

**Table 3** Overview of calibrated model parameters for different construction temperatures

Pre-heating temperature	150°C	350°C	450°C	650°C
$\epsilon^{scan}$	-0.00325	-0.0032	-0.00315	-0.00315
layer delay ( $dn$ )	0	2	4	Post process
$\epsilon^{pt}$	+0.00325	+0.00325	+0.00325	+0.00325
$\epsilon^{cool1}$	-0.00148	-	-	-
$\epsilon^{cool2}$	-	-0.001908	-0.001908	-0.001908

The results of the distortion  $U_{x-x}$  and  $U_{y-y}$  of the calibrated models are visualized as contour plots in Fig. 20. In comparison to the numerical analysis shown in Fig 15 even for higher transformation delays an upward displacement is not shown. These differences in behavior can mainly be attributed to the implemented temperature-dependent flow curves.

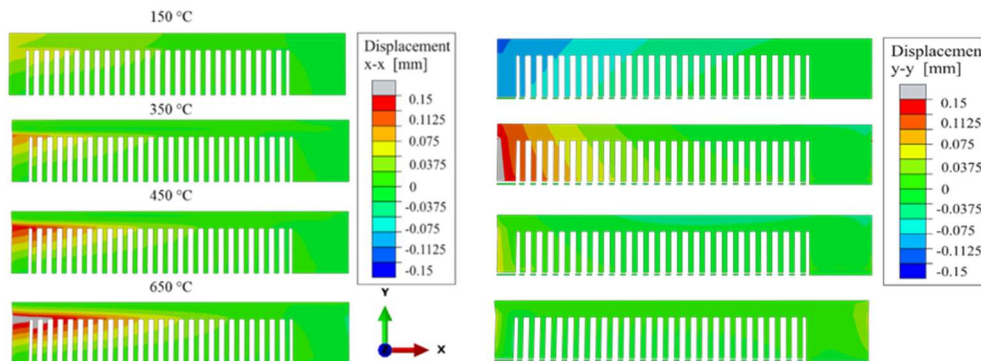


**Fig. 20** Contour plots of numerical distortion calculation with calibrated model parameters in x-direction before separating support (left) and distortion in y-direction after (right)

Fig. 21 represents the comparison of the experimental and simulated results. The values confirm a close correlation of the experiment and the numerical model at low and mid temperature levels. Only for the 650 °C larger deviations can be determined. The proportion of longitudinal shrinkage in the experiment is higher than in the simulation. In this case it is assumed that the real process temperature is significantly below the pre-heating temperature set and the applied material properties are not realistic. However, the simulation shows the same tendency of an increasing longitudinal shrinkage with rising construction temperatures.

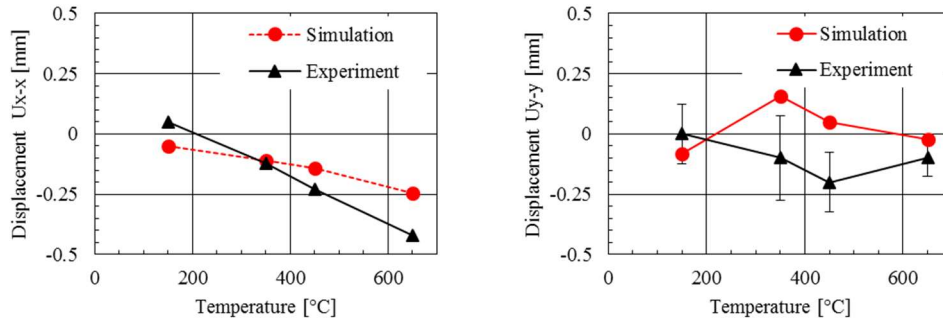


**Fig. 21** Validation of calculated distortion using the new approach with measured distortion of the cantilever

## DISCUSSION

The new developed approach allows for the first time the fast prediction of residual stresses and distortion for martensitic phase transformation steels. The results make clear that a calculation based on the state of the art inherent strain method is not suited for numerical calculation of accurate results for martensitic steels. However, the developed method is still a substitute model that does not represent all physical phenomena. The creep strain can have especially for high process times in combination with high temperatures a relevant influence. Because no temperature and temporal information is available the creep strain could not be considered. Despite the fact that no direct temperature information is available, temperature dependent material properties are introduced to take into account the reduced yield strength at high pre-heating temperatures. In this way the results could improve significantly. But this also increases the effort since the necessary properties have to be determined first.

The chronological sequence of the induced strains has proved to be significant for the quality of the results. This phenomenon should be considered by the segmentation of the standard shrinkage strain  $\varepsilon^{in}$  into the two different strains  $\varepsilon^{scan}$  and  $\varepsilon^{cool}$ . During development of the presented method a subdivision in even more single shrinkage strains has been investigated. Especially a first layer-wise strain from solidification temperature to pre-heating temperature  $\varepsilon_1^{inh}(T_L \rightarrow T_{Bt})$ , in combination with a second shrinkage strain from pre-heating temperature to the middle phase transformation temperature  $\varepsilon_2^{inh}(T_{BT} \rightarrow T_{Pt})$  applied layer delayed together with the transformation strain  $\varepsilon^{pt}$  and a third post process strain  $\varepsilon_3^{inh}(T_{PT} \rightarrow T_{Rt})$  was promising. Also this approach is based on two calibration parameters because the second strain  $\varepsilon_2^{inh}(T_{BT} \rightarrow T_{Pt})$  could be also calculated using a numerical Satoh test. However, the application of more strain tensors is prevented by the process temperature, because the current pre-heating systems are not able to maintain the adjusted pre-heating temperature within the entire specimen. Due to this uncertainty of the temperature, an even finer division is currently not useful for the current machines or without more detailed temperature information and is the restriction for the application of the developed model. The cantilever, which is used for the calibration, just reflects a standard condition with sufficient support structures and therefore an average heat

conduction. For a standard build-up such a condition with an average heat dissipation is intended, which distinguishes the cantilever to a representative sample. If the density of support structures varies widely, then as a consequence the heat dissipation and process temperature may also differ. In this case, a high-quality prediction is even more difficult because the phase transformations are generally initiated by the temperature.

The results confirm the importance of phase transformations for the mechanical behaviour of martensitic steels as already described in [14]. The investigation demonstrates that if the temperatures in the process kept below the middle phase transformation temperature the layer-wise shrinkage compensation enables an almost stress- and distortion-free component. The use of higher construction temperatures therefore should be reconsidered for the martensitic steels.

### SUMMARY AND OUTLOOK

In this research work a new method for the fast numerical prediction of process related residual stresses and distortion for martensitic phase transformation steels in selective laser melting is presented. The approach is based on the inherent strain method, which is further improved by the findings of a performed detailed coupled thermo-mechanical analysis and high temperature experiments. The investigated experiments and simulation indicated the increase of the volume caused by the transformation of austenitic face-centered cubic crystal structure into the martensitic body-centered tetragonal grain structure as a major influence parameter on the mechanical behaviour of the component. Especially the delay of the phase transformation is of great importance and is considered in the model. Another important influencing factor is the time sequence of the applied strains. Therefore the standard inherent strain tensor is distributed into different shrinkage strains. For the further improvement of the quality of the results also for an increased pre-heating temperature-dependent flow curves are introduced in the material model. The newly developed model was extended by one parameter to be calibrated, compared to the standard inherent strain method. Therefore, in addition to the upward deformation, the longitudinal shrinkage before the supports were cut off was introduced as an additional calibration input parameter.

For the following investigations the development of a new specimen for the characterization of the temperature condition in the component is planned. The thermally introduced phase transformation strains at  $M_s$  temperature could be used to analyse the process and machine specific temperature profile across the depths of the component. The presented approach is based on the assumption of a geometry-independent homogeneous heat dissipation. Geometry related hot spots caused by a reduced heat conduction are not taken into account. A further development of the presented method therefore could be the coupling to a fast numerical thermal analysis of the component. Areas with increased heat accumulation could be detected and the time sequence of the applied strains could be further refined for an improvement of accuracy of the numerical prediction.

## REFERENCES

- [1] N. KELLER, V. PLOSHIKHIN: ‘New method for fast predictions of residual stress and distortion of AM parts’, *Solid Freeform Fabrication Symposium*, 2014.
- [2] N. KELLER, J. SCHLASCHE, H. XU, V. PLOSHIKHIN: ‘Simulation Aided Manufacturing: Scanning Strategies for Low Distortion in Laser Beam Melting Processes’, *Fraunhofer Direct Digital Manufacturing Conference*, pp.3-6, 2016.
- [3] M. SCHAENZEL, D. SHAKIROV, A. ILIN, V. PLOSHIKHIN: ‘Development of a cracking criteria for the numerical failure prediction of support structures’, *Fraunhofer Direct Digital Manufacturing Conference*, 2018.
- [4] Y. UEDA, M.G. YUANG: ‘Prediction of Welding Residual Stresses in T and I joints Using Inherent Strains. Report 3’, *Welding International*, (6.4), pp.263-269, 1992.
- [5] Y. UEDA, M.G. YUANG: ‘Prediction of Residual Stresses in Butt Welded Plates Using Inherent Strains’, *Journal of Engineering Materials and Technology*, (115), pp.417-423, 1993.
- [6] Y. UEDA, H. MURAKAWA, N.X. MA: ‘Measuring Method for Residual Stresses in Explosively Clad Plates and a Method of Residual Stress Reduction’, *Journal of Engineering Materials and Technology*, (118), pp.76-582, 1996.
- [7] V. PLOSHIKHIN, A. PRIHODOVSKY, A. ILIN, C. HEIMERDINGER: ‘Advanced numerical method for fast prediction of welding distortions in large aircraft structures’, *International Journal of Microstructure and Materials Properties*, (5), pp.423-435, 2010.
- [8] V. PLOSHIKHIN, A. PRIHODOVSKY, T. FRANK, A. ILIN, D. BÄCHLE, P. KRAFT, C. HEIMERDINGER: ‘Schweißverzüge bei Großbauteilen verstehen und beherrschen’, *Tagungsband Große Schweißtechnische Tagung, DVS-Berichte Band 250*, pp.338-340, 2008.
- [9] V. PLOSHIKHIN, A. PRIHODOVSKY, T. FRANK, A. ILIN, C. HEIMERDINGER: ‘Advanced numerical method for fast prediction of welding distortions of large aircraft structures’, *Proc. 2nd International Conference Distortion Engineering IDE*, 491-498, 2008.
- [10] V. PLOSHIKHIN, A. PRIHODOVSKY, A. ILIN, C. HEIMERDINGER, F. PALM: ‘Beherrschung der Schweißverzüge bei Großbauteilen’, *Tagungsband Große Schweißtechnische Tagung, DVS-Berichte Band 258*, pp.104-107, 2009.
- [11] V. PLOSHIKHIN, A. PRIHODOVSKY, A. ILIN, C. HEIMERDINGER: ‘Advanced numerical method for fast prediction of welding distortions in large aircraft structures’, *International Journal of Microstructure and Materials Properties*, Vol. 5, Nos. 4/5, pp. 423-435, 2010.
- [12] A. PRIHODOVSKY, V. PLOSHIKHIN, A. ILIN, R. LOGVINOV, C. HEIMERDINGER, F. PALM: ‘Efficient numerical method for the prediction of welding distortions and its application to large aircraft structures’, *Mathematical Modelling of Weld Phenomena 9*, Verlag der Technischen Universität Graz, pp. 493-522, 2010
- [13] A. ILIN: *Methode zur effizienten FEM-Simulation der schweißprozessbedingten Deformationen von Großbauteilen*, thesis, University of Bremen, 2013.
- [14] M.SCHAENZEL, D.SHAKIROV, A. ILIN, V. PLOSHIKHIN: ‘Coupled thermo-mechanical process simulation method for selective laser melting considering phase transformation steels’, *International Journal of Computers & Mathematics with Applications*, to be published in 2018.
- [15] J. GOLDAK, A. CHAKRAVARTI, M. BIBBY: ‘A new finite element model for welding heat sources’, *Metallurgical Trans. B 15B*, pp. 299-305, 1984
- [16] D. KOISTINEN, R. MARBURGER: ‘A general equation prescribing the extent of the austenite-martensite transformation in pure iron-carbon alloys and plain carbon steels’, *Acta Metallurgica* 7, 1958
- [17] N. SAUNDERS, U.K.Z. GUO, X. LI ET AL.: ‘JOM 55: 60’, [Online] Available at: [www.doi.org/10.1007/s11837-003-0013-2](http://www.doi.org/10.1007/s11837-003-0013-2), 2003

- [18] DÖRRENBURG EDELSTAHL GMBH: 'Material data sheet 1.4057 X17CrNi16-2', [Online] Available at: [www.doerrenberg.de/uploads/tx\\_c1x1downloads/1.4057\\_de\\_01.pdf](http://www.doerrenberg.de/uploads/tx_c1x1downloads/1.4057_de_01.pdf), 2018
- [19] SIMULIA: *Abaqus analysis User's Manual, 2017*, Providence, Rhode Island, 2017
- [20] E. KARDOULAKI, J. LIN, D. BALINT, D. FARRUGIA: 'Investigation of the effects of thermal gradients present in Gleeble high-temperature tensile tests on the strain state for free cutting steel', *The Journal of Strain Analysis for Engineering Design*, Vol. 49, 2014
- [21] K. SATOH: 'Transient Thermal Stresses of Weld Heat-Affected Zone by Both Ends Fixed Analogy', *Transaction of the Japan Welding Society*, Vol. 3, No.1, 1972





# MULTI-SCALE MULTIPHYSICS SIMULATION OF METAL L-PBF AM PROCESS AND SUBSEQUENT MECHANICAL ANALYSIS

M. BAYAT\*, D. DE BAERE\*, S. MOHANTY\* and J. H. HATTEL\*

*\* Department of Mechanical Engineering, Technical University of Denmark, building 425, room 225, Lyngby, Denmark*

DOI 10.3217/978-3-85125-615-4-55

## ABSTRACT

In this paper, a multi-physics numerical model for multi-track-multi-layer laser powder bed fusion (L-PBF) process is developed and used for analysing the formation and evolution of porosities caused by lack of fusion and improper melting. The simulations are divided into two categories: first and foremost, a multi-physics thermo-fluid model in meso-scale, and second, a mechanical model based on the concept of a unit cell. The thermo-fluid model is used to track and observe the formation of the porosities, and considers phenomena such as multi-phase flow, melting/solidification, radiation heat transfer, capillary and thermo-capillary (Marangoni effect) forces, recoil pressure, geometry dependant absorptivity, and finally evaporation and evaporative cooling. The results for the investigated process parameters indicate that the porosities are mainly formed due to improper fusion of the particles. The probability of presence of pores is also observed to be higher in the first layers. Moreover, the lack of fusion zones are seen to become smaller in the subsequent layers, largely due to better fluid flow and higher temperatures in those layers. Based on the porosity levels determined from the thermo-fluid model, a unit cell mechanical model with an equivalent amount of porosity has been made and subsequently subjected to loading for analysing the part's mechanical behaviour. The unit cell results show that an increase in the porosity can highly affect and deteriorate the part's elastic modulus and its yield strength, as well. The combination of the thermo-fluid and the mechanical unit cell model establishes a direct link between process parameters and mechanical properties for L-PBF.

Keywords: process-property correlation, multi-physics model, thermo-fluid model, multi-layer L-PBF, porosity formation, unit cell approach.

## INTRODUCION

Laser powder bed fusion (L-PBF) method, is categorized as a metal additive manufacturing process [1], where the metallic parts are produced in a layer-wise manner. A simple view of a typical L-PBF machine is shown in Fig. 1. In this process, first a layer of fine spherical metallic particles, whose diameters typically span from approximately 10  $\mu\text{m}$  to 60  $\mu\text{m}$  [2], is distributed on a base plate (which in turn is attached to a build platform) by means of a controllable coating mechanism. Then, the laser starts scanning predefined locations based on the data provided in the CAD files [3]. While the laser scans these zones, the fine metallic particles will get coalesced together, either by being sintered or fully-molten, depending on the intensity of the laser power. After the first layer is shaped, the build platform moves

down and another layer of powder is laid down. Subsequently, the powder feeding and laser scanning continues until the whole part is manufactured [4].

L-PBF has many advantages over the conventional production methods (e.g. Casting, milling, etc) and outweighs them in certain areas such as design freedom, material waste, manufacturing time, etc [5]. However, some of the parts that are manufactured by this process, still suffer from major defects, such as, denudation zones [6], keyhole porosities [7], surface porosities [8] and voids [9].

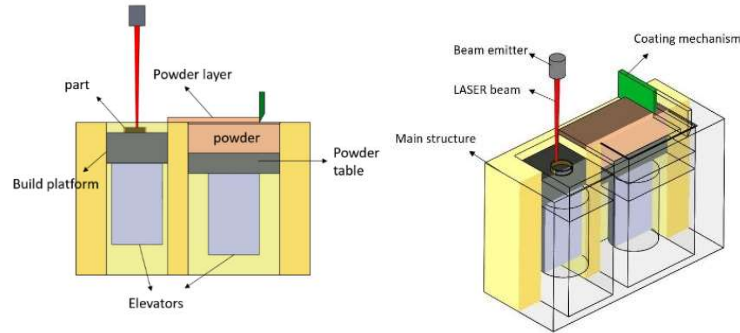


**Fig. 1** L-PBF machine along with its components; (left) cross section and (right) 3-D views.

Depending on the range of the processing parameters (e.g. scanning speed, laser power, hatch distance, etc), the shape and dimensions of the defects might differ considerably. For example, low linear energy density (LED) can result in surface defects as well as lack of fusion zones with unsintered particles [8]. Adoption of high LED levels causes overheated sites that ultimately lead to internal metallurgical or keyhole voids [10].

In the recent years, advanced online monitoring systems have been developed for analysing the thermal maps [11], the solidification time as well as the keyhole evolution [12] during the L-PBF process. However, these research methods, depending on their illumination source and degree of complexity, can either be highly expensive or constitute high safety risks [13].

In the current scenario, developing a multi-physics numerical model for L-PBF process that can predict the evolution of the internal pores can improve the predictability of the process to a large extent. From a numerical point of view, L-PBF contains many physical phenomena, such as: evaporation, melting/solidification, thermal radiation, laser absorption, liquid metal flow, recoil pressure, etc. Numerical models have been developed to address these phenomena, and depending on the complexity and governing physics, they can be categorised into thermal models [14]–[16], thermo-fluid models [17]–[19], thermo-microstructural models [20], [21] and thermo-mechanical models [22]. In particular, thermo-fluid models are best suited for observing the formation and evolution of porosity during the laser powder bed fusion process. Such information regarding the distribution of voids/pores can further be utilized to predict the mechanical response of the corresponding parts through the representative volume element and unit cell methods. Accordingly, by means of these approaches, one might be able to investigate the effect of different patterns of voids or added elements on the overall mechanical response of the parts [23], [24].

In this paper, a multi-physics numerical model for the L-PBF process has been developed which covers multi-phase flow, solidification/melting, evaporation, recoil pressure,

capillary forces, Marangoni effect, buoyancy effect, ray tracing method, radiation and flow in porous medium. The formation of lack-of-fusion defects during the multi-track and multi-layer L-PBF process has been investigated using said model. Moreover, to simulate the actual stochastic distribution of powder layers, a discrete element method (DEM) has been implemented that tracks the position of the powder particles during the powder-feeding step. To consider the effects of surface elevation of the previous sintered/fused layers on the current powder layer's distribution, the results of thermo-fluid simulation of each layer have been exported as CAD data for usage in the DEM simulations. Eventually, the calculated porosity level for all layers has been used to make an equivalent unit cell to study the effect of the porosity on the mechanical behaviour of the samples. An image analysis has been performed on the fluid fraction data to calculate the porosity levels needed for unit cell model.

### NUMERICAL MODEL

During the L-PBF process, usually a relatively high amount of power (50-1000 W) [2] is concentrated on a small surface area, which can easily melt down and even evaporate the powder layer. Physical phenomena such as recoil pressure, capillary and thermo-capillary forces prevail in those harsh conditions and highly affect the material's flow behaviour. To determine the temperature field and observe the material's flow inside the melt regions, it becomes necessary to solve the coupled partial differential equations of balance of mass, linear momentum and energy together. This has been implemented in the thermo-fluid model developed using the commercial software Flow-3D, which in-turn is based on the finite volume method (FVM). Moreover, to better simulate the thermal interaction between laser rays and the fluid (powder and base metal), a ray-tracing method along with a geometry-dependant absorptivity has been implemented. In the following section of the paper, the governing equations for the thermo-fluid model are first described and a detailed description about the laser-material model is also given. Subsequently, the mechanical model for analysing the material behaviour with the unit cell approach and its governing equations are described. The mechanical model has been implemented on the commercial software ABAQUS version 6.16 which works based on the finite element method.

### GOVERNING PHYSICS: THERMO-FLUID MODEL

#### *Fluid flow motion*

The computational domain is divided into two immiscible phases i.e. the ambient air and the metal regions (labelled as void and fluid respectively). Several methods are available in literature to track the free surface of each phase, such as level-set [25], phase field and volume of fluid (VOF) [26] in a fixed mesh (Eulerian framework) approach and Stephan's problem in a moving mesh (Lagrangian framework) approach. In this work, the VOF method has been used for tracking the phase interface. According to the VOF method, the mass balance equation for two-phase flow can be expressed as [26]:

$$\frac{\partial}{\partial t}(\alpha_F \rho_F) + \vec{\nabla} \cdot (\alpha_F \rho_F \vec{V}) = -\dot{m}_{lv} \quad (1)$$

where the subscript  $( )_F$  stands for the fluid phase,  $\rho$  ( $\frac{\text{kg}}{\text{m}^3}$ ) is the density and  $\dot{m}_{lv}$  ( $\frac{\text{kg}}{\text{m}^3 \cdot \text{s}}$ ) is the volumetric rate of mass loss by evaporation.  $\alpha_F$  shows the volume fraction of the fluid phase. To solve equation (1), it is necessary to fulfil the condition that the summation of volume fractions of all present phases equals unity:

$$\alpha_F + \alpha_V = 1 \quad (2)$$

where the subscript  $( )_V$  demonstrates the void phase. This condition also holds an important physical meaning that the cells must not become empty of a medium.

To determine the pressure-velocity field, the system of equations of balance of linear momentum should be solved along with (1) and (2):

$$\rho \left[ \frac{\partial}{\partial t}(\vec{V}) + \vec{\nabla} \cdot \vec{V} \vec{V} \right] = -\vec{\nabla} P + \vec{F}_s + \vec{F}_V + \vec{F}_\theta \quad (3)$$

where  $V$  is the velocity vector and the two vectors  $\vec{F}_s$  and  $\vec{F}_V$  stand for the volumetric forces caused by the spatial variation in fluid stress tensor and solidification drag forces based on Darcy's law for porous medium [27]. The vector of the volumetric forces caused by the spatial variation in internal stresses is defined as:

$$F_s = \nabla \cdot [\tau_{ij}] \quad (4)$$

where  $[\tau_{ij}]$  is the internal stress tensor and is defined as:

$$\tau_{ij} = 2\mu \left[ \frac{1}{2}(V_{i,j} + V_{j,i}) - \frac{1}{3}\delta_{ij} V_{k,k} \right] \quad (5)$$

where  $\delta_{ij}$  is the delta Dirac function. The last term in equation (5) will diminish due to the incompressibility of the present fluid. Since the flow is two-phase, the average values for viscosity and density are used, defined by means of a simple mixing rule:

$$\mu = \alpha_F \mu_F + \alpha_V \mu_V \quad (6)$$

$$\rho = \alpha_F \rho_F + \alpha_V \rho_V \quad (7)$$

To model the moving solidification front, the volumetric forces are defined to be highly dependent on the liquid fraction of the fluid. These forces, also called the solidification drag forces, are supposed to free and freeze the fluid flow depending upon the fluid liquid fraction [28]:

$$\vec{F}_V = -c \frac{(1-f_l)^2}{B+f_l^3} \cdot \vec{V} \quad (8)$$

where  $c \left[ \frac{\text{kg}}{\text{m}^3 \cdot \text{s}} \right]$  and  $B [-]$  are the Karman-Cozeny constants, which, depending on the application, are in the range of  $10^5 - 10^7$  and  $10^{-5} - 10^{-3}$  respectively. Interestingly, the solidification drag forces, according to equation (8), are in the opposite direction of the velocity vectors. Thus, a decrease in liquid volume fraction dramatically increases these forces to an extent that is sufficiently high to freeze the fluid motion.

The last term in equation (3) is the volumetric force which is being imposed on the fluid due to the buoyancy effect. In this work, since the flow is assumed to be incompressible, the Boussinesq approximation is used for calculating the buoyancy force:

$$F_\theta = \rho g \beta (T - T_l) \quad (9)$$

where  $\beta \left( \frac{1}{\text{K}} \right)$  and  $T_l$  are the expansion coefficient and the fluid's liquidus temperature, respectively, and  $g \left( \frac{\text{m}}{\text{s}^2} \right)$  is the gravitational acceleration.

#### *Heat transfer and solidification*

The energy balance equation is applied to the computational domain and subsequently coupled to the velocity field, to find the temperature field and the fluid's fusion condition (liquid or solid state):

$$\rho \left[ \frac{\partial(H)}{\partial t} + \vec{V} \cdot \vec{\nabla} H \right] = \vec{\nabla} \cdot (k \vec{\nabla} T) - \dot{q}'''_{evap}. \quad (10)$$

where  $\dot{q}'''_{evap} \left( \frac{\text{W}}{\text{m}^3} \right)$  is the volumetric heat sink due to the evaporative cooling of fluid and  $H \left( \frac{\text{kJ}}{\text{kg}} \right)$  is called the sensible enthalpy that can be expressed as:

$$H = h_{ref} + \int_{T=T_{amb}}^T C_p dT + f_l \Delta H_{sl}, \quad (11)$$

where  $h_{ref} \left( \frac{\text{kJ}}{\text{kg}} \right)$  and  $\Delta H_{sl} \left( \frac{\text{kJ}}{\text{kg}} \right)$  stand for the reference specific enthalpy of the fluid and the latent heat of fusion, respectively. The enthalpy-porosity method, which has been widely used for melting/solidification modelling [29], is also used in this study. It is assumed that, for the current metal, liquid volume fraction is a linear function of temperature during the solidification interval:

$$f_l = \begin{cases} 0 & , T < T_s \\ \frac{T-T_s}{T_l-T_s} & , T_s < T < T_l \\ 1 & , T_l < T. \end{cases} \quad (12)$$

Since the problem is assumed to be a multi-phase flow, the average sensible enthalpy is used in the heat balance equation, which can be determined by a mixing rule as:

$$H = \frac{\rho_F \alpha_F H_F + \rho_V \alpha_V H_V}{\rho_F \alpha_F + \rho_V \alpha_V} \quad (13)$$

*Recoil, capillary and thermo-capillary forces*

During the L-PBF and welding processes, since high-density heat fluxes are imposed on the fluid's surface, elevated temperatures are attained which cause the material to boil and evaporate. The vaporization of the metal will impart a negative force against the fluid surface, largely due to momentum balance with the escaping vaporized metal, called as the recoil pressure which in extreme cases can even lead to formation of deep keyholes. On the other hand, localized elevated temperature fields will cause large thermal gradients which will subsequently result in thermally-induced shear stresses on the exposed surfaces of the fluid (Marangoni effect). Furthermore, due to the large deflections of the fluid surfaces, capillary forces are also dominant and can affect the fluid motion, especially on the places where big curvatures are formed.

In principal, the saturation pressure of a fluid can be determined by means of thermodynamic relations and equations of state. However, empirical correlations can also be used to find the saturation pressure with a good accuracy, such as the Clausius-Clapeyron equation:

$$P_{sat}(T) = P_{atm} \exp \left[ \frac{\Delta H_{lv}}{C_v(\gamma-1)} \left( \frac{1}{T_g} - \frac{1}{T} \right) \right], \quad (14)$$

where  $P_{atm}$  and  $T_g$  in equation (14) are the atmospheric pressure and the fluid's saturation temperature (boiling temperature) at this pressure, respectively.  $\Delta H_{lv}$  ( $\frac{\text{kJ}}{\text{kg}}$ ) is the latent heat of vaporization and  $C_v$  ( $\frac{\text{kJ}}{\text{kg.K}}$ ) is the specific heat capacity of vaporized fluid at constant volume. There have been a number of investigations on the recoil pressure, and in this study the recoil pressure is assumed to be a function of saturation pressure [30]:

$$P_{recoil}(T) = 0.54 P_{sat}(T), \quad (15)$$

The recoil pressure will thus increase exponentially with increase in temperature beyond the boiling point. According to the statistical thermodynamics, the evaporative mass rate can be approximated as [18]:

$$\dot{m}_{lv} = A_{acom} \cdot \sqrt{\frac{M}{2\pi\bar{R}T}} \cdot P_{sat}(T), \quad (16)$$

where  $A_{acom}$  and  $\bar{R}$  ( $\frac{\text{kJ}}{\text{kmole.K}}$ ) are the accommodation coefficient and the universal gas constant respectively. The thermally-induced shear stresses can be expressed as:

$$\tau = -\vec{\nabla}_s T \cdot \frac{d\sigma}{dT}. \quad (17)$$

## Mathematical Modelling of Weld Phenomena 12

In equation (17),  $\vec{\nabla}_s T \left( \frac{K}{m} \right)$  shows the planar (tangent to the interface) temperature gradient of the fluid and  $\frac{d\sigma}{dT} \left( \frac{N}{m.K} \right)$  represents the temperature dependency of the surface tension. Furthermore, as mentioned before, since the fluid surface might not be smooth, the capillary forces are also present:

$$P_{cap} = \sigma \cdot \kappa. \quad (18)$$

In equation (18),  $\sigma \left( \frac{N}{m} \right)$  and  $\kappa \left( \frac{1}{m} \right)$  are the surface tension between the two phases and the curvature of the free surface respectively. From a mathematical point of view, the mentioned triple forces can be expressed in a single vector form as:

$$F_{V/F} (Pa) = [P_{recoil} + \sigma \cdot \kappa] \vec{n} - [\vec{\nabla} T - \vec{n}(\vec{\nabla} T \cdot \vec{n})] \frac{d\sigma}{dT} \quad (19)$$

According to equation (19), the recoil and capillary effects act as a jump in the pressure on the void/fluid interface and are always normal to the free surface [31]. On the other hand, the thermally-induced shear stresses, as can be seen on the right side of equation (19), are tangent to the free surface. Also, depending on the sign of temperature dependency of the surface tension, the flow might be driven radially outward or inward.  $\vec{n}$  is the void/fluid interface normal vector and is calculated as:

$$\vec{n} = \frac{\vec{\nabla} \varphi}{|\vec{\nabla} \varphi|} \quad (20)$$

where  $\varphi$  is a scalar function which shows the elevation of the void/fluid interface. The curvature mentioned in equation (20) can be determined by:

$$\kappa = - \left[ \nabla \cdot \left( \frac{\vec{n}}{|\vec{n}|} \right) \right] = \frac{1}{|\vec{n}|} \left[ \left( \frac{\vec{n} \cdot \vec{\nabla}}{|\vec{n}|} \right) |\vec{n}| - (\vec{\nabla} \cdot \vec{n}) \right] \quad (21)$$

The mentioned forces are all imposed on the  $\Omega$  boundary, shown in Fig. 2, along with the imposed thermal boundary conditions.



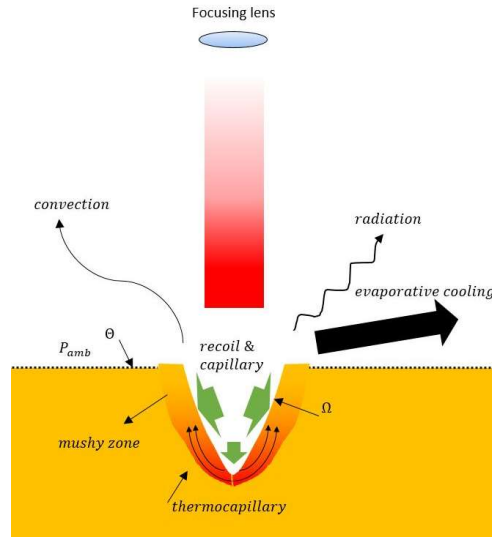


**Fig. 2** Schematic view of the recoil pressure, capillary and thermo-capillary forces along with the thermal boundary conditions on the  $\Omega$  boundary.

Fig. 2 also shows an overall view of the present boundary conditions, where the top boundary is assumed to be a pressure outlet boundary condition, and set to ambient atmospheric pressure allowing both phases to escape the control volume if necessary.

Furthermore, the laser also irradiates the interface, so the thermal boundary condition on this layer can be expressed as:

$$-k \frac{\partial T}{\partial \vec{n}} + \varepsilon \sigma (T_{amb}^4 - T^4) + h_{amb} (T_{amb} - T) + Q''_{i,j} = 0 \quad (22)$$

where  $\varepsilon$  and  $\sigma \left( \frac{W}{m^2.K^4} \right)$  are the fluid's surface emissivity and the Stephan-Boltzmann constants respectively.  $h_{amb} \left( \frac{W}{m^2.K} \right)$  stands for the convective heat transfer coefficient of the void.  $Q''_{i,j}$  in equation (22) is the heat flux of the laser ray "i" after "j" number of recorded collisions.

### *Laser-material interaction*

Depending on the application, there are several ways to model the effect of the laser on the thermal behaviour of the material, such as moving point source, moving heat flux, moving volumetric heat source, equivalent moving volumetric heat source based on optical penetration depth (OPD) and finally ray tracing method. In this work, to better simulate the actual laser-material interaction, the ray-tracing method, along with a geometry-dependent absorptivity, are used. The laser heat flux, which is being emitted from the focusing lens shown in Fig. 2, is assumed to have a planar Gaussian distribution with the following mathematical function:

$$q''_{laser}(x, y) = \frac{2P}{\pi R^2} \exp\left(-\frac{2((x - x_{las})^2 + (y - y_{las})^2)}{R^2}\right), \quad (23)$$

where  $R$  is the beam radius and  $x_{las}, y_{las}$  show the position of the moving laser beam. Depending on the resolution of the computational domain, the analytical expression of the heat flux in equation (23) will be divided into a number of smaller parts while retaining the total beam energy. For each incident ray “ $i$ ”, the new direction of the reflected rays  $\vec{e}_{i,j+1}$  for the “ $j$ ” th collision is determined based on the ray-tracing method as follows:

$$\vec{e}_{i,j+1} = \vec{e}_{i,j} - 2(\vec{e}_{i,j} \cdot \vec{n}_{i,j})\vec{n}_{i,j} \quad (24)$$

The absorptivity of the laser ray at each collision is then assumed to be a geometry-dependant cosine function of the incident angle in this work..

#### GOVERNING PHYSICS: MECHANICAL MODEL

The equilibrium equation is the principal governing partial differential equation which defines the relationship between the applied forces and the material’s mechanical response,

$$\nabla \cdot \sigma_{ij} = 0, \quad (25)$$

where  $\sigma_{ij}$  is the stress tensor in equation (25). The total strain tensor  $\varepsilon_{ij}^{tot}$  can be decomposed into elastic and plastic parts:

$$\varepsilon_{ij}^{tot} = \varepsilon_{ij}^{el} + \varepsilon_{ij}^{pl}, \quad (26)$$

where  $( )_{el}$ ,  $( )_{pl}$  are subscripts standing for elastic and plastic behaviour respectively. The elastic strain is calculated based on the general Hooke’s law:

$$\sigma_{ij} = \frac{E}{1+\nu} \left[ \frac{1}{2} (\delta_{ik}\delta_{jl} + \delta_{il}\delta_{jk}) + \frac{\nu}{1-2\nu} \delta_{ij}\delta_{kl} \right] \varepsilon_{kl}^{el}. \quad (27)$$

where  $E$  (Pa) and  $\nu$  are elastic modulus and Poisson’s ratio, respectively. The J2 flow theory defines the mechanical behaviour of the material in the plastic zone. The corresponding plastic strain increment is calculated as:

$$\dot{\varepsilon}_{ij}^{pl} = \frac{9}{4} \left[ \frac{1}{E_t} - \frac{1}{E} \right] \frac{s_{kl}\dot{\sigma}_{kl}}{\sigma_e^2} s_{ij}. \quad (28)$$

where  $E_t$  (Pa) is the tangent modulus of the material,  $s_{ij}$  is the deviatoric stress tensor and  $\sigma_e$  is the equivalent Mises stress.

$$s_{ij} = \sigma_{ij} - \frac{1}{3} tr(\sigma_{ij}), \quad (29)$$

$$\sigma_e = \sqrt{\frac{3}{2} s_{ij} s_{ij}} \quad (30)$$

METHODOLOGY

As already discussed in the introduction, the L-PBF process consists of two primary steps, namely powder-laying and fusion. In this work, to determine the position of the solid particles during the powder-laying step, a discrete element method (DEM) is used, as shown in Fig. 3. After the DEM simulation, the CAD file containing the laid powder layer is extracted by an in-house code and imported as a fluid region into the thermo-fluid model (fusion model). After the thermo-fluid calculations, the CAD file of the fluid region, along with its stored thermal data, are extracted and the former is fed to the next powder-laying calculation model where it serves as a solid wall with a prescribed restitution coefficient. The latter is used as the initial thermal and fluid boundary condition for the next thermo-fluid (fusion) model. This procedure is repeated for three layers.

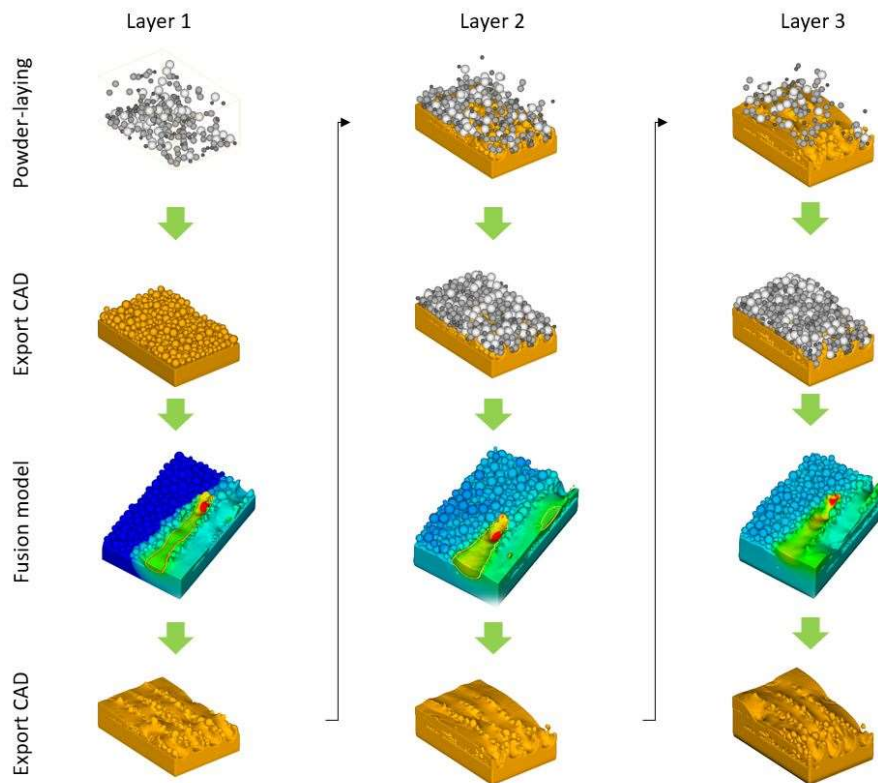


**Fig. 3** The methodology used for the powder-laying and fusion calculations.

To assess the influence of the lack-of-fusion induced porosities on the mechanical behaviour of the manufactured samples, a unit cell approach is implemented in this work. This unit cell method is used to study the effect of porosities on both the yield stress and

the elastic modulus of the samples. First, several cross-sections are made from the 3D CAD geometry extracted from the thermo-fluid model, and the section contours (showing the value of fluid fraction) are transformed into monochromic images. Subsequently, the images are processed by a numerical code developed to determine the amount of porosity in these cross-sections.

Next, a simplified unit cell geometry, i.e. a square with 500  $\mu\text{m}$  edge length, is constructed with a hole (equivalent to the determined porosity) in the middle of the sample. This unit cell is then subjected to the mechanical boundary conditions and loads shown in Fig. 4. The left and bottom boundaries are x-symmetry and y-symmetry respectively, while a uniform x-displacement is imposed on the right boundary in an incremental manner. While the cell is being loaded, the average force on the right boundary is determined. At the same time, the average strain is also calculated, which is defined as the ratio of the x-displacement to the characteristic length of the unit cell.

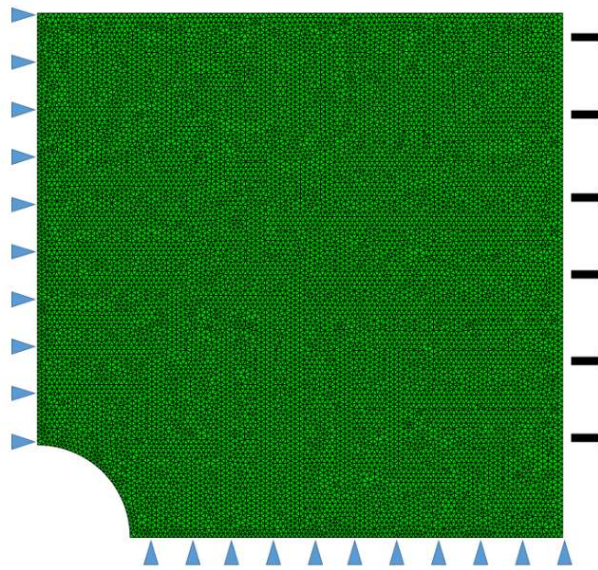


Fig. 4. Mechanical boundary conditions for the unit cell.

## RESULTS AND DISCUSSIONS

### THERMAL FIELDS AND FLUID FLOW

The process parameters and the laser specifications used in this study are all gathered in Table 1. The temperature field during the scanning of first layer along with the melt region are both shown in Fig. 5 for different times.

**Table 1** Process parameters for the multi-layer simulation

Parameter	Value	Parameter	Value
Hatch spacing	100 $\mu\text{m}$	Scanning speed	1600 mm/s
Beam size	60 $\mu\text{m}$	Layer thickness	40 $\mu\text{m}$
Beam power	150 W	Scan length	1000 $\mu\text{m}$

According to Fig. 5 (a), the maximum temperature zone is formed very close to the centre of the moving laser beam. At 400  $\mu\text{s}$ , most of the powder and base-plate are still at their initial temperature of 300 K. Due to the relatively high scanning velocity of the laser and the presence of air between the powders, the flow (propagation) of the heat in the transverse direction is much slower. On the other hand, the thermal resistance of the material (at  $t > 300 \mu\text{s}$ ) on the right side of the scanning beam, is much lower than that of the unmelted powders due to the dense morphology of the metal.

The melt region contour during the scanning of the first layer is also shown in Fig. 5 (b). At  $t = 860 \mu\text{s}$ , it can be clearly observed that the melt region of the two neighbouring tracks do not reach each other and accordingly, lack of fusion sites and unsintered particles are formed between the tracks.

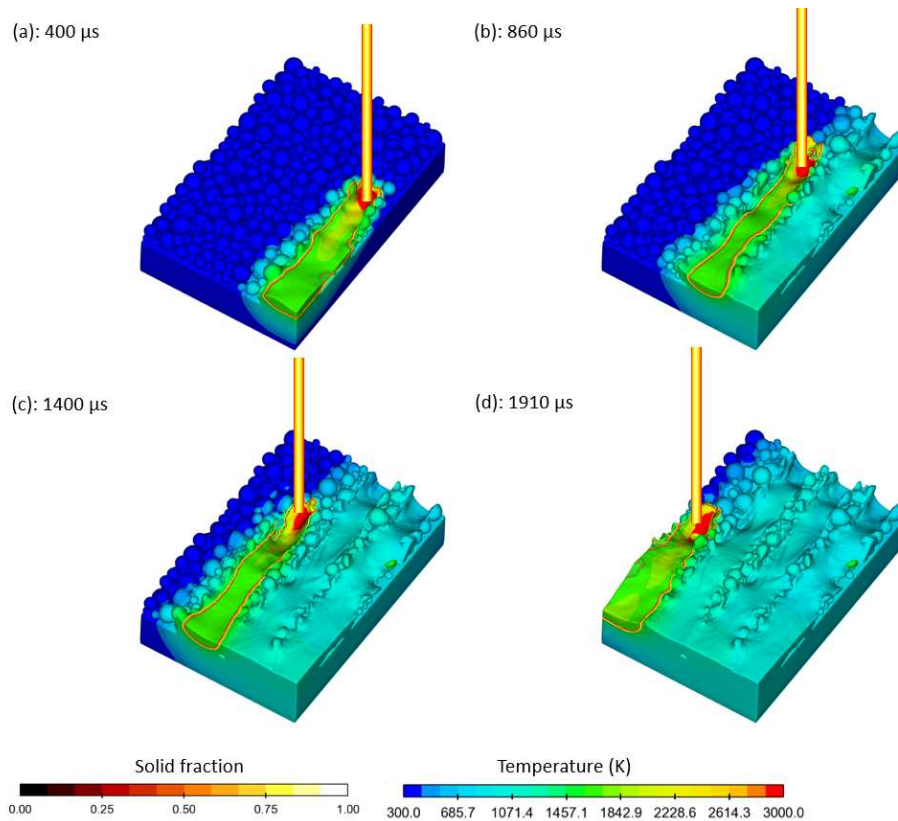


**Fig. 5** Thermal field and melt region during the scanning of the first layer of the powder.

Corresponding to Fig. 5 (c) at  $t = 1400 \mu\text{s}$ , a hole is formed close to the position of the centre of the laser beam. When the temperature in the region goes above the saturation temperature of the metal, the recoil pressure becomes dominant, pushes the deformable liquid down and makes a keyhole. The size of the keyhole increases with further increase in temperature due to greater recoil pressure.

The melting of powder particles during L-PBF is caused either via direct contact with the laser rays or via contact with a hot return flow formed due to the negative pressure gradient present on the fusion front. Starting with the former pathway, when the laser irradiates the powder for the first time, the powder begins to melt, as observed in Fig. 6 (a) and (b), and gains a high flowability. Due to the presence of recoil pressure, the Marangoni effect and the incompressibility of the flow, a large pressure is formed on this front (i.e. the melting front), as shown in the pressure contours in Fig. 7 in the x-z plane.

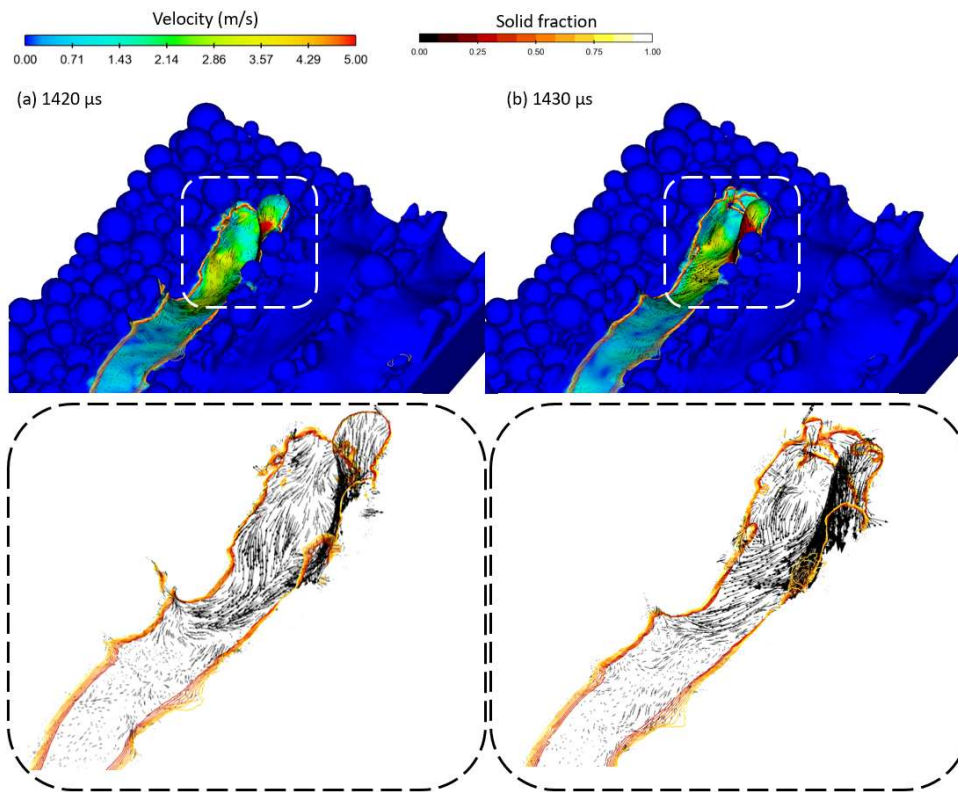


**Fig. 6.** Fluid velocity magnitude and melt region for the first layer at (a)  $1420 \mu\text{s}$  and (b)  $1430 \mu\text{s}$ .

This high-pressure front formed ahead of the laser beam drives the hot fluid (metal) backwards to the already molten zones (see Fig. 6 (a)), thus widening the melt track. As shown in Fig. 7, the coexistence of a high pressure zone in front of the melt pool and a low-pressure one at its rear, forms a local pressure gradient which serves as a driver of hot metal flow back to the relatively colder melted regions.

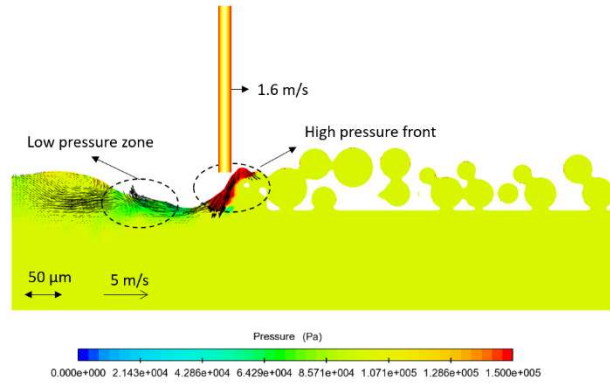


Fig. 7. Pressure front formed ahead of the laser beam for x-z plane.

TRACKING POROSITIES

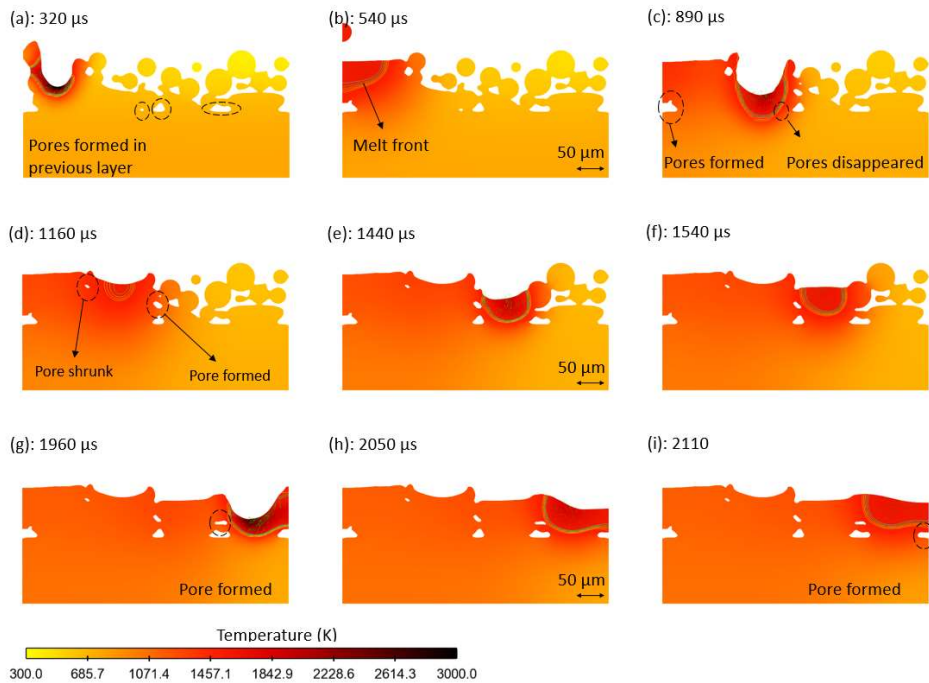


Fig. 8. Fluid region, temperature contour and melt pool dynamics during the scanning of the second layer at  $x=200 \mu\text{m}$  (transverse cross-section) for (a):  $320 \mu\text{s}$ , (b)  $540 \mu\text{s}$ , (c)  $890 \mu\text{s}$ , (d)  $1160 \mu\text{s}$ , (e)  $1440 \mu\text{s}$ , (f)  $1540 \mu\text{s}$ , (g)  $1960 \mu\text{s}$ , (h)  $2050 \mu\text{s}$ , (i)  $2110 \mu\text{s}$ .

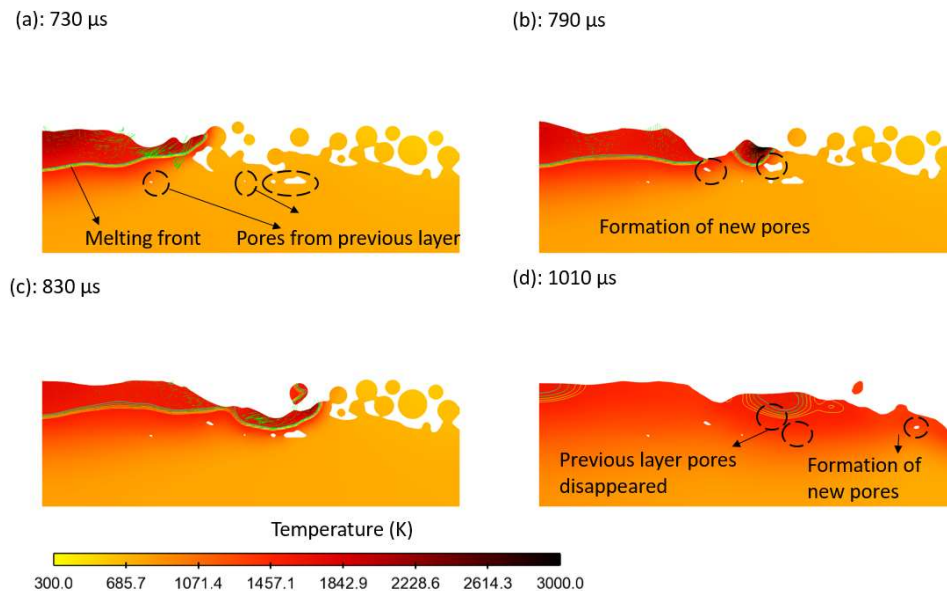
To track how the lack-of-fusion porosities are formed and how they evolve, multiple cross-sections are made in different planes from the 3D domain. Fig. 8. Fluid region, temperature contour and melt pool dynamics during the scanning of the second layer at  $x=200 \mu\text{m}$  (transverse cross-section) shows the fluid region along with its thermal field during the

scanning of the second layer at different times on one of the transverse cross-sections (with respect to direction of laser movement). At  $t = 320 \mu\text{s}$ , the centre of the laser beam reaches the position of the cross-section, and correspondingly the highest temperatures are observed.

At  $t = 540 \mu\text{s}$ , when the laser is farther away from this plane, the melt pool starts to cool down and solidify at the same time. At  $t = 890 \mu\text{s}$ , the laser again reaches the plane while scanning the second track. The keyhole formed due to presence of recoil pressure becomes sufficiently deep to capture some of the pores from the previous layer.

At  $t = 1160 \mu\text{s}$ , subsequent to the collapse of the keyhole walls and solidification of the melt region, another pore is observed to have been formed at the top right side of the track. Simultaneously, some of the pores initially formed at  $t = 890 \mu\text{s}$  are now observed to have shrunk in size. At  $t = 1960 \mu\text{s}$  and  $2110 \mu\text{s}$ , a number of pores are also formed due to the air being trapped below the melt pool. Although these pores have a strong potential to escape the fluid region (because of large density-driven buoyancy force), they cannot move upwards as they are entrapped in either the mushy or the solid zone.

On the other hand, there are a number of occasions where the pores formed during the scanning of the previous layers, coalesce or escape the fluid surface, as shown in Fig. 9.



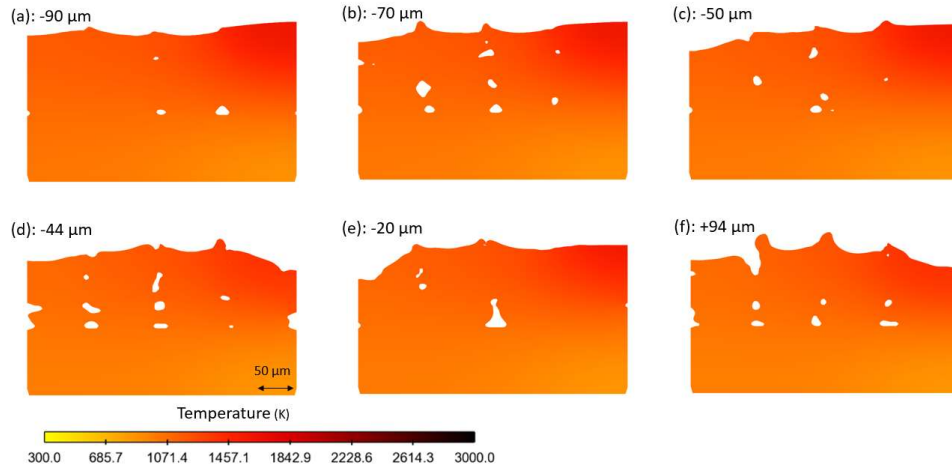
**Fig. 9.** Fluid region, temperature contour and melt pool dynamics during the scanning of the second layer at  $y=200 \mu\text{m}$  (longitudinal cross-section) at: (a)  $730 \mu\text{s}$ , (b)  $790 \mu\text{s}$ , (c)  $830 \mu\text{s}$  and (d)  $1010 \mu\text{s}$ .

Fig. 9 also shows the temperature contour, melt and fluid region in the  $x$ - $z$  longitudinal cross-section at  $y=200 \mu\text{m}$ . Although the particles are molten by the laser scanning, the keyhole is not formed at this position since the cross-section is almost  $50 \mu\text{m}$  away from the hotspots formed closer to the center of the beam. At  $t = 730 \mu\text{s}$ , there are still a number of remnant pores from the previous layer where the entrapped air could not escape the fluid surface – a phenomena which is again observed at  $t = 790 \mu\text{s}$  since the melt region could not penetrate deep enough to capture the void between particles. At  $t = 830 \mu\text{s}$ , the pore



which had been shaped at  $t = 790 \mu\text{s}$  is observed to escape the fluid surface. By  $t = 1010 \mu\text{s}$ , when the laser has finished scanning the second track, some of the pores trapped from the first layer have escaped the melt region.

To demonstrate the entire scanned block's porosity profile, the fluid region along with its temperature contour are depicted on a number of cross-sections in Fig. 10 at the end of the process for all three layers. As shown in Fig. 10, the pores mostly have irregular shapes, with round edges and sizes spanning between  $5 \mu\text{m}$  to  $40 \mu\text{m}$ . Moreover, the first layer has more lack of fusion zones compared to the second and third layers.



**Fig. 10.** Fluid region, temperature contour and melt pool dynamics for the whole three layers, at the end of the fusion process for different cross-sections at x: (a)  $-90 \mu\text{m}$ , (b)  $-70 \mu\text{m}$ , (c)  $-50 \mu\text{m}$ , (d)  $-44 \mu\text{m}$ , (e)  $-20 \mu\text{m}$  and (f)  $+94 \mu\text{m}$ .

Furthermore, as observed in Fig. 10 (b), (e) and (f), the pores are mostly created in the area between the melting tracks and stack above each other in a pattern, especially on the lower levels. This stacking pattern of pores is a well-known outcome observed in samples made without rotation or shifting of scanning strategies between successive layers. Based on the image analysis performed on different cross-sections, the porosity due to the lack of fusion is found to be in the range of 0.43 % to 2.54 %.

#### MECHANICAL ANALYSIS: UNIT CELL

The mechanical response of the unit cell for the upper and lower bounds of porosities are depicted in Fig. 11 and indicates that the porosities have a big influence on the mechanical behaviour of the samples. As seen in Fig. 11, the increase in porosity can reduce the stiffness of the material from a value of 456.7 GPa to 403.2 GPa. The yield limit of the part is affected by the imposed porosities as well, declining from 913 MPa for the unit cell with 0.43 % porosity to 725.8 MPa at 2.54 % porosity. Consequently, these results show that both stiffness and yield limits of the additive manufactured parts can be highly deteriorated because of the presence of even a small amount of porosity.

## UNIT CELL AND MECHANICAL ANALYSIS

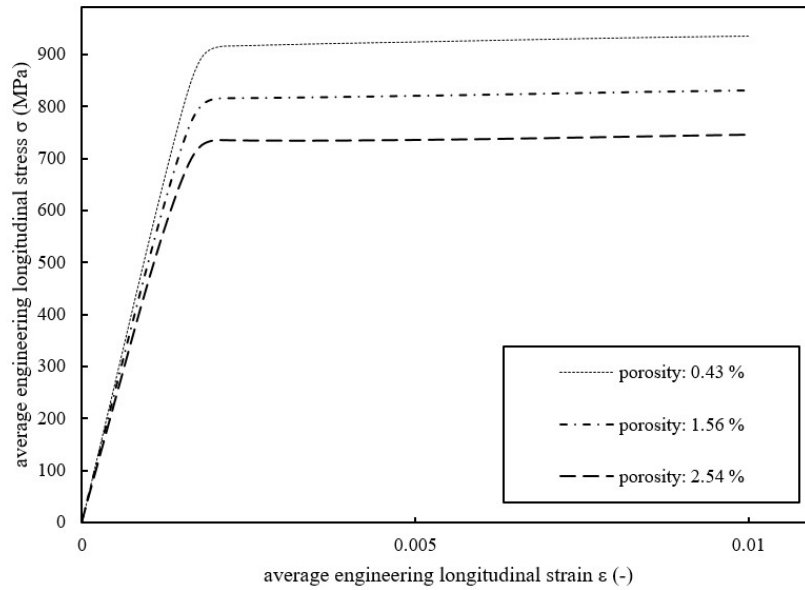


Fig. 11. Calculated average stress-strain curves for the unit cell for different porosities.

## CONCLUSION

In this work, a multi-physics numerical model for the L-PBF process is developed which accounts for multi-phase flow, fluid flow in porous medium, capillary and thermo-capillary forces, solidification and melting, particle-particle interaction, geometry-dependant absorptivity (via ray-tracing method), radiation, recoil pressure, evaporation and evaporative cooling. The model also implements surface tracking algorithms to capture the evolution of the voids and porosities, which are mainly caused by the lack of fusion zones. The results show that a steep pressure gradient prevails on the melt pool front which pumps the fluid back into the molten regions. Furthermore, the results suggest that the lack of fusion defects are mostly found in the lower layers, where the thermal energy of the fluid is lower, compared to higher levels. A detailed discussion about the formation of the pores is also given, which reveals that the pores might form, shrink, coalesce and disappear during the course of the process. Moreover, it is found that most of the pores are formed in the lower levels, where more lack of fusion defects are present. The paper also presents a unit cell model developed to capture the effect of the porosities on the mechanical properties, where it is found that an increase in porosity, decreases both the elastic modulus and the yield strength of the material at the same time. Through the combination of the thermo-fluid model and the mechanical unit cell model, a direct link between process parameters of L-PBF and the emergent mechanical properties of the component has been established. Further developments of the meso-scale thermo-fluid model by inclusion of the plasma plume formation, and by tracking the movements of particles and metal droplets dragged by the vapour/gas flow, would lead to better prediction of the surface of the part being

manufactured by L-PBF as well as allow a more accurate capturing of the keyhole voids formation/evolution. The usage of representative volume elements to model the mechanical response of the L-PBF parts with porosity will also potentially lead to better results. Further, adding a metallurgical model able to predict phase fractions of the metallic alloy, would provide greater inputs to the mechanical analysis and complete the chain of process-materials-property.

### APPENDICES AND ACKNOWLEDGEMENTS

This work has received funding from the European Union Horizon 2020 Marie Skłodowska-Curie ITN PAM<sup>2</sup> project under grant agreement number 721383.

### REFERENCES

- [1] J.O. MILEWSKI, 2017. 'Additive Manufacturing of Metals: From Fundamental Technology to Rocket Nozzles, Medical Implants, and Custom Jewelry', *Springer*, Vol. 258., 2017.
- [2] T. DEBROY et al., 'Additive manufacturing of metallic components – Process, structure and properties' *Prog. Mater. Sci.*, vol. 92, pp. 112–224, 2018.
- [3] V. BHAVAR, P. KATTIRE, V. PATIL, S. KHOT, K. GUJAR, and R. SINGH, 'A review on powder bed fusion technology of metal additive manufacturing', *4th International Conference and Exhibition on Additive Manufacturing Technologies-AM-2014*, 2014.
- [4] C. KAMATH, B. EL-DASHER, G. F. GALLEGOS, W. E. KING, and A. SISTO, 'Density of additively-manufactured, 316L SS parts using laser powder-bed fusion at powers up to 400 W' *Int. J. Adv. Manuf. Technol.*, vol. 74, no. 1–4, pp. 65–78, 2014.
- [5] N. HOPKINSON, R. HAGUE, and P. DICKENS, 'Rapid manufacturing: an industrial revolution for the digital age', *John Wiley & Sons*, 2006.
- [6] M. J. MATTHEWS, G. GUSS, S. A. KHAIRALLAH, A. M. RUBENCHIK, P. J. DEPOND, and W. E. KING, 'Denudation of metal powder layers in laser powder bed fusion processes' *Acta Mater.*, vol. 114, pp. 33–42, 2016.
- [7] W. E. KING et al., 'Observation of keyhole-mode laser melting in laser powder-bed fusion additive manufacturing' *J. Mater. Process. Technol.*, vol. 214, no. 12, pp. 2915–2925, 2014.
- [8] H. GONG, K. RAFI, H. GU, T. STARR, and B. STUCKER, 'Analysis of defect generation in Ti-6Al-4V parts made using powder bed fusion additive manufacturing processes' *Addit. Manuf.*, vol. 1, pp. 87–98, 2014.
- [9] N. T. ABOULKHAIR, N. M. EVERITT, I. ASHCROFT, and C. TUCK, 'Reducing porosity in AlSi10Mg parts processed by selective laser melting' *Addit. Manuf.*, vol. 1, pp. 77–86, 2014.
- [10] R. LIN, H. PING WANG, F. LU, J. SOLOMON, and B. E. CARLSON, 'Numerical study of keyhole dynamics and keyhole-induced porosity formation in remote laser welding of Al alloys' *Int. J. Heat Mass Transf.*, vol. 108, pp. 244–256, 2017.
- [11] P. A. HOOPER, 'Melt pool temperature and cooling rates in laser powder bed fusion' *Addit. Manuf.*, vol. 22, pp. 548–559, 2018.
- [12] C. ZHAO et al., 'Real-time monitoring of laser powder bed fusion process using high-speed X-ray imaging and diffraction' *Sci. Rep.*, vol. 7, no. 1, pp. 1–11, 2017.
- [13] L. J. ZHANG, J. X. ZHANG, A. GUMENYUK, M. RETHMEIER, and S. J. NA, 'Numerical simulation of full penetration laser welding of thick steel plate with high power high brightness laser' *J. Mater. Process. Technol.*, vol. 214, no. 8, pp. 1710–1720, 2014.

- [14] C. BRUNA-ROSSO, A. G. DEMIR, and B. PREVITALI, ‘Selective Laser Melting Finite Element Modeling: Validation with High-Speed Imaging and Lack of Fusion Defects Prediction’ *Mater. Des.*, vol. 156, pp. 143–153, 2018.
- [15] S. MOHANTY AND J. H. HATTEL, ‘Numerical model based reliability estimation of selective laser melting process’ *Phys. Procedia*, vol. 56, pp. 379–389, 2014.
- [16] S. MOHANTY, C. C. TUTUM, AND J. H. HATTEL, ‘grid-based scanning path & parametric approach to thermal homogeneity Cellular scanning strategy for selective laser melting: Evolution of optimal grid-based scanning path & parametric approach to thermal homogeneity’, *Proceedings of SPIE*, October 2016, 2013.
- [17] S. A. KHAIRALLAH, A. T. ANDERSON, A. RUBENCHIK, AND W. E. KING, ‘Laser powder-bed fusion additive manufacturing: Physics of complex melt flow and formation mechanisms of pores, spatter, and denudation zones’ *Acta Mater.*, vol. 108, pp. 36–45, 2016.
- [18] C. QIU, C. PANWISAWAS, M. WARD, H. C. BASOALTO, J. W. BROOKS, and M. M. ATTALLAH, ‘On the role of melt flow into the surface structure and porosity development during selective laser melting’ *Acta Mater.*, vol. 96, pp. 72–79, 2015.
- [19] Y. C. WU et al., ‘Numerical modeling of melt-pool behavior in selective laser melting with random powder distribution and experimental validation’ *J. Mater. Process. Technol.*, vol. 254, July 2017, pp. 72–78, 2018.
- [20] Y. S. LEE AND W. ZHANG, ‘Modeling of heat transfer, fluid flow and solidification microstructure of nickel-base superalloy fabricated by laser powder bed fusion’ *Addit. Manuf.*, vol. 12, pp. 178–188, 2016.
- [21] Z. GAN, H. LIU, S. LI, X. HE, and G. YU, ‘Modeling of thermal behavior and mass transport in multi-layer laser additive manufacturing of Ni-based alloy on cast iron’ *Int. J. Heat Mass Transf.*, vol. 111, pp. 709–722, 2017.
- [22] L. PARRY, I. A. ASHCROFT, and R. D. WILDMAN, ‘Understanding the effect of laser scan strategy on residual stress in selective laser melting through thermo-mechanical simulation’ *Addit. Manuf.*, vol. 12, pp. 1–15, 2016.
- [23] T. ANDRIOLLO and J. H. HATTEL, ‘A micro-mechanical analysis of thermo-elastic properties and local residual stresses in ductile iron based on a new anisotropic model for the graphite nodules’, *Modelling Simul. Mater. Sci. Eng.*, 24, 2016.
- [24] M. TANE, H. NAKAJIMA, Z. REN, and M. VESENJAK, ‘Compressive properties of lotus-type porous iron’, *Computational Materials Science*, vol. 65, pp. 37–43, 2012.
- [25] W. TAN AND Y. C. SHIN, ‘Multi-scale modeling of solidification and microstructure development in laser keyhole welding process for austenitic stainless steel’ *Comput. Mater. Sci.*, vol. 98, pp. 446–458, 2015.
- [26] A. SALEEM, S. FAROOQ, I. A. KARIMI, and R. BANERJEE, ‘A CFD simulation study of boiling mechanism and BOG generation in a full-scale LNG storage tank’ *Comput. Chem. Eng.*, vol. 115, pp. 112–120, 2018.
- [27] S. TIARI, S. QIU, and M. MAHDAVI, ‘Discharging process of a finned heat pipe-assisted thermal energy storage system with high temperature phase change materia’ *Energy Convers. Manag.*, vol. 118, pp. 426–437, 2016.
- [28] V. R. VOLLER and C. PRAKASH, ‘A fixed grid numerical modelling methodology for convection-diffusion mushy region phase-change problems’ *Int. J. Heat Mass Transf.*, vol. 30, no. 8, pp. 1709–1719, 1987.
- [29] H. HAMDI, M. EL GANAOUI, and B. PATEYRON, ‘Thermal Effects on the Spreading and Solidification of a Micrometric Molten Particle Impacting onto a Rigid Substrate Thermal Effects on the Spreading and Solidification of a Micrometric Molten Particle Impacting onto a Rigid Substrate’ *Fluid Dynamics & Materials Processing*, vol. 8, no. 2, pp. 173–195. (2012).
- [30] J. H. CHO and S. J. NA: ‘Implementation of real-time multiple reflection and Fresnel absorption of laser beam in keyhole’ *J. Phys. D. Appl. Phys.*, vol. 39, no. 24, pp. 5372–5378, 2006.

- [31] W. TAN, N. S. BAILEY, and Y. C. SHIN: 'Investigation of keyhole plume and molten pool based on a three-dimensional dynamic model with sharp interface formulation' *J. Phys. D. Appl. Phys.*, vol. 46, no. 5, 2013.

# DEVELOPMENT OF A TWO-DIMENSIONAL AXIAL SYMMETRY MODEL FOR WIRE ARC ADDITIVE MANUFACTURING

S. CADIOU\*, M. COURTOIS\*, M. CARIN\*, P. LE MASSON\*,  
L. GUILMOIS\*\*'\*\*\* and P. PAILLARD\*\*

*\*Univ. Bretagne Sud, UMR CNRS 6027, IRDL, F-56100 Lorient, France, e-mail: Stephen.cadiou@univ-ubs.fr*

*\*\*Polytech Nantes, UMR 6502, IMN F-44000 Nantes, France*

*\*\*\*IRT Jules Verne, Chemin du Chaffault, F-44340 Bouguenais, France*

DOI 10.3217/978-3-85125-615-4-56

## ABSTRACT

In this study, a numerical model taking into account electromagnetism, fluid flow, and heat transfer in the arc and the melt pool is developed using COMSOL Multiphysics®. The level set method is used to simulate the layer-by-layer addition of materials along the vertical axis to form a cylindrical rod. This shape has the advantage to be simulated with a 2D axial-symmetry model in order to reduce computation time. The implementation of the arc plasma model is first validated by comparing predictions with literature data. Then, the arc pressure, arc shear stress, Lorentz forces and heat flux are analysed and used to define source terms for the additive manufacturing model. In this model, the building of a 308 stainless steel rod is simulated by adding molten metal droplet along the vertical axis. The adding of droplets and heat source are periodically stopped in order to simulate the layer-by-layer build-up of the rod. The calculated shape and the temperature field are analysed and compared to experimental data.

Keywords: Modeling, Multiphysics, Additive Manufacturing, WAAM

## INTRODUCTION

The additive manufacturing (AM) of metal parts is a revolutionary process with great potential. A large number of additive manufacturing methods are now available. The current work focuses on the Wire Arc Additive Manufacturing (WAAM), which is a highly promising process due to its high deposition rate and efficiency (100%). This process uses an electric arc as a heat source and a wire as feedstock and is very similar to the GMA (Gas Metal Arc) welding process. However, a thorough understanding of the physical phenomena involved in WAAM is desirable to produce defect-free and reliable AM parts. Numerical simulation provides an efficient way to understand the influence of the operating parameters on the geometry, the thermal cycles, the microstructure, the distortions and the residual stresses observed in the AM parts.

In the literature, there are different models concerning the numerical simulation of arc welding and additive arc wire fabrication. The most complete models are those dealing with

the physical phenomena in the arc. Many authors have proposed arc model without filler material to simulate Tungsten Inert Gas (TIG) welding process (Hsu [1], Tanaka [2] [3] [4], Brochard [5], Traidia [6], Lago [7], Li [8], Yau [9]). These models have the advantage of describing the main physical phenomena only from the operating parameters and material properties and can be regarded as self-consistent models. In parallel, models simulating Gas Metal Arc Welding (GMAW) and Wire Arc Additive Manufacturing (WAAM) were developed. Murphy [10] and Luo [11] have developed models focusing on the evolution of the droplet in the arc. Fan [12], Hu [13], [14] have developed models able to track the formation as well as the detachment of droplets from the wire electrode, and its transfer through the arc and into the weld pool. In these studies, a stationary two-dimensional axisymmetric GMAW system is considered. The Volume of Fluid (VOF) method is employed for tracking the free surface of the droplets and the melt pool. With this method, the mass conservation is well satisfied, but the interface reconstruction is quite difficult and the implementation in 3D is tedious and time consuming [15]. It is also possible to use a level set method to track the gas-metal interface. Desmaison [16] used this method to simulate in 3D the material supply at the melt pool surface during a laser/GMAW welding process. However, there are very limited numerical studies in 3D to simulate multilayer deposition such as in WAAM processes, since a complete 3D modeling has to face prohibitive calculation times. In order to reduce calculation times, these models are generally simplified and based on empirical laws requiring a calibration of input parameters with experimental data. The droplet formation and detachment, droplet flight in arc plasma and impingement of droplets are not explicitly simulated. Bai [17] developed a 3D model to investigate the fluid flow and heat transfer behaviours in multilayer deposition of plasma arc welding (PAW). A VOF method is used to track the melt pool surface. The mass feeding process is modelled as a source term in the mass conservation equation. The location of the mass input is determined according to experimental data. The heat of arc is also simplified using a modified double-ellipsoidal volumetric heat source model based on calibrated parameters with IR imaging. This model is used to simulate the 1<sup>st</sup>, 2<sup>nd</sup> and 21<sup>st</sup> layer depositions. However, due to prohibitive computation time, the simulation of the 21<sup>st</sup> layer is initialized with the experimental profile of the 20<sup>th</sup> layer. Hejripour [18] used an Arbitrary Lagrangian-Eulerian (ALE) method to predict the shape of the first layer in a WAAM process. Gaussian functions are chosen to describe the heat input, the current density and the arc pressure. The profile of the free surface is calculated by minimizing the total potential energy of the surface resulting from a balance condition between surface tension, hydrostatic pressure and arc pressure. However, this method is difficult to apply for multilayer deposition. Note that in all these studies, in order to validate the models, the comparisons are limited to the shape of geometry and to macrographs for fusion zone.

In this paper, a two-dimensional axial-symmetric model taking into account electromagnetism, fluid flow, and heat transfer in the arc and the melt pool is first presented. This arc model is used to define the heat input of a WAAM model. A level set method is used for simulating the layer-by-layer addition of materials along the vertical axis. In this model, the manufacturing of a 308 stainless steel rod by a WAAM process is simulated. The calculated shape and the temperature field are analysed and compared to experimental data.

## MODELING OF ARC WELDING

In order to determine the heat input induced by the arc based solely on the operating parameters, an arc model is developed in the case of tungsten cathode. Many physical phenomena have to be considered in the arc and the melt pool as shown in Fig. 1.

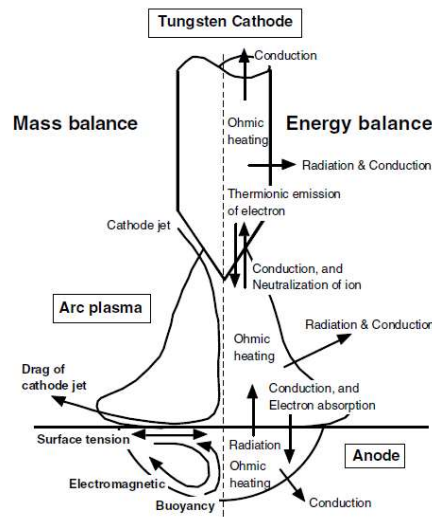


**Fig.1** Main physical phenomena taken into account in the numerical modeling of arc welding [2].

## THE COMPUTATIONAL MODEL

The mathematical modeling of such a process involves different physics like heat transfer, fluid flow, or electromagnetism. The present model is focused on these three physics, which is also refer to a Magneto-Hydro Dynamics (MHD) model. The aim of this approach is to predict the heat transfer and fluid flow in both the arc plasma and the weld pool. This model is based on that of Hsu [1] and Tanaka [2] [3] [4]. Their works have been used as references for many researchers [5-8] in order to validate MHD models of arc welding.

Based on these reference cases, the following assumptions are considered:

- The model is solved in 2D axisymmetric, since the TIG torch is static,
- The plasma is in local thermodynamic equilibrium (LTE). This assumption means that species such as ions, neutrons are supposed to have the same temperature. However this assumption is not valid near cathode / plasma interface and anode / plasma interface. To overcome this, conditions are applied to these interfaces as done in [2-8]. Moreover, Haidar [19] showed that the plasma is in LTE, if arc length is superior to 2 mm and the temperature reaches 12 000 K. This is the case with our model.
- The fluid flow in the plasma is considered to be Newtonian laminar with a weakly compressible approach,



## Mathematical Modelling of Weld Phenomena 12

- A Newtonian laminar incompressible flow is considered in the melt pool,
- The cathode and anode are not considered deformable. Traidia showed that for low current welding (up to 180 A) the free surface depression is negligible [6]. To reduce computational time, the anode is not deformable.
- Buoyancy force is taken into account using the Boussinesq approximation.
- The effect of metal vapours coming from the vaporisation of the melt pool surface on the transport properties of the arc is not included in the model.

When the arc interacts with the anode, metal vapor can be generated if the surface temperature reaches the evaporation point. Several studies have been carried out on the understanding of the influence of these metallic vapors. Lago, [7], shows through his numerical model that metal vapors tend to cool the plasma essentially at the edges. Current densities, in the presence of metal vapors, increase at the center of the arc and decrease at the edges. Moreover, the vapors increase the current densities at the anode. The greater flux comes from the increase of the electrical flux due to the electrical conductivities increase. These remarks are consistent with Mougnot [20]. Murphy and Tanaka et al [21] have shown that the maximum value of the current density is slightly lower (5.5% difference) when the metal vapors are taken into account. In our case, we chose to neglect the metallic vapors since their effect is rather small but also in order to simplify the calculations.

With these assumptions, the governing equations of heat and mass transfer for arc and metal transport are given below:

- Conservation of mass

$$\frac{\partial \rho}{\partial t} + \text{div}(\rho \vec{v}) = 0 \quad (1)$$

where  $\rho$  is the density,  $t$  the time and  $\vec{v}$  the velocity vector.

- Conservation of momentum

$$\begin{aligned} \rho \left( \frac{\partial \vec{v}}{\partial t} + \overline{\text{grad}}(\vec{v}) \cdot \vec{v} \right) \\ = \overline{\text{div}} \left[ -P \bar{I} + \mu_f \left( \overline{\text{grad}}(\vec{v}) + {}^t \overline{\text{grad}}(\vec{v}) \right) \right. \\ \left. - \frac{2}{3} \text{div}(\vec{v}) \bar{I} \right] + \vec{F}_v \end{aligned} \quad (2)$$

where  $P$  is the pressure,  $\bar{I}$  the identity matrix,  $\mu_f$  the dynamic viscosity and  $\vec{F}_v$  the volume force detailed below.

In the plasma, this volume force is an electromagnetic force:

$$\vec{F}_v = \vec{F}_{mag} = \vec{j} \times \vec{B} \quad (3)$$

where  $B$  is the magnetic flux density and  $j$  is the current density.

In the melt pool, the volume force is expressed as follows:

$$\vec{F}_v = \vec{F}_{mag} + \vec{F}_b + \vec{F}_{Darcy} = \vec{j} \times \vec{B} - \rho_{ref} \beta (T - T_{ref}) \vec{g} - C \frac{(1 - f_L)^2}{f_L^3 + b} \vec{v} \quad (4)$$

where  $\vec{F}_b$  is the buoyancy force,  $\vec{F}_{Darcy}$  is the Darcy law. The Darcy law enables to stop the fluid flow in the solid region.  $\rho_{ref}$  is the density at the reference temperature  $T_{ref}$ ,  $\beta$  is the thermal expansion coefficient,  $\vec{g}$  is the acceleration due to gravity,  $C$  is a relatively huge constant that ensures the decrease of the velocity field in the solid region,  $b$  is a relatively low constant introduced to avoid division by zero and  $f_L$  is the liquid fraction function. This function is assumed to vary linearly with temperature in the mushy zone as follows:

$$f_L = \begin{cases} 1 & \text{if } T > T_L \\ \frac{T - T_S}{T_L - T_S} & \text{if } T_S \leq T \leq T_L \\ 0 & \text{if } T < T_S \end{cases} \quad (5)$$

where  $T$  is the temperature,  $T_S$  and  $T_L$  are the solidus and liquidus temperatures of the workpiece material.

- Conservation of energy

$$\rho C_p^{eq} \left( \frac{\partial T}{\partial t} + \vec{v} \cdot \overrightarrow{grad}(T) \right) = div \left( \bar{k} \overrightarrow{grad}(T) \right) + S_v \quad (6)$$

where  $\rho$  is the density,  $C_p$  is an equivalent specific heat, that equals  $C_p$  in the cathode and arc-plasma domains, and is modified to  $C_p + L_f \frac{df_L}{dT}$  in the anode domain to account for the latent heat of fusion  $L_f$ ,  $k$  is the thermal conductivity,  $T$  is the temperature, and  $S_v$  is a volumetric heat source term.

In the plasma, this source term is expressed as follows:

$$S_v = S_j + S_{rad} = \vec{j} \cdot \vec{E} - 4\pi\epsilon_N \quad (7)$$

where  $S_j$  is the heating Joule effect (with  $j$  is current density, and  $E$  is electric field), and  $S_{rad}$  is the radiation losses with  $\epsilon_N$  the emission coefficient of Argon.

Inside the cathode and the anode, the heat source term is only the heating Joule effect.

The electromagnetic force and the Joule heating are obtained from the resolution of electromagnetic equations:

$$\begin{aligned} div \left( \sigma_e \overrightarrow{grad}(V) + \sigma_e \frac{\partial \vec{A}}{\partial t} \right) &= 0 \\ \sigma_e \frac{\partial \vec{A}}{\partial t} + \frac{1}{\mu_0} \overrightarrow{rot} \left( \overrightarrow{rot}(\vec{A}) \right) + \sigma_e \overrightarrow{grad}(V) &= \vec{0} \end{aligned} \quad (8)$$

## Mathematical Modelling of Weld Phenomena 12

where  $\sigma_e$  is the electrical conductivity,  $V$  is the electrical potential,  $\mu_0$  is the magnetic permeability and  $A$  is the magnetic vector potential.

At the cathode/plasma interface, specific phenomena must be taken into account in the energy balance such as cathode ion neutralization, thermionic emission, and radiation losses from the cathode surface. This energy balance is formulated as follows [2]:

$$\vec{q}_c \cdot (-\vec{n}) = \vec{q}_{pl} \cdot (-\vec{n}) + q_{ions} + q_{thermionic} + q_{radiation} \quad (9)$$

where:

- $\vec{q}_c = -k_c \overrightarrow{grad}(T_c)$  with  $k_c$  is the cathode thermal conductivity and  $T_c$  is the temperature field in the cathode
- $\vec{q}_{pl} = -k_{pl} \overrightarrow{grad}(T_{pl})$  with  $k_{pl}$  is the plasma thermal conductivity and  $T_c$  is the temperature field in the plasma
- $q_{ions} = j_i V_i$  with  $j_i$  is the ion current and  $V_i$  is the gas ionisation potential
- $q_{thermioni} = -j_e \phi_c$  with  $j_e$  is the electron current and  $\phi_c$  is the cathode work function
- $q_{radiation} = -\varepsilon \sigma_B T^4$  with  $\varepsilon$  is the anode emissivity,  $\sigma_B$  is the Stefan-Boltzmann constant and  $T$  is the temperature at the interface.

As for the cathode / plasma interface, specific phenomena must be taken into account in the energy balance such as the absorption of electrons by the anode, and the radiation losses. This energy balance is expressed, according to Tanaka et al. [2], as follows:

$$\vec{q}_a \cdot (-\vec{n}) = \vec{q}_{pl} \cdot (-\vec{n}) + q_{electrons,condensation} + q_{radiation} \quad (10)$$

where:

- $\vec{q}_a = -k_a \overrightarrow{grad}(T_a)$  with  $k_a$  is the anode thermal conductivity and  $T_a$  is the temperature field in the anode,
- $\vec{q}_{pl} = -k_{pl} \overrightarrow{grad}(T_{pl})$  with  $k_{pl}$  is the plasma thermal conductivity and  $T_{pl}$  is the temperature field in the plasma,
- $q_{electrons,condensation} = |\vec{j} \cdot \vec{n}| \phi_a$  with  $|\vec{j} \cdot \vec{n}|$  is the normal current density and  $\phi_a$  is the anode work function,
- $q_{radiation} = -\varepsilon \sigma_B T^4$  with  $\varepsilon$  is the anode emissivity,  $\sigma_B$  is the Stefan-Boltzmann constant and  $T$  is the temperature at the interface.

Since the anode surface is considered as non-deformable, only drag force induced by the plasma jet on the melt pool surface and Marangoni effect are taken into account at the anode surface and can be formulated as follows:

$$F_{anode} = F_{shear} + F_{marangoni} \quad (11)$$

where:

## Mathematical Modelling of Weld Phenomena 12

- $F_{shear} = (\bar{\tau} - P_{pl}\bar{I}) \cdot \vec{n}) \cdot \vec{t}$  with  $\bar{\tau}$  the shear stress tensor,  $P_{pl}$  the plasma pressure applied to the top surface of the melt pool and  $\vec{t}$  the tangential vector at the top surface of the melt pool.
- $F_{marangoni} = f_L \frac{\partial \gamma}{\partial T} \frac{\partial T}{\partial r}$  with  $\gamma$  the surface tension coefficient. With the introduction of the liquid fraction  $f_L$  in this expression, Marangoni force becomes zero at the anode surface in the solid phase.

### VALIDATION OF THE MODEL

The aim of this section is to compare the results calculated by our model to those available in the literature. As mentioned previously, two reference cases have been used: Hsu [1] and Tanaka et al [3]. In [2], a copper anode cooled with water is considered, so the anode stays at the solid state. This reference case is used to compare the calculated results in the plasma. In particular, comparisons will focus on:

- Arc-plasma temperature
- The evolution of axial velocity in the arc column along the axis of symmetry.

In the second reference case [3], the anode is composed of stainless steel, which is heated by the arc until a melt pool is created. For this configuration, the shape of the weld pool, the shear forces applied to the melt pool surface, the heat flux as well as the current density at the surface of the anode are analysed and compared to the literature data.

All these results have been obtained with a computational domain meshed using standard Lagrangian quadratic triangular elements. The mesh size densities are as follows  $8 \cdot 10^{-4}$  m in the plasma,  $5 \cdot 10^{-5}$  m in melt pool domains, and  $1 \cdot 10^{-4}$  m in the cathode domain,  $1 \cdot 10^{-5}$  m at the top surface of the weld pool and the cathode, where high thermal gradients occur. Computations are performed within 1 hour on 8 processors computer (3.47GHz and 96 GB RAM DDR3) for a stationary calculation and 12 hours for a unsteady calculation.

Before presenting the results of our numerical models and in order to have a better analysis of the results, Table 1 summarizes the main differences between the different models of the literature as well as with our numerical model.

**Table 1** Comparisons of assumptions used by the different authors [1], [4], [5], [6], [7]

	<b>Brochard</b>	<b>Traidia</b>	<b>Lago</b>	<b>Hsu</b>	<b>Tanaka</b>	<b>Our model</b>
<b>Software</b>	Cast3m	Comsol	FIUENT	Not specified	SIMPLEC	Comsol
<b>Configurations</b>	2D axisymmetric / Stationary	2D axisymmetric / Stationary	2D axisymmetric / Stationary	2D axisymmetric / Stationary	2D axisymmetric / Time-dependent	2D axisymmetric / Time-dependant
<b>Assumptions</b>						
<b>Plasma</b>	LTE	LTE	LTE	LTE	LTE	LTE
<b>Plasma : Fluid</b>	Incompressible	Incompressible	Weakly compressible	Not specified	Weakly compressible	Weakly compressible
<b>Fluid flow</b>	Laminar	Laminar	Laminar	Laminar	Laminar	Laminar
<b>Anode surface</b>	Not deformable	Not deformable	Not deformable	Not deformable	Not deformable	Not deformable
<b>Cathode</b>	Present	Present	Not present	Not present	Present	Present
<b>Electromagnetic calculation</b>	Method of least squares	Magnetic approach	Potential approach and magnetic approach	Magnetic approach	Not specified	General approach
<b>Normal current density at the surface</b>	$j = \frac{I}{\pi R_c^2}$	$j = \frac{I}{\pi R_c^2}$	$j(r) = J_{max} \exp(-br)$ $J_{max} = \frac{I}{\pi R_c^2}$	$j(r) = J_{max} \exp(-br)$ $J_{max} = \frac{I}{\pi R_c^2}$	$j(r) = J_{max} \exp(-br)$ $J_{max} = \frac{I}{\pi R_c^2}$	$j(r) = J_{max} \exp(-br)$ $J_{max} = \frac{I}{\pi R_c^2}$

One of the strongly criticisable assumptions is the normal current density applied. Indeed, it is virtually impossible to measure the plasma temperature as well as the electric field exactly near the tip of the cathode. It is therefore necessary to choose a reasonable profile of the current as Hsu formulated [1]:

$$j(r) = J_{max} \exp(-br) \tag{12}$$

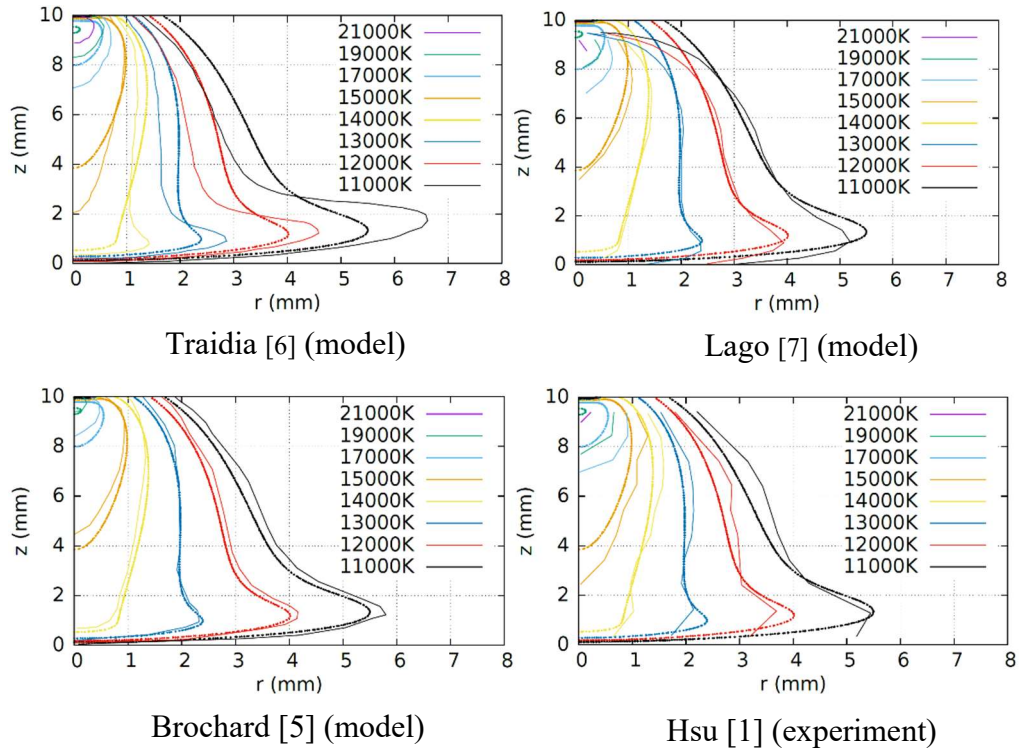
Therefore, we have chosen to apply this same profile in our model. However, the constant b of equation (12) is determined using the equation (13):

$$I = \int_{\partial\Omega} -\vec{n} \cdot \vec{j} dS = 2\pi \int_0^{R_c} j(r)r dr \tag{13}$$

*Configuration of Hsu*

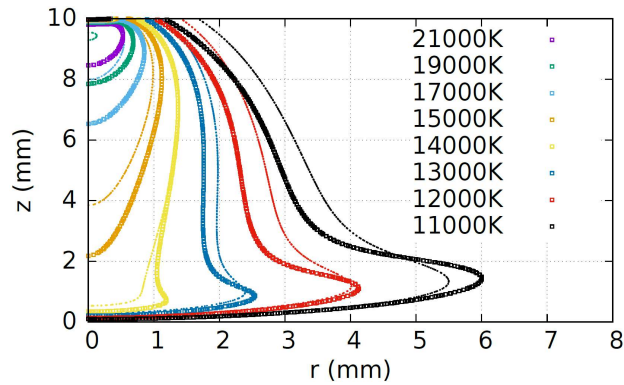
In this configuration of Hsu [2], a thoriated tungsten cathode is used, with a copper anode and argon as a shielding gas. The arc current is fixed to I = 200A, the electrode-tip has an angle of 60° with a truncation radius of 0.3 mm, and the inter-electrode distance (arc length) is set to 10 mm. Many authors have reproduced this configuration like Brochard [5], Traidia [6], and Lago[7]. The material properties are temperature-dependant. The values of the properties and other parameters are given in these references.

Fig. 2 shows a comparison of the isotherms in the plasma calculated by our model and given by other authors [6], [7], [5], [1]



**Fig. 2** Comparisons of isotherms of a free-burning between authors (dashed lines) and our model (continuous lines).

It can be observed that our model gives temperatures consistent with the numerical results of Traidia, Lago and Brochard and also the experimental data of Hsu. The differences between authors are relatively minor, in the range of several hundred kelvins. Nevertheless, the Lago's model lacks precision near the cathode. This shows that it is essential to take into account the cathode to predict the temperature field in this zone. However, the temperature field near the anode gives satisfactory results. The Traidia's model has wider isotherms than our model. One of its assumptions is the incompressible fluid flow in plasma. To highlight the effect of this assumption, a calculation with an incompressible fluid flow in our model was realized. The Fig. 3 shows that this assumption is too penalizing.



**Fig. 3** Comparisons of isotherms of a free-burning between our model with an incompressible fluid flow (square lines) in plasma and with a weakly compressible fluid flow (dashed lines).

The Fig. 4 gives a comparison of the flow velocity along the axis of symmetry calculated by our model and the model of [1], [7], [5].

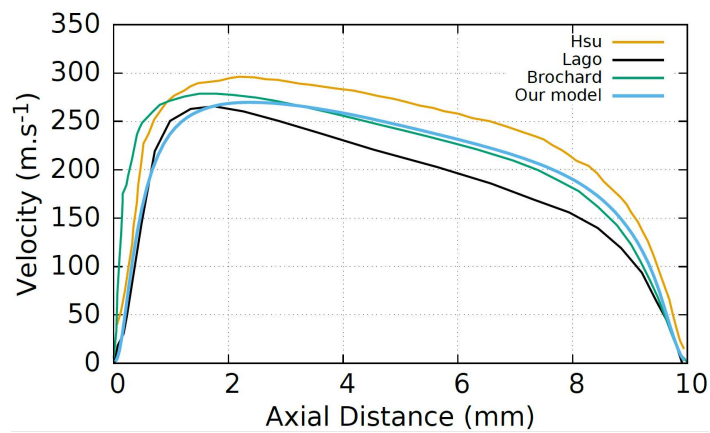


**Fig. 4** Comparisons of flow velocity along the axis of the arc calculated by [1], [7], [5] and our model.

From Fig. 4, it can be observed that our model gives results consistent with the models of Hsu, Lago and Brochard. The flow velocities calculated by our model are close to the average velocities given by the different authors.

These comparisons show that our model gives consistent values for temperature and velocity in the plasma.

#### *Configuration of Tanaka*

In the configuration of Tanaka [3], a thoriated tungsten cathode is used with a 304 stainless steel anode and argon as a shielding gas. The arc current is fixed to  $I = 150$  A, the electrode-tip has an angle of  $60^\circ$  with a truncation radius of 0.3 mm, and the inter-electrode distance (arc length) is set to 5 mm [2],[4]. Many authors are reproduced this study like Brochard

[5], Traidia [6]. The description of the model and all data used for this configuration are detailed in these references. The advantage of this second configuration is that it enables to validate the calculated temperatures and velocities in the melt pool.

The Fig. 5 shows the temperature field and velocity vectors in the whole geometry Fig. 5a) and in the melt pool (Fig. 5b). In the plasma, the order of magnitude of temperatures and velocities is consistent with the previous study. In the melt pool, the fluid flow velocity is also consistent with the Brochard's results. Brochard obtained a velocity of 0.31 m/s and our model gives a velocity of 0.34 m/s.

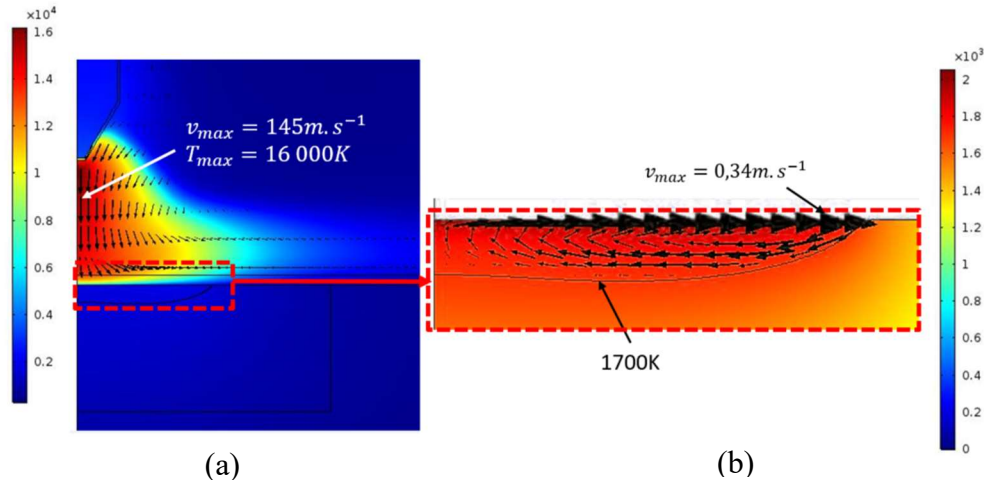


**Fig. 5** Temperature field (K) and velocity vector in the whole geometry (a) as well as in the melt pool (b).

The results calculated by our model is compared to those given by Tanaka [2] [3], Brochard [5], and Traidia [6], in terms of :

- shear stress at the anode surface,
- current density at the anode surface,
- heat flux density at the anode surface,
- temperature at the anode surface.

The results can be seen in Fig. 6. Note that some authors do not present all these values. So our model is compared only with the available data presented in the literature.



# Mathematical Modelling of Weld Phenomena 12

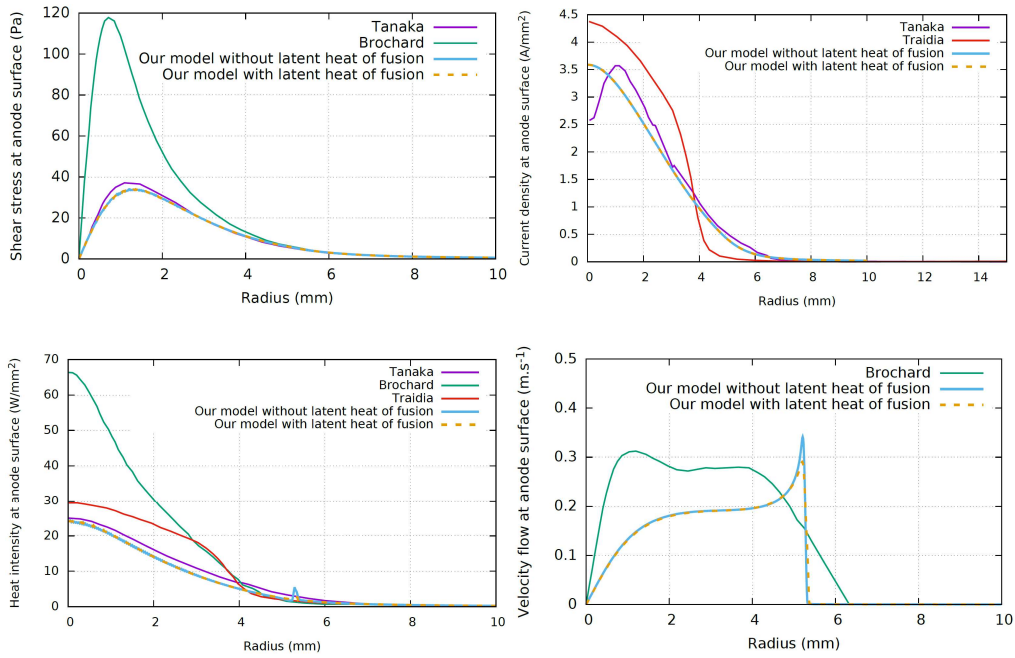


**Fig. 6** Comparisons of shear stress, current density, heat intensity, and velocity flow at the surface of anode between authors and our model [2], [3], [5], [6].

These comparisons show that our model is overall consistent with the different authors. Only, Brochard has different results regarding shear stress and heat intensity at the anode surface. It is difficult to explain why Brochard obtained such discrepancies with other models of literature and our model. Note that such models are relatively complex and the authors do not give all the details of their model. Some material properties are not clearly indicated. The numerical methods used to solve the equations can differ. Different softwares are employed. The physics near the electrodes are very complicated due to the non Local Thermodynamic Equilibrium. The authors do not used the same method to treat the interfaces, as detailed in [8]. The arc initiation is also a delicate issue to simulate in such models. In order to further validate the model, the shape of the melt pool is compared with results given by [2], [5] (Fig. 7).

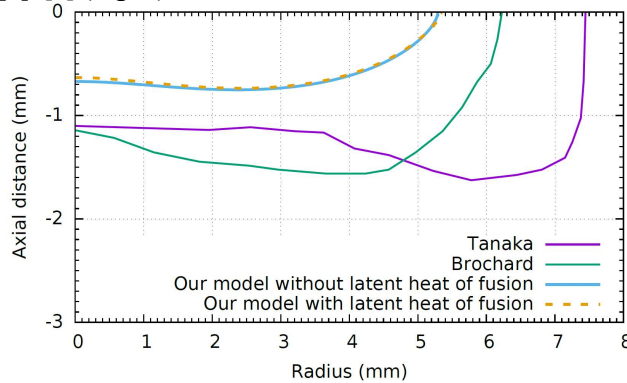


**Fig. 7** Comparisons of shape of melt pool between authors and our model [2], [5].

Fig. 7 shows significant differences in the melt pool shapes calculated by the different authors. Tanaka and Brochard predict the same penetration depth but the melt pool width is larger for Tanaka. The global shape differs also. Our model predicts a smaller melt pool. Brochard obtained a larger melt pool than Tanaka and our model. From Fig. 6, it is possible to observe that the shear stress calculated by Brochard is higher than that given by our model, this could explain why our melt pool is narrower. However, it is more difficult to give an explanation for the difference observed for our model and Tanaka, since the results presented in Fig. 5 are very close between Tanaka and our model. One possible explanation could come from a different thermal boundary condition at the bottom of the anode. In order to better understand the observed differences, experiments will be planned in the future.

With regard to the latent heat of fusion, the Fig.6 and Fig. 7 shows that it has a very small influence on the results. Consequently, can be neglected in a stationary approach.

This first section enables to validate the model of arc welding. This model can be used to define boundary conditions for a model restricted to the melt pool. It provides the net heat flux, electromagnetic forces and shear stress caused by the drag force of arc at the melt pool surface as a function of only operating parameters such as arc length, electrode shape, or electrical current. Nevertheless, this model must be modified in order to represent a GMA process (or a WAAM process) in which the electrode is consumable. The melting of the anode creates droplets. The presence of these droplets in the plasma and their fall modify also the physical phenomena in the plasma. The boundary conditions for the electrical problem are also different since the electrons move in the opposite direction. The complete modelling of all these unsteady phenomena is more complex than the GTA modelling and a simplified approach is proposed in the next section. Indeed, the WAAM process is well adapted for the manufacturing of large parts. However, numerical models need to be simplify to reduce computational time for large geometries.

### MODELING OF THE BUILDING OF THE ROD

In this section, a numerical model of wire arc additive manufacturing (WAAM) is presented. The aim is to build a rod along the vertical axis. This shape has the advantage to be simulated with a 2D axial-symmetry model in order to reduce computation time.

### EXPERIMENTAL PROCEDURES

The definition and validation of the model are based on experimental data obtained by the Jean Rouxel Institute of Materials at University of Nantes (IMN) in France. In arc processes, various modes of metal transfer exist depending on many operating variables such as the arc current. Here, a pulsed metal inert gas (MIG) process is chosen. During this process, one droplet per pulse is created at the electrode tip with a detachment frequency of 25 Hz. The droplets then travel the arc plasma and fall into the melt pool. To build the rod, a first series of droplets are deposited on a cylindrical substrate of 12,7 mm diameter and 40 mm of height composed of 304 stainless steel. The wire is 308LSi stainless steel, its

## Mathematical Modelling of Weld Phenomena 12

diameter is 1 mm and is speed is 2 mm/min. The shielding gas is Argon, and the flow is 14 L/min. The distance between the nozzle and the cylindrical substrate is 12 mm. The arc height is fixed at 2 mm during one layer. One layer is composed of 62 droplets. The next layer is created when the temperature is below 300°C. This temperature is measured by an infrared camera.

During the process, a high-speed camera is also used to measure the diameter of the droplets and to obtain the evolution of the geometry of the layers.

The Fig. 8 illustrates the different rods obtained by additive manufacturing.



**Fig. 8** Photographies of different rods by additive manufacturing.

The post mortem observables are obtained using a 3D scan that gives the final geometry of the piece, and by realizing macrographs to obtain the melted zone.

### PRESENTATION OF THE MODEL

The developed model simulates the heating of the substrate by the arc, the falling of droplets in the melt pool and the solidification of the layer after arc extinguishes. To simplify the model, the droplet formation and detachment are not simulated. Indeed, the droplet enters at the top of the computation domain with a given size, velocity and temperature based on experimental data. The creation of the arc is also not integrated in this model, but the arc model presented in the previous section is used to define a heat source term applied at the free surface of the liquid phase. Note that this heat source terms needs to be adapted for a WAAM process. Lorentz forces, shear stress at the melt pool surface and Marangoni effect are also omitted in this first model in order to reduce computational time. An experimental validation will enable to discuss these strong assumptions. The Fig. 9 illustrates the main steps of this simplified model.

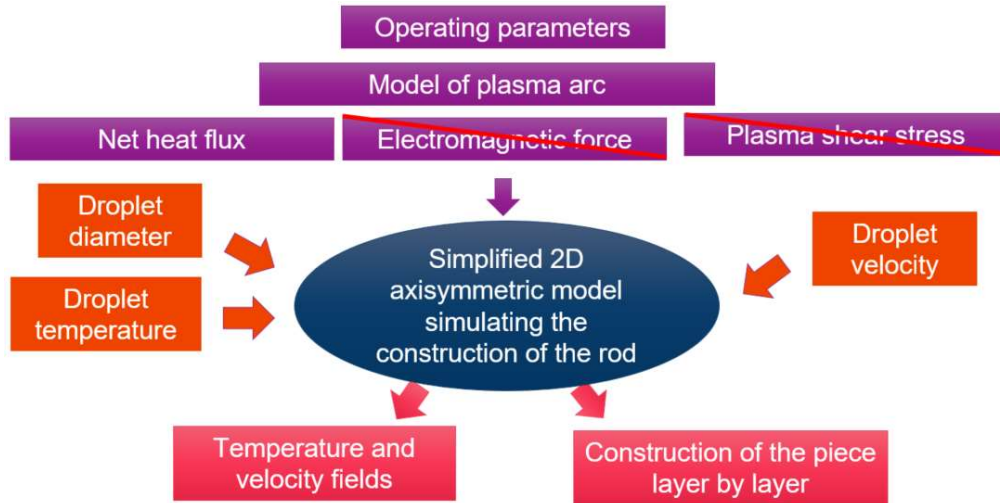


Fig. 9 Schematic diagram of the simplified approach for WAAM process.

Given the assumptions used for this model, only heat transfer and fluid flow are considered. The impingement of molten metal droplets into the melt pool and the resulting change in the melt pool shape are simulated using the level set method. This method is described in the next section.

#### PRESENTATION OF THE LEVEL SET METHOD

The level set method [22] consists in defining a  $\phi$  variable on a fixed Cartesian grid to represent the interface between gas and metal. This variable  $\phi$  is defined to 0 in gas, and 1 in metal. The interface is identified by the isovalue  $\phi = 0.5$ . This variable also serves for defining the appropriate properties in each material (gas or metal). So, for example, the density is defined as follows:

$$\rho = \rho_{gas} + (\rho_{steel} - \rho_{gas})\phi \quad (14)$$

where  $\rho_{gas}$  represents the gas density and  $\rho_{steel}$  the metal density. These properties can be temperature-dependant. Note that, at the interface, a mean value for the material properties is set. At the vicinity of the gas/metal interface, a continuous variation in properties is modelled using a smooth step function (Fig. 10). However, the thickness of this transition must be small enough to represent the interface accurately but not too small, in order to avoid numerical convergence problems.

Once the variable is correctly defined, the interface is usually determined by simply locating the variable  $\phi = 0.5$ . The displacement of the interface is obtained by solving a transport equation related to the velocity of the fluids. The transport equation used is:

$$\frac{\partial \phi}{\partial t} + \vec{v} \cdot \overline{\text{grad}}(\phi) = \gamma_{ls} \overline{\text{div}} \left( \varepsilon_{ls} \overline{\text{grad}}(\phi) - \phi(1 - \phi) \frac{\overline{\text{grad}}(\phi)}{|\overline{\text{grad}}(\phi)|} \right) \quad (15)$$

where  $\gamma_{ls}$  is the reinitialization parameter and  $\varepsilon_{ls}$  is the interface thickness controlling parameter.

Moreover, the  $\phi$  variable is also used to define a Dirac function  $\delta(\phi)$ . This function makes it possible to apply all the existing boundary conditions between the two fluids in the computational domain through source terms introduced into the conservation equations.

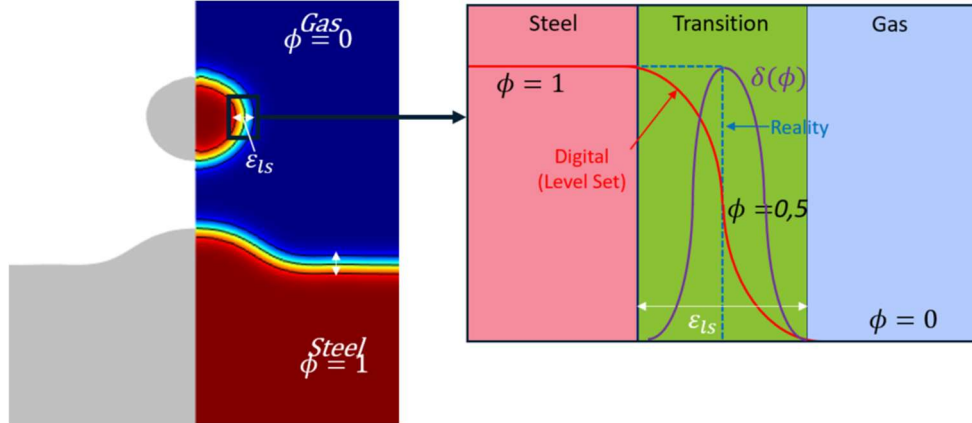


**Fig. 10** Schematic drawing illustrating the level set method and the evolution of the  $\phi$  variable and Dirac function along the interface.

#### PRESENTATION OF THE EQUATIONS

In addition to the previously mentioned assumptions, the plasma and liquid metal are supposed to be incompressible Newtonian fluids in a laminar flow.

With these assumptions, the governing equations of heat and mass transfer for plasma and metal transport are given below:

- Conservation of mass

$$\text{div}(\vec{v}) = 0 \quad (16)$$

- Conservation of momentum

$$\rho \left( \frac{\partial \vec{v}}{\partial t} + \overline{\text{grad}}(\vec{v}) \cdot \vec{v} \right) = \overline{\text{div}} \left[ -P\vec{i} + \mu_f \left( \overline{\text{grad}}(\vec{v}) + {}^t\overline{\text{grad}}(\vec{v}) \right) - \frac{2}{3} \text{div}(\vec{v})\vec{i} \right] + \vec{F}_v \quad (17)$$

The term source of momentum equation is expressed as follows:

## Mathematical Modelling of Weld Phenomena 12

$$\begin{aligned}\vec{F}_v &= \vec{F}_g + \vec{F}_{Darcy} \times (\phi > 0,5) + \vec{F}_{st} \\ &= \rho \vec{g} + \left( -C \frac{(1-f_L)^2}{f_L^3 + b} \vec{v} \right) \times (\phi > 0,5) + \text{div}(\gamma(\vec{i} - (\vec{n} \cdot \vec{n}^T))\delta(\phi))\end{aligned}\quad (18)$$

The Darcy law is necessary only for steel, because it is the only material to have a solid and liquid phase.

Conservation of Energy

$$\rho C_p \left( \frac{\partial T}{\partial t} + \vec{v} \cdot \overrightarrow{\text{grad}}(T) \right) = \text{div}(\overrightarrow{\lambda \text{ grad}}(T)) + S_v \times \delta(\phi) \quad (19)$$

The source term of energy is:

$$S_v = S_{NetHeatFlux} \times \delta(\phi) \quad (20)$$

where  $S_{NetHeatFlux}$  is calculated by the model of arc and corresponds to the net heat flux at the melt pool surface (Fig. 11).

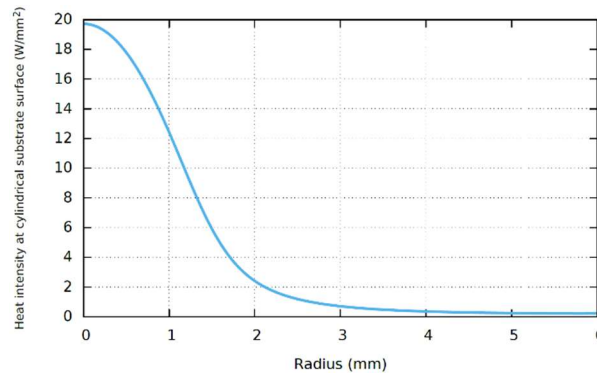


**Fig. 11** The net heat flux at the melt pool surface ( $S_{NetHeatFlux}$ ).

The droplets are introduced at the top of the computation domain with an initial diameter  $D_d$  dependent on the wire electrode feed rate  $v_w$  and radius  $r_w$ , and the droplet detachment frequency  $f_d$  according to the following equation [10]:

$$D_d = \left( 6r_w^2 \frac{\rho_w v_w}{\rho_d f_d} \right)^{1/3} \quad (21)$$

where  $\rho_w$  and  $\rho_d$  are the density of the wire and the droplet, respectively.

The diameter obtained by the equation (21) is 1.26 mm with the experimental parameters. Moreover, using the high speed camera, it is possible to measure the diameter of the droplet which is 1.27 mm. Consequently, the equation (21) gives a good estimation of the diameter of the droplet.

It was not possible to measure the temperature of the droplet with the used infrared camera since it is limited to 1500°C. The value of the droplet temperature is based on

## Mathematical Modelling of Weld Phenomena 12

literature data which is 2100 K [23]. The velocity of the droplet is obtained from the high speed camera. Its velocity is 0.063 m/s.

The material properties used in our calculations are given in Table 2.

**Table 2** Material properties of 304 stainless steel and shielding gas used in our calculations.

	304 stainless steel	Gas
Thermal conductivity (W/m/K)	$k(T)$ [24]	0.08
Specific heat (J/kg/K)	$C_p(T)$ [24]	510
Density (kg/m <sup>3</sup> )	6725	1
Dynamic Viscosity (Pa.s)	$1.10^{-3}$	0.1

The Fig. 12 illustrates the computation domain in order to simulate the building of the rod with different layers.

The computational domain is meshed using standard Lagrangian quadratic elements. The mesh size density is  $5 \cdot 10^{-5}$  m in all domains. Computations are performed within a day on 8 processors computer.

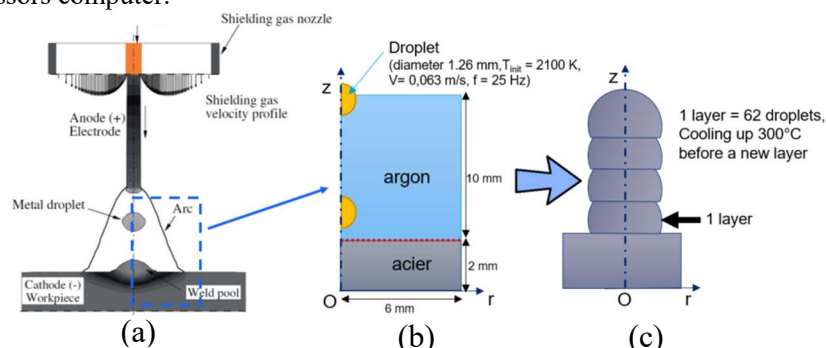


**Fig. 12** (a) Schematic representation of a GMAW system [14], (b) Initial computation domain, (c) Schematic representation of the rod building.

RESULTS AND DISCUSSIONS

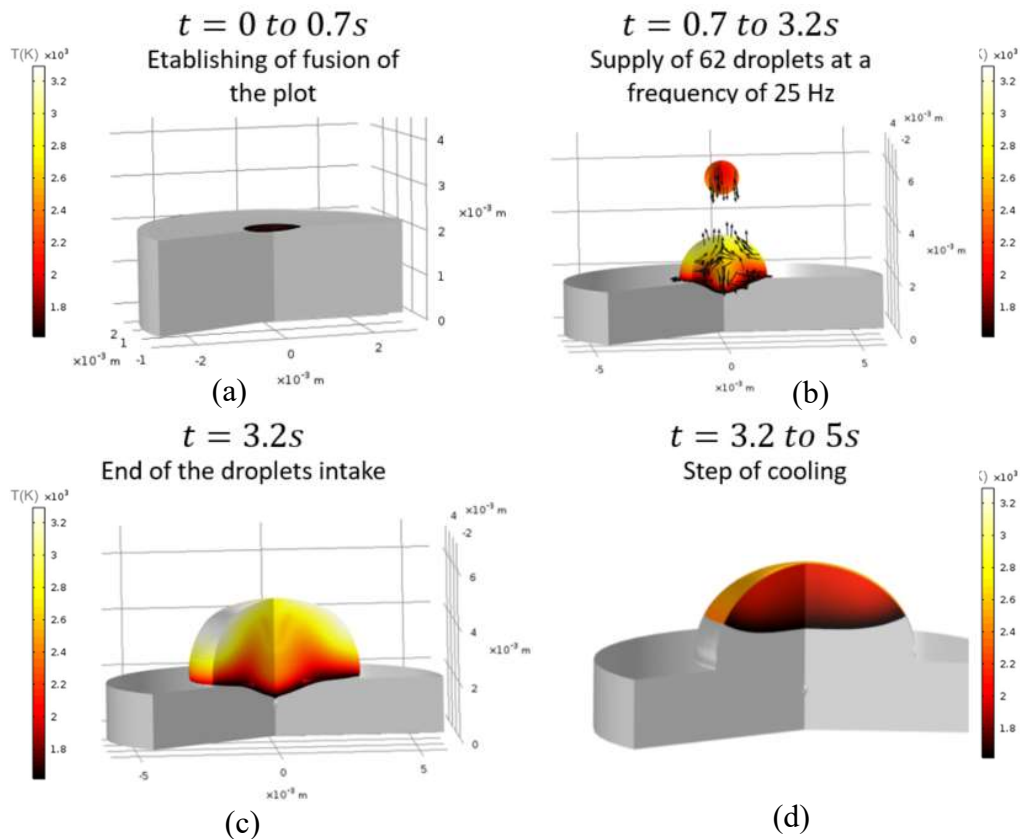


Fig. 13 Shape and temperature field at different times during the building of the first layer.

The Fig. 13 shows the shape of the rod and temperature field at different times during the building of the first layer. The cylindrical substrate is first heated during 0.7 s (Fig. 13a), then droplets are introduced at the top of the computation domain along the z-axis up to 3.2 s. Fig. 13c shows the temperature field and the shape of the first layer before cooling. Note that these figures are presented in 3D geometry during the post-processing procedure, but the calculations are performed in a 2D axial-symmetry geometry. At present, only the first layer has been simulated. The calculated shape of the first layer obtained after cooling is compared to the macrograph in Fig. 14. There is an error of about 8% in terms of volume. Therefore, there is a good agreement between experiment and model despite the strong assumptions.



## Mathematical Modelling of Weld Phenomena 12

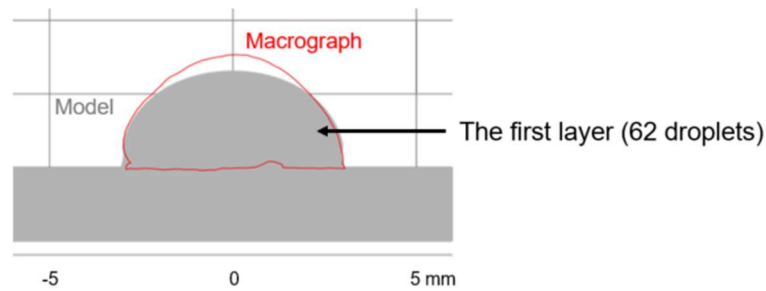


Fig. 14 Comparison of experimental (red) and numerical first layer.

Comparisons between the model and the experimental data are to be continued. The next steps will be to analyse the videos from the fast and thermal cameras, but also to simulate several layers and compare them to the experiments. Moreover, the model must be improved. Simplifying assumptions are to be discussed (electromagnetic forces, Marangoni, shear stress).

### CONCLUSION

In this paper, a model of arc has been developed. It is able to calculate temperature, velocity and electromagnetic fields in the arc and the melt pool. The shape of the melt pool is also calculated from the operating parameters. This model has been used to define heat input for a WAAM model. The building of a cylindrical rod has been simulated. These first results have given satisfactory comparisons with experimental data.

In perspective, it is necessary to continue the comparison between the experiment and the model in terms of heat transfer. In addition, to keep the predictive side of the model, it is necessary to develop an arc model with a fuse electrode using operating parameters.

### REFERENCES

- [1] K. C. HSU, K. ETEMADI, AND E. PFENDER, 'Study of the free-burning high-intensity argon arc', *J. Appl. Phys.*, vol. 54, no. 3, pp. 1293–1301, Mar. 1983.
- [2] M. TANAKA AND J. J. LOWKE, 'Predictions of weld pool profiles using plasma physics', *J. Phys. Appl. Phys.*, vol. 40, no. 1, pp. R1–R23, Jan. 2007.
- [3] M. TANAKA, H. TERASAKI, M. USHIO, AND J. J. LOWKE, 'A unified numerical modeling of stationary tungsten-inert-gas welding process', *Metall. Mater. Trans. A*, vol. 33, no. 7, pp. 2043–2052, 2002.
- [4] M. TANAKA, 'An introduction to physical phenomena in arc welding processes', *Weld. Int.*, vol. 18, no. 11, pp. 845–851, Nov. 2004.
- [5] M. BROCHARD, 'Modèle physique et prédictif du procédé de soudage à l'arc TIG', Université de Provence, 2009.
- [6] A. TRADIA, 'Multiphysics modelling and numerical simulation of GTA weld pools', Ecole Polytechnique, 2011.
- [7] F. LAGO, J. J. GONZALEZ, P. FRETON, AND A. GLEIZES, 'A numerical modelling of an electric arc and its interaction with the anode: Part I. The two-dimensional model', *J. Phys. Appl. Phys.*, vol. 37, no. 6, pp. 883–897, Mar. 2004.

- [8] L. LI, B. LI, L. LIU, AND Y. MOTOYAMA, ‘Numerical Modeling of Fluid Flow, Heat Transfer and Arc–Melt Interaction in Tungsten Inert Gas Welding’, *High Temp. Mater. Process.*, vol. 36, no. 4, Jan. 2017.
- [9] X. YAU, ‘Modélisation numérique instationnaire pour la simulation du soudage TIG avec couplage plasma / bain de fusion’, Aix Marseille université, Marseille, 2018.
- [10] A. B. MURPHY, ‘Influence of droplets in gas–metal arc welding: new modelling approach, and application to welding of aluminium’, *Sci. Technol. Weld. Join.*, vol. 18, no. 1, pp. 32–37, Jan. 2013.
- [11] Y. LUO, J. LI, J. XU, L. ZHU, J. HAN, AND C. ZHANG, ‘Influence of pulsed arc on the metal droplet deposited by projected transfer mode in wire-arc additive manufacturing’, *J. Mater. Process. Technol.*, 2018.
- [12] H. G. FAN AND R. KOVACEVIC, ‘A unified model of transport phenomena in gas metal arc welding including electrode, arc plasma and molten pool’, *J. Phys. Appl. Phys.*, vol. 37, no. 18, pp. 2531–2544, Sep. 2004.
- [13] J. HU AND H. L. TSAI, ‘Heat and mass transfer in gas metal arc welding. Part I: The arc’, *Int. J. Heat Mass Transf.*, vol. 50, no. 5–6, pp. 833–846, Mar. 2007.
- [14] J. HU AND H. L. TSAI, ‘Heat and mass transfer in gas metal arc welding. Part II: The metal’, *Int. J. Heat Mass Transf.*, vol. 50, no. 5–6, pp. 808–820, Mar. 2007.
- [15] S. TANGUY AND A. BERLEMONT, ‘Application of a level set method for simulation of droplet collisions’, *Int. J. Multiph. Flow*, vol. 31, no. 9, pp. 1015–1035, Sep. 2005.
- [16] O. DESMAISON, G. GUILLEMOT, AND M. BELLET, ‘Numerical modelling of hybrid arc/laser welding: a coupled approach to weld bead formation and residual stresses’, p. 12.
- [17] X. BAI ET AL., ‘Numerical analysis of heat transfer and fluid flow in multilayer deposition of PAW-based wire and arc additive manufacturing’, *Int. J. Heat Mass Transf.*, vol. 124, pp. 504–516, Sep. 2018.
- [18] F. HEJRIPOUR, D. T. VALENTINE, AND D. K. AIDUN, ‘Study of mass transport in cold wire deposition for Wire Arc Additive Manufacturing’, *Int. J. Heat Mass Transf.*, vol. 125, pp. 471–484, Oct. 2018.
- [19] J. HAIDAR, ‘Local thermodynamic equilibrium in the cathode region of a free burning arc in argon’, *J. Phys. Appl. Phys.*, vol. 28, no. 12, p. 2494, 1995.
- [20] J. MOUGENOT, J.-J. GONZALEZ, P. FRETON, AND M. MASQUÈRE, ‘Plasma–weld pool interaction in tungsten inert-gas configuration’, *J. Phys. Appl. Phys.*, vol. 46, no. 13, p. 135206, Apr. 2013.
- [21] A. B. MURPHY, M. TANAKA, K. YAMAMOTO, S. TASHIRO, J. J. LOWKE, AND K. OSTRIKOV, ‘Modelling of arc welding: The importance of including the arc plasma in the computational domain’, *Vacuum*, vol. 85, no. 5, pp. 579–584, Nov. 2010.
- [22] S. OSHER AND J. A. SETHIAN, ‘Fronts propagating with curvature-dependent speed: Algorithms based on Hamilton-Jacobi formulations’, *J. Comput. Phys.*, vol. 79, no. 1, pp. 12–49, Nov. 1988.
- [23] X. ZHOU, H. ZHANG, G. WANG, AND X. BAI, ‘Three-dimensional numerical simulation of arc and metal transport in arc welding based additive manufacturing’, *Int. J. Heat Mass Transf.*, vol. 103, no. Supplement C, pp. 521–537, Dec. 2016.
- [24] C. S. KIM, ‘Thermophysical Properties of Stainless Steels’, Argonne National Laboratory III (USA), ANL--75-55, 1975.



## Author Index

### A

Agarwal, G. 465  
Aidun, D. K. 819  
Akita, K. 417  
Akrivos, V. 297  
Alaluss, K. 933  
Amirthalingam, M. 401, 465  
Andersson, J. 485  
Andrieu, A. 505  
Antonissen, J. 125  
Antretter, T. 783  
Anttila, S. 233  
Artinov, A. 695

### B

Bachmann, M. 695  
Bambach, M. 337  
Baumgartner, A. 369  
Bayat, M. 1029  
Becirovic, A. 893  
Behmel, A. 893  
Bendaoud, I. 991  
Biegler, M. 979  
Boellinghaus, T. 443  
Borchert, M. 783  
Bordreuil, C. 139  
Bouchonneau, N. 651

### C

Cadiou, S. 1049  
Cambon, C. 991  
Carin, M. 5, 1049  
Carron, D. 505  
Cesaro, A. 907  
Chen, J. 549  
Chiocca, A. 139  
Courtois, M. 5, 1049  
Cretteur, L. 729, 751

### D

De, A. 795

De Baere, D. 1029  
Delmas, J. 293, 505  
Deschaux-Beaume, F. 139  
De Sousa, G. G. 651  
Dinh-Trong, T. 293  
Doynov, N. 255, 431, 711  
Draxler, J. 485

### E

Ecker, W. 783  
Edberg, P. 485  
Effertz, P. S. 615  
Eftekharimilani, P. 401  
Ehlers, S. 875  
Eisazadeh, H. 819  
Enzinger, N. 369, 615, 639, 805, 841  
Ernst, W. 199  
Erofeev, V. 565  
Ertugrul, G. 27  
Evdokimov, A. 431

### F

Flint, T. F. 149, 219, 861  
Francis, J. A. 149, 861  
Friedrich, N. 875  
Fuchs, F. 615

### G

Gaie, S. 5  
Gao, H. 401, 465  
Gatzen, M. 979  
Geslain, E. 729, 751  
Gkatzogiannis, S. 383  
Goldak, J. 819  
Golubev, I. 665  
Gordon, S. 179  
Grams, M. 907  
Gruber, M. 783  
Guilmois, L. 1049

## H

Haeberle, N. 353  
 Hama-Saleh, R. 337  
 Hamelin, C. J. 149  
 Hattel, J. H. 1029  
 Hendili, S. 293  
 Heppner, E. 681  
 Hermans, M. J. M. 401, 465  
 Hermenegildo, T. F. C. 651  
 Hierl, S. 965  
 Hilpert, B. 783  
 Holly, S. 199  
 Huizenga, R. M. 401  
 Hüntelmann, S. 965

## I

Ikushima, K. 417  
 Ilin, A. 1007  
 Iljkić, D. 167  
 Inoue, H. 93

## J

Jokić, M. 167

## K

Kaars, J. 767  
 Kaboli, R. 27  
 Karkhin, V. 695  
 Käsbauer, J. 965  
 Käß, M. 281  
 Khazan, P. 337, 979  
 Kim, D. C. 93  
 Knoedel, P. 383  
 Kogler, F. 639  
 Kollár, D. 53  
 Koppe, K. 767  
 Kövesdi, B. 53  
 Kozeschnik, E. 199  
 Kramer, R. 27  
 Kzzo, A. 337

## L

Larkiola, J. 233

Launert, B. 255  
 Le Masson, P. 5, 505, 1049  
 Leitz, K.-H. 639  
 Li, W. 533  
 Lindgren, L-E. 485  
 Lisnyi, O. 81  
 Liu, S. 179  
 Loose, T. 965  
 Lu, Y. 907

## M

Ma, T. 533  
 Madigan, M. C. 443  
 Maiwald, F. 965  
 Marie, S. 729  
 Martin, J. 893  
 Martinez, M. 819  
 Maslennikov, A. 565  
 Massoudi Farid, M. 27  
 Matsumura, T. 93  
 Mayr, P. 27, 767, 933  
 Mendez, P. 907  
 Mente, T. 443  
 Michailov, V. 255, 431, 665, 711  
 Mitchell, J. 139  
 Miyasaka, F. 17  
 Mohanty, S. 1029  
 Mokrov, O. 39, 81, 893, 953  
 Montoya, M. 651

## N

Nasiri, M. B. 841  
 Naumov, A. 565  
 Ni, J. 125  
 Nimrouzi, H. 819  
 Nishikawa, S. 417

## O

Ogura, T. 93  
 Oikawa, Y. 93  
 Ossenbrink, R. 431, 711

**P**

Paananen, J. 233  
 Paillard, P. 1049  
 Pantelis, I. 149  
 Panzer, F. 585  
 Pasternak, H. 255  
 Pereira-Alvarez, P. 293  
 Pierre, T. 729, 751  
 Piott, M. 711  
 Pittner, A. 353  
 Ploshikhin, V. 1007  
 Pohjonen, A. 233  
 Pouvreau, C. 729, 751  
 Prabitz, K. M. 783  
 Putz, A. 841

**Q**

Queval, J. 729

**R**

Reheis, N. 639  
 Reisgen, U. 39, 81, 565, 893, 953  
 Rethmeier, M. 353, 695, 979  
 Richardson, I. M. 401, 465  
 Robin, V. 293, 505  
 Robson, J. D. 219  
 Rogeon, P. 729, 751  
 Rouquette, S. 991  
 Rudolph, D. 893

**S**

Saida, K. 93  
 Santos, T. F. A. 651  
 Sato, S. 17  
 Schänzel, M. 1007  
 Schiebahn, A. 39, 81, 565, 953  
 Schleuß, L. 711  
 Schmailzl, A. 965  
 Schmidt, A. 893  
 Schnitzer, R. 199  
 Schubert, H. 783  
 Serizawa, H. 17  
 Shi, L. 549  
 Shibahara, M. 417

Shotri, R. 795  
 Sierlinger, R. 783  
 Simon, M. 39, 81, 893, 953  
 Smith, M. C. 149, 219, 305, 861  
 Smokvina Hanza, S. 167  
 Smoljan, B. 167  
 Soulie, F. 139, 991  
 Stapelfeld, C. 255  
 Štic, L. 167  
 Stodolna, J. 505  
 Stuetz, M. 639  
 Stummer, M. 805  
 Sun, Y. 149, 219, 861

**T**

Tchernov, S. 819  
 Tran-Van, G. 505

**U**

Ummenhofer, T. 383  
 Ünsal, I. 337

**V**

van der Aa, E. M. 401  
 Vasileiou, A. 149, 219, 305, 861  
 Vande Voorde, J. 125

**W**

Wagner, J. 639  
 Wahab, M. A. 125  
 Wang, X. 533  
 Wang, Y. 907  
 Weigl, M. 665  
 Weihe, S. 281, 585  
 Weisheit, A. 337  
 Werber, A. 711  
 Werz, M. 281, 585  
 Wirmsperger, F. 369  
 Woschke, E. 681  
 Wu, C. S. 549  
 Wu, X. 179

**X**

Xiong, Q. 149, 219, 861

**Y**

Yamada, Y. 417

Yang, X. 533

Ye, Q. 533

Yu, L. 93

Yu, Z. 179

**Z**

Zhou, J. 819

Zügner, D. 199